Cover Picture

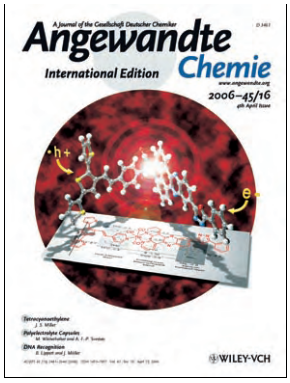

Natasha J. Lundin, Allan G. Blackman, Keith C. Gordon,* and David L. Officer

Modular molecules designed to act as efficient dopants for organic light-emitting diodes (OLEDs) encourage directional transport of electrons and holes, causing them to recombine at the emitting center. In their Communication on page 2582 ff., K. C. Gordon and co-workers describe such a molecule, a phosphorescent dye that comprises an emissive center bound on either side by an electron-transport group and a hole-transport group, as shown in the cover picture.

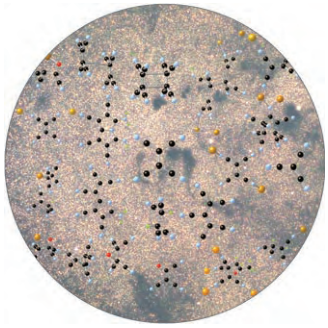

Tetracyanoethylene
Tetracyanoethylene is a highly versatile organic molecule. In his Review on page 2508 ff., J. S. Miller shows how IR spectroscopic data can be used to accurately identify the many structural motifs adopted by this species in compounds and complexes.

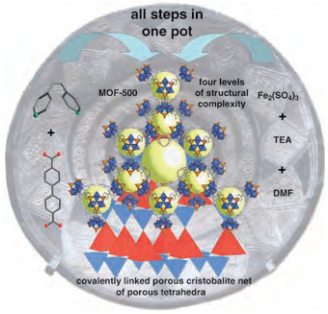

Microporous Materials
The synthesis, structure, and sorption properties of a new metal–organic framework built up from four types of porous tetrahedra is described by O. M. Yaghi and co-workers in their Communication on page 2528 ff.

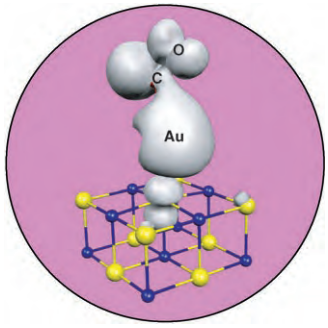

Surface Chemistry
T. Risse et al. have examined Au clusters on MgO surfaces and report the influence of surface color centers (oxygen vacancies) and adsorbed CO molecules in their Communications on pages 2630 ff. and 2633 ff.

Contents

VIP *The following Communications have been judged by at least two referees to be "very important papers" and will be published online at www.angewandte.org soon:*

*Y. Sawada, K. Matsumoto, S. Kondo, H. Watanabe, T. Ozawa, K. Suzuki, B. Saito, T. Katsuki**
Titanium/Salan-Catalyzed Asymmetric Epoxidation with Aqueous Hydrogen Peroxide as Oxidant

*T. B. Phan, M. Breugst, H. Mayr**
Towards a General Scale of Nucleophilicity?

*G. Budroni, A. Corma**
Synthesis of Gold–Organic–Inorganic, High Surface Area Materials as Precursors of Highly Active Catalysts

*H. Nakamichi, T. Okada**
Crystallographic Analyses of Primary Visual Photochemistry

T. Boussie, G. Diamond, C. Goh, K. Hall, A. LaPointe, M. Leclerc, V. Murphy, J. Shoemaker, H. Turner, R. Rosen, J. Stevens,* F. Alfano, V. Busico,* R. Cipullo, G. Talarico*
Non-Conventional Catalysts for Isotactic Propene Polymerization in Solution Developed with High-Throughput-Screening Technologies

*D. Marcus, K. McLachlan, M. Wildman, J. Ehresmann, P. Kletnieks, J. Haw**
Experimental H/D Exchange Evidence of the Failure of Direct C–C Coupling Mechanisms in the Methanol-to-Olefin Process Catalyzed by HSAPO-34

Obituary

Pierre Potier (1934–2006) — *S. Z. Zard* — **2496**

Books

Colloid Science — Terence Cosgrove — *reviewed by D. Wang* — **2498**

Highlights

Microcapsules

M. Winterhalter,*
A. F.-P. Sonnen* — **2500 – 2502**

Stable Air Bubbles—Catch Them If You Can!

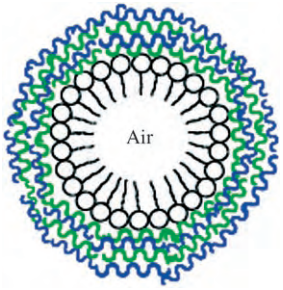

Forever blowing bubbles! Polyelectrolytes are highly charged polymers that can self-assemble at interfaces to form micro- and nanometer-sized structures. A recent report described the coating of air-filled detergent gas bubbles by deposition of polyelectrolyte layers (see picture; black: surfactant; green, blue: polyelectrolyte). These stabilized gas bubbles may be useful, for example, as contrast agents in ultrasound microscopy.

Bioinorganic Chemistry

J. Müller,* B. Lippert* — **2503 – 2505**

Imposing a Three-Way Junction on DNA or Recognizing One: A Metal Triple Helicate Meets Double Helix

In junction: A novel mode of DNA recognition has been identified. A recent X-ray crystal-structure analysis provides a detailed view of how a synthetic $[Fe_2L_3]^{4+}$ helicate binds to a DNA three-way junction by occupying its central hydrophobic cavity (see picture; space-filling model: $[Fe_2L_3]^{4+}$ (gray C, blue N, orange Fe). Ribbon model: DNA (each of the three DNA strands are a different color: blue, red, or yellow)).

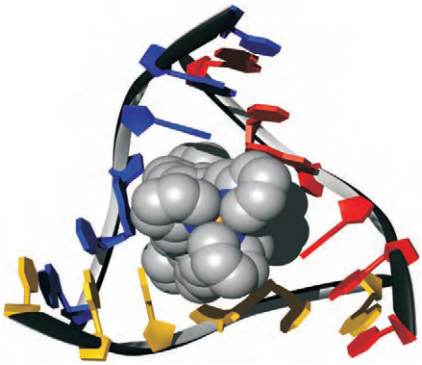

WILEY InterScience DISCOVER SOMETHING GREAT
© 2006 Wiley-VCH Verlag GmbH & Co. KGaA, Weinheim

Reviews

Good vibrations: For tetracyanoethylene (TCNE) many structural motifs are known and their identification is often difficult. The fundamental $\tilde{\nu}_{CN}$ vibrations as well as the length (d) and $\tilde{\nu}_{CC}$ values of the central C—C bond can provide important information on bond order, structure, and charge state (see graph).

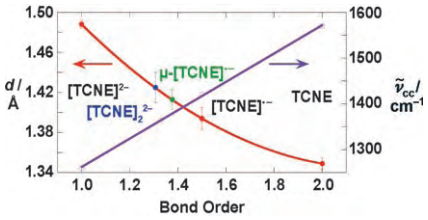

Tetracyanoethylene

J. S. Miller* ——— **2508 – 2525**

Tetracyanoethylene (TCNE): The Characteristic Geometries and Vibrational Absorptions of Its Numerous Structures

Communications

The whole is greater than the sum of its parts: Linking the porous tetrahedra of IRMOP-51 (brown) by connecting their iron-trimer vertices (red) with bipyridine linkers leads to the new metal–organic framework MOF-500, which contains additional smaller (blue) and larger (green and yellow spheres) tetrahedral pores. The sorption capacity of MOF-500 is four times greater than that of the molecular compound IRMOP-51.

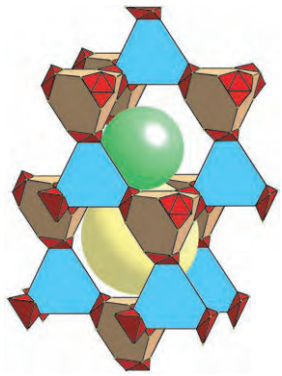

Microporous Materials

A. C. Sudik, A. P. Côté, A. G. Wong-Foy, M. O'Keeffe, O. M. Yaghi* — **2528 – 2533**

A Metal–Organic Framework with a Hierarchical System of Pores and Tetrahedral Building Blocks

Its all done with metals: The title statement is confirmed by comparing the electrocatalytic oxidation of hydrazine at a basal-plane pyrolytic-graphite (BPPG) electrode treated with iron(III) (blue) with that at a multiwalled-carbon-nanotube (MW-CNT)-modified BPPG electrode (red) and at an edge-plane pyrolytic graphite electrode (black; ••••• and –•–• are the responses of iron(III)-treated and MW-CNT-modified BPPG electrode, respectively, in the absence of hydrazine).

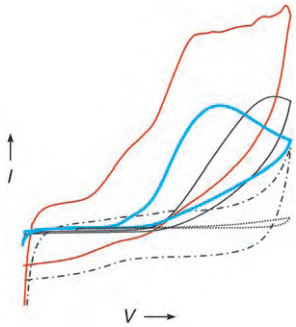

Electrocatalysis

C. E. Banks, A. Crossley, C. Salter, S. J. Wilkins, R. G. Compton* ——— **2533 – 2537**

Carbon Nanotubes Contain Metal Impurities Which Are Responsible for the "Electrocatalysis" Seen at Some Nanotube-Modified Electrodes

For the USA and Canada:
ANGEWANDTE CHEMIE International Edition (ISSN 1433-7851) is published weekly by Wiley-VCH PO Box 191161, D 69451 Weinheim, Germany. Air freight and mailing in the USA by Publications Expediting Inc. 200 Meacham Ave., Elmont, NY 11003. Periodicals postage paid at Jamaica NY 11431. US POSTMASTER: send address changes to *Angewandte Chemie*, Wiley-VCH, 111 River Street, Hoboken, NJ 07030. Annual subscription price for institutions: US$ 5685/5168 (valid for print and electronic / print or electronic delivery); for individuals who are personal members of a national chemical society prices are available on request. Postage and handling charges included. All prices are subject to local VAT/sales tax.

© 2006 Wiley-VCH Verlag GmbH & Co. KGaA, Weinheim

The best in chemistry –

for more than a hundred years

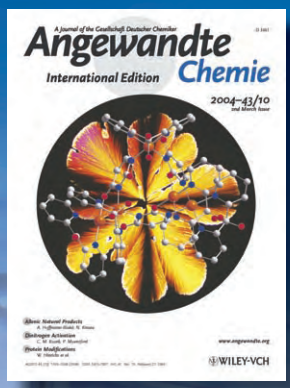

A Journal of the Gesellschaft Deutscher Chemiker

Angewandte
International Edition **Chemie**

www.angewandte.org

1888: ***The beginning of a success story***

Constant Innovations

1962: *First issue of the International Edition*
1976: *Graphical abstracts*
1979: *Cover pictures*
1988: *Centenary of Angewandte*
1989: *Routine use of color*
1991: *New section: Highlights*
1992: *Computerized editorial tracking system*
1995: *Internet service for readers*
1998: *Regular press service; full-text online*
2000: *New section: Essays; EarlyView: Communications available online ahead of the printed version*
2001: *New section: Minireviews*
2002: *Online submission of manuscripts*
2003: *Weekly publication; new section: News; new layout*
2004: *Backfiles (1962-1997); ManuscriptXpress: Online system for authors and referees*

Angewandte's advisors...

Richard R. Ernst
ETH Zürich

*» I support **Angewandte Chemie** because it is a first rank international journal of European origin. More than many other renowned journals, it implements a pioneering spirit, being ready for innovating its form and contents. Its bilingual mode of appearance is another plus. I am looking forward to an equally prosperous future for **Angewandte Chemie**. «*

Angewandte Chemie International Edition *is a journal of the German Chemical Society (GDCh)*

GDCh

WILEY InterScience® DISCOVER SOMETHING GREAT

WILEY-VCH

1821404_gu

Making films: Removal of most of the toluene from a two-phase toluene/water mixture causes nanoparticles present at the liquid–liquid interface to pack closely together in an ordered monolayer film (MLF). This MLF can be removed from the interface for further study.

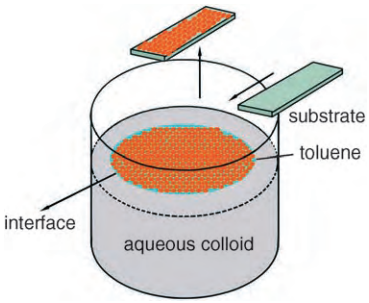

Nanoparticle Assemblies

Y.-J. Li, W.-J. Huang, S.-G. Sun* ——— **2537 – 2539**

A Universal Approach for the Self-Assembly of Hydrophilic Nanoparticles into Ordered Monolayer Films at a Toluene/Water Interface

---

Molecular wires based on through-bond interaction: Strong currents and a gate effect are observed in three terminal conduction devices incorporating σ–π–σ conjugated tercyclohexylidenes. The gate characteristics differ substantially from those of devices based on π-conjugated compounds.

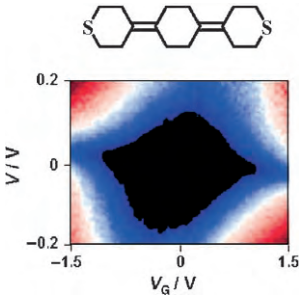

Molecular Electronics

Y.-V. Kervennic, J. M. Thijssen, D. Vanmaekelbergh, R. Dabirian, L. W. Jenneskens, C. A. van Walree,* H. S. J. van der Zant* ——— **2540 – 2542**

Charge Transport in Three-Terminal Molecular Junctions Incorporating Sulfur-End-Functionalized Tercyclohexylidene Spacers

---

Unexpected catalytic activity for the oxidation of CO to CO_2 is exhibited by one of two novel 3D porous metal–organic frameworks in which $[Ni_8L_{12}]^{20-}$ (H_3L = 4,5-imidazoledicarboxylic acid) cubic building blocks (CBBs) are linked by Li^I or Na^I ions. The clathrating ability towards Li^I ions of such CBBs is seen in the X-ray crystal structure, which simulates the potential guest-bonding sites in the building blocks of the MOFs (see picture).

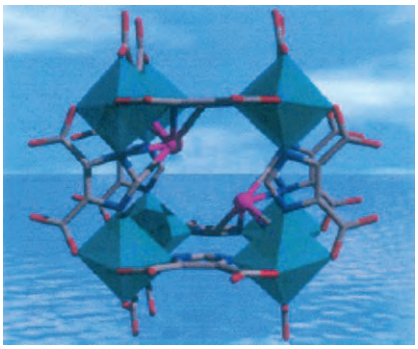

Metal–Organic Frameworks

R.-Q. Zou, H. Sakurai, Q. Xu* ——— **2542 – 2546**

Preparation, Adsorption Properties, and Catalytic Activity of 3D Porous Metal–Organic Frameworks Composed of Cubic Building Blocks and Alkali-Metal Ions

---

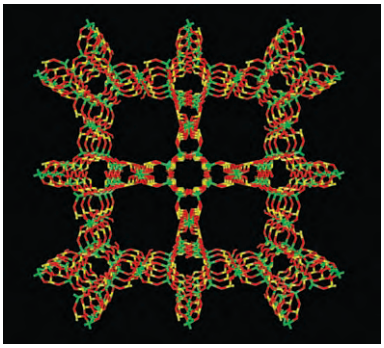

Hydrothermal reaction of $Zn(OAc)_2 \cdot 2H_2O$ and H_3PO_3 in the presence of *n*-butylamine gives the title compound, which contains extra-large 24-ring channels (see framework representation). Each channel is enclosed by a tetragonal array of four 8-ring channels interconnected by corner-sharing 4-ring chains through Zn-O-P linkages.

Microporous Materials

J. Liang, J. Li, J. Yu,* P. Chen, Q. Fang, F. Sun, R. Xu ——— **2546 – 2548**

$[(C_4H_{12}N)_2][Zn_3(HPO_3)_4]$: An Open-Framework Zinc Phosphite Containing Extra-Large 24-Ring Channels

© 2006 Wiley-VCH Verlag GmbH & Co. KGaA, Weinheim

Contents

Asymmetric Catalysts

A. J. Wooten, P. J. Carroll, P. J. Walsh* ——— **2549 – 2552**

Evidence for Substrate Binding by the Lanthanide Centers in $[Li_3(thf)_n(binolate)_3Ln]$: Solution and Solid-State Characterization of Seven- and Eight-Coordinate $[Li_3(sol)_n(binolate)_3Ln(S)_m]$ Adducts

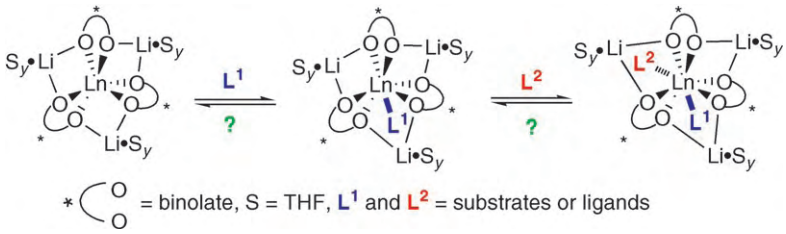

A close bond: The heterobimetallic complexes $[M_3(thf)_n(binolate)_3Ln]$ (M = Li, Na, K) are among the most effective asymmetric Lewis acid catalysts. Previous solution and solid-state studies probing the ability of the lanthanide to bind organic substrates have provided ambiguous results. Definitive support for lanthanide–substrate interactions in solution and the solid state is presented.

Supramolecular Chemistry

A. L. Grzesiak, F. J. Uribe, N. W. Ockwig, O. M. Yaghi, A. J. Matzger* **2553 – 2556**

Polymer-Induced Heteronucleation for the Discovery of New Extended Solids

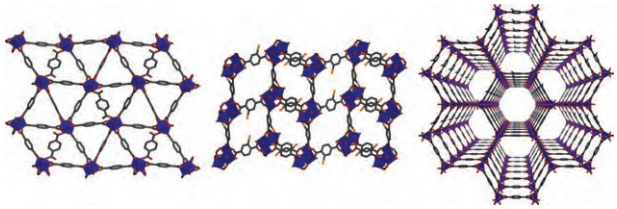

Promoting diversity: Polymer-induced heteronucleation provides kinetic access to three new metal–organic frameworks derived from dicarboxylic acid linkers (see structures). This method is useful as a general approach for discovering extended solids with new topologies that are inaccessible by traditional methods.

Microreactors

D. R. Link,* E. Grasland-Mongrain, A. Duri, F. Sarrazin, Z. Cheng, G. Cristobal, M. Marquez, D. A. Weitz ——— **2556 – 2560**

Electric Control of Droplets in Microfluidic Devices

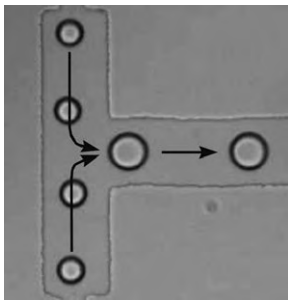

Streamlining microreactors: Electric fields enable the precise manipulation of microreactors in microfluidic channels. One of the key features of such reactors is the ability to combine different chemicals at a precise location to initiate a chemical reaction (see picture).

Natural Product Synthesis

T. Lister, M. V. Perkins* ——— **2560 – 2564**

Total Synthesis of Auripyrone A

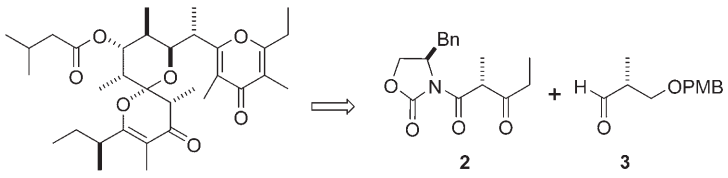

Auripyrone A (**1**)

A natural conclusion: An efficient, asymmetric synthesis of the cytotoxic marine polypropionate auripyrone A (**1**) was achieved from ketone **2** and aldehyde **3**, and the absolute stereochemistry of the natural product was established. The strategy employs substrate control to develop the stereopentad unit.

© 2006 Wiley-VCH Verlag GmbH & Co. KGaA, Weinheim

Shape sensing: The effect of guest complexation on the conformational dynamics of sensors, and its role in signal generation was studied in photoinduced electron transfer (PET) sensors. Based on the obtained results, a new sensor design (see picture) was implemented that uses the influence of conformational dynamics on the PET process.

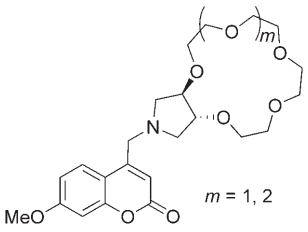

Sensor Design

P. Kele, K. Nagy, A. Kotschy* **2565 – 2567**

The Development of Conformational-Dynamics-Based Sensors

Bull's-eye! ZnS nanostructures consisting of three intersecting ribbons in the form of a dart-shaped tricrystal were prepared by the thermal evaporation of ZnS powder. The ZnS ribbons have lengths of several tens of micrometers, a growth direction of $[\bar{2}2\bar{1}]$, and a width of 0.5–1 μm (see SEM image). The nanostructure is formed by octahedral nucleation and vapor–liquid–solid growth.

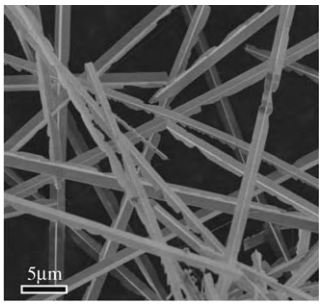

Nanostructures

X. Fan, X.-M. Meng,* X.-H. Zhang,* W.-S. Shi, W.-J. Zhang, J. A. Zapien, C.-S. Lee, S.-T. Lee **2568 – 2571**

Dart-Shaped Tricrystal ZnS Nanoribbons

Choose your favorite shape: A facile, visible-light-assisted, solution-phase approach yields various selenium microstructures, including tubes, rods, shuttles (see picture), and an urchin-like assembly of Se nanorods. The shape of the products is determined by the intensity of the light and the ratio of SeO_2 and poly(vinylpyrrolidone) template.

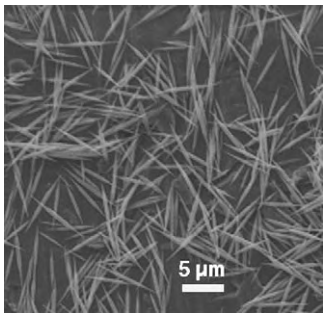

Selenium Microstructures

B. Zhang, W. Dai, X. Ye, F. Zuo, Y. Xie* **2571 – 2574**

Photothermally Assisted Solution-Phase Synthesis of Microscale Tubes, Rods, Shuttles, and an Urchin-Like Assembly of Single-Crystalline Trigonal Selenium

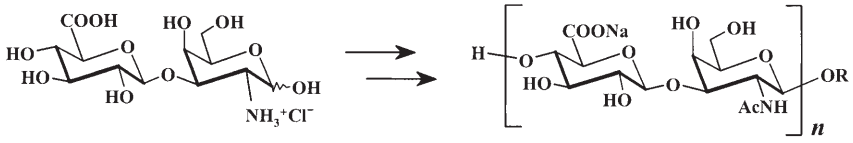

A synthetic short cut: Controlled acid hydrolysis of polymeric chondroitin sulfate affords a tailor-made disaccharidic fragment in good yield. This compound acts as a versatile starting material for the efficient construction of size-defined chondroitin oligosaccharides (see scheme, $n = 1, 2, 3$, etc.) and precursors of various sulfo forms.

Synthesis Design

C. Lopin, J.-C. Jacquinet* **2574 – 2578**

From Polymer to Size-Defined Oligomers: An Expeditious Route for the Preparation of Chondroitin Oligosaccharides

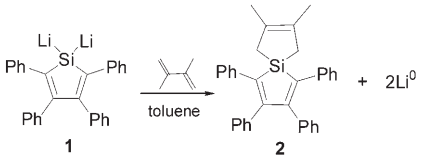

Reducing the reluctant: 1,1-dilithiosilole **1** reacts with 1,3-dienes and undergoes an unusual "oxidative cyclization", in which lithium ions are reduced to metallic lithium and spirosilole adducts like **2** (see scheme) are formed in high yield. This transformation proceeds through well-ordered transition-state geometries, in which the lithium ions play a decisive role.

Silanes

I. S. Toulokhonova, D. R. Friedrichsen, N. J. Hill, T. Müller, R. West* **2578 – 2581**

Unusual Reaction of 1,1-Dilithio-2,3,4,5-tetraphenylsilole with 1,3-Dienes Yielding Spirosilanes and Elemental Lithium

© 2006 Wiley-VCH Verlag GmbH & Co. KGaA, Weinheim

Contents

Electrooptics

N. J. Lundin, A. G. Blackman, K. C. Gordon,* D. L. Officer **2582 – 2584**

Synthesis and Characterization of a Multicomponent Rhenium(I) Complex for Application as an OLED Dopant

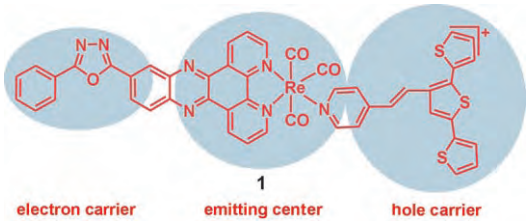

1

Three's not a crowd: A modular approach was used to prepare **1**, an electroactive molecular material that integrates distinct electron-transporting, hole-transporting, and emissive units (see picture). The trifunctional molecule holds promise for use as a dopant in organic light-emitting diodes. Moreover, the units can be easily derivatized, an important factor in the production of devices.

Glycoproteins

J. Müllegger, H. M. Chen, R. A. J. Warren, S. G. Withers* **2585 – 2588**

Glycosylation of a Neoglycoprotein by Using Glycosynthase and Thioglycoligase Approaches: The Generation of a Thioglycoprotein

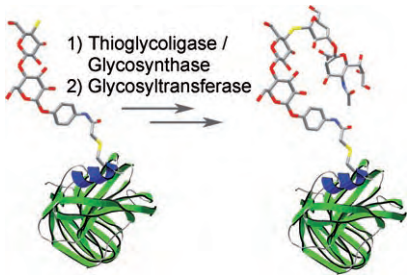

Remodeling: Glycosylation of a neoglycoprotein was achieved in quantitative yields by using a glycosynthase or a thioglycoligase. The resulting glycoproteins function as good acceptors for glycosyl transferases, and the thioglycoprotein proved to be resistant to glycosidase digestion. The established technology will enable the remodeling of natural glycoproteins to make them more stable against degradation in serum.

Fluorinated Peptides

N. Naarmann, B. Bilgiçer, H. Meng, K. Kumar,* C. Steinem* **2588 – 2591**

Fluorinated Interfaces Drive Self-Association of Transmembrane α Helices in Lipid Bilayers

An increased tendency to self-assemble is exhibited by helical peptides with a highly fluorinated interface embedded in phospholipid membranes. A simultaneously hydrophobic and lipophobic surface obtained by replacing all interface leucine residues with hexafluoroleucine results in a significant increase in the ability of transmembrane helices to form higher-order ensembles. A = fluorescence acceptor; D = fluorescence donor.

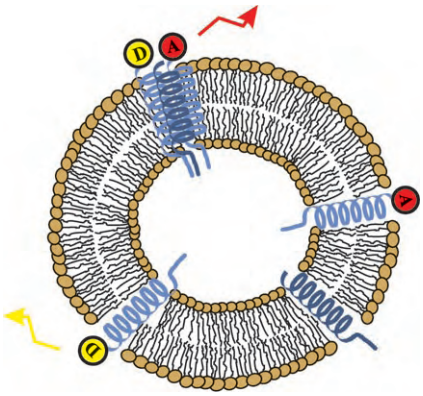

Asymmetric Synthesis

S. Akai,* K. Tanimoto, Y. Kanao, M. Egi, T. Yamamoto, Y. Kita* **2592 – 2595**

A Dynamic Kinetic Resolution of Allyl Alcohols by the Combined Use of Lipases and $[VO(OSiPh_3)_3]$

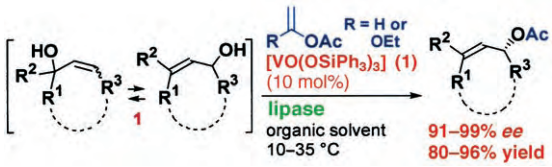

1

Mix and match: A new type of dynamic kinetic resolution of racemic allyl alcohols uses a combination of lipases and $[VO(OSiPh_3)_3]$ (**1**). The 1,3-transposition of allyl alcohols catalyzed by **1** gave thermodynamic mixtures of two regioisomers, which underwent highly enantio- and chemoselective esterification with lipases. Optically enriched allyl acetates were isolated in high yields.

© 2006 Wiley-VCH Verlag GmbH & Co. KGaA, Weinheim

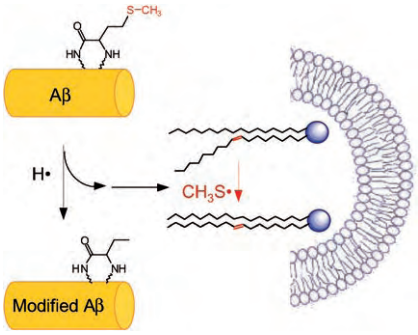

A radical change: A chemical modification of the amyloid-β (Aβ) peptide transformed methionine residue 35 in α-aminobutyric acid. Hydrogen atoms produced by γ irradiation of aqueous solutions selectively attack Met 35, with formation of the modified peptide (see scheme) and sulfur-centered radicals. By using a peptide–liposome model, the formation of *trans*-lipids has also been evaluated as a marker for this radical damage.

Peptide Modification

V. Kadlcik, C. Sicard-Roselli, C. Houée-Levin, M. Kodicek, C. Ferreri, C. Chatgilialoglu* _____ **2595 – 2598**

Reductive Modification of a Methionine Residue in the Amyloid-β Peptide

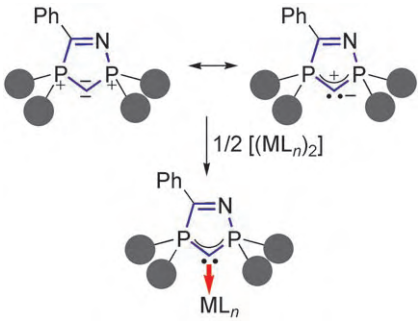

Electron-rich mononuclear complexes of palladium(II) and rhodium(I) were obtained in good yields from dinuclear precursors and a bulky cyclic carbodiphosphorane ligand (see scheme). Their molecular structures show very long M–C distances in agreement with single bonds; that is, the carbodiphosphorane acts as a two-electron σ-donor ligand without π backdonation from the metal center.

Heterocyclic Carbene Ligands

S. Marrot, T. Kato,* H. Gornitzka, A. Baceiredo* _____ **2598 – 2601**

Cyclic Carbodiphosphoranes: Strongly Nucleophilic σ-Donor Ligands

Going solo: The use of $AlH_3{\cdot}NMe_3$ as a hydrogen-transfer agent with β-diketiminatogermanium(II) and β-diketiminatotin(II) halides gives the divalent hydrides [{HC(CMeNAr)$_2$}GeH] and [{HC(CMeNAr)$_2$}SnH] (Ar = 2,6-*i*Pr$_2$C$_6$H$_3$). In the solid state, the compounds exhibit monomeric and dimeric arrangements, respectively, with weak intermolecular Sn–H···Sn contacts for the Sn analogue (see picture).

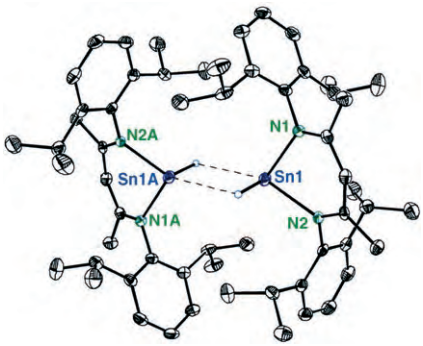

Main-Group Hydrides

L. W. Pineda, V. Jancik, K. Starke, R. B. Oswald, H. W. Roesky* **2602 – 2605**

Stable Monomeric Germanium(II) and Tin(II) Compounds with Terminal Hydrides

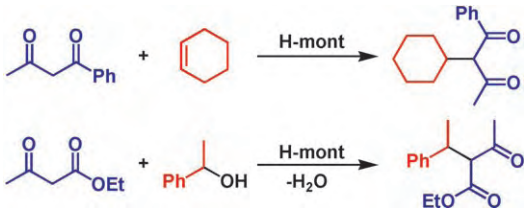

The unique acidity of a proton-exchanged montmorillonite catalyst (H-mont) was exploited in the nucleophilic addition of 1,3-dicarbonyl compounds to simple alkenes (see scheme). The benzylation and allylation of 1,3-dicarbonyl compounds with alcohols and nucleophilic addition of carboxylic acids to alkenes also proceeded smoothly with the H-mont catalyst, which could be recovered easily and recycled at least seven times without loss of activity.

Heterogeneous Catalysis

K. Motokura, N. Fujita, K. Mori, T. Mizugaki, K. Ebitani, K. Kaneda* _____ **2605 – 2609**

Brønsted Acid Mediated Heterogeneous Addition Reaction of 1,3-Dicarbonyl Compounds to Alkenes and Alcohols

© 2006 Wiley-VCH Verlag GmbH & Co. KGaA, Weinheim

Contents

Natural Product Synthesis

K. C. Nicolaou,* M. O. Frederick, G. Petrovic, K. P. Cole, E. Z. Loizidou ——— **2609 – 2615**

Total Synthesis and Confirmation of the Revised Structures of Azaspiracid-2 and Azaspiracid-3

The 39 steps: The recently proposed revised structures of azaspiracid-2 and -3 (see picture), the two most potent members of the azaspiracid family, have been confirmed through the total syntheses of the two compounds. These 39-step syntheses represent a major improvement over the first-generation synthesis of azaspiracid-1 (50 steps).

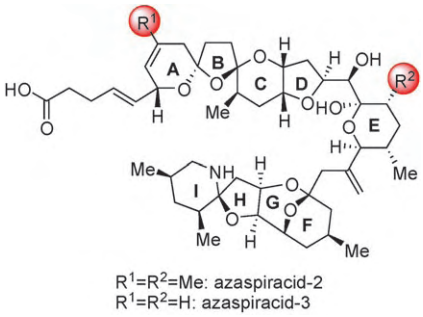

Organocatalysis

M. Rueping,* E. Sugiono, C. Azap ——— **2617 – 2619**

A Highly Enantioselective Brønsted Acid Catalyst for the Strecker Reaction

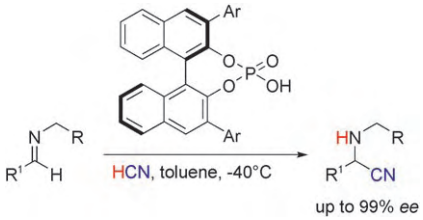

An amenable route to amino acids: An optimized new chiral binol phosphate catalyst (see scheme; Ar = 9-phenanthryl) for the hydrocyanation of imines provides a convenient strategy for the enantioselective synthesis of α-amino acids and diamines.

C–H Bond Activation

L. Ackermann,* A. Althammer, R. Born ——— **2619 – 2622**

Catalytic Arylation Reactions by C–H Bond Activation with Aryl Tosylates

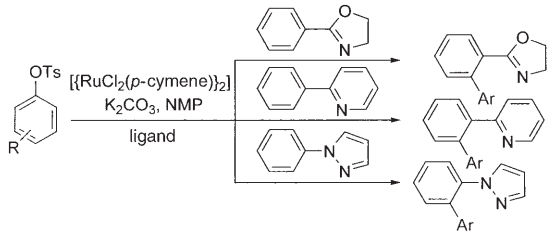

Select and direct: A ruthenium complex derived from an air-stable diaminophosphine oxide preligand allows for highly efficient and selective direct arylation reactions using aryl tosylates. The reactions proceed through C–H bond activation and tolerate pronucleophiles with different directing groups, including pyrazole derivatives (see scheme; NMP = *N*-methylpyrrolidinone, OTs = tosylate).

Benzomorphan Synthesis

E. Klegraf, S. Knauer, H. Kunz* ——— **2623 – 2626**

Stereoselective Synthesis of Benzomorphan Derivatives with Perpivaloylated Galactose as the Chiral Auxiliary

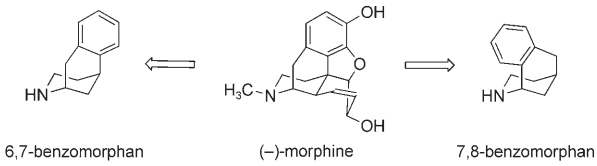

"Which way, sugar?" The cyclization of benzyl-substituted *N*-galactosyl didehydropiperidinones leads stereoselectively to regioisomerically annelated and highly substituted benzomorphan derivatives, which are pharmacophorically relevant structural elements (see scheme). The perpivaloylated *N*-galactosyl auxiliary controls the stereo- as well as the regioselectivity of the reaction.

© 2006 Wiley-VCH Verlag GmbH & Co. KGaA, Weinheim

Erythrocytes as templates can be used for patterning polymer surfaces (see the AFM image). Despite the flexibility of these cells, the imprints show a high selectivity for different blood groups, as revealed by sensor responses with the quartz crystal microbalance (see inset). Thus, the imprinting process creates selective synthetic antibodies for erythrocyte antigens.

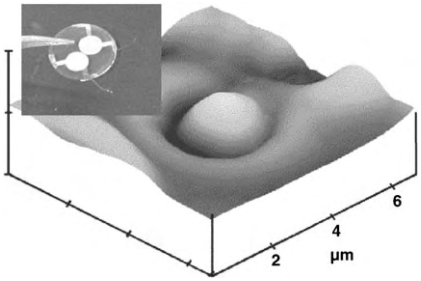

Blood-Group Typing

O. Hayden, K.-J. Mann, S. Krassnig, F. L. Dickert* ——— **2626 – 2629**

Biomimetic ABO Blood-Group Typing

Pricking the surface: STM and EPR spectroscopy demonstrate the presence of color centers on thin MgO(001) films and their interaction with Au atoms. These systems are used to calibrate the IR stretching frequencies of CO bound to Au clusters. Clusters on regular MgO(001) terrace sites remain neutral while nucleation at color centers results in a charge transfer from the surface to the Au cluster.

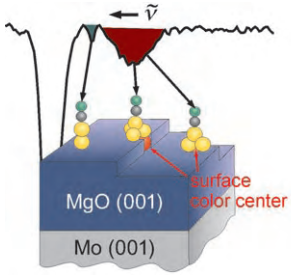

Surface Chemistry (1)

M. Sterrer, M. Yulikov, E. Fischbach, M. Heyde, H.-P. Rust, G. Pacchioni, T. Risse,* H.-J. Freund ——— **2630 – 2632**

Interaction of Gold Clusters with Color Centers on MgO(001) Films

Innocence lost: The IR spectra of Au/CO complexes adsorbed on of a MgO(001) film differ from the corresponding neutral Au clusters. Calculations indicate this shift of 200–250 cm^{-1} can be associated with a negative charge on the Au/CO complex. For Au/CO complexes on so-called color centers a charge transfer is expected, however Au atoms on terrace sites are neutral. Thus, CO in fact induces the charge transfer instead of reporting the charge state of the adsorbed Au atoms.

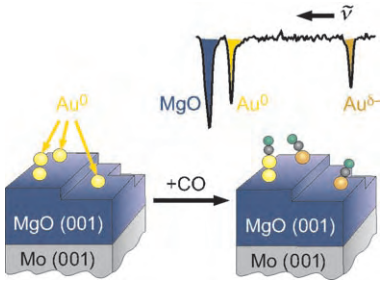

Surface Chemistry (2)

VIP

M. Sterrer, M. Yulikov, T. Risse,* H.-J. Freund, J. Carrasco, F. Illas, C. Di Valentin, L. Giordano, G. Pacchioni ——— **2633 – 2635**

When the Reporter Induces the Effect: Unusual IR spectra of CO on Au_1/MgO(001)/Mo(001)

WILEY InterScience® DISCOVER SOMETHING GREAT

"**Hot Papers**" are chosen by the Editors for their importance in a rapidly evolving field of high current interest. A preview with the graphical abstracts of these articles can be found on the *Angewandte Chemie* homepage in Wiley InterScience at www.angewandte.org.

All articles in *Angewandte Chemie* are published online several weeks ahead of print. They are found under the "**EarlyView**" link on the journal's homepage in Wiley InterScience.

Service

Keywords ——— **2636**

Authors ——— **2637**

Preview ——— **2639**

© 2006 Wiley-VCH Verlag GmbH & Co. KGaA, Weinheim

Contents

For more information on ChemMedChem see www.chemmedchem.org

Corrigendum

Directed Evolution of Enantioselective Enzymes: Iterative Cycles of CASTing for Probing Protein-Sequence Space

M. T. Reetz,* L.-W. Wang, M. Bocola

1236–1241

The penultimate sentence of the first paragraph on page 1237, just above Figure 1, should read: "In each case, only three libraries are necessary, for example, the gene of the best mutant arising from A is used as a template for randomization at sites B, C, and D, etc. (Figure 1)." In a variation of this iterative CASTing, one less branch occurs in each generation until all sites A, B, C, and D have been utilized with termination of the confined protein sequence space.

Angew. Chem. Int. Ed. **2006**, 45

DOI 10.1002/anie.200502746

© 2006 Wiley-VCH Verlag GmbH & Co. KGaA, Weinheim

Pierre Potier (1934–2006)

Pierre Potier, one of France's pre-eminent scientists and benefactors, passed away on February 3, 2006. He spearheaded the discovery of two important anticancer drugs, Navelbine and Taxotere.

Pierre Potier was born in Bois-Colombes, near Paris, on August 22, 1934. He decided upon a career in pharmacy and graduated from the Faculty of Pharmacy of the University of Paris in 1957. His fascination with natural products and their relationship to pharmacy and medicine guided him towards completing a PhD under the joint supervision of Maurice-Marie Janot and Jean Le Men at the Institut de Chimie des Substances Naturelles (ICSN) in Gif-sur-Yvette. These two eminent natural product chemists were at the forefront of the isolation and structural determination of alkaloids.

Potier's early interests were in the lunaria alkaloids, numismine, lunarine, and lunaridine, as well as steroidal alkaloids and ellipticines. His studies on plant alkaloids led to reflections concerning their biogenesis and the possibility that *N*-oxides could be biosynthetic precursors of iminium species, in parallel to their known chemical behavior.[1] Iminium, imine, and enamine intermediates are key players in the biosynthesis and total syntheses of alkaloids hinging on the Mannich, Pictet–Spengler, and other related reactions. The conversion of tertiary amine *N*-oxides into iminium-derived products by the action of acetic anhydride—the so-called Polonovski reaction—suffered in general from complications due to the modest electrophilicity of acetic anhydride and the corresponding nucleophilicity of the ensuing acetate. Potier and his collaborators found that replacement of acetic anhydride with the more reactive trifluoroacetic anhydride transformed this rather obscure reaction into a synthetic tool of tremendous power.[2] The lack of nucleophilicity of the trifluoroacetate anion essentially froze the reaction at the iminium intermediate, at which point typical transformations of iminium salts could be achieved cleanly. Even the simplest and highly reactive iminium trifluoroacetate derived from trimethylamine *N*-oxide could be prepared.

The Polonovski–Potier reaction has since played an important role in the biomimetic syntheses of alkaloids,[3] and its role in the next major topic of Potier's research was decisive. His first wife, Marie-France, died from cancer at a very young age, an event that lead Potier to focus his research on the discovery of drugs to combat this dreadful disease by using substances found in what he called the "good Lord's shop". He was 34 years old with three children to care for.

The Madagascar periwinkle, *Catharanthus roseus*, was locally used as an antidiabetic, and thus the plant extracts were initially examined for possible antidiabetic activity. However, instead of lowering blood sugar levels, the extracts depleted the concentration of white blood cells and thus appeared as potentially useful in treating leukemia. Indeed, two anticancer bis(indole) alkaloids isolated from the periwinkle, namely vinblastine and vincristine, were later marketed. However, the drugs were extremely expensive as a result of the difficulties encountered in obtaining large quantities of the active ingredients. For instance, only 2 g of vincristine could be obtained from 1000 kg of catharanthus (0.0002 % yield).

To remedy this problem, Potier and his team set out to assemble biomimetically, through an iminium intermediate, the two subunits of anhydrovinblastine, namely catharantine and vindoline, which were much more abundant than the more complex bis(indole) alkaloids themselves. Access to the reactive iminium species would rely on the modified Polonovski reaction. This approach was ultimately successful, but serendipity intervened in the attempted conversion of anhydrovinblastine into vinblastine, which called for a second application of the Polonovski–Potier reaction.[4] An unexpected extrusion of one carbon atom occurred to give noranhydrovinblastine, which exhibited strong activity in the tubulin test (vinblastine and vincristine act by binding to tubulin in the mitotic spindle, preventing its polymerization into microtubules). Further studies indicated that the new semisynthetic analogue, now called vinorelbine, was orally active and less neurotoxic than the natural alkaloids. The compound was developed and marketed as Navelbine.

Taxol was another promising anticancer natural product that suffered from a severe supply problem. It is present in minute quantities in the bark of the slow-growing pacific yew tree (*Taxus brevifolia*), and a huge number had to be felled in order to allow extraction of sufficient quantities for complete pharmacological testing. The dilemma of a looming ecological disaster on one hand and dying cancer patients on the other was solved unexpectedly when local authorities decided to build a road through a park in Gif-sur-Yvette. Several century-old European yew trees (*Taxus baccata*) were to be felled, and Potier obtained permission to recover these trees and carried out a systematic study. From the leaves, a substance was isolated whose structure resembled that of taxol but lacked an acetate group and the aliphatic side chain. This compound, 10-deacetylbaccatin III, could solve the supply problem: it was extracted from leave clippings without harm to the tree and could essentially be converted into taxol in a few steps.

During the partial synthesis of taxol from 10-deacetylbaccatin III, serendipity struck yet again. All taxoid derivatives were systematically subjected to the improved tubulin test, and one of the intermediates in the projected synthesis turned out to be more soluble and twice as active as taxol itself.[5] This compound was developed into the drug Taxotere.

Potier's later interests ranged from exploring the biochemistry and therapeutic potential of the ubiquitous nitric oxide to the role of pyruvaldehyde, a glucose metabolite, in type II diabetes. The latter topic was one of his main concerns as he suffered from diabetes. He even tested an ointment based on metformine on himself to heal a recalcitrant wound. A patent was filed following the success of the test, but unfortunately he did not live to see its outcome.

WILEY InterScience DISCOVER SOMETHING GREAT
© 2006 Wiley-VCH Verlag GmbH & Co. KGaA, Weinheim

Pierre Potier rapidly rose through the ranks at the ICSN, becoming a co-director in 1974 and Director in 1990. In the same year, he was also appointed to the prestigious Chair of Chemistry at the Muséum National d'Histoire Naturelle in Paris. He was elected a member of the French Academy of Sciences and was the recipient of numerous prizes, including the Gold Medal of the CNRS, the highest scientific distinction in France. He was appointed Director General of Science and Technology (1994–1996) and later became President of the Fondation de la Maison de la Chimie.

He was a man of many exceptional talents, humanity, and generosity, and had a sharp wit. He once gave me the "French" definition of serendipity, which was "to look for a needle in a haystack and to find the farmer's daughter". Sharing a meal with him was another delightful experience. He was a true *bon vivant* and would regale you with culinary anecdotes and tales of the French *terroir*.

Pierre Potier accomplished much more than any of us could ever dream of doing. Millions of cancer patients are grateful to him for his unwavering search for the "magic bullet". He will be greatly missed by all of us who knew him and remembered by many more.

Samir Z. Zard
Laboratoire de Synthèse Organique
Ecole Polytechnique (France)

[1] V. K. Kansal, P. Potier, *Tetrahedron* **1986**, *42*, 2389.
[2] A. Cavé, C. Kan-Fan, P. Potier, J. Le Men, *Tetrahedron* **1967**, *26*, 4681; A. Ahond, A. Cavé, C. Kan-Fan, H.-P. Husson, J. de R-ostolan, P. Potier, *J. Am. Chem. Soc.* **1968**, *90*, 5622.
[3] P. Potier, *Bull. Soc. Chim. Fr.* **1970**, 28; D. Grierson, *Org. React.* **1990**, *39*, 85.
[4] P. Potier, *J. Nat. Prod.* **1980**, *43*, 72; N. Langlois, F. Guéritte, Y. Langlois, P. Potier, *J. Am. Chem. Soc.* **1976**, *98*, 7024.
[5] P. Potier, *Chem. Soc. Rev.* **1992**, *21*, 113; D. Guénard, F. Guéritte-Voegelein, P. Potier, *Acc. Chem. Res.* **1993**, *26*, 160; J. N. Denis, A. E. Greene, D. Guénard, F. Guéritte-Voegelein, L. Mangatal, P. Potier, *J. Am. Chem. Soc.* **1988**, *110*, 5917.

DOI: 10.1002/anie.200600811

 © 2006 Wiley-VCH Verlag GmbH & Co. KGaA, Weinheim

Microcapsules

DOI: 10.1002/anie.200504526

Stable Air Bubbles—Catch Them If You Can!**

Mathias Winterhalter and Andreas F.-P. Sonnen**

Keywords:
emulsions · imaging agents · interfaces · polyelectrolytes · surfactants

Soap bubbles are fascinating not only for little children.[1] How often have we all tried—in vain—to catch these fragile objects? The importance of bubbles in everyday life is not restricted to the visual pleasures of soap bubbles dancing in the air. Air-filled cavities play an important role in the food industry, for example, with the release of carbon dioxide in beer and sparkling wine.[2] Vivid bubbling is a first quality test for a freshly filled glass.

Recently, micrometer-sized gas bubbles were used as contrast agents in ultrasound microscopy as a result of their large compressibility and scattering elasticity as compared to the surrounding aqueous medium.[3] Although the contrast agent is injected into tissues for imaging, it tends to leak quickly into the blood and other body fluids, thus considerably reducing the quality of the image obtained. Hence, new ways to stabilize gas bubbles are desperately needed. One such possibility was recently offered by Shchukin et al., who described a novel technique to stabilize air-filled detergent bubbles by deposition of a polyelectrolyte.[4]

Hollow polyelectrolyte capsules are readily fabricated by the so-called layer-by-layer deposition technique,[4,5] an approach that was developed in the mid-1990s from investigations on the adsorption of oppositely charged polymer layers at the air–water interface (see Reference [5] for an overview). These investigations led to a new type of material with astonishing properties: for example, they were ultrathin and selectively permeable for various small molecules and their individual layers could be easily functionalized and thus the external polyelectrolyte layer could be tuned with respect to the solvent polarity and for the introduction of protective molecules. The assembly of polyelectolyte capsules starts with the coating of a template, in similar fashion to standard template polymerizations except that ionic rather than covalent bonds are formed between the monomers, which are oppositely and highly charged polymer molecules in this case. A broad range of template materials have been used, including inorganic and organic particles, crystals, and even whole cells such as erythrocytes and yeast cells.

Shchukin et al. employed detergent-coated gas bubbles as a template for the first time (schematically depicted in Figure 1).[4] An ultrasound sonicator was placed at the air–detergent–water interface to create small air-filled, micrometer-sized bubbles. A mixture of the detergents polyoxyethylene sorbitan monooleate (Tween 80) and sorbitan monostearate (Span 60) can stabilize the gas bubbles for a few hours, long enough to allow for coating with poly-

[*] Prof. Dr. M. Winterhalter, A. F.-P. Sonnen
School of Engineering and Science
International University Bremen
28725 Bremen (Germany)
Fax: (+49) 421-200-3249
E-mail: m.winterhalter@iu-bremen.de
andreas@strubi.ox.ac.uk
Prof. Dr. M. Winterhalter
Institut de Pharmacologie et de Biologie Structurale
Université P. Sabatier
205 rte de Narbonne, Toulouse (France)
A. F.-P. Sonnen
The Division of Structural Biology
The Wellcome Trust Centre for Human Genetics
University of Oxford
Roosevelt Drive, Oxford, OX3 7BN (UK)
Fax: (+44) 1865-287-547

[**] Financial support by the Volkswagen Foundation (Nanoengineered Polymer Capsules I/80 054) is acknowledged. We thank M. Lindemann for valuable discussions.

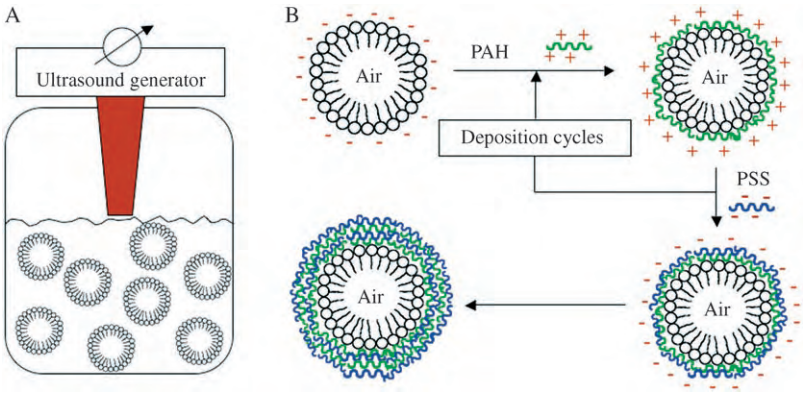

Figure 1. Fabrication of hollow gas-filled polyelectrolyte capsules. A) An aqueous detergent mixture of Tween 80 and Span 60 is used to form gas bubbles through intensive ultrasonication at the air–water interface. The bubbles are characterized by ζ-potential measurements and the values are slightly negative. B) Mixing the bubbles with the cationic PAH results in the deposition of the first polyelectrolyte layer. The capsule now has an overall positive charge. These coated bubbles are separated from the unbound polymer by gentle centrifugation to allow binding of anionic PSS in the following step. The deposition procedure is repeated several times until a desired stability is reached (adapted from Figure 1 of Ref. [4]).

InterScience
© 2006 Wiley-VCH Verlag GmbH & Co. KGaA, Weinheim

electrolytes. The positively charged poly(allylamine hydrochloride) (PAH) binds to the negative surface of the detergent monolayer (Figure 1B), and these primary capsules can be separated from unbound polyelectrolyte by centrifugation at low speeds. After washing, the microspheres are immersed into a solution that contains negatively charged poly(styrene sulfonate) (PSS). The deposition steps are alternated several times to obtain the final coated bubbles, which were characterized using standard biophysical techniques.

Interestingly, ζ-potential measurements of the template gas bubbles gave a slightly negative value (-5 mV) at low salt concentrations. After coating with the first electrolyte layer, the potential jumped to an unexpected high value of $\zeta = +45$ mV. This drastic increase might be ascribed to two phenomena. First, the macroscopic orientation of the detergent molecules at the air–water interface induces a dipole potential, whose negative end is situated at the hydrophilic side towards the water (see Figure 2). This orientation might enhance the binding of the positively charged PAH to the otherwise uncharged detergent molecules, which may lead to changes in their orientation and thus modify their dipole potential and, as a combined effect, eventually lead to an enhanced ζ-potential. As indicated in Figure 3, this hypothesis might easily be tested by measuring the surface potential of a monolayer of Tween 80 and Span 60 at the air–water interface using a vibrating plate.[6] Injection of PAH into the aqueous subphase should then cause a change in the boundary potential, which is the sum of the dipole potential and the potential arising from the surface charge. The relevance of the dipole effect could also be tested by starting the coating process with an anionic polyelectrolyte. The second effect that may enhance the surface potential could originate from the nature of the dielectric media at the interface. Air has a very small dielectric constant, and thus the electric fields of water and air are largely excluded. For such systems, Gouy–Chapman theory predicts an apparent doubling of the surface charge density with subsequently higher surface potentials. Notably, measurements of the ζ-potential of monolayer-coated gas bubbles could be a new way to understand the fundamental differences in surface potentials of mono- and bilayers of lipids and detergents.[6]

The effects of different polyelectrolytes, buffer composition, and temperature on the permeability of water-filled capsules for small molecules have been intensively studied. The mesh size, which ultimately determines the permeability of the capsule, is highly dependent on the growth behavior of the layer. Different interactions between the individual polyelectrolyte layers manifest themselves in two distinct growth behaviors: a linear or an exponential increase in shell thickness with an increasing number of deposited polyelectrolyte layers.[7] These effects must be characterized to find optimal conditions for low gas permeability.

The technique described above allows a straightforward encapsulation of gases, such as perfluorinated hydrocarbons or volatile aromatics. Whereas the former are important echogenic reflectors of ultrasound in medical diagnostics, the latter are of great interest in the food industry. Flavor additives and stabilizers are currently encapsulated using fat dispersions with slow release kinetics, but polyelectrolyte-stabilized gas capsules could be a new way forward, at least for high-quality food products. Moreover, microspheres with a gaseous lumen could also find applications as components of fuel cells, as dispersing containers for the slow and steady release of gases, and as compartments for chemical catalysis.

Ultrasound microscopy is a versatile and noninvasive imaging method in routine diagnostics,[3] however, its resolution is currently limited by the lack of adequate contrast agents. The earlier used agents consisted of micrometer-sized bubbles, which were produced by agitation of saline solution or blood.[3] However, as their half-life in vivo is on the order of several seconds, they can

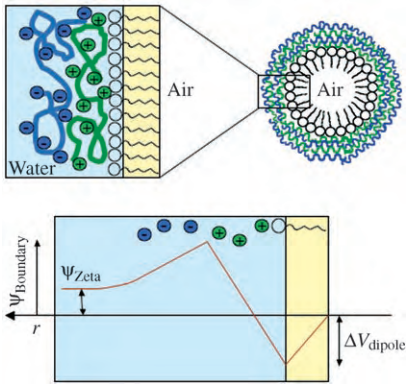

Figure 2. An air bubble covered with a detergent monolayer and coated with a number of alternating polyelectrolyte layers. The otherwise uncharged detergent monolayer is composed of macroscopically oriented dipoles that give rise to a dipole potential (ΔV_{dipole}), which enhances the binding of the positively charged polyelectrolyte and induces a reorientation of the detergent dipoles (see Ref. [6] for details). The Zeta potential (Ψ_{Zeta}) is measured through the electrophoretic mobility and reflects the potential at a certain distance to the interface. The boundary potential, $\Psi_{boundary}$, is the total surface potential at a distance r relative to the gaseous interior of the capsule, where the potential is zero.

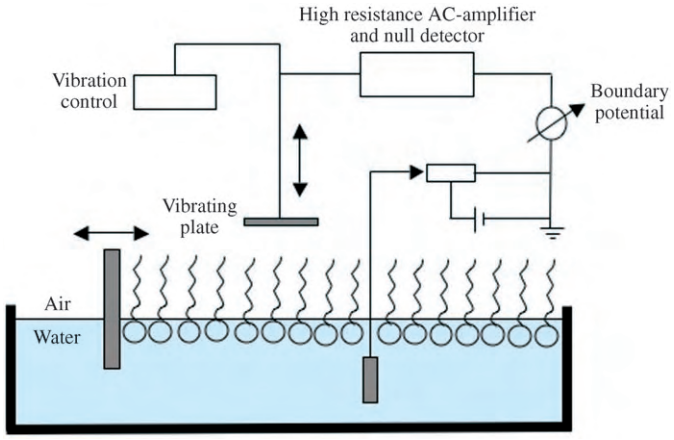

Figure 3. Representation of a monolayer apparatus with a vibrating plate to measure the surface potential.

© 2006 Wiley-VCH Verlag GmbH & Co. KGaA, Weinheim

penetrate only very short distances and are rapidly removed from tissues.

One can think of several ways of how to stabilize gas-filled cavities, with an example being surfactants. However, biodegradability and toxicity must be considered in all in vivo applications, especially in noninvasive imaging techniques, thus proteins such as bovine serum albumin and liposomes have been widely used as stabilizers. From a biophysical point of view, two parameters determine the suitability of gas-filled microcapsules for ultrasound microscopy. The capsules must be large enough to ensure sufficient contrast with the surrounding environment (that is, the scattering cross-section has to be large), yet small enough to efficiently penetrate blood vessels (less than 6–8 μm diameter, depending on the tissue to be imaged).[8] Additionally, the Ostwald coefficient, which describes the ease with which a gas can leave or enter the capsule, must be small; that is, the gas permeability must be low to prolong the in vivo lifetime of the capsule.

Polyelectrolyte microspheres are an exciting advance for the field because their size and permeability can be easily adjusted. The (highly) charged nature of the polyelectrolyte surface could prevent aggregation of the capsules in vivo and thus reduce the risk of blocking blood and lymphatic vessels. Moreover, functionalization of the outer layer may allow targeted molecular imaging of specific tissues or even of individual cells.[9] Initial studies on the functionalization of water-filled polyelectrolyte capsules containing markers and enzymes were promising, and these techniques should readily be implemented in the fabrication of their gas-filled counterparts.

However, as one might expect, the field of targeted in vivo delivery is extremely complex. Many promises have been made to date, but very few solid results have been achieved. Considerable research efforts are still needed as there seems to be no general answers to the numerous biological, physical, and chemical obstacles encountered.

Published online: March 2, 2006

[1] C. Isenberg, *The Science of Soap Films and Soap Bubbles*, Dover, New York, **1992**.
[2] G. Liger-Belair, R. Marchal, B. Robillard, T. Dambrouk, A. Maujean, M. Vignes-Adler, P. Jeandet, *Langmuir* **2000**, *16*, 1889 – 1895.
[3] E. G. Schutt, D. H. Klein, R. M. Mattery, J. G. Reiss, *Angew. Chem.* **2003**, *115*, 3336 – 3355; *Angew. Chem. Int. Ed.* **2003**, *42*, 3218 – 3235.
[4] D. G. Shchukin, K. Köhler, H. Möhwald, G. B. Sukhorukov, *Angew. Chem.* **2005**, *117*, 4610 – 4613; *Angew. Chem. Int. Ed.* **2005**, *44*, 3310 – 3314.
[5] E. Donath, G. B. Sukhorukov, F. Caruso, S. A. Davis, H. Möhwald, *Angew. Chem.* **1998**, *110*, 2323 – 2327; *Angew. Chem. Int. Ed.* **1998**, *37*, 2201 – 2205.
[6] J. A. Cohen, V. B. Gabriel, J. Teissie, M. Winterhalter, in *Planar Lipid Bilayers (BLMs) and Their Applications* (Eds.: H. T. Tien, A. Ottova-Leitmannova), Elsevier, Amsterdam, **2003**.
[7] V. Ball, J.-C. Vogel, P. Schaaf, *Langmuir* **2005**, *21*, 4129 – 4137.
[8] A. Raisinghani, A. N. Demaria, *Am. J. Cardiol.* **2004**, *90*, 3 – 7.
[9] A. L. Kilbanov, *Bioconjugate Chem.* **2005**, *16*, 9 – 17.

 © 2006 Wiley-VCH Verlag GmbH & Co. KGaA, Weinheim

Bioinorganic Chemistry

DOI: 10.1002/anie.200600031

Imposing a Three-Way Junction on DNA or Recognizing One: A Metal Triple Helicate Meets Double Helix

Jens Müller and Bernhard Lippert**

Keywords:
DNA recognition · DNA structure · metal helicate · noncovalent interactions · supramolecular chemistry

Metal triple helicates, supramolecular constructs made up of three bis-ditopic, flexible, linear organic ligands and two octahedrally coordinate metal ions, have presented a synthetic challenge for quite a while. Now well understood, the interactions of such supramolecules with another one, a double-stranded DNA, have lately attracted attention.[1] It was originally the idea to take advantage of the complementarity between charge (positive for the helicate, negative for DNA) and shape (for major-groove binding), which prompted this research. An X-ray crystal structure analysis reported by Hannon, Coll et al. has now revealed an unexpected and truly remarkable interaction between the tetracationic $[Fe_2L_3]^{4+}$ triple helicate (Figure 1, L = bis(pyridylimine) ligand: $C_{25}H_{20}N_4$) and the palindromic DNA sequence 5′-d(CGTACG).[2] Rather than sitting in the major groove of a double-stranded DNA hexamer, as had been expected based on earlier spectroscopic studies,[1c] the metal helicate with its trigonal antiprismatic geometry occupies the central hydrophobic cavity of a three-way (Y-shaped) junction generated by three single strands that are linked by nine Watson–Crick base pairs (Figure 2). The base pairing results in the formation of three minihelices.

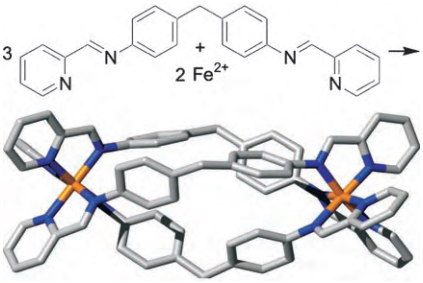

Figure 1. Self-assembly and schematic view of Fe_2 triple helicate; orange Fe, blue N, gray C.[20]

The association between DNA and the metal helicate is accomplished by the interplay of numerous noncovalent forces: In addition to the electrostatic interaction between the positively charged supramolecule and the negatively charged DNA backbone that is also present in related major-groove binding double-helical copper(II) complexes,[3] this new structure also features six extensive π-stacking interactions between the phenyl rings of the helicate and the adenine and thymine bases of the DNA strands as well as strong van der Waals interactions between the helicate and the sugar–phosphate backbone reminiscent of those observed in minor groove binders. Hannon, Coll et al describe this unexpected finding in terms of a selection of an otherwise energetically unfavorable structural element out of a dynamic combinatorial library[4] of palindromic DNA oligomers. On the other hand, it is reasonable to expect that the metal helicate can recognize a naturally occurring three-way junction and bind to it. These two possibilities represent two sides of the same coin. Supportive of this scenario is that the three-way junction is not significantly perturbed from its Y-structure upon binding of the metal complex. This feature suggests that the three-way junction serves as a structural-recognition target not only for proteins as previously observed but also for synthetic small molecules. Helical junctions, such as the three-way junction, are numerous as structural elements in RNA and are significant as intermediates in both homologous and site-spe-

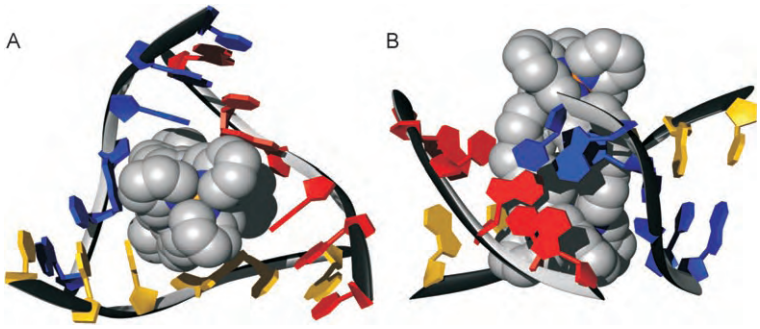

Figure 2. A) Top and B) side view of DNA three-way junction stabilized by Fe_2 triple helicate. Gray spheres C, blue spheres N, orange sphere Fe, all the bases of each of the three DNA strands have a different color: blue, red, or yellow.[20]

[*] Dr. J. Müller, Prof. Dr. B. Lippert
Fachbereich Chemie
Universität Dortmund
44221 Dortmund (Germany)
Fax: (+49) 231-755-3797
E-mail: jens.mueller@uni-dortmund.de
bernhard.lippert@uni-dortmund.de

© 2006 Wiley-VCH Verlag GmbH & Co. KGaA, Weinheim

cific recombination,[5] and in the replication fork during DNA duplication. The replication fork might be seen as one example for a naturally occurring, transient three-way DNA junction.[6]

The binding of small molecules to DNA or to nucleic acids in general is of great interest because of its enormous potential in the fields of anticancer drugs, gene therapy, or biochemical methods for specific DNA recognition and/or modification.[7] The following discussion focuses on the binding of metal complexes to nucleic acids and hence represents a bioinorganic view of DNA recognition.[8]

Although well established, the direct covalent binding of metal ions or complexes to DNA is rather the exception not the rule. Cisplatin (*cis*-$[PtCl_2(NH_3)_2]$), binding to purine nucleobases from the major groove, is a prime example.[9] There are also rare cases of direct binding of $[Mg(H_2O)_n]^{2+}$ ($n = 4$ or 5) to nucleobase donor atoms in nucleic acid structures. Coordinative binding in the minor groove is also known, for example, for sodium ions.[10] However, the recognition process of nucleic acids and their stabilization by most other metal complexes can best be described as a noncovalent interaction. Various nucleic acid structures are known displaying binding of the $[Co(NH_3)_6]^{3+}$ ion, mainly through outer-sphere hydrogen bonding to the DNA donor atoms. A preference of this well-studied complex for a distinct DNA conformation could not be unambiguously delineated to date; apparently its binding merely destabilizes B-type DNA, and the respective nucleic-acid sequence is the main determinant of whether the A- or Z-type conformation is adopted upon interaction with the cobalt complex.[11] Other examples for outer-sphere hydrogen bonding interactions include those of the $[Mg(H_2O)_6]^{2+}$ ion.

Intercalating metal complexes represent another important group of DNA-binding molecules. They are able to attach to the DNA in either groove[12] or even in both grooves at the same time by threading through the DNA.[13] Initially synthesized as square-planar reagents the first metallointercalators were without any significant sequence specificity.[14] However new examples of octahedral metallointercalators permit the targeting of specific DNA sites with high affinity by matching shape, symmetry, and functionalities of the metal complex to that of the nucleic acid target.[12a] The X-ray crystal-structure analysis of a rhodium complex intercalated into DNA provides a rationale how such a sequence specificity can be obtained.[15] By using this strategy of applying specifically designed ligands, even preferential binding to oligonucleotides with mismatches can be observed.[16] Including an alkylating agent in the intercalator conjugate, covalent tagging of mismatched DNA and potentially an application in the development of new chemotherapeutic agents is feasible.[17] However, not every metal complex that could potentially intercalate through its planar aromatic ligand(s) necessarily does so. Several examples are known where the mode of binding has been proposed to depend on various factors including DNA base sequence, substitution pattern of the aromatic ligand, and relative concentrations of DNA and metal coordination compound. The metal compound can under certain conditions be located in either groove without intercalating into the nucleic acid.[18]

The three-way junction-directed binding mode observed for the metal triple helicate by Hannon, Coll et al.[2] opens up an entirely new range of possible DNA-interacting therapeutic agents based on metal complexes. Their cylinder-shaped molecule is reported to potentially have a preference for binding a three-way junction with a central TA sequence, raising the question whether other palindromic sequences might be recognized with structurally related compounds, such as an extended cylinder[1a] or a tetranuclear triple-stranded lanthanide helicate.[19] How the chirality of the complex influences the recognition process is another subject of interest. Time will tell whether a chemistry as rich as that of the intercalating drugs will develop around this new DNA recognition mode.

Published online: March 20, 2006

[1] a) C. Uerpmann, J. Malina, M. Pascu, G. J. Clarkson, V. Moreno, A. Rodger, A. Grandas, M. J. Hannon, *Chem. Eur. J.* **2005**, *11*, 1750 – 1756; b) I. Meistermann, V. Moreno, M. J. Prieto, E. Moldrheim, E. Sletten, S. Khalid, P. M. Rodger, J. C. Peberdy, C. J. Isaac, A. Rodger, M. J. Hannon, *Proc. Natl. Acad. Sci. USA* **2002**, *99*, 5069 – 5074; c) M. J. Hannon, V. Moreno, M. J. Prieto, E. Moldrheim, E. Sletten, I. Meistermann, C. J. Isaac, K. J. Sanders, A. Rodger, *Angew. Chem.* **2001**, *113*, 903 – 908; *Angew. Chem. Int. Ed.* **2001**, *40*, 879 – 884; d) M. J. Hannon, C. L. Painting, A. Jackson, J. Hamblin, W. Errington, *Chem. Commun.* **1997**, 1807 – 1808.

[2] A. Oleksy, A. G. Blanco, R. Boer, I. Usón, J. Aymamí, A. Rodger, M. J. Hannon, M. Coll, *Angew. Chem.* **2006**, *118*, 1249 – 1253; *Angew. Chem. Int. Ed.* **2006**, *45*, 1227 – 1231.

[3] B. Schoentjes, J.-M. Lehn, *Helv. Chim. Acta* **1995**, *78*, 1 – 12.

[4] J.-M. Lehn, *Chem. Eur. J.* **1999**, *5*, 2455 – 2463.

[5] D. M. J. Lilley, *Q. Rev. Biophys.* **2000**, *33*, 109 – 159.

[6] M. R. Singleton, S. Scaife, D. B. Wigley, *Cell* **2001**, *107*, 79 – 89.

[7] S. Neidle, *Nucleic Acid Structure and Recognition*, Oxford University Press, Oxford, **2002**.

[8] for a recent review, see: F. Pierard, A. Kirsch-De Mesmaeker, *Inorg. Chem. Commun.* **2006**, *9*, 111 – 126.

[9] *Cisplatin—Chemistry and Biochemistry of a Leading Anticancer Drug* (Ed.: B. Lippert), Helvetica Chimica Acta, Zürich, **1999**.

[10] a) X. Shiu, L. McFail-Isom, G. G. Hu, L. D. Williams, *Biochemistry* **1998**, *37*, 8341 – 8355; b) N. C. Seeman, J. M. Rosenberg, F. L. Suddath, J. J. P. Kim, A. Rich, *J. Mol. Biol.* **1976**, *104*, 109 – 144.

[11] a) M. C. Wahl, M. Sundaralingam in *Oxford Handbook of Nucleic Acid Structure* (Ed.: S. Neidle), Oxford University Press, Oxford, **1999**, pp. 117 – 144; b) B. Basham, B. F. Eichman, P. S. Ho in *Oxford Handbook of Nucleic Acid Structure* (Ed.: S. Neidle), Oxford University Press, Oxford, **1999**, pp. 199 – 252.

[12] for examples, see: a) K. E. Erkkila, D. T. Odom, J. K. Barton, *Chem. Rev.* **1999**, *99*, 2777 – 2795; b) E. Tuite, P. Lincoln, B. Nordén, *J. Am. Chem. Soc.* **1997**, *119*, 239 – 240.

[13] B. Önfelt, P. Lincoln, B. Nordén, *J. Am. Chem. Soc.* **2001**, *123*, 3630 – 3637.

[14] K. W. Jennette, S. J. Lippard, G. A. Vassiliades, W. R. Bauer, *Proc. Natl. Acad. Sci. USA* **1974**, *71*, 3839 – 3843.

[15] K. L. Kielkopf, K. E. Erkkila, B. P. Hudson, J. K. Barton, D. C. Rees, *Nat. Struct. Biol.* **2000**, *7*, 117 – 121.

[16] H. Junicke, J. R. Hart, J. Kisko, O. Glebov, I. R. Kirsch, J. K. Barton, *Proc.*

 © 2006 Wiley-VCH Verlag GmbH & Co. KGaA, Weinheim

Natl. Acad. Sci. USA **2003**, *100*, 3737 – 3742.
[17] U. Schatzschneider, J. K. Barton, *J. Am. Chem. Soc.* **2004**, *126*, 8630 – 8631.
[18] a) D. Z. M. Coggan, I. S. Haworth, P. J. Bates, A. Robinson, A. Rodger, *Inorg. Chem.* **1999**, *38*, 4486 – 4497; b) C. Hiort, B. Nordén, A. Rodger, *J. Am. Chem. Soc.* **1990**, *112*, 1971 – 1982.
[19] K. Zeckert, J. Hamacek, J.-M. Senegas, N. Dalla-Favera, S. Floquet, G. Bernardinelli, C. Piguet, *Angew. Chem.* **2005**, *117*, 8168 – 8172; *Angew. Chem. Int. Ed.* **2005**, *44*, 7954 – 7958.
[20] Figures have been prepared with MOLMOL: R. Koradi, M. Billeter, K. Wüthrich, *J. Mol. Graphics* **1996**, *14*, 51 – 55.

CGC
Chemical Genomics Centre

The **Max Planck Society** together with **Merck KGaA, N.V. Organon and Schering AG** plans to appoint an

Independent Junior Group Leader in Organic/Bioorganic Chemistry

for the newly established **Chemical Genomics Centre** of the **Max Planck Society.**

The successful candidate should have a strong background in organic chemistry, chemical biology or a related area as proven by an excellent publication record. Junior Group Leaders are usually younger than 35 years old and hold an advanced degree with at least one year post-doctoral experience. The contract is for a group leader at the Junior- or Associate Professor level (up to W2 scale) and is limited to 5 years, starting in the summer of 2006. Funding will be provided in collaboration with Merck, Organon and Schering. Support for laboratory personnel, consumables and equipment will also be provided.

The Chemical Genomics Centre includes groups from six Max Planck Institutes and is designed to develop and apply the approaches of Chemical Genetics to biological systems. The junior group will focus its research activities on organic synthesis, compound library design or lead identification related to a current topic of chemical biology (especially protein-protein interactions or new approaches of kinase inhibition). The junior group will be located in laboratories in the newly established Biologisch-Medizinisches Zentrum Dortmund in the immediate vicinity of the Max-Planck-Institut für molekulare Physiologie.

Applicants considered for the position are expected to participate in a symposium in Dortmund on **May 31st**, **2006.**

The Max Planck Society is committed to employ more disabled persons. The application of disabled persons is strongly encouraged. The Max Planck Society is committed to increase the number of female scientists. Women are particularly encouraged to apply.

Applications including c.v., publication list, a research proposal and two letters of recommendation should be sent to **Sabine Arndt, Chemical Genomics Centre of the Max Planck Society, Otto-Hahn-Str. 15, D–44227 Dortmund, e-mail: Sabine.Arndt@cgc.mpg.de**, before **May 3rd, 2006.** For further information see **www.cgc.mpg.de.**

BAYERISCHE JULIUS-MAXIMILIANS-UNIVERSITÄT WÜRZBURG

Research Training School (DFG Graduiertenkolleg 1221)

Control of Electronic Properties of Aggregated π-Conjugated Molecules

Open Post-Doc and Ph.D. positions

Within the *Research Training School* several post-doc and Ph.D. positions are available.
Candidates for the **Post-Doc positions** shall possess experience in either

a) scanning tunnelling microscopy/spectroscopy (STM/STS) of organic adsorbates on graphite or gold surfaces or
b) in the synthesis and physicochemical characterisation of functional π-electron systems or
c) in method development in quantum chemistry or quantum dynamics.

Candidates for the **Ph.D. positions** shall be interested in an interdisciplinary research work placed between synthesis, spectroscopy and theory. Detailed project descriptions can be viewed at the *Research Training School homepage* http://www.grk1221.de
The Post-Doc positions are limited to two years and the Ph.D. positions to three years. Salary is BATIIa (Post-Doc) and BATIIa/2 (Ph. D. positions)

The University of Würzburg give preference to disabled candidates having the same qualifications as their competitors.

For all positions: Please send applications (CV, diploma or equivalent certificates, list of publications, two names of referees) to the coordinator, Prof. Dr. B. Engels, Institute of Organic Chemistry, University of Würzburg, Am Hubland, D-97074 Würzburg, Germany

 © 2006 Wiley-VCH Verlag GmbH & Co. KGaA, Weinheim

DOI: 10.1002/anie.200503277

Tetracyanoethylene

Tetracyanoethylene (TCNE): The Characteristic Geometries and Vibrational Absorptions of Its Numerous Structures

*Joel S. Miller**

Keywords:
electron transfer · IR spectroscopy · structure elucidation · structure–property relationships · tetracyanoethylene

Dedicated to Eugene E. van Tamelen on the occasion of his 80th birthday

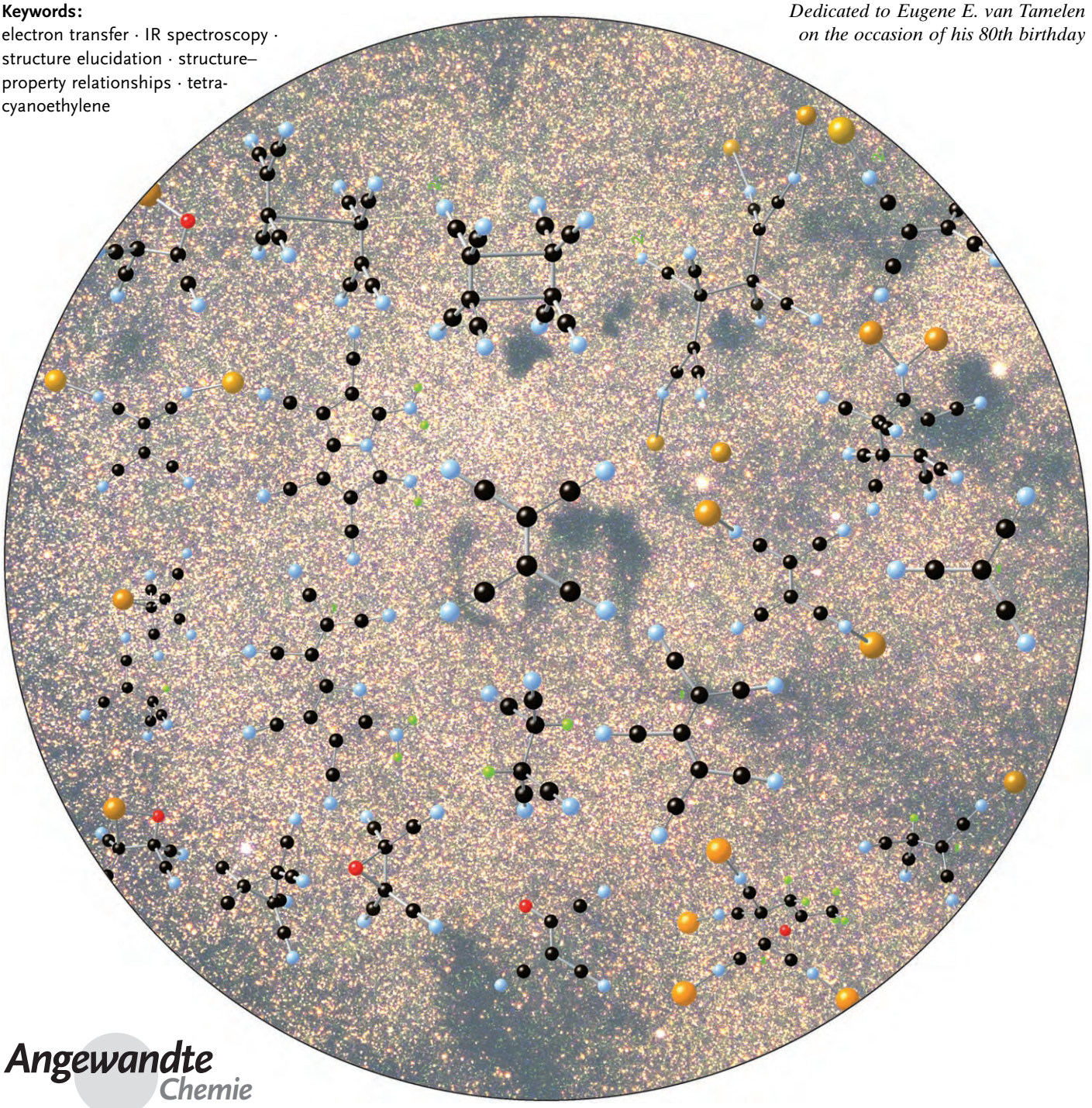

© 2006 Wiley-VCH Verlag GmbH & Co. KGaA, Weinheim

Tetracyanoethylene (TCNE) undergoes numerous reactions and is reported to exist in many structural motifs. Identification of these forms and motifs can be challenging. Nonetheless, the number of $\tilde{\nu}_{CN}$ absorptions and their frequencies provide insight with respect to the specific forms and charge on the TCNE fragment. Particularly informative is the average of the fundamental $\tilde{\nu}_{CN}$ bands, as well as the length of the central C–C bond. This Review discusses the assignment of structure and formal charge for TCNE-containing compounds. Scrutiny of previous assignments reveals some discrepancies which are discussed, and provides a basis for further study of TCNE structure–function relationships. Several multimetal complexes with bridging $[TCNE]^z$ units exhibit mixed valency and extensive delocalization. The scarcity of suitable model compounds, especially those with $M_{d_{\pi}\rightarrow\pi^*}$ backbonding to the CN groups, have thwarted the detailed description of these valence ambiguous compounds; thus, new well-characterized polynuclear compounds are needed.

From the Contents

1. Introduction	2509
2. Reactions of TCNE	2509
3. Bond Lengths and Angles and Infrared Absorptions	2512
4. Discussion	2519
5. Conclusion and Outlook	2522

1. Introduction

Tetracyanoethylene (TCNE; **1**) is one of the most versatile organic compounds as it is used in a many different

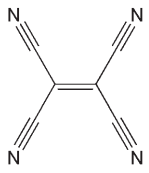

1

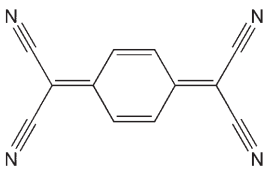

2

of reactions,[1] and in 2007 will be celebrating its Golden Jubilee. The versatility arises from a combination of it being a good dienophile, possessing good leaving groups, and its ease of both oxidation and reduction in addition to it being a good ligand with many modes available for coordination to a metal ion or ions. Furthermore, it has a high electron affinity enabling facile and reversible reduction to form its radical anion and dianion, which have been crystallographically characterized. The ability to accept one or two electrons to form simple anions in conjunction with its ability to bond to as many as four metal ions, leads to the formation of mixed-valence complexes and the classification of TCNE as a "non-innocent" ligand.[2,3] In recognition of the numerous studies using TCNE as an electron acceptor, it has been termed the "*E. coli*" of electron-transfer chemistry.[4]

TCNE was first synthesized at E. I. du Pont de Nemours and Co. in 1957 by the copper-catalyzed thermolysis of dibromomalononitrile, which itself was made from the bromination of malononitrile.[5] It was the first of a series of cyanocarbons, and is the predecessor of 7,7,8,8-tetracyano-*p*-quinodimethane (TCNQ; **2**), among numerous others.[6] The reactivity of TCNE is summarized in Scheme 1.

2. Reactions of TCNE

Reaction of TCNE (**1**) with mercaptoacetic acid or dihydrogen forms H_2TCNE (H_2**1**),[7] a strong acid ($pK_a = 3.6$[8]), while reaction with cyanoform, $HC(CN)_3$, leads to the isolation of hexacyanoethane, $(NC)_3C{-}C(CN)_3$,[9] which is unstable and not crystallographically characterized. TCNE can also lose CN^-,[10] or form Diels–Alder adducts, which resemble H_2TCNE with sp^3-hybridized central carbons, however, they contain the *cis*-$C(CN)_2C(CN)_2$- fragment **3**. The *trans*-conformation (**4**), in addition to being observed for H_2**1**, is observed for the $[TCNQ]_2^{2-}$ σ-dimer,[11] $[C_{12}N_{12}]^{2-}$,[12] and $[C_4(CN)_8]^{2-}$.[13]

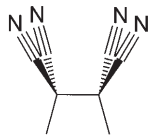

3

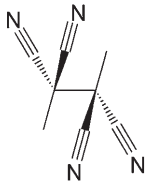

4

TCNE reacts with water in basic solution to form pentacyanopropenide, $[C_3(CN)_5]^-$ (**5**) [Eq. (1); B = base],

$$\underset{\mathbf{1}}{2\,\mathrm{TCNE}} + 2\,H_2O + B \rightarrow \underset{\mathbf{5}}{[C_3(CN)_5]^-} + HB^+ + CO_2 + 3\,HCN \quad (1)$$

and in neutral or acidic solution to form tricyanoethanolate, $[C_2(CN)_3O]^-$ (**6**) [Eq. (2)].[14,15] Furthermore, in the presence

$$\underset{\mathbf{1}}{\mathrm{TCNE}} + H_2O \rightarrow \underset{\mathbf{6}}{[C_2(CN)_3O]^-} + HCN + H^+ \quad (2)$$

[*] Prof. J. S. Miller
Department of Chemistry
University of Utah
Salt Lake City, UT 84112-0850 (USA)
Fax: (+1) 801-581-8433
E-mail: jsmiller@chem.utah.edu

© 2006 Wiley-VCH Verlag GmbH & Co. KGaA, Weinheim

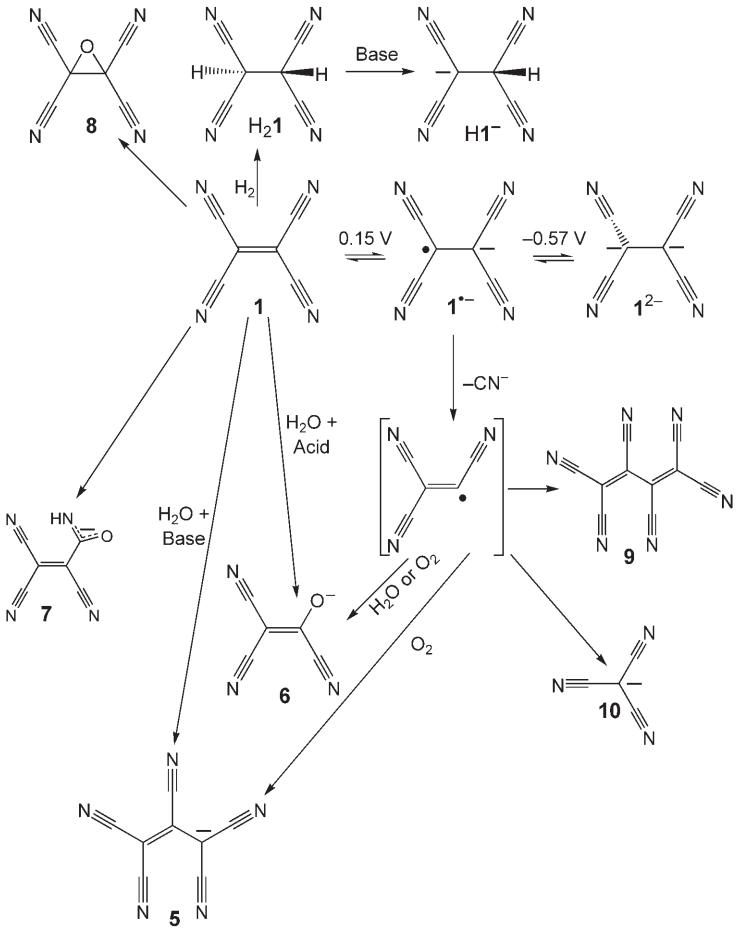

Scheme 1. Oxidation, reduction, and acid-base reactions of TCNE.

of a metal ion 2,3,3-tricyanoacrylamidate, $[(NC)_2C{=}C(CN)\text{-}(CONH)]^-$ (**7**) [Eq. (3)] can also form.[16] The reaction of

$$\underset{\mathbf{1}}{TCNE} + H_2O \rightarrow \underset{\mathbf{7}}{[(NC)_2C{=}C(CN)(CONH)]^-} + H^+ \qquad (3)$$

hydrogen peroxide and TCNE forms the epoxide, TCNEO (**8**),[17] as illustrated in Scheme 1. Numerous physical properties of TCNE are well documented.[18]

Joel S. Miller obtained his PhD from UCLA, and after being a Postdoctoral Associate at Stanford University and several positions with Xerox and Du Pont, he joined the University of Utah where he is now a Distinguished Professor in the Department of Chemistry. He was the recipient of the 2000 American Chemical Society's Chemistry of Materials Award for his discoveries in the area of organic-based magnets. His research focuses upon the preparation of organic-based magnets and the investigation of long carbon–carbon bonds. He is currently on the Advisory Boards of Chem. Eur. J. and Adv. Mater.

The utility of TCNE was significantly expanded when, in 1960, its radical anion, $[TCNE]^{\bullet-}$ ($\mathbf{1}^{\bullet-}$), was found to be stable and characterized.[19] Reduction of TCNE with, for example, iodide or cyanide, forms $[TCNE]^{\bullet-}$, which has been isolated as numerous salts. $[TCNE]^{\bullet-}$ can be further reversibly reduced to form the stable dianion, $[TCNE]^{2-}$ ($\mathbf{1}^{2-}$), which unlike planar (D_{2h}) **1** and $\mathbf{1}^{\bullet-}$, can adopt a twisted D_{2d} structure. The reversible one-electron reduction potentials for TCNE are: $E^{o}_{1/2}$ {0/1−} = 0.15 V, and $E^{o}_{1/2}$ {1−/2−} = −0.57 V (vs. saturated calomel electrode (SCE) in MeCN).[20] In the presence of dry oxygen, $\mathbf{1}^{\bullet-}$ forms both **5**, and **6**, by elusive mechanisms. However, upon reaction with water $\mathbf{1}^{\bullet-}$ only forms **6**.[19c]

The chemistry of $[TCNE]^{\bullet-}$ is richer than that for TCNE, as $[TCNE]^{\bullet-}$ can lose CN^- forming the $[C_2(CN)_3]^{\bullet}$ intermediate, which can dimerize to hexacyanobutadiene (**9**), or form tricyanomethanide, $[C(CN)_3]^-$ (**10**), or **5**, again by unknown mechanisms (Scheme 1). Compound **6** has also been reported to form from the reaction of TCNEO (**8**) and, for example, $[Pt^0(AsPh_3)_4]$, which additionally can form **11** with the *cis*-$C(CN)_2C(CN)_2$- linkage **3** ($\tilde{\nu}_{CN} = 2220\ cm^{-1}$; $\tilde{\nu}_{CO} = 1072\ cm^{-1}$).[21]

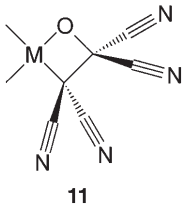

The reaction of Na_2TCNE with $SiMe_3Cl$ and water forms $[C_{11}N_7H_2]^-$ (**12**; Scheme 2), that has been isolated as the Na^+ and $[AsPh_4]^+$ salts (with $\tilde{\nu}_{CN} = 2210$ and 2202 cm^{-1}, and 2221 cm^{-1}, respectively).[22] Compound **12** is a chelating ligand and several $[M(\mathbf{12})_2]$ complexes have been characterized, while acidification forms H**12** ($\tilde{\nu}_{CN} = 2233\ cm^{-1}$).

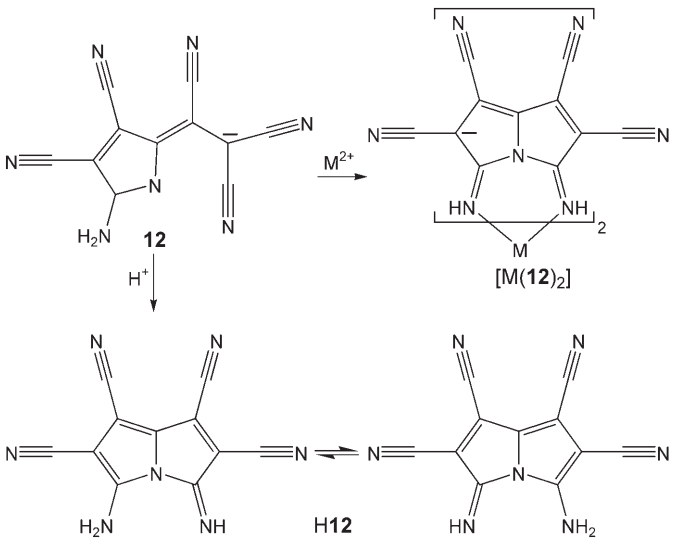

Scheme 2. Formation of **12**, and its reaction chemistry.

Additionally, the cofacial π-$[TCNE]_2^{2-}$ dimer **13** possessing exceptionally long 2.9 Å two-electron–4-center (2e-4c) C–C single bonds has been characterized.[23] The π-$[TCNE]_2^{2-}$ dimer **13a** has also been observed as *trans*-μ- (**13b**),[66a] *cis*-μ- (**13c**), and *trans*-μ_4-$[TCNE]_2^{2-}$ (**13d**)[66b] in which there is no significant change in the C–C bond lengths and the C-C-C

 © 2006 Wiley-VCH Verlag GmbH & Co. KGaA, Weinheim

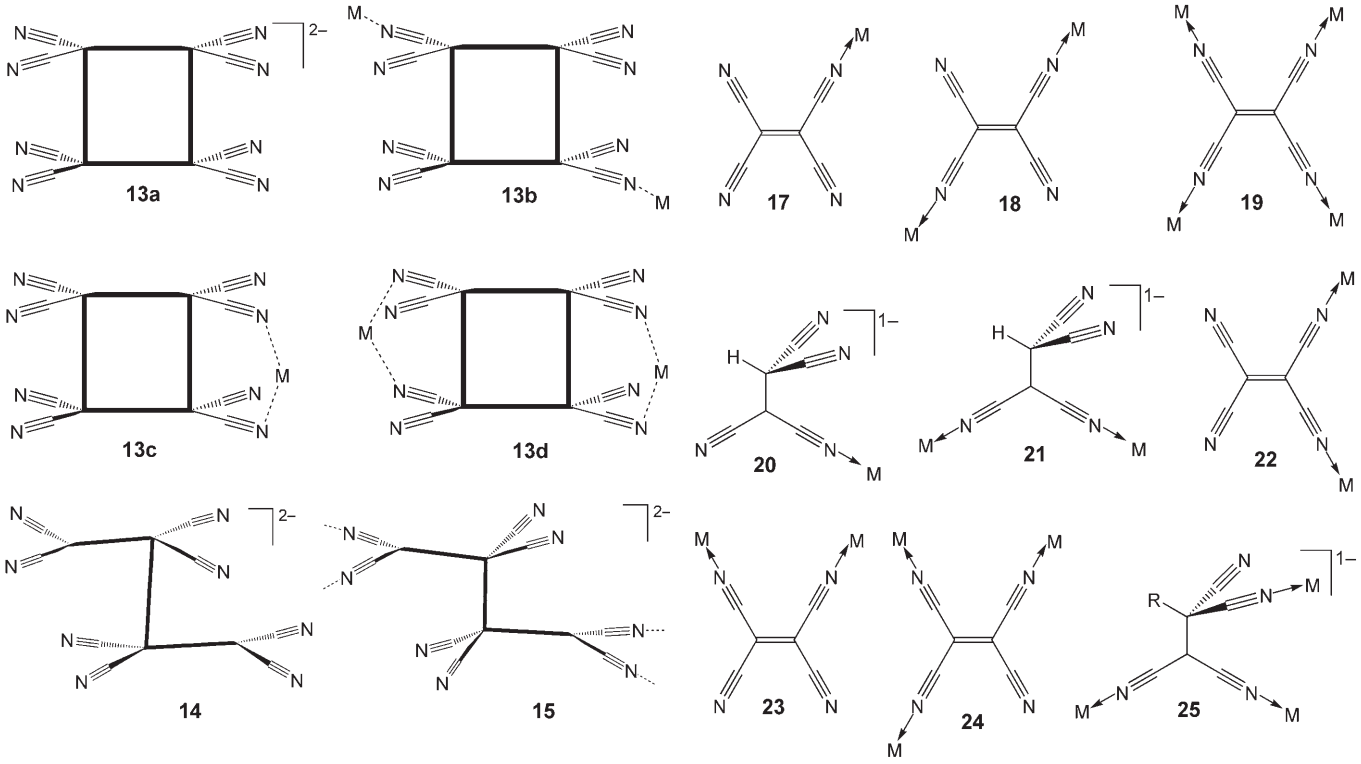

Scheme 3. Transition metal (M) complexes based upon TCNE and reaction products possessing the $C_2(CN)_4$ fragment.

angles (see Table 1) with the exception that the central C–C distances are a bit shorter for **13b,d**.

While seventeen examples of **13** have been reported, a slipped conformation π-$[TCNE]_2^{2-}$ (**14**) has also been reported for $[TTF]^+_2[TCNE]_2^{2-}$ (TTF = tetrathiafulvalene).[24] The σ-dimer, $[C_4(CN)_8]^{2-}$ (**15**) has also been isolated bridging to four M^{II} ions (M = Mn, Fe).[13a]

Reaction of TCNE with $[Pt_3(Ph_2PCH_2PPh_2)_2(CNmes)_2]^{2+}$ (mes = 2,4,6-mesityl) forms the nitrene **16a** ($\tilde{\nu}_{CN}$ = 2188 cm^{-1}),[25a] based upon addition of two TCNEs. Similarly, the reaction of PPh_3 and two TCNEs forms the ylid **16b** ($\tilde{\nu}_{CN}$ = 2201 cm^{-1}).[25b]

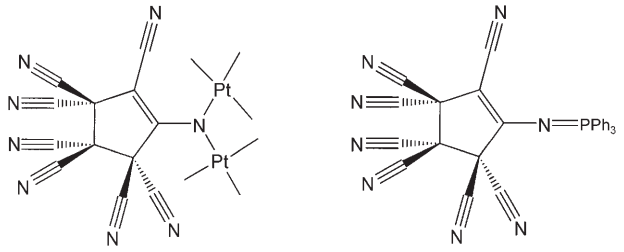

$[TCNE]^z$ ($z = 0, 1-, 2-$) can undergo many reactions with transition metals to form many compounds that range from having the $[TCNE]^z$ moiety as a ligand, to more complex reactions that lead to a ligand possessing the TCNE fragment (Scheme 2 and Scheme 3). For example, TCNE can be a σ-donor ligand and bond to the metal through the lone pair of electrons on the nitrile nitrogen atom (**17**), and can also bridge by μ- and μ_4-TCNE bonding (**18** and **19**, respectively). $[TCNE]^{\bullet-}$ can also form σ bonds (**17**$^{\bullet-}$) and μ bonds (**18**$^{\bullet-}$). $[HTCNE]^-$ has also been reported to form a σ bond (**20**) as well as *cis*-1,1′ bonding (**21**), and other isomers can be envisioned. Compound **22** has been reported for $[Rh_2(O_2CMe)_4(TCNE)]$·benzene,[26a] but because of disorder the structure is too poorly refined to get reliable metric parameters.

Trans-μ-$TCNE^0$ (**18**) bridging has been reported for $[M^{II}(hfac)_2TCNE]$ [27] (hfac = hexafluoracetyacetonate; M = Co, Cu), $[Rh^{II}_2(O_2CMe)_4(TCNE)]$·benzene·xylene[26a] and $[\{Mo^{II}_2(O_2CCF_3)_4\}(TCNE)]$,[26b] and μ_4-TCNE (**19**) has been reported for $[\{Rh^{II}_2(O_2CCF_3)_4\}_2(TCNE)(C_6H_6)_2]$,[28] but the

 © 2006 Wiley-VCH Verlag GmbH & Co. KGaA, Weinheim

structures of the carboxylates are too poor in quality to obtain meaningful metric parameters.

While yet to be reported, 1,2-μ-TCNE (**23**) and μ_3-TCNE (**24**) bridge bonding are anticipated, μ_3- and μ_4-bridging has been noted for $[RTCNE]^-$ (**25** and **26**, respectively). The $[C_4(CN)_8]^{2-}$ σ-dimer (**15**) of $[TCNE]^{\bullet-}$, has been reported to be stabilized by μ_4-bridging to four divalent or trivalent cations,[13] but not with monovalent cations. In addition, TCNE is also a good π-donor ligand and can bond to a metal across the central C–C bond forming η^2-TCNE (**27**). The latter bonding motif is prevalent for later transition metals.

Herein the TCNE bond lengths and angles as well as the $\tilde{\nu}_{CN}$ and $\tilde{\nu}_{CC}$ values are compiled, summarized, and reviewed with the purpose of providing a basis for analysis of the numerous reaction products involving TCNE and selected structural derivatives. There are many theoretical analyses of the structural parameters and vibrational features of TCNE-based materials; they are not discussed herein, but are available.[23,29,30]

3. Bond Lengths and Angles and Infrared Absorptions

Each TCNE-based structure has characteristic structural features, which are diagnostic for the different bonding modes and are summarized in Table 1. The most reliable interatomic distances and angles are obtained from neutron diffraction studies, and the average distances and angles determined in this manner are summarized for TCNE (**1**), TCNEO (**8**), H_2TCNE (H_2**1**), $[TCNE]^{\bullet-}$ (**1**$^{\bullet-}$), and $[TCNE]_2^{2-}$ (**13a**) in Table 2. The $\tilde{\nu}_{CN}$ values, which are also typical of for different bonding modes are listed in Table 3. Table 4 and Table 5 list characteristic $\tilde{\nu}_{CN}$ values of the fragment products that may form from the reaction of TCNE; and where available the $\tilde{\nu}_{CC}$ values are given in Table 3.

3.1. Bond Lengths and Angles

The bond lengths and angles in Table 1 are compiled from either the original publications and/or Cambridge Crystal Database (the CCDC codes are listed in Table 1), as well as in a few cases some unpublished structures from our laboratory, or from recent publications. As a consequence of, for example, poor crystallinity and disorder, some structures are of better quality than others. Hence, for comparative purposes, not only are the reported distances and angles provided, but also the reported estimated standard deviations (esds) are included. The central C–C distance is noted as reported, but in cases with more than one unique TCNE species present in the unit cell, each central C–C distance is reported separately with their esds, averaged values are not given. In contrast, the tabulated C–CN distances as well as NC-C-CN angles (if not unique) are the average for each form of TCNE within the structure, and the highest esd associated with the individual distance or angle is noted.

In Table 1 the range of values for the key distances and angles for each structural form of $[TCNE]^z$ are reported along with an average value obtained from the most precise determination(s). The number of identical structures for each motif is tabulated in the "No." column. For example, there are three reported structures for H_2TCNE (H_2**1**) in addition to one determined by neutron diffraction. Thus "3" is listed in the "No." column because the results from the neutron diffraction studies are reported in Table 2, but are excluded from Table 1. The average data for H_2**1** is listed in Table 1, as each structure was of good quality. For purposes of this summary of the data, good quality simply reflects low esds, at least with respect to related structures for a specific motif. For example, thirteen structures possessing **1**$^{\bullet-}$ have been reported. Six have esds of 0.01 Å, and one has an esd of 0.009 for the C–C bond, and one does not have any reported esds. Of the remaining five structural determinations, two had an esd of 0.006, two of 0.005, and one with 0.004 Å. For averaging purposes only the metric parameters for these latter five structures are included, and 5 is listed in the "No." column. The standard deviation for these five numbers is also reported. Some motifs have only a few reported crystallographically characterized examples, which may have relatively high esds when compared with other motifs, but they are included.

3.1.1. Bond Lengths

The observed central C–C distances have a substantially larger range than the C–CN distances. These C–C distances range from 1.285(8)[31] to 1.641(5) Å, which is 24% with respect to the average, while the C–CN distances range from 1.382(6) to 1.478(13) Å, which is 13% with respect to the average. The C≡N distances do not show any significant changes, and are not reported. The large variation of the central C–C distances is a consequence of the change in bond order (BO), as upon reduction from TCNE to $[TCNE]^{2-}$ the BO decreases from two to one. As a consequence, the central C–C distance is the most diagnostic with respect to form and oxidation state of the TCNE.

TCNE^0: Neutral TCNE, as expected, has the shortest central C–C bond of 1.349(6) Å in accord with its BO of two. Formation of donor(Do)–acceptor complexes with TCNE, Do·TCNE, has been well studied with 23 crystallographically determined examples with esds less than 0.01 Å. Donor–acceptor charge-transfer complexes while having some electron density transferred from the donor to the acceptor do not have electron transfer, unlike electron-transfer salts (sometimes called charge-transfer salts). Hence, from a broad perspective Do·TCNE species are considered neutral compounds. The average central C–C distance for these compounds is 1.337(24) Å, which indicates that there is no significant change in the TCNE structure upon forming Do·TCNE compounds.

Likewise, the central C–C distance for $TCNE^0$ is not altered upon bonding to a metal ion or on bridging between two or four metal ions, with average distances of 1.36(1)[32] 1.347(7),[27] and 1.31(1) Å[28], respectively, for each set of structures (Table 1). Note that the former and latter are relatively poor, disordered structures. Likewise, the sole structure reporting μ_4-TCNE is relatively poor, but its central

 © 2006 Wiley-VCH Verlag GmbH & Co. KGaA, Weinheim

Table 1: Summary of the ranges and average C–C and C–CN distances, and NC-C-CN angles including esds for structurally characterized forms of $[TCNE]^z$ ($z = 0, 1-, 2-$).

TCNE form		No.[a]	C-C [Å]	C-CN [Å]	C-CNM [Å]	C-C-C [°]	MNC-C-C [°]	MNC-C-CNM [°]	C-CR-C [°]	CCDC-Code
$TCNE^0$	**1**	3	1.349(6) [1.344(3)–1.355(2)]	1.435(4) [1.431(1)–1.438(2)]		116.5(12) [115.6(2)–117.8(1)]				TCYETY01;TCYETY02;TCYETY03
TCNE in Do^0·$TCNE^0$	Do·**1**	23	1.337(24) [1.285(8)[31]–1.371(3)]	1.443(14) [1.425(9)–1.484(6)]		118.0(16) [113.0(4)–124.1(4)]				COMHIV;COMHOB;ETCZCE;PACTCN10;PYRCYE02.03;RAYLOS;HORXUH;HORYES;SAMTEF;SISNIR;SKATCE10;MIKTEF;NITRIR;NITRIR01;TEWKOV;VIFFEV;WIGPIL;WUDQAN;XIBGAQ;DIRKIY;YARNAG
σ-$[TCNE]^0$	**17**	2	1.36(1) [1.35(1)–1.37(1)]	1.435(5) [1.43(1)–1.44(1)]	1.43(1) [1.43(1)–1.43(1)]	117.6(5) [117.1(9)–118.2(9)]	118.6(7) [117.9(8)–119.3(8)]			NUYKUN
μ-$[TCNE]^0$	**18**	3	1.347(7) [1.339(5)–1.352(5)]	1.429(9) [1.421(5)–1.438(4)]	1.442(1) [1.441(4)–1.443(4)]		120.1(11) [119.4(3)–121.4(2)]			JOWFEG;JOWFIK; [88b]
μ_4-$[TCNE]^0$	**19**	1	1.31(1)		1.45(1)					YAVVEW
η^2-$TCNE^0$	**27**	10	1.484(19) [1.457(4)–1.512(7)]	1.440(4) [1.434(7)–1.447(8)]		114.4(1) [112.9(5)–116.7(2)]				PUNJUD;BUCNIT10;KAJGUX;MACGIH;NATDAN;NATDIV;NATDOB;QEQHID;ZOYROU
$[TCNE]^{\bullet-}$	**1**$^{\bullet-}$	5	1.394(11) [1.385(6)–1.413(5)]	1.430(12) [1.414(6)–1.445(6)]		118.7(8) [117.9(4)–120.1(4)]				ARDOV;LIBBED;LILVOR;SEJHIY;YAZPIY
σ-$[TCNE]^{\bullet-}$	**17**$^{\bullet-}$	1	1.38(1)	1.44(1)	1.41(1)	116.9[b]	118.2[b]			KATJOE
μ-$[TCNE]^{\bullet-}$	**18**$^{\bullet-}$	17	1.413(10) [1.395(7)–1.425(7)]	1.415(7) [1.396(5)–1.430(5)]	1.409(9) [1.392(5)–1.420(7)]		118.6(8) [117.6(3)–120.2(4)]			MIJYUZ;PILBAN;QIVCED;SAQGUM01;UCIQAY;UCIQEC;UCIQEC;UCIQIG;UCIRAZ;VANDOD;VANFAR;XARCOI;XARCUO;YAGJIZ;YAZPEU[a]
$[TCNE]_2^{2-}$	**13a**	8	1.425(15)[b] [1.408(5)–1.452(6)]	1.421(14) [1.402(7)–1.450(3)]		118.3(8) [117.3(1)–120.0(4)]				MEYEE;KAXLEA;KUGHUP;ODAFAA;XIDVEL;XOKZIG
trans-μ-$[TCNE]_2^{2-}$	*trans*-μ-**13** (**13b**)	1	1.397(5)[c]	1.432(4)	1.430(4)	119.7(3)	118.2(4)			YAZNUI
cis-μ-$[TCNE]_2^{2-}$	*cis*-μ-**13** (**13c**)	1	1.423(4) [1.419(4)–1.428(4)]	1.419(2) [1.416(5)–1.422(5)]	1.408(4) [1.401(5)–1.412(5)]	117.6(12) [116.0(1)–118.6(3)]	118.2(9) [117.4(3)–119.1(3)]			[66b]
trans-μ_4-$[TCNE]_2^{2-}$	*trans*-μ_4-**13** (**13d**)	1	1.409(12)	1.435(14)	1.403(13)		118.1(8)			[66b]
$[TCNE]_2^{2-}$	**14**	1	1.397(3)[d]	1.426(3)		119.3(3)				RIFQAY,01
$[TCNE]^{2-}$	**1**$^{2-}$	1	1.488(4)	1.399(5)		117.4(3)				TUQXUY
μ-$[TCNE]^{2-}$	μ-**1**$^{2-}$	1	1.478(8)	1.417(9)	1.371(9)		118.8(6)			SUGTUJ
H_2TCNE	H_2**1**	3	1.563(2) [1.561(3)–1.565(1)]	1.470(4) [1.466(1)–1.474(2)]					110.9(2) [110.7(1)–111.1(1)]	BUGKIX.02,04
TCNEO	**8**	1	1.496(2)	1.450(1)		117.1(1)				TCYNEO
$TCNECR_2$	**28**	5	1.552(8) [1.542(3)–1.561(4)]	1.449(3) [1.445(2)–1.453(2)]		114.5(12) [112.6(2)–115.5(3)]				TCYCPR,TCYCPR10,TCMPCP10, RiMCAR
-$[C_2(CN)_4]$-Diels–Alder	**3**	5	1.597(7) [1.589(6)–1.605(5)]	1.466(5) [1.458(7)–1.471(5)]		110.7(24) [108.2(3)–114.0(5)]				TCBCUT10,BCYCDO,VILREN,CTCBCU10,CEZCOZ
$R_2[C_4(CN)_8]$, $[TCNQ]_2^{2-}$	**4**	4	1.635(8) [1.626(6)–1.641(5)]	1.482(5) [1.475(7)–1.488(5)]		108.6(1) [107.3(2)–109.7(2)]				EPZTCD;GAXYEJ;OBAPUC[e]
μ_4-$[C_4(CN)_8]^{2-}$	**4,15**	2	1.585(54) [1.508(9)–1.627(9)]	1.497(15) [1.487(11)–1.508(9)]	1.391(3) [1.389(7)–1.393(11)]			118.5(3) [118.2(6)–118.7(4)]	106.3(10) [105.6(5)–107.0(6)]	NUHGIG;NUHGOM
σ-$[HTCNE]^-$	**20**	1	1.511(12)	1.397(13)	1.394(13)		119.8(8)		109.3(9)	IRTCPP10
μ-$[HTCNE]^-$	μ-H**1**$^-$, **21**	1	1.479(9)	1.478(13)	1.399(9)			116.7(5)	108.2(5)	BOQYIP
μ_3-$[RTCNE]^-$	**25**	1	1.536(6)		1.388(6)			120.6(4)	107.4(4)	NACVOC
μ_4-$[RTCNE]^-$	**26**	1	1.514(7)		1.382(6)			118.2(5)	106.0(5)	NACVUI

[a] See text. [b] The intradimer C–C distance for the eight reported structures with esds ≤ 0.006 Å range from 2.800(2) to 2.961(2) Å and average 2.874(55) Å. [c] The intradimer C–C distance is 2.920(5) Å. [d] The intradimer C–C distance for the two reported structures (esds ≤ 0.01 Å) are in the range 3.475(10) to 3.522(3) Å and average 3.50(3) Å. [e] J. S. Miller, unpublished results.

© 2006 Wiley-VCH Verlag GmbH & Co. KGaA, Weinheim

Table 2: Summary of the average C–C, C≡N, and C–CN distances, and NC-C-CN and NC-C-C(CN)$_2$ angles for TCNE (**1**), TCNEO (**8**), H_2TCNE (H_2**1**), $[TCNE]^{\bullet-}$ ($\mathbf{1}^{\bullet-}$), and $[TCNE]_2^{2-}$ (**13**) determined by neutron diffraction.

	T [K]	C-C [Å]	C≡N [Å]	C-CN [Å]	NC-C-CN [°]	NC-C-C(CN)$_2$ [°]	Ref.
TCNE, **1** (monoclinic)	298	1.354(1)	1.146(1)	1.426(1)	117.82(6)	121.09(7)	[100a]
TCNE, **1** (cubic)	298	1.344(3)	1.153(2)	1.439(2)	115.6(1)	122.2(1)	[100b]
H_2TCNE, H_2**1**	158	1.553(1)	1.146(1)	1.466(1)	111.1(1)	110.25(10)	[101]
TCNEO, **8**	298	1.493(3)	1.136(2)	1.446(2)	116.8(1)	118.0(1)	[102]
$[TCNE]^{\bullet-}$, $\mathbf{1}^{\bullet-}$	10	1.429[a]	1.171[a]	1.405[a]	118.6[a]	120.7[a]	[33]
$[TCNE]_2^{2-}$, **13**	50	1.423(4)[b]	1.154(4)	1.411(4)	118.1(2)	120.4(3)	[103]

[a] Esd not reported and unavailable. [b] The intradimer C–C distance is 2.801(1) Å.

C–C distance of 1.31(1) Å[28] is in accord with the other forms of $TCNE^0$. Hence, although data for $TCNE^0$–metal complexes are scare, and of relatively low precision, these central C–C bond lengths are in good agreement with the general criteria set out above for other forms of $TCNE^0$.

[TCNE]$^{\bullet-}$: The monoanion of TCNE is structurally observed in several forms; namely, $[TCNE]^{\bullet-}$ ($\mathbf{1}^{\bullet-}$), σ-$[TCNE]^{\bullet-}$ ($\mathbf{17}^{\bullet-}$), μ-$[TCNE]^{\bullet-}$ ($\mathbf{18}^{\bullet-}$), π-$[TCNE]_2^{2-}$ (**13**, **14**), and σ-$[TCNE]_2^{2-}$, μ_4-$[C_4(CN)_8]^{2-}$ (**15**). The central C–C distance for isolated $\mathbf{1}^{\bullet-}$ ranges from 1.385(6) to 1.413(5) Å for the five higher quality structures that have been reported, and average 1.394(11) Å. These data are depicted in Figure 1, and while the four lower values agree well amongst themselves, the longer 1.413(4) Å value is distinctly at variance to the four other values. This situation makes this determination suspect; however, this compound was also structurally characterized by neutron diffraction and the value is accord with the 1.429 Å determined by this independent method.[33] Hence, the types of cation can play a significant role in $[TCNE]^{\bullet-}$ structures.

The central C–C distance is maintained upon coordination of one $[TCNE]^{\bullet-}$ nitrile to a metal ion (σ-$\mathbf{17}^{\bullet-}$) in the only structure of this type that has been reported, note though that it has a relatively large esd of 0.01 Å. *Trans*-μ-bridging $[TCNE]^{\bullet-}$ between two metal ions ($\mathbf{18}^{\bullet-}$) is more prevalent and the central C–C bond slightly lengthens to 1.413(10) Å for the 17 structurally characterized examples with esd ≤ 0.009 Å. The π-$[TCNE]_2^{2-}$ dimer **13a** has an incrementally longer central C–C bond of 1.425(15) Å. The central C–C distance for μ-$[TCNE]^{\bullet-}$ ($\mathbf{18}^{\bullet-}$) is 1.4% greater than for $[TCNE]^{\bullet-}$, while it is 2.2% greater for π-$[TCNE]_2^{2-}$ (**13**) than for $[TCNE]^{\bullet-}$. While this trend is evident, upon consideration of the associated esds, the lengthening of the central C–C bond in the sequence π-$[TCNE]_2^{2-}$ > μ-$[TCNE]^{\bullet-}$ > $[TCNE]^{\bullet-}$ is less definitive, but supported by analysis of the $\tilde{\nu}_{CC}$ vibrational data (see Section 4).

The σ-$[TCNE]_2^{2-}$ dimer, octacyanobutanediide μ_4-$[C_4(CN)_8]^{2-}$, is especially unusual as it can be viewed a having two types of *trans*-$(NC)_2$C-C$(CN)_2$- (**4**) groups, namely, $[(NC)_2C\text{-}\{C(CN)_2\}_3]^{2-}$ and $[\{(NC)_4C_2\}\text{-}\{C_2(CN)_4\}]^{2-}$ in which the four terminal N atoms coordinate to M ions. The former has C–C distances of 1.615(10) (M = Mn), and 1.508(9) Å (M = Fe), while the latter has C–C distances of 1.59(1) (M = Mn), and 1.627(14) Å (M = Fe).[13a] Hence, for the purposes of the review all four C–C distance were averaged to 1.585(54) Å.

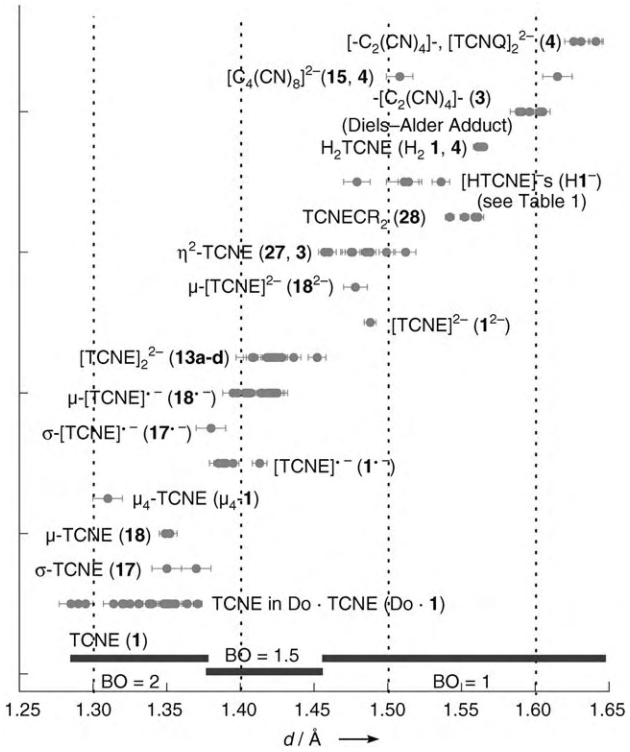

Figure 1. Central C–C distances (*d*), including one esd, for several TCNE-containing species. (BO = bond order of the central C–C bond.)

[TCNE]$^{2-}$: The dianion of TCNE, $[TCNE]^{2-}$ ($\mathbf{1}^{2-}$), has a longer central C–C distance of 1.488 (4) Å in accord with its further reduced bond order of one. Owing to the paucity of structures, insufficient information is available to make generalized trends about the behavior of the dianion when it is a ligand. Nonetheless, in the single example of it bridging to two metal ions, μ-$[TCNE]^{2-}$, the central C–C distance is not altered compared to the free dianion. This distance is comparable to that reported for tetracyanoethylene oxide, TCNEO (**8**; 1.496(2) Å), but is significantly shorter than the 1.563(2) Å observed for H_2TCNE (H_2**1**). $[TCNE]^{2-}$, unlike either $TCNE^0$ or $[TCNE]^{\bullet-}$, is not planar, as free rotation is possible owing to its bond order of one. The dihedral angle between the C$(CN)_2$ units of $[TCNE]^{2-}$ is 87.1° in the charge-transfer salt $[\{CoCp^*_2\}_2]^+[TCNE]^{2-}$[34a] ($Cp^* = C_5Me_5$), 76.6° in the salt $[TDAE]^{2+}[TCNE]^{2-}$[34b] [TDAE = tetrakis(dime-

 © 2006 Wiley-VCH Verlag GmbH & Co. KGaA, Weinheim

thylamino)ethylene], and 67.2° in the complex [{Ir^{I}(CO)-$(PPh_3)_2$}$_2$(TCNE)].[34c]

TCNE fragments in organic compounds: The central C–C distances for systems with -$(NC)_2$C-C$(CN)_2$- moieties, either *cis*- (**3**) or *trans*- (**4**), have been reported for many systems. The *cis*-$(NC)_2$C-C$(CN)_2$- (**3**) group in three membered rings with C, O, or M heteroatoms have also been reported. The epoxide, TCNEO (**8**), has a short central C–C bond (1.496(2) Å). Cyclopropanes, TCNECR$_2$ (**28**), have a longer central C–C bond that ranges from 1.542(3) to 1.561(4) Å (average = 1.552(8) Å), values which are approximately 0.04 Å shorter than those observed for four-membered ring Diels–Alder adducts, which average 1.597(7) Å. The metallocyclopropane, η^2-TCNE (**27**), which has ten structurally characterized examples with esds less than 0.008 Å, has an average central C–C distance of 1.484(19) Å, comparable to TCNEO, Figure 1.

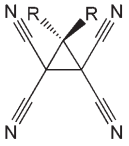

28

For either **3**, as occurs for Diels–Alder adducts, or **4**, as occurs for σ-dimers of $[TCNQ]_2^{2-}$ and $[TCNE]_2^{2-}$ {μ_4-$[C_4(CN)_8]^{2-}$}, the central C–C bond lengths are significantly longer than the often-quoted longest sp^3–sp^3 C–C bond of 1.54 Å reported for diamond. The average central C–C distances are 1.597(7), 1.635(8), and 1.585(54) for Diels–Alder adducts and σ-dimers of $[TCNQ]_2^{2-}$ and {μ_4-$[C_4(CN)_8]^{2-}$}, respectively. Likewise, the *cis*-$(NC)_2$C-C$(CN)_2$- bonds in **16** are also long as they average 1.585(30) and 1.544(30) Å for **16a** and **16b**, respectively. Hence, these central C–C distances exceed the long C–C distance observed of 1.563(2) Å for H_2**1**.

The central C–C distances for $[HTCNE]^-$ (H**1**$^-$) are shorter than those for H_2**1**, albeit for the few structurally characterized examples: σ-$[HTCNE]^-$ (**20**; 1.511(12) Å,[35] μ-$[HTCNE]^-$ (**21**; 1.479(9) Å),[36] μ_3-$[RTCNE]^-$ (**25**; 1.536(6) Å), and μ_4-$[RTCNE]^-$ (**26**; 1.514(7) Å when R = $CH_2C(O)Me$).[37] These values are in the range observed for η^2-$TCNE^0$ (**27**), and TCNECR$_2$ (**28**).

A summary of the central C–C distances including their associated esds as a function of TCNE-containing species is presented in Figure 1. Overall, when central C–C distances are $< \approx 1.38$ Å, it is attributed to $TCNE^0$ with a C=C bond (BO = 2). The C–C distances in the range of ≈1.38 to 1.46 Å, have a bond order of 1.5 characteristic of $[TCNE]^{\bullet -}$ or π-$[TCNE]_2^{2-}$ (**13**, **14**). Central C–C distances of 1.46 Å and greater are attributed to sp^3-hybridized central C–C single bonds (BO = 1), as observed for $[TCNE]^{2-}$ (**1**$^{2-}$), η^2-TCNE (**27**), $[HTCNE]^-$ (H**1**$^-$), H_2TCNE (H_2**1**), σ-$[TCNE]_2^{2-}$ (**15**), Diels–Alder adducts with TCNE, as well as σ-$[TCNQ]_2^{2-}$, Figure 1.

3.1.2. Bond Angles

The NC-C-CN bond angles can vary significantly for a specific form of TCNE. For example, for the 23 examples of Do·TCNE complexes summarized in Table 1 the NC-C-CN angle ranges from 113.0(4) to 121.4(4)°. This spread is a 7.1% deviation from the average of 118.0(16)°, and exceeds the deviation of an individual determination. The large differences are presumably due to the specific solid-state packing interactions, and as a consequence do not provide any meaningful information regarding the TCNE form. Likewise, bonding of one or more nitrile groups to a metal, that is, M-NC-C-CN or M-NC-C-CN-M, does not lead to a NC-C-CN angle that differs from the observed NC-C-CN angles. The C-CR-C angles range from 105.6(5) to 111.1(1)°, as expected for the formal sp^3 hybridization of the central carbon atom. For example, the σ-$[TCNE]_2^{2-}$ dimer μ_4-$[C_4(CN)_8]^{2-}$ (**15**) has average MNC-C-CNM angles of 118.5(3)° in accord with its sp^2 central carbon atom, and the internal NC-C-CN angle averages 106.3(10)° in accord with its sp^3 central carbon. The C-C≡N angles are essentially linear with minimal deviations as expected for the formal sp hybridization, and like the NC-C-CN angles are not discussed further.

3.2. Infrared Spectra

The infrared spectra $\tilde{\nu}_{CN}$ values, and where available those of the Raman $\tilde{\nu}_{CC}$ vibrations, listed in Table 3 are complied from either the original publications or unpublished results from our group. The $\tilde{\nu}_{CC}$ vibrations are typically not observed as they are IR forbidden. (For structures **13** and **14** the $\tilde{\nu}_{CC}$ vibration becomes IR allowed and is observed.) Although the $\tilde{\nu}_{CC}$ bands are Raman active, they are not routinely reported. Furthermore, as a consequence of different groups reporting data taken from different spectrometers, with different resolution as well as different standardizations, and under different conditions (solution or in the solid state (KBr, CsI, Nujol)), some data are of better quality than others. More importantly, weak IR-forbidden bands and shoulders of bands may or may not be reported. Intensity designations, weak (w), medium (m), strong (s), and very strong (vs) and identification of shoulders (sh) are, unfortunately, arbitrary and are spectrum dependent and are a source of confusion. For example, nitriles, are weak to medium $\tilde{\nu}_{CN}$ absorbers,[54] nonetheless, their $\tilde{\nu}_{CN}$ absorptions are frequently designated as strong (s). In contrast CO and in particular metal-bound CO groups are strong absorbers.[38a] Hence, for complexes with both metal-bound CO and nitriles, the $\tilde{\nu}_{CN}$ band may be is dwarfed by the $\tilde{\nu}_{CO}$ absorption, and while under other circumstances it might be labeled as medium (m) or strong (s), the relative intensity of the $\tilde{\nu}_{CO}$ absorption might perhaps lead to the labeling of the $\tilde{\nu}_{CN}$ band as weak (w). Furthermore, the intensity of the $\tilde{\nu}_{CN}$ absorptions for $[TCNE]^z$ increases as z becomes more negative, because the electronic dipole increases as z becomes more negative. As a consequence, the $\tilde{\nu}_{CN}$ bands for $TCNE^0$ are more than an order of magnitude weaker than those of $[TCNE]^{\bullet -}$ on a mole basis,[39a] as observed for $[(FeCpCp^*)_2(TCNE)_2TCNE^0]$·Solv (Solv = CH_2Cl_2, THF; Cp = C_5H_5).[39b] Hence, in general when data is reported, and we have independently obtained the data, we used our data, simply to minimize errors of interpretation. Figure 2 summarizes the $\tilde{\nu}_{CN}$ absorptions for the different TCNE-bases species, which have been unambiguously characterized.

© 2006 Wiley-VCH Verlag GmbH & Co. KGaA, Weinheim

Table 3: Summary of the $\tilde{\nu}_{CN}$ and $\tilde{\nu}_{CC}$ values for structurally characterized forms of TCNE.

TCNE form		$\tilde{\nu}_{CN}$ [cm^{-1}] (KBr or Nujol)	No. of peaks	Average $\tilde{\nu}_{CN}$ [cm^{-1}]	$\tilde{\nu}_{CC}$ [cm^{-1}]
TCNE	**1**	2262 (s);2228 (m); 2214 (w) (KBr); 2254 (s);2247 (m) (CH_2Cl_2)[b]	3	2235 2250	1570R[a][52]
TCNE in Do^0·TCNE^0	Do·**1**	2247(7) [2241–2261] 2222(3) [2218–2228] 2209(3) [2207–2214][88a]	3	2226	1565R[52]
σ-[TCNE]^0	**17**	[c]			[c]
μ-[TCNE]^0	**18**	2258[27]–2221 (w)[26b, 27, 88b]	2	2240	[c]
μ_4-[TCNE]^0	**19**	2245 [2230–2259] 2215 [2210–2221][26b, 28]	2	2230	[c]
η^2-TCNE^0	**27**	2222(6) (KBr) [2209–2230][89] 2223(8) (CH_2Cl_2) [2207–2235]	1	2222	[c]
[TCNE]$^{\bullet-}$	**1**$^{\bullet-}$	2183 (m); 2144 (m)[b]	2	2164	1421[55]
σ-[TCNE]$^{\bullet-}$	**17**$^{\bullet-}$	2197 (m) [2189–2205] 2160 [2152–2175] 2127 (m), [2110–2136 (m)][2, 56, 58, 84b]	2/3	2161	1410[56, 58]
μ-[TCNE]$^{\bullet-}$	**18**$^{\bullet-}$	2196(5) (m) [2189–2206] 2142(12) (s) [2126–2163][b],[65, 66]	2	2169	[c]
$[TCNE]_2^{2-}$	**13a**	2191(1.4) (m) [2189–2193] 2173(1.7) (m) [2170–2175] 2161(1.7) (m) [2159–2163][90]	3	2175	1364[23]
trans-μ-$[TCNE]_2^{2-}$	**13b**	2193 (m); 2173 (m); 2162 (m)[23, 66]	3	2176	1365[23]
cis-μ- und *trans*-μ_4-$[TCNE]_2^{2-}$	**13c,d**	2195 (m), 2176 (s), 2162 (s), 2137 (w)[66c]	4	2168	1360[66c]
$[TCNE]_2^{2-}$	**14**	2216 (m); 2197 (s); 2180 (m)[91]	3	2198	1385[23]
$[TCNE]^{2-}$	**1**$^{2-}$	2142 (s) [2140–2143] 2074 (w) [2069–2078][92]	2	2108	1260[56]
μ-$[TCNE]^{2-}$	μ-**1**$^{2-}$	2176 (m); 2097 (s)[34c, 93]	2	2137	1256[93]
H_2TCNE	H_2**1**	2273[b]	1	2273	[c]
TCNEO	**8**	2278[b]	1	2278	[c]
$TCNECR_2$	**28**	2269 [2260–2273][f]	1	2269	[c]
-[$C_2(CN)_4$]- Diels–Alder RCN (R = Alkyl) k conjugated[54]	**3**	2244(8) [2250–2230][94–96]	1	2244	[c]
		2250 [2260–2240] 2231 [2240–2222]	1	2250 2231	[c]
$R_2[C_4(CN)_8]$, $[TCNQ]_2^{2-}$	**4**	[d]			[c]
μ_4-$[C_4(CN)_8]^{2-}$	**4**,**15**	2215(4.5) (m) [2212–2223] 2157(2.8) (s) [2153–2160] 2107(4) (w) [2101–2111][b],[13a]	3	2160	[c]
σ-$[HTCNE]^-$	**20**	[e]			[c]
μ-$[HTCNE]^-$	μ-H**1**$^-$, **21**	2213 (m) [2208–2213] 2172 (s) [2165–2178][36]	2	2193	[c]
μ_3-$[RTCNE]^-$	**25**	2220 (m); 2153 (s) 2127 (s)[37]	3	2167	[c]
μ_4-$[RTCNE]^-$	**26**	2213 (m); 2162 (s)[37]	3	2188	[c]

[a] Determined by Raman spectroscopy. [b] Data taken on a Bruker Tensor 37 FT-IR spectrometer (± 1 cm^{-1}). [c] Not reported. [d] No characteristic $\tilde{\nu}_{CN}$ absorption because of the presence of other nitriles, but all occur in the range 2125–2225 cm^{-1}; a diagnostic δ_{CH} vibration at 804 cm^{-1} occurs for $[TCNQ]_2^{2-}$.[97] [e] No characteristic $\tilde{\nu}_{CN}$ absorption owing to the presence of other nitriles, but all occur at 2233(sh), 2220(s), 2168(vs), and 1355(w).[98] [f] For R = CN, that is, $C_3(CN)_6$ absorptions occur at 2290, 2250, 2220 cm^{-1}.[99]

3.2.1. *TCNE^0*

The four nitrile groups for D_{2h} TCNE gives rise to two IR and two Raman allowed absorptions, which occur at 2262 and 2228 cm^{-1} and 2247 and 2235 cm^{-1}, respectively.[29,40] Our routine solid-state IR spectra obtained for TCNE^0 exhibit three $\tilde{\nu}_{CN}$ absorptions at 2262(s), 2228(m), and 2214(w) in KBr, which differ from the spectra with peaks at 2254(s) and 2247(m) observed in CH_2Cl_2, Figure 3. In KBr the average $\tilde{\nu}_{CN}$ absorption is at 2235 cm^{-1}, while it is 2250 cm^{-1} in CH_2Cl_2. The literature is confusing as in some cases two, three, or four bands are reported. Clearly TCNE exhibits two major and one or more weaker peaks, and different authors may or may not include weak, and even shoulders when they report these absorptions.

Upon forming a classical Do·TCNE donor–acceptor complex, these three bands are found in the ranges of 2261–2241, 2228–2218, and 2214–2207 cm^{-1}, respectively, in KBr, Table 3. These values represent small shifts to lower wavenumber and are in the range of differences reported for TCNE by other authors throughout the years. Similar small shifts are observed in solution with the stronger electron donors giving the larger shifts.[41] Donor–acceptor charge complexes involve configurational interaction (mixing of excited states with the ground state) orbital mixing that leads to removal of electron density or weakening of the CN

 © 2006 Wiley-VCH Verlag GmbH & Co. KGaA, Weinheim

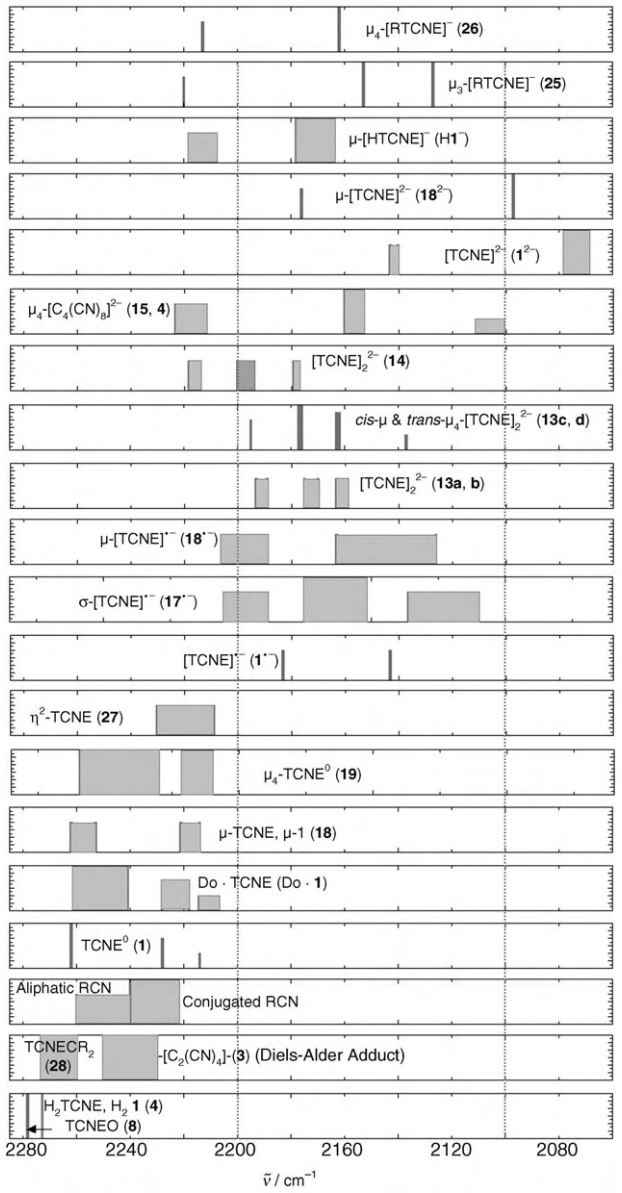

Figure 2. $\tilde{\nu}_{CN}$ IR absorption ranges for structurally characterized forms of TCNE.

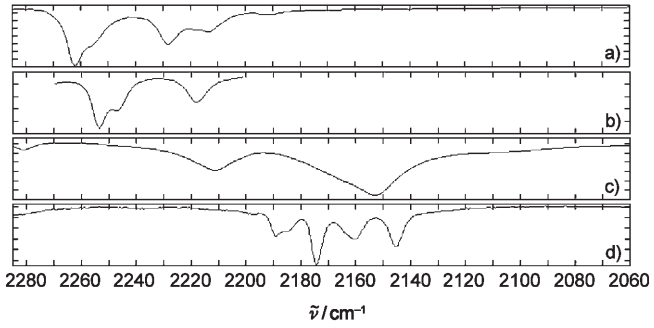

Figure 3. $\tilde{\nu}_{CN}$ region of the IR spectra for a) $TCNE^0$ (**1**; KBr), b) $TCNE^0$ (**1**; CH_2Cl_2), c) μ_4-$[C_4(CN)_8]^{2-}$ (**15**) present in $[Mn\{C_4(CN)_8\}(NCMe)_2]$ and d) $[TCNE]_2^{2-}$ (**13**) and $[TCNE]^{\bullet-}$ (**1**$^{\bullet-}$) present in $[\{Pt^{II}(\mu\text{-}PtBu_2)H(PtBu_2H_2)\}^+_3[TCNE]_2^{2-}[TCNE]^{\bullet-}]$.[75b]

bond; hence, a small shift in the $\tilde{\nu}_{CN}$ absorptions to lower energy is expected, as observed.

Donation of the lone pair of electrons by a nitrile group (e.g. MeCN) to a Lewis acid shifts the $\tilde{\nu}_{CN}$ vibration to higher energy; thus, as for cyanide and carbon monoxide this shift is attributed to σ-donation that removes weakly antibonding electron density.[38b] For example, MeCN has an IR absorption of A_1 symmetry at 2266 cm^{-1}[42a] (although other values appear in the literature[43]). This value increases to 2306 cm^{-1} for $[Zn^{II}(NCMe)_4]^{2+}$.[42a] Even higher values are observed for other homoleptic transition-metal complexes, as significant $M_{d_{\pi}\text{–}\pi^*}$ backbonding, which occurs for divalent or reduced metals, especially with strong-field ligands, such as CN^- or CO, is not present in accord with nitriles not being strong-field ligands.[42b,44] Even N-bonded $[TCNE]^{\bullet-}$ which has a lower lying π* orbital, with respect to $TCNE^0$, is a weak-field ligand as observed for $[M^{II}(TCNE)_2]\cdot x\,Solv$ (M = Mn, Fe, Co)[45] and $[M^{II}C_4(CN)_8(NCMe)_2]\cdot Solv$ (M = Mn, Fe) being high-spin complexes.[13a] This trend is expected for the σ bonding of $[TCNE]^z$ to a metal ion, M, although less so for $z = 1-$ than for $z = 0$. Furthermore, unlike nitriles, such as acetonitrile, where the nitrogen atom does or does not bond, $[TCNE]^z$ has four nitrogen atoms and all may or may not participate in bonding. It should be noted that while nitrile groups are not strong-field ligands they can exist on low-spin complexes, which is imposed by other strong-field ligands that are present. Hence, owing to the low-spin metal ion, more d_π electron density will be available to backbond to the nitrile groups. This trend for $TCNE^0$ is problematic owing to the lack of well-characterized examples, and IR data has not been reported for the lone structurally characterized example where σ-$TCNE^0$ is present. Data for μ-$TCNE^0$ reveals that while the highest wavenumber $\tilde{\nu}_{CN}$ band at 2260 cm^{-1} is essentially identical to 2262 cm^{-1} observed for $TCNE^0$, the two lower energy absorptions shift to higher energy (Figure 2) in accord with this trend.

The backbonding of nitrile groups to Ru^{II} centers however, has been established as the $\tilde{\nu}_{CN}$ value for $[Ru^{II}(NH_3)_5(NCR)]^{2+}$ (R = Me, Ph, etc.) is reduced with respect to the free RCN by 43 and 15 cm^{-1}, for R = Me, Ph, respectively.[43] This is not the situation for either $[Ru^{III}(NH_3)_5(NCR)]^{3+}$[43] or for $[M^{II}_2(NCMe)_{10}]^{4+}$ complexes with M^{II} = Mo^{II}, Tc^{II}, Rh^{II}, where the $\tilde{\nu}_{CN}$ band shifts to higher wavenumber with respect to free MeCN (M = Mo,[46] Tc,[47] Rh[48]). Therefore, shifting $\tilde{\nu}_{CN}$ to higher values, while the general trend, may not always occur, particularly if backbonding is significant. To date, only Ru^{II} backbonding to nitrile groups has been documented, but perhaps it may be important for other second (and third) row divalent metal ions or first row metal ions in formal oxidation states less than two.

Likewise, μ-TCNE, as reported for $[M^{II}(hfac)_2(TCNE)]$ (M = Co, Cu), also has three $\tilde{\nu}_{CN}$ absorptions at 2260, 2240, and 2217 cm^{-1}.[27] Both $[\{Mo_2(O_2CCF_3)_4\}(TCNE)]$ and $[\{Rh_2(O_2CCF_3)_4\}_2(TCNE)(C_6H_6)_2]$ possess μ_4-$TCNE^0$ ligands and have two absorptions at 2259 and 2221 cm^{-1} (average = 2230 cm^{-1})[26b] and 2230 and 2210 cm^{-1} (average = 2220 cm^{-1}),[28] respectively (Figure 2). The absorptions are in accord for a $TCNE^0$ ligand, as they are nominally higher in energy than that observed for free $TCNE^0$, as expected from

© 2006 Wiley-VCH Verlag GmbH & Co. KGaA, Weinheim

the above trend (Figure 2). Likewise, albeit not crystallographically characterized, $[\{Re^{I}(CO)_4Cl\}_4(TCNE)]$ has $\tilde{\nu}_{CN}$ absorptions at 2225 and 2205 cm^{-1} (average = 2215 cm^{-1})[49] and $[\{Fe^{II}Cp(CO)_2\}_4(TCNE)]^{4+}$ has absorptions at 2269(w) and 2238(m) cm^{-1} (average = 2254 cm^{-1})[50] indicative of $TCNE^0$.[51] Hence, the presence of three absorptions for $[\{Fe^{II}Cp(CO)_2\}_4(TCNE)]^{4+}$, with two above 2230 cm^{-1}, indicates $TCNE^0$ in some form. The $\tilde{\nu}_{CC}$ Raman peak for TCNE (1570 cm^{-1}) and Do·TCNE (1565 cm^{-1}) are effectively identical and are in accord with BO = 2.[40,52,53]

3.2.2. TCNE Fragments in Organic Compounds

TCNEO (**8**), η^2-TCNE (**27**), $TCNECR_2$ (**28**), and Diels–Alder products possessing the *cis* fragment **3** are each reported to have a single $\tilde{\nu}_{CN}$ absorption. TCNEO (**8**) has a $\tilde{\nu}_{CN}$ absorption at 2278 cm^{-1}. Likewise, η^2-TCNE (**27**), has a single $\tilde{\nu}_{CN}$ absorption in the range of 2230 to 2209 cm^{-1} (average = 2222 cm^{-1}). Three-membered rings $TCNECR_2$ (**28**) have their $\tilde{\nu}_{CN}$ absorption between 2273 and 2260 cm^{-1} (average = 2269 cm^{-1}), which exceeds that of the four-membered ring Diels–Alder products with their $\tilde{\nu}_{CN}$ absorption in the range of 2250 and 2230 cm^{-1} (average = 2244 cm^{-1}). Thus, for the three-membered rings, the wavenumbers are TCNEO > $TCNECR_2$ > η^2-TCNE, which is reverse of the trend for central C–C distances (i.e. TCNEO < $TCNECR_2$ < η^2-TCNE. For comparison, H_2TCNE (H_2**1**) possesses the *trans* **4** fragment and also has a single $\tilde{\nu}_{CN}$ absorption at 2273 cm^{-1}.

The observed values are in accord with the expectation for aliphatic nitriles, which range from 2260 to 2240(m) cm^{-1}, and exceed the range of 2240 to 2222(m) cm^{-1} assigned to conjugated nitriles.[54] Thus, all of these neutral TCNE-based species have $\tilde{\nu}_{CN}$ absorption(s) above 2210 cm^{-1} (Figure 4). $\tilde{\nu}_{CN}$ absorptions below 2210 cm^{-1} are indicative of anionic species (see Sections 3.2.3 and 3.2.4).

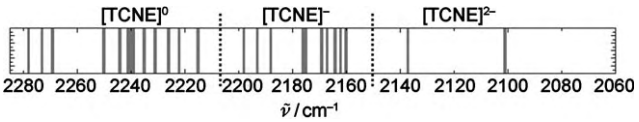

Figure 4. Average $\tilde{\nu}_{CN}$ absorption (Table 3) as a function of charge *z* in $[TCNE]^z$ for crystallographically characterized forms of TCNE. Above 2210 cm^{-1} $z = 0$, between 2210 and 2150 cm^{-1} $z = 1-$, and below 2150 cm^{-1} $z = 2-$.

3.2.3. [TCNE]$^{\bullet-}$

Isolated $[TCNE]^{\bullet-}$ ($\mathbf{1}^{\bullet-}$), exhibits two $\tilde{\nu}_{CN}$ absorptions at 2183 and 2144 cm^{-1}, and a $\tilde{\nu}_{CC}$ peak at 1421 cm^{-1}.[55] With respect to σ-$[TCNE]^{\bullet-}$ ($\mathbf{17}^{\bullet-}$), only two structurally characterized examples of σ-$[TCNE]^{\bullet-}$ have been reported; namely, $[V^{IV}Cp_2X(TCNE)]$ (X = Cl, Br, I)[56-59] and $[Mn^{II}Cp(CO)_2(TCNE)]$ (see Section 4).[60] Owing to the lower symmetry intrinsic to σ-bonding, $\tilde{\nu}_{CN}$ absorptions occur at 2197(s), 2160(s), and 2127(w) cm^{-1} (in addition to much weaker peak at 2219 cm^{-1}) as well as a $\tilde{\nu}_{CC}$ peak at 1405 cm^{-1} for the vanadium complexes, and 2205(s) and 2136(s) cm^{-1} for the manganese.[61] Therefore, in one case three vibrational bands are reported, whereas in the other case only two absorptions are reported. Hence, this bonding motif may be problematic with respect to identification owing to the variation of the number of peaks. Nonetheless, in the case of the vanadium compound its $\tilde{\nu}_{CC}$ peak at 1405 cm^{-1} is diagnostic for $[TCNE]^{\bullet-}$. It should be noted that while not structurally characterized, $[Cp'Co(CO)(TCNE)]$ ($\tilde{\nu}_{CN}$(Nujol) = 2221(vs), 2175(vs) cm^{-1}),[62] $[Cp'Co(PPh_3)(TCNE)]$ $\tilde{\nu}_{CN}$(Nujol) = 2218(vs), 2160(vs) cm^{-1},[62] $[Cp'Co(P(OMe)_3)(TCNE)]$ ($\tilde{\nu}_{CN}$(Nujol) = 2215(s,sh), 2199(vs), 2177(s,sh), 2155(s,sh) cm^{-1}),[62b] and $[Cp'Co(NC_5H_5)(TCNE)]$ ($\tilde{\nu}_{CN}$(Nujol) = 2213(s,sh), 2198 (vs), 2178(m,sh), 2160(w,sh) cm^{-1})[62b] (Cp′ = C_5H_4Me) are assigned to have the $\mathbf{17}^{\bullet-}$ unit, and the number of absorptions vary in the solid state, while four absorptions are present in solution. The related $[CpCo(PMe_3)(TCNE)]$, also not structurally characterized, has $\tilde{\nu}_{CN}$(KBr) = 2210 cm^{-1}[63] indicative of the η^2-TCNE (**27**) motif.

For the 42 compounds with *trans*-μ-$[TCNE]^{\bullet-}$ ($\mathbf{18}^{\bullet-}$) units, the average values of the $\tilde{\nu}_{CN}$ absorptions can be found in the ranges of 2206–2189 and 2163–2126 cm^{-1}. Of these compounds, 40 are members of the family of molecule-based magnets of $[Mn^{III}(por)][TCNE]\cdot Solv$ composition (por = substituted *meso*-tetraphenylporphyrinate),[64] one is an Fe^{III} analogue,[65] and one is $[(CN)Cu^{I}(PPh_3)_2(TCNE)Cu(PPh_3)_2]$.[66] The higher energy absorption shifts to higher energy by 6 to 23 cm^{-1} compared to free $[TCNE]^{\bullet-}$, while the lower energy absorption either increases or decreases by up to ± 19 cm^{-1}.

Whereas free $[TCNE]^{\bullet-}$ reliably has $\tilde{\nu}_{CN}$ absorptions at 2183 and 2144 cm^{-1} deviations from both of these two values suggest that $[TCNE]^{\bullet-}$ is bonded to a metal ion. Both σ-$[TCNE]^{\bullet-}$ ($\mathbf{17}^{\bullet-}$) and μ-$[TCNE]^{\bullet-}$ ($\mathbf{18}^{\bullet-}$) have absorptions in the same region, but while the latter has two allowed IR peaks, the lower symmetry σ-$[TCNE]^{\bullet-}$ motif, although it may exhibit two absorptions, should, and frequently does, exhibit more.

$[TCNE]^{\bullet-}$ has also been isolated as π-$[TCNE]_2^{2-}$ and σ-$[TCNE]_2^{2-}$ dimers. The π-$[TCNE]_2^{2-}$ dimers **13a** have characteristic $\tilde{\nu}_{CN}$ absorptions at 2191(m), 2173(m), and 2161(m) cm^{-1} (Figure 2 and Figure 3).[23] These values do not change (Table 1) even upon *trans*-μ-bridging structure, as observed for $[(Ph_3P)_3Cu^{I}([TCNE]_2)Cu^{I}(PPh_3)_3]$,[23,66a] (**13b**), cis-μ-bridging as observed for $[Mn^{II}(amtp)(NCMe)(TCNE)_2]$ (amtp = tris(pyrazol-1-ylmethyl)amine][66b] (**13c**), and *cis*-μ_4-bridging as observed for $[\{Mn^{II}(amtp)(NCMe)\}_2(TCNE)_2]^{2+}$[66b] (**13d**) as each exhibit an IR active $\tilde{\nu}_{CC}$ absorption at 1364 cm^{-1}.[23,66b,c] $[TTF]^+_2[TCNE]_2^{2-}$[24] has a different conformation of $[TCNE]_2^{2-}$ (**14**), and similar, but different $\tilde{\nu}_{CN}$ absorptions at 2216(m), 2197(s), and 2180(m) cm^{-1} (Figure 2),[23] and a $\tilde{\nu}_{CC}$ absorption shifted to higher wavenumber at 1385(s) cm^{-1}.[23] In contrast, σ-$[TCNE]_2^{2-}$ dimers, μ_4-$[C_4(CN)_8]^{2-}$ (**15**) have distinctly different $\tilde{\nu}_{CN}$ absorptions at 2215(5)(m), 2157(3)(s), and 2107(4)(w) cm^{-1} (Figure 2 and Figure 3).[13] Thus, species with a single negative charge per TCNE moiety have average $\tilde{\nu}_{CN}$ absorptions between 2150 and 2210 cm^{-1} (Figure 4), and dimerized species have three $\tilde{\nu}_{CN}$ absorptions, while monomeric species have two $\tilde{\nu}_{CN}$ absorptions.

 © 2006 Wiley-VCH Verlag GmbH & Co. KGaA, Weinheim

3.2.4. [TCNE]$^{2-}$

Dianionic TCNE species have their average $\tilde{\nu}_{CN}$ absorptions below 2150 cm^{-1} (Figure 4). The $\tilde{\nu}_{CN}$ absorptions for isolated [TCNE]$^{2-}$ occur at 2142(s) and 2074(w) cm^{-1}, which are shifted to 2176 and 2097 cm^{-1} for μ-[TCNE]$^{2-}$.

Characteristic assignments for the $\tilde{\nu}_{CN}$ absorption(s) in bonded and bridging [RTCNE]$^{-}$ (R = H, $CH_2C(O)Me$) are not well documented. Nonetheless, a few species have been reported and their absorptions occur between 2220 and 2162 cm^{-1} and average 2180 cm^{-1} in accord with one negative charge per TCNE fragment.

Overall, a few trends are evident, namely, a) the average $\tilde{\nu}_{CN}$ absorption for a [TCNE]$^{z-}$-based species occurs above 2210 cm^{-1} for $z = 0$, between 2210 and 2150 cm^{-1} for $z = 1-$, and below 2150 cm^{-1} for $z = 2-$ (Figure 4, Table 3; note only the significant, fundamental absorptions are averaged and weak and very weak absorptions are excluded in the average; however, some data in the literature neglects to include this information and their assignment is intrinsically subjective). b) Two $\tilde{\nu}_{CN}$ absorptions are expected for [TCNE]$^{z-}$ ($z = 1-$, $2-$), and three $\tilde{\nu}_{CN}$ absorptions are expected for [TCNE]$^{z-}$ ($z = 0$) and dimers (σ or π) of [TCNE]$^{z-}$ ($z = 1-$). A single $\tilde{\nu}_{CN}$ absorption is expected for H_2TCNE (H_2**1**), TCNEO (**8**), η^2-TCNE (**27**), and related compounds, such as Diels–Alder adducts and $TCNECR_2$ (**28**). Since these latter TCNE-based compounds are neutral the single $\tilde{\nu}_{CN}$ absorption is expected above 2210 cm^{-1}, and typically occurs at a substantially higher frequency.

Table 4 lists characteristic $\tilde{\nu}_{CN}$ absorptions for products that may form from the reaction of TCNE. Hexacyanobutadiene (**9**) is a one of many reduction products from TCNE reactions and can exist in many forms, and its $\tilde{\nu}_{CN}$ absorptions are in Table 5.

4. Discussion

Analysis of the metric parameters associated with a single-crystal structure determination, when available, and the IR spectra in the region of 2300 to 2050 cm^{-1} provide complementary information with respect to the bond order and charge on the TCNE fragment. To satisfy the curiosity of those making a new material, its IR spectrum is among the first pieces of the data that can be used for characterization. The number and average wavenumber of the $\tilde{\nu}_{CN}$ bands provides a quick clue as to the important characteristics of the TCNE moiety, and may in some cases unambiguously identify the TCNE form. This ability to correlate the $\tilde{\nu}_{CN}$ signature with specific form (or forms) arises from an analysis of a structure–property ($\tilde{\nu}_{CN}$) relationship, which itself is due to numerous structures where the form of the TCNE can be unambiguously described. As noted herein, this is more reliable for some forms where several good-quality structures as well as IR data are available. In cases where albeit one mediocre, if not poor, structure is available, or in cases where the $\tilde{\nu}_{CN}$ data are not reported, the form of the TCNE is less reliably assigned. The ability to assign charge or bonding motif is further hindered in cases where model compounds have yet to be structurally characterized and the $\tilde{\nu}_{CN}$ data unambiguously assigned.

The above correlations enable the revisiting of several assignments for different TCNE-containing compounds in the literature. First is a reviewing of the description of metallocyclopropanes, η^2-TCNE (**27**). Formally, it can either be described as one of the two limiting structures, namely, [M^{x}η^2-(TCNE)^0] or [M^{x+2}η^2-(TCNE)$^{2-}$]. The average central C–C distance for η^2-TCNE, as noted earlier, is 1.484(19) Å (Figure 1, Table 1). This distance is in the range observed for [TCNE]$^{2-}$ (that is, 1.478(8)–1.488(4) Å), and is much

Table 4: Significant $\tilde{\nu}_{CN}$ bands for CN^-, $[C(CN)_3]^-$ (**7**), $[C_3(CN)_5]^-$ (**8**), $[C_2(CN)_3O]^\bullet$ (**9**), $[(NC)_2C{=}C(CN)(CON]^\bullet$ (**7**), μ-$OC_2(CN)_4$, and $NC(C(CN)_2)_3C(CN)$- (**16**).

Cyanocarbon	$\tilde{\nu}_{CN}$ [cm^{-1}]	Compound
CN^-	2053 (s)	$[NEt_4][CN]$
$[C(CN)_3]^-$ (**10**)	2163 (s)	$[NEt_4][C(CN)_3]$
$[C_3(CN)_5]^-$ (**5**)	2196 (vs), 1500(m) ($\tilde{\nu}_{CC}$)	$[FeCp^*_2][C_3(CN)_5]$
$[C_2(CN)_3O]^\bullet$ (**6**)	2210 (m), 2200 (m), 2179 (m), 1608 (vs) ($\tilde{\nu}_{CO}$),1487 (s) ($\tilde{\nu}_{CC}$)	$[NMe_4][C_2(CN)_3O]$
$[(NC)_2C{=}C(CN)(CONH]^\bullet$ (**7**)	2200 (s), 2179 (m)	$[Mo_2(O_2CBut)_3[(NC)_2C{=}C(CN)(CONH)]$[16]
$Pt(OC_2(CN)_4)$ (**11**)	2220, 1072 ($\tilde{\nu}_{CO}$)	$[Pt^0(AsPh_3)_2(OC_2(CN)_4)]$[21]
$NC(C(CN)_2)_3C(CN)$- (**16**)	2197	**16a**[25a] and **16b**[25b]

Table 5: Summary of the significant $\tilde{\nu}_{CN}$ bands as a function of bonding modes of $[C_4(CN)_6]^z$ ($z = 0$, $1-$, $2-$).

$[C_4(CN)_6]^z$ bonding mode	$\tilde{\nu}_{CN}$ [cm^{-1}]			$\tilde{\nu}_{CO}$ [cm^{-1}]	Ref.
π-$C_4(CN)_6^0$	2247 (s)	2238 (s)	2211 (m)		[104, 105]
π-$[C_4(CN)_6]^{\bullet-}$	2185 (s)	2168 (m)			[106]
trans-1,4-$[C_4(CN)_6]^{\bullet-}$	2193 (s)	2150 (s)			[107]
trans-2,3-$[C_4(CN)_6]^{\bullet-}$	2217 (w)	2190 (m)			[108]
σ-4-$[C_4(CN)_6]^{\bullet-}$	2185 (m)	2170 (s)	2153 (m)		[109]
π-$[C_4(CN)_6]_2^{2-}$	2185 (s)	2170 (m)	2128 (m)		[109]
π-$[C_4(CN)_6]^{2-}$	2200 (m)	2152 (s)	2124 (w)		[109]
π-*i*-$[C_4(CN)_6]^{2-}$	2174 (s)	2158 (m)			[104, 106]
trans-1,4-$Na_2[C_4(CN)_6]$	2229 (m)	2174 (s)	2142 (s)		[105, 110]
cis-1,4-$Na_2[C_4(CN)_6]$	2173 (s)	2123 (m)			[105, 110]
$[C_4(CN)_5O]^-$	2235 (w,sh)	2226 (m)	2218 (s)	1557 (m)	[109]

© 2006 Wiley-VCH Verlag GmbH & Co. KGaA, Weinheim

longer than that expected for $TCNE^0$ (that is, <1.37 Å). Nonetheless, based on other considerations, especially the $\tilde{\nu}_{CN}$ absorptions above 2200 cm^{-1}, η^2-TCNE is best formulated as η^2-$TCNE^0$, and not η^2-$[TCNE]^{2-}$. In $[HTCNE]^-$ ($H\mathbf{1}^-$), the central C–C distances are shorter than those for $H_2\mathbf{1}$, albeit there are only a few structurally characterized examples of σ-$[HTCNE]^-$ (**20**; 1.511(12)),[68] μ-$[HTCNE]^-$ (**21**; 1.479(9)),[69] μ_3-$[RTCNE]^-$ (**25**; 1.536(6)), and μ_4-$[RTCNE]^-$ (**26**; 1.514(7), where $R=CH_2C(O)Me$).[70] Nonetheless, they are in the range observed for η^2-$TCNE^0$ (**27**). These species, however, have $\tilde{\nu}_{CN}$ absorption(s) significantly below 2210 cm^{-1} in addition to the one in the 2220 to 2213 cm^{-1} region characteristic of η^2-$TCNE^0$. These lower wavenumbers are in accord with the negative charge, which shifts the absorptions to lower energies.

Diamagnetic $[VCp_2X(TCNE)]$ ($X=Cl$, Br, I)[56,57] and paramagnetic $[MnCp(CO)_2(TCNE)]$[60,61] are the only two structurally characterized examples of σ-$[TCNE]^{\bullet-}$ ($\mathbf{17}^{\bullet-}$) albeit the structures are too poor to get meaningful metric parameters. Thus, the vanadium complex might be better described as $[V^{III}Cp_2X(TCNE)]$ (which should be diamagnetic) or $[V^{IV}Cp_2X(TCNE^-)]$ (which should be paramagnetic (and antiferromagnetic coupled)), or $[V^{V}Cp_2X(TCNE^{2-})]$ (which should be diamagnetic). While the manganese complex can be $[Mn^{II}Cp(CO)_2(TCNE^-)]$ (paramagnetic (and antiferromagnetic coupled)) or $[Mn^{I}Cp(CO)_2(TCNE)]$ (diamagnetic). Owing to the lower symmetry associated with the σ-bonding, $\tilde{\nu}_{CN}$ absorptions occur at 2192(m), 2152(m), and 2128(m) cm^{-1} (average = 2157 cm^{-1}; there is also a much weaker peak at 2211 cm^{-1}) for the vanadium complex, and 2205 and 2136 cm^{-1} (average = 2170 cm^{-1}) for the manganese complex. The values for both complexes are in accord with the trend of shifting to higher energy with respect to unbound $[TCNE]^{\bullet-}$ (Figure 2), and the average wavenumbers also suggest $[TCNE]^{\bullet-}$ (Figure 3). Hence, as suggested $[V^{IV}Cp_2X(TCNE)]$ and $[Mn^{II}Cp(CO)_2(TCNE)]$ are the assigned structures, and are in agreement with the magnetic data.

The same trend is also evident for μ-$[TCNE]^z$ ($z=1-$, $2-$). In isolated $[TCNE]^z$, the $\tilde{\nu}_{CN}$ absorptions are 2183 and 2144 cm^{-1} ($z=1-$) and 2142 and 2074 cm^{-1} ($z=2-$). Where as in μ-$[TCNE]^z$ these bands shift on average to 2196 and 2142 cm^{-1} ($z=1-$) and 2176 and 2097 cm^{-1} ($z=2-$; Figure 1). For $z=1-$ the higher energy absorption is always shifted to higher energy reflecting bonding to a metal center. In contrast, the lower energy absorption shifts either to lower or higher energy by approximately 19 cm^{-1}, and does not follow the trend as it is not bonded to a metal center. In contrast to $[TCNE]^{\bullet-}$, both $\tilde{\nu}_{CN}$ absorptions for $[TCNE]^{2-}$ shift to higher wavenumbers, but unlike $[TCNE]^{\bullet-}$ with many examples enabling a meaningful trend, only one pair of examples exist for $[TCNE]^{2-}$, hence, more examples are needed.

No $\tilde{\nu}_{CN}$ data, however, are available for σ-$[TCNE]^{2-}$, μ_3-$[TCNE]^z$, and μ_4-$[TCNE]^z$ ($z=1-$, $2-$), as well-characterized compounds possessing these moieties do not exist at present. Nonetheless, the same trend of $\tilde{\nu}_{CN}$ values is expected to be followed as no unbound nitrile nitrogen would exist for μ_4-$[TCNE]^z$ and μ_3-$[TCNE]^z$ would have only one. Hence, for μ_4-$[TCNE]^{\bullet-}$ and μ_3-$[TCNE]^{\bullet-}$ $\tilde{\nu}_{CN}$ absorption should occur above 2144 cm^{-1}, and absorptions at lower wavenumbers should be attributed to μ_3-$[TCNE]^{2-}$ and μ_4-$[TCNE]^{2-}$. Other factors, however, may become important leading to a lower $\tilde{\nu}_{CN}$ value.

This central C–C distance increases as the bond order decreases; it is 1.349(6) Å for $[TCNE]^z$ ($z=0$; BO = 2), 1.394(11) Å for $[TCNE]^z$ ($z=1-$; BO = 1.5), 1.488(4) Å ($z=2-$; BO = 1; Figure 5). These distances are nominally main-

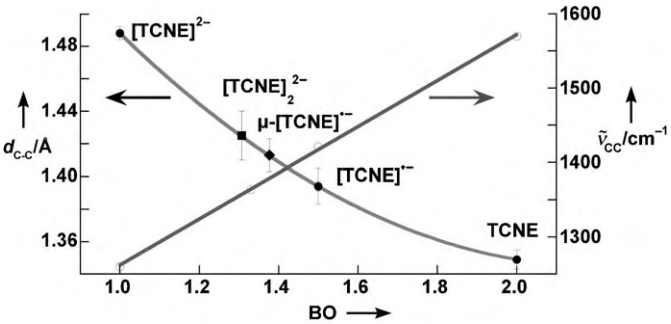

Figure 5. Average central C–C distance (*d* with esd) and $\tilde{\nu}_{CC}$ value for TCNE, $[TCNE]^{\bullet-}$, μ-$[TCNE]^{\bullet-}$, $[TCNE]_2^{2-}$, and $[TCNE]^{2-}$ as a function of bond order (BO).

tained upon coordination of one nitrile to a metal ion in the few σ-$[TCNE]^z$ ($z=0$, $1-$) complexes that have been reported; but, it should be noted that each of these structures have large esds of 0.01 Å that could obscure small changes in distances. In contrast, *trans*-bridging structure of μ-$[TCNE]^{\bullet-}$ between two metal ions slightly lengthens the central C–C bond to 1.413(10) Å (see Section 3.1.1). This change corresponds to a weakening of the central C–C bond, and reduction of the BO to 1.38 (Figure 5). The $[TCNE]_2^{2-}$ dimer (**13a**) has an incrementally longer average central C–C bond 1.425(15) Å, and concomitantly further reduced BO of 1.31. Thus, the central C–C distance for μ-$[TCNE]^{\bullet-}$ is 1.4% greater than for $[TCNE]^{\bullet-}$, while it is 2.2% greater for $[TCNE]_2^{2-}$ with respect to $[TCNE]^{\bullet-}$. This trend is expected as for constant BO, the bond length increases with increasing p contribution to hybridization,[71] and $[TCNE]_2^{2-}$ has $sp^{2.17}$ compared to sp^2 for $[TCNE]^{\bullet-}$. The change in the length of the central C–C bond as $[TCNE]_2^{2-} > \mu\text{-}[TCNE]^{\bullet-} > [TCNE]^{\bullet-}$ is best supported by the trend observed for the $\tilde{\nu}_{CC}$ vibrations. The $\tilde{\nu}_{CC}$ peak is observed at 1570, 1421, 1364, and 1260 cm^{-1}, for TCNE, $[TCNE]^{\bullet-}$, $[TCNE]_2^{2-}$, and $[TCNE]^{2-}$, respectively, and the shifting of the $\tilde{\nu}_{CC}$ values for this related series of compounds is in accord with the lengthening of the central C–C bond (Figure 6). The $\tilde{\nu}_{CC}$ values decrease linearly with decreasing BO, and give a BO of 1.33 for $[TCNE]_2^{2-}$ (Figure 5), in good agreement with that obtained from the aforementioned C–C distance correlation.

Opposite to the trend for the central C–C lengths, the C–CN distances slightly decrease with increasing negative charge for TCNE, $[TCNE]^{\bullet-}$, μ-$[TCNE]^{\bullet-}$, $[TCNE]_2^{2-}$, and $[TCNE]^{2-}$ (Figure 7). The range is 25% of the variation of that observed for the central C–C bond. As a consequence, the central C–C and C–CN bonds are essentially are identical

 © 2006 Wiley-VCH Verlag GmbH & Co. KGaA, Weinheim

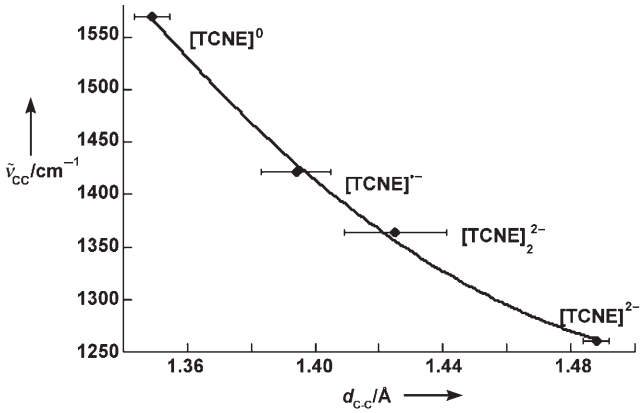

Figure 6. The dependence of the $\tilde{\nu}_{CC}$ wavenumber as a function of the average central C–C distance *d* for isolated TCNE^0, [TCNE]$^{\bullet-}$, [TCNE]$_2^{2-}$, and [TCNE]$^{2-}$. The esds of the average central C–C distances are noted, while esds for the $\tilde{\nu}_{CC}$ wavenumber (± 1 cm^{-1}) are smaller than the symbol and thus are not observed.

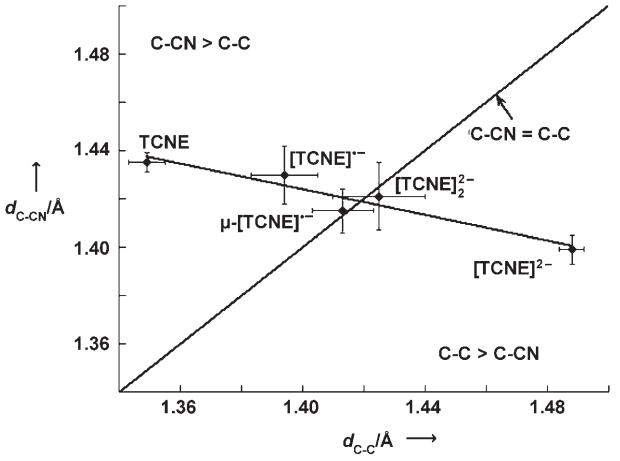

Figure 7. Average central C–C distances (d_{C-C} with esd) for TCNE, [TCNE]$^{\bullet-}$, μ-[TCNE]$^{\bullet-}$, [TCNE]$_2^{2-}$, and [TCNE]$^{2-}$ as a function of their average C–CN distances (d_{C-CN} with esds). Note that the range of C–CN distances is 25% that of the range in the central C–C distance.

for μ-[TCNE]$^{\bullet-}$ and [TCNE]$_2^{2-}$ in accord with their resonance structures.

Upon analyzing the bond lengths and angles as well as the $\tilde{\nu}_{CN}$ and $\tilde{\nu}_{CC}$ wavenumbers for the many forms for which TCNE has been reported, in a few cases discrepancies between the aforementioned conclusions with respect to the central C–C distance and bond order and/or $\tilde{\nu}_{CN}$ absorption(s) and charge for TCNE-based species and the reported assignments exist.

[Fe^{II}{(DMGBPh$_2$)$_2$}(NC$_5$H$_5$)(TCNE)] (**29**; DMG = dimethylglyoximato) is reported to hae a σ-TCNE fragment based upon its structure, with a central C–C distance of 1.388(10) Å.[72a] The $\tilde{\nu}_{CN}$ and $\tilde{\nu}_{CC}$ values are reported at 2178 and 1452 cm^{-1},[72b] respectively. The 2178 cm^{-1} $\tilde{\nu}_{CN}$ band is at substantially lower wavenumber than the TCNE^0 absorptions, which occur above 2210 cm^{-1} (Table 1, Figure 4), and is in the 2210–2150 cm^{-1} range assigned to [TCNE]$^{\bullet-}$. The [TCNE]$^{\bullet-}$ characterization is further supported by the 1452 cm^{-1} $\tilde{\nu}_{CC}$ band, which is also substantially lower than that reported for TCNE^0, and closer to the 1430 cm^{-1} value reported for [TCNE]$^{\bullet-}$.[55] The 1.388(10) Å C–C distance lies on the high end of distances for bonded or nonbonded TCNE, and the low end of distances for bonded or nonbonded [TCNE]$^{\bullet-}$. The large esd of 0.01 Å indicates sufficient ambiguity as to which grouping the C–C distance can be assigned and hence, it should not be relied on for assignment of oxidation state of the TCNE. Note that the Fe–N$_{TCNE}$ distance is 1.850(6) Å and noted to be "*significantly shorted that the 1.94 Å length observed in…*" other Fe^{II} complexes.[72a] The 1.850(6) Å is in excellent agreement with the 1.889(2) Å Fe^{III}–N$_{TCNE}$ distances reported for [Fe^{III}(TPP)]$^+$[TCNE]$^{\bullet-}$ (H$_2$TPP = *meso*-tetraphenylporphyrin),[65] and for Fe^{III}-N$_{TCNQ}$ in [Fe^{III}(TPP)]$^+$-[TCNQ]$^{\bullet-}$,[73] and the 1.865(2) Å for [{Fe^{III}(TPP)(NC$_5$H$_5$)}$_2$-(TCNQ)].[73] Hence, **29** is best described as [Fe^{III}-{(DMGBPh$_2$)$_2$}(NC$_5$H$_5$)([TCNE]$^{\bullet-}$)].

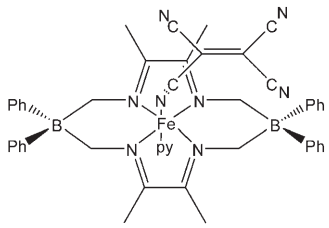

29

While not characterized in detail until recently, evidence for the presence of [TCNE]$_2^{2-}$[23] has previously been reported. The [TCNE]$_2^{2-}$ dimer has a diagnostic 3-line $\tilde{\nu}_{CN}$ absorption pattern that occurs at 2191, 2173, and 2161 cm^{-1}. The purple isomer of [Co(acacen)(NC$_5$H$_5$)]$_2$[TCNE] [acacen = *N*,*N*′-ethylenebis(acetylacetonate)] has absorptions at 2158sh, 2170s, and 2180s,[74] which while not precisely those noted in Table 3 for [TCNE]$_2^{2-}$, they are reasonably close in value, and in conjunction with the purple color (also characteristic of [TCNE]$_2^{2-}$[23]) strongly indicate the presence of [TCNE]$_2^{2-}$.

The reaction of [Pt^{II}(μ-P*t*Bu$_2$)H(P*t*Bu$_2$H)] and TCNE is reported to form the charge-transfer complex, [{Pt^{II}(μ-P*t*Bu$_2$)H(P*t*Bu$_2$H)}$_2$(TCNE)] with $\tilde{\nu}_{CN}$ absorptions at 2189, 2174, 2161, and 2145 cm^{-1}.[75a] The first three peaks are suspiciously similar to the pattern expected for [TCNE]$_2^{2-}$, and upon revisiting the spectra with a higher resolution FT-IR spectrometer absorptions at 2189, 2185, 2174, 2160, and 2145 cm^{-1} characteristic of both [TCNE]$_2^{2-}$ and [TCNE]$^{\bullet-}$ being present are observed (Figure 3).[75b] Hence, this compound is best formulated as [{Pt^{II}(μ-P*t*Bu$_2$)H(P*t*Bu$_2$H)}$_2$]$^+_3$-[TCNE]$_2^{2-}$[TCNE]$^{\bullet-}$. In THF the compound is reported to rearrange to [{Pt^{II}(μ-P*t*Bu$_2$)H(P*t*Bu$_2$H)}$_2$]$^+$[TCNE]$^{\bullet-}$ with $\tilde{\nu}_{CN}$ absorptions at 2188 and 2159 cm^{-1}.[75b] Our spectra shows the peaks to be at 2188 and 2144 cm^{-1} that are characteristic of isolated [TCNE]$^{\bullet-}$.[75b]

The detailed studies of the IR and Raman spectra taken putatively on the alkali-metal salts of [TCNE]$^{\bullet-}$, undoubtedly are in fact for [TCNE]$_2^{2-}$.[53,76] Finally, the suggestion that the soluble product from the reaction of TCNE and poly(ferrocenylethylene) with absorptions at 2218, 2199, and 2148 cm^{-1} possesses [TCNE]$_2^{2-}$,[77] is unlikely as these values are at

© 2006 Wiley-VCH Verlag GmbH & Co. KGaA, Weinheim

variance with respect to the expected values for $[TCNE]_2^{2-}$ (Table 3, Figure 3).

The reaction of copper metal and TCNE in acetonitrile was originally claimed to form $Cu^{+}[TCNE]^{\bullet-}$.[19c] Upon revisiting this material it was reformulated as $Cu^{2+}[TCNE]^{2-}$, with $\tilde{\nu}_{CN}$ absorptions at 2210 and 2162 cm^{-1} that average 2186 cm^{-1}.[78,79] These signals are consistent with bridging $[TCNE]^{\bullet-}$, which gives signals in the ranges of 2206–2180 and 2163–2126 cm^{-1} and with an average wavenumber in the range of 2210–2150 cm^{-1} as measured for the copper species. This value is too high in energy for $[TCNE]^{2-}$, as one peak is expected under 2100 cm^{-1}. Magnetic susceptibility and/or EPR studies should clarify this as the Landé *g* factor for Cu^{II} is larger than for $[TCNE]^{\bullet-}$.

The TCNE adduct with 3_3(1,3,5)cyclophane is reported to have a $\tilde{\nu}_{CN}$ at 2134 cm^{-1},[80] which suggests reduced TCNE, not $TCNE^0$, as reported. Most likely this is a misprint, but perhaps it indicates formation of the electron-transfer salt $[3_3$-(1,3,5)cyclophane$]^{\bullet+}[TCNE]^{\bullet-}$, as also the dark purple color might indicate. Further characterization is needed.

The reaction of $[Cp(Ph_3P)_2Ru^{II}NC_3Ph][PF_6]$ with TCNE was reported to form $[Cp(Ph_3P)_2Ru^{II}(TCNE)Ru^{II}(PPh_3)_2Cp][PF_6]_2$ possessing a μ-$TCNE^0$ moiety.[81a] Its reported central C–C bond of 1.393(11) Å is longer than the known examples of TCNE, Do·TCNE, σ-$[TCNE]^0$, and μ-$[TCNE]^0$, but is in accord with than expected for $[TCNE]^{\bullet-}$. Likewise, the reported $\tilde{\nu}_{CN}$ absorption at 2164(sh) and 2134 cm^{-1} (average = 2149 cm^{-1}) are far too low in wavenumber for $TCNE^0$, but are also consistent with $[TCNE]^{\bullet-}$. Hence, the reported compound is probably mixed-valent $[Cp(Ph_3P)_2Ru^{III}(TCNE^{\bullet-})Ru^{II}(PPh_3)_2Cp][PF_6]_2$ and the reinvestigation of this interesting compound is in progress.[81b]

$[FeCp(Ph_2PC_2H_4PPh_2)(TCNE)][PF_6]$ with $\tilde{\nu}_{CN}$ absorptions at 2171, 2059, and 1995 cm^{-1} that average 2175 cm^{-1}, and binuclear $[\{FeCp(Ph_2PC_2H_4PPh_2)_2\}(TCNE)][PF_6]_2$ with $\tilde{\nu}_{CN}$ absorptions at 2197(sh), 2173 cm^{-1} that average 2180 cm^{-1} have been reported.[82] These average $\tilde{\nu}_{CN}$ absorptions are in accord with $[TCNE]^{\bullet-}$ suggesting $[Fe^{III}Cp(Ph_2PC_2H_4PPh_2)(TCNE^{-})]^{+}$ for the former and the mixed-valent formula of $[\{Fe^{II/III}{}_2Cp_2(Ph_2PC_2H_4PPh_2)_2\}(TCNE^{\bullet-})]^{2+}$ for the latter.

5. Conclusion and Outlook

TCNE is an important component in many different types of reactions ranging for classical organic synthesis to materials chemistry, and as noted earlier, is the "*E. coli*" of electron-transfer chemistry.[4] The numerous reactivity modes leads to complex reactions and ultimately a broad array of products, and understanding the structure and properties of the products, not to mention the mechanistic pathway(s), can be challenging. ^{13}C NMR spectroscopic methods, in principle, could be helpful, but in practice little useful information is available. IR spectroscopy, especially in the $\tilde{\nu}_{CN}$ region, provides a wealth of information, if it can be unambiguously interpreted. Metric parameters from single-crystal structure determinations are essential, but not always available. Herein, by using the best-available structure determinations in conjunction with the $\tilde{\nu}_{CN}$ absorptions, as well as ancillary data when available, a structure–$\tilde{\nu}_{CN}$-absorption relationship has been developed and used to analyze the charge and bond order assignments for many reaction products based on TCNE. Key is the average $\tilde{\nu}_{CN}$ absorption which is used to assign the formal charge for the $[TCNE]^z$ fragment, as values exceeding 2210 cm^{-1} are assigned $z = 0$, those between 2210 and 2150 cm^{-1} are assigned $z = 1-$, and those below 2150 cm^{-1} are assigned $z = 2-$ (Figure 4).

The 2-electron 4-center C–C intradimer bond in $[TCNE]_2^{2-}$ (**13a** and μ$_4$-**13**, **13d**) and admixture of some sp^3-hybridization in the formally sp^2 central carbon atoms[23] suggest a lengthening of the central C–C bond. While the central C–C distance increases as $[TCNE]_2^{2-}$ (1.425(15) Å) > $[TCNE]^{\bullet-}$ (1.394(11) Å) inclusion of the esd data makes this trend less definitive. However, consideration of the more accurately determined $\tilde{\nu}_{CC}$ absorptions shows a decrease of wavenumber from $[TCNE]^{\bullet-}$ (1421 cm^{-1}) to $[TCNE]_2^{2-}$ (1364 cm^{-1}) which indicates bond weakening and consequently lengthening in $[TCNE]_2^{2-}$ with respect to $[TCNE]^{\bullet-}$ as anticipated from the long, 2-electron 4-center C–C intradimer bonding in $[TCNE]_2^{2-}$.

Numerous fascinating compounds have been made that clearly have four, three, and sometimes only two metal ions are bridged by a $[TCNE]^z$ fragment, but assignment of TCNE charge and bond order has been limited by paucity of well-characterized model compounds, and even with the studies described herein, this is still a major limitation. These di-, tri-, and tetranuclear compounds are even more problematic with respect to assignment if they are composed of mixtures of metal centers. Hence, speculation of charge and bond order assignments without well-characterized model compounds is risky.

To date only one structural determination of a μ$_4$-TCNE complex (**19**) has been reported and it has large esds,[28] while more than six examples of μ$_3$- and μ$_4$-$[TCNE]^z$ have been claimed, most from Kaim and co-workers.[2,4,58,61,83–86] Owing to their valence ambiguous nature, further analysis is warranted, especially structural determinations. The tetranuclear complexes $[\{Re^{I}(CO)_4Cl)\}_4][TCNE]$ and $[\{Fe^{II}Cp(CO)_2\}_4(TCNE)]^{4+}$[50] have average $\tilde{\nu}_{CN}$ absorptions of 2215 and 2254 cm^{-1},[49] respectively, that are clearly characteristic of $TCNE^0$. In contrast, $[\{Cu(Me_3TAC)\}_4(TCNE)]^{4+}$ (Me_3TAC = 1,4,7-trimethyltriazacyclononane) has an average $\tilde{\nu}_{CN}$ absorption at 2189 cm^{-1} indicative of $[TCNE]^{\bullet-}$ which suggests that its composition is mixed-valent $[\{Cu^{I}{}_3Cu^{II}(Me_3TAC)_4\}([TCNE]^{\bullet-})]^{4+}$.[83] The complexes $[\{OsHCl(CO)(PPr_3)_2\}_4(TCNE)]$,[58] $[\{MnCp^*(CO)_2\}_4(TCNE)]$,[4,84] and $[\{Ru(NH_3)_5\}_4(TCNE)]^{8+}$[86] have average $\tilde{\nu}_{CN}$ absorptions at 2140, 2135, and 2137 cm^{-1}, respectively, suggesting the presence of $[TCNE]^{2-}$, as $[Os^{II}{}_2Os^{III}{}_2\{HCl(CO)(PPr_3)_2\}_4([TCNE]^{2-})]$, $[Mn^{I}{}_2Mn^{II}{}_2\{Cp^*(CO)_2\}_4([TCNE]^{2-})]$, and $[Ru^{II}{}_2Ru^{III}{}_2(NH_3)_{20}([TCNE]^{2-})]^{8+}$, respectively. The latter ruthenium-containing complex can either be oxidized or reduced, whereby the average $\tilde{\nu}_{CN}$ absorptions for these redox species are shifted to lower values.[86] This result indicates that the ruthenium ions are either oxidized or reduced, as it is unlikely that $[TCNE]^{\bullet3-}$ is present. These formulations assume a localized model for the electronic structure, which may not be valid. These assignments also assume that the

 © 2006 Wiley-VCH Verlag GmbH & Co. KGaA, Weinheim

average $\tilde{\nu}_{CN}$ absorption, as illustrated in Figure 4, is indicative of the charge state for these tetranuclear complexes. Undoubtedly, as Ru^{II} is known to backbond to nitriles reducing the $\tilde{\nu}_{CN}$ absorptions (see Section 3.2.1), this simplistic analysis needs refinement. Likewise, the low-spin Os^{II} and Mn^{II} centers in these tetranuclear complexes may backbond to $[TCNE]^{z}$, complicating the interpretation. The ranges for the charge assignments is expected to be modified as new well-characterized examples are reported, and different ranges may be operative for TCNE complexes of different nuclearity, as well as with the degree of backbonding with $[TCNE]^{z}$.

In addition to these polynuclear species, magnetically ordered materials of $M[TCNE]_x$ ($x \approx 2$; M = V, Mn, Fe, Co, Ni) composition are particularly hard to assign charge and bond order. These materials are formulated as 3D network structures composed of μ- (**18**, **22**, **23**), μ_3- (**24**), and μ_4- (**19**) $[TCNE]^{\bullet -}$ fragments. This formulation is consistent with the observed broad, overlapping $\tilde{\nu}_{CN}$ absorptions arising from multiple M–N bonding modes as well as mixtures of different $[TCNE]^{z}$ units bonding to a different number of metal centers in different ways, which vary with preparation. While backbonding is not thought to be significant for these high-spin M^{II} magnets, the lack of suitable μ- (**22**, **23**), μ_3- (**24**), and μ_4- (**19**) $[TCNE]^{\bullet -}$ model compounds has thwarted the detailed interpretation of the structure from the $\tilde{\nu}_{CN}$ absorptions. Nonetheless, the assignment of nominal composition as $M^{II}[\{TCNE\}^{\bullet -}]_x$ is possible as their average $\tilde{\nu}_{CN}$ absorptions fall in the 2210–2050 cm^{-1} region[45,87] that is attributed to $[TCNE]^{\bullet -}$.

In due time, crucially needed new model compounds will become available. This development will occur as synthetic skills increase and as the ability to solve not only smaller crystals, but to refine the structures of more complicated disordered crystals improves. It is a goal of this review to encourage the synthesis of new TCNE-based materials by providing an enhanced ability to analyze and assign the structure of new materials.

The author gratefully acknowledges the Raman and FT-IR spectra obtained by M. L. Taliaferro, K. I. Pokhodnya, and T. D. Selby, and numerous discussions with P. J. Low (Durham), J. J. Novoa (Barcelona), K. I. Pokhodnya (Utah), T. G. Richmond (Utah), A. L. Rheingold (San Diego) R. E. Del Sesto (LANL), W. W. Shum (Utah), and G. T. Yee (Virginia Polytechnic Institute), as well as the continued partial support from the U. S. Department of Energy (No. DEFG 03-93ER45504) and the Air Force Office of Scientific Research (No. F49620-03-1-0175).

Received: September 15, 2005

[1] A. J. Fatiadi, *Synthesis* **1986**, 249.
[2] W. Kaim, M. Moscherosch, *Coord. Chem. Rev.* **1994**, *129*, 157.
[3] M. D. Ward, J. A. McCleverty, *J. Chem. Soc. Dalton* **2002**, 275; C. K. Jørgenson, *Coord. Chem. Rev.* **1966**, 1, 164.
[4] B. Olbrich-Deussner, W. Kaim, R. Gross-Lannert, *Inorg. Chem.* **1989**, *28*, 3113.
[5] T. L. Cairns, R. A. Carboni, D. D. Coffman, V. A. Engelhardt, R. E. Heckert, E. L. Little, E. G. McGeer, B. C. McKusick, W. J. Middleton, *J. Am. Chem. Soc.* **1957**, *79*, 2340.
[6] W. R. Hertler, W. Mahler, L. R. Melby, J. S. Miller, R. E. Putscher, O. W. Webster, *Mol. Cryst. Liq. Cryst.* **1989**, *171*, 205.
[7] L. R. Milgrom, *Tetrahedron* **1983**, *39*, 3895.
[8] W. J. Middleton, R. E. Heckert, E. L. Little, C. G. Krespan, *J. Am. Chem. Soc.* **1958**, *80*, 2783.
[9] S. Trofimenko, B. C. McKusick, *J. Am. Chem. Soc.* **1962**, *84*, 3677.
[10] H. Hartmann, W. Kaim, M. Wanner, A. Klein, S. Frantz, C. Duboc-Toia, J. Fiedler, S. Zális, *Inorg. Chem.* **2003**, *42*, 7018.
[11] S. Mikami, K.-i. Sugiura, J. S. Miller, Y. Sakata, *Chem. Lett.* **1999**, 413; H. Zhao, R. A. Heinz, K. R. Dunbar, R. D. Rogers, *J. Am. Chem. Soc.* **1996**, *118*, 12844; R. H. Harms, H. J. Keller, D. Nöthe, M. Werner, D. Grundel, H. Sixl, Z. G. Soos, R. M. Metzger, *Mol. Cryst. Liq. Cryst.* **1981**, *65*, 179; S. K. Hoffman, P. J. Corvan, P. Singh, C. N. Sethuklekshmi, R. M. Metzer, W. E. Hatfield, *J. Am. Chem. Soc.* **1983**, *105*, 4608; V. Dong, H. Endres, H. J. Keller, W. Moroni, D. Nöthe, *Acta Crystallogr. Sect. B* **1977**, *33*, 2428.
[12] W. E. Buschmann, A. M. Arif, J. S. Miller, *J. Chem. Soc. Chem. Commun.* **1995**, 2343.
[13] a) J. Zhang, L. M. Liable-Sands, A. L. Rheingold, R. E. Del Sesto, D. C. Gordon, B. M. Burkhart, J. S. Miller, *Chem. Commun.* **1998**, 1385; b) J. W. Raebiger, J. S. Miller, *Inorg. Chem.* **2002**, *41*, 3308.
[14] W. J. Middleton, E. L. Little, D. D. Coffman, V. A. Engelhardt, *J. Am. Chem. Soc.* **1958**, *80*, 2795.
[15] $C_2(CN)_3OH$ (**H6**) forms, but being stongly acidic ($pK_a \approx 1.9$), it ionizes.[14]
[16] F. Conan, B. Le Gall, J. M. Kerbaol, S. Le Stang, J. Sala-Pala, Y. Le Mest, J. Basca, X. Ouyang, K. R. Dunbar, C. F. Campana, *Inorg. Chem.* **2004**, *43*, 3673.
[17] W. J. Linn, O. W. Webster, R. E. Benson, *J. Am. Chem. Soc.* **1963**, *85*, 2030.
[18] A. J. Fatiadi, *Synthesis* **1987**, 959.
[19] a) W. D. Phillips, J. C. Rowell, *J. Chem. Phys.* **1960**, *33*, 626; b) O. W. Webster, O. W. Mahler, R. E. Benson, *J. Org. Chem.* **1960**, *25*, 1470; c) O. W. Webster, O. W. Mahler, R. E. Benson, *J. Am. Chem. Soc.* **1960**, *82*, 3678.
[20] M. D. Ward, *Electroanal. Chem.* **1989**, *16*, 182.
[21] R. Schlodder, J. A. Ibers, M. Lenarda, M. Graziani, *J. Am. Chem. Soc.* **1974**, *96*, 6893.
[22] A. Flamini, T. D. Selby, J. S. Miller, *Inorg. Synth.* **2004**, *34*, 68.
[23] R. E. Del Sesto, J. S. Miller, J. J. Novoa, P. Lafuente, *Chem. Eur. J.* **2002**, *8*, 4894.
[24] S. A. Clemente, A. Marzotto, *J. Mater. Chem.* **1996**, *6*, 941.
[25] a) T. Tanase, M. Hamaguchi, R. A. Bergum, E. Goto, *Chem. Commun.* **2001**, 1072; b) P. J. Butterfield, J. C. Tebby, T. J. King, *J. Chem. Soc. Dalton* **1978**, 1237; T. Mohan, R. O. Day, R. R. Holmes, *Inorg. Chem.* **1992**, *31*, 2271.
[26] a) A. L. Cotton, Y. Kim, J. Lu, *Inorg. Chim. Acta* **1994**, *221*, 1; b) B. Le Gall, F. Conan, J.-M. Kerbaol, J. P. Sala, E. Vigier, M. M. Kubicki, Y. Le Mest, *C. R. Chim* **2005**, *8*, 977.
[27] Splitting of the $\tilde{\nu}_{CN}$ absorption occurs: A. G. Bunn, P. J. Carroll, B. B. Wayland, *Inorg. Chem.* **1992**, *31*, 1297.
[28] F. A. Cotton, Y. Kim, *J. Am. Chem. Soc.* **1993**, *115*, 8511.
[29] D. A. Dixon, J. S. Miller, *J. Am. Chem. Soc.* **1987**, *109*, 3656.
[30] B. Milián, R. Pou-Amérigo, M. Merchan, M. Merchán, E. Ortí *ChemPhysChem* **2005**, *6*, 503.
[31] This curiously short distance was reported for *trans*-1,1′-Azonorbornane-*N*-oxide·TCNE: M. L. Greer, S. C. Blackstock, *J. Org. Chem.* **1996**, *61*, 7895.
[32] R. Dreos, S. Geremia, G. Nardin, L. Randaccio, G. Tauzher, S. Vuano, *Inorg. Chim. Acta* **1998**, *272*, 74.

 © 2006 Wiley-VCH Verlag GmbH & Co. KGaA, Weinheim

[33] A. Zheludev, A. Grand, E. Ressouche, J. Schweizer, B. Morin, A. J. Epstein, D. A. Dixon, J. S. Miller, *J. Am. Chem. Soc.* **1994**, *116*, 7243.

[34] a) D. A. Dixon, J. S. Miller, *J. Am. Chem. Soc.* **1987**, *109*, 3656; b) J. R. Fox, B. M. Foxman, D. Guarrera, J. S. Miller, J. C. Calabrese, A. H. Reis, Jr., *J. Mater. Chem.* **1996**, *6*, 1627; c) G. T. Yee, J. C. Calabrese, C. Vazquez, J. S. Miller, *Inorg. Chem.* **1993**, *32*, 377.

[35] J. S. Ricci, J. A. Ibers, *J. Am. Chem. Soc.* **1971**, *93*, 2391.

[36] V. Jacob, S. Mann, G. Huttner, O. Walter, L. Zsolnai, E. Kaifer, P. Rutsch, P. Kircher, E. Bill, *Eur. J. Inorg. Chem.* **2001**, 2625.

[37] L. Carlucci, G. Ciani, D. M. Proserpio, A. Sironi, *Angew. Chem.* **1996**, *108*, 1170; *Angew. Chem. Int. Ed. Engl.* **1996**, *35*, 1088.

[38] a) K. Nakamoto, *Infrared and Raman Spectra of Inorganic and Coordination Compounds*, 5th ed., Part B, Wiley, New York, **1997**, p. 126; b) K. Nakamoto, *Infrared and Raman Spectra of Inorganic and Coordination Compounds*, 5th ed., Part B, Wiley, New York, **1997**, p. 105.

[39] a) J. S. Miller, D. T. Glatzhofer, C. Vazquez, R. S. McLean, J. C. Calabrese, W. J. Marshall, J. W. Raebiger, *Inorg. Chem.* **2001**, *40*, 2058; b) M. L. Taliaferro, J. S. Miller, unpublished results.

[40] F. A. Miller, O. Sala, J. P. Devlin, J. Overend, E. Lippert, W. Lunder, J. Moser, J. Varchim, *Spectrochim. Acta* **1964**, *20*, 1233.

[41] J. C. Stires IV, E. J. McLaurin, C. P. Kubiak, *Chem. Commun.* **2005**, 3532.

[42] a) K. F. Purcell, R. S. Drago, *J. Am. Chem. Soc.* **1966**, *88*, 919; b) W. E. Buschmann, J. S. Miller, *Chem. Eur. J.* **1998**, *4*, 1731.

[43] R. E. Clarke, P. C. Ford, *Inorg. Chem.* **1970**, *9*, 227.

[44] NCMe has a ligand-field strength slightly stronger that OH_2 and first-row $[M^{II}(NCMe)_6]^{2+}$ complexes are all high spin.[42b]

[45] J. Zhang, J. Ensling, V. Ksenofontov, P. Gütlich, A. J. Epstein, J. S. Miller, *Angew. Chem.* **1998**, *110*, 676; *Angew. Chem. Int. Ed.* **1998**, *37*, 657.

[46] F. A. Cotton, K. J. Wiesinger, *Inorg. Chem.* **1991**, *30*, 871.

[47] J. C. Bryan, F. A. Cotton, L. M. Daniel, S. C. Haefner, A. P. Sattelberger, *Inorg. Chem.* **1995**, *34*, 1875.

[48] K. R. Dunbar, *J. Am. Chem. Soc.* **1988**, *110*, 8247.

[49] M. Leirer, G. Knör, A. Vogler, *Inorg. Chem. Commun.* **1992**, *2*, 110.

[50] A. N. Maity, B. Schwederski, W. Kaim, *Inorg. Chem. Commun.* **2005**, *8*, 600.

[51] Since the compound is not crystallographically characterized, it is not included in Table 2.

[52] K. Kaya, A. Nakatsuka, N. Kubota, M. Ito, *J. Raman Spectrosc.* **1973**, *48*, 495.

[53] J. Stanley, D. Smith, B. Latimer, J. P. Devlin, *J. Phys. Chem.* **1966**, *70*, 2011; J. J. Hinkel, J. P. Devlin, *J. Chem. Phys.* **1973**, *58*, 4750.

[54] R. M. Silverstein, G. C. Bassler, T. C. Morill, *Spectrochemical Identification of Organic Compounds*, 5th ed., Wiley, New York, **1991**, pp. 126–127.

[55] D. L. Jeanmaire, M. R. Suchanski, R. P. van Duyne, *J. Am. Chem. Soc.* **1975**, *97*, 1699.

[56] M. F. Rettig, R. M. Wing, *Inorg. Chem.* **1969**, *8*, 2685; The preliminary structure cited in this paper does not report bond lengths or angles.

[57] The spins undoubtedly antiferromagnetically couple, and in the case of strong coupling appear to be a diamagnetic.

[58] F. Baumann, M. Heilmann, W. Matheis, A. Schulz, W. Kaim, J. Jordanov, *Inorg. Chim. Acta* **1996**, *251*, 239.

[59] Similar $\tilde{\nu}_{CN}$ absorptions are observed for [VCp*$_2$Br(TCNE)] at 2189, 2174(s), and 2110(m) cm^{-1} (average = 2158 cm^{-1}), and $\tilde{\nu}_{CC} = 1420\ cm^{-1}$.[58]

[60] H. Braunwarth, F. Hutter, L. Zsolnai, *J. Organomet. Chem.* **1989**, *372*, C23.

[61] Likewise, [MnCp*(CO)$_2$(TCNE)] and [Mn(C$_5$H$_4$Me)(CO)$_2$-(TCNE)] exhibit key $\tilde{\nu}_{CN}$ absorptions at 2202(s) and 2122(m) (average 2162 cm^{-1}),[60] and 2205(s) and 2130(s) (average 2168 cm^{-1}) suggesting that although their structures are unknown, they are similar. B. Olbrich-Duessner, R. Gross, W. Kaim, *J. Organomet. Chem.* **1989**, *366*, 155.

[62] a) M. J. Macazaga, M. S. Delgado, J. R. Masaguer, *J. Organomet. Chem.* **1986**, *299*, 377; b) M. J. Macazaga, M. S. Delgado, J. R. Masaguer, *J. Organomet. Chem.* **1986**, *310*, 249.

[63] H. Werner, B. Juthani, *J. Organomet. Chem.* **1981**, *209*, 211.

[64] J. S. Miller, A. J. Epstein, *Chem. Commun.* **1998**, 1319.

[65] S. Mikami, K-i. Sugiura, T. Maruta, Y. Maeda, M. Ohba, N. Usuki, H. Ohkawa, T. Akutagawa, S. Nishihara, T. Nakamura, K. Iwasaki, N. Miyazaki, S. Hino, E. Asato, J. S. Miller, Y. Sakata, *J. Chem. Soc. Dalton Trans.* **2001**, 448.

[66] a) M. M. Olmstead, G. Speier, L. Szabo, *Chem. Commun.* **1994**, 541; b) G. Wang, H. Zhu, J. Fan, C. Slebodnick, G. T. Yee, *Inorg. Chem.* **2006**, *45*, 1406; c) G. T. Yee, personal communication.

[67] See ref. [13].

[68] See ref. [35].

[69] See ref. [36].

[70] See ref. [37].

[71] H. A. Bent, *Chem. Rev.* **1961**, *61*, 275.

[72] a) I. Vernik, D. V. Stynes, *Inorg. Chem.* **1996**, *35*, 6210; b) D. G. A. H. de Silva, D. B. Leznoff, G. Impey, I. Vernik, Z. Jin, D. V. Stynes, *Inorg. Chem.* **1995**, *34*, 4015.

[73] K.-i. Sugiura, J. S. Miller, unpublished results.

[74] A. L. Crumbliss, F. Basolo, *Inorg. Chem.* **1971**, *10*, 1676.

[75] a) P. Leoni, M. Pasquali, A. Fortunelli, G. Germano, A. Albinati, *J. Am. Chem. Soc.* **1998**, *120*, 9564; b) M. L. Taliaferro, P. Leoni, J. S. Miller, unpublished results.

[76] J. J. Hoagland, K. W. Hipps, *Langmuir* **1989**, *5*, 849; J. C. Moore, D. Smith, Y. Yohne, J. P. Devlin, *J. Phys. Chem.* **1971**, *75*, 325.

[77] J. M. Melson, P. Nuguyen, R. Peterson, H. Rengel, P. M. Macdonald, A. J. Lough, I. Manners, N. P. Raju, J. E. Greedan, S. Barlow, D. O'Hare, *Chem. Eur. J.* **1997**, *3*, 573.

[78] A. Rockenbauer, G. Speier, L. Szabó, *Inorg. Chim. Acta* **1992**, *201*, 5.

[79] We observe these absorptions at 2212 (m) and 2165 (s) cm^{-1} (KBr) (M. L. Taliaferro, J. S. Miller, unpublished results).

[80] M. Yasutake, T. Koga, Y. Sakamoto, S. Komatsu, M. Zhou, K. Sako, H. Tatemitsu, S. Onaka, Y. Aso, S. Inoue, T. Shinmyozu, *J. Am. Chem. Soc.* **2002**, *124*, 10136.

[81] a) R. L. Cordiner, D. Corcoran, D. S. Yufit, A. E. Goeta, J. A. K. Howard, P. J. Low, *Dalton Trans.* **2003**, 3541; b) P. J. Low, J. S. Miller, unpublished results.

[82] C. Diaz, A. Arancibia, *Polyhedron* **2000**, *19*, 137.

[83] S. Berger, H. Hartmann, M. Wanner, J. Fiedler, W. Kaim, *Inorg. Chim. Acta* **2001**, *314*, 22.

[84] a) R. Gross-Lannert, W. Kaim, B. Olbrich-Deussner, *Inorg. Chem.* **1990**, *29*, 5046; W. Kaim, T. Roth, B. Olbrich-Deussner, R. Gross-Lannert, J. Jordanov, E. K. H. Roth, *J. Am. Chem. Soc.* **1992**, *114*, 5693; b) R. Gross, W. Kaim, *Angew. Chem.* **1987**, *99*, 257; *Angew. Chem. Int. Ed. Engl.* **1987**, *26*, 251.

[85] A. N. Maity, B. Schwederski, W. Kaim, *Inorg. Chem. Commun.* **2005**, *8*, 600.

[86] M. Moscherosch, E. Waldhoer, H. Binder, W. Kaim, J. Fiedler, *Inorg. Chem.* **1995**, *34*, 4326; S. I. Amer, T. P. Dasgupta, P. M. Henry, *Inorg. Chem.* **1983**, *22*, 1970.

[87] J. M. Manriquez, G. T. Yee, R. S. McLean, A. J. Epstein, J. S. Miller, *Science* **1991**, *252*, 1415; J. S. Miller, G. T. Yee, J. M. Manriquez, A. J. Epstein, in *Proceedings of Nobel Symposium #NS-81 Conjugated Polymers and Related Materials: The Interconnection of Chemical and Electronic Structure*, Oxford University Press, 461, **1993**; *La Chimica & La Industria* **1992**, *74*, 845; K. I. Pokhodnya, N. Petersen, J. S. Miller, *Inorg. Chem.* **2002**, *41*, 1996; K. I. Pokhodnya, A. J. Epstein, J. S. Miller, *Adv. Mater.* **2000**, *12*, 410; D. C. Gordon, L. Deakin, A. M. Arif, J. S. Miller, *J. Am. Chem. Soc.* **2000**, *122*, 290; K. I. Pokhodnya, V.

 © 2006 Wiley-VCH Verlag GmbH & Co. KGaA, Weinheim

Burtman, A. J. Epstein, J. W. Raebiger, J. S. Miller, *Adv. Mater.* **2003**, *15*, 1211; E. B. Vickers, A. Senesi, J. S. Miller, *Inorg. Chim. Acta* **2004**, *357*, 3889; K. I. Pokhodnya, E. B. Vickers, M. Bonner, A. J. Epstein, J. S. Miller, *Chem. Mater.* **2004**, *16*, 3218.

[88] a) G. Bocelli, L. Cardellini, G. de Meo, A. Ricci, C. Rizzoli, G. Tosi, *J. Crystallogr. Spectrosc. Res.* **1990**, *20*, 561; M. L. Greer, S. C. Blackstock, *J. Org. Chem.* **1996**, *61*, 7895; S. Kyushin, M. Ikarugi, K. Takatsuna, M. Goto, H. Matsumoto, *J. Organomet. Chem.* **1996**, *510*, 121; P. Bruni, G. Bocelli, A. Cantoni, E. Giorgini, M. Iacussi, E. Maurelli, G. Tosi, *J. Chem. Crystallogr.* **1995**, *25*, 683; b) S. Delgato, A. Muñoz, M. E. Medina, C. J. Pastor, *Inorg. Chim. Acta* **2006**, *359*, 109.

[89] M. I. Bruce, B. G. Ellis, B. W. Skelton, A. H. White, *J. Organomet. Chem.* **2000**, *607*, 131; A. Horsken, G. Zheng, M. Stradiotto, C. T. C. McCrory, L. Li, *J. Organomet. Chem.* **1998**, *558*, 1; W. E. Meyer, A. J. Amoroso, M. Jaeger, J. Le Bras, W.-T. Wong, J. A. Gladysz, *J. Organomet. Chem.* **2000**, *616*, 44; A. Maisonnat, J.-J. Bonnet, R. Poilblanc, *Inorg. Chem.* **1980**, *19*, 3168; L. Li, G. D. Enright, K. F. Preston, *Organometallics* **1994**, *13*, 4686; M. Kranenburg, J. G. P. Delis, P. C. J. Kamer, P. W. N. M. van Leeuwen, K. Vrieze, N. Veldman, A. L. Spek, K. Goubitz, J. Fraanje, *J. Chem. Soc. Dalton Trans.* **1997**, 1839; A. Tsubouchi, N. Nakamura, A. Sugimoto, H. Inoue, T. Adachi, *J. Heterocycl. Chem.* **1994**, *31*, 1337; Y. Yamaguchi, H. Nagashima, *Organometallics* **2000**, *19*, 725; M. Bottrill, M. Green, A. G. Orpen, D. R. Saunders, I. D. Williams, *J. Chem. Soc. Dalton Trans.* **1989**, 511.

[90] R. E. Del Sesto, J. S. Miller, J. J. Novoa, P. Lafuente, *Chem. Eur. J.* **2002**, *8*, 4894.

[91] D. A. Clemente, A. Marzotto, *J. Mater. Chem.* **1986**, *6*, 941.

[92] D. A. Dixon, J. S. Miller, *J. Am. Chem. Soc.* **1987**, *109*, 3656; J. R. Fox, B. M. Foxman, D. Guarrera, J. S. Miller, J. C. Calabrese, A. H. Reis, Jr., *J. Mater. Chem.* **1986**, *6*, 1627.

[93] W. Beck, R. Schlodder, K. H. Lechler, *J. Organomet. Chem.* **1973**, *54*, 303.

[94] Y. Tobe, A. Takemura, M. Jimbo, T. Takahashi, K. Kobiro, K. Kakiuchi, *J. Am. Chem. Soc.* **1992**, *114*, 3479.

[95] M. I. Bruce, T. W. Hambley, J. R. Rodgers, M. R. Snow, A. G. Swincer, *J. Organomet. Chem.* **1982**, *226*, C1.

[96] A value of 2200 cm^{-1} is reported, but because the value is anomalous and as other nitriles are present, it is excluded from this Table (J. M. Fang, C. C. Yang, Y. W. Wang, *J. Org. Chem.* **1989**, *54*, 477).

[97] H. Zhao, R. A. Heinz, X. Ouyang, K. R. Dunbar, C. Campana, R. D. Rogers, *Chem. Mater.* **1999**, *11*, 736.

[98] J. S. Ricci, J. A. Obers, M. S. Fraser, W. H. Baddley, *J. Am. Chem. Soc.* **1970**, *92*, 3489.

[99] V. M. Anisimov, A. B. Zolotoi, M. Y. Antipin, P. M. Lukin, O. E. Nasakin, Yu. T. Struchkov, *Mendeleev Commun.* **1992**, 24.

[100] a) U. Drück, H. Güth, *Z. Kristallogr.* **1982**, *161*, 103; b) R. G. Little, D. Pautler, P. Coppens, *Acta Crystallogr. B* **1971**, *27*, 1493.

[101] J. P. Declercq, B. Tinant, A. Parfonry, M. van Meerssche, E. Legrand, M. S. Lehmann, *Acta Crystallogr. Sect. C* **1983**, *39*, 1401.

[102] D. A. Matthews, J. Swanson, M. H. Mueller, G. D. Stucky, *J. Am. Chem. Soc.* **1971**, *93*, 5945.

[103] L. N. Dawe, P. M. B. Piccoli, A. J. Schultz, A. M. Arif, M. L. Taliaferro, J. S. Miller, unpublished results.

[104] D. A. Dixon, J. C. Calabrese, J. S. Miller, *J. Phys. Chem.* **1991**, *95*, 3139; D. A. Dixon, J. C. Calabrese, J. S. Miller, *J. Phys. Chem.* **1991**, *95*, 7960.

[105] O. W. Webster, *J. Am. Chem. Soc.* **1964**, *86*, 2898.

[106] J. S. Miller, J. Zhang, W. M. Reiff, *J. Am. Chem. Soc.* **1987**, *109*, 4584.

[107] J. S. Miller, C. Vazquez, N. Jones, R. S. Mclean, A. J. Epstein, *J. Mater. Chem.* **1995**, *5*, 707.

[108] K.-i. Sugiura, A. M. Arif, D. R. Rittenberg, A. J. Epstein, J. S. Miller, *Chem. Eur. J.* **1997**, *3*, 138.

[109] D. K. Rittenberg, K.-i. Sugiura, A. M. Arif, C. D. Incarvito, A. L. Rheingold, Y. Sakata, J. S. Miller, *Chem. Eur. J.* **2000**, *6*, 1811.

[110] T. D. Selby, J. S. Miller, unpublished results.

© 2006 Wiley-VCH Verlag GmbH & Co. KGaA, Weinheim

Communications

DOI: 10.1002/anie.200600175

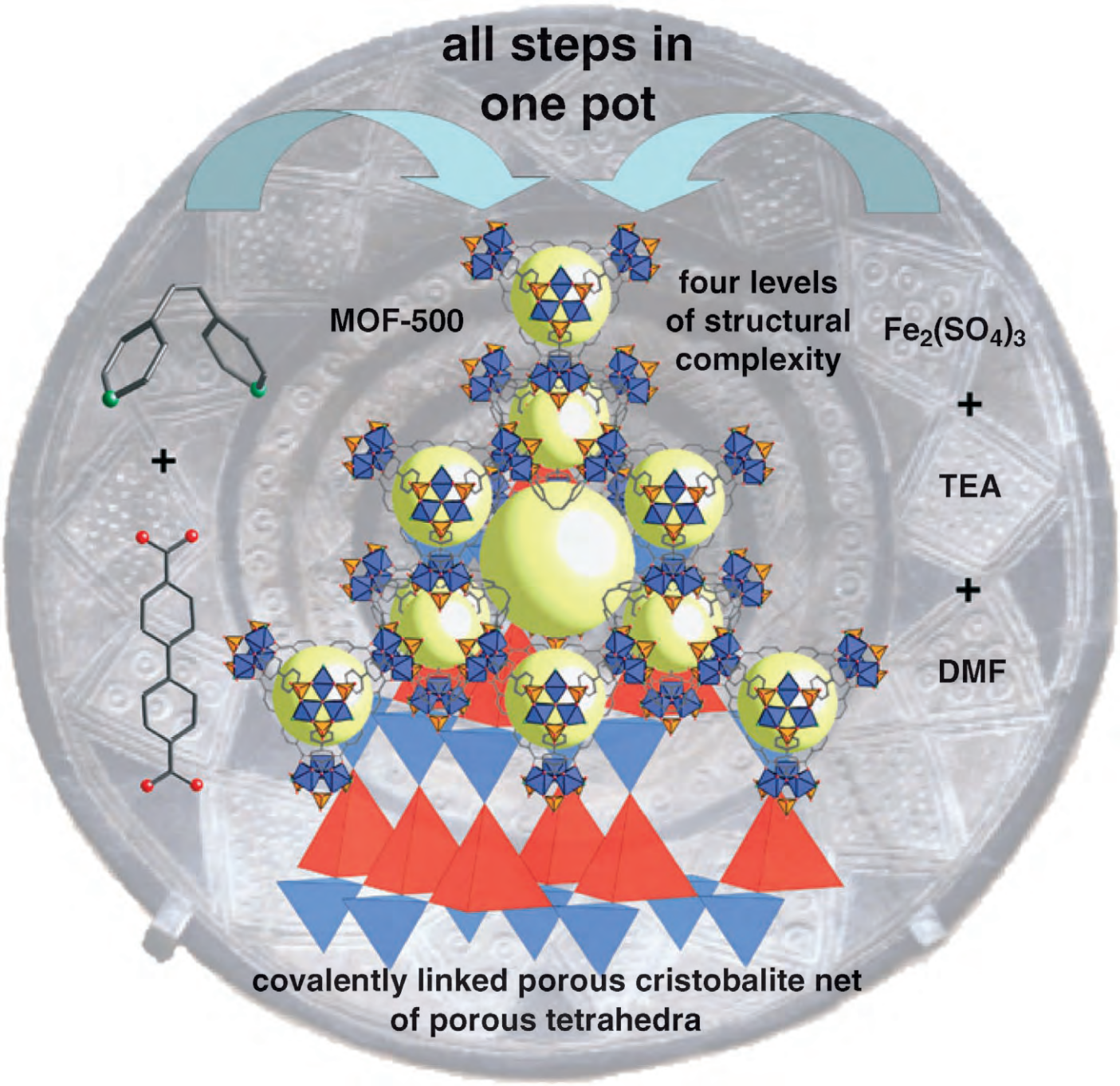

The step-by-step synthesis of hierarchical solid-state structures is hindered by the insolubility of the intermediates. In their Communication on the following pages, O. M. Yaghi and co-workers describe how the metal–organic framework MOF-500 is targeted on the basis of the crystal structure of its porous tetrahedral building blocks and prepared by a one-pot synthesis.

WILEY InterScience DISCOVER SOMETHING GREAT
© 2006 Wiley-VCH Verlag GmbH & Co. KGaA, Weinheim

Microporous Materials

DOI: 10.1002/anie.200600175

A Metal–Organic Framework with a Hierarchical System of Pores and Tetrahedral Building Blocks**

*Andrea C. Sudik, Adrien P. Côté, Antek G. Wong-Foy, Michael O'Keeffe, and Omar M. Yaghi**

Hierarchical chemical structures that incorporate some of the complexity typical of biological assemblies now exist and are being developed for use as highly selective catalysts, sensors, and ion- and drug-transport materials. Generally, such synthetic systems are based on supramolecular structures, for which it is possible to design step-by-step reactions that progressively lead to complex architectures of discrete molecular components.[1] In contrast, the stepwise synthesis of analogous extended (nonmolecular) networks is not feasible, because the intermediates are insoluble. Herein, we present the synthesis of MOF-500, a new metal–organic framework (MOF), to illustrate how a "one-pot" reaction can yield a crystalline solid with four distinct levels of complexity (defined by structural elements of increasing size, with distinct compositions, structures, and pores). Prior knowledge of reaction conditions that yield the porous tetrahedral level-3 building blocks of MOF-500 (Figure 1) obviates the need for a multistep synthesis.[2] We highlight the remarkable similarities between the structure of the extended network MOF-500 and that of its molecular building blocks (IRMOP-51). Furthermore, we demonstrate that a concomitant fourfold increase in gas uptake and surface area occurs on going from the crystals of the molecular building blocks IRMOP-51 to those of the extended network MOF-500.

Figure 1 outlines the conceptual and practical aspects of the synthesis and structure of MOF-500, in the context of four levels of increasing complexity. Dissolution of $Fe_2(SO_4)_3$ in *N*,*N*′-dimethylformamide (DMF) and triethylamine (TEA) yields solvated Fe^{III} ions (level 1), which in the presence of carboxylates, aggregate into trigonal $\{(Fe_3O)(CO_2)_3(SO_4)_3\}$ units (level 2).[2] In the absence of the sulfate capping groups, each of these units has six carboxylate ligands, $\{(Fe_3O)(CO_2)_6\}$, and can be viewed as a trigonal-prismatic building block. Such metal–carboxylate trigonal-prismatic units can be joined by multitopic organic linkers to form MOFs at the next level of structural hierarchy (level 3).[3–5] For example, Férey and co-workers used structural hierarchy to computationally predict and subsequently synthesize a series of highly porous MOFs (MIL-100, MIL-101, MIL-hypo-1, and MIL-hypo-2) based on trigonal-prismatic $\{(Cr_3O)(CO_2)_6\}$ units and 1,4-benzenedicarboxylate or 1,3,5-benzenetricarboxylate linkers.[6] We have recently shown that the sulfate-capped $\{(Fe_3O)(CO_2)_3(SO_4)_3\}$ units of level 2 can be joined by multitopic organic linkers (for example, 4,4′-biphenyldicarboxylate (BPDC)) in the presence of pyridine (py) to give the series of discrete porous tetrahedra IRMOP-51–53 at level 3.[2] These compounds have the same topology and are, thus, termed isoreticular metal–organic polyhedra (IRMOP). In these

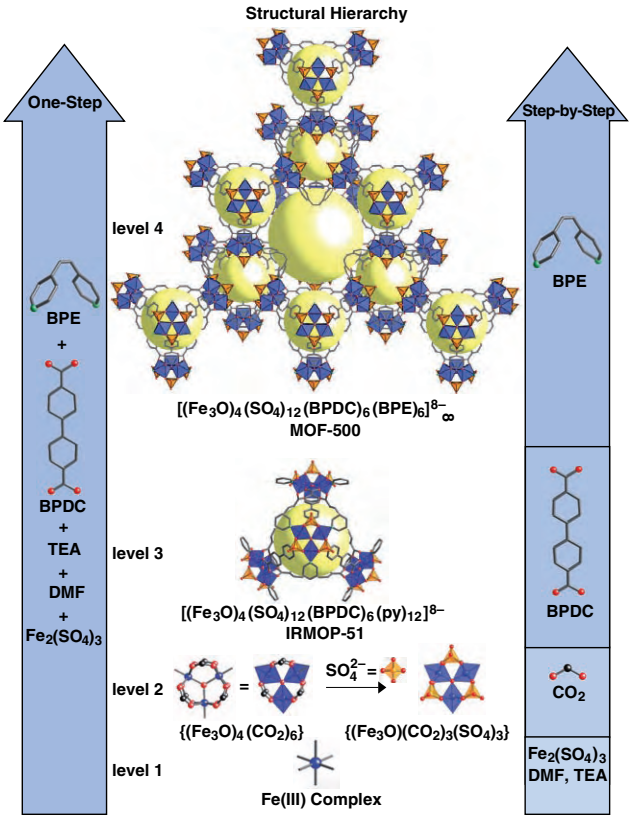

Figure 1. Conceptual representation of the synthesis and hierarchical structure of MOF-500. MOF-500 is built up from four distinct levels of structural hierarchy. Progression from one level to the next proceeds with the addition of a linking component. Although the step-by-step assembly (right arrow) of MOF-500 is not feasible in practice, a one-step synthesis (left arrow) is successful. See text for details. Fe blue atoms and polyhedra, S orange polyhedra, O red, N green, C gray; yellow spheres represent the tetrahedral pore space. Hydrogen atoms and the minor disorder components of the BPDC linkers are omitted.

[*] Dr. A. P. Côté, Prof. O. M. Yaghi
Department of Chemistry and Biochemistry
University of California, Los Angeles
Los Angeles, CA 90095-1569 (USA)
Fax: (+1) 310-206-4038
E-mail: yaghi@chem.ucla.edu
Dr. A. C. Sudik, Dr. A. G. Wong-Foy
Materials Design and Discovery Group
Department of Chemistry, University of Michigan
Ann Arbor, MI 48109-1055 (USA)
Prof. M. O'Keeffe
Department of Chemistry and Biochemistry
Arizona State University, Tempe, AZ 85287-1604 (USA)

[**] This work was supported by the National Science Foundation (DMR 0242630) and the Department of Energy (DOE). We thank Dr. Matthias Thommes from Quantachrome Instruments for helpful discussions concerning DFT calculations and Mr. Andrew R. Millward for assistance in adsorption studies. A.P.C. thanks the Natural Sciences and Engineering Research Council of Canada (NSERC) for a postdoctoral fellowship.

Supporting information for this article is available on the WWW under http://www.angewandte.org or from the author.

 © 2006 Wiley-VCH Verlag GmbH & Co. KGaA, Weinheim

IRMOP, three terminal pyridine ligands coordinate to each trigonal $\{(Fe_3O)(CO_2)_3(SO_4)_3\}$ unit. Herein, we use the level-3 compound IRMOP-51 as a building block for a fourth level of complexity, by replacing the pyridine ligands with a bipyridine linker, *cis*-1,2-bis-4-pyridylethane (BPE), to yield the extended network MOF-500. In so doing, four types of interconnected pores are created, which can be fully utilized for gas storage.

Conceptually, there are two pathways that can be employed to achieve the structure of MOF-500: a step-by-step addition of the required components or a one-pot reaction combining all components (Figure 1). The first strategy is difficult to implement in this system, because the level-3 compound IRMOP-51 is insoluble. Therefore, it was necessary to synthesize MOF-500 by the second strategy, by finding reaction conditions that combine all the steps.

The reaction conditions that produce MOF-500 are based on the procedure used to prepare the level-3 compound IRMOP-51. Equimolar amounts of $Fe_2(SO_4)_3{\cdot}x\,H_2O$ and H_2BPDC were heated (100 °C, 24 h) in a solution of DMF, TEA, and BPE to afford orange crystals of MOF-500 (15 % yield, based on H_2BPDC; see Supporting Information). A single crystal selected from the resulting MOF-500 sample was analyzed using X-ray diffraction.[7] FT-IR spectroscopy, thermogravimetric analysis (TGA), and powder X-ray diffraction (PXRD) were used to confirm the structural assignment and phase purity of the bulk sample (see Supporting Information). Elemental analysis revealed a formula of $[(Fe_3O)_4(SO_4)_{12}(BPDC)_6(BPE)_6]^{8-}\cdot 8\,[NH_2(CH_3)_2]^+\cdot 13\,H_2O\cdot 8\,DMF$ for the as-synthesized crystals of MOF-500. The negative charge of the anionic MOF-500 framework (−8 per formula unit) is balanced by eight dimethylammonium counterions, which are formed through the well-established decarbonylation of DMF upon heating in the presence of TEA.[8] The cations are completely disordered in the crystal and, thus, difficult to locate using X-ray diffraction techniques. In addition, it is difficult to accurately determine the stoichiometry of the neutral guests (DMF and water), owing to their volatility, which can lead to changes in their stoichiometry during post-synthesis sample handling. Similar obstacles are commonly encountered in MOF chemistry. Nevertheless, given that the neutral guests will ultimately be evacuated or exchanged from the pores, and that the structure of the framework was determined definitively from the single-crystal X-ray diffraction data, any ambiguity in the formulation of the guest molecules does not preclude the use of MOF-500 as a porous material.

Generally, we and others have found that MOF crystals containing large guest-filled pores (78.5 % of the free volume (see Table 1 for definition) in MOF-500) diffract X-rays to a limited resolution (ca. 1 Å) and produce a large diffuse-scattering background, because of the liquid-like packing of the guest entities within the framework.[6b,9] These factors do not inhibit the full and proper refinement of the metal–organic framework, as illustrated for MOF-5,[10] but do make identification and refinement of the guests (solvent and cations) unfeasible. The final anisotropically refined model for MOF-500 ($R_1 = 0.1005$, $wR_2 = 0.2598$) confirms that BPE molecules link the IRMOP-51 tetrahedra in the structure, as the assignment of atom types to electron-density peaks was unambiguous, and the average bond lengths and angles for the $\{(Fe_3O)(CO_2)_3(SO_4)_3\}$ units (Fe–Fe 3.325(3), Fe–O_{CO} 2.009(7), Fe–μ_3-O 1.921(2) Å), and the BPDC and BPE linkers (C–C 1.31(2), C–O 1.271(9), C–N 1.29(2) Å; C-C-C 124(3), O-C-O 124(2)°) fall within the expected ranges.[11,12]

There are four different types of porous tetrahedral units (A–D; Figure 2) in the MOF-500 framework. Tetrahedra A

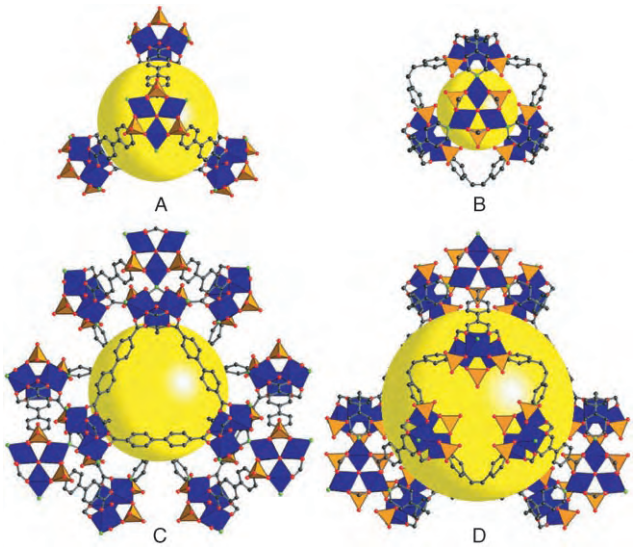

Figure 2. Tetrahedral building blocks A–D of MOF-500. The yellow sphere inside each tetrahedron is the largest sphere that can fit inside the pore without contacting the interior van der Waals surface. Fe blue polyhedra, S orange polyhedra, O red, N green, C gray. Hydrogen atoms and the minor disorder components of the BPDC linkers are omitted.

are the IRMOP-51 building blocks. Tetrahedra B are defined by four iron trimers, each belonging to a separate A-type tetrahedron, linked by six BPE molecules. The *cis* conformation of the BPE linkers provides the 70.5° angle necessary to covalently link the iron trimers of adjacent A-type tetrahedra. Tetrahedra C and D, which encompass the remaining void space, are actually truncated tetrahedra. Both are constructed from the iron-trimer vertices, and the BPDC and BPE edges of the A- and B-type tetrahedra. The BPE linkers protrude into the cavities of the C-type tetrahedra, but not those of the D-type tetrahedra.

The arrangement of the tetrahedral units in MOF-500 corresponds to the high-symmetry β-cristobalite (SiO_2) topology;[13] the central μ_3-oxygen atoms of each iron trimer serve as the vertices (X) in a cubic TX_2 net of corner-sharing $\{TX_4\}$ tetrahedra. The centers of the A- and B-type tetrahedra (T) are arranged in what can be described as a diamond net, or since there are two types of tetrahedra, as a binary sphalerite (ZnS) net (Figure 3). Note that, as two types of tetrahedra alternate in MOF-500, only nets with even-numbered rings are possible candidates for the topology; in particular, nets with 5-membered rings are ruled out.[5,6a] The further requirement of 180° T-X-T angles limits the possible T nets to either sphalerite or its hexagonal analogue wurtzite.

 © 2006 Wiley-VCH Verlag GmbH & Co. KGaA, Weinheim

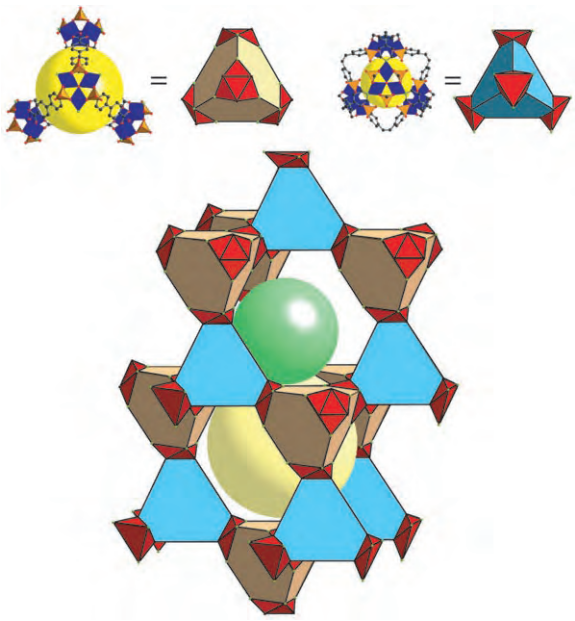

Figure 3. The topology of MOF-500 is based on alternating A-type (brown) and B-type (blue) tetrahedra linked through their shared iron trimers (red). Spheres represent the pore space of tetrahedra C (green) and D (light yellow).

The large cavities of the C- and D-type tetrahedra correspond to the holes delineated by adamantoid cages in the diamond (or sphalerite) net.

The level-3 compound IRMOP-51 crystallizes in two modifications: a stable triclinic form, and a metastable cubic form of much greater specific volume, which provided the inspiration for the present work. Remarkably, the crystal structures of MOF-500 and cubic IRMOP-51 are superimposable and have the same $F\bar{4}3m$ symmetry; contractions of only 0.4 Å between adjacent tetrahedra in IRMOP-51 are required for connection to occur in MOF-500 (Figure 4). Correspondingly, the unit-cell lengths of MOF-500 ($a =$ 38.509(1) Å) and IRMOP-51 ($a = 38.508(9)$ Å) are virtually identical. However, in MOF-500 the interstitial space of IRMOP-51 has been transformed into a rigid system of interconnected pores that can now be fully accessed by guests. Specifically, in MOF-500, tetrahedra A–D surround four unique pore types, whose properties are summarized in Table 1. The fixed pore diameter (see Table 1 for definition) of tetrahedron A (the IRMOP-51 building block) is maintained at 10.4 Å, and the smaller pore of tetrahedron B has a fixed diameter of 5.2 Å; the larger pores of tetrahedra C and D have fixed diameters of 13.0 and 18.0 Å, respectively. All four types of pore are interconnected by virtue of each tetrahedron having open faces with free pore diameters (see Table 1 for definition) ranging from 3.4 Å for tetrahedron B to 9.5 Å for tetrahedra C and D. The pores of MOF-500 not only vary in metrics, but also have distinctive chemical environments (Table 1). Organic BPDC linkers and iron trimers line the walls of the A-type pores, whereas BPE linkers and iron trimers, with their sulfate caps facing inwards, line the walls of the B-type pores. Both the C- and D-type pores are lined with BPDC and BPE organic linkers, but only

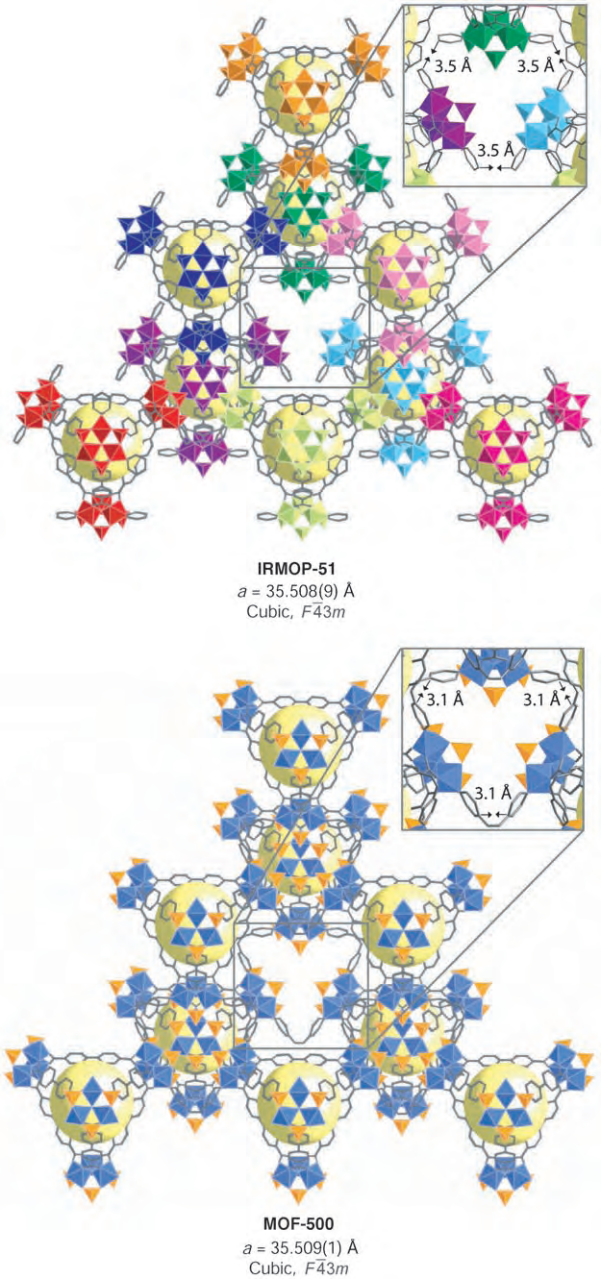

Figure 4. Comparison of the structures of IRMOP-51 and MOF-500, which are nearly isostructural. In IRMOP-51, the individual tetrahedra (each depicted in a different color; Fe and S polyhedra, C gray; yellow spheres represent the tetrahedral pore space) are isolated, but in MOF-500, the A-type tetrahedra (Fe blue polyhedra, S orange polyhedra, O red, N green, C gray; yellow spheres represent the tetrahedral pore space) are linked by BPE molecules, as shown in the enlarged sections of the structures. Hydrogen atoms and the minor disorder components of the BPDC linkers are omitted.

the D-type pores have direct exposure to sulfate units. In the crystals of MOF-500, 78.5 % of the free volume is distributed among the pores in amounts ranging from 6.6 % for B-type pores to 32.4 % for D-type pores (Table 1).

Comparison of the gas sorption isotherms for evacuated samples of MOF-500 and cubic IRMOP-51 indicates a significant enhancement in the sorption capacity of MOF-

 © 2006 Wiley-VCH Verlag GmbH & Co. KGaA, Weinheim

Table 1: Properties of the pores in MOF-500.

Property	Pore type A	B	C	D
Diameter (Å), X-ray[a,b]	10.4	5.2	13.0	18.0
Aperture (Å), X-ray[a,c]	6.4	3.4	9.5	9.5
Fraction of free volume (%), X-ray[a,d]	15.5	6.6	24.0	32.4
Diameter (Å), sorption[e]	9.6	–	14.8	20.0
Chemical environment:				
Fe_3O	4	4	–	–
SO_4	–	12	–	12
BPDC	6	–	12	6
BPE	–	6	6	12

[a] Calculated from the crystal structure of MOF-500 using Cerius^2.[16] [b] Fixed pore diameter: the diameter of the largest sphere that can occupy the pore without contacting the van der Waals surface of the framework. [c] Free pore diameter: the diameter of the largest sphere that pass through the aperture of the pore without contacting the van der Waals surface of the framework. [d] Free volume: the free crystal volume bounded by the van der Waals surface of the framework. [e] Calculated from a NLDFT fit to the argon adsorption data for MOF-500 in Figure 5 a.

500. The argon sorption isotherms for MOF-500 and IRMOP-51 at 87 K reveal reversible uptakes of 1127 and 278 mg g^{-1} (at $P/P_o = 0.1$), corresponding to 128 and 30 argon atoms per formula unit, respectively (Figure 5 a). Thus, a fourfold increase in argon sorption capacity is attained by linking IRMOP-51 into a rigid framework. Whereas typical Type-I behavior is observed for IRMOP-51, a distinct reversible step is evident at $P/P_o \approx 0.01$ in the argon and N_2 sorption isotherms of MOF-500, followed by a plateau at $P/P_o \gtrsim 0.15$ (see Supporting Information for the N_2 sorption isotherm). The specific surface areas (A_s) of MOF-500 and IRMOP-51, determined by the Brunauer–Emmett–Teller (BET) method using the adsorption branches of the argon isotherms, are 2274 and 544 m^2 g^{-1}, respectively.[14] For MOF-500, A_s represents the cumulative specific surface area for both steps in the micropore region; a similar A_s value of 2224 m^2 g^{-1} was calculated from the N_2 sorption isotherm of MOF-500 at 78 K.

The multistep features observed in the micropore region of both the argon and N_2 sorption isotherms of MOF-500 confirm the presence of multiple types of pores, a characteristic known from the crystal structure. To evaluate the pore size distribution of MOF-500, the argon sorption isotherm at 87 K was analyzed using nonlocal density functional theory (NLDFT) implementing a hybrid kernel for argon adsorption at liquid-argon temperature based on a zeolite/silica model containing cylindrical pores.[15] The distribution calculated by fitting the MOF-500 adsorption data revealed three types of pores with widths centered around 9.6, 14.8, and 20.0 Å (Figure 5 b, histogram). Moreover, these values are consistent with the dimensions of pores A, C, and D in the MOF-500 crystal structure (Table 1). The contribution from pore B is not observed, because its pore aperture (3.4 Å) is very similar in size to the kinetic diameter of argon (3.4 Å).[14] Further analysis of the pore size distribution reveals that the contribution of micropores (widths < 20 Å) to the total pore volume is 0.61 cm^3 g^{-1} or 65% (Figure 5 b, curve), which compares favorably to the sum of the free volumes in pores A, C, and D (72%). The value of 0.61 cm^3 g^{-1}, however, is in excellent agreement with the value of 0.63 cm^3 g^{-1} derived from a Dubinin–Radushkevich (DR) treatment of the argon sorption isotherm. In contrast, a DR analysis of the IRMOP-51 argon sorption isotherm yielded a micropore volume of only 0.15 cm^3 g^{-1}. The sorption data validate the accessibility and permanently porous nature of three types of cavities in MOF-500, while only one type of cavity was identified for MOF-500.

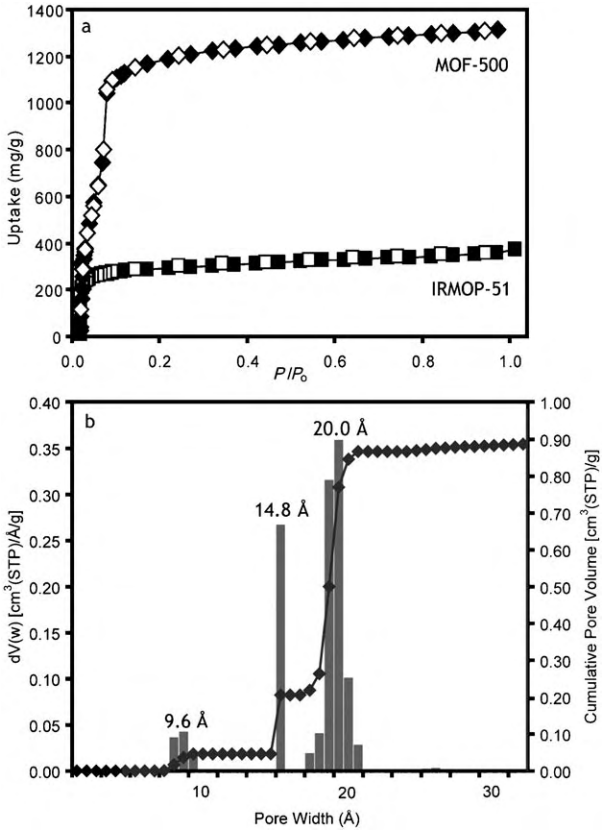

Figure 5. a) Argon sorption isotherms for MOF-500 (◆, ◇) and IRMOP-51 (■, □) at 87 K (filled symbols: adsorption, open symbols: desorption). b) Pore size distribution (left axis, histogram) and cumulative pore volume (right axis, ◆) for MOF-500, calculated from a NLDFT fit to the argon adsorption data for MOF-500 in (a). See text for details. STP = normalized to standard temperature and pressure.

This study illustrates at least two unique features of MOF-500: 1) conceptually, its structure is built up from four levels of hierarchy, and 2) its sorption capacity is significantly enhanced relative to that of its level-3 building units (IRMOP-51). The general applicability of this hierarchical approach to solid-state synthesis is virtually unlimited, given the large number of crystalline molecular solids.

Received: January 16, 2006

Keywords: iron · metal–organic frameworks · microporous materials · nanostructures · sorption

 © 2006 Wiley-VCH Verlag GmbH & Co. KGaA, Weinheim

[1] a) D. T. Bong, T. D. Clark, J. R. Granja, M. R. Ghadiri, *Angew. Chem.* **2001**, *113*, 1016 – 1041; *Angew. Chem. Int. Ed.* **2001**, *40*, 988 – 1011; b) S. I. Stupp, V. Le Bonheur, K. Walker, L. S. Li, K. E. Huggins, M. Keser, A. Amstutz, *Science* **1997**, *276*, 384 – 389; c) V. Berl, M. J. Krische, I. Huc, J.-M. Lehn, M. Schmutz, *Chem. Eur. J.* **2000**, *6*, 1938 – 1946; d) M. C. T. Fyfe, J. F. Stoddart, *Acc. Chem. Res.* **1997**, *30*, 393 – 401; e) D. Zhao, J. S. Moore, *Chem. Commun.* **2003**, 807 – 818; f) M. Fujita, D. Oguro, M. Miyazawa, H. Oka, *Nature* **1995**, *378*, 469 – 471; g) N. I. Kovtyukhova, T. E. Mallouk, *Chem. Eur. J.* **2002**, *8*, 4355 – 4363; h) T. K. Holman, A. M. Pivovar, M. D. Ward, *Science* **2001**, *294*, 1907 – 1911; i) M. W. Hosseini, *Acc. Chem. Res.* **2005**, *38*, 313 – 323.

[2] A. C. Sudik, A. W. Millward, N. W. Ockwig, A. P. Côté, J. Kim, O. M. Yaghi, *J. Am. Chem. Soc.* **2005**, *127*, 7110 – 7118.

[3] G. Férey, *J. Solid State Chem.* **2000**, *152*, 37 – 48.

[4] A. C. Sudik, A. P. Côté, O. M. Yaghi, *Inorg. Chem.* **2005**, *44*, 2998 – 3000.

[5] C. Serre, F. Millange, S. Surblé, G. Férey, *Angew. Chem.* **2004**, *116*, 6445 – 6449; *Angew. Chem. Int. Ed.* **2004**, *43*, 6285 – 6289.

[6] a) G. Férey, C. Mellot-Draznieks, C. Serre, F. Millange, *Acc. Chem. Res.* **2005**, *38*, 217 – 225; b) G. Férey, C. Serre, C. Mellot-Draznieks, F. Millange, S. Surblé, J. Dutour, I. Margiolaki, *Angew. Chem.* **2004**, *116*, 6456 – 6461; *Angew. Chem. Int. Ed.* **2004**, *43*, 6296 – 6301; c) C. Mellot-Draznieks, J. Dutour, G. Férey, *Z. Anorg. Allg. Chem.* **2004**, *630*, 2599 – 2604.

[7] MOF-500: refined formula: $Fe_{12}S_{12}C_{156}H_{96}N_{12}O_{86.61}$ (see Supporting Information for details), $T = 258(2)$ K, cubic, space group $F\bar{4}3m$ (No. 216), $a = 38.509(1)$ Å, $V = 57107(3)$ Å^3, $Z = 4$, $\rho_{calcd} = 0.533$ g cm^{-3}, $\mu(Mo_{K\alpha}) = 0.372$ mm^{-1}, 72106 measured reflections, 2889 unique reflections ($R_{int} = 0.4268$), 128 parameters, no restraints, $R_1 = 0.1005$ for 1721 observed reflections ($I > 2\sigma(I)$), wR_2(all data) $= 0.2598$, $S = 1.062$, $\Delta\rho_{elec} = 0.407$ e Å^{-3}. CCDC-294671 (MOF-500) contains the supplementary crystallographic data (and details of the data handling and structure refinement) for this paper. These data can be obtained free of charge from The Cambridge Crystallographic Data Centre via www.ccdc.cam.ac.uk/data_request/cif.

[8] D. D. Perrin, W. L. F. Armarego, *Purification of Laboratory Chemicals*, 3rd ed. Pergamon, Oxford, **1988**.

[9] a) M. E. Kosal, J.-H. Chou, S. R. Wilson, K. S. Suslick, *Nat. Mater.* **2002**, *1*, 118 – 121; b) G. J. McManus, Z. Wang, M. Zaworotko, *Cryst. Growth Des.* **2004**, *4*, 11 – 13; c) D. J. Hoffart, S. J. Loeb, *Angew. Chem.* **2005**, *117*, 923 – 926; *Angew. Chem. Int. Ed.* **2005**, *44*, 901 – 904; d) B. D. Chandler, A. P. Côté, D. T. Cramb, J. T. Hill, G. K. H. Shimizu, *Chem. Commun.* **2002**, 1900 – 1901; e) H. K. Chae, D. Y. Siberio-Pérez, J. Kim, Y. Go, M. Eddaoudi, A. J. Matzger, M. O'Keeffe O. M. Yaghi, *Nature* **2004**, *427*, 523 – 527.

[10] a) H. Li, M. Eddaoudi, M. O'Keeffe, O. M. Yaghi, *Nature* **1999**, *402*, 276 – 279; b) M. Eddaoudi, D. B. Moler, H. Li, B. Chen, T. M. Reineke, M. O'Keeffe, O. M. Yaghi, *Acc. Chem. Res.* **2001**, *34*, 319 – 330.

[11] R. D. Cannon, R. P. White, *Prog. Inorg. Chem.* **1988**, *36*, 195 – 298.

[12] F. H. Allen, O. Kennard, D. G. Watson, L. Brammer, G. Orpen, *J. Chem. Soc. Perkin Trans. 2* **1987**, S1 – S19. Note, the elevated uncertainties for the geometric parameters of the BPE and BPDC linkers are primarily due to disorder.

[13] M. O'Keeffe, B. G. Hyde, *Crystal Structures: I. Patterns and Symmetry*, Mineralogical Society of America, Washington DC, **1996**.

[14] F. Rouquerol, J. Rouquerol, K. S. W. Sing, *Adsorption by Powder and Porous Solids*, Academic Press, London, **1999**.

[15] a) J. P. Olivier, W. B. Conklin, M. Szombathely in *Characterization of Porous Solids III* (Eds.: F. Rodriguez-Reinoso, J. Rouquerol, K. S. W. Sing, K. K. Unger), Elsevier, Amsterdam, **1994**, pp. 81 – 89; b) P. I. Ravikovitch, D. Wei, W. T. Chueh, G. L. Haller, A. V. Neimark, *J. Phys. Chem. B* **1997**, *101*, 3671 – 3679.

[16] Cerius^2 Modeling Environment, Molecular Simulations Inc., San Diego CA, **1999**.

 © 2006 Wiley-VCH Verlag GmbH & Co. KGaA, Weinheim

Electrocatalysis

DOI: 10.1002/anie.200600033

Carbon Nanotubes Contain Metal Impurities Which Are Responsible for the "Electrocatalysis" Seen at Some Nanotube-Modified Electrodes

*Craig E. Banks, Alison Crossley, Christopher Salter, Shelley J. Wilkins, and Richard G. Compton**

Carbon nanotubes (CNTs) have emerged as a novel class of nanomaterials and consequently receive considerable interest in a plethora of areas,[1–7] none more so than in electrochemistry and electrocatalysis where their use has escalated over the last decade owing to the reported "electrocatalytic" properties of carbon-nanotube-modified electrodes, that is, electrodes usually made of carbon with a film of nanotubes.[8–13] These properties include reductions in overpotentials, increments in the voltammetric peak heights which facilitates lower detection limits and enhanced sensitivities in analytical sensing coupled with little or no observed surface fouling.[8–10,13]

We have compared the electroreduction of ferricyanide and the oxidation of epinephrine in aqueous solutions at carbon-nanotube-modified electrodes with the response of an edge-plane pyrolytic graphite (EPPG) electrode.[11,12] The EPPG electrode is an electrode constructed from highly ordered pyrolytic graphite where the graphite layers are perpendicular to the disc surface and are separated with an interlayer spacing of 3.35 Å. Surface defects occur in the form of steps exposing the edges of the graphite layers (see Figure 1 A). Conversely a basal-plane pyrolytic graphite (BPPG) electrode is fabricated such that the layers of graphite lie parallel to the surface. When a CNT-modified electrode was compared with an EPPG electrode, an analogous response in the voltammetry was observed at both electrodes (see Figure 1 B) allowing us to demonstrate that

[*] Dr. C. E. Banks, Prof. Dr. R. G. Compton
Physical and Theoretical Chemistry Laboratory
Oxford University
South Parks Road, Oxford OX1 3QZ (UK)
Fax: (+44) 1865-275-410
E-mail: richard.compton@chem.ox.ac.uk
Dr. A. Crossley, C. Salter, Dr. S. J. Wilkins
Materials Department
University of Oxford, Parks Road, Oxford OX1 3PH (UK)

© 2006 Wiley-VCH Verlag GmbH & Co. KGaA, Weinheim

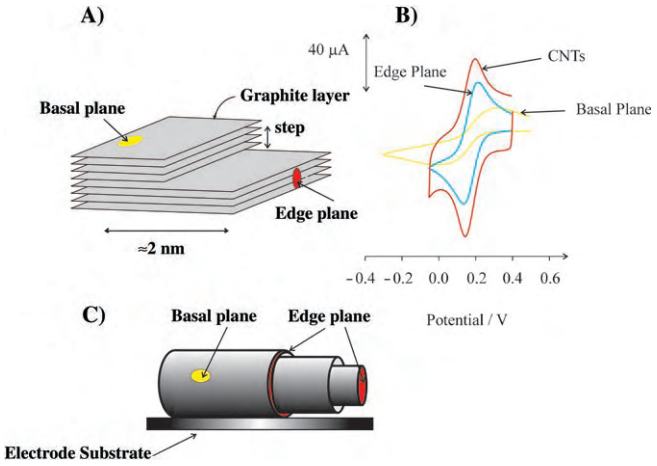

Figure 1. A) Schematic representation of a crystal of highly ordered pyrolytic graphite where the layers of graphite have an interlayer spacing of 3.35 Å. B) The difference in the voltammetric response for the reduction of ferricyanide in an aqueous solution using basal-plane and edge-plane pyrolytic graphite electrodes. Note the identical response for the CNT-modified electrode compared with the edge-plane pyrolytic graphite electrode. C) A single MW-CNT on an electrode surface where the edge-plane-like sites are shown at the end of the tube and along the tube axis.

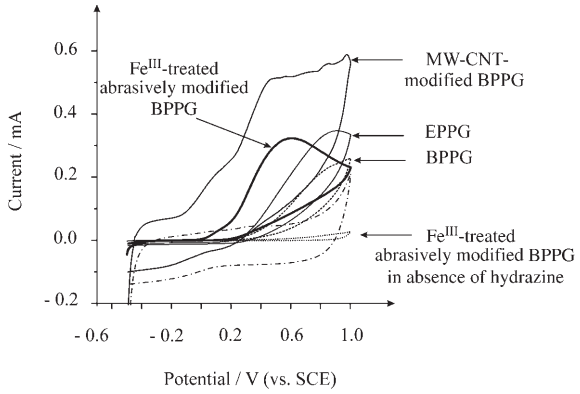

Figure 2. Cyclic voltammetric profiles resulting from the electrochemical oxidation of 6.5 mM hydrazine in a pH 7.2 phosphate buffer solution. Note that the unmarked dot-dash-dot line is the response of the MW-CNT-modified BPPG in the absence of hydrazine.

the electrochemical reactivity of carbon nanotubes resides solely in edge-plane-like sites, defects which occur at the end of the nanotubes or along the tube axis (see Figure 1 C).[11–14] Similar observations have now been made for several diverse chemical systems.[15–17]

In particular, we have shown that the electrocatalytic oxidation of NADH observed at multi-walled CNT electrodes produced exactly the same response as that at an EPPG electrode allowing insights into the electrochemical reactivity of NADH at carbon nanotubes.[15] Notably, the reported lack of surface passivation of NADH oxidation products at the CNTs was shown to adsorb at edge plane sites. However, owing to the high density of edge-plane-like sites on CNTs (and the EPPG electrode) they were unsusceptible to surface passivation.[15] We have also advocated the routine use of EPPG electrodes for sensing applications where electrocatalysis with CNT-modified electrodes is claimed. This recommendation is based on the longer life of the EPPG electrodes as compared to the CNT-modified electrodes and for greater simplicity of the measurement.[12–17]

We have recently noted examples where the response of a CNT-modified electrode when compared directly with an EPPG electrode indicates that the electrochemical reactivity is not consistent with the hypothesis that it should arise solely from edge-plane-like sites/defects on the CNTs. One such example is in the electrocatalytic oxidation of hydrazine at multi-walled carbon nanotube (MW-CNT) modified electrodes. In particular, Zhao et al. have reported that superior electrocatalytic oxidation of hydrazine was possible at a MW-CNT paste electrode in comparison to a graphite-powder paste electrode;[18] it is this observation we consider herein.

Figure 2 shows the voltammetric response corresponding to the electrochemical oxidation of hydrazine in a phosphate buffer solution at a MW-CNT-modified BPPG electrode. This occurs at approximately +0.46 V (versus saturated calomel electrode (SCE)) which, in comparison to a bare BPPG electrode a barely defined oxidation peak is seen (Figure 2) owing to the very low proportion of edge-plane sites, shows a considerable reduction in the overpotential coupled with an appreciable increase in the peak magnitude. A control experimental to verify the observed "electrocatalysis" of CNT was conducted as necessary to claim electrocatalysis;[11–14] we compared the observed response of the MW-CNT-modified electrode with an EPPG electrode. The EPPG electrode was cut from a high quality piece of highly ordered pyrolytic graphite with the graphite layers perpendicular to the disc face and as the names implies produces an electrode with a surface purely formed from edge-plane graphite. Figure 2 shows the voltammetric response of an EPPG electrode which exhibits an oxidation wave with a peak potential at +0.91 V (vs. SCE). Comparison of this EPPG-electrode response with that of the CNT-modified electrode in Figure 2 indicates that the observed electrocatalysis signal observed at the later is not due to edge-plane sites/defects on the CNTs but must derive from other causes; it is this we next address. Specifically we address the issue of possible impurities in the CNT samples.[19,20]

In our work, we use multi-walled "bamboo" carbon nanotubes (from NanoLab, Brighton, MA) with a 10–20 nM diameter and are 5–20 μm in length with a purity of >95%. We took a sample of these MW-CNTs and placed these into a covered beaker containing 2 M nitric acid and stirred the solution for 20 h. The MW-CNTs were collected by filtration and washed with copious amounts of water after which are allowed to dry overnight at room temperature; this procedure is that advocated by Wang et al. the pioneering group in this area.[19,20] These nanotubes will be referred to as "washed MW-CNTs". Another sample of the unwashed MW-CNTs was taken and subjected to a "super wash". The only difference between this and the washed MW-CNTs is the length of time which they are stirred in 2 M nitric acid, this being 36 h for super-washed MW-CNTs. Energy-dispersive X-ray (EDX) analysis was conducted on the washed MW-CNTs and the super-washed MW-CNTs and compared with an

 © 2006 Wiley-VCH Verlag GmbH & Co. KGaA, Weinheim

unwashed nanotube sample. Figure 3 shows a typical EDX spectrum where we observe that the sulfur signal, initially present on the unwashed MW-CNTs decreases to approximately half its initial magnitude after the sample has been

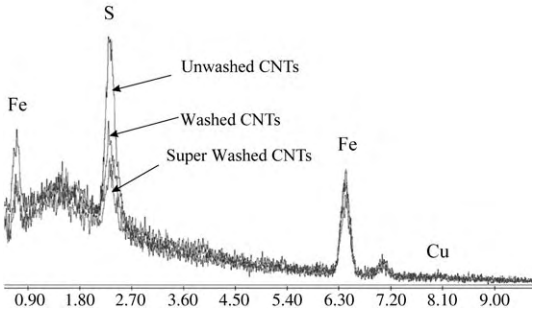

Figure 3. Typical EDX spectra comparing the response of unwashed, washed, and super-washed MW-CNTs.

washed but remains of similar intensity after being super washed. The spectrum also indicates the presence of significant amounts of iron, which was not removed with either washing or even super washing.

The extent of the iron present on the unwashed MW-CNTs was explored with wavelength dispersive X-ray (WDX) analysis on an electron microprobe. Figure 4 shows an SEM image of the unwashed MW-CNTs where close inspection reveals areas on the MW-CNTs (seen as white) which are attributed to metal impurities. These metal impurities are better identified with WDX, the results of which are also shown in Figure 4, where the distribution of iron can be seen over the MW-CNT sample, as indicated by the color intensity. The resolution of the electron microprobe is insufficient to identify the individual regions along a MW-CNT but it does indicate that the surface is dotted with small nuclei (>50 nm) of iron rather than large "clumps".

X-ray photoelectron spectroscopy (XPS) was conducted to acquire information about the oxidation state of the iron in the unwashed MW-CNT sample. A binding energy position of 710.3 (eV) was found agreeing well with a literature value for Fe^{III} [21] indicating that the iron present on the MW-CNTs is likely Fe_2O_3.[21] XPS data analysis of the unwashed MW-CNTs indicated that the sample was 98.9 atomic% carbon, 1.0 atomic% oxygen, 0.1 atomic% iron, and trace (<0.1 atomic%) copper and sulfur was observed.

Typically the MW-CNTs are grown using a metal catalysis which can either be nickel or cobalt but is most commonly iron.[22] After fabrication the MW-CNTs undergo an acid purification which leaches away the metals to a purity of 95% or better.[22,23] After the purification, the CNTs are tested using thermogravimetry where 1 g of CNTs are oxidized in a way such that the remaining weight should be less than 0.05 g (which is due to metal impurities). Therefore in 1 g of CNTs, 0.05 g is due to metal impurities. It is also of note that Nanolab independently have conducted EDX on their carbon nanotubes and have found that typically the CNTs contains about 1% weight iron along with 0.1% by weight of sulfur.[23]

What is important from the above observations is that iron cannot be simply removed by washing and is likely trapped in graphite-like planes along the tube axis, or at the ends of the nanotubes, or contained within the carbon nanotubes; clearly washing the nanotubes in acid has no significant effect in respect of the complete removal of iron.

Given that we know that the iron present is Fe^{III}, an abrasively modified BPPG electrode of Fe^{III} oxide was next prepared. This involves first cellotaping the BPPG.[11] This procedure involves polishing a BPPG electrode surface on carborundum paper and then pressing cellotape on the cleaned BPPG surface before removing the cellotape along with general attached graphite layers. This process is repeated several times. The electrode was then cleaned in acetone to remove any adhesive. The freshly prepared BPPG electrode is then gently rubbed on a fine piece of quality filter paper containing Fe^{III} (Fe_2O_3). This abrasively modified electrode was then investigated in the presence and absence of 6.5 mM hydrazine in pH 7.2 phosphate buffer solution. As depicted in Figure 2, a large oxidation wave occurring at approximately $+0.56$ V (vs. SCE) is observed which is in excellent agreement with the response of the MW-CNT-modified BPPG electrode. Note that no oxidation wave is observed in the absence of hydrazine in the pH 7.2 phosphate buffer solution indicating that the observed wave is due to the catalytic oxidation of hydrazine at the Fe^{III} surface.

Note that the electrochemical oxidation of hydrazine occurs at metallic substrates such as palladium,[24] platinum,[25,26] nickel,[25] and cobalt[25] in which case, surface oxides are likely to place a key in the electrocatalysis mechanism.[26] Whilst the exact electrochemical mechanism is unknown it will almost certainly involve the chemically irreversible oxidation of hydrazine to nitrogen.

The above study shows proof-of-concept in respect of observed apparent electrocatalysis at the carbon-nanotube-modified electrode is likely due to the role of metal

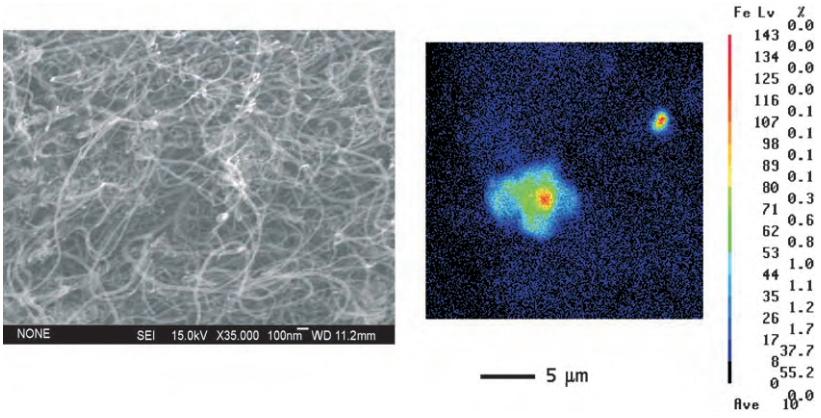

Figure 4. Left: A typical SEM image of the unwashed MW-CNTs. Right: WDX analysis of the unwashed MW-CNTs. The color scale indicates the Fe signal intensity (red = high signal intensity).

 © 2006 Wiley-VCH Verlag GmbH & Co. KGaA, Weinheim

impurities in the carbon nanotubes; the catalysis has been shown to be most likely due to Fe_2O_3 impurities. Furthermore note that a similar oxidation wave was observed (ca. +0.58 V vs. SCE) using an abrasively modified Fe^{II} (FeO) BPPG electrode indicating that other oxidation states of the iron impurities might exist and could contribute to the observed electrocatalytic signal at the MW-CNT-modified electrode.

Note that XPS only identifies elements on the surface (< 10 nm depth) of the bundle of MW-CNTs so that any metal impurities in the center of a MW-CNT bundle may not be detected.

We also note that Lin and Leu[27] have shown that hydrogen peroxide can be electrocatalytically detected using a Fe_3O_4-based chemical sensor. We speculate that the reported electrocatalytic reduction of hydrogen peroxide observed at MW-CNT-modified electrodes[20] may possibly be due to the presence of iron impurities on/within the CNTs used by Wang et al.[20]

In summary:

a) The protocol of washing CNTs,[16,17] which are already at 95% or greater purity prior to use, has little effect as evidenced by "super washing", the electroactive metal impurities on/within the carbon nanotubes are not further removed.
b) Metal impurities in some instances may cause the observed "electrocatalysis" associated with carbon-nanotube-modified electrodes.

We therefore advocate that all electrochemical experiments where carbon-nanotube-modified electrodes are employed should be compared with EPPG electrodes. This will show that either edge-plane sites/defects are responsible or suggest that metal impurities may provide a facile electrochemical reaction.

Experimental Section

All chemicals used were of analytical grade and were used as received without any further purification. These were: hydrazine sulfate (99+ % A.C.S Reagent), iron(II) oxide (99.99%, Aldrich) iron(III) oxide (99.999% Aldrich). All solutions were prepared with deionized water of resistivity not less than 18.2 MΩ cm (Vivendi water systems, UK).

Multi-walled carbon nanotubes (> 95% purity (10–20 nM diameter, 5–20 μm length) were obtained from NanoLab (Brighton, MA). The MW-CNTs were washed in 2 M nitric acid for 20 h and are referred to as washed MW-CNTs, while super-washed refers to the MW-CNTs washed for 35 h in a 2 M nitric acid solution.

Voltammetric measurements were carried out using a μ-Autolab II (ECO-Chemie, The Netherlands) potentiostat. All measurements were conducted using a three-electrode configuration.

Edge and basal plane pyrolytic graphite, (BPPG, EPPG, Le Carbone, Ltd. Sussex, UK) were used a working electrodes. In the former case discs of pyrolytic graphite were machined into a 4.9 mm diameter, which was oriented with the disc face parallel with the edge plane, or basal plane as required. The EPPG electrodes were polished on alumina lapping compounds (BDH) of decreasing sizes (0.1–5 μm) on soft lapping pads prior to use. The counter electrode was a bright platinum wire, with a saturated calomel electrode (Radiometer, Copenhagen, Denmark) completing the circuit.

The BPPG was prepared for modification by renewing the electrode surface with cellotape. This procedure involves polishing the old BPPG-electrode surface on carborundum paper and then pressing cellotape on the cleaned BPPG surface before removing it along with general attached graphite layers. This was repeated several times. The electrode was then cleaned in acetone to remove any adhesive.

The MW-CNTs were cast onto a freshly prepared BPPG. This involves first dispersing MW-CNTs (2 mg) into ethanol (2 mL). The suspension is then placed into an ultrasonic bath for 1 min before 20 μL of it is pippetted onto the BPPG surface. This solution is allowed to volatize at room temperature producing a random distribution of carbon nanotubes on the BPPG surface.

XPS analysis: The samples were pressed onto a conducting carbon pad, completely covering the pad which was attached to an aluminum stub. The samples were introduced into the XPS instrument through a turbo-pumped chamber (10^{-6} Torr). XPS was performed in a VG nine-channel CLAM4 system using 300-W monochromated Al X-rays. The X-rays are focused onto an area of the sample 1 mm × 5 mm. The largest slits and apertures (5 mm) were used to maximize the signal. The survey scan was obtained with the analyzer operating at a constant pass energy of 100 eV (1.0 eV step, 0.1 s per channel, 5 scans). Detailed scans were performed with a constant pass energy of 20 eV. The Fe and Cu regions were scanned at 0.1 eV step and 0.2 s per channel, 100 scans were performed. Base pressure of the ion-pumped analysis chamber was 1×10^{-9} Torr. The area under the principal peak of each element in the spectrum, divided by an empirically derived sensitivity factor,[21] is proportional to the concentration of that element on the surface (top 10 nm).

SEM and EDX were carried out using a JEOL 6500F instrument. The compositional analysis of the MW-CNTs on the electrode surface was carried out by employing wavelength dispersive X-ray analysis (WDX; JEOL JXA-8800 microprobe).

Received: January 4, 2006
Published online: March 17, 2006

Keywords: carbon nanotubes · electrocatalysis · electrochemistry · oxidation · pyrolytic graphite electrodes

[1] S. E. Kooi, U. Schlecht, M. Burghard, K. Kern, *Angew. Chem.* **2002**, *114*, 1409 – 1411; *Angew. Chem. Int. Ed.* **2002**, *41*, 1353 – 1355.
[2] T. Sun, H. Liu, W. Song, X. Wang, L. Jiang, L. Li, D. Zhu, *Angew. Chem.* **2004**, *116*, 4763 – 4766; *Angew. Chem. Int. Ed.* **2004**, *43*, 4663 – 4666.
[3] E. Joselevich, *Angew. Chem.* **2004**, *116*, 3052 – 3054; *Angew. Chem. Int. Ed.* **2004**, *43*, 2992 – 2994.
[4] G. G. Wildgoose, C. E. Banks, R. G. Compton, *Small* **2006**, *2*, 182 – 193.
[5] E. Bekyarova, Y. Ni, E. B. Malarkey, V. Montana, J. L. McWilliams, R. C. Haddon, V. Parpura, *J. Biomed. Nanotechnol.* **2005**, *1*, 3 – 17.
[6] I. S. Chronakis, *J. Mater. Process. Technol.* **2005**, *167*, 283 – 293.
[7] P. Poulin, Philippe, *Actual. Chim.* **2005**, *282*, 13 – 17.
[8] J. J. Gooding, *Electrochim. Acta* **2005**, *50*, 3049 – 3060.
[9] Y. Lin, W. Yantasee, J. Wang, *Front. Biosci.* **2005**, *10*, 492 – 505.
[10] J. Wang, *Electroanalysis* **2005**, *16*, 7 – 14.
[11] R. R. Moore, C. E. Banks, R. G. Compton, *Anal. Chem.* **2004**, *76*, 2677 – 2682.
[12] C. E. Banks, R. R. Moore, T. J. Davies, R. G. Compton, *Chem. Commun.* **2004**, *16*, 1804 – 1805.
[13] C. E. Banks, R. G. Compton, *Analyst* **2006**, *131*, 15 – 21.
[14] C. E. Banks, T. J. Davies, G. G. Wildgoose, R. G. Compton, *Chem. Commun.* **2005**, *7*, 829 – 841.
[15] C. E. Banks, R. G. Compton, *Analyst* **2005**, *130*, 1232 – 1239.
[16] F. Wantz, C. E. Banks, R. G. Compton, *Electroanalysis* **2005**, *16*, 1529 – 1533.

 © 2006 Wiley-VCH Verlag GmbH & Co. KGaA, Weinheim

[17] R. R. Moore, C. E. Banks, R. G. Compton, *Analyst* **2004**, *129*, 755 – 758.
[18] Y.-D. Zhao, W.-D. Zhang, H. Chen, Q.-M. Luo, *Talanta* **2002**, *58*, 529 – 534.
[19] M. Musameh, J. Wang, A. Merkoci, Y. Lin, *Electrochem. Commun.* **2002**, *4*, 743 – 746.
[20] J. Wang, M. Musameh, Y. Lin, *J. Am. Chem. Soc.* **2003**, *125*, 2408 – 2409.
[21] *Practical Surface Analysis, 2nd ed., Vol. 1* (Eds.: D. Briggs, M. P. Seah), Wiley, New York, **1990**.
[22] E. Mendoza, S. J. Henley, C. H. P. Poa, G. Y. Chen, C. E. Giusca, A. A. D. T. Adikaari, J. D. Carey, S. R. P. Silva, *Sens. Actuators B* **2005**, *109*, 75 – 80.
[23] http://www.nano-lab.com/nanotubes-research-grade.html.
[24] C. Batchelor-McAuley, C. E. Banks, A. O. Simm, T. G. J. Jones, R. G. Compton, *Analyst* **2006**, *131*, 106 – 110.
[25] I. P. Kolesnikova, A. N. Sofronkov, *Ukr. Khim. Zh.* **1977**, *43*, 13 – 16.
[26] A. J. Bard, *Anal. Chem.* **1963**, *35*, 1602 – 1607.
[27] M. S. Lin, H. J. Leu, *Electroanalysis* **2005**, *16*, 2068 – 2073.

 © 2006 Wiley-VCH Verlag GmbH & Co. KGaA, Weinheim

Nanoparticle Assemblies

DOI: 10.1002/anie.200504595

A Universal Approach for the Self-Assembly of Hydrophilic Nanoparticles into Ordered Monolayer Films at a Toluene/Water Interface**

*Yong-Jun Li, Wei-Jun Huang, and Shi-Gang Sun**

Since Yogev et al. first reported that liquid metal-like films of silver could be obtained under certain conditions at dichloromethane–water interfaces,[1] the self-assembly of nanoparticles at liquid–liquid interfaces has attracted extensive interest, which has effectively opened the door for the self-assembly of hydrophilic nanoparticles.[2–7] Generally, aqueous charged nanoparticles are assembled into nanostructured films at a liquid–liquid interface by electrostatic interactions with interfacial oppositely charged molecules.[8,9]

It has been demonstrated[10–12] that hydrophilic nanoparticles can be trapped at liquid–liquid (or liquid–air) interfaces by bringing the contact angle of particles with the interface close to 90°. Vanmaekelbergh and co-workers,[10] for example, have found that ethanol forces the contact angle of citrate-stabilized Au nanoparticles with a heptane–water interface close to 90°, which causes these nanoparticles to form a monolayer film (MLF). However, in many cases where nanoparticle films assemble at liquid–liquid interfaces the nanoparticles were found to be randomly distributed and did not form an ordered structure.[1,10,11] Furthermore, it is well known that hydrophilic nanoparticles are more difficult to assemble into ordered MLFs than hydrophobic nanoparticles.

We report herein a universal approach for the self-assembly of hydrophilic nanoparticles into ordered MLFs at toluene–water interfaces. Ordered MLFs with a large area have been assembled from some typical hydrophilic colloid systems, including Au, Pt, and SiO_2, by subtly controlling the interfacial tension of the two phases.

The hydrophilic nanoparticles (Au, Pt, and SiO_2) were assembled into ordered MLFs at a toluene–water interface by following the procedure illustrated in Scheme 1. First, nanoparticles are trapped at the interface by using ethanol as an inducer in a process similar to that described in reference [10]. In this process, the number of hydrophilic nanoparticles escaping from the aqueous phase to the interface of the two phases depends on the volume of ethanol added. We found that too much ethanol results in the folding of the as-prepared MLFs, and we also sonicated the mixture gently to accelerate the interfacial assembly of nanoparticles in the presence of a small quantity of ethanol. The addition of an appropriately small quantity of ethanol is therefore beneficial to the formation of a perfect film. The nanoparticle MLF assembled at the toluene–water interface is not dense initially; it can be observed that the nanoparticles are mobile at the interface and are randomly distributed in the films, as reported previously.[1,10,11]

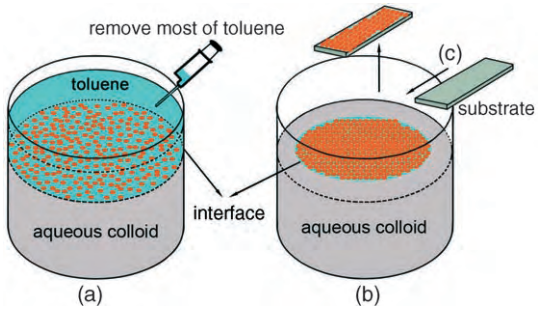

Scheme 1. Schematic representation of the formation and transfer of an interfacial MLF. The MLF formed initially is incompact and disordered (a); nanoparticles assemble into a close-packed MLF after most of toluene has been removed (b); the MLF is transferred onto a solid substrate (c).

[*] Dr. Y.-J. Li, W.-J. Huang, Prof. S.-G. Sun
State Key Laboratory of Physical Chemistry of Solid Surfaces
Department of Chemistry
College of Chemistry and Chemical Engineering
Xiamen University
Xiamen 361005 (P.R. China)
Fax: (+86) 592-218-0181
E-mail: sgsun@xmu.edu.cn
Dr. Y.-J. Li
Department of Chemistry
College of Chemistry and Chemical Engineering
Hunan University
Changsha 410082 (P.R. China)

[**] This study was supported financially by grants from the National Natural Science Foundation of China (20021002, 90206039) and the Major State Basic Research Project of China (2002CB211804).

Supporting Information for this article is available on the WWW under http://www.angewandte.org or from the author.

© 2006 Wiley-VCH Verlag GmbH & Co. KGaA, Weinheim

The interfacial tension at the toluene–water interface provides surface pressure in the Langmuir–Blodgett (LB) technique that compresses the interfacial nanoparticles into a close-packed structure, which is the key to obtaining ordered MLFs. We used a syringe to remove most of the toluene from the top of the container, and the contact area (interface area) between toluene and water therefore decreased. Due to the action of the interfacial tension, the interfacial MLFs shrank to form a close-packed structure. These close-packed structures could then be easily transferred onto the surface of different substrates, such as a nonconductive material (glass slide), a Si wafer, or a conductive material (glassy carbon). The conductive substrates were employed together with metallic nanoparticles for subsequent electrochemical studies. Scheme 1 illustrates the formation and transfer of an interfacial MLF. Typically, the clean substrate is immersed into the solution at an angle (5–10°) and the MLF is deposited onto one side of the substrate by pulling it slowly from the solution. Generally, the smaller the angle the more favorable the film transfer.

Figure 1 shows a photo taken with a digital camera of an MLF formed from Au nanoparticles (18 nm) deposited on a Petri dish. The area of the MLF is about 19 cm^2. Note that the area of the MLF can be controlled simply by adjusting the concentration of nanoparticles in solution and the interfacial area of the two phases.

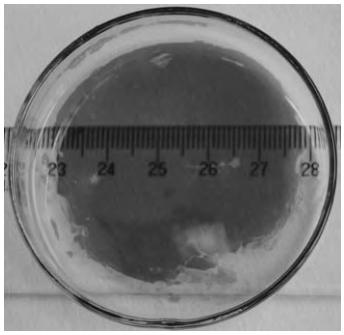

Figure 1. Photograph of an Au nanoparticle film deposited on the bottom of a Petri dish. Each mark on the ruler represents 1 mm.

Figure 2 shows SEM images of MLFs formed from Au and SiO_2 nanoparticles by modifying the interfacial tension. Both these types of nanoparticles are packed closely in their respective MLFs, although some aggregates (congeries) are also observed in the MLFs. The interspaces of the nanoparticles and their conglomeration behavior are directly related to the surface charge and to species absorbed on the nanoparticles; for example, the MFLs of Pt nanoparticles synthesized using polyvinylpyrrolidone (PVP) as stabilizer exhibit another type of film structure (Figure 3). The TEM images of these Pt nanoparticle MFLs show that the interspaces between the Pt nanoparticles are about 3 nm, which is close to the size of the Pt nanoparticles themselves. No large congeries can be observed in the MFLs.

In addition, domains of close-packed Au or Pt nanoparticles coexist in their MFLs with small voids (about 100–200 nm), as already reported.[10,11] These voids may arise from either adsorption of the small bubbles that form during the process of ethanol addition onto the films or a structural change of the MLFs during the transfer process—the particles transferred were observed to float around on the surface of the substrate before drying. No difference in film morphology before and after transfer could be distinguished, however, because the arrangement of nanoparticles at the interface of the two phases is very difficult to characterize directly.

All the nanoparticles studied in their different colloid systems assemble into ordered MLFs over a short range, although small congeries of nanoparticles (< 150 nm) can be observed in all the MLFs. Under certain conditions we were able to obtain films completely constructed from aggregates of nanoparticles, which is inconsistent with the conclusion of Vanmaekelbergh's group that particles do not coalesce into clumps.[10] We also found that the rate of addition of ethanol

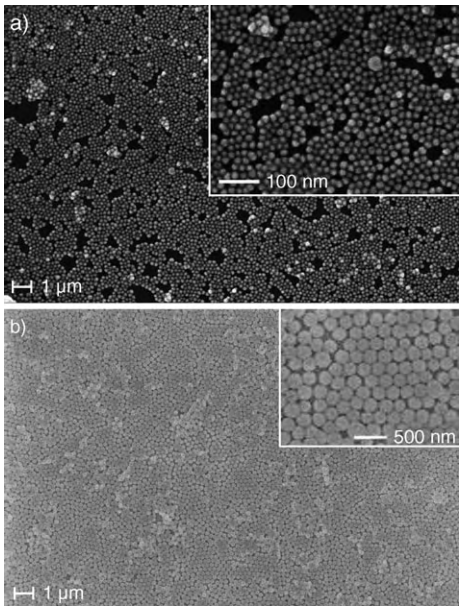

Figure 2. SEM photographs of MLFs of a) Au and b) SiO_2 nanoparticles. The insets are higher magnification images of the respective samples.

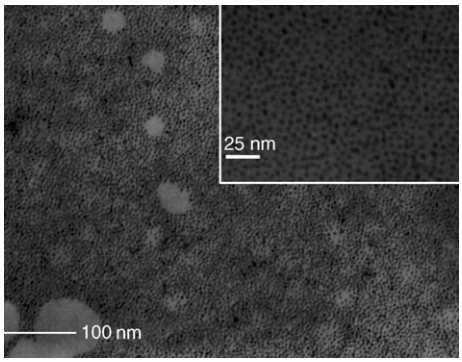

Figure 3. TEM images of the MLF formed from Pt nanoparticles synthesized using PVP as stabilizer.

 © 2006 Wiley-VCH Verlag GmbH & Co. KGaA, Weinheim

during formation of the MLFs can be used to control the interaction between different nanoparticles. Thus, if ethanol is injected into the colloids rapidly the nanoparticles are apt to aggregate and the resultant nanoparticle film exhibits a fractal structure (see Supporting Information). Furthermore, addition of too much ethanol can lead to folding of the MLF (not shown). It is therefore important to control the injection rate and the volume of ethanol in order to form the desired films.

The type of stabilizer (surfactants) has no effect on the formation of nanoparticle MLFs, although too much surfactant in solution does not allow effective trapping of the nanoparticles at the interface. This method also works well with nanoparticles prepared in aqueous solution without any surfactant, and this finding not only opens up a new way to assemble nanoparticles from dilute colloidal solution but also makes it possible to investigate the real surface properties of colloidal particles. Figure 2b shows an ordered MLF of SiO_2 nanoparticles obtained from an aqueous SiO_2 suspension without any surfactant or other impurities. Except for some small congeries, the SiO_2 nanoparticles are arranged in a more ordered manner than that of Au nanoparticles, and no voids are present in the whole film. This property may be very useful for the preparation of photonic arrays.

It has been demonstrated that an inorganic salt is able to induce nanoparticles to overcome the energy barrier to reach a water–air interface spontaneously.[12,13] However, the area of the resultant film was rather small and the particles sparsely distributed on the substrates did not form a continuous thin film. Moreover, it took about two days for the Ag colloidal particles to be trapped to form a film at the interface.[13] In the present method, ethanol serves as a mediator instead of an inorganic salt and the hydrophilic nanoparticles are rapidly extracted from the solution to fluctuate at the interface. Such an effect has been discussed by considering that ethanol decreases the surface charge of the nanoparticles.[10] However, if a defined quantity of ethanol was added to the colloid solution before addition of the toluene phase only a few nanoparticles were extracted from the solution. When toluene was subsequently added instead of air the number of nanoparticles at the interface did not increase, even after several days. In our method, however, nanoparticles are always immediately released from the sites where ethanol is added and reach the toluene–water interface. Therefore, the existence of a toluene phase before addition of ethanol should also be considered a key factor for the formation of MLFs along with the role of ethanol at the liquid–liquid interface. Toluene is directly involved in the trapping of nanoparticles and does not simply act as an interfacial phase. The mechanism of the assembly of nanoparticles is still under investigation.

In summary, a universal assembly method has been developed whereby hydrophilic nanoparticles form ordered MLFs with a large area at a liquid–liquid interface. This method is simple and convenient, and the MLF can easily be transferred onto solid substrates from the interface. The MLFs prepared by this method could be used as catalysts, electrodes, and as the plating layer in the electronic industry, and can also be employed in fundamental studies in physical chemistry, colloidal science, and surface science.

Experimental Section

Au nanoparticles with an average size of 18 nm were synthesized according to Frens' method,[14] and used directly for the assembly. Pt nanoparticles stabilized by PVP (Acros Co.), with an average size of 3.3 nm, were synthesized by the reduction of $H_2[PtCl_6]$ with methanol.[15] The solvent was then evaporated and the Pt nanoparticles were redispersed in Milli-Q water before nanoparticle assembly. SiO_2 nanospheres of diameter 200 nm were synthesized following the traditional Stöber method;[16] they were also redispersed in Milli-Q water before use.

MLFs of the different nanoparticles were transferred onto Si(100) wafers ($1.0 \times 1.0\ cm^2$) for characterization by scanning electron microscopy (LEO-1530, Germany). The size of the cubic Pt nanoparticles is only about 3.3 nm, so the Pt nanoparticle MLFs were transferred onto a carbon-coated Cu grid and characterized by transmission electron microscopy (JEM-CX100-II, Japan).

Received: December 27, 2005
Published online: March 17, 2006

Keywords: interfaces · monolayers · nanoparticles · self-assembly

[1] D. Yogev, S. Efrima, *J. Phys. Chem.* **1988**, *92*, 5754–5760.
[2] Y. Lin, H. Skaff, T. Emrick, A. D. Dinsmore, T. P. Russell, *Science* **2003**, *299*, 226–229.
[3] L. L. Dai, R. Sharma, C.-Y. Wu, *Langmuir* **2005**, *21*, 2641–2643.
[4] H. Schwartz, Y. Harel, S. Efrima, *Langmuir* **2001**, *17*, 3884–3892.
[5] A. Kumar, S. Mandal, S. P. Mathew, P. R. Selvakannan, A. B. Mandale, R. V. Chaudhari, M. Sastry, *Langmuir* **2002**, *18*, 6478–6483.
[6] A. Berman, N. Belman, Y. Golan, *Langmuir* **2003**, *19*, 10962–10966.
[7] R. A. W. Dryfe, A. O. Simm, B. Kralj, *J. Am. Chem. Soc.* **2003**, *125*, 13014–13015.
[8] K. S. Mayya, M. Sastry, *Langmuir* **1999**, *15*, 1902–1904.
[9] D. Wyrwa, N. Beyer, G. Schmid, *Nano Lett.* **2002**, *2*, 419–421.
[10] F. Reincke, S. G. Hickey, W. K. Kegel, D. Vanmaekelbergh, *Angew. Chem.* **2004**, *116*, 464–468; *Angew. Chem. Int. Ed.* **2004**, *43*, 458–462.
[11] H. Duan, D. Wang, D. G. Kurth, H. Möhwald, *Angew. Chem.* **2004**, *116*, 5757–5760; *Angew. Chem. Int. Ed.* **2004**, *43*, 5639–5642.
[12] B. P. Binks, *Curr. Opin. Colloid Interface Sci.* **2002**, *7*, 21–41.
[13] J.-W. Hu, G.-B. Han, B. Ren, S.-G. Sun, Z.-Q. Tian, *Langmuir* **2004**, *20*, 8831–8838.
[14] G. Frens, *Nature* **1973**, *241*, 20.
[15] T. Teranishi, M. Hosoe, T. Tanaka, M. Miyake, *J. Phys. Chem. B* **1999**, *103*, 3818–3827.
[16] W. Stöber, A. Fink, E. Bohn, *J. Colloid Interface Sci.* **1968**, *26*, 62.

 © 2006 Wiley-VCH Verlag GmbH & Co. KGaA, Weinheim

Molecular Electronics

DOI: 10.1002/anie.200503591

Charge Transport in Three-Terminal Molecular Junctions Incorporating Sulfur-End-Functionalized Tercyclohexylidene Spacers**

Yann-Vaï Kervennic, Jos M. Thijssen, Daniel Vanmaekelbergh, Reza Dabirian, Leonardus W. Jenneskens, Cornelis A. van Walree, and Herre S. J. van der Zant**

Molecular electronics using single molecules as active components is a promising technological concept of fast-growing interest.[1–3] Two-[4–8] and three-terminal[9–14] systems have been studied, often employing π-conjugated compounds with thiol end groups. Experimental results at low temperatures indicate that the three-terminal devices studied so far operate in the weak coupling regime in which the discrete molecular energy-level structure remains essentially intact.

Herein we present charge-transport phenomena in three-terminal molecular junctions based on bis(sulfur-end-functionalized) tercyclohexylidene **1**. Compound **1** and the

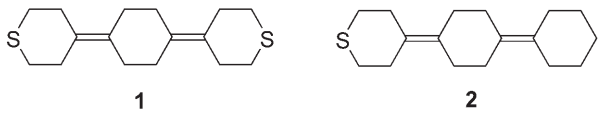

1 **2**

monosulfur reference compound **2** are oligo(cyclohexylidenes), which consist of cyclohexane-type rings interconnected by double bonds.[15] Their σ–π–σ orbital topology allows transannular electronic interactions and mediates charge transport through the partly saturated hydrocarbon framework, as demonstrated by the occurrence of long-range photoinduced charge separation.[16–18] Photoelectron spectroscopy and NBO studies show that there is a strong electronic coupling between the electron lone pairs of the sulfur atoms in bis(sulfur-end-capped) oligo(cyclohexylidenes) owing to σ–π–σ through-bond interactions.[19] In common with other sulfides, the sulfur atoms can bind to gold substrates by physisorption,[20,21] thus enabling the formation of self-assembled monolayers.[22]

The three-terminal devices used consist of gold leads and an oxidized aluminum film that serves as a gate. They were constructed with a technique published elsewhere (see also the Supporting Information).[23] In short, nanogaps in a 15-nm-thick gold wire were created by using a combination of e-beam lithography and electrochemical etching. This approach allows the creation of gaps with subnanometer precision by monitoring the gap conductance in situ during etching.[23] For the tercyclohexylidenes (length 1.2 nm), the gap distance was between 1.2 and 1.5 nm. After creation of the gap and drying, the samples were dipped in solutions of **1** and **2** in ethanol (1.0 mM) and dried. Compounds **1** and **2** were available from previous studies.[19] In all cases (nine junctions) and for both molecules a dramatic decrease in resistance (from >1 GΩ to the MΩ range) was observed. Ten other junctions were dipped in pure ethanol and did not exhibit an increase in conductance which shows that the decrease in resistance is due to the presence of the tercyclohexylidenes. The zero-bias room-temperature resistance varied from junction to junction (Figures 1 and 3; see also the Supporting Information). These

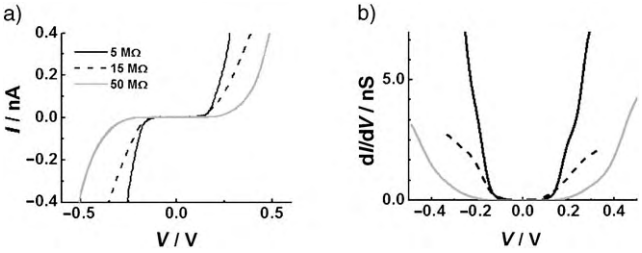

Figure 1. a) Current–voltage characteristics (trace and retrace) of three different molecular junctions based on **1** measured at 7–10 K. b) Corresponding numerically obtained differential conductance (trace only) in the same pattern. Zero-bias room-temperature resistances are indicated in the legend of a).

differences may reflect differences in bonding strength or in molecule-lead geometries, that is, in the exact physisorption of the molecule to the leads.[24] Another factor may be the number of molecules between the gold leads. We cannot be sure that it concerns only a single molecule, but several reasons suggest that, at most, only a few molecules are involved (see Supporting Information).

Figure 1 shows the low-temperature (7–10 K) current–voltage characteristics and differential conductance (dI/dV) traces of molecular junctions based on **1**. Single curves (no averaging) were recorded back (trace) and forth (retrace) with a sweep rate of 10 mV s^{-1} and proved to be stable for days. Different curves represent devices with different room-temperature resistances, but all are virtually symmetric around $V=0$. In general, currents in the nA range and conductance values in the nS range were obtained. Before

[*] R. Dabirian, Prof. L. W. Jenneskens, Dr. C. A. van Walree
Debye Institute, Organic Chemistry and Catalysis
Utrecht University
Padualaan 8, 3584 CH Utrecht (The Netherlands)
Fax: (+31) 30-253-4533
E-mail: c.a.vanwalree@chem.uu.nl
Dr. Y.-V. Kervennic, Dr. J. M. Thijssen, Dr. H. S. J. van der Zant
Kavli Institute of Nanoscience
Delft University of Technology
PO Box 5046, 2600 GA, Delft (The Netherlands)
Fax: (+31) 15-278-3251
E-mail: herre@qt.tn.tudelft.nl
Prof. D. Vanmaekelbergh
Debye Institute, Condensed Matter and Interfaces
Utrecht University
Princetonplein 1, 3584 CC Utrecht (The Netherlands)

[**] Financial support was obtained from the Dutch Organization for Fundamental Research on Matter (FOM).

Supporting information for this article is available on the WWW under http://www.angewandte.org or from the author.

InterScience
© 2006 Wiley-VCH Verlag GmbH & Co. KGaA, Weinheim

discussing the data further, it is important to note that in total five junctions based on **1** were characterized which, despite the variation in current magnitude, together evoke a consistent picture.

At low temperatures, a strong influence of the gate voltage on the current is observed for the junctions based on **1** (Figure 2). The gate coupling, that is, the ratio of the gate

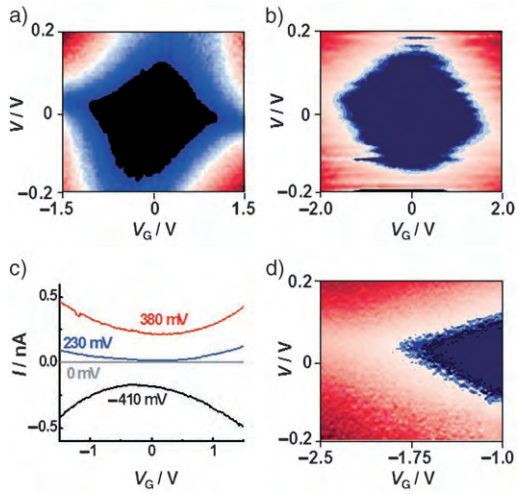

Figure 2. a) Stability diagram at 8 K of the device based on **1** with a room-temperature resistance of 15 MΩ. Plotted is d*I*/d*V* as a function of bias and gate voltage. The conductance ranges from 0 (black) to 10 nS (red). b) Stability diagram at 8 K of the sample **1** with a room-temperature resistance of 5 MΩ. The conductance ranges from 0 (blue) to 25 nS (red). c) Current versus gate voltage for the same sample as in a) plotted for four different bias voltages (indicated). d) High-resolution stability diagram of the same sample as in b). The conductance ranges from 0 (blue) to 40 nS (red). The stability diagrams are composed of more than 100 curves.

capacitance to the total capacitance of the molecular island within Coulombic theory,[25] can be estimated by dividing the diamond height by the width. For both the junctions in Figure 2a,b the gate coupling is about 0.1, implying that a change of 1 V in the gate potential induces a shift of 0.1 eV in the molecular electrostatic energy. Interestingly, the differential conductance plots (Figure 2a,b,d) do not show the sharp features commonly observed in weakly coupled molecular junctions.[9–13] A related surprising aspect is the absence of well-defined degeneracy points along the gate axis at low bias.[25] Sharp current peaks are usually observed upon recording the current as a function of gate potential and correspond to the appearance of new charge states when crossing discrete energy levels.[9,10] In contrast, in the case of **1** the current steadily increases with the gate voltage (Figure 2c) leading to the appearance of a single, broad, diamondlike feature in the d*I*/d*V* plots. The absence of sharp Coulombic blockade features makes it very unlikely that gold grains are responsible for the features reported in this study.

The presence of two sulfur atoms in **1** is essential for the observed behavior. This is revealed by the strongly different current–voltage characteristics of the asymmetric junctions based on monosulfide **2**. In **2**, the sulfur-functionalized site is expected to be well coupled to the gold electrode, whereas the other side is—most likely—bound by a weak van der Waals contact. At low temperature, all four devices based on **2** show current–voltage curves with discrete steps. The step size is sample-dependent and varies between 50 and 200 mV; two examples are shown in Figure 3a. The step position changes

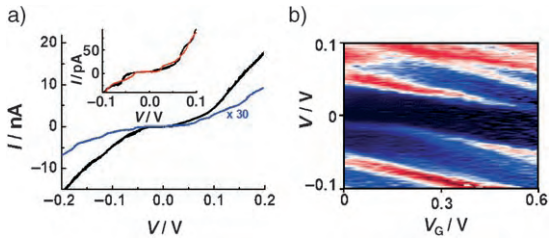

Figure 3. a) Current–voltage characteristics at 5 K of two junctions based on **2** with a room-temperature resistance of 8 MΩ (black) and 500 MΩ (blue). The current level of the blue curve has been multiplied by a factor of 30. Inset: Current–voltage characteristics of the molecular junction with a room-temperature resistance of 500 MΩ for two different gate voltages. b) Stability diagram of the 500-MΩ sample measured at 5 K. The differential conductance ranges from 0 (black) to 3 nS (red).

when applying a voltage to the gate, thus leading to current–voltage characteristics that are generally asymmetric[26] (Figure 3a (inset), Figure 3b). The steps resemble Coulombic staircases that are regularly observed in asymmetrically coupled quantum dots.[27] However, it cannot be completely excluded that the steps originate from vibrational modes in the molecules.[28–30] A remarkable observation that is not yet understood is that at low temperatures junctions based on **1** give larger currents than those based on **2**.

The absence of sharp features and degeneracy points in junctions based on **1** can be rationalized in two ways. First, it suggests the presence of broad transport levels, which must then arise from substantial hybridization between molecule and gold orbitals. A second possibility is that energy levels (which are not necessarily broadened) shift when they align with the chemical potential of one of the leads. Both scenarios rest on a substantial interaction between **1** and the electrodes. In this respect, it is important to realize that the contact between π-conjugated aromatic thiols and gold electrodes leads to decoupling of the sulfur atoms from the aromatic hydrocarbon moiety and the formation of high potential barriers at the molecule–lead interface.[31,32] The phenomena observed for junctions based on **1** reflect a more-favorable molecule–lead contact. This might be related to a different bonding mode of the sulfur atoms in the alkyl sulfide **1** (compared with the covalent Au–S bond for thiols) and the efficient coupling between the terminal sulfur atoms through the σ–π–σ framework.[19]

In conclusion, we have shown that electron transport in three-terminal devices prepared by electrochemical etching that contain σ–π–σ conjugated tercyclohexylidene **1** molecular wires is considerably different from that in junctions involving π-conjugated systems. This presumably finds its

 © 2006 Wiley-VCH Verlag GmbH & Co. KGaA, Weinheim

origin in a substantial coupling between the molecules and the leads.

Received: October 11, 2005
Revised: February 8, 2006
Published online: March 20, 2006

Keywords: charge transfer · conjugation · molecular electronics · sulfur · through-bond interactions

[1] C. Joachim, J. K. Gimzewski, A. Aviram, *Nature* **2000**, *408*, 541.
[2] A. Nitzan, M. A. Ratner, *Science* **2003**, *300*, 1384.
[3] J. R. Heath, M. A. Ratner, *Phys. Today* **2003**, (May), 43.
[4] M. A. Reed, C. Zhou, C. J. Muller, T. P. Burgin, J. M. Tour, *Science* **1997**, *278*, 252.
[5] C. Kergueris, J.-P. Bourgoin, S. Palacin, D. Esteve, C. Urbina, M. Magoga, C. Joachim, *Phys. Rev. B* **1999**, *59*, 12505.
[6] J. Reichert, R. Ochs, D. Beckmann, H. B. Weber, M. Mayor, H. v. Löhneysen, *Phys. Rev. Lett.* **2002**, *88*, 176804–1.
[7] R. H. M. Smit, Y. Noat, C. Untiedt, N. D. Lang, M. C. van Hemert, J. M. van Ruitenbeek, *Nature* **2002**, *419*, 906.
[8] B. Xu, N. J. Tao, *Science* **2003**, *301*, 1221.
[9] H. Park, J. Park, A. K. L. Lim, E. H. Anderson, A. P. Alivisatos, P. L. McEuen, *Nature* **2000**, *407*, 57.
[10] J. Park, A. N. Pasupathy, J. I. Goldsmith, C. Chang, Y. Yaish, J. R. Petta, M. Rinkoski, J. P. Sethna, H. D. Abruna, P. L. McEuen, D. C. Ralph, *Nature* **2002**, *417*, 722.
[11] W. Liang, M. P. Shores, M. Bockrath, J. R. Long, H. Park, *Nature* **2002**, *417*, 725.
[12] N. B. Zhitenev, H. Meng, Z. Bao, *Phys. Rev. Lett.* **2002**, *88*, 226801–1.
[13] S. Kubatkin, A. Danilov, M. Hjort, J. Cornil, J.-L. Brédas, N. Stuhr-Hansen, P. Hedegård, T. Bjørnholm, *Nature* **2003**, *425*, 698.
[14] B. Xu, X. Xiao, X. Yang, L. Zang, N. Tao, *J. Am. Chem. Soc.* **2005**, *127*, 2386.
[15] F. J. Hoogesteger, R. W. A. Havenith, J. W. Zwikker, L. W. Jenneskens, H. Kooijman, N. Veldman, A. L. Spek, *J. Org. Chem.* **1995**, *60*, 4375.
[16] F. J. Hoogesteger, C. A. van Walree, L. W. Jenneskens, M. R. Roest, J. W. Verhoeven, W. Schuddeboom, J. J. Piet, J. M. Warman, *Chem. Eur. J.* **2000**, *6*, 2948.
[17] W. D. Oosterbaan, C. Koper, T. W. Braam, F. J. Hoogesteger, J. J. Piet, B. A. J. Jansen, C. A. van Walree, H. J. van Ramesdonk, M. Goes, J. W. Verhoeven, W. Schuddeboom, J. M. Warman, L. W. Jenneskens, *J. Phys. Chem. A* **2003**, *107*, 3612.
[18] E. P. A. M. Bakkers, A. W. Marsman, L. W. Jenneskens, D. Vanmaekelbergh, *Angew. Chem.* **2000**, *112*, 2385; *Angew. Chem. Int. Ed.* **2000**, *39*, 2297.
[19] A. W. Marsman, R. W. A. Havenith, S. Bethke, L. W. Jenneskens, R. Gleiter, J. H. van Lenthe, M. Lutz, A. L. Spek, *J. Org. Chem.* **2000**, *65*, 4584.
[20] D. J. Lavrich, S. M. Wetterer, S. L. Bernasek, G. Scoles, *J. Phys. Chem. B* **1998**, *102*, 3456.
[21] H. Takiguchi, K. Sato, T. Ishida, K. Abe, K. Yase, K. Tanabe, *Langmuir* **2000**, *16*, 1703.
[22] R. Dabirian, A. N. Zdravkova, P. Liljeroth, C. A. van Walree, L. W. Jenneskens, *Langmuir* **2005**, *21*, 10497.
[23] Y. V. Kervennic, D. Vanmaekelbergh, L. P. Kouwenhoven, H. S. J. van der Zant, *Appl. Phys. Lett.* **2003**, *83*, 3782. "Electrochemically fabricated nanometer-sized molecular junctions": Y. V. Kervennic, PhD Thesis, Delft **2004**, chap. 7. (can be downloaded from http://med.tn.tudelft.nl/publi/papers.php).
[24] X. Xiao, B. Xu, N. J. Tao, *Nano Lett.* **2004**, *4*, 267.
[25] For an example, see: L. P. Kouwenhoven, D. G. Austing, S. Tarucha, *Rep. Prog. Phys.* **2001**, *64*, 701.
[26] Asymmetric current–voltage characteristics have also been observed for an asymmetric metal–molecule contact configuration in two-terminal measurements on oligo(phenylene ethynylene) molecules: J. G. Kushmerick, D. B. Holt, J. C. Yang, J. Naciri, M. H. Moore, R. Shashidhar, *Phys. Rev. Lett.* **2002**, *89*, 086802.
[27] "Single Charge Tunneling": G.-L. Ingold, Y. V. Nazarov in *NATO ASI Series* (Eds: H. Grabert, M. H. Devoret), Plenum, New York, **1993**, chap. 2.
[28] W. Wang, T. Lee, I. Kretzschmar, M. A. Reed, *Nano Lett.* **2004**, *4*, 643.
[29] L. H. Yu, Z. K. Keane, J. W. Ciszek, L. Cheng, M. P. Stewart, J. M. Tour, D. Natelson, *Phys. Rev. Lett.* **2004**, *93*, 266802.
[30] J. G. Kushmerick, J. Lazorcik, C. H. Patterson, R. Shashidhar, D. S. Seferos, C. G. Bazan, *Nano Lett.* **2004**, *4*, 639.
[31] Y. Xue, M. A. Ratner, *Phys. Rev. B* **2003**, *68*, 115406.
[32] Y. Xue, M. A. Ratner, *Phys. Rev. B* **2003**, *68*, 115407.

 © 2006 Wiley-VCH Verlag GmbH & Co. KGaA, Weinheim

Metal–Organic Frameworks

DOI: 10.1002/anie.200503923

Preparation, Adsorption Properties, and Catalytic Activity of 3D Porous Metal–Organic Frameworks Composed of Cubic Building Blocks and Alkali-Metal Ions**

*Ru-Qiang Zou, Hiroaki Sakurai, and Qiang Xu**

Open metal–organic frameworks (MOFs) are regarded as promising materials for a range of applications.[1–5] Especially MOFs with inner cavities are known to include gas molecules in their cavities and exhibit unique gas-storage or catalysis properties, for which high regioselectivity, stereoselectivity, and shape selectivity are observed.[6] However, to the best of our knowledge, catalysis of gas-phase reactions by MOFs is rare, although there are a few reports on liquid-phase catalytic

[*] R.-Q. Zou, Prof. Dr. Q. Xu
National Institute of Advanced Industrial Science and Technology (AIST)
Ikeda, Osaka 563-8577 (Japan)
and
Graduate School of Science and Technology
Kobe University
Nada Ku, Kobe, Hyogo 657-8501 (Japan)
Fax: (+81)72-751-9629
E-mail: q.xu@aist.go.jp
Dr. H. Sakurai
National Institute of Advanced Industrial Science and Technology (AIST)
Ikeda, Osaka 563-8577 (Japan)

[**] We thank the reviewers for valuable suggestions, Midori Goto for single-crystal X-ray diffraction measurements, and AIST and Kobe University for financial support.

Supporting information for this article is available on the WWW under http://www.angewandte.org or from the author.

WILEY InterScience DISCOVER SOMETHING GREAT
© 2006 Wiley-VCH Verlag GmbH & Co. KGaA, Weinheim

reactions.[6] On the other hand, the preparation of these materials still suffers from a general lack of control over the structure and properties of the solids produced by traditional synthetic methods, which is directly related to the fact that the starting entities do not maintain their structures during the reaction, so that correlation between reactants and products is poor. Therefore, the development of rational synthetic routes for the construction of structurally well-defined solids is most significant for the creation of porous MOFs. A promising approach to the rational assembly of networks is the use of molecular building blocks (MBBs), which are most commonly metal-containing aggregates that dictate the direction of polymer extension.[3,5,7] As a suitable route toward the construction of functional MOFs, the MBB approach has promoted the search for and development of new synthetic strategies as a means to tune and/or enhance the respective properties. Until now, MBBs have mainly been singled out from three-dimensional (3D) metal–organic frameworks, in which they only act as the basal unit of the framework and cannot be self-existent apart from the whole framework.

Herein, we present a new route for the construction of functional MOFs by using the discrete metal–organic cubic building block $[Ni_8L_{12}]^{20-}$ (H_3L = 4,5-imidazoledicarboxylic acid),[8] which is bridged by different alkali-metal ions (Li^+ and Na^+). In this process, the discrete cubic building block remains intact. Interestingly, such MOFs exhibit not only significant gas-adsorption properties but also stable catalytic activity for the oxidation of CO to CO_2. The clathrating ability toward Li^I ions of such cubic building blocks is also directly revealed in the X-ray crystal structure, which fully simulates the potential guest-bonding sites inside the building blocks of the porous MOFs.

Heating a solution of $Ni(NO_3)_2$, 4,5-imidazoledicarboxylic acid (H_3L), and LiOH or NaOH in H_2O/CH_3OH at 90 °C in a teflon-capped scintillation vial for 4 d afforded two crystalline products: $\{[Li_{11}(Ni_8L_{12})(H_2O)_{12}]Li_9(H_2O)_{20}\}_n$ (**1**) and $\{[Na_{20}(Ni_8L_{12})(H_2O)_{28}](H_2O)_{13}(CH_3OH)_2\}_n$ (**2**), respectively.

Complex **1** crystallizes in the trigonal space group $R\bar{3}c$ and consists of $[Ni_8L_{12}]^{20-}$ cubic building blocks bridged by Li^I ions.[9] Figure 1a illustrates the cubic building block $[Ni_8L_{12}]^{20-}$ with two Li^I ions included in the cavity. Each $[M_8L_{12}]^{20-}$ unit consists of eight Ni^{II} ions which occupy the vertices of the cube and are linked in a bichelating fashion by twelve L ligands. Each Ni^{II} ion is coordinated to three N and three O atoms from three separate L ligands in a slightly distorted octahedral coordination geometry. The Ni–N and Ni–O bond lengths lie in the normal ranges of 2.019(4)–2.032(4) and 2.096(4)–2.110(4) Å, respectively. The cubic building blocks offer many open coordination sites for alkali-metal ions. In the $[Ni_8L_{12}]^{20-}$ unit, each L ligand adopts a carboxylate O atom and an imidazolyl N atom to chelate two individual Ni^{II} ions and form two five-membered rings coplanar with the imidazole rings. The carboxylate O atoms not coordinated to Ni^{II} centers chelate two kinds of individual Li^I ions: Li(1), which bridges two adjacent cubic building blocks to form a 3D network with tetrahedral coordination geometry (Figure 1b), and Li(2), which also has a tetrahedral coordination environment but is coordinated to the other two terminal water molecules.

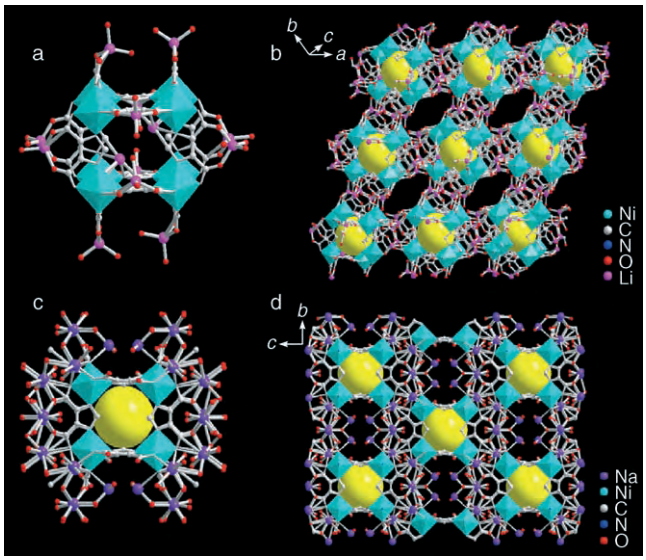

Figure 1. a) The cubic building block of **1** with the coordinated and clathrated Li^I ions. b) The 3D MOF of **1** with open channels. c) The cubic building block of **2** surrounded by the coordinated Na^I ions. d) The 3D MOF of **2** with open channels.

The firm inclusion of the two Li^I ions in the corners of such cubic cavities near the vertex Ni^{II} ions with strong Li–Ni, Li–C, and Li–N interactions (Li(3)–Ni(1) 2.89(5), Li(3)–C(1) 2.518(18), Li(3)–N(1) 2.59(4) Å) is unprecedented. These represent potential bonding sites for gas adsorption in cubic building blocks in MOFs. The cubic building blocks self-assemble into a 3D network with open channels through coordination of three pairs of chelating carboxylate O atoms to Li(1) centers (Figure 1b). Another 1.5 uncoordinated Li^I ions are incorporated in each asymmetric unit of **1** to obtain charge balance.

Complex **2** crystallizes in the orthorhombic space group *Pnnm* and consists of $[M_8L_{12}]^{20-}$ cubic building blocks bridged by Na^I ions. Figure 1c illustrates the cubic building block of **2** surrounded by Na^I ions through strong Na–O bonds. It is different from our recently reported unsaturated building block[8b] in that the 1D hydrophobic open channels of **2** are formed by two kinds of Na^I ions bridging adjacent $[M_8L_{12}]^{20-}$ cubic building blocks, and the hydrophilic open channels of **2** are partly filled by the coordinated Na^I ions. All of the sodium ions assemble into a 3D network with normal Na–O and Na–Na interactions. Furthermore, most of the carboxylate groups in **2** are coordinated in the μ_2-O mode through Na-O-Na bonds, which further rigidifies the framework of **2**. These adjacent cubic building blocks self-assemble into a 3D MOF with water and methanol molecules trapped in the hydrophilic channels (Figure 1d).

The thermal stability of these porous networks was studied by thermogravimetric (TG) analysis and powder X-ray diffraction (PXRD; Supporting Information). The TG curves of **1** and **2** indicate release of guest molecules up to 160 °C to give the desolvated form, and at 380 °C the ligand molecules start to be released. The PXRD patterns of **2** indicate that its framework is stable up to 380 °C, while that of **1** decomposes at a lower temperature, which is mainly

 © 2006 Wiley-VCH Verlag GmbH & Co. KGaA, Weinheim

ascribed to the weaker coordinative interactions of Li–O bonds compared to Na–O bonds.

The BET surface areas of **1** and **2** are 145 and 186 $m^2 g^{-1}$, and the micropore volumes are 0.28 and 0.33 $cm^3 g^{-1}$, respectively. The surface areas observed for **1** and **2** are consistent with their effective free volumes of 23 and 38%, respectively, as calculated with Platon. The N_2 adsorption behavior of **1** and **2** was examined at 77 K. Nitrogen adsorption isotherms were recorded with automatic volumetric adsorption equipment (ASAP2010, Micromeritics). A known weight (500 mg) of the synthesized sample was placed in a quartz sample tube and dried under high vacuum at 160 °C for 10 hours to remove solvent molecules prior to measurements. Approximately 53 and 121 mL of N_2 was adsorbed per 1.0 g of desolvated sample at 1 atm, respectively (Supporting Information).

Unexpectedly, **2** exhibits stable catalytic activity in the oxidation of CO to CO_2, while complex **1** lacks such activity as a result of its lesser thermal stability. Oxidation of CO to CO_2 on metal catalysts, especially on gold nanoparticles, has been extensively investigated.[10] Figure 2 shows the rate of CO oxidation, R_{QMS}, obtained by quadrupole mass spectroscopy (QMS; see Experimental Section) in comparison with those for Ni-Y zeolite and nickel oxide (NiO).[11a] The specific activities of Cu-, Fe-, Ni-, Co-, and Cr-exchanged Y zeolite are generally lower than those of their corresponding oxides,[11b] while the reaction rate over **2** was between those of NiO and Ni-Y zeolite, and the activation energy of **2** (64.9 kJ mol^{-1}) was also between those of NiO (39.8 kJ mol^{-1}) and Ni-Y zeolite (108.8 kJ mol^{-1}).[11b] Importantly, the activity of **2** is temporally stable, while those of Ni-Y zeolite and NiO decreased rapidly at 200 °C and took more than 50 minutes to reach steady state.[11a] Figure 3 shows a plot of reaction rate R_{QMS} against temperature. Reaction rates calculated from GC analyses (R_{GC}) are also plotted in this figure and almost agree with the R_{QMS} values.

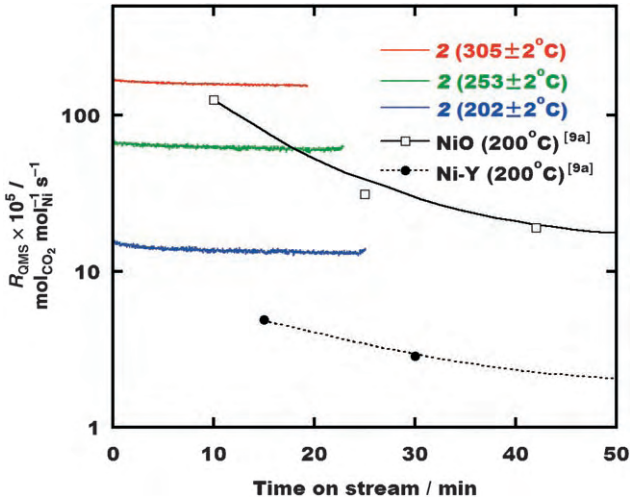

Figure 2. Catalytic activity of **2** in CO oxidation at 202, 253, and 305 °C, measured on a flowing CO (1%) + O_2 (20%) + He (balance) gas mixture (SV = 20000 mL h^{-1} g(cat.)$^{-1}$). The activity data of NiO and zeolite Ni-Y were taken from reference [9a] for comparison.

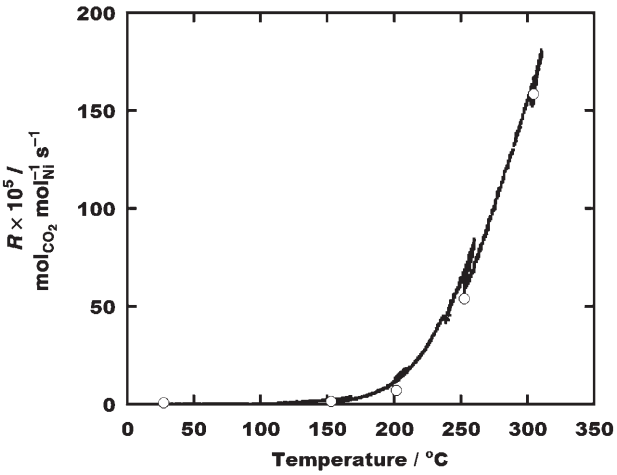

Figure 3. Rate of CO oxidation over **2** versus temperature. R_{QMS} (line) calculated from QMS data and R_{GC} (circles) calculated from GC data.

Complex **2** showed stable activity for the initial 20 minutes of reaction time at a fixed temperature of 202 °C or higher. The instability of the active site of Ni-Y zeolite has been ascribed to small clusters of Ni ions bonded through oxygen or hydroxy linkages or small crystallites of NiO.[11a] Nearly comparable activity of **2** to NiO is noteworthy because all Ni sites are completely isolated and no oxygen is bound between them, as can be seen in the crystal structure. The PXRD patterns of **2** (Supporting Information) indicate that the framework of **2** remains intact after the catalytic reaction and that no crystalline NiO is present. Complex **2** is the first example of a porous MOF catalyst for the oxidation of CO to CO_2, and the stable catalytic activity makes an intriguing forerunner for other new environmentally relevant materials. The catalytically active sites may be ascribable to the Ni^{II} clusters in **1** and **2**, and further studies such as impregnation of an inert matrix (for example, silica gel) with these Ni^{II} clusters will be used to investigate the catalytic reaction mechanism.

In conclusion, we have presented two novel 3D multifunctional MOFs with predesigned cubic building blocks that exhibit significant N_2 adsorption. The clathrating ability toward Li^{I} ions of such cubic building blocks was directly observed in the X-ray crystal structure of **1**, which fully simulates the potential guest-bonding sites inside the building blocks of the porous MOF materials. Unexpectedly, complex **2** exhibits stable catalytic activity in the oxidation of CO to CO_2. These observations should allow optimization of a new generation of structurally well-defined multifunctional MOFs.

Experimental Section

Synthesis of **1** and **2**: A solution of $Ni(NO_3)_2 \cdot 6H_2O$ (582 mg, 2 mmol) in water (10 mL) was added to a solution of H_3L (468 mg, 3 mmol) and LiOH (**1**; 90%, 80 mg, 3 mmol) or NaOH (**2**; 126 mg, 3 mmol) in methanol (5 mL), and the mixture was heated to 90 °C in a teflon-capped scintillation vial. Single crystals suitable for X-ray diffraction were obtained from the bottom of the vial after 4 days. The crystals were rinsed with water, methanol, and Et_2O and dried in air. Yields: 70% (**1**), 85% (**2**).

© 2006 Wiley-VCH Verlag GmbH & Co. KGaA, Weinheim

X-ray structure determinations: Single-crystal X-ray diffraction data for **1** and **2** were collected on a Bruker Smart 1000 CCD diffractometer at 183(2) K with $Mo_{K\alpha}$ radiation ($\lambda = 0.71073$ Å) in ω scan mode. The program SAINT was used for integration of the diffraction profiles. The crystals of **1** are sensitive to air and were measured in a sealed capillary tube. Both structures were solved by direct methods with the SHELXS program and refined by full-matrix least-squares methods with SHELXL (semi-empirical absorption corrections were applied by using the program SADABS). Metal atoms in each complex were located from the *E* maps, and other non-hydrogen atoms were located in successive difference Fourier syntheses and refined with anisotropic thermal parameters on F^2. The hydrogen atoms of the ligand were generated theoretically on the specific atoms and refined isotropically with fixed thermal factors.

Gas-sorption measurements: Sample tubes of known weight were loaded with 500 mg of sample and sealed with a TranSeal. Samples were degassed at 160 °C for 10 h on a Micromeritics ASAP 2010 analyzer until the outgas rate was no more than 1 mTorr min^{-1}. The degassed sample and sample tube were weighed precisely and then transferred back to the analyzer. The TranSeal prevented exposure of the sample to the air after degassing. The outgas rate was again confirmed to be less than 1 mTorr min^{-1}. Adsorption isotherms were measured at 77 K in a liquid-nitrogen bath.

Catalysis studies: A multipurpose temperature-programmed desorption (TPD) instrument (TP-5000, Ohkura Riken) was used as a reactor for CO oxidation. Pure CO, O_2, and He were supplied through mass-flow controllers and mixed with each other, and then the final reactant gas (200 mL min^{-1}) was passed through the catalyst bed (0.3 g). After pretreatment of catalyst with flowing O_2 (20 %) + He (balance) at 300 °C for 30 min and cooling to room temperature, the flow was changed to the reactant gas, the composition of which was CO (1 vol %) + O_2 (20 vol %) + He (balance), and the hourly space velocity (SV) was 20000 mL h^{-1} g(cat.)$^{-1}$. The reaction temperature was programmed between room temperature and 305 °C and monitored by thermocouple (see Supporting Information).

Reactants and products were analyzed with a QMS analyzer (MMC-200, Ulvac), and a TCD-GC (GC-14B, Shimadzu) equipped with a methanizer (MT-221, GL Science). QMS signals were monitored throughout the reaction, and GC analyses were carried out after stabilization of the temperature at 152, 202, 253, and 305 °C.

QMS signals having *m*/*z* values of 28 (CO) and 44 (CO_2) were used for the calculation of reaction rate. Signal intensities of these are referred to as S_{28} and S_{44}, respectively. From the calibration experiment, in which the signal intensities were measured under a flowing mixture of pure gases at known rates, a linear relationship was confirmed between S_{44} and CO_2 concentration, and between S'_{28} and CO concentration. S'_{28} was calculated using $S'_{28} = S_{28} - S_{28}(CO_2)$ where $S_{28}(CO_2)$ is the contribution of the *m*/*z* 28 fragment from CO_2, which was calculated from S_{44} and the fragment pattern of pure CO_2. The reaction rate R_{QMS} [$mol_{CO_2}\,mol_{Ni}^{-1}\,s^{-1}$] was calculated from $R_{QMS} = [k\,S_{44}/(k\,S_{44} + S'_{28})]\,F_{CO}/M_{Ni}$. The factor $k = 1.05$ was determined from a calibration experiment in order to correct the difference in molar sensitivity of signals S_{44} and S'_{28}. F_{CO} [$mol\,s^{-1}$] is the flow rate of CO in the reactant gas, and M_{Ni} is the amount of Ni [mol] in used catalyst.

IR spectra were recorded on a Jasco FT/IR-230 spectrometer. Powder X-ray diffraction data were collected with $Cu_{K\alpha}$ ($\lambda = 1.5406$ Å) radiation on a Rigaku X-ray diffractometer, whereby the sample was heated for 1 h at each temperature before data collection. Thermogravimetric analysis was carried out at a ramp rate of 5 °C min^{-1} in a helium atmosphere on a Shimadzu DTG-50 instrument.

Received: November 5, 2005
Published online: March 17, 2006

Keywords: adsorption · alkali metals · heterogeneous catalysis · metal–organic frameworks · nickel

[1] D. Maspoch, D. Ruiz-Molina, K. Wurst, N. Domingo, M. Cavallini, F. Biscarini, J. Tejada, C. Rovira, J. Veciana, *Nat. Mater.* **2003**, *2*, 190.

[2] a) S. Noro, S. Kitagawa, M. Kondo, K. Seki, *Angew. Chem.* **2000**, *112*, 2161; *Angew. Chem. Int. Ed.* **2000**, *39*, 2081; b) M. Eddaoudi, J. Kim, N. Rosi, D. Vodak, J. Wachter, M. O'Keeffe, O. M. Yaghi, *Science* **2002**, *295*, 469; c) K. Uemura, S. Kitagawa, M. Kondo, K. Fukui, R. Kitaura, H.-C. Chang, T. Mizutani, *Chem. Eur. J.* **2002**, *8*, 3587; d) S. Takamizawa, E. Nakata, H. Yokoyama, K. Mochizuki, W. Mori, *Angew. Chem.* **2003**, *115*, 4467; *Angew. Chem. Int. Ed.* **2003**, *42*, 4331.

[3] a) N. L. Rosi, J. Eckert, M. Eddaoudi, D. T. Vodak, J. Kim, M. O'Keeffe, O. M. Yaghi, *Science* **2003**, *300*, 1127; b) D. N. Dybtsev, H. Chun, S. H. Yoon, D. Kim, K. Kim, *J. Am. Chem. Soc.* **2004**, *126*, 32; c) S. S. Kaye, J. R. Long, *J. Am. Chem. Soc.* **2005**, *127*, 6506; d) M. Dinca, J. R. Long, *J. Am. Chem. Soc.* **2005**, *127*, 9376; e) B. Kesanli, Y. Cui, M. R. Smith, E. W. Bittner, B. C. Bockrath, W. Lin, *Angew. Chem.* **2005**, *117*, 74; *Angew. Chem. Int. Ed.* **2005**, *44*, 72; f) Y. Kubota, M. Takata, R. Matsuda, R. Kitaura, S. Kitagawa, K. Kato, M. Sakata, T. C. Kobayashi, *Angew. Chem.* **2005**, *117*, 851; *Angew. Chem. Int. Ed.* **2005**, *44*, 920; g) B. Chen, N. W. Ockwig, A. R. Millward, D. S. Contreras, O. M. Yaghi, *Angew. Chem.* **2005**, *117*, 4823; *Angew. Chem. Int. Ed.* **2005**, *44*, 4745; h) J. L. Rowsell, O. M. Yaghi, *Angew. Chem.* **2005**, *117*, 4748; *Angew. Chem. Int. Ed.* **2005**, *44*, 4670.

[4] a) G. J. Halder, C. J. Kepert, B. Moubaraki, K. S. Murray, J. D. Cashion, *Science* **2002**, *298*, 1762; b) L.-Y. Kong, Z.-H. Zhang, H.-F. Zhu, H. Kawaguchi, T. Okamura, M. Doi, Q. Chu, W.-Y. Sun, N. Ueyama, *Angew. Chem.* **2005**, *117*, 4426; *Angew. Chem. Int. Ed.* **2005**, *44*, 4352; c) L. Pan, M. B. Sander, X. Huang, J. Li, M. Smith, E. Bittner, B. Bockrath, J. K. Johnson, *J. Am. Chem. Soc.* **2004**, *126*, 1308.

[5] a) O. M. Yaghi, H. Li, *J. Am. Chem. Soc.* **1995**, *117*, 10401; b) O. M. Yaghi, H. Li, *J. Am. Chem. Soc.* **1996**, *118*, 295; c) A. Kamiyama, T. Noguchi, T. Kajiwara, T. Ito, *Angew. Chem.* **2000**, *112*, 3260; *Angew. Chem. Int. Ed.* **2000**, *39*, 3130.

[6] a) M. Fujita, Y. J. Kwon, S. Washizu, K. Ogura, *J. Am. Chem. Soc.* **1994**, *116*, 1151; b) J. S. Seo, D. Whang, H. Lee, S. I. Jun, J. Oh, Y. Jeon, K. Kim, *Nature* **2000**, *404*, 982; c) C.-D. Wu, A. Hu, L. Zhang, W. Lin, *J. Am. Chem. Soc.* **2005**, *127*, 8940.

[7] a) L. Pan, K. M. Adams, H. E. Hernandez, X. Wang, C. Zheng, Y. Hattori, K. Kaneko, *J. Am. Chem. Soc.* **2003**, *125*, 3062; b) Y. Liu, V. C. Kravtsov, D. A. Beauchamp, J. F. Eubank, M. Eddaoudi, *J. Am. Chem. Soc.* **2005**, *127*, 7266.

[8] a) Y.-L. Liu, V. Kravtsov, R. D. Walsh, P. Poddar, H. Srikanthc, M. Eddaoudi, *Chem. Commun.* **2004**, 2806; b) R.-Q. Zou, L. Jiang, H. Senoh, N. Takeichi, Q. Xu, *Chem. Commun.* **2005**, 3526.

[9] Crystal data for **1**: trigonal, space group $R\bar{3}c$, $a = 17.6646(9)$, $b = 17.6646(9)$, $c = 78.413(7)$ Å, $V = 21190(2)$ Å^3, $Z = 12$, $\rho_{calcd} = 1.472$ g cm^{-3}. Least-squares refinement based on 42116 reflections with $I > 2\sigma(I)$ and 5618 parameters led to convergence with final $R_1 = 0.1139$, $wR_2 = 0.3602$, and GOF = 1.737. Crystal data for **2**: orthorhombic, space group *Pnnm*, $a = 16.441(2)$, $b = 16.539(4)$, $c = 25.639(4)$ Å, $V = 6972(2)$ Å^3, $Z = 8$, $\rho_{calcd} = 1.704$ g cm^{-3}. Least-squares refinement based on 21256 reflections with $I > 2\sigma(I)$ and 7870 parameters led to convergence with final $R_1 = 0.0817$, $wR_2 = 0.2238$, and GOF = 1.036. Although data for both compounds were collected at low temperature, ready loss of water of crystallization resulted in slightly higher *R* values. CCDC-288366 (**1**) and CCDC-288367 (**2**) contain the supplementary crystallographic data for this paper. These data

 © 2006 Wiley-VCH Verlag GmbH & Co. KGaA, Weinheim

can be obtained free of charge from The Cambridge Crystallographic Data Centre via www.ccdc.cam.ac.uk/data_request/cif.

[10] a) M. Haruta, *Nature* **2005**, *437*, 1098; b) M. Haruta, *Catal. Today* **1997**, *36*, 153; c) M. Haruta, T. Kobayashi, H. Sano, N. Yamada, *Chem. Lett.* **1987**, *16*, 405; d) M. Haruta, N. Yamada, T. Kobayashi, S. Iijima, *J. Catal.* **1989**, *115*, 301; e) M. Haruta, S. Tsubota, T. Kobayashi, H. Kageyama, M. J. Genet, B. Delmon, *J. Catal.* **1993**, *144*, 175.

[11] a) F. C. Hong, H. H. Kung, *J. Catal.* **1982**, *77*, 561; b) I. E. Maxwell, *Adv. Catal.* **1982**, *31*, 1.

 © 2006 Wiley-VCH Verlag GmbH & Co. KGaA, Weinheim

Table 1: Examples for open-framework materials with 24-ring channels.[a]

Compound	Ref.
$[Zn_3(PO_4)_2(PO_3OH)][(C_6H_{16}N_2)]\cdot 2H_2O$ (ND-1)	[5a]
$[Zn_3(O_3PCH_2COO)_2(O_3PCH_2COOH)][(NH_3CH_2CH_2NH_3)(btc)]$	[5b]
$[Ga_2(deta)(PO_4)_2]\cdot 2H_2O$ (NTHU-1)	[5c]
$[Ge_9O_{17}(OH)_4][N(CH_2CH_2NH_3)_3]_{2/3}[HCON(CH_3)_2]_{1/6}(H_2O)_{11/3}$ (FDU-4)	[5d]
$[Ge_{14}O_{29}F_4][H_2dab]_3[dab]_{0.5}\cdot 16H_2O$ (ASU-16)	[5e]
$[Ni_{18}(HPO_4)_4(OH)_3F_9][(H_3O,NH_4)_4]\cdot 12H_2O$ (VSB-1)	[5f]
$[Ni_{20}(HPO_4)_8(PO_4)_4][(OH)_{12}(H_2O)_6]\cdot 12H_2O$ (VSB-5)	[5g]
$[Ni@Ge_{14}O_{24}(OH)_3]\cdot 2NiL_3$ (FJ-1; L = en or enMe)	[5h]

[a] btc = 1,3,5-benzenetricarboxylic acid; deta = diethylenetriamine; dab = 1,4-diaminobutane; en = ethylenediamine; enMe = 1,2-diaminopropane.

Microporous Materials

DOI: 10.1002/anie.200504134

$[(C_4H_{12}N)_2][Zn_3(HPO_3)_4]$: An Open-Framework Zinc Phosphite Containing Extra-Large 24-Ring Channels**

Jing Liang, Jiyang Li, Jihong Yu, Peng Chen, Qianrong Fang, Fuxing Sun, and Ruren Xu*

Microporous materials with open-framework structures are of great importance due to their potential applications in catalysis, separation, and ion-exchange processes.[1] The discovery of the aluminophosphate molecular sieve VPI-5, which contains 18-ring channels, in 1988[2] promoted the search for new open-framework structures with increasing pore sizes for use in catalysis and the separation of large molecules.[3–5] A few open-framework structures with extra-large 24-ring windows have been described (Table 1). More recently, Zou et al. reported a mesoporous germanium oxide (SU-M) with the largest primitive cell and lowest framework density of any inorganic material and channels that are defined by 30-rings.[5i]

Several approaches toward the design and synthesis of extra-large-pore materials have been explored in the past few years.[6] One feasible method for the preparation of such frameworks is based on the charge-density matching of host and guest by the appropriate selection of framework elements and organic structure-directing agents.[7] An alternative strategy is to make interrupted open-frameworks with terminal P–OH and P=O groups, such as the 20-ring gallophosphate cloverite[4a] and the 20-ring aluminophosphate JDF-20.[4b] The replacement of tetrahedral phosphate groups PO_4^{3-} by pyramidal phosphite units HPO_3^{2-} can reduce the M-O-P connectivity and generate more-open interrupted framework structures. Recently, metal phosphites with novel open-framework structures and compositions have been prepared by using various template molecules,[8] including several vanadium hydrogenphosphites with 14-ring channels[9e] and zinc phosphites with 16-ring channels.[9a–d] Here, we report the first metal phosphite, $[(C_4H_{12}N)_2][Zn_3(HPO_3)_4]$ (denoted ZnHPO-CJ1; CJ stands for China Jilin University), with extra-large 24-ring channels and a unique framework topology.

ZnHPO-CJ1 was prepared by the hydrothermal reaction of a mixture of $Zn(OAc)_2\cdot 2H_2O$, *n*-butylamine, H_3PO_3, and H_2O in a 1:4.5:3:488 ratio at 180 °C for three days in a Teflon-lined stainless-steel autoclave.

Single-crystal structural analysis revealed that ZnHPO-CJ1 consists of a macroanionic $[Zn_3(HPO_3)_4]^{2-}$ framework and *n*-butylammonium counterions, $CH_3(CH_2)_3NH_3^+$. Each asymmetric unit contains two crystallographically distinct P atoms and two crystallographically distinct Zn sites, with Zn(2) located on a twofold axis (see Figure S1 in the Supporting Information). Each P atom connects three O atoms to nearby Zn atoms, leaving a terminal P–H bond. All Zn atoms are in tetrahedral environments. The P–O and Zn–O bond lengths ($P-O_{av.} = 1.505$, $Zn-O_{av.} = 1.956$ Å) are in agreement with those observed in other zinc phosphites.[9] The existence of P–H bonds is confirmed by the characteristic band of the phosphite anion ($\tilde{\nu}_{H-P} = 2399\ cm^{-1}$) in the IR spectrum (see Figure S2).

The open framework of ZnHPO-CJ1 is made up of strictly alternating ZnO_4 tetrahedra and HPO_3 pseudo-pyramids, which are arranged in parallel 24-ring and 8-ring channels extending along the crystallographic *c* axis (Figure 1a). The approximate size of the 24-ring window is 11.0×11.0 Å^2, which is comparable with those of the 24-ring channels in NTHU-1[5c] (diameter 10.4 Å) and FDU-4[5d] (12.65 Å). Eight $CH_3(CH_2)_3NH_3^+$ ions reside in each 24-ring window. The alkyl groups of these cations extend into the hollow space of the 24-ring channel and their NH_3^+ groups form H-bonds with the framework oxygen atoms (Figure 1b). The center space of the channels between the organic cations is empty, as in ND-1,

[*] J. Liang, Dr. J. Li, Prof. J. Yu, P. Chen, Q. Fang, F. Sun, Prof. R. Xu
State Key Laboratory of Inorganic Synthesis and Preparative Chemistry
College of Chemistry
Jilin University
Changchun 130012 (P.R. China)
Fax: (+86) 431-516-8608
E-mail: jihong@mail.jlu.edu.cn

[**] This work was supported by the National Natural Science Foundation of China.

Supporting Information for this article is available on the WWW under http://www.angewandte.org or from the author.

InterScience
© 2006 Wiley-VCH Verlag GmbH & Co. KGaA, Weinheim

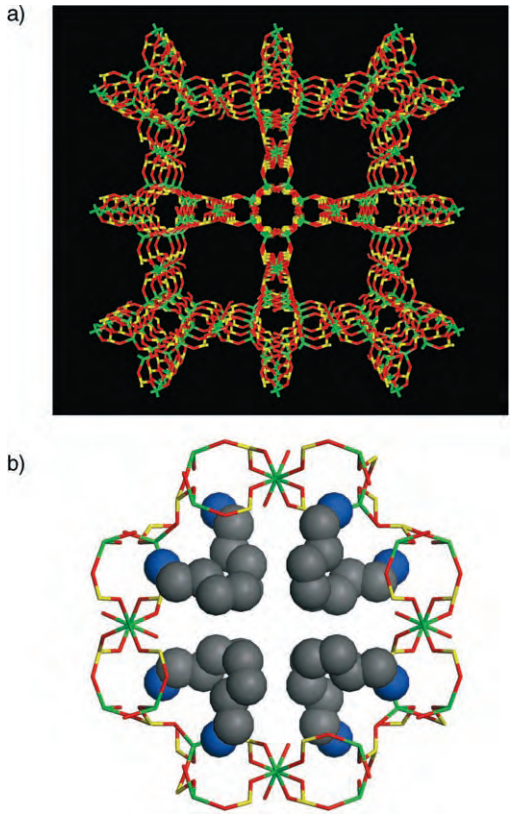

Figure 1. a) The open-framework structure of ZnHPO-CJ1 viewed along the [001] direction showing the extra-large 24-ring and the 8-ring channels. The atoms O4′, O5′, O6′, and all H atoms have been omitted for clarity; b) eight $CH_3(CH_2)_3NH_3^+$ ions reside in one 24-ring pore. Hydrogen atoms have been omitted for clarity. Color code: Zn green, P yellow, O red, N blue, C gray.

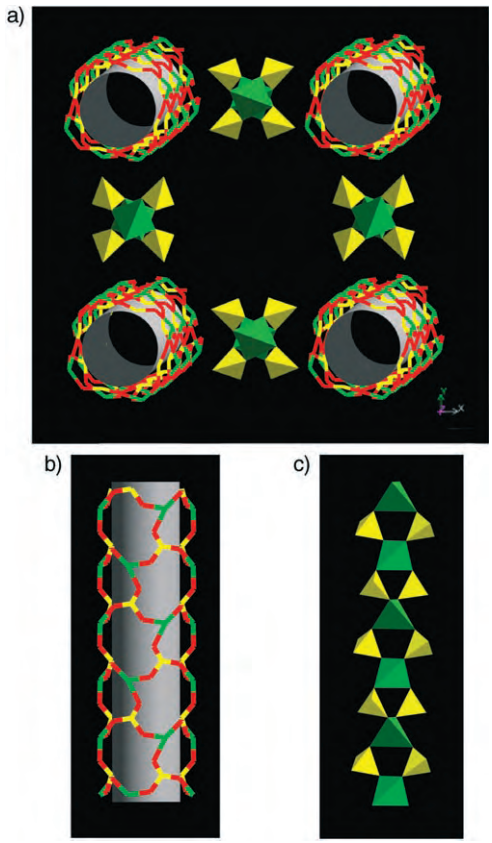

Figure 2. a) The tetragonal array of four 8-ring channels; b) one 8-ring channel with 6-ring side pockets; c) the corner-sharing 4-ring chain. Color code: Zn green, P yellow, O red.

with a distance of about 2.6 Å between the end carbon atoms of two *n*-butylamine cations across the channels.

Figure 2a shows the tetragonal array of four 8-ring channels in the structure. These 8-ring channels with 6-ring side pockets (Figure 2b) are further connected by four corner-sharing 4-ring chains (Figure 2c) through Zn-O-P linkages to form the 24-ring channels. Strikingly, the 8-ring channels are hollow but do not contain encapsulated molecules. The pore size (ca. 3.4×3.4 Å^2) is typical for molecular sieves containing eight-ring channels, such as ABW (3.4×3.8 Å^2), AFX (3.4×3.6 Å^2), PAU (3.6×3.6 Å^2), and RHO (3.6×3.6 Å^2). The PH groups of the $HP(1)O_3$ units point into the 8-ring channels, which partially reduces the free volume available.

TG analysis (Figure S3) showed a weight loss of 24.02% between 160 and 395 °C, which is attributed to the decomposition of the *n*-butylammonium cations (calcd 22.35%). An XRD study showed that the structure collapses after heating at 280 °C for 3 h, which suggests that the inorganic framework structure is unstable upon removal of the organic molecules.

To the best of our knowledge, the largest pore opening found in metal phosphites to date is 16-rings,[9] therefore ZnHPO-CJ1 is the first metal phosphite with extra-large 24-ring channels. Its framework density, 11.6 polyhedra per 1000 Å^3, is similar to the values of 12.1 for ND-1,[5a] 11.1 for FDU-4,[5d] and 10.9 for NTHU-1.[5c] The structure of ZnHPO-CJ1 provides useful information on the host–guest relationship in the formation of extra-large pores. As opposed to the extra-large-pore high-silica zeolites UTD-1 and CIT-5, which are templated by bulky organic cations with low charge density, many metal phosphates and phosphites with extra-large pores have been prepared in the presence of relatively small organic amines which yield ammonium ions with high charge density. Examples include the 20-ring aluminophosphate JDF-20, templated by triethylamine,[4b] the 16-ring gallophosphate ULM-5, templated by 1,6-hexanediamine,[10] the 16-ring gallophosphate ULM-16, templated by cyclopentylamine,[11] the 18-ring gallophosphate MIL-31, templated by $NH_2(CH_2)_nNH_2$ ($n = 9,10$),[12] and the 24-ring zinc phosphate ND-1, templated by 1,2-diaminocyclohexane,[5a] where several ammonium ions are included in one extra-large pore. This exemplifies the idea of a supramolecular templating process being used for the preparation of mesoporous molecular sieves.[13]

Experimental Section

Synthesis and characterization: Typically, $Zn(OAc)_2 \cdot 2H_2O$ (0.25 g) was first dissolved in H_2O (10 mL), and then *n*-butylamine (0.51 mL) was added while stirring. Finally, H_3PO_3 (0.280 g) was added to the above reaction mixture. A homogeneous reaction gel (pH ≈ 6) was formed after stirring for 1 h, and this gel was sealed in a 15-mL Teflon-

 © 2006 Wiley-VCH Verlag GmbH & Co. KGaA, Weinheim

lined stainless-steel autoclave and heated at 180 °C for three days under static conditions. The colorless, rod-shaped single crystals obtained were separated by sonication, washed with distilled water, and then dried in the air.

X-ray powder diffraction (XRD) data were collected on a Siemens D5005 diffractometer with $Cu_{K\alpha}$ radiation ($\lambda = 1.5418$ Å). The experimental XRD pattern agreed well with the simulated one generated on the basis of the single-crystal analysis (Figure S4). A Perkin–Elmer TGA 7 unit was used for the thermogravimetric analysis in air (heating rate 20 K min^{-1}). ICP analysis was performed with a Perkin–Elmer Optima 3300 DV ICP instrument (calcd (wt %): Zn 29.52, P 18.65; found: Zn 28.95, P 18.03). Elemental analysis was carried out with a Perkin–Elmer 2400 elemental analyzer (calcd (wt %): C 14.46, H 4.25, N 4.22; found: C 14.65, H 3.89, N 4.33).

Structure determination: Structural analysis of a single crystal ($0.20 \times 0.06 \times 0.06$ mm^3) was performed with a Siemens SMART CCD diffractometer using graphite-monochromated $Mo_{K\alpha}$ radiation ($\lambda = 0.71073$ Å). The data were collected at $T = (20 \pm 2)$ °C. Data processing was accomplished with the SAINT processing program.[14] The structure was solved by direct methods and refined on F^2 by full-matrix least-squares using SHELXTL97.[15] All Zn, P, and O atoms were determined directly; C and N atoms were subsequently found in the difference Fourier map. The H atoms of the HPO_3 groups were found in the final difference Fourier map, H atoms of the *n*-butylammonium cations were placed geometrically. The thermal parameter of H(1) was fixed at 0.08. The O(4), O(5), and O(6) atoms were disordered over two positions with an equal occupancy to the O(4′), O(5′), and O(6′) atoms. P(1) is tetrahedrally coordinated either to O(4), O(5), O(6′), and H1 or to O(4′), O(5′), O(6), and H1. Zn(1) is tetrahedrally coordinated either to O(3), O(4), O(5′), and O(6) or to O(3′), O(4′), O(5), and O(6′). All non-hydrogen atoms of the inorganic framework were refined anisotropically.

Crystal data: $C_8H_{28}N_2O_{12}P_4Zn_3$, $M_r = 664.32$, tetragonal, space group $P4cc$ (no. 103), $a = 16.4797(8)$, $b = 16.4797(8)$, $c = 8.8635(6)$ Å, $V = 2407.2(2)$ Å^3, $Z = 4$, $\mu = 3.283$ mm^{-1}, $\rho_{calcd} = 1.833$ g cm^{-3}, 13489 reflections measured, 2664 unique ($R_{int} = 0.0688$). The final wR_2 (all data) was 0.0727 and R_1 was 0.0374. CCDC-290109 contains the supplementary crystallographic data for this paper. These data can be obtained free of charge from The Cambridge Crystallographic Data Centre via www.ccdc.cam.ac.uk/data_request/cif.

Received: November 21, 2005
Revised: January 25, 2006
Published online: March 17, 2006

Keywords: hydrothermal synthesis · materials science · phosphites · template synthesis · zinc

[1] a) A. K. Cheetham, G. Férey, T. Loiseau, *Angew. Chem.* **1999**, *111*, 3466; *Angew. Chem. Int. Ed.* **1999**, *38*, 3268, and references therein; b) J. M. Thomas, R. Raja, G. Sankar, R. G. Bell, *Acc. Chem. Res.* **2001**, *34*, 191; c) J. Yu, R. Xu, *Acc. Chem. Res.* **2003**, *36*, 481, and references therein; d) Ch. Baerlocher, W. M. Meier, D. H. Olson, *Atlas of Zeolite Framework Types 5th rev. ed.*, Elsevier, London, **2001**; IZA Structure Commission website: http://www.iza-structures.org/database/.

[2] M. E. Davis, C. Saldarriaga, C. Montes, J. M. Graces, C. Crowder, *Nature* **1988**, *331*, 698.

[3] a) G. Férey, A. K. Cheetham, *Science* **1999**, *283*, 1125; b) H. L. Li, A. Laine, M. O'Keeffe, O. M. Yaghi, *Science* **1999**, *283*, 1145; c) Q. Fang, G. Zhu, M. Xue, J. Sun, Y. Wei, S. Qiu, R. Xu, *Angew. Chem.* **2005**, *117*, 3913; *Angew. Chem. Int. Ed.* **2005**, *44*, 3845.

[4] a) M. Estermann, L. B. McCusker, Ch. Baerlocher, A. Merrouche, H. Kessler, *Nature* **1991**, *352*, 320; b) Q. Huo, R. Xu, S. Li, Z. Ma, J. M. Thomas, R. H. Jones, A. M. Chippindale, *J. Chem. Soc. Chem. Commun.* **1992**, 875.

[5] a) G. Yang, S. C. Sevov, *J. Am. Chem. Soc.* **1999**, *121*, 8389; b) J. Zhu, X. Bu, P. Feng, G. D. Stucky, *J. Am. Chem. Soc.* **2000**, *122*, 11563; c) C. H. Lin, S. L. Wang, K. H. Lii, *J. Am. Chem. Soc.* **2001**, *123*, 4649; d) Y. Zhou, H. Zhu, Z. Chen, M. Chen, Y. Xu, H. Zhang, D. Zhao, *Angew. Chem.* **2001**, *113*, 2224; *Angew. Chem. Int. Ed.* **2001**, *40*, 2166; e) J. Plévert, T. M. Gentz, A. Laine, H. Li, V. G. Young, O. M. Yaghi, M. O'Keeffe, *J. Am. Chem. Soc.* **2001**, *123*, 12706; f) N. Guillou, Q. Gao, M. Nogués, R. E. Morris, M. Hervieu, G. Férey, A. K. Cheetham, *C. R. Acad. Sci. Paris Ser. IIc* **1999**, *2*, 387; g) N. Guillou, Q. Gao, P. M. Forster, J.-S. Chang, M. Nogués, S.-E. Park, G. Férey, A. K. Cheetham, *Angew. Chem.* **2001**, *113*, 2913; *Angew. Chem. Int. Ed.* **2001**, *40*, 2831; h) Z. Lin, J. Zhang, J. Zhao, S. Zheng, C. Pan, G. Wang, G. Yang, *Angew. Chem.* **2005**, *117*, 7041; *Angew. Chem. Int. Ed.* **2005**, *44*, 6881; i) X. Zou, T. Conradsson, M. Klingstedt, M. S. Dadachov, M. O'Keeffe, *Nature* **2005**, *437*, 716.

[6] a) M. E. Davis, *Chem. Eur. J.* **1997**, *3*, 1745; b) T. E. Gier, G. D. Stucky, *Nature* **1991**, *349*, 508; c) T. M. Nenoff, W. T. A. Harrison, T. E. Gier, G. D. Stucky, *J. Am. Chem. Soc.* **1991**, *113*, 378; d) W. T. A. Harrison, T. E. Gier, K. L. Moran, J. M. Nicol, H. Eckert, G. D. Stucky, *Chem. Mater.* **1991**, *3*, 27; e) D. E. Akporiaye, *Angew. Chem.* **1998**, *110*, 2594; *Angew. Chem. Int. Ed.* **1998**, *37*, 2456; f) K. J. Balkus, Jr., *Progress in Inorganic Chemistry, Vol. 50*, Wiley, New York, **2001**, p. 217.

[7] P. Feng, X. Bu, G. D. Stucky, *Nature* **1997**, *388*, 735.

[8] a) S. Fernández, J. L. Mesa, J. L. Pizarro, L. Lezama, M. I. Arriortua, T. Rojo, *Angew. Chem.* **2002**, *114*, 3835; *Angew. Chem. Int. Ed.* **2002**, *41*, 3683; b) G. Bonavia, J. DeBord, R. C. Haushalter, D. Rose, J. Zubieta, *Chem. Mater.* **1995**, *7*, 1995; c) J. A. Rodgers, W. T. A. Harrison, *Chem. Commun.* **2000**, *23*, 2385; d) J. Liang, Y. Wang, J. Yu, Y. Li, R. Xu, *Chem. Commun.* **2003**, 882.

[9] a) W. T. A. Harrison, *J. Solid State Chem.* **2001**, *160*, 4; b) W. T. A. Harrison, M. L. F. Phillips, T. M. Nenoff, *Int. J. Inorg. Mater.* **2001**, *3*, 1033; c) Z. Lin, J. Zhang, S. Zheng, G. Yang, *J. Mater. Chem.* **2004**, *14*, 1652; d) W. Chen, N. Li, S. Xiang, *J. Solid State Chem.* **2004**, *177*, 3229; e) R. K. Chiang, N. T. Chuang, *J. Solid State Chem.* **2005**, *178*, 3040.

[10] T. Loiseau, G. Férey, *J. Solid State Chem.* **1994**, *111*, 403.

[11] C. Sassoye, J. Marrot, T. Loiseau, G. Férey, *Chem. Mater.* **2002**, *14*, 1340.

[12] C. Sassoye, T. Loiseau, F. Taulelle, G. Férey, *Chem. Commun.* **2000**, 943.

[13] H. O. Pastore, S. Coluccia, L. Marchese, *Annu. Rev. Mater. Res.* **2005**, *35*, 351.

[14] SMART and SAINT (software package), Siemens Analytical X-ray Instruments Inc., Madison, WI, **1996**.

[15] SHELXTL, version 5.1, Siemens Industrial Automation, Inc., Madison, WI, **1997**.

 © 2006 Wiley-VCH Verlag GmbH & Co. KGaA, Weinheim

Asymmetric Catalysts

DOI: 10.1002/anie.200504275

Evidence for Substrate Binding by the Lanthanide Centers in $[Li_3(thf)_n(binolate)_3Ln]$: Solution and Solid-State Characterization of Seven- and Eight-Coordinate $[Li_3(sol)_n(binolate)_3Ln(S)_m]$ Adducts**

*Alfred J. Wooten, Patrick J. Carroll, and Patrick J. Walsh**

Dedicated to Professor Larry Sneddon on the occasion of his 60th birthday.

The heterobimetallic $[M_3(thf)_n(binolate)_3Ln]$ (binol = 1,1′-bi-2-naphthol; M = Li, Na, K; thf = tetrahydrofuran) catalysts (Figure 1) developed by Shibasaki and co-workers have

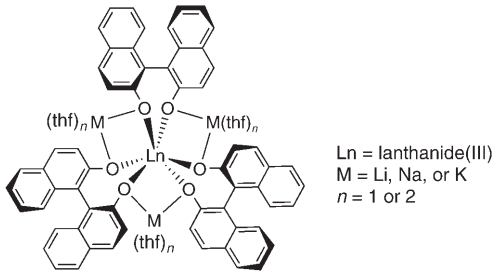

Figure 1. $[M_3(thf)_n(binolate)_3Ln]$ catalysts developed by Shibasaki and co-workers.

proven to be among the most versatile and successful asymmetric Lewis acid catalysts introduced to date.[1–3] Central to mechanistic proposals involving $[M_3(thf)_n(binolate)_3Ln]$ heterobimetallic compounds is Lewis acid activation of the substrate by the lanthanide.[2–4] Prior efforts to detect lanthanide–substrate interactions, however, have not been successful. Herein, we disclose solid-state and solution evidence that $[Li_3(thf)_n(binolate)_3Ln]$ catalysts can bind organic substrates and substrate analogues to form seven- and eight-coordinate Ln centers.

Several $[M_3(thf)_n(binolate)_3Ln]$[5,6] and $[M_3(thf)_n(binolate)_3Ln(OH_2)]$[1,5,7,8] complexes have been characterized crystallographically.[9] The lanthanide centers in these structures are either six-coordinate (Figure 1) or seven-coordinate when bound to a water molecule. Each main-group-metal center is bound by one or two organic solvent molecules. The lanthanide centers in sterically hindered $[M_3(thf)_n(binolate)_3Ln]$ complexes have a much higher affinity for water than for organic ligands, evidence for which was found by crystallization of the hydrates above from THF and Et_2O. In this regard, the absence of structurally characterized $[M_3(thf)_n(binolate)_3Ln(S)]$ (S = substrate or solvent) complexes with Lewis basic organic ligands bound to the lanthanide atom raises questions concerning the ability of the lanthanide center to bind and activate substrates in asymmetric catalysis.

One approach used by prior investigators to address these concerns involved probing Ln–substrate binding interactions in solution by using paramagnetic Pr, Eu, and Yb analogues. Paramagnetic complexes provide greater chemical-shift dispersions than their diamagnetic counterparts, thereby allowing the study of normally unobservable metal–substrate interactions.[10] Previously reported ^{1}H NMR spectroscopic binding studies of $[Na_3(thf)_6(binolate)_3Pr]$ and $[Na_3(thf)_6(binolate)_3Eu]$ with cyclohexenone showed small chemical-shift differences for the α-vinyl proton of 0.1 and 0 ppm, respectively.[8] Similarly, addition of pivalaldehyde to $[Li_3(thf)_6(binolate)_3Pr]$ resulted in a shift of the signal for the formyl hydrogen atom of only 0.1 ppm.[11] These small lanthanide-induced shifts (LISs) could be attributed to coordination of the carbonyl groups to the main-group atoms. Alternatively, the small LIS may indicate weak, reversible substrate binding to the lanthanide center. A related NMR spectroscopic study with paramagnetic $[Na_3(thf)_6(binolate)_3Yb]$ showed that the small Yb center does not even bind water.[6]

To reconcile some of the differences in proposed mechanisms and experimental observations for this important class of catalysts, we set out 1) to assess whether the lanthanide in $[Li_3(sol)_n(binolate)_3Ln]$ complexes could bind organic substrates and substrate analogues in solution and in the solid state, and 2) to examine the coordination numbers and geometries of the resultant adducts.

Binding studies of $[Li_3(thf)_6(binolate)_3Eu]$ in solution are complicated by the presence of two different Lewis acidic metal centers, both of which can bind the substrate, thus causing a LIS. To simplify the analysis of our binding studies, we sought to inhibit substrate binding to the lithium centers by addition of a tightly binding diamine. Thus, addition of *N,N*′-dimethylethylenediamine (dmeda) to $[Li_3(thf)_6(binolate)_3Ln]$ (**1**: Ln = Eu, **2**: Ln = La)[1] in THF resulted in the formation of $[Li_3(dmeda)_3(binolate)_3Ln]$ (**3**: Ln = Eu, **4**: Ln = La) as crystalline solids. The ^{1}H NMR spectra of **3** and **4** suggest that they are single diastereomers. Importantly, the diamine backbone of **3** experiences a LIS to lower frequencies with the resonances being observed as two broad singlets at $\delta = -3.59$ and -3.82 ppm. The diamine backbone is diastereotopic due to the chiral environment of the binolate ligands and indicates that the diamine is not dissociating from the lithium on the NMR timescale.

A comparison of the LISs of **1** and **3** could reveal whether the cyclohexenone carbonyl group binds to the lithium or the

[*] Dr. A. J. Wooten, Dr. P. J. Carroll, Prof. P. J. Walsh
P. Roy and Diana T. Vagelos Laboratories
Department of Chemistry, University of Pennsylvania
231 South 34th Street, Philadelphia, PA 19104-6323 (USA)
Fax: (+1) 215-573-6743
E-mail: pwalsh@sas.upenn.edu

[**] We thank the National Institutes of Health and the National Institute of General Medical Sciences (GM058101) for a postdoctoral fellowship to A.J.W. We are grateful to Professor John F. Hartwig of Yale University for helpful discussions. sol = solvent; S = substrate or solvent.

Supporting information for this article is available on the WWW under http://www.angewandte.org or from the author.

 © 2006 Wiley-VCH Verlag GmbH & Co. KGaA, Weinheim

lanthanide centers. If cyclohexenone binds to the lithium centers, the LISs of **1** and **3** will be significantly different because the lithium centers in **3** are coordinatively saturated and cannot bind the substrate. If binding takes place at the lanthanide center, however, cyclohexenone will exhibit similar LISs with both **1** and **3**. The addition of 6 equivalents of cyclohexenone to **1** in [D_8]THF resulted in significant LIS of the vinyl α- and β-hydrogen atoms to higher frequencies, giving chemical-shift differences consistent with reversible substrate binding of 0.56 and 0.16 ppm, respectively (Table 1). At the same concentration ratio for the dmeda adduct **3**, the resonances of the cyclohexenone vinyl α- and β-hydrogen atoms shifted to similarly high frequencies, giving LISs of 0.66 and 0.18 ppm, with the diamine backbone remaining diastereotopic.

Table 1: Measured induced shifts of cyclohexenone and DMF with various shift reagents at given concentration ratios.[a]

Shift reagent and substrate	[SR]/[Sub] [M/M]	LIS $\Delta\delta$ H_α [ppm]	LIS $\Delta\delta$ H_β [ppm]	LIS $\Delta\delta$ H (formyl) [ppm]	LIS $\Delta\delta$ CH_3 [ppm]	LIS $\Delta\delta$ CH_3 [ppm]
1 + cyclohexenone	0.032/0.193	0.56	0.16	–	–	–
3 + cyclohexenone	0.037/0.186	0.66	0.18	–	–	–
5 + cyclohexenone	0.032/0.193	0.46	0.28	–	–	–
[Eu(hfc)$_3$] + cyclohexenone	0.032/0.193	0.05	0.00	–	–	–
[Eu(hfc)$_3$] + cyclohexenone	0.193/0.193	0.30	0.06	–	–	–
4 + cyclohexenone	0.032/0.194	0.03	0.02	–	–	–
1 + DMF	0.032/0.258	–	–	1.14	1.26	0.61
3 + DMF	0.032/0.258	–	–	2.30	1.06	0.77
4 + DMF	0.032/0.258	–	–	0.09	0.04	0.02

[a] Internal reference: mesitylene at $\delta = 6.73$ ppm (H) and $\delta = 2.22$ ppm (CH_3). Solvent: [D_8]THF at $\delta = 3.58$ and 1.73 ppm.

Further support for substrate binding was obtained with [Li_3(thf)$_6$(binolate)$_3$Pr] (**5**), which induced LISs to lower frequencies for the vinyl α- and β-hydrogen atoms of cyclohexenone of 0.46 and 0.28 ppm, respectively. The contrasting effect of Pr and Eu complexes on the chemical shifts of bound substrates to lower and higher frequencies, respectively, is well-known.[10,12] The LISs observed with cyclohexenone and **1, 3**, and **5** can only arise from binding of the carbonyl oxygen atom to the lanthanide centers. To put these LISs in perspective, the LISs of cyclohexenone was examined in the presence of the well-known chiral shift reagent [Eu(hfc)$_3$] (hfc = 3-(heptafluoropropylhydroxymethylene)-*d*-camphorato). At the above concentration ratio in [D_8]THF, [Eu(hfc)$_3$] caused only a small LIS for the vinyl α-hydrogen atom (0.05 ppm, Table 1). A 1:1 molar ratio of [Eu(hfc)$_3$] to cyclohexenone, however, resulted in a LIS of 0.30 ppm. These shifts are smaller than would be observed in non-coordinating solvents owing to competition between [D_8]THF and cyclohexenone for binding at the europium center. We attribute the larger LIS of the Eu–binolate-based complexes over [Eu(hfc)$_3$] to the greater steric hindrance about the lanthanide center in the binolate derivatives, which results in a greater selectivity for the less-crowded carbonyl oxygen atom over the THF oxygen atom. For comparison, diamagnetic **4** induced shifts of < 0.03 ppm in the resonances of the vinyl group of cyclohexenone.

To obtain a larger LIS, we examined a substrate analogue that would have an affinity for the lanthanide center greater than that of cyclohexenone. Addition of 8 equivalents of *N,N*-dimethylformamide (DMF) to **1** and **3** resulted in a LIS of 1.14 and 2.30 ppm, respectively, for the signals of the formyl hydrogen atom. In contrast, addition of DMF to diamagnetic **4** resulted in a shift of 0.09 ppm. The binding studies with cyclohexenone and DMF attest to the advantages of using paramagnetic lanthanides to probe interactions that would be otherwise difficult to evaluate.

Additional support for lanthanide–substrate binding in solution was obtained by demonstrating that **4**, which contains coordinatively saturated lithium atoms, is an active catalyst. Complex **2** often gives the highest enantioselectivities and product yields.[3] Therefore, the reaction of 1.2 equivalents of dimethyl phosphite with benzaldehyde[13] in the presence of **4** (10 mol%) at −78 °C in THF produced the α-hydroxy phosphonate in 92% yield with 78% *ee*. In the asymmetric Henry reaction,[14] nitromethane (10 equiv) was added to benzaldehyde in the presence of **4** (10 mol%) at −50 °C in THF to generate the nitroaldol product in 76% yield with 25% *ee*. Finally, addition of 1,3-cyclopentadiene (10 equiv) to 3-(1-oxo-2-propenyl)-2-oxazolidinone in CH_2Cl_2 at 0 °C in the presence of **4** (10 mol%) produced the Diels–Alder product in 54% yield with 32% *ee*.[15]

Inspired by the observation of substrate binding to the lanthanide center in THF, we explored the solid-state structure of the substrate adducts. Pentane was diffused into THF solutions of **1** and **2** at room temperature. Pale crystals were obtained, and their structures determined. An ORTEP diagram of seven-coordinate [Li_3(thf)$_4$(binolate)$_3$La(thf)] (**7**) is shown in Figure 2.[16] Isostructural [Li_3(thf)$_4$(binolate)$_3$Eu(thf)][17] (**6**) is illustrated in the Supporting Information. These structures are consistent with competitive binding of [D_8]THF in the solution studies outlined above.

The gross structural features of **6** and **7** consist of a LnO_7 core that can be described as a trigonally compressed capped octahedron with THF as the capping group. In addition to the chirality of the binolate ligands, the lanthanide ions are stereogenic centers. As observed with the hydrates, use of (*R*)-binol led to the Δ configuration at the lanthanide. Slight differences in the bond lengths of **6** and **7** were observed owing to the smaller ionic radius of Eu (1.09 Å) relative to La (1.17 Å). The binolate La–O bond lengths in **7** ranged from 2.403(5) to 2.485(3) Å, and the dative La–O_{THF} bond length was 2.567(5) Å. The Eu–O bond lengths for the binolate ligands ranged from 2.302(3) to 2.400(4) Å, with a Eu–O_{THF} bond length of 2.482(4) Å. Binding of THF to the lanthanide pulled the La 0.767(4) Å out of the Li_3 plane, whereas the smaller Eu was displaced by 0.737(3) Å. Smaller displace-

 © 2006 Wiley-VCH Verlag GmbH & Co. KGaA, Weinheim

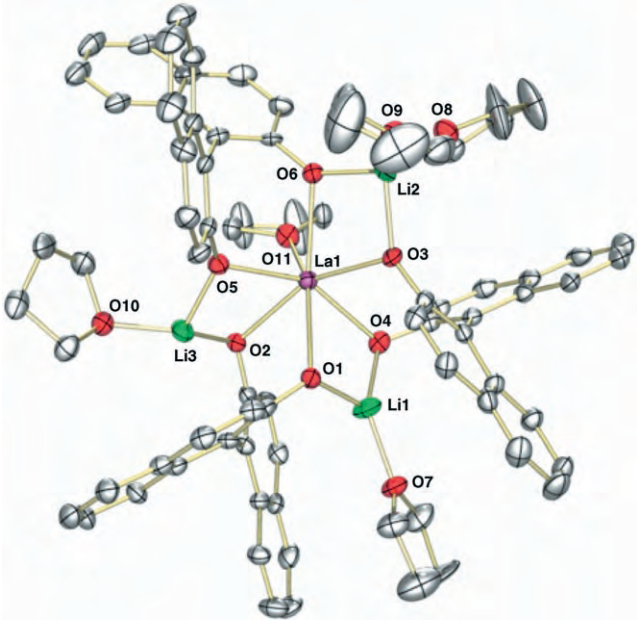

Figure 2. Structure of $[Li_3(thf)_4(binolate)_3La(thf)]$ (**7**).

ments were observed for the seven-coordinate aqua adducts $[Na_3(thf)_6(binolate)_3Eu(OH_2)]$ (0.387 Å) and $[Li_3(OEt_2)_3(binolate)_3Eu(OH_2)]$ (0.326 Å).[5]

To probe the binding of softer ligands to the lanthanide center, we crystallized $[Li_3(py)_5(binolate)_3La(py)_2]$ (**8**) (py = pyridine) by diffusion of pentane into a solution of **2** in pyridine at room temperature. An ORTEP diagram of **8** is shown in Figure 3.[18] The complex consists of an eight-coordinate lanthanum center with two pseudo-*trans* pyridine molecules (N–La–N = 150.87(8)°; La–N bond lengths: La1–N6 = 2.812(3) Å, La1–N7 = 2.773(3) Å). The observed *trans*

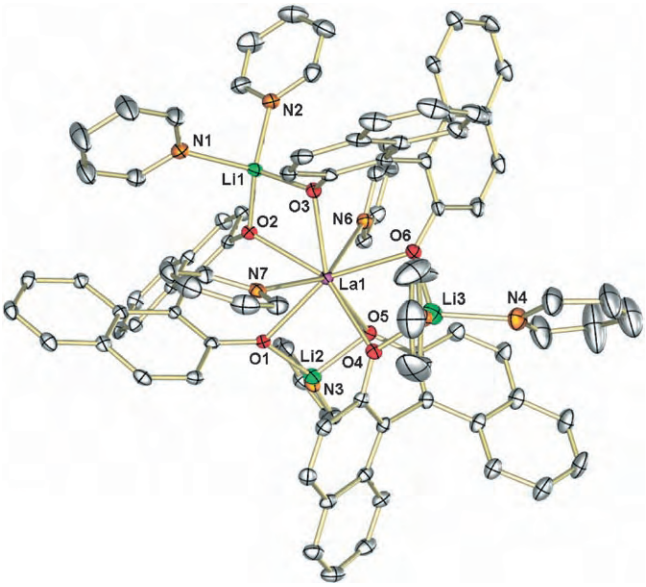

Figure 3. Structure of $[Li_3(py)_5(binolate)_3La(py)_2]$ (**8**).

coordination may explain why the chelating diamine dmeda does not bind to the lanthanide centers in **3** and **4**. The binolate La–O bond lengths in **8** ranged from 2.439(2)–2.536(2) Å and were, on average, longer than the La–O bond lengths in THF adduct **7** (2.403(5)–2.485(3) Å). The La atom in eight-coordinate **8** was displaced by only 0.042 Å from the Li_3 plane. Although the eight-coordinate pyridine adduct has not been used in asymmetric reactions to date, it is quite relevant, because it clearly demonstrates that sterically hindered $[Li_3(thf)_n(binolate)_3Ln]$ catalysts can achieve a coordination number of eight. In solution, there is probably rapid equilibria between six-, seven-, and eight-coordinate complexes that result in signal averaging on the NMR timescale.[19]

In summary, the solution and solid-state structures of the seven- and eight-coordinate complexes described herein provide the first definitive evidence that the lanthanide in $[Li_3(thf)_n(binolate)_3Ln]$ complexes can bind substrates and substrate analogues. Furthermore, several reactions catalyzed by $[Li_3(thf)_n(binolate)_3Ln]$ complexes require an additive, such as water, to allow high enantioselectivity. It has been proposed that in the aldol reaction, the seven-coordinate water adduct, $[Li_3(thf)_6(binolate)_3La(OH_2)]$, binds the substrate to give eight-coordinate $[Li_3(thf)_6(binolate)_3La(OH_2)(substrate)]$.[20,21] The characterization of eight-coordinate $[Li_3(py)_5(binolate)_3La(py)_2]$ lends support to this proposal for larger lanthanides and indicates that the lanthanide centers can expand their coordination number beyond seven, the proposed maximum for this important class of compounds.[22]

Experimental Section

Determination of induced chemical shifts: The ^{1}H NMR spectra in this study were obtained on a Bruker DMX-300 Fourier transform NMR spectrometer at 300 MHz. Mesitylene was used as an internal-referencing standard for all experiments, and $[D_8]$THF was used as the solvent. Induced chemical shifts of cyclohexenone and DMF were obtained by incremental addition of known masses of the solid lanthanide complex to a substrate solution of known concentration. The first shift reagent (SR) used with cyclohexenone and DMF was $[Li_3(thf)_3(binolate)_3Eu]$, at a concentration ratio ([SR]:[Substrate]) of 0.032 M:0.193 M and 0.032 M:0.258 M, respectively. $[Li_3(dmeda)_3(binolate)_3Eu]$ was then used with cyclohexenone and DMF at a concentration ratio of 0.037 M:0.186 M and 0.032 M:0.258 M, respectively. Finally, $[Li_3(thf)_3(binolate)_3Pr]$ was used with cyclohexenone at a concentration ratio of 0.032 M:0.193 M. Each sample was allowed to equilibrate for 15 min before acquisition of NMR data. All spectra can be found in the Supporting Information.

4: Under nitrogen, dmeda (0.143 mL, 0.118 g, 1.34 mmol) was added to a solution of **2** (0.500 g, 0.407 mmol) in THF (40 mL). This solution was stirred at room temperature for 4 h, after which all volatile materials were removed in vacuo. The remaining white solid was placed on a frit and washed with diethyl ether (3 × 5 mL) to afford the desired compound after drying under reduced pressure (0.470 g, 91% yield based on **2**). ^{1}H NMR (300 MHz, $[D_8]$THF, 25 °C, tetramethylsilane (TMS)): $\delta = 0.61$ (br s, 2H; NH), 1.60 (s, 6H; N–CH_3), 1.69 (br d, 2H; N–CH_2), 1.96 (br d, 2H; N–CH_2), 6.83 (d, 2H), 6.91 (m, 4H), 7.23 (d, 2H), 7.67 ppm (t, 4H); ^{13}C{^{1}H} NMR (75 MHz, $[D_8]$THF): $\delta = 36.1$ (N–CH_3), 50.7 (N–CH_2), 119.4, 120.4, 125.0, 126.1, 127.2, 127.9, 128.2, 128.6, 136.6, 163.8 ppm; IR (KBr): $\tilde{\nu}$ = 3341, 3299, 3043, 2981,2952, 2890, 2855, 2802, 1612, 1588, 1553, 1499,

 © 2006 Wiley-VCH Verlag GmbH & Co. KGaA, Weinheim

1463, 1422, 1342, 1283, 1247, 1177, 1140, 1096, 1069, 994, 959, 935, 882, 822, 746, 665, 632, 591, 574 cm^{-1}; elemental analysis: calcd (%) for $C_{72}H_{72}Li_3O_6N_6La$ (1277.11 $g\,mol^{-1}$): C 67.71, H 5.68, N 6.58; found: C 67.35, H 5.67, N 6.30.

3: Under nitrogen, dmeda (0.141 mL, 0.117 g, 1.33 mmol) was added to a solution of **1** (0.500 g, 0.403 mmol) in THF (40 mL). This solution was stirred at room temperature for 4 h, after which all volatile materials were removed in vacuo. The remaining solid was placed on a frit and washed with diethyl ether (3 × 5 mL) to afford the desired compound after drying under reduced pressure (0.440 g, 85% yield based on **1**). ^1H NMR (300 MHz, [D$_8$]THF, 25 °C, TMS): $\delta = -9.16$ (br s, 2H; NH), −3.82 (br s, 2H; N−CH_2), −3.59 (br s, 2H; N−CH_2), 0.366 (s, 6H; N−CH_3), −1.69 (d, 2H), 3.04 (t, 2H), 5.56 (t, 2H), 7.65 (d, 2H), 13.76 (br s, 2H), 40.56 ppm (br s, 2H); $^{13}C\{^1H\}$ NMR (75 MHz, [D$_8$]THF): $\delta = 33.2$ (N−CH_3), 43.8 (N−CH_2), 85.99, 116.43, 116.86, 122.07, 122.58, 128.64, 130.49, 132.39, 134.54, 180.40 ppm; IR (KBr): $\tilde{\nu} = 3342$, 3299, 3043, 2985, 2952, 2875, 2856, 2803, 1612, 1589, 1554, 1501, 1463, 1423, 1342, 1283, 1248, 1175, 1138, 1096, 1069, 995, 959, 935, 898, 821, 746, 665, 642, 591, 574 cm^{-1}; elemental analysis: calcd (%) for $C_{72}H_{72}Li_3O_6N_6Eu{\cdot}THF$ (1362.27 $g\,mol^{-1}$): C 67.01, H 5.92, N 6.17; found: C 67.26, H 6.35, N 5.99.

8: Complex **2** (30 mg) was added to a vial and dissolved in pyridine (1.0 mL). This vial was then placed within a 20-mL screw-capped vial that was half-filled with dry pentane. After several days, pale crystals suitable for an X-ray diffraction study were formed. ^1H NMR (500 MHz, [D$_8$]THF, 25 °C, TMS): $\delta = 6.79$ (m, 4H), 6.89 (m, 2H), 6.98 (d, J(H,H) = 8.7 Hz, 2H), 7.22 (m, 7H), 7.58 (d, J(H,H) = 8.8 Hz, 2H), 7.60 (d, J(H,H) = 8.0 Hz, 2H), 7.65 (m, 3H), 8.52 ppm (m, 7H); $^{13}C\{^1H\}$ NMR (125 MHz, [D$_8$]THF): $\delta = 119.1$, 120.4, 124.4, 124.8, 126.8, 126.9, 128.1, 128.4, 128.5, 136.4, 136.7, 150.9, 163.5 ppm; elemental analysis: calcd (%) for $C_{95}H_{71}Li_3O_6N_7La$ (1566.35 $g\,mol^{-1}$): C 72.85, H 4.57, N 6.26; found: C 72.98, H 4.78, N 6.12.

Received: December 1, 2005
Published online: March 17, 2006

Keywords: asymmetric catalysis · lanthanides · Lewis acids · paramagnetic compounds · reaction mechanisms

[1] H. Sasai, T. Suzuki, N. Itoh, K. Tanaka, T. Date, K. Okamura, M. Shibasaki, *J. Am. Chem. Soc.* **1993**, *115*, 10372.
[2] M. Shibasaki, M. Kanai, K. Funabashi, *Chem. Commun.* **2002**, 1989.
[3] M. Shibasaki, N. Yoshikawa, *Chem. Rev.* **2002**, *102*, 2187.
[4] N. Yamagiwa, S. Matsunaga, M. Shibasaki, *J. Am. Chem. Soc.* **2003**, *125*, 16178.
[5] H. C. Aspinall, J. F. Bickley, J. L. M. Dwyer, N. Greeves, R. V. Kelly, A. Steiner, *Organometallics* **2000**, *19*, 5416.
[6] L. Di Bari, M. Lelli, G. Pintacuda, G. Pescitelli, F. Marchetti, P. Salvadori, *J. Am. Chem. Soc.* **2003**, *125*, 5549.
[7] E. Takaoka, N. Yoshikawa, Y. M. A. Yamada, H. Sasai, M. Shibasaki, *Heterocycles* **1997**, *46*, 157.
[8] H. Sasai, T. Arai, Y. Satow, K. N. Houk, M. Shibasaki, *J. Am. Chem. Soc.* **1995**, *117*, 6194.
[9] H. C. Aspinall, *Chem. Rev.* **2002**, *102*, 1807.
[10] A. F. Cockerill, G. L. O. Davies, R. C. Harden, D. M. Rackham, *Chem. Rev.* **1973**, *73*, 553.
[11] Y. M. A. Yamada, N. Yoshikawa, H. Sasai, M. Shibasaki, *Angew. Chem.* **1997**, *109*, 1942; *Angew. Chem. Int. Ed. Engl.* **1997**, *36*, 1871.
[12] W. D. Horrocks, J. P. Sipe, *J. Am. Chem. Soc.* **1971**, *93*, 6800.
[13] H. Sasai, M. Bougauchi, T. Arai, M. Shibasaki, *Tetrahedron Lett.* **1997**, *38*, 2717.
[14] T. Arai, Y. M. A. Yamada, N. Yamamoto, H. Sasai, M. Shibasaki, *Chem. Eur. J.* **1996**, *2*, 1368.
[15] T. Morita, T. Arai, H. Sasai, M. Shibasaki, *Tetrahedron: Asymmetry* **1998**, *9*, 1445.
[16] Crystal data for **7**: $C_{80}H_{76}O_{11}LaLi_3$, $M_r = 1373.18$; monoclinic, space group $P21$, $a = 18.532(4)$, $b = 11.479(3)$, $c = 19.262(5)$ Å, $\beta = 101.379(2)^\circ$, $V = 4017(2)$ Å^3, $Z = 2$, $\rho_{calcd} = 1.135\,g\,cm^{-3}$, μ ($Mo_{K\alpha}$) = 5.84 cm^{-1}, $F_{000} = 1420$, 2θ range = 5.24–54.94°, crystal size = 0.25 × 0.12 × 0.05 mm^3, $T = 143$ K; 28983 reflections measured with 14622 used in refinement; $R_1 = 0.0585$, $wR_2 = 0.1237$ (11601 reflections with $F > 4\sigma(F)$); $R_1 = 0.0767$, $wR_2 = 0.1357$, GoF = 1.035 (14622 unique, nonzero reflections and 857 variables).
[17] Crystal data for **6**: $C_{80}H_{76}O_{11}EuLi_3$, $M_r = 1386.24$; monoclinic, space group $P21$, $a = 18.2048(6)$, $b = 11.4818(4)$, $c = 18.9389(7)$ Å, $\beta = 100.190(1)$(, V=3896.2(2) Å^3, $Z = 2$, $\rho_{calcd} = 1.182\,g\,cm^{-3}$, μ ($Mo_{K\alpha}$) = 8.59 cm^{-1}, $F_{000} = 1432$, 2θ range = 5.28–55.12°, crystal size = 0.38 × 0.27 × 0.08 mm^3, $T = 143$ K; 28807 reflections measured with 28807 used in refinement; $R_1 = 0.0518$, $wR_2 = 0.1584$ (28033 reflections with $F > 4\sigma(F)$); $R_1 = 0.0536$, $wR_2 = 0.1608$, GoF = 1.151 (28807 unique, nonzero reflections and 858 variables).
[18] Crystal data for **8**: $C_{100}H_{76}O_6N_8LaLi_3$, $M_r = 1645.45$; monoclinic, space group $P21$, $a = 13.3600(8)$, $b = 13.5347(8)$, $c = 23.066(2)$ Å, $\beta = 101.9270(10)^\circ$, $V = 4080.9(4)$ Å^3, $Z = 2$, $\rho_{calcd} = 1.316\,g\,cm^{-3}$, μ ($Mo_{K\alpha}$) = 5.84 cm^{-1}, $F_{000} = 1664$, 2θ range = 5.22–54.96°, crystal size = 0.42 × 0.40 × 0.22 mm^3, $T = 143$ K; 23262 reflections measured with 13727 used in refinement; $R_1 = 0.0308$, $wR_2 = 0.0742$ (13052 reflections with $F > 4\sigma(F)$); $R_1 = 0.0334$, $wR_2 = 0.0768$, GoF = 1.082 (13727 unique, nonzero reflections and 1064 variables). CCDC-284685, -284686, and -284687 (**7, 8, 6**, respectively) contain the supplementary crystallographic data for this paper. These data can be obtained free of charge from The Cambridge Crystallographic Data Centre via www.ccdc.cam.ac.uk/data_request/cif.
[19] T. Kowall, F. Foglia, L. Helm, A. E. Merbach, *J. Am. Chem. Soc.* **1995**, *117*, 3790.
[20] N. Yoshikawa, Y. M. A. Yamada, J. Das, H. Sasai, M. Shibasaki, *J. Am. Chem. Soc.* **1999**, *121*, 4168.
[21] N. Yoshikawa, T. Suzuki, M. Shibasaki, *J. Org. Chem.* **2002**, *67*, 2556.
[22] N. Yamagiwa, J. Tian, S. Matsunaga, M. Shibasaki, *J. Am. Chem. Soc.* **2005**, *127*, 3413.

 © 2006 Wiley-VCH Verlag GmbH & Co. KGaA, Weinheim

Supramolecular Chemistry

DOI: 10.1002/anie.200504312

Polymer-Induced Heteronucleation for the Discovery of New Extended Solids**

*Adam L. Grzesiak, Fernando J. Uribe, Nathan W. Ockwig, Omar M. Yaghi, and Adam J. Matzger**

The assembly of components from solution into the solid state can be accomplished in numerous manners, and each of these pathways can give rise to unique materials. The effects of the assembly pathway can be relatively subtle, as in the crystallization of pharmaceuticals into polymorphic crystals,[1] or more dramatic, involving changes in strong bonding, as is often encountered in the preparation of extended solids.[2] In general, there is no explicit connection between the growth conditions and the structure of the resultant phase. Indeed, spectacular changes in structure can arise from subtle differences in experimental conditions. Recently, we have introduced the use of heterogeneous nucleation from insoluble polymers as a powerful technique for efficiently discovering and selecting among different polymorphic forms of pharmaceuticals.[3] It is proposed that the polymer serves to direct the formation of one phase over others at the time of nucleation by selectively stabilizing one mode of aggregation under conditions (solvent, temperature, extent of supersaturation, etc.) that are otherwise identical. We sought to examine the applicability of this technique towards the emergent area of metal–organic frameworks (MOFs), where it is highly desirable to establish a relationship between the crystallization conditions and the outcome of the MOF synthesis. Herein, we show that polymer substrates of varying functionality can be successfully employed to access MOF structures that otherwise are not obtainable.

We chose, as initial objects of study, MOF-2 and MOF-5 (Figure 1), two of the early reported MOFs based on the well-studied system of 1,4-benzenedicarboxylate (BDC) and Zn^{2+} ions. Either paddle-wheel (MOF-2) or basic zinc acetate (MOF-5) secondary building units (SBUs) are interconnected to produce square-grid or primitive-cubic framework structures, respectively.[2d,e] It was anticipated that, in analogy to the phase selection obtained for polymorphic pharmaceuticals,[3] selection between these two extended solids might be achieved under a single set of conditions by changing only the identity of a polymer heteronucleant present during network formation.

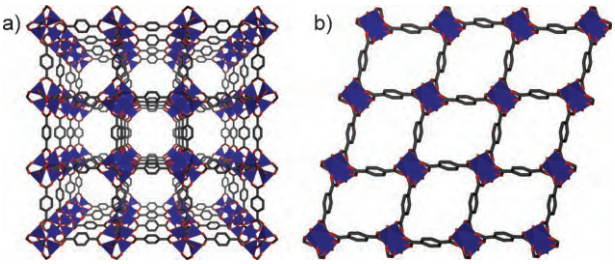

Figure 1. Packing diagrams of a) MOF-5 and b) MOF-2, which are derived from identical synthetic components, but have different crystal structures. Dark blue polyhedra represent the coordination environments of the Zn atoms; C gray, O red.

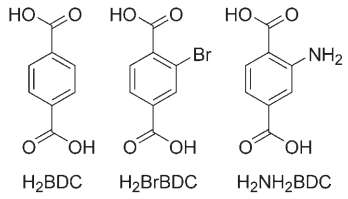

In initial experiments, the composition of the polymer substrate onto which crystallization occurs was varied to study MOF phase selection in the presence of acidic or basic functional groups. Such substrates could interact with the reactants, by hydrogen bonding to the MOF linkers or by direct coordination to the metal, to initiate crystal growth. The monomers methacrylic acid (MAA) and 4-vinylpyridine (4VP) were each individually cross-linked with divinylbenzene (DVB) in various ratios (see Experimental Section) to create insoluble copolymers with discrete percentages of acidic or basic functionality. This approach allows systematic exploration of the effect of substrate composition. Reagents dissolved in *N*,*N*-diethylformamide (DEF) were loaded into the wells of a microtiter plate, each of which contained a polymer of discrete composition that is completely insoluble, owing to extensive cross-linking. Utilizing cross-linked polymers assures a heteronucleation process and also facilitates high-throughput screening by optical microscopy. Secondary screening carried out by vibrational spectroscopy and powder X-ray diffraction (PXRD) provides unambiguous phase characterization.

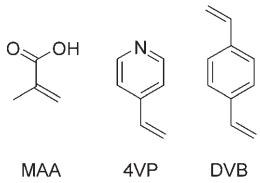

To explore phase selection between MOF-2 and MOF-5, crystallization experiments were conducted with solvent and concentration conditions which were optimized for the syn-

[*] A. L. Grzesiak, F. J. Uribe, N. W. Ockwig, Prof. O. M. Yaghi, Prof. A. J. Matzger
Department of Chemistry
University of Michigan
Ann Arbor, MI 48109-1055 (USA)
Fax: (+1) 734-615-8853
E-mail: matzger@umich.edu

[**] This work was supported by the U.S. Department of Energy and the Beckman Foundation. A.L.G. was a fellow of the NSF-sponsored IGERT program for Molecularly Designed Electronic, Photonic, and Nanostructured Materials at the University of Michigan.

Supporting information for this article is available on the WWW under http://www.angewandte.org or from the author.

© 2006 Wiley-VCH Verlag GmbH & Co. KGaA, Weinheim

thesis of MOF-5 (see Experimental Section). Under these conditions, but with the addition of insoluble copolymers of MAA/DVB, both MOF-5 and an additional phase, identified as distinct from MOF-2, were formed. The new phase, designated PNMOF-1 (PNMOF = polymer-nucleated metal–organic framework), has a plate-like morphology and was observed in the presence of MAA/DVB copolymers with less than 30% MAA.[4] This phase is readily distinguished from MOF-5 by its characteristic morphology, Raman spectrum, and PXRD pattern (see Supporting Information). Its structure was determined by single-crystal X-ray diffraction, and a formula of $Zn_3(BDC)_3(DEF)_2$ was found for the framework.[5] The structure of PNMOF-1 is composed of trinuclear zinc carboxylate clusters joined through linear BDC linkers (Figure 2a). The clusters consist of a single octahedrally coordinated zinc center surrounded by two peripheral tetrahedrally coordinated zinc centers. One peripheral zinc center is bound to the central zinc atom through three bridging carboxylate groups. The other peripheral zinc center is bound to the central zinc atom through two bridging carboxylate groups and a single μ_2-bridging carboxylate oxygen atom. Finally, the tetrahedral coordination sphere of the peripheral zinc centers is completed by the coordination of DEF oxygen atoms. Each of these clusters is joined to six adjacent clusters through the linear BDC linkers to yield an overall 2D triangular-grid structure containing cavities large enough to include additional solvent molecules.

PNMOF-1 was also found in the majority of crystallizations employing polymers containing 5–25% of base-functionalized 4VP cross-linked with DVB. This observation and the appearance of the PNMOF-1 phase with lower percentages of acid-functionalized MAA in the MAA/DVB polymers indicate that more nonpolar surfaces, rather than acidic or basic functionalities, facilitate the formation of PNMOF-1. To confirm this hypothesis, crystals were grown in polypropylene vessels, and PNMOF-1 was observed as the major product (see Supporting Information).

One of the outstanding features of MOFs, particularly in the isoreticular MOF (IRMOF) series, of which MOF-5 is the parent member, is the possibility of tuning their properties by altering the functionality and size of the linker.[6] Therefore, with the aim of producing additional networks with the same topology as PNMOF-1, a bromine-substituted 1,4-benzenedicarboxylic acid (H_2BrBDC) was employed as the linking component in the MOF synthesis. In the absence of added polymers, the crystalline product is the cubic IRMOF-2,[6] which is topologically identical to MOF-5. However, when the synthesis is conducted in the presence of cross-linked polymers, an additional morphologically distinct MOF phase is formed. This new phase, termed PNMOF-2, has a plate-like morphology, as well as a unique Raman spectrum and PXRD pattern (see Supporting Information). Crystals of PNMOF-2 were routinely observed in the presence of polymers containing up to 20% MAA or 30% 4VP cross-linked with DVB. The structure of PNMOF-2, as determined by single-crystal X-ray diffraction,[5] is monoclinic and, surprisingly, has a different topology than PNMOF-1 (Figure 2b). The framework of PNMOF-2 has a formula of $(Zn_3O)(BrBDC)_2(H_2BrBDC)(DEF)_4$, and is built from zinc-oxo clusters consisting of one tetrahedrally and two octahedrally coordinated zinc centers. The three zinc centers are bridged by the carboxylate groups of four BrBDC linkers, which extend the structure in three dimensions. The remaining zinc coordination sites are occupied by four oxygen atoms of terminal DEF molecules, one carbonyl oxygen atom of a linking diacid, and one μ_3-bridging oxide anion. As in the case of PNMOF-1, PNMOF-2 grows in larger quantities from relatively more nonpolar surfaces. A common theme in these structures is the presence of DEF solvent molecules bound to zinc atoms, which perhaps favors nucleation from relatively nonpolar surfaces.

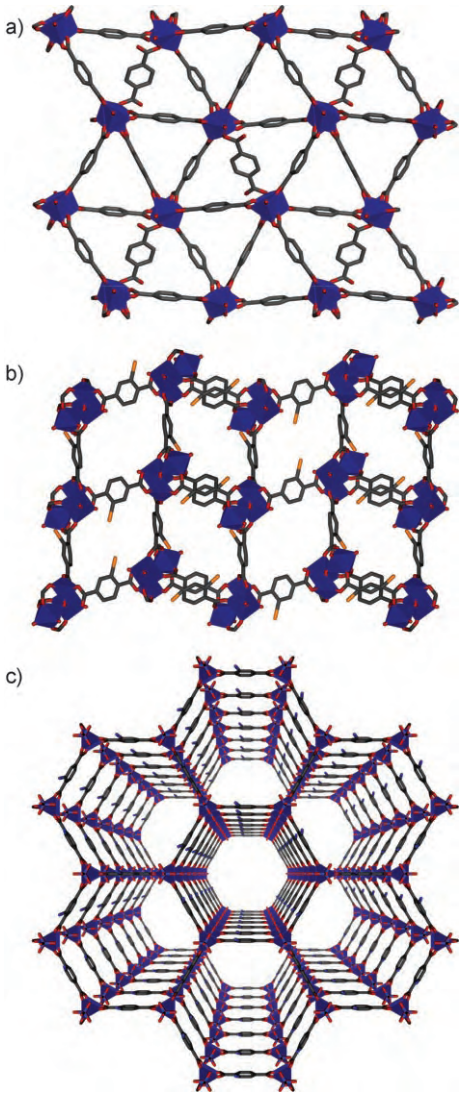

Figure 2. Crystal structures of a) PNMOF-1 ($Zn_3(BDC)_3(DEF)_2$), b) PNMOF-2 ($(Zn_3O)(BrBDC)_2(H_2BrBDC)(DEF)_4$), and c) PNMOF-3 ($Zn_4(NH_2BDC)_3(NO_3)_2(H_2O)_2$). Solvent molecules and hydrogen atoms are omitted for clarity, and disordered atoms are shown in their highest-occupancy positions. Dark blue polyhedra represent the coordination environments of the Zn atoms; C gray, O red, N light blue, Br yellow.

To further explore the generality of the polymer-induced heteronucleation approach to the discovery of new MOF phases, an amine-substituted dicarboxylic acid (H_2NH_2BDC) was employed as a component in the MOF synthesis. This

 © 2006 Wiley-VCH Verlag GmbH & Co. KGaA, Weinheim

relatively more polar linking unit is found in IRMOF-3,[6] a network isostructural to MOF-5. Crystallization from conditions identical to those employed above, with the exception of a higher temperature, results in the cubic phase IRMOF-3. However, the new phase PNMOF-3 is additionally observed in crystallizations containing cross-linked MAA/DVB copolymers, but is not observed when 4VP/DVB copolymers or polydivinylbenzene are utilized. PNMOF-3 is readily recognized because its crystals express hexagonal faces and are distinct from the crystals of the cubic IRMOF-3 phase. The crystal structure of PNMOF-3 reveals a framework of composition $Zn_4(NH_2BDC)_3(NO_3)_2(H_2O)_2$ (Figure 2c).[5] The structure is composed of trigonal clusters, in which two zinc atoms are bridged by the carboxylate functionalities of three NH_2BDC linkers. The remaining coordination site of each zinc atom is occupied by either a nitrate anion or a water molecule (statistically disordered) to maintain the charge neutrality of the structure. The clusters are assembled through linear NH_2BDC linkers to generate hexagonal-grid layers that are arranged in registry, yielding unusually large infinite channels of 14.9 Å diameter,[7] which are orthonormal to the layer and are occupied by crystallographically unresolved solvent molecules (see Experimental Section).

The production of PNMOF-3, in contrast to the cases of PNMOF-1 and PNMOF-2, requires the presence of MAA in the polymer heteronucleant, which demonstrates the importance of acid functionality in the selection of this framework. An increase in the yield of PNMOF-3 to approximately 75% of the product was achieved by utilizing MAA/DVB copolymers composed of 20% MAA. This success demonstrates that suitable conditions for phase production can be found on the basis of initial combinatorial discovery experiments. Notably, in contrast to the two other new MOF phases described herein, the framework of PNMOF-3 is charged, which demonstrates that a variety of extended network types may be produced by utilizing the polymer-induced heteronucleation method.

In summary, the discovery of extended solid phases using insoluble polymer substrates has been illustrated for MOFs. In these studies, conditions that yielded isostructural phases in the absence of added polymers were used. Polymer-induced heteronucleation is a simple way to increase the diversity of conditions during the crystallization of extended networks. Furthermore, the formation of a particular phase is dependent upon the polymer composition, which allows optimized production of new phases by altering polymer polarity and functionality. Studies are ongoing to identify suitable procedures for producing larger quantities of these new MOFs to thoroughly establish their properties for gas storage and catalysis applications.

Experimental Section

Polymer synthesis: MAA and 4VP were individually copolymerized with the cross-linker DVB to create copolymers with 5, 10, 15, 20, 25, 30, 40, 50, 60, and 70% (by volume) acidic (MAA) or basic (4VP) monomer. All samples were irradiated with an array of four 15-watt UVA lamps for 3 h using 1 mol% 2,2'-azobisisobutyronitrile (AIBN) as an initiator. Following irradiation, the polymers were annealed at 85°C in a vacuum oven (< 1 Torr) for 4 h to remove residual monomer, short oligomers, and solvent molecules.

MOF synthesis: MOFs were produced by heating approximately 125 μL of a DEF solution containing a dicarboxylic acid (26.7 mM) and $Zn(NO_3)_2{\cdot}4H_2O$ (80.0 mM) to 85 (PNMOF-1) or 100°C (PNMOF-2 and 3) for 1 day, in the presence of cross-linked copolymers, or as controls, polydivinylbenzene or polypropylene. The microtiter plates were sealed with polyethylene plugs and pressed firmly between aluminum plates to prevent solvent loss upon heating. Each experiment was repeated 8 times within each trial, and at least 2 trials were carried out to gauge reproducibility. Only consistently reproduced results are reported. The same reactions lead exclusively to MOF-5, IRMOF-2, or IRMOF-3 when performed with the appropriate linker in glass vials without the addition of a polymer, under otherwise identical conditions.

X-ray diffraction: PXRD was performed on a Bruker AXS D8 DISCOVER GADDS diffractometer (for combinatorial screening) equipped with a $Cu_{K\alpha}$ source ($\lambda = 1.5406$ Å) and an area detector. Single-crystal X-ray diffraction was performed on a Bruker SMART CCD-based diffractometer with a $Mo_{K\alpha}$ source ($\lambda = 0.71073$ Å). Intensity data were integrated with the SAINT software package and corrected for absorption by using SADABS. The structure was then solved by direct methods and refined by using the SHELXTL (v6.10) software package. All non-hydrogen atoms, with the exception of those of free solvent molecules and severely disordered bound solvent molecules, were refined anisotropically. For PNMOF-1 and 2, hydrogen atoms were generated at idealized positions and refined as riding atoms. For all three structures, the contribution of free solvent molecules was calculated through the use of the SQUEEZE subroutine of the PLATON software suite.[8]

Received: December 4, 2005
Published online: March 14, 2006

Keywords: crystal growth · metal–organic frameworks · microporous materials · polymers · supramolecular chemistry

[1] a) H. G. Brittain, *Polymorphism in Pharmaceutical Solids*, Marcel Dekker, New York, **1999**; b) B. Rodríguez-Spong, C. P. Price, A. Jayasankar, A. J. Matzger, N. Rodríguez-Hornedo, *Adv. Drug Delivery Rev.* **2004**, *56*, 241 – 274.

[2] a) D. T. Vodak, K. Kim, L. Iordanidis, P. G. Rasmussen, A. J. Matzger, O. M. Yaghi, *Chem. Eur. J.* **2003**, *9*, 4197 – 4201; b) R. Kitaura, K. Seki, G. Akiyama, S. Kitagawa, *Angew. Chem.* **2003**, *115*, 444 – 447; *Angew. Chem. Int. Ed.* **2003**, *42*, 428 – 431; c) S. Kitagawa, R. Kitaura, S. Noro, *Angew. Chem.* **2004**, *116*, 2388 – 2430; *Angew. Chem. Int. Ed.* **2004**, *43*, 2334 – 2375; d) H. Li, M. Eddaoudi, T. L. Groy, O. M. Yaghi, *J. Am. Chem. Soc.* **1998**, *120*, 8571 – 8572; e) H. Li, M. Eddaoudi, M. O'Keeffe, O. M. Yaghi, *Nature* **1999**, *402*, 276 – 279; f) N. L. Rosi, J. Kim, M. Eddaoudi, B. L. Chen, M. O'Keeffe, O. M. Yaghi, *J. Am. Chem. Soc.* **2005**, *127*, 1504 – 1518.

[3] a) M. Lang, A. L. Grzesiak, A. J. Matzger, *J. Am. Chem. Soc.* **2002**, *124*, 14834 – 14835; b) C. P. Price, A. L. Grzesiak, A. J. Matzger, *J. Am. Chem. Soc.* **2005**, *127*, 5512 – 5517.

[4] In this context, it is interesting to note that recently the growth of MOF-5 from self-assembled monolayers of 16-mercaptohexadecancoic acid on gold has been reported. S. Hermes, F. Schröder, R. Chelmowski, C. Wöll, R. A. Fischer, *J. Am. Chem. Soc.* **2005**, *127*, 13744 – 13745.

[5] Crystal data: a) PNMOF-1 ($Zn_3(BDC)_3(DEF)_2$): colorless plate, $0.22 \times 0.11 \times 0.06$ mm^3, 153(2) K, monoclinic, space group $C2/c$ (no. 15), $a = 25.032(5)$, $b = 20.812(4)$, $c = 17.738(3)$ Å, $\beta = 114.396(3)°$, $V = 8416(3)$ Å^3, $Z = 8$, $\rho_{calcd} = 1.404$ g cm^{-3}, $\mu(Mo_{K\alpha}) = 1.757$ mm^{-1}, $F(000) = 3624$, 9740 unique reflections, $2.64 \le 2\theta \le 57.06°$, $T_{max} = 0.90$, $T_{min} = 0.70$, $R_1 = 0.0566$, $R_w =$

 © 2006 Wiley-VCH Verlag GmbH & Co. KGaA, Weinheim

0.1197; b) PNMOF-2 ($(Zn_3O)(BrBDC)_2(H_2BrBDC)(DEF)_4$): colorless block, $0.22\times0.18\times0.13\ mm^3$, 153(2) K, monoclinic, space group $C2/c$ (no. 15), $a=43.028(13)$, $b=13.000(4)$, $c=22.077(7)$ Å, $\beta=114.964(6)°$, $V=11195(6)$ Å^3, $Z=8$, $\rho_{calcd}=1.410\ g\,cm^{-1}$, $\mu(Mo_{K\alpha})=3.118\ mm^{-1}$, $F(000)=4588$, 11414 unique reflections, $2.08\le2\theta\le52.74°$, $T_{max}=0.67$, $T_{min}=0.53$, $R_1=0.1411$, $R_w=0.3913$; c) PNMOF-3 ($Zn_4(NH_2BDC)_3(NO_3)_2(H_2O)_2$): orange plate, $0.43\times0.17\times0.14\ mm^3$, 258(2) K, hexagonal, space group $P6/mmm$ (no. 191), $a=18.3385(7)$, $c=14.2657(10)$ Å, $V=4154.8(4)$ Å^3, $Z=4$, $\rho_{calcd}=0.376\ g\,cm^{-3}$, $\mu(Mo_{K\alpha})=0.589\ mm^{-1}$, $F(000)=459$, 1914 unique reflections, $3.84\le2\theta\le55.18°$, $T_{max}=0.92$, $T_{min}=0.79$, $R_1=0.0959$, $R_w=0.2686$. CCDC-286534 (PNMOF-1), CCDC-286535 (PNMOF-2), and CCDC-286536 (PNMOF-3) contain the supplementary crystallographic data for this paper. These data can be obtained free of charge from The Cambridge Crystallographic Data Centre via www.ccdc.cam.ac.uk/data_request/cif.

[6] M. Eddaoudi, J. Kim, N. Rosi, D. Vodak, J. Wachter, M. O'Keefe, O. M. Yaghi, *Science* **2002**, *295*, 469 – 472.

[7] This value is the distance across the channel from aromatic carbon to aromatic carbon (18.3 Å) minus two carbon van der Waals radii (each 1.70 Å). A. Bondi, *J. Phys. Chem.* **1964**, *68*, 441 – 451.

[8] A. L. Spek, *Acta Crystallogr. Sect. A* **1990**, *46*, C34.

 © 2006 Wiley-VCH Verlag GmbH & Co. KGaA, Weinheim

Microreactors

DOI: 10.1002/anie.200503540

Electric Control of Droplets in Microfluidic Devices**

Darren R. Link, Erwan Grasland-Mongrain, Agnes Duri, Flavie Sarrazin, Zhengdong Cheng, Galder Cristobal, Manuel Marquez, and David A. Weitz*

The precision manipulation of streams of fluids with microfluidic devices is revolutionizing many fluid-based technologies and enabling the development of high-throughput reactors that use minute quantities of reagents. However, as the scale of these reactors shrinks, contamination effects due to surface adsorption and diffusion limit the smallest quantities that can be used. The confinement of reagents in droplets in an immiscible carrier fluid overcomes these limitations, but demands new fluid-handling technology. We present a platform technology based on charged droplets and electric fields that enables electrically addressable droplet generation, highly efficient droplet coalescence, precision droplet breaking and recharging, and controllable droplet sorting. This is an essential enabling technology for a high-throughput droplet microfluidic reactor.

Networks of small channels are a flexible platform for the precision manipulation of small amounts of fluids.[1,2] The utility of such microfluidic devices depends critically on enabling technologies such as the microfluidic peristaltic pump,[3] electrokinetic pumping,[4,5] and dielectrophoretic-pump or electrowetting-driven[6] flow; these technologies can form the essential building blocks for the assembly of fluid-handling modules.[7] These modules can be used to perform a variety of key tasks including the measurement of precise aliquots of fluids, the combination of fluid streams, and the mixing of multiple fluid components. The assembly of such modules into complete systems provides a convenient and robust way to construct microfluidic devices. These have myriad uses; for example, high-throughput screening,[8] the exploration of chemical phase diagrams, assays of biological molecules,[9–11] single-cell analysis,[12–17] and combinatorial approaches to protein crystallization[18] can all be performed with only minimal consumption of reagents. However, virtually all microfluidic devices are based on flows of streams of fluids; this sets a limit on the smallest volume of reagent that can be used effectively because of the contaminating effects of diffusion and surface adsorption. As the dimensions of small volumes are decreased, diffusion becomes the dominant mechanism for mixing leading to dispersion of reactants. Moreover, surface adsorption of reactants, although small, can be highly detrimental at low concentrations and small volumes. As a result current microfluidic technologies cannot be reliably used for applications involving minute quantities of reagent—for example, bioassays at levels down to the single molecule are not easily performed. An approach that overcomes these limitations is the use of aqueous droplets in an immiscible carrier fluid;[19] these droplets provide a well-defined, encapsulated microenvironment that eliminates cross-contamination or changes in concentration caused by diffusion or surface interactions. Droplets provide the ideal microcapsule that can isolate reactive materials, cells, or small particles for further manipulation and study. Moreover, by making droplets as small as one femtoliter, reactions of single biomolecules can be investigated. However, essentially all enabling technology for microfluidic systems developed thus far has focused on single-phase fluid flow, and there are few corresponding, active means to manipulate droplets. In particular, manipulating, mixing, and combining reagents in microfluidic geometries is much more difficult for droplets than for single streams,[19,20] especially when the droplets are stabilized with

[*] Dr. D. R. Link, E. Grasland-Mongrain, A. Duri, F. Sarrazin, Prof. Z. Cheng, G. Cristobal, Prof. D. A. Weitz
Department of Physics and DEAS
Harvard University
Cambridge, MA 02138 (USA)
Fax: (+1) 203-458-2514
E-mail: dlink@raindancetechnologies.com
M. Marquez
Los Alamos National Laboratory
Chemistry Division
Los Alamos, NM 87545 (USA)
M. Marquez
INEST Group
Philip Morris USA Research Center
Richmond, VA 23234 (USA)

[**] This work was supported by Kraft Foods, Rhodia Corporation, and the NSF through the Harvard MRSEC (DMR-0213805 and DMR-0243715). The authors thank H. A. Stone and M. P. Brenner for valuable discussions.

Supporting information for this article is available on the WWW under http://www.angewandte.org or from the author.

InterScience
© 2006 Wiley-VCH Verlag GmbH & Co. KGaA, Weinheim

surfactant, as they must be for more-complex processing. This difficulty has precluded the widespread use of droplet technology as robust microreactors in microfluidic devices.

Herein we present a generic and robust platform technology for manipulating and controlling individual droplets in microfluidic devices. By combining electrostatic charge on the droplets and electric fields on the devices, we develop modules that create, recombine, split, and sort droplets one by one, thus providing fine control over individual microreactors while retaining high purity and enabling very high throughput. By incorporating the forces that result from charging the aqueous fluid in an electric field E, we can produce smaller droplets with more precise control of their individual timing than is feasible with other strategies that rely solely on viscous forces to overcome surface tension;[21–25] this provides a robust droplet-generation module that allows us to produce microreactors with volumes as small as femtoliters, while using orifices whose dimensions are significantly larger than the one-micron-diameter droplet size, thereby reducing potential clogging problems. By incorporating charges of opposite sign on different droplets we can merge droplets controllably and reliably, thus overcoming the stabilizing forces caused by surface tension and lubrication; this provides a robust droplet-coalescence module that allows us to mix precise aliquots of reactants. By incorporating the extensional force induced by an electric field we can controllably split large droplets into smaller aliquots for further analysis and simultaneously recharge neutral drops for further processing; this provides a robust splitting or charging module that allows us to perform multiple assays on the same materials. By incorporating the forces produced by electric fields on charged droplets we can steer individual droplets into selected channels; this provides a robust droplet-sorting module that allows us to select desired reaction products. These modules are the essential tools for high-speed manipulation and control of individual droplets and can serve as the enabling technology for droplet-based microfluidic devices. Moreover, because all control is carried out by switching electric fields, there are no moving parts and frequencies as high as 10^5 Hz are feasible; this facilitates very high throughput combinatorial technology.

We use soft lithography to pattern channels in polydimethylsiloxane (PDMS), a transparent polymer material.[26] A glass slide forms the top of the channel. We incorporate electric fields by patterning indium tin oxide (ITO) electrodes on the surface of the glass slide adjacent to the channels and seal the slide to the PDMS by using oxygen plasma. Devices fabricated in PDMS have the advantage of being strongly hydrophobic, which ensures that the oil carrier phase wets their surfaces and that the water droplets do not contact the channel walls, which facilitates the isolation of biomolecules and eliminates cross-contamination caused by surface interactions.

We use a flow-focusing geometry to form the drops. A water stream is infused from one channel through a narrow constriction; oil streams hydrodynamically focus the water stream and reduce its size as it passes through the constriction (Figure 1 A). This droplet generator can be operated in a flow regime that produces a steady stream of uniform droplets of water in oil. The size of the water droplets is controlled by the relative flow rates of the oil and the water; the viscous forces overcome surface tension to create uniform droplets. If the flow rate of the water is too high, a longer jet of fluid passes through the orifice and breaks up into droplets further downstream; these droplets are less uniform in size. If the flow rate of the water is too low, the droplet breakup in the orifice becomes irregular again, which produces a wider range of droplet sizes. Although this emulsification technology is robust, it is limited to producing droplets of one size at any given flow rate; this droplet size is largely determined by the channel dimensions. Moreover, the timing of the droplet production cannot be controlled.

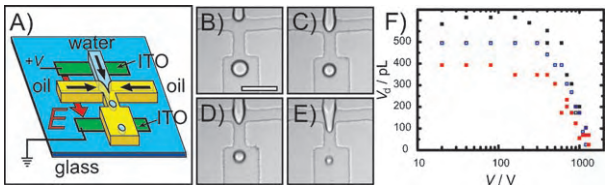

Figure 1. Charged-droplet generation. A) Oil and water streams converge at a 30-micron orifice. A voltage V applied to indium tin oxide (ITO) electrodes on the glass produces an electric field E, which capacitively charges the water–oil interface. The drop size is independent of charge at low field strengths but decreases at higher field strengths, as shown in the photomicrographs (scale bar: 100 μm): B) $V=0$ V, C) $V=400$ V, D) $V=600$ V, E) $V=800$ V. F) Droplet size as a function of voltage showing the crossover between flow-dominated and field-dominated droplet snap-off for three different flow rates of the continuous phase oil ($Q_c=80$ nL s^{-1} black; 110 nL s^{-1} blue; and 140 nL s^{-1} red). The infusion rate of the water is constant ($Q_d=20$ nL s^{-1}).

We overcome these limitations by incorporating electric fields to create an electrically addressable emulsification system. To achieve this, we apply high voltage to the aqueous stream and charge the oil–water interface, as shown schematically in Figure 1 A. The water stream behaves as a conductor whereas the oil is an insulator; electrochemical reactions charge the fluid interface like a capacitor. Upon droplet formation, the charge of the interface remains on the droplet. Furthermore, the droplet volume (V_d) and frequency (f) can be tailored over nearly three orders of magnitude without changing the infusion rate of the oil or the water. The size and frequency of the droplet are not independent; instead, their product is determined by the infusion rate of the dispersed phase $Q_d=fV_d$. The droplet size decreases with increasing field strength, as shown in Figure 1 B–E. The dependence of the droplet size on applied voltage for three different flow rates is summarized in Figure 1 F. The electric field has a negligible effect at low applied voltages, and droplet formation is driven exclusively by the competition between surface tension and viscous flow. By contrast, at high electric-field strengths, there is a significant additional force F on the growing drop given by $F=qE$ where q is the charge on the droplet. Since the droplet interface behaves as a capacitor, q is proportional to the applied voltage V. This leads to a V^2 dependence of F, which accounts for the decrease in droplet size with increasing applied field (Figure 1 F). If the electric field becomes too large, the charged interface of the water

 © 2006 Wiley-VCH Verlag GmbH & Co. KGaA, Weinheim

stream is repelled by the highly charged drops; this destabilizes the production and increases the variation in droplet size.

The electronic control afforded by the field-induced droplet formation provides an additional valuable benefit: it allows the phase of the droplet break-off to be adjusted within the production cycle. This is accomplished by increasing the field above the critical break-off field only at the instant the droplet is required. This provides a convenient means to synchronize precisely the production and arrival of individual droplets at specific locations.

An essential component in any droplet-based reaction-confinement system is a mixer that combines two or more reagents to initiate a chemical reaction. Multicomponent droplets can easily be generated by bringing together streams of materials at the point where droplets are made.[27] However, all but the simplest reactions require multiple steps in which new reagents are added during each step. This can be accomplished by merging a new stream of fluid with large droplets passing the orifice;[28] however, this technique precludes the use of stabilizing surfactants, which limits its applicability when multiple processing steps require highly stable droplets. Instead, mixing can be best accomplished in droplet-based microfluidic reactors by combining different droplets, each containing individual reactants. However, this combination of droplets is particularly difficult to achieve in a microfluidic device because surface tension, surfactant stabilization, and drainage forces all hinder droplet coalescence;[29] moreover, the droplets must cross the stream lines that define their respective flows and must be perfectly synchronized to arrive at a precise location for coalescence.

The use of electrostatic charge overcomes these difficulties; placing charges of opposite sign on each droplet and applying an electric field forces them to coalesce. As an example we show a device consisting of two separate nozzles that generate droplets with different compositions and opposite charges (Figure 2A). The droplets are brought together at the confluence of the two streams. The electrodes used to charge the droplets upon formation also provide the electric field to force the droplets across the stream lines, thus leading to coalesce. Slight variations in the structure of the two nozzles result in slight differences in the frequency and phase of the droplet generation in the absence of a field. Thus the droplets differ in size even though the infusion rates are identical. Moreover, the droplets do not arrive at the point of confluence at exactly the same time. As a result the droplets do not coalesce, as shown in Figure 2B. By contrast, upon application of an electric field, the droplet formation becomes exactly synchronized, which ensures that pairs of identically sized droplets each reach the point of confluence simultaneously. Moreover, the droplets are oppositely charged, which forces them to traverse the stream lines and contact each other, thereby causing them to coalesce, as shown in Figure 2C. The remarkable synchronization of the droplet formation results from coupling of the break-off of each of the pair of droplets as mediated by the electric field; the magnitude of the electric field varies as the separation between the leading edges of the two droplets changes and the frequency of droplet break-off is mode-locked to the

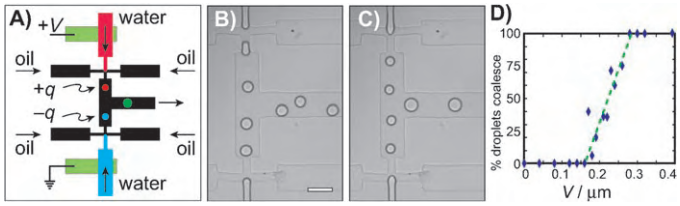

Figure 2. Coalescing drops. A) Drops having opposite sign of electrostatic charge can be generated by applying a voltage across the two aqueous streams. B) In the absence of an electric field the frequency and timing of drop formation at the two nozzles are independent and each nozzle produces a different-sized drop at a different frequency; the infusion rates are the same at both nozzles. After the confluence of the two streams, the drops from the upper and lower nozzles stay in their respective halves of the stream and, owing to the presence of surfactant, do not coalescence even in the case of large droplets that fill the width of the channel (scale bar: 100 µm). C) With an applied voltage of 200 V across the 500-micron separation of the nozzles, the drops simultaneously break off from the two nozzles and are identical; simultaneous drop formation can be achieved for unequal infusion rates of the aqueous streams even up to a factor of two difference in volumes. D) The fraction of the drops that encounter each other and coalesce increases linearly above a critical field when the surfactant sorbitol monooleate (3%) is present.

electric field. A minimum charge is required to cause droplets to coalesce, presumably because of the stabilizing effects of the surfactant coating; this is evident from Figure 2D, which shows the voltage dependence of the percentage of drops that contact each other that actually coalesce.

The use of oppositely charged droplets and an electric field to combine and mix reagents is an extremely robust method, and 100% of the droplets coalesce with their partner from the opposite stream. However, after they coalesce the resultant drops carry no electrostatic charge. Although it is convenient to charge droplets during formation, other methods must be employed in any robust droplet-based microfluidic system to recharge the mixed droplets if necessary for further processing. This is readily accomplished through the use of extensional flow to split neutral droplets in the presence of an electric field, which polarizes them and results in two oppositely charged daughter droplets (Figure 3A). The photomicrograph in Figure 3B shows neutral droplets entering a bifurcation and splitting into charged daughter droplets. The dashed region in Figure 3B is enlarged in Figure 3C to illustrate the asymmetric stretching of the charged droplets in the electric field. The vertical dashed lines indicate the edges of the electrodes, where the droplets return to their symmetric spherical shape. The electric field also allows precision control of the droplet splitting and provides the basis for a robust droplet-division module that allows the splitting of the contents into two or more aliquots of identical reagent, which could facilitate multiple assays on the contents of the same microreactor.

A final component essential for the construction of microfluidic droplet-reaction systems is a droplet sorter. The contents of individual droplets must be probed, and selected droplets sorted into discreet streams. Such sorting in microfluidic devices can be accomplished through the use of mechanical valves.[16] Droplets can be passively sorted by size,

 © 2006 Wiley-VCH Verlag GmbH & Co. KGaA, Weinheim

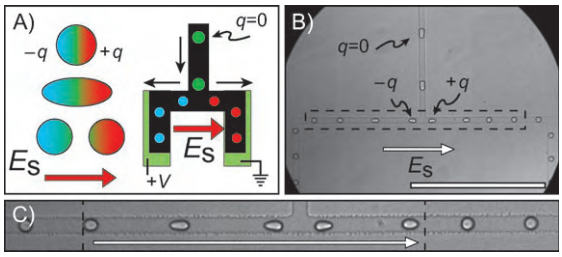

Figure 3. Recharging neutral drops. A) Neutral drops are recharged by breaking them apart in the presence of an electric field. Uncharged drops ($q=0$) are polarized in an electric field ($E_S \neq 0$), and provided E_S is sufficiently large, as shown in the photomicrograph of (B; scale bar: 500 μm), they break into two oppositely charged daughter drops in the extensional flow at a bifurcation. The enlargement of the dashed rectangle, shown in (C), reveals that the charged drops are stretched in the electric field but become spherical again upon contact with the electrodes indicated by dashed vertical lines.

through creative use of flow geometry;[20] however, sorting is most useful when based on content rather than size. The use of electrostatic charging of droplets provides an alternate means that can be precisely controlled, can be switched at high frequencies, and requires no moving parts. The electrostatic charge on the droplets enables drop-by-drop sorting based on the linear coupling of charge to an external electric field. As an example, a T-junction bifurcation that splits the flow of carrier fluid equally will also randomly split the droplet population equally into the two streams, as shown in Figure 4A. However, a small electric field applied at the bifurcation precisely dictates which channel the drops enter; a schematic of the electrode configuration is shown in Figure 4B. Varying the direction of the field varies the direction of the sorted droplets as shown in Figure 4C and D. The large forces that can be imparted on the droplets and the high switching frequency make this a fast and robust sorting engine

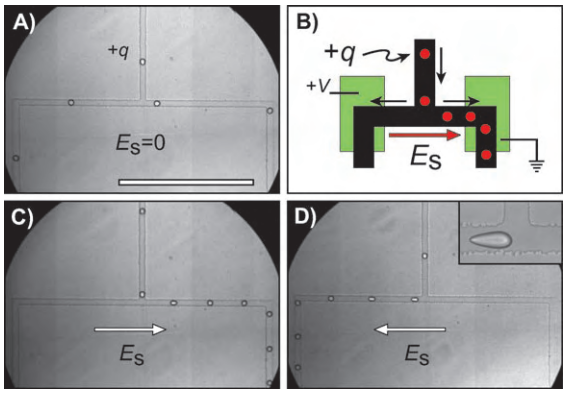

Figure 4. Manipulating charged drops. A) Charged drops alternately enter the right and left channels when no field is applied ($E_S=0$; scale bar: 500 μm). B) Layout for using an electric field E_S to select the channel that charged drops will enter at a bifurcation. C) When an electric field is applied to the right, the drops enter the right branch at the bifurcation. D) The drops enter the left branch when the field is reversed. After the bifurcation, the distance between drops is reduced to half of what it was before, which indicates that the oil stream is evenly divided. The inset of (D) shows the deformation in the shape of a highly charged drop in an electric field.

with no moving parts; thus the processing rate is limited only by the rate of droplet generation.

The enhanced functionality that electrostatic charge brings to droplets in microfluidic devices has the potential to enable an expansive list of microfluidics applications. This toolkit of techniques for manipulating droplets will enable modular integration of systems for transporting and carrying out reaction of small numbers of molecules. High-throughput screening, combinatorial chemistry, and the search for rare biological function in libraries of biomolecules could all potentially benefit from electrostatic manipulation of droplets in microchannels. Droplet-based microfluidic technology can also be used to develop a chip-scale fluorescence-activated cell sorter (FACS) with enhanced activation functionality that goes beyond fluorescence to include multiple reagent-based assays between the droplet formation and sorting steps. Moreover by using femtoliter droplets, which are a few microns in diameter, even a single biomolecule represents a concentrations of approximately 1 nM, which is sufficient for efficient chemical reactivity and single-molecule assays.[30]

Many of the potential uses of droplet-based microfluidic devices are driven by a need to encapsulate a varied population or library of molecules, cells, or particles into microreactors, perform an assay on the contents, perhaps through the addition of reagents, and then, finally, to remove selectively specific microreactors from the collection in a search for rare events. This requires processing rates of approximately 10^3 per second to sort through the smallest libraries in a reasonable time whereas rates on the order of 10^5 per second are desirable for larger libraries. These rates are feasible with the charged-droplet paradigm. Moreover, because the microfluidic devices are stamped, parallel flow streams can be fabricated, further enhancing the total throughput. Combined, the advantages of droplets and high-throughput manipulation provide significant opportunity for widespread application. The platform technology presented herein will facilitate the potential application of droplet-based microfluidic technology.

Received: October 6, 2005
Revised: December 19, 2005
Published online: March 17, 2006

Keywords: droplets · high-throughput screening · microfluidics · microreactors

[1] H. A. Stone, A. D. Stroock, A. Ajdari, *Annu. Rev. Fluid Mech.* **2004**, *36*, 381.
[2] S. A. Sundberg, *Curr. Opin. Biotechnol.* **2000**, *11*, 47.
[3] M. A. Unger, H.-P Chou, T. Thorsen, A. Scherer, S. R. Quake, *Science* **2000**, *288*, 113.
[4] R. A. Mathies, X. C. Huang, *Nature* **1992**, *359*, 167.
[5] D. J. Harrison, K. Fluri, K. Seiler, Z. Fan, C. S. Effenhauser, A. Manz, *Science* **1993**, *261*, 895.
[6] M. G. Pollack, A. D. Shendorov, R. B. Fair, *Lab Chip* **2002**, *2*, 96.
[7] T. Thorsen, S. J. Maerkl, S. R. Quake, *Science* **2002**, *298*, 580.
[8] J. Khandurina, A. Guttman, *Curr. Opin. Chem. Biol.* **2002**, *6*, 359.
[9] G. H. Seong, R. M. Crooks, *J. Am. Chem. Soc.* **2002**, *124*, 13360.

 © 2006 Wiley-VCH Verlag GmbH & Co. KGaA, Weinheim

[10] M. A. Burns, B. N. Johnson, S. N. Brahmasandra, K. Handique, J. R. Webster, M. Krishnan, T. S. Sammarco, P. M. Man, D. Jones, D. Heldsinger, C. H. Mastrangelo, D. T. Burke, *Science* **2002**, *282*, 484.
[11] C. B. Cohen, E. Chin-Dixon, S. Jeong, T. T. Nikiforov, *Anal. Biochem.* **1999**, *273*, 89.
[12] A. Y. Fu, H.-P. Chou, C. Spence, F. H. Arnold, S. R. Quake, *Anal. Chem.* **2002**, *74*, 2457.
[13] H. Wu, A. Wheeler, R. N. Zare, *Proc. Natl. Acad. Sci. USA* **2004**, *101*, 12809.
[14] J. Sinclari, J. Pihl, J. Olofsson, M. Karlsson, K. Jardemark, D. T. Chiu, O. Orwar, *Anal. Chem.* **2002**, *74*, 6133.
[15] J. Farinas, A. W. Chow, H. G. Wada, *Anal. Biochem.* **2001**, *295*, 138.
[16] A. Y. Fu, C. Spence, A. Scherer, F. H. Arnold, S. R. Quake, *Nat. Biotechnol.* **1999**, *17*, 1109.
[17] J. W. Hong, V. Studer, G. Hang, W. F. Anderson, S. R. Quake, *Nat. Biotechnol.* **2004**, *22*, 435.
[18] C. L. Hansen, E. Skordalakes, J. M. Berger, S. R. Quake, *Proc. Natl. Acad. Sci. USA* **2002**, *99*, 16531.
[19] Y.-C. Tan, J. S. Fisher, A. I. Lee, V. Cristini, A. P. Lee, *Lab Chip* **2004**, *4*, 292.
[20] Y.-C. Tan, A. P. Lee, *Lab Chip* **2005**, *5*, 1178.
[21] T. Thorsen, R. W. Roberts, F. H. Arnold, S. R. Quake, *Phys. Rev. Lett.* **2001**, *86*, 4163.
[22] S. Sugiura, M. Nakajima, S. Iwamoto, M. Seki, *Langmuir* **2001**, *17*, 5562.
[23] S. L. Anna, N. Bontoux, H. A. Stone, *Appl. Phys. Lett.* **2003**, *82*, 364.
[24] Y. C. Tan, V. Cristini, A. P. Lee, *7th International Conference on Micro Total Analysis Systems* **2003**, 963.
[25] D. R. Link, S. L. Anna, H. A. Stone, D. A. Weitz, *Phys. Rev. Lett.* **2004**, *92*, 054503.
[26] J. C. McDonald, D. C. Duffy, J. R. Anderson, D. T. Chiu, H. Wu, O. J. A. Schueller, G. M. Whitesides, *Electrophoresis* **2000**, *21*, 27.
[27] H. Song, J. D. Tice, R. F. Ismagilov, *Angew. Chem.* **2003**, *115*, 792; *Angew. Chem. Int. Ed.* **2003**, *42*, 768.
[28] B. Zheng, R. F. Ismagilov, *Angew. Chem.* **2003**, *115*, 2576; *Angew. Chem. Int. Ed.* **2005**, *44*, 2520.
[29] I. Shestopalov, J. D. Tice, R. F. Ismagilov, *Lab Chip* **2004**, *4*, 316.
[30] P. S. Dittrich, M. Jahnz, P. Schwille, *ChemBioChem* **2005**, *6*, 811.

 © 2006 Wiley-VCH Verlag GmbH & Co. KGaA, Weinheim

Natural Product Synthesis

DOI: 10.1002/anie.200504573

Total Synthesis of Auripyrone A**

*Troy Lister and Michael V. Perkins**

Dolabella auricularia, a sea hare from the *aplysiidae* family of marine opisthobranchs, has been a prolific source of bioactive metabolites, which range from peptides and depsipetides to polyketides, for over 40 years.[1] In 1996, the auripyrones A (**1**) and B (**2**) were added to this list when they were isolated

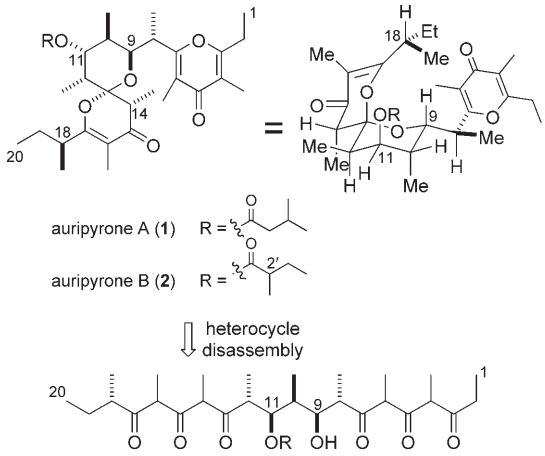

by Suenaga et al.[2] from the methanol extract of specimens of *D. auricularia* collected near Mie Prefecture, Japan. Structural elucidation revealed a characteristic polypropionate architecture, with a unique spiroacetal dihydropyrone core tethered to a γ-pyrone ring. Auripyrones A (**1**) and B (**2**) were shown to differ only in the nature of their respective C11 acyloxy side chains and exhibited moderate cytotoxicity against HeLa S_3 cells with IC_{50} values of 0.26 and 0.48 μg mL^{-1}, respectively. Suenaga et al.[2] assigned the complete relative stereochemistry of **1** using extensive ^{1}H NMR experiments, but they were unable to assign the configuration of the C2′ stereocenter of **2** or the absolute stereochemistry[3] of the natural products.

[*] T. Lister, Dr. M. V. Perkins
School of Chemistry, Physics and Earth Sciences
Flinders University
PO Box 2100, Adelaide, South Australia 5001 (Australia)
Fax: (+61) 8-8201-2905
E-mail: mike.perkins@flinders.edu.au

[**] We thank Flinders University and the Australian Research Council for financial support. T.L. acknowledges the receipt of an Australian Post Graduate Award. We thank Prof. H. Kigoshi and Prof. K. Suenaga (Department of Chemistry, University of Tsukuba, Japan) for kindly providing copies of NMR spectra of authentic auripyrones A and B.

Supporting information for this article is available on the WWW under http://www.angewandte.org or from the author.

WILEY InterScience DISCOVER SOMETHING GREAT
© 2006 Wiley-VCH Verlag GmbH & Co. KGaA, Weinheim

At the heart of the auripyrones, as evidenced by unraveling the heterocycles, is a *meso* stereopentad, flanked on both sides by two tricarbonyl systems. The C2 symmetry of this stereochemical array is broken only by the C19–C20 ethyl extension and the acyl group on the C11 oxygen atom. The presence of the C11 acyloxy moiety may constitute a biosynthetic protecting group, thus guiding the observed spiro cyclization in preference to competing cyclization events.

Herein, we describe the first total synthesis of auripyrone A (**1**) and identify the absolute stereochemistry of the natural product. We chose the reterosynthetic approach shown in Scheme 1.

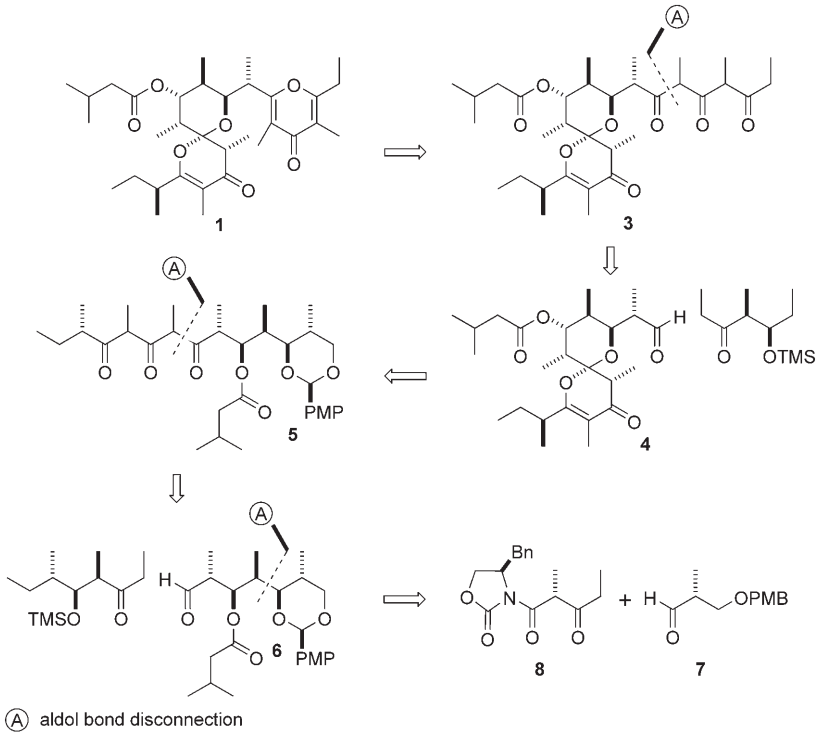

Scheme 1. Retrosynthetic analysis of auripyrone A (**1**). Bn = benzyl, PMB = *para*-methoxybenzyl, PMP = *para*-methoxyphenyl, TMS = trimethylsilyl.

It was anticipated that a final-stage pyrone formation, which would give **1**, could be accomplished from triketone **3**, despite the potentially sensitive nature of the spiroacetal core. Formation of **3** was proposed from spiroacetal aldehyde **4** through a sequence of aldol addition, deprotection, and oxidation. One of the critical elements in the strategy was the formation of the correct stereoisomer of the spiroacetal dihydropyrone found in **4**, which was foreseen to arise from a thermodynamically controlled cyclization after removal of the acetal protecting group in **5**. Aldol addition, deprotection, and oxidation would provide tricarbonyl **5** from aldehyde **6**. To generate the correct stereopentad in **6**, we proposed the use of substrate control by employing the Evans dipropionate equivalent **8**,[4] in an aldol reaction with known[5] chiral aldehyde **7**, followed by *syn* reduction of the resultant β-hydroxy ketone.

Previous work[6] has shown that the formation of the sprioacetal dihydropyrone was unsuccessful without differentiation between the C9 and C11 hydroxy groups. We chose to use the acyloxy moiety found in **1** as the C11 protecting group, thus minimizing the reliance on formal protection sequences. Indeed, the final strategy does not require the introduction of any protecting groups within the linear sequence.

We began our synthesis from dipropionate equivalent **8** (available[4] from (*R*)-phenylalanine in five steps; Scheme 2). The Sn^{II} enolate of β-ketoimide **8**[7] underwent a highly selective double stereodifferentiating aldol addition with known[5] α-methyl aldehyde **7** to give the 9,10-*syn*,10,12-*anti* aldol product **9**. Subsequent reduction with DIBAL-H[7] of the adduct gave diol **10** as a single isomer, thus completing the construction of the stereopentad. The necessity for the reduction with DIBAL-H to be performed on the unprotected substrate is a small drawback to this highly efficient protocol.

Migration of the PMB group introduced with aldehyde **7** provided an efficient solution to the selective protection of diol **10**. In practice, treatment of **10** with DDQ under anhydrous conditions[8] afforded the crystalline *p*-methoxybenzilidene acetal **11** in good yield, thus selectively protecting the C9 hydroxy group. Treatment of **11** with isovaleric acid under conditions developed by Yamaguchi and co-workers[9] gave **12** in near quantitative yield. Thus, the required C11 acyloxy function for **1** was installed, thereby negating the use of a formal protecting group.

The treatment of **12** with $LiBH_4$[10] gave the desired primary alcohol **13** in good yield (70%), with only minor amounts of diol **14** (20%). The overall yield of **13** could be increased by processing the by-product **14** through the following sequence: 1) protection of the primary alcohol group with a PMB ether, 2) Yamaguchi esterification, and 3) DDQ-mediated cleavage of the PMB ether. Oxidation of **13** with DMP[11] gave aldehyde **6** in excellent yield.

The stereochemistry of the stereopentad in **10** was confirmed by using the simple strategy shown in Scheme 3. Treatment of the diol **10** with dimethoxypropane and catalytic PPTS gave the acetonide **15**, whose characteristic ^{13}C NMR shifts[12] of $\delta = 19.4$ and 30.1 ppm indicated a *syn*-diol relationship. Subsequent DDQ-mediated cleavage of the PMB ether and reductive removal of the auxiliary gave the *meso*-diol **16**, which displayed only nine ^{13}C NMR resonances and no optical rotation.

The preparation of the spiroacetal dihydropyrone **17** is shown in Scheme 4. Reaction of the Ti^{IV} enolate[7,13] of pentan-3-one (**18**) with (*S*)-2-methylbutanal (**19**; obtained from the oxidation of the commercially available (*S*)-2-methylbutanol) gave two separable aldol products **20** (15%) and **21** (65%). The major product was assigned as the *anti*-Felkin isomer **21** on the basis of a literature precedent.[14] Silyl protection of **21** with TMSOTf/lutidine completed this short

 © 2006 Wiley-VCH Verlag GmbH & Co. KGaA, Weinheim

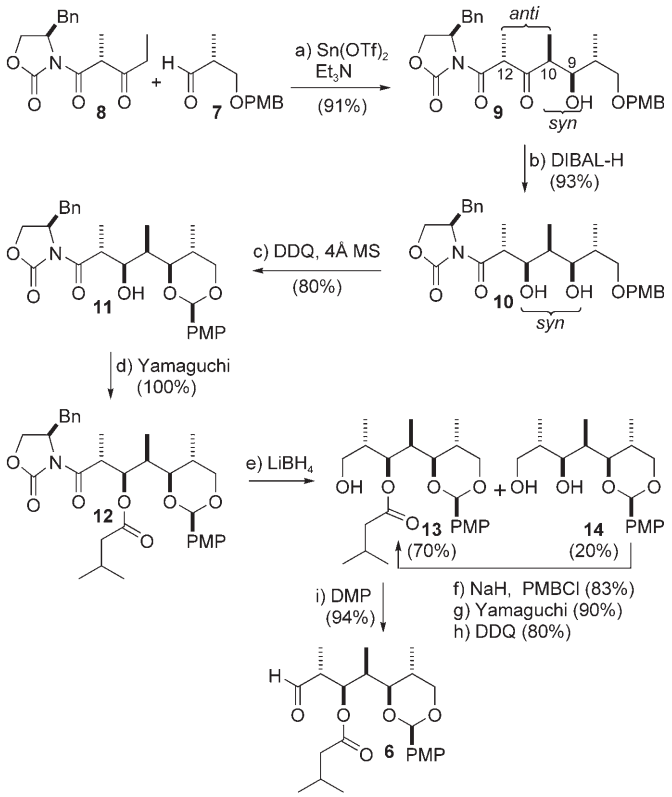

Scheme 2. Installation of the stereopentad, differential protection, and construction of the aldehyde **6**. Reagents and conditions: a) $Sn(OTf)_2$ (1.3 equiv), Et_3N (1.3 equiv), **7** (1.5 equiv), CH_2Cl_2, −78 °C, 30 min, 91 %; b) DIBAL-H (4.0 equiv), Et_2O, −78 °C, 1 h, 93 %; c) DDQ (1.2 equiv), 4-Å powdered molecular sieves, CH_2Cl_2, 0 °C, 5 h, 80 %; d) 2,4,6-trichlorobenzoyl chloride (8.5 equiv), 4-DMAP (19.0 equiv), Et_3N (9.0 equiv), isovaleric acid (5.0 equiv), toluene, −78 °C→RT, 1.5 h, 100 %; e) $LiBH_4$ (1.2 equiv), EtOH (1.2 equiv), Et_2O, −10 °C, 3.5 h, 63 %; f) NaH (3.0 equiv), PMBCl (1.2 equiv), THF, room temperature, 3 h, 83 %; g) 2,4,6-trichlorobenzoyl chloride (17.0 equiv), 4-DMAP (38.0 equiv), Et_3N (18.0 equiv), isovaleric acid (10.0 equiv), toluene, −78 °C→RT, 1.5 h, 90 %; h) DDQ (1.3 equiv), phosphate buffer (pH 7), CH_2Cl_2, 0 °C, 3 h, 80 %; i) DMP (1.5 equiv), CH_2Cl_2, room temperature, 1 h, 94 %. OTf = trifluoromethanesulfonate, DDQ = 2,3-dichloro-5,6-dicyano-1,4-benzoqinone, DIBAL-H = diisobutylaluminum hydride, 4-DMAP = 4-(dimethylamino)pyridine, DMP = Dess–Martin periodinane, $LiBH_4$ = lithium borohydride, PMBCl = *p*-methoxybenzyl chloride.

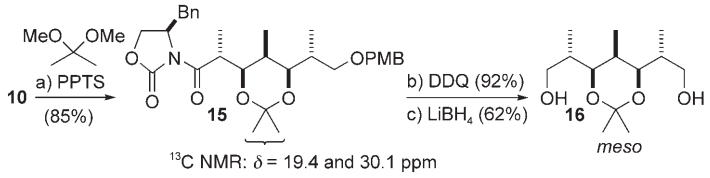

Scheme 3. Construction of the *meso*-diol **16** to confirm of the relative stereochemistry of the stereopentad. Reagents and conditions: a) $(MeO)_2C(CH_3)_2$, PPTS (cat.), CH_2Cl_2, room temperature, 3 h, 85 %; b) DDQ (1.5 equiv), phosphate buffer (pH 7), CH_2Cl_2, 0 °C, 3 h, 92 %; c) $LiBH_4$ (2.4 equiv), EtOH (2.4 equiv), Et_2O, −10 °C, 1.5 h, 62 %. PPTS = pyridinium *p*-toluenesulfonate.

synthesis of enantiomerically pure ketone **22** required for coupling with aldehyde **6**.

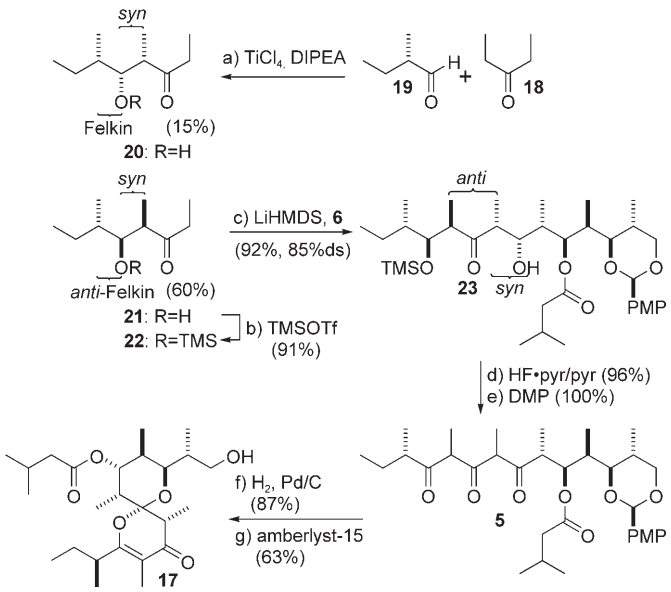

Scheme 4. Construction of the spiroacetal dihydropyrone **17**. Reagents and conditions: a) **18**, $TiCl_4$ (1.2 equiv), DIPEA (1.4 equiv), **19** (1.5 equiv), CH_2Cl_2, −78 °C, 1 h, 60 %; b) TMSOTf (1.5 equiv), 2,6-lutidine (2.0 equiv), CH_2Cl_2, −90 °C, 10 min, 91 %; c) LiHMDS (1.1 equiv), **6** (0.5 equiv), THF, −78 °C, 2 h, 92 %, 85 % *de*; d) HF·pyr/pyr, THF, room temperature, 45 min, 96 %; e) DMP (3.0 equiv), H_2O (2.0 equiv), CH_2Cl_2, room temperature, 1 h, 100 %; f) H_2, Pd/C (70 % w/w), EtOH, room temperature, 30 min, 87 %; g) amberlyst-15 (50 % w/w), CH_2Cl_2, −50 °C→RT, 5 h, 63 %. DIPEA = *N*,*N*-diisopropylethylamine, LiHMDS = lithium hexamethyldisilazide, Pd/C = palladium on activated carbon 10 % w/w, pyr = pyridine.

Ketone **22** was treated with LiHMDS at −78 °C, and the addition of aldehyde **6** gave the major aldol product **23** (78 %) and other isomers (11 %) after quenching. The configuration of the newly generated stereocenters in the major product **23** were tentatively assigned on the assumption that the *syn*/*anti* preference of the ketone[15] dominates in this double stereodifferentiating aldol reaction. In any case, the configuration of these newly formed stereocenters was not critical as they were either lost upon oxidation or became epimerizable in subsequent steps. To that end, the TMS group was removed with buffered HF·pyridine, and double oxidation with DMP afforded triketone **5** as a mixture of the keto and enol forms.

After extensive experimentation, spiroacetal dihydropyrone **17** was found to be most readily available from hydrogenolysis (H_2, Pd/C) of acetal **5** followed by stirring of the purified reaction product with amberlyst-15 resin[16] in CH_2Cl_2 for several hours. Gratifyingly, the cascade cyclization proceeded under thermodynamic control, thus giving **17** in good yield (63 %) and with high diastereoselectivity (94 % *ds*).[17] Two-dimensional NOE interaction experiments allowed us to confirm the total relative stereochemistry and, importantly, establish the configuration of the dioxaspiro center unambiguously.[18] There was also a good correlation of the ^1H and ^{13}C NMR chemical shifts and coupling constants with those reported[2] for the sprioacetal dihydropyrone core of **1**.

The second aldol extension and final stages of the synthesis of **1** is shown in Scheme 5. Oxidation of alcohol **17** with DMP gave aldehyde **4** (91 %), ready for aldol extension.

 © 2006 Wiley-VCH Verlag GmbH & Co. KGaA, Weinheim

The coupling of **4** with a single enantiomer of ketone (4*S*,5*R*)-**24** was anticipated to lower the number of isomeric products and thus simplify their isolation and characterization. The synthesis of **24** was readily achieved and began with *N*-acyloxazolidinone **25**[4] in a four-step sequence which consisted of *syn*-aldol addition, transamination,[19] addition of Grignard reagents, and finally silyl protection (66% over four steps). Enolization of **24** with LiHMDS followed by reaction with **4** gave the elaborate adduct **26** in excellent yield (94%) and as a separable mixture of two diastereomers (88% *ds*). The configuration of the major product **26** was again tentatively assigned on the assumption that the *syn*/*anti* preference of the ketone[15] dominated in this double stereodifferentiating aldol reaction. Pleasingly, the use of the mild enolization conditions and the enantiomerically pure ketone had again enabled isolation of the desired aldol product in high yield and with good stereoselectivity.

The silyl group was removed with HF·pyr/pyr and the resultant diol **27** was oxidized with DMP to give the precursor triketone **3** as a mixture of the keto and enol forms. With the key precursor in hand, we turned our attention to the final formation of the pyrone ring. The methods developed by Yamamura and co-workers (PPh_3/CCl_4 and dimethylsulfoxide (DMSO)/$(COCl)_2$)[20] for the conversion of 1,3,5-triketones into the corresponding γ-pyrones under mild conditions have proved successful when employed by Paterson[9,21] and Arimoto[22] on relatively simple systems. Unfortunately the application of either of these conditions to **3** led to mixtures of decomposition products, in which the spiroacetal dihydropyrone ring was absent, despite apparent formation of a pyrone ring in a number of cases.

Recent studies[23] in our group have shown that the pyrone ring system found in tridachiahydropyrone can be formed in good yield from the appropriate β,δ-diketoacids by treatment with P_2O_5 supported on celite. Application of these conditions to **3** proved successful, and the reaction was further optimized by the addition of amberlyst-15 resin, which is thought to aid the reaction by increasing the rate of the triketone tautomerization. In the optimized procedure, **3** was stirred with the amberlyst-15 resin for several minutes, before P_2O_5 supported on celite was added and the reaction mixture stirred overnight. After filtration and flash chromatography, **1** was isolated in 39% yield. Synthetic **1** exhibited identical spectral data (^1H and ^{13}C NMR, UV/Vis, IR, and MS), as well as melting point, to those reported by Suenaga et al.[2] Notably, the optical rotation of synthetic **1**, $[\alpha]_D^{20} = +33°$ ($c = 0.2$, $CHCl_3$), was the same sign as that reported $[\alpha]_D^{26} = +28°$ ($c = 0.083$, $CHCl_3$),[2] thus establishing the absolute configuration of the natural product **1** (see Table 1).

The chemistry described herein constitutes an efficient, asymmetric synthesis of the cytotoxic marine polypropionate auripyrone A (**1**) in 16 steps and 6.2% yield from ketone **8** and aldehyde **7**, and thus establishes the absolute stereochemistry of the natural product. Our strategy employs substrate control to develop the stereopentad unit and introduces a novel method for the installation of γ-pyrone rings from 1,3,5-triketones.

Received: December 23, 2005
Published online: March 17, 2006

Keywords:
γ-pyrone · aldol reaction · cytotoxicity · natural products · total synthesis

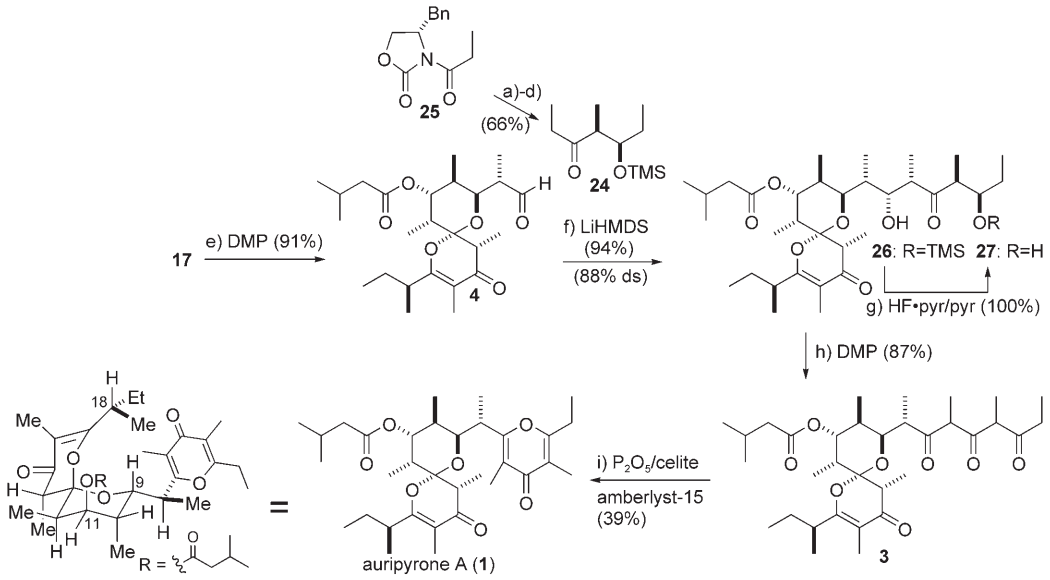

Scheme 5. Construction of the γ-pyrone ring and completion of the synthesis of **1**. Reagents and conditions: a) Bu_2BOTf (1.2 equiv), Et_3N (1.3 equiv), propanal (2.0 equiv), CH_2Cl_2, −78→0°C, 1.5 h, 88%; b) MeONH(Me)·HCl (2.0 equiv), $AlMe_3$ (2.0 equiv), CH_2Cl_2, room temperature, overnight, 100%; c) EtMgBr (3.0 equiv), Et_2O, room temperature, overnight, 88%; d) TMSOTf (1.5 equiv), 2,6-lutidine (2.0 equiv), CH_2Cl_2, −90°C, 30 min, 85%; e) DMP (1.5 equiv), CH_2Cl_2, room temperature, 1 h, 91%; f) LiHMDS (1.0 equiv), **4** (0.13 equiv), THF, −78°C, 1 h, 94%, 88% *de*; g) HF·pyr/pyr, THF, room temperature, 45 min, 100%; h) DMP (4.0 equiv), CH_2Cl_2, room temperature, 1 h, 87%; i) amberlyst-15 (50% w/w), P_2O_5 (4.0 equiv), celite, CH_2Cl_2, room temperature, overnight, 39% (based on 40% recovery of starting material).

 © 2006 Wiley-VCH Verlag GmbH & Co. KGaA, Weinheim

Table 1: Selected physical properties for **17, 27**, and **1**.

17: $R_f = 0.25$ (silica gel, Et_2O/CH_2Cl_2 15:85); $[\alpha]_D^{20} = +107.5°$ ($c = 0.4$, CH_2Cl_2); IR (film): $\tilde{\nu} = 3478, 1732, 1669, 1624, 1462, 1387, 1371, 1294, 1166, 1095, 1058, 1038, 1010, 986, 918\ cm^{-1}$; ^1H NMR (600 MHz, C_6D_6): $\delta = 4.93$ (t, $J = 3.6$ Hz, 1H), 3.83 (dd, $J = 10.2$, 2.4 Hz, 1H), 3.49 (dd, 10.8, $J = 5.4$ Hz, 1H), 3.37–3.34 (m, 1H), 2.50–2.44 (m, 1H), 2.43 (q, $J = 6.6$ Hz, 1H), 2.20–2.13 (m, 3H), 1.89 (s, 3H), 1.87 (qd, $J = 7.2$, 4.2 Hz, 1H), 1.81–1.73 (m, 2H), 1.61–1.55 (m, 1H), 1.54–1.40 (m, 2H), 1.14 (d, $J = 6.6$ Hz, 3H), 1.06 (d, $J = 6.6$ Hz, 3H), 0.89 (d, $J = 6.0$ Hz, 3H), 0.88 (t, $J = 7.8$ Hz, 3H), 0.88 (d, $J = 6.0$ Hz, 3H), 0.80 (d, $J = 7.2$ Hz, 3H), 0.67 (d, $J = 7.2$ Hz, 3H), 0.56 ppm (d, $J = 7.2$ Hz, 3H); ^{13}C NMR (75.5 MHz, C_6D_6): $\delta = 192.8, 172.0, 167.3, 108.0, 105.3, 75.1, 71.8, 66.6, 44.6, 44.0, 37.7, 36.6, 34.2, 31.9, 27.4, 26.3, 22.4, 22.3, 16.6, 12.6, 12.4, 12.0, 10.0, 9.4, 8.0$ ppm; HR ESI MS: calcd for $C_{25}H_{42}O_6Na^+$ [$M + Na^+$]: 461.2874; found: 461.2879; EI MS m/z (%): 197 (15), 149 (22), 111 (17), 97 (30), 85 (55), 83 (67), 72 (51), 70 (59), 57 (100), 55 (71).

27: $R_f = 0.26$ (silica gel, Et_2O/CH_2Cl_2 20:80); $[\alpha]_D^{20} = +76.9°$ ($c = 0.4$, CH_2Cl_2); IR (film): $\tilde{\nu} = 3505, 1734, 1670, 1620, 1459, 1388, 1373, 1346, 1294, 1254, 1212, 1166, 1120, 1094, 1058, 1009, 986, 964, 918\ cm^{-1}$; ^1H NMR (600 MHz, C_6D_6): $\delta = 4.96$ (t, $J = 3.6$ Hz, 1H), 4.15 (br s, 1H), 3.98 (dd, $J = 10.2$, 1.8 Hz, 1H), 3.77 (br m, 1H), 2.81 (br s, 1H), 2.63 (qd, $J = 7.2$, 4.2 Hz, 1H), 2.53–2.43 (m, 3H), 2.39 (q, $J = 6.6$ Hz, 1H), 2.24–2.16 (m, 3H), 1.95–1.84 (m, 3H), 1.84 (s, 3H), 1.61–1.55 (m, 1H), 1.55–1.50 (m, 1H), 1.49–1.43 (m, 1H), 1.37–1.31 (m, 1H), 1.14 (d, $J = 7.2$ Hz, 3H), 1.08 (d, $J = 6.6$ Hz, 3H), 1.07 (d, $J = 6.6$ Hz, 3H), 1.03 (d, $J = 7.2$ Hz, 3H), 0.99 (t, $J = 7.2$ Hz, 3H), 0.94 (t, $J = 7.2$ Hz, 3H), 0.92 (d, $J = 6.0$ Hz, 3H), 0.91 (d, $J = 6.0$ Hz, 3H), 0.80 (d, $J = 6.6$ Hz, 3H), 0.76 (d, $J = 6.6$ Hz, 3H), 0.76 ppm (d, $J = 7.2$ Hz, 3H); ^{13}C NMR (75.5 MHz, $CDCl_3$): $\delta = 220.2, 194.0, 172.1, 168.4, 107.5, 105.5, 75.2, 73.8, 70.3, 68.8, 50.5, 49.6, 44.5, 44.0, 38.2, 37.9, 34.1, 32.0, 27.6, 27.1, 26.3, 22.5, 22.4, 16.6, 12.4, 12.0, 11.0, 10.9, 10.7, 9.9, 9.8, 9.3, 7.9$ ppm; HR ESI MS: calcd for $C_{33}H_{56}O_8Na^+$ [$M + Na^+$]: 603.3867; found: 603.3863; EI MS m/z (%): 197 (52), 168 (9), 139 (14), 109 (15), 85 (24), 57 (100).

1: m.p.: 171–173 °C (172–176 °C)[2]; $R_f = 0.27$ (silica gel, Et_2O/CH_2Cl_2 50:50); $[\alpha]_D^{20} = +33.3°$ ($c = 0.2$, $CHCl_3$); IR (film): $\tilde{\nu} = 1729, 1656, 1626, 1618, 1459, 1419, 1386, 1374, 1291, 1251, 1166, 1091, 1058, 1010, 984, 963, 919\ cm^{-1}$; UV/Vis (MeOH) λ_{max} (ε): 260 (18200), 220 nm (10100 $M^{-1}cm^{-1}$); ^1H NMR (600 MHz, C_6D_6): $\delta = 4.92$ (t, $J = 3.3$ Hz, 1H), 3.98 (dd, $J = 10.2$, 2.1 Hz), 2.76 (dq, $J = 10.2$, 7.2 Hz, 1H), 2.32 (q, $J = 6.6$ Hz, 1H), 2.31 (dq, $J = 15.0$, 7.5 Hz, 1H), 2.26 (dqd, $J = 7.2$, 7.2, 3.6 Hz, 1H), 2.21–2.16 (m, 1H), 2.18–2.11 (m, 2H), 2.10 (dq, $J = 15.0$, 7.5 Hz, 1H), 2.03 (s, 3H), 1.98 (s, 3H), 1.85 (qd, $J = 7.2$, 3.6 Hz, 1H), 1.83–1.80 (m, 1H), 1.64 (s, 3H), 1.56–1.48 (m, 1H), 1.41–1.34 (m, 1H), 1.12 (d, $J = 6.6$ Hz, 3H), 0.99 (d, $J = 7.2$ Hz, 3H), 0.91 (d, $J = 6.0$ Hz, 3H), 0.90 (d, $J = 6.6$ Hz, 3H), 0.90 (t, $J = 7.5$ Hz, 3H), 0.84 (t, $J = 7.5$ Hz, 3H), 0.78 (d, $J = 7.2$ Hz, 3H), 0.74 (d, $J = 7.2$ Hz, 3H), 0.65 ppm (d, $J = 7.2$ Hz, 3H); ^{13}C NMR (151 MHz, $CDCl_3$): $\delta = 191.8, 178.5, 172.0, 166.2, 162.1, 161.6, 121.3, 118.1, 107.8, 105.0, 75.2, 70.6, 44.5, 44.0, 37.2, 36.7, 34.1, 31.7, 26.4, 26.3, 24.7, 22.5, 22.3, 16.0, 12.1, 12.0, 11.9, 11.0, 10.7, 9.7, 9.5, 8.9, 8.1$ ppm; HR ESI MS: calcd for $C_{33}H_{50}O_7Na^+$ [$M + Na^+$]: 581.3449; found: 581.3448; EI MS m/z (%): 558 (M^+, 43), 501 (9), 457 (11), 391 (6), 317 (20), 261 (12), 221 (31), 193 (100), 180 (43), 151 (11), 137 (18), 85 (17), 83 (22), 57 (68), 55 (15).

[1] K. Yamada, H. Kigoshi, *Bull. Chem. Soc. Jpn.* **1997**, *70*, 1479–1489; C. Tiringal, *Bioactive Compounds from Natural Sources*, Taylor and Francis, London, **2001**, pp. 580–621.

[2] K. Suenaga, H. Kigoshi, K. Yamada, *Tetrahedron Lett.* **1996**, *37*, 5151–5154.

[3] The structure drawn by Suenaga et al.[2] in the report on the isolation of the natural product was an arbitrary choice for the absolute stereochemistry of the auripyrones. We chose to target the enantiomer of that depicted by Suenaga et al. because of the commercial availability of only the *S* enantiomer of 2-methylbutanol, which we used to gain access to the remote C18 stereocenter.

[4] D. A. Evans, J. R. Gage, *Org. Synth.* **1989**, *68*, 77–91; D. A. Evans, M. D. Ennis, T. Le, *J. Am. Chem. Soc.* **1984**, *106*, 1154–1156; D. A. Evans, H. P. Ng, J. S. Clark, D. L. Rieger, *Tetrahedron* **1992**, *48*, 2127–2142.

[5] R. D. Walkup, R. J. Kane, P. D. Boatman, Jr., R. T. Cunningham, *Tetrahedron Lett.* **1990**, *31*, 7587–7590; D. W. Jeffery, M. V. Perkins, *Tetrahedron Lett.* **2004**, *45*, 8667–8671.

[6] M. V. Perkins, S. Jahangiri, M. R. Taylor, *Tetrahedron Lett.* **2006**, *47*, 2025–2028; M. V. Perkins, R. A. Sampson, J. Joannou, M. R. Taylor, *Tetrahedron Lett.* **2006**, in press..

[7] D. A. Evans, J. S. Clark, R. Metternich, V. J. Novack, G. S. Sheppard, *J. Am. Chem. Soc.* **1990**, *112*, 866–868.

[8] Y. Oikawa, T. Nishi, O. Yonemitsu, *Tetrahedron Lett.* **1983**, *24*, 4037–4040; L. A. Paquette, M. Duan, I. Konetzki, C. Kempmann, *J. Am. Chem. Soc.* **2002**, *124*, 4257–4270.

[9] I. Paterson, D. Y. Chen, J. L. Aceña, A. S. Franklin, *Org. Lett.* **2000**, *2*, 1513–1516; M. Hikotam, Y. Sakurai, K. Horita, O. Yonemitsu, *Tetrehedron Lett.* **1990**, *31*, 6367–6370; J. Inanaga, K. Hirata, H. Saeki, T. Katsuki, M. Yamaguchi, *Bull. Chem. Soc. Jpn.* **1979**, *52*, 1989–1993.

[10] D. A. Evans, A. M. Ratz, B. E. Huff, G. S. Sheppard, *J. Am. Chem. Soc.* **1995**, *117*, 3448–3467.

[11] D. B. Dess, J. C. Martin, *J. Org. Chem.* **1983**, *48*, 4155–4156; D. B. Dess, J. C. Martin, *J. Am. Chem. Soc.* **1991**, *113*, 7277–7287.

[12] S. D. Rychnovsky, D. J. Skalitzky, *Tetrahedron Lett.* **1990**, *31*, 945–948.

[13] D. A. Evans, F. Urpý, T. C. Somers, J. S. Clark, M. T. Bilodeau, *J. Am. Chem. Soc.* **1990**, *112*, 8215–8216; D. A. Evans, D. L. Rieger, M. T. Bilodeau, F. Urpi, *J. Am. Chem. Soc.* **1991**, *113*, 1047–1049; D. A. Evans, M. J. Dart, J. L. Duffy, D. L. Rieger, *J. Am. Chem. Soc.* **1995**, *117*, 9073–9074.

[14] W. R. Roush, *J. Org. Chem.* **1991**, *56*, 4151–4157.

[15] P. A. McCarthy, M. Kageyama, *J. Org. Chem.* **1987**, *52*, 4681–4686; D. A. Evans, M. G. Yang, M. J. Dart, J. L. Duffy, *Tetrahedron Lett.* **1996**, *37*, 1957–1960.

[16] J. J. Young, L. J. Jung, K. M. Cheng, *Tetrahedron Lett.* **2000**, *41*, 3411–3413; S. V. Ley, I. R. Baxendale, R. N. Bream, P. S. Jackson, A. G. Leach, D. A. Longbottom, M. Nesi, J. S. Scott, R. I. Storer, S. J. Taylor, *J. Chem. Soc. Perkin Trans. 1* **2000**, 3815–4195; M. V. Perkins, W. Kitching, R. A. I. Drew, C. J. Moore, W. A. Konig, *J. Chem. Soc. Perkin Trans. 1* **1990**, 1111–1117.

[17] A small amount of an inseparable isomer ($\approx 6\%$) was present in the purified product; this contaminant was carried through the synthesis and is seen as a minor impurity in the spectra of the final product auripyrone A.

[18] The major product was predicted and found to be the isomer in which both oxygen atoms are in the anomerically favorable axial positions; see P. Deslongchamps, D. D. Rowan, N. Pothier, T. Sauve, J. K. Saunders, *Can. J. Chem.* **1981**, *59*, 1105–1121.

[19] A. Basha, M. Lipton, S. M. Weinreb, *Tetrahedron Lett.* **1977**, *18*, 4171–4174; D. A. Evans, A. S. Kim, R. Metternich, V. J. Novack, *J. Am. Chem. Soc.* **1998**, *120*, 5921–5942.

[20] H. Arimoto, S. Nishiyama, S. Yamamura, *Tetrahedron Lett.* **1990**, *31*, 5619–5620.

[21] I. Paterson, A. S. Franklin, *Tetrahedron Lett.* **1994**, *35*, 6925–6928.

[22] H. Arimoto, R. Yokoyama, K. Nakamura, Y. Okumura, D. Uemura, *Tetrahedron* **1996**, *52*, 13901–13908.

[23] D. W. Jeffery, M. V. Perkins, J. M. White, *Org. Lett.* **2005**, *7*, 407–409; D. W. Jeffery, M. V. Perkins, J. M. White, *Org. Lett.* **2005**, *7*, 1581–1584.

 © 2006 Wiley-VCH Verlag GmbH & Co. KGaA, Weinheim

Sensor Design

DOI: 10.1002/anie.200504335

The Development of Conformational-Dynamics-Based Sensors**

*Péter Kele, Krisztina Nagy, and András Kotschy**

The majority of present-day fluorescent sensors consisting of a receptor and a fluorophore unit exploit the so-called photoinduced electron transfer (PET) phenomenon.[1] In PET sensors, guest binding to the receptor module invokes the shift of a donor atom's (or site's) redox potential and reversal of its ability to quench the fluorescence of the fluorophore part, thereby resulting in a measurable change in the fluorescent signal. The generality and efficiency of this switching process led to the regular use of PET sensors in numerous fields from simple-ion sensing to logic gates.[2,3]

The effect of guest binding is mostly rationalized by the guest's coordinative interaction with the donor site, although the effect of conformational dynamics on the transfer of the electrons from the donor site to the fluorophore has also been studied.[4] There are certain cases, however, in which the formation of secondary interactions between the host and guest does not give a satisfactory explanation for the enhanced fluorescent signal. This suggests that, in these sensors, the conformational dynamics of the receptor part might also play a significant role.[5] An intriguing example is the commercial sensor developed for monitoring sodium and potassium levels in blood, where the conformational change in the receptor, driven by guest binding, is the origin of the change in the PET process.[6,7] Although these sensors demonstrate nicely the marked effect of conformational changes on the PET process, their unique structure hinders the extension of their design to the selective detection of other guests, such as organic molecules.[8]

To understand how changes in the dynamic behavior of sensor molecules influence their emitted signal, we initiated a systematic study. The test system we chose is a well-established sensor design in which a nitrogen atom acts as a donor site in the PET process and is isolated from the fluorophore by a methylene spacer. The first set of experiments was aimed at establishing the influence of the conformational dynamics of the surroundings of the nitrogen atom on its participation in the PET process. This was determined by the preparation of a coumarine-based sensor series in which the donor nitrogen atom was part of saturated heterocycles of similar structures but different ring sizes (**1a**–**h**, Scheme 1).[9] For comparison, we also included a sensor in the study where the substituents on the donor nitrogen atom did not form a ring (**1i**).

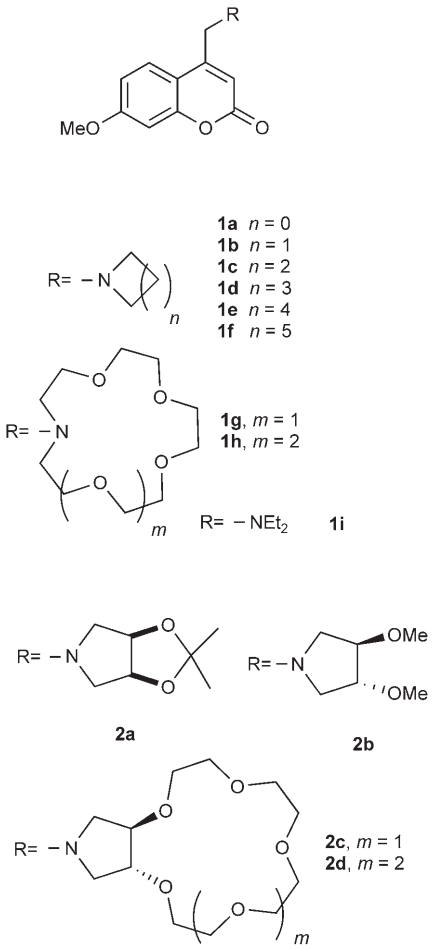

Scheme 1. The studied coumarylmethylamine sensors.

The efficiency of the PET process in these sensors was determined by comparing, in solution, the fluorescence of the basic sensor molecules with the fluorescence of their protonated forms when the PET process is completely blocked. The process was blocked by the excess addition of a strong acid (HBF_4) that protonates the amine moiety. The proportion of the measured fluorescence values (also know as fluorescence enhancement (FE), shown in Figure 1) represents the signaling potential (maximal achievable FE) of these sensors. Molecules with ring sizes of 6 (**1d**) or 8 (**1f**), as well as the macrocyclic aza-crown derivatives (**1g,h**) have an inherent signaling potential of 38–50, whereas other sensors fall well outside this range. The aziridine-containing **1a** has a very limited potential (3.9) probably because of its rigid structure, whereas the azetidine- (**1b**; 77) and azepine- (**1e**; 135) containing sensors as well as the noncyclic diethylamino compound (**1I**; 77) show larger fluorescence enhancements.

[*] Dr. P. Kele, K. Nagy, Prof. A. Kotschy
Institute of Chemistry
Eötvös Loránd University
1117 Budapest, Pázmány Péter sétány 1/A (Hungary)
Fax: (+36) 1-372-2909
E-mail: kotschy@chem.elte.hu

[**] Financial support from the Hungarian Ministry of Education (BÖ125/2003) and Hungarian Research Fund (OTKA F047125, F048739), as well as the technical assistance of Mr. Tibor Zs. Nagy is gratefully acknowledged.

Supporting information for this article is available on the WWW under http://www.angewandte.org or from the author.

© 2006 Wiley-VCH Verlag GmbH & Co. KGaA, Weinheim

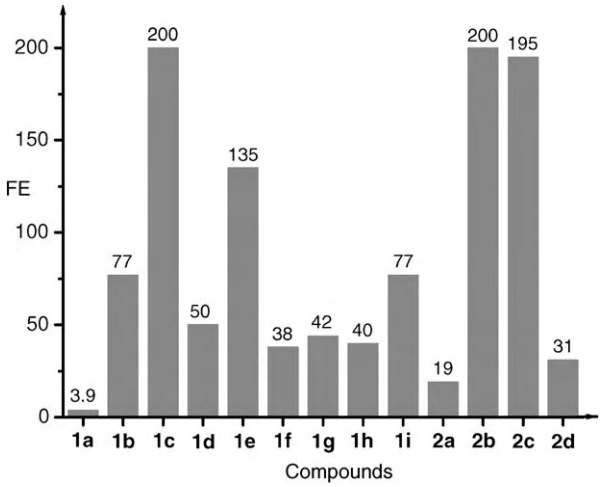

Figure 1. Protonation induced fluorescence enhancements in the studied coumaryl sensors (FE = fluorescence enhancement, I/I_0).

There is one sensor, **1c**, in which the nitrogen donor atom extinguishes the fluorescence so efficiently in the free sensor that the FE value, upon protonation, is 200.

As these data show, the signaling potential of the similar sensor molecules varies greatly with the size of the ring in which the nitrogen atom is settled. An explanation of the observed differences probably lies in understanding the conformational and orientational control of the dynamics of the electron-transfer process, an area little studied so far in related systems.[10]

We assumed that the outstanding signaling potential of **1c** was connected with the pyrrolidine ring as the key structural element, so the next set of experiments was aimed at establishing the influence of the conformational dynamics of the five-membered ring on the fluorescent signal. First, the analogue of **1c**, in which the mobility of the ring was practically frozen by introducing a condensed five-membered ring in the form of acetonide **2a**, was prepared. This simple change had a drastic effect on the signaling potential by reducing it to a tenth of its value (Figure 1; compare FE = 200 for **1c** with FE = 19 for **2a**). To prove that this is a conformational effect, the dimethoxy analogue of **2a** (**2b**) was also prepared and showed practically the same signaling potential (FE = 200) as that of the parent compound **1c**.

These findings imply the possibility of designing a sensor in which the methyl groups of sensor **2b** are replaced by a crown ether unit. This sensor, which is anticipated to show very weak fluorescence in the free state, could bind guest molecules by its crown ether part. We expected that the guest binding would decrease the conformational mobility of the macrocycle, and through it, the pyrrolidine ring. This in turn would reduce the involvement of the nitrogen atoms in the PET process and increase the fluorescent signal. To test this hypothesis, we prepared sensors **2c** and **2d** with 15- and an 18-membered crown ether receptor units, respectively, condensed to the pyrrolidine ring.[11] The signaling potential of the pyrrolidinocrown sensors, determined by protonation, showed a remarkable dependence on the size of the crown moiety (Figure 1). Although the incorporation of the [15]crown-5 moiety (**2c**) had a negligible effect on the donor properties of the pyrrolidine unit, the analogous [18]crown-6 compound (**2d**) showed a decreased signaling potential (compare FE = 195 for **2c** with FE = 31 for **2d**). This finding, which underlines the sensitivity of the donor ability of the nitrogen atom in the pyrrolidine ring to changes in the ring's conformational dynamics, was quite unexpected in light of the similar characteristics of the parent crown ether sensors **1g** (FE = 42) and **1h** (FE = 40).

Having established the signaling potential of the new sensor molecules **2c** and **2d**, we conducted a series of coordination experiments with different organic ammonium salts. Our selection included *n*-butyl- (**3a**), cyclohexyl- (**3b**), isopropyl- (**3c**), *tert*-butyl- (**3d**), and neopentylammonium perchlorate (**3e**) as guests. The choice of the amines was driven by our desire to have a set of guests with the same binding modes, but various steric demand. For complexation experiments, the parent sensors **1g** and **1h** were also included in the study. The measured fluorescence enhancement values for the different guest–sensor combinations are shown in Figure 2.[9]

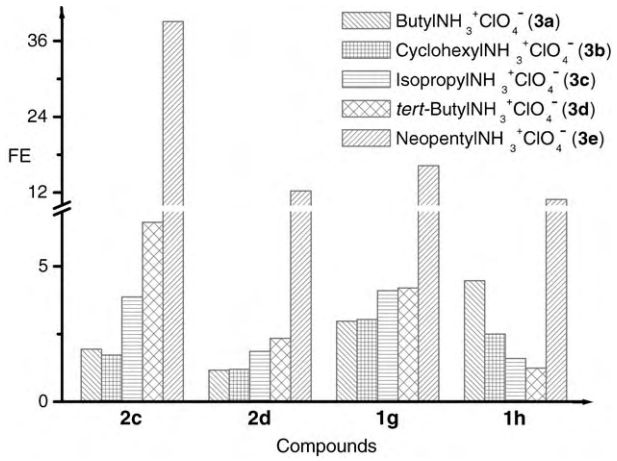

Figure 2. Enhancement of the fluorescent signal of sensors **2c, 2d, 1g**, and **1h** in the presence of different ammonium perchlorates **3a–e** (FE = fluorescence enhancement, I/I_0).

At first sight one can see that the pattern of fluorescence enhancements and measured values vary from sensor to sensor for the different ammonium salts. The first conclusion we could draw from these data by comparison of the FE values in the **2c** and **2d** series is that the guest in these sensors binds to the crown ether moiety, as expected. If the ammonium salts formed secondary interactions with the nitrogen atom in the pyrrolidine ring, or underwent acid–base reactions with the same site, we should have observed similar fluorescence enhancements for both sensors.

Both **2c** and **2d** react sensitively to the steric demand of the guest. Increasing the bulkiness of the ammonium ion resulted, in both series, in a marked signal enhancement particularly for neopentylammonium perchlorate (**3e**). Comparison of these data sets also reveals that the change in the conformational dynamics of the [15]crown-5-based sensor upon guest complexation exceeds changes with the

 © 2006 Wiley-VCH Verlag GmbH & Co. KGaA, Weinheim

[18]crown-6 analogue. This is evident by the measured signals for **2c** being usually twice as high as for **2d**.

By comparing the effect of the binding of ammonium ions **3a–e** to the parent sensor molecules **1g** and **1h**, one can also make some interesting observations. For the ammonium salts **3a–d**, the trend in the change of the observed fluorescence enhancements is opposite for the two sensors. Although the signal strength for the [15]crown-5 system (**1g**) increased with the steric demand of the ammonium salt, in the case of the [18]crown-6 sensor, we see a reverse variation. The highest signal was observed for **3a**, and **3d** gave the weakest signal. To rationalize these seemingly contradictory results one also has to consider the varying hydrogen-donor ability (acidity) of the ammonium salts, which decreases in the order of **3a–3d**. This might also be important on the grounds that, in these systems, the binding of the ammonium ion might include the direct interaction of the ammonium ion and the donor nitrogen atom that is responsible for signal generation. So, it is the combination of the dynamic effects (the sterically more demanding the ammonium ion, the more it decreases the mobility of the ring system) and the secondary interactions (the stronger the hydrogen donating ability of the ammonium ion, the more it depletes the electron density of the donor nitrogen atom) that determine the observed fluorescence enhancement. Although one can expect a similar contribution from the secondary interactions in both sensors, the results suggest that, in the case of the 15-membered crown ether (**1g**), the dynamic effects outweigh the secondary interactions in influencing the PET process. In the case of the 18-membered crown ether (**1h**), however, dynamic effects are less significant. This is also in agreement with our previous finding that sensor **2c**, which contains a 15-membered crown host, was more sensitive to the steric demand of the ammonium salts than **2d**, which contains an 18-membered ring. In the case of ammonium ions possessing an "extreme steric demand", such as **3e**, this factor becomes predominant and all sensors show outstanding fluorescence-enhancement values. The pyrrolidine-based dynamic sensor **2c** gave by far the highest signal (FE = 40).

A third interesting aspect of this study is the comparison of the parent sensors with the newly developed ones. We can state that sensors **2c** and **2d**, which use the effects invoked by changes in the conformational dynamics, in general are of comparable efficiency to the well-established parent sensors **1g** and **1h**. At the same time, however, they exhibit an increased sensitivity towards the size of the guest and a decreased sensitivity towards its hydrogen-donating ability. On the basis of the presented results, we can state that the change of conformational dynamics in molecular hosts during recognition processes can provide a significant contribution to the observed signal in PET sensors.[12] By establishing the influence of molecular flexibility on the fluorescent signal in PET sensors, we were able to tune this dynamics based signal to give comparable or even higher signal strengths than regular PET sensors. A potential advantage of this new sensor family is its enhanced sensitivity towards the steric demand of guests. We believe that the combination of the accumulated results on the PET sensors and the utilization of changes in conformational dynamics occurring during molecular recognition might lead to the development of more effective sensor molecules in the near future.

In summary, our studies directed at understanding the contribution of conformational dynamics to the signaling ability of sensor molecules revealed that the conformational mobility of the donor atom's surroundings has a profound effect on its signaling potential. Based on the obtained results, we implemented a new sensor design that uses the influence of conformational dynamics on the PET process and gives signals comparable to, or even greater than, conventional sensors. A salient feature of this new sensor class is its enhanced sensitivity towards the steric demand of guests. Besides leading to the introduction of a new sensor family, our study also underlines the important contribution of changes in the conformational dynamics in the working of common sensor families.

Received: December 6, 2005
Published online: March 15, 2006

Keywords: conformational dynamics · crown compounds · fluorescence · photoinduced electron transfer · sensors

[1] J. F. Callan, A. P. de Silva, D. C. Magri, *Tetrahedron* **2005**, *61*, 8551, and references therein.
[2] A. P. de Silva, H. Q. N. Gunaratne, T. Gunnlaugsson, A. J. M. Huxley, C. P. McCoy, J. T. Rademacher, T. E. Rice, *Chem. Rev.* **1997**, *97*, 1515.
[3] a) F. M. Raymo, *Adv. Mater.* **2002**, *14*, 401; b) A. P. de Silva, N. D. McClenaghan, *Chem. Eur. J.* **2002**, *8*, 4935.
[4] a) M. Cotlet, S. Masuo, G. Luo, J. Hofkens, M. van der Auweraer, J. Verhoeven, K. Müllen, X. S. Xie, F. De Schryver, *Proc. Natl. Acad. Sci. USA* **2004**, *101*, 14343; b) I. V. Sazanovich, C. Kirmaier, E. Hindin, L. Yu, D. F. Bocian, J. S. Lindsey, D. Holten, *J. Am. Chem. Soc.* **2004**, *126*, 2664.
[5] R. E. Gawley, S. Pinet, C. M. Cardona, P. K. Datta, T. Ren, W. C. Guida, J. Nydick, R. M. Leblanc, *J. Am. Chem. Soc.* **2002**, *124*, 13449.
[6] H. He, M. Mortellaro, M. J. P. Leiner, R. J. Fraatz, J. Tusa, *J. Am. Chem. Soc.* **2003**, *125*, 1468.
[7] H. He, M. Mortellaro, M. J. P. Leiner, S. T. Young, R. J. Fraatz, J. Tusa, *Anal. Chem.* **2003**, *75*, 549.
[8] P. Kele, J. Orbulescu, T. L. Calhoun, R. E. Gawley, R. M. Leblanc, *Tetrahedron Lett.* **2002**, *43*, 4413.
[9] Materials, methods, and measured FE values are available as Supporting Information.
[10] L. R. Khundkar, J. W. Perry, J. E. Hanson, P. B. Dervan, *J. Am. Chem. Soc.* **1994**, *116*, 9700.
[11] Although sensors **2c** and **2d** were synthesized in an enantiopure form, their potential for enantioselective recognition is not part of the presented study.
[12] There are two possible explanations for the effect exerted by conformational dynamics on the fluorescent signal. The first builds on the changes of the stochastic frequency and amplitude profile of intramolecular movements caused by covalent substitution, whereas the other advocates a change in the static equilibrium structure accompanying the supramolecular modification. At present, we presume that simple sensor molecules are better described by the first approach, whereas for the characterization of supramolecular complexes, the second approach might be more relevant. Experimental and modeling studies aimed at refining this picture are in progress.

 © 2006 Wiley-VCH Verlag GmbH & Co. KGaA, Weinheim

Nanostructures

DOI: 10.1002/anie.200504069

Dart-Shaped Tricrystal ZnS Nanoribbons**

Xia Fan, Xiang-Min Meng, Xiao-Hong Zhang,* Wen-Sheng Shi, Wen-Jun Zhang, Juan A. Zapien, Chun-Sing Lee, and Shuit-Tong Lee*

Structural parameters such as size and shape have a significant influence on the properties of nanostructures, and extensive efforts have been expended on controlling these parameters during synthesis.[1,2] Novel applications might emerge if complex nanocrystals, such as three-terminal ballistic junctions or Y-branch junctions,[3,4] and well-defined three-dimensional (3D) architectures could be synthesized in a controllable manner.[5–7] To date, the shape/morphology control typically relies on anisotropic nanocrystal nucleation and growth from a liquid medium. Another standard approach uses a static template and the differential growth rates of different crystal facets. This makes possible the controlled growth of branched inorganic nanostructures.[8,9] In comparison to the large amount of work on 1D nanostructures (wires and tubes), there are relatively few reports on 3D nanostructures. Recently, some special 3D architectures, such as comb-, windmill-, and tetrapod-like, and nanopropellor array structures, with nanometer and micrometer sizes have been observed in Group II–VI semiconductors (ZnO, CdS, CdSe, and ZnSe).[10–14]

ZnS, a wide direct-bandgap (3.68 eV at 300 K) II–VI semiconductor, has been considered as a promising material for the fabrication of blue electroluminescent (EL) diodes and lasers.[15,16] Many efforts have been made on the synthesis of 1D ZnS nanostructures,[17–22] which have unique properties for optical and electrical applications. We have reported the synthesis of ZnS bicrystal ribbons and explained their growth mechanism by combining the vapor–liquid–solid (VLS) and oxide-assisted growth (OAG) models.[23] More recently, Zhu et al.[24] reported the growth of ZnS architectures with core rods covered with a spine-type array. Herein, we report a simple thermal evaporation technique for the fabrication of a novel ZnS architecture made of three intersecting ribbons that form a dart-shaped tricrystal (DST) nanostructure.

The synthesis of dart-tail-like ZnS nanoribbons was carried out in a vacuum tube furnace. An alumina tube was mounted inside the tube furnace and used as the vacuum chamber. Trace SiO powder was placed at the center of the tube, and ZnS powder was placed 10 cm away (in the downstream direction) from the SiO powder. Si wafers in an alumina boat were placed near the downstream end of the tube, which was sealed and evacuated to a pressure of 2×10^{-5} Torr. The furnace was then heated to 1100 °C at a rate of approximately 10 °C min^{-1} and kept at this temperature for 4 h. Throughout the entire heating and cooling process, a constant flow of high-purity Ar premixed with 5 % H_2 was fed into the tube at a flow rate of 50 standard cubic centimeters per minute and a pressure of 30 Torr. After the furnace had cooled to room temperature, the white products deposited at around 900 °C on the inner wall of the alumina boat were collected and characterized by scanning electron microscopy (SEM; Hitachi S-4300FEG).

Figure 1 a reveals that the product is not primitive 1D rods, but consists of 3D objects with a complex dart-tail-like structure and a length of tens of micrometers. A high-magnification SEM image (Figure 1 b) clearly shows that the

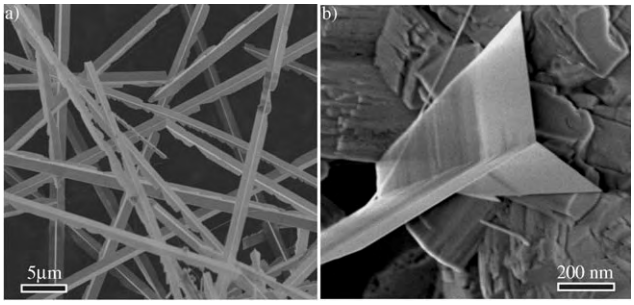

Figure 1. a) SEM image of the ZnS dart-shaped tricrystal (DST) synthesized by simple thermal evaporation. b) Enlarged SEM image of the end of a DST.

dart-tail-like structure is made of three intersecting ribbons sharing a common "spine" over the entire length of the structure, and each ribbon within this architecture has a width of 0.5–1 μm. Notably, the deposition product consists almost entirely of the DST structure. Nanostructures of other morphologies, such as particles, were seldom observed.

X-ray diffraction analysis shows that the product has the wurtzite (hexagonal) ZnS structure with lattice constants of $a = 0.382$ and $c = 0.626$ nm (JCPDS: 36-1450). No characteristic peaks from other impurities, such as ZnO and Si, can be detected from the XRD data, which suggests that the deposition product has high phase purity.

The detailed microstructure and composition of the product were characterized by transmission electron microscopy (TEM), selected-area electron diffraction (SAED), and

[*] Dr. X. Fan,[+] Prof. X.-M. Meng, Prof. X.-H. Zhang, Prof. W.-S. Shi, Prof. S.-T. Lee
Nano-organic Photoelectronic Laboratory
Technical Institute of Physics and Chemistry
Chinese Academy of Sciences, Beijing 100101 (P.R. China)
Fax: (+86) 10-6487-9375
E-mail: xmmeng@mail.ipc.ac.cn
xhzhang@mail.ipc.ac.cn
Dr. W.-J. Zhang, Dr. J. A. Zapien, Prof. C.-S. Lee, Prof. S.-T. Lee
Center of Super-Diamond and Advanced Films (COSDAF)
and Department of Physics and Materials Science
City University of Hong Kong, Hong Kong SAR (China)
[+] Also at: Graduate School of Chinese Academy of Sciences
Beijing 100039 (P.R. China)

[**] We thank the Chinese Academy of Sciences and the CAS–Croucher Funding Scheme for Joint Laboratories of the Croucher Foundation for financial support and the National Natural Science Foundation of China (No. 50572109). The work in Hong Kong was supported by the Research Grants Council of Hong Kong SAR, China, through a central allocation project (No. CityU 3/04C).

InterScience DISCOVER SOMETHING GREAT
© 2006 Wiley-VCH Verlag GmbH & Co. KGaA, Weinheim

energy-dispersive X-ray spectrometry (EDS). Figure 2a shows a bright-field image of the DST ZnS nanostructures, with three intersecting ribbons sharing a common spine over the entire length. Several tens of these structures have been examined, and most of them have a diameter of approximately 500 nm, while DSTs with a diameter up to 1 μm were occasionally observed. An arrow-shaped tip is shown in the upper right inset in Figure 2a. Figure 2b is a SAED pattern from the single DST nanoribbon marked by an arrow in Figure 2a. The pattern shows two sets of diffraction spots having a twin relationship with a common $(0\bar{1}3)$ plane, and each set can be indexed with a [131] axis of a wurtzite ZnS crystal. Figure 2c shows one end of a DST ZnS nanostructure, in which two branches stretch out their widest facets, while the third protrudes vertically on the common spine. Figure 2d is a high-resolution (HR) TEM image taken from the interface region of the two nonvertical branch ribbons in Figure 2c. It can be seen that the boundary is uniform and straight, and the angle between the two $(10\bar{1})$ planes of the two branch ribbons is around 109.5°.

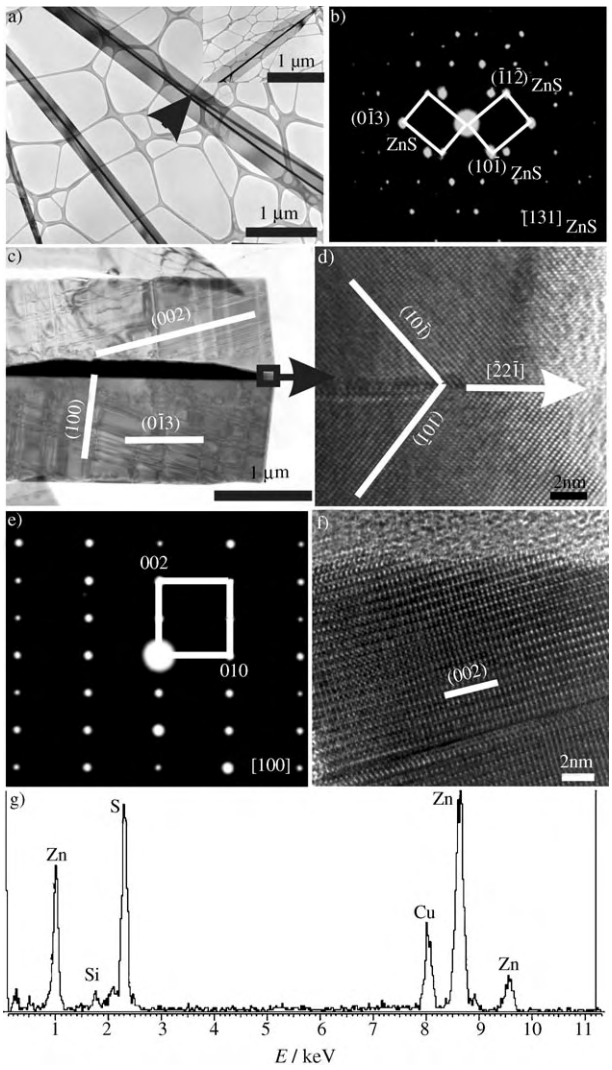

Figure 2. a) Bright-field TEM image of the dart-shaped nanoribbons. Inset: arrow-shaped tip. b) SAED pattern of the DST marked with a dark arrow in (a). c) Bright-field TEM image of the end of a DST. d) HRTEM image of the region marked with a rectangle in (c). e) SAED pattern and f) HRTEM image of the dart-shaped nanoribbon after tilting by an angle of 30°. g) EDS spectrum of a DST ribbon.

To obtain further structural information on the ribbons, the DST was analyzed in detail by a TEM tilting experiment. The SAED of one of the intersection ribbons reveals a single set of spots along the [100] zone axis of the wurtzite-2H ZnS structure (Figure 2e), which suggests that the flat surface of the ribbon is along the $(2\bar{1}0)$ plane. Figure 2f is an HRTEM image corresponding to Figure 2e, in which stacking faults can be seen along the (002) plane. The angle between the (002) plane and the edge of the nanoribbon is about 17°. The growth direction of the ribbon was determined to be $[\bar{2}2\bar{1}]$. Similar observations were obtained from the other ribbons in this and a couple of other DSTs.

Figure 2g is an EDS spectrum of a DST ZnS structure, which reveals the presence of Zn, S, Si, and O (the Cu signal comes from the TEM grid) with atomic ratios of 48:46:2:4. Together with the above results, we deduce that the DST structure consists of a ZnS wurtzite crystal with a trace amount of amorphous silicon oxide on the surface.

Figure 3 shows a typical photoluminescence (PL) spectrum of the synthesized ZnS DSTs measured at room temperature with Nd:YAG laser excitation at 266 nm. The spectrum with a peak centered at 332 nm is similar to that of ZnS nanowires.[21]

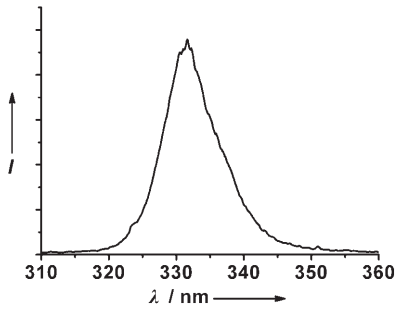

Figure 3. Room-temperature photoluminescence spectrum of the as-synthesized ZnS DSTs.

SEM investigation reveals several kinds of morphology of the ends of the DST ZnS nanostructures. Figure 4a shows a

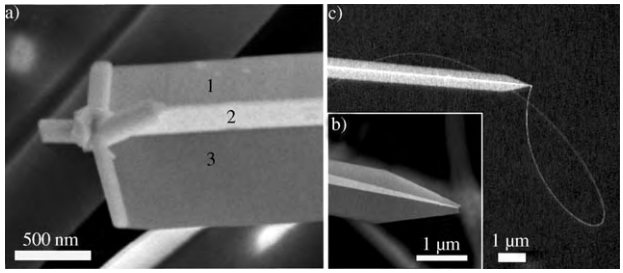

Figure 4. SEM images of ZnS DST nanoribbon: a) tip region, b,c) end region.

 © 2006 Wiley-VCH Verlag GmbH & Co. KGaA, Weinheim

DST nanoribbon with a tetrapod tail, which directly indicates the orientation relationship between three intersecting dart-shaped ribbons. Figure 4b shows an SEM image of the tip of a DST nanoribbon, whose size gradually decreases from body to tip. In Figure 4c, a single nanowire with [001] growth direction was found to grow from the tip of a DST nanoribbon.

In our experiment, the source is high-purity ZnS powder with a sphalerite structure which has a sublimation point of about 1020 °C. The growth direction of the DST is $[\bar{2}2\bar{1}]$, which is different from the [120] growth direction of ZnS nanoribbons synthesized by the vapor–solid (VS) method,[17] and from the [121] and [131] directions of ZnS bicrystalline nanoribbons and the [001] direction of ZnS nanowires synthesized by the VLS method.[21,22] Importantly, when SiO is removed, no DST structure can be formed.

The growth mechanisms of the present ZnS DST nanoribbons are not fully understood, and therefore a preliminary growth model is proposed here for discussion. On the basis of the present observations, a combination of two different processes, namely metal-catalyzed VLS growth and catalyst-free OAG,[14,25,26] is used to explain the growth of the DST structure. First, the ZnS source material reacts with H_2 in the carrier gas to form Zn and H_2S vapors. Concurrently, the SiO source sublimes to form SiO vapor. All vapors are then transported by the carrier gas to a low-temperature zone and deposited on the inner wall of the alumina boat. The SiO vapor reacts with O_2 (or H_2O) to form SiO_x vapor in the transport process. The mixture of Zn and SiO_x vapor forms liquid droplets of solid solution in the low-temperature region. The liquid droplets would continuously absorb more Zn, H_2S, and SiO_x from the vapor. Inside the droplets, Zn and H_2S react to form ZnS and H_2. SiO_x decomposes into SiO_2 and Si. When the concentrations of ZnS, Si, and SiO_2 reaches supersaturation with respect to the local temperature, ZnS would precipitate from the droplet and form the nanoscale ZnS core.

It has been reported that nuclei are often in the form of multiply twinned octahedrons during solidification of some hexagonal materials such as ZnO and ZnSe.[27,28] Self-organization in superstructures has also been proposed to explain the formation of unusual geometries in solutions such as PbSe.[29,30] It is believed that the present DST structure shares a similar initial nucleation mechanism to that of these tetrapod nanostructures. The ZnS would first precipitate as octahedrons (Figure 5a) composed of twinned crystals.[31] As a result of the polarity of ZnS, these octahedral nuclei would then grow along the fastest growth direction to form a nanoscale tetrapod (Figure 5b). When the tetrapod grows to a size similar to that of the original liquid droplet, surface tension would draw the tetrapod to the side of the liquid droplet. Effectively, the liquid droplet would now be captured by three legs of the tetrapod (Figure 5c). When more source vapors are absorbed into the liquid, precipitation of ZnS would continue by growth along the interface of the tetrapod and the liquid droplet. This would lead to the formation of the DST structure shown in Figure 5d. SiO_2 segregates from the droplet and wraps on the surface of the DST structure. Eventually, when the supply of the source vapors is terminated, further growth of the DST would reduce the size of the liquid droplet. These steps explain the gradual size reduction in the DST structure near the end (Figures 5e,f and 4b). Finally, the liquid droplet would become too small to support further growth of the DST. Depending on the local temperature, the tiny liquid droplet might simply solidify or grow into a nanowire (Figures 5g and 4c) according to the VLS mechanism.

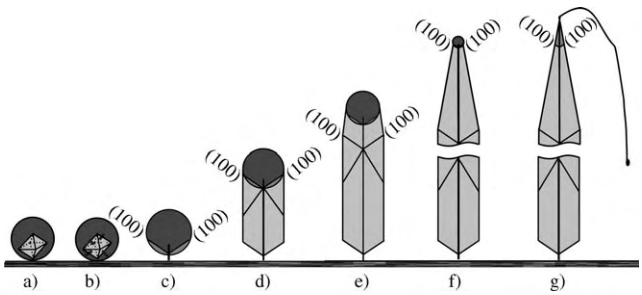

Figure 5. Schematic diagram of the growth mechanism of ZnS DST nanoribbons; see text for details.

In conclusion, dart-shaped ZnS semiconductor nanostructures made of three intersecting ribbons have been synthesized by a simple SiO-assisted thermal evaporation process. The tricrystalline ribbons have a wurtzite-2H structure. As-grown ZnS ribbons have lengths of several tens of micrometers, and each intersected ribbon within a DST structure has a width of 500 nm to 1 μm. The growth direction of the DST nanoribbons was observed to be $[\bar{2}2\bar{1}]$ of the ZnS wurtzite structure. The room-temperature PL spectrum of the DST nanostructure revealed a strong, sharp UV emission band at 332 nm. The mechanism of formation of the DST structures was explained by the production of tetrapod nuclei followed by growth at the interface of the tetrapod and the liquid catalyst.

Received: November 16, 2005
Revised: January 26, 2006
Published online: March 17, 2006

Keywords: crystal growth · electron microscopy · nanostructures · semiconductors · zinc

[1] A. P. Alivisatos, *Science* **1996**, *271*, 933.
[2] C. M. Lieber, *Solid State Commun.* **1998**, *107*, 607.
[3] K. Hieke, M. Ulfward, *Phys. Rev. B* **2000**, *62*, 16727.
[4] Rashmi, L. Bednarz, B. Hackens, G. Farhi, V. Bayot, I. Huynen, *Solid State Commun.* **2005**, *134*, 217.
[5] T. S. Ahmadi, Z. L. Wang, T. C. Green, A. Henglein, M. A. El-Sayed, *Science* **1996**, *272*, 1924.
[6] X. G. Peng, L. Manna, W. D. Yang, J. Wickham, E. Scher, A. Kadavanich, A. P. Alivisatos, *Nature* **2000**, *404*, 59.
[7] E. Shevchenko, D. Talapin, A. Kornowski, F. Wiekhorst, J. Kötzler, M. Haase, A. Rogach, H. Weller, *Adv. Mater.* **2002**, *14*, 287.
[8] J. Tanori, M. P. Pileni, *Langmuir* **1997**, *13*, 639.
[9] M. Li, H. Schnablegger, S. Mann, *Nature* **1999**, *402*, 393.
[10] L. Manna, D. J. Milliron, A. Meisel, E. C. Scher, A. P. Alivisatos, *Nat. Mater.* **2003**, *2*, 382.

 © 2006 Wiley-VCH Verlag GmbH & Co. KGaA, Weinheim

[11] H. Q. Yan, R. G. He, J. Johnson, M. Law, R. J. Saykally, P. D. Yang, *J. Am. Chem. Soc.* **2003**, *125*, 4728.
[12] C. Ma, D. Moore, J. Li, Z. L. Wang, *Adv. Mater.* **2003**, *15*, 228.
[13] J. Q. Hu, Y. Bando, D. Goldberg, *Small* **2005**, *1*, 95.
[14] P. X. Gao, Z. L. Wang, *Appl. Phys. Lett.* **2004**, *84*, 2883.
[15] P. Thioulouse, *J. Cryst. Growth* **1985**, *72*, 545.
[16] R. Nakano, H. Matsumoto, T. Endo, J. Shimada, N. Sakagami, N. Miura, *Jpn. J. Appl. Phys.* **1988**, *27*, L2103.
[17] Y. Jiang, X. M. Meng, J. Liu, Z. Y. Xie, C. S. Lee, S. T. Lee, *Adv. Mater.* **2003**, *15*, 323.
[18] Y. Jiang, X. M. Meng, J. Liu, Z. R. Hong, C. S. Lee, S. T. Lee, *Adv. Mater.* **2003**, *15*, 1195.
[19] J. Q. Hu, Y. Bando, J. H. Zhan, D. Goldberg, *Angew. Chem.* **2004**, *116*, 4706; *Angew. Chem. Int. Ed.* **2004**, *43*, 4606.
[20] O. Wu, N. Zheng, Y. Ding, Y. Li, *Inorg. Chem. Commun.* **2002**, *5*, 671.
[21] X. M. Meng, J. Liu, Y. Jiang, W. W. Chen, I. Bello, C. S. Lee, S. T. Lee, *Chem. Phys. Lett.* **2003**, *382*, 434.
[22] X. Fan, X. M. Meng, X. H. Zhang, S. T. Lee, S. K. Wu, *Appl. Phys. Lett.* **2005**, *86*, 173111.
[23] X. M. Meng, Y. Jiang, C. S. Lee, S. T. Lee, *Appl. Phys. Lett.* **2003**, *83*, 2244.
[24] Y. C. Zhu, Y. Bando, L. W. Yin, *Adv. Mater.* **2004**, *16*, 331.
[25] R. S. Wagner, W. C. Ellis, *Appl. Phys. Lett.* **1964**, *4*, 89.
[26] R. Q. Zhang, Y. Lifshitz, S. T. Lee, *Adv. Mater.* **2003**, *15*, 635.
[27] J. Q. Hu, Y. Bando, D. Golberg, *Small* **2005**, *1*, 95.
[28] Y. Dai, Y. Zhang, Z. L. Wang, *Solid State Commun.* **2003**, *126*, 626.
[29] K. S. Cho, D. V. Talapin, W. Gascher, C. B. Murray, *J. Am. Chem. Soc.* **2005**, *127*, 7140.
[30] Z. Y. Tang, N. A. Kotov, M. Giersig, *Science* **2002**, *297*, 237.
[31] S. Takeuchi, H. Iwanaga, M. Fujii, *Philos. Mag. A* **1994**, *69*, 1125.

 © 2006 Wiley-VCH Verlag GmbH & Co. KGaA, Weinheim

Selenium Microstructures

DOI: 10.1002/anie.200504131

Photothermally Assisted Solution-Phase Synthesis of Microscale Tubes, Rods, Shuttles, and an Urchin-Like Assembly of Single-Crystalline Trigonal Selenium**

*Bin Zhang, Wei Dai, Xingchen Ye, Fan Zuo, and Yi Xie**

Trigonal selenium (t-Se) is one of the most widely studied materials owing to its fundamental significance in theoretical studies and its potential applications in many fields.[1] Considerable effort has been devoted to generating selenium nanorods, nanowires, nanobelts, and nanowire networks by employing techniques such as laser ablation,[2] sonochemical approaches,[3] solution-mediated transformations,[4] refluxing,[5] hydrothermal methods,[6] CVD,[7] and biomolecule-assisted methods.[8] Recently, a great deal of attention has been focused on the synthesis of tubular selenium.[9] Ultralong Se microtubes were recently fabricated by a one-step solution-phase method in our group,[10] and we also found that the morphology of the selenium products has a remarkable influence on their capacity for electrochemical hydrogen storage,[10] which inspired us to search for a simple, inexpensive, and efficient approach to the morphology-controlled synthesis of Se nanostructures/microstructures, especially those with novel and interesting morphologies.

Recently, photochemical and irradiation synthesis has proven to be a promising route for the preparation of various nanomaterials. These simple processes yield uniform products while the growth mechanism of the resulting materials can be resolved conveniently.[11–14] Current photochemical methods focus mainly on the use of UV light. For instance, Yang et al. have successfully prepared uniform gold nanorods upon UV irradiation,[11] and the morphology-controlled synthesis of Au nanorods has also been realized in a combined chemical reduction/UV photochemical approach.[12] γ-Irradiation from a ^{60}Co source has been used in the preparation of semiconductor/polymer nanocables and Ag/Pt alloy nanoparticles.[14] It is therefore important to design a safer, cheaper, and more convenient light-assisted approach to 1D nanomaterials/micromaterials.

As for the solution-phase synthesis of trigonal selenium materials, the transformation of amorphous Se (a-Se) into t-Se is still considered to be an important step.[1,3–6,9–11] Ishida et al. have reported, on the basis of Raman spectrocopic obeservations, that laser light with a wavelength of 633 nm can induce the anisotropic crystallization of a-Se, which then forms t-Se.[15] Thus, it is reasonable to assume that visible light (380–800 nm) should also be able to accelerate the transformation of a-Se into t-Se. In this communication, we report the first facile one-step method for the controlled synthesis of single-crystalline Se 1D microstructures upon irradiation with visible light from a commercial lawn lamp in the presence of poly(vinylpyrrolidone) (PVP, K-30). Selenium microtubes, nanorods, novel shuttle-like needles, and urchin-like assemblies of selenium nanorods can be fabricated on a large scale by varying the experimental parameters. The photo and thermal effects of visible light are thought to be significant in this morphology-controlled synthesis of Se materials. In addition, we demonstrate that the selenium microtubes and microshuttles have distinctly different electrochemical hydrogen-storage capacities.

Various selenium materials with unusual morphologies can be synthesized in this visible-light-assisted approach by controlling the relative amounts of SeO_2 and PVP. The as-prepared products were first examined by field emission scanning electron microscopy (FESEM; Figure 1). When a mixture of 0.1 g of SeO_2 and 0.01 g of PVP was illuminated with a lawn lamp (see the Supporting Information), the samples obtained were found to contain Se microtubes with a

[*] Dr. B. Zhang, W. Dai, X. Ye, F. Zuo, Prof. Y. Xie
Department of Nanomaterials and Nanochemistry
Hefei National Laboratory for Physical Sciences at Microscale
University of Science and Technology of China
Hefei, Anhui 230026 (P.R. China)
Fax: (+86) 551-360-3987
E-mail: yxie@ustc.edu.cn

[**] This work was supported by the National Nature Science Foundation (NSF) of China.

Supporting Information for this article is available on the WWW under http://www.angewandte.org or from the author.

 © 2006 Wiley-VCH Verlag GmbH & Co. KGaA, Weinheim

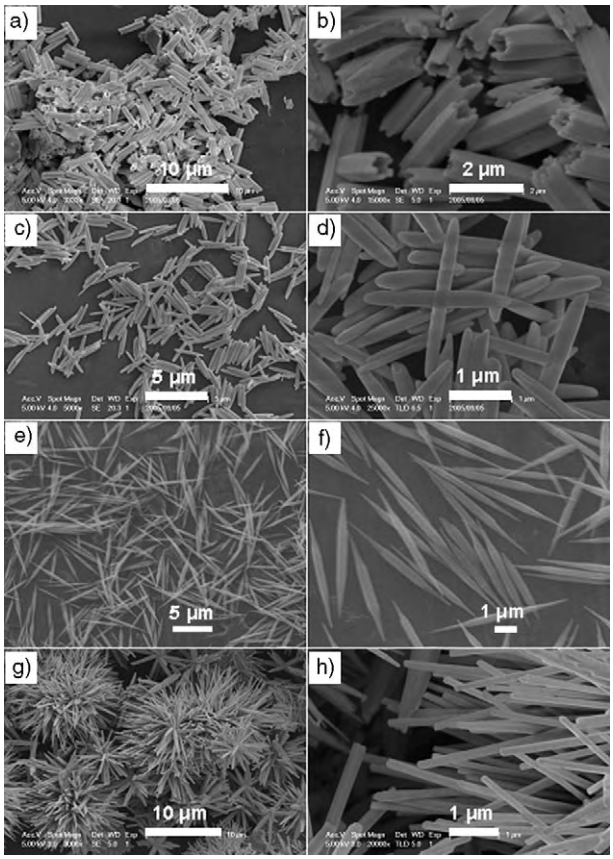

Figure 1. FESEM images of four selenium samples with different morphologies prepared from different amounts of SeO_2 and PVP: microtubes (0.1 g SeO_2 + 0.01 g PVP) (a and b); microrods (0.1 g SeO_2 + 0.05 g PVP) (c and d); microshuttles (0.1 g SeO_2 + 0.005 g PVP) (e and f); urchin-like assembly of selenium nanorods (0.05 g SeO_2 + 0.01 g PVP) (g and h).

uniform size distribution, as shown by the low-magnification FESEM image (Figure 1a). The FESEM image at higher magnification (Figure 1b) clearly shows the products' tubular structure, with a diameter of 900 nm and a length of about 2.5 μm. When the amount of PVP was increased to 0.05 g, with the other conditions remaining unchanged, selenium microrods were obtained; some cross-like rod structures could also be observed in the final products (Figure 1c and d). As shown in Figure 1e and f, shuttle-like t-Se, which has not been observed in previous reports, was obtained when only 0.005 g of PVP was used. These shuttles are about 6.5 μm long and end in two very sharp tips. Interestingly, selenium nanorods with a diameter of 160 nm assembled spontaneously to form a novel urchin-like shape (Figure 1g and h), which has not been reported in previous approaches, when the amount of SeO_2 was decreased to 0.05 g with other conditions remaining unchanged. The successful preparation of these abundant and new Se morphologies suggests that this visible-light-assisted approach could be applied to synthesize Se, Te, and other anisotropic materials with novel morphologies.

The XRD pattern and the Raman and EDAX spectra of the as-prepared products identifies them as trigonal selenium of high crystallinity and purity (see the Supporting Information). The morphology and structure of the Se microshuttles were further characterized by TEM and selected-area electron diffraction (SAED). Figure 2a display the TEM images of the obtained selenium shuttles, which reveal that the ends of the shuttle-like samples are very sharp. The indexing of the spots in the SAED pattern (Figure 2b) and HRTEM observations (Figure 2c and d) indicate that the microshuttle is a single crystal that grows predominantly along the [001] direction (*c* axis).

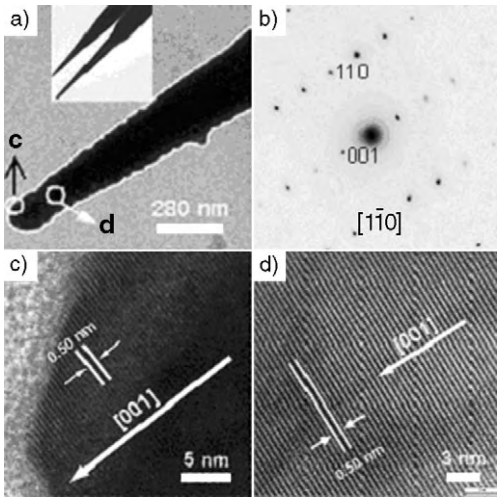

Figure 2. a) TEM image of one t-Se microshuttle. The inset shows the low-magnification TEM image. b) The associated SAED pattern. The [1$\bar{1}$0] zone axis of the trigonal selenium microshuttle is identified, thus indicating the preferential growth along the [001] direction. (c and d) HRTEM images of different areas (indicated in a) of an individual shuttle. The fringe spacing of 0.5 nm observed in this image corresponds to the separation of the (001) lattice planes.

To determine the role of light and heat in the formation of these selenium materials we performed a series of control experiments in which the amount of the reagents was controlled to be identical to that of the microtubes, unless otherwise stated. In this approach, we found that the solution-phase temperature was about 100 °C when a 500-W lawn lamp was used (the intensity of the light shining on the reaction mixture was around 340 mW cm^{-2}). Therefore, to clarify the role of the light a conventional reflux technique was applied to the four different solution systems, but only broken selenium tubes (Supporting Information) were obtained when refluxing the solution with different amounts of SeO_2 and PVP, which are obviously different from the microtubes, microrods, microshuttles, and urchin-like assemblies of nanorods obtained with the visible-light-assisted technique (Figure 1).

We also found that refluxing the reaction mixtures gave only small differences in the products' morphologies for different amounts of SeO_2 and PVP (Supporting Information). In contrast, the morphology obtained is very sensitive to the amount of SeO_2 and PVP in the photothermally assisted method (Figure 1). This indicates that the visible light from the lawn lamp induces and greatly enhances the directing role of PVP in the preparation of selenium materials. Moreover, we found that only Se particles were obtained when the

 © 2006 Wiley-VCH Verlag GmbH & Co. KGaA, Weinheim

reaction mixture was irradiated with an ultrahigh-pressure mercury lamp of an ultraviolet spot curing system (HG-250, Mejiro Precision Inc.), which confirms the critical role of thermal effects in controlling the morphology. This conclusion is also supported by the formation of broken multi-armed tubes and Se particles (Figure 3a) when the light intensity of the lawn lamp was decreased from 340 to 210 mW cm^{-2} (the power of the lamp was decreased from 500 to 300 W).

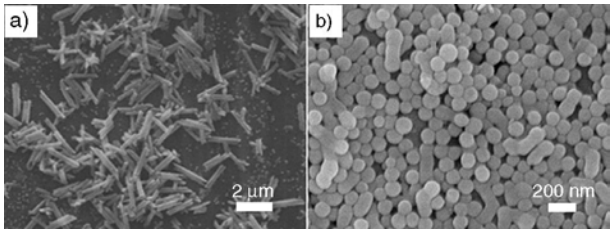

Figure 3. SEM images of selenium samples prepared by other methods: a) mixture of broken multi-armed tubes and Se particles synthesized by illumination with a lawn lamp at 210 mW cm^{-2}; b) uniform selenium spheres fabricated by gamma irradiation.

When the same system was irradiated with γ-radiation from a 2.59×10^{15} Bq ^{60}Co γ-ray source with a dose of 30 kGy, the brick-red products obtained were found to be uniform amorphous selenium spheres (Figure 3b). Thus, our visible-light-assisted approach is obviously different from both the conventional refluxing technique and the reported methods that require UV or γ-ray irradiation. We suppose that photoirradiation and thermal effects contribute simultaneously to the controlled synthesis of Se tubes, rods, shuttles, and urchin-like assemblies. As for the role of light, we assume that it accelerates the transformation of a-Se into t-Se and that it orients the growth along the *c* axis of t-Se. In fact, besides the laser-induced anisotropic crystallization of a-Se,[15a] a similar anisotropic crystallization of selenium has been observed when investigating the Raman spectrum of an amorphous selenium film.[16] We therefore decided to carry out a Raman analysis of our amorphous Se intermediates to confirm that visible light can also accelerate the transformation of a-Se into t-Se (Supporting Information). It is reasonable to assume that visible light breaks covalent bonds[15,16] in our approach and makes the products grow along the *c*-axis, but further investigations are necessary.

Although the exact mechanism of the photothermally assisted morphology-controlled preparation of t-Se 1D structures is still unclear, the directing role of PVP is undoubtedly significant. In the absence of PVP, only sphere-like Se particles were synthesized rather than 1D Se materials. As discussed above, tube-like, rod-like, shuttle-like, and urchin-like selenium materials can be fabricated by adjusting the ratio of SeO_2 to PVP, which suggests the key role of PVP in controlling the Se products' shape. Furthermore, intersecting, needle-like selenium was obtained (Supporting Information) when PVP was replaced by the nonionic surfactant polyoxyethylene (20) sorbitan monolaurate (Tween-20). However, under hydrothermal conditions no needle-like selenium was obtained when Tween-20 was adopted as the capping agent.[12] This further testifies that PVP or other surfactants may exhibit more significant directing roles upon illumination with visible light, and that this photothermally assisted technique is a better way of synthesizing selenium materials with new morphologies. Our preliminary TEM observations of the intermediates have also shown that Se nanostructures/microstructures experience an Ostwald-type ripening during the conversion of a-Se into t-Se and the following nucleation and growth process, similar to what Xia et al. have proposed for other Se and Te systems (Supporting Information).[1a,b,17]

Interestingly, our electrochemical study demonstrated that the discharge capacity of Se microtubes is higher than that of shuttle-like selenium and that the morphology of the selenium products exerts a noticeable influence on the electrochemical hydrogen storage ability (Supporting Information).

In summary, a facile photothermally assisted solution-phase approach has been developed for the synthesis of selenium micromaterials. Tubular, rod-like, and shuttle-like Se as well as an urchin-like assembly of selenium nanorods can be synthesized on a large scale by varying the relative amounts of SeO_2 and PVP. Both light and thermal effects play significant roles in this visible-light-assisted technique. We have observed that the light from a lawn lamp can induce and enhance the directing role of PVP in the morphology-controlled synthesis of selenium materials. In addition, the electrochemical hydrogen-storage capacity has been demonstrated to be susceptible to the morphology of the Se materials. Although detailed investigations concerning the exact photothermal role and the growth mechanism and hydrogen-storage process are still in progress, this novel approach can be potentially extended to fabricate 1D nanostructures/microstructures of Te and other anisotropic materials with interesting morphologies in the presence of PVP or other surfactants. Furthermore, the preparation and electrochemical studies of Se materials with different shapes will offer great opportunities to explore the dependence of the properties of the material on its morphology and be essential for the subsequent manufacture of potential optoelectronic devices.

Experimental Section

All chemicals were of analytical grade and were used as received. In a typical procedure, a given amount of poly(vinylpyrrolidone) (PVP, K-30) and hydrazine hydrate ($N_2H_4 \cdot H_2O$, 85%, 1 mL) were added to distilled water (50 mL) and the mixture was dispersed to form a homogeneous solution by constant strong stirring. Then, distilled water (50 mL) containing a given amount of SeO_2 was quickly added dropwise to the above solution at room temperature, and the solution quickly became orange-yellow. Once the solution had turned salmon pink (about 30 min), the mixture was irradiated for 6 h with visible light from a commercial lawn lamp (halogen bulb) at a distance of 5 cm (340 mW cm^{-2}). The black precipitate was collected and washed three times each with distilled water and absolute ethanol. The sample was then dried in vacuo at 50 °C for six hours. The XRD, Raman, SEM, TEM, and EDAX apparatus and the electrochemical measurements are described in the Supporting Information.

Received: November 21, 2005
Revised: January 5, 2006
Published online: March 17, 2006

 © 2006 Wiley-VCH Verlag GmbH & Co. KGaA, Weinheim

Keywords: materials science · microstructures · selenium · semiconductors

[1] a) B. Gates, B. Mayers, B. Cattle, Y. N. Xia, *Adv. Funct. Mater.* **2002**, *12*, 219; b) B. Gates, Y. D. Yin, Y. N. Xia, *J. Am. Chem. Soc.* **2000**, *122*, 12582; c) X. C. Jiang, B. Mayers, T. Herricks, Y. N. Xia, *Adv. Mater.* **2003**, *15*, 1740; d) B. Mayers, X. C. Jiang, D. Sunderland, B. Cattle, Y. N. Xia, *J. Am. Chem. Soc.* **2003**, *125*, 13364; e) S. Nath, S. K. Ghosh, S. Panigahi, T. Thundat, T. Pal, *Langmuir* **2004**, *20*, 7880.
[2] Z. Y. Jiang, Z. X. Xie, S. Y. Xie, X. H. Zhang, R. B. Huang, L. S. Zheng, *Chem. Phys. Lett.* **2003**, *368*, 425.
[3] B. T. Mayers, K. Liu, D. Sunderland, Y. N. Xia, *Chem. Mater.* **2003**, *15*, 3825.
[4] a) B. Cheng, E. T. Samulski, *Chem. Commun.* **2003**, 2024; b) Z. Y. Tang, Y. Wang, K. Sun, N. A. Kotov, *Adv. Mater.* **2005**, *17*, 358.
[5] B. Gates, B. Mayers, B. Cattle, Y. N. Xia, *Adv. Funct. Mater.* **2002**, *12*, 219.
[6] Z. H. Wang, X. Y. Chen, J. W. Liu, X. G. Yang, Y. T. Qian, *Inorg. Chem. Commun.* **2003**, *6*, 1329.
[7] a) L. Ren, H. Z. Zhang, P. H. Tan, Y. F. Chen, Z. S. Zhang, Y. Q. Chang, J. Xu, F. H. Yang, D. P. Yu, *J. Phys. Chem. B* **2004**, *108*, 4627; b) X. B. Cao, Y. Xie, S. Y. Zhang, F. Q. Li, *Adv. Mater.* **2004**, *16*, 649; c) X. B. Cao, Y. Xie, L. Y. Li, *Adv. Mater.* **2003**, *15*, 1914.
[8] B. Zhang, X. C. Ye, W. Dai, W. Y. Hou, F. Zuo, Y. Xie, *Nanotechnology* **2006**, *17*, 385.
[9] a) H. Zhang, D. R. Yang, Y. J. Ji, X. Y. Ma, J. Xu, D. L. Que, *J. Phys. Chem. B* **2004**, *108*, 1179; b) S. Y. Zhang, J. Zhang, Y. Liu, X. Ma, H. Y. Chen, *Electrochim. Acta* **2005**, *50*, 4365; c) Y. R. Ma, L. M. Qi, J. M. Ma, H. M. Cheng, *Adv. Mater.* **2004**, *16*, 1023.
[10] B. Zhang, W. Dai, X. C. Ye, W. Y. Hou, Y. Xie, *J. Phys. Chem. B* **2005**, *109*, 22830.
[11] F. Kim, J. H. Song, P. D. Yang, *J. Am. Chem. Soc.* **2002**, *124*, 14316.
[12] Y. Niidome, K. Nishioka, H. Kawasaki, S. Yamada, *Chem. Commun.* **2003**, 2376.
[13] D. Cheng, X. Zhou, H. Xia, H. S. O. Chan, *Chem. Mater.* **2005**, *17*, 3578.
[14] a) Y. Xie, Z. Qiao, M. Chen, X. Liu, Y. Qian, *Adv. Mater.* **1999**, *11*, 1512; b) C. M. Doudna, M. F. Bertino, F. D. Blum, A. T. Tokuhiro, D. Lahiri-Dey, S. Chattopadhyay, J. Terry, *J. Phys. Chem. B* **2003**, *107*, 2966.
[15] a) K. Ishida, K. Tanaka, *Phys. Rev. B* **1997**, *56*, 206; b) V. Lyubin, M. Klebanov, M. Mitkova, T. Petkova, *Appl. Phys. Lett.* **1997**, *71*, 2118.
[16] a) S. N. Yannopoulos, K. S. Andrikopoulos, *J. Chem. Phys.* **2004**, *121*, 4747; b) V. V. Poborchii, A. V. Kolobov, K. Tanaka, *Appl. Phys. Lett.* **1999**, *74*, 215; c) V. V. Poborchii, A. V. Kolobov, K. Tanaka, *Appl. Phys. Lett.* **1998**, *72*, 1167.
[17] a) B. Mayers, Y. N. Xia, *Adv. Mater.* **2002**, *14*, 279; b) B. Mayers, Y. N. Xia, *J. Mater. Chem.* **2002**, *12*, 1875.

 © 2006 Wiley-VCH Verlag GmbH & Co. KGaA, Weinheim

Synthesis Design

DOI: 10.1002/anie.200503551

From Polymer to Size-Defined Oligomers: An Expeditious Route for the Preparation of Chondroitin Oligosaccharides**

*Chrystel Lopin and Jean-Claude Jacquinet**

Chondroitin sulfates are structurally complex, polyanionic, microheterogeneous, linear polysaccharides belonging to the glycosaminoglycan family. They are ubiquitous components of the extracellular matrix of all connective tissues, but are also found on mammalian cell surfaces and in neural tissues.[1] They are copolymers made of dimeric units composed of D-glucuronic acid (GlcA) and 2-acetamido-2-deoxy-D-galactose (GalNAc) arranged in the sequence $[\rightarrow 4)$-β-D-GlcA-$(1\rightarrow 3)$-β-D-GalNAc-$(1\rightarrow]_n$, and contain on average one sulfate group per disaccharide unit, but other types with sulfate(s) at various positions are also known. These sulfation patterns give rise to numerous biologically important functions, such as cell–cell recognition,[2] brain development and regeneration,[3] or binding to selectins,[4] and many other that are not completely deciphered at the molecular level. Unfortunately, structurally defined oligosaccharide fragments of chondroitin and its sulfo forms are not easily prepared, even though they are in great demand. Thus, rapid and efficient methods for the preparation of chondroitin sulfate oligomers are critical to advance our understanding of this important class of biomolecules. Synthetic approaches should ideally provide ready access and involve a small number of steps. Several syntheses of chondroitin sulfate oligosaccharides have recently been reported,[5] all starting from monomeric units. Since D-GalNAc is a rare and somewhat expensive sugar, its derivatives have been generally prepared by long routes. In a continued effort to try to reduce the number of transformations in a multistep procedure, we turned our attention towards the possible chemical hydrolysis of chondroitin sulfate polymers. These compounds are abundant and readily available, and were formerly mainly obtained from bovine cartilage. However, the discovery of bovine spongiform encephalopathy has meant that they cannot be used anymore, at least for medical purposes. Commercial products are now obtained from cartilage of marine origin (shark, skate), and

[*] Dr. C. Lopin, Dr. J.-C. Jacquinet
Institut de Chimie Organique et Analytique—UMR CNRS 6005
Faculté des Sciences
Université d'Orléans, BP 6759
45067 Orléans Cedex (France)
Fax: (+33) 2-3841-7281
E-mail: jean-claude.jacquinet@univ-orleans.fr

[**] This research was supported by the "Programme National de Recherche sur les Maladies Ostéoarticulaires" (INSERM Pro-A 0401) and by the Action Concertée Incitative "Mécanismes Fondamentaux des Maladies" (BCMS 0152).

Supporting information for this article is available on the WWW under http://www.angewandte.org or from the author.

WILEY InterScience DISCOVER SOMETHING GREAT
© 2006 Wiley-VCH Verlag GmbH & Co. KGaA, Weinheim

they should constitute an attractive starting material for organic chemists.

Since the pioneering works of Levene[6] and of Davidson and Meyer[7] on the structure of chondroitin sulfates, chondrosine, the basic repeating unit of chondroitin sulfates, can be obtained by acid hydrolysis of the polymer, a process that also results in desulfation and N-deacetylation of the resulting disaccharide. This product contains a number of attractive features. Besides its backbone, which still possesses D-GlcA and D-GalNH$_2$ arranged in the correct manner, there is an interesting possibility to substitute the free amine group with a powerful stereocontrolling auxiliary such as a trichloroacetyl group,[8] a process that was used successfully for the synthesis of chondroitin sulfate oligosaccharides.[9] We thus reinvestigated and improved the protocol devised by Davidson and Meyer, and the known[7] methyl ester **1** (Scheme 1)

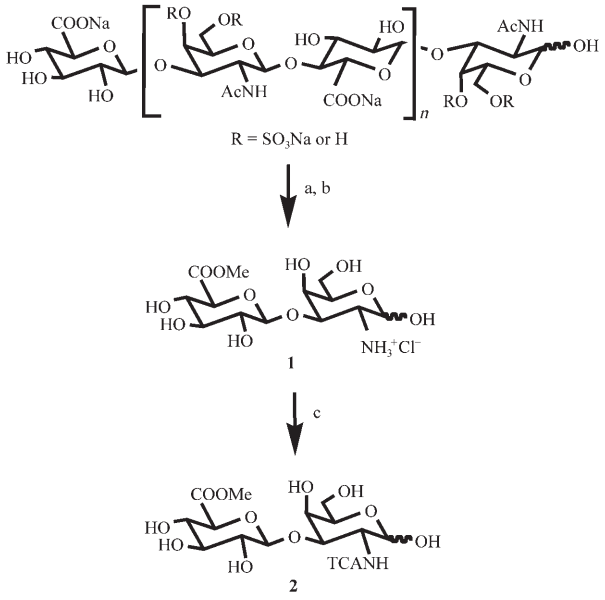

Scheme 1. Preparation of building block **2**. Reagents and conditions: a) IR-120 [H$^+$] resin, H_2O; then 0.5 M H_2SO_4, 100 °C, 6 h; b) AcCl, MeOH, 0 °C, 72 h; c) Cl_3CCOCl, pyridine, 0 °C, 4 h; then CH_2Cl_2/MeOH/pyridine, room temperature, 3 h. TCA = trichloroacetyl.

was obtained in good yield. Attempted chemoselective N-trichloroacetylation of **1** failed, but trichloroacetamide **2** was readily obtained through O,N-pertrichloroacetylation followed by selective solvolysis of the trichloroacetate esters.

Unfortunately, acetylation of **2** was troublesome (Scheme 2), and variation of the conditions (acetylating reagent, solvent, temperature) led systematically to mixtures of pyranose **3** and furanose **4** in an approximately 3/1 ratio. This result is not a surprising[10] outcome in the D-galacto series as a consequence of the unfavorable interaction of the 4-axial hydroxy group in the pyranoid derivative. To avoid this ring equilibrium, **2** was first treated with benzaldehyde and trifluoroacetic acid under thermodynamic control to lock the galactosamine unit in the pyranose conformation through formation of a 4,6-benzylidene acetal, and then was peracetylated in situ to give **5**. Mild acid hydrolysis of **5** followed by

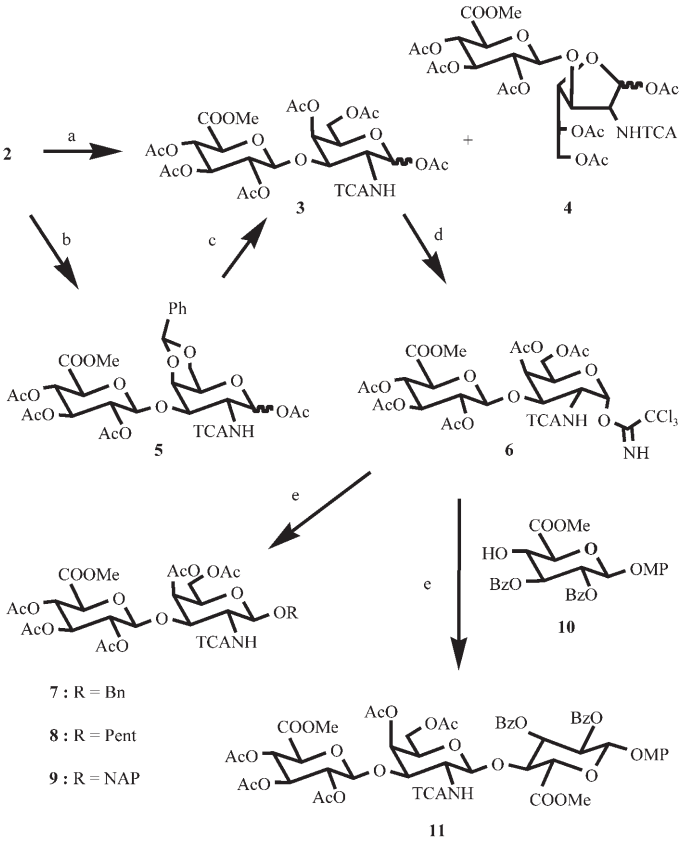

Scheme 2. Synthesis of glycosides **7**–**9** and **11**. Reagents and conditions: a) Ac_2O, pyridine, 0 °C, 8 h; b) PhCHO, TFA, 24 h; then Ac_2O, pyridine, room temperature, 16 h, 72%; c) 75% TFA, CH_2Cl_2, 0 °C, 4 h; then Ac_2O, pyridine, room temperature, 6 h, 78%; d) hydrazine acetate, DMF, 30 min; then Cl_3CCN, DBU, CH_2Cl_2, 30 min, 70%; e) alcohol, TMSOTf, CH_2Cl_2, 30 min, 80–90%. Bn = benzyl, Pent = pentenyl, NAP = 2-naphthylmethyl, MP = 4-methoxyphenyl, TFA = trifluoroacetic acid, DMF = *N*,*N*-dimethylformamide, DBU = 1,8-diazabicyclo-[5,4,0]undec-7-ene, TMSOTf = trimethylsilyl trifluoromethanesulfonate.

acetylation gave exclusively **3** in good yield. Removal of the 4,6-benzylidene acetal on **5** is a prerequisite since it has been demonstrated[11] that derivatives in the D-galacto series locked in an activated 4,6-acetal arrangement, despite the presence of a participating group at C-2, led to mixtures of glycosides in which the 1,2-*cis* species were predominant. The peracetate **3** was then transformed in two steps into the crystalline α-trichloroacetimidate **6**. The glycosylating power of **6** was then tested towards a set of alcohols. The coupling of imidate **6** with benzyl alcohol, 4-pentenol, 2-naphthylmethanol, and the poorly reactive **10**[12] in the presence of a trimethylsilyl triflate catalyst gave exclusively the corresponding 1,2-*trans*-glycosides **7**–**9** and **11** in excellent yields.

A block approach was designed for the construction of oligomers in which crucial coupling reactions were achieved by using Schmidt's trichloroacetimidate glycosylation procedure.[13] The 2-naphthylmethyl (NAP)-substituted glycoside **9** was selected as a starting material since the NAP group[14] should be retained after deprotection of the other hydroxy groups and serve as a fluorophore in biological assays or easily removed to afford reducing species—both useful tools

 © 2006 Wiley-VCH Verlag GmbH & Co. KGaA, Weinheim

for the preparation of microarrays. Transesterification of **9** (Scheme 3) followed by acetalation with 2-methoxypropene and CSA under kinetic control gave the crystalline bisacetal **12** together with a small amount of its 3′,4′ isomer, which was easily recycled by acid hydrolysis. Levulinoylation of **12** gave **13**, which was submitted to mild acid hydrolysis and acetylation to afford the crystalline key intermediate **14**. This was then transformed into either acceptor **15** through selective cleavage of the levulinoyl group or crystalline donor **16** by treatment with DDQ[15] followed by imidoylation. Coupling of alcohol **15** with donor **16** in the presence of a TMSOTf catalyst gave the crystalline tetrasaccharide derivative **17**, which was readily transformed into acceptor **18** in good yield. Further coupling of **18** with imidate **6** or **16** under the same conditions gave hexasaccharide derivatives **19** and **20**, respectively, in 65% yield. Deprotection of **19** was achieved through transformation of the *N*-trichloroacetyl groups into their *N*-acetyl congeners by radical reduction with tributylstannane[8] followed by a two-step saponification with lithium hydroperoxide[16] and sodium hydroxide, to give the target hexasaccharide glycoside **21** in good yield. Thus, an efficient route is now open for the preparation of size-defined chondroitin oligomers containing a fluorescent glycoside as useful probes for the study of the biosynthesis as well as the polymerization of chondroitin sulfate chains.

The possibility was next examined of differentiating each sugar unit so as to prepare the way for the synthesis of chondroitin sulfo forms with important biological functions. Another route was explored in which the more economical 4-methoxyphenyl group was used as a temporary protection at the anomeric reducing center. Surprisingly, the attempted coupling of **3** or **6** with 4-methoxyphenol under various conditions led to anomeric mixtures of glycosides ($\beta \approx \alpha \approx 2:1$). Since anomerization of the β-glycoside was not observed in the reactions, this lack of stereoselectivity was attributed to the 2-deoxy-2-trichloroacetamido group participating too slowly, possibly as a result of the presence of the bulky group at O-3 which prevents a rapid change in the conformation of the D-galacto unit. To overcome this problem, the trichloromethyl oxazoline **22** (Scheme 4) was prepared directly from **3** by using a protocol reported for the D-gluco series.[8] Indeed, reaction of **22** with 4-methoxyphenol in the presence of TMSOTf at 0°C gave exclusively the β-glycoside **23** in excellent yield. It is to be noted that the NAP-substituted glycoside **9** could be obtained from **3** in 80% overall yield via **22**. Glycoside **9** was finally selected as a starting material on the basis of its accessability and because of the greater solubility of its derivatives compared to those of its 4-methoxyphenyl analogues. Transesterification of **9** followed by 4,6-benzylidene formation, 2′,3′-isopropylidenation, and 4′-levulinoylation, as reported previously, gave the intermediate **24** in 56% overall yield. Interestingly, the 2′,3′-isopropylidene acetal on **24** could be selectively removed in the presence of the 4,6-benzylidene group through mild acid hydrolysis to give the crystalline diol **25** in 79% yield. Variants in which the D-GalNAc moiety was sulfated were planned to be synthesized later on from the common precursor **31**, in which benzoate esters were selected as permanent protection for hydroxy groups that were not to be

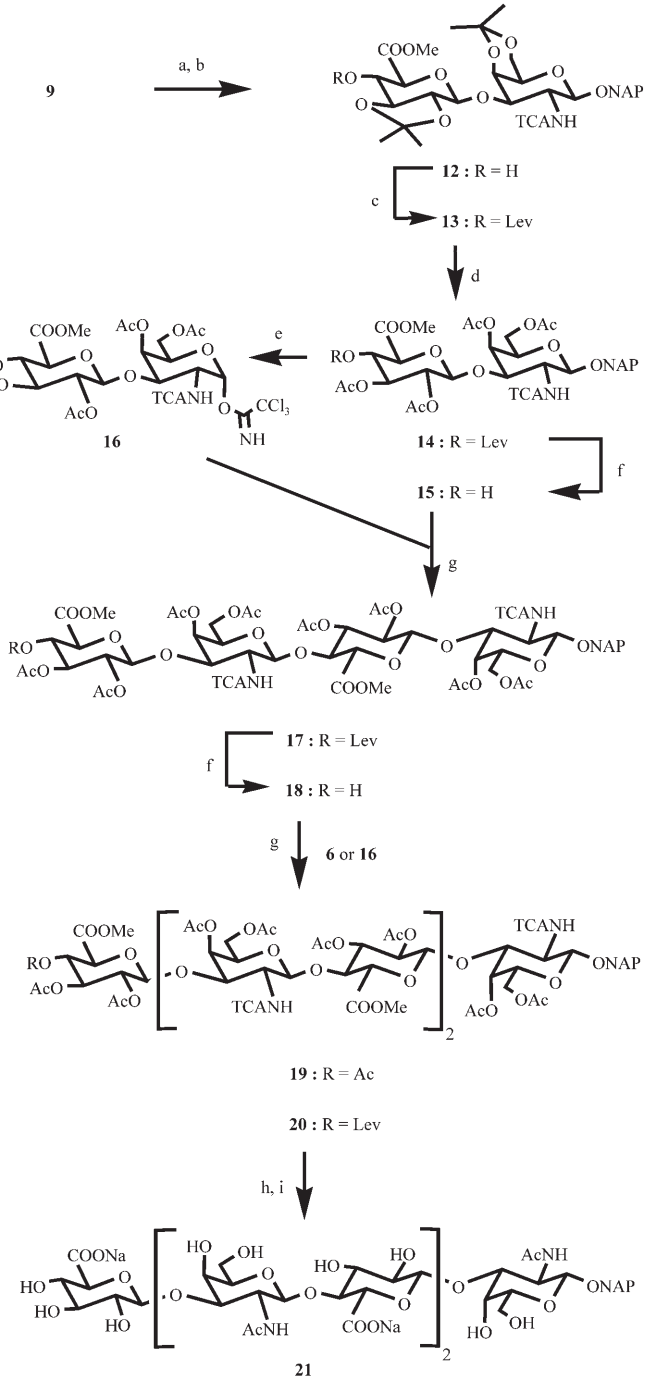

Scheme 3. Synthesis of chondrosine hexasaccharide glycoside **21**. Reagents and conditions: a) NaOMe, MeOH; b) 2-methoxypropene, CSA, DMF, 90 min, 67% from **9**; c) LevOH, DCC, DMAP, CH_2Cl_2, 3 h, 90%; d) 60% AcOH, 100°C, 1 h; then Ac_2O, pyridine, 16 h, 71%; e) DDQ, CH_2Cl_2/MeOH, 24 h; then Cl_3CCN, DBU, CH_2Cl_2, 30 min, 66%; f) hydrazine acetate, pyridine, 8 min, 89%; g) TMSOTf, CH_2Cl_2, 30 min, 57% for **17**, 65% for **19** and **20**; h) Bu_3SnH, AIBN, DMAC, 80°C, 2 h, 78%; then $LiOH/H_2O_2$, THF, −10°C to room temperature, 16 h; then 4 M NaOH, MeOH, room temperature, 4 h, 75%. CSA = camphorsulfonic acid, LevOH = 4-oxopentanoic acid, DCC = *N*,*N*-dicyclohexylcarbodiimide, DMAP = 4-dimethylaminopyridine, DDQ = 2,3-dichloro-5,6-dicyanobenzoquinone, AIBN = 2,2′-azobis(2-methylpropionitrile), DMAC = *N*,*N*-dimethylacetamide.

 © 2006 Wiley-VCH Verlag GmbH & Co. KGaA, Weinheim

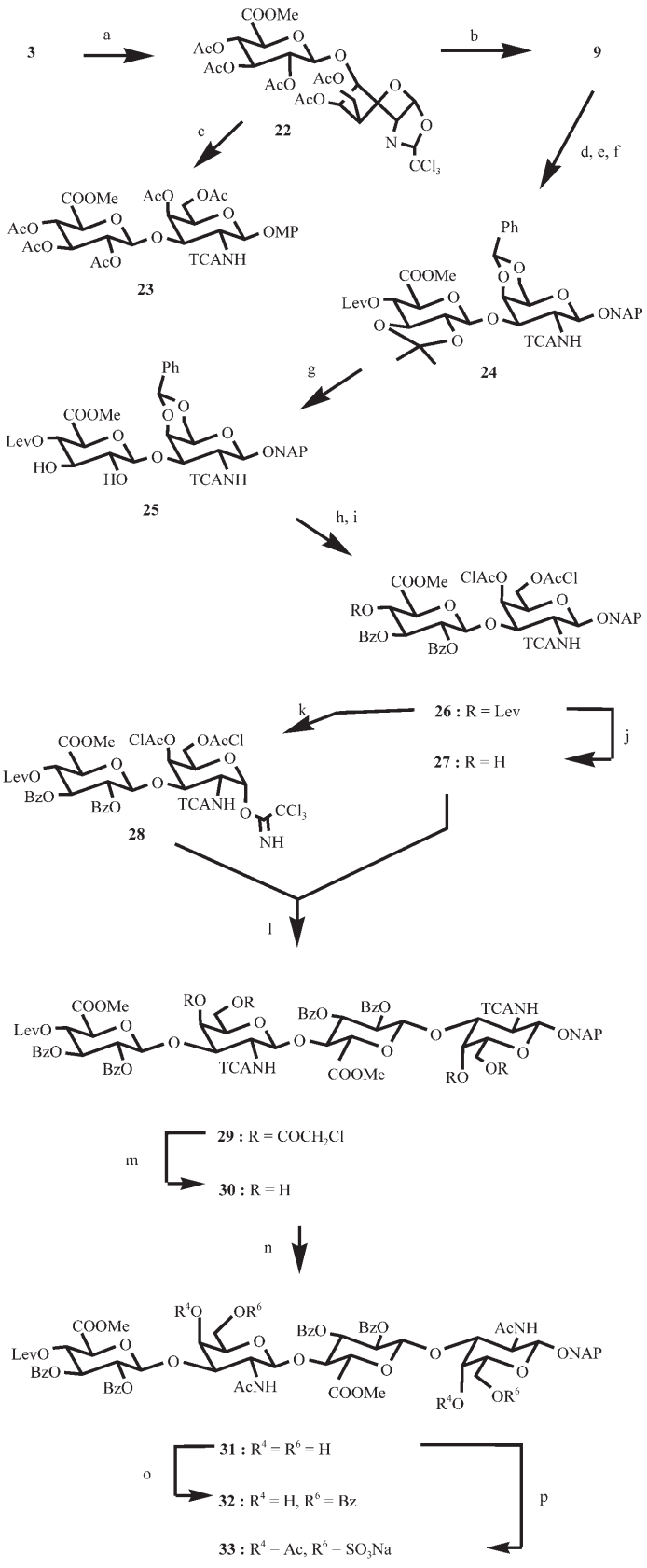

O-sulfonated. To achieve this goal, the intermediate **25** was submitted to 2′,3′-dibenzoylation, mild acid hydrolysis of the 4,6-benzylidene acetal, and chloroacetylation of the resulting 4,6-diol to give **26** in 76% overall yield. This latter compound was either transformed into acceptor **27**, through selective cleavage of the levulinoyl group, or donor **28**, through oxidative removal of the NAP glycoside with DDQ followed by imidoylation. Coupling of alcohol **27** with imidate **28** in the presence of a TMSOTf catalyst gave the tetrasaccharide derivative **29** in 71% yield. This intermediate should be ready for further elongation at the nonreducing end after selective cleavage of the *O*-lev group. Removal of the chloroacetate esters with thiourea gave the tetrol **30**, the *N*-trichloroacetyl groups of which were reduced by a radical method to give the key intermediate **31**, a precursor of the 4,6-disulfated species (chondroitin sulfate E). Selective benzoylation at O-6 of **31** with benzoyl cyanide gave **32**, a precursor of the 4-sulfated species (chondroitin sulfate A), whereas controlled regioselective sulfation at C-6[17] with the sulfur trioxide/trimethylamine complex followed by O-acetylation at C-4 (to assess the positions of sulfation) afforded **33**, a direct precursor of the 6-sulfated species (chondroitin sulfate C).

Differentiation between O-2′ and O-3′ was next studied (Scheme 5), and was achieved starting from diol **25**. Treatment of **25** with benzoyl cyanide gave exclusively the crystalline 3′-benzoate **34** in 80% yield. This was then transformed in good yield into the key intermediate **35** through chloroacetylation at O-2′, hydrolysis of the 4,6-benzylidene acetal, selective chloroacetylation at O-6 at −20 °C, and benzoylation at O-4, thus opening the way for the preparation of the 6,2′-sulfo form (chondroitin sulfate D). Tin-mediated[18] benzoylation of **25** gave the 2′-benzoate **36** in 68% yield, along with its 3′ isomer **34** (16% yield). It should now be possible to transform the 2′-benzoate **36** by the same strategy into precursors of the less common sulfo forms such as 4,3′-disulfated (chondroitin sulfate K), 6,3′-disulfated (chondroitin sulfate L), and 4,6,3′-trisulfated species (chondroitin sulfate M).

Scheme 4. Synthesis of precursors of chondroitin sulfates E (**31**), A (**32**), and C (**33**). Reagents and conditions: a) $BF_3{\cdot}OEt_2$, TMSBr, 2,4,6-collidine, Bu_4NBr, CH_2Cl_2, 48 h, 89%; b) 2-naphthylmethanol, TMSOTf, CH_2Cl_2, 30 min, 90%; c) 4-methoxyphenol, TMSOTf, CH_2Cl_2, 0 °C, 30 min, 90%; d) MeONa, MeOH; then PhCHO, TFA, 4 h, 75%; e) 2-methoxypropene, CSA, DMF, 90 min, 83%; f) LevOH, DCC, DMAP, CH_2Cl_2, 1 h, 92%; g) 80% AcOH, CH_2Cl_2, 20 h, 79%; h) PhCOCl, pyridine, 0 °C, 1 h, 95%; i) 75% AcOH, 100 °C, 30 min; then $(ClAc)_2O$, pyridine, CH_2Cl_2, 0 °C, 1 h, 80%; j) hydrazine acetate, pyridine, room temperature, 8 min, 89%; k) DDQ, CH_2Cl_2/MeOH, room temperature, 24 h; then Cl_3CCN, DBU, CH_2Cl_2, 20 min, 68%; l) TMSOTf, CH_2Cl_2, room temperature, 1 h, 71%; m) thiourea, pyridine/EtOH, 80 °C, 2 h, 90%; n) Bu_3SnH, AIBN, DMAC, 80 °C, 2 h, 89%; o) PhCOCN, pyridine, room temperature, 6 h, 88%; p) $Me_3N{\cdot}SO_3$, DMF, 40 °C, 2 h 30; then Ac_2O, pyridine, room temperature, 16 h; then SP-C25 [Na^+] resin, 81%. Bz = benzoyl.

 © 2006 Wiley-VCH Verlag GmbH & Co. KGaA, Weinheim

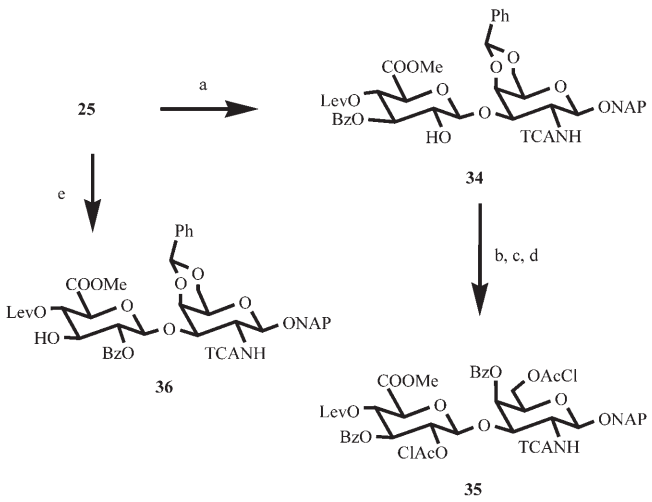

Scheme 5. Access to precursors of CS-D (**35**) and chondroitin sulfates K, L, and M (**36**). Reagents and conditions: a) PhCOCN, pyridine, room temperature, 6 h, 80%; b) $(ClAc)_2O$, pyridine, 0°C, 1 h, 95%; c) 75% AcOH, 100°C, 20 min; then $(ClAc)_2O$, pyridine, CH_2Cl_2, −20°C, 30 min, 72%; d) PhCOCl, pyridine, 0°C, 1 h, 91%; e) Bu_2SnO, dioxane/benzene, reflux, 7 h; then PhCOCl, room temperature, 8 h, 68%.

In conclusion, **1** can be readily prepared on a multigram scale and its versatility has been demonstrated. This shortened sequence renders this approach very attractive and competitive for the preparation of size-defined chondroitin oligomers. Also relevant is the rapid access to precursors for the preparation of various sulfo forms starting from the common intermediate **25**. This route can also be applied to other biologically important members of the glycosaminoglycan family such as dermatan sulfate and hyaluronic acid. The synthesis of a collection of chondroitin oligomers and their various sulfo forms based on this approach is underway, and will be reported elsewhere in due course.

Received: October 6, 2005
Revised: November 12, 2005
Published online: March 13, 2006

Keywords: carbohydrates · glycosaminoglycans · oligosaccharides · synthesis design

[1] a) L. Kjellèn, U. Lindahl, *Annu. Rev. Biochem.* **1991**, *60*, 443–475; b) R. V. Iozzo, *Annu. Rev. Biochem.* **1998**, *67*, 609–652.
[2] M. Jalkanen, M. Jalkanen, *J. Cell Biol.* **1992**, *116*, 817–825.
[3] N. B. Schwartz, N. Domowicz, *Glycoconjugate J.* **2004**, *21*, 329–341.
[4] H. Kawashima, K. Atarashi, M. Hirose, S. Yamada, K. Sugahara, M. Misayaka, *J. Biol. Chem.* **2002**, *277*, 12921–12930.
[5] a) N. Karst, J. C. Jacquinet, *Eur. J. Org. Chem.* **2002**, 815–825; b) N. A. Karst, R. J. Linhardt, *Curr. Med. Chem.* **2003**, *10*, 1993–2031; c) J. I. Tamura, M. Tokuyoshi, *Biosci. Biotechnol. Biochem.* **2004**, *68*, 2436–2443; d) S. E. Tully, R. Mabon, C. I. Gama, S. M. Tsai, X. Liu, L. C. Hsieh-Wilson, *J. Am. Chem. Soc.* **2004**, *126*, 7736–7737.
[6] P. A. Levene, *J. Biol. Chem.* **1941**, *140*, 267–277.
[7] E. A. Davidson, K. Meyer, *J. Am. Chem. Soc.* **1954**, *76*, 5686–5689.
[8] G. Blatter, J. M. Beau, J. C. Jacquinet, *Carbohydr. Res.* **1994**, *260*, 189–202.
[9] a) C. Coutant, J. C. Jacquinet, *J. Chem. Soc. Perkin Trans. 1* **1995**, 1573; b) F. Belot, J.-C. Jacquinet, *Carbohydr. Res.* **2000**, *326*, 88–97.
[10] N. Karst, J.-C. Jacquinet, *J. Chem. Soc. Perkin Trans. 1* **2000**, 2709–2717.
[11] a) D. Qiu, S. S. Gandhi, R. R. Koganty, *Tetrahedron Lett.* **1996**, *37*, 595–598; b) F. Belot, J. C. Jacquinet, *Carbohydr. Res.* **2000**, *325*, 93–106.
[12] F. Belot, J. C. Jacquinet, *Carbohydr. Res.* **1996**, *290*, 79–86.
[13] R. R. Schmidt, *Angew. Chem.* **1986**, *98*, 213–236; *Angew. Chem. Int. Ed. Engl.* **1986**, *25*, 212–235.
[14] M. J. Gaunt, J. Yu, J. B. Spencer, *J. Org. Chem.* **1998**, *63*, 4172–4173.
[15] J. Xia, S. A. Abbas, R. D. Locke, C. F. Piskorz, J. L. Alderfer, K. L. Matta, *Tetrahedron Lett.* **2000**, *41*, 169–173.
[16] H. Lucas, J. E. M. Basten, T. G. van Dinther, D. G. Meuleman, S. F. van Aelst, C. A. A. van Boeckel, *Tetrahedron* **1990**, *46*, 8207–8228.
[17] J.-C. Jacquinet, L. Rochepeau-Jobron, J.-P. Combal, *Carbohydr. Res.* **1998**, *314*, 283–288.
[18] S. David, S. Hanessian, *Tetrahedron* **1985**, *41*, 643–663.

 © 2006 Wiley-VCH Verlag GmbH & Co. KGaA, Weinheim

Silanes

DOI: 10.1002/anie.200503362

Unusual Reaction of 1,1-Dilithio-2,3,4,5-tetraphenylsilole with 1,3-Dienes Yielding Spirosilanes and Elemental Lithium**

*Irina S. Toulokhonova, Dennis R. Friedrichsen, Nicholas J. Hill, Thomas Müller, and Robert West**

Silole dianions[1–6] are important species in organometallic chemistry, both because of their high reactivity and their unique electronic structure. Silole dianions possess six

[*] Dr. I. S. Toulokhonova, D. R. Friedrichsen, Dr. N. J. Hill, Prof. Dr. R. West
Department of Chemistry
University of Wisconsin, Madison
1101 University Ave., Madison, WI 53706 (USA)
Fax: (+1) 608-262-6143
E-mail: west@chem.wisc.edu
Dr. T. Müller
Institut für Anorganische und Analytische Chemie der Universität Frankfurt
Marie-Curie-Strasse 11, 60439 Frankfurt (Germany)
Fax: (+49) 69-798-29188

[**] This research was supported by grants from the National Science Foundation. We thank Dr. Ilia A. Guzei (UW-Madison) for solving and refining the twinned crystal structure of **5**.

Supporting information for this article is available on the WWW under http://www.angewandte.org or from the author.

WILEY InterScience DISCOVER SOMETHING GREAT
© 2006 Wiley-VCH Verlag GmbH & Co. KGaA, Weinheim

π electrons, and it is well established from theoretical calculations[2] and X-ray data that silole dianions (**A**)[3–6] and their benzannulated analogues (**B**, **C**)[7–10] have aromatic character. Silole dianions act as nucleophiles in reactions with halogenated alkyl groups, silanes,[1,4–12] and adamantanone,[13] and have strong reducing properties.[14]

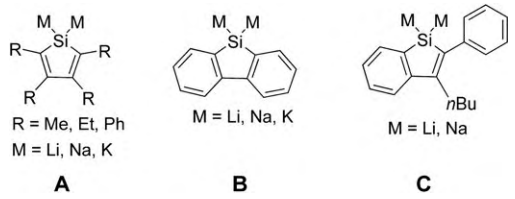

Here, we report the unexpected reaction of 1,1-dilithio-2,3,4,5-tetraphenylsilole (**1**) with 2,3-dimethyl-1,3-butadiene (DMB) and 1,3-cyclohexadiene to yield the spirosilole products **2** and **3** (Scheme 1). Remarkably, the lithium ions

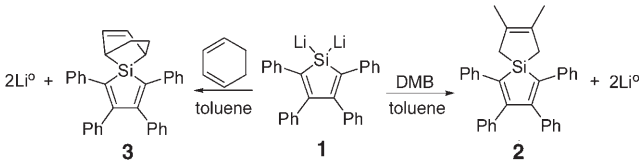

Scheme 1. Reaction of silole dianion **1** with DMB and with 1,3-cyclohexadiene.

are reduced in these reactions to metallic lithium. The elemental lithium appeared as a gray powder at the bottom of the reaction vessel and was identified by reaction with 2-propanol to produce dihydrogen, by interaction with benzyl chloride to give 1,2-diphenylethane, and by titration of a hydrolyzed sample with HCl. The crystal structure of **2** is presented in Figure 1. A similar reaction occurs between 9,9-

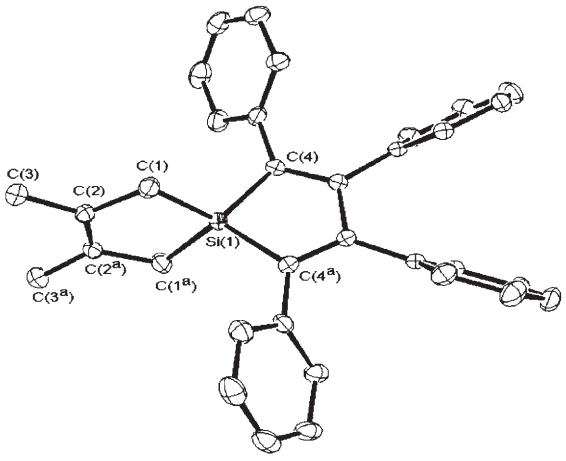

Figure 1. Thermal-ellipsoid diagram of **2**. Selected bond lengths and angles: Si(1)-C(1) 1.8812(17), C(1)-C(2) 1.518(2), Si(1)-C(4) 1.8738(16), C(2)-C(2a) 1.337(3); C(1a)1-Si(1)-C(1) 95.25(11), C(4a)-Si(1)-C(1) 120.45(7).

dilithio-9-silafluorene (**4**) and DMB to yield spirosilafluorene **5**, also in high yield (Scheme 2).

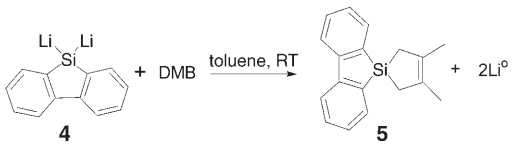

Scheme 2. Reaction of silafluorene dianion **4** with DMB.

Reactions with 1,3-dienes to yield 1,4-cyclic products are characteristic of silylenes.[15] Indeed, compound **2** was first reported from the reaction of photochemically generated silylene **6** with DMB.[16] Thus, we considered that the reactions in Scheme 1 might proceed through the same silylene **6**. No

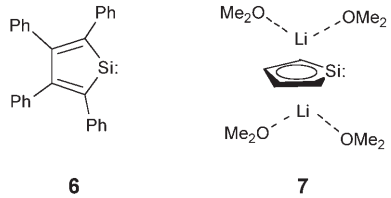

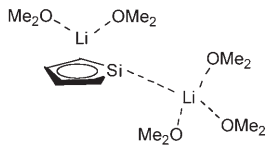

reaction occurred, however, with phenyldimethylsilane, a typical silylene-scavenger reagent. In contrast, a fast reaction of silylene **6** with ethyldimethylsilane is reported.[16] This observation suggests that **6** is not an intermediate in the reaction of **1** with DMB. Instead, we propose, on the basis of DFT calculations,[17,18] the mechanism which is shown in Scheme 3 for the model reaction of compound **7** with 1,3-butadiene.

Our starting point is the experimental observation that **1** exists in toluene as a THF solvate. Comparison of experimental ^{29}Si NMR data for **1** with computed NMR chemical shifts for the model compounds **7** and **8** indicates that, in solutions of aromatic hydrocarbons, **1** adopts an η^5–η^5 structure, which is similar to the computed structure of **7**[19,20] (^{29}Si NMR shift of **1** in [D$_6$]benzene: $\delta = 53.1$ ppm; computed: $\delta = 58.8$ (**7**), 39.3 ppm (**8**)).[21] After formation of the encounter complex **9**, the dilithiosilole **7** undergoes a nucleophilic addition to butadiene, which is assisted by complexation of the diene to the Li cation, thus yielding the monoalkylated silole **10**. Attack of the negatively charged δ-carbon atom on the silicon atom completes the 1,4-addition sequence with the formation of the reduced spiro compound **11**. The formation of compound **11** is exergonic by 16.3 kcal mol^{-1}. Finally, **11** collapses by loss of elemental lithium and dimethyl ether to yield the final product **12**. The reaction

 © 2006 Wiley-VCH Verlag GmbH & Co. KGaA, Weinheim

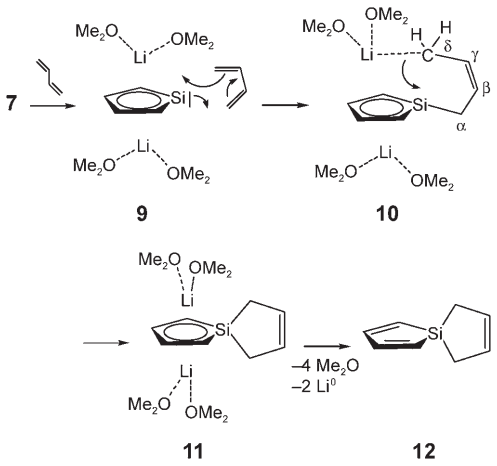

Scheme 3. Proposed mechanism for the cycloaddition of 1,3-butadiene to **7**.

profile of the proposed reaction mechanism, along with computed structures of the intermediates **10** and **11** as well as the transition states (TS) **TS(9/10)** and **TS(10/11)**, is given in Figure 2. The free-enthalpy barrier for the first step ($\Delta G^{298} = 16.6$ kcal mol^{-1}) is rate-determining, and the height of the barrier is in qualitative agreement with a reaction which proceeds smoothly at room temperature. The barrier for the second step is only 2.4 kcal mol^{-1}; therefore, an intermediate monoalkylated silole similar to **10** would be hard to observe experimentally. The transformation of **11** to the final products **12**, Me_2O, and Li^0 would be strongly endergonic if all the products remained in solution. In the actual reactions, the transformation may be driven by the precipitation of lithium, thus removing it from equilibrium.

The above reactions were carried out in toluene. When the reaction of **1** with DMB was carried out in THF, the yield of spirosilane **2** (ca. 25%) was much lower. This result may have come about because the excess THF solvated the lithium cations and removed them from the diene, thus making the reaction with the double bond less favorable. The reaction of disodium tetraphenylsilole with DMB also gave spirosilane **2**, but again in much lower yield (ca. 20%). This result indicates the importance of the size and the coordination ability of the alkali-metal cation for the cyclization reaction, which emerges also from the highly oriented transition-state geometries (Figure 2), as predicted by the computations.

The scope of this new "oxidative-cyclization" reaction will be further explored in our laboratories. Preliminary results indicate that reactions take place between **1** and acetylenes and diynes, but are much more complex.

Experimental Section

All procedures with air- and moisture-sensitive compounds were carried out by using a Schlenk line under nitrogen or argon. 2,3-Dimethyl-1,3-butadiene (DMB) and 1,3-cyclohexadiene were purchased from Aldrich and used without further purification. Solvents were distilled from sodium benzophenone ketyl. NMR spectra were recorded at room temperature on a Varian INOVA or Varian Unity-500 spectrometer. The chemical shifts are expressed in ppm relative to TMS as an internal standard.

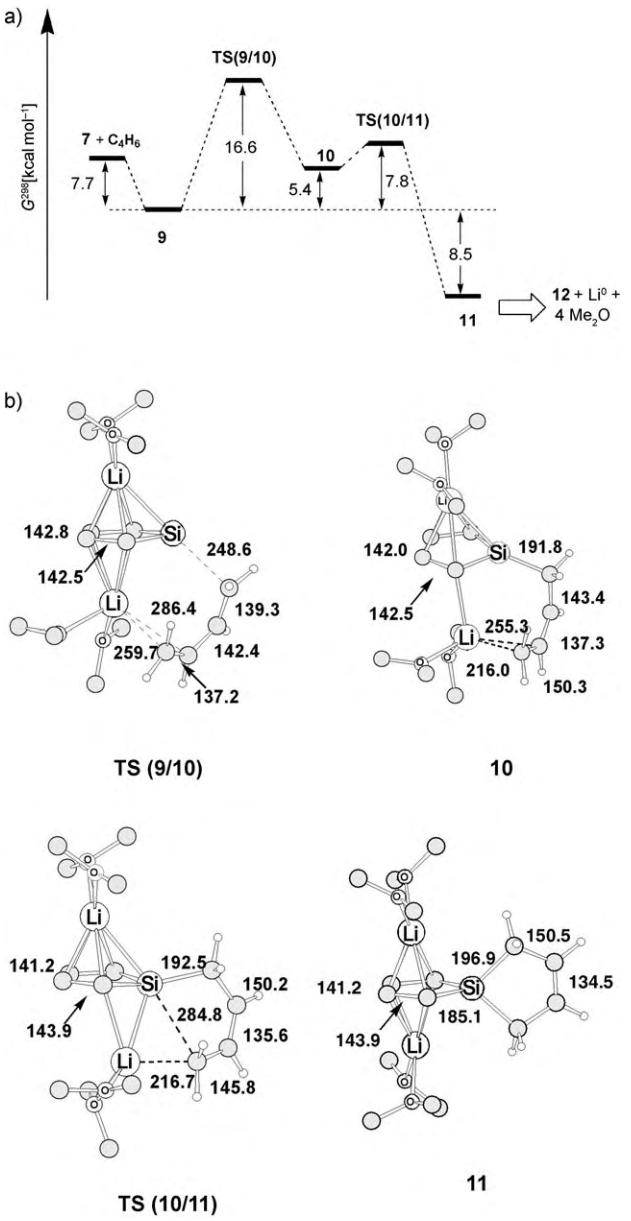

Figure 2. a) Calculated reaction coordinate for the reaction of **7** with 1,3-butadiene.[18] b) Optimized geometries of compounds **TS(9/10)**, **10**, **TS(10/11)**, and **11** (bond lengths are given in pm).

X-ray data collection and structural refinement for **2**: Intensity data were collected by using a Bruker SMART CCD area detector,[22] mounted on a Bruker Platform goniometer, with graphite-monochromated $Mo_{K\alpha}$ radiation ($\lambda = 0.71073$ Å). The samples were cooled to 133(2) K. For **2**, the monoclinic space group $P2_1/n$ (no. 14) was determined by systematic absences and statistical tests, and verified by subsequent refinement. The structure was solved by direct methods and refined by full-matrix least-squares methods on F^2. X-ray data collection and structural refinement for **5** are presented in the Supporting Information. CCDC-284150 and CCDC-284149 contain the supplementary crystallographic data for this paper. These data can be obtained free of charge from The Cambridge Crystallographic Data Centre via www.ccdc.cam.ac.uk/data_request/cif.

2: Compound **1** was prepared from 1,1-dichloro-2,3,4,5-tetraphenylsilole (0.5 g, 2.2 mmol) and Li (0.033 g, 4.8 mmol) in THF (7.5 mL)

 © 2006 Wiley-VCH Verlag GmbH & Co. KGaA, Weinheim

under argon as described previously.[3] The THF was removed by vacuum and replaced with toluene. A solution of DMB (0.18 g, 2.2 mmol) in toluene (10 mL) was added to the solution of **1** (2.2 mmol) in toluene (10 mL) at −78 °C. After warming the mixture to room temperature over 3 h, the reaction mixture was hydrolyzed with a saturated solution of aqueous ammonium chloride. The organic layer was extracted into diethyl ether, separated from the aqueous layer, and dried over $MgSO_4$. The solvents were evaporated in vacuo, and the residue was crystallized from hexane/diethyl ether. Yield: 95 %. ^{1}H NMR (500.0 MHz, C_6D_6): $\delta = 1.6$ (s, 6H, CH_3), 2.2 (s, 4H, CH_2), 7.13–7.48 ppm (br m, 20H, Ar); ^{13}C NMR (125.75 MHz, C_6D_6): $\delta = 19.4$ (s, CH_3), 29.5 (s, CH_2), 121.33–147.30 ppm (br m, Ar); ^{29}Si NMR (99.38 MHz, C_6D_6): $\delta = 15.2$ ppm. The reaction of **1** with DMB in THF was performed by a similar procedure.

3: The reaction of **1** with 1,3-cyclohexadiene was performed as described above for the experiment of **1** with DMB. Yield: 25%. ^{1}H NMR (500.0 MHz, C_6D_6): $\delta = 1.59$ (s, 4H, CH_2), 2.55 (s, 2H, CH), 6.84–7.16 ppm (br m, 20H, Ar); ^{13}C NMR (125.75 MHz, C_6D_6): $\delta =$ 20.40 (s, CH), 36.26 (s, CH_2), 124.63–149.95 ppm (br m, Ar); ^{29}Si NMR (99.38 MHz, C_6D_6): $\delta = 4.00$ ppm.

Reaction of 1,1-disodium-2,3,4,5-tetraphenylsilole with DMB: 1,1-disodium-2,3,4,5-tetraphenylsilole was prepared as in ref. [1]. The reaction was conducted as described above for **1** and DMB in toluene. A complicated mixture of unidentified products was observed in the reaction. **2** (20 %) was detected by ^{1}H NMR spectroscopy.

5: Compound **4** was prepared from 9,9-dichloro-9-silafluorene and lithium as described by Liu et al.[7] A solution of DMB (2.2 mmol) in toluene (10 mL) was added at −78 °C to a solution of **4** (2.2 mmol) in toluene (10 mL). The reaction mixture was worked up as described above for **2**. The product was crystallized from hexane/diethyl ether. Yield: 87 %. ^{1}H NMR (500.0 MHz, C_6D_6): $\delta = 0.81$ (s, 4H, CH_2), 1.82 (s, 6H, CH_3), 6.64–6.85 ppm (br m, 8H, Ar); ^{13}C NMR (125.75 MHz, C_6D_6): $\delta = 21.41$ (s, CH_3), 28.56 (s, CH_2), 121.35–150.53 ppm (br m, Ar); ^{29}Si NMR (99.38 MHz, C_6D_6): $\delta = 6.54$ ppm.

Received: September 21, 2005
Revised: January 5, 2006
Published online: March 14, 2006

Keywords: reduction · silicon · silole dianions · spiro compounds

[1] W. C. Joo, J. H. Hong, S. B. Choi, H. E. Son, C. H. Kim, *J. Organomet. Chem.* **1990**, *391*, 27–36.
[2] B. Goldfuss, P. von R. Schleyer, F. Hampel, *Organometallics* **1996**, *15*, 1755–1757.
[3] a) R. West, H. Sohn, U. Bankwitz, J. Calabrese, Y. Apeloig, T. Müller, *J. Am. Chem. Soc.* **1995**, *117*, 11608–11610; b) R. West, H. Sohn, D. R. Powell, T. Müller, Y. Apeloig, *Angew. Chem.* **1996**, *108*, 1095–1097; *Angew. Chem. Int. Ed. Engl.* **1996**, *35*, 1002–1004.
[4] U. Bankwitz, H. Sohn, D. R. Powell, R. West, *J. Organomet. Chem.* **1995**, *499*, C7–C9.
[5] W. P. Freeman, T. D. Tilley, G. P. A. Yap, A. L. Rheingold, *Angew. Chem.* **1996**, *108*, 960–962; *Angew. Chem. Int. Ed. Engl.* **1996**, *35*, 882–884.
[6] W. P. Freeman, T. D. Tilley, L. M. Liable-Sands, A. L. Rheingold, *J. Am. Chem. Soc.* **1996**, *118*, 10457–10468.
[7] Y. Liu, T. C. Stringfellow, D. Ballweg, I. A. Guzei, R. West, *J. Am. Chem. Soc.* **2002**, *124*, 49–57.
[8] Y. Liu, D. Ballweg, T. Müller, I. A. Guzei, R. W. Clark, R. West, *J. Am. Chem. Soc.* **2002**, *124*, 12174–12181.
[9] S.-B. Choi, P. Boudjouk, P. Wei, *J. Am. Chem. Soc.* **1998**, *120*, 5814–5815.
[10] S.-B. Choi, P. Boudjouk, *Tetrahedron Lett.* **2000**, *41*, 6685–6688.
[11] T. Sanji, T. Sakai, C. Kabuto, H. Sakurai, *J. Am. Chem. Soc.* **1998**, *120*, 4552–4553.
[12] I. S. Toulokhonova, T. C. Stringfellow, S. A. Ivanov, A. Masunov, R. West, *J. Am. Chem. Soc.* **2003**, *125*, 5767–5773.
[13] I. S. Toulokhonova, I. A. Guzei, R. West, *J. Am. Chem. Soc.* **2004**, *126*, 5336–5337.
[14] Y. Liu, D. Ballweg, R. West, *Organometallics* **2001**, *20*, 5769–5770.
[15] a) J. Grobe, T. Schierholt in *Organosilicon Chemistry II: From Molecules to Materials* (Eds.: N. Auner, J. Weis), Wiley-VCH, Weinheim **1996**, pp. 317–319; b) G. Manuel, P. Mazerolles, G. Cauguy, *Synth. React. Inorg. Met.-Org. Nano-Met. Chem.* **1974**, *4*, 133–138; c) J. Dunogues, R. Arreguy, C. Biran, R. Calas, F. Pisciotti, *J. Organomet. Chem.* **1973**, *63*, 119–131; d) P. Mazerolles, F. Gregoire, *J. Organomet. Chem.* **1986**, *301*, 153–160.
[16] M. Kako, S. Oba, R. Uesugi, S. Sumiishi, Y. Nakadaira, K. Tanaka, T. Takada, *J. Chem. Soc. Perkin Trans. 2* **1997**, 1251–1253.
[17] All calculations were carried out by using Gaussian 03, Gaussian Inc., Pittsburgh, **2003**.
[18] The structures were optimized by using DFT calculations at the B3LYP/6-31G(d) level. Refined energies were obtained at the B3LYP/6-311+G(2d,p) level, and corrections for the free enthalpy *G* at 298 K were computed at the B3LYP/6-31G(d) level. These corrections were added to the energies obtained at the B3LYP/6-311+G(2d,p) level. Each stationary point was identified either as an intermediate or transition state (TS) by a subsequent frequency calculation. Intrinsic reaction coordinate (IRC) computations were used to connect the transition states with the appropriate minima. The influence of the basis-set size on the computed geometries and relative energies was tested at the B3LYP/6-311+G(d,p) level of theory for several compounds and was found to be insignificant in all cases. All calculated data are presented in the Supporting Information.
[19] The dilithium salt **1** crystallizes from THF in the η^1–η^5 form (see ref. [3]); in solution, however, the η^5–η^5 isomer prevails (see ref. [20]).
[20] T. Müller, Y. Apeloig, H. Sohn, R. West in *Organosilicon Chemistry III: From Molecules to Materials* (Eds.: N. Auner, J. Weis), Wiley-VCH, Weinheim, **1998**, pp. 144–151.
[21] Computed at GIAO/B3LYP/6-311+G(2d,p)//B3LYP/6-31G(d). Calculated σ(Si) for TMS: 329.3.
[22] Bruker-AXS. (2000–2003) SADABS V.2.05, SAINT V.6.22, SHELXTL V.6.10 & SMART 5.622 Software Reference Manuals. Bruker-AXS, Madison, Wisconsin, USA.

 © 2006 Wiley-VCH Verlag GmbH & Co. KGaA, Weinheim

Electrooptics

DOI: 10.1002/anie.200504532

Synthesis and Characterization of a Multicomponent Rhenium(I) Complex for Application as an OLED Dopant**

Natasha J. Lundin, Allan G. Blackman, Keith C. Gordon, and David L. Officer*

Dedicated to Professor John J. McGarvey

Current studies in the field of organic light-emitting diodes (OLEDs) are aimed at improving display technology through production of devices with increased efficiency, flexibility, and long lifetimes.[1] An OLED converts electrical energy into light by allowing holes and electrons, which are transported from opposing electrodes, to combine to form an exciton, or localized excited state, in an emissive material. Subsequent relaxation of the exciton results in the emission of light.[1] A successful OLED requires facile and balanced charge transport as well as a high conversion efficiency of excitons to light.[2] As electrons and holes are transported through the lowest unoccupied molecular orbitals (LUMOs) and highest occupied molecular orbitals (HOMOs), respectively, in OLED components, the relative band gap and HOMO and LUMO energies of these materials is of crucial importance to the efficiency and brightness of an OLED.[3] Balanced charge injection is required so that charge recombination does not occur close to the electrode/polymer interface, because a metal electrode can deactivate excitons, lowering the efficiency of electroluminescence of the device.[2]

To fulfill these requirements, OLEDs often contain a number of layers that individually perform the roles of charge transport and light emission.[4] Each layer requires materials with the correct HOMO and LUMO energies to either promote or disrupt the flow of charge in the device. In many devices the emissive layer consists of a polymer such as poly(*N*-vinylcarbazole) (PVK) doped with a transition-metal complex, which acts as the charge-recombination and emission center.[5,6] Maximization of the brightness of a device is a key consideration in the production of OLEDs, which is why phosphorescent metal complexes are favored over fluorescent organic materials in many situations.[7] The dopant used also greatly affects the wavelength and broadness of the emission, as well as the efficiency of the device, so that an OLED may be tuned by appropriate selection of the metal center and ligand(s).

Herein, we describe our endeavors to design an electroactive material composed of simple modular units, each of which performs a specific function, namely electron transfer, hole transfer, and emission. Furthermore, we chose units that may be easily derivatized, thereby giving great flexibility to this design strategy. Wong et al.[8] and Gong et al.[9] have synthesized integrated molecules containing all three functionalities and shown that they are effective as a single charge-transport and emitting layer in OLEDs. Trifunctional polymers have also been prepared.[10] We designed and synthesized a trifunctional molecule that comprises the key units for an OLED material: an emissive chromophore based on a Re^{I} polypyridyl complex containing dipyrido[3,2-*a*:2′,3′-*c*]phenazine (dppz), an electron-transporting 1,3,4-oxadiazole group, and a hole-transporting terthiophene unit. Re^{I} polypyridyl complexes are known to be highly emissive[11,12] and have been used as emitting dopants in a variety of OLED structures.[13–15] 1,3,4-Oxadiazole heterocycles are widely used as electron-transporting groups owing to their electron deficiency and good thermal stability.[2] The terthiophene subunit can act as a hole-transport group[16] and can also be easily functionalized and polymerized.[17] These units were linked to form a trifunctional molecule as outlined in Scheme 1.

Ligand 2-(11-dipyrido[3,2-*a*:2′,3′-*c*]phenazine)-5-phenyl-1,3,4-oxadiazole (**2**), which was prepared from dppz-CO_2H,[18] was treated with $[Re(CO)_5Cl]$ to give *fac*-**3**. Ag^+-induced solvolysis of **3** in MeCN[19] and reaction of the resulting complex **4** with (*E*)-1-((2,2′:5′,2″-terthiophen)-3′-yl)-2-(4′-pyridyl)ethane (**5**) gave the multifunctional complex **6** as the hexafluorophosphate salt (Scheme 1). Elemental analysis suggested the presence of a single molecule of solvent (ethyl acetate), and both ^1H and ^{13}C NMR spectra were consistent with the desired product. Despite numerous attempts using different solvents and counterions, we were unable to grow crystals of **6** of suitable quality for X-ray analysis.

Spectroscopic data for dppz, **2**, **3**, **5**, and **6** are presented in Table 1 and Figure 1. The ligand dppz is commonly thought to contain partitioned orbitals, as it displays limited communication between the phenazine and bipyridyl sections of the ligand.[20,21] If ligand **2** behaves in a similar manner, it is expected that introduction of an electron-withdrawing oxadiazole moiety, or coordination of a metal center, should have little effect on the properties of the ligand. However, both ligand substitution and metal coordination resulted in a shift in the absorption maxima. The emission maximum of **2** is at the same wavelength as that of dppz but exhibits a higher quantum yield of emission. Complexes **3** and **6** both display broader emission bands than **2**, showing the influence of the rhenium(I) center. The absorption spectra of **3** and **6** show tails

[*] N. J. Lundin, Dr. A. G. Blackman, Prof. K. C. Gordon
Department of Chemistry
The MacDiarmid Institute for Advanced Materials and Nanotechnology
University of Otago
P.O. Box 56, Dunedin (New Zealand)
Fax: (+64) 3-479-7906
E-mail: kgordon@chemistry.otago.ac.nz
Prof. D. L. Officer
Department of Chemistry
Nanomaterials Research Centre
Massey University
P.O. Box 11222, Palmerston North (New Zealand)

[**] We acknowledge financial support from the MacDiarmid Institute for Advanced Materials and Nanotechnology. OLED = organic light-emitting diode.

Supporting information for this article is available on the WWW under http://www.angewandte.org or from the author.

InterScience
© 2006 Wiley-VCH Verlag GmbH & Co. KGaA, Weinheim

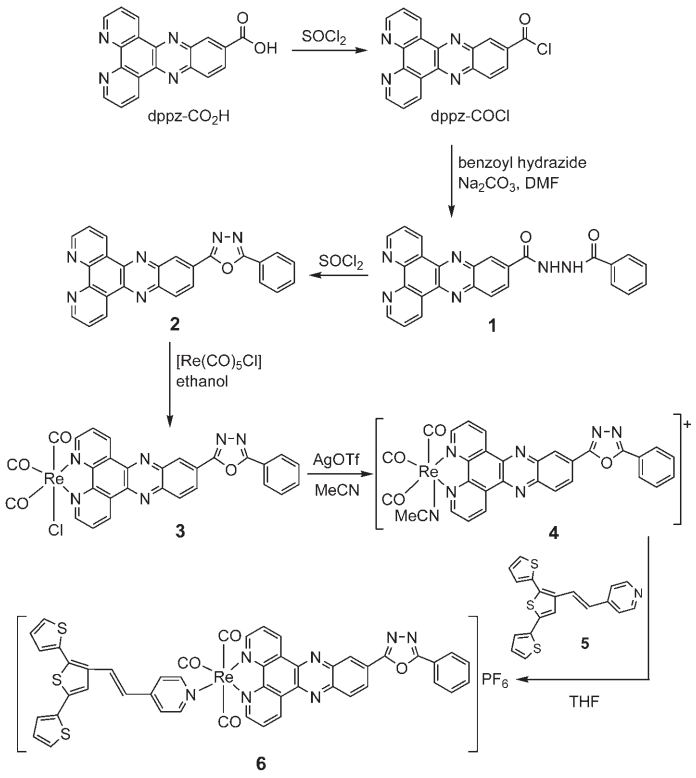

Scheme 1. Synthesis of the multicomponent molecule **6**. dppz = dipyrido-[3,2-*a*:2′,3′-*c*]phenazine; DMF = *N*,*N*-dimethylformamide; Tf = trifluoromethanesulfonyl.

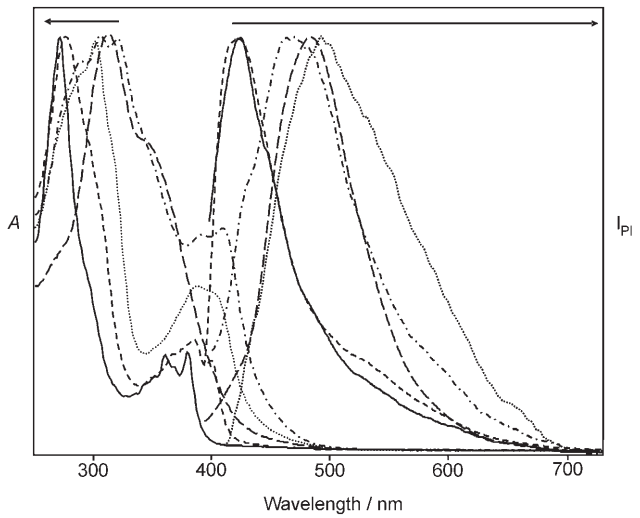

Figure 1. Normalized absorption (*A*) and photoluminescence (PL) data of dppz (——), **2** (----), **3** (••••), **5** (– – –), and **6** (–•–•). Data were collected at room temperature from solutions (≈10^{-5} M) in CH_2Cl_2 degassed with N_2.

Table 1: Spectroscopic data for dppz, **2**, **3**, **5**, and **6**.

Compound	λ_{max} [nm][a]	ε [$M^{-1}cm^{-1}$]	λ_{PL} [nm][b]	Quantum yield[c]	Stokes shift [cm^{-1}][d]
dppz	380	18000	427	0.009	2900
2	400	1300	427	0.040	1600
3	388	29000	497	0.001	2600
5	342	21000	487	0.130	8700
6	409	3400	474	0.003	3400

[a] Data were collected at room temperature from solutions in CH_2Cl_2 (concentrations in the 10^{-5} M range) degassed with N_2. [b] Maximum wavelength of photoluminescence upon excitation at $\lambda = 380$ nm. [c] Absolute values, calculated by the method of Wang et al.[22] [d] Calculated from the difference between the lowest energy absorption maximum and the emission wavelength maximum.

at lower energy, indicative of a metal–ligand state that is not present in the free ligand.

The Stokes shifts of dppz, **2**, **3**, **5**, and **6** were calculated in wavenumbers from the difference between the lowest energy absorption maximum and the emission maximum of each compound.[23] The oxadiazole moiety decreases the size of the Stokes shift of **2** relative to that of dppz. However, coordination of the rhenium(I) center increases the Stokes shift, as seen by a comparison of the data for **3** and **6** with those of **2** (see Table 1). The large Stokes shift as observed for **5** may be caused by significant structural differences between the ground state and excited state, as has been predicted for **5** and related molecules.[16] The Stokes shift of **6** is closer to that of **3** than of **5**, which suggests that the HOMO and LUMO of **6** are more similar to those of **3** than of **5**.[24]

Electrochemical data for dppz, **2**, **3**, **5**, and **6** are presented in Table 2 and Figure 2. HOMO and LUMO energies were calculated from the electrochemical data by known methods.[25] The introduction of an electron-withdrawing oxadiazole group had the predicted effect, with compounds **2, 3**, and **6** being reduced at less-negative potential than dppz. Complex **6** was reduced at less-negative potential than its components, and its LUMO is correspondingly lower in energy. This observation correlates with the complex being easier to reduce than dppz, **2**, **3**, or **5** and thus a suitable candidate for electron transport. The presence of a terthiophene moiety in **5** and **6** was reflected in the oxidation potentials of the compounds: Compounds **5** and **6** were oxidized at less-positive potentials than dppz, **2**, or **3**, indicating a greater propensity for **5** and **6** to lose an electron. Resultantly, the HOMO energies of **5** and **6** are greater than

Table 2: Electrochemical data for dppz, **2**, **3**, **5**, and **6**.

Compound	Reduction potential [mV][a]	Oxidation potential [mV][a]	*E*(HOMO) [eV][b]	*E*(LUMO) [eV][b]
dppz	−1600[26]	n.d.	−6.22[27]	−2.96[27]
2	−851 (irr)	1690 (irr)	−5.87	−3.31
3	−746	1620 (irr)	−5.79	−3.36
5	−1030 (irr)	1110	−5.35	−3.13
6	−648	1170 (irr)	−5.38	−3.45

[a] Potentials were measured with reference to decamethylferrocenium/decamethylferrocene. Determined from solutions in dichloromethane (1.0 mM), containing tetrabutylammonium perchlorate (0.10 M) as the supporting electrolyte. Samples were purged with N_2 for 5 min before use. Scan rate: 100 Mvs^{-1}. n.d. = not determined; irr indicates an irreversible process. [b] Calculated using the method of Li et al.[25]

 © 2006 Wiley-VCH Verlag GmbH & Co. KGaA, Weinheim

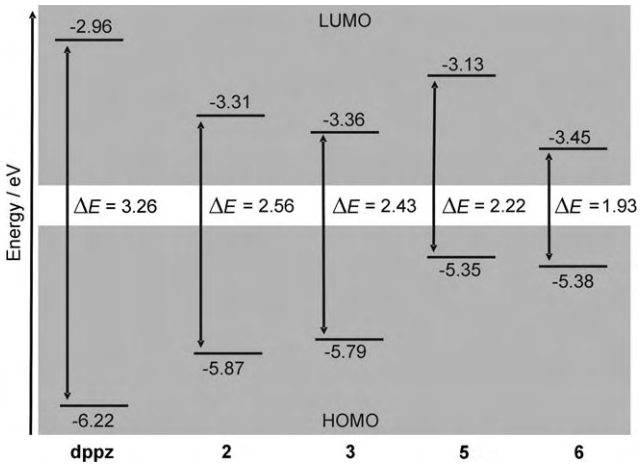

Figure 2. HOMO, LUMO, and band gap energies of dppz, **2**, **3**, **5**, and **6**.

those of dppz, **2**, or **3**, and thus **5** and **6** are expected to be better hole-transporting materials. The electrochemical data show that **6** has the smallest band gap energy of the compounds studied, and the relative energies of its HOMO and LUMO suggest that it favors transport of both holes and electrons.

Note that the HOMO and LUMO energies of **6** lie within the band gap of the host polymer PVK (Figure 3), so that the charges should accumulate and recombine on **6** rather than on

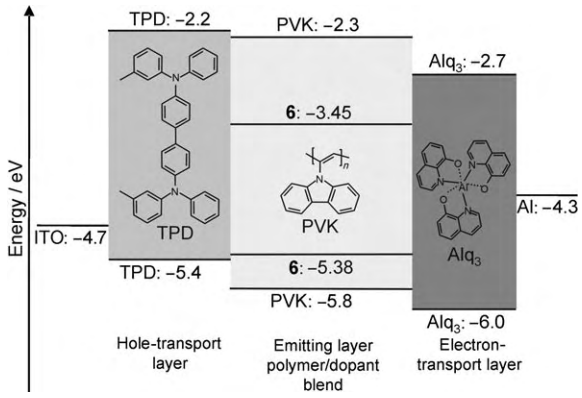

Figure 3. HOMO and LUMO energy levels of **6** superimposed onto a theoretical device containing *N,N*′-diphenyl-*N,N*′-bis(3-methylphenyl)-1,1′-biphenyl-4,4′-diamine (TPD), poly(*N*-vinylcarbazole) (PVK), and tris(8-hydroxyquinoline)aluminum (Alq_3). ITO = indium tin oxide.

PVK and emission should then occur from the relaxation of excitons localized on **6**. Theoretically, **6** looks to be a promising candidate as an OLED dopant as the small band gap should allow efficient charge transport. However, the small band gap of **6** may also cause inefficient conversion of excitons into radiation, as is reflected in the low quantum yield (Table 1). Nonetheless, the modular nature of complex **6** means that the individual components can be readily derivatized prior to assembly of the trifunctional molecule, thus allowing the electronic properties of the multifunctional compound to be tuned. We are currently engaged in studies aimed at derivatizing the modular components and making devices containing **6** and its derivatives.

Received: January 21, 2006

Keywords: electron transport · heterocycles · molecular electronics · rhenium

[1] E. Holder, B. M. W. Langeveld, U. S. Schubert, *Adv. Mater.* **2005**, *17*, 1109.
[2] G. Hughes, M. R. Bryce, *J. Mater. Chem.* **2005**, *15*, 94.
[3] H. Yersin, *Top. Curr. Chem.* **2004**, *241*, 1.
[4] J. Kido, Y. Okamoto, *Chem. Rev.* **2002**, *102*, 2357.
[5] Y. Kawamura, S. Yanagida, S. R. Forrest, *J. Appl. Phys.* **2002**, *92*, 87.
[6] J. Wang, R. Wang, J. Yang, Z. Zheng, M. D. Carducci, T. Cayou, N. Peyghambarian, G. E. Jabbour, *J. Am. Chem. Soc.* **2001**, *123*, 6179.
[7] M. Baldo, M. Segal, *Phys. Status Solidi A* **2004**, *201*, 1205.
[8] W.-Y. Wong, Z. He, S.-K. So, K.-L. Tong, Z. Lin, *Organometallics* **2005**, *24*, 4079.
[9] X. Gong, P. K. Ng, W. K. Chan, *Adv. Mater.* **1998**, *10*, 1337.
[10] A. P. Kulkarni, C. J. Tonzola, A. Babel, S. A. Jenekhe, *Chem. Mater.* **2004**, *16*, 4556.
[11] H. D. Stoeffler, N. B. Thornton, S. L. Temkin, K. S. Schanze, *J. Am. Chem. Soc.* **1995**, *117*, 7119.
[12] R. Argazzi, E. Bertolasi, C. Chiorboli, C. A. Bignozzi, M. K. Itokazu, N. Y. M. Iha, *Inorg. Chem.* **2001**, *40*, 6885.
[13] S. Ranjan, S.-Y. Lin, K.-C. Hwang, Y. Chi, W.-L. Ching, C.-S. Liu, Y.-T. Tao, C.-H. Chien, S.-M. Peng, G.-H. Lee, *Inorg. Chem.* **2003**, *42*, 1248.
[14] S. Kan, X. Liu, F. Shen, J. Zhang, Y. Ma, G. Zhang, Y. Wang, J. Shen, *Adv. Funct. Mater.* **2003**, *13*, 603.
[15] Y. Li, Y. Wang, Y. Zhang, Y. Wu, J. Shen, *Synth. Met.* **1999**, *99*, 257.
[16] T. M. Clarke, K. C. Gordon, D. L. Officer, S. B. Hall, G. E. Collis, A. K. Burrell, *J. Phys. Chem. A* **2003**, *107*, 11505.
[17] A. K. Burrell, J. Chen, G. E. Collis, D. K. Grant, D. L. Officer, C. O. Too, G. G. Wallace, *Synth. Met.* **2003**, *135–136*, 97.
[18] D. Ossipov, E. Zamaratski, J. Chattopadhyaya, *Helv. Chim. Acta* **1999**, *82*, 2186.
[19] J. V. Caspar, T. J. Meyer, *J. Phys. Chem.* **1983**, *87*, 952.
[20] M. K. Brennaman, T. J. Meyer, J. M. Papanikolas, *J. Phys. Chem. A* **2004**, *108*, 9938.
[21] M. K. Kuimova, D. C. Grills, P. Matousek, A. W. Parker, X.-Z. Sun, M. Towrie, M. W. George, *Vib. Spectrosc.* **2004**, *35*, 219.
[22] K. Wang, L. Huang, L. Gao, L. Jin, C. Huang, *Inorg. Chem.* **2002**, *41*, 3353.
[23] The electronic spectra are complicated for these systems, with many chromophores in the visible region, thus the Stokes shift calculated are phenomenological.
[24] These data pertain to solution-phase spectra, and some of the reorganization energy that leads to the Stokes shift will be reduced in the film phase because reorganization of the solvent cage will not be present. Thus, the band gaps will be smaller than estimated by our method. To obtain more accurate estimates of the band gaps is a topic of current investigation.
[25] Y. Li, Y. Cao, J. Gao, D. Wang, G. Yu, A. J. Heeger, *Synth. Met.* **1999**, *99*, 243.
[26] J. Fees, M. Ketterle, A. Klein, J. Fiedler, W. Kaim, *J. Chem. Soc. Dalton Trans.* **1999**, 2595.
[27] G. David, P. J. Walsh, K. C. Gordon, *Chem. Phys. Lett.* **2004**, *383*, 292.

 © 2006 Wiley-VCH Verlag GmbH & Co. KGaA, Weinheim

Glycoproteins

DOI: 10.1002/anie.200503900

Glycosylation of a Neoglycoprotein by Using Glycosynthase and Thioglycoligase Approaches: The Generation of a Thioglycoprotein**

*Johannes Müllegger, Hong Ming Chen, R. Antony J. Warren, and Stephen G. Withers**

Glycan structures, both intracellular and exposed on the surface of cells, play important roles in a large number of biological processes, such as cell–cell recognition, ligand–receptor binding, immunomodulation, and protein folding.[1,2] Elucidation of the biological function of glycoproteins is currently hampered mainly by the fact that they are not easily available as homogenous isoforms but exist as complex mixtures of different glycoforms.[3,4] As of yet, there are no generally useful strategies for the direct glycosylation of a protein to generate a natural glycoprotein: the strategies of Wong, Schultz, and co-workers are technically impressive but not yet applicable to the general production of glycoproteins on any scale.[5,6] Strategies therefore involve partial, specific deglycosylation of existing glycoproteins to create more homogenous populations of the glycoprotein, followed by chemoenzymatic remodeling.[7,8] These steps are required as the synthetic chemical assembly of larger glycostructures is essentially impossible on native proteins owing to the harsh conditions required. Two general strategies are to use glycosyl transferases[9] or the transglycosylation activity of glycosidases.[10] Only modest yields of shorter glycopeptides have generally been obtained by using the transglycosylation activity of *endo* glycosidases, although one very recent publication reports the high-yielding transglycosylation of a core N-glycan structure by using an activated oxazoline-donor sugar and a synthetic glycopeptide containing one N-linked β-*N*-acetylglycosaminyl residue as an acceptor.[11]

Glycosynthases and thioglycoligases are two new classes of mutant glycosidases recently developed for oligosaccharide synthesis, but they have not yet been applied to glycoprotein synthesis.[12,13] Indeed, the relatively high K_M values for their acceptors has caused concern that they would not be useful in this role. The goal of this study was to explore the applicability of these two classes of enzymes for the synthesis of glycoproteins by first using a neoglycoprotein acceptor as a model system to simplify the analysis. A particular goal was to explore the generation of glycoproteins in which the terminal sugar is linked through a glycosidase-resistant thioglycosidic bond and determine if such thioglycoproteins are recognized by other glycan-modifying enzymes. Through appropriate applications of such technology, it should be possible to generate therapeutic glycoproteins in which the terminal sugar is sulfur-linked. Such proteins should enjoy considerably longer serum half-lives.

The *endo* xylanase from *Bacillus circulans* (Bcx) was chosen as the protein base for a model neoglycoprotein for several reasons. First, it is a small, highly characterized protein of approximately the same size as cytokines; for some cytokines glycosylation is extremely important both for activity and serum half-life.[14] Second, as it is an enzyme, the effects of chemical and enzymatic manipulations on overall structural integrity can easily be followed by activity-based assays. Third, the three-dimensional structure of Bcx has been solved by X-ray crystallography and extensive NMR spectroscopy assignments.[15,16] Furthermore, the native protein contains no cysteines, thus unique thiol groups can be introduced at the surface by in vitro mutagenesis. This allows site-selective modification of Bcx with sugar entities through thiol-reactive reagents.[17] The sugar structures selected for conjugation were cellobiose and its 4′-thio analogue because these sugars function as good acceptors for *Agrobacterium* sp. (Abg) glycosynthase and Abg thioglycoligase, respectively. These are the enzymes that were used as glycosylation catalysts.

Thiol-reactive cellobioside **1** was synthesized by reduction and bromoacetylation of *p*-nitrophenyl cellobioside (see Supporting Information). After reaction with Bcx S22C for 1 h, analysis with MALDI-TOF MS showed complete labeling with a mass increase equivalent to one incorporated label (+474.2 Da) resulting in neoglycoprotein G2-Bcx (Figure 1A, B). This neoglycoprotein was then tested as an acceptor for Abg 2F6 glycosynthase[18] by using α-galactopyranosyl fluoride (α-GalF) as a donor and monitoring the reaction with MALDI-TOF MS. Complete conversion of the G2-Bcx into a glycoprotein bearing three sugar units (named LacG-Bcx) was observed after overnight incubation (Figure 1C, Figure 2G, Scheme 1A). No incorporation was observed in control reactions that used Bcx wild-type (wt) or the unlabeled mutant Bcx S22C as acceptors. Likewise, no reaction occurred upon incubation of G2-Bcx with only α-GalF over extended periods of time. The time course for this reaction showed conversion of $\geq 80\,\%$ in 200 minutes (see Supporting Information) when a molar ratio of 19:1 for acceptor/glycosynthase was used.

[*] Dr. J. Müllegger, Dr. H. M. Chen, Prof. Dr. S. G. Withers
Protein Engineering Network of Centres of Excellence
Department of Chemistry
University of British Columbia
Vancouver, B. C. V6T 1Z1 (Canada)
Fax: (+1) 604-822-8869
E-mail: withers@chem.ubc.ca
Dr. R. A. J. Warren
Protein Engineering Network of Centres of Excellence
Department of Microbiology and Immunology
University of British Columbia
Vancouver, B. C. V6T 1Z1 (Canada)

[**] The authors would like to thank Prof. L. P. McIntosh and Prof. W. W. Wakarchuk for Bcx clones, Dr. Y. W. Kim for Abg 2F6 glycosynthase, and L. Lairson for glycosyl transferases, as well as the proteomics core facility of UBC for providing assistance with, and access to, the mass spectrometer. The project was funded by the Natural Sciences and Engineering Research Council of Canada (NSERC) and the Protein Engineering Network of Centres of Excellence of Canada (PENCE). J.M. was financed by a Schrödinger Fellowship from the Austrian FWF.

Supporting information for this article is available on the WWW under http://www.angewandte.org or from the author.

 © 2006 Wiley-VCH Verlag GmbH & Co. KGaA, Weinheim

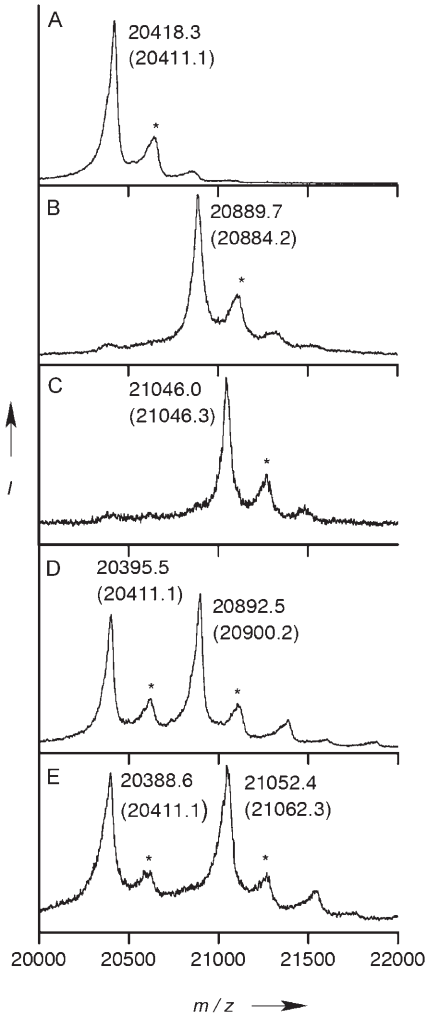

Figure 1. MALDI-TOF MS spectra of Bcx S22C before chemical glycosylation (A), G2-Bcx (B), LacG-Bcx (C), 4SG2-Bcx (D), and GalSG-Bcx (E). Average measured masses for the protein and calculated masses (in brackets) are shown. Asterisks (*) denote artifact peaks from sinapinic acid (SPA) matrix addition to the protein (≈206–224 Da). *I* = intensity.

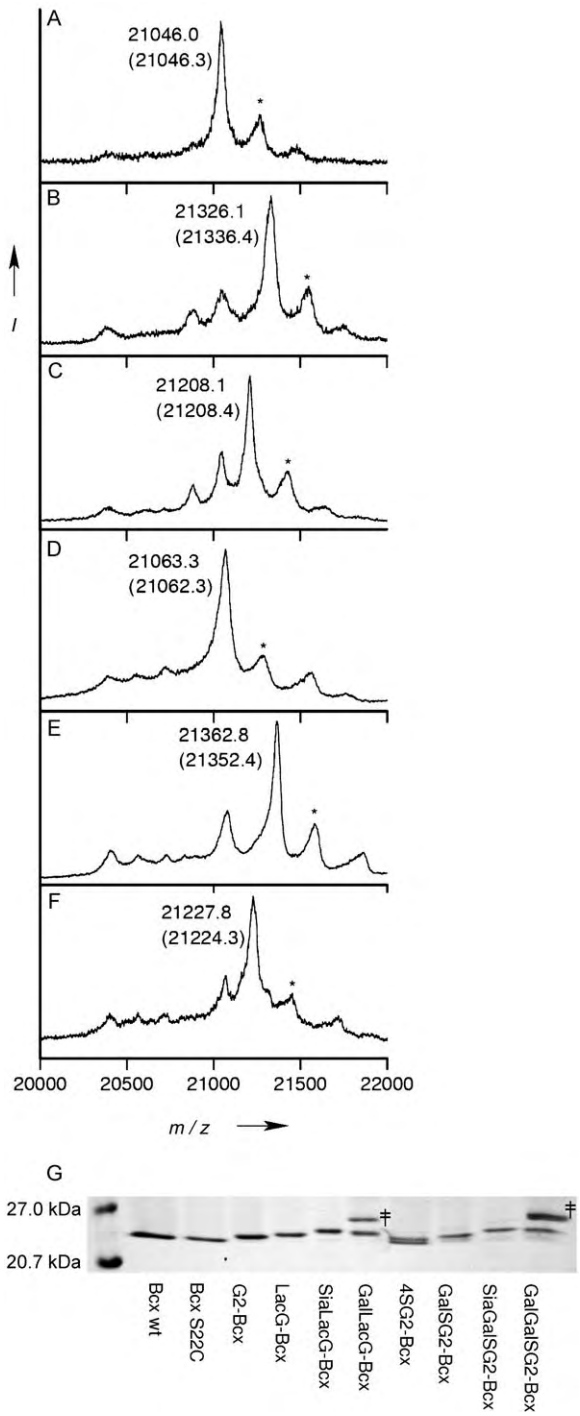

Figure 2. MALDI-TOF MS spectra of LacG-Bcx (A), and the products of glycosylation by Cst1 (B) and LgtC (C). Panels (D, E, F) show the respective spectra for GalSG2-Bcx. Asterisks (*) denote artifact peaks from SPA matrix addition to the protein (≈206–224 Da). Average masses measured for the protein and calculated masses (in brackets) are shown. (G) SDS-PAGE analysis of all Bcx neoglycoprotein variants. Small shifts in migration are observed, but more importantly the complete conversions achieved in the glycosynthase and thioglycoligase reactions are demonstrated. ‡ indicates protein contamination introduced with LgtC. *I* = intensity.

Two sets of experiments were undertaken to confirm the type of linkage formed by the glycosynthase on the surface of the neoglycoprotein. Cleavage of the terminal galactose by jack-bean β-galactosidase (β-Gal) and both the galactose and the glucose by β-glucosidase from Abg (bifunctional β-galactosidase/glucosidase), as shown by MALDI-TOF MS (see Supporting Information), clearly shows formation of the expected β linkage.[19] Confirmation of the terminal lactose structure on the neoglycoprotein was provided by the action of two glycosyl transferases with high specificities for lactose as an acceptor: LgtC, an α-1,4-galactosyl transferase from *Neisseria meningitides*,[20] and Cst1, an α-2,3-sialyltransferase from *Campylobacter jejuni*.[21] Both enzymes used LacG-Bcx as an acceptor, resulting in the formation of the Pk antigen (Gal α-1,4-lactose) and sialyllactose epitopes, respectively, on the surface of Bcx (Figure 2B, C). Finally, to confirm that all manipulations were carried out on a properly folded protein and that the glycosylation did not affect this conformation, the xylanase activities of Bcx wt, Bcx S22C, and LacG-Bcx were measured with 2,5-dinitrophenyl xylobioside as the

 © 2006 Wiley-VCH Verlag GmbH & Co. KGaA, Weinheim

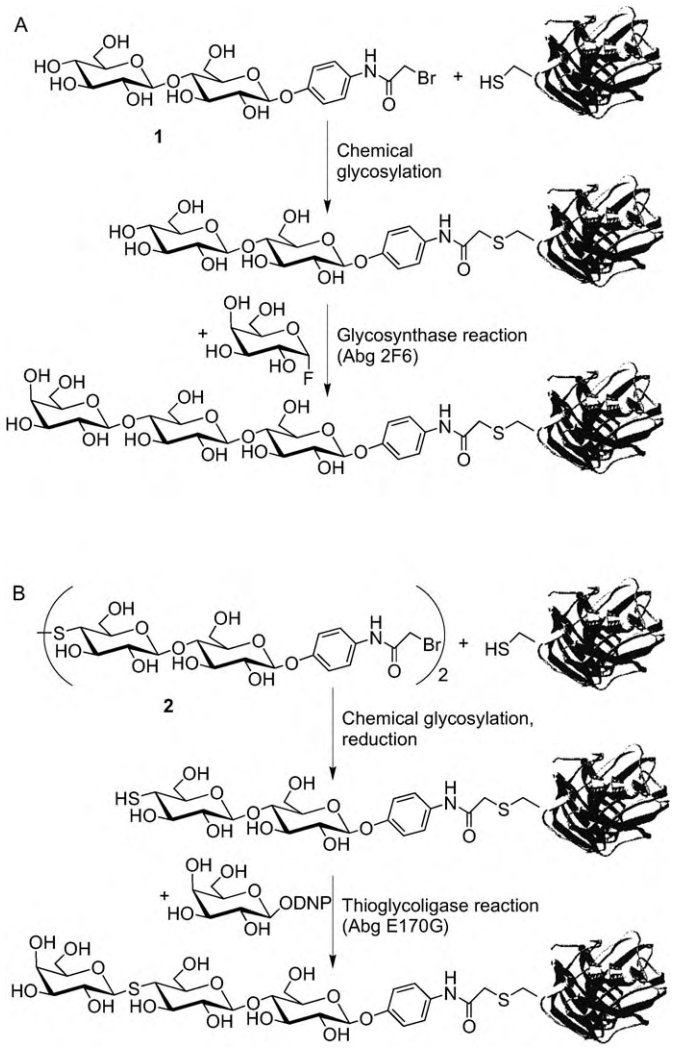

Scheme 1. Reaction scheme for the chemical glycosylation and subsequent transfer of a galactose by Abg glycosynthase (A) or Abg thioglycoligase (B).

substrate. No significant differences in k_{cat} or K_M from literature values were observed,[22] confirming the integrity of the protein (see Supporting Information).

Parallel studies to test the thioglycoligase approach required incorporation of a 4′-deoxy-4′-thiocellobiosyl moiety onto the neoglycoprotein. This was achieved by incubating Bcx S22C with an excess of **2** (used in its disulfide form to minimize self-polymerization) overnight, followed by reduction with dithiothreitol (DTT). MALDI-TOF MS analysis revealed about 50% incorporation to create thio-neoglycoprotein Bcx-4SG2 (Figure 1D). This mixture of labeled and unlabeled protein was directly used as an acceptor for the Abg thioglycoligases, with the unreacted Bcx S22C acting as a useful internal control. Three different thioglycoligase mutants, namely Abg E170A, Abg E170G, and Abg E170Q, were tested by using 2,4-dinitrophenyl β-D-glucopyranoside (DNPGlc) and 2,5-dinitrophenyl β-D-galactopyranoside (DNPGal) as donors. Glycosylation of Bcx-4SG2 was observed by MALDI-TOF MS when each of the thioglycoligase mutants were used with DNPGlc (creating GSG2-Bcx), whereas only Abg E170G was active when using DNPGal as a donor (creating GalSG2-Bcx; Figure 1E and Figure 2G). This specificity is in full accordance with earlier observations.[23] Control reactions carried out with Bcx wt and the "internal" control Bcx S22C showed no signs of glycosylation, suggesting specific attachment of the hexose unit to the thioglycoside part of the thio-neoglycoprotein. The presence of a thioglycosidic linkage was established in three ways. First, the mixture of GalSG2-Bcx and Bcx S22C was treated with the thiol-reactive compound (+)-biotinyl-iodoacetamidyl-3,6-dioxaoctanediamine (Pierce), and the reaction mixture analyzed by MALDI-TOF MS. The mass of Bcx S22C, but not that of GalSG2-Bcx, increased by the mass of the biotin label (+415.5 Da), confirming the absence of a free thiol in the latter case and thus selective glycosylation of the 4-thio residue on the thio-neoglycoprotein. Further, GalSG2-Bcx was then easily separated from the contaminating Bcx S22C by capturing the biotin-labeled protein on streptavidin beads (Pierce). Second, GalSG2-Bcx was glycosylated by LgtC and Cst1, with the thio-neoglycoprotein proving to be a good acceptor for both transferases, as shown by MALDI-TOF MS (Figure 2D,E,F). This confirms that a thiolactose structure is present and that the presence of sulfur does not affect the action of the transferase. Third, the formation of a glycosidase-resistant thioglycoside linkage by the thioglycoligase was confirmed by subjecting the samples of GalSG2-Bcx to digestion with jack-bean β-Gal and Abg.[24,25] In both cases cleavage was not observed by MALDI-TOF MS. Thus, not only is a thioglycoprotein produced for the first time, but it has also proven to be resistant to glycosidase digestion.

In summary, we demonstrate unambiguously the utility of the glycosynthase and thioglycoligase approaches for the remodeling of glycoproteins, and describe the first generation of a thioglycosylated glycoprotein. This work thereby complements the recent demonstration of the synthesis of thioglycoside-containing glycolipids by using the very low inherent activities of a few glycosyltransferases to catalyze thioglycoside formation.[26,27] The resistance of this thioglycoprotein, but not of its oxygen analogue, to glycosidase digestion and the further glycosylation of both structures by glycosyl transferases directly demonstrates the potential of this approach for generating metabolically stable glycoprotein structures. Work is currently underway to extend this strategy with other glycosynthases and thioglycoligases to other glycosylated structures, particularly those which terminate in a thiosialoside, and to install these in natural glycoproteins.

Received: November 4, 2005
Revised: January 21, 2006
Published online: March 10, 2006

Keywords: enzyme models · glycoproteins · glycosylation · thioglycoligases · thioglycoproteins

[1] P. Van den Steen, P. M. Rudd, R. A. Dwek, G. Opdenakker, *Crit. Rev. Biochem. Mol. Biol.* **1998**, *33*, 151–208.

 © 2006 Wiley-VCH Verlag GmbH & Co. KGaA, Weinheim

[2] A. Helenius, M. Aebi, *Science* **2001**, *291*, 2364 – 2369.
[3] J. F. Nemeth, G. P. Hochgesang, Jr., L. J. Marnett, R. M. Caprioli, *Biochemistry* **2001**, *40*, 3109 – 3116.
[4] C. Neususs, U. Demelbauer, M. Pelzing, *Electrophoresis* **2005**, *26*, 1442 – 1450.
[5] R. Xu, S. R. Hanson, Z. Zhang, Y. Y. Yang, P. G. Schultz, C. H. Wong, *J. Am. Chem. Soc.* **2004**, *126*, 15654 – 15655.
[6] Z. Zhang, J. Gildersleeve, Y. Y. Yang, R. Xu, J. A. Loo, S. Uryu, C. H. Wong, P. G. Schultz, *Science* **2004**, *303*, 371 – 373.
[7] B. G. Davis, *Chem. Rev.* **2002**, *102*, 579 – 602.
[8] M. J. Grogan, M. R. Pratt, L. A. Marcaurelle, C. R. Bertozzi, *Annu. Rev. Biochem.* **2002**, *71*, 593 – 634.
[9] K. Witte, P. Sears, R. Martin, C. H. Wong, *J. Am. Chem. Soc.* **1997**, *119*, 2114 – 2118.
[10] K. Yamamoto, S. Kadowaki, J. Watanabe, H. Kumagai, *Biochem. Biophys. Res. Commun.* **1994**, *203*, 244 – 252.
[11] B. Li, Y. Zeng, S. Hauser, H. Song, L. X. Wang, *J. Am. Chem. Soc.* **2005**, *127*, 9692 – 9693.
[12] M. Jahn, S. G. Withers, *Biocatal. Biotransform.* **2003**, *21*, 159 – 166.
[13] G. Perugino, A. Trincone, M. Rossi, M. Moracci, *Trends Biotechnol.* **2004**, *22*, 31 – 37.
[14] L. C. Wasley, G. Timony, P. Murtha, J. Stoudemire, A. J. Dorner, J. Caro, M. Krieger, R. Kaufman, *Blood* **1991**, *77*, 2624 – 2632.
[15] W. W. Wakarchuk, R. L. Campbell, W. L. Sung, J. Davoodi, M. Yaguchi, *Protein Sci.* **1994**, *3*, 467 – 475.
[16] L. A. Plesniak, W. W. Wakarchuk, L. P. McIntosh, *Protein Sci.* **1996**, *5*, 1118 – 1135.
[17] D. Macmillan, R. M. Bill, K. A. Sage, D. Fern, S. L. Flitsch, *Chem. Biol.* **2001**, *8*, 133 – 145.
[18] Y. W. Kim, S. S. Lee, R. A. Warren, S. G. Withers, *J. Biol. Chem.* **2004**, *279*, 42787 – 42793.
[19] L. F. Mackenzie, Q. P. Wang, R. A. J. Warren, S. G. Withers, *J. Am. Chem. Soc.* **1998**, *120*, 5583 – 5584.
[20] L. L. Lairson, C. P. Chiu, H. D. Ly, S. He, W. W. Wakarchuk, N. C. Strynadka, S. G. Withers, *J. Biol. Chem.* **2004**, *279*, 28339 – 28344.
[21] M. Gilbert, J. R. Brisson, M. F. Karwaski, J. Michniewicz, A. M. Cunningham, Y. Wu, N. Young, W. Wakarchuk, *J. Biol. Chem.* **2000**, *275*, 3896 – 3906.
[22] L. Ziser, I. Setyawati, S. G. Withers, *Carbohydr. Res.* **1995**, *274*, 137 – 153.
[23] J. Müllegger, M. Jahn, H. M. Chen, R. A. J. Warren, S. G. Withers, *Protein Eng. Des. Sel.* **2005**, *18*, 33 – 40.
[24] M. Jahn, J. Marles, R. A. J. Warren, S. G. Withers, *Angew. Chem.* **2003**, *115*, 366 – 368; *Angew. Chem. Int. Ed.* **2003**, *42*, 352 – 354; .
[25] C. Orgeret, E. Seillier, C. Gautier, J. Defaye, H. Driguez, *Carbohydr. Res.* **1992**, *224*, 29 – 40.
[26] J. Rich, W. Wakarchuk, D. Bundle, *Chemistry* **2005**, *12*, 845 – 848.
[27] J. Rich, A. Szpacenko, M. Palcic, D. Bundle, *Angew. Chem.* **2004**, *116*, 623 – 625; *Angew. Chem. Int. Ed.* **2004**, *43*, 613 – 615.

 © 2006 Wiley-VCH Verlag GmbH & Co. KGaA, Weinheim

Fluorinated Peptides

DOI: 10.1002/anie.200503567

Fluorinated Interfaces Drive Self-Association of Transmembrane α Helices in Lipid Bilayers**

Natascha Naarmann, Başar Bilgiçer, He Meng, Krishna Kumar, and Claudia Steinem**

Integral membrane proteins represent roughly a third of the human proteome[1] and are responsible for a host of fundamental cellular processes including signaling, trafficking, photosynthesis, and respiration. Furthermore, they function as ion channels, pores, and transporters and are targets of the majority of pharmaceuticals in use today.[2] Membrane proteins are embedded in a hydrophobic lipid bilayer, and the question arises as to what the determinants that drive and stabilize a discrete protein conformation and protein–protein interactions in this particular environment are. An emerging answer to this question is that the primary forces are relatively weak van der Waals packing, occasional hydrogen bonding, and electrostatic interactions.[3] We recently reported a de novo design strategy to control oligomerization of independent transmembrane helices that relies on the unique properties of fluorinated interfaces.[4,5] These "fluorous" interfaces[6,7] self-sort from similar aliphatic protein surfaces[6,8] and also are capable of directing helix–helix interactions in the context of the nonpolar environment of detergent micelles.[9] Herein we show that coupled with hydrogen bonds as mediators of protein–protein interactions,[10] fluorinated interfaces, which are simultaneously hydrophobic and lipophobic, are superior and more efficient at directing oligomer

[*] Prof. Dr. K. Kumar
Cancer Center
Tufts-New England Medical Center
Boston, MA 02110 (USA)
Fax: (+1) 617-627-3443
E-mail: krishna.kumar@tufts.edu
Dr. N. Naarmann, Prof. Dr. C. Steinem
Institut für Analytische Chemie, Chemo- und Biosensorik
Universität Regensburg
93040 Regensburg (Germany)
Fax: (+49) 943-4491
E-mail: claudia.steinem@chemie.uni-regensburg.de
Dr. B. Bilgiçer,[+] H. Meng,[+] Prof. Dr. K. Kumar
Department of Chemistry
Tufts University
Medford, MA 02155-5813 (USA)
[+] These authors contributed equally to this work.

[**] We thank Dr. J. D. Lear for helpful discussions. This work was supported in part by the National Institutes of Health (Grants GM65500 and 1S10RR017948) and by the National Science Foundation (Grants CHE-0236846 and CHE-0320783). Additional support to C.S. was provided by the Fonds der Chemischen Industrie. K.K. is a DuPont Young Professor.

Supporting information for this article is available on the WWW under http://www.angewandte.org or from the author.

InterScience
© 2006 Wiley-VCH Verlag GmbH & Co. KGaA, Weinheim

structures in phospholipid membranes than those based on natural aliphatic side chains alone.

Our design is based on the heptad [(abcdefg)$_n$] repeat of coiled coils characterized by a 4–3 (a and d positions) disposition of hydrophobic residues.[11] Interhelical interactions in membranes have been compared to the "knobs-into-holes" packing adopted by soluble coiled coils.[12] Furthermore, both the left-handed crossing angles of helices ($\approx 20°$) and the rotamer distribution of the leucine residues in membrane proteins are similar to those observed in coiled coils.[13] Peptide TH1 (Figure 1) is adorned with leucine residues at all a and d positions with the exception of a single asparagine at position 14, and it was demonstrated previously that similar peptides form trimeric assemblies in detergent micelles driven by interhelical hydrogen bonding.[14–16] As a control, peptide TH2 (Figure 1) was synthesized in which the asparagine was replaced by leucine, thereby removing the sole interhelical hydrogen-bonding interaction and leading to monomeric helical structures in detergent micelles. The designed peptides were rendered membrane soluble by replacement of the hydrophilic and charged residues that are usually in contact with water with randomly selected hydrophobic residues. To investigate the effect of fluorination on the aggregation properties of such peptides, all canonical positions that constitute the helix-packing interface in TH1 were replaced by 5,5,5,5′,5′,5′-(2*S*)-hexafluoroleucine (**L**)[17] in TF1 (Figure 1) to yield a simultaneously hydrophobic and lipophobic interhelical interface. A single tryptophan at position 4 was included to function as an environment-sensitive spectroscopic marker.

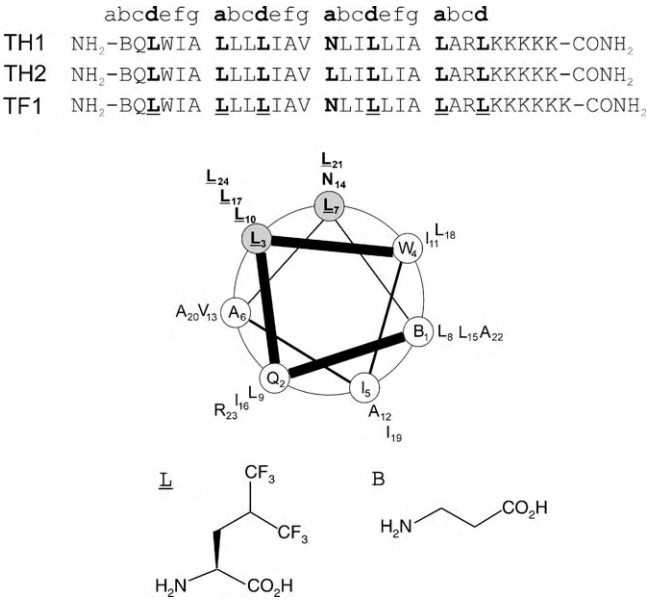

Figure 1. Sequences of peptides TH1, TH2, and TF1 shown with a helical wheel representation of TF1. Residues at the a and d positions that form the putative interhelical surfaces are shaded. TH1 and TH2 contain leucines at the a and d positions of the 4–3 heptad repeat, whereas TF1 is decorated with hexafluoroleucine (**L**) at all canonical membrane embedded interface positions. Lysine residues at the C terminus were added to preserve modest solubility in HPLC solvents to aid purification.

The fluorescence of tryptophan was monitored for peptides inserted into large unilamellar vesicles (LUVs) composed of 1-palmitoyl-2-oleoyl-*sn*-glycero-3-phosphocholine (POPC) as a function of different lipid/peptide ratios. In all cases, a hypsochromic shift of tryptophan emission was observed relative to that of tryptophan in aqueous solution ($\lambda_{max,em} = 350$ nm) indicative of a more-hydrophobic environment of the tryptophan residue. For lipid/peptide ratios greater than 300:1, the maximum of fluorescence emission was 334 nm for TH1, 340 nm for TH2, and 337 nm for TF1. Tryptophan is frequently located at the bilayer–water interface[18] and it is likely that it is positioned similarly in this instance. The slight differences in the observed λ_{max} values for tryptophan emission therefore are presumably a consequence of the exact localization of the indole chromophore in the lipid bilayer and also of the differential tendency of the peptides to aggregate (see below). Circular dichroism spectra established that all peptides are α helical in POPC vesicles, with characteristic negative maxima at 222 and 208 nm (Figure 2). It is possible that the lower CD amplitude of TH2 relative to that of TH1 and TF1 may be due to its non-self-associated state in the vesicles.

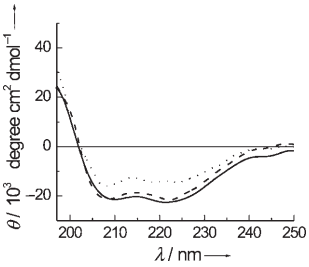

Figure 2. Circular dichroism spectra of TH2 (••••), TH1 (----), and TF1 (——) in POPC show that all peptides are helical in membrane environments. Buffer conditions: tris–HCl (10 mM), NaCl (100 mM), pH 7.5.

Fluorescence resonance energy transfer (FRET) experiments were recently used to assess the oligomeric state of peptides not only in detergent micelles[19,20] but also in vesicles.[21,22] In this case, FRET between donor- and acceptor-labeled peptides embedded in large unilamellar vesicles composed of POPC was used to determine the oligomeric state of the peptide ensembles and the dissociation constants of the corresponding aggregates. Peptides equipped with 7-nitrobenz-2-oxa-1,3-diazole (NBD) attached to the N terminus through a β-alanine linker were used as fluorescence donors, whereas 5(6)-carboxytetramethylrhodamine (TAMRA)-labeled peptides were used as acceptors. Self-association of peptides within the lipid bilayer results in an increased quenching of the NBD fluorescence with increasing amounts of TAMRA-labeled peptides[23–27] and a concomitant increase in TAMRA fluorescence (see Supporting Information). The total peptide concentration and the peptide/lipid ratio were kept constant. A plot of the relative fluorescence of

 © 2006 Wiley-VCH Verlag GmbH & Co. KGaA, Weinheim

the quenched donor F to that in the absence of quenching F_0 as a function of the mole fraction of the TAMRA-labeled peptide (χ_A) for different lipid/peptide ratios resulted in the data sets depicted in Figure 3. It was shown earlier that control peptide TH2 forms monomeric structures in detergent solutions. The observed quenching of the fluorescence of randomly distributed donors as a function of acceptor concentration in vesicles (Figure 3 A) is characteristic of the statistical occurrence of FRET due to the presence of several acceptors in any given vesicle. On the basis of the assumption that TH2 is monomeric, the Förster radius R_0 can be fitted to the two data sets shown in Figure 3 A according to the theoretical description of Wolber and Hudson[28] and leads to a value of $R_0 = 5.6$ nm (see Supporting Information). This value is in close agreement with the Förster radius reported in the literature.[15] The numerical value is independent of a parallel or antiparallel orientation of the peptides as it exceeds the estimated interchromophore distance in either mode of assembly. The degree of association of TH1 and TF1 in POPC LUVs can be determined by assuming a binomial distribution of donors and acceptors in an oligomeric ensemble after accounting for statistical occurrence of FRET. From a global fit analysis of the three data sets shown in Figure 3 B and C for different lipid/peptide ratios, the best fits were obtained when assuming a monomer–trimer equilibrium for TH1 and TF1 (see Supporting Information). Dissociation constants attending this equilibrium were extracted, with $K_D = (1.8 \pm 0.2) \times 10^{-5}$ MF^2 for TH1 and a significantly tighter trimeric assembly with $K_D = (0.56 \pm 0.05) \times 10^{-5}$ MF^2 for TF1. These values unambiguously demonstrate that the fluorinated interface in TF1 has a considerable effect on its self-assembly properties. The fluorinated helix interface increases the affinity of the peptide helices owing to the increased tendency of fluorinated residues to face away from the hydrocarbon lipid, thus forming a "fluorous" core. An alternative explanation may be found in the strength of the interhelical hydrogen bonding that may be enhanced within the highly fluorinated core. Figure 4 shows the relative fluorescence as a function of TAMRA-labeled peptides at a lipid/peptide ratio of 600:1 and highlights the relative aggregation propensity of all three peptides. TF1 displays the greatest proclivity to form trimeric assemblies followed by TH1, whereas TH2 is merely monomeric.

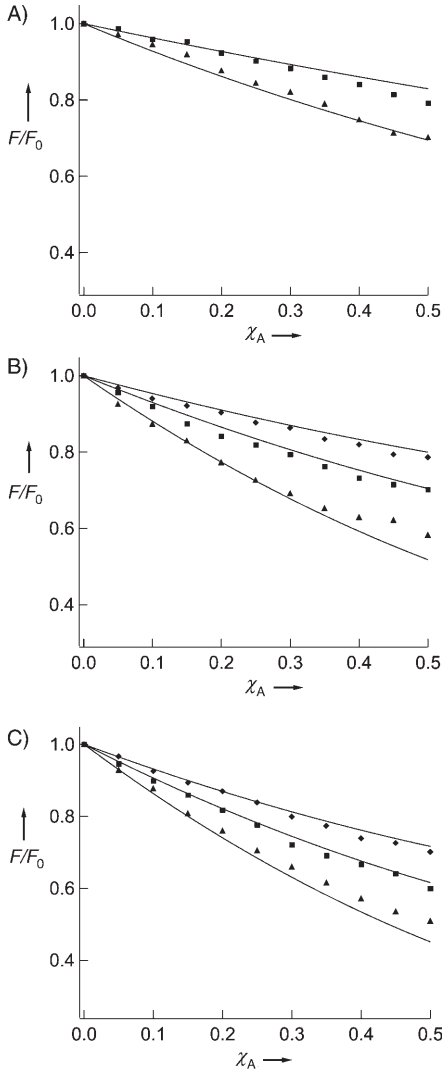

Figure 3. Association of A) TH2, B) TH1, and C) TF1 as determined by FRET. The ratio of fluorescence intensity in the presence (F) and absence (F_0) of acceptor was measured as a function of the mole fraction χ_A of TAMRA-labeled peptides. The experiments were performed for three different lipid/peptide ratios: 300:1 (▲, 1.65 mM), 600:1 (■, 3.30 mM) and 900:1 (◆, 4.95 mM). The mole fraction of TAMRA-labeled peptide χ_A was varied in the range 0–0.5 μM, while the total peptide concentration was kept constant by using unlabeled peptide. The solid lines are results of global fits based on the assumption of a monomer–trimer equilibrium (B, C), whereas TH2 (A) was assumed to be monomeric.[30]

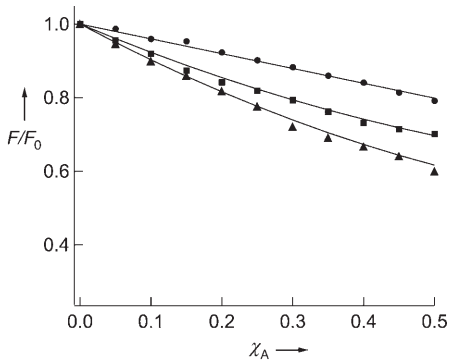

Figure 4. Comparison of the association propensity of TH2 (●), TH1 (■), and TF1 (▲) at a constant lipid/peptide ratio of 600:1 as judged by FRET.

In conclusion, we have demonstrated that incorporation of a nonbiological fluorinated interface is both robust and efficient at mediating helix–helix interactions in phospholipid membranes. Such supramolecularly assembled fluorous surfaces are orthogonal in their noncovalent self-association behavior with side chains found in nature and might present a unique opportunity to reengineer membrane-embedded protein systems.

 © 2006 Wiley-VCH Verlag GmbH & Co. KGaA, Weinheim

Experimental Section

POPC was purchased from Avanti Polar Lipids (Alabaster, AL, USA) and used without further purification. Peptides were synthesized manually on 4-methylbenzhydrylamine (MBHA) resin by using the in situ neutralization protocol for *t*Boc chemistry on a 0.15-mmol scale. 4-Fluoro-7-nitrobenz-2-oxa-1,3-diazole (NBD-F) and activated 5-(and -6)-carboxytetramethylrhodamine (TAMRA) were coupled through the β-alanine linker to the N terminus. Details of the chemical synthesis were reported previously.[9]

POPC LUVs with the requisite amount of peptide were prepared according to the extrusion method.[29] Peptide concentrations were determined by UV/Vis spectroscopy by using NBD absorbance ($\varepsilon_{460} = 23000\,\text{M}^{-1}\,\text{cm}^{-1}$) or TAMRA absorbance ($\varepsilon_{550} = 92000\,\text{M}^{-1}\,\text{cm}^{-1}$) in the case of labeled peptides, whereas those of unlabeled peptides were determined by using the absorbance of the single tryptophan residue ($\varepsilon_{280} = 5690\,\text{M}^{-1}\,\text{cm}^{-1}$). Lipids dissolved in chloroform and peptides dissolved in ethanol were added to a glass tube and the solvents were evaporated in a stream of nitrogen followed by several hours in vacuo to obtain a lipid–peptide film. Multilamellar vesicles were obtained by swelling the lipid–peptide film in water for 30 min with periodic vortexing for 30 s. The resulting multilamellar vesicles were then sized by extrusion through stacked polycarbonate membranes (nominal pore diameters of 100 nm) with a miniextruder (LiposoFast, Avestin) to obtain large unilamellar vesicles.

Fluorescence emission spectra were recorded on a Cary Eclipse fluorescence spectrometer (Varian, Darmstadt). Emission spectra were obtained by excitation at 280 nm and recorded in the wavelength range of 290–450 nm with continuous stirring. Fluorescence spectra were corrected for vesicle scattering and dilution of peptide solution if necessary. Excitation and emission bandwidths were set at 5 nm. All spectra were recorded at room temperature.

FRET was used to determine the strength of peptide association in lipid membranes. Fluorescence spectra were obtained by excitation at 485 nm with emission recorded in the range 500–700 nm with continuous stirring of the solution at room temperature. Corrections for scattering were applied by subtracting a spectrum of a vesicle suspension lacking peptides. NBD-labeled peptides were used as donors (2.75 μM) and TAMRA-labeled peptides as acceptors (0–0.5 μM). The total peptide concentration was kept constant at 5.5 μM by using unlabeled peptides. The FRET measurements were performed for different lipid/peptide ratios by changing the POPC concentration: 300:1 (1.65 mM POPC), 600:1 (3.30 mM POPC) and 900:1 (4.95 mM POPC). All samples were prepared in water and diluted with tris–HCl (10 mM), NaCl (100 mM), pH 7.5.

Circular dichroism spectra were recorded between 195–250 nm on a Jasco J-714 CD spectrometer (Jasco, Easton, MD, USA) at room temperature in a 10-mm-pathlength quartz cuvette for TF1 and 1-mm cuvettes for TH1 and TH2. A total of 10 scans were obtained and averaged with a scanning rate of 50 nm min^{-1} with a resolution of 1 nm and bandwidth of 1 nm with a response time of 2 s. For TH1 and TH2, a lipid/peptide ratio of 100:1 was used, whereas for TF1 this ratio was 125:1. The peptide concentrations were set to 25 μM for TH1 and TH2 and 20 μM for TF1. The reference spectra of the respective POPC vesicle suspensions were subtracted.

Received: October 7, 2005
Revised: December 20, 2005
Published online: March 13, 2006

Keywords: FRET (fluorescence resonance energy transfer) · membrane proteins · membranes · peptides · protein engineering

[1] T. J. Stevens, I. T. Arkin, *Proteins* **2000**, *39*, 417–420.
[2] T. Klabunde, G. Hessler, *ChemBioChem* **2002**, *3*, 929–944.
[3] T. Haltia, E. Freire, *Biochim. Biophys. Acta* **1995**, *1228*, 1–27.
[4] B. Bilgiçer, K. Kumar, *J. Chem. Educ.* **2003**, *80*, 1275–1281.
[5] N. C. Yoder, K. Kumar, *Chem. Soc. Rev.* **2002**, *31*, 335–341.
[6] B. Bilgiçer, X. Xing, K. Kumar, *J. Am. Chem. Soc.* **2001**, *123*, 11815–11816.
[7] Y. Tang, G. Ghirlanda, N. Vaidehi, J. Kua, D. T. Mainz, I. W. Goddard, W. F. DeGrado, D. A. Tirrell, *Biochemistry* **2001**, *40*, 2790–2796.
[8] B. Bilgiçer, K. Kumar, *Tetrahedron* **2002**, *58*, 4105–4112.
[9] B. Bilgiçer, K. Kumar, *Proc. Natl. Acad. Sci. USA* **2004**, *101*, 15324–15329.
[10] J. D. Lear, H. Gratkowski, W. F. DeGrado, *Biochem. Soc. Trans.* **2001**, *29*, 559–564.
[11] A. Lupas, *Trends Biochem. Sci.* **1996**, *21*, 375–382.
[12] D. Langosch, J. Heringa, *Proteins* **1998**, *31*, 150–159.
[13] A. K. Chamberlain, J. U. Bowie, *Biophys. J.* **2004**, *87*, 3460–3469.
[14] H. Gratkowski, J. D. Lear, W. F. DeGrado, *Proc. Natl. Acad. Sci. USA* **2001**, *98*, 880–885.
[15] C. Choma, H. Gratkowski, J. D. Lear, W. F. DeGrado, *Nat. Struct. Biol.* **2000**, *7*, 161–166.
[16] F. X. Zhou, H. J. Merianos, A. T. Brunger, D. M. Engelman, *Proc. Natl. Acad. Sci. USA* **2001**, *98*, 2250–2255.
[17] X. Xing, A. Fichera, K. Kumar, *Org. Lett.* **2001**, *3*, 1285–1286.
[18] J. A. Killian, G. von Heijne, *Trends Biochem. Sci.* **2000**, *25*, 429–434.
[19] J. D. Lear, A. L. Stouffler, H. Gratkowski, V. Nanda, W. F. DeGrado, *Biophys. J.* **2004**, *87*, 3421–3429.
[20] R. M. Johnson, C. L. Heslop, C. M. Deber, *Biochemistry* **2004**, *43*, 14361–14369.
[21] E. Li, M. You, K. Hristova, *Biochemistry* **2005**, *44*, 352–360.
[22] M. You, E. Li, W. C. Wimley, K. Hristova, *Anal. Biochem.* **2005**, *340*, 154–164.
[23] B. D. Adair, D. M. Engelman, *Biochemistry* **1994**, *33*, 5539–5544.
[24] L. A. Chung, J. D. Lear, W. F. DeGrado, *Biochemistry* **1992**, *31*, 6608–6616.
[25] M. Li, L. G. Reddy, R. Bennett, N. D. Silva, Jr., L. R. Jones, D. D. Thomas, *Biophys. J.* **1999**, *76*, 2587–2599.
[26] E. London, H. G. Khorana, *J. Biol. Chem.* **1982**, *257*, 7003–7011.
[27] L. G. Reddy, L. R. Jones, D. D. Thomas, *Biochemistry* **1999**, *38*, 3954–3962.
[28] P. K. Wolber, B. S. Hudson, *Biophys. J.* **1979**, *28*, 179–210.
[29] R. C. MacDonald, R. I. MacDonald, B. P. M. Menco, K. Takeshita, N. K. Subbarao, L. Hu, *Biochim. Biophys. Acta* **1991**, *1061*, 297–303.
[30] N. Naarmann, B. Bilgiçer, K. Kumar, C. Steinem, *Biochemistry* **2005**, *44*, 5188–5195.

 © 2006 Wiley-VCH Verlag GmbH & Co. KGaA, Weinheim

Asymmetric Synthesis

DOI: 10.1002/anie.200503765

A Dynamic Kinetic Resolution of Allyl Alcohols by the Combined Use of Lipases and $[VO(OSiPh_3)_3]$**

Shuji Akai, Kouichi Tanimoto, Yukiko Kanao, Masahiro Egi, Tomoko Yamamoto, and Yasuyuki Kita**

The lipase-catalyzed dynamic kinetic resolution (DKR) of racemic alcohols has drawn increasing attention over the last few years. The DKR protocol combines the lipase-catalyzed kinetic resolution (KR) of racemic alcohols[1] with an in situ racemization of the less reactive enantiomers, thus producing optically enriched esters in up to quantitative yields,[2–4] whereas the original KR has the inherent limitation of 50% product yield at best. In previously reported DKRs, ruthenium complexes were used as effective catalysts to bring about the racemization of optically active alcohols through oxidation/reduction reactions. Similarly, the combined use of lipases with other transition-metal-based racemization catalysts has the potential to produce diverse DKR methods. However, although some rhodium, iridium, ruthenium, and aluminum complexes are known to catalyze the racemization of alcohols,[5] only a few have proven to be compatible with enzymatic reactions.[5a,6]

Optically enriched allyl alcohols and their derivatives are especially important as useful intermediates in the synthesis of natural and non-natural compounds.[7] Therefore, their asymmetric synthesis has been extensively investigated, with much of the attention focused on the transition-metal-catalyzed KR and DKR of allyl alcohols and their esters[8,9] and the asymmetric reduction of enones.[10,11] From the viewpoint of the synthetic utility of the allyl alcohols as well as the extension of the lipase-catalyzed DKR methodology, we report herein a very different DKR of allylic alcohols by the combination of lipases with $[VO(OSiPh_3)_3]$.[12]

It has been known for more than three decades that the oxovanadium(v) compounds, $[VO(OR)_3]$ (**1**), catalyze the interconversion of allylic alcohols (**2** and **3**) through the formation of the allyl vanadates **A** [Eq. (1)].[13]

However, because the reactions are usually performed at high temperatures (150–170 °C) and afford thermodynamic

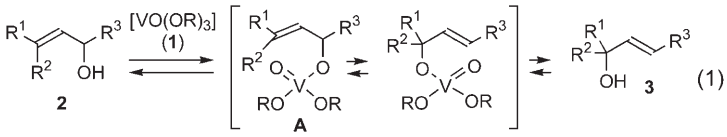

(1)

mixtures of two regioisomers (**2** and **3**), this isomerization has found limited application.[14,15] If these vanadium-catalyzed isomerization reactions could be combined with the lipase-catalyzed KR, a new DKR method would be established by virtue of the high enantio- and chemoselective abilities of the lipases.[16] To examine the feasibility of this idea, a lipase-catalyzed KR of (±)-**2a** was examined first without and then with a catalytic amount of the stable compound, $[VO(OSiPh_3)_3]$ (**1a**).

First, after screening a number of commercially available lipases and organic solvents, we found that ordinary KR took place effectively. For instance, *Candida antarctica* lipase fr.B (CAL-B, Roche Diagnostics) and the acyl donor ethoxyvinyl acetate[17] (**4a**, 2 equiv) in acetone at 25 °C for 21 h completed the resolution to give (*R*)-**5a** (92% *ee*, 51% yield) and (*S*)-**2a** (97% *ee*, 49% yield) (Table 1, entry 1).

Table 1: KR and DKR of (±)-**2a**.[a]

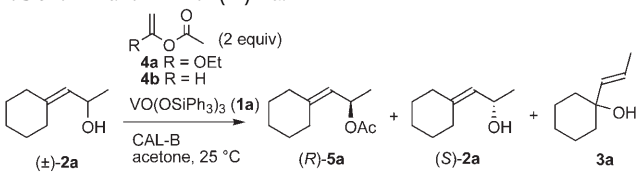

Entry	4	1a [mol%]	t [h]	(R)-5a[b] ee [%]	(R)-5a[b] Yield [%]	(S)-2a[b] ee [%]	(S)-2a[b] Yield [%]	3a Yield [%]
1	**4a**	–	21	92	51[c]	97	49[c]	–
2	**4a**	10	16	99	66[d]	5	5[d]	29[d]
3	**4a**	10	60	98	95[c]	–	trace	< 5[d]
4	**4b**	10	72	93	89[c]	–	< 5[d]	6[d]

[a] The reaction was carried out as stated in the text. [b] The optical purities of **2a** and **5a** were determined by GC with a chiral column, TCI Chiraldex G-TA. The absolute stereochemistry of the recovered **2a** was determined to be *S* by the modified Mosher method, and thereby that of **5a** to be *R*. [c] Yield of isolated product after SiO_2-column chromatography. [d] Yield based on ^1H NMR spectroscopic data.

Next, **1a** in acetone was found to effect 1,3-transposition at 25 °C. The reaction of (*S*)-**2a** (98% *ee*) with **1a** (10 mol%) reached thermodynamic equilibrium after about 12 h to give a mixture of (±)-**2a** and **3a** (15:85), while the racemization of (*S*)-**2a** proceeded [Eq. (2)] (Figure 1).

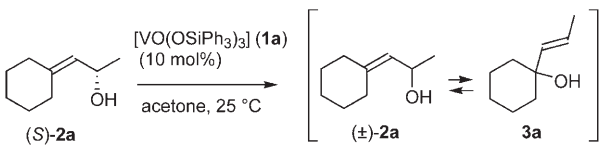

(2)

[*] Prof. Dr. S. Akai, Dr. M. Egi, T. Yamamoto
School of Pharmaceutical Sciences
University of Shizuoka
52-1, Yada, Suruga-ku, Shizuoka 422-8526 (Japan)
Fax: (+81) 54-264-5672
E-mail: akai@u-shizuoka-ken.ac.jp
Dr. K. Tanimoto, Y. Kanao, Prof. Dr. Y. Kita
Graduate School of Pharmaceutical Sciences
Osaka University
1-6, Yamadaoka, Suita, Osaka 565-0871 (Japan)
Fax: (+81) 6-6879-8229
E-mail: kita@phs.osaka-u.ac.jp

[**] This work was supported by Grants-in-Aid for Scientific Research (S and C) from the Ministry of Education, Culture, Sports, Science, and Technology, Japan. We thank Roche Diagnostics K. K., Japan and Amano Enzyme Inc., Japan for the generous gift of the lipases.

InterScience
© 2006 Wiley-VCH Verlag GmbH & Co. KGaA, Weinheim

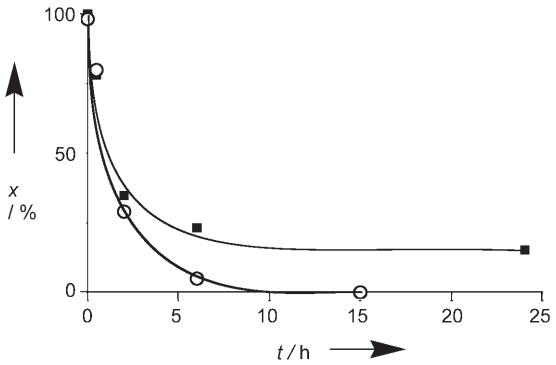

Figure 1. Time course of the isomerization of (*S*)-**2a** (98% *ee*) catalyzed by **1a** in acetone at 25°C. ■ Mol ratio **2a**/(**2a** + **3a**), ○ optical purity of (*S*)-**2a**.

We then investigated the DKR of **2a** by the combined use of CAL-B and **1a**. A mixture of **2a, 4a** (2 equiv), **1a** (10 mol%), and CAL-B was stirred in anhydrous acetone at 25°C. After 16 h, a mixture of (*R*)-**5a** (99 *ee*, 66% yield), (*S*)-**2a** (5% *ee*, 5% yield), and **3a** (29% yield) was obtained (Table 1, entry 2). These results indicated that the lipase and **1a** had little adverse affect on each other. Prolonged stirring for 2.5 days resulted in the conversion of **3a** into (*R*)-**5a** (98% *ee*, 95% yield) (Table 1, entry 3). The use of vinyl acetate (**4b**, 2 equiv), currently the most popular acyl donor, also brought about a similar DKR that produced (*R*)-**5a** (93% *ee*, 89% yield) after 3 days (Table 1, entry 4), although its optical and chemical yields were slightly lower than those obtained using **4a** (Table 1, entry 3). In these reactions, the formation of the acetate of the tertiary alcohol **3a** was not observed, which was expected from the high chemoselectivity of the lipase-catalyzed reactions.[16]

The preparation of the ester (*R*)-**5a** from the tertiary alcohol **3a** is a unique feature of this DKR protocol. The alcohol, which is readily available by the alkynylation of cyclohexanone followed by reduction,[18] can be converted into (*R*)-**5a** (99% *ee*, 91% yield) under the same conditions as entry 3 of Table 1 (Scheme 1).[19]

This DKR method was also effective for the cyclic allylic alcohol (±)-**2b**. In this case, both *Pseudomonas fluorescens* lipase (AK, Amano Enzyme) and *Burkholderia cepacia* lipase immobilized on diatomaceous earth (PS-D, Amano Enzyme) in toluene was suitable for ordinary KR, and DKR using these lipases with **1a** produced (*R*)-**5b** (91–95% *ee*) in 83–93% yield [Eq. (3)].[20,21] Although a related DKR of the

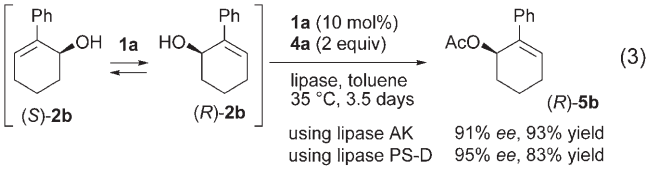

(3)

racemic acetate (±)-**5b**, in which the lipase-catalyzed hydrolysis and the palladium(II)-catalyzed racemization were combined to yield optically enriched **2b** (96% *ee*, 81% yield), was previously reported, the reaction took 19 days for completion.[22]

The DKR protocol was successfully applied to other racemic secondary alcohols (±)-**2c–g** as well as the tertiary alcohol **3e** with either **4a** or **4b** (Table 2). All reactions were carried out at around room temperature to produce the esters

Table 2: DKR of (±)-**2** and **3** to give (*R*)-**5**.[a]

Entry	Alcohol	4	Lipase	Solvent	*T* [°C]	*t* [days]	5[b]	*ee* [%]	Yield [%]
1	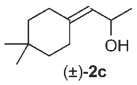 (±)-**2c**	**4a**	CAL-B	acetone	25	2	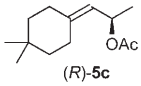 (*R*)-**5c**	97[c]	88
2		**4b**	CAL-B	acetone	25	2		98[c]	94
3	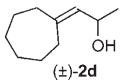 (±)-**2d**	**4a**	CAL-B	acetone	10	2	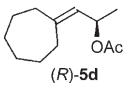 (*R*)-**5d**	97[c]	88
4		**4b**	CAL-B	acetone	10	2		98[c]	80
5	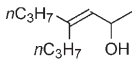 (±)-**2e**	**4a**	CAL-B	acetone	25	3		99[d]	91
6		**4b**	CAL-B	acetone	25	3		99[d]	85
7	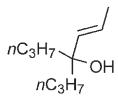 **3e**	**4a**	CAL-B	acetone	25	4	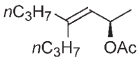 (*R*)-**5e**	98[d]	93
8		**4b**	CAL-B	acetone	25	4		99[d]	93
9	(±)-**2f**: R = Ph	**4a**	PS-D	toluene	35	2	(*R*)-**5f** R = Ph	97[e]	91
10		**4b**	PS-D	toluene	35	2		99[e]	96
11	(±)-**2g** R = C≡CSiMe$_3$	**4a**	PS-D	toluene	35	4	(*R*)-**5g**: R = C≡CSiMe$_3$	91[c]	81

[a] The reaction was carried out as stated in the text. [b] Yield of isolated product after SiO_2-column chromatography. [c] Optical purity was determined by HPLC with a Daicel Chiralcel OD-H column (for **5c** and **5g**) or a Daicel Chiralpak AD-H column (for **5d**), after conversion into the corresponding alcohol **2**. [d] Optical purity was determined by GC with a chiral column, TCI Chiraldex G-TA, after conversion into the corresponding alcohol **2e**. [e] Optical purity was determined by HPLC with a Daicel Chiralcel OD-H column.

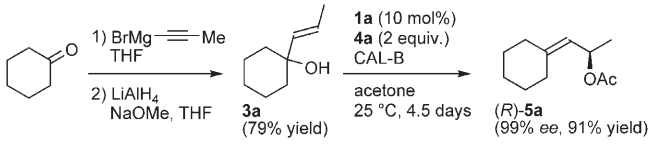

Scheme 1. Preparation of **3a** and its conversion into (*R*)-**5a** by DKR.

(*R*)-**5c–g** with 91–99% *ee* in 80–96% yields, which demonstrates the similar high efficacy of both **4a** and **4b**. The use of ethoxyvinyl esters, in particular, will enable us to apply the DKR method to the domino-type reactions that we recently developed.[3,17] Among the products, (*R*)-**5g** was reported to be a key synthetic intermediate of medicinally important

 © 2006 Wiley-VCH Verlag GmbH & Co. KGaA, Weinheim

compounds.[23] It was previously prepared by the ordinary KR of (±)-**2g** to give (*R*)-**5g** and (*S*)-**2g**, followed by Mitsunobu reaction of the mixture. Although the enantioselectivity of the KR was excellent (99% *ee* for both products), the Mitsunobu inversion suffered partial racemization to give (*R*)-**5g** with 88% *ee*.[23a] Our DKR method produced (*R*)-**5g** (91% *ee*, 81% yield) directly (Table 2, entry 11).

In conclusion, we have shown that the combination of the oxovanadium compound **1a** with lipases produces a novel DKR process with excellent enantiomer resolution and chemical yields. The 1,3-transposition of allyl alcohols was catalyzed by **1a** and resulted in a thermodynamic equilibrium of two regioisomers, which underwent highly enantio- and chemoselective esterification under the action of the lipases. Because the **1a**-catalyzed 1,3-transposition reactions are not very sensitive to oxygen and moisture, this DKR method offers the advantage of a facile experimental procedure without the need for special apparatus.[24] Furthermore, it features a unique preparation of optically active esters of secondary alcohols from the corresponding ketones via the readily available tertiary alcohols; this synthesis is not attainable by existing DKRs with ruthenium complexes.

Experimental Section

Typical procedure: (±)-**2a** (50 mg, 0.36 mmol), **4a** (93 mg, 0.71 mmol), **1a** (32 mg, 0.036 mmol), CAL-B (150 mg), and anhydrous acetone (4 mL) were added to a round-bottomed flask. The flask was sealed and the reaction mixture was stirred at 25 °C for 2.5 days. The reaction mixture was then filtered and concentrated in vacuo. The residue was purified by flash column chromatography on SiO_2 (hexane/Et_2O, 20:1 to 2:1) to give (*R*)-**5a** as a colorless oil (62 mg, 95% yield, 98% *ee* (GC analysis with TCI chiraldex G-TA)). $[\alpha]_D^{20} = +35.0$ ($c = 0.96$, $CHCl_3$); ^1H NMR (300 MHz, $CDCl_3$): $\delta = 1.26$ (d, $J = 7.0$ Hz, 3H), 1.48–1.58 (m, 6H), 2.02 (s, 3H), 2.06–2.09 (m, 2H), 2.18–2.23 (m, 2H), 5.11 (br d, $J = 9.0$ Hz, 1H), 5.63 ppm (qd, $J = 7.0$, 9.0 Hz, 1H); ^{13}C NMR (75 MHz, $CDCl_3$): $\delta = 21.3$, 21.5, 26.6, 27.7, 28.4, 29.4, 36.8, 67.4, 121.5, 144.1, 170.5 ppm; IR (KBr): $\nu = 1715\ cm^{-1}$; elemental analysis: calcd (%): C 72.49, H 9.95; found: C 72.26, H 9.89.

Received: October 24, 2005
Revised: January 13, 2006
Published online: March 17, 2006

Keywords: allyl alcohols · asymmetric synthesis · dynamic kinetic resolution · lipases · vanadium

[1] For recent reviews, see: a) S. M. Roberts, *J. Chem. Soc. Perkin Trans. 1* **2001**, 1475–1499; b) T. Ema, *Curr. Org. Chem.* **2004**, *8*, 1009–1025; c) A. Ghanem, H. Y. Aboul-Enein, *Chirality* **2005**, *17*, 1–15; d) E. Garcia-Urdiales, I. Alfonso, V. Gotor, *Chem. Rev.* **2005**, *105*, 313–354.

[2] For reviews, see: a) O. Pàmies, J.-E. Bäckvall, *Chem. Rev.* **2003**, *103*, 3247–3261; b) N. J. Turner, *Curr. Opin. Chem. Biol.* **2004**, *8*, 114–119; c) M.-J. Kim, Y. Ahn, J. Park, *Bull. Korean Chem. Soc.* **2005**, *26*, 515–522.

[3] S. Akai, K. Tanimoto, Y. Kita, *Angew. Chem.* **2004**, *116*, 1431–1434; *Angew. Chem. Int. Ed.* **2004**, *43*, 1407–1410.

[4] For some recent improvements and applications of the lipase–ruthenium(II)-catalyzed DKRs, see: a) J. H. Choi, Y. K. Choi, Y. H. Kim, E. S. Park, E. J. Kim, M.-J. Kim, J. Park, *J. Org. Chem.* **2004**, *69*, 1972–1977; b) M. Edin, J. Steinreiber, J.-E. Bäckvall, *Proc. Natl. Acad. Sci. USA* **2004**, *101*, 5761–5766; c) B. Martin-Matute, M. Edin, K. Bogár, F. B. Kaynak, J.-E. Bäckvall, *J. Am. Chem. Soc.* **2005**, *127*, 8817–8825; d) P. Kielbasinski, M. Rachwalski, M. Mikolajczyk, M. A. H. Moelands, B. Zwanenburg, F. P. J. T. Rutjes, *Tetrahedron: Asymmetry* **2005**, *16*, 2157–2160; e) G. K. M. Verzijl, J. G. de Vries, Q. B. Broxterman, *Tetrahedron: Asymmetry* **2005**, *16*, 1603–1610.

[5] a) P. M. Dinh, J. A. Howarth, A. R. Hudnott, J. M. J. Williams, W. Harris, *Tetrahedron Lett.* **1996**, *37*, 7623–7626; b) O. Pàmies, J.-E. Bäckvall, *Chem. Eur. J.* **2001**, *7*, 5052–5058; c) M. Ito, A. Osaku, S. Kitahara, M. Hirakawa, T. Ikariya, *Tetrahedron Lett.* **2003**, *44*, 7521–7523; d) S. Wuyts, D. E. de Vos, F. Verpoort, D. Depla, R. de Gryse, P. A. Jacobs, *J. Catal.* **2003**, *219*, 417–424.

[6] For a related DKR of racemic secondary amines with palladium(0) on carbon as a racemization catalyst, see: M. T. Reetz, K. Schimossek, *Chimia* **1996**, *50*, 668–669; see also: Y. K. Choi, M. J. Kim, Y. Ahn, M.-J. Kim, *Org. Lett.* **2001**, *3*, 4099–4101.

[7] For examples, see: R. M. Hanson, *Org. React.* **2002**, *60*, 1–156.

[8] For a recent review, see: E. Vedejs, M. Jure, *Angew. Chem.* **2005**, *117*, 4040–4069; *Angew. Chem. Int. Ed.* **2005**, *44*, 3974–4001.

[9] For recent examples, see: B. J. Lüssem, H.-J. Gais, *J. Am. Chem. Soc.* **2003**, *125*, 6066–6067; H.-J. Gais, O. Bondarev, R. Hetzer, *Tetrahedron Lett.* **2005**, *46*, 6279–6283.

[10] For typical reviews, see: R. Noyori, T. Ohkuma, *Angew. Chem.* **2001**, *113*, 40–75; *Angew. Chem. Int. Ed.* **2001**, *40*, 40–73; S. Itsuno, *Org. React.* **1998**, *52*, 395–576.

[11] For other recent examples based on different methodologies, see: H. Li, P. J. Walsh, *J. Am. Chem. Soc.* **2004**, *126*, 6538–6539; S. F. Kirsch, L. E. Overman, *J. Am. Chem. Soc.* **2005**, *127*, 2866–2867.

[12] The first preparation of **1a** was reported independently by two groups: a) N. F. Orlov, B. N. Dolgov, M. G. Voronkov, *Dokl. Akad. Nauk SSSR* **1958**, *122*, 246–249; b) F. E. Granchelli, G. B. Walker, US 2863891, **1958** [*Chem. Abstr.* **1959**, *53*, 50997]; for a precise preparation of **1a**, see: c) B. M. Trost, C. Jonasson, *Angew. Chem.* **2003**, *115*, 2109–2112; *Angew. Chem. Int. Ed.* **2003**, *42*, 2063–2066.

[13] a) P. Chabardes, E. Kuntz, J. Varagnat, *Tetrahedron* **1977**, *33*, 1775–1783; for a review, see: b) S. Bellemin-Laponnaz, J.-P. Le Ny, *C. R. Chim.* **2002**, *5*, 217–224.

[14] The related isomerization of propargyl and allenyl alcohols has found synthetic use for producing conjugated carbonyl compounds after irreversible enol–keto transformation (for an example, see: C. Tode, Y. Yamano, M. Ito, *J. Chem. Soc. Perkin Trans. 1* **2001**, 3338–3345) and was applied to the aldol reaction of the intermediate vanadium enolates.[12c]

[15] The vanadium catalyst prepared in situ from $[VO(acac)_2]$ and $Me_3SiOOSiMe_3$ caused isomerization at room temperature: S. Matsubara, T. Okazoe, K. Oshima, K. Takai, H. Nozaki, *Bull. Chem. Soc. Jpn.* **1985**, *58*, 844–849.

[16] The lipase-catalyzed reactions of tertiary alcohols are usually slow, probably due to steric hindrance: U. T. Bornscheuer, R. J. Kazlauskas, *Hydrolases in Organic Synthesis: Regio- and Stereoselective Biotransformations*, Wiley-VCH, Weinheim, **1999**, p. 95.

[17] For a review, see: Y. Kita, S. Akai, *Chem. Rec.* **2004**, *4*, 363–372; for a recent example, see: S. Akai, K. Tanimoto, Y. Kanao, S. Ohmura, Y. Kita, *Chem. Commun.* **2005**, 2369–2371.

[18] For the *E*-selective reduction of alkynes with $LiAlH_4$/NaOMe, see: I. Fleming, N. K. Terrett, *J. Organomet. Chem.* **1984**, *264*, 99–118.

[19] The reaction of **3a** with **1a** (10 mol%) in acetone at 25 °C reached equilibrium after about 6 h to afford a mixture of **2a** and **3a** (15:85).

 © 2006 Wiley-VCH Verlag GmbH & Co. KGaA, Weinheim

[20] The optical purity was determined by HPLC with a Daicel Chiralpak AD-H column; $[\alpha]_D^{22} = +169$ ($c = 1.0$, $CHCl_3$) (lit: $[\alpha]_D^{25} = -157$ ($c = 0.57$, $CHCl_3$) for (*S*)-**5b** with 96% *ee*).[21]
[21] M. Frohn, X. Zhou, J.-R. Zhang, Y. Tang, Y. Shi, *J. Am. Chem. Soc.* **1999**, *121*, 7718–7719.
[22] J. V. Allen, M. J. Williams, *Tetrahedron Lett.* **1996**, *37*, 1859–1862.
[23] a) S. Takano, M. Suzuki, K. Ogasawara, *Tetrahedron: Asymmetry* **1993**, *4*, 1043–1046; b) M. M. Kabat, J. Kiegiel, N. Cohen, K. Toth, P. M. Wovkulich, M. R. Uskoković, *J. Org. Chem.* **1996**, *61*, 118–124.
[24] The ruthenium-catalyzed racemization reported so far needed strict anaerobic conditions because the interfusion of oxygen often caused the formation of significant amounts of side products, that is, ketones.[2–4] However, just before submitting this Communication, a novel ruthenium complex was reported to produce the DKR of alcohols with a lipase in air (N. Kim, S.-B. Ko, M. S. Kwon, M.-J. Kim, J. Park, *Org. Lett.* **2005**, *7*, 4523–4526).

 © 2006 Wiley-VCH Verlag GmbH & Co. KGaA, Weinheim

Peptide Modification

DOI: 10.1002/anie.200503942

Reductive Modification of a Methionine Residue in the Amyloid-β Peptide**

*Vojtech Kadlcik, Cécile Sicard-Roselli, Chantal Houée-Levin, Milan Kodicek, Carla Ferreri, and Chryssostomos Chatgilialoglu**

Amyloid-β peptide (Aβ) is a 39–43 amino acid peptide strongly involved in the development of Alzheimer's disease. In the plasma, the major form is Aβ(1–40), which aggregates to form neuritic plaques and neurofibrillary tangles in the diseased brain.[1] Special attention has been paid to the role of methionine residue 35 (Met35), which has been shown to play a critical role in the oxidative-stress and neurotoxicity properties exhibited by Aβ. This was demonstrated by replacing Met35 with other amino acids.[2,3] The molecular basis of this stress involves oxidation to the methionine radical cation and subsequent formation of methionine sulfoxide and/or electron transfer to other residues.[4,5] However, a clear picture of the chemical degradation paths and their influence on the disease aetiology is far from being achieved.

In the context of free-radical damage, the concept of reductive stress has received much less attention than that of oxidative stress.[6] The reductive attack of H· atoms on methionine is known to cause degradation, with formation of α-aminobutyric acid and CH_3SH.[7] The sulfur-centered radical intermediates involved in such degradation have been recently connected with a type of tandem protein–lipid damage, based on the reaction of thiyl radicals with unsaturated fatty acids.[8] We were interested in applying a chemical biology approach to focus on radical damage of Aβ, by replacement of Met35 with α-aminobutyric acid in the peptide sequence. The replacement of methionine by other amino acids in Aβ is known to occur by genetic mutation, as in the case of valine, which causes the disease to appear at very early ages.[9] In this paper we describe the reaction of H· atoms with the 40-residue Aβ(1–40) or its reversed sequence Aβ(40–1), the detection of tandem protein–lipid damage, and the isolation and identification of the peptide modified at the Met35 residue.

To begin with, the reaction of H· atoms with the methionine moiety was monitored by using *trans*-lipids as markers.[8,10] Liposomes were prepared from 1-palmitoyl-2-oleoyl phosphatidylcholine (POPC), in the form of large unilamellar vesicles (LUVETs) with a 100 nm diameter; these vesicles were obtained by membrane extrusion with LiposoFast.[10,11] Aβ(1–40) or Aβ(40–1) was added to this suspension. A small amount of *tert*-butanol (0.20 M), which did not exceed 1% of the total volume, was also added. The oleate (*cis*-9-octadecenoic acid) content of POPC was kept at 8.7 mM, whereas three peptide concentrations (150, 300, 450 μM), corresponding to lipid/peptide ratios of 58:1, 58:2, and 58:3, respectively, were used. In at least two of these conditions (58:1 and 58:2 ratios), the membrane association of the peptide could be neglected, according to recent data.[12] The mixtures were saturated with N_2O prior to γ irradiation at a dose rate of 12.0 Gy min^{-1}. After irradiation, lipid isolation, and derivatization to the corresponding fatty acid methyl esters,[13] GC analysis was used to determine the *cis*/*trans* ratio.[11]

Figure 1a shows the percentage of elaidate (*trans*-9-octadecenoic acid) residues formed after exposure to 1033 Gy, for Aβ(1–40) and the reversed sequence Aβ(40–1). In all experiments, the geometrical isomerization of the lipid chains of the POPC vesicles occurred, and it can be seen that the more peptide present, the more the isomerization progresses. The reactivity of the two peptides in water was quite similar. Control experiments in the absence of peptide showed that elaidate formation is less than 0.8% after exposure to 1033 Gy. The conditions with Aβ(1–40) and a lipid/peptide ratio of 58:2 were chosen for a dose profile of the *cis*–*trans* isomerization. Aliquots (30 μL) of the suspension were withdrawn at different irradiation times (4–86 min) for lipid isolation, derivatization, and GC analysis. Figure 1b

[*] Dr. C. Ferreri, Dr. C. Chatgilialoglu
ISOF, Consiglio Nazionale delle Ricerche
Via P. Gobetti 101, 40129 Bologna (Italy)
Fax: (+39) 051-639-8349
E-mail: chrys@isof.cnr.it
V. Kadlcik, Dr. C. Sicard-Roselli, Prof. C. Houée-Levin
Laboratoire de Chimie Physique, UMR 8000
Université Paris-Sud
91405 Orsay cedex (France)
Prof. M. Kodicek
Department of Biochemistry and Microbiology
Institute of Chemical Technology
16628 Prague (Czech Republic)

[**] Work supported in part by the European Community's Marie Curie Research Training Network under contract HPRN-CT-2002–000184 [SULFRAD].

 © 2006 Wiley-VCH Verlag GmbH & Co. KGaA, Weinheim

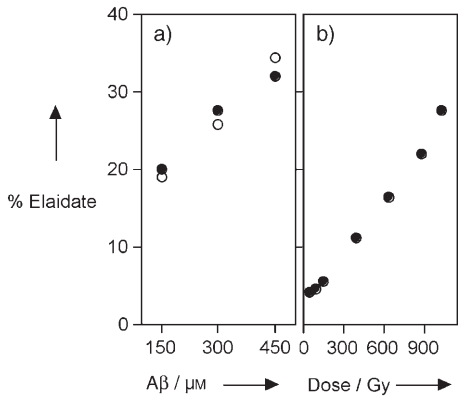

Figure 1. Formation of elaidate residues from γ irradiation of POPC (8.7 mM) vesicles containing Aβ(1–40) (●) or Aβ(40–1) (○) and 0.2 M *t*BuOH in N_2O-saturated water. a) After 1033 Gy of γ irradiation with varying Aβ concentrations; b) irradiation dose profile for 300 μM Aβ(1–40).

shows that the formation of elaidate increased linearly with the dose exposure.

The reaction sequence starts with primary reactive species from water (e_{aq}^-, HO•, H•), obtained by γ radiolysis of aqueous suspensions. The presence of N_2O (about 0.02 M) efficiently transforms e_{aq}^- into HO• radicals ($k = 9.1 \times 10^9\,M^{-1}s^{-1}$). Under these conditions, H• atoms and HO• radicals accounted for 10% and 90%, respectively, of the reactive species. With 0.2 M *t*BuOH, HO• radicals are scavenged efficiently ($k = 6.0 \times 10^8\,M^{-1}s^{-1}$), whereas H• atoms react only slowly ($k = 1.7 \times 10^5\,M^{-1}s^{-1}$) [Eq. (1)].[14,15]

$$HO^{\cdot}/H^{\cdot} + (CH_3)_3COH \rightarrow H_2O/H_2 + (CH_3)_2C(OH)CH_2 \qquad (1)$$

Hydrogen atoms are known to selectively attack Met residues, thereby resulting in the formation of α-aminobutyric acid and CH_3SH.[7,8] We suggest that H• atoms react with Met35 of Aβ(1–40) or Aβ(40–1) to afford the diffusible thiyl radical that catalytically isomerizes the double bond of POPC (Scheme 1).[10]

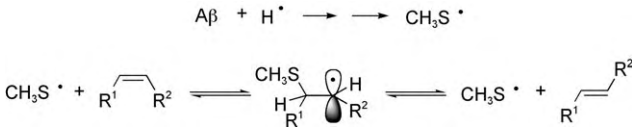

Scheme 1. Methanethiyl-radical-catalyzed isomerization of *cis*-phospholipids.

To address the Met35 modification in the Aβ peptide by H• atoms, the reaction was studied in the absence of liposomes by HPLC and mass spectrometry. Furthermore, the reaction was performed under acidic conditions and Ar atmosphere, where the reaction of e_{aq}^- with H^+ ions to yield H• atoms ($k = 2.3 \times 10^{10}\,M^{-1}s^{-1}$) becomes relevant,[14] thereby increasing the radiation chemical yield of H• atoms. Indeed, in the presence of 0.06 M $HClO_4$ with 1% *t*BuOH (pH 1.5), no hydrolysis of peptide takes place and the yield of H• atoms is about 6 times higher than in pure water. Owing to the low solubility of Aβ(1–40) under acidic conditions, only Aβ(40–1) was used for this experiment. The HPLC analysis after radiolysis of 100 μM Aβ(40–1) in acidic medium showed that a number of products are formed at 200 Gy. Peptide consumption was $2.8 \times 10^{-7}\,mol\,J^{-1}$. The analogous experiment at the natural pH value and saturated with N_2O showed a slightly lower peptide consumption ($1.9 \times 10^{-7}\,mol\,J^{-1}$).[16]

Figure 2 shows the MALDI-TOF analysis of the reaction mixture at a low pH value in the range 4250–4500 Da. Four

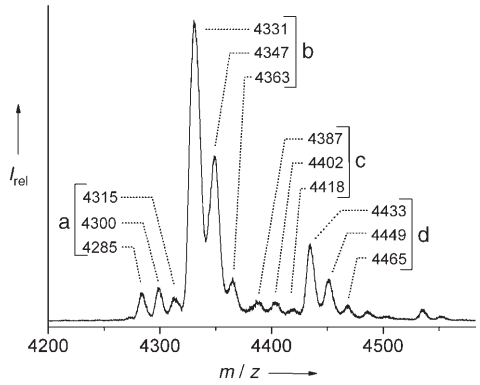

Figure 2. MALDI-TOF mass spectrum of the reaction mixture after 200 Gy of γ irradiation of a solution containing 100 μM Aβ(40–1), 0.06 M $HClO_4$, and 1% *t*BuOH (pH 1.5). Average [*M*+H] masses are given in the figure. The four clusters (a–d) with three peaks each are discussed in the text.

clusters (a–d) with three peaks each are the main feature. Cluster b shows the [*M*+H] peak of Aβ at 4331 Da together with the two average masses of 4347 and 4363 Da that correspond to products containing one (+16 Da) or two (+32 Da) oxygen atoms. Cluster d, which is absent at the natural pH value, shows average masses at 4433, 4449, and 4465 Da that match well with the addition of a $HClO_4$ moiety to the masses in cluster b. Cluster a contains products with average masses of 4285, 4300, and 4315 Da that are 46 Da lighter than the peaks of cluster b, whereas cluster c represents the addition of $HClO_4$ to the cluster a. The mass difference of 46 Da corresponds to the loss of the CH_2S moiety from Met35 and, therefore, to the peptide containing α-aminobutyric acid.

The HPLC chromatogram of the reaction mixture after γ radiolysis at pH 1.5 is shown in Figure 3. In order to correlate the mass spectra to this chromatogram, HPLC fractions were collected and analyzed by MALDI-TOF MS. For both radiolytical systems (at pH 1.5 and the natural pH value), a product with a monoisotopic [M+H] mass of 4282.2 Da (corresponding to average mass of 4285 Da in Figure 2) was detected in the fraction with an elution time of 40.0–41.5 min. At the pH 1.5, the peak at 4282.2 Da was the main one, together with a peak at 4344.2 Da (Figure 3, inset), whereas the peak at 4282.2 Da is less intense than the peaks at 4328.2 Da and 4344.2 Da for the natural pH value.[17] These results suggest that the yield of α-aminobutyric acid is much higher at pH 1.5 than at the natural pH value, a finding in agreement with the increased yield of H• atoms in the acidic medium.

 © 2006 Wiley-VCH Verlag GmbH & Co. KGaA, Weinheim

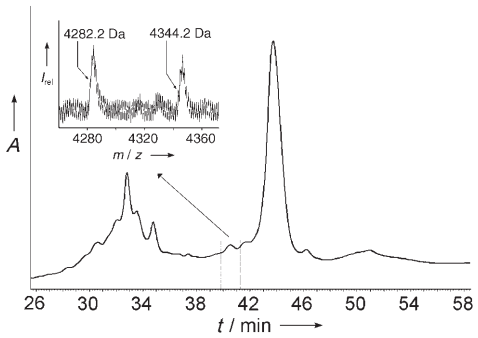

Figure 3. HPLC chromatogram of Aβ(40–1) after γ radiolysis at pH 1.5. Experimental conditions: 100 μM Aβ(40–1) in 0.06 M $HClO_4$ and 1% *t*BuOH with a dose of 200 Gy. The inset shows the MALDI-TOF mass spectrum of the HPLC fraction collected at $t = 40.0$–41.3 min. Two species with monoisotopic [M + H] masses of 4282.2 Da (Aβ − 46 Da) and 4344.2 Da (Aβ + 16 Da) were detected.

To confirm the identification of the 4282.2-Da product, trypsin digestion of the 40–41.5-min HPLC fraction of Aβ(40–1) after radiolysis at a low pH value was performed, and the resulting peptide mixture was analyzed by MALDI-TOF MS. Peptides corresponding to the sequence of residues 27–1 were detected unchanged. The [M + H] peak corresponding to the peptide comprising residues 40–28 (1213.7 Da) was very weak. Instead, an intense peak at 1167.7 Da (−46 Da) and a peak at 1229.8 Da (+16 Da) were present in the spectrum. This result shows that the observed mass difference of 46 Da is located in the sequence of residues 40–28, which contains the Met35 residue, and is thus consistent with the identification of the 4282.2-Da product as the α-aminobutyric acid containing peptide.

In summary, the Aβ peptide suffers from the highly selective attack of H· atoms on the Met35 residue, with the formation of a modified peptide containing an α-aminobutyric acid residue. This chemical reactivity could represent the molecular basis of a posttranslational modification of the Aβ peptide[18] which could infer interesting biological effects. The formation of *trans*-lipids as a marker of radical damage to methionine-containing peptides was also evaluated. The system of POPC vesicles containing Aβ modeled the occurrence of radical damage that is transferred from the peptide to the lipid domain. This suggests a link between lipidomics and proteomics, due to the known interaction of the Aβ protein with cell membranes.[19]

Experimental Section

LUVETs were prepared as previously described[10] from POPC (1.9 mg; 0.0025 mmol) in water (950 μL) purified with a Millipore system (Milli-Q). Aβ peptide (0.6 mg in 50 μL of Milli-Q water) and *t*BuOH (0.2 M) were added to the LUVET suspension. The suspension was then transferred to a vial, equipped with an open-top screw cap and a teflon-faced septum, and saturated with N_2O prior to γ irradiation. Workup and analysis of the irradiated reaction mixture was carried out as previously reported.[10]

1% *t*BuOH was added to Aβ peptide (100 μM; Bachem, Switzerland) in water (230 μL) purified with a Elga Maxima system or in 0.06 M $HClO_4$. The solution was saturated with Ar prior to γ irradiation. HPLC was performed on a Beckman Gold 168 (Beckman Coulter) instrument with diode array detection. The analytical column was a Zorbax C18 reversed-phase column (4.6 × 25 cm). The mobile-phase eluents were A) 0.1% trifluoroacetic acid (TFA) in water and B) 0.1% TFA and 70% CH_3CN in water. The gradient elution used was 35% B for 10 min, 35→45% B over 20 min, 45% B for 10 min, and 45→80% B over 40 min.

For trypsin cleavage, lyophilized products isolated by HPLC were solubilized in 25 mM $(NH_4)_2CO_3/(NH_4)HCO_3$ buffer (50 μL; pH 8.4) containing 10% CH_3CN (v/v). Trypsin (1 μL; 1 mg mL^{-1}) was added to this solution and the mixture was incubated for 1 h at room temperature.

MALDI-TOF MS analyses were carried out with a Biflex IV Bruker Daltonic mass spectrometer, equipped with a UV nitrogen laser (337 nm) and a dual microchannel plate detector. Spectra were obtained in the positive mode at an accelerating voltage of 19 kV. Linear and reflector modes were used for each sample to check for possible fragmentation. Spectra were externally calibrated with trypsin-cleaved human serum albumin or Bruker Protmix I for each measurement. Samples for MALDI-TOF MS were prepared by mixing analyte (1 μL) and matrix solution (2,5-dihydroxybenzoic acid; 9 μL; 15 mg mL^{-1} in 0.1% TFA/CH_3CN (2:1 v/v)). A total of 1 μL of this mixture was deposited on the probe plate and spectra were recorded after evaporation of the solvent.

Received: November 7, 2005
Published online: March 15, 2006

Keywords: lipids · methionine · peptides · radicals · radiolysis

[1] D. J. Selkoe, *Physiol. Rev.* **2001**, *81*, 741–766.
[2] S. M. Yatin, S. Varadarajian, C. D. Link, D. A. Butterfield, *Neurobiol. Aging* **1999**, *20*, 325–330.
[3] J. Kanski, M. Aksenova, C. Schöneich, D. A. Butterfield, *Free Radical Biol. Med.* **2002**, *32*, 1205–1211.
[4] B. L. Miller, K. Kuczera, C. Schöneich, *J. Am. Chem. Soc.* **1998**, *120*, 3345–3356.
[5] C. Schöneich, D. Pogocki, G. L. Hug, K. Bobrowski, *J. Am. Chem. Soc.* **2003**, *125*, 13700–13713.
[6] B. Lipinski, *Br. J. Nutr.* **2002**, *87*, 93–94.
[7] a) R. Shapira, G. Stein, *Science* **1968**, *162*, 1489–1491; b) L. K. Mee, S. J. Adelstein, G. Stein, *Radiat. Res.* **1972**, *52*, 588–602; c) N. N. Lichtin, J. Ogdan, G. Stein, *Radiat. Res.* **1973**, *55*, 69–80; d) L. K. Mee, S. J. Adelstein, *Radiat. Res.* **1974**, *60*, 422–431; e) N. N. Lichtin, A. Shafferman, *Radiat. Res.* **1974**, *60*, 432–440; f) L. K. Mee, S. J. Adelstein, C. M. Steihart, N. N. Lichtin, *Radiat. Res.* **1977**, *71*, 493–504.
[8] C. Ferreri, I. Manco, M. R. Faraone-Mennella, A. Torreggiani, M. Tamba, C. Chatgilialoglu, *ChemBioChem* **2004**, *5*, 1710–1712.
[9] H. Houlden, R. Crook, R. J. Dolan, J. McLaughlin, T. Revesz, J. Hardy, *Neurosci. Lett.* **2001**, *313*, 93–95.
[10] a) C. Chatgilialoglu, C. Ferreri, *Acc. Chem. Res.* **2005**, *38*, 441–448; b) C. Ferreri, C. Chatgilialoglu, *ChemBioChem* **2005**, *6*, 1722–1734.
[11] a) C. Chatgilialoglu, C. Ferreri, M. Ballestri, Q. G. Mulazzani, L. Landi, *J. Am. Chem. Soc.* **2000**, *122*, 4593–4601; b) C. Ferreri, C. Costantino, L. Perrotta, L. Landi, Q. G. Mulazzani, C. Chatgilialoglu, *J. Am. Chem. Soc.* **2001**, *123*, 4459–4468; c) C. Ferreri, A. Samadi, F. Sassatelli, L. Landi, C. Chatgilialoglu, *J. Am. Chem. Soc.* **2004**, *126*, 1063–1072.
[12] M. Bokvist, F. Lindström, A. Watts, G. Gröbner, *J. Mol. Biol.* **2004**, *335*, 1039–1049.
[13] J. F. K. Kramer, V. Fellner, M. E. R. Dugan, F. D. Sauer, M. M. Mossoba, M. P. Yurawecz, *Lipids* **1997**, *32*, 1219–1228.
[14] a) G. V. Buxton, C. L. Greenstock, W. P. Helman, A. B. Ross, *J. Phys. Chem. Ref. Data* **1988**, *17*, 513–886; b) A. B. Ross, W. G.

 © 2006 Wiley-VCH Verlag GmbH & Co. KGaA, Weinheim

Mallard, W. P. Helman, G. V. Buxton, R. E. Huie, P. Neta, *NDRL-NIST Solution Kinetic Database—Version 3*, Notre Dame Radiation Laboratory, Notre Dame, IN, and NIST Standard Reference Data, Gaithersburg, MD, **1998**.

[15] The rate constant for the reaction of e_{aq}^- with the Aβ peptide is unknown but for analogous reactions with proteins like RNase A or lysozyme, values of approximately $2\times10^{10}\,\text{M}^{-1}\,\text{s}^{-1}$ are reported (see: M. Faraggi, M. H. Klapper, L. M. Dorfman, *J. Phys. Chem.* **1978**, *82*, 508–512). With the assumption of a similar rate constant for the reaction of e_{aq}^- with Aβ, it was calculated that more than 90% of e_{aq}^- are scavenged by N_2O under our conditions, even at the highest concentration of Aβ used.

[16] Sodium dodecylsulfate PAGE analysis showed the formation of dimers in both radiolytical systems. Dimers are the main products when HO• radicals or one-electron oxidants react with Aβ. See: V. Kadlcik, C. Sicard-Roselli, T. A. Mattioli, M. Kodicek, C. Houée-Levin, *Free Radical Biol. Med.* **2004**, *37*, 881–891.

[17] The presence of a 4344.2-Da peak is not surprising, because this peak is also present and is even more intense in fractions with both shorter and longer elution times. It is probable that a mixture of 4344.2-Da products, corresponding to hydroxylation isomers, forms a background in this elution range.

[18] S. Li, R. W. Roberts, *Chem. Biol.* **2003**, *10*, 233–239.

[19] S. Kim, T.-J. Jeon, A. Oberai, D. Yang, J. J. Schmidt, J. U. Bowie, *Proc. Natl. Acad. Sci. USA* **2005**, *102*, 14278–14283.

 © 2006 Wiley-VCH Verlag GmbH & Co. KGaA, Weinheim

Heterocyclic Carbene Ligands

DOI: 10.1002/anie.200504396

Cyclic Carbodiphosphoranes: Strongly Nucleophilic σ-Donor Ligands**

Sebastien Marrot, Tsuyoshi Kato, Heinz Gornitzka, and Antoine Baceiredo**

The importance of highly active complexes with bulky and electron-rich ligands has been well recognized. In particular, palladium- and nickel-catalyzed cross-coupling reactions are accelerated in the presence of phosphoxides,[1] proazaphosphatranes[2] or N-heterocyclic carbenes (NHC).[3] Over the last few years, and largely as a result of the pioneering works by Herrmann et al. and Grubbs et al.,[4] the NHC ligands were most intensively studied. They are considered to be strong σ-donor ligands with very weak π-acceptor character which stabilize the active species and accelerate important catalytic steps. Another important aspect is the steric protection provided by these ligands, which also promote dissociation reactions to generate coordinatively unsaturated species and protect them. Recently, several new carbene ligands exhibiting enhanced strong nucleophilic character have become available (Scheme 1), for example, cyclic amino alkyl carbenes (CAAC),[5] remote N-heterocyclic carbenes (rNHC),[6] and diphosphinocarbenes (PHC).[7]

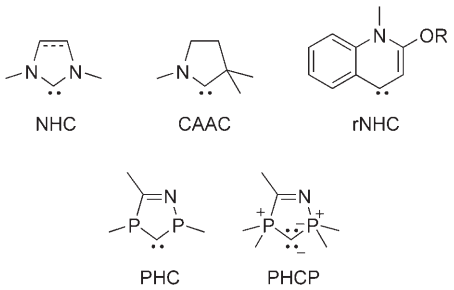

Scheme 1. Heterocyclic carbene ligands.

Carbodiphosphoranes contain two cumulated ylide functions and a formally divalent central carbon atom with two negative charges which are stabilized by two phosphonio groups.[8] As this type of compounds has a bent structure and shows very strong nucleophilicity,[8a] they are potential electron-rich carbon-centered ligands. Several complexes with these ligands were synthesized,[9] and recently a pincer-type Rh^{III} complex was reported with hexaphenylcarbodiphosphorane as a two-electron σ ligand without any π backdonation from the metal center.[10] Despite their potential, the variety of carbodiphosphoranes is very limited, due to synthetic difficulties, particularly in the cyclization, and only one cyclic carbodiphosphorane has been isolated.[11] In fact, almost all work on the coordination behavior of these ligands has been performed with hexamethyl- or hexaphenylcarbodiphosphorane. Another problem is ligand degradation, which can be caused by dissociation of phosphine,[9f] Wittig-type reactions,[12] and phenyl *ortho*-metalation.[9a,b,10]

Here we present the synthesis of rigid P-heterocyclic carbodiphosphoranes (PHCP, Scheme 1) and their Pd^{II} and Rh^{I} complexes. The five-membered heterocyclic cations **1a**,**b**, precursors for the cyclic carbodiphosphoranes, were prepared by the previously reported method that exploits the reactivity of transient diphosphino carbocations as 1,3-dipoles.[13] The reaction of bis(diisopropylamino)phosphino diazomethane with a bis(dialkylamino)phosphenium salt in CH_2Cl_2 solution at 0 °C in the presence of a large excess of benzonitrile leads cleanly, after evolution of nitrogen, to the desired heterocyclic cations **1a**,**b** in good yields (79 and 86%, respectively; Scheme 2). The cyclization is totally regioselective in the case of **1b** and gives the product in which the imine nitrogen atom is bound to the less hindered phosphorus atom.

The PHCPs **2a,b** were cleanly generated at −78 °C by deprotonation of the corresponding salts **1a,b** with potassium

[*] S. Marrot, Dr. T. Kato, Dr. H. Gornitzka, Dr. A. Baceiredo
Laboratoire Hétérochimie Fondamentale et Appliquée (UMR 5069)
Université Paul Sabatier
118, route de Narbonne, 31062 Toulouse Cedex 9 (France)
Fax: (+33) 5-6155-8204
E-mail: kato@chimie.ups-tlse.fr
baceired@chimie.ups-tlse.fr

[**] We are grateful to the CNRS for financial support of this work and to the FSE for a grant to S.M.

Supporting information for this article is available on the WWW under http://www.angewandte.org or from the author.

© 2006 Wiley-VCH Verlag GmbH & Co. KGaA, Weinheim

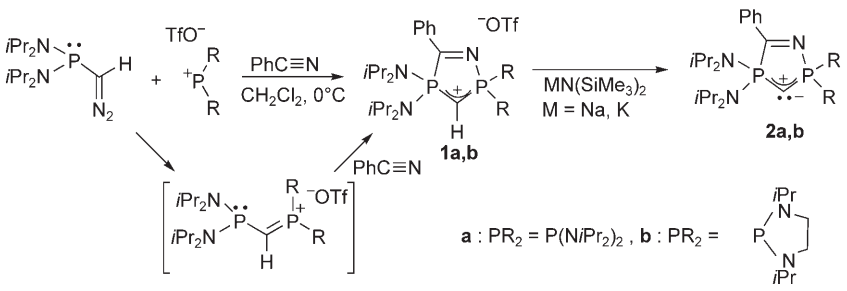

Scheme 2. Synthesis of carbodiphosphoranes **2a,b**. TfO^- = trifluoromethanesulfonate.

or sodium hexamethyldisilazide and were isolated by crystallization (Scheme 2). In the ^{31}P NMR spectra, **2a,b** display a characteristic AB system for the two different phosphorus atoms (**2a**: $\delta = 63.1$, 73.3 ppm, $^2J_{PP} = 160$ Hz; **2b**: $\delta = 60.0$, 71.5 ppm, $^2J_{PP} = 153$ Hz). The ^{13}C NMR signal for the central carbon atom appears as a doublet of doublets for **2a** ($\delta =$ 21.5 ppm, $^1J_{CP} = 10.6$, 25.6 Hz) and as a doublet for **2b** ($\delta =$ 15.3 ppm, $^1J_{CP} = 12.1$ Hz), shifted downfield relative to linear carbodiphosphoranes.[14] In contrast to the only reported stable cyclic carbodiphosphoranes, which decompose at 20–35 °C (depending on the ring size),[11] no significant decomposition was observed when a solution of **2a** or **2b** in C_6D_6 was heated at 80 °C for a few hours. Moreover, these ligands melt without decomposition (**2a**: 135 °C, **2b**: 145 °C) and can be stored under inert gas atmosphere.

The molecular structure of **2b** is shown in Figure 1.[15] The central five-membered ring is planar and the P-C-P bond angle (104.8°) is much more acute than those of known

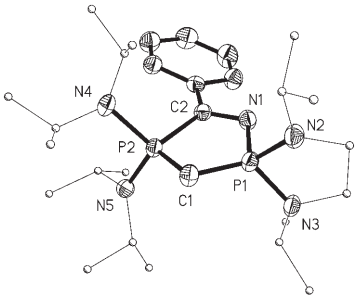

Figure 1. Molecular structure of **2b**. Carbon atoms of substituents on the amino groups are simplified for clarity. Thermal ellipsoids are at 50% probability. Selected bond lengths [Å] and angle [°]: C1–P1 1.644(19), C1–P2 1.657(17), P1–N1 1.759(15), P2–C2 1.917(18), C2–N1 1.285(2); P2-C1-P1 104.82(10).

carbodiphosphoranes (117–143°).[11,16] As expected, the two P–C1 bonds (1.64 and 1.66 Å) are as short as P–C double bonds, in agreement with delocalization of the negative charges on the central carbon atom onto the phosphonio fragments.

To test their coordinating ability, PHPC ligands **2** were treated with Pd^{II} and Rh^{I} complexes in THF at room temperature. While with the more sterically hindered ligand **2a**, no complexation was detected, the less hindered **2b** reacted with $[\{PdCl(allyl)_2\}_2]$, $[\{RhCl(nbd)_2\}_2]$ (nbd = norbornadiene), and $[\{RhCl(CO)_2\}_2]$ to give the corresponding Pd^{II} and Rh^{I} complexes **3**–**5** in nearly quantitative yield (Scheme 3).

Complexes **3** and **4** are air-sensitive and were isolated as brown crystals. X-ray diffraction studies[15a] confirmed the nearly planar environments around the Pd (**3**) and Rh (**4**) centers (Figure 2).[15b] In both complexes, the central carbon atom of ligand **2b** is trigonal-planar (sum of angles: 359.9° for **4** and 359.8° for **5**) and the P–C1 bond lengths lie between those

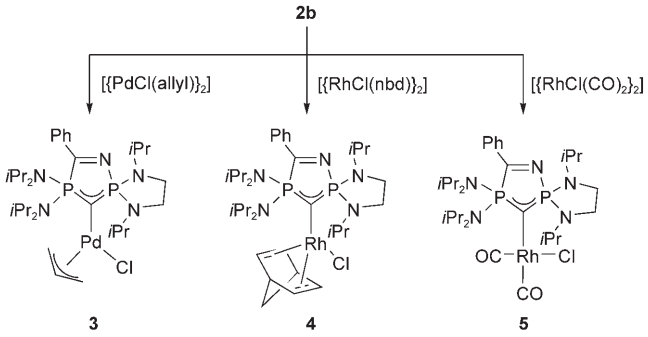

Scheme 3. Synthesis of PHCP complexes **3**–**5**.

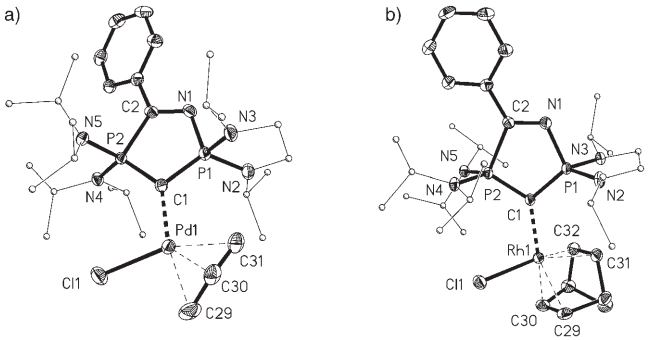

Figure 2. Molecular structures of **3** (a) and **4** (b). Carbon atoms of substituents on the amino groups are simplified for clarity. Thermal ellipsoids are at 50% probability. Selected bond lengths [Å] and angles [°]: **3**: Pd1–C1 2.120(2), C1–P1 1.673(2), C1–P2 1.694(2), Pd1–C29 2.169(3), Pd1–C30 2.125(4), Pd1–C31 2.130(3), Pd1–Cl1 2.368(7); P2-C1-P1 106.66(13). **4**: Rh1–C1 2.115(18), C1–P1 1.676(18), C1–P2 1.702(18), Rh1–C29 2.144(19), Rh1–C30 2.137(19), Rh1–C31 2.106(19), Rh1–C32 2.099(19), Rh1–Cl1 2.387(5); P2-C1-P1 106.86(10).

of single and double bonds, that is, the remaining carbon lone pair is well stabilized by the two phosphonio groups. In **3**, the Pd1–C1 bond (2.120 Å) is longer than those reported for Pd–NHC complexes (2.00–2.06 Å)[17] and can be regarded as a single bond. The same tendency was observed with **4**, which has a very long Rh1–C1 single bond (2.115 Å) that suggests very weak π donation from the metal atom to the carbodiphosphorane ligand. Interestingly, in both complexes **2b** behaves as an "inert" monodentate ligand, although all the

 © 2006 Wiley-VCH Verlag GmbH & Co. KGaA, Weinheim

reported carbodiphosphorane complexes of Rh^{I} and Pt^{II} generally undergo phenyl *ortho*-metalation to give cyclic complexes.[9b,10] We observed similar behavior in the reaction of hexaphenylcarbodiphosphorane with $[\{PdCl(allyl)\}_2]$, which gives complex **6** in near-quantitative yield (Scheme 4).[18]

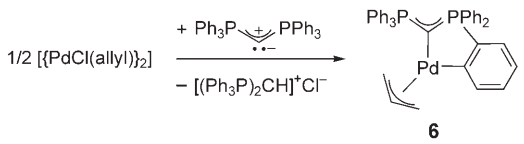

6

Scheme 4. Reaction of hexaphenylcarbodiphosphorane with $[\{PdCl(allyl)\}_2]$.

The carbonyl stretching frequencies of *cis*-$[RhCl(CO)_2L]$ complexes are recognized as an excellent measure for the donor and acceptor properties of the ligand L.[17a,b,19,20] The IR spectrum of **5** exhibits two bands at 2042 and 1960 cm^{-1}, which can be assigned to the ν(CO) I and ν(CO) II vibrations, respectively. Comparison with IR data for previously reported $[RhCl(CO)_2L]$ complexes of NHCs and PHCs (Table 1)[7] shows that PHCP ligand **2b** is a much stronger donor than the NHC and PHC ligands.

Table 1: Carbonyl IR frequencies $\tilde{\nu}$ [cm^{-1}] for *cis*-$[RhCl(CO)_2L]$ complexes.

L	$\tilde{\nu}$(CO) I	$\tilde{\nu}$(CO) II	Reference
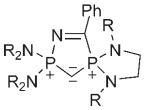	2042	1960	this work
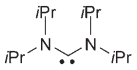	2057	1984	[17a]
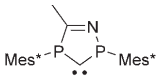	2059	1985	[7]
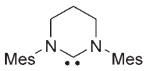	2062	1976	[19]
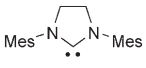	2081	1996	[17a]
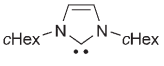	2076	2006	[17a]

In conclusion, the rigid and stable cyclic carbodiphosphorane (PHPC) ligands and some of their complexes are now readily available. Their electronic properties, as superior electron-donating ligands to NHC and PHC ligands, were confirmed by IR spectroscopy. The synthesis of new electron-rich complexes and their applications in homogeneous catalysis are under investigation.

Experimental Section

All manipulations were performed under an inert atmosphere of argon by using standard Schlenk techniques. Dry, oxygen-free solvents were employed. ^1H, ^{13}C, and ^{31}P NMR spectra were recorded on Bruker AC200, WM250, or Avance 300 spectrometers. IR spectra were recorded on a Perkin-Elmer 1600 spectrometer. ^1H NMR[18] and ^{13}C NMR chemical shifts are reported in ppm relative to Me_4Si as external standard. ^{31}P NMR downfield chemical are expressed in ppm relative to 85% H_3PO_4. Compounds **1a** and **1b** were prepared according to the previously reported method.[13]

2a,**b**: THF (5 mL) was added to a mixture of sodium hexamethyldisilazide (0.41 mmol) and **1** (0.41 mmol) at −80 °C, and then the cold bath was removed. The solution became clear after 30 min of stirring at room temperature, and the solvent was removed under vacuum. After filtration of the pentane extract of **2a** (8 mL), the solution was concentrated (2 mL). Dark red crystals of **2a** were obtained at −30 °C. Pentane-insoluble **2b** was washed with pentane (5 mL) and extracted with Et_2O (2 mL). Product **2b** was obtained as red crystals from this solution at −30 °C. **2a**: 86%, m.p. 135 °C; $^{31}P\{^1H\}$ NMR ([D$_8$]THF, 25 °C, 81 MHz): $\delta = 63.1$, 73.3 ppm ($^2J_{PP} = 160$ Hz); ^{13}C NMR ([D$_8$]THF, 25 °C, 75 MHz): $\delta = 21.5$ (dd, $J_{CP} = 10.6$, 25.6 Hz; PCP), 23.4 (d, $J_{CP} = 4$ Hz; CH_3), 24.2 (d, $J_{CP} = 4$ Hz; CH_3), 25.0 (d, $J_{CP} = 3$ Hz; CH_3), 25.7 (d, $J_{CP} = 3$ Hz; CH_3), 46.1 (d, $J_{CP} = 7$ Hz; NCH), 46.7 (d, $J_{CP} = 6$ Hz; NCH), 128.6 (s; CH_{arom}), 129.0 (s; CH_{arom}), 129.9 (s; CH_{arom}), 130.5 (s; CH_{arom}), 131.6 (s; CH_{arom}), 131.8 (s; CH_{arom}), 138.3 (dd, $J_{CP} = 13$, 26 Hz; C_{ipso}), 185.0 ppm (dd, $J_{CP} = 12$, 16 Hz; C=N). **2b**: 74%; m.p. 145 °C; $^{31}P\{^1H\}$ NMR ([D$_8$]THF, 25 °C, 81 Hz): $\delta = 60.0$, 71.5 ppm ($J_{PP} = 153$ Hz); ^{13}C NMR ([D$_8$]THF, 25 °C, 75 Hz): $\delta = 15.3$ (d, $J_{CP} = 12.1$ Hz; PCP), 20.2 (d, $J_{CP} = 5$ Hz; CH_3), 21.1 (d, $J_{CP} = 4$ Hz; CH_3), 23.0 (d, $J_{CP} = 4$ Hz; CH_3), 25.0 (d, $J_{CP} = 2$ Hz; CH_3), 37.3 (d, $J_{CP} = 6.1$ Hz; NCH_2), 42.2 (d, $J_{CP} = 6$ Hz; NCH), 47.0 (d, $J_{CP} = 5.5$ Hz; NCH), 127.6 (s; CH_{arom}), 129.0 (s; CH_{arom}), 130.1 (s; CH_{arom}), 138.0 (dd, $J_{CP} = 12$ Hz, $J_{CP} = 27$ Hz; C_{ipso}), 182.5 ppm (dd, $J_{CP} = 8$, 15 Hz; C=N).

3–**5**: A solution of **2b** (0.3 mmol) was added to a solution of the corresponding complex (0.074 mmol) in THF (2 mL) at room temperature. After 30 min, the solvent was evaporated under vacuum. Then the product was extracted into Et_2O. After removal of the solvent under vacuum, the desired complexes were purified by recrystallization or precipitation. **3**: 68%, m.p. 143 °C (decomp); $^{31}P\{^1H\}$ NMR (C_6D_6, 25 °C, 81 MHz): $\delta = 61.2$, 71.9 ppm ($J_{PP} = 225$ Hz); ^{13}C NMR ($CDCl_3$, 25 °C, 75 Hz): $\delta = 1.50$ (dd, $J_{CP} = 86$, 88 Hz; PCP), 20.8 (d, $J = 6.1$ Hz; CH_3), 21.5 (s; CH_3), 23.6 (d, $J_{CP} = 5.1$ Hz; CH_3), 26.1 (d, $J_{CP} = 4$ Hz; CH_3), 36.9 (dd, $J_{CP} = 1.6$, 9.2 Hz; CH_2), 42.5 (d, $J_{CP} = 7.8$ Hz; NCH), 48.6 (d, $J_{CP} = 6.1$ Hz; NCH), 48.5 (s; $CH_{2\,allyl}$), 72.1 (s; $CH_{2\,allyl}$), 108.5 (s; CH_{allyl}), 128.1 (s; CH_{arom}), 129.9 (s; CH_{arom}), 131.5 (s; CH_{arom}), 136.8 (dd, $J_{CP} = 24.8$, 31.5 Hz; C_{ipso}), 185.6 ppm (dd, $J_{CP} = 7$, 53 Hz; C=N). **4**: 81%; m.p. 195 °C (decomp); $^{31}P\{^1H\}$ NMR (C_6D_6, 25 °C, 81 Hz): $\delta = 64.6$, 75.7 ppm ($J_{PP} = 230$ Hz); ^{13}C NMR (C_6D_6, 25 °C, 75 Hz): $\delta = 9.10$ (ddd, $J_{CP} = 39$, 71 Hz, $J_{CRh} = 104$ Hz; CRh), 20.4 (d, $J_{CP} = 6.5$ Hz; CH_3), 21.2 (s; CH_3), 25.7 (d, $J_{CP} = 4$ Hz; CH_3), 26.1 (d, $J_{CP} = 4$ Hz; CH_3), 37.3 (dd, $J_{CP} = 2$, 6.5 Hz; CH_2), 42.8 (d, $J_{CP} = 7.5$ Hz; NCH), 44.0 (d, $J_{CRh} = 12$ Hz; CH=CH_{nbd}), 48.9 (d, $J_{CP} = 6.5$ Hz; NCH), 49.2 (s; CH_{nbd}), 49.3 (s; CH_{nbd}), 57.8 (d, $J_{CRh} = 8$ Hz; CH=CH_{nbd}), 61.4 (d, $J_{CRh} = 6$ Hz; $CH_{2\,nbd}$), 128.5 (s; CH_{arom}), 129.3 (s; CH_{arom}), 131.6 (s; CH_{arom}), 136.0 (dd, $J_{CP} = 7.5$, 24 Hz; C_{ipso}), 185.4 ppm (ddd, $J_{CP} = 49$, 4 Hz, $J_{CRh} = 3$ Hz; C=N). **5**: 59%, IR (CaF_2): $\tilde{\nu}$(CO) = 2042, 1960 cm^{-1}; $^{31}P\{^1H\}$ NMR ($CDCl_3$, 25 °C, 81 MHz): $\delta = 68.2$, 75.6 ppm ($^2J_{PP} = 224$ Hz); ^{13}C NMR ($CDCl_3$, 25 °C, 75 MHz): $\delta = 16.9$ (ddd, $J_{CP} = 32$, 87 Hz, $J_{CRh} = 44$ Hz; CRh), 19.9 (d, $J_{CP} = 5$ Hz; CH_3), 21.3 (d, $J_{CP} = 5$ Hz; CH_3), 23.1 (d, $J_{CP} = 4$ Hz; CH_3), 25.7 (d, $J_{CP} = 3$ Hz; CH_3), 36.6 (dd, $J_{CP} = 2$, 8 Hz; NCH_2), 42.6 (d, $J_{CP} = 6$ Hz; NCH), 49.2 (d, $J_{CP} = 6$ Hz; NCH), 128.1 (s; CH_{arom}), 129.0 (s; CH_{arom}), 131.9 (s; CH_{arom}), 136.7 (dd, $J_{CP} = 5.6$ Hz, 26 Hz; C_{ipso}), 182.1 (dd, $J_{CP} = 46$, 70.5 Hz; C=N), 184.4 (dd, $J_{CP} =$

 © 2006 Wiley-VCH Verlag GmbH & Co. KGaA, Weinheim

6.75 Hz, $J_{CRh}=49$ Hz; RhCO), 185.5 (ddd, $J_{CP}=57$, 4 Hz, $J_{CRh}=3$ Hz; C=N), 186.2 ppm (dd, $J_{CP}=8$ Hz, $J_{CRh}=76$ Hz, RhCO).

Received: December 10, 2005
Revised: January 20, 2006
Published online: March 14, 2006

Keywords: palladium · phosphorus heterocycles · rhodium · ylides

[1] Phosphoxides $R_2P(=O)H$ are masked air-stable forms of electron-rich phosphinous acid ligands R_2POH: a) G. Y. Li, *Angew. Chem.* **2001**, *113*, 1561 – 1564; *Angew. Chem. Int. Ed.* **2001**, *40*, 1513 – 1516; b) L. Ackermann, R. Born, *Angew. Chem.* **2005**, *117*, 2497 – 2500; *Angew. Chem. Int. Ed.* **2005**, *44*, 2444 – 2447.

[2] W. Su, S. Urgaonkar, P. A. McLaughlin, J. G. Verkade, *J. Am. Chem. Soc.* **2004**, *126*, 16433 – 16439.

[3] a) C. W. K. Gstöttmayr, V. P. W. Böhm, E. Herdtweck, M. Grosche, W. A. Herrmann, *Angew. Chem.* **2002**, *114*, 1421 – 1423; *Angew. Chem. Int. Ed.* **2002**, *41*, 1363 – 1365; b) J. Huang, S. P. Nolan, *J. Am. Chem. Soc.* **1999**, *121*, 9889 – 9890; c) W. A. Herrmann, K. Öfele, D. von Preysing, S. K. Schneider, *J. Organomet. Chem.* **2003**, *687*, 229 – 248.

[4] W. A. Herrmann, *Angew. Chem.* **2002**, *114*, 1342 – 1362; *Angew. Chem. Int. Ed.* **2002**, *41*, 1290 – 1309.

[5] a) V. Lavallo, Y. Canac, C. Präsang, B. Donnadieu, G. Bertrand, *Angew. Chem.* **2005**, *117*, 5851 – 5855; *Angew. Chem. Int. Ed.* **2005**, *44*, 5705 – 5709; b) V. Lavallo, Y. Canac, A. Dehope, B. Donnadieu, G. Bertrand, *Angew. Chem.* **2005**, *117*, 7402 – 7405; *Angew. Chem. Int. Ed.* **2005**, *44*, 7236 – 7239.

[6] S. K. Schneider, P. Roembke, G. R. Julius, C. Loschen, H. G. Raubenheimer, G. Frenking, W. A. Herrmann, *Eur. J. Inorg. Chem.* **2005**, 2973 – 2977.

[7] D. Martin, A. Baceiredo, H. Gornitzka, W. W. Schoeller, G. Bertrand, *Angew. Chem.* **2005**, *117*, 1728 – 1731; *Angew. Chem. Int. Ed.* **2005**, *44*, 1700 – 1703.

[8] Recent review on ylides and carbodiphosphorane chemistry: a) O. I. Kolodiazhnyi, *Tetrahedron*, **1996**, *52*, 1855 – 1929, and references therein; b) O. I. Kolodiazhnyi, *Phosphorus Ylides: Chemistry and Application in Organic Synthesis*, Wiley-VCH, Weinheim, **1999**.

[9] a) J. C. Baldwin, W. C. Kaska, *Inorg. Chem.* **1979**, *18*, 686 – 691; b) W. Petz, C. Kutschera, B. Neumüller, *Organometallics* **2005**, *24*, 5038 – 5043; c) J. Vicente, A. R. Singhal, *Organometallics* **2002**, *21*, 5887 – 5900; d) W. Petz, F. Weller, J. Uddin, G. Frenking, *Organometallics* **1999** *18*, 619 – 626; e) J. Sundermeyer, K. Weber, K. Peters, H. G. von Schnering *Organometallics* **1994**, *13*, 2560 – 2562; f) A. D. Bruce, A. S. Gamble, T. L. Tonker, J. L. Templeton *Organometallics* **1987**, *6*, 1950 – 1952; g) H. Schmidbaur, C. E. Zybill, G. Müller, C. Krüger, *Angew. Chem.* **1983**, *95*, 753 – 755; *Angew. Chem. Int. Ed. Engl.* **1983**, *22*, 729 – 730.

[10] K. Kubo, N. D. Jones, M. J. Ferguson, R. MacDonald, R. G. Cavell, *J. Am. Chem. Soc.* **2005**, *127*, 5314 – 5315.

[11] H. Schmidbaur, T. Costa, B. Milewski-Mahrla, U. Schubert, *Angew. Chem.* **1980**, *92*, 557 – 558; *Angew. Chem. Int. Ed. Engl.* **1980**, *19*, 555 – 556.

[12] W. C. Kaska, D. K. Mitchell, R. F. Reichelderfer, W. D. Korte, *J. Am. Chem. Soc.* **1973**, *95*, 2847 – 2854.

[13] T. Kato, A. Baceiredo, H. Gornitzka, W. W. Schoeller, G. Bertrand, *J. Am. Chem. Soc.* **2002**, *124*, 2506 – 2512.

[14] E. Fluck, B. Neumüller, R. Braun, G. Heckmann, *Z. Anorg. Allg. Chem.* **1988**, *567*, 23 – 38.

[15] a) Crystal data: **2b:** $C_{28}H_{51}N_5P_2$, $M_r=519.68$, triclinic, $P\bar{1}$, $a=9.384(1)$, $b=9.688(1)$, $c=18.443(1)$ Å, $\alpha=96.936(1)$, $\beta=90.360(1)$, $\gamma=114.052(1)°$, $V=1517.1(2)$ Å^3, $Z=2$, $T=193(2)$ K. 9003 reflections (6120 independent, $R_{int}=0.0192$) were collected. Max. residual electron density: 0.426 e Å^{-3}, $R_1=0.0432$ ($I>2\sigma(I)$) and $wR_2=0.1171$ (all data) with $R_1=\Sigma||F_o|-|F_c||/\Sigma|F_o|$ and $wR_2=(\Sigma w(F_o^2-F_c^2)^2/\Sigma w(F_o^2)^2)^{0.5}$. **3**: $C_{35}H_{66}ClN_5OP_2Pd$, $M_r=776.72$, monoclinic, $P2_1/c$, $a=18.003(2)$ Å, $b=10.262(2)$ Å, $c=22.707(2)$ Å, $\beta=111.460(2)°$, $V=3904.1(6)$ Å^3, $Z=4$, $T=133(2)$ K. 22283 reflections (7984 independent, $R_{int}=0.0342$) were collected. Max. residual electron density: 0.649 e Å^{-3}, $R_1=0.0326$ ($I>2\sigma(I)$) and $wR_2=0.0821$ (all data). **4**: $C_{37}H_{63}Cl_5N_5P_2Rh$, $M_r=920.02$, monoclinic, $P2_1/n$, $a=11.237(1)$, $b=17.036(1)$, $c=22.6864(1)$ Å, $\beta=95.536(1)°$, $V=4322.9(4)$ Å^3, $Z=4$, $T=133(2)$ K. 24979 reflections (8865 independent, $R_{int}=0.0217$) were collected. Max. residual electron density: 0.756 e Å^{-3}, $R_1=0.0267$ ($I>2\sigma(I)$) and $wR_2=0.0680$ (all data). All data for all structures represented in this paper were collected at low temperature for oil-coated shock-cooled crystals on a Bruker-AXS CCD 1000 diffractometer with $Mo_{K\alpha}$ radiation ($\lambda=0.71073$ Å). The structures were solved by direct methods (SHELXS-97: G. M. Sheldrick, *Acta Crystallogr. Sect. A* **1990**, *46*, 467 – 473) and all non-hydrogen atoms were refined anisotropically by the least-squares method on F^2 (G. M. Sheldrick, SHELXL-97, Program for Crystal Structure Refinement, Universität Göttingen, **1997**). CCDC-292498 (**2b**), CCDC-292499 (**3**), and CCDC-292500 (**4**) contain the supplementary crystallographic data for this paper. These data can be obtained free of charge from The Cambridge Crystallographic Data Centre via www.ccdc.cam.ac.uk/data_request/cif; b) Mean deviations from the best planes formed by the four coordination sites and the metal atoms are 0.0261 Å for Pd (**3**) and 0.0194 Å for Rh (**4**).

[16] a) H. Schmidbaur, G. Hasslberger, U. Deschler, U. Schubert, C. Kappenstein, A. Frank, *Angew. Chem.* **1979**, *91*, 437 – 438; *Angew. Chem. Int. Ed. Engl.* **1979**, *18*, 408 – 409; b) G. E. Hardy, J. I. Zink, W. C. Kaska, *J. Am. Chem. Soc.* **1978**, *100*, 8001 – 2002; c) U. Schubert, C. Kappenstein, B. Milewski-Mahrla, H. Schmidbaur, *Chem. Ber.* **1981**, *114*, 3070.

[17] a) K. Denk, P. Sirsch, W. A. Herrmann, *J. Organomet. Chem.* **2002**, *649*, 219 – 224; b) W. A. Herrmann, K. Öfele, D. von Preysing, E. Herdtweck, *J. Organomet. Chem.* **2003**, *684*, 235 – 248; c) A. W. Coleman, P. B. Hitchcock, M. F. Lappert, R. K. Maskell, J. H. Müller, *J. Organomet. Chem.* **1985**, *296*, 173 – 196; d) W. A. Herrmann, M. Elison, J. Fischer, C. Köcher, G. R. J. Artus, *Chem. Eur. J.* **1996**, *2*, 772 – 780; e) D. Enders, H. Gielen, J. Runsink, K. Breuer, S. Brode, K. Boehn, *Eur. J. Inorg. Chem.* **1998**, 913 – 919.

[18] See Supporting Information.

[19] M. Mayr, K. Wurst, K.-H. Ongania, M. R. Buchmeiser, *Chem. Eur. J.* **2004**, *10*, 1256 – 1266.

[20] C. Präsang, B. Donnadieu, G. Bertrand, *J. Am. Chem. Soc.* **2005**, *127*, 10182 – 10183.

 © 2006 Wiley-VCH Verlag GmbH & Co. KGaA, Weinheim

Main-Group Hydrides

DOI: 10.1002/anie.200504337

Stable Monomeric Germanium(II) and Tin(II) Compounds with Terminal Hydrides**

*Leslie W. Pineda, Vojtech Jancik, Kerstin Starke, Rainer B. Oswald, and Herbert W. Roesky**

Metal hydrides and their complexes are considered valuable synthons in chemistry. It was demonstrated that main-group and transition-metal hydrides are important intermediates in some industrial processes and also function as catalysts.[1] Furthermore, in the quest for alternative energy sources, metal hydrides have been considered as potential feedstocks for hydrogen storage.[2] Group 14 hydrides such as R_3SiH, R_3GeH, and R_3SnH are important reagents for some key reactions in organic synthesis. The preparation of these species is commonly carried out by reduction of the corresponding chloride compounds with lithium aluminum hydride.[3] However, the isolation and structural characterization of monomeric, terminal low-valent Group 14 hydrides seem to be difficult as a result of the potential reactivity and instability of these species. So far, only [{2,6-$Trip_2C_6H_3Sn(\mu$-H)}$_2$] (Trip = 2,4,6-*i*$Pr_3C_6H_2$) has been structurally characterized and exhibits a dimeric structure with the tin(II) atoms connected by bridging hydride ligands,[4] although the existence of MH_2 (M = Si to Pb) has been anticipated by theoretical calculations.[5] Previously, we reported on the preparation of the germanium(II) and tin(II) precursors [{HC(CMeNAr)$_2$}GeCl] (**1**; Ar = 2,6-*i*$Pr_2C_6H_3$) and [{HC(CMeNAr)$_2$}SnCl] (**2**).[6,7] Treatment of **1** with $LiAlH_4$ or $NaBH_4$ did not afford the terminal germanium(II) hydride, but rather, the four-coordinate adduct [{HC(CMeNAr)$_2$}Ge(H)BH_3] was formed. Moreover, attempts to prepare a terminal tin(II) hydride from **2** in reactions with reducing reagents such as $NaBH_4$, KBH_4, and KH were unsuccessful. In contrast, the reactions of **1** and **2** with $AlH_3{\cdot}NMe_3$[8–10] in toluene at −4 °C yield the first monomeric and terminal germanium(II) and tin(II) hydrides [{HC(CMeNAr)$_2$}GeH] (**3**, Scheme 1)[11] and [{HC(CMeNAr)$_2$}SnH] (**4**). Elimination of trimethylamine as a volatile by-product was observed during the course of the reactions of **1** and **2** with $AlH_3{\cdot}NMe_3$. The color of the reaction mixture changed from yellow to orange-red in the synthesis of **3**, and from pale yellow to green in the synthesis of **4**. No further color change was observed for either reaction mixture upon warming to ambient temperature.

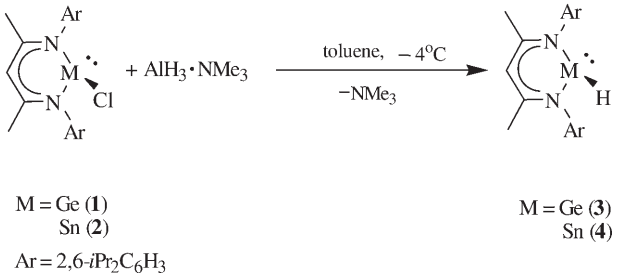

Scheme 1. Formation of **3** and **4**.

Compound **3** is thermally stable over a long period of time when stored in an inert atmosphere in a glove box, whereas **4** decomposes slowly under the same conditions to form an insoluble gray solid within four days. However, **4** is stable at −32 °C over a longer period of time. Both **3** and **4** are air- and moisture-sensitive and were characterized by IR spectroscopy, multinuclear NMR spectroscopy, single-crystal X-ray structural analysis, and DFT calculations. In the IR spectrum of **3**, a strong absorption was observed at 1733 cm^{-1}, which can be attributed to the Ge–H stretching mode and compares well with that reported for Ar′(H)GeGe(H)Ar′[13] (1785 cm^{-1}; Ar′ = 2,6-$Dipp_2C_6H_3$, Dipp = 2,6-*i*$Pr_2C_6H_3$), but is found at a lower frequency than that for [{HC(CMeNAr)$_2$}Ge(H)BH_3] (1928 cm^{-1}).[7] Hydride complexes of germanium(IV) show Ge–H absorptions in the range from 1953 to 2175 cm^{-1}.[3a,14–16] The Sn–H stretching mode of **4** (1849 cm^{-1}) is comparable to those in the hydrogen-bridged tin compound [{2,6-$Trip_2C_6H_3Sn(\mu$-H)}$_2$] (1828, 1771 cm^{-1}).[4] In the ^{1}H NMR spectrum of **3**, the Ge–H hydrogen atom resonates at lower field (δ = 8.08 ppm) than those in Ar′(H)GeGe(H)Ar′ (δ = 3.48 ppm) and $Ar'(H)_2GeGeAr'{\cdot}PMe_3$ (δ = 3.81 ppm).[13] Interestingly, the Ge–H proton resonance of **3** is in the range of germanium(IV) hydrides.[17] The Sn–H proton resonance of **4** is found at a surprisingly low-field shift (δ = 13.83 ppm) relative to that in [{2,6-$Trip_2C_6H_3Sn(\mu$-H)}$_2$] (δ = 7.87 ppm), and is flanked by Sn satellites ($^1J(^{119}Sn,^1H)$ = 64 Hz).[4] The Sn–H resonance of **4** is the lowest-field chemical shift observed for a tin hydride.[3a,18–20] The ^{119}Sn NMR resonance of **4** (δ = −224.7 ppm) is in accordance with a three-coordinate tin(II) environment ([{HC(CMeNAr)$_2$}SnCl]: δ = −224 ppm;[7] [{$H_2B(pz)_2$}SnCl]: δ = −305 ppm; [{$Ph_2B(pz)_2$}SnCl]: δ = −353 ppm; [{$H_2B(pz')_2$}SnCl]: δ = −271 ppm; pz = pyrazole, pz′ = 3-methylpyrazole).[21]

Orange-red single crystals of **3** and green crystals of **4** suitable for X-ray structural analysis[22] were grown from saturated hexane solutions at −32 °C within two days (**3**) or

[*] Dipl.-Chem. L. W. Pineda, Dr. V. Jancik, Dipl.-Chem. K. Starke, Prof. Dr. H. W. Roesky
Institut für Anorganische Chemie
Universität Göttingen
Tammannstrasse 4, 37077 Göttingen (Germany)
Fax: (+49) 551-39-3373
E-mail: hroesky@gwdg.de
Dr. R. B. Oswald
Institut für Physikalische Chemie
Universität Göttingen
Tammannstrasse 6, 37077 Göttingen (Germany)

[**] This work was supported by the Fonds der Chemischen Industrie and the Göttinger Akademie der Wissenschaften. L.W.P. thanks the Deutscher Akademischer Austauschdienst (DAAD) for a predoctoral fellowship.

Supporting information for this article is available on the WWW under http://www.angewandte.org or from the author.

InterScience
© 2006 Wiley-VCH Verlag GmbH & Co. KGaA, Weinheim

after one week (**4**). Compound **3** crystallizes in the monoclinic space group $P2_1/n$ with two independent isostructural monomers in the asymmetric unit. Although the Ge–H hydrogen atom in **3** could not be localized in the difference electron-density map, the Ge–H linkage was unequivocally confirmed by IR and ^{1}H NMR spectroscopy (see above). In **3**, the germanium atom is tetrahedrally coordinated by the β-diketiminato ligand, a hydrogen atom, and, we assume, a lone pair of electrons at the fourth coordination site (Figure 1). Compound **3** exhibits Ge–N bond lengths of 1.989(2) Å (molecule 1) as well as 1.994(2) and 1.988(2) Å (molecule 2), and these lengths are very similar to those of **1** (1.988(2), 1.997(2) Å).[6]

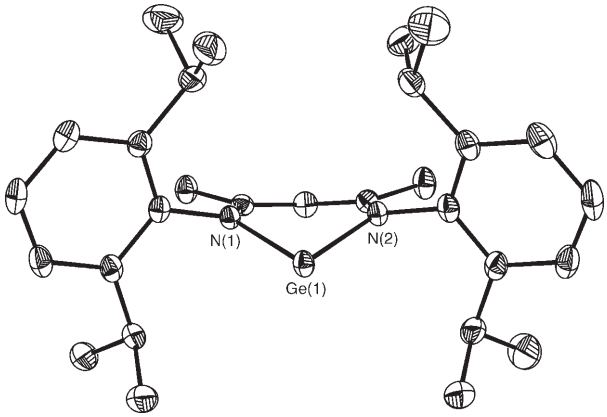

Figure 1. Thermal-ellipsoid plot of one molecule of **3** at the 50% probability level. Hydrogen atoms are omitted for clarity. The Ge–H hydrogen atom could not be localized. Only the numbering scheme of molecule 1 is depicted. Selected bond lengths [Å] and angles [°]: molecule 1: Ge(1)–N(1) 1.989(2), Ge(1)–N(2) 1.989(2), N(1)-Ge(1)-N(2) 90.3(1); molecule 2: Ge(2)–N(1A) 1.994(2), Ge(2)–N(2A) 1.988(2), N(1A)-Ge(2)–N(2A) 90.5(1).

Compound **4** crystallizes in the monoclinic space group $C2/c$ with one monomer in the asymmetric unit. Weak intermolecular contacts between the lone pair of electrons on the tin atom and the Sn–H hydrogen atom from another molecule generate hydrogen bridges and formation of a dimer (d(Sn(1)···H(1A)): 4.01(3) Å; d(Sn···Sn): 3.71 Å). Compound **4** comprises a distorted tetrahedral geometry at the tin atom, which coordinates to a monoanionic β-diketiminato ligand, a hydrogen atom, and, we assume, a lone pair of electrons at the fourth coordination site (Figure 2). The Sn–H hydrogen atom was localized from the residual electron density. The most prominent structural feature of **4** is the Sn–H bond length of 1.74(3) Å, which is in good agreement with Sn–H bond lengths predicted by theoretical calculations (1.77 Å).[5,25] However, this length is shorter than those of [{2,6-$Trip_2C_6H_3$Sn(μ-H)}$_2$], which exhibits two different μ-hydrogen bonds (d(Sn–H): 1.89(3), 1.95(3) Å).[4]

To investigate the electronic properties of **3** and **4**, ab initio calculations were carried out by using the Gaussian program package[26] with the well-established DFT-variant B3LYP.[27–29] Two different basis sets were employed to achieve a suitable description of the electronic structure. The LANL2DZ[30] basis set (for Ge and Sn) and the 6-

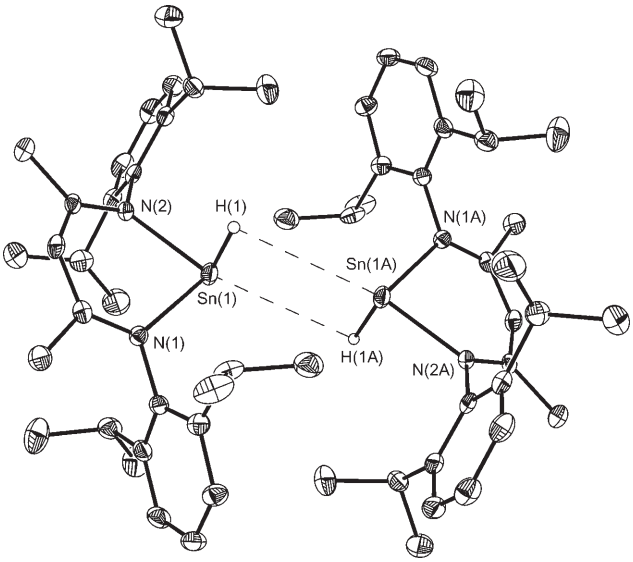

Figure 2. Thermal-ellipsoid plot of **4** at the 50% probability level. Carbon-bound H atoms are omitted for clarity. Selected bond lengths [Å] and angles [°]: Sn(1)–H(1) 1.74(3), Sn(1)–N(1) 2.195(2), Sn(1)–N(2) 2.198(2), Sn(1)···H(1A) 4.01(3); H(1)-Sn(1)-N(1) 93.4(8), H(1)-Sn(1)-N(2) 92.6(8), N(1)-Sn(1)-N(2) 85.1(1).

31G[31,32] basis set (for the remaining atoms) with additional double-diffuse functions were used. The structures of both complexes were determined by full geometry optimization. The obtained equilibrium geometries were in good agreement with the X-ray data. Since the structural parameters are the result of the calculated molecular orbitals, an analysis of the electronic structure was perfomed with the natural bond order (NBO)[33] procedure, which makes it possible to describe and quantify the contribution of the atomic orbitals to the molecular orbitals. The calculations showed that the electron density of the lone pair on the central atom in each of **3** and **4** contributes to the bonding in the complex. The NBO analysis of the M–H bond shows that the contribution of the lone pair of electrons on germanium can best be described as an $sp^{0.32}$ hybrid, while the hybrid for tin is of the type $sp^{0.25}$ (see the Supporting Information). The larger p character at the Ge center in compound **3** (20% greater than that at the Sn center in **4**) leads to an enhanced delocalization of π electrons over the neighboring p orbitals of the nitrogen atoms. Remarkably, in the case of **4**, there is no participation of the hydrogen s orbital in the lone pair of electrons.

Analysis of the metal–hydrogen bond by using the natural localized molecular orbitals (NLMO) reveals significant differences between **3** and **4**. For the Ge–H bond in **3**, the hydrogen atom contributes 65%, and the corresponding hydrogen atom in the Sn–H bond contributes 70%. Analysis of the molecular orbitals of **4** also shows that there is no participation of the hydrogen s orbital in the wave function describing the lone pair of electrons. Another factor that influences the electron density at the hydrogen atom is the amount of donor–acceptor interaction with the nitrogen atoms of the ring system. This interaction occurs mainly through two-electron stabilization in a donor–acceptor situation[34] involving the bonding Ge–H orbital and nonbond-

 © 2006 Wiley-VCH Verlag GmbH & Co. KGaA, Weinheim

ing orbitals of the ring system, which transfers electron density from the nitrogen atoms into the Ge–H bond. This effect is 50% larger for **3** than for **4**. Taking these findings into account, the low-field chemical shift of the hydrogen atom in **4** might be deduced. The lack of further stabilization from delocalization causes the tin atom to pull out electron density strongly from the hydride ligand to compensate for its electron-deficient character. Hence, the "naked" nature of the hydrogen atom in the Sn–H bond is a reflection of extreme deshielding and leads to such a low-field chemical shift.

In summary, we were able to isolate and structurally characterize compounds of composition [{HC(CMeNAr)$_2$}GeH] and [{HC(CMeNAr)$_2$}SnH] by the reactions of $AlH_3{\cdot}NMe_3$ with the appropriate chloride precursors. These compounds represent the first examples of terminal, monomeric hydrides of germanium(II) and tin(II).

Experimental Section

All manipulations were performed in a dry and oxygen-free atmosphere (N_2 or Ar) by using Schlenk-line and glove-box techniques. Solvents were purified prior to use by distillation over appropriate drying agents under nitrogen.

3: A solution of $AlH_3{\cdot}NMe_3$ (1.18 mL, 1.0 M in toluene) was slowly added to a solution of **1** (0.62 g, 1.18 mmol) in toluene (25 mL) at −4 °C, and the yellow solution immediately turned to orange-red. The cooling bath was removed after 20 min, and stirring of the solution was continued until the elimination of NMe_3 had ceased. All volatiles were removed in vacuum, and the remaining orange-red residue was extracted with *n*-hexane (15 mL). The solvent was removed in vacuo to yield **3** as an orange-red powder. Yield: 0.32 g (60%); m.p. 170 °C (decomp); IR (KBr pellet): $\tilde{\nu}$ = 1733 cm^{-1} (s, GeH); ^{1}H NMR (300 MHz, C_6D_6, 25 °C, TMS): δ = 8.08 (s, 1H, GeH), 7.15–7.07 (m, 6H, ArH), 4.92 (s, 1H, γ-CH), 3.58 (sept, ^3J(H,H) = 6.8 Hz, 2H, C*H*(CH$_3$)$_2$), 3.41 (sept, ^3J(H,H) = 6.8 Hz, 2H, C*H*(CH$_3$)$_2$), 1.55 (s, 6H, CH$_3$), 1.37 (d, ^3J(H,H) = 6.8 Hz, 6H, CH(C*H*$_3$)$_2$), 1.29 (d, ^3J(H,H) = 6.8 Hz, 6H, CH(C*H*$_3$)$_2$), 1.19 (d, ^3J(H,H) = 6.8 Hz, 6H, CH(C*H*$_3$)$_2$), 1.17 ppm (d, ^3J(H,H) = 6.8 Hz, 6H, CH(C*H*$_3$)$_2$); ^{13}C NMR (125.8 MHz, C_6D_6, 25 °C, TMS): δ = 167.5 (CN), 146.5, 143.5, 141.6, 127.3, 124.6, 124.3 (Ar), 97.8 (γ-CH), 29.0 (CH$_3$), 28.2 (*C*H(CH$_3$)$_2$), 27.0 (*C*H(CH$_3$)$_2$), 24.8 (CH(*C*H$_3$)$_2$), 24.4 (CH(*C*H$_3$)$_2$), 23.7 (CH(*C*H$_3$)$_2$), 22.8 ppm (CH(*C*H$_3$)$_2$); EI-MS (70 eV): *m*/*z* (%): 491 (100) [*M*−H]$^+$, 449 (40) [*M*−*i*Pr]$^+$. Elemental analysis (%) calcd for $C_{29}H_{42}GeN_2$ (491.26): C 70.69, H 8.60, N 5.70; found: C 70.20, H 8.53, N 5.36.

4: A solution of **2** (1.85 g, 3.24 mmol) in toluene (30 mL) was cooled to −4 °C and added slowly to a solution of $AlH_3{\cdot}NMe_3$ (3.24 mL, 1.0 M in toluene). The cooling bath was removed after 15 min, and the solution was stirred further until NMe_3 elimination had ceased. The color of the solution changed from pale yellow to green. The solvent was removed in vacuo, and the green residue was extracted with *n*-hexane. The solvent was removed to afford **4** as a green powder. Yield: 1.58 g (91%); m.p. 125 °C (decomp); IR (KBr pellet): $\tilde{\nu}$ = 1849 cm^{-1} (m, SnH); ^{1}H NMR (500 MHz, C_6D_6, 25 °C, TMS): δ = 13.83 (s, ^1J(^{119}Sn,^{1}H) = 64 Hz, 1H, SnH), 7.15–7.06 (m, 6H, ArH), 4.89 (s, 1H, γ-CH), 3.52 (sept, ^3J(H,H) = 6.8 Hz, 2H, C*H*(CH$_3$)$_2$), 3.46 (sept, ^3J(H,H) = 6.8 Hz, 2H, C*H*(CH$_3$)$_2$), 1.62 (s, 6H, CH$_3$), 1.34 (d, ^3J(H,H) = 6.8 Hz, 6H, CH(C*H*$_3$)$_2$), 1.27 (d, ^3J(H,H) = 6.8 Hz, 6H, CH(C*H*$_3$)$_2$), 1.19 (d, ^3J(H,H) = 6.8 Hz, 6H, CH(C*H*$_3$)$_2$), 1.17 ppm (d, ^3J(H,H) = 6.8 Hz, 6H, CH(C*H*$_3$)$_2$); ^{13}C NMR (125.8 MHz, C_6D_6, 25 °C, TMS): δ = 167.7 (CN), 145.5, 143.0, 142.8, 126.8, 124.7, 124.3 (Ar), 98.3 (γ-CH), 29.0 (CH$_3$), 27.8 (*C*H(CH$_3$)$_2$), 26.8 (*C*H(CH$_3$)$_2$), 24.8 (CH(*C*H$_3$)$_2$), 24.4 (CH(*C*H$_3$)$_2$), 24.0 (CH(*C*H$_3$)$_2$), 23.4 ppm (CH(*C*H$_3$)$_2$); ^{119}Sn NMR (186.5 MHz, C_6D_6, 25 °C, Me_4Sn): δ = −224.7 ppm; EI-MS (70 eV): *m*/*z* (%): 537 (5) [*M*−H]$^+$. Elemental analysis (%) calcd for $C_{29}H_{42}N_2Sn$ (537.36): C 64.82, H 7.88, N 5.21; found: C 64.20, H 7.45, N 5.33.

Received: December 6, 2005
Revised: January 25, 2006
Published online: March 14, 2006

Keywords: density functional calculations · germanium · Group 14 elements · hydrides · tin

[1] a) H. D. Kaesz, R. B. Saillant, *Chem. Rev.* **1972**, *72*, 231–281; b) G. S. McGrady, G. Guilera, *Chem. Soc. Rev.* **2003**, *32*, 383–392; c) S. Aldridge, A. J. Downs, *Chem. Rev.* **2001**, *101*, 3305–3365; d) H.-J. Himmel, *Dalton. Trans.* **2003**, 3639–3649; e) H.-J. Himmel, *Z. Anorg. Allg. Chem.* **2005**, *631*, 1551–1564; f) N. W. Mitzel, *Angew. Chem.* **2003**, *115*, 3984–3986; *Angew. Chem. Int. Ed.* **2003**, *42*, 3856–3858; g) W. M. Mueller, J. P. Blackledge, G. G. Libowitz, *Metal Hydrides*, Academic Press, London, **1968**, pp. 1–21; h) F. Lefebvre, J.-M. Basset, *Main Group Met. Chem.* **2002**, *25*, 15–32; i) J. Zhao, A. S. Goldman, J. F. Hartwig, *Science* **2005**, *307*, 1080–1082.

[2] a) R. F. Service, *Science* **2004**, *305*, 958–961; b) J. A. Turner, *Science* **2004**, *305*, 972–974; c) W. Grochala, P. P. Edwards, *Chem. Rev.* **2004**, *104*, 1283–1315; d) F. Schüth, B. Bogdanović, M. Felderhoff, *Chem. Commun.* **2004**, 2249–2258.

[3] a) E. J. Kupchik in *Organotin Compounds*, *Vol. 1* (Ed.: A. K. Sawyer), Marcel Dekker, New York, **1971**, pp. 7–72; b) A. G. Davies, P. J. Smith in *Comprehensive Organometallic Chemistry*, *Vol. 2* (Eds.: G. Wilkinson, F. G. A. Stone, E. W. Abel), Pergamon, Oxford, **1982**, pp. 584–585; c) M. Lesbre, P. Mazerolles, J. Satgé, *The Organic Compounds of Germanium*, Wiley, London, **1971**, pp. 259–265; d) P. Rivière, M. Rivière-Baudet, J. Satgé, in *Comprehensive Organometallic Chemistry*, *Vol. 2* (Eds.: G. Wilkinson, F. G. A. Stone, E. W. Abel), Pergamon, Oxford, **1982**, pp. 424–425; for some selected applications of Group 14 hydrides in organic synthesis, see: e) V. I. Dodero, M. B. Faraoni, D. C. Gerbino, L. C. Koll, A. E. Zuñiga, T. N. Mitchell, J. Podestá, *Organometallics* **2005**, *24*, 1992–1995; f) D. S. Hays, G. C. Fu, *J. Org. Chem.* **1997**, *62*, 7070–7071; g) V. I. Dodero, L. C. Koll, M. B. Faraoni, T. N. Mitchell, J. Podestá, *J. Org. Chem.* **2003**, *68*, 10087–10091; h) V. I. Dodero, T. N. Mitchell, J. Podestá, *Organometallics* **2003**, *22*, 856–860; i) K. Sasaki, Y. Kondo, K. Maruoka, *Angew. Chem.* **2001**, *113*, 425–428; *Angew. Chem. Int. Ed.* **2001**, *40*, 411–414.

[4] B. E. Eichler, P. P. Power, *J. Am. Chem. Soc.* **2000**, *122*, 8785–8786.

[5] G. Trinquier, *J. Am. Chem. Soc.* **1990**, *112*, 2130–2137.

[6] Y. Ding, H. Hao, H. W. Roesky, M. Noltemeyer, H.-G. Schmidt, *Organometallics* **2001**, *20*, 4806–4811.

[7] Y. Ding, H. W. Roesky, M. Noltemeyer, H.-G. Schmidt, *Organometallics* **2001**, *20*, 1190–1194.

[8] R. A. Kovar, J. O. Callaway, *Inorg. Synth.* **1976**, *22*, 37–47.

[9] H. W. Roesky, *Aldrichimica Acta* **2004**, *37*, 103–108.

[10] S. S. Kumar, H. W. Roesky, *Dalton Trans.* **2004**, 3927–3937.

[11] Alternatively, compound **3** could also be prepared in good yield by the reaction of [{HC(CMeNAr)$_2$}GeOH][12] and $AlH_3{\cdot}NMe_3$.

[12] L. W. Pineda, V. Jancik, H. W. Roesky, D. Neculai, A. M. Neculai, *Angew. Chem.* **2004**, *116*, 1443–1445; *Angew. Chem. Int. Ed.* **2004**, *43*, 1419–1421.

[13] A. F. Richards, A. D. Phillips, M. M. Olmstead, P. P. Power, *J. Am. Chem. Soc.* **2003**, *125*, 3204–3205.

[14] A. Castel, P. Rivière, J. Satgé, H. Y. Ko, *Organometallics* **1990**, *9*, 205–210.

 © 2006 Wiley-VCH Verlag GmbH & Co. KGaA, Weinheim

[15] F. Riedmiller, G. L. Wegner, A. Jockisch, H. Schmidbaur, *Organometallics* **1999**, *18*, 4217 – 4324.

[16] P. Rivière, J. Satgé, *Bull. Soc. Chim. Fran.* **1967**, *11*, 4039 – 4046.

[17] G. H. Spikes, J. C. Fettinger, P. P. Power, *J. Am. Chem. Soc.* **2005**, *127*, 12232 – 12233.

[18] M. L. Maddox, N. Flitcroft, H. D. Kaesz, *J. Organomet. Chem.* **1965**, *4*, 50 – 56.

[19] G. Yamamoto, S. Ohta, M. M. Kaneko, K. Mouri, M. Ohkuma, R. Mikami, Y. Uchiyama, M. Minoura, *Bull. Chem. Soc. Jpn.* **2005**, *78*, 487 – 497.

[20] F. Schager, R. Goddard, K. Seevogel, K.-R. Pörschke, *Organometallics* **1998**, *17*, 1546 – 1551.

[21] M. N. Hansen, K. Niedenzu, J. Serwatowska, J. Serwatowski, K. R. Woodrum, *Inorg. Chem.* **1991**, *30*, 866 – 868.

[22] a) Crystal data for **3**: $C_{29}H_{42}GeN_2$, $M_r = 491.24$, crystal dimensions $0.10 \times 0.05 \times 0.02$ mm^3, monoclinic, space group $P2_1/n$, $a = 15.238(3)$, $b = 18.201(4)$, $c = 20.485(4)$ Å, $\beta = 99.11(3)°$, $V = 5610(2)$ Å^3, $Z = 8$, $\rho_{calcd} = 1.163$ g cm^{-3}, $F(000) = 2096$, $\lambda = 1.54178$ Å, $T = 100(2)$ K, $\mu(Cu_{K\alpha}) = 1.593$ mm^{-1}. Of the 35990 measured reflections, 7983 were independent (R(int) = 0.0418). The final refinements converged to $R1 = 0.0388$ for $I > 2\sigma(I)$, $wR2 = 0.1035$ for all data. The final difference Fourier synthesis gave a min/max residual electron density of $-0.476/+1.47$ e Å^{-3}; b) crystal data for **4**: $C_{29}H_{42}SnN_2$, $M_r = 537.34$, crystal dimensions $0.10 \times 0.05 \times 0.05$ mm^3, monoclinic, space group $C2/c$, $a = 25.209(5)$, $b = 15.139(3)$, $c = 14.682(3)$ Å, $\beta = 94.92(3)°$, $V = 5583(2)$ Å^3, $Z = 8$, $\rho_{calcd} = 1.279$ g cm^{-3}, $F(000) = 2240$, $\lambda = 1.54178$ Å, $T = 100(2)$ K, $\mu(Cu_{K\alpha}) = 7.392$ mm^{-1}. Of the 22645 measured reflections, 4000 were independent (R(int) = 0.0315). The final refinements converged to $R1 = 0.0216$ for $I > 2\sigma(I)$, $wR2 = 0.0548$ for all data. The final difference Fourier synthesis gave a min/max residual electron density of $-0.745/+0.749$ e Å^{-3}; c) data for the structures were collected on a Bruker three-circle diffractometer, which was equipped with a SMART 6000 CCD detector. Intensity measurements were performed on a rapidly cooled crystal in the ranges $6.54 \le 2\theta \le 117.94°$ (**3**) and $6.82 \le 2\theta \le 117.80°$ (**4**). The structures were solved by direct methods with SHELXS-97[23] and refined for all data by full-matrix least squares on F^2.[24] All non-H atoms for **3** and **4** were refined anisotropically, and all H atoms for **3** and **4**, except for the γ-C–H hydrogen atoms H(3A) and H(3AA) in **3** (the packing diagram shows chain formation through weak intermolecular interactions between the lone pair of electrons at the Ge atom and the γ-C–H hydrogen atom of another molecule), were included in geometrically idealized positions and refined with the riding model. Localization of the H(3A) and H(3AA) atoms from the electron-density maps in **3** proved to be more accurate than fixing the atoms in the idealized positions and led to lower $R1$ and $wR2$ values. The Sn–H hydrogen atom in **4** was localized from the difference electron-density map and refined isotropically with U_{ij} tied to the parent atom. CCDC-291156 and CCDC-291157 contain the supplementary crystallographic data for this paper. These data can be obtained free of charge from The Cambridge Crystallographic Data Centre via www.ccdc.cam.ac.uk/data_request/cif.

[23] SHELXS-97, Program for Structure Solution: G. M. Sheldrick, *Acta Crystallogr. Sect. A* **1990**, *46*, 467 – 473.

[24] G. M. Sheldrick, SHELXL-97, *Program for Crystal Structure Refinement*, University of Göttingen, Göttingen (Germany), **1997**.

[25] K. Balasubramanian, *J. Chem. Phys.* **1988**, *89*, 5731 – 5738.

[26] Gaussian 03 (Revision C.02): M. J. Frisch et al., see the Supporting Information.

[27] C. Lee, W. Yang, R. G. Parr, *Phys. Rev. B* **1988**, *37*, 785 – 789.

[28] B. Miehlich, A. Savin, H. Stoll, H. Preuss, *Chem. Phys. Lett.* **1989**, *157*, 200 – 206.

[29] A. D. Becke, *J. Chem. Phys.* **1993**, *98*, 5648 – 5652.

[30] a) P. J. Hay, W. R. Wadt, *J. Chem. Phys.* **1985**, *82*, 270 – 283; b) W. R. Wadt, P. J. Hay, *J. Chem. Phys.* **1985**, *82*, 270 – 298; c) P. J. Hay, W. R. Wadt, *J. Chem. Phys.* **1985**, *82*, 299 – 310.

[31] G. A. Petersson, M. A. Al-Laham, *J. Chem. Phys.* **1991**, *94*, 6081 – 6090.

[32] G. A. Petersson, A. Bennett, T. G. Tensfeldt, M. A. Al-Laham, W. A. Shirley, J. Mantzaris, *J. Chem. Phys.* **1988**, *89*, 2193 – 2218.

[33] a) J. E. Carpenter, F. Weinhold, *J. Mol. Struct.* **1988**, *169*, 41 – 62; b) J. P. Foster, F. Weinhold, *J. Am. Chem. Soc.* **1980**, *102*, 7211 – 7218; c) A. E. Reed, F. Weinhold, *J. Chem. Phys.* **1985**, *83*, 1736 – 1740; d) A. E. Reed, L. A. Curtiss, F. Weinhold, *Chem. Rev.* **1988**, *88*, 899 – 926.

[34] F. Weinhold, C. Landis, *Valency and Bonding*, University Press, Cambridge, **2005**, pp. 19 – 20; F. Weinhold, C. Landis, *Valency and Bonding*, University Press, Cambridge, **2005**, pp. 94 – 96; F. Weinhold, C. Landis, *Valency and Bonding*, University Press, Cambridge, **2005**, pp. 125 – 128; F. Weinhold, C. Landis, *Valency and Bonding*, University Press, Cambridge, **2005**, pp. 184 – 188.

 © 2006 Wiley-VCH Verlag GmbH & Co. KGaA, Weinheim

Heterogeneous Catalysis

DOI: 10.1002/anie.200504609

Brønsted Acid Mediated Heterogeneous Addition Reaction of 1,3-Dicarbonyl Compounds to Alkenes and Alcohols**

*Ken Motokura, Noriaki Fujita, Kohsuke Mori, Tomoo Mizugaki, Kohki Ebitani, and Kiyotomi Kaneda**

From the standpoint of atom efficiency,[1] nucleophilic additions to alkenes or alcohols instead of alkyl halides are attractive salt-free methods (Scheme 1). Simple alkenes are readily accessible and abundant carbon-atom sources, but intermolecular additions of 1,3-dicarbonyl compounds to simple alkenes remain problematic. In traditional acid- or base-catalyzed Michael reactions of 1,3-dicarbonyl com-

[*] Dr. K. Motokura, N. Fujita, Dr. K. Mori, Dr. T. Mizugaki, Dr. K. Ebitani, Prof. Dr. K. Kaneda
Department of Materials Engineering Science
Graduate School of Engineering Science
Osaka University
1-3 Machikaneyama, Toyonaka, Osaka 560-8531 (Japan)
Fax: (+81) 6-6850-6260
E-mail: kaneda@cheng.es.osaka-u.ac.jp

[**] This investigation was supported by a Grant-in-Aid for Scientific Research from the Ministry of Education, Culture, Sports, Science, and Technology of Japan (16206078). We thank the Center of Excellence (21COE; "Creation of Integrated Ecochemistry" program, Osaka University). We are also grateful to Prof. Dr. S. Namba (Teikyo University) for catalyst preparation and Dr. K. Mori, Dr. Y. Senga, and Dr. S. Yamakita (Bel Japan) for TPD measurement. K.M. thanks the JSPS for a Research Fellowship for Young Scientists.

Supporting information for this article is available on the WWW under http://www.angewandte.org or from the author.

© 2006 Wiley-VCH Verlag GmbH & Co. KGaA, Weinheim

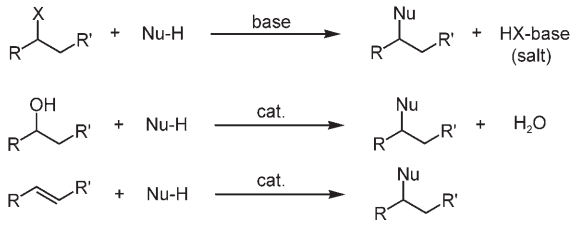

Scheme 1. A comparison of nucleophilic additions to halides (with salt formation) and to alkenes or alcohols (without salt formation).

pounds, only reactive, electron-deficient alkenes, such as α,β-unsaturated ketones, have been utilized. Attempts to overcome this limitation have focused mainly on the development of homogeneous metal catalysts to which the alkenes can coordinate;[2,3] however, these catalyst systems require expensive metals and halogenated solvents. We have pursued a new concept that involves dual activation of the olefinic double bond and the reacting C–H bond of the nucleophile[4] by catalytic sites to promote a highly efficient intermolecular addition reaction.

Recently, solid acid catalysts based on montmorillonites (monts)[5] and zeolites,[6] which have uniformly sized pores and voids, have received attention. Their adjustable acidity derived from enwrapped protons enables a variety of highly selective organic reactions. The use of solid montmorillonite and zeolite catalysts in liquid-phase organic synthesis also allows a simple workup and the potential to recycle catalysts in an environmentally acceptable process. Previously, we reported that montmorillonites that enwrap metal cations (M^{n+}-monts) act as strong solid acid catalysts for various organic transformations.[7] Herein, we describe a novel synthetic method in which montmorillonites are used in addition reactions of 1,3-dicarbonyl compounds to alkenes (Scheme 2). Not only does this heterogeneous catalytic system enable a simple workup and the use of recyclable catalysts, but it also has high activity owing to unique acid sites in the montmorillonite. Furthermore, the catalytic system can be used for the benzylation and allylation of 1,3-dicarbonyl compounds with alcohols and for the nucleophilic addition of carboxylic acids to alkenes.

Proton-exchanged montmorillonite (H-mont) was prepared from Na^+-mont by using an aqueous solution of

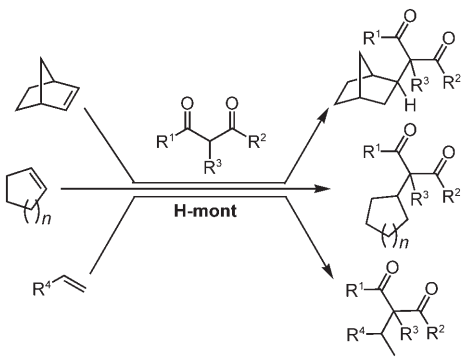

Scheme 2. Use of a proton-exchanged montmorillonite as the catalyst in addition reactions of 1,3-dicarbonyl compounds to alkenes.

hydrogen chloride (see Experimental Section). X-ray diffraction verified retention of a layered structure. The degree of exchange of the sodium cations in the H-mont was 98.9%. NH_3-TPD (temperature programmed desorption) analysis revealed the strength (ΔH)[8,9] and quantity of the acid sites in the H-mont to be 111 kJ mol^{-1} and 0.86 mmol g^{-1}, respectively. Other zeolites, such as H-USY, H-mordenite, and H-ZSM-5, were commercially available. Al-MCM-41, which has large pores, was prepared according to the literature.[10]

The reaction of acetyl acetone (**1a**) with norbornene (**2a**) was examined in the presence of several acid catalysts (Table 1). The H-mont catalyst displayed excellent activity and gave **3a** in 83% yield (Table 1, entry 1). Substitution of

Table 1: Addition of **1a** to **2a** in the presence of various acid catalysts.[a]

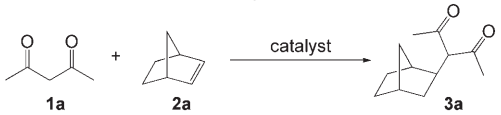

Entry	Catalyst	Acid sites [mmol g^{-1}][b]	Pore size [Å]	Conv. **2a** [%][c]	Yield **3a** [%][c]
1	H-mont	0.86	–	87	83
2	H-USY	0.53	7.4×7.4	37	37
3	mont K10	0.25	–	9	8
4	Al-MCM-41	0.15	27×27	7	5
5	H-mordenite	1.07	6.5×7.0	11	trace[d]
6	H-ZSM-5	0.87	5.1×5.5	n.r.	n.r.
7	SO_4^{2-}/ZrO_2	n.m.	–	n.r.	n.r.
8	Na^+-mont	n.m.	–	n.r.	n.r.
9	H_2SO_4[e]	–	–	29	4
10	*p*-TsOH·H_2O[e]	–	–	n.r.	n.r.
11	none	–	–	n.r.	n.r.

[a] Reaction conditions: **1a** (1.3 mmol), **2a** (1.0 mmol), catalyst (0.03 g), *n*-heptane (2 mL), 0.5 h, 150 °C. [b] Estimated from the *h* and h^+ peaks in the NH_3-TPD spectra. [c] Determined by GC analysis and ^{1}H NMR spectroscopy. [d] Oligomers of **2a** are the main products. [e] Quantity used: 0.1 mmol. n.m. = not measured, n.r. = no reaction.

H-mont for H-USY led to just a moderate yield of the product (Table 1, entry 2). Other solid acids, such as mont K-10, Al-MCM-41, and H-mordenite, were significantly less active (Table 1, entries 3–5). The reaction scarcely occurred in the presence of H-ZSM-5 as a result of its restricted pore size (Table 1, entry 6). The homogeneous acids H_2SO_4 and *p*-toluenesulfonic acid were not effective catalysts under these reaction conditions (Table 1, entries 9 and 10).

The H-mont-catalyzed addition reaction was extended to other 1,3-dicarbonyl compounds and alkenes, as shown in Table 2. Compound **2a** reacted with a variety of β-diketones to afford the addition products in excellent yields (Table 2, entries 1–3 and 6). Notably, the reactions of β-ketoesters and a β-lactone proceeded smoothly; the hydrodecarboxylation of the ester groups was suppressed (Table 2, entries 4, 5, and 7).[11] Intermolecular additions of β-ketoesters to norbornene were previously unknown. Interestingly, less reactive cyclic alkenes, such as cyclopentene (**2b**) and cyclohexene (**2c**), were good substrates for this H-mont catalyst system (Table 2, entries 8–10). The reaction of the terminal aliphatic olefins 1-pentene (**2d**) and 1-hexene (**2e**) gave the dione compounds in

 © 2006 Wiley-VCH Verlag GmbH & Co. KGaA, Weinheim

Table 2: Addition reaction of 1,3-dicarbonyl compounds **1** to alkenes **2**.[a]

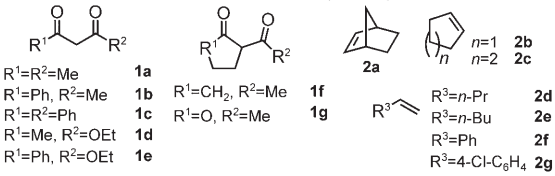

Entry	**1**	**2**	*t* [h]	*T* [°C]	Yield [%][b]
1	**1a**	**2a**	1	150	90
2	**1b**	**2a**	1	150	88
3	**1c**	**2a**	1	150	93
4	**1d**	**2a**	1	150	(71)
5	**1e**	**2a**	1	150	74
6	**1f**	**2a**	1	150	83
7	**1g**	**2a**	1	150	87
8[c]	**1c**	**2b**	24	180	(66)
9[c]	**1b**	**2c**	24	180	78
10[c]	**1c**	**2c**	24	180	(80)
11[d,e]	**1c**	**2d**	24	150	53, 9:1[f]
12[d,e]	**1c**	**2e**	24	150	60, 5:1[f]
13[e,g]	**1e**	**2f**	3	150	72[h]
14[i]	**1f**	**2g**	3	150	72[h]

[a] Reaction conditions: **1** (1 mmol), **2** (1.3 mmol), H-mont (0.15 g), *n*-heptane (2 mL). [b] Yield of the isolated product based on the dicarbonyl starting material. Values in parentheses are yields as determined by GC analysis. Diastereomers were formed in a 1:1 ratio from asymmetric dicarbonyl compounds (^{1}H NMR). Only the *exo* product was isolated in the reaction of **2a**. [c] Quantity of **2**: 5 mmol. [d] Quantity of **2**: 15 mmol. [e] The alkene was added in portions. [f] Ratio of the 2-adduct to the 3-adduct (^{1}H NMR). [g] Quantity of **1e**: 3 mmol, **2f**: 1 mmol. [h] Yield of the isolated product based on the alkene. [i] Quantity of **1f**: 1.3 mmol, **2g**: 1 mmol.

Table 3: Reuse of the H-mont catalyst for the addition reaction of **1a** to **2a**.[a]

Recycle number	fresh	1	2	3	4	5	6	7
Yield of **3a** [%][b]	93	92	93	93	92	94	92	93

[a] Reaction conditions: **1a** (1 mmol), **2a** (1.3 mmol), H-mont (0.15 g), *n*-heptane (2 mL), 1 h, 150 °C. [b] Determined by GC analysis.

Table 4: α-Benzylation and allylation of 1,3-dicarbonyl compounds **1** by treatment with alcohols.[a]

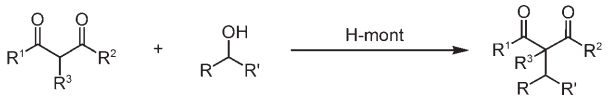

Entry	**1**	Alcohol R, R′	*T* [°C]	Yield [%][b]
1	**1a**	Ph, Me	100	90
2	**1a**	*p*-Cl-C$_6$H$_4$, Me	150	80
3[c]	**1a**	2-naphthyl, Me	150	72
4	**1a**	Ph, Ph	100	91
5	**1a**		90	80[d]
6[e]	**1b**	Ph, Me	100	86[f]
7[c]	**1f**	Ph, Me	150	86[f]
8	**1d**	Ph, Me	100	88[f]
9	**1e**	Ph, Me	100	51[f]
10	**1d**		90	48[f]

[a] Reaction conditions: **1** (1.5 mmol), alcohol (1 mmol), H-mont (0.15 g), *n*-heptane (2 mL), 1 h, 100 °C. [b] Yield of the isolated product based on the alcohol. [c] Reaction time: 0.5 h. [d] Yield as determined by GC analysis. [e] Quantity of **1b**: 1 mmol. [f] Diastereomers were formed in a 1:1 ratio (^{1}H NMR).

moderate yields along with small amounts of isomerization products (Table 2, entries 11 and 12). Styrene derivatives also functioned as good substrates in the H-mont-catalyzed addition reaction (Table 2, entries 13 and 14).[12]

The high activity of the H-mont catalyst system and the simplicity of the workup procedure are exemplified by the following: After the reaction of dibenzoylmethane (**1c**; 22.4 g, 0.10 mol) with **2a** (11.3 g, 0.12 mol) at 150 °C for 3 h in the presence of the H-mont catalyst (0.3 g), the spent catalyst was readily separated from the reaction mixture. Direct recrystallization then gave pure 2-(bicyclo-[2.2.1]heptan-2-yl)-1,3-diphenylpropane-1,3-dione (31.3 g, 98 % yield of the isolated product).[9] The turnover number (TON) and turnover frequency (TOF) of this catalytic reaction (TON: 380, TOF: 127 h^{-1}, based on the active acid sites of the H-mont) were considerably greater than those of a previously reported homogeneous $AuCl_3$/AgOTf catalyst system (TON: 16, TOF: 3.2 h^{-1}).[3a] Additionally, the recovered H-mont catalyst could be reused at least seven times without any loss of its activity (Table 3). Dimethyl malonate, which has a high pK_a value, did not react.

The high reactivity of 1,3-dicarbonyl compounds in the H-mont-catalyzed reactions prompted investigations of the α-benzylation and allylation of the 1,3-dicarbonyl compounds by treatment with alcohols (Table 4). The reaction of **1a** with 1-phenylethanol in the presence of the H-mont catalyst gave the α-benzylated product 3-(1-phenylethyl)pentane-2,4-dione in 90 % yield (Table 4, entry 1). The sterically hindered alcohol 1-(2-napthyl)ethanol was also a good substrate for this reaction (Table 4, entry 3). In the case of 2-cyclohexen-1-ol, α-allylation proceeded efficiently (Table 4, entries 5 and 10). Furthermore, β-ketoesters underwent both benzylation (Table 4, entries 8 and 9) and allylation (Table 4, entry 10). Halides are usually used for the α-benzylation and allylation of active methylene groups;[13] methods in which an alcohol is used as a benzylating or allylating reagent are highly atom efficient candidates.[14,15] Unfortunately, reactions with primary alcohols resulted in low yields owing to the formation of ethers under the present reaction conditions.

In the reaction of **1a** with **2a**, the addition of the radical trap 2,6-di-*tert*-butyl-*p*-cresol to the reaction medium had hardly any influence.[16] The IR spectrum of the H-mont upon treatment with pyridine showed a new peak at 1543 cm^{-1} due to protonated pyridine molecules.[9,17] The catalytic activity of a variety of Brønsted acids was shown not to depend on their acidity, as determined by NH_3-TPD (Table 1); H-mordenite, which has strong Brønsted acidity ($\Delta H = 160$ kJ mol^{-1}) was less active than the H-mont and H-USY catalysts, which have ΔH values of 111 and 122 kJ mol^{-1}, respectively.[8,9] These results suggest that a suitable strength of the Brønsted acid sites is required for efficient addition reactions of 1,3-dicarbonyl compounds to alkenes. In the intermolecular

 © 2006 Wiley-VCH Verlag GmbH & Co. KGaA, Weinheim

competitive reaction of **2a** with an equimolar mixture of **1a** ($pK_a = 9.0$)[18] and nitroethane ($pK_a = 8.6$),[18] the H-mont catalyst favored the formation of **3a** (97% yield) exclusively (Scheme 3).

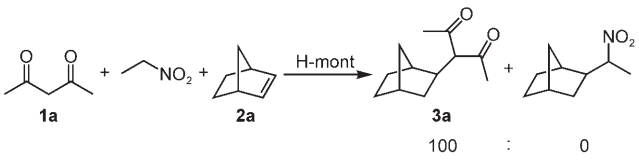

Scheme 3. Intermolecular competitive reaction of **2a** with an equimolar mixture of **1a** and nitroethane under H-mont catalysis.

After treatment of the H-mont catalyst with **1a**, IR absorptions due to both the keto and enol forms of **1a** (1537(enol), 1592(enol), and 1698(keto) cm^{-1})[9] were detected, similar to those found for adsorbed **1a** onto the Brønsted acid site of Z12H zeolite (1540(enol), 1592(enol), and 1700(keto) cm^{-1}).[19] A proposed reaction path involves the dual activation of the alkene and the 1,3-dicarbonyl compound: 1) protonation of an alkene at an acid site and coordination of a 1,3-dicarbonyl compound to a neighboring H^+ site;[20] 2) formation of an activated enol intermediate; 3) nucleophilic attack of the enol (Scheme 4). Kinetic studies showed first-order dependence on **2a** and an inverse first-order relationship with respect to **1a**,[9] and thus indicated that alkene protonation may be a rate-determining step that is impeded by adsorbed 1,3-dicarbonyl compounds. The negatively charged silicate layers are capable of acting as delocalized counter anions to stabilize cationic intermediates.

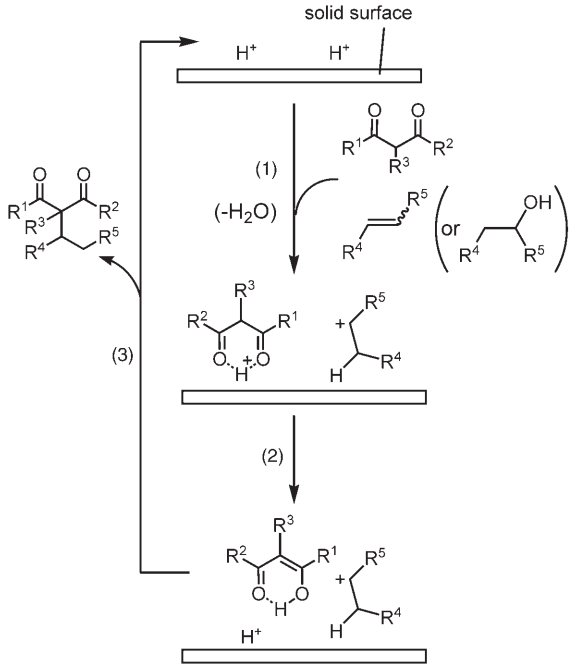

Scheme 4. A proposed dual-activation reaction pathway for the addition of 1,3-dicarbonyl compounds to alkenes or alcohols in the presence of the H-mont catalyst.

Furthermore, the higher activity of the H-mont catalyst relative to that of the homogeneous acids can be attributed to concentrated protonic acid sites in the interlayer space of the H-mont.

The strong protonation ability of the H-mont catalyst is further applicable to the addition reactions of carboxylic acids to alkenes (Scheme 5). For example, the reaction of benzoic acid with **2a** in the presence of the H-mont catalyst gave 2-benzoyloxynorbornane in 89% yield. Even with less reactive simple alkenes, such as cyclopentene and cyclohexene, the corresponding esters were obtained in excellent yields. Furthermore, the H-mont catalyst promoted the intramolecular reaction of 2-cyclopentene-1-acetic acid in excellent yield.

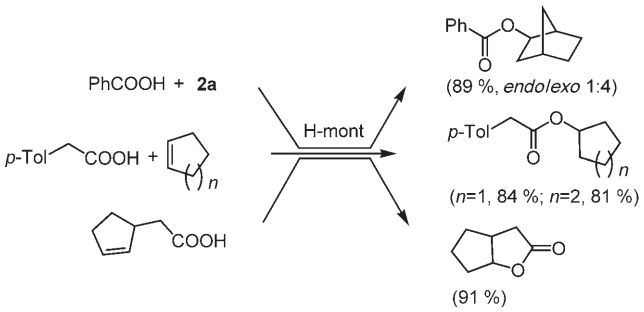

Scheme 5. The H-mont-catalyzed addition of carboxylic acids to alkenes. Tol = tolyl.

In summary, environmentally benign addition reactions of various 1,3-dicarbonyl compounds to alkenes and alcohols in the presence of solid acid catalysts have been described. Unique acid sites with delocalized counter anions of two-dimensional silicate sheets will allow additional novel C–C bond-forming reactions.

Experimental Section

A mixture of the parent Na^+-montmorillonite (3.0 g; $Na_{0.66}(OH)_4Si_8(Al_{3.34}Mg_{0.66}Fe_{0.19})O_{20}$; Na 2.69, Al 11.8, Fe 1.46, Mg 1.97%; Kunipia F, Kunimine Industry, Japan) and aqueous HCl (1.1 wt%, 200 mL) was stirred at 90°C for 24 h. The slurry obtained was filtered and washed with distilled water (1 L) to remove chlorine, then dried at 110°C in air to afford the H-mont as a whitish-gray powder. Elemental analysis: Na 0.03, Mg 1.73, Al 10.1, Fe 1.34%.

Typical procedure: H-mont (0.15 g), *n*-heptane (2 mL), **1a** (1 mmol), and **2a** (1.3 mmol) were placed in a pressure tube, and the resulting mixture was stirred vigorously at 150°C. After 1 h, the catalyst was separated by filtration. GC analysis of the filtrate showed that **3a** had formed in 93% yield. The filtrate was concentrated by evaporation, and the crude product was purified by column chromatography on silica (diethyl ether/*n*-hexane 1:9) to afford the pure product (90% yield). The recovered catalyst could be reused at least seven times without appreciable loss of activity and selectivity: The yields of the first, second, and seventh runs were 92, 93, and 93%, respectively.

Received: December 29, 2005
Published online: March 17, 2006

 © 2006 Wiley-VCH Verlag GmbH & Co. KGaA, Weinheim

Keywords: 1,3-dicarbonyl compounds · addition reactions · alcohols · alkenes · heterogeneous catalysis

[1] a) B. M. Trost, *Science* **1991**, *254*, 1471; b) R. A. Sheldon, *CHEMTECH* **1994**, 38; c) R. A. Sheldon, *Pure Appl. Chem.* **2000**, *72*, 1233.

[2] a) T. Pei, R. A. Widenhoefer, *J. Am. Chem. Soc.* **2001**, *123*, 11290; b) T. Pei, R. A. Widenhoefer, *Chem. Commun.* **2002**, 650; c) X. Wang, T. Pei, X. Han, R. A. Widenhoefer, *Org. Lett.* **2003**, *5*, 2699; d) D. Yang, J.-H. Li, Q. Gao, Y.-L. Yan, *Org. Lett.* **2003**, *5*, 2869; e) A. Leitner, J. Larsen, C. Steffens, J. F. Hartwig, *J. Org. Chem.* **2004**, *69*, 7552; for oxidative additions, see: f) T. Pei, X. Wang, R. A. Widenhoefer, *J. Am. Chem. Soc.* **2003**, *125*, 648; g) X. Wang, R. A. Widenhoefer, *Chem. Commun.* **2004**, 660.

[3] a) X. Yao, C.-J. Li, *J. Am. Chem. Soc.* **2004**, *126*, 6884; b) R.-V. Nguyen, X.-Q. Yao, D. S. Bohle, C.-J. Li, *Org. Lett.* **2005**, *7*, 673; c) X. Yao, C.-J. Li, *J. Org. Chem.* **2005**, *70*, 5752.

[4] For the addition of benzoyl acetates to cyclic dienes in the presence of $Ga(TfO)_3$ and TfOH through the activation of both the donor and the diene, see: R.-V. Nguyen, C.-J. Li, *J. Am. Chem. Soc.* **2005**, *127*, 17184.

[5] For clay-catalyzed organic synthesis, see: a) T. J. Pinnavaia, *Science* **1983**, *220*, 365; b) P. Laszlo, *Acc. Chem. Res.* **1986**, *19*, 121; c) Y. Izumi, M. Onaka, *Adv. Catal.* **1992**, *38*, 245.

[6] For zeolite catalysis, see: a) J. A. Horsley, *CHEMTECH* **1997**, *27*, 45; b) V. Ramamurthy, P. Lakshminarasimhan, C. P. Grey, L. J. Johnston, *Chem. Commun.* **1998**, 2411; c) C. W. Jones, K. Tsuji, M. E. Davis, *Nature* **1998**, *393*, 52; d) A. Corma, L. T. Nemeth, M. Renz, S. Valencia, *Nature* **2001**, *412*, 423.

[7] For Brønsted acid catalysis, see: a) K. Ebitani, T. Kawabata, K. Nagashima, T. Mizugaki, K. Kaneda, *Green Chem.* **2000**, *2*, 157; b) K. Motokura, N. Fujita, K. Mori, T. Mizugaki, K. Ebitani, K. Kaneda, *J. Am. Chem. Soc.* **2005**, *127*, 9674; for Lewis acid catalysis, see: c) T. Kawabata, T. Mizugaki, K. Ebitani, K. Kaneda, *J. Am. Chem. Soc.* **2003**, *125*, 10486; d) T. Kawabata, M. Kato, T. Mizugaki, K. Ebitani, K. Kaneda, *Chem. Eur. J.* **2005**, *11*, 288.

[8] a) M. Niwa, N. Katada, M. Sawa, Y. Murakami, *J. Phys. Chem.* **1995**, *99*, 8812; b) R. Nakao, Y. Kubota, N. Katada, N. Nishiyama, K. Kunimori, K. Tomishige, *Appl. Catal. A* **2004**, *273*, 63.

[9] See Supporting Information.

[10] T. Kugita, M. Ezawa, T. Owada, Y. Tomita, S. Namba, N. Hashimoto, M. Onaka, *Micro. Meso. Mater.* **2001**, *44–45*, 531.

[11] The decomposition of esters was observed with the previously reported Au catalyst system; see reference [3a].

[12] In several cases, H-USY was found to be a good catalyst for the reaction of styrenes. For example, the reaction of **1a** with **2f** in the presence of H-USY afforded the corresponding product in 75% yield, whereas the product was obtained in only 51% yield when the H-mont catalyst was used.

[13] a) M. Moreno-Mañas, A. González, C. Jaime, M. E. Lloris, J. Marquet, A. Martinez, A. C. Siant, A. Vallribera, *Tetrahedron* **1991**, *47*, 6511; b) S. Arumugam, D. McLeod, J. G. Verkade, *J. Org. Chem.* **1998**, *63*, 3677.

[14] Benzhydrol is the only alcohol that has been used in previously reported acid-catalyzed benzylation reactions of active methylene groups: a) F. Bisaro, G. Prestat, M. Vitale, G. Poli, *Synlett* **2002**, *11*, 1823; b) G. C. Gullickson, D. E. Lewis, *Aust. J. Chem.* **2003**, *56*, 385.

[15] The allylation of 1,3-dicarbonyl compounds with allylic alcohols has usually been performed with Pd catalysts, see: a) X. Lu, X. Jiang, X. Tao, *J. Organomet. Chem.* **1988**, *344*, 109; b) F. Ozawa, H. Okamoto, S. Kawagishi, S. Yamamoto, T. Minami, M. Yoshifuji, *J. Am. Chem. Soc.* **2002**, *124*, 10968.

[16] For the radical addition of active methylene compounds to alkenes, see: K. Hirase, T. Iwahama, S. Sakaguchi, Y. Ishii, *J. Org. Chem.* **2002**, *67*, 970.

[17] For a recent example, see W. Daniell, N.-Y. Topsøe, H. Knözinger, *Langmuir* **2001**, *17*, 6233.

[18] R. G. Person, R. L. Dillon, *J. Am. Chem. Soc.* **1953**, *75*, 2439.

[19] S. M. Alexander, D. M. Bibby, R. F. Howe, R. H. Meinhold, *Zeolite* **1993**, *13*, 441.

[20] For previous examples of two activated substrates at neighboring catalytic sites on solid surfaces, see: a) K. Yamaguchi, K. Ebitani, T. Yoshida, H. Yoshida, K. Kaneda, *J. Am. Chem. Soc.* **1999**, *121*, 4526; b) T. Seki, H. Tachikawa, T. Yamada, H. Hattori, *J. Catal.* **2003**, *217*, 117.

 © 2006 Wiley-VCH Verlag GmbH & Co. KGaA, Weinheim

Natural Product Synthesis

DOI: 10.1002/anie.200600295

Total Synthesis and Confirmation of the Revised Structures of Azaspiracid-2 and Azaspiracid-3**

K. C. Nicolaou, Michael O. Frederick, Goran Petrovic, Kevin P. Cole, and Eriketi Z. Loizidou*

Dedicated to Professor Dieter Enders on the occasion of his 60th birthday

The azaspiracids are a group of notorious marine neurotoxins whose accumulation in mussels causes serious human poisoning known as azaspiracid poisoning syndrome (AZP) upon their consumption.[1] In a series of papers,[2–4] we recently reported the revision of the originally proposed structure, **1a**, and the total synthesis of the revised structure of azaspiracid-1 (**1**, Figure 1). Isolated from *Mytilus edulis* and first reported in 1998,[5] azaspiracid-1 (**1**) is the most abundant member of this class of marine natural products. Herein, we report the total synthesis of the revised structures of azaspiracid-2 (**2**) and -3

[*] Prof. Dr. K. C. Nicolaou, M. O. Frederick, Dr. G. Petrovic, K. P. Cole, E. Z. Loizidou
Department of Chemistry and
The Skaggs Institute for Chemical Biology
The Scripps Research Institute
10550 North Torrey Pines Road, La Jolla, CA 92037 (USA)
Fax: (+1) 858-784-2469
E-mail: kcn@scripps.edu
and
Department of Chemistry and Biochemistry
University of California, San Diego
9500 Gilman Drive, La Jolla, CA 92093 (USA)

[**] We thank Dr. D. H. Huang and Dr. G. Siuzdak for NMR spectroscopic and mass spectrometric assistance, respectively. Financial support for this work was provided by The Skaggs Institute for Chemical Biology, the National Institutes of Health (USA), a predoctoral fellowship from the National Science Foundation (to M.O.F.), and grants from Amgen and Merck.

© 2006 Wiley-VCH Verlag GmbH & Co. KGaA, Weinheim

(**3**, Figure 1), the two most potent members of the azaspiracid family (azaspiracid-1: LD_{50}(against mice) = 0.20 mg kg^{-1}; azaspiracid-2: LD_{50} = 0.11 mg kg^{-1}; azaspiracid-3: LD_{50} = 0.14 mg kg^{-1}),[6,7] by a route that differs significantly from that employed[2–4] to construct azaspiracid-1 (**1**). The reported

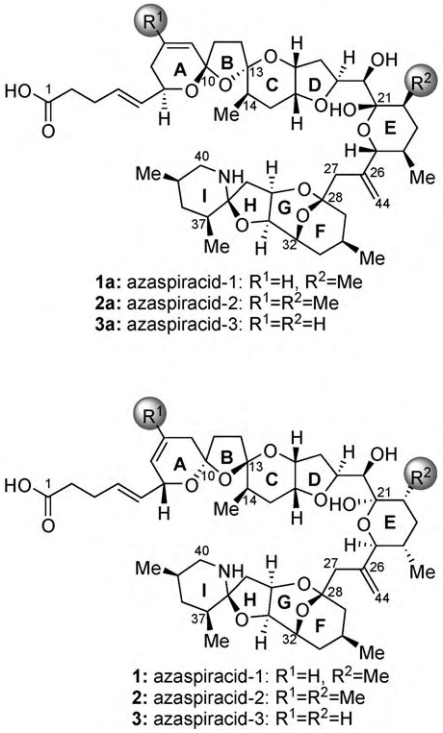

Figure 1. Originally proposed (**1a**–**3a**) and revised (**1**–**3**) structures of azaspiracid-1, -2, and -3.

total syntheses are shorter by eleven steps and deliver the product in considerably higher overall yield. They also confirm our recently proposed structures[4a] for the titled compounds and, furthermore, should be applicable to the synthesis of azaspiracid-1 (**1**).

As in the case of azaspiracid-1, our devised synthetic strategy for the total syntheses of azaspiracid-2 and -3 was based on a retrosynthetic analysis that involved a dithiane coupling[8] (C20–C21 bond) and a Stille reaction[9] (C27–C28 bond), and required the key building blocks, pentafluorophenyl esters **4** and **5**, dithianes **6** and **7**, and stannane **8** (Figure 2).

It was in the construction of the ABCD ring systems **16** and **21** of azaspiracid-2 and -3 (**2** and **3**, Figure 1) that the new total syntheses shined over the original synthesis of azaspiracid-1 (**1**) in terms of both brevity and efficiency. Owing to their similarity, only the synthesis of azaspiracid-2 (**2**) will be described in detail, while the route leading to azaspiracid-3 (**3**) is only summarized in the schemes. Starting from the known alcohol **9** (Scheme 1),[10] the corresponding allylic chloride was synthesized by the action of NCS and Me_2S and treated with the lithium derivative of dithiane **10** (*n*BuLi, THF, −30 °C) to afford coupling product **11** in 70% overall

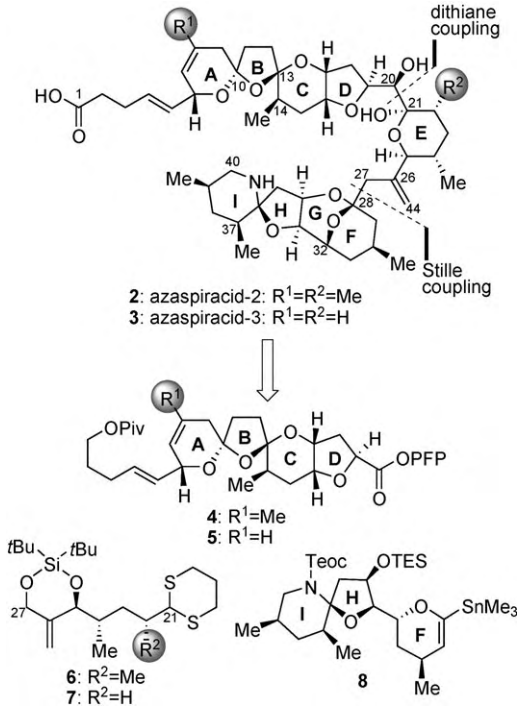

Figure 2. Retrosynthetic analysis of azaspiracid-2 (**2**) and -3 (**3**). Piv = trimethylacetyl, PFP = pentafluorophenyl, Teoc = 2-(trimethylsilyl)-ethoxycarbonyl, TES = triethylsilyl.

yield (two steps from **9**). Exposure of **11** to $HgCl_2$ in the presence of ethylene glycol resulted in the exchange of the dithiane group with an ethylene ketal. Subsequent removal of the silyl group (TBAF) from the newly generated compound followed by exposure to Ph_3P, I_2, and imidazole furnished iodide **12** in 41% overall yield for the three steps. Upon iodine–lithium exchange (*t*BuLi), the resulting lithium derivative of **12** added smoothly to aldehyde **14**, which was generated from previously synthesized alcohol **13**[11] by 1) selective removal of the TBS group with TMSOTf, 2) formation of the bis(TES) derivative with TESCl and imidazole, and 3) selective oxidation of the primary TES ether[12] with $(COCl)_2$, DMSO, and Et_3N. Oxidation of the resulting secondary alcohol with DMP led to ketone **15** in 81% overall yield from **12**. The much anticipated cascade reaction of precursor **15** with the $\Delta^{7,8}$ double bond in place proceeded smoothly under the influence of TMSOTf[13] in CH_2Cl_2 at −90 °C to afford the desired tetracyclic system **16** in 72% yield, together with its chromatographically separable C10 diastereomer in a favorable 6:1 ratio (Scheme 1). Indeed, the presence of the C7–C8 double bond during the cyclization allowed the shortening of the route by several steps and improved the overall efficiency in the construction of the ABCD ring system of the azaspiracids.

With multigram quantities of the ABCD tetracycle **16** in hand, the extension of its side chain to afford the requisite pentafluorophenyl ester **4** was accomplished as depicted in Scheme 2. Thus, the hydroxy group at C5 of **16** was oxidized under carefully controlled conditions (DMP, no buffer), and the resulting, rather labile γ,δ-unsaturated aldehyde was

 © 2006 Wiley-VCH Verlag GmbH & Co. KGaA, Weinheim

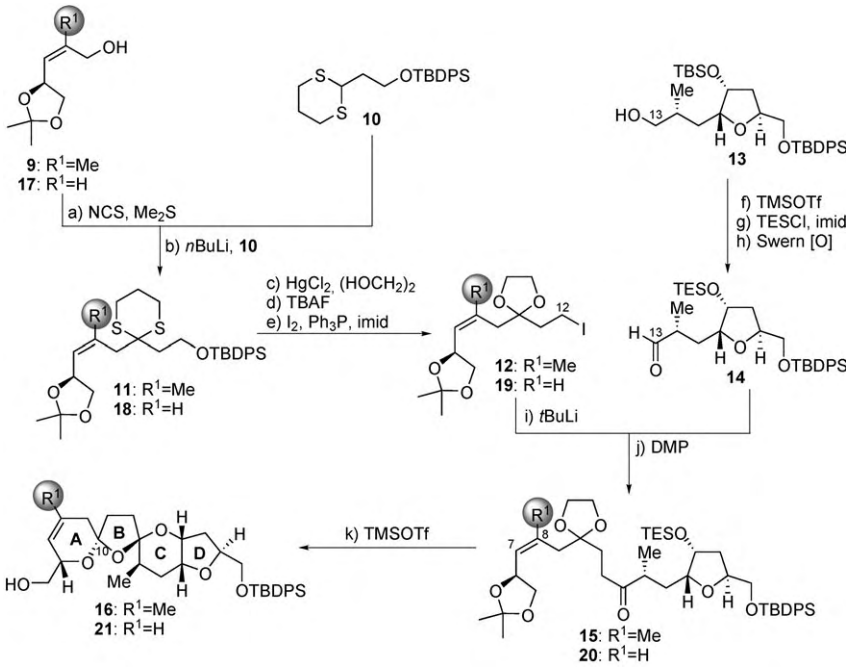

Scheme 1. Synthesis of ABCD precursors **16** and **21**. Reagents and conditions: a) NCS (1.3 equiv), Me_2S (1.4 equiv), CH_2Cl_2, −40→0°C, 1 h; b) **10** (1.4 equiv), *n*BuLi (1.3 equiv), THF, −30°C, 2 h; then chlorides from **9** or **17**; then −30→0°C, 1 h, 70% for **11** (from **9**), 68% for **18** (from **17**); c) $HgCl_2$ (3.5 equiv), $CaCO_3$ (10 equiv), $(HOCH_2)_2/CH_3CN$ (1:3), 0°C, 30 min; d) TBAF (1.0 M in THF, 1.1 equiv), THF, 25°C, 12 h; e) I_2 (1.3 equiv), imid (1.5 equiv), Ph_3P (1.5 equiv), THF, 25°C, 30 min, 41% over three steps for **12**, 33% over three steps for **19**; f) TMSOTf (3.0 equiv), CH_2Cl_2, −30°C, 3 h, 75%; g) TESCl (3.0 equiv), imid (5.0 equiv), CH_2Cl_2, 25°C, 1 h, 100%; h) $(COCl)_2$ (2.0 equiv), DMSO (4.0 equiv), CH_2Cl_2, −78°C, 1 h; then Et_3N (8.0 equiv), −78→0°C, 97%; i) *t*BuLi (2.0 equiv), **12** or **19** (1.0 equiv), Et_2O, −78°C, 1 h; then **14**, 30 min; j) DMP (1.2 equiv), $NaHCO_3$ (10 equiv), CH_2Cl_2, 25°C, 1 h, 81% over two steps for **15**, 74% over two steps for **20**; k) TMSOTf (1.0 M in CH_2Cl_2, 5.0 equiv), CH_2Cl_2, −90°C, 72% for **16**, 65% for **21**. NCS = *N*-chlorosuccinimide, TBDPS = *tert*-butyldiphenylsilyl, TBAF = tetra-*n*-butylammonium fluoride, imid = imidazole, TBS = *tert*-butyldimethylsilyl, TMS = trimethylsilyl, Tf = trifluoromethanesulfonyl, DMSO = dimethyl sulfoxide, DMP = Dess–Martin periodinane.

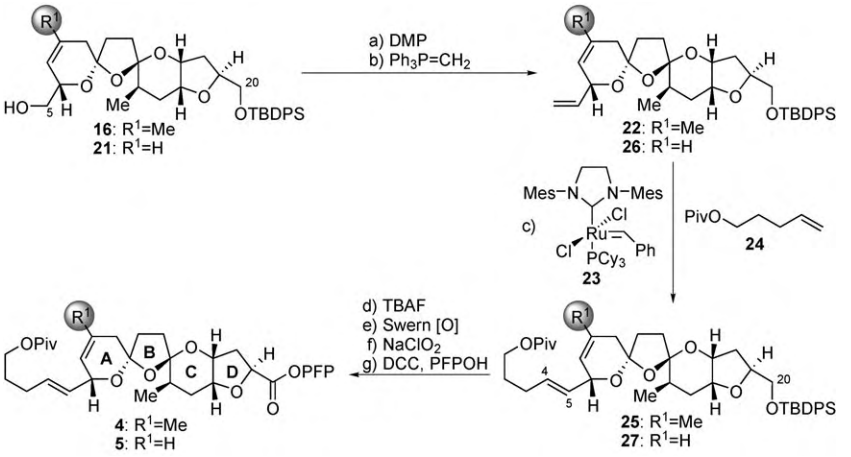

Scheme 2. Construction of pentafluorophenol esters **4** and **5**. Reagents and conditions: a) DMP (2.0 equiv), CH_2Cl_2, 25°C, 1 h; b) $Ph_3PCH_3^+Br^-$ (5.0 equiv), *n*BuLi (1.6 M in hexanes, 4.0 equiv), THF, 0°C, 1 h; then −78°C; then aldehyde from **16** or **21**, −78→25°C, 18 h, 55% over two steps for **22**, 49% over two steps for **26**; c) **23** (0.1 equiv), **24** (3.0 equiv), CH_2Cl_2, 40°C, 14 h, 60% for **25** with 35% recovered **22** (repeat two more times, 90% for the three cycles), 60% for **27** with 35% recovered **26** (repeat two more times, 90% for the three cycles); d) TBAF (1.0 M in THF, 2.0 equiv), THF, 25°C, 14 h; e) $(COCl)_2$ (5.0 equiv), DMSO (10 equiv), CH_2Cl_2, −78°C, 1 h; then Et_3N (20 equiv), −78→0°C; f) $NaClO_2$ (10 equiv), NaH_2PO_4 (10 equiv), 2-methyl-2-butene (excess), *t*BuOH/H_2O (4:1), 25°C, 1 h; g) DCC (2.0 equiv), PFPOH (1.5 equiv), CH_2Cl_2, 25°C, 2 h, 72% over four steps for **4**, 75% over four steps for **5**. DCC = dicyclohexylcarbodiimide.

treated immediately and without purification with the ylide derived from $Ph_3P^+CH_3Br^-$ and *n*BuLi to afford terminal olefin **22** in 55% overall yield for the two steps. Engagement of **22** with a threefold excess of pivaloate **24** in an olefin metathesis reaction under the initiating influence of Grubbs' catalyst II (**23**) afforded, after three reiterations, bis-(olefin) **25** in 90% yield together with minor amounts of its $\Delta^{4,5}$ *cis* isomer, which was removed by chromatography. The functionality at C20 was then elaborated through a four-step sequence, involving 1) TBAF-induced removal of the TBDPS group, 2) Swern oxidation to the aldehyde with $(COCl)_2$, DMSO, and Et_3N, 3) oxidation with $NaClO_2$ to the carboxylic acid, and 4) DCC-mediated coupling with pentafluorophenol, to afford the coveted intermediate **4** in 72% overall yield (Scheme 2).

While the dithiane fragment required for azaspiracid-2 (**2**) was the same as that needed for azaspiracid-1, that is, **6** (Figure 2),[2a] the dithiane desired for incorporation into azaspiracid-3 (see **7**, Figure 2) required new chemistry for its construction (Scheme 3). Thus, hydroxy methyl ester **28** was converted into its iodide **29** by known chemistry[14] and treated with the anion derived from 1,3-dithiane and *n*BuLi to afford dithiane derivative **30** in 93% yield. Further elaboration of the latter compound (TBAF; $(COCl)_2$, DMSO, and Et_3N) led to aldehyde **31**, which was coupled with vinyl iodide **32** under Nozaki–Hiyama–Kishi conditions[15] ($CrCl_2/NiCl_2$) to afford allylic alcohol **33** in 69% overall yield from **30**, in favor of the desired C25 diastereomer (ca. 2:1 ratio). Removal of the TBS group (TBAF) followed by transformation of the generated 1,3-diol system to a cyclic silyl ether ($tBu_2Si(OTf)_2$) furnished the desired intermediate **7** in 62% overall yield after chromatographic separation from its undesired C25 epimer (Scheme 3).

The advancement of pentafluorophenyl ester **4** to allylic acetate **36**, the required Stille coupling partner, is shown in Scheme 4. Note that the new Stille partner differs from the one originally used in the synthesis of azaspiracid-1 (**1**)[3b] in that the hydroxy group at C25 is now internally engaged in a six-membered lactol ring, a feature that allowed it to perform in a superior manner in the

 © 2006 Wiley-VCH Verlag GmbH & Co. KGaA, Weinheim

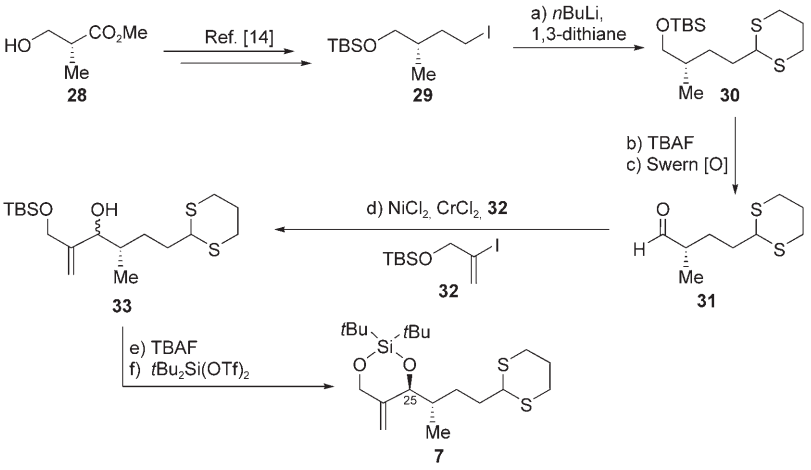

Scheme 3. Construction of dithiane fragment **7**. Reagents and conditions: a) 1,3-dithiane (2.0 equiv), *n*BuLi (1.6 M in THF, 1.9 equiv), THF, −30 °C, 3 h; then **29**, −30 °C, 20 min 93 %; b) TBAF (1.0 M in THF, 1.2 equiv), THF, 25 °C, 7 h, 98 %; c) $(COCl)_2$ (1.2 equiv), DMSO (2.4 equiv), CH_2Cl_2, −78 °C, 1 h; then Et_3N (5.0 equiv), −78→0 °C; d) $CrCl_2$ (4.0 equiv), $NiCl_2$ (0.02 equiv), **32**, DMF, 0 °C, 30 min, 71 % over two steps, ca. 2:1 ratio; e) TBAF (1.0 M in THF, 2.2 equiv), THF, 25 °C, 3 h, 99 %; f) $tBu_2Si(OTf)_2$ (1.5 equiv), 2,6-lutidine (4.0 equiv), CH_2Cl_2, −30 °C, 30 min, 62 %. DMF = dimethylformamide.

intended Stille coupling (see below) as compared to its TBS-protected, open-chain counterpart.[3b] The organometallic species derived from dithiane **6** and *n*BuLi/nBu_2Mg[16] was treated with **4** at −90 °C to afford ketone **34** in 65 % yield. Treatment of **34** with DIBAL-H at −90 °C led to reduction of the carbonyl group at C20 and concomitantly cleaved the pivaloate ester group to give a dihydroxy compound from which the cyclic silyl ether was dismantled (TBAF) to afford tetraol **35** (47 % overall yield for the two steps). The assigned stereochemistry at C20 was based on our previous findings with a related compound[3b,17] and was subsequently confirmed by the arrival at the final target, azaspiracid-2 (**2**, see below). The primary hydroxy groups within **35** were then selectively acetylated through reaction with AcCl and 2,4,6-collidine[18] at −78 °C, and the dithiane moiety was removed by exposure to $PhI(OCOCF_3)_2$,[19] which led to spontaneous collapse of the incipient hydroxy ketone to give lactol **36** in 80 % overall yield for the two steps. Compound **39** was similarly prepared as summarized in Scheme 4.

Scheme 5 outlines the final stages of the total synthesis of azaspiracid-2 (**2**) and -3 (**3**) starting with the Stille coupling of allylic acetate **36** with vinyl stannane **8**.[4a] The reaction was admirably catalyzed by $[Pd_2(dba)_3]$ in the presence of LiCl, $AsPh_3$, and iPr_2NEt in DMF at ambient temperature, leading to intermediate **40** in 80 % yield (see Table 1 for characterization). It was pleasing to note the improvement of this final coupling as a consequence of the reengineering of the allylic acetate component which relieved it from the steric hindrance of the original partner that carried a protecting group at C25.[3b] Selective removal of the TES group from compound **40** (TBAF) followed by NIS-induced iodoetherification led to product **41** (48 % yield for the two steps). Iodoether **41** was then exposed to the action of TESCl and imidazole, leading to the bis(TES) ether (C20 and C25) of its open hydroxy-keto form which was treated with nBu_3SnH and Et_3B to remove the now redundant iodine residue to furnish the advanced intermediate **42** in 86 % overall yield.

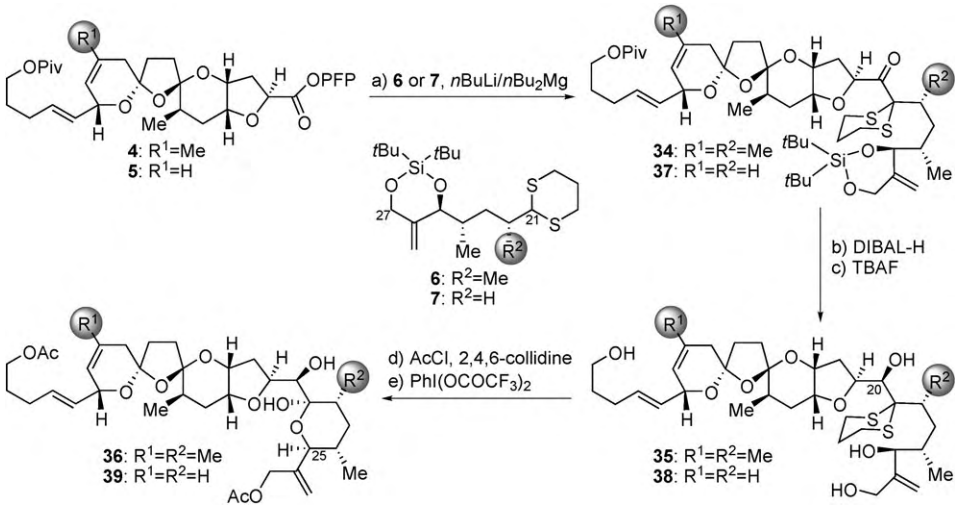

Scheme 4. Synthesis of allylic acetate Stille coupling partners **36** and **39**. Reagents and conditions: a) **6** or **7** (6.0 equiv), *n*BuLi/nBu_2Mg (1.1 M in hexanes, 5.3 equiv), THF, 25 °C, 1.5 h; then −90 °C; then **4** or **5**, 30 min, 65 % for **34**, 74 % for **37**; b) DIBAL-H (1.0 M in CH_2Cl_2, 10 equiv), CH_2Cl_2, −90 °C, 30 min; c) TBAF (1.0 M in THF, 3.0 equiv), THF, 25 °C, 16 h, 47 % over two steps for **35**, 44 % over two steps for **38**; d) AcCl (20 equiv), 2,4,6-collidine (40 equiv), CH_2Cl_2, −78 °C, 6 h; e) $PhI(OCOCF_3)_2$ (0.01 M in CH_3CN, 1.2 equiv), CH_3CN/pH 7 buffer (4:1), 0 °C, 15 min, 80 % over two steps for **36**, 72 % over two steps for **39**. DIBAL-H = diisobutylaluminum hydride.

 © 2006 Wiley-VCH Verlag GmbH & Co. KGaA, Weinheim

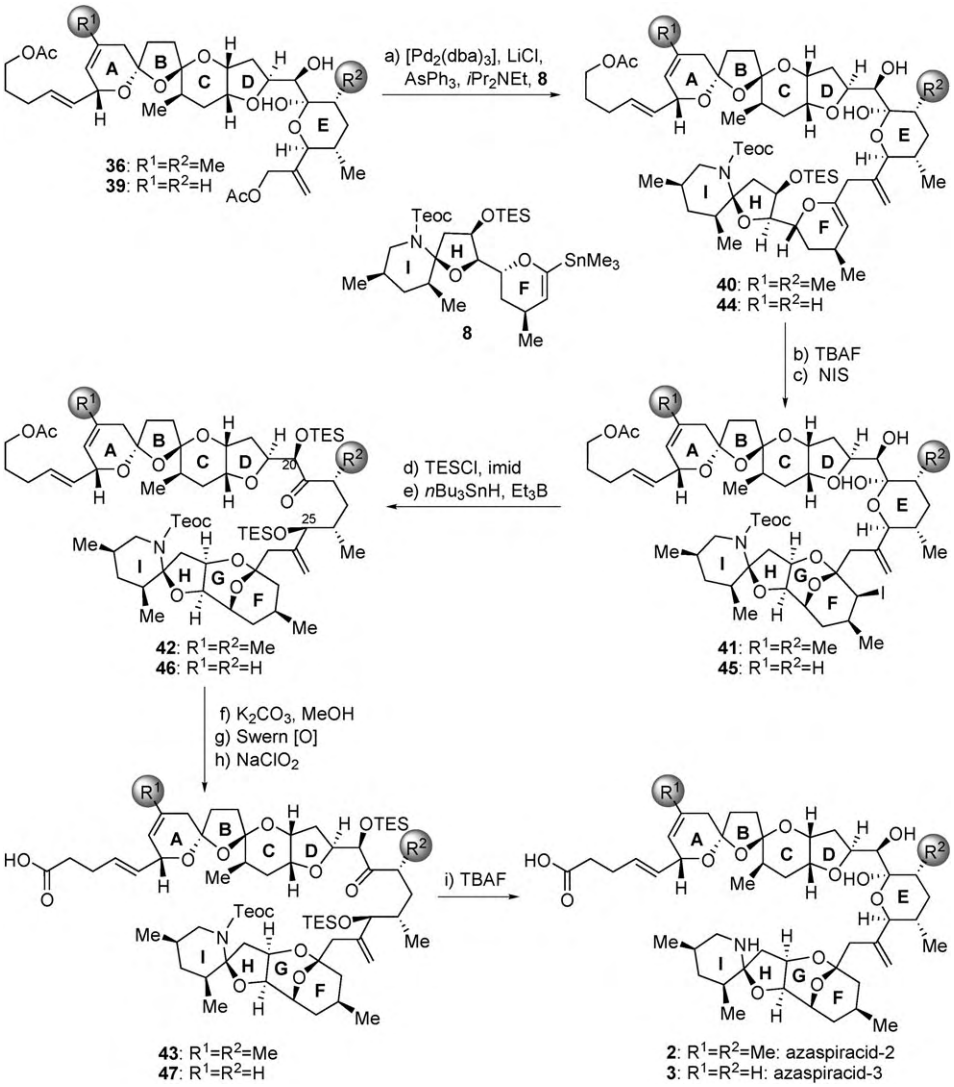

Scheme 5. Completion of the total syntheses of azaspiracid-2 (**2**) and -3 (**3**). Reagents and conditions: a) **8** (2.0 equiv), $[Pd_2(dba)_3]$ (0.3 equiv), $AsPh_3$ (0.3 equiv), LiCl (6.0 equiv), iPr_2NEt (10 equiv), DMF, 25 °C, 1 h, 80% for **40**, 69% for **44**; b) TBAF (1.0 M in THF, 1.5 equiv), THF, 0 °C, 30 min; c) NIS (2.0 equiv), $NaHCO_3$ (10 equiv), THF, 0 °C, 12 h, 48% over two steps for **41**, 51% over two steps for **45**; d) TESCl (30 equiv), imid (60 equiv), CH_2Cl_2, 25 °C, 16 h; e) Et_3B (1.0 M in hexanes, 0.2 equiv), nBu_3SnH/toluene (1:2), 0 °C, 5 min, 86% over two steps for **42**, 88% over two steps for **46**; f) K_2CO_3 (5.0 equiv), MeOH, 25 °C, 1 h; g) $(COCl)_2$ (20 equiv), DMSO (40 equiv), CH_2Cl_2, −78 °C, 1 h; then Et_3N (80 equiv), −78→0 °C; h) $NaClO_2$ (10 equiv), NaH_2PO_4 (10 equiv), 2-methyl-2-butene (excess), $tBuOH/H_2O$ (4:1), 25 °C, 1.5 h; i) TBAF (1.0 M in THF, 5.0 equiv), THF, 25 °C, 15 h, 26% over four steps for **2**, 21% over four steps for **3**. dba = dibenzylideneacetone, NIS = *N*-iodosuccinimide.

Compound **42** was tailored so as to allow its selective conversion to carboxylic acid **43** by a three-step sequence involving 1) deacetylation (K_2CO_3, MeOH), 2) Swern oxidation to the aldehyde, and 3) further oxidation with $NaClO_2$. Finally, exposure of **43** to TBAF in THF led to the removal of all three protecting groups and the spontaneous folding of the molecule into its natural form (azaspiracid-2, **2**). In a similar way, azaspiracid-3 (**3**) was synthesized from key building blocks **5, 7**, and **8** as summarized in Schemes 1–5. The spectral data for synthetic azaspiracid-2 (**2**) and -3 (**3**) were identical to those reported[6] for the naturally occurring substances, thus confirming their revised structures[4a] as **2** and **3**.

The described syntheses confirm the newly proposed[4a] structures for azaspiracid-2 (**2**) and -3 (**3**) and should be applicable to the synthesis of azaspiracid-1 (**1**). As the approach described herein is considerably shorter than our previous route[4] to azaspiracid-1 (**1**; 39 linear steps versus 50) and given the extreme natural scarcity of these long sought after natural products, the present strategy also renders them readily available for much needed biological investigations.[20]

Received: January 23, 2006
Published online: March 20, 2006

Keywords: azaspiracids · fused-ring systems · natural products · spiro compounds · total synthesis

 © 2006 Wiley-VCH Verlag GmbH & Co. KGaA, Weinheim

Table 1: Selected physical properties for compound **40**, azaspiracid-2 (**2**), compound **44**, and azaspiracid-3 (**3**).

40: $R_f = 0.59$ (silica gel, EtOAc/hexanes 2:3); $[\alpha]_D^{25} = 7.9$ ($c = 0.93$, CH_2Cl_2); IR (film): $\nu_{max} = 3450, 2955, 2910, 2868, 1737, 1654, 1458\ cm^{-1}$; ^1H NMR (500 MHz, C_6D_6): $\delta = 5.67–5.56$ (m, 2H), 5.43 (s, 1H), 5.24 (s, 1H), 5.09 (s, 1H), 5.00 (br s, 1H), 4.71–4.67 (m, 1H), 4.65 (d, $J = 4.0$ Hz, 1H), 4.55 (q, $J = 6.8$ Hz, 1H), 4.38–4.35 (m, 1H), 4.30–4.26 (m, 2H), 4.22 (d, $J = 9.5$ Hz, 1H), 4.00–3.96 (m, 1H), 3.90 (t, $J = 7.0$ Hz, 2H), 3.81 (d, $J = 5.5$ Hz, 1H), 3.74–3.73 (m, 1H), 3.68 (br s, 1H), 3.48 (dd, $J = 14.5$, 6.0 Hz, 1H), 3.38 (t, $J = 12.5$ Hz, 1H), 2.99 (d, $J = 16.0$ Hz, 1H), 2.86 (d, $J = 16.0$ Hz, 1H), 2.58 (dd, $J = 14.5$, 6.5 Hz, 1H), 2.34–2.00 (m, 9H), 1.97–1.85 (m, 2H), 1.83–1.70 (m, 2H), 1.64 (s, 6H), 1.58 (s, 3H), 1.47–1.40 (m, 4H), 1.38–1.27 (m, 8H), 1.07 (d, $J = 7.0$ Hz, 3H), 1.06 (d, $J = 7.0$ Hz, 3H), 1.03 (t, $J = 8.0$ Hz, 9H), 0.98 (d, $J = 7.0$ Hz, 3H), 0.80 (d, $J = 7.0$ Hz, 3H), 0.79 (d, $J = 7.0$ Hz, 3H), 0.78 (d, $J = 7.0$ Hz, 3H), 0.65 (q, $J = 8.0$ Hz, 6 Hz), 0.06 ppm (s, 9H); ^{13}C NMR (125 MHz, $CDCl_3$): $\delta = 170.7, 156.9, 152.7, 146.2, 143.4, 133.7, 131.0, 130.0, 126.8, 123.3, 114.4, 111.0, 105.0, 104.9, 100.6, 99.1, 97.5, 87.8, 84.7, 80.5, 79.0, 77.2, 72.8, 72.2, 72.1, 71.9, 68.0, 63.7, 50.1, 47.2, 40.0, 39.1, 37.7, 37.5, 37.5, 35.7, 33.3, 32.3, 32.2, 30.8, 29.6, 29.5, 29.0, 27.9, 26.7, 26.0, 25.7, 24.2, 21.1, 19.5, 18.6, 17.6, 17.2, 7.8, 5.7, −0.9$ ppm; HRMS (ESI): calcd for $C_{62}H_{103}NO_{14}Si_2Na^+$ [M+Na^+]: 1164.6814; found 1164.6789.

2: $R_f = 0.48$ (silica gel, $CHCl_3$/MeOH/H_2O 40:9:1); $[\alpha]_D^{25} = -11.9$ ($c = 0.21$, MeOH); IR (film): $\nu_{max} = 3450, 2955, 2910, 2868, 1737, 1654, 1458\ cm^{-1}$; ^1H NMR (600 MHz, CD_3OD): $\delta = 5.70$ (dt, $J = 13.2$, 6.0 Hz, 1H), 5.41 (dd, $J = 13.2$, 6.0 Hz, 1H), 5.35 (s, 2H), 5.17 (s, 1H), 4.99 (br s, 1H), 4.72 (br s, 1H), 4.61 (br s, 1H), 4.44–4.41 (m, 1H), 4.35 (br s, 1H), 4.20 (s, 1H), 4.04–4.00 (m, 1H), 3.98 (d, $J = 9.0$ Hz, 1H), 3.92–3.86 (m, 2H), 2.88–2.85 (m, 1H), 2.82–2.78 (t, $J = 12.6$ Hz, 1H), 2.61 (dd, $J = 14.4$, 4.8 Hz, 1H), 2.44–2.41 (m, 3H), 2.36–2.29 (m, 5H), 2.27–2.20 (m, 2H), 2.18–2.15 (m, 1H), 2.07–1.93 (m, 8H), 1.85–1.80 (m, 3H), 1.76–1.72 (m, 1H), 1.68 (s, 3H), 1.68–1.62 (m, 4H), 1.53–1.48 (m, 1H), 1.45–1.27 (m, 5H), 0.97 (d, $J = 6.6$ Hz, 3H), 0.95 (d, $J = 6.6$ Hz, 3H), 0.93 (d, $J = 6.6$ Hz, 6H), 0.91 (d, $J = 6.6$ Hz, 3H), 0.84 ppm (d, $J = 6.0$ Hz, 3H); ^{13}C NMR (150 MHz, CD_3OD): $\delta = 177.8, 149.1, 133.0, 132.95, 131.9, 123.8, 118.1, 112.1, 108.2, 101.0, 99.5, 97.5, 82.3, 80.4, 80.0, 79.0, 77.6, 75.6, 74.1, 73.6, 73.4, 50.1, 47.0, 44.9, 43.1, 42.5, 41.1, 39.0, 38.5, 38.2, 37.8, 37.5, 36.5, 36.1, 35.6, 34.0, 33.4, 31.7, 30.2, 29.6, 27.2, 24.3, 23.8, 19.3, 18.9, 17.4, 17.2, 16.2$ ppm; HRMS (ESI): calcd for $C_{48}H_{73}NO_{12}H^+$ [M+H^+]: 856.5208; found 856.5208.

44: $R_f = 0.60$ (silica gel, EtOAc/hexanes 2:3); $[\alpha]_D^{25} = -5.5$ ($c = 1.1$, CH_2Cl_2); IR (film): $\nu_{max} = 3447, 2954, 2907, 2861, 1735, 1700, 1654, 1458\ cm^{-1}$; ^1H NMR (500 MHz, C_6D_6): $\delta = 5.69–5.54$ (m, 4H), 5.19 (s, 1H), 5.07 (s, 1H), 5.00 (br s, 1H), 4.67 (d, $J = 4.0$ Hz, 1H), 4.63 (dt, $J = 9.5$, 6.5 Hz, 1H), 4.57 (q, $J = 6.0$ Hz, 1H), 4.43–4.39 (m, 1H), 4.34 (d, $J = 10.0$ Hz, 1H), 4.32–4.26 (m, 2H), 4.16 (br s, 1H), 4.01–3.98 (m, 1H), 3.94 (t, $J = 7.0$ Hz, 1H), 3.89 (t, $J = 6.5$ Hz, 2H), 3.76–3.74 (m, 1H), 3.57 (d, $J = 6.5$ Hz, 1H), 3.53 (dd, $J = 14.5$, 5.5 Hz, 1H), 3.38 (t, $J = 12.0$ Hz, 1H), 2.97 (d, $J = 15.5$ Hz, 1H), 2.90 (d, $J = 15.5$ Hz, 1H), 2.58 (dd, $J = 14.5$, 6.0 Hz, 1H), 2.40–2.24 (m, 4H), 2.20–2.06 (m, 6H), 2.03–1.97 (m, 4H), 1.89–1.82 (m, 4H), 1.78–1.73 (m, 2H), 1.64 (s, 6H), 1.53–1.47 (m, 4H), 1.37–1.32 (m, 4H), 1.08 (d, $J = 7.0$ Hz, 3H), 1.04 (t, $J = 8.0$ Hz, 9H), 0.81 (d, $J = 6.5$ Hz, 3H), 0.80 (d, $J = 6.5$ Hz, 3H), 0.76 (d, $J = 6.5$ Hz, 3H), 0.73 (d, $J = 7.5$ Hz, 3H), 0.66 (q, $J = 8.0$ Hz, 6H), 0.07 ppm (s, 9H); ^{13}C NMR (125 MHz, C_6D_6): $\delta = 171.8, 156.3, 152.0, 145.4, 142.7, 131.1, 131.0, 130.2, 126.1, 122.7, 114.6, 110.3, 105.9, 104.3, 99.8, 97.4, 96.9, 83.9, 80.8, 79.3, 78.8, 77.2, 72.7, 72.1, 71.7, 71.2, 63.6, 63.0, 49.4, 38.8, 38.1, 37.9, 37.2, 37.1, 35.1, 33.0, 32.6, 31.7, 30.7, 30.2, 30.0, 28.9, 28.3, 27.8, 25.1, 23.2, 18.8, 18.1, 18.0, 17.0, 16.4, 7.2, 5.1, −1.5$ ppm; HRMS (ESI): calcd for $C_{60}H_{99}NO_{14}Si_2Na^+$ [M+Na^+]: 1136.6496; found 1136.6468.

3: $R_f = 0.48$ (silica gel, $CHCl_3$/MeOH/H_2O 40:9:1); $[\alpha]_D^{25} = -25.0$ ($c = 0.10$, MeOH); IR (film): $\nu_{max} = 3450, 2955, 2910, 2868, 1737, 1654, 1458\ cm^{-1}$; ^1H NMR (600 MHz, CD_3OD): $\delta = 5.75–5.72$ (m, 2H), 5.64 (d, $J = 10.2$ Hz, 1H), 5.46 (dd, $J = 15.0$, 7.2 Hz, 1H), 5.34 (s, 1H), 5.18 (s, 1H), 5.00 (s, 1H), 4.81 (br s, 1H), 4.44–4.40 (m, 1H), 4.36 (s, 1H), 4.22 (s, 1H), 4.08–4.05 (m, 2H), 3.90 (s, 1H), 3.64–3.62 (m, 1H), 2.90–2.88 (m, 1H), 2.83 (t, $J = 12.0$ Hz, 1H), 2.64–2.61 (m, 1H), 2.54–2.41 (m, 3H), 2.39–2.22 (m, 7H), 2.16–2.04 (m, 5H), 2.00–1.89 (m, 5H), 1.87–1.83 (m, 2H), 1.77–1.74 (m, 1H), 1.70–1.60 (m, 4H), 1.56–1.53 (m, 2H), 1.39–1.26 (m, 3H), 1.02–0.95 (m, 12H), 0.87 ppm (d, $J = 6.6$ Hz, 3H); ^{13}C NMR (150 MHz, CD_3OD): $\delta = 177.8, 149.1, 133.0, 132.95, 131.9, 123.8, 118.1, 112.1, 108.2, 101.0, 99.5, 97.5, 82.3, 80.4, 80.0, 79.0, 77.6, 75.6, 74.1, 73.6, 73.4, 50.1, 47.0, 44.9, 43.1, 42.5, 41.1, 39.0, 38.5, 38.2, 37.8, 37.5, 36.5, 36.1, 35.6, 34.0, 33.4, 31.7, 30.2, 29.6, 27.2, 24.3, 23.8, 19.3, 18.9, 17.4, 17.2, 16.2$ ppm; HRMS (ESI): calcd for $C_{46}H_{69}NO_{12}H^+$ [M+H^+]: 828.4892; found 828.4893.

[1] T. McMahon, J. Silke, *Harmful Algae News* **1996**, *14*, 2.

[2] a) K. C. Nicolaou, Y. Li, N. Uesaka, T. V. Koftis, S. Vyskocil, T. Ling, M. Govindasamy, W. Qian, F. Bernal, D. Y.-K. Chen, *Angew. Chem.* **2003**, *115*, 3771–3776; *Angew. Chem. Int. Ed.* **2003**, *42*, 3643–3648; b) K. C. Nicolaou, D. Y.-K. Chen, Y. Li, W. Qian, T. Ling, S. Vyskocil, T. V. Koftis, M. Govindasamy, N. Uesaka, *Angew. Chem.* **2003**, *115*, 3777–3781; *Angew. Chem. Int. Ed.* **2003**, *42*, 3649–3653.

[3] a) K. C. Nicolaou, S. Vyskocil, T. V. Koftis, Y. M. A. Yamada, T. Ling, D. Y.-K. Chen, W. Tang, G. Petrovic, M. O. Frederick, Y. Li, M. Satake, *Angew. Chem.* **2004**, *116*, 4412–4418; *Angew. Chem. Int. Ed.* **2004**, *43*, 4312–4318; b) K. C. Nicolaou, T. V. Koftis, S. Vyskocil, G. Petrovic, T. Ling, Y. M. A. Yamada, W. Tang, M. O. Frederick, *Angew. Chem.* **2004**, *116*, 4418–4424; *Angew. Chem. Int. Ed.* **2004**, *43*, 4318–4324.

[4] a) K. C. Nicolaou, P. M. Pihko, F. Bernal, M. O. Frederick, W. Qian, N. Uesaka, N. Diedrichs, J. Hinrichs, T. V. Koftis, E. Loizidou, G. Petrovic, M. Rodriquez, D. Sarlah, N. Zou, *J. Am. Chem. Soc.* **2006**, *128*, 2244–2257; b) K. C. Nicolaou, D. Y.-K. Chen, Y. Li, N. Uesaka, G. Petrovic, T. V. Koftis, F. Bernal, M. O. Frederick, M. Govindasamy, T. Ling, P. M. Pihko, W. Tang, S. Vyskocil, *J. Am. Chem. Soc.* **2006**, *128*, 2258–2267; c) K. C. Nicolaou, T. V. Koftis, S. Vyskocil, G. Petrovic, W. Tang, M. O. Frederick, D. Y.-K. Chen, Y. Li, T. Ling, Y. M. A. Yamada, *J. Am. Chem. Soc.* **2006**, *128*, 2859–2872.

[5] M. Satake, K. Ofuji, H. Naoki, K. J. James, A. Furey, T. McMahon, J. Silke, T. Yasumoto, *J. Am. Chem. Soc.* **1998**, *120*, 9967–9968.

[6] K. Ofuji, M. Satake, T. McMahon, J. Silke, K. J. James, H. Naoki, Y. Oshima, T. Yasumoto, *Nat. Toxins* **1999**, *7*, 99–102.

[7] a) K. Ofuji, M. Satake, T. McMahon, K. J. James, H. Naoki, Y. Oshima, T. Yasumoto, *Biosci. Biotechnol. Biochem.* **2001**, *65*, 740–742; b) K. J. James, M. Diaz Sierra, M. Lehane, A. Brana, A. Furey, *Toxicon* **2003**, *41*, 277–283; c) E. Ito, M. Satake, K. Ofuji, N. Kurita, T. McMahon, K. James, T. Yasumoto, *Toxicon* **2000**, *38*, 917–930; d) E. Ito, M. Satake, K. Ofuji, M. Higashi, K. Harigaya, T. McMahon, T. Yasumoto, *Toxicon* **2002**, *40*, 193–203; e) E. Ito, M. O. Frederick, T. V. Koftis, W. Tang, G. Petrovic, T. Ling, K. C. Nicolaou, *Harmful Algae*, ASAP.

[8] E. J. Corey, D. Seebach, *Angew. Chem.* **1965**, *77*, 1134–1135; *Angew. Chem. Int. Ed. Engl.* **1965**, *4*, 1075–1077.

[9] a) J. K. Stille, *Angew. Chem.* **1986**, *98*, 504–519; *Angew. Chem. Int. Ed. Engl.* **1986**, *25*, 508–524; b) L. Del Valle, J. K. Stille, L. S. Hegedus, *J. Org. Chem.* **1990**, *55*, 3019–3023.

 © 2006 Wiley-VCH Verlag GmbH & Co. KGaA, Weinheim

[10] For the synthesis of **9**, see: A. B. Smith, Q. Lin, K. Nakayama, A. M. Boldi, C. S. Brook, M. D. Mcbriar, W. H. Moser, M. Sobukawa, L. Zhuang, *Tetrahedron Lett.* **1997**, *38*, 8675 – 8678. For the synthesis of **17**, see: S. G. Koenig, S. M. Miller, K. A. Leonard, R. S. Löwe, B. C. Chen, D. J. Austin, *Org. Lett.* **2003**, *5*, 2203 – 2206.
[11] K. C. Nicolaou, W. Qian, F. Bernal, N. Uesaka, P. M. Pihko, J. Hinrichs, *Angew. Chem.* **2001**, *113*, 1302 – 1304; *Angew. Chem. Int. Ed.* **2001**, *40*, 4068 – 4071.
[12] G. A. Tolstikov, M. S. Miftakhov, M. E. Adler, N. G. Komissarova, O. M. Kuznetsov, N. S. Vostrikov, *Synthesis* **1989**, 940 – 942.
[13] V. Bou, J. Vilarrasa, *Tetrahedron Lett.* **1990**, *31*, 567 – 568.
[14] Y. Nakamura, K. Mori, *Biosci. Biotechnol. Biochem.* **2000**, *64*, 1713 – 1721.
[15] For recent reviews of Cr^{II}-mediated reactions, see: a) A. Furstner, *Chem. Rev.* **1999**, *99*, 991 – 1046; b) L. A. Wessjohann, G. Scheid, *Synthesis* **1999**, 1 – 36.
[16] M. Ide, M. Nakata, *Bull. Chem. Soc. Jpn.* **1999**, *72*, 2491 – 2499.
[17] The DIBAL-H reduction of **37** to **38** (azaspiracid-3 series) gave a mixture of C20 epimers (ca. 1.2:1) from which the desired isomer **38** was separated chromatographically, while the undesired isomer could be recycled by oxidation–reduction. The stereochemical identity of **38** was based on ^{1}H NMR spectroscopic comparisons with those of its counterpart encountered en route to azaspiracid-1[3b] and was finally proven by its conversion to azaspiracid-3.
[18] K. Ishihara, H. Kurihara, H. Yamamoto, *J. Org. Chem.* **1993**, *58*, 3791 – 3793.
[19] G. Stork, K. Zhao, *Tetrahedron Lett.* **1989**, *30*, 287 – 290.
[20] For other studies directed toward the synthesis of azaspiracids, see: a) R. G. Carter, D. J. Weldon, *Org. Lett.* **2000**, *2*, 3913 – 3916; b) R. G. Carter, D. E. Graves, *Tetrahedron Lett.* **2001**, *42*, 6035 – 6039; c) R. G. Carter, T. C. Bourland, D. E. Graves, *Org. Lett.* **2002**, *4*, 2177 – 2179; d) R. G. Carter, D. E. Graves, M. A. Gronemeyer, G. S. Tschumper, *Org. Lett.* **2002**, *4*, 2181 – 2184; e) R. G. Carter, T. C. Bourland, X. T. Zhou, M. A. Gronemeyer, *Tetrahedron* **2003**, *59*, 8963 – 8974; f) X.-T. Zhou, R. G. Carter, *Chem. Commun.* **2004**, *19*, 2138 – 2140; g) X.-T. Zhou, R. G. Carter, *Angew. Chem.* **2006**, *118*, 1819 – 1822; *Angew. Chem. Int. Ed.* **2006**, *45*, 1787 – 1790; h) C. J. Forsyth, J. L. Hao, J. Aiguade, *Angew. Chem.* **2001**, *113*, 3775 – 3779; *Angew. Chem. Int. Ed.* **2001**, *40*, 3663 – 3667; i) A. B. Dounay, C. J. Forsyth, *Org. Lett.* **2001**, *3*, 975 – 978; j) J. L. Hao, J. Aiguade, C. J. Forsyth, *Tetrahedron Lett.* **2001**, *42*, 817 – 820; k) J. L. Hao, J. Aiguade, C. J. Forsyth, *Tetrahedron Lett.* **2001**, *42*, 821 – 824; l) J. Aiguade, J. L. Hao, C. J. Forsyth, *Org. Lett.* **2001**, *3*, 979 – 982; m) L. K. Geisler, S. Nguyen, C. J. Forsyth, *Org. Lett.* **2004**, *6*, 4159 – 4162; n) M. Sasaki, Y. Iwamuro, J. Nemoto, M. Oikawa, *Tetrahedron Lett.* **2003**, *44*, 6199 – 6201; o) Y. Ishikawa, S. Nishiyama, *Tetrahedron Lett.* **2004**, *45*, 351 – 354; p) Y. Ishikawa, S. Nishiyama, *Heterocycles* **2004**, *63*, 539 – 565; q) Y. Ishikawa, S. Nishiyama, *Heterocycles* **2004**, *63*, 885 – 893.

 © 2006 Wiley-VCH Verlag GmbH & Co. KGaA, Weinheim

Organocatalysis

DOI: 10.1002/anie.200504344

A Highly Enantioselective Brønsted Acid Catalyst for the Strecker Reaction**

Magnus Rueping, Erli Sugiono, and Cengiz Azap*

The hydrocyanation of imines, the Strecker reaction, is a practical and direct method to α-amino acids.[1] Consequently, various attempts to develop asymmetric Strecker reactions have been made.[2] In addition to metal-catalyzed cyanations using chiral Al, Ti, Zr, and lanthanide catalysts,[3] promising metal-free, enantioselective variants of this reaction have recently been disclosed. These include processes based on chiral guanidines,[4] ureas and thioureas,[5] bis(*N*-oxides),[6] and ammonium salts.[7] Given the importance of the Strecker reaction and the resulting products, we report herein a new type of Brønsted acid catalyst[8] for this transformation, a chiral binol phosphate (binol = 2,2′-dihydroxy-1,1′-binaphthyl).

The starting point for our development of this new catalyst for the enantioselective Strecker reaction was the successful application of Brønsted acid catalysts of type **1** in asymmetric transformations,[9,10] originally reported by Akiyama and Terada. Recently we reported a Brønsted acid catalyzed transfer hydrogenation of imines and quinolines[10] using binol phosphates **1**. Based on this reaction, we reasoned that activation of imine **2** by catalytic protonation would generate the iminium **3** which would subsequently undergo addition of HCN to give the desired amino nitrile **4** and the regenerated Brønsted acid **1** (Scheme 1). Thus we prepared

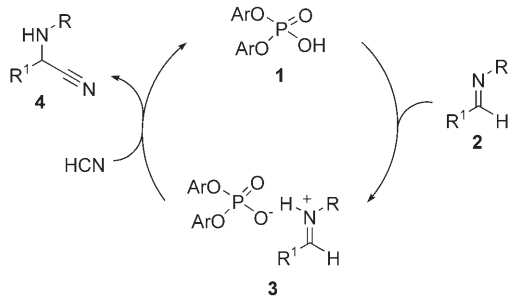

Scheme 1. Assumed catalytic cycle for imine activation by binol phosphate **1**.

[*] Prof. M. Rueping, E. Sugiono, C. Azap
Degussa Endowed Professorship
Institute for Organic Chemistry und Chemical Biology
Johann Wolfgang Goethe University Frankfurt am Main
Marie-Curie-Strasse 11, 60439 Frankfurt am Main (Germany)
Fax: (+49) 69-798-29248
E-mail: M.rueping@chemie.uni-frankfurt.de

[**] The authors acknowledge Degussa AG for generous funding.
Supporting information for this article is available on the WWW under http://www.angewandte.org or from the author.

several binol phosphates and tested the corresponding catalysts **1a–g** in the enantioselective Strecker reaction. Initial explorations, however, concentrated on varying reaction parameters, such as different protected imines, cyanide sources, catalyst loading, temperature, and concentration.[11] The best results, with respect to yield and selectivity, were obtained with benzyl-protected imines and HCN at −40 °C using 10 mol % of catalyst.

The influence of the substituent Ar′ on the catalytic behavior was studied (Table 1). From this survey sterically more congested Brønsted acids emerged as catalysts with good to excellent levels of enantioselectivity. Best selectivities were obtained with catalyst **1g** providing the benzyl-protected amino nitrile **4** in 93 % *ee* (Table 1, entry 7).

Table 1: Survey of chiral Brønsted acid catalysts **1a–g** for the Strecker reaction.

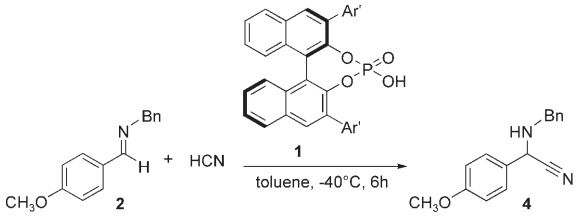

Entry[a]	Ar′	*ee* [%][b]
1	phenyl (**1a**)	26
2	4-biphenyl (**1b**)	60
3	1-naphthyl (**1c**)	84
4	2-naphthyl (**1d**)	32
5	3,5-$(CF_3)_2C_6H_3$ (**1e**)	38
6	3,5-$(C_6H_5)_2C_6H_3$ (**1f**)	*rac*
7	9-phenanthryl (**1g**)	93

[a] Reactions were performed with imine **2** (Bn = benzyl), HCN (1.5 equiv) at 0.15 M concentration in toluene using 10 mol % of catalyst **1**. [b] Determined by HPLC analysis using a Chiralcel OD-H column.

Futher examinations concentrated on the solvent employed (Table 2). While the hydrocyanations could be performed in all the solvents tested, the best selectivities were achieved in nonpolar aromatic solvents (Table 2, entry 1), followed by chlorinated solvents (entries 2 and 3). This trend

Table 2: Influence of solvent on the enantioselectivity of the Strecker reaction.

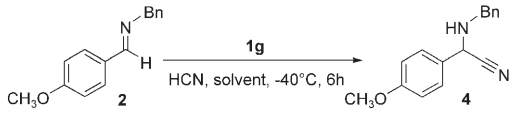

Entry[a]	Solvent	*ee* [%][b]
1	toluene	93
2	chloroform	60
3	dichloromethane	44
4	acetonitrile	*rac*
5	THF	*rac*

[a] Reactions were performed with imine **2**, HCN (1.5 equiv) at 0.15 M concentration using 10 mol % of catalyst. [b] Determined by HPLC analysis using a Chiralcel OD-H column.

© 2006 Wiley-VCH Verlag GmbH & Co. KGaA, Weinheim

is in accordance with our observations on Brønsted acid catalyzed hydride transfer reactions.[10]

With the optimized conditions we explored the scope of the Brønsted acid catalyzed hydrocyanation of various imines (Table 3). In general, aromatic and heteroaromatic, *N*-benzyl- and *N*-*para*-methoxybenzyl-protected amines, bearing either electron-withdrawing or electron-donating groups were obtained in high enantioselectivities and good yields.[12]

Important products from the Strecker reaction are the amino nitriles which can be converted into amino acids and diamines. Hence, to demonstrate the preparation of these compounds and to determine the absolute configuration of the products, amino nitrile **5l** was reduced and deacetylated to afford the corresponding diamine **6** (Scheme 2).[13] In addition, the formylated amino nitrile **7** was subjected to hydrolysis with subsequent debenzylation to yield amino acid **8**.[5b]

Table 3: Scope of the Strecker reaction.

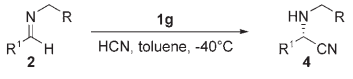

Entry[a]	2	R	4	Yield [%][b]	*ee* [%][c]
1	**2a**	Ph	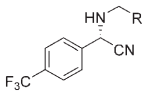	75	97
2	**2b**	*p*-$H_3COC_6H_4$		53	96
3	**2c**	Ph	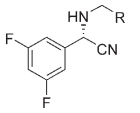	59	98
4	**2d**	Ph, $R^2=H$	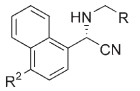	85	99
5	**2e**	Ph, $R^2=OCH_3$		70	94
6	**2f**	Ph	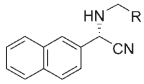	71	85
7	**2g**	Ph	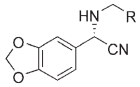	88	93
8	**2h**	Ph, X=S, $R^2=H$	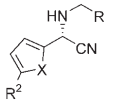	77	95
9	**2i**	Ph, X=O, $R^2=H$		84	89
10	**2j**	Ph, X=O, $R^2=CH_3$		85	92
11	**2k**	*p*-$H_3COC_6H_4$	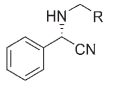	87	89
12	**2l**	Ph, $R^2=OCH_3$	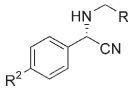	97	93
13	**2m**	Ph, $R^2=CH_3$		55	87
14	**2n**	Ph	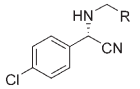	69	85
15	**2o**	*p*-$H_3COC_6H_4$		60	86

[a] Reactions were performed with imine **2**, HCN (1.5 equiv) at −40 °C in toluene at 0.15 M concentration for 2–3 days using 10 mol% of catalyst. [b] Yield of the isolated trifluoroacetamides **5** after acetylation of the corresponding amino nitriles **4** and chromatography. [c] Determined by HPLC analysis using Chiralcel OD-H or ADH-columns.

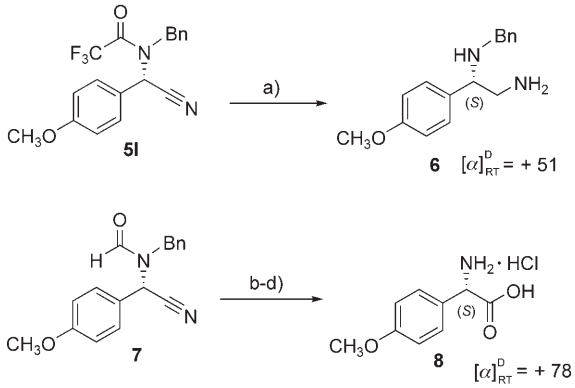

Scheme 2. Reduction and hydrolysis of amino nitriles **5l** and **7**. a) $LiAlH_4$, Et_2O; b) 65% (w/v) H_2SO_4, 45 °C, 20 h; c) HCl (conc.), 70 °C, 12 h; d) H_2/Pd-C, MeOH.

The observed *S*-configuration of the products can be explained by a stereochemical model derived from the X-ray crystal structure of binol phosphate **1g**. In the transition state, the imine is activated by the Brønsted acid **1g**, thereby forming iminium **3**. This process favors the approach of the cyanide nucleophile from the less hindered *Re*-face rather than the *Si*-face which is efficiently shielded by the large phenanthryl group of the catalyst (Figure 1).

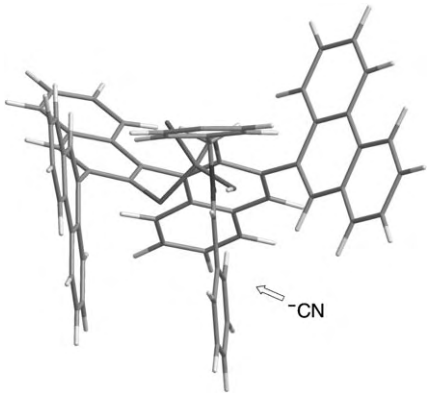

Figure 1. Conceivable transition structure derived from an X-ray crystal structure of chiral Brønsted acid **1g** and optimization calculations.

In summary, we have developed an organocatalytic hydrocyanation of imines, which provides direct access to a diverse range of aromatic amino nitriles and the corresponding amino acids and diamines in high enantioselectivity. The use of binol phosphates as efficient Brønsted acid catalysts in the enantioselective Strecker reaction not only increases the diversity of possible transformations with this catalyst but also shows the great potential of this type of Brønsted acid in asymmetric catalysis. Experiments to establish a more detailed mechanism of activation and the application of this

 © 2006 Wiley-VCH Verlag GmbH & Co. KGaA, Weinheim

catalyst to the hydrocyanation of ketimines and to other reactions of imines with related nucleophiles are currently under investigation.

Received: December 6, 2005
Published online: March 17, 2006

Keywords: amino acids · binol phosphate · Brønsted acids · organocatalysis · Strecker reaction

[1] A. Strecker, *Ann. Chem. Pharm.* **1850**, *75*, 27.
[2] For reviews, see: a) H. Gröger, *Chem. Rev.* **2003**, *103*, 2795; b) L. Yet, *Angew. Chem.* **2001**, *113*, 900; *Angew. Chem. Int. Ed.* **2001**, *40*, 875; c) C. Spino, *Angew. Chem.* **2004**, *116*, 1796; *Angew. Chem. Int. Ed.* **2004**, *43*, 1764.
[3] Al catalysts: a) M. S. Sigman, E. N. Jacobsen, *J. Am. Chem. Soc.* **1998**, *120*, 5315; b) M. Takamura, Y. Hamashima, H. Usuda, M. Kanai, M. Shibasaki, *Angew. Chem.* **2000**, *112*, 1716; *Angew. Chem. Int. Ed.* **2000**, *39*, 1650; Ti catalysts: c) C. A. Krueger, K. W. Kuntz, C. D. Dzierba, W. G. Wirschun, J. D. Gleason, M. L. Snapper, A. H. Hoveyda, *J. Am. Chem. Soc.* **1999**, *121*, 4284; d) J. J. Byrne, M. Chavarot, P.-Y. Chavant, Y. Valleé, *Tetrahedron Lett.* **2000**, *41*, 873; e) N. S. Josephsohn, K. W. Kuntz, M. L. Snapper, A. H. Hoveyda, *J. Am. Chem. Soc.* **2001**, *123*, 11594; Zr catalysts: f) H. Ishitani, S. Komiyama, S. Kobayashi, *Angew. Chem.* **1998**, *110*, 3369; *Angew. Chem. Int. Ed.* **1998**, *37*, 3186; g) S. Kobayashi, H. Ishitani, *Chirality* **2000**, *12*, 540; Lathanide catalysts: h) M. Chavarot, J. J. Byrne, P.-Y. Chavant, Y. Valleé *Tetrahedron: Asymmetry* **2001**, *12*, 1147; i) S. Masumoto, H. Usuda, M. Suzuki, M. Kanai, M. Shibasaki, *J. Am. Chem. Soc.* **2003**, *125*, 5634.
[4] E. J. Corey, M. J. Grogan, *Org. Lett.* **1999**, *1*, 157.
[5] a) M. S. Sigman, E. N. Jacobsen, *J. Am. Chem. Soc.* **1998**, *120*, 4901; b) M. S. Sigman, P. Vachal, E. N. Jacobsen, *Angew. Chem.* **2000**, *112*, 1336; *Angew. Chem. Int. Ed.* **2000**, *39*, 1279; c) P. Vachal, E. N. Jacobsen, *Org. Lett.* **2000**, *2*, 867; d) P. Vachal, E. N. Jacobsen, *J. Am. Chem. Soc.* **2002**, *124*, 10012; e) A. G. Wenzel, M. P. Lalonde, E. N. Jacobsen, *Synlett* **2003**, 1919; f) S. B. Tsogoeva, D. A. Yalalov, M. J. Hateley, C. Weckbecker, K. Huthmacher, *Eur. J. Org. Chem.* **2005**, 4995.
[6] For the application of stoichiometric amounts of bis(*N*-oxides), see: a) B. Liu, X. Feng, F. Chen, G. Zhang, X. Cui, Y. Jiang, *Synlett* **2001**, 1551; b) Z. Jiao, X. Feng, B. Liu, F. Chen, G. Zhang, Y. Jiang, *Eur. J. Org. Chem.* **2003**, 3818.
[7] J. Huang, E. J. Corey, *Org. Lett.* **2004**, *6*, 5027.
[8] For reviews on chiral Brønsted acid catalysis, see: a) P. R. Schreiner, *Chem. Soc. Rev.* **2003**, *32*, 289; b) P. M. Pihko, *Angew. Chem.* **2004**, *116*, 2110; *Angew. Chem. Int. Ed.* **2004**, *43*, 2062; c) C. Bolm, T. Rantanen, I. Schiffers, L. Zani, *Angew. Chem.* **2005**, *117*, 1788; *Angew. Chem. Int. Ed.* **2005**, *44*, 1758.
[9] a) T. Akiyama, J. Itoh, K. Yokota, K. Fuchibe, *Angew. Chem.* **2004**, *116*, 1592; *Angew. Chem. Int. Ed.* **2004**, *43*, 1566; b) D. Uraguchi, M. Terada, *J. Am. Chem. Soc.* **2004**, *126*, 5356; c) D. Uraguchi, K. Sorimachi, M. Terada, *J. Am. Chem. Soc.* **2004**, *126*, 11804; d) T. Akiyama, H. Morita, J. Itoh, K. Fuchibe, *Org. Lett.* **2005**, *7*, 2583; e) S. Hofmann, A. M. Seayad, B. List, *Angew. Chem.* **2005**, *117*, 7590; *Angew. Chem. Int. Ed.* **2005**, *44*, 7424; f) M. Terada, K. Sorimachi, D. Uraguchi, *Synlett* **2006**, 13; g) T. Akiyama, Y. Tamura, J. Itoh, H. Morita, K. Fuchibe, *Synlett* **2006**, 141; h) R. I. Storer, D. E. Carrera, Y. Ni, D. W. C. MacMillan, *J. Am. Chem. Soc.* **2006**, *128*, 84.
[10] a) M. Rueping, C. Azap, E. Sugiono, T. Theissmann, *Synlett* **2005**, 2367; b) M. Rueping, E. Sugiono, C. Azap, T. Theissmann, M. Bolte, *Org. Lett.* **2005**, *7*, 3781, c) M. Rueping, A. P. Antonchick, T. Theissmann, *Angew. Chem./Angew. Chem. Int. Ed.* **2006**, in press.
[11] *N*-Boc-, *N*-tosyl-, *N*-phenyl-, *N*-benzhydryl-, and *N*-phosphinoyl-protected imines gave inferior results compared to the *N*-benzyl-protected ones. As cyanide sources we tested acetone cyanohydrine, trimethylsilyl cyanide, and HCN. Reduction of catalyst loading, temperature, and concentration resulted in loss of enantioselectivities.
[12] Enantioselectivities decreased in the case of aliphatic imines, for example, 2-(benzylamino)-3-methylbutane nitrile was obtained in 55% *ee*.
[13] N. A. Hassan, E. Bayer, J. C. Jochims, *J. Chem. Soc. Perkin Trans. 1* **1998**, 3747.

 © 2006 Wiley-VCH Verlag GmbH & Co. KGaA, Weinheim

C–H Bond Activation

DOI: 10.1002/anie.200504450

Catalytic Arylation Reactions by C–H Bond Activation with Aryl Tosylates**

Lutz Ackermann, Andreas Althammer, and Robert Born*

Transition-metal-catalyzed cross-coupling reactions of organometallic reagents with aryl iodides, bromides, and triflates as electrophiles are reliable tools for the regioselective syntheses of compounds with $C(sp^2)$–$C(sp^2)$ linkages.[1,2] The organometallic compounds are often not commercially available or are expensive, and give rise to the formation of undesired byproducts. The direct arylation of organic compounds by C–H bond functionalization offers an attractive alternative.[3–6]

For traditional cross-coupling reactions of organometallic species the development of electron-rich stabilizing ligands allowed the use of readily available aryl chlorides as electrophiles.[7] Contrarily, generally applicable methods for regioselective direct arylation reactions employing aryl chlorides were reported only recently. Intramolecular direct arylation reactions with aryl chlorides were reported by the groups of Bedford,[8] Buchwald,[9] Fagnou,[10,11] and others[12] to proceed in the presence of palladium complexes derived from electron-rich tertiary phosphines, such as $P(t\mathrm{Bu})_3$, or 2-(di-

[*] Dr. L. Ackermann, Dipl.-Chem. A. Althammer, Dipl.-Chem. R. Born
Ludwig-Maximilians-Universität München
Department Chemie und Biochemie
Butenandtstrasse 5–13, Haus F, 81377 München (Germany)
Fax: (+49) 89-2180-77425
E-mail: lutz.ackermann@cup.uni-muenchen.de

[**] Support by Professor Paul Knochel, the DFG (Emmy Noether-Programm), the Fonds der Chemischen Industrie, and the Ludwig-Maximilians-Universität is gratefully acknowledged.

Supporting information for this article is available on the WWW under http://www.angewandte.org or from the author.

© 2006 Wiley-VCH Verlag GmbH & Co. KGaA, Weinheim

tert-butylphosphino)biphenyl.[13,14] We developed a general method for ruthenium-catalyzed[15] intermolecular arylation reactions using aryl chlorides.[16,17] An additional advantage of our method is the use of secondary phosphine oxide[18,19] (1-Ad)$_2$P(O)H (**4**; 1-Ad = 1-adamantyl)[20] as preligand, which makes the catalytic system air- and moisture-stable.

The possibility of using tosylates as electrophiles in cross-coupling chemistry is attractive, since they can be prepared from readily available phenols or ketones with reagents that are less expensive than those used to prepare the corresponding triflates. Further, tosylates are more convenient to use, because they are more stable to water than triflates and are highly crystalline. However, this greater stability makes tosylates less reactive in transition-metal-catalyzed processes. Recently, methods for traditional cross-coupling reactions between aryl tosylates and organometallic complexes have been developed.[21] In contrast, catalytic, direct arylation reactions through C–H bond activation using tosylates have proven elusive. We report herein a highly active ruthenium catalyst derived from an air-stable heteroatom-substituted secondary phosphine oxide,[22] which allows for the first general direct arylation by C–H bond activation, and tolerates a variety of highly functionalized aryl tosylates and pronucleophiles with different directing groups. Furthermore, the findings document the first use of an air-stable secondary phosphine oxide in the challenging catalytic conversion of aryl tosylates.

Ruthenium complexes generated from different preligands were evaluated in the arylation of oxazoline derivative **1**, because 2-oxazolinyl substituents can be easily converted into valuable functionalities, such as the corresponding carboxylic acids.[23] The catalytic activity was probed in the conversion of electron-rich, thereby electronically deactivated, tosylate **2a** (Table 1). While alkyl-substituted secondary phosphine oxide **4** (Table 1, entry 1) as well as heteroatom-substituted derivatives **5**–**7** (Table 1, entries 2–4) enabled conversion of tosylate **2a**, most efficient catalysis was achieved with the sterically hindered diaminophosphine oxide **8** (Table 1, entries 5–7). NMP proved to be the best solvent tested (Table 1, entry 5).[24]

Table 1: Intermolecular C–H bond arylation with tosylate **2a**.[a]

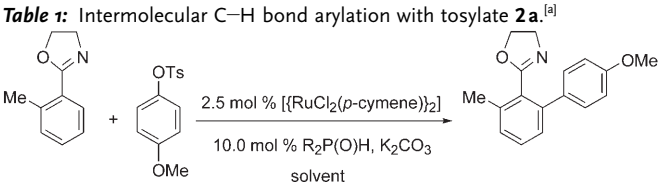

1 **2a** **3a**

Entry	$R_2P(O)H$		Solvent	Yield [%]
1	(1-Ad)$_2$P(O)H	**4**	NMP	55
2	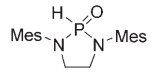	**5**	NMP	10
3	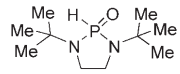	**6**	NMP	59
4	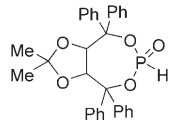	**7**	NMP	58
5	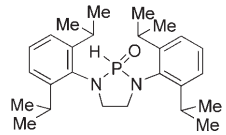	**8**	NMP	76
6			*t*BuOH	21
7			DMPU	40

[a] Reaction conditions: **1** (1.0 mmol), **2a** (1.2 mmol), [{RuCl$_2$(*p*-cymene)}$_2$] (2.5 mol%), $R_2P(O)H$ (10.0 mol%), solvent (2 mL), 120°C, 22 h; GC analysis versus *n*-decane as internal standard. NMP = *N*-methylpyrrolidinone, DMPU = 1,3-dimethyltetrahydro-2-pyrimidinone.

The scope of the optimized ruthenium catalyst was probed in the regioselective direct arylation of oxazoline **1** with diversely substituted tosylates **2** (Table 2). Note that electron-rich aryl tosylates (Table 2, entries 1–4), even those bearing an *ortho*-substituent (Table 2, entry 4), were efficiently converted. Furthermore, the catalyst tolerated a number of important functional groups, such as an alkene (Table 2, entry 5), an ester (Table 2, entries 6 and 7), a nitrile (Table 2, entry 8), and (enolizable) ketones (Table 2, entries 10–12). Importantly, a comparable yield of isolated product was also obtained in larger scale reactions (Table 2, entry 12).

The high catalytic activity also allowed for efficient arylation reactions of pyridine derivatives[25] as pronucleophiles by using aryl tosylates. Interestingly, the selectivity of the C–H bond activation could be controlled through the choice of electrophile (Table 3). Aryl chloride **10a** gave rise to double arylated product **11a**, even at lower reaction temperature (Table 3, entries 1, and 2), or shorter reaction times (Table 3, entries 3–5), with a catalytic activity superior to that observed using **4** as the preligand.[16] In contrast, on employing aryl tosylate **2k** as the electrophile the monoarylated product **12a** was formed selectively and isolated in good yield (Table 3, entry 6).

Importantly, this selectivity was also observed for differently substituted electrophiles and pyridine derivatives **9** (Table 4, entries 1–6). Furthermore, the catalyst allowed for the development of the first ruthenium-catalyzed regioselective arylation using a pyrazole as the directing group (Table 4, entries 7–11). Importantly, both aryl chlorides (Table 4, entry 7) as well as aryl tosylates (Table 4, entries 8–11) were applicable as electrophiles. As observed for pyridine derivatives (see above), the formation of either di- or monoarylated products was controlled through choice of electrophile.

In summary, we report the first direct arylation reactions through C–H bond activation using aryl tosylates. A highly active ruthenium catalyst derived from an air-stable secondary diaminophosphine oxide tolerates a wide variety of important functional groups and is applicable to pronucleophiles with different directing groups. In addition, the unprecedented use of pyrazole derivatives as the directing groups in ruthenium-catalyzed directed arylation reactions was demonstrated. The selective formation of either mono- or diarylated products can be controlled through the choice of electrophile.

 © 2006 Wiley-VCH Verlag GmbH & Co. KGaA, Weinheim

Table 2: Scope of C–H bond activation with oxazoline **1**.[a]

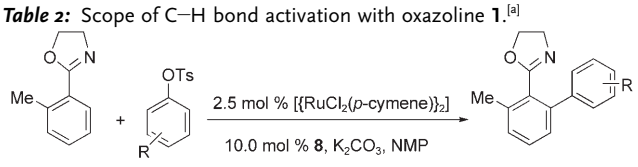

1 **2** **3**

Entry	Tosylate	Product	Yield [%]
1	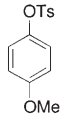 **2a**	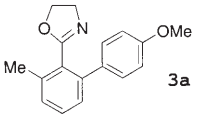 **3a**	71
2	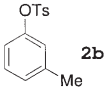 **2b**	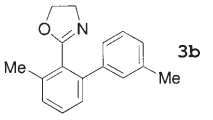 **3b**	81
3	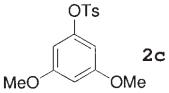 **2c**	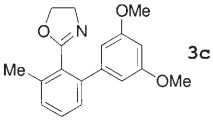 **3c**	51
4	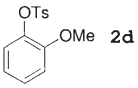 **2d**	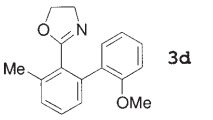 **3d**	50
5	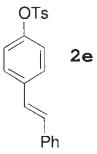 **2e**	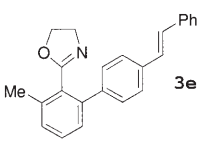 **3e**	85
6	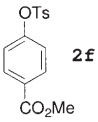 **2f**	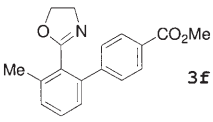 **3f**	93
7	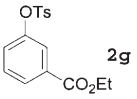 **2g**	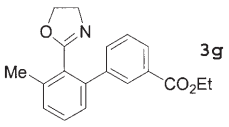 **3g**	73
8	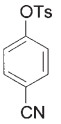 **2h**	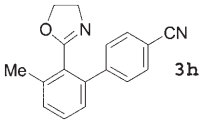 **3h**	59
9	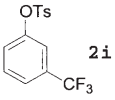 **2i**	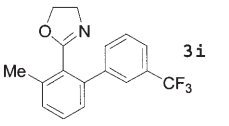 **3i**	96
10	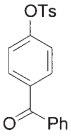 **2j**	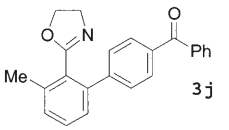 **3j**	94
11	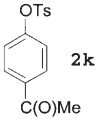 **2k**	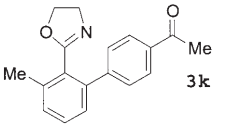 **3k**	93
12	**2k**	**3k**	92[b]

[a] Reaction conditions: **1** (1.0 mmol), **2** (1.2 mmol), [{$RuCl_2$(*p*-cymene)}$_2$] (2.5 mol%), **8** (10.0 mol%), NMP (2 mL), 120°C, 23 h; yield of isolated product. [b] Performed on a 15 mmol scale.

Table 3: Selective C–H bond arylation of phenyl pyridine **9a**.[a]

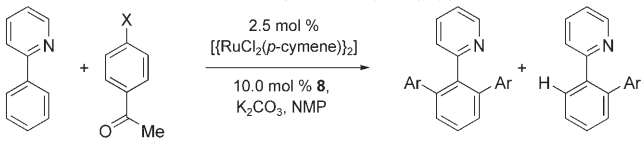

9a X = Cl **10a**; X = OTs **2k** **11a** **12a**

Entry	X	*T* [°C]	*t* [h]	**11a** [%]	**12a** [%]
1	Cl (**10a**)	85	24	58 (52)[b]	18
2	Cl (**10a**)	105	24	91 (85)[b]	7
3	Cl (**10a**)	120	1	56	38
4	Cl (**10a**)	120	2	71	26
5	Cl (**10a**)	120	5	91	9
6	OTs (**2k**)	120	24	<1	78 (65)[b]

[a] Reaction conditions: **9a** (1.0 mmol), **2k** or **10a** (2.2 mmol), [{$RuCl_2$(*p*-cymene)}$_2$] (2.5 mol%), **8** (10.0 mol%), NMP (2 mL); GC-analysis; Ar = 4-Me(O)CC_6H_4. [b] Yield of isolated product.

Experimental Section

Representative procedure for ruthenium-catalyzed cross-coupling reactions of aryl tosylates (Table 2, entry 10): A solution of [{$RuCl_2$(*p*-cymene)}$_2$] (15 mg, 0.025 mmol, 2.5 mol%), **8** (43 mg, 0.10 mmol, 10 mol%), K_2CO_3 (207 mg, 1.50 mmol), **1** (163 mg, 1.01 mmol), and **2j** (424 mg, 1.20 mmol) in dry NMP (2.0 mL) was stirred for 23 h at 120°C under N_2. Et_2O (75 mL) and H_2O (75 mL) were added to the reaction mixture at ambient temperature. The separated aqueous phase was extracted with Et_2O (2×75 mL). The combined organic layers were washed with H_2O and brine, dried over $MgSO_4$, and concentrated in vacuo. The remaining residue was purified by column chromatography on silica gel (*n*-pentane/Et_2O, 1/1→1/3) to yield **3j** as a pale brown solid (320 mg, 94%).

Received: December 14, 2005
Published online: March 17, 2006

Keywords: C–C coupling · C–H bond activation · homogeneous catalysis · ruthenium · secondary phosphine oxides

[1] M. Beller, C. Bolm, *Transition Metals for Organic Synthesis*, 2nd ed., Wiley-VCH, Weinheim, **2004**.
[2] A. de Meijere, F. Diederich, *Metal-Catalyzed Cross-Coupling Reactions*, 2nd ed., Wiley-VCH, Weinheim, **2004**.
[3] G. Dyker, *Handbook of C-H Transformations*, Wiley-VCH, Weinheim, **2005**.
[4] F. Kakiuchi, N. Chatani, *Adv. Synth. Catal.* **2003**, *345*, 1077–1101.
[5] V. Ritleng, C. Sirlin, M. Pfeffer, *Chem. Rev.* **2002**, *102*, 1731–1769.
[6] M. Miura, M. Nomura, *Top. Curr. Chem.* **2002**, *219*, 212–237.
[7] A. F. Littke, G. C. Fu, *Angew. Chem.* **2002**, *114*, 4350–4386; *Angew. Chem. Int. Ed.* **2002**, *41*, 4176–4211.
[8] R. B. Bedford, C. S. J. Cazin, *Chem. Commun.* **2002**, 2310–2311.
[9] E. Hennessy, S. L. Buchwald, *J. Am. Chem. Soc.* **2003**, *125*, 12084–12085.
[10] M. Leblanc, K. Fagnou, *Org. Lett.* **2005**, *7*, 2849–2852.
[11] L.-C. Campeau, M. Parisien, M. Leblanc, K. Fagnou, *J. Am. Chem. Soc.* **2004**, *126*, 9186–9187.
[12] M. Miura, T. Satoh, *Top. Organomet. Chem.* **2005**, *14*, 55–83.
[13] For recent use of palladium complexes generated from N-heterocyclic carbenes, see: L.-C. Campeau, P. Thansandote, K. Fagnou, *Org. Lett.* **2005**, *7*, 1857–1860.

 © 2006 Wiley-VCH Verlag GmbH & Co. KGaA, Weinheim

Table 4: Selective C–H bond arylation with aryl chlorides **10** or aryl tosylates **2**.[a]

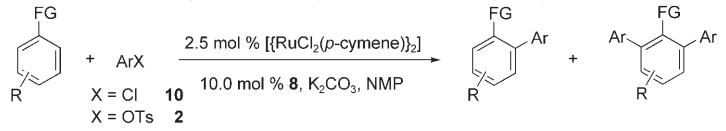

Entry	Pronucleophile	Electrophile	Product	Yield [%]
1	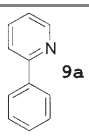 **9a**	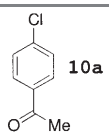 **10a**	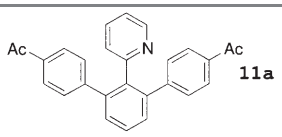 **11a**	87
2	**9a**	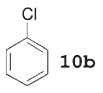 **10b**	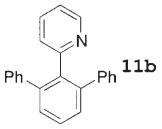 **11b**	99[b]
3	**9a**	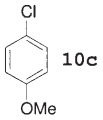 **10c**	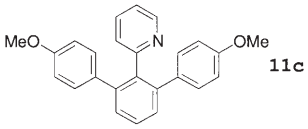 **11c**	91
4	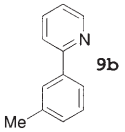 **9b**	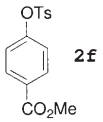 **2f**	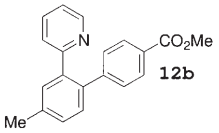 **12b**	56
5	**9b**	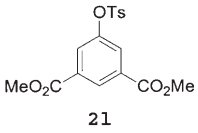 **2l**	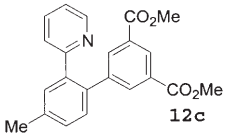 **12c**	56
6	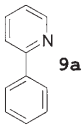 **9a**	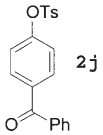 **2j**	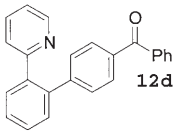 **12d**	54
7	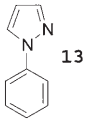 **13a**	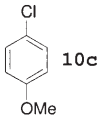 **10c**	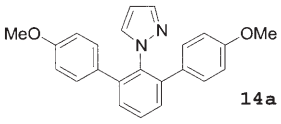 **14a**	81
8	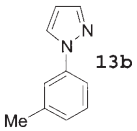 **13b**	**2f**	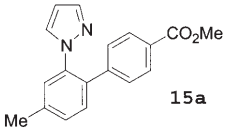 **15a**	61
9	**13b**	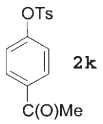 **2k**	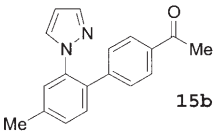 **15b**	51
10	**13a**	**2f**	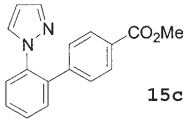 **15c**	55
11	**13a**	**2k**	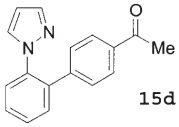 **15d**	57

[a] Reaction conditions: **9** or **13** (1.0 mmol), **2** (1.0–1.2 mmol) or **10** (2.2 mmol), [{$RuCl_2$(*p*-cymene)}$_2$] (2.5 mol%), **8** (10.0 mol%), NMP (2 mL), 120°C, 24 h; yield of isolated product; FG = functional group. [b] 8 h.

[14] Miura and co-workers reported on an elegant palladium-catalyzed arylation through C–C bond cleavage by using aryl chlorides as electrophiles and electron-rich PCy_3 as ligand: Y. Terao, H. Wakui, M. Nomoto, T. Satoh, M. Miura, M. Nomura, *J. Org. Chem.* **2003**, *68*, 5236–5243.

[15] F. Kakiuchi, N. Chatani in *Ruthenium in Organic Synthesis* (Ed.: S.-I. Murahashi), Wiley-VCH, Weinheim, **2004**, pp. 219–255.

[16] L. Ackermann, *Org. Lett.* **2005**, *7*, 3123–3125.

[17] For elegant ruthenium-catalyzed arylation reactions with aryl bromides, see: S. Oi, E. Aizawa, Y. Ogino, Y. Inoue, *J. Org. Chem.* **2005**, *70*, 3113–3119, and references therein.

[18] For traditional cross-coupling reactions with an alkyl-substituted secondary phosphine oxide, see: G. Y. Li, *Angew. Chem.* **2001**, *113*, 1561–1564; *Angew. Chem. Int. Ed.* **2001**, *40*, 1513–1516.

[19] L. Ackermann, R. Born, *Angew. Chem.* **2005**, *117*, 2497–2500; *Angew. Chem. Int. Ed.* **2005**, *44*, 2444–2447.

[20] J. R. Goerlich, A. Fischer, P. G. Jonas, R. Schmutzler, *Z. Naturforsch. B* **1994**, *49*, 801–811.

[21] Selected examples: a) V. Percec, G. M. Golding, J. Smidrkal, O. Weichold, *J. Org. Chem.* **2004**, *69*, 3447–3452; b) Z.-Y. Tang, Q.-S. Hu, *J. Am. Chem. Soc.* **2004**, *126*, 3058–3059; c) J. Zhou, G. C. Fu, *J. Am. Chem. Soc.* **2003**, *125*, 12527–12530; d) M. E. Limmert, A. H. Roy, J. F. Hartwig, *J. Org. Chem.* **2005**, *70*, 9364–9370; e) A. H. Roy, J. F. Hartwig, *J. Am. Chem. Soc.* **2003**, *125*, 8704–8705.

[22] For the use in nickel-catalyzed cross-coupling reactions of aryl chlorides and fluorides, see: L. Ackermann, R. Born, J. H. Spatz, D. Meyer, *Angew. Chem.* **2005**, *117*, 7382–7386; *Angew. Chem. Int. Ed.* **2005**, *44*, 7216–7219.

[23] T. G. Gant, A. I. Meyers, *Tetrahedron* **1994**, *50*, 2297–2360.

[24] Reactions conducted in either PhMe, DMF, or DMSO gave no conversion of aryl tosylate **2a** under otherwise identical reaction conditions.

[25] Representative examples for the use of pyridine groups as directing groups in direct arylation reactions: a) S. Oi, S. Fukita, Y. Inoue, *Chem. Commun.* **1998**, 2439–2440; b) S. Oi, S. Fukita, N. Hirata, N. Watanuki, S. Miyano, Y. Inoue, *Org. Lett.* **2001**, *3*, 2579–2581; c) D. Kalyani, N. R. Deprez, L. V. Desai, M. S. Sanford, *J. Am. Chem. Soc.* **2005**, *127*, 7330–7331; d) D. Shabashov, O. Daugulis, *Org. Lett.* **2005**, *7*, 3657–3659.

© 2006 Wiley-VCH Verlag GmbH & Co. KGaA, Weinheim

Benzomorphan Synthesis

DOI: 10.1002/anie.200504090

Stereoselective Synthesis of Benzomorphan Derivatives with Perpivaloylated Galactose as the Chiral Auxiliary**

*Ellen Klegraf, Stephan Knauer, and Horst Kunz**

Chiral bicyclic piperidine derivatives are important pharmacophoric structural elements. Despite its undesired side effects, morphine **1**, the prototype of current opiod analgesics,

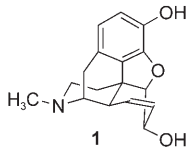

1

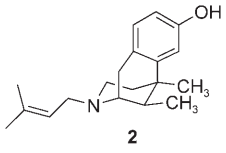

2

is still indispensable in pain management.[1] Starting from morphine as a lead structure, many analogues have been synthesized. These differ in the spectrum of side effects, but they most often also show lower activity on the opiod receptors. Pentazocine **2**, a representative of this structural class, has potent analgesic properties but has lower affinity to the μ receptor responsible for the addictive effect.[2]

In pentazocine **2** the polycyclic structure of morphine **1** is reduced to a tricyclic benzomorphan system. It still contains the pharmacologically essential hydroxy functionality on the aromatic ring. The substituted benzomorphan scaffold therefore has potential as a lead structure in the search for new drug candidates with selective activity on opiate receptors.

We report short stereoselective syntheses of 6,7- and 7,8-benzomorphans. To obtain the 6,7-annelated derivatives, 2-benzyl-substituted 5,6-didehydropiperidin-4-ones were applied to a domino Suzuki–Heck coupling sequence. 7,8-Benzomorphans were accessible by an acid-catalyzed cyclization of 4-benzyl-substituted 5,6-didehydropiperidin-2-ones. The employed *O*-pivaloylated D-galactose auxiliary determined the stereoselectivity of both reactions.

The synthesis of the 6,7-benzomorphan derivatives started with the condensation of halogen-substituted phenylacetic aldehydes[3] **4** and 2,3,4,6-tetra-*O*-pivaloyl-β-D-galactopyranosylamine[4] (**3**). The formation of the corresponding *N*-galactosyl imines **5** proceeded smoothly at room temperature under dehydrating conditions. Higher temperatures, longer reaction times, and acid catalysis led preferentially to the formation of the undesired conjugated enamines. In a Lewis acid catalyzed tandem Mannich–Michael reaction[5] the aldimines **5** were reacted with 1-methoxy-3-trimethylsiloxybutadiene[6] (**6**) to form *N*-galactosyl 2-benzyl-didehydropiperidinones **7** (Scheme 1).

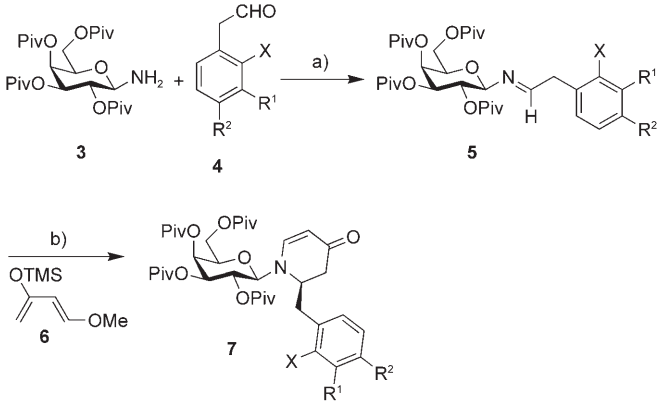

X = Cl, R^1 = H, R^2 = H, 53 %, d.r. 90:10
X = Br, R^1 = H, R^2 = H, 70 %, d.r. 94:6
X = I, R^1 = H, R^2 = H, 32 %, d.r. 95:5
X = Br, R^1 = OBn, R^2 = OMe, 38 %, d.r. 95:5

Scheme 1. Diastereoselective synthesis of 2-benzyl-5,6-dehydropiperidinones **7**: a) MS (4 Å), *i*PrOH, room temperature, 1 h; b) $ZnCl_2$, **6**, THF, −78 °C→−20 °C, 1 d, then 1 N HCl.

The efficient shielding of the *Re* face of the imine double bond by the bulky pivaloyloxy group in the 2-position of the carbohydrate moiety led to a highly stereoselective formation of the asymmetric center in the heterocycle. The diastereoselectivity of the ring formation increased with the size of the *o*-halogen substituent on the aromatic moiety. Unfortunately, the yields decreased in the same order. Upon treatment with L-Selectride, the didehydropiperidinones **7** easily underwent a chemoselective conjugate hydride addition to the enone system.[7] The corresponding enolates were *O*-sulfonated by the addition of *N*-phenylbis(trifluoromethanesulfonyl)-imide[8] to the reaction mixture which gave the enol triflates **8** (Scheme 2).

As previously described, enol triflates of type **8** are suitable substrates for palladium-catalyzed cross-couplings. In Suzuki–Miyaura reactions with aromatic boronic acids they formed 2,4-disubstituted 4,5-didehydropiperidines.[7] In the case of the *o*-bromobenzyl derivatives **8** the reaction proceeded further after the initial coupling with the boronic acid in 4-position and led to tricyclic benzomorphan structures **9** (Scheme 2). The subsequent intramolecular Heck cyclization stereoselectively formed a new quaternary carbon center in the 4-position of the piperidine ring. The attack was controlled by the configuration of the benzyl substituent in the 2-position and thus occurred exclusively from the top face of the *endo* double bond. A Heck olefination on a similar structure has already been used in the enantioselective synthesis of (−)-morphine by Overman et al. to build the

[*] Dr. E. Klegraf, Dr. S. Knauer, Prof. Dr. H. Kunz
Institut für Organische Chemie
Johannes Gutenberg-Universität Mainz
Duesbergweg 10–14, 55128 Mainz (Germany)
Fax: (+49) 6131-392-4786
E-mail: hokunz@uni-mainz.de

[**] This work was supported by the Deutsche Forschungsgemeinschaft, Aventis Pharma Deutschland GmbH, and the Fonds der Chemischen Industrie. We thank Dr. Dieter Schollmeyer, Institut für Organische Chemie of the Universität Mainz, for the X-ray structure analysis.

 © 2006 Wiley-VCH Verlag GmbH & Co. KGaA, Weinheim

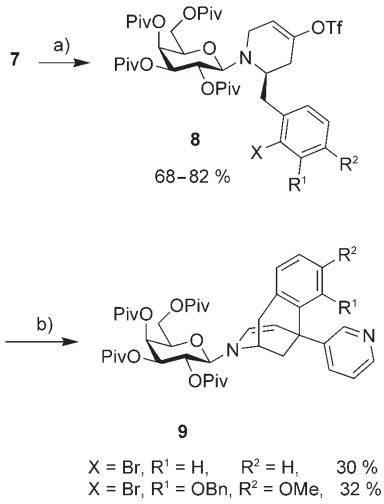

Scheme 2. Formation of the enol triflates **8** and domino Suzuki–Heck coupling to give the corresponding benzomorphans: a) L-Selectride, $PhNTf_2$, THF, −78 °C→ room temperature, 2 h; b) 3-pyridineboronic acid, $[Pd(PPh_3)_2Cl_2]$, Cs_2CO_3, DMF (trace of H_2O), *hν*, 20 min at 80 °C, then 20 min at 100 °C. Tf = trifluoromethanesulfonyl.

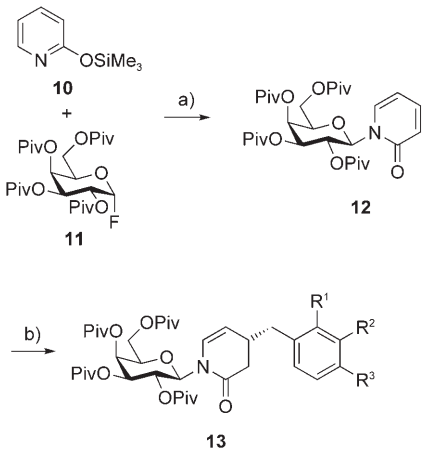

Scheme 3. Regio- and diastereoselective synthesis of **13**: a) 1,2-dichloroethane, 70 °C, $TiCl_4$, 2 h, 99%; b) TIPSOTf, DCM, room temperature, 1 h, then 2,6-lutidine, RMgX, 20 °C, 2 h (Table 1).

quaternary carbon in the 5-position of the benzomorphan structure as a key step.[9]

Further investigations into the domino Suzuki–Heck reaction with 3-pyrimidine boronic acid as the coupling partner showed that traces of water and the choice of the employed halogen were essential for the outcome of the reaction. In the absence of water no conversion was observed because the initial Suzuki cross-coupling did not occur. On the other hand, the presence of too much water led to side reactions in the Heck cyclization. Best results were achieved with microwave irradiation which resulted in a significant reduction of the reaction time to give the *N*-galactosyl 3,4-didehydro-6,7-benzomorphans **9** in moderate yields (Scheme 2).

The stereochemical course of the Heck coupling and the formation of the quaternary center are determined by the configuration of **8**. The orientation of the halogenated benzyl substituent in **8** allows approach of the coupling partner only from the *Si* face of the double bond and only one diastereomer results. In contrast, iodobenzyl derivatives did not undergo the Heck cyclization. Instead a (second) Suzuki cross coupling with the *ortho* position of the benzylic substituent took place. The corresponding chloro compound could be selectively converted to the 2,4-disubstituted 4,5-didehydropiperidine but further Heck olefination did not proceed even when tri-*tert*-butylphosphine ligands were used.[10]

An alternative strategy led to the stereoselective formation of 7,8-benzomorphans. β-Selective *N*-glycosylation of 2-(trimethylsilyloxy)pyridine **10** with *O*-pivaloylated galactosyl fluoride **11** gave the *N*-galactosyl 2-pyridone **12** in excellent yield (Scheme 3).[11] This unsaturated heterocyclic structure was transformed regio- and stereoselectively by reaction with benzyl Grignard reagents. After activating *O*-silylation using triisopropylsilyltrifluoromethanesulfonate (TIPSOTf), the Grignard addition gave 4-benzylated 5,6-didehydropiperidin-2-ones **13** in moderate to excellent yields (Table 1). The regioselectivity and the high diastereomeric ratio of this process was determined by the facial differentiation of the carbohydrate auxiliary.[12] Previously published syntheses using the same benzylpiperidine moiety to form 7,8-benzomorphans required highly activated aromatic systems and proceeded in a nonregioselective manner.[13,14]

Table 1: Stereoselective synthesis of 4-substituted *N*-galactosyl 4-benzyldidehydropiperidinones (Scheme 3).

Cmpd.	RMgX	Yield [%]	d.r. (*R*/*S*)[a]
13a	BnMgCl	73	>99:1
13b	*m*-$MeC_6H_4CH_2MgCl$	83	92:8
13c	*m*-$MeOC_6H_4CH_2MgCl$	41	86:14
13d	*m*-$ClC_6H_4CH_2MgCl$	66	>99:1
13e	*m*-$BrC_6H_4CH_2MgBr$	30	>99:1
13f	*p*-$MeC_6H_4CH_2MgCl$	88	85:15
13g	*p*-$MeOC_6H_4CH_2MgCl$	98	92:8
13h	*p*-$ClC_6H_4CH_2MgCl$	61	94:6
13i	*o*-$MeC_6H_4CH_2MgCl$	98	91:9
13j	*o*-$BrC_6H_4CH_2MgBr$	52	>99:1
13k	2,5-$Me_2C_6H_3CH_2MgCl$	63	92:8
13l	2,4-$Me_2C_6H_3CH_2MgCl$	34	89:11
13m	3,5-$(MeO)_2C_6H_3CH_2MgCl$	54	82:18
13n	1-NaphtCH_2MgCl[b]	68	>99:1

[a] 400 MHz ^1H NMR spectrum and analytical HPLC. [b] Napht = naphthyl; the C-6 regioisomer is formed in < 5% yield.

In the case of the 4-benzyldidehydropiperidinones **13**, the intramolecular aminoalkylations took place at low temperatures in the presence of a mixture of $HCl/SnCl_4$. The intermediate *N*-acyl iminium ion **14** underwent cyclization to yield the tricyclic benzazocinones **15** (Scheme 4). Thus, this synthesis provided 7,8-benzomorphans **15** in high yields and is a significant improvement over previous syntheses of the tricyclic core via *N*-acyl iminium species.[13c,d,14] The electrophilic attack at the phenyl ring occurred exclusively from the *cis* side. The X-ray structure analysis of **15a** shows the diaxial

 © 2006 Wiley-VCH Verlag GmbH & Co. KGaA, Weinheim

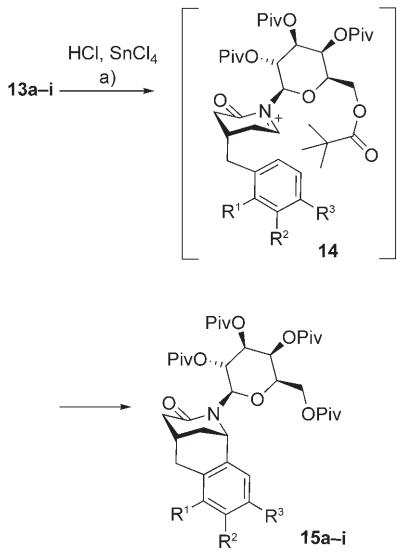

Scheme 4. Acid-catalyzed intramolecular aminoalkylation: a) HCl (4 equiv), $SnCl_4$ (2 equiv), CH_2Cl_2, −78 °C→20 °C.

configuration on the piperidine ring of the 7,8-benzomorphan (Figure 1).[15]

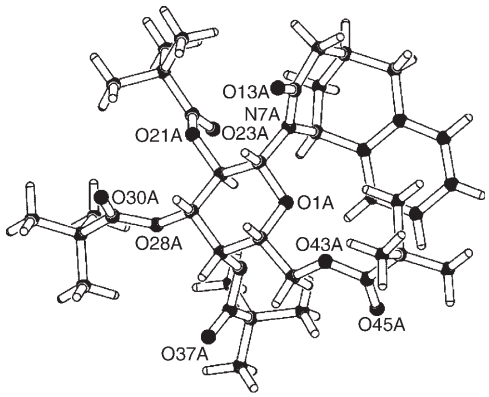

Figure 1. X-ray structure analysis of **15a**.

The diversity of the stereoselective ring formation was demonstrated by applying a large variety of differently substituted 4-benzyldidehydropiperidinones **13b–13n** (Scheme 4, Table 2). Benzyl derivatives with electron-donating groups (+I and +M) as well as halogen-substituted compounds were easily transformed into the corresponding 7,8-benzomorphans **15** (Table 2). The conversions of the deactivated aromatics (**13d**, **13e**, **13h**, **13j**) were incomplete.[16] The regioselectivity of the cyclization of the *meta*-substituted derivatives **13b–e** ($R^1 = H$) is supported by the favored reaction in *para* position, and, in addition, by the 6-pivaloyloxy group of the galactose auxiliary (Scheme 4). The aminoalkylation of the disubstituted benzylic compounds **13k–m** as well as the naphthylmethyl derivative **13n** proceeded regio- and stereoselectively in high yields (Table 3).

Table 2: Cyclization of monosubstituted compounds **13a–j** (Scheme 4).

Cmpd.	R^1	R^2	R^3	Yield [%]	*t* [h]
15a	H	H	H	85	18
15b	H	Me	H	83	8
15c	H	OMe	H	85	10
15d	H	Cl	H	48[a]	20
15e	H	Br	H	58[a]	15
15f	H	H	Me	84	8
15g	H	H	OMe	67	12
15h	H	H	Cl	52[a]	22
15i	Me	H	H	71	8
15j	Br	H	H	69[a]	48

[a] Incomplete conversion.

Table 3: Intramolecular reaction of disubstituted compounds **13k–13n**.

Starting cmpd.	Product[a]		Yield [%]	*t* [h]
13k	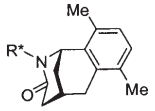	**15k**	83	8
13l	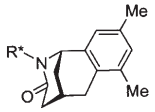	**15l**	88	8
13m	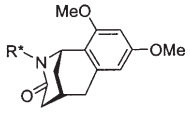	**15m**	87	8
13n	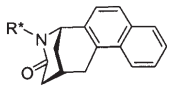	**15n**	72	8

[a] R* = 2,3,4,6-Tetra-*O*-pivaloyl-galactose.

To release the 7,8-benzomorphan moiety from the carbohydrate auxiliary the diastereomerically pure benzazocine **15a** was treated with Lawesson's reagent[17] to give the corresponding thioamide, which was subsequently desulfurated on Raney nickel to give **16** (Scheme 5). Acidic cleavage of the *N*-glycosidic bond using aqueous HCl in methanol gave the 7,8-benzomorphan hydrochloride **17** in almost quantitative yield.

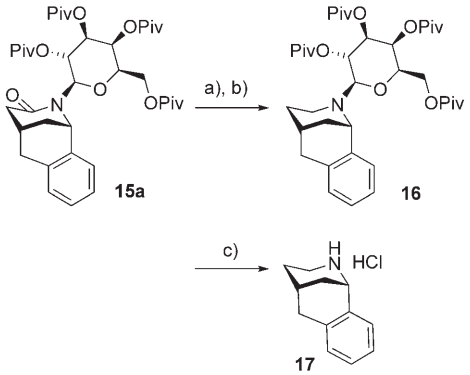

Scheme 5. Synthesis of 7,8-benzomorphan: a) Lawesson's reagent (0.5 equiv), toluene, 110 °C, 1.5 h, 83%; b) Raney Ni, H_2, *i*PrOH, 70 °C, 2 h, 74%; c) 2 N HCl in methanol, 20 °C, 24 h, 96%.

 © 2006 Wiley-VCH Verlag GmbH & Co. KGaA, Weinheim

Herein we have described a stereoselective approach to the regioisomeric series of 6,7- and 7,8-benzomorphans employing benzyl-substituted *N*-galactosyl didehydropiperidinones. In both processes the galactosyl auxiliary exhibits excellent stereo- and regiocontrol in the key steps. The corresponding enantiomeric products are accessible by use of the quasi-enantiomerc D-arabinosyl auxiliary.[18]

Received: November 17, 2005
Published online: March 20, 2006

Keywords: aminoalkylation · asymmetric synthesis · benzomorphans · chiral auxiliaries · domino reactions

[1] J. Frackenpohl, *Chem. Unserer Zeit* **2000**, *34*, 99 – 112.
[2] a) D. H. Jenkinson, E. A. Barnard, D. Hoyer, P. P. A. Humphrey, P. Leff, N. P. Shankley, *Pharmacol. Rev.* **1995**, *47*, 255 – 266; b) T. Christoph, H. Buschmann, *Pharm. Unserer Zeit* **2002**, *31*, 40 – 43; c) R. N. Brodgen, T. M. Speight, C. S. Avery, *Drugs* **1978**, *16*, 473 – 505.
[3] a) P. Mosset, R. Grée, *Synth. Commun.* **1985**, *15*, 749 – 757; d) B. C. Ranu, U. Jana, *J. Org. Chem.* **1998**, *63*, 8212 – 8216; c) S. Wiegand, H. J. Schäfer, *Tetrahedron* **1995**, *51*, 5341 – 5350; b) S. E. Gibson, N. Guillo, R. J. Middleton, A. Thuilliez, M. J. Tozer, *J. Chem. Soc. Perkin Trans. 1* **1997**, 447 – 455.
[4] H. Kunz, W. Sager, D. Schanzenbach, M. Decker, *Liebigs Ann. Chem.* **1991**, 649 – 654.
[5] a) H. Kunz, W. Pfrengle, *Angew. Chem.* **1989**, *101*, 1041 – 1042; *Angew. Chem. Int. Ed. Engl.* **1989**, *28*, 1067 – 1068; b) M. Weymann, W. Pfrengle, D. Schollmeyer, H. Kunz, *Synthesis* **1997**, 1151 – 1160; c) M. Weymann, M. Schultz-Kukula, H. Kunz, *Tetrahedron Lett.* **1998**, *39*, 7835 – 7838; d) M. Weymann, M. Schultz-Kukula, S. Knauer, H. Kunz, *Monatsh. Chem.* **2002**, *133*, 571 – 587.
[6] S. J. Danishefsky, T. Kitahara, *J. Am. Chem. Soc.* **1974**, *96*, 7807 – 7808.
[7] S. Knauer, H. Kunz, *Tetrahedron: Asymmetry* **2005**, *16*, 529 – 539.
[8] D. L. Comins, L. A. Morgan, *Tetrahedron Lett.* **1991**, *32*, 5919 – 5922.
[9] C. Y. Hong, N. Kado, L. E. Overman, *J. Am. Chem. Soc.* **1993**, *115*, 11028 – 11029.
[10] A. F. Littke, G. C. Fu, *Angew. Chem.* **2002**, *114*, 4350 – 4386; *Angew. Chem. Int. Ed.* **2002**, *41*, 4176 – 4211.
[11] a) M. Follmann, H. Kunz, *Synlett* **1998**, *9*, 989 – 990; b) M. Follmann, A. Rösch, E. Klegraf, H. Kunz, *Synlett* **2001**, *10*, 1569 – 1570.
[12] E. Klegraf, M. Follmann, D. Schollmeyer, H. Kunz, *Eur. J. Org. Chem.* **2004**, 3346 – 3360.
[13] a) K. Mitsuhashi, S. Shiotani, R. Oh-Uchi, K. Shiraki, *Chem. Pharm. Bull.* **1969**, *17*, 434 – 453; b) T. Kometani, S. Shiotani, *J. Med. Chem.* **1978**, *21*, 1105 – 1110; c) J. Bosch, J. Bonjoch, A. Diez, A. Linares, M. Moral, M. Rubiralta, *Tetrahedron* **1985**, *41*, 1753 – 1762, and references therein; d) J. Bosch, M. Rubiralta, M. Moral, J. Arino, *J. Chem. Soc. Perkin Trans. 1* **1986**, 1533 – 1539.
[14] a) J. Bosch, J. Canals, R. Granados, *J. Heterocycl. Chem.* **1975**, *12*, 1117 – 1121; b) M. Rubiralta, A. Diez, J. Bosch, *Heterocycles* **1988**, *27*, 785 – 788.
[15] X-ray structure analysis of **15a** (MeOH): triclinic, space group $P1$, $a = 10.951(2)$, $b = 13.406(2)$, $c = 15.086(3)$ Å, $\alpha = 105.61\ (2)$, $\beta = 106.08(1)$, $\gamma = 104.65\ (1)°$. At a cell volume of $V = 1917.0(7)$ Å^3, two independent molecules and $M_r = 685.83$ results in a density of $d = 1.188\ \mathrm{g\,cm^{-3}}$. Total number of electrons per elemental cell $F(000) = 740$. Diffractometer CAD4, $Cu_{K\alpha}$ graphite monochromator. Scan type $\omega/2\theta$, scan width $0.9 + 0.15\tan(\theta)$. Measuring range $2° \le \theta < 70°$, $-13 \le h \le 13$, $-16 \le k \le 16$, $-18 \le l \le 18$. Measured reflex number: 14163, independent: 13426 ($R_{int} = 0.0130$), observed: 13229 ($|F|/\sigma(F) > 4.0$). Corrections: Lorentz and polarization correction. Intensity decline of ca. 5% corrected with cubic spline; solution: program: SIR-92 (direct method), refinement: program: SHELXL-97. CCDC 283243 contains the supplementary crystallographic data for this paper. These data can be obtained free of charge from The Cambridge Crystallographic Data Centre via www.ccdc.cam.ac.uk/data_request/cif.
[16] With long reaction times, cleavage of the 6-pivaloyl protecting group (ca. 10%) from the cyclized product was observed.
[17] S. Scheibye, B. S. Pedersen, S.-O. Lawesson, *Bull. Soc. Chim. Belg.* **1978**, *87*, 229 – 238.
[18] B. Kranke, D. Hebrault, M. Schultz-Kukula, H. Kunz, *Synlett* **2004**, 671 – 674.

 © 2006 Wiley-VCH Verlag GmbH & Co. KGaA, Weinheim

Blood-Group Typing

DOI: 10.1002/anie.200502857

Biomimetic ABO Blood-Group Typing**

*Oliver Hayden, Karl-J. Mann, Stefan Krassnig, and Franz L. Dickert**

Dedicated to Professor Rolf W. Saalfrank on the occasion of his 66th birthday

Molecularly imprinted polymers (MIPs) with synthetic recognition sites are capable of detecting chemical species in complex environments.[1] These properties are of increasing interest for bioanalytical applications.[2,3] The most significant advantages of MIPs are mechanical and chemical stability, low cost, and ease of preparation.[4] Recently, surface imprinting has been applied to form artificial receptors on polymer thin films accessible for proteins,[5] plant viruses,[6] and yeasts.[7] Here, we demonstrate surface imprinting for the recognition of mammalian cells. Erythrocyte-specific interactions are achieved with recognition sites on surface-imprinted polyurethane applicable for blood-group (BG) typing of the main ABO antigens. This finding in establishing MIPs to recognize bulky analytes is highly relevant for clinical applications such as serology.

[*] Dr. O. Hayden, Dr. K.-J. Mann, Mag. S. Krassnig, Prof. F. L. Dickert
Institute of Analytical Chemistry and Food Chemistry
University of Vienna
Währingerstrasse 38, 1170 Vienna (Austria)
Fax: (+43) 1-4277-9523
E-mail: franz.dickert@univie.ac.at

[**] This work was supported by the FWF, the Austrian Science Fund (project number P15512).

Supporting information for this article is available on the WWW under http://www.angewandte.org or from the author.

WILEY InterScience DISCOVER SOMETHING GREAT
© 2006 Wiley-VCH Verlag GmbH & Co. KGaA, Weinheim

The blood groups A, B, AB, and O are usually determined by passing a sample through a dextran gel containing immobilized antibodies followed by centrifugation. If the blood group corresponds to the antibody, a precipitate forms.[8] Innovative automated systems are available that monitor this reaction on a surface by changes in the reflectance of a laser beam. The MIPs we propose function reversibly, however, and no expensive reagents are necessary.

Our surface-imprinting concept depicted in Figure 1 is based on a soft-lithographic synthesis of MIPs directly on a transducer coated with a polymerizing thin film. This rational

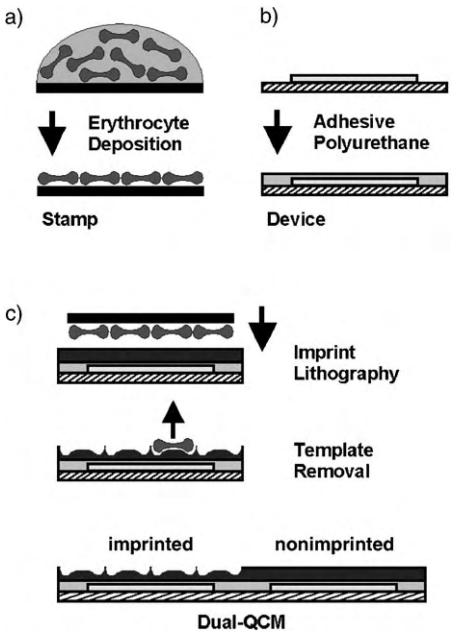

Figure 1. Surface imprinting with soft lithography. a) Erythrocyte or "ghost" monolayers were deposited from a suspension on a microscope slide used as the stamp. b) Microbalances were precoated with a 100-nm polyurethane layer to improve the adhesion of the MIP layer. c) The stamp was pressed onto a prepolymerized polyurethane layer covering the sensitive electrode. After curing, the stamp and templates were removed in hot water and 0.5% sodium dodecylsulfate (SDS) solution. The reference channel on the dual microbalance was coated with nonimprinted polyurethane.

fabrication of closely packed recognition sites is compatible with technological processes for potential large-scale production and does not require expensive antibodies. Stamps covered with monolayers of red blood cells were prepared on microscope slides (Figure 2a). The cavities on the molded polyurethane surface correspond to the doughnut-shaped topography of the erythrocytes (Figure 2b,c). The cells form imprints with depths up to 500 nm (Figure 2d). The nonimprinted layer on the reference electrode, which is produced by spin coating, is smooth (see Supporting Information).

The bioimprinting was performed on microbalances with two electrodes for differential measurements; one electrode was used as a nonimprinted reference to eliminate viscosity effects.[9] We take advantage of the dual construction to observe selective and nonselective adsorption of red blood

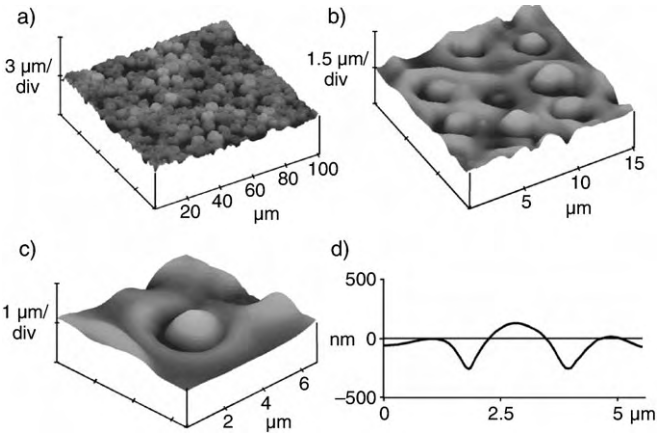

Figure 2. AFM characterization of the erythrocyte imprinting. a) The AFM micrograph shows a densely packed layer of erythrocytes deposited on the stamp. b) The templating red blood cells mold the polyurethane layer **I** during imprinting. c) Imprint site of a single red blood cell. The annular cavities with a central elevation depict the doughnut shape of the templating erythrocytes. d) Section analyses of the single imprint shown in (c).

cells on imprinted and nonimprinted polyurethane under identical conditions.

The adsorption of suspensions of red blood cells on polyurethane imprinted with or nonimprinted with blood group A (BG A) erythrocytes is shown in Figure 3a. The erythrocyte concentration is more than two orders of magnitude more dilute than that in whole blood ($4–5 \times 10^9$ cells mL^{-1}). Imprinted surfaces show selective adsorption of erythrocytes of blood group A, whereas minor nonselective adsorption is observed with nonimprinted polyurethane. The nonselective adsorption increases from about 5% of the specific effect under flow conditions to 20% when the flow has stopped because of sedimentation. Erythrocytes of type B show only one-third of the adsorption of blood group A, indicating a blood-type-selective recognition. It is noteworthy that the nonselective adsorption of BG B cells is the same as that of BG A.

To demonstrate the selectivity of the MIP layers for intact cells, we exposed the sensor to a suspension of mechanically ruptured blood cells (Figure 3b). The rupturing of the blood cells was performed with a peristaltic pump and monitored by optical microscopy. The ruptured BG A cells show the same nonselective adsorption on both the imprinted and nonimprinted polyurethane layers, whereas the injection of a fresh sample of intact BG A cells resulted again in selective recognition on the imprinted polyurethane. Cellular integrity is therefore a necessity for the cell-recognition event.

The cross-selectivities of polyurethane-imprinted layers **I** (see Experimental Section) are summarized in Figure 4a. All erythrocyte concentrates were diluted to 1×10^7 cells mL^{-1}, and the adsorption was recorded under stopped-flow conditions with response times of 10 min. In all cases the imprinted sensor layers showed the highest sensitivity for the template blood group. The nonselective response on the reference channel was approximately 2 kHz for all blood types tested. The same selectivity pattern was observed with

 © 2006 Wiley-VCH Verlag GmbH & Co. KGaA, Weinheim

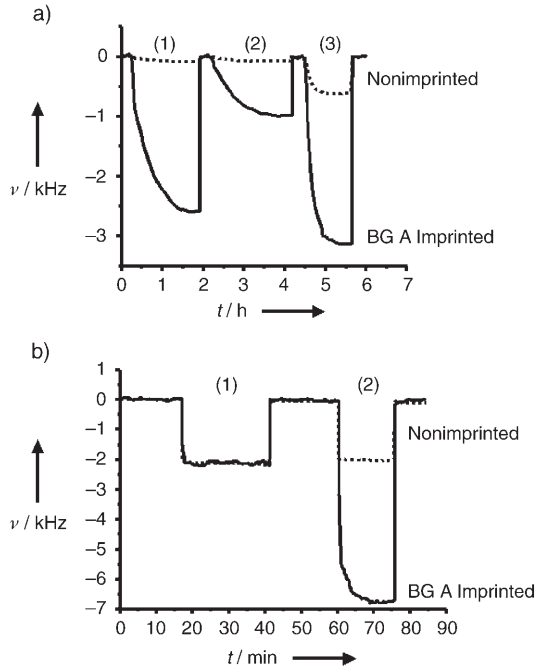

Figure 3. Characterization of coated dual QCM for differential measurements. a) The selective and nonselective adsorption of red blood cells is shown on BG A-imprinted (——) and nonimprinted polyurethane **I** (•••••), respectively. Suspensions of (1) 1×10^7 cells mL^{-1} of BG A and (2) BG B were injected with a flow rate of 2 mL min^{-1} in a flow cell with a volume of 150 µL. For comparison, (3) 1×10^7 cells mL^{-1} of BG A was adsorbed without flow. b) The frequency shift due to the adsorption of degraded (1) and freshly prepared (2) BG A samples of 1×10^9 cells mL^{-1} are shown on imprinted (——) and nonimprinted polyurethane **II** (•••••) after injection of the blood sample.

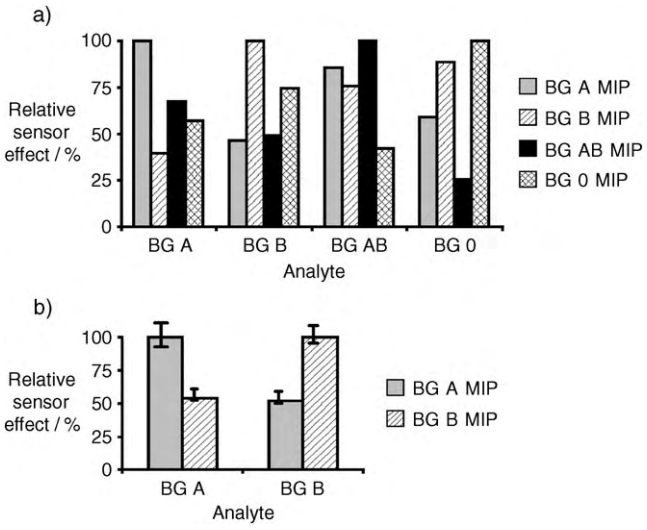

Figure 4. Selectivity of ABO-specific MIP sensors consisting of polyurethanes **I** and **II**. a) The selectivity of ABO-imprinted layers (differential measurements); the highest sensitivities were observed when the analyte and template were the same type of erythrocyte. All measurements were performed with blood samples of 1×10^7 cells mL^{-1} under stopped-flow conditions. b) Blood-group typing with whole blood samples. Polyurethane **II** imprinted with either BG A or BG B cells was selective for the detection of template-analogue erythrocytes (differential measurements).

red blood cell concentrations of 1×10^7 and 10^9 cells mL^{-1}. The frequency response of polyurethane **II** imprinted with blood group AB to different blood types is illustrated in the Supporting Information.

The size and shape of the erythrocytes is the same for all blood groups. The selective recognition of the erythrocytes by the MIPs therefore depends on differences in cell surface rather than geometric form. This is quite remarkable since simple sedimentation of bulky red blood cells results in a strong frequency decrease, and it should not be possible to determine subtle changes in the recognition event.

The carbohydrate antigens of the ABO system are the most dominant antigens on the glycocalix surface of erythrocytes.[10] The density of ABO antigens on red blood cells (10^5–10^6 antigen copies per cell),[11] is up to 100 times higher than those of protein epitopes of the Rhesus system or other antigens. Specifically, the density of ABO antigens exceeds that of the Rhesus proteins by a factor of approximately 10–30,[12] and consequently ABO antigens are decisive for detection. Furthermore, all of our blood samples were Rhesus positive. Therefore, we can assume a negligible influence of other erythrocyte antigens on the cellular imprinting.

The main difference between the A and B antigens is determined by the terminal carbohydrate units on the BG O antigen, *N*-acetylgalactosamine and galactose, respectively. Unmodified O-antigen sites are also present on membrane surfaces of erythrocytes of blood group A (up to 10%) and B (up to 50%).[9] The BG O-imprinted layers thus display appreciable cross-sensitivity to BG A and BG B cells (Figure 4). Furthermore, since BG B is more similar to BG O, the sensor response is more pronounced for BG B than for BG A. As Figure 4 shows an unambiguous assignment of the blood-group types is possible. The strongest sensor response was always obtained when the analyte was identical to the template. The signals of BG A and BG B differ appreciably depending on which imprinted MIP was used, and the signals are nearly identical when MIP imprinted with BG AB was used. BG O and BG AB are also easily distinguished in Figure 4.

The selective recognition obtained in buffered suspension was even observed with whole blood from eight donors as well as with concentrated erythrocyte samples. Freshly prepared whole blood samples of types A and B were diluted to give suspensions with a concentration of 1×10^7 erythrocytes mL^{-1}. Figure 4b shows the selectivity pattern achieved with these samples on polyurethane **II**, which was imprinted with BG A and BG B. The cross-selectivity of each MIP layer in experiments with whole blood was identical to that obtained with the erythrocyte concentrate though the absolute frequency decreased threefold. The decrease in sensitivity is attributed to the blood serum, which leads to increased nonspecific adsorption on imprinted surfaces. These results confirm that imprinted polymers can be applied to real-life samples.

From the selectivities obtained with the biomolecularly imprinted layers it can be concluded that during the surface-imprinting procedure the cells do not only leave behind cavities in the appropriate size and shape. The surface of the

 © 2006 Wiley-VCH Verlag GmbH & Co. KGaA, Weinheim

red blood cells acts as a template for their recognition on the polymer surface. The polyurethanes applied contain excess hydroxy functionalities. It is therefore supposed that the selective recognition is driven by hydrogen bonds to sugar residues defining the major blood group type on the cell membrane. In future work we will apply the bioimprinting concept for further in-depth studies of cell antigen recognition.

Experimental Section

Preparation of erythrocyte stamps and "ghost" (erythrocyte membrane) stamps: Whole blood samples from individual donors were provided by the Medical University of Vienna. Erythrocyte concentrates of individual donors containing approximately 5×10^9 erythrocytes mL^{-1} were purchased from the Red Cross Blood Donation Center in Vienna. The buffer system of the concentrates was exchanged with an isotonic NaCl (190 mM) solution. Erythrocyte ghosts were generated by osmolysis in dilute buffers or distilled water at 4 °C for 15 min.[13] Ghosts were centrifuged at 4000 g for 15 min. The procedure was repeated to achieve the desired purity of the ghosts. The stamp was made by applying several microliters of this sample to a microscope slide. The excess suspension was removed by spinning at 3000 rpm after sedimentation.

Polyurethane layers and soft lithography: Equimolar mixtures of 4,4′-diisocyanatodiphenylmethane (MDI, 48.8 mg) and bisphenol A (51.2 mg) in 100 μL of anhydrous THF were prepolymerized up to the gelling point at 65 °C under inert gas. The prepolymer was diluted to 1:25, spin-coated onto the QCMs at 4000 rpm, and cured in nitrogen at 125 °C for 3 h. This layer was used as an adhesive layer for improved adhesion of the MIP layer.

Polyurethanes consisting of MDI, bisphenol A, and phloroglucinol as the cross-linker with an excess of hydroxy groups were used for surface imprinting. The polymer layers with the following ratios of functionalities were pre-polymerized as described before with the adhesive layer: **I**: OH/NCO = 2:1 and **II**: OH/NCO = 1.5:1 with 12% cross-linker. The 1:5-diluted solution was spinned onto the coated QCMs at 2000 rpm. The erythrocyte-covered stamp was gently pressed into the polymerizing layer and cured over night at room temperature. The rupturing of dehydrated red blood cells during imprinting can be avoided by appropriate handling.[14] The stamp was removed in hot water, and the templating cells were washed off with 0.5% sodium dodecylsulfate solution. AFM measurements in contact mode were performed with a DI Nanoscope IIIa using oxide-sharpened silicon nitride probes (spring constant 0.06 Nm^{-1}).

Piezoacoustic devices and measurement set-up: Dual electrode geometries were screen-printed (brilliant gold paste from Heraeus) onto quartz discs (10 MHz, AT-cut, 15.5 mm diameter) and burned-in at 400 °C overnight.[6] The electrodes facing the aqueous face were grounded and their diameters were twice that of the electrodes oriented towards the gas phase.[15] The QCMs were mounted horizontally in flow cells with volumes of either 150 μL or 5 μL. Samples and flow cells were thermostatted at 25 °C. We used custom-built oscillator circuits[16] with self-programmed frequency read-out and processing software. The oscillator frequency was measured with a HP 53131A frequency counter, and the data was transferred via a HP-IB bus to a PC. The sensor effects were confirmed with network analyzer measurements.

Gravimetric measurements: Flow measurements were performed with a flow rate of 2 mL min^{-1} at 25 °C. Dilutions were made with SAG-M buffer at pH 7.4 and with 10 mM EDTA. Before the measurements, the red blood cell suspension was gently shaken to break up formed rouleaux (stacks). Erythrocyte suspensions were injected with a piston pump to minimize mechanical rupture of the red blood cells. Suspensions were used for only one adsorption measurement. The flow cells were flushed offline with 0.1% solution of sodium dodecylsulfate and then washed with buffer after each erythrocyte adsorption test. Red blood cell concentrations were determined using a Neubauer erythrometer.

Received: August 11, 2005
Revised: December 16, 2005
Published online: March 17, 2006

Keywords: blood groups · molecular recognition · scanning probe microscopy · sensors · surface chemistry

[1] K. Haupt, K. Mosbach, *Chem. Rev.* **2000**, *100*, 2495–2504.
[2] a) K. J. Shea, *Trends Polym. Sci.* **1994**, *2*, 166–173; b) S. A. Piletsky, A. P. F. Turner, *Electroanalysis* **2002**, *13*, 317–323.
[3] C. Alexander, E. V. Vulfson, *Adv. Mater.* **1997**, *9*, 751–755.
[4] M. Khayyami, B. Danielsson, P. Larsson, K. Mosbach, D. Kriz, *Biosens. Bioelectron.* **1994**, *9*, 551–556.
[5] H. Shi, W.-B. Tsai, M. D. Garrison, S. Ferrari, B. D. Ratner, *Nature* **1999**, *398*, 593–597.
[6] F. L. Dickert, O. Hayden, R. Bindeus, K.-J. Mann, D. Blaas, E. Waigmann, *Anal. Bioanal. Chem.* **2004**, *378*, 1929–1934.
[7] O. Hayden, F. L. Dickert, *Adv. Mater.* **2001**, *13*, 311–313.
[8] K. Dörner, *Klinische Chemie und Haematologie, 5th ed.*, Thieme, Stuttgart, **2003**, pp. 60–61; K. Dörner, *Klinische Chemie und Haematologie, 5th ed.*, Thieme, Stuttgart, **2003**, pp. 322–325.
[9] a) K. K. Kanazawa, J. G. Gordon, *Anal. Chim. Acta* **1985**, *175*, 99–105; b) O. Hayden, R. Bindeus, C. Haderspöck, K.-J. Mann, B. Wirl, F. L. Dickert, *Sens. Actuators B* **2003**, *91*, 316–319.
[10] M. Ferencik, *Handbook of Immunochemistry*, Chapman & Hall, London, **1993**.
[11] L. Thomas, *Use and Assessment of Clinical Laboratory Results*, TH-Books, Frankfurt/Main, **1998**.
[12] H. Schenkel-Brunner, *Human Blood Groups, Chemical and Biochemical Basis of Antigen Specifity*, Springer, Heidelberg, **2000**, p. 413.
[13] J. T. Dodge, C. Mitchell, D. J. Hanahan, *Arch. Biochem. Biophys.* **1979**, *100*, 119–130, 119–130.
[14] N. Mohandasm, M. R. Clakr, M. S. Jacobs, S. B. Shohet, *J. Clin. Invest.* **1980**, *66*, 563–573.
[15] M. Rodahl, F. Höök, B. Kasemo, *Anal. Chem.* **1996**, *68*, 2219–2227.
[16] F. Eichelbaum, R. Borngräber, J. Schröder, R. Lucklum, P. Hauptmann, *Rev. Sci. Instrum.* **1999**, *70*, 2537–2545.

 © 2006 Wiley-VCH Verlag GmbH & Co. KGaA, Weinheim

Surface Chemistry (1)

DOI: 10.1002/anie.200504443

Interaction of Gold Clusters with Color Centers on MgO(001) Films**

Martin Sterrer, Maxim Yulikov, Esther Fischbach, Markus Heyde, Hans-Peter Rust, Gianfranco Pacchioni, Thomas Risse, and Hans-Joachim Freund*

For a long time gold was considered catalytically inactive. However, it came under scrutiny after experiments showed distinct catalytic activity for small, supported, gold-nanoparticle catalysts.[1–3] This discovery has triggered a burst of activity to understand the microscopic mechanisms of these systems.[4,5] One strategy to unravel the details was to characterize model systems of gold atoms deposited on defined supports both experimentally as well as theoretically.[6–11] A variety of different effects were considered in which particle size and electronic effects were among the most important ones. In this respect, the interaction with the underlying support is of paramount importance for a detailed understanding. For the supported system the situation is rather complicated because of the large variety of surface sites that need to be taken into account. For oxide supports, such as MgO, low-coordinate sites as well as surface oxygen vacancies (surface color centers or F_S-centers) are considered particularly important, because it is expected that these sites may alter the properties of the adsorbed atoms and clusters with respect to regular surface terrace sites. Recent density functional theory (DFT) calculations show a strong binding of gold atoms and dimers at defects with the highest binding energies found for gold on singly charged (F^+) and neutral (F^0) color centers.[9] Furthermore, charge transfer from the defect site to the gold atom was also proposed.[9] This result is in agreement with calculations of Landman et al. for small gold clusters (Au_8). Based on theoretical predictions and IR spectra taken for Au_8 clusters deposited on MgO films with different roughness it was concluded that the observed difference in catalytic activity towards CO oxidation is due to an interaction of the Au_8 clusters with color centers on the MgO surface.[7]

However, a direct experimental correlation between the presence of color centers on the surface, their interaction with metal atoms and clusters, and the properties of the metal atoms and clusters adsorbed to these sites (as probed, for example, by the CO stretching frequency), has never been established. Herein we are aiming to demonstrate this correlation using color centers on single crystalline MgO and their interaction with gold as a prototype example. A combination of electron paramagnetic resonance (EPR) and scanning tunneling microscopy (STM) is used to verify the existence of color centers as well as the nucleation of Au onto these defects. These characterized systems then serve as reference systems in which the CO stretching frequencies can be correlated with the properties of Au clusters nucleated at regular as well as defect sites.

The upper STM image in Figure 1 a was measured on a 3–4 monolayer (ML) thick, single-crystalline MgO(001) film grown on Ag(001) after electron bombardment. The image is characterized by rectangular MgO terraces which have edges running parallel to the [100] directions of the MgO lattice. The additional bright spots located at the edges, corners, and kinks of the MgO facets are introduced by electron-bombardment and were assigned to surface color centers.[12] Note that the non-electron bombarded, pristine film shows only a minute number of color centers. Subsequently, this film was

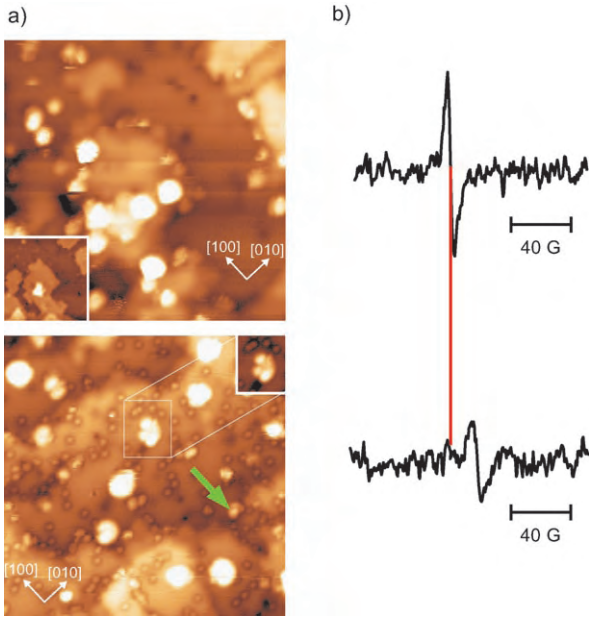

Figure 1. a) STM images (30×30 nm^2). Top: 3–4 ML MgO(001)/Ag-(001) taken after electron bombardment, $V_s=-3.0$ V, $I_t=8$ pA; inset: same area $V_s=3.5$ V, $I_t=9$ pA; bottom: the same preparation after deposition of 0.035 ML Au at 5–8 K; a dimer is indicated by a green arrow; inset: nucleation on a color center, with adjusted contrast; $V_s=1.3$ V, $I_t=10$ pA; 30×30 nm^2. b) EPR spectra around $g=2$, top: MgO(001) film on Mo(001) after low-dose electron bombardment; bottom: the same preparation after deposition of 0.015 ML Au at 30 K. The red line indicates the position of the color-center signal in both spectra.

[*] Dr. M. Sterrer, Dr. M. Yulikov, Dipl.-Chem. E. Fischbach, Dr. M. Heyde, Dr. H.-P. Rust, Dr. T. Risse, Prof. Dr. H.-J. Freund
Fritz Haber Institute of the Max Planck Society
Department of Chemical Physics
Faradayweg 4–6, 14195 Berlin (Germany)
Fax: (+49 30-8413-4316
E-mail: risse@fhi-berlin.mpg.de
Prof. Dr. G. Pacchioni
Dipartimento di Scienza dei Materiali
Università di Milano-Bicocca
via R. Cozzi, 53, 20125 Milano (Italy)

[**] M.S. is grateful for financial support by the Austrian Science Fund (FWF), Erwin Schroedinger Fellowship No. J2345-B10, E.F. acknowledges support of the Studienstiftung des deutschen Volkes, and G.P. thanks the Alexander von Humboldt foundation for supporting his visit at the FHI. This work was partially supported by the European Union through STRP GSOMEN. Support of the Fonds der Chemischen Industrie is gratefully acknowledged.

InterScience
© 2006 Wiley-VCH Verlag GmbH & Co. KGaA, Weinheim

exposed to a small amount of Au atoms (0.035 ML) at 5–8 K. As seen from the lower STM image in Figure 1a, Au atoms and Au_2 dimers (e.g. marked by the green arrow) are found on the terraces of the MgO film. From the fine structure observed within the bright protrusions (see inset) as well as scanning tunneling spectroscopy it is inferred that small gold clusters of a few atoms nucleate on these centers.

The upper trace in Figure 1b shows the EPR spectrum around the free electron *g*-value of a 20 ML thick, single-crystalline MgO(001) film grown on Mo(001) after bombardment with electrons. The EPR signal was previously assigned to paramagnetic color centers located at edge sites of the MgO surface.[12] The signal only occurs after electron bombardment. The pristine film shows no EPR signal, which means that the number of paramagnetic color centers on this film is lower than 7×10^{11} centers cm^{-2}. This value is in accord with STM results from the MgO films grown on Ag. After deposition of 0.015 ML of Au at 30 K the EPR signal of the color center is quenched. This result is a direct consequence of the nucleation of Au at the color centers. This behavior arises from the coupling of the doublet ground states of the color center and the Au atom to a singlet ground state of the adsorption complex. However, the quenching of the signal is also consistent with the formation of small Au clusters at these sites, as seen by STM. Concomitant to the decrease of the color-center signal a new EPR signal appears at higher field. This line is part of a quartet of lines with a large isotropic hyperfine coupling constant of about 1400 MHz, which is characteristic of single Au atoms. A detailed analysis of angular dependence of the signals shows that these Au atoms are nucleated on the terraces of the MgO film, directly above the oxygen ions.[13] The Au dimers seen by STM cannot be detected directly by EPR spectroscopy, however, the presence of oligomers is inferred from dosage-dependent measurements. From these experiments it can be concluded that:

1. The pristine films do not exhibit a measurable amount of point defects (color centers).
2. Color centers are produced by electron bombardment and can be characterized by EPR and STM.
3. Au nucleates at color centers as well as on regular terrace sites.

These systems are now used to calibrate the stretching frequency of CO molecules bound to different Au centers. Figure 2a shows the IR spectrum of an electron bombarded MgO film grown on Mo(001) after deposition of 0.05 ML Au at 30 K and subsequent saturation dosage of CO at 30 K. The spectrum shows a broad peak around 2160 cm^{-1} which consists of a doublet of lines at 2163 and 2153 cm^{-1} arising from CO adsorbed to low-coordinate sites as well as regular terrace sites of the MgO surface, respectively.[14] In addition, two bands one at 2120 and a broad one around 2070 cm^{-1} are observed. These bands correspond to CO bound to Au as IR measurements on the bare, electron-bombarded film exposed to CO, but not Au, shows only the peaks at 2163 and 2153 cm^{-1}, and only differs from the spectrum of the CO-treated pristine film in that the relative intensity of the peak at 2163 cm^{-1} increases at the expense of the intensity of the peak

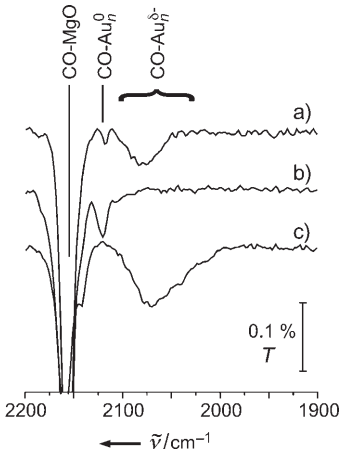

Figure 2. IR spectra after saturation coverage by CO on Au clusters formed on differently pretreated MgO films. a) film after medium-dose electron bombardment and deposition of 0.05 ML Au at 30 K; b) pristine MgO film after deposition of 0.025 ML Au at 80 K; c) film after high-dose electron bombardment and deposition of 0.025 ML Au at 30 K; film annealed to 90 K prior to CO adsorption; *T* = transmission.

at 2153 cm^{-1} (data not shown). The band at 2120 cm^{-1} is in perfect agreement with expectations for CO adsorbed to small, neutral Au clusters, which are known to show bands that are slightly blue shifted with respect to those of CO adsorbed to large Au clusters or Au single-crystal surfaces (2110 cm^{-1}).[4] For the amount of Au used in our experiment no signal arising from CO bound to single gold atoms is observed. A discussion of the unexpected properties of the IR signals of CO bound to single gold-atoms, is given in the next Communication in this issue.[15] To further corroborate the assignment, Au was adsorbed on a pristine MgO film without electron bombardment which, according to STM and EPR measurements, has a negligible amount of color centers. The IR spectrum of this preparation treated with CO (Figure 2b) shows a signal at 2120 cm^{-1}, in addition to the bands of the MgO film, confirming the assignment of this peak to CO adsorbed to neutral Au clusters. Notice the complete absence of bands in the 2000–2100 cm^{-1} range.

For the electron-bombarded sample, the signal observed at 2070 cm^{-1} (Figure 2a) can be readily explained by CO adsorbed to negatively charged Au clusters, which are predicted to be produced by the adsorption of Au to color centers. The red shift of the band is due to the greater π-back-donation from the negatively charged Au than from the neutral Au. Theoretically, a red shift of the CO stretching frequency of 25 to 80 cm^{-1} depending on the charge on the Au_8 clusters was predicted which corresponds rather well with the observed values.[7] From the width of the IR line it is clear that a variety of different species are present. This situation is even more pronounced for a film which was heavily bombarded with electrons (Figure 2c). First, the signal at 2120 cm^{-1} has vanished after this treatment indicating that the prolonged electron bombardment has decreased the amount of terrace sites considerably. Second, the signal for CO bound to the negatively charged Au clusters is even broader and extends down to 2000 cm^{-1}. The intensity distribution in the range between 2000 and 2070 cm^{-1} depends

 © 2006 Wiley-VCH Verlag GmbH & Co. KGaA, Weinheim

on the amount of gold and the preparation (electron dosage, deposition temperature, annealing steps etc.). From a variety of different experiments it can be concluded that the lines at lower wavenumber correspond to CO bound to smaller gold particles. In addition, structural inhomogeneities of the various species will contribute to the width of the signal. The effect of cluster size on the stretching frequency is in agreement with a simple model: the influence of the charge on the stretching frequency should decrease with increasing cluster size owing to the distribution of the charge over the cluster. A similar behavior was also found for gold clusters in the gas phase.[16]

These results can be compared to values reported for Au particles on various catalytically interesting samples as shown in Figure 3.[4,17–19] The values presented herein for a well

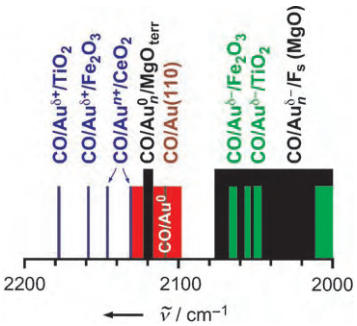

Figure 3. Comparison of IR stretching frequencies observed for the systems reported herein (back bars, terr = terrace) with measurements on other catalytically relevant systems (blue: positively charged Au particles; red: neutral Au particles; green: negatively charged Au particles).

defined model system fit perfectly with findings for neutral Au clusters on a variety of supports. The stretching frequencies for CO on the negatively charged Au clusters differ from those of CO on neutral clusters in a way that depends strongly on the size of the particles. The difference ranges from about 100 cm^{-1} for very small clusters down to about 40 cm^{-1} for larger particles.

In conclusion, these experiments provide the first direct correlation between the presence of color centers on a single-crystalline oxide surface, the nucleation of metal atoms to these centers, and the impact of the nucleation site on the properties of the metal particle as probed by the IR stretching frequency of adsorbed CO molecules. Based on the IR data it was shown that Au particles adsorbed to color centers are indeed charged as expected from theoretical predictions, while Au particles on regular terrace sites are neutral. In addition, we find good indications that the red shift of the stretching frequency for CO on negatively charged Au clusters is strongly dependent on the size of the Au particle as rationalized by simple electronic considerations.

Experimental Section

EPR and IR experiments were performed at 30 K on a 20 monolayer (ML) thick MgO(001) film grown on Mo(001). Au atoms were deposited at 30 K unless otherwise stated. The Mo substrate was cleaned by oxidation with O_2 at 1500 K and subsequent flash heating to 2300 K. The MgO films were prepared by deposition of Mg in an oxygen atmosphere (1×10^{-6} mbar) at a substrate temperature of 600 K and a rate of 1 ML MgO/min. The films were subsequently annealed to 1100 K for 10 min. The EPR spectra of Au atoms were measured with a microwave power of 2 mW in a TE_{102} cavity using a modulation amplitude of 4 G. IR spectra were taken with a spectral resolution of 4 cm^{-1}. 1000 scans were accumulated to obtain a reasonable signal-to-noise ratio. Details of the experimental setup are described elsewhere.[20] STM experiments were carried out in a custom-built low-temperature STM which has been described in detail elsewhere.[21] For the STM experiments a 3–4 ML thick MgO(001) film was grown on Ag(001) by reactive deposition of Mg at 550 K. Au was deposited at 5–8 K. In all cases color centers were produced by electrons with an energy of 100 eV extracted from a filament.

Received: December 14, 2005
Published online: March 13, 2006

Keywords: color centers · EPR spectroscopy · gold · IR spectroscopy · magnesium oxide

[1] M. Haruta, T. Kobayashi, H. Sano, N. Yamada, *Chem. Lett.* **1987**, 405.
[2] G. C. Bond, D. T. Thompson, *Catal. Rev. Sci. Eng.* **1999**, *41*, 319.
[3] M. Haruta, *Nature* **2005**, *437*, 1098.
[4] R. Meyer, C. Lemire, S. K. Shaikhutdinov, H.-J. Freund, *Gold Bull.* **2004**, *37*, 72.
[5] M. S. Chen, D. W. Goodman, *Catal. Today* **2006**, *111*, 22.
[6] H. Grönbeck, P. Broqvist, *J. Phys. Chem. B* **2003**, *107*, 12239.
[7] B. Yoon, H. Häkkinen, U. Landman, A. S. Wörz, J. M. Antonietti, S. Abbet, K. Judai, U. Heiz, *Science* **2005**, *307*, 403.
[8] G. Pacchioni, L. Giordano, M. Baistrocchi, *Phys. Rev. Lett.* **2005**, *94*, 226104/1.
[9] A. Del Vitto, G. Pacchioni, F. Delbecq, P. Sautet, *J. Phys. Chem. B* **2005**, *109*, 8040.
[10] H. Häkkinen, S. Abbet, A. Sanchez, U. Heiz, U. Landman, *Angew. Chem.* **2003**, *115*, 1335; *Angew. Chem. Int. Ed.* **2003**, *42*, 1297.
[11] K. Højrup-Hansen, S. Ferrero, C. R. Henry, *Appl. Surf. Sci.* **2004**, *226*, 167.
[12] M. Sterrer, E. Fischbach, T. Risse, H.-J. Freund, *Phys. Rev. Lett.* **2005**, *94*, 186101/1.
[13] M. Yulikov, M. Sterrer, M. Heyde, H. P. Rust, T. Risse, H.-J. Freund, G. Pacchioni, A. Scagnelli, unpublished results.
[14] M. Sterrer, T. Risse, H.-J. Freund, *Surf. Sci.* **2005**, *596*, 222.
[15] M. Sterrer, M. Yulikov, T. Risse, H.-J. Freund, J. Carrasco, F. Illas, C. Di Valentin, L. Giordano, G. Pacchioni, *Angew. Chem.* **2006**, *118*, 2695; *Angew. Chem. Int. Ed.* **2006**, *45*, 2633.
[16] A. Fielicke, G. von Helden, G. Meijer, D. B. Pedersen, B. Simard, D. M. Rayner, *J. Am. Chem. Soc.* **2005**, *127*, 8416.
[17] J. Guzman, S. Carrettin, A. Corma, *J. Am. Chem. Soc.* **2005**, *127*, 3286.
[18] F. Boccuzzi, A. Chiorino, M. Manzoli, D. Andreeva, T. Tabakova, *J. Catal.* **1999**, *188*, 176.
[19] A. S. Wörz, U. Heiz, F. Cinquini, G. Pacchioni, *J. Phys. Chem. B* **2005**, *109*, 18418.
[20] J. Schmidt, T. Risse, H. Hamann, H.-J. Freund, *J. Chem. Phys.* **2002**, *116*, 10861.
[21] M. Heyde, M. Kulawik, H.-P. Rust, H.-J. Freund, *Rev. Sci. Instrum.* **2004**, *75*, 2446.

 © 2006 Wiley-VCH Verlag GmbH & Co. KGaA, Weinheim

Surface Chemistry (2)

DOI: 10.1002/anie.200504473

When the Reporter Induces the Effect: Unusual IR spectra of CO on Au_1/MgO(001)/Mo(001)**

Martin Sterrer, Maxim Yulikov, Thomas Risse, Hans-Joachim Freund, Javier Carrasco, Francesc Illas, Cristiana Di Valentin, Livia Giordano, and Gianfranco Pacchioni*

Since Haruta's discovery that nanometer-sized gold particles supported on titanium dioxide act as effective catalysts for oxidation reactions,[1,2] a large number of experimental and theoretical studies has been dedicated to the origin of the enhanced chemical activity of nanosized gold (e.g. refs. [3–8]). Recently, Haruta et al. concluded that for high-activity Au catalysts, the contact structure between the Au particles and the support is more important than the mean particle size,[9] thus emphasizing the role of the oxide substrate in the chemistry of supported metal clusters. A key aspect in the activation of gold seems to be the charge transfer from the support to the metal. By studying size-selected Au_8 clusters on regular and defective MgO surfaces, Heiz and co-workers came to the conclusion that in the presence of surface defects the activity of Au_8 is considerably enhanced,[10] and proposed that oxygen vacancies (so-called color centers or F centers), an often addressed class of point defects on oxide surfaces,[11] efficiently transfer charge to the cluster thus increasing its chemical activity. A similar effect in terms of reactivity was found for negatively charged Au clusters in the gas-phase.[12] Even before this report it was clear that defects on the oxide support can have a crucial role in modifying the properties of a nanocluster and that it is important to quantify the extent of charge transfer to establish correlations with the chemical activity. However, the experimental determination of the charged state of an entity on a surface is challenging. It is mostly done by indirect measurements, for example photoelectron spectroscopy,[13] thus care must be taken when interpreting the results. For instance, for Au atoms adsorbed on regular terrace sites of MgO films, the isotropic hyperfine coupling constant as measured by electron paramagnetic resonance (EPR) spectroscopy is reduced by about 50% as compared to the gas phase.[14] This reduction is not due to charge transfer but to polarization and hybridization effects, in fact, gold atoms bound to the non-defective MgO surface are essentially neutral as shown by theoretical calculations.[6,14,15]

The IR stretching frequency of CO adsorbed to metal atoms or particles is a common way to probe the electron density of the metal centers.[16,17] For CO on metal surfaces the CO stretching frequency (2143 cm^{-1} in the gas-phase) is shifted to 1950–2140 cm^{-1} when CO is adsorbed on one metal atom (on-top position), to 1800–2000 cm^{-1} for CO bridging two metal sites, and to 1700–1900 cm^{-1} for CO on threefold-hollow sites (see e.g. ref. [18]). This trend correlates with the number of metal atoms interacting with CO, hence with the extent of back-donation into the CO $2\pi^*$ antibonding orbital. It is, however, important to note that assignments based on this scheme have led to misinterpretations as shown by photoelectron diffraction experiments.[19] A large body of data exists for CO adsorbed on Au particles on oxides, and, depending on the nature of the support and on the size of the particles, the stretching frequency is always between 2000 and 2170 cm^{-1}.[20–23] Signals below 2090 cm^{-1} were assigned to negatively charged Au nanoclusters nucleated at defect sites, while values between 2140 and 2100 cm^{-1} are typical of neutral Au clusters. For isolated, supported, transition-metal atoms, such as Pd bound to regular terrace MgO sites, CO stretching frequencies above 2000 cm^{-1} were found. Very low frequencies, in the range 1800–1900 cm^{-1}, are more typical of $[MCO]^-$ transition-metal complexes in the gas phase.[17,24]

Herein we will compare the CO stretching frequencies of CO bound to Au atoms deposited on regular terrace sites with those of CO attached to Au atoms nucleated at color centers on MgO surfaces. The first situation was realized by deposition of 0.0125 monolayer (ML) Au at 30 K onto a well annealed, 20 ML thick MgO(001) film which was shown to be free of color centers.[25] From EPR spectroscopy it was unambiguously shown that under these conditions Au atoms are nucleated on the terrace sites of the MgO film. This situation is in agreement with STM results on MgO(001) films grown on Ag(001),[14] which exhibit similar surface morphology and adsorption sites compared to films appropriately prepared on Mo surfaces.[26–29] Saturation coverage of CO was dosed at 30 K and the system was annealed to 63 K to desorb CO bound to the terrace sites of MgO (see the typical IR band of low-coordinate sites of MgO at 2163 cm^{-1}, Figure 1).[28] Under these conditions two bands at 2122 and 1852 cm^{-1} corresponding to Au species are observed (see Figure 1a). From the coverage dependence of the line intensities in combination with the EPR results it is readily deduced that the 1852 cm^{-1} band is due to CO bound to Au atoms while the 2122 cm^{-1} band is due to CO adsorbed on small Au clusters.[14] In addition, isotope mixing experiments (gray trace in

[*] Dr. M. Sterrer, Dr. M. Yulikov, Dr. T. Risse, Prof. Dr. H.-J. Freund
Fritz Haber Institute of the Max Planck Society
Department of Chemical Physics
Faradayweg 4–6, 14195 Berlin (Germany)
Fax: (+49) 30-8413-4316
E-mail: risse@fhi-berlin.mpg.de
J. Carrasco, Prof. Dr. F. Illas
Departament de Química Física
Universitat de Barcelona
C/Martí i Franquès 1, 08028 Barcelona (Spain)
Dr. C. Di Valentin, Dr. L. Giordano, Prof. Dr. G. Pacchioni
Dipartimento di Scienza dei Materiali
Università di Milano-Bicocca
via R. Cozzi, 53, 20125 Milano (Italy)

[**] M.S. is grateful for financial support by the Austrian Science Fund (FWF), Erwin Schroedinger Fellowship No. J2345-B10, G.P. thanks the Alexander von Humboldt foundation for supporting his visit at the FHI. This work was partially supported by the European Union through STRP GSOMEN. Support of the Fonds der Chemischen Industrie is gratefully acknowledged.

Supporting information for this article is available on the WWW under http://www.angewandte.org or from the author.

 © 2006 Wiley-VCH Verlag GmbH & Co. KGaA, Weinheim

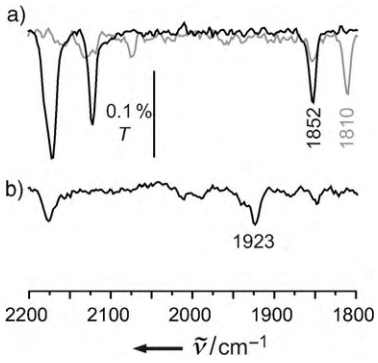

Figure 1. IR spectra of Au/CO complexes adsorbed on a) an annealed MgO(001) film (black trace 100% ^{12}CO; gray trace 25% ^{12}CO, 75% ^{13}CO) and b) an electron bombarded MgO(001) film (^{12}CO); T = transmission.

Figure 1 a) show unambiguously the presence of a one-to-one complex of CO and Au. The band at 1852 cm^{-1} is an unusually low frequency for CO adsorbed on supported metal atoms. It is red-shifted by 291 cm^{-1} with respect to gas-phase CO, and is much below any other reported value of the CO stretching frequency on supported Au.[20–23] With respect to a matrix-isolated Au/CO complex, $\tilde{\nu}_e$(CO) = 2039 cm^{-1},[30] the line is shifted by about 180 cm^{-1}. This result indicates that the MgO terrace sites have a huge effect on the properties of supported Au/CO complexes.

This situation is compared to Au adsorbed on a film containing surface color centers. The color centers are produced by electron bombardment of films prepared according to the recipe used for the above experiment. The color centers are predominately located at steps, corners, and kinks, but almost never on terraces as previously shown by STM as well as by EPR spectroscopy.[25] 0.0025 ML Au was deposited at 30 K on these films and EPR as well as STM reveal a nucleation of Au atoms at the color centers as well as a small fraction on regular terrace sites of the MgO facets.[31] The IR spectrum shown in Figure 1 b was taken after saturating the surface with CO at 30 K and subsequent annealing to 75 K to desorb most of the CO bound to MgO sites. In comparison to the spectrum in Figure 1 a additional bands are found at 1923 cm^{-1} and between 1980 and 2020 cm^{-1}. The band at 1852 cm^{-1} is strongly diminished indicating that only a minority of Au atoms remains on the terrace sites, and the band at 2120 cm^{-1} is completely absent for this preparation condition. From coverage-dependent measurements the band at 1923 cm^{-1} can be attributed to Au/CO complexes formed on neutral (F^0) or singly charged (F^+) color centers while the blue-shifted signal, which extents up to 2070 cm^{-1} depending on the preparation condition (Au coverage, deposition temperature, annealing, etc), belongs to CO adsorbed to small Au clusters nucleated at color centers.[31]

The observed blue shift of the CO stretching frequency of the CO/Au/color-center complex as compared to gold adsorbed on regular terrace sites is surprising because the color centers are usually considered the stronger Lewis bases and the frequency of CO adsorbed on these defects is normally red-shifted compared to the same atoms bound to oxide anions.[16]

This surprising result was investigated in a series of theoretical calculations. The methods used range from periodic supercell density functional theory (DFT) calculations (plane wave basis sets, PW91 exchange-correlation functional as implemented in the VASP code[32]) to embedded cluster DFT calculations (atomic orbital basis sets, PW91 or B3LYP exchange-correlation functionals), to coupled cluster calculations at the CCSD(T) level (Gaussian 03;[33] for full details of all the calculations see the Supporting Information). The reason for using so many different methods, and in particular the computationally intensive CCSD(T), is that pure DFT functionals tend to give too low an energy for the CO 2π^* orbital and to overestimate the metal-to-CO back-donation (which greatly influences the CO stretching frequency), a problem partially resolved by the use of hybrid functionals. Figure 2 a shows the optimized geometry of the

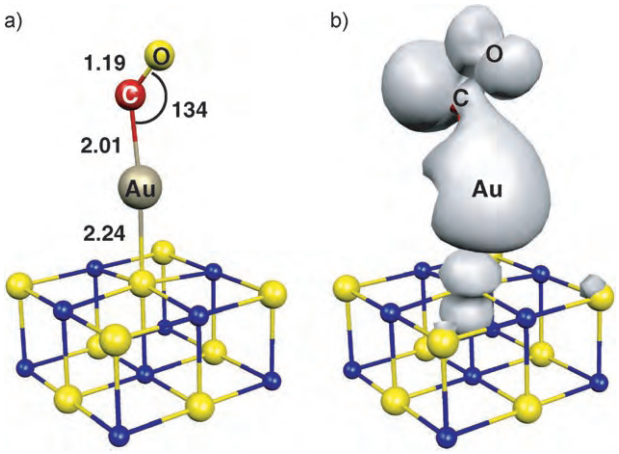

Figure 2. a) Optimal geometry and b) spin-density plot of an Au/CO complex adsorbed on-top of an oxygen anion on a MgO(001) terrace (embedded cluster calculations; distances [Å], angle [°]).

Au/CO complex on a five-coordinate oxygen anion (O_{5c}) of the MgO surface. The molecule is tilted (the Au-C-O angle is approximately 134°) and has an elongated C–O bond. As shown in Table 1, both the binding geometry and the CO stretching frequency vary little with the method used. All models predict large red-shifts of $\tilde{\nu}$(CO), between 275 and 301 cm^{-1}. At the highest level of theory, CCSD(T), $\tilde{\nu}$(CO) is 1863 cm^{-1} and $\Delta\tilde{\nu}$ = 298 cm^{-1} (with respect to the gas phase);

Table 1: Properties of Au/CO complex formed at the (001) surface of MgO obtained with various computational methods.

Model	Method	α(Au-C-O) [°]	r_e(C–O) [Å]	Δr_e(C-O) [Å]	$\tilde{\nu}$(CO) [cm^{-1}]	$\Delta\tilde{\nu}^{[a]}$ [cm^{-1}]
supercell	DFT(PW91)	137	1.182	0.040	1848	−281
O_9Mg_9	DFT(PW91)	134	1.187	0.049	1854	−275
O_9Mg_9	DFT(B3LYP)	132	1.175	0.037	1910	−301
OMg_5	CCSD(T)	136	1.181	0.044	1863	−298

[a] With respect to free CO. r_e = Equilibrium bond length.

 © 2006 Wiley-VCH Verlag GmbH & Co. KGaA, Weinheim

these values are in nearly quantitative agreement with experiment.

The large red-shift of the CO stretching frequency reflects a substantial charge transfer from Au to CO. The unpaired electron is about 10% on the surface O_{5c} ion, 30% on Au, and 60% on CO, see Figure 2b; in the surface complex the $2\pi^*$ orbital of CO becomes occupied thus resulting in a large vibrational shift. The Lewis acidic CO promotes charge flow from the O^{2-} ion to Au (an atom with high electron affinity, 2.3 eV) and from Au to CO. The occurrence of a net charge transfer is confirmed by the fact that a $[AuCO]^-$ gas-phase complex, computed at the B3LYP level, has a $\tilde{\nu}$(CO) red-shifted by 271 cm^{-1} compared to free CO. Note that the tilt of the CO molecule is very unusual for CO bound to metals. It is also a direct consequence of the charge transfer. The molecule NO, which is valence isoelectronic with CO^-, also binds to metals by forming nonlinear bonds (e.g. refs. [34,35]).

The net charge transfer, however, occurs only after CO adsorption; the gold atom adsorbed to a terrace site of MgO is neutral[6,14,15] This situation means that the CO stretching frequency measures a final-state effect and cannot be considered as a reporter of the properties of the Au/MgO complex as usually assumed.

The occurrence of a large charge transfer on the defect-free MgO surface explains why no further red-shift is observed for the Au/CO complex bound to color centers; experimentally a blue shift of approximately 60 cm^{-1} is observed with respect to the terrace sites. This result has been modeled by adsorbing an Au/CO complex on an F^0 center on a MgO terrace (in this respect the calculation is not fully representative of the experiment as F centers are located on steps and corners). Periodic supercell calculations as used above show a linear complex with $\tilde{\nu}(CO) = 1876$ cm^{-1}, which is 28 cm^{-1} higher than for the same complex formed on a terrace, fully consistent with the experimental results. The electron-withdrawing ability of the Au/CO complex is so strong that it can withdraw an electron more easily from the five-coordinate oxygen anion on an MgO terrace than from an F^0 center.

In conclusion, we report on the large influence of CO on the properties of Au atoms adsorbed on MgO terrace sites. The atoms adsorbed to O_{5c} anions of the MgO terraces are neutral, but change their chemical nature dramatically by simple adsorption of the Lewis acid CO. This adsorption induces a net charge transfer from the surface to the Au/CO complex, leading to a dramatic red-shift of the CO stretching frequency. In fact, the charge transfer is so large that the Au/CO complex adsorbed to electron-rich defects such as color centers shows a blue-shifted band with respect to the complex on regular terrace sites. It is possible that other π ligands can induce similar effects and thus may result in a modified chemical activity. Finally, it is important to stress that the CO stretching frequency does not serve as a reporter of the nature of the adsorbed Au atoms; CO induces significant chemical modifications of the supported gold species. Thus, care is required in the interpretation of vibrational spectra of CO.

Received: December 16, 2005
Published online: March 20, 2006

Keywords: ab initio calculations · color centers · gold · IR spectroscopy · magnesium oxide

[1] M. Haruta, *Catal. Today* **1997**, *36*, 153.
[2] M. Haruta, N. Yamada, T. Kobayashi, S. Iijima, *J. Catal.* **1989**, *115*, 301.
[3] H. Häkkinen, S. Abbet, A. Sanchez, U. Heiz, U. Landman, *Angew. Chem.* **2003**, *115*, 1335; *Angew. Chem. Int. Ed.* **2003**, *42*, 1297.
[4] M. S. Chen, D. W. Goodman, *Science* **2004**, *306*, 252.
[5] C. Lemire, R. Meyer, S. Shaikhutdinov, H.-J. Freund, *Angew. Chem.* **2004**, *116*, 121; *Angew. Chem. Int. Ed.* **2004**, *43*, 118.
[6] G. Pacchioni, L. Giordano, M. Baistrocchi, *Phys. Rev. Lett.* **2005**, *94*, 226104/1.
[7] H. Grönbeck, P. Broqvist, *J. Phys. Chem. B* **2003**, *107*, 12239.
[8] K. Højrup-Hansen, S. Ferrero, C. R. Henry, *Appl. Surf. Sci.* **2004**, *226*, 167.
[9] M. Okumura, S. Tsubota, M. Haruta, *J. Mol. Catal. A* **2003**, *199*, 73.
[10] A. Sanchez, S. Abbet, U. Heiz, W.-D. Schneider, H. Häkkinen, R. N. Barnett, U. Landman, *J. Phys. Chem. A* **1999**, *103*, 9573.
[11] G. Pacchioni, *ChemPhysChem* **2003**, *4*, 1041.
[12] W. T. Wallace, R. L. Whetten, *J. Am. Chem. Soc.* **2002**, *124*, 7499.
[13] C. C. Chusuei, X. Lai, K. Luo, D. W. Goodman, *Top. Catal.* **2001**, *14*, 71.
[14] M. Yulikov, M. Sterrer, M. Heyde, H. P. Rust, T. Risse, H.-J. Freund, G. Pacchioni, A. Scagnelli, unpublished results.
[15] A. Del Vitto, G. Pacchioni, F. Delbecq, P. Sautet, *J. Phys. Chem. B* **2005**, *109*, 8040.
[16] S. Abbet, E. Riedo, H. Brune, U. Heiz, A. M. Ferrari, L. Giordano, G. Pacchioni, *J. Am. Chem. Soc.* **2001**, *123*, 6172.
[17] M. Frank, M. Bäumer, R. Kuehnemuth, H.-J. Freund, *J. Phys. Chem. B* **2001**, *105*, 8569.
[18] N. Sheppard, T. T. Nguyen in *Advances in Infrared and Raman Spectroscopy, Vol. 5* (Eds.: R. E. Hester, R. J. H. Clark), Heyden, London, **1978**, p. 67, and references therein.
[19] D. P. Woodruff, A. M. Bradshaw, *Rep. Prog. Phys.* **1994**, *57*, 1029.
[20] R. Meyer, C. Lemire, S. K. Shaikhutdinov, H.-J. Freund, *Gold Bull.* **2004**, *37*, 72.
[21] A. S. Wörz, U. Heiz, F. Cinquini, G. Pacchioni, *J. Phys. Chem. B* **2005**, *109*, 18418.
[22] B. Yoon, H. Häkkinen, U. Landman, A. S. Wörz, J. M. Antonietti, S. Abbet, K. Judai, U. Heiz, *Science* **2005**, *307*, 403.
[23] F. Boccuzzi, A. Chiorino, M. Manzoli, D. Andreeva, T. Tabakova, *J. Catal.* **1999**, *188*, 176.
[24] A. Fielicke, G. von Helden, G. Meijer, B. Simard, D. M. Rayner, *J. Phys. Chem. B* **2005**, *109*, 23935.
[25] M. Sterrer, E. Fischbach, T. Risse, H.-J. Freund, *Phys. Rev. Lett.* **2005**, *94*, 186101/1.
[26] S. Schintke, S. Messerli, M. Pivetta, F. Patthey, L. Libioulle, M. Stengel, A. De Vita, W. D. Schneider, *Phys. Rev. Lett.* **2001**, *87*.
[27] Z. Dohnalek, G. A. Kimmel, S. A. Joyce, P. Ayotte, R. S. Smith, B. D. Kay, *J. Phys. Chem. B* **2001**, *105*, 3747.
[28] M. Sterrer, T. Risse, H.-J. Freund, *Surf. Sci.* **2005**, *596*, 222.
[29] H. M. Benia, S. Benedetti, N. Nilius, unpublished results.
[30] L. Jiang, Q. Xu, *J. Phys. Chem. A* **2005**, *109*, 1026.
[31] M. Sterrer, M. Yulikov, E. Fischbach, M. Heyde, H. P. Rust, G. Pacchioni, T. Risse, H.-J. Freund, *Angew. Chem.* **2006**, *118*, 2692; *Angew. Chem. Int. Ed.* **2006**, *45*, 2630.
[32] G. Kresse, J. Furthmüller, *Phys. Rev. B* **1996**, *54*, 11169.
[33] Gaussian 03 (Revision B.04), M. J. Frisch et al. Gaussian, Inc., Pittsburgh, PA, **2003**, see Supporting Information.
[34] I. P. Batra, C. R. Brundle, *Surf. Sci.* **1976**, *57*, 12.
[35] G. Doyen, G. Ertl, *Surf. Sci.* **1977**, *69*, 157.

 © 2006 Wiley-VCH Verlag GmbH & Co. KGaA, Weinheim

Cover Picture

Bruno Botta, Fabiana Caporuscio, Deborah Subissati, Andrea Tafi,* Maurizio Botta, Antonello Filippi, and Maurizio Speranza*

Protein allosterism is the basis for the molecular control of fundamental processes in living systems, but despite its importance, basic questions on the mechanisms involved remain unanswered. A gas-phase approach to the problem is described by M. Speranza et al. in their Communication on page 2717 ff., in which they report the highly enantioselective, 2-aminobutane-induced loss of D- and L-tryptophan from the achiral hydrophobic rim of a chiral resorcin[4]arene.

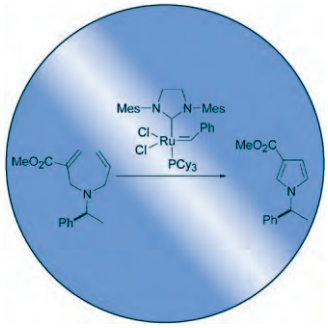

Ring-Closing Metathesis
Ring-closing metathesis is often used as a key step in the construction of heterocyclic and carbocyclic arenes. An overview is provided by T. J. Donohoe et al. in their Minireview on page 2664 ff.

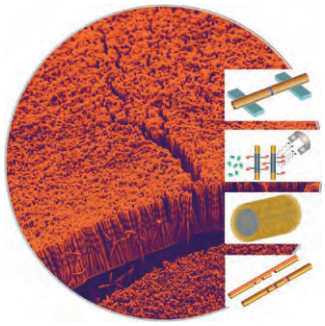

One-Dimensional Nanostructures
Recent advances in the template synthesis of multisegmented one-dimensional nanorods and nanowires as well as applications of these multicomponent nanomaterials are discussed in detail in the Review by C. A. Mirkin et al. on p. 2672 ff.

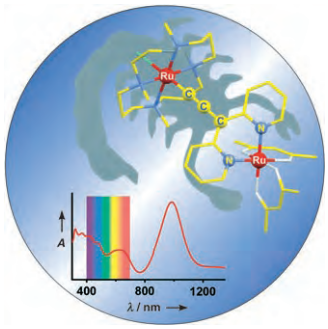

Metalloligands
In their Communication on page 2694 ff., C.-M. Che et al. report a ruthenium(II) complex with π-conjugated hydrocarbon chains and chelating pyridyl groups that serves as a metalloligand for metal ions. The complex with $\{Ru(acac)_2\}$ gives rise to an intense near-IR absorption.

Contents

VIP *The following Communications have been judged by at least two referees to be "very important papers" and will be published online at www.angewandte.org soon:*

*V. Lavallo, Y. Canac, B. Donnadieu, W. Schoeller, G. Bertrand**
CO Fixation to Stable Acyclic and Cyclic Alkyl Amino Carbenes: Stable Amino Ketenes with a Small HOMO–LUMO Gap

*D. Rohde, C.-J. Yan, H.-J. Yan, L.-J. Wan**
From Lamellar to Hexagonal Self-Assembly of Bis(dioxaborin) Molecules

*T. Adler, N. Borho, M. Reiher, M. Suhm**
Chirality-Induced Hydrogen-Bond Topology Switch: Tetrameric Methyl Lactate Clusters in the Gas Phase

*D. Bang, B. Pentelute, S. H. Kent**
Kinetically Controlled Ligation for the Convergent Chemical Synthesis of Proteins

*H. Chen, Z. Ouyang, R. G. Cooks**
Thermal Production and Reactions of Organic Ions at Atmospheric Pressure

*Y. Sawada, K. Matsumoto, S. Kondo, H. Watanabe, T. Ozawa, K. Suzuki, B. Saito, T. Katsuki**
Titanium/Salan-Catalyzed Asymmetric Epoxidation with Aqueous Hydrogen Peroxide as Oxidant

News

Awards of the Chemical Society of Japan 2005 ——— **2656**

Books

Modern Organonickel Chemistry — Yoshinao Tamaru — *reviewed by Y. Masuyama* ——— **2657**

The World's Greatest Fix — G. J. Leigh — *reviewed by M. D. Fryzuk* ——— **2658**

Highlights

Receptor Libraries

B. de Bruin, P. Hauwert, J. N. H. Reek* ——— **2660 – 2663**

Dynamic Combinatorial Chemistry: The Unexpected Choice of Receptors by Guest Molecules

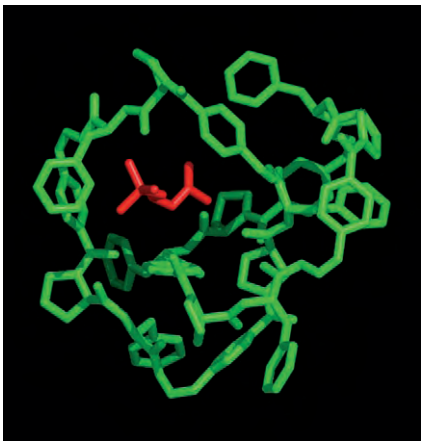

Survival of the fittest? Amplification of the best receptor from a dynamic combinatorial library does not always proceed according to survival of the "fittest". However, it has recently resulted in the discovery of some unexpected receptors for various substrates, as illustrated by the example of a catenane receptor (see picture; green) for the neurotransmitter acetylcholine (red).

© 2006 Wiley-VCH Verlag GmbH & Co. KGaA, Weinheim

Minireviews

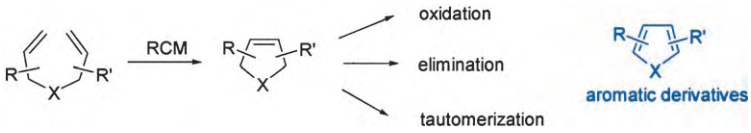

Openings from ring closing: Ring-closing metathesis (RCM) is an extremely useful technique for constructing heterocyclic and carbocyclic ring systems, which can be transformed into aromatic derivatives by a variety of different strategies. This Minireview brings together the different approaches reported to date.

Ring-Closing Metathesis

T. J. Donohoe,* A. J. Orr, M. Bingham ——— **2664 – 2670**

Ring-Closing Metathesis as a Basis for the Construction of Aromatic Compounds

Reviews

Each component does its part: Multisegmented 1D nanostructures can be reliably synthesized within the micro- or nanosized pores of hard templates. When released from these templates (see picture), the individual components of these structures can be used to perform multiple tasks simultaneously. In this way, these single structures provide possibilities for novel applications and new directions in fundamental areas of study.

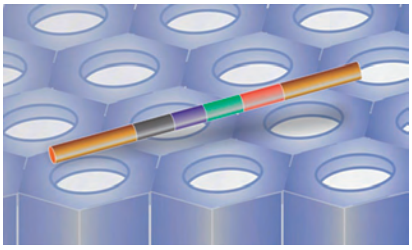

Nanostructures

S. J. Hurst, E. K. Payne, L. Qin, C. A. Mirkin* ——— **2672 – 2692**

Multisegmented One-Dimensional Nanorods Prepared by Hard-Template Synthetic Methods

Communications

Making the band: A bis(pyridyl)allenylidene–ruthenium complex acts as a metalloligand for the binding of metal ions. The dinuclear complex $[(16\text{-TMC})ClRu{=}C{=}C{=}C(2\text{-py})_2Ru(acac)_2]^+$ (16-TMC = 1,5,9,13-tetramethyl-1,5,9,13-tetraazacyclohexadecane) features an intense low-energy metal-to-ligand charge transfer in an excited state delocalized over both Ru ions and the allenylidene bridge (see plot of the LUMO).

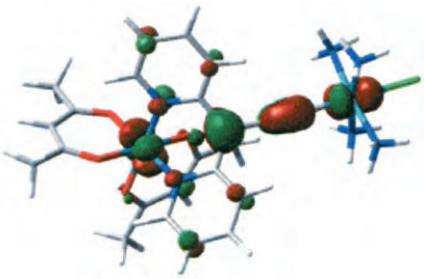

Molecular Electronics

C.-Y. Wong, G. S. M. Tong, C.-M. Che,* N. Zhu ——— **2694 – 2698**

A Bis(pyridyl)allenylidene Complex of Ruthenium: A "Molecular Clip" That Displays Intense Near-Infrared Absorption upon Coordination to a Ruthenium(II) Center

For the USA and Canada:
ANGEWANDTE CHEMIE International Edition (ISSN 1433-7851) is published weekly by Wiley-VCH PO Box 191161, D 69451 Weinheim, Germany. Air freight and mailing in the USA by Publications Expediting Inc. 200 Meacham Ave., Elmont, NY 11003. Periodicals postage paid at Jamaica NY 11431. US POSTMASTER: send address changes to *Angewandte Chemie*, Wiley-VCH, 111 River Street, Hoboken, NJ 07030. Annual subscription price for institutions: US$ 5685/5168 (valid for print and electronic / print or electronic delivery); for individuals who are personal members of a national chemical society prices are available on request. Postage and handling charges included. All prices are subject to local VAT/sales tax.

© 2006 Wiley-VCH Verlag GmbH & Co. KGaA, Weinheim

The best in chemistry – for more than a hundred years

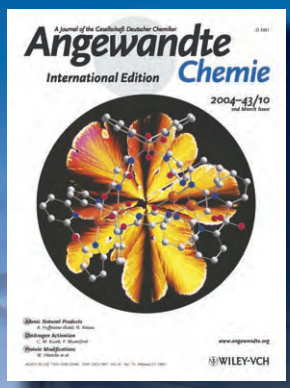

A Journal of the Gesellschaft Deutscher Chemiker

Angewandte International Edition **Chemie**

www.angewandte.org

1888: ***The beginning of a success story***

Constant Innovations

1962: *First issue of the International Edition*
1976: *Graphical abstracts*
1979: *Cover pictures*
1988: *Centenary of Angewandte*
1989: *Routine use of color*
1991: *New section: Highlights*
1992: *Computerized editorial tracking system*
1995: *Internet service for readers*
1998: *Regular press service; full-text online*
2000: *New section: Essays; EarlyView: Communications available online ahead of the printed version*
2001: *New section: Minireviews*
2002: *Online submission of manuscripts*
2003: *Weekly publication; new section: News; new layout*
2004: *Backfiles (1962-1997); ManuscriptXpress: Online system for authors and referees*

Angewandte's advisors...

Horst Kessler
Institut für Organische und Biochemie, Technische Universität München

» If you want to be recognized send your best papers to ***Angewandte Chemie****. The journal is scientifically of top quality; the layout makes the articles easy to read and contributes to the overall impact. An important step forward was the coverage in Medline making the life sciences community aware of the journal's content. Now the field of bioorganic chemistry is also becoming stronger in* ***Angewandte Chemie****. «*

Angewandte Chemie International Edition *is a journal of the German Chemical Society (GDCh)*

GDCh

WILEY InterScience® DISCOVER SOMETHING GREAT

WILEY-VCH

1831404_gw

Insight into amyloids: Four identical segments of the amyloid β-peptide, which is associated with Alzheimer's disease by fibril formation, were successfully attached to a cyclic decapeptide template. The assembly forms soluble protofibrils (see picture) that reveal a cross-β-sheet structure, with fast controllable kinetics and without a lag phase.

Peptide Assemblies

G. T. Dolphin, P. Dumy,*
J. Garcia* ——— **2699 – 2702**

Control of Amyloid β-Peptide Protofibril Formation by a Designed Template Assembly

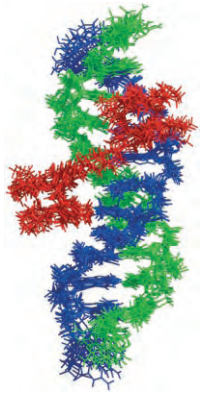

Feeling groovy: A large dimeric calix[4]-arene hexaaniline binds selectively to double-stranded DNA and especially RNA with submicromolar K_D values. The picture shows a simulation of the complex between a 12-base-pair B-DNA (green and blue) and an anilinocalixarene dimer (red), which fits snugly into the major groove. Several physical and spectroscopic characteristics strongly indicate insertion into the major groove.

DNA Intercalation

R. Zadmard, T. Schrader* — **2703 – 2706**

DNA Recognition with Large Calixarene Dimers

Seeing the light: An androgen promotes interactions between the androgen-receptor ligand-binding domain (AR LBD) and a coactivator protein. This results in an increase in the fluorescence resonant energy transfer (FRET) from cyan fluorescent protein (CFP) to yellow fluorescent protein (YFP). The indicator distinguishes ligands of different potencies for the AR.

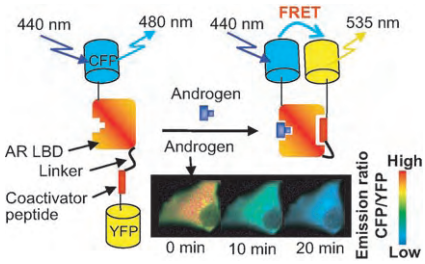

Binding Assays

M. Awais, M. Sato, X. Lee, Y. Umezawa* ——— **2707 – 2712**

A Fluorescent Indicator To Visualize Activities of the Androgen Receptor Ligands in Single Living Cells

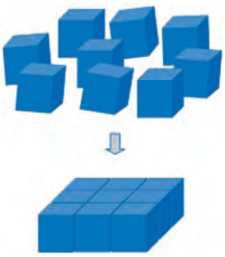

Attractive exteriors: Surface reduction of Co_3O_4 nanocubes leads to the formation of ordered 2D arrays (see picture), in which the nanocubes are connected through isotropic superparamagnetic interactions. This method provides an efficient means for generating assemblies of nanoparticles, without using organic surfactants or external magnetic fields.

Self-Assembly

H. M. Chen, R.-S. Liu, H. L. Li, H. C. Zeng* ——— **2713 – 2717**

Generating Isotropic Superparamagnetic Interconnectivity for the Two-Dimensional Organization of Nanostructured Building Blocks

© 2006 Wiley-VCH Verlag GmbH & Co. KGaA, Weinheim

Contents

Host–Guest Systems

B. Botta, F. Caporuscio, D. Subissati, A. Tafi,* M. Botta, A. Filippi, M. Speranza* ——— **2717 – 2720**

Flattened Cone 2,8,14,20-Tetrakis (L-valinamido)[4]resorcinarene: An Enantioselective Allosteric Receptor in the Gas Phase

A get-out clause: Displacement of the enantiomers of tryptophan from the achiral hydrophobic rim of a flattened cone resorcinarene derivative is induced by 2-aminobutane (**B**). The displacement exhibits a marked enantioselectivity which is traced to a conformational coupling between the achiral hydrophobic rim of the resorcinarene host and its chiral hydrophilic rim wherein the 2-aminobutane enantiomers are trapped.

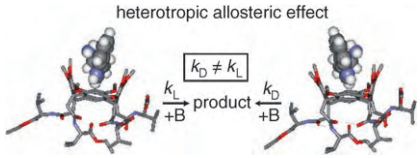

Synthetic Methods

H. Sun, S. G. DiMagno* ——— **2720 – 2725**

Room-Temperature Nucleophilic Aromatic Fluorination: Experimental and Theoretical Studies

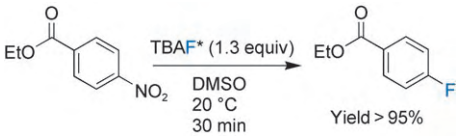

Taming the reagent: The use of anhydrous tetrabutylammonium fluoride ($TBAF_{anh}$) in nucleophilic aromatic substitution reactions, including variants of the selective halogen-exchange and fluorodenitration processes (see scheme), was investigated. It was shown that $TBAF_{anh}$ permits these reactions to be performed under surprisingly mild conditions if it is used in relatively nonpolar media.

Protein Engineering

K. Sugimoto, S. Kanamaru, K. Iwasaki, F. Arisaka, I. Yamashita* ——— **2725 – 2728**

Construction of a Ball-and-Spike Protein Supramolecule

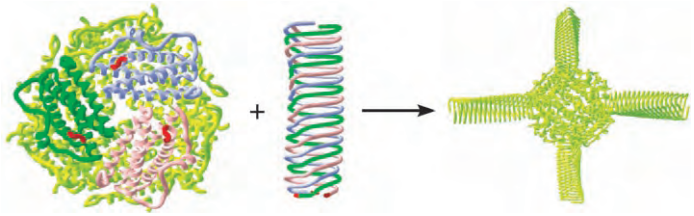

On the ball: Fusion of gp5C (spike) to LisDps (ball) through a flexible linker connecting the respective C and N termini allowed the engineered construction of a ball-and-spike protein supramolecule. The two symmetric protein components self-assemble to form a large protein supramolecule made of artificial components.

Non-natural Amino Acids

A. Deiters, D. Groff, Y. Ryu, J. Xie, P. G. Schultz* ——— **2728 – 2731**

A Genetically Encoded Photocaged Tyrosine

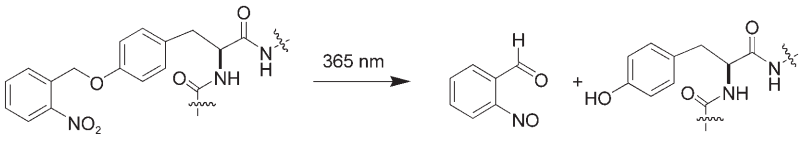

Activating proteins with light: A photocaged tyrosine was genetically encoded in *E. coli* in response to the amber codon TAG. Substitution of Tyr503 in the active site of β-galactosidase allowed photoactivation of this enzyme in vitro or directly in bacteria with 360-nm light. This method should allow photoregulation of the activity of a variety of biological processes including transcription, signal transduction, and cellular trafficking.

© 2006 Wiley-VCH Verlag GmbH & Co. KGaA, Weinheim

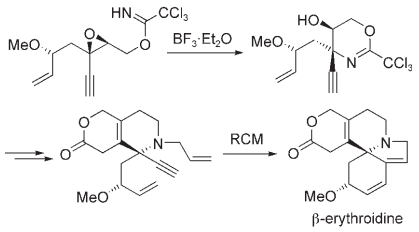

Enyne enyne oh! The first total synthesis of (+)-β-erythroidine, a non-aromatic *Erythrina* alkaloid, is demonstrated. The key steps involved are Lewis acid promoted cyclization of an epoxy–trichloroacetimidate intermediate and tandem ring-closing metathesis (RCM) of the dienyne (see scheme).

Natural Product Synthesis

H. Fukumoto, K. Takahashi, J. Ishihara, S. Hatakeyama* ——— **2731 – 2734**

Total Synthesis of (+)-β-Erythroidine

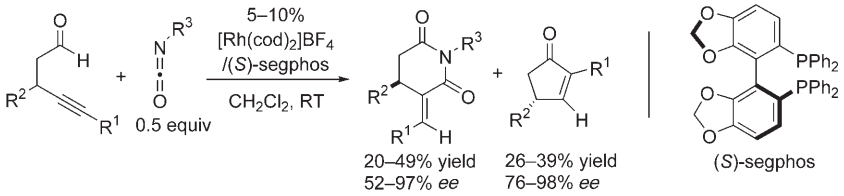

Enantioenriched 2-alkylideneglutarimides and cyclopentenones are prepared by parallel kinetic resolution of 3-substituted 4-alkynals with a cationic Rh^{I}/(*S*)-segphos catalyst system. This is an attractive route to the above-mentioned products given the one-step access to 4-alkynals from readily available terminal alkynes.

Cycloaddition

K. Tanaka,* Y. Hagiwara, M. Hirano ——— **2734 – 2737**

Rh-Catalyzed [4+2] Annulation of 4-Alkynals with Isocyanates and Its Application to the Parallel Kinetic Resolution of Unfunctionalized 4-Alkynals

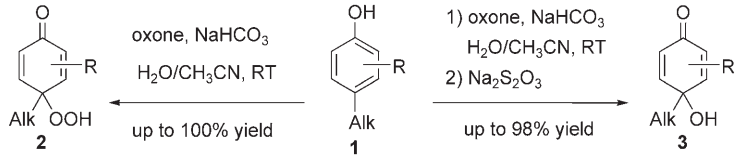

Easy does it: Easily handled and environmentally safe oxone generates singlet oxygen which effects the simple and selective oxidative de-aromatization of *para*-alkyl phenols **1** into *para*-peroxyquinols **2** under very mild conditions with good to excellent yields. A one-pot access to *para*-quinols **3** from **1** is also possible after treatment of the crude reaction mixture with sodium thiosulfate.

Oxidation

M. C. Carreño,* M. González-López, A. Urbano* ——— **2737 – 2741**

Oxidative De-aromatization of *para*-Alkyl Phenols into *para*-Peroxyquinols and *para*-Quinols Mediated by Oxone as a Source of Singlet Oxygen

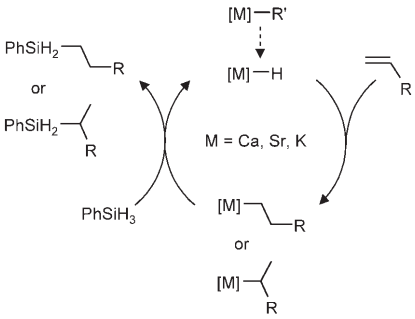

Clean conversion of conjugated alkenes with exclusive formation of one regioisomer is achieved by using a new class of hydrosilylation catalysts based on early main-group metals (Ca, Sr, and K). The regioselectivity can be switched to the other isomer through the choice of the metal and solvent polarity.

Synthetic Methods

F. Buch, J. Brettar, S. Harder* ——— **2741 – 2745**

Hydrosilylation of Alkenes with Early Main-Group Metal Catalysts

© 2006 Wiley-VCH Verlag GmbH & Co. KGaA, Weinheim

Contents

Biosensors

S. Hwang, W. Cha, M. E. Meyerhoff* ——— 2745 – 2748

Polymethacrylates with a Covalently Linked Cu^{II}–Cyclen Complex for the In Situ Generation of Nitric Oxide from Nitrosothiols in Blood

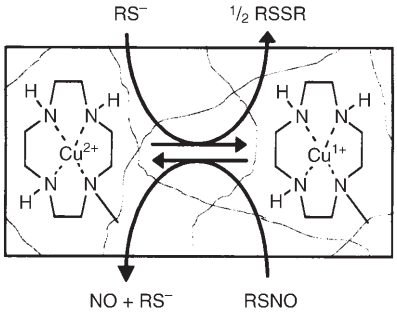

In the matrix: A new cross-linked hydrogel polymer, poly(2-hydroxyethyl methacrylate) (pHEMA), containing appended Cu^{II}–cyclen sites (cyclen = 1,4,7,10-tetraazacyclododecane) was prepared and shown to generate nitric oxide from endogenous *S*-nitrosothiol species (RSNO) typically found in circulating whole blood.

Glycosylations

S. A. Borisova, C. Zhang, H. Takahashi, H. Zhang, A. W. Wong, J. S. Thorson, H.-w. Liu* ——— 2748 – 2753

Substrate Specificity of the Macrolide-Glycosylating Enzyme Pair DesVII/DesVIII: Opportunities, Limitations, and Mechanistic Hypotheses

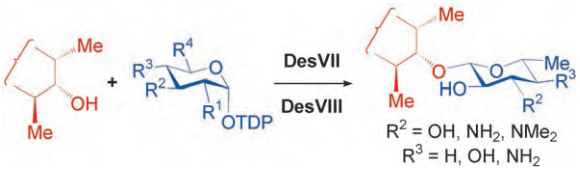

Two's Company: DesVII, a glycosyltransferase involved in the biosynthesis of macrolide antibiotics, is unusual in that it requires an additional protein partner, DesVIII, for its full activity. The level of substrate tolerance of the DesVII/DesVIII pair was explored.

Synthesis Design

J.-C. Lee, C.-Y. Wu, J. V. Apon, G. Siuzdak, C.-H. Wong* ——— 2753 – 2757

Reactivity-Based One-Pot Synthesis of the Tumor-Associated Antigen N3 Minor Octasaccharide for the Development of a Photocleavable DIOS-MS Sugar Array

Sweet and light: Readily available thioglycosides with defined relative reactivity values were used as building blocks in a one-pot strategy to synthesize the tumor-associated carbohydrate antigen N3 minor (**1**). The target molecule was attached covalently to a porous silicon surface through a photocleavable linker for direct characterization in a mass spectrometer equipped with a laser source.

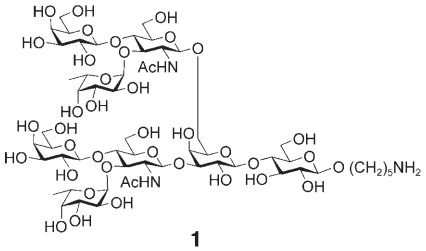

1

Bioinorganic Chemistry

M. Guo,* I. Harvey, D. J. Campopiano, P. J. Sadler* ——— 2758 – 2761

Short Oxo–Titanium(IV) Bond in Bacterial Transferrin: A Protein Target for Metalloantibiotics

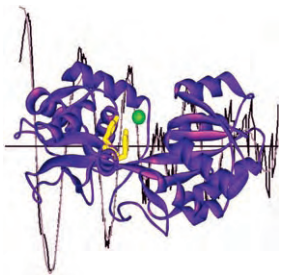

A competitive edge? Ti^{IV} binding to a bacterial transferrin (ferric-ion-binding protein, FBP; see picture, foreground) is rapid, competes with Fe^{III} binding, and results in a short oxo–Ti^{IV} bond (EXAFS studies; see picture, background). Inhibitors of iron uptake by FBP should be active against diseases caused by bacterial pathogens. The results suggest that Ti complexes could provide such inhibition.

© 2006 Wiley-VCH Verlag GmbH & Co. KGaA, Weinheim

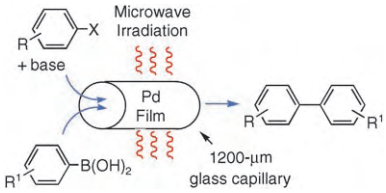

Finally ... metal in a microwave! Thin films of Pd black deposited onto the inner surface of microcapillaries are efficient for metal-catalyzed transformations under flow conditions including the Suzuki–Miyama and Heck couplings. The reaction mixture is flowed through these miniature capillaries while being microwaved, and conversion times are on the order of seconds.

Continuous-Flow Reactions

G. Shore, S. Morin, M. G. Organ* ——— **2761 – 2766**

Catalysis in Capillaries by Pd Thin Films Using Microwave-Assisted Continuous-Flow Organic Synthesis (MACOS)

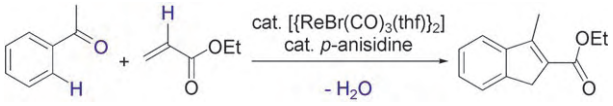

Several reaction steps, including C–H activation, lead to indene derivatives in good yields in the rhenium-catalyzed reaction of aromatic ketimines and ethyl acrylate. Indene derivatives can also be obtained by the reactions of aromatic ketones with α,β-unsaturated esters in the presence of a catalytic rhenium complex and *p*-anisidine (see scheme).

Annulation Reactions

Y. Kuninobu,* Y. Nishina, M. Shouho, K. Takai* ——— **2766 – 2768**

Rhenium- and Aniline-Catalyzed One-Pot Annulation of Aromatic Ketones and α,β-Unsaturated Esters Initiated by C–H Bond Activation

All sewn up: A "three-staged stitch" was used to append the A–C rings of desoxohexacyclinol (**1**), which was further converted into the related compounds hexacyclinol (**2**) and 5-*epi*-hexacyclinol (**3**). Screening of the late-staged intermediates indicated that precursors to **1** retain potent antimalarial activity. The mechanism of this action is suggested to involve a three-step prodrug-like activation.

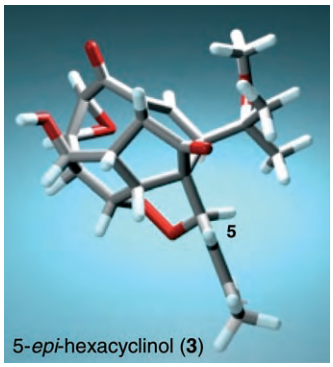

Antimalarial Drugs

J. J. La Clair* ——— **2769 – 2773**

Total Syntheses of Hexacyclinol, 5-*epi*-Hexacyclinol, and Desoxohexacyclinol Unveil an Antimalarial Prodrug Motif

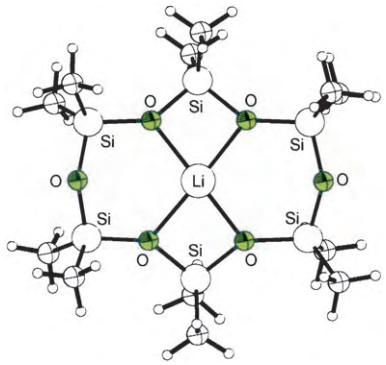

An unexpected guest: The salts $LiD_5[Al_F]$, $LiD_6[Al_F]$, and $LiD_6[Al_{PhF}]$ ($D_n = (Me_2SiO)_n$; $[Al_F] = Al\{OC(CF_3)_3\}_4$; $[Al_{PhF}] = Al\{OC(CF_3)_2Ph\}_4$) are the first host–guest complexes to be synthesized directly from cyclic dimethylsiloxanes, alkali-metal ions, and weakly coordinating anions. Their experimental and calculated structures imply that the cyclic dimethylsiloxanes act as pseudo crown ethers (see structure of $[LiD_6]^+$).

Host–Guest Complexes

A. Decken, J. Passmore,* X. Wang ——— **2773 – 2777**

Cyclic Dimethylsiloxanes as Pseudo Crown Ethers: Syntheses and Characterization of $Li(Me_2SiO)_5[Al\{OC(CF_3)_3\}_4]$, $Li(Me_2SiO)_6[Al\{OC(CF_3)_3\}_4]$, and $Li(Me_2SiO)_6[Al\{OC(CF_3)_2Ph\}_4]$

© 2006 Wiley-VCH Verlag GmbH & Co. KGaA, Weinheim

Contents

Photoelectrochemistry

T. Abe,* K. Nagai,* S. Kabutomori, M. Kaneko, A. Tajiri, T. Norimatsu _____ **2778 – 2781**

An Organic Photoelectrode Working in the Water Phase: Visible-Light-Induced Dioxygen Evolution by a Perylene Derivative/Cobalt Phthalocyanine Bilayer

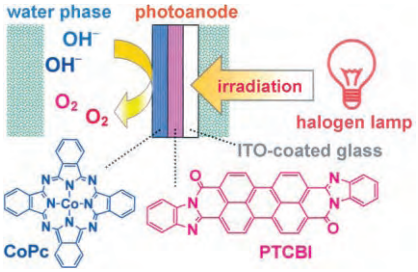

Two layers are better than one: The organic bilayer composed of 3,4,9,10-perylenetetracarboxylic acid bisbenzimidazole (PTCBI, an n-type semiconductor) and cobalt phthalocyanine (CoPc, a p-type semiconductor) was found to act as a novel photoanode that is responsive to visible light under 750 nm to induce efficiently the photoelectrochemical splitting of water to evolve dioxygen.

Polymer Chemistry

A. Amgoune, C. M. Thomas,* S. Ilinca, T. Roisnel, J.-F. Carpentier* **2782 – 2784**

Highly Active, Productive, and Syndiospecific Yttrium Initiators for the Polymerization of Racemic β-Butyrolactone

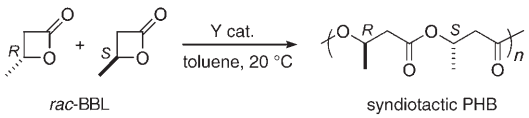

Alternate tacticities: The ring-opening polymerization of *rac*-β-butyrolactone (*rac*-BBL) using a six-coordinate yttrium complex bearing a dianionic amine-bis(phenolate) ligand as initiator proceeds readily at room temperature to give the corresponding poly(3-hydroxybutyrate) (PHB) with up to 94% syndiotacticity and narrow molecular-weight distributions (see scheme).

Reduction

D. Lee, D. Kim, J. Yun* _____ **2785 – 2787**

Highly Enantioselective Conjugate Reduction of β,β-Disubstituted α,β-Unsaturated Nitriles

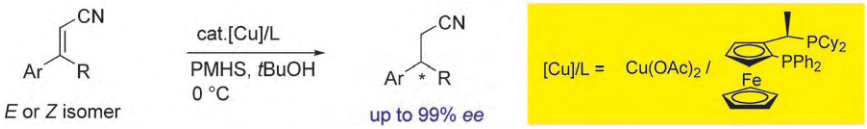

Easy access: The highly enantioselective conjugate reduction of α,β-unsaturated nitriles is achieved by employing bench-top stable copper(II) acetate and josiphos (L) as the ligand in the presence of polymethylhydrosiloxane (PMHS). This protocol provides ready access to valuable chiral β-aryl substituted nitriles in good yields and with excellent enantioselectivities.

Homogeneous Catalysis

R. B. C. Jagt, P. Y. Toullec, D. Geerdink, J. G. de Vries,* B. L. Feringa,* A. J. Minnaard* _____ **2789 – 2791**

A Ligand-Library Approach to the Highly Efficient Rhodium/Phosphoramidite-Catalyzed Asymmetric Arylation of *N*,*N*-Dimethylsulfamoyl-Protected Aldimines

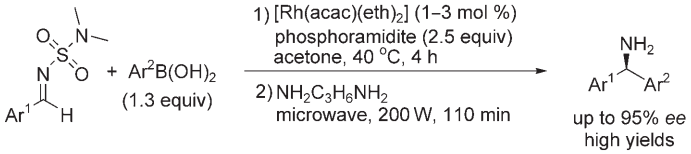

Small but effective: The title reaction, after microwave-assisted removal of the *N*,*N*-dimethylsulfamoyl protecting group, leads to chiral diarylmethyl amines. The use of 1 mol% catalyst and 1.3 equivalents of aryl boronic acid results in excellent yields (up to 98%) and enantioselectivities (up to 95% *ee*) of the isolated products. acac = acetylacetonate; eth = ethylene.

© 2006 Wiley-VCH Verlag GmbH & Co. KGaA, Weinheim

What happens in between? A nonanuclear gallium(III) cluster (see structure: white H, gray C, red O, orange Br, beige Ga) is a potential intermediate in the assembly of a dinuclear helicate. The cluster could be isolated because of conformational restrictions at the ligand which disfavor the formation of the triple-stranded helical complex.

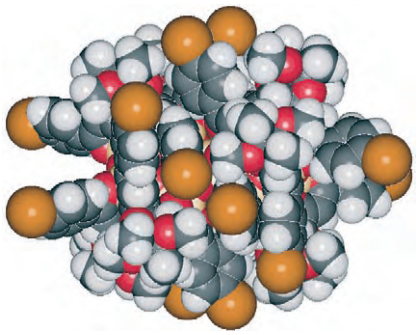

Helical Structures

M. Albrecht,* S. Dehn, R. Fröhlich ——— **2792 – 2794**

A Nonanuclear Gallium(III) Cluster: An Intermediate in the Formation of Dinuclear Triple-Stranded Helicates?

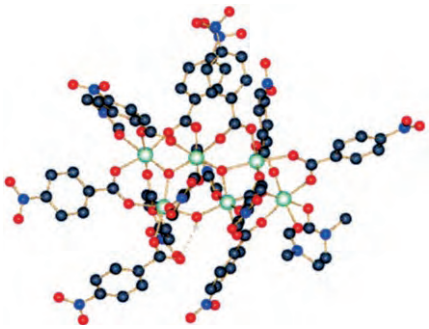

Six of one: A hexanuclear iron *p*-nitrobenzoate compound (see structure; green Fe, red O, blue N, gray C), a novel type of iron cluster was prepared and characterized. The complex has an $[Fe_6(\mu_3\text{-}O)_3(\mu_2\text{-}OH)]^{11+}$ core and shows a remarkable catalytic activity in the oxidation of cyclohexane.

Cluster Compounds

G. Trettenhahn, M. Nagl, N. Neuwirth, V. B. Arion,* W. Jary, P. Pöchlauer, W. Schmid* ——— **2794 – 2798**

A Hexanuclear Iron(III) Carboxylate with an $[Fe_6(\mu_3\text{-}O)_3(\mu_2\text{-}OH)]^{11+}$ Core as an Efficient Catalyst for Cycloalkane Oxidation

The Ti dimer is fairly weakly bound, but highly reactive, and completely cleaves the strong N_2 triple bond in just one step without activation energy (see scheme; Ti red, N blue). In contrast, a Ti atom in its ground electronic state does not react with N_2.

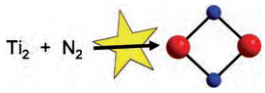

N_2 Activation

H.-J. Himmel,* O. Hübner, W. Klopper, L. Manceron ——— **2799 – 2802**

Cleavage of the N_2 Triple Bond by the Ti Dimer: A Route to Molecular Materials for Dinitrogen Activation?

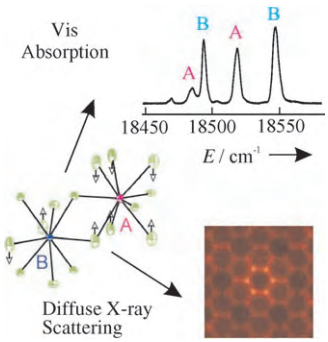

Illuminating disorder: Many highly efficient light emitters are members of the family β-$NaLnF_4$ (Ln = Y, La–Lu). Diffuse X-ray scattering is combined with single-crystal absorption spectroscopy at cryogenic temperatures to unambiguously identify and characterize two crystallographically inequivalent spectroscopic sites (A and B). The high light yield is correlated with the existence and nature of these sites.

Upconversion

A. Aebischer, M. Hostettler, J. Hauser, K. Krämer, T. Weber, H. U. Güdel,* H.-B. Bürgi* ——— **2802 – 2806**

Structural and Spectroscopic Characterization of Active Sites in a Family of Light-Emitting Sodium Lanthanide Tetrafluorides

© 2006 Wiley-VCH Verlag GmbH & Co. KGaA, Weinheim

Sources

Product and Company Directory

You can start the entry for your company in "Sources" in any issue of *Angewandte Chemie*.

If you would like more information, please do not hesitate to contact us.

Wiley-VCH Verlag – Advertising Department
Tel.: 0 62 01 - 60 65 65
Fax: 0 62 01 - 60 65 50
E-Mail: MSchulz@wiley-vch.de

Service

Keywords ____ *2808*

Authors ____ *2809*

Angewandte's Sister Journals ____ *2810 – 2811*

Preview ____ *2813*

For more information on ChemMedChem see www.chemmedchem.org

© 2006 Wiley-VCH Verlag GmbH & Co. KGaA, Weinheim

CSJ Awards

H. Kobayashi

H. Kobayashi

Hayao Kobayashi (Institute for Molecular Science, Myodaiji, Okazaki) has been awarded by the Chemical Society of Japan (CSJ) for his work on magnetic organic superconductors and single-component molecular metals. He recently reported in *Angewandte Chemie* on the dielectric properties of porous molecular crystals that contain polar guest molecules.[1] Kobayashi completed his PhD at the University of Tokyo in 1966. He then joined the faculty at Toho University in 1980. Since 1995, he is affiliated with the Institute for Molecular Science.

K. Komatsu

K. Komatsu

Koichi Komatsu has been recognized for his research at Kyoto University on the structures and properties of carbonaceous conjugated systems. His research group recently reported on fullerenes, in particular on open-cage structures[2a] and alkylated C_{70} cations.[2b] Komatsu obtained his PhD in 1974 from Kyoto University and remained there as an assistant professor. He then carried out postdoctoral research at the University of Wisconsin, Madison, during 1975–76, before returning to Kyoto. In 1995 he was appointed Professor at the Institute of Chemical Research at the University of Kyoto.

H. Masuhara

H. Masuhara

Hiroshi Masuhara (Osaka University) has received a CSJ Award for his work on laser nanochemistry. Masuhara is a member of the editorial board of *ChemPhysChem*, where he recently described the enhancement of Förster energy transfer within a microscopic spherical cavity.[3] Masuhara completed his PhD at Osaka University in 1971 and remained there until 1984. He then accepted a professorship at the Kyoto Institute of Technology, and returned to Osaka University in 1991.

K. Tatsumi

K. Tatsumi

Kazuyuki Tatsumi (Nagoya University) completed his PhD in 1976 on theoretical inorganic chemistry. He then carried out postdoctoral fellowships at Texas A&M (M. Tsutsui) and Cornell University (R. Hoffmann). He returned to Osaka University in 1982 as an assistant professor. In 1994 he accepted a professorship at Nagoya University. He has been awarded by the CSJ for his work on the molecular architecture and bioinorganic chemistry of transition metal chalcogenides. He recently described in *Angewandte Chemie* a half-sandwich ruthenium(II) complex with a coordinatively unsaturated 2,6-dimesitylphenyl thiolate ligand.[4] Tatsumi serves on advisory boards for *The Chemical Record* and *Chemistry – An Asian Journal*.

D. Uemura

Daisuke Uemura (Nagoya University) receives his award for his research in the area of bioorganic chemistry of marine natural products. Uemura reported recently in *Angewandte Chemie* on the enantioselective synthesis of the spirotetracyclic core of mangicols through a stereoselective transannular Diels–Alder reaction.[5] Uemura completed his PhD in 1975 at Nagoya University (Y. Hirata). Until 1997, he held a professorship at Shizuoka University and was a postdoc with Y. Kishi (Harvard) in 1982. He chairs the organizing committee for the IUPAC congress on biodiversity and natural products in Kyoto in July.

D. Uemura

Y. Umezawa

Y. Umezawa

Yoshio Umezawa (University of Tokyo) has been awarded for the development of methods for imaging and detecting ions and molecules. Recently, in *Angewandte Chemie* he reported a fluorescent indicator for the visualization of the activity of androgen receptor ligands in single living cells.[6] Umezawa obtained his PhD from the University of Tokyo in 1972 and subsequently worked as a postdoc in Cincinnati, Chapel Hill (NC), Ohio, and Budapest until he became a Professor at the Hokkaido University in 1985 and in Tokyo in 1992. Umezawa is a member of the advisory boards for *The Chemical Record* and *Chemistry – An Asian Journal*.

[1] H.-B. Cui, K. Takahashi, Y. Okano, H. Kobayashi, Z. Wang, A. Kobayashi, *Angew. Chem.* **2005**, *117*, 6666; *Angew. Chem. Int. Ed.* **2005**, *44*, 6508.

[2] a) H. Sawa, Y. Wakabayashi, Y. Murata, M. Murata, K. Komatsu, *Angew. Chem.* **2005**, 117, 2017; *Angew. Chem. Int. Ed.* **2005**, *44*, 1981; b) T. Kitagawa, Y. Lee, N. Masaoka, K. Komatsu, *Angew. Chem.* **2005**, *117*, 1422; *Angew. Chem. Int. Ed.* **2005**, *44*, 1398.

[3] H. Fujiwara, K. Sasaki, H. Masuhara, *ChemPhysChem* **2005**, *6*, 2410.

[4] Y. Ohki, H. Sadohara, Y. Takikawa, K. Tatsumi, *Angew. Chem.* **2004**, *116*, 2340; *Angew. Chem. Int. Ed.* **2004**, *43*, 2290.

[5] K. Araki, K. Saito, H. Arimoto, D. Uemura, *Angew. Chem.* **2004**, *116*, 83; *Angew. Chem. Int. Ed.* **2004**, *43*, 81.

[6] M. Awais, M. Sato, X. Lee, Y. Umezawa, *Angew. Chem.* **2006**, *118*, 2773; *Angew. Chem. Int. Ed.* **2006**, *45*, 2707.

DOI: 10.1002/anie.200601201

WILEY InterScience DISCOVER SOMETHING GREAT

© 2006 Wiley-VCH Verlag GmbH & Co. KGaA, Weinheim

Receptor Libraries

DOI: 10.1002/anie.200504480

Dynamic Combinatorial Chemistry: The Unexpected Choice of Receptors by Guest Molecules

*Bas de Bruin, Peter Hauwert, and Joost N. H. Reek**

Keywords:
dynamic combinatorial chemistry · molecular recognition · receptors · supramolecular chemistry

Although our knowledge in the broad field of chemistry has increased enormously over the past decades, we are still unable to give precise predictions on the behavior of molecules in solution. Therefore, combinatorial approaches and high-throughput experimentation have become increasingly important by facilitating the rapid discovery of lead compounds and the optimization of processes in which trial-and-error is the dominant approach. In the mid-1990s, a fundamentally new concept in this area, dynamic combinatorial chemistry (DCC), was introduced by the groups of Sanders,[1] Lehn,[2] and others.[3,4] Whereas traditional combinatorial libraries are based on the preparation of kinetically stable compounds and subsequent screening for their function, this new concept takes advantage of reversible bonds, covalent or noncovalent, by generating a random (virtual) library whose members are in dynamic equilibrium.

The formation of the library is under thermodynamic control, which gives rise to new properties such as adaptation; that is, the library readjusts its distribution by external stimuli. Upon addition of a target molecule, the mixture of potential receptors in the library re-equilibrates in favor of the best receptor(s) for the target. By using this strategy the preparation and screening of the receptor for a certain target is integrated in one step,[4d] as the receptor is chosen by the target. Libraries of receptors of variable complexity have been constructed, with the simplest comprised of a mixture of macrocycles of variable sizes based on identical building blocks (type A; Figure 1a).

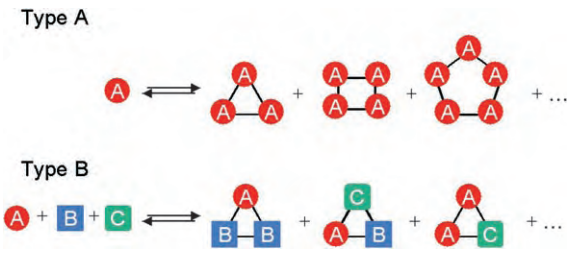

Figure 1. A dynamic combinatorial library (DCL) consisting of macrocycles of variable sizes based on identical building blocks (type A), and a DCL of similar-sized macrocycles based on different building blocks (type B).

More complex systems are composed of a mixture of different building blocks, thus forming receptors based on homo- and heteroaggregates (type B; Figure 1b). These approaches have been successfully applied to obtain a variety of receptors to bind different classes of guests, such as Li^+ and ammonium ions, and even a neurotransmitter.[5–7]

The elegance and power of the concept of amplification (and thus identification) of the best receptor was an issue of recent debate. Computer simulations[8] and thermodynamic/statistical analysis, supported by experimental data,[8a,9] on dynamic combinatorial libraries (DCLs) of the types shown in Figure 1 indicated that certainly not in all situations does the best receptor need to be amplified by the addition of the target. In these complex systems, in which receptors are in dynamic equilibrium, the energetically most favorable situation of the entire system determines the outcome of an amplification experiment. In situations where the concentration of the receptor depends on the composition of the library, the best receptor is not likely to be amplified at the expense of a lower total concentration of receptor. This problem does not arise for conventional, kinetically stable receptors because the composition of the receptor remains the same during the entire experiment. The amplification of a receptor from a DCL can only happen because the receptors compete simultaneously for both the building blocks that they are built from *and* the target guest. As different receptors are commonly built from the same building blocks, an increase in the concentration of certain receptors causes a decrease in the concentration of others (Figure 1).

Importantly, a shift in the equilibrium as a result of binding the guest leads in some scenarios to a decrease in the total concentration of relevant receptors. For example, amplification of the larger macrocycles of type A (A_n) leads to a decrease in the number of the smaller ones and, thus, reduces the total concentration of receptors available for guest binding. A comparable situation can occur for the type B receptors (Figure 1) if significant binding of the target guest requires the presence of a specific building block (e.g. building

[*] Dr. B. de Bruin, P. Hauwert, Prof. Dr. J. N. H. Reek
Van't Hoff Institute for Molecular Sciences
University of Amsterdam
Nieuwe Achtergracht 129
1018 WS Amsterdam (The Netherlands)
Fax: (+31) 20525-6437
E-mail: reek@science.uva.nl

InterScience
© 2006 Wiley-VCH Verlag GmbH & Co. KGaA, Weinheim

Table 1: Free-energy "economics" in the relative concentrations (c_{rel}) of library members of type B (Figure 1) as a function of the relative binding affinities (K_{rel}) of targets.

Entry		AAA	AAB	BBA	BBB	BBC	BCC	CCC	AAC	ACC	ABC
1	K_{rel}	1	1	1	1	1	1	1	1	1	1
	c_{rel} [%]	3.7	11.1	11.1	3.7	11.1	11.1	3.7	11.1	11.1	22.2
	$\Delta\Delta G^0$ [kcal mol^{-1}]	0	0	0	0	0	0	0	0	0	0
2	K_{rel}	1000	1	1	1	1	1	1	1	1	1
	c_{rel} [%]	28.1	0.5	3.4	7.2	21.5	21.5	7.2	0.5	3.4	6.8
	$\Delta\Delta G^0$ [kcal mol^{-1}]	−4.1	0	0	0	0	0	0	0	0	0
3	K_{rel}	900	600	300	1	1	1	1	600	300	300
	c_{rel} [%]	0.1	2.1	22.8	0.5	1.6	1.6	0.5	2.1	22.8	45.7
	$\Delta\Delta G^0$ [kcal mol^{-1}]	−4.0	−3.8	−3.4	0	0	0	0	−3.8	−3.4	−3.4

block A, as shown in entry 3 of Table 1). Amplification of the homoreceptors entirely built from this building block (A-A-A) occurs at the expense of the heteroreceptors that contain this building block (e.g. A-A-B, A-B-C, etc.) and thus leads to a decrease in the *total* concentration of receptors that make a significant contribution to the total free energy of the entire system. This phenomenon can easily lead to amplification of the weaker binding receptors at the cost of the better receptors, because the total free energy gained by guest binding by a few strong receptors can be less beneficial than a multitude of somewhat weaker interactions (see Table 1, entry 3). This effect is especially important when the relative free energies ($\Delta G^0 = -RT\ln K$) associated with binding of the target are of the same order of magnitude[8–10] and when the concentration of the target is relatively high.[9b,10]

To explain this phenomenon, the selection procedure in a DCC can be compared to the economic trade situation of retailers with respect to their customers. If sufficient customers (guests) are available, the most profitable situation is reached when as many shops (receptors) as possible are available to satisfy (bind) as many customers (guests) as possible, even though the profit per shop (binding energy per receptor) is not as high for all shops as that for the most profitable one. A turning point is reached at lower demands, and below a critical value the situation is reversed and a higher profit (binding energy) per shop (receptor) becomes most important. Therefore, the target-induced amplification in a DCL depends on the relative concentration of the guest. This behavior was first simulated by Severin and co-workers[8] and was recently experimentally confirmed by Otto, Sanders, and co-workers, as well as by Saur and Severin.[9] Indeed, at high concentrations of guest competition among receptors that are based on the same building blocks dominates the selection procedure, whereas at low concentrations of guest the receptor with the largest affinity is selected by the guest according to the best fit (most profit) principle. A recent theoretical analysis by Otto, Sanders, and co-workers[10] revealed that also in very large DCLs, which consist of many potential receptors, moderately good hosts that are already present in relatively high concentrations in the absence of the guest are likely to be amplified further upon addition of an excess of the guest.

On the basis of these findings, the groups of Sanders and Severin have reported a general strategy to select the best receptor from a DCL: 1) It is recommended to use conditions under which the building blocks (not the assemblies) are the dominant species in solution. 2) A DCL should be designed such that all receptors contain a common building block, which should be present in substoichiometric amounts with respect to the other subunits. 3) A relatively low concentration of the target should be used during the amplification experiment (a 1:10 ratio with respect to the total concentration of building blocks is used as a rule of thumb, taking the detection limitations into account).

These results show that the field of DCL is more complex than previously anticipated and amplification of the best receptor is not always obvious. On the other hand, one might argue that problems occur only when the differences between the receptors are small. The value of the DCC approach has been recently demonstrated by some interesting examples that reveal receptors with exceptionally strong affinities for the target. A common feature of these examples is that the hosts have unexpected structures, and it is very unlikely that these receptors would have been discovered by more traditional design and synthesis strategies.[11,7] For example, the DCL depicted in Figure 2 is

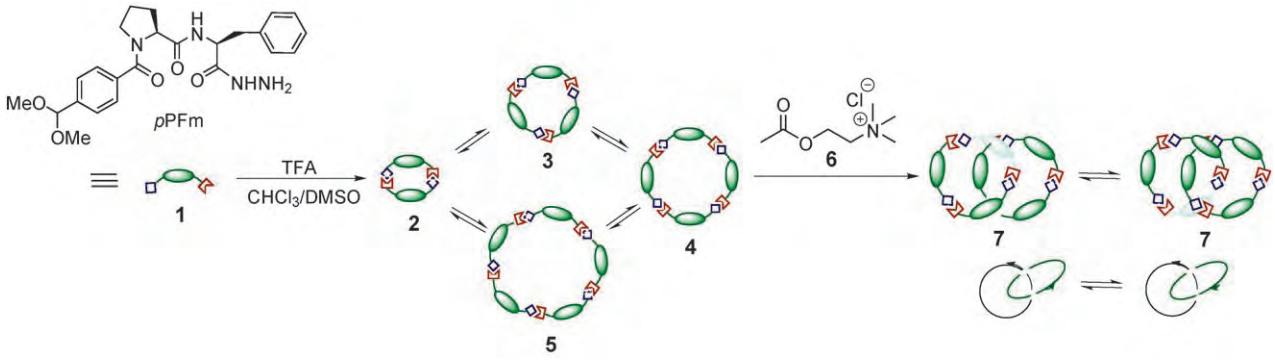

Figure 2. Unexpected amplification of a catenane receptor from a DCL of cyclic peptides by the addition of the neurotransmitter acetylcholine.[7] TFA = trifluoroacetic acid; DMSO = dimethyl sulfoxide.

 © 2006 Wiley-VCH Verlag GmbH & Co. KGaA, Weinheim

based on the reversible formation of a hydrazone from the hydrazide and a latent aldehyde (acetal functionality) of the peptide building block *p*PFm (**1**), which is a pseudopeptide based on proline and phenylalanine residues. The library consists of mostly cyclic oligomers **2**–**5** (**2**–**4** dominate). Most remarkably, addition of the neurotransmitter acetylcholine (**6**) causes a gradual increase in catenane **7**, which comprises two interlocked three-membered rings **3** and is not detected in the absence of the target. Acetylcholine binds to a single diastereoisomer of **7** in one specific conformation from the many possibilities, with an exceptionally high binding constant ($1.4 \times 10^7\,M^{-1}$). The affinity of the trimer **3** and tetramer **4** for acetylcholine proved to be much weaker (1.5×10^3 and $5.7 \times 10^3\,M^{-1}$, respectively). These results are remarkable because, first, the amplification of a catenane is highly unexpected. From rational design one would never have predicted that two interlocked rings would form the most suitable binding motif for the neurotransmitter, as there are no other catenane structures known that strongly bind cations.[12] Second, the DCC method proves useful as a synthetic method to prepare a catenane receptor that would have been most difficult to prepare without the template.[13]

A second remarkable example was recently reported in which tetramethylammonium salts were used as target guests during the amplification process (Figure 3). The initial DCL consisted of macrocycles based on **8** and a smaller disulfide formed by reversible S–S bond formation, and surprisingly the large macrocycle **11** was discovered as a good receptor. On the basis of size match–mismatch arguments, one would expect NMe_4^+ to bind much less strongly to the macrocyle *meso*-**11** than to the macrocyles *rac*-**9** and *rac*-**10** (Figure 3). Detailed studies revealed that *meso*-**11** is by far the best host in the mixture (reported binding constants of $4 \times 10^6\,M^{-1}$ and $8 \times 10^2\,M^{-1}$ for *meso*-**11** and *rac*-**9**, respectively). This unexpected result, which is unlikely to have been discovered by traditional strategies, was explained by the induced-fit character of the host; *meso*-**11** encapsulates the NMe_4^+ ion by folding completely around it (Figure 4).[11]

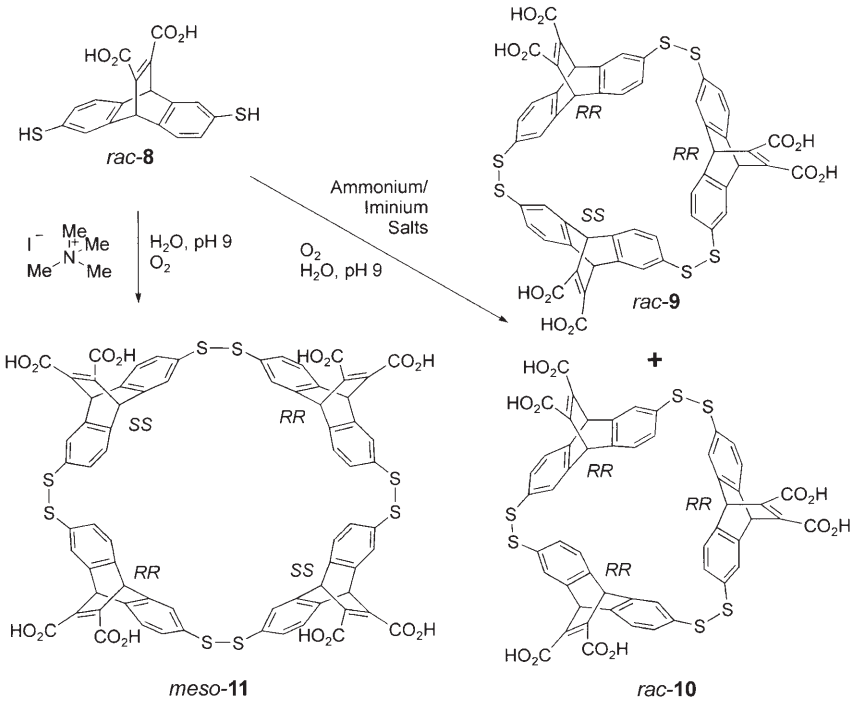

Figure 3. Unexpected amplification of a large, size-mismatched cyclic host from a DCL by the addition of NMe_4^+.[11]

Although "selection of the fittest" from a DCL does not necessarily always provide the "fittest", the importance of dynamic combinatorial chemistry is clearer than ever before. DCLs are theoretically well understood now and it is clear that they behave as complex systems. Examples of amplification of unexpected receptors with high target affinities superbly demonstrate the proof of principle. The next challenge is to apply the DCC approach to existing problems that are hard to solve by traditional strategies. In addition, the application of DCC in new research areas should be explored. In this regard, supramolecular catalysis in which the catalytic activity is based on the complexation of the transition state seems a particularly promising area. An example of the successful application of DCC in catalysis has already been reported.[6b] A DCL that is similar to the one depicted in Figure 3 was used to select a supramolecular catalyst for a Diels–Alder reaction by the addition of a transition-state analogue (in this case the product). The host that was amplified indeed accelerated (although moderately) the envisioned Diels–Alder reaction. The relevance of DCC in, for example, transition-metal catalysis is still open to investigation. However, in general, unexpected results, new synthetic methods, and new applications are likely to result from future studies.

Figure 4. CPK models of the complex formed from *meso*-**11** and NMe_4^+ in a) extended and b) folded conformations. The host binds the guest through an induced-fit mechanism. Reprinted with permission from Reference [11]

[1] a) P. A. Brady, R. P. Bonar-Law, S. J. Rowan, C. J. Suckling, J. K. M. Sanders, *Chem. Commun.* **1996**, 319–320; b) S. J. Rowan, P. A. Brady, J. K. M. Sanders, *Angew. Chem.* **1996**, *108*, 2283–2285; *Angew. Chem. Int. Ed. Engl.* **1996**, *35*, 2143–2145; c) S. J. Rowan, D. G. Hamilton, P. A. Brady, J. K. M. Sanders, *J. Am. Chem. Soc.* **1997**, *119*, 2578–2579; d) S. J. Rowan, J. K. M. Sanders, *Chem. Commun.* **1997**, 1407–1408.

[2] a) B. Hasenknopf, J.-M. Lehn, B. O. Kneisel, G. Baum, D. Fenske, *Angew.*

 © 2006 Wiley-VCH Verlag GmbH & Co. KGaA, Weinheim

Chem. **1996**, *108*, 1987 – 1990; *Angew. Chem. Int. Ed. Engl.* **1996**, *35*, 1838 – 1840; b) B. Hasenknopf, J.-M. Lehn, N. Boumediene, A. Dupont-Gervais, A. Van Dorsselaer, B. Kneisel, D. Fenske, *J. Am. Chem. Soc.* **1997**, *119*, 10956 – 10962; c) I. Huc, J.-M. Lehn, *Proc. Natl. Acad. Sci. USA* **1997**, *94*, 2106 – 2110; d) J.-M Lehn, A. V. Eliseev, *Science* **2001**, *291*, 2331 – 2332.

[3] a) T. Hayashi, T. Asai, H. Hokazono, H. Ogoshi, *J. Am. Chem. Soc.* **1993**, *115*, 12210 – 12211; b) B. A. Katz, J. Finer-Moore, R. Mortezaei, D. H. Rich, R. M. Stroud, *Biochemistry* **1995**, *34*, 8264 – 8280; c) P. G. Swann, R. A. Casanova, A. Desai, M. M. Frauenhoff, M. Urbancic, U. Slomcznska, A. J. Hopfinger, G. C. LeBreton, D. L. Venton, *Biopolymers* **1996**, *40*, 617 – 625; d) S. Sakai, Y. Shigemase, T. Sasaki, *Tetrahedron Lett.* **1997**, *38*, 8145 – 8148; e) A. V. Eliseev, M. I. Nelen, *J. Am. Chem. Soc.* **1997**, *119*, 1147 – 1148; f) B. Klekota, M. H. Hammond, B. L. Miller, *Tetrahedron Lett.* **1997**, *38*, 8639 – 8642; g) H. Hioki, W. C. Still, *J. Org. Chem.* **1998**, *63*, 904 – 905.

[4] For selected reviews, see: a) S. Otto, *Curr. Opin. Drug Discovery Dev.* **2003**, *6*, 509 – 520; b) S. J. Rowan, S. J. Cantrill, G. R. L. Cousins, J. K. M. Sanders, J. F. Stoddart, *Angew. Chem.* **2002**, *114*, 938 – 993; *Angew. Chem. Int. Ed.* **2002**, *41*, 898 – 952; c) O. Ramström, T. Bunyapaiboonsri, S. Lohmann, J.-M. Lehn, *Biochim. Biophys. Acta* **2002**, *1572*, 178 – 186; d) A. Ganesan, *Angew. Chem.* **1998**, *110*, 2989 – 2992; *Angew. Chem. Int. Ed.* **1998**, *37*, 2828 – 2831; e) J.-M. Lehn, *Chem. Eur. J.* **1999**, *5*, 2455 – 2463; f) J.-L. Reymond, *Angew. Chem.* **2004**, *116*, 5695 – 5697; *Angew. Chem. Int. Ed.* **2004**, *43*, 5577 – 5579.

[5] a) I. Saur, R. Scopelliti, K. Severin, *Chem. Eur. J.* **2006**, *12*, 1058 – 1066; b) S. Otto, S. Kubik, *J. Am. Chem. Soc.* **2003**, *125*, 7804 – 7805; c) T. Nishinaga, A. Tanatani, K. C. Oh, J. S. Moore, *J. Am. Chem. Soc.* **2002**, *124*, 5934 – 5935; d) O. Storm, U. Lüning, *Chem. Eur. J.* **2002**, *8*, 793 – 798; e) A. L. Kieran, A. D. Bond, A. M. Belenguer, J. K. M. Sanders, *Chem. Commun.* **2003**, 2674 – 2675; f) B. Fuchs, A. Nelson, A. Star, J. F. Stoddart, S. B. Vidal, *Angew. Chem.* **2003**, *115*, 2618 – 2622; *Angew. Chem. Int. Ed.* **2003**, *42*, 4220 – 4224; g) R. Cacciapaglia, S. Di Stefano, L. Mandolini, *J. Am. Chem. Soc. 127*, **2005**, 13666 – 13671; h) Y. Kubota, S. Sakamoto, K. Yamaguchi, M. Fujita, *Proc. Natl. Acad. Sci. USA* **2002**, *99*, 4854 – 4856; i) M. Hochgürtel, H. Kroth, D. Piecha, M. W. Hofmann, C. Nicolau, S. Krause, O. Schaaf, G. Sonnenmoser, A. V. Eliseev, *Proc. Natl. Acad. Sci. USA* **2002**, *99*, 3382 – 3387.

[6] a) S. Otto, R. L. E. Furlan, J. K. M. Sanders, *Science* **2002**, *297*, 590 – 593; b) B. Brisig, J. K. M. Sanders, S. Otto, *Angew. Chem.* **2003**, *115*, 1308 – 1311; *Angew. Chem. Int. Ed.* **2003**, *42*, 1270 – 1273.

[7] R. T. S. Lam, A. Belenguer, S. L. Roberts, C. Naumann, T. Jarrosson, S. Otto, J. K. M. Sanders, *Science* **2005**, *308*, 667 – 669.

[8] a) Z. Grote, R. Scopelliti, K. Severin, *Angew. Chem.* **2003**, *115*, 3951 – 3955; *Angew. Chem. Int. Ed.* **2003**, *42*, 3821 – 3825; b) K. Severin, *Chem. Eur. J.* **2004**, *10*, 2565 – 2580.

[9] a) P. T. Corbet, J. K. M. Sanders, S. Otto, *J. Am. Chem. Soc.* **2005**, *127*, 9390 – 9392; b) I. Saur, K. Severin, *Chem. Commun.* **2005**, 1471 – 1473.

[10] P. T. Corbett, S. Otto, J. K. M. Sanders, *Chem. Eur. J.* **2004**, *10*, 3139 – 3143.

[11] P. T. Corbett, L. H. Tong, J. K. M. Sanders, S. Otto, *J. Am. Chem. Soc.* **2005**, *127*, 8902 – 8903.

[12] a) For two examples of catenane receptors for anions, see: A. Andrievsky, F. Ahuis, J. L. Sessler, F. Vögtle, D. Gudat, M. Moini, *J. Am. Chem. Soc.* **1998**, *120*, 9712 – 9713; b) M. R. Sambrook, P. D. Beer, J. A. Wisner, R. L. Paul, A. R. Cowley, *J. Am. Chem. Soc.* **2004**, *126*, 15364 – 15365.

[13] T. J. Hubin, D. H. Busch, *Coord. Chem. Rev.* **2000**, *20*, 5 – 52.

 © 2006 Wiley-VCH Verlag GmbH & Co. KGaA, Weinheim

Ring-Closing Metathesis

DOI: 10.1002/anie.200503512

Ring-Closing Metathesis as a Basis for the Construction of Aromatic Compounds

Timothy J. Donohoe, Allan J. Orr, and Matilda Bingham*

Keywords:
arenes · carbocycles · heterocycles · metathesis · synthetic methods

The use of metathesis, especially in the context of ring-closing metathesis (RCM) to form five- and six-membered rings, is widespread in organic chemistry today. However, there are surprisingly few examples of the reaction being used to form aromatic compounds. The central place of aromatic compounds in both medicinal chemistry and natural products synthesis, coupled with the efficiency and functional group tolerance of RCM catalysts, means that there is now an interesting opportunity to use RCM for the synthesis of arenes. Although the formation of an aromatic compound was viewed in many early examples as an undesirable degradation product, several rationally designed methods towards the preparation of aromatic compounds by RCM have recently been developed.

1. Introduction

The word metathesis is derived from the Greek for "change position". The olefin metathesis reaction itself involves the exchange of groups around double bonds. It is promoted by a metal carbene complex and is believed to proceed through a series of reversible [2+2] cycloadditions and cycloreversions.[1–8] The ring-closing metathesis (RCM) variant of this general reaction has become one of the most powerful ways of forming cyclic structures and yields a wide range of ring sizes. This powerful method for closing rings is often followed by hydrogenation to remove the alkene that was introduced by the RCM reaction. The notion of using RCM processes to form unsaturated cyclic structures is but a short step away from the construction of an aromatic ring system. Despite this small step, there are relatively few examples of the use of the RCM reaction to deliberately construct aromatic compounds.

An examination of the literature reveals that the calculated synthesis of aromatic compounds by RCM has followed four strategies, which will be discussed in turn. First, ring closure followed by an aromatization step through oxidation yields arenes. Second, RCM to give an appropriate cyclic compound then an elimination of a suitable leaving group gives arenes directly. Third, the construction of new rings fused to existing aromatic frameworks can give rise to fused arenes in one step. Finally, a combination of RCM with tautomerization of the products is a powerful new idea that promises much for the future.

2. RCM Followed by Oxidation

Perhaps the simplest route to aromatic compounds through the RCM process is ring closure followed by an allylic oxidation. In 1985, the industrial chemists Warwel and Winkelmüller reported the synthesis of some alkyl benzenes through cross-metathesis (using a poorly defined $WCl_6/Et_2O/SnBu_4$ catalyst) followed by oxidative aromatization of the cyclohexenylalkene products.[9] However, further work in this area had to wait for the development of more powerful and versatile metathesis catalysts.[10–15]

In early work, Grigg and co-workers mentioned the formation of a pyrrole **4** by RCM in a single experiment using Grubbs' first generation catalyst **1**, at elevated temperatures, whilst attempting to close the rings for a series of aniline derivatives, such as **2** (Scheme 1).[16]

[*] Prof. T. J. Donohoe, A. J. Orr
Department of Chemistry
University of Oxford
Chemistry Research Laboratory
Mansfield Road, Oxford, OX1 3TA (UK)
Fax: (+44) 1865-275-708
E-mail: timothy.donohoe@chem.ox.ac.uk
Dr. M. Bingham
Department of Medicinal Chemistry
Organon Laboratories Ltd.
Newhouse, Lanarkshire ML1 5SH, Scotland (UK)

InterScience
© 2006 Wiley-VCH Verlag GmbH & Co. KGaA, Weinheim

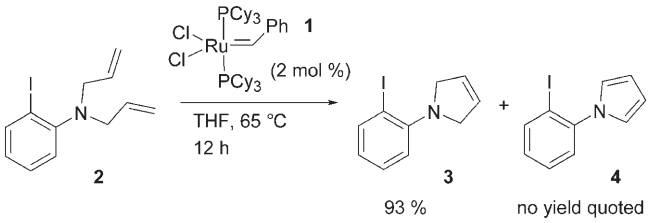

Scheme 1. Formation of pyrroles as a by-product of RCM. Cy = cyclohexyl.

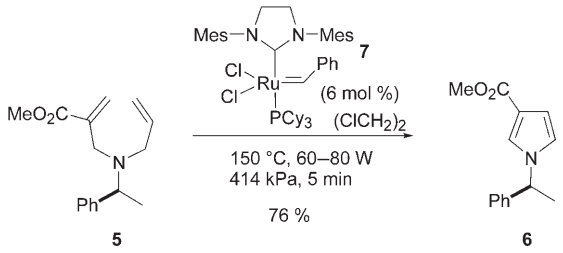

Scheme 2. Serendipitous formation of pyrroles through microwave-promoted RCM. Mes = mesityl.

Wilson and co-workers also reported the serendipitous synthesis of a pyrrole following an RCM reaction under microwave conditions.[17] Exposure of the N-protected diene **5** (Scheme 2) to Grubbs' second generation catalyst **7** in a microwave for 5 minutes resulted in isolation of pyrrole **6** in 76% yield. Only one other pyrrole was formed in this study and was obtained as a mixture along with the corresponding dihydropyrrole (these were the desired products of the investigation). Surprisingly, all of the other examples detailed therein returned the expected dihydropyrroles after the RCM reaction.

Robertson et al. also adopted this approach during their investigation into the synthesis of roseophilin. They detailed an experiment, as a footnote, designed to target the bis-aromatic portion of the target molecule.[18] An RCM reaction on pyrrole **8** proceeded smoothly at room temperature to form the ring-closed product **9** in 88% yield (Scheme 3). However, subsequent allylic oxidation proved extremely difficult; the pyrrole-furan **10** was eventually obtained in 8% yield after reaction of **9** with NiO_2 for five days.

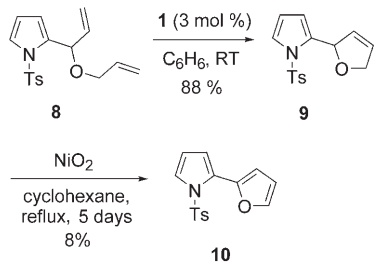

Scheme 3. Synthesis of pyrrole-furan biaryls by an RCM/oxidation protocol. Ts = tosyl.

Stevens and co-workers also used the oxidation strategy and employed a tandem Grubbs' carbene/$RuCl_3$ catalytic system to effect ring closure and subsequent dehydrogenation (promoted by $RuCl_3$) in situ to give a pyrrole (Scheme 4).[19] The strategy met with some degree of success, and a series of different N-protected pyrroles could be formed in moderate yield. Unfortunately, substitution could only be incorporated onto the pyrrole backbone itself in one instance (**14**, Scheme 4). When electron-withdrawing groups were present on the nitrogen atom, no oxidation was observed. The authors suggested, therefore, that coordination of the ruthenium species onto nitrogen is implicated in the oxidation and, hence, that the basicity of the nitrogen atom is crucial in this process. However, in follow-up work, the authors managed to improve upon the yields in this sequence by altering the (in situ) oxidant to the quinone derivative, chloroanil (**17**).[20] Thus, for example, a 90% conversion was observed in the case of **15**→**16** under the new conditions (Scheme 4).

Another example of this RCM/oxidation method was disclosed by Nakagawa and co-workers in 2001[21] and expanded upon by Bennasar et al. in 2005.[22] Nakagawa and collaborators obtained the quinoline **20** after an RCM

Timothy J. Donohoe studied chemistry at the University of Bath and obtained his DPhil with S. Davies at Oxford (1992). Following a postdoctoral stay with P. Magnus in the USA, he joined the University of Manchester in 1994 as a lecturer and was promoted to Reader in 2000. In 2001 he joined the Dyson Perrins Laboratory, Oxford, as Lecturer in Chemistry and Fellow of Magdalen College, and in 2004 he was appointed Professor of Chemistry at Oxford University. His research interests encompass asymmetric synthesis, total synthesis, catalysis, and redox reactions.

Matilda Bingham studied chemistry at Imperial College London and completed her PhD on the synthesis of artificial enzyme catalysts using molecular imprinting (W. Motherwell) at University College London in 2000. Following two years as a postdoctoral fellow, working first with S. Zard at the Institut de Chimie des Substances Naturelles at Gif-sur-Yvette (France) and then J. Winkler at the University of Pennsylvania, she joined the Medicinal Chemistry Department at Organon (UK), where she is currently a team leader and research scientist in the CNS therapeutic area.

Allan J. Orr was born in Motherwell (UK) and received his MSc degree from the University of Strathclyde in Glasgow, following a year in industry, in 2001. He commenced his studies for his DPhil in 2002 under the supervision of Prof. Timothy J. Donohoe, investigating the synthesis of aromatic compounds using the ring-closing metathesis reaction.

© 2006 Wiley-VCH Verlag GmbH & Co. KGaA, Weinheim

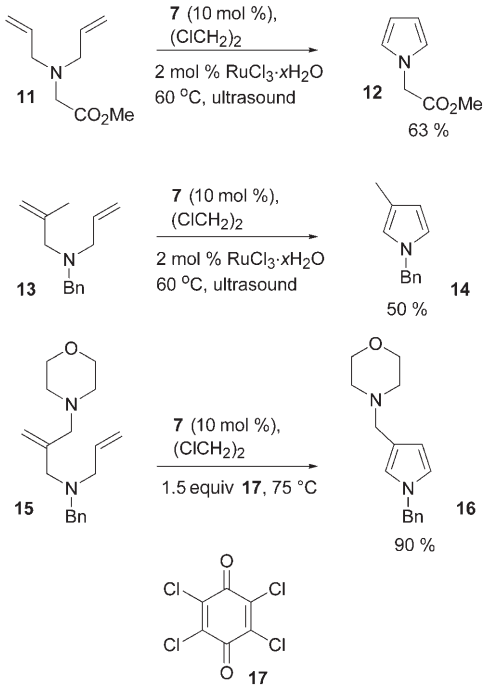

Scheme 4. Formation of pyrroles through an RCM/dehydrogenation strategy. Bn = benzyl.

reaction on the N-protected diene **18**, followed by deprotection of the nitrogen from **19** during silica gel chromatography, and then spontaneous oxidation in air (Scheme 5).[21] Both steps proceeded in near-quantitative yields. Bennasar et al. recently synthesized two quinolines **24** and **25** from their respective 1,4-dihydroquinoline analogues **22** and **23**, which were themselves constructed by an RCM reaction (Scheme 5).[22] The enamides **21** (R = H, Me) were prepared from the corresponding amides through an olefination process and then subjected to standard RCM conditions in toluene. Subsequent treatment of the ring-closed products with 5% Pd/C under an O_2 atmosphere afforded the fully aromatic products.

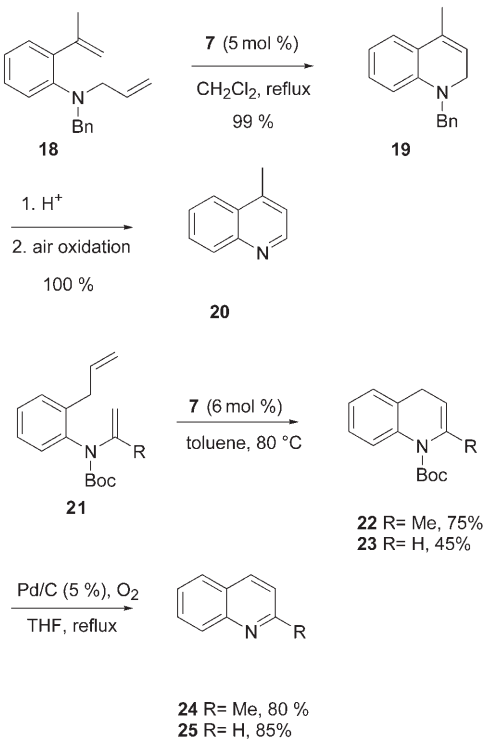

Scheme 5. Synthesis of quinolines by an RCM/oxidation protocol. Boc = *tert*-butyloxycarbonyl.

This RCM/oxidation protocol has also been used to synthesize aromatic five- and six-membered B,N-containing heterocycles, namely azaborolides and azaborines, respectively.[23]

3. RCM Followed by Elimination of a Leaving Group

Another way of forming aromatic compounds after a RCM reaction is to incorporate a leaving group in the ring thus formed; subsequent elimination then completes the sequence.

During their investigations into spirocycle assembly through tandem RCM, Harrity and co-workers showed that their methodology was more suited to the construction of sensitive [4,4]-spiroacetals than traditional acid-catalyzed techniques.[24] They demonstrated the sensitivity of the products from RCM by treating spiroacetal **27** with TsOH at room temperature and showed that it decomposed to furan **28** within one hour (Scheme 6).

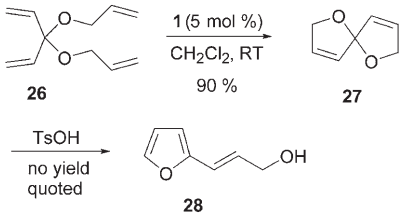

Scheme 6. Decomposition of a spiroacetal to a furan.

Our own ongoing efforts towards the synthesis of aromatic frameworks by RCM recently led to the disclosure of a palladium coupling/RCM/elimination protocol.[25] We were able to construct our acyclic diene RCM precursors **30** and **33** in good yields by using palladium(II)-catalyzed coupling of an alcohol (or a sulfonamide) with methoxyallene (Scheme 7).[26–29] Subsequent treatment of the mixed acetals and aminals **30** and **33** with Grubbs' second generation catalyst **7**, followed by exposure of the ring-closed intermediates to TFA, resulted in the elimination of methanol to afford substituted furans **31** and pyrroles **34** in good overall yields. Note that Rutjes and co-workers had previously reported the formation of *N*-tosylpyrrole itself as a result of similar decomposition of a corresponding RCM intermediate on silica.[28]

We then applied this methodology to the construction of some interesting α-linked biaryl systems, first in a similar

 © 2006 Wiley-VCH Verlag GmbH & Co. KGaA, Weinheim

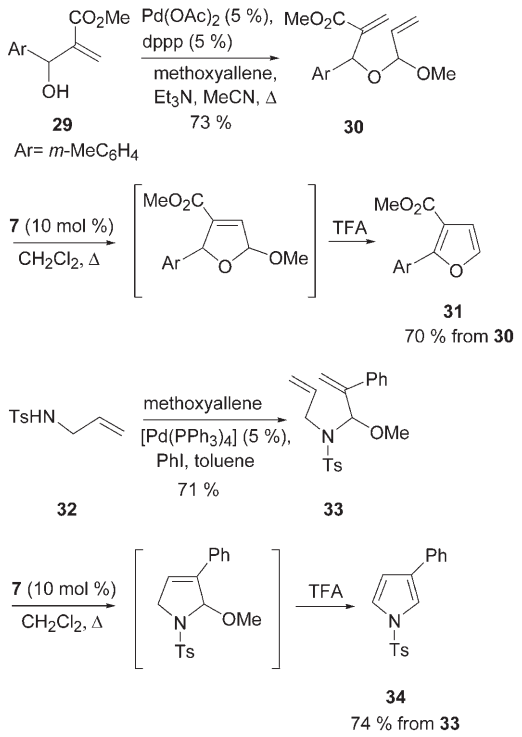

Scheme 7. Palladium coupling/RCM/elimination route to furans and pyrroles. TFA = trifluoroacetic acid, dppp = 1,3-bis(diphenylphosphino)propane.

manner to that described above, then by an intriguing double palladium coupling/RCM/elimination strategy (Scheme 8).[24,30] Hence, the pyrrole-furan **37** and the bifuranyl **40** were synthesized in good yield and in a rapid and efficient manner.

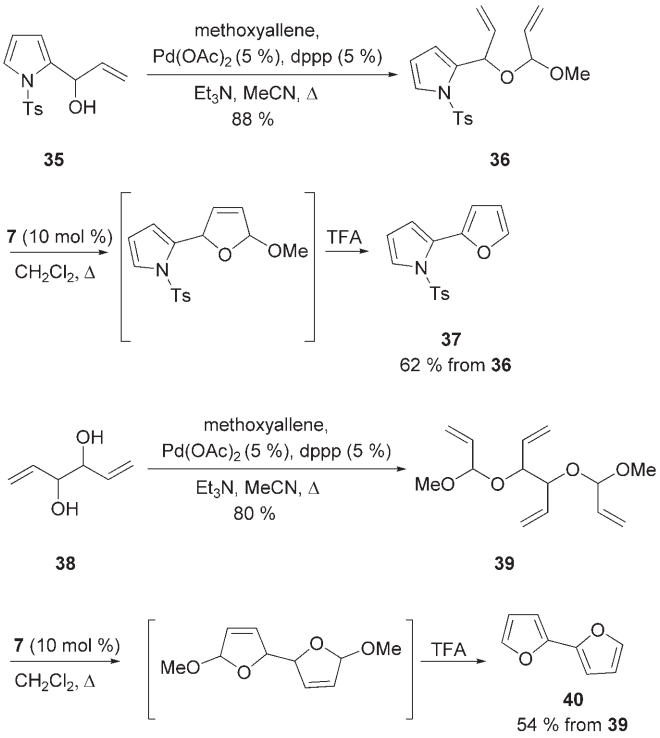

Scheme 8. Synthesis of linked biaryls by RCM/elimination.

A similar approach was used by Lovely and co-workers in the synthesis of a benzimidazole as part of their investigation into the formation of a series of bicyclic imidazoles (Scheme 9).[31] The bicyclic structure was formed by an RCM reaction of the diene **41** with Grubbs' second generation catalyst, and elimination of water in situ furnished the benzimidazole **42**, albeit in 45 % yield.

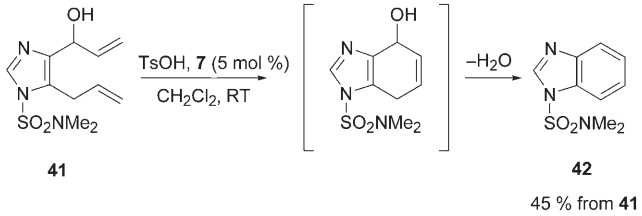

Scheme 9. Synthesis of a benzimidazole by RCM/elimination.

Fürstner et al. used enyne metathesis to construct N-heterocylic rings en route to a synthesis of the antibiotic metacycloprodigiosin (Scheme 10).[32] Here, compound **43**

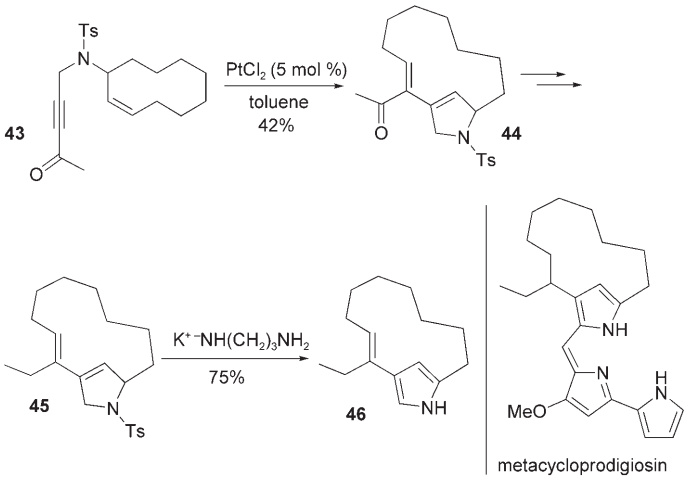

Scheme 10. Enyne metathesis route to pyrroles.

was transformed to the rearranged derivative **44** in 42 % yield using platinum dichloride as catalyst. After a small amount of manipulation, the aromatization of **45**, by treatment with a strong base, was accomplished to give **46** in 75 % yield. Compound **46** is a known intermediate in the synthesis of metacycloprodigiosin, and so this work constituted a formal synthesis of the target.

A related and general approach to the synthesis of several substituted pyrroles was reported by Lamaty and co-workers and involved an aza-Baylis–Hillman/RCM/aromatization sequence.[33] Accordingly, the aza-Baylis–Hillman reaction between **47**, an aryl aldehyde, and methyl acrylate produced the trimethylsilylethylsulfonyl (SES)-protected β-aminoesters **48** (Scheme 11). These sulfonamides could be allylated to

 © 2006 Wiley-VCH Verlag GmbH & Co. KGaA, Weinheim

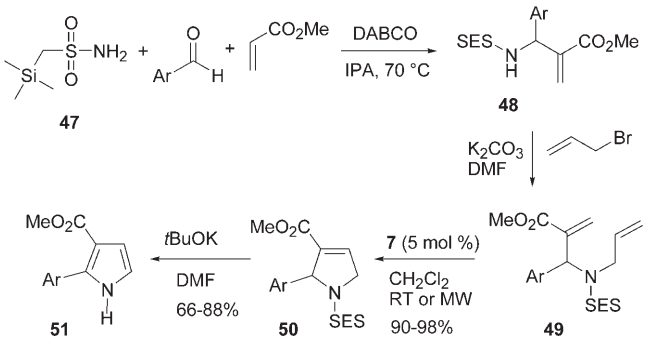

Scheme 11. Aza-Baylis–Hillman/RCM/aromatization sequence to substituted pyrroles. Ar can be any one of 11 different substituted aryl groups;[33] DABCO = 1,4-diazabicyclo[2.2.2]octane; IPA = isopropyl alcohol; MW = microwave.

the RCM precursor diene **49**, which, upon treatment with Grubbs' second generation catalyst at ambient temperature or in a microwave, afforded the ring-closed products **50** in high yields. The aromatization step was achieved through a base-induced elimination of the sulfonyl group, resulting in the formation of 2-aryl,3-methoxycarbonylpyrroles **51** in good overall yields.

In 2001, Huang and Wang reported the synthesis of a number of naphthalene derivatives by an RCM/elimination method (Scheme 12).[34] The diene precursors **52** were constructed through a Claisen rearrangement and subsequently ring-closed using Grubbs' first generation catalyst **1**. Elimination of water in situ afforded naphthalenes **53** in good overall yields (80–92%).

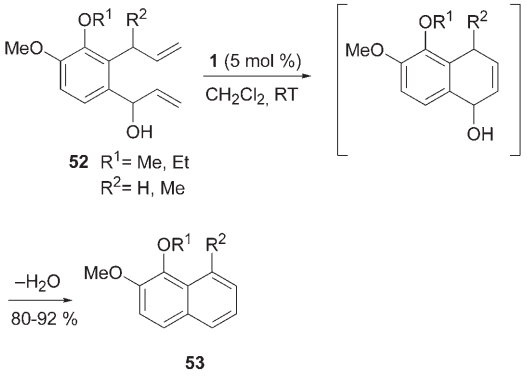

Scheme 12. Synthesis of naphthalene derivatives by RCM/elimination.

Yamamoto and co-workers recently disclosed an interesting approach to naphthalene derivatives through an enyne metathesis catalyzed by $PtBr_2$ (Scheme 13).[35] In this case, the platinum catalyst had a dual role: first, to facilitate the enyne metathesis of **54** to **55**, and, second, as a Lewis acid to induce elimination of methanol to give the fully aromatic product **56**. In this manner, several substituted naphthalene derivatives were synthesized with yields ranging from 35–76%.

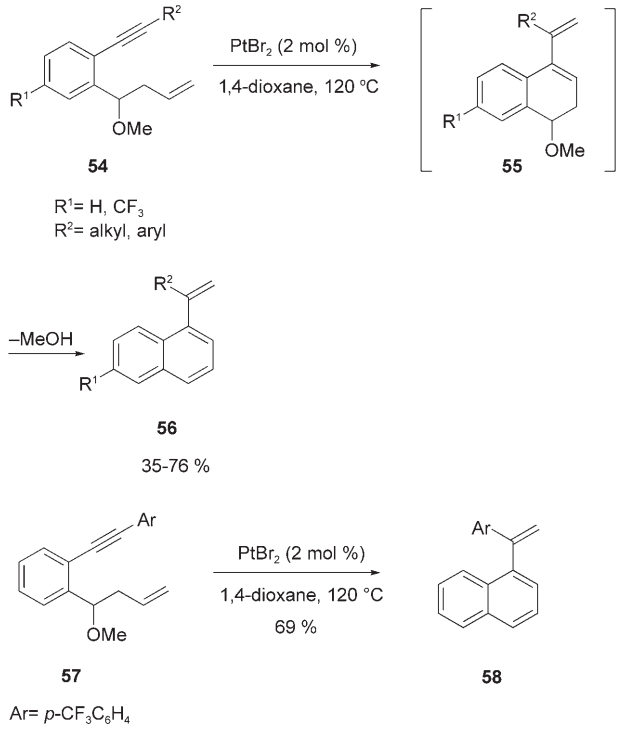

Scheme 13. Synthesis of naphthalene derivatives by enyne metathesis.

4. Fused Aromatic Compounds Formed Directly by RCM

The use of RCM to form a new ring that is fused to an existing unsaturated framework can also result in the formation of a new aromatic ring system, purely as a consequence of the structure of the RCM product. This approach has been used in the construction of benzofurans, indoles, and phenanthrenes.

In 1994, Grubbs and co-workers reported the synthesis of several cyclic enol ethers by RCM, initiated by Schrock's molybdenum catalyst **59**.[36] They also disclosed that 2-substituted benzofurans could be efficiently prepared by this method. Hence, ring closures of enol ethers **60** and **62** proceeded in 87% yield in both cases to deliver early examples of aromatic compounds prepared directly by RCM (Scheme 14).

In a similar manner, Nishida and co-workers prepared four substituted indoles through an RCM strategy (Scheme 15).[37] Note that the starting enamines **65** were prepared from the *N*-allyl compound **64**, which underwent isomerization in the presence of catalyst **7** and vinyloxytrimethylsilane. Sulfonamide **65** was then treated with 5 mol% of catalyst **7**, and RCM afforded the substituted indole **66** directly in 83% yield.

Iuliano et al. recently constructed a series of differently substituted phenanthrenes, which are useful intermediates in natural product synthesis, by RCM of 2,2′-divinylbiphenyls **67** (these were conveniently prepared by Wittig olefination of benzaldehyde precursors; Scheme 16).[38] They reported that the metathesis reactions proceeded in good yields under mild conditions using second generation catalyst **68**, irrespective of

© 2006 Wiley-VCH Verlag GmbH & Co. KGaA, Weinheim

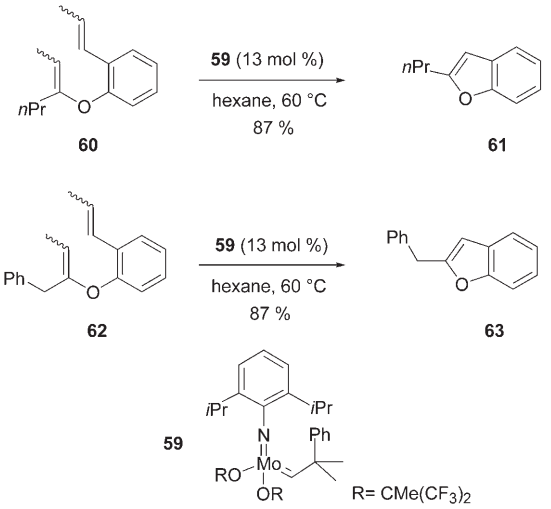

Scheme 14. Synthesis of benzofurans by RCM.

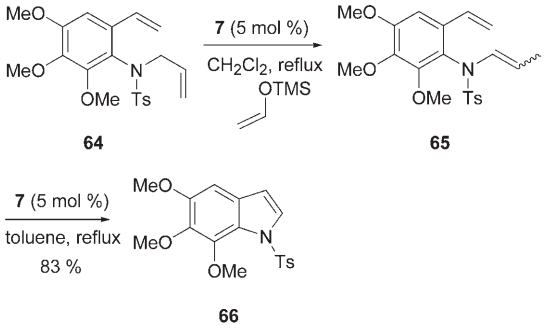

Scheme 15. Synthesis of indoles by RCM. TMS = trimethylsilyl.

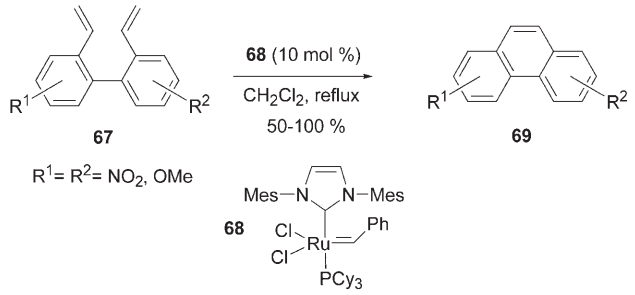

Scheme 16. Synthesis of substituted phenanthrenes by RCM.

the nature and position of the substituents present on the starting material.

5. RCM Combined with Tautomerization

The combination of RCM reactions with a tautomerization reaction of the products is an ingenious way of making aromatic compounds directly. So far, only carbocyclic arenes have been prepared this way but there is much promise here for the future.

Van Otterlo et al. reported the first example of an aromatic compound synthesized through an RCM/tautomerization protocol in 2003. They obtained the naphthol derivative **72** in 69% yield, as an isolated example, during their study into the formation of benzo-fused bicyclic compounds (Scheme 17).[39] Hence, oxidation of alcohol **70** by MnO_2 and subsequent ring closure provided naphthol **72**, which was presumably formed by tautomerization of a corresponding cyclic ketone intermediate derived from **71**.

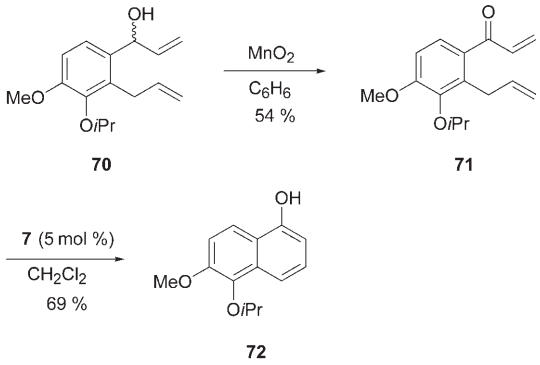

Scheme 17. Synthesis of a naphthol derivative by RCM/tautomerization.

This approach was also successfully used by Yoshida and Imamoto, who constructed a series of substituted phenol derivatives in a process related to that described above. Hence, a range of substituted trienes **73** (prepared by standard synthetic sequences) were subjected to RCM with catalyst **7** (2.5–7.5 mol%) in dichloromethane to afford the proposed ketone intermediates **74**, which spontaneously tautomerized to phenols **75** (Scheme 18).[40] A maximum number of three substituents could be placed on the ring, including alkyl, phenyl, alkyloxy, silyl, and silyloxy groups. In most cases, the reaction proceeded in very good yield and

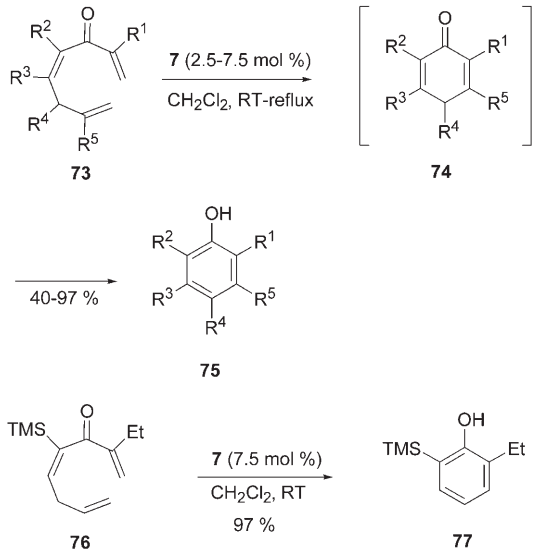

Scheme 18. Synthesis of substituted phenol derivatives by RCM/tautomerization. R^1 = H, alkyl, C_2H_4OH, C_2H_4OAc; R^2 = H, *n*Pr, Ph, TMS; R^3 = *n*Pr, H, D; R^4 = H, TBS; R^5 = H, Me. TBS = *tert*-butyldimethylsilyl.

 © 2006 Wiley-VCH Verlag GmbH & Co. KGaA, Weinheim

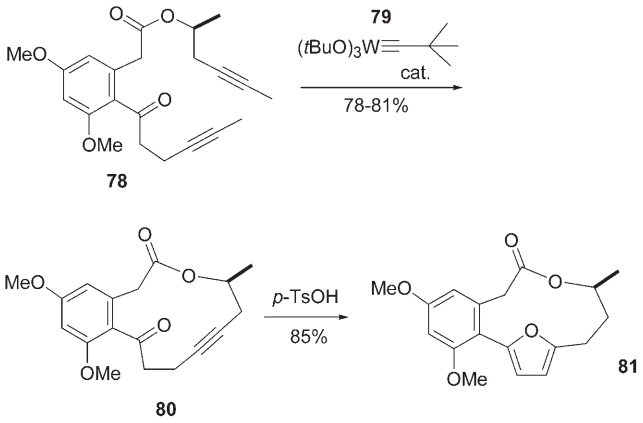

Scheme 19. Synthesis of a furan using an RCAM reaction.

promises to become a general method for the synthesis of phenols.

Finally, Fürstner et al. used the ring-closing alkyne metathesis reaction (RCAM) as a key C–C bond-forming reaction en route to a furan.[41] The RCAM reaction of **78** gave macrocyclic alkyne **80** in good yield. This compound was then treated with acid to accomplish formation of furan **81** (Scheme 19);[42] double deprotection of the two phenylmethyl ethers within **81** in one step then gave the natural product citreofuran.

6. Summary and Outlook

From this survey, it is clear that the synthesis of aromatic compounds by RCM is an important emerging area and one that will continue to grow in the coming years. The four main strategies that have been used to construct arenes are likely to be developed and expanded until RCM-based chemistry becomes a method of choice for preparing complex substituted aromatic carbocycles or heterocycles.

We thank the EPSRC and Organon for funding.

Received: October 4, 2005
Published online: March 20, 2006

[1] R. H. Grubbs, S. J. Miller, G. C. Fu, *Acc. Chem. Res.* **1995**, *28*, 446.
[2] R. H. Grubbs, S. Chang, *Tetrahedron* **1998**, *54*, 4413.
[3] S. K. Armstrong, *J. Chem. Soc. Perkin Trans. 1* **1998**, 371.
[4] A. Fürstner, *Angew. Chem.* **2000**, *112*, 3140; *Angew. Chem. Int. Ed.* **2000**, *39*, 3012.
[5] T. M. Trnka, R. H. Grubbs, *Acc. Chem. Res.* **2001**, *34*, 18.
[6] A. Deiters, S. F. Martin, *Chem. Rev.* **2004**, *104*, 2199.
[7] M. D. McReynolds, J. M. Dougherty, P. R. Hanson, *Chem. Rev.* **2004**, *104*, 2239.
[8] K. C. Nicolaou, P. G. Bulger, D. Sarlah, *Angew. Chem.* **2005**, *117*, 4564; *Angew. Chem. Int. Ed.* **2005**, *44*, 4490.
[9] S. Warwel, W. Winkelmüller, *J. Mol. Catal.* **1985**, *28*, 247.
[10] R. R. Schrock, J. S. Murdzek, G. C. Bazan, J. Robbins, M. Dimare, M. Oregan, *J. Am. Chem. Soc.* **1990**, *112*, 3875.
[11] G. C. Bazan, E. Khosravi, R. R. Schrock, W. J. Feast, V. C. Gibson, M. B. Oregan, J. K. Thomas, W. M. Davis, *J. Am. Chem. Soc.* **1990**, *112*, 8378.
[12] K. Yamano, K. Konno, H. Shirahama, *Chem. Lett.* **1991**, 1541.
[13] P. Schwab, M. B. France, J. W. Ziller, R. H. Grubbs, *Angew. Chem.* **1995**, *107*, 2179; *Angew. Chem. Int. Ed. Engl.* **1995**, *34*, 2039.
[14] M. Scholl, S. Ding, C. W. Lee, R. H. Grubbs, *Org. Lett.* **1999**, *1*, 953.
[15] M. Scholl, T. M. Trnka, J. P. Morgan, R. H. Grubbs, *Tetrahedron Lett.* **1999**, *40*, 2247.
[16] P. Evans, R. Grigg, M. Monteith, *Tetrahedron Lett.* **1999**, *40*, 5247.
[17] C. M. Yang, W. V. Murray, L. J. Wilson, *Tetrahedron Lett.* **2003**, *44*, 1783.
[18] J. Robertson, N. Kuhnert, Y. Zhao, *Heterocycles* **2000**, *53*, 2415.
[19] N. Dieltiens, C. V. Stevens, D. De Vos, B. Allaert, R. Drozdzak, F. Verpoort, *Tetrahedron Lett.* **2004**, *45*, 8995.
[20] N. Dieltiens, C. V. Stevens, B. Allaert, F. Verpoort, *Arkivoc* **2005**, 92.
[21] M. Arisawa, C. Theeraladanon, A. Nishida, M. Nakagawa, *Tetrahedron Lett.* **2001**, *42*, 8029.
[22] M. L. Bennasar, T. Roca, M. Monerris, D. Garcia-Diaz, *Tetrahedron Lett.* **2005**, *46*, 4035.
[23] A. J. Ashe, X. D. Fang, *Org. Lett.* **2000**, *2*, 2089.
[24] M. J. Bassindale, P. Hamley, A. Leitner, J. P. A. Harrity, *Tetrahedron Lett.* **1999**, *40*, 3247.
[25] T. J. Donohoe, A. J. Orr, K. Gosby, M. Bingham, *Eur. J. Org. Chem.* **2005**, 1969.
[26] F. P. J. T. Rutjes, T. M. Kooistra, H. Hiemstra, H. E. Schoemaker, *Synlett* **1998**, 192.
[27] R. Grigg, E. Mariani, V. Sridharan, *Tetrahedron Lett.* **2001**, *42*, 8677.
[28] S. S. Kinderman, R. Doodeman, J. W. van Beijma, J. C. Russcher, K. C. M. F. Tjen, T. M. Kooistra, H. Mohaselzadeh, J. H. van Maarseveen, H. Hiemstra, H. E. Schoemaker, F. P. J. T. Rutjes, *Adv. Synth. Catal.* **2002**, *344*, 736.
[29] S. S. Kinderman, R. de Gelder, J. H. van Maarseveen, H. E. Schoemaker, H. Hiemstra, F. P. J. T. Rutjes, *J. Am. Chem. Soc.* **2004**, *126*, 4100.
[30] M. P. Heck, C. Baylon, S. P. Nolan, C. Mioskowski, *Org. Lett.* **2001**, *3*, 1989.
[31] Y. Z. Chen, H. V. R. Dias, C. J. Lovely, *Tetrahedron Lett.* **2003**, *44*, 1379.
[32] A. Fürstner, H. Szillat, B. Gabor, R. Mynott, *J. Am. Chem. Soc.* **1998**, *120*, 8305.
[33] V. Declerck, P. Ribiere, J. Martinez, F. Lamaty, *J. Org. Chem.* **2004**, *69*, 8372.
[34] K. S. Huang, E. C. Wang, *Tetrahedron Lett.* **2001**, *42*, 6155.
[35] G. B. Bajracharya, I. Nakamura, Y. Yamamoto, *J. Org. Chem.* **2005**, *70*, 892.
[36] O. Fujimura, G. C. Fu, R. H. Grubbs, *J. Org. Chem.* **1994**, *59*, 4029.
[37] M. Arisawa, Y. Terada, M. Nakagawa, A. Nishida, *Angew. Chem.* **2002**, *114*, 4926; *Angew. Chem. Int. Ed.* **2002**, *41*, 4732.
[38] A. Iuliano, P. Piccioli, D. Fabbri, *Org. Lett.* **2004**, *6*, 3711.
[39] W. A. L. van Otterlo, E. L. Ngidi, E. M. Coyanis, C. B. de Koning, *Tetrahedron Lett.* **2003**, *44*, 311.
[40] K. Yoshida, T. Imamoto, *J. Am. Chem. Soc.* **2005**, *127*, 10470.
[41] A. Fürstner, G. Seidel, *Angew. Chem.* **1998**, *110*, 1758; *Angew. Chem. Int. Ed.* **1998**, *37*, 1734.
[42] A. Fürstner, A.-S. Castanet, K. Radkowski, C. W. Lehmann, *J. Org. Chem.* **2003**, *68*, 1521

© 2006 Wiley-VCH Verlag GmbH & Co. KGaA, Weinheim

Nanostructures

DOI: 10.1002/anie.200504025

Multisegmented One-Dimensional Nanorods Prepared by Hard-Template Synthetic Methods

*Sarah J. Hurst, Emma Kathryn Payne, Lidong Qin, and Chad A. Mirkin**

Keywords:
molecular electronics · nanostructures · nanotechnology · template synthesis

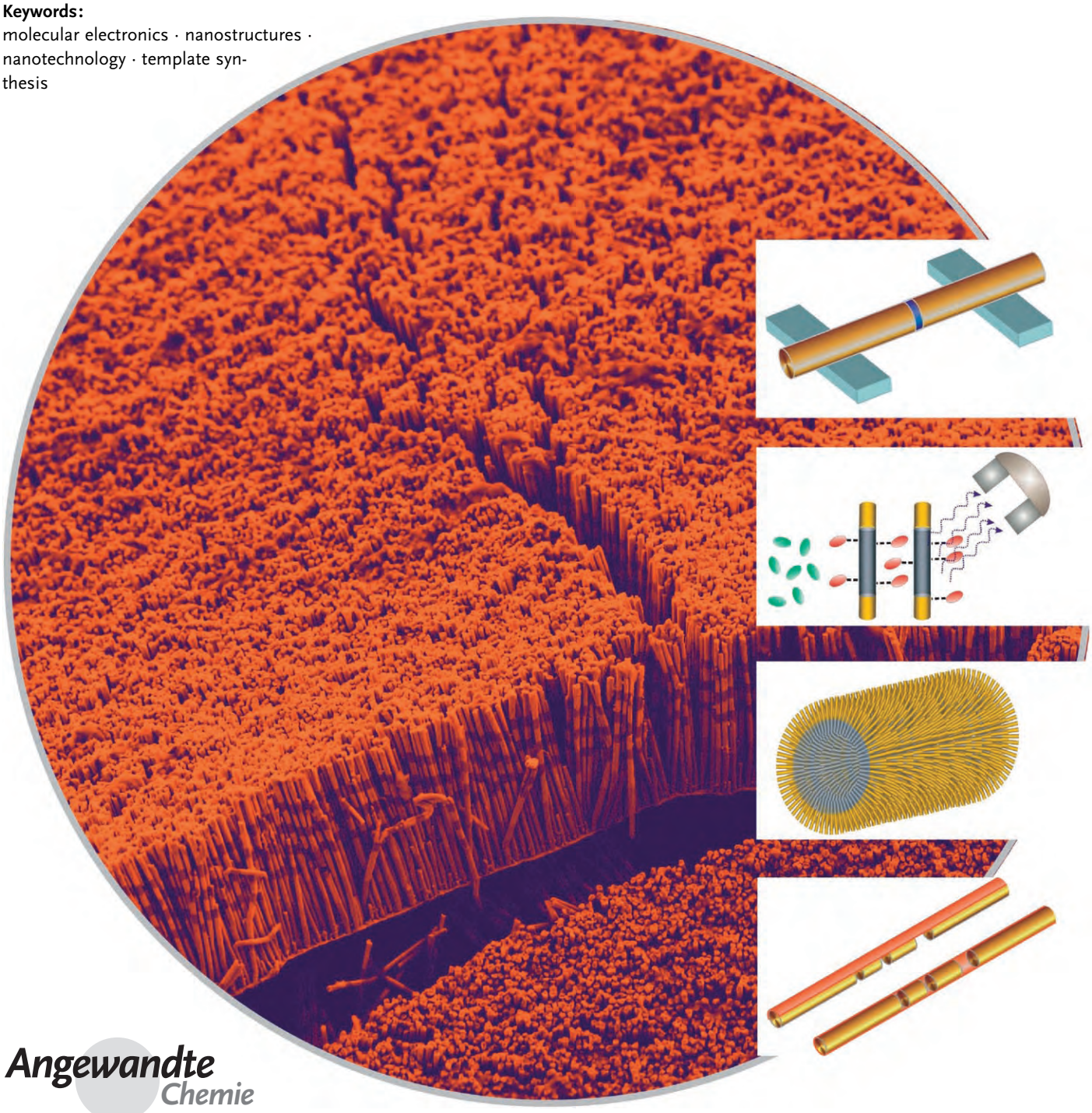

© 2006 Wiley-VCH Verlag GmbH & Co. KGaA, Weinheim

In the science and engineering communities, the nanoscience revolution is intensifying. As many types of nanomaterials are becoming more reliably synthesized, they are being used for novel applications in all branches of nanoscience and nanotechnology. Since it is sometimes desirable for single nanomaterials to perform multiple functions simultaneously, multicomponent nanomaterials, such as core–shell, alloyed, and striped nanoparticles, are being more extensively researched. Nanoscientists hope to design multicomponent nanostructures and exploit their inherent multiple functionalities for use in many novel applications. This review highlights recent advances in the synthesis of multisegmented one-dimensional nanorods and nanowires with metal, semiconductor, polymer, molecular, and even gapped components. It also discusses the applications of these multicomponent nanomaterials in magnetism, self-assembly, electronics, biology, catalysis, and optics. Particular emphasis is placed on the new materials and devices achievable using these multicomponent, rather than single-component, nanowire structures.

From the Contents

1. Introduction 2673

2. Synthesis: Templates and Deposition Techniques 2674

3. Properties and Applications of Multisegmented One-dimensional Nanostructures 2677

4. Summary and Outlook 2689

1. Introduction

Nanoscience is a field that focuses on developing new synthetic and analytical tools for building and studying structures with submicrometer, and more typically sub-100-nm, dimensions.[1] Moreover, it is a field that utilizes such capabilities and the fundamental property differences associated with such highly miniaturized structures to construct novel functional materials and devices. The field is highly interdisciplinary, encompassing aspects of physics, chemistry, biology, materials science and engineering, and medicine. It is a field whose emergence has been long anticipated,[2] yet is still in its infancy and has just begun to progress towards its full potential. Owing to widespread interest and investment, however, nanoscience is growing and progressing at an unprecedented rate.

Initially, nanoscience research focused on the study of isotropic, noble metal particles, most of which were synthesized in the solution phase as colloids or sols.[3] Now, numerous and diverse synthetic methodologies, surface analytical techniques, and materials fabrication methods exist for building structures of many compositions and shapes on the nanometer length scale. While wet-chemical techniques[4] are still extensively used, other methods, such as hard-template-directed,[5] lithographic,[6] and vapor phase[7] syntheses, have been developed. These methods are being used to create isotropic nanoparticles as well as novel anisotropic nanostructures, such as disks,[8] prisms,[9] cubes,[10] rods,[5,11] wires,[5,12] and branched structures.[11d,13] These nanomaterials are typically composed of noble metals or semiconductors.

These nanomaterials, especially anisotropic structures, have turned out to be ideal for the study of the physical and chemical consequences of miniaturization, or the changes that arise in bulk materials as they are scaled down to clusters that consist of tens to thousands of atoms.[3] By altering the size, composition, and shape of the nanomaterial, the optical, electronic, magnetic, mechanical, and chemical properties of a material change and, therefore, can be manipulated. These effects are found to be the most profound as the dimensions of the material reach the sub-100-nm level. As the effects of miniaturization are becoming more clearly understood and controlled, isotropic and anisotropic nanoparticles are beginning to be used in many applications, such as ultra-sensitive and ultra-selective biosensing,[14] catalysis,[4b,15] and nanoelectronics and photonics.[16]

Since nanoparticles are being used in more applications, it is becoming increasingly desirable for single structures to perform many functions simultaneously. One way single structures can be manipulated to perform multiple functions is if they are synthesized such that they consist of more than one component. In nature, multifunctional systems are ubiquitous and range from simple organic amphiphiles[17] to more complicated macromolecules, such as proteins and enzymes.[18] Taking inspiration from nature, chemists and nanoscientists are designing and synthesizing multifunctional systems. Chemists have, for example, synthesized copolymers,[18] which are single polymer chains that are composed of multiple subunits of more than one type of monomer, and supramolecular catalysts,[19] which are designed to mimic allosteric enzymes. Active research in nanoscience has currently focused on synthesizing core–shell[20] and alloyed[21] nanoparticles, which are composed of more than one material. In these core–shell systems, in particular, the favorable properties of the core are maintained (e.g., optical properties, magnetism), while the shell functions to provide additional stabilization, passivation, or chemical functionality. In all of these examples, both natural and synthetic, it is easily seen

[*] S. J. Hurst, E. K. Payne, L. Qin, Prof. C. A. Mirkin
Department of Chemistry and
International Institute for Nanotechnology
Northwestern University
2145 Sheridan Road, Evanston, IL 60208-3113 (USA)
Fax: (+1) 847-467-5123
E-mail: chadnano@northwestern.edu

© 2006 Wiley-VCH Verlag GmbH & Co. KGaA, Weinheim

that multicomponent structures can provide exciting new avenues for study.

Nanorods, wires, belts, and tubes make up one particular class of anisotropic nanomaterials, which are considered quasi one-dimensional structures.[22] These structures have extremely high aspect ratios and offer researchers the potential to build striped structures with multiple chemical components aligned along the long axis of the structure. These multicomponent materials have recently been synthesized by high-temperature catalytic processes,[23] pulsed-laser ablation/chemical vapor deposition (PLA-CVD),[24] vapor–solid–liquid (VLS) growth processes,[25] evaporation of mixed powders,[26] epitaxial growth processes,[12,27] and deposition, using various techniques, into hard templates.[5,28] As increasing emphasis is placed on low cost, high throughput, high volume, and ease of production, template synthesis is becoming the method of choice for the synthesis of multicomponent nanorods and nanowires.

For this reason, we focus in this review on multisegmented one-dimensional nanorods and nanowires prepared in hard templates by using various deposition techniques and the inherent multiple functionalities that these structures provide. The articles we highlight here are those that are currently the most relevant to this specific topic. Although hollow multisegmented metallic nanotubes have recently been developed as well,[29] we chose to focus this review on the analogous solid structures. The text is organized into three sections. Section 2 highlights template synthesis and deposition methods, focusing on those syntheses that are important for creating multisegmented one-dimensional structures. It covers the main types of templates that are utilized as well as electrochemical and non-electrochemical deposition techniques. Section 3 focuses on the properties of and applications for multisegmented nanorods and nanowires, and is broken up into six main subsections based upon application. Section 3.1 highlights the use of multisegmented nanowires for studies of fundamental magnetic phenomena. Section 3.2 discusses new self-assembly possibilities involving multisegmented one-dimensional structures which use driving forces made possible by their segmentation. Section 3.3 focuses on multisegmented rods in relation to their use as nanocircuit elements and potential electrical measurement platforms. Section 3.4 discusses the importance of multisegmented structures for detection and separation of biological molecules and their further application in therapeutics. Sections 3.5 and 3.6 address the use of the multisegmented rods in catalysis and optics, respectively. This review concludes with Section 4, which summarizes the main concepts that were outlined and proposes future directions for research in the area of multisegmented one-dimensional nanostructures.

2. Synthesis: Templates and Deposition Techniques

2.1. Hard Templates

Micro- and nanoporous templates are routinely used to fabricate one-dimensional multisegmented rods because their pores can be filled with a variety of materials using a number of techniques.[5,28] In addition, the pores of the templates are uniform and dense providing a means to synthesize monodisperse nanomaterials in high yield. Another advantage of

Chad A. Mirkin earned his B.S. at Dickinson College (1986) and his Ph.D. from Pennsylvania State University (1989). After an NSF Postdoctoral Fellowship at MIT, he joined the faculty of Northwestern University where he is currently the Director of the NU International Institute for Nanotechnology and the George B. Rathmann Professor of Chemistry, Professor of Medicine, and Professor of Materials Science and Engineering. He has authored over 250 manuscripts and 50 patents, founded two companies (Nanosphere and NanoInk), and co-founded the journal Small. He has received numerous awards, including the NIH Director's Pioneer Award, the American Chemical Society (ACS) Pure Chemistry Award, and the ACS Nobel Signature Award.

Emma Kate Payne was born in Montgomery, Alabama and grew up in Birmingham, Alabama. In 2003, she earned a B.S. degree in Chemistry with a minor in Biology from Sweet Briar College in Virgina. She is currently a Chemistry Ph.D. candidate at Northwestern University under the supervision of Chad A. Mirkin.

Sarah J. Hurst was born in Joliet, Illinois, and grew up in Fort Walton Beach, FL. In 2002, she earned B.S. degrees in both Chemistry and Physics from the University of Florida in Gainesville. She is currently a Chemistry Ph.D. candidate at Northwestern University under the supervision of Chad A. Mirkin.

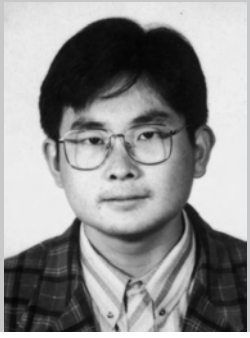

Lidong Qin was born and grew up in Lu'an city, Anhui Province of China. In 1999, he received his B.S. degree in Chemistry from Jilin University, China. At the same university, he went on to complete his M.S. in Polymer Chemistry and Physics under the supervision of Prof. Jiacong Shen and Prof. Lixin Wu (2002). He is currently working to complete his Ph.D. in Chemistry at Northwestern University under the supervision of Chad A. Mirkin.

 © 2006 Wiley-VCH Verlag GmbH & Co. KGaA, Weinheim

hard templates is that, during synthesis, the placement and dimensions of the different components of the rods can be controlled. There are many materials, such as zeolites,[30] glass,[31] nanoporous solids,[32] mica,[33] and block copolymer films[34] which have been and are currently being used as templates for the fabrication of nanorods and nanowires, but ion-track-etched membranes and anodic aluminum oxide templates are the most commonly used materials.

2.1.1. *Ion-Track-Etched Membranes*

Ion-track-etched membranes are commercially available as filters and are usually prepared from either polycarbonate or polyester thin films.[5,28] Nonporous films of these materials are first bombarded with ions, which produce randomly spaced damage tracks through the membranes. These tracks are then chemically etched to form uniform pores through the membrane, which can range from 10 to 2000 nm in diameter, at densities as high as 10^9 pores per square centimeter (Figure 1 A). The random nature of pore formation during this process can result in a large number of intersecting pores that will detrimentally affect the number, homogeneity, and dimensions of the multisegmented rods during their synthesis. For this reason, anodic aluminum oxide (AAO) templates are often used for the synthesis of multisegmented rods depending on the specific application.

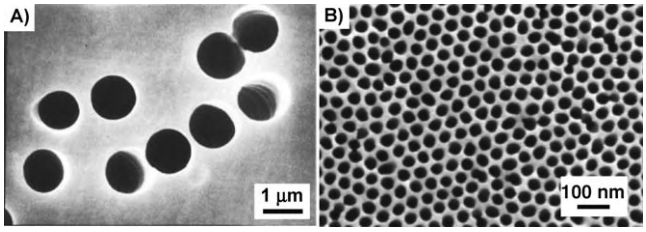

Figure 1. A) Scanning electron microscopy (SEM) image of a polycarbonate membrane with ≈1-μm diameter pores. B) SEM image of an AAO membrane (pore diameters ≈35 nm).

2.1.2. *Anodic Aluminum Oxide (AAO) Templates*

AAO templates are also commercially available in a limited number of pore diameters (e.g., 10, 20, 100, 200 nm).[28a] Fortunately, AAO templates of many diameters (5–267 nm) can be synthesized following the two-step anodization process established by Masuda and co-workers[35] in which nanosized pores are grown in an insulating oxide film of alumina. In this process, a thin sheet of high-purity aluminum is first annealed and then subjected to an electropolishing solution, which removes the top layers of aluminum oxide on the surface leaving it with a mirrorlike shine. Subsequently, the aluminum is subjected to an anodization step in an acidic electrolyte solution. The sheet is then placed in a chromate solution to remove the barrier oxide layer, and a second anodization is performed in the same acidic solution. Finally, the aluminum is removed. The resulting membrane contains cylindrical pores of uniform diameter arranged in a hexagonal array with pore densities as high as 10^{11} pores per square centimeter (Figure 1 B). Unlike the ion-track-etch membranes, these pores do not intersect.

The dimensions of the AAO templates can be easily tailored by using this scheme.[28b] The template thickness is dependent, for example, on the time of anodization, with longer anodizations resulting in thicker templates. These thicker templates allow rods having longer lengths to be synthesized. In addition, different pore diameters can be produced by varying the composition and concentration of the acidic electrolyte solution and the temperature and voltage of the anodization. Pore diameters of 5–33 nm, 30–70 nm, and 150–267 nm can be achieved by using H_2SO_4, oxalic acid, and H_3PO_4, respectively, under varying temperatures and voltages.[28b]

2.2. *Electrochemical Deposition*

Electrochemical deposition can be used to deposit materials into ion-track-etched or AAO templates (see Section 2.1).[5,28] Electrochemical deposition offers marked advantages over other methods for the synthesis of one-dimensional nanostructures. Electrochemical deposition does not require expensive instrumentation, high temperatures, or low-vacuum pressures. This method is also not time-consuming, since nanomaterials grown in this fashion have a high growth rate. Multisegmented rods can be easily synthesized by changing the plating solution and accordingly varying the potential of the deposition. Also, by varying the shape of the electrical pulse bringing about the deposition, the interface between multiple electrodeposited components can be controlled.

Regardless of the type of materials to be deposited, the same general scheme applies for the creation of nanowires through electrochemical deposition (Figure 2). In the first step of the general process, a thin metal film is evaporated onto one face of the template. This metal film is used as a working electrode that is responsible for electrodepositing materials in the pores. Typically, before the desired components are deposited, a layer of sacrificial metal is deposited into the pores to prevent a "puddling" effect, which causes one end of the rod to have a deformed mushroom shape. Then, deposition of the desired components is performed

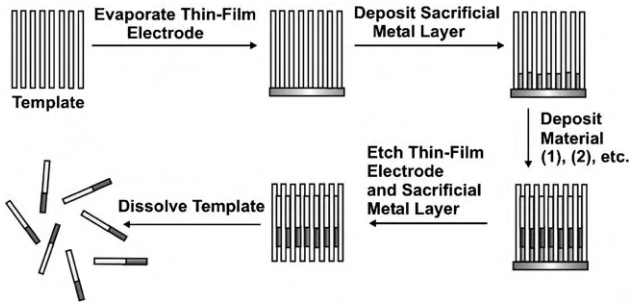

Figure 2. General scheme for the synthesis of one-dimensional nanostructures (nanowires and nanorods) by the deposition of materials into nanoporous templates.

© 2006 Wiley-VCH Verlag GmbH & Co. KGaA, Weinheim

sequentially. After deposition of the desired components, the nanowires are released by chemically dissolving the thin film electrode, sacrificial metal layer, and template.

Several review articles already have discussed such electrochemical deposition procedures for the preparation of nanostructures in detail.[5,28] Herein, the deposition methods of metals, semiconductors, and conducting polymers, which are heavily used as components in multisegmented nanowires, are briefly discussed.

2.2.1. Metals

The first example of electrochemical metal deposition into a hard template was shown by Possin and co-workers[33a] in 1970. Possin and co-workers prepared Zn, Sn, and In nanowires in small pores that were track-etched in mica, to study their superconducting properties. The template method was later introduced and popularized as a nanofabriation strategy by Martin and co-workers[5,28a] and Moskovitz and co-workers.[36] In these methods, metal ions are reduced from electrolytic solutions through the application of a negative potential, typically in a three-electrode electrochemical cell. Since the pioneering syntheses, nanowires consisting of many different metals (e.g., Au, Ag, Sn, Cu, Ni, Co, Pt, Pd, Pb, Fe, Zn, Bi)[5,33a,37–44] have been synthesized in hard templates. The diameters of the nanowires are dictated by the pore size of the template, while their lengths are directly related to the amount of negative charge passed through the system according to Faraday's Law.

Pulsed electrochemical deposition[45] is a technique that was developed specifically for the preparation of multisegmented metal nanowires with precise interfaces. In this technique, a single electrolyte bath, containing multiple metal ions, is used. In the two-component bath system, for example, the more noble metal is kept at a low concentration and the less noble metal is kept at a much higher concentration. If the two metals have well-separated redox potentials, as the potential of the system is held at the less negative potential, the more noble metal is deposited exclusively. As the potential is pulsed to a more negative potential, however, the less noble metal is deposited along with only a small amount of the more noble metal. This method allows multilayers to be grown with monolayer precision.

2.2.2. Conducting Polymers

The main difference between metal deposition and polymer deposition is that a negative potential (reduction) is applied to the system for metal deposition, while a positive potential (oxidation) is applied for polymer deposition. When a positive potential is applied to an organic electrolyte solution containing the appropriate monomers, polymerization takes place within the pores of the template. Martin and co-workers[5,46] pioneered the synthesis of polypyrrole (Ppy), polyaniline, and poly(3-methylthiophene) (P3MT) nanotubes and nanorods. Burford and co-workers[47] investigated the morphology of Ppy nanostructures prepared in different templates. Polymer segments also were incorporated into multicomponent nanowires by our group in an effort to synthesize mesoscopic amphiphiles and to study their assembly[48] and electrical transport properties[49] (see Sections 3.2.1 and 3.3, respectively).

2.2.3. Semiconductors

Sweep techniques have been used to stoichiometrically deposit II–VI semiconducting materials into porous templates. For instance, Martin, Sailor, and co-workers[50,51] have shown sequential monolayer deposition of CdSe using cyclic voltammetry. This monolayer deposition is accomplished by plating out a small amount of Se and a large amount of Cd during the deposition and subsequently stripping off excess Cd during the reverse potential sweep. Moskovitis and co-workers[52] also discovered an AC electrochemical deposition strategy for preparing semiconducting nanowire arrays. Semiconductor-metal multisegmented structures were synthesized by Chakarvarti and Vetter[53] under constant current conditions. In their studies, Cu–Se nanostructures were characterized by SEM and their tubular structure and photoconductivity were discussed. In recent years, the electrical transport properties of semiconducting structures have been studied by our group[49] and the Mallouk[54] group in the context of nanoelectronic circuitry.

Recently, electrochemical methods also have been developed to deposit semiconducting metal oxide nanowires into hard templates. Zheng et al.[55] have, for example, produced ZnO nanowires by applying a cathodic current to an aqueous zinc nitrate solution. To achieve better crystallinity and larger crystal size, Wang et al.[56] extended this technique by electrochemically depositing ZnO nanowires from a nonaqueous solution. In this method, the nanowires were cathodically deposited from a solution of dimethyl sulfoxide (DMSO) containing zinc chloride and a molecular oxygen precursor. ZnO segments, due to their optical, electronic, and piezoelectric properties, could be incorporated into multisegmented rods to create optoelectronic devices.[57]

2.3. Other Types of Deposition

One drawback of electrochemical deposition methods is that the material to be deposited must be both easily reduced and conductive. Also, the template itself must be modified with a metal backing in order to be used in the context of an electrochemical experiment.[5,28] Other methods exist, however, that allow materials that are poor conductors and not easily reduced to be deposited into hard templates, which do not need to be conductive. These methods provide another way to deposit metals and conducting polymers, yet also allow nonconducting polymers, semiconducting metal oxides, and biological molecules, such as DNA and proteins, to be deposited. Most of these methods involve an alternating-immersion method, where the template is first immersed in a solution that prepares the surface to accept the desired deposition material in a second immersion step. These methods provide avenues to deposit components that can lead to extended functionality in multisegmented nanorods and nanowires.

 © 2006 Wiley-VCH Verlag GmbH & Co. KGaA, Weinheim

2.3.1. Metals

Metals, predominantly Au, have been deposited into polycarbonate, AAO, and plastic membranes without the use of electrochemical methods.[28a,58] Briefly, in this method, a sensitizer, typically Sn^{2+}, is applied to the membrane surfaces, including both the pores and the walls. This sensitizer binds to the surfaces through complexation with surface functionalities such as amino, carbonyl, and hydroxy groups. The sensitized membrane is then exposed to Ag^{+} ions resulting in the formation of nanoscopic Ag particles on the activated membrane. Finally, the template is immersed into a solution containing Au^{+} ions and a reducing agent, which results in Au metal plating on the surfaces and pores of the membrane. This method can be used to make both hollow nanotubes and solid nanorods by varying the amount of time the membrane is immersed in the Au ion solution.

2.3.2. Nonconducting and Conducting Polymers

Electroless techniques also can be used to deposit polymers into the pores of a membrane. In the chemical polymerization technique, the membrane is immersed into a solution containing both the desired monomer and a polymerization agent.[5b,58] Polymer deposition occurs when these two species meet inside the pores of the membrane. These methods are used to deposit both conducting polymers as well as plastics, such as polyacrylonitrile, into the membrane pores. Polymers also have been successfully deposited into the pores of hard templates using layer-by-layer deposition techniques.[59] In these strategies, the template is immersed in solutions of positive and negative polyelectrolytes in an alternating fashion. The oppositely charged polyelectrolytes assemble into layers on the template walls due to electrostatic interactions. Each subsequent immersion decreases the inner diameter of the growing nanotubes.

2.3.3. Semiconductors

Semiconductors can be deposited into the pores of a template by using a sol–gel deposition process.[28a,60,61] The sol–gel process starts by making a sol, which is a suspension of colloidal particles, through the hydrolysis of a precursor molecule (e.g., titanium isopropoxide, zinc acetate, WCl_6, or $SiCl_4$). The template is then immersed into the sol for a given period of time, and the sol deposits onto the walls of the pores. After heat treatment, tubes or rods made from a variety of semiconducting metal oxides, such as TiO_2, ZnO, WO_3, and SiO_2 are formed. Metal oxides of this type also can be synthesized through room-temperature techniques that are analogous to biomineralization.[62]

2.3.4. Biological Molecules

Recently, methods have been developed by Martin and co-workers[63,64] to deposit biological molecules, such as DNA and proteins, inside the pores of template membranes. The DNA nanotubes can be synthesized using a scheme in which the membrane is first functionalized with a layer of an α,ω-diorganophosphonate(DOP)–zirconium(IV) complex. The initial layer of DNA is attached to this DOP–Zr layer. Subsequent layers of DNA then can be hybridized on this initial layer of DNA using standard Watson–Crick base-pairing chemistry. In a similar alternate-immersion strategy, protein tubes, made from glucose oxidase or hemoglobin, were synthesized. The primary immersion solution in this technique was 3-aminopropylphosphonic acid. The phosphonate groups of this molecule were then used to attach a layer of glutaraldehyde, which acts as a protein-immobilization agent, to the walls of the pores. Next, the membrane was immersed in the protein solution. Alternating immersion of the membrane in glutaraldehyde and protein solutions were performed until the desired nanotube thickness was obtained.

3. Properties and Applications of Multisegmented One-dimensional Nanostructures

The deposition methods outlined in Section 2 are some of the most popular techniques in template synthesis. Multisegmented one-dimensional structures of many types have been synthesized by using a sequential combination of these techniques in a single synthetic method. The properties of these materials and their applications in various areas of nanoscience, including magnetism, self-assembly, electronics, biology, catalysis, and optics, have been extensively studied and are discussed below.

3.1. Fundamental Magnetism

Both single-segment and multisegmented nanorods and nanowires have several unique magnetic properties as a result of their low dimensionality.[65,66] This low dimensionality brings about anisotropy in the fundamental magnetic properties (e.g., easy axis, coercivity, remanence, saturation magnetization, Curie temperature) of these nanomaterials depending on whether a magnetic field is applied parallel or perpendicular to their long axes.[40,41,67] These properties also can be tuned by varying parameters such as nanorod composition, length, diameter and, in multisegmented structures, layer thickness and spacing. This magnetic anisotropy has even been exploited to assemble such structures (see Section 3.2.2). Giant magnetoresistance (GMR) is one magnetic property that arises solely due to the segmented structure of multilayered nanorods and nanowires. Therefore, we discuss this particular property in greater detail.

3.1.1. Early Findings and the Origin of Giant Magnetoresistance (GMR) in Multisegmented Structures

In the late 1980s, there was an explosion of interest in the fundamental magnetic behavior of multicomponent thin films composed of alternating layers of magnetic and nonmagnetic metals. This explosion was spurred by the initial discovery that these bulk thin films exhibited giant magnetoresistance (GMR), which is the unusually large decrease in the electrical resistance of a material in response to an applied magnetic

© 2006 Wiley-VCH Verlag GmbH & Co. KGaA, Weinheim

field. This discovery was made simultaneously and independently by Baibich et al.[68] and Binasch et al.[69] in films produced by molecular beam epitaxy (MBE). A few years later, GMR was demonstrated in bulk thin films prepared by sputter coating[70] as well as electrochemical deposition.[71] The use of electrochemical deposition in this field of research began with the development of the pulsed electrochemical deposition technique (see Section 2.2.1).[45]

Pulsed electrochemical deposition, when combined with template synthesis, culminated in the synthesis of multilayered magnetic nanowires, which were also found to exhibit GMR. The first nanowires of this kind were produced within the pores of track-etched polycarbonate membranes and were composed of thin Co–Cu[72–74] (Figure 3A, B) and NiFe–Cu[73,75] layers. The shapes of the MR curves (measured with the current in the plane (CIP) geometry) for the Co–Cu nanowires were similar to those observed for the conventional Co–Cu multilayered films, although smaller in magnitude in these initial experiments (Figure 3C).[72] After these experiments, many other nanowires synthesized from magnetic-non-magnetic couples, such as Ni–Cu,[67c–d] Fe–Cu,[76] and CoNiCu–Cu,[75,77] also were found to exhibit GMR effects.

The giant magnetoresistance of multilayered nanowires is a consequence of the electronic structures of the magnetic and nonmagnetic layers.[78] As mentioned above, the magnetic properties of nanowires of a single metallic component (e.g., Fe, Co, or Ni) have been studied extensively, but these nanowires do not exhibit GMR.[66] The function of each nanowire component in producing the GMR effect can be qualitatively understood using the Mott model.[78] The premise of the Mott model is that electrical conductivity in metals can be described in terms of two independent conduction channels formed by the spin-up and spin-down electrons. Further, it states that, in ferromagnetic metals, the resistance of these spin-up and spin-down electron conduction channels can be different.

These concepts can be taken together to explain GMR in the commonly studied Co–Cu multicomponent nanowire system.[78] In this system, the nonmagnetic Cu layers function as spacer layers. Due to these spacer layers, each magnetic Co layer can be viewed as a single magnetic domain in which the individual electron spins are aligned such that a magnetic moment of the layer is produced in one direction. In the absence of an applied magnetic field, the directionality of the magnetic moment in each of the Co layers is random with respect to one another. As a consequence, resistance is high for both the spin-up and spin-down electron conduction channels and thus in the nanowire as a whole. When a magnetic field is applied, the magnetic moments of each Co layer will align in the same direction as that of the magnetic field. Therefore, one electron conduction channel will experience high resistance, whereas the other will experience little or no resistance. In this way, with the application of the magnetic field, the resistance of the multicomponent nanowire is decreased.

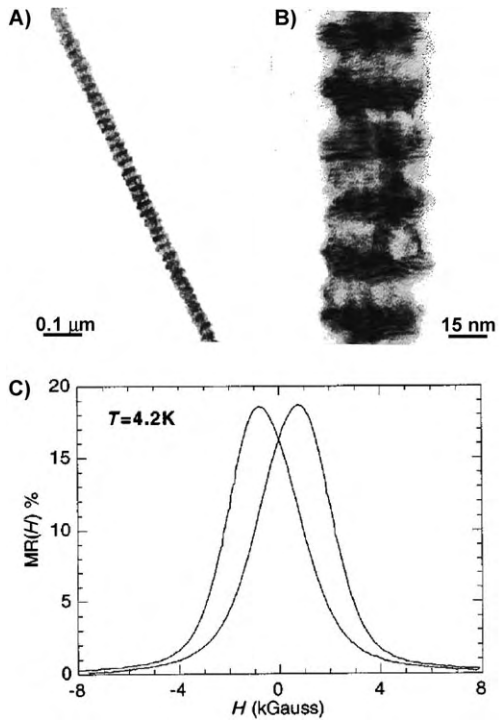

Figure 3. A), B) Transmission electron microscopy (TEM) images of a single nanowire with 10-nm thick Co (light bands) and Cu (dark bands) layers. C) Plot of magnetoresistance (MR) versus applied magnetic field (parallel to the film of nanowires) at $T = 4.2$ K. The forward and reverse curves display little overlap, indicative of a large coercive, or switching, field. Room-temperature measurements ($T = 290$ K) display a similar shaped curve with a smaller maximum (ca. 15%) and a smaller coercive field (not shown). Reprinted with permission from reference [72]. Copyright 1994, American Institute of Physics.

3.1.2. *New Studies Made Possible by Hard Templates and Multisegmented Nanowires*

The technique of electrochemical deposition into templates allowed important magnetic studies of GMR to be performed on these multisegmented nanowires that were difficult or impossible using other methods. These studies, in fact, highlight some of the first uses for hard templates and the multisegmented nanowire structures produced within their pores.

The use of both anodic aluminum oxide (AAO) and polycarbonate templates allowed unique experiments to be performed. Both types of templates were used as a measurement platform for the nanowires within their pores, but for different purposes.[79] In AAO templates, due to their high pore densities, the magnetic interactions between nanowires could be studied. Alternatively, polycarbonate templates, due to their low pore densities, allowed single, magnetically isolated nanowires to be studied.[66] Also, since AAO templates are stable at high temperatures, the effects of the annealing process on the GMR of the nanowires was studied.[77] In general, it was found that the GMR responses of nanowires deposited into AAO templates were larger than those deposited into polycarbonate membranes.[77,80]

More importantly, the multicomponent nanowires turned out to be the ideal structures for the study of several aspects of GMR. The multilayered nanowires were used to study, for example, the dependence of current directionality, temper-

 © 2006 Wiley-VCH Verlag GmbH & Co. KGaA, Weinheim

ature, and layer thickness and number on GMR effects. In studies of current directionality, the two geometries of interest are the current in plane (CIP) geometry and the current perpendicular to the plane (CPP) geometry, where the magnetism is measured with the current flow parallel and perpendicular to the plane of the layers, respectively. CPP-GMR had been predicted to be larger than CIP-GMR.[81] Unfortunately, this prediction was difficult to confirm since the necessary experiments were difficult to perform. While several CIP-GMR studies had been performed, CPP-GMR was hard to measure due to the low resistance of the layers as measured in the CPP geometry. Previously, the experiments were only undertaken by groups using either ultra-sensitive superconducting quantum interference device (SQUID)-based systems[82] or pillared samples[83] and, more recently, grooved substrates.[84,85] Using nanowire samples, however, the larger magnitude of CPP-GMR has been easily verified and extensively studied.[86] Large signals were produced and, therefore, more precise measurements could be made due to the large aspect ratio of the nanowires.[66]

Up until this point, the temperature dependence of GMR, and CPP-GMR in particular, was impossible to study because the most popular methods, as mentioned above, require liquid helium temperatures. Multisegmented nanowires, however, do not have this restriction and can be studied at temperatures ranging from 4.2 K to room temperature (298 K). Belliard and co-workers[87] were the first to carry out such studies on Co–Cu multilayered nanowires and to fit their experimental data to theoretical calculations. In general, it was found experimentally that the GMR effect decreases with increasing temperature.

The multisegmented wires also allowed convenient study of the effect of the layer thickness and layer number on GMR. Both of these parameters could be easily varied through electrochemistry without detriment to the interface quality. By varying the layer thickness over the nanometer to micrometer range, Piraux et al.[87,88] studied the change in the GMR of Co–Cu nanowires as a function of temperature. These experimental data were then used to calculate important physical values such as interface and bulk scattering parameters and spin-diffusion lengths (SDL) for these metals. Searson and co-workers[67e] later found that the layer thickness, in addition to affecting GMR, also affected other magnetic properties such as the easy axis, the Curie temperature, the coercivity, and remanent magnetization of the nanowires. Ansermet and co-workers[80] found that, for Co–Cu nanowires, the GMR of the nanowires increased as the number of magnetic–nonmagnetic bilayers increased. They found that this result held for nanowires that were from two to several hundred bilayers thick in both AAO and polycarbonate templates. This group also observed spin-valve resistance switching in trilayer Co–Cu–Co nanowires.[80]

These important studies helped elucidate very fundamental physical theories. They also suggested that multisegmented, multifunctional nanowires could have future applications in areas of high-density magnetic recording, memory storage, and switching, although the problem of integrating the AAO and polymer templates into an electronic circuit does exist. The nanowires also have attracted interest for their application in bioelectronics and medical devices since they are biocompatible under certain circumstances.[66]

3.2. Self-Assembly

Self-assembly generally refers to the autonomous organization of components into patterns or structures without human intervention.[89] Recently, some self-assembly strategies have focused on using biological molecules[90] or biological templates[91] to spatially control small isotropic building blocks. The assembly of single-component metallic nanowires[92] also has been studied. Multisegmented nanowires and nanorods, however, offer additional degrees of freedom in assembly. By taking advantage of the different properties and functions of the individual components, multiple avenues for self-assembly are possible for a single system.

3.2.1. Template-Assisted Assembly

Our group[48] has utilized the template synthesis method to prepare two-component rod structures that behave as mesoscopic amphiphiles. These structures were made of Au hydrophilic blocks and polypyrrole (Ppy) hydrophobic blocks. In a typical experiment, Au–Ppy nanorods were synthesized in an AAO template and subsequently released from the template through its dissolution. These novel amphiphilic structures have a pseudo-conical shape because of a difference in diameter between the Au (large) and polymer (small) sections. Therefore, they assemble into three-dimensional bundle- and tubular-shaped microscale architectures (Figure 4 A).

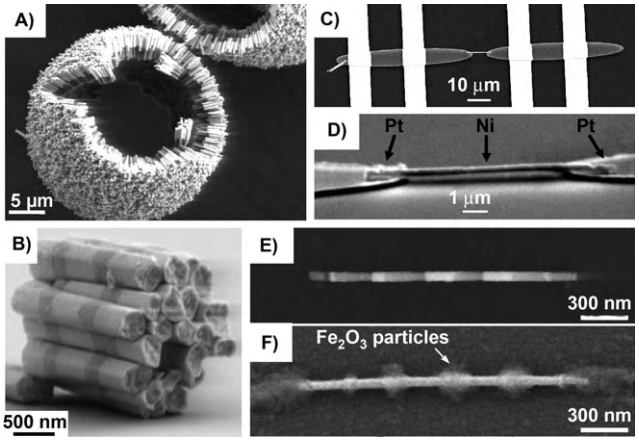

Figure 4. A) SEM image of Au-Ppy rods self-assembled into a tubular shape. B) SEM image of a bundle of Au-Ni rods showing the alignment of the ferromagnetic sections. SEM images showing C) a top view and D) a close-up view (substrate tilted 70°) of a Pt-Ni-Pt wire trapped by elliptical Ni magnetic electrodes. E) SEM image of a Au-CoNi rod and F) the same rod after treatment with 8-nm Fe_2O_3 nanoparticles. In images A), B), E), and F), the brighter segments of the rods are the Au segments. A) and B) were reproduced with permission from references [48] and [93], respectively. C) and D) were reproduced with permission from reference [94]; copyright 2002, American Institute of Physics. E) and F) were reproduced with permission from reference [98].

© 2006 Wiley-VCH Verlag GmbH & Co. KGaA, Weinheim

Subsequent experiments showed that the template plays a critical role in producing such structures by pre-aligning the rods, as it dissolves, such that only certain rod–rod interactions are possible. The bundles and tubes that form are a result, in part, of the strong van der Waals attractions between the organic ends of the individual rods as well as the steric repulsion between the Au ends of the different nanorods. The diameter of these superstructures can be controlled by varying the ratio of the lengths between the Au and Ppy segments of the nanorods. Larger Au/Ppy ratios result in tubes of smaller diameter and conversely, smaller Au/Ppy ratios produce tubes with larger diameters. Two-dimensional sheet superstructures formed from Au–Ppy–Au nanorods, which have an hour-glass as opposed to a conical shape. This work is important because it suggests that templates can play a role in guiding the assembly of mesoscopic structures in addition to serving their synthetic role in controlling the dimensions of the building blocks.

3.2.2. *Magnetic Assembly*

Bundle structures of a different type also have been formed by using magnetic interactions. Whitesides and co-workers[93] designed multisegmented nanorods made of ferromagnetic Ni sections separated by diamagnetic Au spacer segments. The Au segments function to increase the stability of the assembly by producing multiple, simultaneous magnetic interactions along the length of the nanorod. The magnetic interactions between the Ni segments of the nanorods are responsible for the assembly. In these nanorods, the Ni sections are disklike and have smaller thickness than diameters ($t < d$). This type of structure causes the magnetic moments of the Ni segments to align perpendicular to the long axis of the nanorod.[67d–e] Therefore, individual nanorods bundle side-to-side so that their ferromagnetic sections align (Figure 4B).

There are many other important examples of magnetic assembly of multisegmented electrodeposited nanorods. Magnetic assembly has sparked interest, for example, in the field of micro- and nanoscale electronics due to its importance in magnetic trapping. Magnetic trapping can be used to assemble individual nanowires, which contain either interior or terminal magnetic segments, on lithographically defined magnetic microelectrode patterns for the purpose of electrical measurements. Without the use of the magnetic trapping technique, immobilization of nanowires onto microelectrodes for electrical measurements can be a time-consuming and difficult process. Since the nanowire positioning is left to capillary forces acting in the solution during evaporation, several attempts at immobilization must typically be made before a single nanowire with the correct orientation can be found contacting the microelectrodes.[49] Conversely, using the magnetic trapping technique, the immobilization of nanowires can be precisely controlled by using an external magnetic field.[43,94,95]

For this reason, several groups are vigorously researching magnetic trapping. First, Tanase et al.[94] achieved magnetic trapping about 50% of the time, with three-segment, ≈350-nm diameter nanorods composed of an 8-μm Ni central segment with 2-μm Pt caps on each end. The Pt caps were used to provide low-resistance electrical contacts, while the Ni segment could be magnetically manipulated. These nanorods were assembled in a 6-μm gap between a pair of Ni electrodes, which were fabricated by using optical lithography and thermal evaporation (Figure 4C,D). The ellipse-shaped Ni electrodes were magnetized parallel to their long axis prior to assembly, and a small external field was applied during the trapping to assist the alignment of the nanowires before precipitation. Similar work involving magnetic trapping was also accomplished by Crone and co-workers[95] using Ni–CuSn(bronze)–Ni nanorods and by Myung and co-workers[43] using Ni–Au–Ni and Ni–Bi–Ni nanorods.

In addition to nanoelectronics, magnetic assembly also has become a subject of increased interest in the fields of biology and biochemistry.[96] Magnetic nanoparticles have been used to separate biomolecules and cells from multicomponent mixtures, to stimulate cells mechanically, and to enhance contrast in magnetic resonance imaging (MRI). To enable the study of biological processes at the subcellular level, however, magnetic nanoparticles must be able to be positioned with submicron precision. While advances have been made in the synthesis and derivatization of magnetic nanoparticles,[21b,97] little progress has been made in controlling their positioning.

Whitesides and co-workers[98] have demonstrated one solution to this problem by employing multisegmented electrochemically deposited nanorods. These nanorods comprised very short (20–100 nm) diamagnetic Au sections separated by longer (≈350 nm) ferromagnetic CoNi alloy sections (Figure 4E). The Au sections functioned to set up a series of magnetic gaps along the length of the nanorods that, unlike a magnetic gap filled with air, provided mechanical stabilization for the nanorod. These magnetic gaps produce sub-100-nm areas of intense magnetic field gradients that are confined to the region of that gap. Owing to these intense gradients, 8-nm iron oxide particles were attracted to and assembled around these gaps (Figure 4F). The size and shape of the magnetic field gradient, and hence, the spatial confinement of this assembly can be controlled by changing the size of the ferromagnetic sections and the magnetic susceptibilities of the components of the nanorod.

3.2.3. *Surface Modification*

Nanoscale building blocks also can be assembled by using their distinct surface chemistry.[99] It is widely known that bulk metallic films and nanoparticles of various shape and composition can be functionalized with self-assembled monolayers (SAM) of small molecules containing, for example, thiol, cyanide, amine, and carboxylic acid groups. Molecules as sophisticated as modified proteins and nucleic acids have been used to prepare monolayer structures. For multisegmented nanomaterials, each component has a different surface reactivity, thus it is possible to achieve spatially selective chemical functionalization along the long axis of the nanowire.

Several groups have demonstrated various ways to selectively functionalize multisegmented nanorods and nanowires. Our group,[100,101] for example, has shown that histidine-

 © 2006 Wiley-VCH Verlag GmbH & Co. KGaA, Weinheim

tagged proteins preferentially bind to the Ni segments of Au–Ni–Au nanorods and has exploited this property in bioseparation strategies (see Section 3.4.2). Also, Mallouk and co-workers[37a] were able to show that orthogonal assembly of 2-mercaptoethylamine and 1-butaneisocyanide occurred on the surfaces of Au and Pt segments, respectively, of an electrochemically synthesized nanorod. Similar studies, which were performed by Meyers et al.,[102] show that the Au and Ni components of a nanorod could be selectively functionalized with nonylmercaptan and Heme IX porphyrin, respectively. Another study by Meyers et al.[103] showed that mouse IgG protein and its antibody selectively absorbed onto palmitic acid monolayers of the Ni components of a Au–Ni rod. Taking the concept of selective functionalization on multicomponent nanorods one step further, it was shown that further selective chemistry could be performed on these monolayers through amide, thiourea, and thioether coupling reactions.[102]

Several cases of self-assembly have been reported that take advantage of these affinity binding events. Searson and co-workers,[104] for instance, reported the directed end-to-end linkage of Au–Pt–Au and Au–Ni–Au multisegmented nanorods using a biotin–avidin linkage (Figure 5). In these systems,

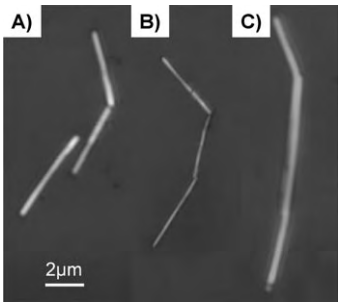

Figure 5. Optical microscope images of Au–Ni–Au nanorods: A) a single (left) and two linked nanorod chains (right); B), C) chains of three and four nanowires, respectively. Reproduced with permission from reference [104b].

the central Pt or Ni segments, which are considered essential to avoid nonspecific binding and minimize lateral nanorod assembly, were passivated with 1-butaneisocyanide or palmitic acid, respectively. The Au segments were functionalized with biotin-terminated 1-undecanethiol. Assembly of these rods then was achieved in one of two different ways. In the first method, avidin-terminated rods were prepared by exposing a solution of biotin-terminated nanorods to avidin. End-to-end assembly, as dictated by the biotin–avidin linkages on the Au segments, then was observed when equal amounts of avidin- and biotin-terminated nanorods were mixed. Alternatively, end-to-end assembly was achieved through the addition of free avidin to biotin-terminated nanowires. In a similar scheme, Searson and co-workers[105] patterned avidin on a Ag-coated surface using a poly(dimethylsiloxane) (PDMS) stamping technique. Subsequently, bicomponent nanorods consisting of biotinylated Au segments and Ni segments passivated with palmitic acid were assembled on this substrate using the biotin–avidin linkage.

There is no conceivable end to the superstructures that can be formed using this methodology. Once these types of second-order superstructures are formed it would be interesting to find ways to assemble them into even higher-order macroscopic superstructures. When this type of assembly can be achieved, the full potential of building materials and tailoring their properties from the bottom up will begin to be realized.

3.3. Electronics

Electronic properties of one-component nanowire systems have been studied extensively over the past couple of decades.[106] The focus of the majority of this research deals with utilizing nanowires for transport measurements and as elements in nanoscale device preparation. Unfortunately, single-component nanowires are difficult to position for measurement, limited in terms of functionalization, and have contact resistances, which are large enough to interfere with the actual measurement of the nanoscale device. Multisegmented nanowires solve some of these problems. For example, within a single multisegmented wire, one magnetic component can be used to control positioning, another can be a noble metal, which insures contact conductance and possibilities for surface functionalization, and the last segment can be the material of interest for measurement. With these structures, electrical properties in nanowires, such as resistance and semi- and superconductivity, can be studied.

Electronic properties of these multisegmented nanorods are typically measured by integrating them in a microscale circuit. This integration is usually accomplished by using microfluidic,[106b] electric-field-driven,[107] top-contact metal evaporation,[108] solvent evaporation,[49] and magnetic trapping (as mentioned in Section 3.2.2) techniques.[43,94,95]

3.3.1. Resistors

Resistors, which are defined by their linear current–voltage behavior, are one of the simplest nanowire devices; they require only two terminal connections.[109] So far, resistors have been fabricated using multicomponent nanorods that solely contain metal segments, as well as those that contain polymers sandwiched by metal segments. Tanase et al.[94] and Myung and co-workers[43] have successfully fabricated resistors from Pt–Ni–Pt and Ni–Au–Ni nanowires, respectively. Tanase et al.[94] found that trapped Pt–Ni–Pt wires exhibited linear current–voltage (I–V) curves for currents up to 1 mA at both room and liquid nitrogen temperatures (Figure 6 A, B). Myung and co-workers[43] also measured an ohmic response at room temperature for a single Ni–Au–Ni nanowire. Similarly, Wang and co-workers[110] synthesized Au–Sn–Au sandwiched structures and studied the mechanisms for intermetallic phase formation and the effect of these phases on the nanowire superconductivity.

In addition to metals, polymers have been employed as components in nanoresistors. Our group[49] has prepared metal–polymer nanowires (324 nm in diameter) by electrochemically depositing Au and polypyrrole (Ppy) into an AAO

© 2006 Wiley-VCH Verlag GmbH & Co. KGaA, Weinheim

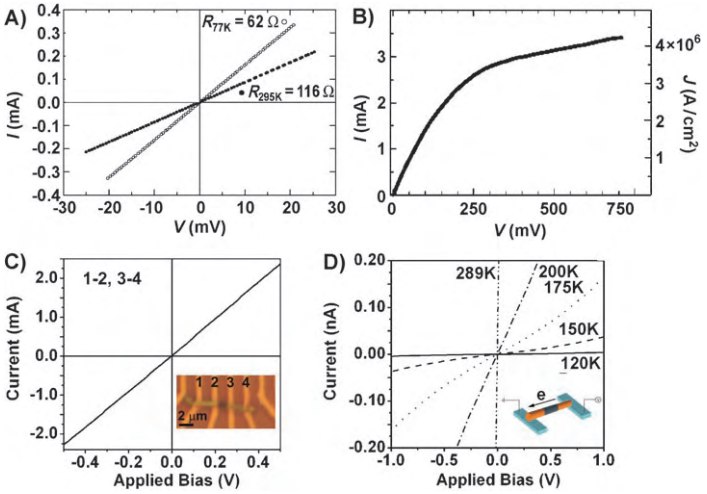

Figure 6. A) *I–V* behavior of a Pt–Ni–Pt nanowire showing an ohmic response at 77 K and 295 K. B) Extension of the $T = 295$ K *I–V* curve to higher current showing the effect of local heating on the nanowire. C) *I–V* characteristics of the Au segments of a single Au–Ppy–Au nanorod (shown in the inset) connected between Au microelectrode fingers. D) *I–V* characteristics, at a variety of temperatures, of the Ppy segment shown in the inset in C). The electrical responses in C) and D) were measured across terminals 1–2 or 3–4 and terminal 2–3, respectively. A) and B) were reprinted with permission from reference [94]; copyright 2002, American Institute of Physics. C) and D) were reproduced with permission from reference [49].

template. The Au–Ppy–Au segmented nanowires were deposited onto a microelectrode array (inset Figure 6C), and *I–V* measurements were carried out. The *I–V* plot shown in Figure 6C again confirms the linear, ohmic behavior for the Au metal segments of the nanowire at room temperature. Figure 6D, however, shows the ohmic behavior of the Ppy segment at room temperature and the nonlinearity of the *I–V* curve at temperatures below 175 K. This nonlinearity is characteristic of semiconducting behavior in conducting polymers.

3.3.2. *Transistors*

Transistors are semiconductor-based three-terminal devices, which can be used for purposes such as amplification, switching, voltage stabilization, and signal modulation.[109] For transistors to be integrated into circuits, each component device is required to be individually gated. Multisegmented nanowires are therefore ideal for fabricating these devices.

Using a multisegmented nanowire system, Mallouk and co-workers[54] have demonstrated a "wrap-around gate" approach to nanoscale thin-film transistors (TFT). As shown in the scheme in Figure 7A, SiO_2 nanotubes were deposited onto the pore walls of a Ag-backed AAO membrane by using repeated $SiCl_4$ adsorption–hydrolysis cycles. This treated membrane was then used to electroplate Au–CdS(or CdSe)–Au nanowires. Finally, when the template was dissolved, rods were released which were sheathed in silica. One of these structures was immobilized on a microelectrode contact such that the Au, CdS, and Au segments of the rod acted as the source, channel, and drain for the device, respectively (Figure 7B). The silica sheath acted as the gate oxide and the central Au electrode on the substrate served as the gate. The *I–V* characteristics between the drain and the source of the Au–CdS–Au@$(SiO_2)_n$ nanowire devices (Figure 7C) showed the behavior of a field-effect transistor (FET).

Field-effect transistors also have been made from organic polymer components in multisegmented nanowire systems. Polypyrrole exhibits good stability at room temperature and can be used to make devices that act as FETs and can be used for chemical sensors. For example, FETs were produced by electrochemically fabricating Co–Ppy–Co nanowires in AAO templates and patterning a gate on one side of the wire.[111] The measured output and transfer characteristics exhibited results similar to thin-film FETs containing only Ppy.[112]

3.3.3. *Switches*

Diodes are devices that allow current flow in one direction, but block current flow in the other. In this regard, they are typically employed as switches in electrical circuits.[109] Diodes are primarily synthesized by building a junction between a p-type (hole-rich) and a n-type (electron-rich) semiconductor. Recently, as a proof-of-concept experiment, our group[49] prepared nanodiodes from Au–Ppy–Cd–Au multisegmented nanowires (Figure 8A) and studied their electronic transport properties. In this system, the Ppy forms a

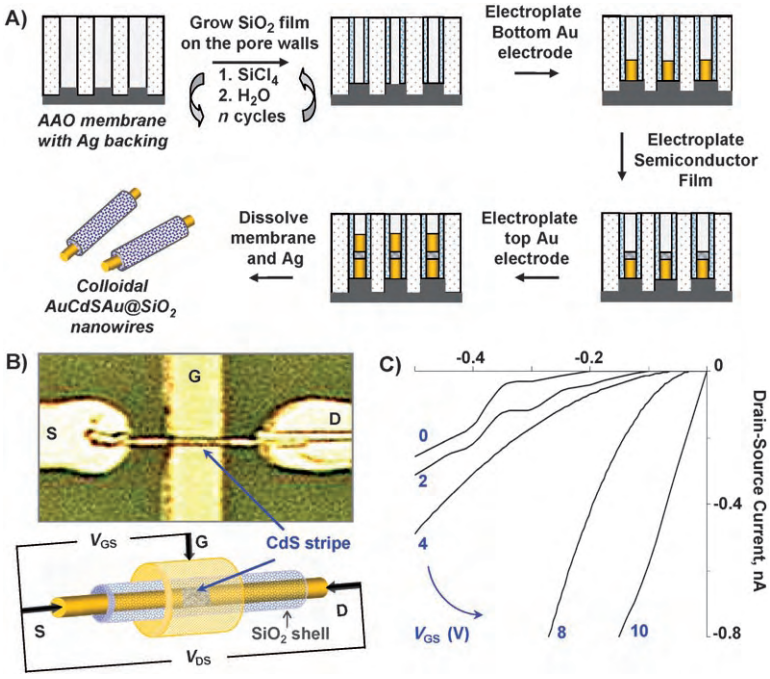

Figure 7. A) Scheme for the template synthesis of coaxially gated in-wire TFTs. B) Optical microscope image and schematic of a SiO_2-sheated Au–CdS–Au nanowire aligned for electrical measurement. C) Typical I_{DS}–V_{DS} characteristics of a nanowire as shown in B) for different values of gate voltage. Reproduced with permission from reference [54].

 © 2006 Wiley-VCH Verlag GmbH & Co. KGaA, Weinheim

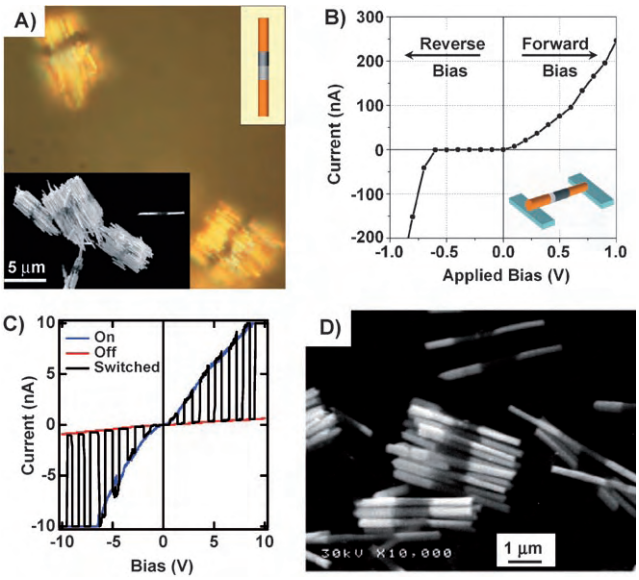

Figure 8. A) Optical microscope image of Au–Ppy–Cd–Au nanorod with insets showing schematic (upper right) and SEM image (lower left) of the same. B) *I–V* characteristics of nanorods shown in A) under forward and reverse bias. C) *I–V* curves of nanorods shown in D) with light on, light off, and switched between on and off at 5-s intervals. D) SEM image of 350-nm diameter Au–CdSe–Au nanorods. A) and B) were reproduced with permission from reference [49]. C) and D) were reproduced with permission from reference [114].

Schottky-like junction with Cd due to the difference in work functions between the two materials, and the Au caps serve to provide efficient electrical contact. The *I–V* curves measured for these devices exhibited non-ohmic, asymmetric diode behavior at room temperature (Figure 8B). Metal nanowires with layered carbon nanotube/polymer/semiconductor shells also have been synthesized and were found to behave as diodes.[113]

Devices exhibiting photoconductivity, an increase in conductivity under illumination by light, also, like diodes, can be used for electrical switching. These devices have on- and off-states that are dictated by the intensity of illumination. Template synthesis of photoconductive Au–CdSe–Au nanowires (Figure 8D) were reported by Mallouk and co-workers.[114] The nanowires were significantly more resistive in the dark than when illuminated by a Xe lamp. The nanowire was switched between two different resistivities several times at 5-s intervals with no degradation of the response (Figure 8C).

Silica-sheathed Ga–ZnS nanowires also have been synthesized.[115] The junction between the Ga and ZnS layers was found to be highly sensitive to electron beam irradiation (EBI) inside an electron microscope. Therefore, these structures have potential application as EBI-driven switches.

3.3.4. *Gaps*

In the field of nanoelectronics, precise electrical measurements depend on the ability to fabricate and functionalize electrode gaps less than 20-nm wide. Fabricating such structures is far from routine and often involves low-yielding and imprecise procedures such as break-junction techniques and gap narrowing by electroplating.[116]

Recently, our group[117] developed a new strategy to control the gap size in a one-dimensional wire structure down to the 5-nm length scale and create new nanoelectronic devices. This process, called on-wire lithography (OWL), is based on the concept that multisegmented nanowires of at least two materials can be designed such that one of the materials is susceptible to wet-chemical etching, while the other is not (Figure 9A). In this way, the susceptible component serves as a sacrificial layer for gap creation, and the other layer serves as a support and a connection for further measurement. The key innovation in OWL is the chemical vapor deposition (CVD) of a layer of insulating silica on one side of the nanowires. This layer holds the nanowire segments in place, while also leaving them accessible to fill (Figure 9B). The *I–V* curves show that 13-nm gaps within the OWL-fabricated nanowires are insulating. However, after selectively functionalizing the gap with a nanoscopic amount of conductive polymer using dip-pen nanolithography (DPN),[118] the *I–V* curve showed a response typical of the conducting polymer (Figure 9C). Using the OWL procedure and relatively inexpensive instrumentation, gap or notched nanowire structures can be made that will facilitate the study of the electronic properties of nanomaterials.

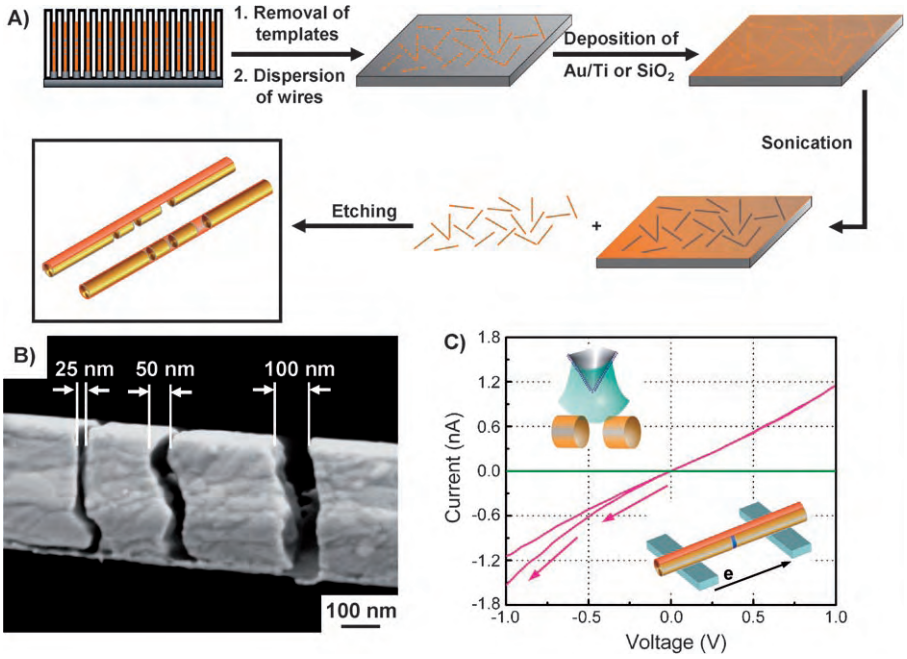

Figure 9. A) Scheme of OWL process. B) SEM image of side view of nanogap wire with gap sizes of 25 nm, 50 nm, and 100 nm. C) *I–V* measurements on the gapped nanowires. The green line is the measurement for an empty gap, while the pink line is after the addition, by dip-pen nanolithography, of a PEO/Ppy mixture into the gap. The red arrows indicate a conductivity change when the filled gap is irradiated with a Xe lamp. Reproduced with permission from reference [117].

© 2006 Wiley-VCH Verlag GmbH & Co. KGaA, Weinheim

Bao and co-workers[119] have presented another approach to fabricating gapped multisegmented nanowires. In their scheme, Au–Ag–Au multicomponent nanowires were first immobilized on microelectrodes. Then, gapped nanowire electrodes of controlled gap size were created by either chemically etching or using heat to remove the Ag segment (Figure 10 A). Unlike the OWL method, this technique does not utilize a nanowire support layer so once the Ag segment is removed the nanowire is physically broken. By filling a 100-nm gapped nanowire with poly(3-hexylthiophene) (P3HT), organic field-effect transistors were subsequently fabricated (Figure 10 B) and electrically characterized (Figure 10 C, D).

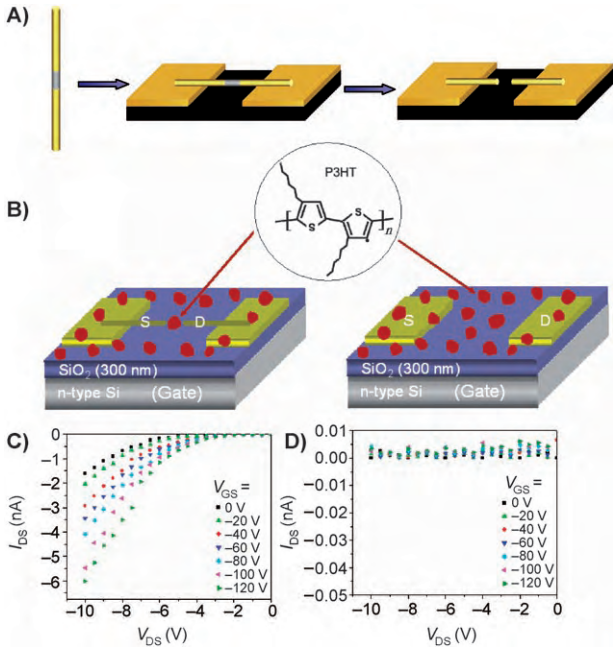

Figure 10. A) Schematic for the nanowire electrode fabrication process. The Au–Ag–Au nanowire is first immobilized on a larger microelectrode pattern and the Ag segment of the wire is then selectively etched. B) Schematic showing spin-casting of P3HT on the microelectrode surface with (left) and without (right) an immobilized, gapped nanowire. C), D) I_{DS}–V_{DS} behavior of systems shown left and right, respectively, in B). Reproduced with permission from reference [119].

Keating and co-workers[120] have taken yet another approach to produce gapped nanorod structures. In contrast to both our group and Bao's group, who employ techniques that partially enclose and do not enclose their gapped nanostructures, respectively, Keating and co-workers have demonstrated a method to completely encase gapped nanorods in a silica shell. These encased gapped nanorods were then used to study the optical properties of gapped nanostructures (see Section 3.6).

3.3.5. *Molecular Junctions*

Multisegmented nanowires also have been used to study the electronic properties of molecular junctions. Metal nanowires, 70 nm in diameter, containing in-wire monolayer junctions of 16-mercaptohexadecanoic acid were studied by Mallouk and co-workers.[121] These Au–molecular monolayer–Au junctions were prepared through combined electroplating/molecular assembly/electroless plating steps and then aligned between metal fingers on an insulating substrate. *I–V* measurements of individual nanowires confirmed that the organic monolayer could be contacted electrically without introducing electrical short circuits that penetrate the monolayer. The measured values for zero-bias resistance, current density, and breakdown field strength were all within range for an ordered alkanethiol SAM of the same experimental thickness.[122] Junctions of different organic monolayers, such as dodecane, oligo(phenylene ethylene), and oligo(phenylene vinylene), were also explored by this group.[123,124]

3.4. *Biological Applications*

To date, many single-component nanostructures, primarily Au, semiconducting, and magnetic nanoparticles, have been investigated for their use in biological applications.[14,96] These nanostructures have proven to be very effective at a large number of tasks. Au and semiconducting nanoparticles have been used to detect species, such as proteins, DNA, and disease markers, at low concentrations. Magnetic nanoparticles are used for cell separations and studies of cellular function. Silica nanotubes, which were functionalized on their inner surface with a layer of Fe_3O_4 (magnetite) nanoparticles, have even been used for chemical extractions and protein separations.[125] Single-component structures are limited, however, in terms of multiplexing in detection, separations, and therapeutics. Multisegmented nanorods provide platforms for simultaneous detection and separation of multiple species in solution as well as multiple modes for species identification. Multicomponent nanomaterials, especially those having magnetic segments, also can be utilized for in vivo therapeutics, where it is important that materials are able to deliver a species to a cell as well as apply force to it. Biological detection, separation, and therapeutic schemes, which employ multisegmented nanorods, are discussed in Sections 3.4.1 to 3.4.3. Nanorod functionalization through affinity binding events, which also was discussed in Section 3.2.3, is a widespread technique in many of these applications[126] and plays an essential role in separation and therapeutic strategies.

3.4.1. *Detection and Sensing*

Natan, Keating, and co-workers[44] have shown multiplexed detection and sensing of biological analytes using striped metallic nanorods, referred to as nanobarcodes (NBC) (Figure 11 A, B). Through sequential electrochemical deposition of metal into AAO and polycarbonate templates, NBCs with complex striping patterns were prepared by using a combination of metals (Au, Ag, Pt, Pd, Ni, Co, and/or Cu). These metal segments showed distinguishable contrast in both optical and electron microscopy with varying thickness and composition. In this way, NBCs that have different metallic patterns (e.g., 10010 and 01000, where 0 = Au and 1 = Ag) can

 © 2006 Wiley-VCH Verlag GmbH & Co. KGaA, Weinheim

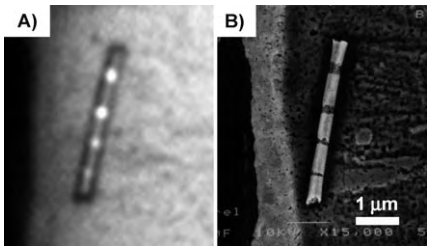

Figure 11. Optical (A) and SEM (B) images of a Au–Ag multicomponent rod with ≈550-nm Au stripes (brighter segments) and Ag stripes of 240, 170, 110, and 60 nm (top to bottom). Reproduced with permission from reference [44].

be distinguished using optical microscopy in the reflectance mode. When detecting different analytes, these patterns can be used as an identification system that can be conveniently read-out using optical microscopy. Multiple striping patterns can be used to identify multiple species simultaneously in solution.

Nanobarcodes composed of Ag and Au segments have been used for both DNA[44,127] and protein[44] detection. The DNA detection strategy employed a sandwich assay in which the striped rods were first functionalized with a 12-nucleotide capture sequence capable of binding a 24-nucleotide target sequence. After capture, the target sequence is then detected by the addition of a fluorophore-tagged 12-nucleotide probe sequence complementary to the remaining bases of the target strand. When the target strand was present, each segment of the metal barcodes could be seen in the optical reflectance and in the fluorescence images (Figure 12A, B). However, when the target strand was omitted, the NBCs were visible only in the reflectance image (Figure 12C, D). For the detection of proteins, the surfaces of the NBCs were coated with a specific capture antibody. The target protein is then captured and a second fluorophore-labeled antibody sandwiches the target protein for detection. Read-out was performed, using the same scheme as in the case of DNA detection, in a simultaneous immunoassay on two different barcoded particles (Figure 12E–G).

Natan, Keating, and co-workers[128,129] further increased the ease and speed of the NBC assay by incorporating software programs to manage the optical read-out. This software analyzes optical microscope images and provides automated nanobarcode identification and fluorescence measurements as well as data on particle position, length, and diameter. This software was developed in the context of a library of the more than 100 different nanorod patterns that could be created by using an eight-stripe system of different combinations of Ag and Au segments. At its current stage, the software can distinguish 70 striping patterns with greater than 90% accuracy. These 70 patterns provide a massive library of nanoparticle markers that can be used for biodetection and multiplexing.

Mallouk and co-workers[130] have developed a different strategy for multicomponent rod-based biodetection. While, in the NBC assay, the rods are modified with the capture, target, and probe strands after synthesis, Mallouk and co-workers have incorporated capture proteins into the multi-

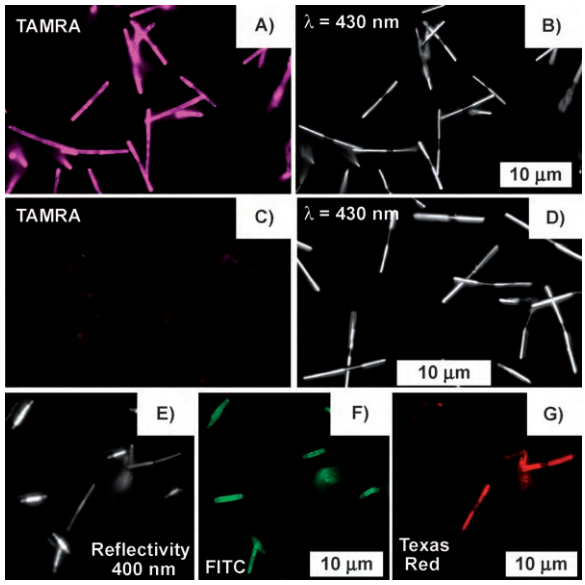

Figure 12. A–D) "Sandwich" DNA hybridization assay. The optical microscope images in B) and D) show reflectance optical read-out, which give NBC and accordingly analyte ID. The fluorescence images in A) and C) confirm the presence or absence, respectively, of the DNA target sequence. E)–G) Read-out of a simultaneous sandwich immunoassay performed by using NBCs. E) Optical reflectance image showing two different NBCs. F) and G) Fluorescence images, taken with FITC and Texas Red filter sets, respectively, that simultaneously confirm the presence of two fluorophore-tagged proteins in solution. Images A) and B), images C) and D), and images E)–G) show the same grouping of rods. Reproduced with permission from reference [44].

component rods during synthesis (Figure 13). In separate experiments, avidin and streptavidin were each immobilized in the polypyrrole (Ppy) segment of Au–Ppy–Au rods by

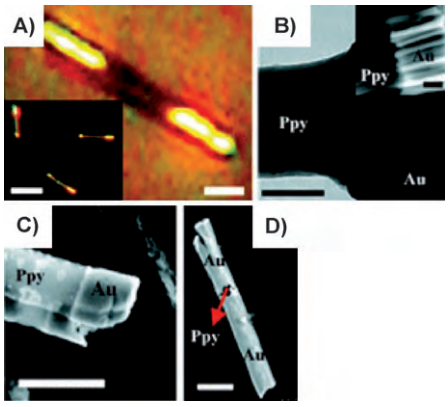

Figure 13. A) Optical microscope images (bright field) of a Au–Ppy–Au nanowire (scale bar = 1 μm). Diameter and total length of the nanowire are 314 nm and 4 μm, respectively. The inset shows a dark-field image of the same nanowire (scale bar = 4 μm). B) TEM image of a Au–Ppy junction (scale bar = 100 nm). The inset shows an environmental scanning electron microscopy (ESEM) image of the same junction (scale bar = 1 μm). C) SEM image of a Au–Ppy junction after electroless deposition of the second Au cap (scale bar = 600 nm). D) Field-emission(FE)-SEM image of a Au–Ppy–Au nanowire after electrochemical deposition of the second Au cap (scale bar = 600 nm). Reproduced with permission from reference [130].

 © 2006 Wiley-VCH Verlag GmbH & Co. KGaA, Weinheim

physical entrapment during the Ppy polymerization. The entrapped proteins maintained their ability to bind to fluorophore-tagged biotin after the physical entrapment. Accordingly, the rods could be used as biosensors in fluorescent detection schemes.

3.4.2. Separations

Histidine (His) is known to have a high binding affinity for Ni, and this interaction is already used in Ni columns to separate His-tagged proteins from biological solutions.[131] Our group[100] has demonstrated that Au–Ni–Au rods can be used to achieve the same goal (Figure 14), but with rapid-

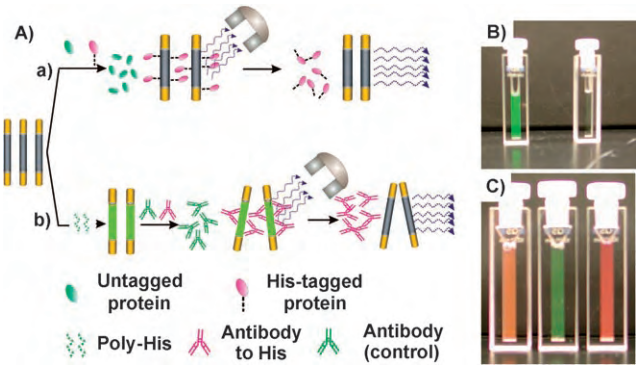

Figure 14. A) Scheme for separation of His-tagged proteins from untagged proteins (route a) and for separation of antibodies to poly-His from other antibodies (route b). B) Two cuvettes showing solutions of fluorescein-tagged poly-His before (left) and after (right) exposure to Au–Ni–Au nanorods. C) Left cuvette (orange): dye-labeled His-tagged (red) and untagged proteins (green) before exposure to nanorods. After exposure to nanorods, red His-tagged proteins are removed; the middle cuvette (green) contains only untagged proteins. Right cuvette (red): after release of the red His-tagged proteins from the nanorods. Reproduced with permission from reference [100].

binding kinetics. When these rods were introduced to a solution containing both His-tagged and untagged proteins, the His-tagged proteins attached to the Ni portion of the rod and could be removed from solution using an applied magnetic field. Similarly, it was demonstrated that Au–Ni–Au rods functionalized with poly-His could be used to efficiently separate mixtures of anti-His proteins from control antibodies. For these experiments, the Au portions of the rods were passivated with thiolated poly(ethylene glycol) (PEG-SH) to minimize nonspecific binding of proteins to Au surfaces and to minimize aggregation caused by bare gold surface–surface interactions.

However, the Au segments also provide an additional degree of freedom that can be used to perform simultaneous separation of another molecular species. This concept was demonstrated by our group[101] using Au–Ni–Au triblock structures. These structures were synthesized, as described above, but the Au segments were functionalized with 11-amino-1-undecanethiol. The primary amine group tethered to the Au surface was chemically modified to bind nitrostreptavidin. Then, the Au segments were used to bind biotin-tagged bovine serum albumin (BSA), while His-tagged ubitquitin was bound to the Ni segment. Again, the Ni components of the rods also enabled separation of these two attached proteins from solution through the application of a magnetic field. The nanorods were able to capture and remove more than 90% of the His-tagged and biotin-tagged proteins based on fluorescence measurements.

3.4.3. Therapeutics

In addition to detection and separations, multisegmented rods also have been used in preliminary gene therapy experiments.[132,133] Currently, synthetic gene-delivery systems have been limited by their relatively low transfection efficiency, which limits the ability of the system to incorporate foreign DNA inside a target cell.[134] This problem stems from the difficulty in controlling the properties of present gene delivery systems on the nanoscale. The fabrication of the segmented rods provides an outlet of control in nanosized dimensions. In addition, multisegmented rods can be engineered with different functionalities in spatially defined regions offering precise control of antigen placement and the possibility of stimulating multiple immune responses.

Searson and co-workers[132] showed one example of using electrochemically synthesized Au–Ni rods for therapeutics. Once removed from the AAO template, the Ni segment of the nanorod was functionalized with 3-[(2-aminoethyl)dithiol]-propionic acid (AEDP) through its carboxylic acid terminus.

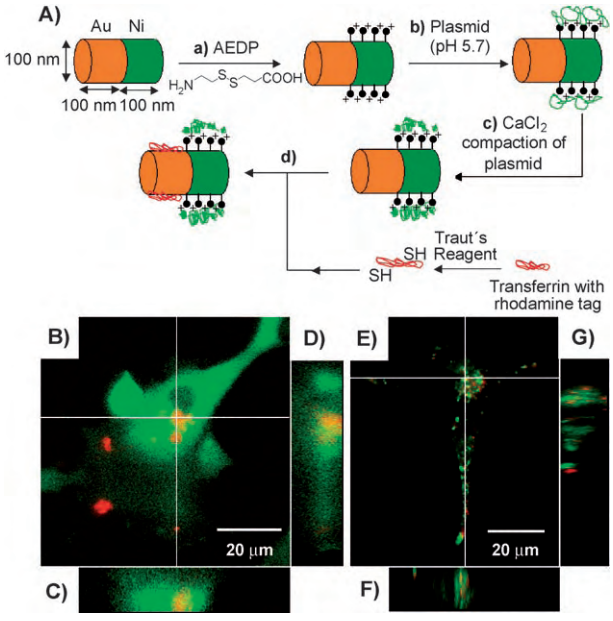

Figure 15. A) Scheme for the spatially selective binding of DNA plasmids and transferrin to multicomponent nanorods. B)–G) Stacked laser scanning confocal microscope images of transfected cells. B) A live HEK293 cell. Rhodamine (red) identifies the subcellular location of the nanorods, GFP (green) expression confirms transfection. C), D) orthogonal sections confirm nanorods are within the cell. E) A live HEK293 cell stained with Lysotracker Green, which identifies the location of the nanorods (Rhodamine) in relation to acidic organelles; F), G) orthogonal sections. Reproduced with permission from reference [132].

 © 2006 Wiley-VCH Verlag GmbH & Co. KGaA, Weinheim

Plasmid DNA was then electrostatically bound to the protonated amine groups of the AEDP (Figure 15A). The Au segment of the nanorod then was functionalized with transferrin, a cell-targeting protein, which was chemically modified with a thiol. Transfection studies using these loaded rods were conducted on human embryonic kidney (HEK293) mammalian cell lines (Figure 15B–G), and the multicomponent rods were proven to be more efficient in transfection than transferrin-modified single-component rods.

In addition, Searson and co-workers[133] have carried out in vivo studies (in mice) of the ability of multisegmented rods to provide gene therapy. For these studies, a series of experiments were carried out to test the ovalbumin-specific antibody response in mice immunized with various antigen or plasmid Au–Ni rods. In these studies, the strongest immunostimulatory responses were invoked using rods selectively functionalized with ovalbumin antigen (Ni segment) and plasmid DNA encoding ovalbumin (Au segment). The response was stronger than when rods modified with only ovalbumin antigen or ovalbumin antigen with plasmid DNA not encoding ovalbumin were used. It also was higher than the response observed when Au nanoparticles were used, which were functionalized with either only ovalbumin antigen or only ovalbumin-encoded plasmid DNA. Therefore, multicomponent rods potentially could provide an advantage in gene therapy applications. This approach can be extended to other gene targets through the use of different DNA strands, proteins, and nanorod components.

3.5. Catalysis

The template synthesis method is an ideal way to make multisegmented nanowires and nanowire arrays with controllable composition, size, distribution, surface area, and morphology. Therefore, these structures, if synthesized with catalytically active components, provide a model system to study the effect of these parameters on catalytic activity. Bai and co-workers[135] prepared a layered Ni–Cu nanowire array, in which the Ni segments were used to study the electrochemical reduction of nitroethane, while the Cu segments served as non-catalytically active spacer layers. The Ni–Cu nanowire arrays were more active catalysts than Ni nanowire arrays and bulk Ni substrates. The Ni segment also can be used for catalyst recovery through application of a magnetic field.

Similarly, Lee and co-workers[136] utlilized the dimensionality and compositional advantages of the template synthesis to fabricate multisegmented nanowires that could be used as methanol electro-oxidation catalysts. The catalytic properties of both Pt–Ni[136a] and Pt–Ru[136b] nanorods were investigated. In each case, the Pt segment serves to activate the C−H bond cleavage of methanol adsorbed to its surface. The other component (Ni or Ru) provides oxygen that reacts with CO species on the Pt surface to create CO_2 and render the Pt surface active for the next round of activation. For both types of multisegmented nanorods, cyclic voltammetry studies showed increased catalytic activity as the number of Pt−Ni or Pt−Ru interfaces was increased. Since template synthesis allows such precision in the placement and number of components and interfaces, these experiments provide direct evidence of the role of interfacial pair sites in the bifunctional catalytic mechanism.

The placement of catalytic components along the nanorods also has been used to control the motion of these nanoscale and microscale objects. The Mallouk group[137,138] and Ozin and Manners and co-workers[139] have studied the non-Brownian motion of Pt–Au and Ni–Au nanowires in an aqueous hydrogen peroxide solution, respectively. In one study, the motion of Pt–Au nanorods was charted as the Au segment was propelled by the released oxygen gas formed by catalytic decomposition of H_2O_2 at the Pt segment (Figure 16). The observed velocities of the Pt–Au nanowires were comparable to those of flagellar bacteria and similar mobile microorganisms. When Ni segments were incorporated into these nanorods, the directionality of their motion could be controlled remotely using an applied magnetic field. In another study, the rotary motion of Ni–Au nanorods that were tethered by their Au end to a silicon surface were studied. Known techniques potentially could be used to tether or couple other nanoscale objects to these nanoengines in spatially defined ways to create catalytically powered nano- and micromachines.

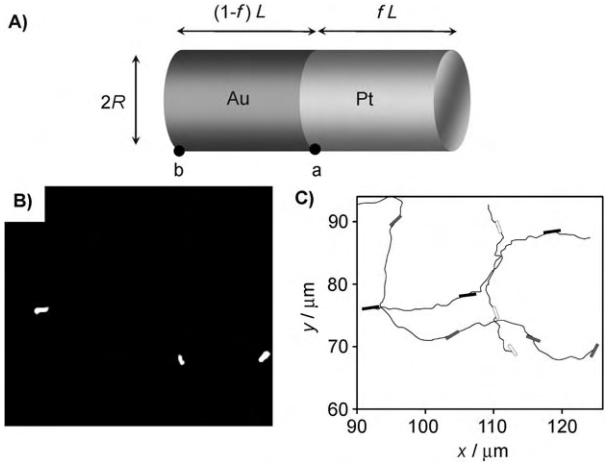

Figure 16. A) Schematic diagram of a Pt–Au nanorod showing the dimensions used to calculate interfacial forces. B) Optical microscope image of three, 2-µm (in length) Pt–Au rods. C) Trajectory of the Pt–Au rods shown in B) in 2.5% aqueous hydrogen peroxide over the subsequent 5 s. Reproduced with permission from reference [137].

3.6. Optical Applications

As discussed in Section 3.4.1, the optical properties, specifically the reflectance, of multisegmented metallic nanowires have been exploited for biosensing and biodetection applications.[44] These studies were conducted on rods having dimensions greater than 100 nm. It is well known, however, that the optical properties of metals change dramatically when their dimensions are reduced below 100 nm.[3] In this size regime, surface plasmon resonance (SPR) dictates the optical properties of the metal. Two distinct SPR responses are generated by the anisotropy of the multicomponent rods.

© 2006 Wiley-VCH Verlag GmbH & Co. KGaA, Weinheim

One response is parallel to the short axis (transverse) and the other is parallel to the long axis (longitudinal). As a result, rods with sub-100-nm dimensions could be used to probe these SPR responses of the metal segments as a function of length, composition, and periodicity. Template synthesis of multicomponent rods makes these investigations easy to perform.

Nanoscale particles 50–80-nm in diameter have previously been shown to be highly efficient elastic scatterers.[140] Shultz and co-workers[141] expanded this concept by studying the scattering properties of the individual segments of 30-nm diameter multicomponent rods, consisting of Au, Ag, and Ni segments (Figure 17). In these studies, only the excited

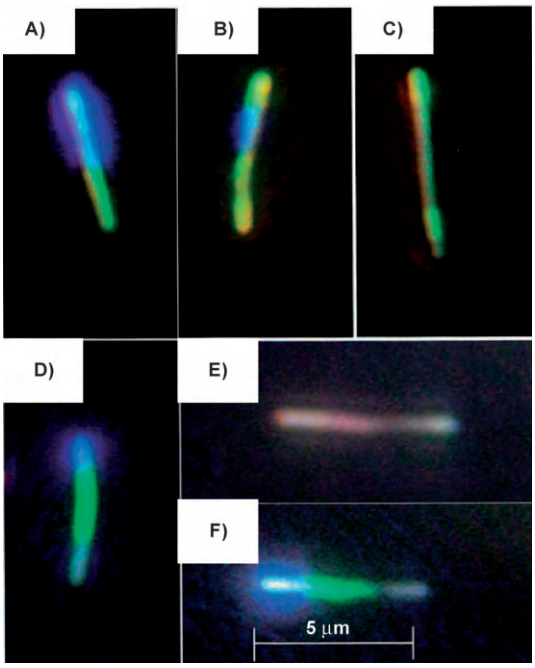

Figure 17. Digital camera color images of selected nanowires using the 100X oil immersion objective. A) Ag–Au, B) Au–Ag–Au, C) Au–Ni–Au–Ni, D) Ag–Au–Ni, E) Ag–Au–Ni, F) Ag–Au–Ni. For A)–D) and F) the white light is polarized along the short axis of each nanowire; for E), the light is polarized along the long axis. Reproduced with permission from reference [141].

transverse plasmon resonances were investigated. These transverse plasmon resonances were found to be polarization-dependent. Polarization along the long axis of the rod resulted in a loss of plasmon resonance information since the dimension of this rod was greater than 100 nm in this direction. On the other hand, plasmon resonance information was retained for polarization along the short axis having dimensions less than 100 nm. When illuminated under the optical microscope, each rod had a specific spectral signature that was dependent on the sizes of the segments. These distinct spectral signatures could be used for optical identification, much like the larger NBCs, in biodiagnostic assays and sensing. Further spectral signatures of multicomponent rods, resulting from other SPR modes, also could be studied and used for these purposes.

In another study, Keating and co-workers[120] investigated the optical extinction of the individual segments of multicomponent rods as a function of the spacing between the segments. Tricomponent Au, Ni, and Ag segmented wires with diameters of 320 nm, 100 nm, and 32 nm and various lengths were electrochemically deposited into AAO templates. The wires were then removed from the templates and coated completely with SiO_2 (Figure 18 A). The Ni segments were selectively etched by sulfuric acid, as was demonstrated in the OWL process, since the silica layer was porous enough to allow chemical penetration. This etching resulted in Au and Ag segments separated by gaps and encased in transparent silica (Figure 18 B–D). The gap spacing could be accurately controlled by changing the length of the sacrificial Ni segments. When the Ni segments were removed, optical absorption peaks characteristic of Au or Ag particles were observed. When the gaps between the Au and/or Ag segments were reduced to sizes smaller than the diameters of the segments, the maximums of the extinction spectra broadened and red-shifted. These changes were attributed to the increase in interparticle coupling between the segments. Therefore, by varying the composition of and the gap size between the components of the rods, control could be exercised over the optical properties of the nanorods. This concept could be extended to include other metals and gap sizes, resulting in novel spectral features. Gapped nanostructures also have been considered as candidates for plasmonic waveguides.[117,142]

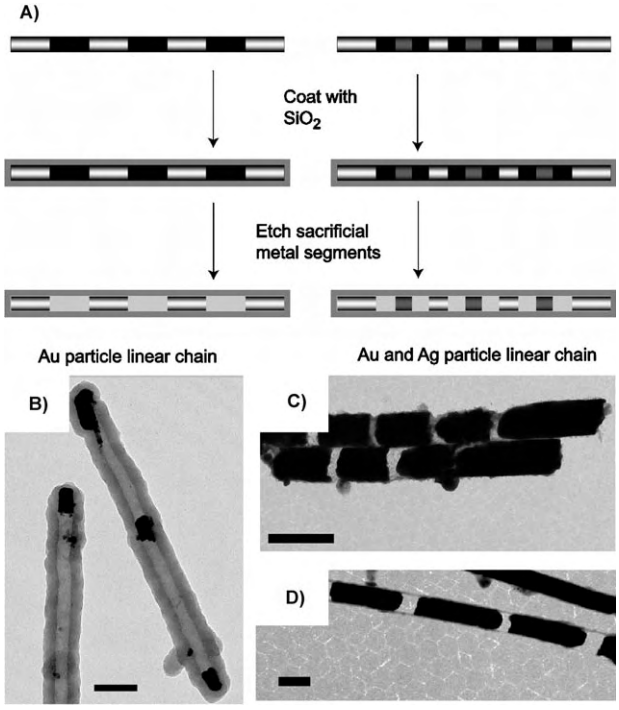

Figure 18. A) Scheme for preparation of a chain of metal nanoparticles. B)–D) TEM images of representative nanoparticle chains. B) Chain of Au particles (ca. 60×36 nm) with ≈400-nm gap sizes (scale bar = 100 nm). C), D) Chain of Ag nanoparticles with varying lengths and 100-nm widths with interparticle spacings smaller than the particle size (scale bar = 200 nm). Reproduced with permission from reference [120].

 © 2006 Wiley-VCH Verlag GmbH & Co. KGaA, Weinheim

4. Summary and Outlook

Recent advances in the study of the synthesis, properties, and applications of multisegmented one-dimensional nanostructures that were prepared through hard-template-directed synthesis have been discussed in this review. The nanostructures mentioned here contain a combination of metallic, semiconducting, polymeric, molecular, and gapped components. These multiple different components each possess unique physical and chemical properties that provide nanostructures formed from them with multifunctionality. This multifunctionality allows the nanostructure as a whole to perform several tasks simultaneously. As a result, a variety of applications for multicomponent structures have been developed in several areas, such as magnetics, self-assembly, electronics, biology, catalysis, and optics.

In addition to expanding the types of building blocks that can be used in the hard-template synthesis of multisegmented nanowires, there are two major challenges. The first involves creating higher throughput methods for synthesizing such structures. The second involves simple methods for integrating such structures into functional device architectures. At present, in a research setting, about 10^{11} multisegmented nanorods can be produced in a single synthesis using one commercially-available AAO template (13-mm diameter). Depending on the length and composition of the targeted nanorod, this synthesis can require several hours to complete. While one way to increase the production and throughput of the template synthesis is to perform several syntheses at once, this requires additional instrumentation and manpower. Therefore, it could be advantageous to develop templates that have larger areas and pore densities. For anyone to capitalize on such structures for industrial applications, automation of the electrodeposition process would be required. Attempts in this direction are underway.[143]

Integration is a more challenging issue. It is clear that such structures could be used as probes or additives to increase the performance or enhance the properties of bulk materials, but for them to be used as individually addressable components in electronic and photonic devices, methods must be developed to position them in the context of existing architectures (e.g., a circuit). Epitaxially grown nanowires, for example, can be grown at specified locations on a substrate.[12,27] In the case of template-synthesized nanowires, however, positioning is more difficult and will likely be addressed by a combination of chemistry and mechanically driven approaches.

The mechanical properties of multisegmented structures also will become an important issue as these structures and their applications are commercialized. The multicomponent structures and the integrity of their interfaces will need, for example, to be strong and stable both while the given application is carried out as well as in long-term storage situations. Investigations of the stability of the multicomponent nanostructures when they are mechanically (e.g., stretched, compressed, bent) and environmentally (e.g., heated, cooled, different solvents) stressed over varying lengths of time will be necessary. In some cases, multisegmented nanostructures and their interfaces will need to be mechanically or chemically reinforced for use in certain applications.

These investigations into the mechanical properties of multicomponent nanostructures also could initiate a new series of future fundamental studies and applications. For instance, mechanical stresses that change the size, shape, or composition of the nanostructure would change the chemical and physical properties of the multicomponent materials. As a result of these changes, these nanomaterials could be potentially used as nanoscale actuators. These nanoscale actuators would function such that the change in properties would signal the presence of a particular stress.

It is clear that a great deal of progress has been made over the past decade in the synthesis of multisegmented one-dimensional nanostructures through hard-template-assisted methods. As a result, knowledge of their properties and applications also has been developed significantly. Several important issues still remain that will be the subject of intense research in this field for many years to come.[144]

The Air Force Office of Scientific Research (AFOSR), the National Institute of Health (NIH) Director's Pioneer Award, the NIH Centers for Cancer Nanotechnology Excellence (NIH-CCNE), the Office of Naval Research (ONR), the National Science Foundation (NSF) Nanoscale Science and Engineering Center (NSEC), and the NSF Materials Research Science and Engineering Center (MRSEC) are all acknowledged for their support.

Received: November 11, 2005
Published online: March 29, 2006

[1] a) C. A. Mirkin, *Science* **1999**, *286*, 2095; b) C. A. Mirkin, *Small* **2005**, *1*, 14.
[2] R. Feynman, *The Pleasure of Finding Things Out* (Ed.: J. Robbins), Perseus Books, New York, **1999**.
[3] See, for example: a) *Nanomaterials: Synthesis, Properties, and Applications* (Eds.: A. S. Edelstein, R. C. Cammarata), Institute of Physics, Philadelphia, **1996**; b) *Nanostructured Materials: Clusters, Composites, and Thin Films* (Eds.: V. M. Shalaev, M. Moskovits), American Chemical Society, Washington, DC, **1997**; c) *Handbook of Nanostructured Materials and Nanotechnology* (Ed.: H. S. Nalwa), Academic Press, New York, **2000**; d) *Metal Nanoparticles: Synthesis Characterization, and Application* (Eds.: D. L. Feldheim, C. A. Foss, Jr.), Marcel Dekker, New York, **2002**.
[4] a) B. L. Cushing, V. L. Kolesnichenko, C. J. O'Connor, *Chem. Rev.* **2004**, *104*, 3893; b) C. Burda, X. Chen, R. Narayanan, M. A. El-Sayed, *Chem. Rev.* **2005**, *105*, 1025.
[5] a) R. M. Penner, C. R. Martin, *Anal. Chem.* **1987**, *59*, 2625; b) C. R. Martin, *Adv. Mater.* **1991**, *3*, 457; c) C. R. Martin, *Science* **1994**, *266*, 1961; d) C. R. Martin, *Chem. Mater.* **1996**, *8*, 1739.
[6] B. D. Gates, Q. Xu, M. Stewart, D. Ryan, C. G. Wilson, G. M. Whitesides, *Chem. Rev.* **2005**, *105*, 1171.
[7] a) H. Dai, *Acc. Chem. Res.* **2002**, *35*, 1035; b) M. T. Swihart, *Curr. Opin. Colloid Interface Sci.* **2003**, *8*, 127.
[8] a) M. Maillard, S. Giorgio, M.-P. Pileni, *Adv. Mater.* **2002**, *14*, 1084; b) E. Hao, K. L. Kelly, J. T. Hupp, G. C. Schatz, *J. Am. Chem. Soc.* **2002**, *124*, 15182; c) S. Chen, D. L. Carroll, *Nano Lett.* **2002**, *2*, 1003.

© 2006 Wiley-VCH Verlag GmbH & Co. KGaA, Weinheim

[9] a) J. C. Hulteen, R. P. Van Duyne, *J. Vac. Sci. Technol. A* **1995**, *13*, 1553; b) R. Jin, Y. Cao, C. A. Mirkin, K. L. Kelly, G. C. Schatz, J. G. Zheng, *Science* **2001**, *294*, 1901; c) R. Jin, Y. C. Cao, E. Hao, G. S. Métraux, G. C. Schatz, C. A. Mirkin, *Nature* **2003**, *425*, 487; d) J. E. Millstone, S. Park, K. L. Shuford, L. Qin, G. C. Schatz, C. A. Mirkin, *J. Am. Chem. Soc.* **2005**, *127*, 5312.

[10] a) T. S. Ahmadi, Z. L. Wang, T. C. Green, A. Henglein, M. A. El-Sayed, *Science* **1996**, *272*, 1924; b) Y. Sun, X. Xia, *Science* **2002**, *298*, 2176; c) D. Yu, V. W. Yam, *J. Am. Chem. Soc.* **2004**, *126*, 13200.

[11] a) X. Peng, L. Manna, W. Yang, J. Wickham, E. Scher, A. Kadavanich, A. P. Alivisatos, *Nature* **2000**, *404*, 59; b) N. R. Jana, L. Gearheart, C. J. Murphy, *J. Phys. Chem. B* **2001**, *105*, 4065; c) F. Kim, J. H. Song, P. Yang, *J. Am. Chem. Soc.* **2002**, *124*, 14316; d) Z. A. Peng, X. Peng, *J. Am. Chem. Soc.* **2002**, *124*, 3343.

[12] J. Hu, T. W. Odom, C. M. Lieber, *Acc. Chem. Res.* **1999**, *32*, 435.

[13] a) L. Manna, D. J. Milliron, A. Meisel, E. C. Scher, A. P. Alivisatos, *Nat. Mater.* **2003**, *2*, 382; b) S. Chen, Z. L. Wang, J. Ballato, S. H. Foulger, D. L. Carroll, *J. Am. Chem. Soc.* **2003**, *125*, 16186; c) E. Hao, R. C. Bailey, G. C. Schatz, J. T. Hupp, S. Li, *Nano Lett.* **2004**, *4*, 327.

[14] a) M. Bruchez, Jr., M. Moronne, P. Gin, S. Weiss, A. P. Alivisatos, *Science* **1998**, *281*, 2013; b) T. A. Taton, C. A. Mirkin, R. L. Letsinger, *Science* **2000**, *289*, 1757; c) S.-J. Park, T. A. Taton, C. A. Mirkin, *Science* **2002**, *295*, 1503; d) Y. C. Cao, R. Jin, C. A. Mirkin, *Science* **2002**, *297*, 1536; e) J.-M. Nam, C. S. Thaxton, C. A. Mirkin, *Science* **2003**, *301*, 1884; f) W. J. Parak, D. Gerion, T. Pellegrino, D. Zanchet, C. Micheel, S. C. Williams, R. Boudreau, M. A. L. Gros, C. A. Larabell, A. P. Alivisatos, *Nanotechnology* **2003**, *14*, R15; g) E. Katz, I. Willner, *Angew. Chem.* **2004**, *116*, 6166; *Angew. Chem. Int. Ed.* **2004**, *43*, 6042; h) J.-M. Nam, S. I. Stoeva, C. A. Mirkin, *J. Am. Chem. Soc.* **2004**, *126*, 5932; i) D. G. Georganopoulou, L. Chang, J.-M. Nam, C. S. Thaxton, E. J. Mufson, W. L. Klein, C. A. Mirkin, *Proc. Natl. Acad. Sci. USA* **2005**, *102*, 2273; j) N. L. Rosi, C. A. Mirkin, *Chem. Rev.* **2005**, *105*, 1547.

[15] a) H. Bönnemann, R. M. Richards, *Eur. J. Inorg. Chem.* **2001**, 2455; b) A. T. Bell, *Science* **2003**, *299*, 1688.

[16] Special issue: "Synthesis and Plasmonic Properties of Nanostructures": *Mater. Res. Soc. Bull.* **2005**, *30*.

[17] L. G. Wade, Jr., *Organic Chemistry*, 4th ed., Prentice Hall, Upper Saddle River, **1999**.

[18] L. Stryer, *Biochemistry*, 4th ed., W. H. Freeman, New York, **1995**.

[19] a) N. C. Gianneschi, P. A. Bertin, S. T. Nguyen, C. A. Mirkin, L. N. Zakharov, A. L. Rheingold, *J. Am. Chem. Soc.* **2003**, *125*, 10508; b) N. C. Gianneschi, S.-H. Cho, S. T. Nguyen, C. A. Mirkin, *Angew. Chem.* **2004**, *116*, 5619; *Angew. Chem. Int. Ed.* **2004**, *43*, 5503; c) N. C. Gianneschi, S. T. Nguyen, C. A. Mirkin, *J. Am. Chem. Soc.* **2005**, *127*, 1644.

[20] a) L. M. Liz-Marzán, M. Giersig, P. Mulvaney, *Langmuir* **1996**, *12*, 4329; b) F. Caruso, A. S. Susha, M. Giersig, H. Mohwald, *Adv. Mater.* **1999**, *11*, 950; c) F. Caruso, *Adv. Mater.* **2001**, *13*, 11; d) Y. Cao, R. Jin, C. A. Mirkin, *J. Am. Chem. Soc.* **2001**, *123*, 7961; e) M. Green, *Small* **2005**, *1*, 684; f) R. G. Sanedrin, D. G. Georganopoulou, S. Park, C. A. Mirkin, *Adv. Mater.* **2005**, *17*, 1027; g) S. I. Stoeva, F. Huo, J.-S. Lee, C. A. Mirkin, *J. Am. Chem. Soc.*, **2005**, *127*, 15362.

[21] a) S. Link, Z. L. Wang, M. A. El-Sayed, *J. Phys. Chem. B* **1999**, *103*, 3529; b) T. Hyeon, *Chem. Commun.* **2003**, 927; c) F. Raimondi, G. G. Scherer, R. Kötz, A. Wokaun, *Angew. Chem.* **2005**, *117*, 2228; *Angew. Chem. Int. Ed.* **2005**, *44*, 2190; d) J.-M. Léger, *Electrochim. Acta* **2005**, *50*, 3123; e) Y. Liang, L. Zhai, X. Zhao, D. Xu, *J. Phys. Chem. B* **2005**, *109*, 7120.

[22] Y. Xia, P. Yang, Y. Sun, Y. Wu, B. Mayers, B. Gates, Y. Yin, F. Kim, H. Yan, *Adv. Mater.* **2003**, *15*, 353.

[23] J. Hu, M. Ouyang, P. Yang, C. M. Lieber, *Nature* **1999**, *399*, 48.

[24] Y. Wu, R. Fan, P. Yang, *Nano Lett.* **2002**, *2*, 83.

[25] a) M. S. Gudiksen, L. J. Lauhon, J. Wang, D. C. Smith, C. M. Lieber, *Nature* **2002**, *415*, 617; b) M. T. Björk, B. J. Ohlsson, T. Sass, A. I. Persson, C. Thelander, M. H. Magnusson, K. Deppert, L. R. Wallenberg, L. Samuelson, *Nano Lett.* **2002**, *2*, 87.

[26] J. Jie, G. Wang, X. Han, J. G. Hou, *J. Phys. Chem. B* **2004**, *108*, 17027.

[27] See, for example: M. A. Herman, H. Sitter, *Molecular Beam Epitaxy*, Springer, New York, **1989**.

[28] a) J. C. Hulteen, C. R. Martin, *J. Mater. Chem.* **1997**, *7*, 1075; b) T. L. Wade, J.-E. Wegrowe, *Eur. Phys. J. Appl. Phys.* **2005**, *8*, 3, and references therein.

[29] W. Lee, R. Schlotz, K. Nielsch, U. Gösele, *Angew. Chem.* **2005**, *117*, 6204; *Angew. Chem. Int. Ed.* **2005**, *44*, 6050.

[30] a) C.-G. Wu, T. Bein, *Science* **1994**, *264*, 1757; b) J. S. Beck, J. C. Vartuli, W. J. Roth, M. E. Leonowicz, C. T. Kresge, K. D. Schmitt, C. T. W. Chu, D. H. Olson, E. W. Sheppard, S. B. McCullen, J. B. Higgins, J. L. Schlenker, *J. Am. Chem. Soc.* **1992**, *114*, 10834.

[31] R. J. Tonucci, B. L. Justus, A. J. Campillo, C. E. Ford, *Science* **1992**, *258*, 783.

[32] G. A. Ozin, *Adv. Mater.* **1992**, *4*, 612.

[33] a) G. R. Possin, *Rev. Sci. Instrum.* **1970**, *41*, 772; b) L. Sun, P. C. Searson, C. L. Chein, *Appl. Phys. Lett.* **1999**, *74*, 2803.

[34] a) T. Thurn-Albrecht, J. Schotter, G. A. Kästle, N. Emley, T. Shibauchi, L. Krustin-Elbaum, K. Guarini, C. T. Black, M. T. Tuominen, T. P. Russell, *Science* **2000**, *290*, 2126; b) T. Thurn-Albrecht, R. Steiner, J. DeRouchey, C. M. Stafford, E. Huang, M. Bal, M. Tuominen, C. J. Hawker, T. P. Russell, *Adv. Mater.* **2000**, *12*, 787.

[35] H. Masuda, K. Fukuda, *Science* **1995**, *268*, 1466.

[36] C. K. Preston, M. J. Moskovits, *J. Phys. Chem.* **1993**, *97*, 8495.

[37] a) B. R. Martin, D. J. Dermody, B. D. Reiss, M. Fang, L. A. Lyon, M. J. Natan, T. E. Mallouk, *Adv. Mater.* **1999**, *11*, 1021; b) D. Peña, B. Razavi, P. A. Smith, J. K. N. Mbindyo, M. J. Natan, T. S. Mayer, T. E. Mallouk, C. D. Keating, *Mater. Res. Soc. Symp. Proc.* **2001**, *636*, D4.6.1; c) N. I. Kovtyukhova, T. E. Mallouk, *Chem. Eur. J.* **2002**, *8*, 4355.

[38] Y.-G. Guo, L.-J. Wan, J.-R. Gong, C.-L. Bai, *Phys. Chem. Chem. Phys.* **2002**, *4*, 3422.

[39] Y.-K. Su, D.-H. Qin, H.-L. Zhang, H. Li, H.-L. Li, *Chem. Phys. Lett.* **2004**, *388*, 406.

[40] D. S. Xue, H. G. Shi, M. S. Si, *J. Phys. Condens. Matter* **2004**, *16*, 8775.

[41] F. de Menten de Horne, L. Piraux, S. Michotte, *Appl. Phys. Lett.* **2005**, *86*, 152510.

[42] J.-G. Wang, M.-L. Tian, N. Kumar, T. E. Mallouk, *Nano Lett.* **2005**, *5*, 1247.

[43] C. M. Hangarter, N. V. Myung, *Chem. Mater.* **2005**, *17*, 1320.

[44] S. R. Nicewarner-Peña, R. G. Freeman, B. D. Reiss, L. He, D. J. Peña, I. D. Walton, R. Cromer, C. D. Keating, M. J. Natan, *Science* **2001**, *294*, 137.

[45] J. Yahalom, O. Zadok, *J. Mater. Sci.* **1987**, *22*, 1573.

[46] a) R. M. Penner, C. R. Martin, *J. Electrochem. Soc.* **1986**, *133*, 2206; b) L. S. Van Dyke, C. R. Martin, *Langmuir* **1990**, *6*, 1118.

[47] R. P. Burford, T. Tongtam, *J. Mater. Sci.* **1991**, *26*, 3264.

[48] S. Park, J.-H. Lim, S.-W. Chung, C. A. Mirkin, *Science* **2004**, *303*, 348.

[49] S. Park, S.-W. Chung, C. A. Mirkin, *J. Am. Chem. Soc.* **2004**, *126*, 11772.

[50] A. M. Kressin, V. V. Doan, J. D. Klein, M. J. Sailor, *Chem. Mater.* **1991**, *3*, 1015.

[51] J. D. Klein, R. D. Herrick II, D. Palmer, M. J. Sailor, C. J. Brumlik, C. R. Martin, *Chem. Mater.* **1993**, *5*, 902.

 © 2006 Wiley-VCH Verlag GmbH & Co. KGaA, Weinheim

[52] D. Routkevitch, T. Bigioni, M. Moskovits, J. M. Xu, *J. Phys. Chem.* **1996**, *100*, 14037.
[53] S. K. Chakarvarti, J. Vetter, *J. Micromech. Microeng.* **1993**, *3*, 57.
[54] N. I. Kovtyukhova, B. K. Kelley, T. E. Mallouk, *J. Am. Chem. Soc.* **2004**, *126*, 12738.
[55] M. J. Zheng, L. D. Zhang, G. H. Li, W. Z. Shen, *Chem. Phys. Lett.* **2002**, *363*, 123.
[56] Q. Wang, G. Wang, B. Xu, J. Jie, X. Han, G. Li, Q. Li, J. G. Hou, *Mater. Lett.* **2005**, *59*, 1378.
[57] C. Liu, J. A. Zapien, Y. Yao, X. Meng, C. S. Lee, S. Fan, Y. Lifshitz, S. T. Lee, *Adv. Mater.* **2003**, *15*, 838, and references therein.
[58] V. P. Menon, C. R. Martin, *Anal. Chem.* **1995**, *67*, 1920.
[59] a) Z. Liang, A. S. Susha, A. Yu, F. Caruso, *Adv. Mater.* **2003**, *15*, 1849; b) S. Hou, C. C. Harrell, L. Trofin, P. Kohli, C. R. Martin, *J. Am. Chem. Soc.* **2004**, *126*, 5674.
[60] B. B. Lakshmi, P. K. Dorhout, C. R. Martin, *Chem. Mater.* **1997**, *9*, 857.
[61] N. I. Kovtyukhova, T. E. Mallouk, T. S. Mayer, *Adv. Mater.* **2003**, *15*, 780.
[62] Y. Mao, S. S. Wong, *J. Am. Chem. Soc.* **2004**, *126*, 15245.
[63] S. Hou, J. Wang, C. R. Martin, *J. Am. Chem. Soc.* **2005**, *127*, 8586.
[64] S. Hou, J. Wang, C. R. Martin, *Nano Lett.* **2005**, *5*, 231.
[65] G. P. Heydon, S. R. Hoon, A. N. Farley, S. L. Tomlinson, M. S. Valera, K. Attenborough, W. Schwarzacher, *J. Phys. D* **1997**, *30*, 1083.
[66] A. Fert, L. Piraux, *J. Magn. Magn. Mater.* **1999**, *200*, 338.
[67] a) W. Schwarzacher, K. Attenborough, A. Michel, G. Nabiyouni, J. P. Meier, *J. Magn. Magn. Mater.* **1997**, *165*, 23; b) S. Valizadeh, L. Hultman, J.-M. George, P. Leisner, *Adv. Funct. Mater.* **2002**, *12*, 766; c) Y.-G. Guo, L.-J. Wan, C.-F. Zhu, D.-L. Yang, D.-M. Chen, C.-L. Bai, *Chem. Mater.* **2003**, *15*, 664; d) M. Chen, P. C. Searson, C. L. Chien, *J. Appl. Phys.* **2003**, *93*, 8253; e) M. Chen, L. Sun, J. E. Bonevich, D. H. Reich, C. L. Chien, P. C. Searson, *Appl. Phys. Lett.* **2003**, *82*, 3310; f) A. Robinson, W. Schwarzacher, *J. Appl. Phys.* **2003**, *93*, 7250; g) H.-P. Liang, Y.-G. Guo, J.-S. Hu, C.-F. Zhu, L.-J. Wan, C.-L. Bai, *Inorg. Chem.* **2005**, *44*, 3013.
[68] M. N. Baibich, J. M. Broto, A. Fert, F. Nguyen Van Dau, F. Petroff, P. Eitenne, G. Creuzet, A. Friederich, J. Chazelas, *Phys. Rev. Lett.* **1988**, *61*, 2472.
[69] G. Binasch, P. Grünberg, F. Saurenbach, W. Zinn, *Phys. Rev. B* **1989**, *39*, 4828.
[70] S. S. P. Parkin, N. More, K. P. Roche, *Phys. Rev. Lett.* **1990**, *64*, 2304.
[71] M. Alper, K. Attenborough, R. Hart, S. J. Lane, D. S. Lashmore, C. Younes, W. Schwarzacher, *Appl. Phys. Lett.* **1993**, *63*, 2144.
[72] L. Piraux, J. M. George, J. F. Despres, C. Leroy, E. Ferain, R. Legras, K. Ounadjela, A. Fert, *Appl. Phys. Lett.* **1994**, *65*, 2484.
[73] A. Blondel, J. P. Meier, B. Doudin, J.-P. Ansermet, *Appl. Phys. Lett.* **1994**, *65*, 3019.
[74] K. Liu, K. Nagodawithana, P. C. Searson, C. L. Chien, *Phys. Rev. B* **1995**, *51*, 7381.
[75] S. Dubois, C. Marchal, J. M. Beuken, L. Piraux, J. L. Duvail, A. Fert, J. M. George, J. L. Maurice, *Appl. Phys. Lett.* **1997**, *70*, 396.
[76] S. Dubois, E. Chassaing, J. L. Duvail, L. Piraux, M. G. Waals, *J. Chim. Phys. PCB* **1999**, *96*, 1316.
[77] P. R. Evans, G. Yi, W. Schwarzacher, *Appl. Phys. Lett.* **2000**, *76*, 481.
[78] E. Y. Tsymbal, D. G. Pettifor in *Solid State Physics, Vol. 56* (Eds.: H. Ehrenreich, F. Spaepen), Academic Press, **2001**, pp. 113.
[79] T. M. Whitney, J. S. Jiang, P. C. Searson, C. L. Chein, *Science* **1993**, *261*, 1316.
[80] T. Ohgai, X. Hoffer, L. Gravier, J.-E. Wegrowe, J.-P. Ansermet, *Nanotechnology* **2003**, *14*, 978.
[81] T. Valet, A. Fert, *Phys. Rev. B* **1993**, *48*, 7099.
[82] W. P. Pratt, Jr., S.-F. Lee, J. M. Slaughter, R. Loloee, P. A. Schroeder, J. Bass, *Phys. Rev. Lett.* **1991**, *66*, 3060.
[83] M. A. M. Gijs, S. K. J. Lenczowski, J. B. Giesbers, *Phys. Rev. Lett.* **1993**, *70*, 3343.
[84] T. Ono, T. Shinjo, *J. Phys. Soc. Jpn.* **1995**, *64*, 363.
[85] M. A. M. Gijs, M. T. Johnson, A. Reinders, P. E. Huisman, R. J. M. van de Veerdonk, S. K. J. Lenczowski, R. M. J. van Gansewinkel, *Appl. Phys. Lett.* **1995**, *66*, 1839.
[86] J. Bass, W. P. Pratt, Jr., *J. Magn. Magn. Mater.* **1999**, *200*, 274.
[87] L. Piraux, S. Dubois, A. Fert, L. Belliard, *Eur. Phys. J. B* **1998**, *4*, 413.
[88] L. Piraux, S. Dubois, A. Fert, *J. Magn. Magn. Mater.* **1996**, *159*, L287.
[89] G. M. Whitesides, B. Grzybowski, *Science* **2002**, *295*, 2418.
[90] a) C. A. Mirkin, R. L. Letsinger, R. C. Mucic, J. J. Storhoff, *Nature* **1996**, *382*, 607; b) A. P. Alivisatos, K. P. Johnsson, X. Peng, T. E. Wilson, C. J. Loweth, M. P. Bruchez, Jr., P. G. Schultz, *Nature* **1996**, *382*, 609.
[91] a) E. Dujardin, C. Peet, G. Stubbs, J. N. Culver, S. Mann, *Nano Lett.* **2003**, *3*, 413; b) C. Mao, D. J. Solis, B. D. Reiss, S. T. Kottmann, R. Y. Sweeney, A. Hayhurst, G. Georgiou, B. Iverson, A. M. Belcher, *Science* **2004**, *303*, 213; c) Z. Li, S.-W. Chung, J.-M. Nam, D. S. Ginger, C. A. Mirkin, *Angew. Chem.* **2003**, *115*, 2408; *Angew. Chem. Int. Ed.* **2003**, *42*, 2306; d) V. Berry, S. Rangaswamy, R. F. Saraf, *Nano Lett.* **2004**, *4*, 939; e) N. L. Rosi, C. S. Thaxton, C. A. Mirkin, *Angew. Chem.* **2004**, *116*, 5616; *Angew. Chem. Int. Ed.* **2004**, *43*, 5500.
[92] B. R. Martin, S. K. St. Angelo, T. E. Mallouk, *Adv. Funct. Mater.* **2002**, *12*, 759.
[93] J. C. Love, A. R. Urbach, M. G. Prentiss, G. M. Whitesides, *J. Am. Chem. Soc.* **2003**, *125*, 12696.
[94] M. Tanase, D. M. Silevitch, A. Hultgren, L. A. Bauer, P. C. Searson, G. J. Meter, D. H. Reich, *J. Appl. Phys.* **2002**, *91*, 8549.
[95] A. K. Bentley, J. S. Trethewey, A. B. Ellis, W. C. Crone, *Nano Lett.* **2004**, *4*, 487.
[96] a) C. C. Berry, A. S. G. Curtis, *J. Phys. D* **2003**, *36*, R198; b) C. C. Berry, *J. Mater. Chem.* **2005**, *15*, 543.
[97] A. K. Gupta, M. Gupta, *Biomaterials* **2005**, *26*, 3995.
[98] A. R. Urbach, J. C. Love, M. G. Prentiss, G. M. Whitesides, *J. Am. Chem. Soc.* **2003**, *125*, 12704.
[99] J. C. Love, L. A. Estroff, J. K. Kriebel, R. G. Nuzzo, G. M. Whitesides, *Chem. Rev.* **2005**, *105*, 1103.
[100] K.-B. Lee, S. Park, C. A. Mirkin, *Angew. Chem.* **2004**, *116*, 3110; *Angew. Chem. Int. Ed.* **2004**, *43*, 3048.
[101] B.-K. Oh, S. Park, S. W. Lee, K.-B. Lee, C. A. Mirkin, *J. Am. Chem. Soc.* **2006**, in press.
[102] L. A. Bauer, D. H. Reich, G. J. Meyer, *Langmuir* **2003**, *19*, 7043.
[103] N. S. Birenbaum, B. T. Lai, C. S. Chen, D. H. Reich, G. J. Meyer, *Langmuir* **2003**, *19*, 9580.
[104] a) A. K. Salem, M. Chen, J. Hayden, K. W. Leong, P. C. Searson, *Nano Lett.* **2004**, *4*, 1163; b) M. Chen, L. Guo, R. Ravi, P. C. Searson, *J. Phys. Chem. B* **2006**, *110*, 211; c) M. Chen, P. C. Searson, *Adv. Mater.* **2005**, *17*, 2765.
[105] A. K. Salem, J. Chao, K. W. Leong, P. C. Searson, *Adv. Mater.* **2004**, *16*, 268.
[106] a) X. Duan, Y. Huang, Y. Cui, J. Wang, C. M. Lieber, *Nature* **2001**, *409*, 66; b) Y. Huang, X. Duan, Q. Wei, C. M. Lieber, *Science* **2001**, *291*, 630; c) D. H. Cobden, *Nature* **2001**, *409*, 32; d) G. Y. Tseng, J. C. Ellenbogen, *Science* **2001**, *294*, 1293; e) R. F. Service, *Science* **2001**, *293*, 782.
[107] P. A. Smith, C. D. Nordquist, T. N. Jackson, T. S. Mayer, B. R. Martin, J. Mbindyo, T. E. Mallouk, *Appl. Phys. Lett.* **2000**, *77*, 1399.

 © 2006 Wiley-VCH Verlag GmbH & Co. KGaA, Weinheim

[108] Y. Wu, J. Xiang, C. Yang, W. Lu, C. M. Lieber, *Nature* **2004**, *430*, 61.
[109] D. Jiles, *Introduction to the Electronic Properties of Materials*, Chapman and Hall, London, **1994**.
[110] J. Wang, M. Tian, T. E. Mallouk, M. H. W. Chan, *Nano Lett.* **2004**, *4*, 1313.
[111] H.-J. Chung, H. H. Jung, Y.-S. Cho, S. Lee, J.-H. Ha, J. H. Choi, Y. Kuk, *Appl. Phys. Lett.* **2005**, *86*, 213113.
[112] U. S. Ramelow, J. H. Ma, R. Darbeau, *Mater. Res. Innovations* **2001**, *5*, 40.
[113] N. I. Kovtyukhova, T. E. Mallouk, *Adv. Mater.* **2005**, *17*, 187.
[114] D. J. Peña, J. K. N. Mbindyo, A. J. Carado, T. E. Mallouk, C. D. Keating, B. Razavi, T. S. Mayer, *J. Phys. Chem. B* **2002**, *106*, 7458.
[115] J. Hu, Y. Bando, J. Zhan, D. Golberg, *Adv. Mater.* **2005**, *17*, 1964.
[116] a) M. A. Reed, C. Zhou, C. J. Muller, T. P. Burgin, J. M. Tour, *Science* **1997**, *278*, 252; b) H. Park, A. K. L. Lim, A. P. Alivisatos, *Appl. Phys. Lett.* **1999**, *75*, 301; c) C. Z. Li, H. X. He, N. J. Tao, *Appl. Phys. Lett.* **2000**, *77*, 3995; d) J. Reichert, R. Ochs, D. Beckmann, H. B. Weber, M. Mayor, H. v. Löhneysen, *Phys. Rev. Lett.* **2002**, *88*, 176804; e) J. Xiang, B. Liu, S.-T. Wu, B. Ren, F.-Z. Yang, B.-W. Mao, Y. L. Chow, Z.-Q. Tian, *Angew. Chem.* **2005**, *117*, 3127; *Angew. Chem. Int. Ed.* **2005**, *44*, 1265.
[117] L. Qin, S. Park, L. Huang, C. A. Mirkin, *Science* **2005**, *309*, 113.
[118] a) R. D. Piner, J. Zhu, F. Xu, S. Hong, C. A. Mirkin, *Science* **1999**, *283*, 661; b) D. S. Ginger, H. Zhang, C. A. Mirkin, *Angew. Chem.* **2004**, *116*, 30; *Angew. Chem. Int. Ed.* **2004**, *43*, 30; c) K. Salaita, S. W. Lee, X. Wang, L. Huang, T. M. Dellinger, C. Liu, C. A. Mirkin, *Small* **2005**, *1*, 940.
[119] S. Liu, J. B.-H. Tok, Z. Bao, *Nano Lett.* **2005**, *5*, 1071.
[120] J. A. Sioss, C. D. Keating, *Nano Lett.* **2005**, *5*, 1779.
[121] J. K. N. Mbindyo, T. E. Mallouk, J. B. Mattzela, I. Kratochvilova, B. Razavi, T. N. Jackson, T. S. Mayer, *J. Am. Chem. Soc.* **2002**, *124*, 4020.
[122] a) M. D. Porter, T. B. Bright, D. L. Allara, C. E. D. Chidsey, *J. Am. Chem. Soc.* **1987**, *109*, 3559; b) V. A. Sundar, B. Liedberg, D. L. Allara, *Langmuir* **1995**, *11*, 3882.
[123] L. T. Cai, H. Skulason, J. G. Kushmerick, S. K. Pollack, J. Naciri, R. Shashidhar, D. L. Allara, T. E. Mallouk, T. S. Mayer, *J. Phys. Chem. B* **2004**, *108*, 2827.
[124] I. Kratochvilova, M. Kocirik, A. Zambova, J. Mbindyo, T. E. Mallouk, T. S. Mayer, *J. Mater. Chem.* **2002**, *12*, 2927.
[125] S. J. Son, J. Reichel, B. He, M. Schuchman, S. B. Lee, *J. Am. Chem. Soc.* **2005**, *127*, 7316.
[126] a) D. H. Reich, M. Tanase, A. Hultgren, L. A. Bauer, C. S. Chen, G. J. Meyer, *J. Appl. Phys.* **2003**, *93*, 7275; b) L. A. Bauer, N. S. Birenbaum, G. J. Meyer, *J. Mater. Chem.* **2004**, *14*, 517.
[127] S. R. Nicewarner-Peña, A. J. Carado, K. E. Shale, C. D. Keating, *J. Phys. Chem. B* **2003**, *107*, 7360.
[128] B. D. Reiss, R. G. Freeman, I. D. Walton, S. M. Norton, P. C. Smith, W. G. Stonas, C. D. Keating, M. J. Natan, *J. Electroanal. Chem.* **2002**, *522*, 95.
[129] I. D. Walton, S. M. Norton, A. Balasingham, L. He, D. F. Oviso, Jr., D. Gupta, P. A. Raju, M. J. Natan, G. R. Freeman, *Anal. Chem.* **2002**, *74*, 2240.
[130] R. M. Hernández, L. Richter, S. Semancik, S. Stranick, T. E. Mallouk, *Chem. Mater.* **2004**, *16*, 3431.
[131] a) R. H. Clemmit, H. A. Chase, *Biotechnol. Bioeng.* **2000**, 67, 206; b) H. Stiborova, J. Kostal, A. Mulchandani, W. Chen, *Biotechnol. Bioeng.* **2003**, 82, 605; c) A. M. Noubhani, W. Dieryck, N. Bakalara, L. Latxague, X. Santarelli, *J. Chromatogr. B* **2003**, *790*, 153.
[132] A. K. Salem, P. C. Searson, K. W. Leong, *Nat. Mater.* **2003**, *2*, 668.
[133] A. K. Salem, C. F. Hung, T. W. Kim, T. C. Wu, P. C. Searson, K. W. Leong, *Nanotechnology* **2005**, *16*, 484.
[134] a) P. J. Carter, R. J. Samulski, *Int. J. Mol. Med.* **2000**, *6*, 17; b) C. W. Pouton, L. W. Seymour, *Adv. Drug Delivery Rev.* **2001**, *46*, 187.
[135] H. Zhang, Y. Guo, L. Wan, C.-L. Bai, *Chem. Commun.* **2003**, *24*, 3022.
[136] a) F. Liu, J. Y. Lee, W. Zhou, *J. Phys. Chem. B* **2004**, *108*, 17959; b) F. Liu, J. Y. Lee, W. Zhou, *Adv. Funct. Mater.* **2005**, *15*, 1459.
[137] W. F. Paxton, K. C. Kistler, C. C. Olmeda, A. Sen, S. K. St. Angelo, Y. Cao, T. E. Mallouk, P. E. Lammert, V. H. Crespi, *J. Am. Chem. Soc.* **2004**, *126*, 13424.
[138] T. R. Kline, W. F. Paxton, T. E. Mallouk, A. Sen, *Angew. Chem.* **2005**, *117*, 754; *Angew. Chem. Int. Ed.* **2005**, *44*, 744.
[139] S. Fournier-Bidoz, A. C. Arsenault, I. Manners, G. A. Ozin, *Chem. Commun.* **2005**, 441.
[140] S. Schultz, D. R. Smith, J. J. Mock, D. A. Schultz, *Proc. Natl. Acad. Sci. USA* **2000**, *97*, 996.
[141] J. J. Mock, S. J. Oldenburg, D. R. Smith, D. A. Schultz, S. Schultz, *Nano Lett.* **2002**, *2*, 465.
[142] S. A. Maier, P. G. Kik, H. A. Atwater, S. Meltzer, E. Harel, B. E. Koel, A. A. G. Requicha, *Nat. Mater.* **2003**, *2*, 229.
[143] For one example of commercially-available multicomponent nanorods, see: Nanoplex Technologies, Inc. at www.nanoplex-tech.com, **2006**.
[144] Additional references concerning multisegmented nanorods that have appeared since the submission of this manuscript include: a) F. Liu, J. Y. Lee, W. J. Zhou, *Small* **2006**, *2*, 121; b) P. Dhar, T. M. Flacher, Y. Wang, T. E. Mallouk, W. F. Paxton, A. Sen, *Nano Lett.* **2006**, *6*, 66; c) M. Chen, C.-L. Chien, P. C. Searson, *Chem. Mater.* **2006**, DOI: 10.1021/cm052262b.

 © 2006 Wiley-VCH Verlag GmbH & Co. KGaA, Weinheim

Communications

DOI: 10.1002/anie.200600139

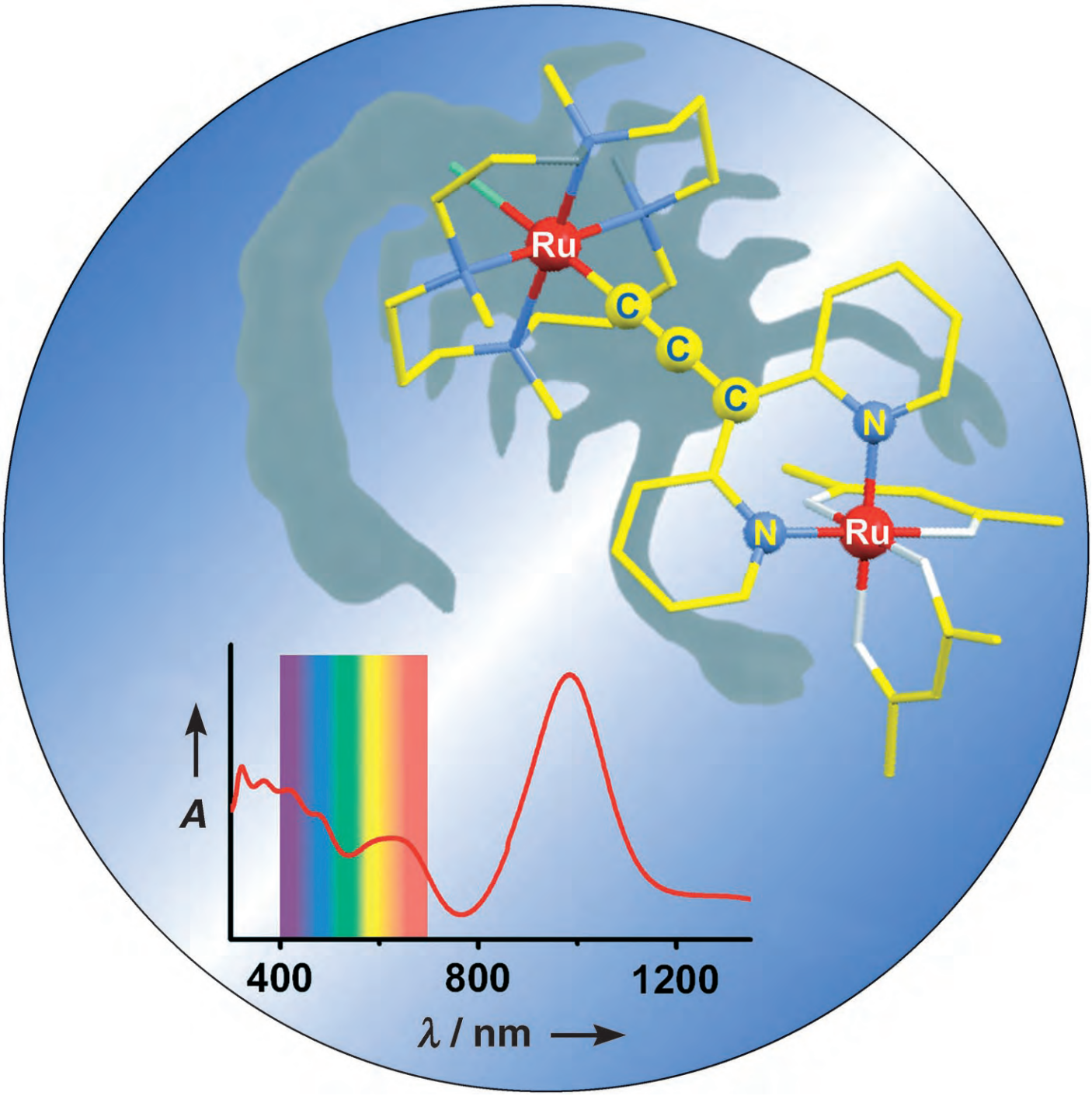

Upon complexation of $\{Ru(acac)_2\}$ to a ruthenium(II) "molecular clip", electron density is delocalized over the $\{Ru{=}C{=}C{=}C(2\text{-}py)_2Ru\}$ chain, and an intense near-infrared absorption appears. For more details, see the Communication by C.-M. Che et al. on the following pages.

WILEY InterScience DISCOVER SOMETHING GREAT
© 2006 Wiley-VCH Verlag GmbH & Co. KGaA, Weinheim

Molecular Electronics

DOI: 10.1002/anie.200600139

A Bis(pyridyl)allenylidene Complex of Ruthenium: A "Molecular Clip" That Displays Intense Near-Infrared Absorption upon Coordination to a Ruthenium(II) Center**

Chun-Yuen Wong, Glenna So Ming Tong, Chi-Ming Che, and Nianyong Zhu*

Organometallic complexes with π-conjugated carbon-chain bridges have attracted considerable interest for their potential applications in molecular-scale electronic devices.[1] In this context, the pursuit of allenylidene–metal complexes [M=C=C=CR^{1}R^2] is prevalent because the presence of π interactions between the metal ion and the rigid, linear allenylidene bridge allows delocalization of electron density and thus electronic communication between remote functional groups.[2] Multinuclear systems with allenylidene bridges have generally been obtained by the coupling of organometallic allenylidenes to allenylidene–, carbyne–, or acetylide–metal complexes[2,3] in which the presence of a M–C bond in the bridge termini seems to be a prerequisite for connecting two or more metal centers. Herein, we report a bis(pyridyl)allenylidene–ruthenium(II) complex, *trans*-[(16-TMC)ClRu=C=C=C(2-py)$_2$]$^+$ (**1**, 16-TMC = 1,5,9,13-tetramethyl-1,5,9,13-tetraazacyclohexadecane, py = pyridyl), that can be used as a "molecular clip" for metal-ion binding. The 16-TMC ligand has the virtue of being optically and electrochemically silent, thus facilitating spectroscopic investigation of the {Ru=C=C=CR^{1}R^2} unit. Complexation of **1** with [Ru(acac)$_2$] (acac = acetylacetonate), as shown below, leads to a metal-to-ligand charge-transfer (MLCT) excited state which is delocalized over *both* Ru^{II} ions and the allenylidene bridge (Ru=C=C=C(2-py)$_2$Ru). This delocalization results in an intense lowest-energy absorption in the near-infrared (NIR) region (λ_{max} = 989 nm).

trans-[(16-TMC)ClRu=C=C=C(2-py)$_2$]$^+$ (**1**) was synthesized by employing the strategy developed for *trans*-[(16-TMC)ClRu=C=C=CAr$_2$]$^+$.[4] *trans*-[Ru(16-TMC)Cl$_2$]Cl was first reduced to a Ru^{II} species with zinc amalgam in methanol, and the resultant pale green solution was filtered and heated at reflux with HC≡CC(OH)(2-py)$_2$ in the absence of zinc amalgam (Scheme 1). Complex **1**-PF$_6$ was isolated as a deep-red solid with an intense IR stretching band at 1885 cm^{-1} ($\nu_{C=C=C}$) and characteristic ^{13}C NMR signals at δ = 143.0, 143.6 (C_γ), 284.8, 287.3 (C_β), 313.4, and 319.2 ppm (C_α).[5] The UV/Vis absorption spectrum of **1** in CH$_3$CN features an intense absorption band at λ_{max} = 468 nm ($\varepsilon = 1.9 \times 10^4$ dm^3 mol^{-1} cm^{-1}, Figure 1). This absorption is assigned to a metal-perturbed π→π* allenylidene intraligand transition, and is slightly blue-shifted from the corresponding absorption for *trans*-[(16-TMC)ClRu=C=C=CPh$_2$]$^+$ (λ_{max} = 479 nm).[4] The cyclic voltammogram of **1** displays a reversible reduction couple at $E_{1/2}$ = −1.11 V and an irreversible oxidation wave at E_{pa} = 0.73 V (vs. Fc$^+$/Fc, Figure 2; Fc$^+$/Fc = ferrocenium/ferrocene),[6] both of which are slightly more positive than the corresponding potentials of *trans*-[(16-TMC)ClRu=C=C=CPh$_2$]$^+$ ($E_{1/2}$ = −1.27, E_{pa} = 0.64 V).[4]

The ligation of **1** with metal ions can be verified by UV/Vis spectroscopy and cyclic voltammetry. Addition of metal

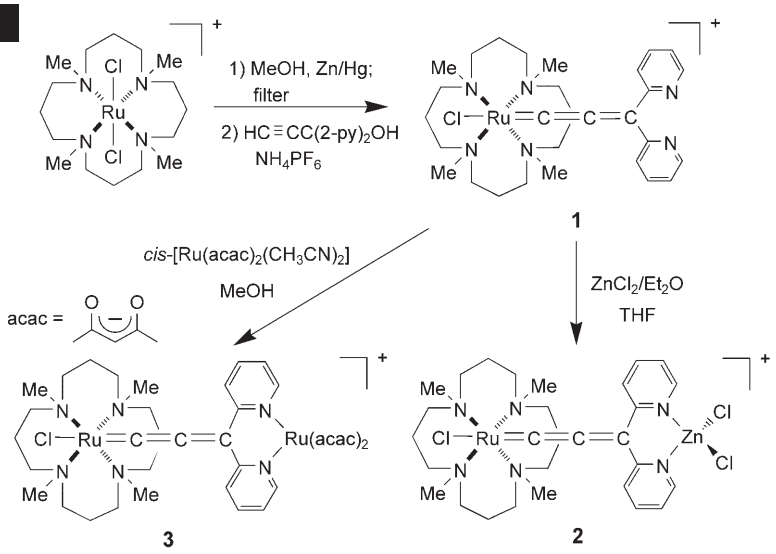

Scheme 1. Preparation of **1**–**3**.

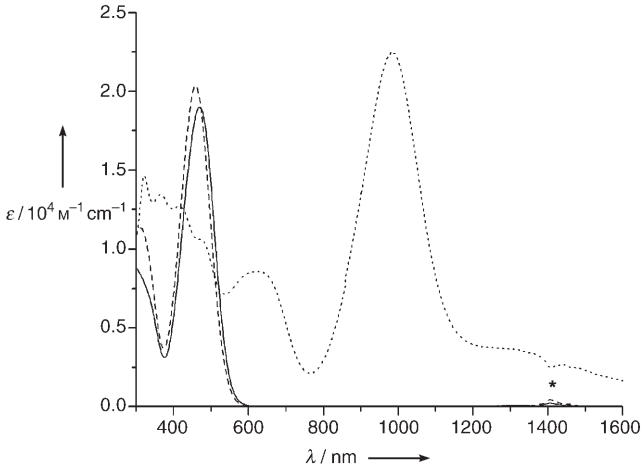

Figure 1. UV/Vis spectra of **1** (solid line), **2** (dashed line), and **3** (dotted line) in CH$_3$CN at 298 K (instrumental artefacts are marked by *).

[*] Dr. C.-Y. Wong, Dr. G. S. M. Tong, Prof. Dr. C.-M. Che, Dr. N. Zhu
Department of Chemistry and
HKU–CAS Joint Laboratory on New Materials
The University of Hong Kong
Pokfulam Road, Hong Kong (P.R. China)
Fax: (+852) 2857-1586
E-mail: cmche@hku.hk

[**] This work was supported by the Research Grants Council of the Hong Kong SAR, China (HKU 7077/01P) and the University of Hong Kong.

Supporting information for this article is available on the WWW under http://www.angewandte.org or from the author.

 © 2006 Wiley-VCH Verlag GmbH & Co. KGaA, Weinheim

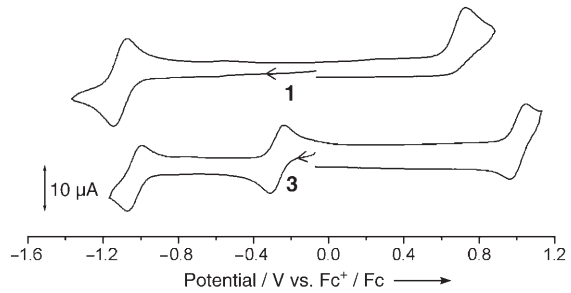

Figure 2. Cyclic voltammograms of **1** and **3** (0.1 M nBu_4NPF_6 in CH_3CN).

ions to a solution of **1** in CH_3CN (with 0.1 M nBu_4NPF_6) induces a shift in the λ_{max} value and redox potentials. For example, addition of 100 equivalents of $Zn(ClO_4)_2$ to a solution of **1** in CH_3CN was accompanied by an isosbestic spectral change with a shift in λ_{max} from 469 to 459 nm, and the redox potentials were shifted from −1.11 ($E_{1/2}$) and 0.73 V (E_{pa}) to −0.75 (E_{pc}) and 0.95 V (E_{pa}; see the Supporting Information).

The dinuclear complexes [(16-TMC)ClRu=C=C=C(2-py)$_2$ZnCl$_2$]$^+$ (**2**) and [(16-TMC)ClRu=C=C=C(2-py)$_2$Ru(acac)$_2$]$^+$ (**3**) were isolated from the reactions of **1** with $ZnCl_2$ and *cis*-[Ru(acac)$_2$(CH_3CN)$_2$], respectively. The crystal structures of complexes **2**-PF_6 and **3**-PF_6·CH_3CN were determined (Figure 3). In each case, the Ru(1) atom adopts a distorted octahedral environment, and the two pyridyl rings are non-coplanar (the interplanar angles between the rings are 139.26 and 140.54° for **2** and **3**, respectively).[7] The Zn atom in **2** is in a distorted tetrahedral geometry, and the Λ and Δ forms cocrystallize as a racemic mixture in **3**. Although the Ru-C_α-C_β and C_α-C_β-C_γ angles for both complexes approach linearity (171.7(6)–175.8(6)°), the six-membered rings formed by the chelating pyridyl groups and the Zn or Ru atoms are in boat conformation and are oriented away from the {Ru=C=C=C} moieties (Ru-C_α-Zn/Ru angles: 144.42/159.44°). The Ru-C_α (**2**: 1.835(6) Å, **3**: 1.894(6) Å), C_α-C_β (**2**: 1.258(8) Å, **3**: 1.243(7) Å), and C_β-C_γ (**2**: 1.356(8) Å, **3**: 1.380(7) Å) bond lengths are comparable to those reported for related allenylidene–ruthenium complexes.[2,4]

The cyclic voltammogram of **2** displays a reversible couple at $E_{1/2} = -0.73$ V and an irreversible wave at $E_{pa} = 0.96$ V, which are assigned as the reduction and oxidation, respectively, that originate from the {(16-TMC)ClRu=C=C=C(py-2)$_2$}$^+$ unit. The cyclic voltammogram of **3** displays three reversible/quasi-reversible couples at $E_{1/2} = -1.03$, −0.27, and 1.01 V (vs. Fc^+/Fc, Figure 2). The redox waves at $E_{1/2} = -1.03$ and 1.01 V are assigned to the reduction and oxidation couples, respectively, that originate from the {(16-TMC)ClRu=C=C=C(2-py)$_2$}$^+$ unit, and the couple at $E_{1/2} = -0.27$ V is assigned to the Ru^{III}/Ru^{II} couple of the {Ru(acac)$_2$} moiety. It is noted that the {Ru(acac)$_2$} moiety is oxidized at a similar potential as in *cis*-[Ru(acac)$_2$(CH_3CN)$_2$] ($E_{1/2} = -0.28$ V)[8] and *cis*-[Ru(acac)$_2$(pyrazine)$_2$] ($E_{1/2} = -0.29$ V vs. Fc^+/Fc),[9] although one may expect that the positive charge of the metalloligand would have an effect on the $E_{1/2}(Ru^{III}/Ru^{II})$ value of the {Ru(acac)$_2$} moiety. The $E_{1/2}$ value attributed to the {Ru(acac)$_2$} oxidation lies between those of the reduction and oxidation couples from {(16-TMC)ClRu=C=C=C-(2-py)$_2$}$^+$, thus suggesting that the highest filled {Ru(acac)$_2$} electronic level lies between the π and π* levels of {(16-TMC)ClRu=C=C=C(2-py)$_2$}$^+$.

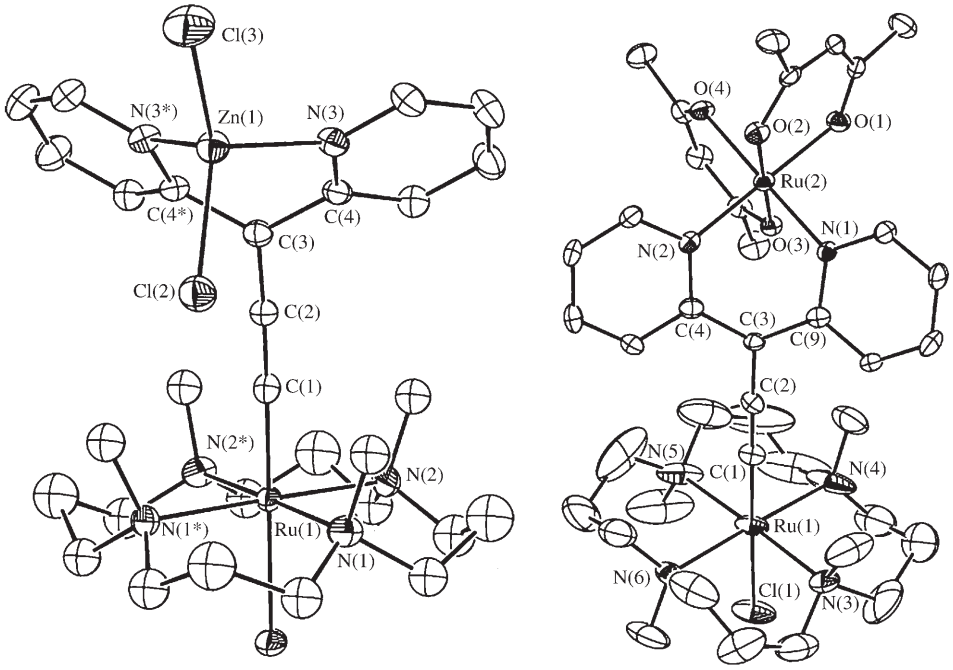

Figure 3. Perspective views of the cations in **2**-PF_6 (left) and **3**-PF_6·CH_3CN (right); thermal ellipsoids are set at 30% probability. Selected bond lengths [Å] and angles [°]: **2**-PF_6: Ru-C(1) 1.835(6), C(1)-C(2) 1.258(8), C(2)-C(3) 1.356(8), Ru-Cl(1) 2.425(2), mean Ru-N 2.254, Zn-N 2.053(3), mean Zn-Cl 2.208; N(3)-Zn(1)-N(3*) 91.2(2), Cl(2)-Zn(1)-Cl(3) 121.6(1), Ru(1)-C(1)-C(2) 175.6(5), C(1)-C(2)-C(3) 171.7(6). **3**-PF_6·CH_3CN: Ru(1)-C(1) 1.894(6), C(1)-C(2) 1.243(7), C(2)-C(3) 1.380(7), Ru(1)-Cl(1) 2.496(2), mean Ru(1)-N 2.261, mean Ru(2)-N 1.986, mean Ru(2)-O 2.037; N(1)-Ru(2)-N(2) 87.7(2), Ru(1)-C(1)-C(2) 174.0(5), C(1)-C(2)-C(3) 175.8(6).

The UV/Vis spectrum of **2** shows a resemblance to that of **1** (see Figure 1). The intense absorption at $\lambda_{max} = 457$ nm ($\varepsilon = 2.0 \times 10^4$ dm^{3}mol^{-1}cm^{-1}) is assigned as a metal-perturbed π→π* allenylidene intraligand transition. For **3**, the UV/Vis spectrum features an intense low-energy absorption band at $\lambda_{max} = 989$ nm ($\varepsilon = 2.3 \times 10^4$ dm^{3}mol^{-1}cm^{-1}), which is significantly red-shifted from the lowest-energy absorption band of **1** by about 11300 cm^{-1}. In addition, there is a shoulder peak at $\lambda > 1200$ nm. The one-electron-oxidized, mixed-valent complex [(16-TMC)ClRu=C=C=C(2-py)$_2$Ru(acac)$_2$]$^{2+}$ could be generated by electrochemical oxidation of **3** at −0.10 V versus Fc^+/Fc, whereby isosbestic UV/Vis spectral changes were

 © 2006 Wiley-VCH Verlag GmbH & Co. KGaA, Weinheim

observed with a diminishment in the intensity of the band at 989 nm (Figure 4).

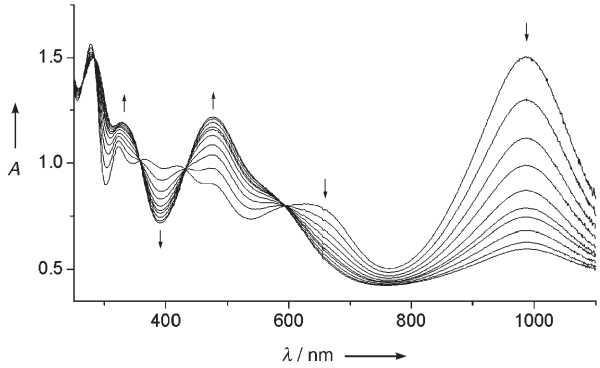

Figure 4. Thin-layer UV/Vis spectra (1-minute traces) of **3** in CH_3CN at 298 K during electrochemical oxidation at −0.10 V versus Fc^+/Fc.

Density functional theory (DFT) and time-dependent DFT (TDDFT) calculations were performed on the model complex $[(NH_3)_4ClRu{=}C{=}C{=}C(py\text{-}2)_2Ru(acac)_2]^+$ (**3M**, Figure 5a). The fully optimized structure of **3M** is in good agreement with the X-ray structure of **3**, and the calculated transition energies correspond well to the spectroscopic data of **3** (see the Supporting Information for the optimized coordinates and the transition energies of **3M**). We can thus use the calculations to gain further insight into the electronic structure of **3**.

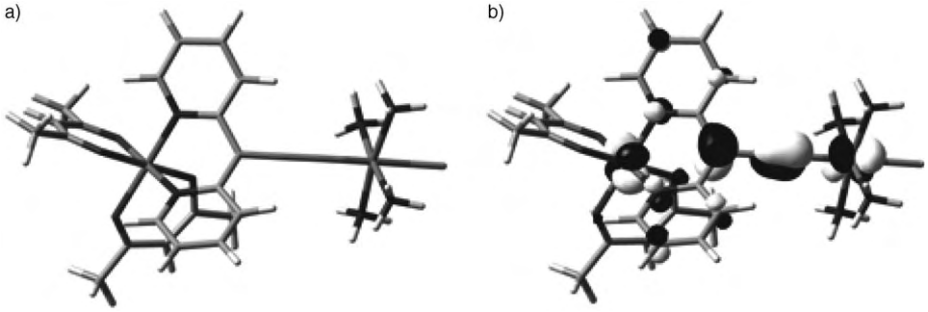

Figure 5. a) Fully optimized structure and b) LUMO surface contour plots (isovalue = 0.05 a.u.) of the model complex $[(NH_3)_4ClRu{=}C{=}C{=}C(2\text{-}py)_2Ru(acac)_2]^+$ (**3M**).

The highest occupied molecular orbitals HOMO, HOMO−1, and HOMO−3 of **3M** are mainly localized on the Ru_{acac} atom while the HOMO−2 and HOMO−5 are essentially of $\pi(Ru{=}C{=}C{=}C(2\text{-}py)_2)$ character (see the Supporting Information for the nature of the frontier MOs). Thus, in the ground state, there is no electronic communication between the two Ru ions. However, the lowest unoccupied molecular orbital (LUMO) of **3M** is composed of both $\pi^*(Ru{=}C{=}C{=}C(2\text{-}py)_2)$ and $d_\pi(Ru_{acac})$ contributions such that the electron density is delocalized over both Ru ions and the allenylidene bridge (Figure 5b). Hence, in the excited state, there is electronic communication between the $\{Ru(acac)_2\}$ moiety and the metalloligand. This MO description is in accordance with the redox measurements of **3** which indicate that the highest filled electronic level of the $\{Ru(acac)_2\}$ moiety lies between the π and π* levels of the $\{(16\text{-}TMC)ClRu{=}C{=}C{=}C(2\text{-}py)_2\}^+$ unit, as discussed above.

TDDFT calculations showed that the intense lowest-energy absorption of **3M** is in the NIR region ($\lambda = 801$ nm, overestimation of the intense band of **3** at 989 nm by ca. 2400 cm^{-1}; oscillator strength $f = 0.2461$). The major contributing excitation is the HOMO−3→LUMO (42%) transition, with a smaller contribution from the HOMO−1→LUMO (10%) transition. A weaker band was also calculated at $\lambda = 1317$ nm ($f = 0.0078$), which is also derived from the same transitions as the intense excitation calculated at $\lambda =$ 801 nm, with the HOMO−1→LUMO transition (54%) giving the larger contribution (HOMO−3→LUMO: 28%). This weaker band may correspond to the shoulder peak of **3** at $\lambda > 1200$ nm. The smaller oscillator strength of this transition ($\lambda = 1317$ nm) is a result of poorer overlap between the HOMO−1 and LUMO. From the MO descriptions above, the absorptions calculated at $\lambda = 801$ and 1317 nm are assigned as Ru_{acac}-to-π*(Ru=C=C=C(2-py)$_2$Ru) charge-transfer transitions. The large red shift in absorption energy from $\lambda_{max} =$ 457 nm in **1** to 989 nm in **3** is thus a result of 1) the localization of the HOMO−1 on the Ru_{acac} center in **3** which has a higher energy than the $\pi(Ru{=}C{=}C{=}C(2\text{-}py)_2)$ orbital in **1** and 2) the greater delocalization of the LUMO between the two Ru^{II} ions in **3**. This spectral assignment is also consistent with the fact that neither **1** nor *cis*-$[Ru(acac)_2(CH_3CN)_2]$ exhibits optical absorptions at $\lambda > 600$ nm.

In conclusion, we have synthesized an allenylidene–ruthenium complex that can be used as a "molecular clip" for metal-ion binding. DFT/TDDFT calculations revealed delocalization along the $\{Ru{=}C{=}C{=}C(2\text{-}py)_2Ru\}$ moiety in the MLCT excited states with NIR absorption energies. The present findings highlight the potential application of the allenylidene ligand as a molecular bridge to allow electronic communication between remote functional groups.

Experimental Section

1-PF_6: A methanolic solution (20 mL) of *trans*-$[Ru(16\text{-}TMC)Cl_2]Cl$ (0.10 g, 0.20 mmol) was refluxed in the presence of zinc amalgam for 10 min. This mixture was filtered to give a green solution, and excess $HC{\equiv}CC(2\text{-}py)_2OH$ (0.40 mol) was then added. After heating the solution at reflux for 2 h, the resultant deep-red solution was filtered and added to a saturated methanolic solution of NH_4PF_6 to afford a red crystalline solid. The crude red solid was dissolved in a minimum volume of CH_2Cl_2, and slow diffusion of Et_2O into this solution afforded deep-red crystals. Yield: 0.12 g, 79%; ^1H NMR (500 MHz, [D_6]acetone): $\delta = 1.34$–1.48, 1.62–2.25 (m, 16H, CH_2), 2.19, 2.46, 2.51 (singlets, 12H, NCH_3), 3.09–4.10 (m, 8H, CH_2), 7.88–7.92 (m, 4H, py), 8.42–8.46 (m, 2H, py), 8.66–8.69 ppm (m, 2H, py); $^{13}C\{^1H\}$ NMR

 © 2006 Wiley-VCH Verlag GmbH & Co. KGaA, Weinheim

(126 MHz, [D$_6$]acetone): $\delta = 20.9$, 21.0 (NCH_2CH_2), 48.3, 50.8 (NCH_3), 57.7, 66.2, 70.1 (NCH_2), 123.3, 123.5, 138.3, 151.2 (C_{py}), 143.0, 143.6 (C_γ), 165.6 (C_{ipso}), 284.8, 287.3 (C_β), 313.4, 319.2 ppm (C_α); IR (KBr): $\tilde{\nu}_{C=C=C} = 1885$, $\tilde{\nu}_{PF} = 841$ cm^{-1}; FAB-MS: m/z: 613 [M^+]. Elemental analysis (%) calcd for $C_{29}H_{44}N_6RuClPF_6$: C 45.94, H 5.85, N 11.08; found: C 46.16, H 5.85, N 10.95.

2-PF_6: A solution of $ZnCl_2$ in Et_2O (1 mL, 1M) was added to a solution of **1**-PF_6 (0.10 g, 0.13 mmol) in THF (30 mL), and this mixture was heated at reflux for 10 h. The resultant red solid was isolated by filtration and washed with Et_2O (2 × 10 mL). This solid was recrystallized by slow diffusion of Et_2O into a CH_2Cl_2 solution to give red crystals. Yield: 0.14 g, 78%; ^{1}H NMR (500 MHz, [D$_6$]acetone): $\delta = 1.42$–2.00 (m, 16H, NCH_2), 2.18, 2.32, 2.41, 2.46 (singlets, 12H, NCH_3), 3.38–3.96 (m, 8H, CH_2), 8.25–8.28 (m, 4H, py), 8.59–8.63 (m, 2H, py), 8.71–8.72 ppm (m, 2H, py); ^{13}C{^{1}H} NMR (126 MHz, [D$_6$]acetone): $\delta = 21.5$ (NCH_2CH_2), 45.9, 52.1 (NCH_3), 58.7, 63.0, 67.0, 67.8 (NCH_2), 123.1, 126.2, 143.3, 149.5, 167.4 (C_{py}), 132.2 (C_γ), 210.0 (C_β, another signal may be obscured by that of the solvent), 309.2, 312.7 ppm (C_α); IR (KBr): $\tilde{\nu}_{C=C=C} = 1896$, $\tilde{\nu}_{PF} = 844$ cm^{-1}; FAB-MS: m/z: 750 [M^+]. Elemental analysis (%) calcd for $C_{29}H_{44}N_6RuCl_3ZnPF_6$: C 38.94, H 4.96, N 9.40; found: C 38.89, H 5.00, N 9.36.

3-PF_6: A methanolic solution (20 mL) of **1**-PF_6 (0.10 g, 0.13 mmol) and [Ru(acac)$_2$(CH_3CN)$_2$] (0.10 g, 0.26 mmol) was heated at reflux for 10 h. The resultant deep-green solution was filtered, and the dark green residue was washed with methanol (2 × 5 mL). This solid was recrystallized by slow diffusion of Et_2O into a CH_2Cl_2 solution to give brown crystals. Yield: 0.13 g, 95%; ^{1}H NMR (500 MHz, [D$_6$]acetone): $\delta = 1.45$–2.59 (m, 40H, NCH_3, NCH_2, CH_3(acac)), 3.35–3.99 (m, 8H, CH_2), 5.49 (brs, 2H, CH(acac)), 7.67–7.68 (m, 2H, py), 7.78 (brs, 2H, py), 8.11 (brs, 2H, py), 8.84–8.85 ppm (m, 2H, py); ^{13}C{^{1}H} NMR (126 MHz, [D$_6$]acetone): $\delta =$ 21.6, 21.7 (NCH_2CH_2), 27.8 (CH_3(acac), another signal may be obscured by that of the solvent), 48.9, 51.9 (NCH_3), 58.5, 62.6, 66.7, 71.0 (NCH_2), 99.4 (CH(acac)), 119.9, 130.4, 136.0, 158.7, 172.2 (C_{py}), 126.8 (C_γ), 186.9, 189.9 (CO(acac)), 245.6, 246.6 (C_β), 269.4, 274.8 ppm (C_α); IR (KBr): $\tilde{\nu}_{C=C=C} = 1871$, $\tilde{\nu}_{PF} = 842$ cm^{-1}; FAB-MS: m/z: 913 [M^+]. Elemental analysis (%) calcd for $C_{39}H_{58}N_6O_4Ru_2ClPF_6$: C 44.30, H 5.53, N, 7.95; found: C 44.56, H 5.44, N 7.61.

Crystal data and structural refinement parameters: **2**-PF_6: $C_{29}H_{48}Cl_3F_6N_6PRuZn$, $M_r = 898.49$, orthorhombic, space group $Pnma$, $a = 16.395(3)$, $b = 11.684(2)$, $c = 19.700(4)$ Å, $\alpha = \beta = \gamma = 90°$, $V = 3773.7(13)$ Å^3, $Z = 4$, $\rho_{calcd} = 1.581$ g cm^{-3}, $\mu(Mo_{K\alpha}) = 1.350$ mm^{-1}, $T = 253$ K, $F(000) = 1832$, $R1 = 0.0462$ ($wR2 = 0.1331$) for 3629 unique reflections ($R_{int} = 0.0513$) with a GOF of 1.126. **3**-PF_6·CH_3CN: $C_{41}H_{61}ClF_6N_7O_4PRu_2$, $M_r = 1098.53$, monoclinic, space group $P2_1/c$, $a = 20.864(4)$, $b = 13.426(3)$, $c = 16.458(3)$ Å, $\alpha = \gamma = 90$, $\beta = 99.07(3)°$, $V = 4552.6(16)$ Å^3, $Z = 4$, $\rho_{calcd} = 1.603$ g cm^{-3}, $\mu(Mo_{K\alpha}) = 0.831$ mm^{-1}, $T = 253$ K, $F(000) = 2248$, $R1 = 0.0483$ ($wR2 = 0.1024$) for 7149 unique reflections ($R_{int} = 0.0727$) with a GOF of 0.834. Data were collected with $\omega/2\theta$ ($2\theta_{max} = 50.94$ and 51.06° for **2** and **3**, respectively) on a MAR diffractometer with graphite-monochromated $Mo_{K\alpha}$ radiation ($\lambda = 0.71073$ Å). The structures were solved by direct methods employing the SIR-97 program[10] and refined on F^2 using SHELXL-97.[11] CCDC-294797 (**2**) and CCDC-294798 (**3**) contain the supplementary crystallographic data for this paper. These data can be obtained free of charge from The Cambridge Crystallographic Data Centre via www.ccdc.cam.ac.uk/data_request/cif.

Computational details: DFT geometry optimizations and subsequent TDDFT calculations were performed on the model complex [$(NH_3)_4ClRu{=}C{=}C{=}C(2\text{-py})_2Ru(acac)_2$]$^+$ (**3M**) by using the Perdew–Wang 1991 exchange and correlation functionals.[12] Stuttgart 16-valence-electron relativistic effective-core potentials were used for Ru,[13] and the 6-31G* basis set for all other atoms (H, C, N, O, and Cl).[14] The conductor-like polarizable continuum model (C-PCM)[15] was employed to model the solvent (CH_3CN) effects in the TDDFT calculations. All calculations were performed with Gaussian 03.[16]

Received: January 12, 2006
Published online: April 4, 2006

Keywords: cyclic voltammetry · density functional calculations · pi interactions · ruthenium · UV/Vis spectroscopy

[1] P. F. H. Schwab, M. D. Levin, J. Michl, *Chem. Rev.* **1999**, *99*, 1863.
[2] M. I. Bruce, *Chem. Rev.* **1998**, *98*, 2797.
[3] S. Rigaut, D. Touchard, P. H. Dixneuf, *Coord. Chem. Rev.* **2004**, *248*, 1585.
[4] C.-Y. Wong, C.-M. Che, M. C. W. Chan, K.-H. Leung, D. L. Phillips, N. Zhu, *J. Am. Chem. Soc.* **2004**, *126*, 2501.
[5] Multiple resonances are observed in the ^{1}H and ^{13}C{^{1}H} NMR spectra as the 16-TMC ligand can exhibit several possible conformations upon coordination to the metal center; see reference [4] and the following: a) C.-M. Che, W.-K. Cheng, T.-F. Lai, C.-K. Poon, T. C. W. Mak, *Inorg. Chem.* **1987**, *26*, 1678; b) C.-M. Che, K.-Y. Wong, T. C. W. Mak, *J. Chem. Soc. Chem. Commun.* **1985**, 988; c) T. C. W. Mak, C.-M. Che, K.-Y. Wong, *J. Chem. Soc. Chem. Commun.* **1985**, 986; d) C.-M. Che, K.-Y. Wong, T. C. W. Mak, *J. Chem. Soc. Chem. Commun.* **1985**, 546.
[6] Conditions: working electrode, glassy carbon; scan rate 100 mV s^{-1}, nBu$_4$NPF$_6$ (0.1M in CH_3CN) as supporting electrolyte. The oxidation wave becomes more reversible at higher scan rates.
[7] The interplanar angle is defined by the planes formed by the six non-hydrogen atoms of the pyridyl rings.
[8] Recorded in this work.
[9] T. Hasegawa, T. C. Lau, H. Taube, W. P. Schaefer, *Inorg. Chem.* **1991**, *30*, 2921.
[10] SIR-97: A. Altomare, M. C. Burla, M. Camalli, G. Cascarano, C. Giacovazzo, A. Guagliardi, A. G. G. Moliterni, G. Polidori, R. Spagna, *J. Appl. Crystallogr.* **1999**, *32*, 115.
[11] SHELXL-97 (release 97-2), G. M. Sheldrick, Programs for Crystal Structure Analysis, University of Göttingen, Germany, **1997**.
[12] J. P. Perdew in *Electronic Structure of Solids* (Eds.: P. Ziesche, H. Eschrig), Akademie Verlag, Berlin, **1991**.
[13] D. Andrae, U. Haeussermann, M. Dolg, H. Stoll, H. Preuss, *Theor. Chim. Acta* **1990**, *77*, 123.
[14] a) P. C. Hariharan, J. A. Pople, *Theor. Chim. Acta* **1973**, *28*, 213; b) M. M. Francl, W. J. Petro, W. J. Hehre, J. S. Binkley, M. S. Gordon, D. J. DeFree, J. A. Pople, *J. Chem. Phys.* **1982**, *77*, 3654.
[15] a) V. Barone, M. Cossi, *J. Phys. Chem. A* **1998**, *102*, 1995; b) V. Barone, M. Cossi, J. Tomasi, *J. Chem. Phys.* **1997**, *107*, 3210.
[16] Gaussian 03 (Revision B.05), M. J. Frisch et al. See the Supporting Information for the full reference.

 © 2006 Wiley-VCH Verlag GmbH & Co. KGaA, Weinheim

Peptide Assemblies

DOI: 10.1002/anie.200600395

Control of Amyloid β-Peptide Protofibril Formation by a Designed Template Assembly**

Gunnar T. Dolphin, Pascal Dumy, and Julian Garcia**

Amyloid fibrillar deposits, which consist mainly of the amyloid β-peptides, $A\beta_{1-40}$ and $A\beta_{1-42}$,[1] are characteristic of the neurodegenerative disorder Alzheimer's disease. Amyloid fibrils of Aβ have a high content of β sheets and are similar to fibrils associated with other neurodegenerative diseases such as Parkinson's and Huntington's diseases. Aβ normally exists as a soluble random coil, but through formation of intermediate oligomers it misfolds into protofibrils, and further aggregation of the protofibrils forms amyloid. To aid the search for therapeutic strategies, detailed knowledge of the mechanisms of formation as well as structural information of protofibrils is of current interest. As a result of short-lived intermediates and the insoluble nature of amyloid fibrils, detailed structural information has not been available to date. However, experimental data from solid-state NMR spectroscopy, EPR measurements, and X-ray scattering studies have revealed key features of the organization of Aβ in fibrillar structures, such as the cross-β-sheet structural motif, where β strands are perpendicular to the fibril axis and form intermolecular parallel β sheets that extend along the length of the fibril.[2] On the basis of present knowledge, Tycko and co-workers have recently proposed a structural model with minimum dimensions for the $A\beta_{1-40}$ protofibril.[3] A cross-section of this protofilament contains a dimer of $A\beta_{1-40}$ peptides, each of which forms a strand–loop–strand, and a disordered N-terminal segment. Recently, a number of different configurations of the strand–loop–strand fold have been presented, and the controversy demonstrates the need for a detailed structural analysis.[3–6] Our first aim was to design a stable and water-soluble Aβ protofilament for high-resolution structural determination by NMR spectroscopy. Herein, we present our strategy for attaching four identical sequences formed by residues 16–37 of full-length Aβ to a cyclic decapeptide scaffold, designed to create a high local concentration, to induce the formation of protofibrils. The sequence was mutated at three positions to increase the solubility and to reduce the propensity of the protofibrils to further aggregate and form an amyloid.

The assembly, $(A\beta_{16-37}Y_{20}K_{22}K_{24})_4$, was designed to form a building block of the Aβ protofilament and is composed of two cross-sections (as compared to native Aβ fibrils), each containing two Aβ segments that fold through side-chain–side-chain hydrophobic interactions. Cross-β-sheets are formed between the cross-sections, and aggregation of assemblies forms protofibrils. The success of the presented template assembly is demonstrated through observation of folding with no lag phase, the binding of dyes that are specific to cross-β-sheets, and control of the kinetics of formation of protofibrils by the concentration of the divalent anion HPO_4^{2-}. From electron microscopy the observed dimensions of the protofibrils are found to correspond well with our model. Control of folding of a soluble protofilament associated with Alzheimer's disease may give insight into the mechanisms of formation of fibrils and also be used as a tool for the screening of fibril inhibitors.

As the starting point for the design of the assembly, we used present structural knowledge of Aβ fibrils[3,5] in combination with the template-assembled synthetic protein approach (Figure 1).[7] For the scaffold a cyclic decapeptide with controlled conformation was chosen that offers two opposite faces for attachment (Figure 1c).[8] The Aβ fragments were ligated to the face with fourfold attachment possibilities by chemoselective oxime bond formation.[9] The Aβ sequence was reduced to residues 16–37 of full-length Aβ, which contains the highly ordered β-strand segments (Figure 1d). As this segment is highly hydrophobic and has a calculated isolectric point of $pI = 0$ at neutral pH, difficulties with solubility and aggregation are expected. To increase solubility, by a net positive charge, and to minimize uncontrolled aggregation, through charge repulsions between the protofilaments, three mutations were introduced into the sequence that forms the hydrophilic surface of the protofilament. Thus, Glu22 and Val24 were mutated to Lys, and Phe20 was mutated to Tyr for increased solubility and to serve as a chromophore. This Aβ segment is termed $A\beta_{16-37}Y_{20}K_{22}K_{24}$. These mutations on the hydrophilic surface were expected to have minor effects on the desired protofibril structure as compared to the native protofibril, and only change the protofibril–protofibril association behavior. To further increase solubility and protofibril–protofibril charge repulsions, the scaffold contains two Arg residues on the opposite face. One or both of these can be replaced by probes or affinity tags in future designs.

Figure 1a shows the modelled structure of $(A\beta_{16-37}Y_{20}K_{22}K_{24})_4$. The assembly is constructed of two protofibril cross-sections, each of which consists of four β strands. The two C-terminal strands in parallel form a central hydrophobic core. The core is shielded from the solvent by the hydrophilic scaffold, the loops, and the two outer β strands with the mutations. The tertiary structure of the assembly reveals C_{2y} symmetry, and by the formation of parallel cross-β-sheets the assembly would form protofibrils with a quaternary structure as shown in Figure 1b.[6]

Oxime bond ligation reactions are commonly performed between unprotected peptide fragments, one with an amino-

[*] Dr. G. T. Dolphin, Prof. P. Dumy, Prof. J. Garcia
LEDSS, UMR 5616, ICMG-FR
Université Joseph Fourier
BP 53, 38041 Grenoble Cedex 9 (France)
Fax: (+33) 4-7651-4431
E-mail: pascal.dumy@ujf-grenoble.fr
julian.garcia@ujf-grenoble.fr

[**] We thank Dr. Serge Perez for access to an electron microscope and Isabelle Paintrand for performing the study. This work was supported by grants from AFM-INSERM GIS "maladies rares amyloses héréditaires" (no. AE02013 KSA), IUF, and ACI.

Supporting information for this article is available on the WWW under http://www.angewandte.org or from the author.

 © 2006 Wiley-VCH Verlag GmbH & Co. KGaA, Weinheim

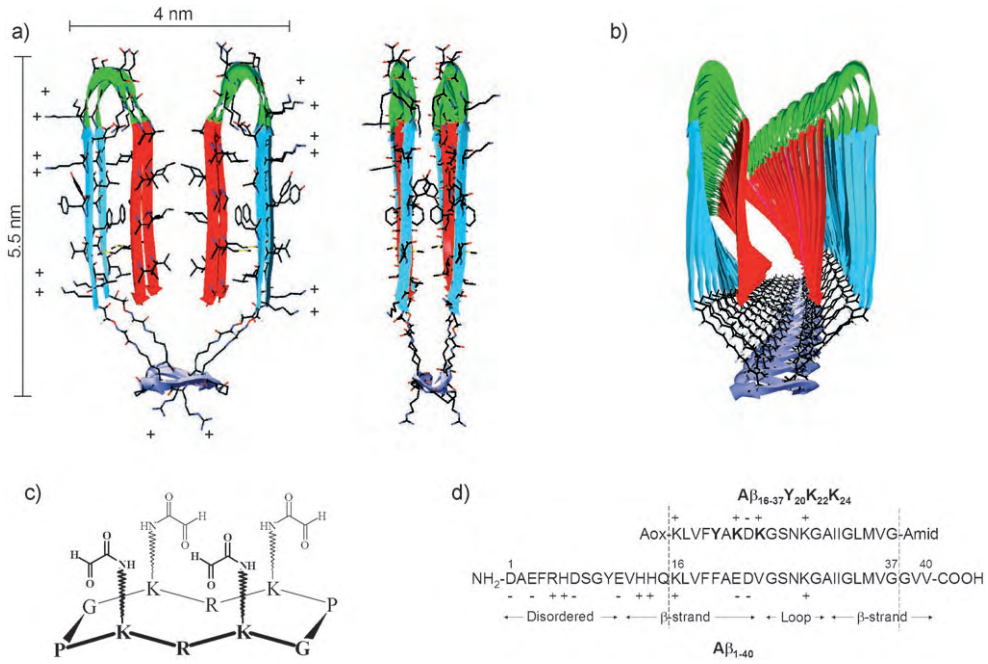

Figure 1. a) Modeled representation of $(A\beta_{16-37}Y_{20}K_{22}K_{24})_4$, viewed along and perpendicular to the protofibril axis. b) Representation of the quaternary structure for the $(A\beta_{16-37}Y_{20}K_{22}K_{24})_4$ protofibril. c) Chemical structure of the cyclic decapeptide scaffold with four glyoxyl-aldehyde-functionalized lysines. d) Amino acid sequences of the $A\beta_{16-37}Y_{20}K_{22}K_{24}$ fragment and full-length $A\beta_{1-40}$. Mutated residues are shown in bold. Aox denotes the aminooxy function. Indications of the secondary structure of $A\beta_{1-40}$ are taken from reference [3].

oxy function and the other with an aldehyde function, in aqueous polar organic mixtures.[10] The solid-phase peptide synthesis of the aminooxy fragment of $A\beta_{16-37}Y_{20}K_{22}K_{24}$ and the aldehyde-functionalized scaffold were performed under standard activation with PyBOP/DIPEA (benzotriazole-1-yl-oxytripyrrolidinophosphonium hexafluorophosphate/diisopropylethylamine). Aβ sequences are known to be difficult to synthesize and purify, thus the preparation of $(A\beta_{16-37}Y_{20}K_{22}K_{24})_4$ was a challenge. For the $A\beta_{16-37}Y_{20}K_{22}K_{24}$ sequence, each coupling was monitored by the Kaiser test and performed until completion. The aminooxy function was introduced to the N terminus by acylation with the succinimide ester of *N*-Boc-*O*-(carboxymethyl)hydroxylamine as the final coupling step before cleavage from the solid support using trifluoroacetic acid (TFA). Purification by RP-HPLC provided the aminooxy-$A\beta_{16-37}Y_{20}K_{22}K_{24}$ fragment. The cyclic decapeptide scaffold containing four glyoxyl-aldehyde-functionalized Lys side chains was prepared by the strategy described previously.[11] The fourfold ligation was performed in DMSO at 40 °C, monitored by analytical RP-HPLC, and was complete within 23 h (Figure 2). The assembly was purified by C5 RP-HPLC and characterized by ES-MS: mass calculated for $[M+H]^+$: 10813.0 Da; found: 10812.6 Da.

The formation of the characteristic amyloid cross-β-sheet structure was determined by far-UV circular dichroism (CD) spectroscopy and specific binding of the dyes thioflavine T (ThT) and Congo Red (CR) in phosphate buffer (5 mM, pH 7.1). The CD spectrum is shown in Figure 3a and is characteristic of a β-sheet structure, with a maximum at $\lambda = 200$ nm and a minimum at $\lambda = 218$ nm. Under the same conditions, the CD spectrum of the unligated segment $A\beta_{16-37}Y_{20}K_{22}K_{24}$ displays a random-coil profile with the typical minimum at $\lambda = 195$ nm. These results show that the strategy of ligating four $A\beta_{16-37}Y_{20}K_{22}K_{24}$ segments to the scaffold, as designed, induces formation of a β-sheet, whereas the unligated segment remains unstructured.

Amyloid structures are identified by binding of the fluorescent dye ThT, which is highly specific for the cross-β-sheet structure. This binding of ThT is accompanied by a large red shift in its excitation spectra, allowing selective excitation of bound ThT.[12] In the study of ThT and its interaction with $(A\beta_{16-37}Y_{20}K_{22}K_{24})_4$, a strongly enhanced fluorescence intensity is seen at 480 nm compared to ThT alone (Figure 3b). The assembly was also tested for binding of CR as another indicator of fibril formation (Figure 3c). The spectrum of CR alone has an absorbance maximum at 503 nm. Upon binding of CR to $(A\beta_{16-37}Y_{20}K_{22}K_{24})_4$ the absorbance

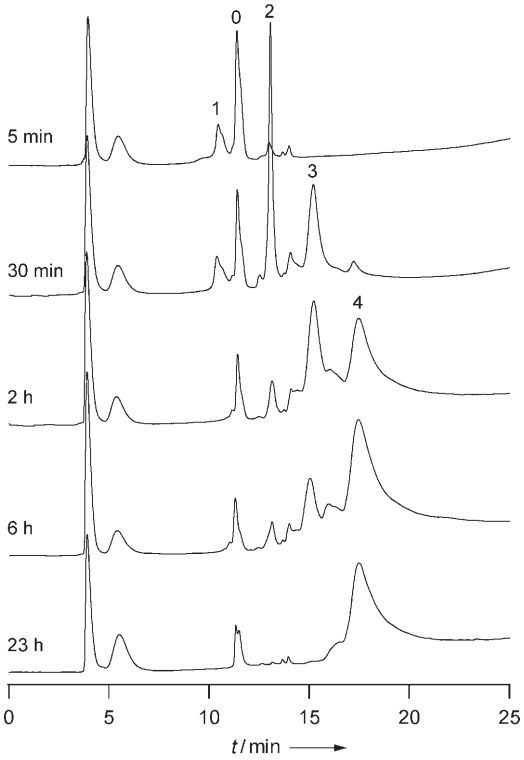

Figure 2. Fourfold chemoselective ligation of $A\beta_{16-37}Y_{20}K_{22}K_{24}$ to the scaffold was monitored by analytical reverse-phase (RP)-HPLC (C18 column; chromatograms obtained at 250 nm are shown). Free $A\beta_{16-37}Y_{20}K_{22}K_{24}$ is labeled as 0; peaks labeled 1 to 4 correspond to the number of $A\beta_{16-37}Y_{20}K_{22}K_{24}$ units ligated to the scaffold. The final product $(A\beta_{16-37}Y_{20}K_{22}K_{24})_4$ is seen after 2 h as a broad peak with a retention time of 18 min. A gradient of 27 to 90% acetonitrile during 30 min was used, and 0.1% TFA was used to provide the counterion.

 © 2006 Wiley-VCH Verlag GmbH & Co. KGaA, Weinheim

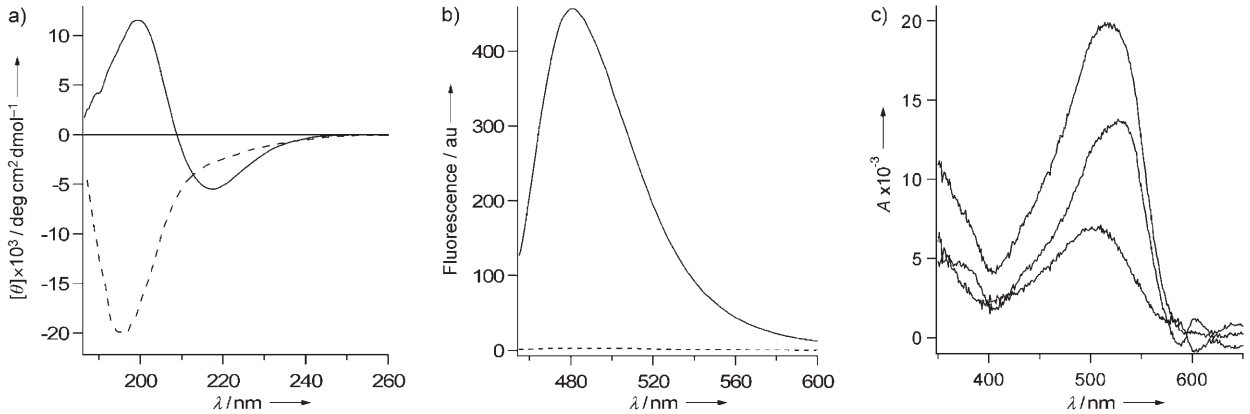

Figure 3. Characterization of $(A\beta_{16-37}Y_{20}K_{22}K_{24})_4$ in phosphate buffer (5 mM, pH 7.1) at 21 °C. a) Far-UV CD spectra of 7 μM $(A\beta_{16-37}Y_{20}K_{22}K_{24})_4$ (——) and 17 μM $A\beta_{16-37}Y_{20}K_{22}K_{24}$ (-----). b) Fluorescence spectra (excitation at 435 nm) of ThT (10 μM) alone (-----) and in the presence of $(A\beta_{16-37}Y_{20}K_{22}K_{24})_4$ (3 μM; ——). c) Spectra of Congo Red (CR; 2.5 μM; bottom) alone and upon interaction with $(A\beta_{16-37}Y_{20}K_{22}K_{24})_4$ (3 μM; top); the difference spectrum is that shown in the middle.

of CR is increased, and from the difference spectrum the point of maximal difference is found at 530 nm, indicating a cross-β-sheet structure.[13] We confirmed the formation of protofibrils by performing transmission electron microscopy (TEM) studies (see Figure 4). In the TEM image, short fibrils

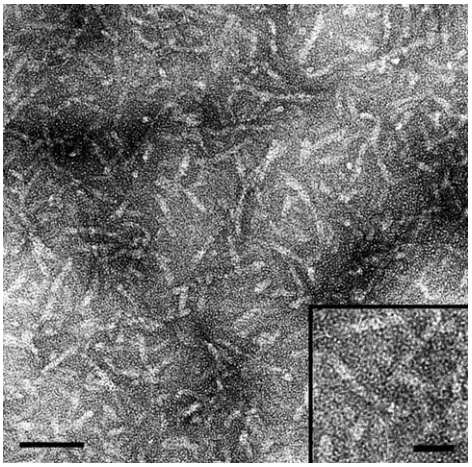

Figure 4. Electron micrograph of protofibril made from $(A\beta_{16-37}Y_{20}K_{22}K_{24})_4$ (scale bar: 50 nm). The fibrils were formed in phosphate buffer (4 mM, pH 7.1) for 1.5 h at 21 °C. Inset: magnified view (scale bar: 20 nm).

with diameters of 5–6 nm are seen that correspond well with the dimensions of our modelled structure (Figure 1). Aβ fibrils are known to fold into different morphologies: Recently, Petkova et al. presented solid-state NMR data that support a quaternary structure for Aβ protofibrils with C_{2z} symmetry, where the two C-terminal strands in each cross-section are antiparallel in the central hydrophobic core.[6] As a result of our template-assembled module, the formed protofibrils are locked into an approximate C_{2y} symmetry, where the two C-terminal strands are parallel in the core (Figure 1a). The formation of protofibrils shows that the quaternary structure with C_{2y} symmetry is possible for Aβ protofibrils.

Folding kinetics from the random coil to the cross-β-sheet structure was monitored by CD spectroscopy and binding to ThT. From the kinetic studies, it is seen that folding is highly sensitive to the concentration of HPO_4^{2-} ions and that no lag phase is observed, contrary to what is found for native Aβ. The sensitivity was demonstrated with different mixtures (10 mM total concentration) of phosphate and TRIS buffers at pH 7.1 (Figure 5). In TRIS buffer alone, no folding was observed. With a mixture of 1 mM HPO_4^{2-} and 9 mM TRIS, the β-sheet is formed but still the peptide is mostly found as a random coil after 5000 s (Figure 5b). With a mixture of 5 mM HPO_4^{2-} and 5 mM TRIS buffers a complete β-sheet conformation is formed, and with an increasing concentration of HPO_4^{2-} the kinetics are much faster. These results indicate that the divalent anion HPO_4^{2-} stabilizes the formation of protofibrils, presumably through charge neutralization. The kinetic data from CD spectroscopy and ThT binding experiments are the same within experimental error: the data from 5 mM and 10 mM HPO_4^{2-} solutions fit well to single-exponential functions, and the measured rate constants for fully folded protofibrils are 0.052 min^{-1} and 0.092 min^{-1}, respectively. The data from CD and ThT binding measurements with 20 mM HPO_4^{2-} solution only fit well to a double-exponential function, indicating the presence of two folding processes at higher concentrations of HPO_4^{2-}; the slower process has a rate constant of 0.15 min^{-1}, whereas the faster process has a rate constant of 0.49 min^{-1}.

It is also seen in the CD profile at higher concentrations of HPO_4^{2-} (20 mM) that $[\theta]_{200}$ after reaching a maximum decreases without notable change of $[\theta]_{218}$, which indicates the formation of another structural conformation (Figure 5a,b). Our interpretation of these results is that the protofibril forms first and that higher concentration of HPO_4^{2-} stabilizes further aggregation of the protofibril towards amyloid structures. The most notable difference in the CD profiles is the ratio of the absolute values of the CD signals at $\lambda = 200$ and 218 nm. The $[\theta]_{200}/[\theta]_{218}$ ratio found for

 © 2006 Wiley-VCH Verlag GmbH & Co. KGaA, Weinheim

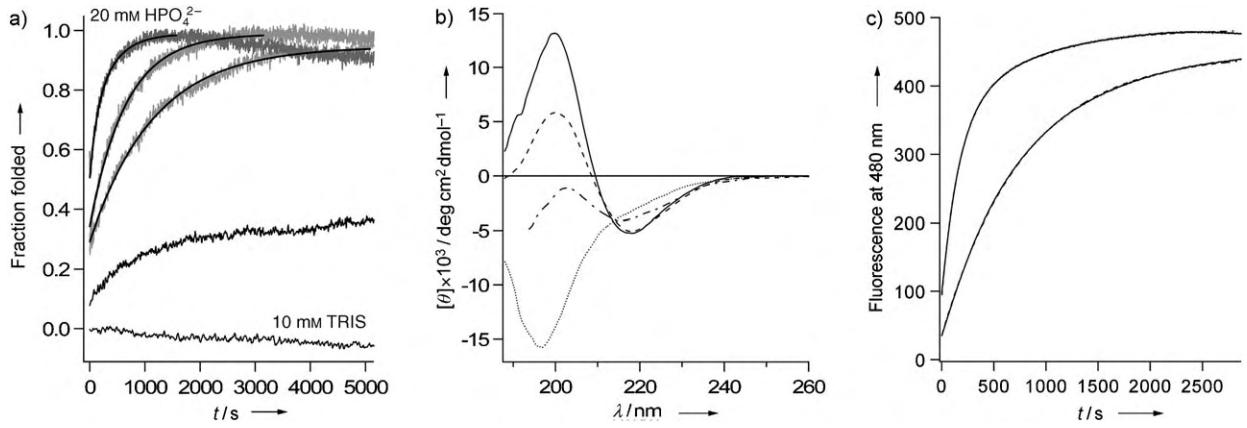

Figure 5. a) Folding kinetics of $(A\beta_{16-37}Y_{20}K_{22}K_{24})_4$ (3 μM) followed by the change of $[\theta]_{200}$ in phosphate/TRIS buffer mixtures (10 mM total, except for one sample at 20 mM phosphate) at pH 7.1 and 20°C, presented as the fraction folded. The concentration of phosphate buffer from bottom to top are 0 mM, 1 mM, 5 mM, 10 mM, and 20 mM. Solid lines are the exponential fits of the curves. b) Corresponding CD spectra after the kinetic studies at different concentrations of phosphate buffer: 0 mM (••••), 1 mM (–•–•), 5 mM (——), and 20 mM -----). c) Folding kinetics of $(A\beta_{16-37}Y_{20}K_{22}K_{24})_4$ (3 μM) monitored by the fluorescence of bound ThT (10 μM) at 480 nm, pH 7.1, and 20°C, at different concentrations of phosphate buffer: 5 mM (bottom) and 20 mM (top). Dashed lines are the exponential fits of the curves.

the protofibril formed in 5 mM HPO_4^{2-} solution is 2.5, and that found for the aggregated protofibril in 20 mM HPO_4^{2-} solution is 1.1. This result indicates that different morphologies of aggregated $(A\beta_{16-37}Y_{20}K_{22}K_{24})_4$ may be identified by the CD profile.

In conclusion, we have successfully prepared $(A\beta_{16-37}Y_{20}K_{22}K_{24})_4$, which forms a module of the Aβ protofibril, constructed of four Aβ segments attached to a cyclic decapeptide scaffold. The presented results show the formation of protofibrils with fast controllable kinetics and without a lag phase. The structure is highly soluble and the cross-β-sheet structure and formation of protofibril was confirmed by TEM studies and specific binding of ThT and CR. The designed mutations combined with the templated assembly strategy apparently allow the formation of a protofibril structure. Also, the need for the template strategy was demonstrated by CD analysis of the unligated segment, which remained unstructured. Detailed solution-structural analysis by NMR spectroscopy in the future should provide information on the nature of the folded protofibril and folded intermediates such as that observed in 1 mM HPO_4^{2-} solution. Detailed structural information of the intermediates and the protofibril on the pathway towards amyloid will aid research towards fibril inhibitors. Also, the presented model may prove to be a valuable tool in screening experiments of amyloid inhibitors, as the fast kinetics of protofibril formation without a lag phase is desirable for high-throughput screening.

Received: January 30, 2006
Published online: March 23, 2006

Keywords: amyloids · peptides · protein design · protein folding · template synthesis

[1] G. G. Glenner, C. W. Wong, *Biochem. Biophys. Res. Commun.* **1984**, *120*, 885–890.
[2] R. Tycko, *Curr. Opin. Struct. Biol.* **2004**, *14*, 96–103.
[3] A. T. Petkova, Y. Ishii, J. J. Balbach, O. N. Antzutkin, R. D. Leapman, F. Delaglio, R. Tycko, *Proc. Natl. Acad. Sci. USA* **2002**, *99*, 16742–16747.
[4] S. Shivaprasad, R. Wetzel, *Biochemistry* **2004**, *43*, 15310–15317.
[5] T. Lührs, C. Ritter, M. Adrian, D. Riek-Loher, B. Bohrmann, H. Döbeli, D. Schubert, R. Riek, *Proc. Natl. Acad. Sci. USA* **2005**, *102*, 17342–17347.
[6] A. T. Petkova, W.-M. Yau, R. Tycko, *Biochemistry* **2006**, *45*, 498–512.
[7] M. Mutter, P. Dumy, P. Garrouste, C. Lehmann, M. Mathieu, C. Peggion, S. Peluso, A. Razaname, G. Tuchscherer, *Angew. Chem.* **1996**, *108*, 1588–1591; *Angew. Chem. Int. Ed. Engl.* **1996**, *35*, 1482–1485.
[8] P. Dumy, I. M. Eggleston, S. Cervigni, U. Sila, X. Sun, M. Mutter, *Tetrahedron Lett.* **1995**, *36*, 1255–1258.
[9] K. Rose, *J. Am. Chem. Soc.* **1994**, *116*, 30–33.
[10] J. Shao, J. P. Tam, *J. Am. Chem. Soc.* **1995**, *117*, 3893–3899.
[11] O. Renaudet, P. Dumy, *Org. Lett.* **2003**, *5*, 243–246.
[12] H. LeVine III, *Methods Enzymol.* **1999**, *309*, 274–284.
[13] W. E. Klunk, R. F. Jacob, R. P. Mason, *Methods Enzymol.* **1999**, *309*, 285–305.

 © 2006 Wiley-VCH Verlag GmbH & Co. KGaA, Weinheim

DNA Intercalation

DOI: 10.1002/anie.200502946

DNA Recognition with Large Calixarene Dimers**

*Reza Zadmard and Thomas Schrader**

DNA-binding molecules are of eminent medicinal significance because they constitute a large part of all anticancer drugs.[1] In nature, DNA recognition mainly follows four different paths: efficient binding agents either target the phosphodiester backbone,[2] intercalate into the basepairs,[3] or occupy the minor[4] or major groove.[5] Interestingly enough, the zinc finger[6] and the leucine zipper motifs,[7] two typical protein domains that fit snuggly into the major groove of DNA, have similar dimensions (averaged α-helix diameters of ca. 1.3 nm) and also a comparable overall topology. Both motifs have a large basic cylinder with a polar protic face that reads the nucleic bases on the groove's floor. Recently, Hannon et al. reported on the first artificial noncovalent major groove binder, a tetracationic metallosupramolecular cylinder with a size of approximately $2 \times 1\ nm^2$.[8] This remarkable molecule binds tightly to the floor of the major groove and induces DNA bending and intramolecular coiling. We have now found that a calixarene dimer with six protonatable aniline NH_2 groups at its upper rims, connected by a suitable flexible linker, is also able to recognize double-stranded (ds) DNA.[9] This molecule is even larger than the triple-helix cylinder, with an average size of about $3 \times 1\ nm^2$. Its dimensions therefore exclude a potential intercalation or minor groove insertion.

Various dimeric cationic calixarenes are accessible by a straightforward synthetic avenue. Triple protection of the parent tetraaniline[10] with *tert*-butoxycarbonyl (Boc) groups followed by amide coupling with diacid dichlorides leads to dimeric protected precursors that are converted into the cationic hosts by cleavage of the Boc groups under mild conditions with trifluoroacetic acid. Reciprocal cross-peaks between all adjacent aromatic calixarene protons (NOESY) prove the existence of a regular cone conformation, whereas a variable-temperature experiment revealed a fast dynamic rotation of the calixarene around the bridge. A molecular dynamics calculation confirmed the assumed high degree of preorganization within the calixarene dimer **1b** carrying the rigid aromatic spacer, whereas much more flexibility was found for the aliphatic bridge in **1a** (Figure 1a).

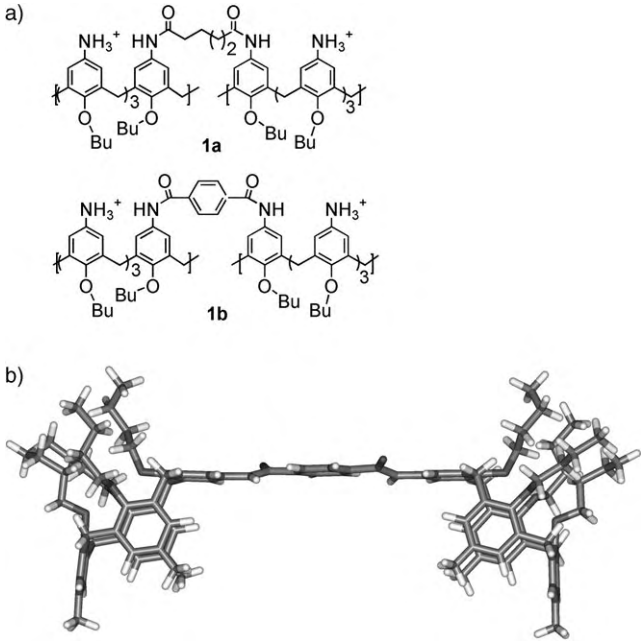

Figure 1. a) Calix[4]arene dimers **1a**/**1b** based on trifunctional anilinium building blocks. b) Molecular mechanics calculation for the rigid hexaanilinium calixarene dimer **1b**. The *syn* conformer is energetically almost identical to its *anti* counterpart ($\Delta H \approx 1$ kcal mol^{-1}).[11]

Preliminary binding experiments with negatively charged substrates (see below) showed large upfield shifts for the peripheral calixarene protons that are exposed to the approaching guest. Such a shift was also seen for guest protons that point towards the anisotropy cone of the calixarene cavity. Subsequent ^{1}H NMR spectroscopy and fluorescence titrations[12] helped to characterize the binding profile of compounds **1a** and **1b**: the sugars showed no response, and the acidic peptides and the di- and oligophosphates were all weakly bound (except for oligonucleotides such as fluorescein-labeled triadenosine).[13]

To investigate ds-DNA recognition, one of two complementary primer fragments containing 12 nucleic bases was fluorescein-labeled at its 5′-terminus, and the resulting duplex was incubated with increasing amounts of calixarene dimer. A marked decrease in fluorescence intensity indicated a strong interaction, producing a sharply kinked titration curve that corresponds to an approximate 9:1 dimer/DNA stoichiometry (Job plot)[14] with an association constant for each individual dimer binding event of $1 \times 10^5\ M^{-1}$ (assuming no cooperativity). In buffer solutions that were tenfold more dilute, the affinity increased to micromolar K_D values, thus providing experimental evidence for a certain contribution of polar interactions. These, however, are most likely complemented

[*] R. Zadmard,[+] Prof. T. Schrader
Fachbereich Chemie
Universität Marburg
Hans-Meerwein-Strasse, 35032 Marburg (Germany)
Fax: (+49) 6421-28-25544
E-mail: schradet@staff.uni-marburg.de

[+] Present address:
Chemistry and Chemical Engineering Research Center of Iran
P.O. Box 14335-186, Tehran (Iran)

[**] We are indebted to the Carell group (Munich) for a sample of fluorescein-labeled triadenosine, as well as to the Marahiel group (Marburg) for 45-bp DNA samples. Valuable advice came from Dr. Mohamad Mofid. We also thank the Pingoud group (Giessen) for the measurements of CD spectra. Funding by the Deutsche Forschungsgemeinschaft is gratefully acknowledged.

Supporting information for this article is available on the WWW under http://www.angewandte.org or from the author.

 © 2006 Wiley-VCH Verlag GmbH & Co. KGaA, Weinheim

by strong hydrophobic forces[15] and possibly even reinforced by the formation of aggregates.[16] The highest affinity, however, was found for longer ds DNA with 45 nucleic bases containing the whole primer (up to $6 \times 10^7\,\text{M}^{-1}$ in 2-[4-(2-hydroxyethyl)-1-piperazinyl]ethanesulfonic acid (HEPES) buffer solution (0.1 mM)).[17] Interestingly, the stiff linear dimer **1b** greatly laged behind the flexible **1a** by two orders of magnitude; it simply could not adjust to the helical curvature of the duplex. The relatively small dependence on ionic strength and the high, variable stoichiometry factor could be explained by major groove binding, with several dimers filling up the groove where they engage in salt bridges with the phosphodiester backbone. The DNA and RNA sequences used herein are shown in Table 1.

To elucidate the binding mechanism, we measured UV as well as fluorescence melting curves for various ds DNA before and after addition of the dimer. In each case, we obtained almost the same melting points, ruling out extensive cross-linking of the complementary DNA strands and intercalation or minor groove insertion.[18] However, the UV melting curves of ds DNA in the presence of the calixarene dimers looked drastically different from those of pure DNA; they were inverted and strongly enhanced with respect to their absorption intensity (Figure 2). This is not an effect of the calixarene dimer, which produced a straight horizontal line under identical conditions. Clearly, complexation affects the nucleic base chromophores and strongly increases UV absorption for the duplex but quenches it for the single-strand (ss) DNA. This is in perfect agreement with an insertion of the extended unpolar calixarene dimer corpus into the major groove accompanied by hydrogen bonding to the nucleic bases (Hogsteen sites). As AT pairs present a methyl group into the major groove and GC pairs do not, pure $(GC)_n$ DNA strands should be preferred for insertion into the calixarene dimer owing to additional hydrogen bond contacts. This sequence selectivity was indeed established with fluorescein-labeled $(GC)_{12}$ and $(AT)_{12}$ model DNA, which produced a pronounced difference in the K_D value of one order of magnitude (Table 2). In sharp contrast, crystal structures for spermine–DNA complexes show that polyamines also bridge the minor groove and thus lead to considerable duplex stabilization.[19] Moreover, most backbone binders are known to distort the DNA conformation from the structure of B-DNA towards that of A-DNA.[20] However, in CD measurements before and after complexation with a 50-fold excess of the calixarene dimer, no major conformational changes were indicated in the critical region between 200 and 270 nm (data not shown).[18]

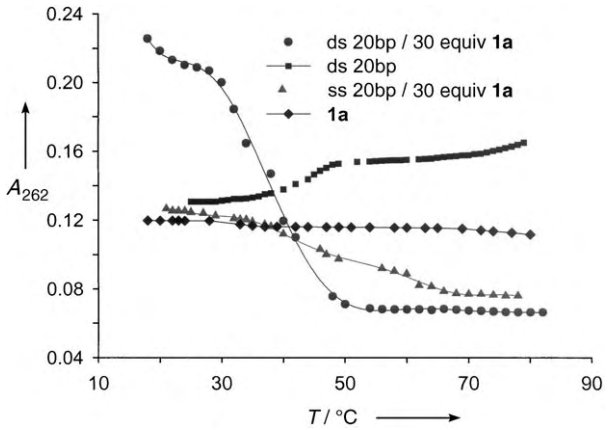

Figure 2. Melting curves of ss DNA and ds DNA before and after complexation by a large excess of the dimer.

Table 1: DNA and RNA sequences used.[a]

Entry	Abbreviation	Sequence
1	ds Fl-DNA (12 bp)	5′-[Fl]GTGACGAACCTC-3′/5′-GAGGTTCGTCAC-3′
2	ds Fl-DNA (12 bp, 3 mm)	5′-[Fl]GTGACGAACCTC-3′/5′-GAGCTTGGTAAC-3′
3	ds Fl-DNA [$(GC)_{12}$]	5′-[Fl]GGGGGGGGGGGG-3′/5′-CCCCCCCCCCCC-3′
4	ds Fl-DNA [$(AT)_{12}$]	5′-[Fl]AAAAAAAAAAAA-3′/5′-TTTTTTTTTTTT-3′
5	ds Fl-RNA [$(AU)_{12}$]	5′-[Fl]AAAAAAAAAAAA-3′/5′-UUUUUUUUUUUU-3′
6	ds DNA (45 bp)	5′-AATTCACTGCTTGGAGCCACCCGCAGTTCGAAAAATAAGCATGCA-3′/ 5′-CTAGTGCATGCTTATTTTTCGAACTGCGGGTGGCTCCAAGCAGTG-3′

[a] Fl = fluorescein.

Molecular mechanics calculations of our 12-bp DNA duplex complexed by the flexible ligand **1a** showed intriguing minimum-energy structures in which the two ammonium groups of the calixarene units were deeply buried within the major groove. Depending on the base sequence, up to six additional hydrogen bond contacts were established during the minimization procedure; they all involve carbonyl oxygen and imino nitrogen atoms of the nucleic bases and NH_2 as well as NH_3^+ groups of the calixarene (Figure 3). Subsequent

Table 2: Association constants between various DNA strands and dimeric receptors **1**.

Entry	Receptor	Guest	Solvent	K_a [M^{-1}][d]	Stoichiometry
1	**1a**	ds Fl-DNA (12 bp)	HEPES (0.1 mM)[a]	2×10^6 (±20%)	9:1[c]
2	**1a**	ds Fl-DNA (12 bp)	HEPES (1 mM)[b]	1×10^5 (±27%)	8:1[c]
3	**1a**	ds Fl-DNA (12 bp, 3 mm)	HEPES (1 mM)[b]	1×10^5 (±16%)	6:1[c]
4	**1a**	ds Fl-DNA [$(GC)_{12}$]	HEPES (1 mM)[b]	1×10^6 (±7%)	8:1[c]
5	**1a**	ds Fl-DNA [$(AT)_{12}$]	HEPES (1 mM)[b]	1×10^5 (±9%)	8:1[c]
6	**1a**	ds Fl-RNA [$(AU)_{12}$]	HEPES (1 mM)[b]	6×10^6 (±35%)	30:1
7	**1a**	ds Fl-RNA [$(AU)_{12}$]	HEPES (100 mM)[b]	8×10^5 (±31%)	35:1
8	**1a**	ds DNA (45 bp)	HEPES (0.1 mM)[a]	6×10^7 (±52%)	30:1[c]
9	**1b**	ds Fl-DNA (12 bp)	HEPES (1 mM)[b]	4×10^3 (±45%)	9:1[d]

[a] HEPES buffer in methanol/water (9:1). [b] HEPES buffer in methanol/water (1:1). [c] From best-curve fitting. [d] Statistical error from the curve fitting.

 © 2006 Wiley-VCH Verlag GmbH & Co. KGaA, Weinheim

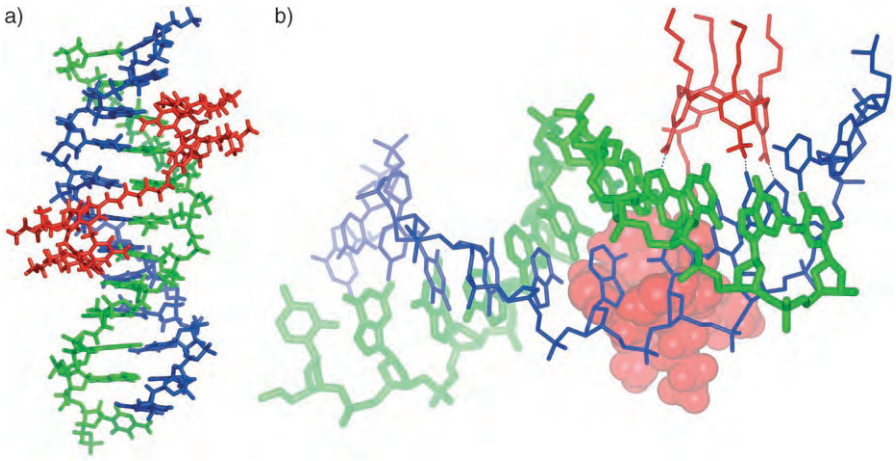

Figure 3. a) B-DNA (12 bp, green and blue) with tightly bound anilinocalixarene dimer (red). b) View along the major groove, revealing three hydrogen bond contacts between the ligand NH_2/NH_3^+ groups and various nucleic bases at the groove floor (MacroModel 7.0, MMFFs, water, 1000 steps).

molecular dynamics calculations demonstrate the remarkable stability of this arrangement: the overall structure is well maintained for 100 ps and even keeps five of six hydrogen bonds between DNA and the ligand.

Major grooves in RNA molecules are typically much more confined, with a maximum width of about 10 Å and a phosphate–phosphate distance of even less. Their profile (cross section) matches exactly the shape of our dimeric calixarene binder. If its preferred nucleic acid binding mode is truly insertion in the major groove, RNA should offer a superior microenvironment for **1a** through maximizing the van der Waals interactions. Remarkably, RNA affinities are 60-fold greater than that of DNA binding, and are only slightly lowered in 100 mM buffer (from 170 nM to 1.3 μM), indicating a perfect fit inside the major groove of the RNA (Table 2).[21]

A standard test for efficient DNA binding is the replacement of already intercalated ethidium bromide. At 1 μM, nonfluorescent 20-bp ds DNA with zero to three built-in mismatches shows a steady increase in fluorescence emission, which is in all cases almost completely quenched by an excess (30 equivalents) of added dimer; its occupance of the major groove consequently expels the ethidium bromide into the free solution. Although the values for the concentration at 50% dye displacement (C_{50}) are modest (owing to the high stoichiometric factor), the corresponding charge excess ratio at 50% dye displacement (CE_{50}) are, even at high salt loads, among the lowest ever reported for DNA binders, owing to the relatively low total charge of the calixarene (Figure 4, Table 3). Interestingly, the short 20-mer DNA strand bound just as well as the calf thymus DNA (ca. 10000 bp). Direct comparison with spermine revealed again the striking difference to polyamines: at physiological NaCl concentration, the dimer–DNA interaction is hardly weakened, whereas C_{50} and CE_{50} values for spermine drop by a factor of 300. We therefore conclude that the calixarene dimer does not attack the phosphodiester backbone by mere multiple salt bridges, but rather inserts into the spacious major groove where it can tolerate large amounts of competing ions.

According to recent reports, the DNA recognition efficiency of major groove binders can also be quantitatively characterized by ethidium bromide displacement assays;[22] hence, the respective K_a values for 20-mer ds DNA were calculated by the competitive method and surpass $10^6\,M^{-1}$, even at 100 mM NaCl.[23]

With the hexaaniline calixarene dimer, we have introduced a large amphiphilic molecule that selectively binds ds DNA and RNA with submicromolar K_D values in buffered aqueous solution; contrary to most other DNA binders, it most likely targets exclusively the major groove and causes no conformational change or (de)stabilization in the DNA duplex.

We will, in the future, try to investigate in detail the postulated binding mode by employing linear dichroism, NOESY, and atomic force microscopy techniques. Most importantly, however, an element of sequence selectivity can be introduced into the bridge, in the form of amide, ester, and thioether groups or amino acid side chains that interact with the base pairs on the floor of the major groove. Owing to

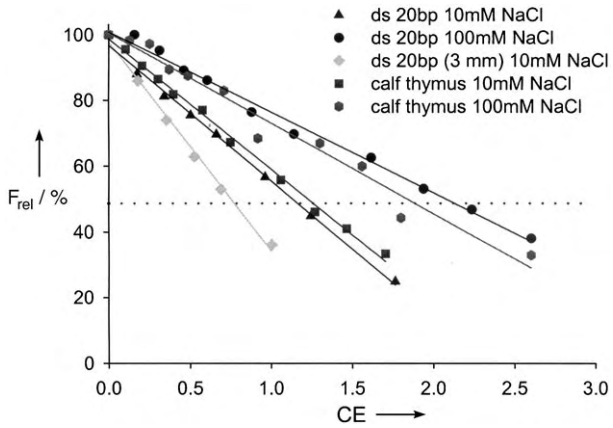

Figure 4. Ethidium bromide displacement from unlabeled DNA duplexes ($c = 1$ μM) by dimer **1a** (H_2O/MeOH 1:1, 9 mM or 100 mM NaCl, 2 mM HEPES, pH 7.0). F_{rel} = relative fluorescence emission intensity; CE = charge excess ratio.

Table 3: Ethidium bromide displacement assay for different double-stranded DNAs at different concentrations of NaCl.

DNA	[NaCl] [mM]	Nominal charge	C_{50} [μM]	CE_{50}
1a + 20 bp (3 mm)	9	+2	7.0	0.7
1a + 20 bp (0 mm)	9	+2	10.0	1.2
1a + 20 bp (0 mm)	100	+2	19.4	2.0
1a + calf thymus DNA	9	+2	9.0	1.3
1a + calf thymus DNA	100	+2	16.3	1.65
spermine + calf thymus DNA	9	+4	1.3	5.3
spermine + calf thymus DNA	150	+4	390	1560

© 2006 Wiley-VCH Verlag GmbH & Co. KGaA, Weinheim

this new binding mode, we expect the dimeric calixarene to find numerous applications as a sensitive analytical tool in DNA chemistry with a promising potential to control gene expression.

Received: August 18, 2005
Revised: January 20, 2006
Published online: March 20, 2006

Keywords: calixarenes · DNA · intercalation · major groove · supramolecular chemistry

[1] D. J. Newman, G. M. Cragg, K. M. Snader, *J. Nat. Prod.* **2003**, *66*, 1022 – 1037.
[2] H. Deng, V. A. Bloomfield, J. M. Benevides, G. J. Thomas, Jr., *Nucleic Acids Res.* **2000**, *28*, 3379 – 3385; For cationic DNA binders as transfection agents, see: A. D. Miller, *Angew. Chem.* **1998**, *110*, 1862 – 1880; *Angew. Chem. Int. Ed.* **1998**, *37*, 1768 – 1785, (liposomes); S. E. Stiriba, H. Frey, R. Haag, *Angew. Chem.* **2002**, *114*, 1385 – 1390; *Angew. Chem. Int. Ed.* **2002**, *41*, 1329 – 1334, (dendrimers); Y. Kakizawa, K. Kataoka, *Adv. Drug Delivery Rev.* **2002**, *54*, 203 – 222, (polymers).
[3] For a review on DNA intercalators, see: W. D. Wilson in *Comprehensive Natural Products Chemistry* (Eds.: K. Nakanishi, D. Barton), Elsevier, New York, **1999**, pp. 427 – 476.
[4] W. C. Tse, D. L. Boger, *Chem. Biol.* **2004**, *11*, 1607 – 1617; P. B. Dervan, *Bioorg. Med. Chem.* **2001**, *9*, 2215 – 2235; S. Neidle, *Nat. Prod. Rep.* **2001**, *18*, 291 – 309.
[5] For DNA binding agents, see: D. S. Johnson, D. L. Boger in *Comprehensive Supramolecular Chemistry* (Ed.: Y. Murakami), Elsevier, Oxford, **1996**, pp. 73 – 176; W. I. Sundquist, S. J. Lippard, *Coord. Chem. Rev.* **1990**, *100*, 293 – 322; P. D. Lawley, D. H. Philipps, *Mutat. Res.* **1996**, *355*, 13 – 40. For bulky adamantyl polyamines with a pronounced DNA preference, see: N. Lomadze, H.-J. Schneider, *Tetrahedron Lett.* **2002**, *43*, 4403 – 4405.
[6] A. Klug, D. Rhodes, *Trends Biochem. Sci.* **1988**, *13*, 465 – 469; M. Elrod-Erickson, T. E. Benson, C. O. Pabo, *Structure* **1998**, *6*, 451 – 464.
[7] W. H. Landschultz, P. F. Johnson, S. L. McKnight, *Science* **1988**, *240*, 1759 – 1764; Y. Fujii, T. Toda, M. Yanagida, T. Hakoshima, *Nat. Struct. Biol.* **2000**, *7*, 889 – 893.
[8] M. J. Hannon, V. Moreno, M. J. Prieto, E. Moldrheim, E. Sletten, I. Meistermann, C. J. Isaac, K. J. Sanders, A. Rodger, *Angew. Chem.* **2001**, *113*, 903 – 908; *Angew. Chem. Int. Ed.* **2001**, *40*, 879 – 884; I. Meistermann, V. Moreno, M. J. Prieto, E. Moldrheim, E. Slatten, S. Khalid, P. M. Rodger, J. C. Peberdy, C. J. Isaac, A. Rodger, M. J. Hannon, *Proc. Natl. Acad. Sci. USA* **2002**, *99*, 5069 – 5077.
[9] For permanently charged aminocalixarenes that stabilize ion-pairing interactions with ds DNA, see: Y. Shi, H.-J. Schneider, *J. Chem. Soc. Perkin Trans. 2* **1999**, 1797 – 1803; similar guanidinium calixarenes forming complexes with plasmid DNA: M. Dudic, A. Colombo, F. Sansone, A. Casnati, G. Donofrio, R. Ungaro, *Tetrahedron* **2004**, *60*, 11 613 – 11 618.
[10] R. Zadmard, M. Junkers, T. Schrader, T. Grawe, A. Kraft, *J. Org. Chem.* **2003**, *68*, 6511 – 6521.
[11] Similar observations have been reported by Gutsche and also Arduini: J. Wang, S. G. Bodige, W. H. Watson, C. D. Gutsche, *J. Org. Chem.* **2000**, *65*, 8260 – 8263; A. Arduini, A. Pochini, A. Secchi, *Eur. J. Org. Chem.* **2000**, 2325 – 2334.
[12] H. J. Schneider, R. Kramer, S. Simova, U. Schneider, *J. Am. Chem. Soc.* **1988**, *110*, 6442; C. S. Wilcox in *Frontiers in Supramolecular Chemistry* (Ed.: H. J. Schneider), VCH, Weinheim, **1991**, p. 123.
[13] Courtesy of the Carell group, LMU Munich, Germany.
[14] P. Job, *Ann. Chim.* **1928**, *9*, 113 – 203; M. T. Blanda, J. H. Horner, M. Newcomb, *J. Org. Chem.* **1989**, *54*, 4626 – 4636.
[15] A pK_a titration of the monomeric parent tetraanilinium calixarene, although hampered by its low solubility, pointed to an upper limit of p$K_a \approx 7.0$ for the last two deprotonation steps. Thus, at neutral pH, it seems probable that each calixarene unit carries no more than one positive charge. This value might be slightly altered by the considerable methanol content in most solvent mixtures.
[16] Dilution and variable temperature NMR experiments with **1a** produced only small chemical shift changes; dynamic light scattering (D. Joester, M. Losson, R. Pugin, H. Heinzelmann, E. Walter, H. P. Merkle, F. Diederich, *Angew. Chem.* **2003**, *115*, 1524 – 1528; *Angew. Chem. Int. Ed.* **2003**, *42*, 1486 – 1490) or GPC measurements would perhaps identify small oligomeric aggregates. However, it is also conceivable, that these are only formed after docking onto the DNA strand.
[17] In these cases, the calixarene dimer was precomplexed with calcein, forming a quite efficient 2:1 complex ($80\,000\,\text{M}^{-1}$). This highly fluorescent reporter molecule was subsequently replaced by the unlabeled native DNA in a competition experiment (indicator displacement assay, IDA).
[18] M. H. Hou, S.-B. Lin, J.-M. P. Yuann, W.-C. Lin, A. H.-J. Wang, L.-S. Kan, *Nucleic Acids Res.* **2001**, *29*, 5121 – 5128.
[19] L. W. Tari, A. S. Secco, *Nucleic Acids Res.* **1995**, *23*, 2065 – 2073.
[20] L. van Dam, N. Korolev, L. Nordenskiöld, *Nucleic Acids Res.* **2002**, *30*, 419 – 428.
[21] The minor groove of RNA is much more shallow, but has the same diameter as its major groove. It cannot, therefore, be ruled out that the calixarene dimer also binds to this well accessible cleft; such a recognition mode would also explain the high observed stoichiometry factor of 30:1.
[22] Y.-H. Shim, P. B. Arimondo, A. Laigle, A. Garbesi, S. Lavielle, *Org. Biomol. Chem.* **2004**, *2*, 915 – 921.
[23] We used the competitive method, with the binding constant for ethidium bromide $K_{EB} = 10^7\,\text{M}^{-1}$ for calf thymus DNA, as referenced in the literature. The noncompetitive method introduced by Boger et al. seems not to be applicable, because the intercepts with the *x*-axis point to large binding site sizes of > 2 (compare the high stoichiometries found in fluorescence titrations): D. L. Boger, B. E. Fink, M. P. Hedrick, *J. Am. Chem. Soc.* **2000**, *122*, 6382 – 6394.

 © 2006 Wiley-VCH Verlag GmbH & Co. KGaA, Weinheim

Binding Assays

DOI: 10.1002/anie.200503185

A Fluorescent Indicator To Visualize Activities of the Androgen Receptor Ligands in Single Living Cells**

*Muhammad Awais, Moritoshi Sato, Xianfen Lee, and Yoshio Umezawa**

Androgens are essential steroid hormones for the expression of the male phenotype. They play characteristic roles in the differentiation and development of the male embryo and in the initiation and maintenance of spermatogenesis. The biological activity of androgens is mediated by binding to the androgen receptor (AR).[1] The AR is a member of the nuclear receptor (NR) superfamily and regulates transcription of AR-specific target genes in response to its natural androgens such as testosterone and 5α-dihydrotestosterone (DHT).[1–3] The AR is an important pharmaceutical target for the treatment of prostate cancer. The transcriptional activity of the AR is suppressed in prostate-cancer treatment by using drugs that act as AR antagonists.[4,5] Certain environmental/industrial chemicals have been linked to the developmental and reproductive defects in wildlife and humans.[6] These chemicals mimic or block the natural androgen activities in the living body by binding with the AR. In vitro receptor binding[7,8] and reporter-gene assays[9–11] are used routinely to evaluate interactions of ligands with the AR. For a receptor-binding assay, a large amount of purified receptor protein is required and it is not possible to distinguish between the agonistic and antagonistic effects of a ligand. Reporter-gene assays, however, distinguish between agonist and antagonist ligands but require the incubation for more than 24 h of a ligand and a reporter gene in the culture media containing mammalian cells or yeast. To overcome these limitations, we developed a genetically encoded fluorescent indicator to visualize, in real time, the activities of AR ligands with different potencies in single living cells. In contrast to the previous assay methods, the present indicator discriminates agonists from antagonists within a few minutes.

The principle of the present indicator is shown schematically in Figure 1a. The ligand-binding domain (LBD) of an AR was connected to a coactivator peptide (^{488}HERAM**L**KR**LL**QRIDSKC^{503}) of Tat interactive protein-60 (Tip60)[12,13] through a flexible linker, $(GGNGG)_3$. This fusion protein was sandwiched between two spectral variants of green fluorescent protein (GFP)—cyan fluorescent protein (CFP, a donor) and yellow fluorescent protein (YFP, an acceptor)—in such a way that the excitation and emission spectra of these GFP mutants were suitable for fluorescence resonant energy transfer (FRET) from CFP to YFP.[14–17] This fusion protein functions as a *f*luorescent *i*ndicator to probe ligand-induced *c*onformational changes in the *a*ndrogen *r*eceptor (ficaro) thus allowing interaction with the coactivator peptide (Figure 1b) in an intramolecular FRET fashion.[14] The binding of an agonist to a receptor LBD induces a conformational change within the LBD that results in the creation of a recognition surface for a coactivator protein. A coactivator binds to that surface on LBD and this interaction stimulates transcription activity.[3,18–20] Most coactivator proteins contain conserved leucine-rich **L**XX**LL** motifs (L = leucine, X = any amino acid) that are responsible for interaction with agonist-bound AR LBD and other NRs.[3,13,19–23] The binding of an antagonist to a receptor, however, induces a different conformational change in which the extreme C-terminal helix 12 of the LBD invades the site for coactivator binding and does not allow the coactivator to interact with the receptor.[19,24] Addition of an AR agonist to cultured cells expressing ficaro promotes binding between the AR LBD and the Tip60 coactivator peptide and results in an increase in FRET from CFP to YFP. In contrast, addition of an antagonist does not result in an increase in the FRET response. The FRET approach has been used by several laboratories, including our own, for other proteins.[14–17] We applied this approach to a very important clinical target, the AR, to assay AR ligands in live cells.

After we confirmed the expression of the expected 85-kDa ficaro (Figure 1b) by western blotting analysis (Figure 1c), the response of ficaro was evaluated under a fluorescence microscope. Cultured cells were expressed with ficaro and stimulated with DHT (100 nM), an AR agonist. The CFP/YFP emission ratio decreased for several minutes and reached a plateau after approximately 20 min; no detectable change was observed in the control sample (without DHT) under otherwise identical experimental conditions. The time course of the CFP/YFP ratio change is shown Figure 2a, which indicates that FRET from CFP to YFP increases upon binding of DHT with ficaro. Figure 2b shows pseudocolor images of a cell expressed with ficaro when stimulated with DHT, illustrating a DHT-induced change in the CFP/YFP emission ratio of ficaro throughout the cell. To confirm that the increase in FRET was actually triggered by the AR LBD–coactivator interaction upon DHT stimulation, we made a ficaro mutant, ficaro/3A, by replacing all the hydrophobic leucine (L) residues of the LXXLL motif with alanine (A) residues (Figure 1b). As expected, the mutant ficaro did not show any significant change in the emission ratio of CFP/YFP upon DHT stimulation (Figure 2a). To confirm the binding of DHT to the AR LBD within ficaro, we performed a whole-cell binding assay.[31] As shown in Figure 2c, [^{3}H]DHT specifically binds with the ficaro. In contrast, the binding of

[*] Dr. M. Awais, Dr. M. Sato, X. Lee, Prof. Dr. Y. Umezawa
Department of Chemistry, School of Science
The University of Tokyo and
Japan Science and Technology Agency
Hongo, Bunkyo-ku, Tokyo 113-0033 (Japan)
Fax: (+81) 3-5841-8349
E-mail: umezawa@chem.s.u-tokyo.ac.jp
Dr. M. Sato
PRESTO
Japan Science and Technology Agency
4-1-8 Honcho Kawaguchi, Saitama (Japan)

[**] This work was supported by grants from the Japan Science and Technology Agency (JST) and the Japan Society for the Promotion of Science (JSPS).

 © 2006 Wiley-VCH Verlag GmbH & Co. KGaA, Weinheim

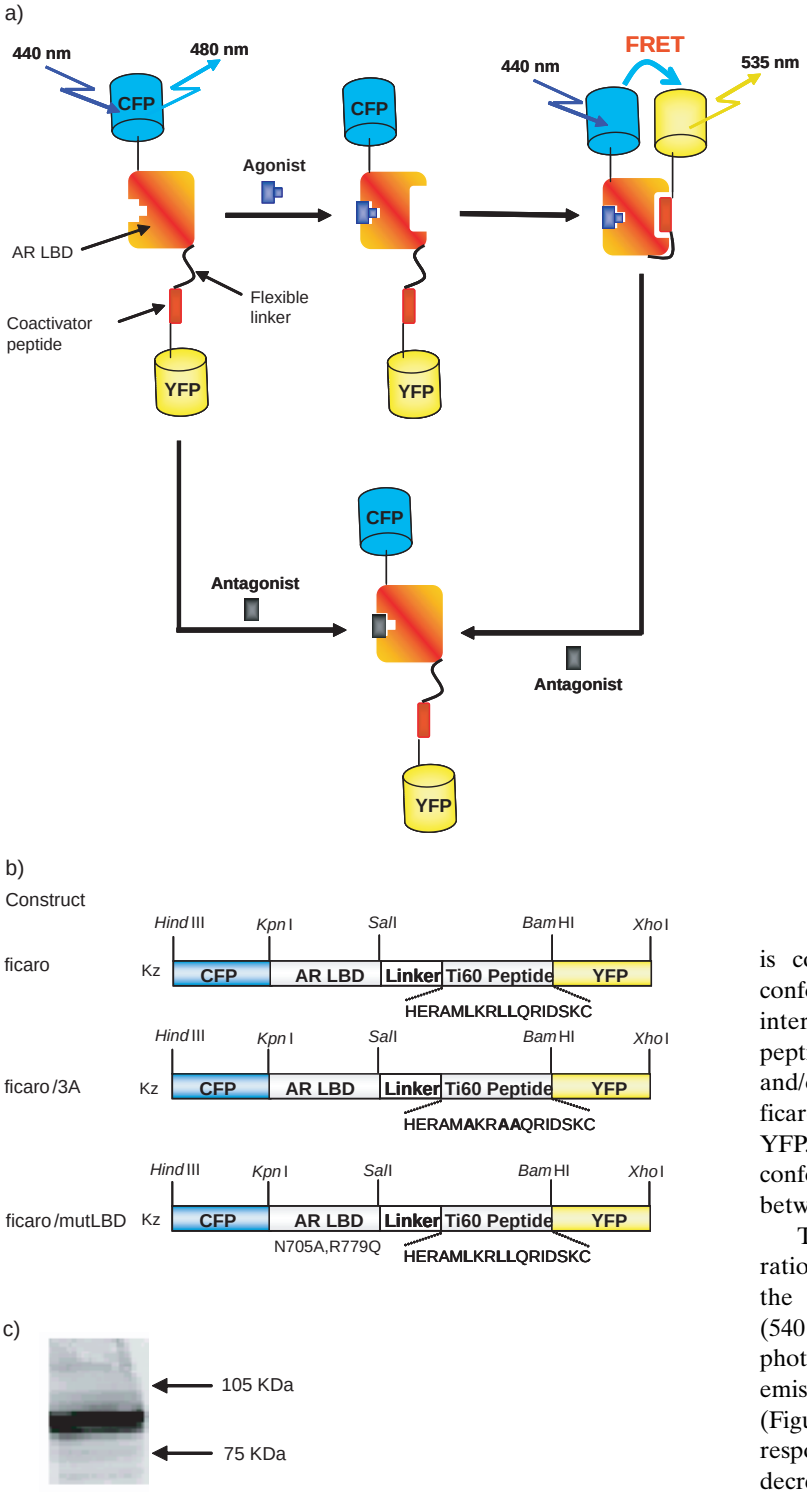

Figure 1. Fluorescent indicator for the ligand-induced coactivator recruitment to the AR LBD in living cells. a) Principle of the ficaro, based on intramolecular FRET, to visualize the ligand-dependent interaction between the AR LBD and the Tip60 coactivator peptide that contains the LXXLL motif. An agonist promotes binding between the AR LBD and the coactivator peptide. Consequently, CFP is oriented in close proximity to YFP, resulting in an increase in the FRET response. In contrast, an antagonist prevents binding of the coactivator peptide to the AR LBD. Replacement of an agonist with an antagonist results in dissociation of the receptor/coactivator complex to abolish the FRET change. The magnitude of the FRET strongly depends on the relative orientation and distance between the donor (CFP) and acceptor (YFP) fluorophore. b) Construct of indicators for expression and imaging in mammalian cells. Shown at top of each bar are the restriction sites. The Tip60 peptide contains 16 residues (488–503 amino acids). $(GGNGG)_3$ is a flexible linker that consists of 15 amino acids. AR LBD contains residues from 672–910 amino acids. CFP and YFP are different-colored mutants of GFP derived from *Aequorea victoria* with mammalian codons and the following additional mutations: CFP, F64L/S65T/Y66W/N146I/M153T/V163A/N212K, and YFP, S65G/V68L/Q69K/S72A/T203Y. Kz is an abbreviation for Kozak sequence, which allows optimal translation initiation in mammalian cells. In ficaro/3A, all the hydrophobic leucine (L) residues of the LXXLL motif of the Tip60 peptide were replaced with alanine (A) residues. To construct ficaro/mutLBD, Asn^{705} and Arg^{779} were replaced with alanine and glutamine,[25] respectively, in the AR LBD of ficaro. mutLBD = mutant ligand binding domain. c) Immunoblot analysis was performed as described in the Experimental Section using the whole-cell extract of PK-15 cells transfected with an expression vector encoding the ficaro construct and the expression of expected the 85-kDa protein was confirmed by western blotting.

[^{3}H]DHT with ficaro/mutLBD (Figure 1b), in which the Asn^{705} and Arg^{779} residues of AR LBD (which are essential for binding AR ligands) were replaced with alanine and glutamine, respectively,[25] is negligible relative to ficaro without any mutation in the AR LBD. In a cell-imaging experiment, no considerable change in the CFP/YFP emission ratio was obtained when cells expressed with ficaro/mutLBD were stimulated with DHT (Figure 2d). Taken all together, it is concluded that DHT binding to the AR induced a conformational change in the AR LBD that promoted interactions between the AR LBD and the coactivator peptide. This interaction resulted in a decrease in the distance and/or a change in orientation between CFP and YFP within ficaro, thereby increasing the efficiency of FRET from CFP to YFP. This allows real-time imaging of the DHT-induced conformation change in the AR LBD and interactions between AR and the coactivator in live cells.

To confirm that the decrease in the CFP/YFP emission ratio was caused by FRET, we carried out photobleaching of the acceptor fluorophore, YFP, within ficaro. Excitation (540 ± 12.5 nm) of a cell that expresses ficaro resulted in photobleaching of YFP and caused an increase in the donor emission from CFP owing to a breakdown in energy transfer (Figure 3a). As expected, the photobleached cell did not respond to DHT, although the unbleached cell gave a decrease in the CFP/YFP emission ratio after DHT stimulation (Figure 3b). This confirmed that the FRET response of ficaro was, in fact, due to the energy transfer from CFP to YFP upon coactivator-peptide binding to the AR within ficaro.

It has been demonstrated that AR LBD (C-terminal domain) preferably interacts with the FXXLF motif in the N-terminal domain of the same AR in an androgen-dependent manner.[26] When the Tip60 peptide in ficaro was replaced with the AR N-terminal domain peptide (^{20}RGAFQNLFQSV^{30}), which contains a FXXLF motif, a

 © 2006 Wiley-VCH Verlag GmbH & Co. KGaA, Weinheim

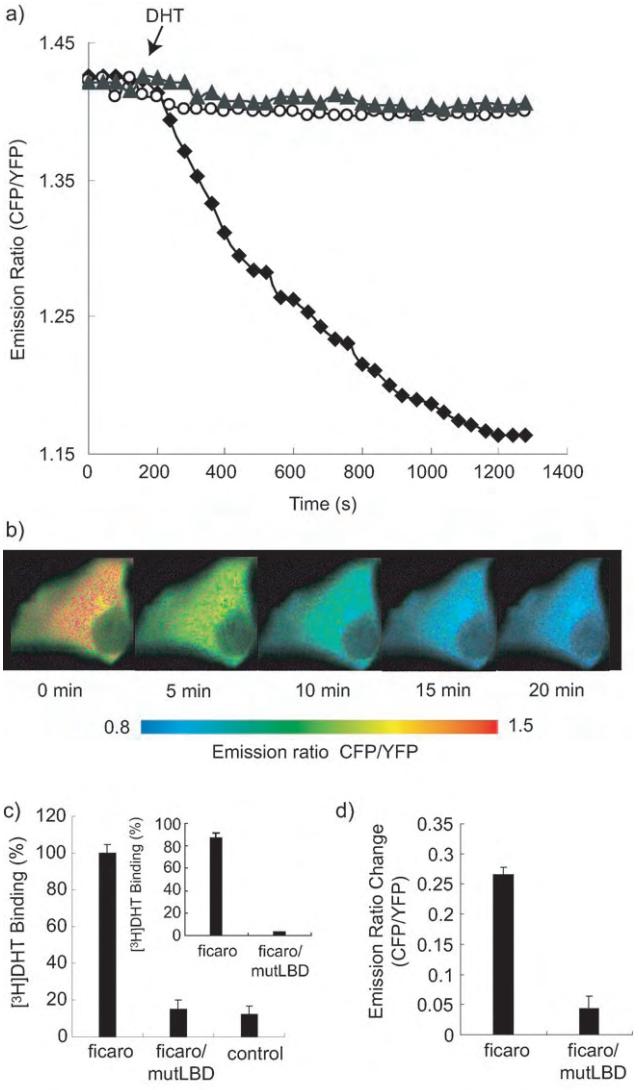

Figure 2. FRET was expressed as the CFP/YFP emission ratio. a) Time course of the FRET responses of ficaro upon (♦) DHT addition in live PK-15 cells, (○) with blank (in the absence of DHT), and (▲) response of the ficaro/3A (mutated ficaro) upon addition of DHT (100 nM) to PK-15 cells. For each experiment, the expression vector (0.8 μg) encoding ficaro was transfected into cultured PK-15 cells in 3.5-cm glass-bottomed dishes. Results represent typical observations from five independent trials. b) Pseudocolor images of the CFP/YFP emission ratio before ($t = 0$ min) and 5, 10, 15, and 20 min after the addition of DHT (100 nM), obtained from a cell expressed with ficaro. c) Specificity of the [^{3}H]DHT binding to ficaro. Whole-cell binding assays were performed as described in the Experimental Section. The specific binding of [^{3}H]DHT (5 nM) with ficaro, ficaro/mutLBD, and a control sample was obtained after subtraction of nonspecific binding of a 100-fold excess of [^{3}H]DHT with ficaro, ficaro/mutLBD, and control sample, respectively. The specific binding of [^{3}H]DHT with ficaro was considered as 100 percent. Inset: The specific binding value of the control sample was subtracted from the specific binding value of the ficaro and ficaro/mutLBD to evaluate the net specific binding of [^{3}H]DHT with ficaro and ficaro/mutLBD, respectively. The data are representative of three independent experiments. d) Comparison of the CFP/YFP emission ratio changes of ficaro and ficaro/mutLBD. PK-15 cells expressed with each ficaro and ficaro/mutLBD, respectively were stimulated with DHT (100 nM). The results are the means ± S.D. (standard deviation) of emission ratios from three different cells/experiments.

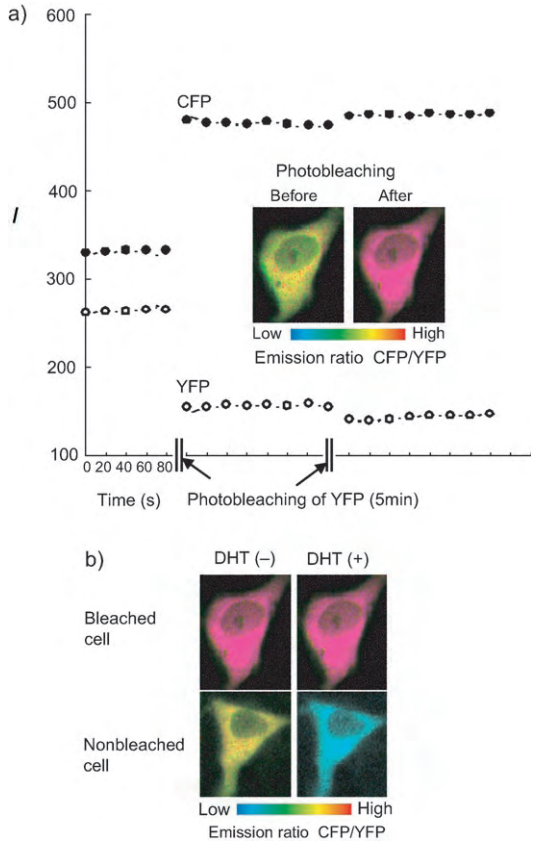

Figure 3. Photobleaching of YFP to assess the efficiency of FRET in ficaro. a) Photobleaching study of ficaro. Changes in the fluorescence intensity (I in arbitrary units) of CFP and YFP and in the CFP/YFP emission ratio (inset) after the cell expressing ficaro was excited at 540 ± 12.5 nm to photobleach the acceptor fluorophore, YFP. b) Pseudocolor images of the CFP/YFP emission ratio in the absence and presence of 100 nM DHT in bleached and nonbleached cells expressed with ficaro, respectively.

considerable increase in the FRET response was observed upon DHT stimulation (data not shown). This shows the ability of the AR LBD to interact with the LXXLL motif as well as the FXXLF motif. To construct ficaro for visualizing the activities of AR ligands in live cells, we adopted a general approach that can be applied not only to AR[13,22,27] but also to other NRs,[3,19–21,23] that is, the ligand-induced interaction of a receptor LBD with a coactivator LXXLL motif.

The response of the ficaro was imaged in other cell lines such as CHO-K1, HeLa, and human prostate cancer cells LNCaP and PC-3. The expression of ficaro in all these cells was very good, and no significant difference was observed in the CFP/YFP emission ratio change among PK15, CHO-K1, HeLa, LNCaP, and PC-3 cells (Figure 4a). Next, the response of ficaro was evaluated in the absence and presence of overexpressed Tip60 coactivator. The PK-15 cells transfected with ficaro in the absence and presence of overexpressed Tip60 exhibited similar responses (Figure 4b). The data in Figure 4a,b show that the endogenous Tip60 with differing concentrations in different cell lines does not interfere with the function of ficaro.

Androgens and other steroid compounds such as DHT, testosterone, progesterone, and cortisol were also applied to

 © 2006 Wiley-VCH Verlag GmbH & Co. KGaA, Weinheim

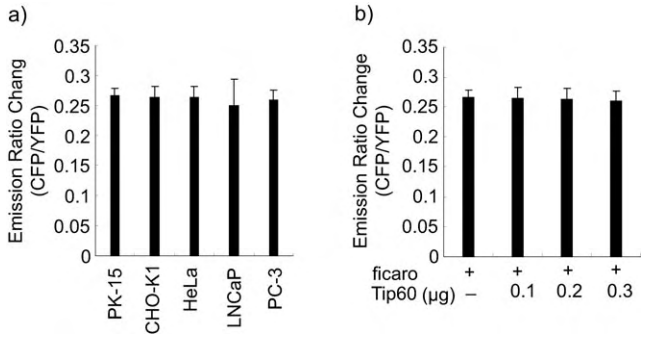

Figure 4. a) CFP/YFP emission ratio change of the ficaro expressed in PK-15, CHO-K1, HeLa, LNCaP, and PC-3 cells with stimulation by DHT (100 nM). For each experiment, cultured cells in 3.5-cm glass-bottomed dishes were transfected with pcDNA3.1 (+) vector (0.8 μg) encoding the ficaro. b) Response of the ficaro expressed in PK-15 cells in the absence and presence of overexpressed Tip60, respectively. The results in (a) and (b) are the means ± S.D. of emission ratios from three different cells/experiments.

ficaro to assess their ability to promote interactions between the AR LBD and the coactivator, as shown in dose-response curves (Figure 5). The effective concentration required for

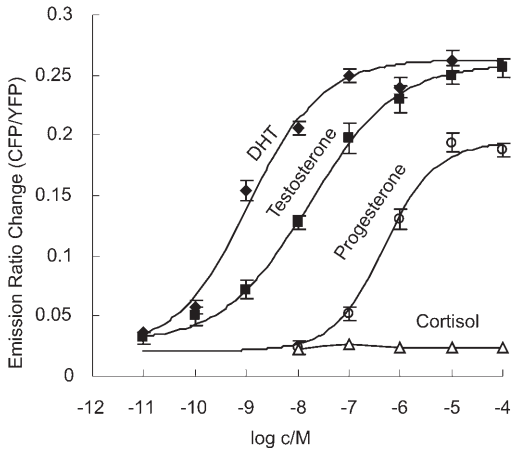

Figure 5. FRET responses of ficaro for various concentrations of DHT (◆), testosterone (■), progesterone (○), and cortisol (△). The results are the means ± S.D. of emission ratios from five different cells/experiments.

half-maximum CFP/YFP ratio change, EC_{50}, for DHT, testosterone, and progesterone were 1.1×10^{-9}, 1.7×10^{-8}, and 4.7×10^{-7} M, respectively. Cortisol did not show any response at all tested concentrations. The EC_{50} values of DHT, testosterone, and progesterone are comparable to those by a reporter-gene assay.[11] Testosterone induced the same extent of FRET response as that of DHT but with a 10-fold higher concentration than DHT. In contrast, progesterone did not display the same extent of the FRET level as induced by DHT even at the highest concentration used in the experiment. This difference in FRET levels between progesterone and DHT suggests that although progesterone promotes considerable binding of the coactivator peptide to the AR, it probably does not induce a conformation change in precisely the same way as a full agonist such as DHT or testosterone. The suboptimal conformation induced by progesterone in the AR LBD might be responsible for a weak binding between the AR LBD and the coactivator peptide that resulted in a submaximal response by progesterone in Figure 5. Progesterone was previously shown to bind with AR and exert partial agonist activity at high concentrations in mammalian cells.[28] Thus, our indicator discriminates between full and partial agonists.

Next, we evaluated the response of ficaro with AR antagonists. Cells expressing ficaro were treated with flutamide (1.0 μM), an AR antagonist.[5,10] No change in the CFP/YFP ratio was observed (Figure 6a). Flutamide and other AR antagonists[9,10,29] such as genistein (Gen, a phytoestrogen), bisphenol-A (Bis-A, an environmental endocrine disruptor (ED)), procymidone (a fungicide and an ED), and nonylphenol (NP, an environmental ED) were each added to cells at concentrations of 0.01–100 μM to determine their ability to induce FRET. No increase in FRET was observed with these chemicals (data not shown). Next, we visualized the ability of flutamide to replace testosterone from the AR LBD within ficaro. Cells were stimulated first with testosterone (100 nM).

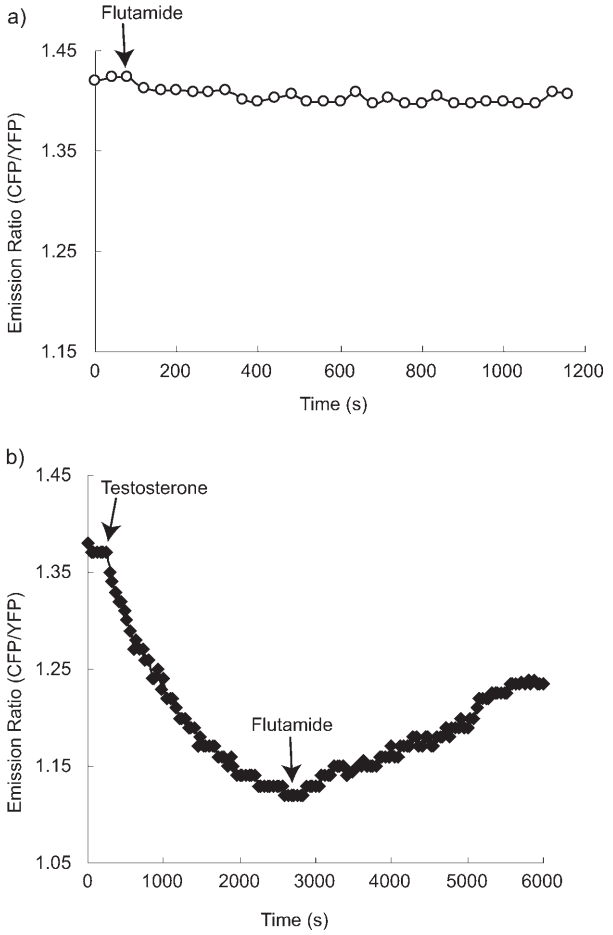

Figure 6. a) Time course of the FRET response of ficaro upon addition of flutamide (1.0 μM) to a cultured cell expressing ficaro. b) Time course of the FRET response upon stimulating the cell expressing ficaro with testosterone (100 nM) followed by the addition of flutamide (10 μM) in the same cell without washing the testosterone.

 © 2006 Wiley-VCH Verlag GmbH & Co. KGaA, Weinheim

A clear decrease in the CFP/YFP emission ratio (increase in the FRET) was observed. Upon reaching a plateau, flutamide (10 μM) was added. A significant increase in the emission ratio of CFP/YFP (decrease in the FRET) was observed (Figure 6b), whereas there was no detectable change in the ratio upon the addition of a compound that has a very weak binding affinity for AR (neither agonist nor antagonist), such as cortisol[8,10] or in a control sample under otherwise identical experimental conditions (data not shown). The flutamide-induced decrease in the FRET response of ficaro represents the ability of flutamide to convert AR from an activated conformation into an inactivated mode by displacing testosterone from the LBD of the receptor, the process of which corresponds to hormone therapy for prostate cancer.[4,5] The results demonstrate the usefulness of ficaro to screen both agonism and antagonism of compounds in a single run of the screening.

Figure 7 displays data showing the abilities of AR antagonists such as flutamide, Gen, Bis-A, procymidone, and NP to inhibit the activity of DHT. The response of ficaro for DHT (10 nM) was measured at different concentrations of each antagonist. Flutamide inhibited the activity of DHT in a dose-dependent manner. Gen and Bis-A also inhibited the action of DHT; in both cases a full dose-response curve was obtained. The concentration required for a half-maximum inhibition of DHT activity, IC_{50}, for flutamide, Gen, and Bis-A obtained from the response curves (Figure 7) were converted into equilibrium dissociation constants, K_i, using the Cheng–Prusoff equation.[30] The K_i values for flutamide, Gen, and Bis-A were 8.1×10^{-6}, 5.0×10^{-5}, and 9.1×10^{-5} M, respectively.

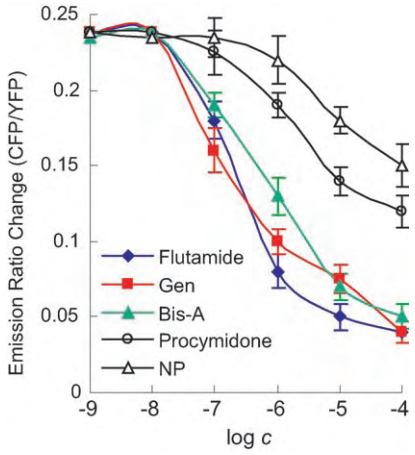

Figure 7. Emission ratio change for DHT (10 nM) was assessed in the presence of flutamide, Gen, Bis-A, procymidone, and NP, respectively, at various concentrations. For each experiment, the antagonist of various concentrations (1.0 nM–100 μM) was added to glass-based dishes containing PK-15 cells expressing the ficaro indicator and the resultant mixture incubated for 10–12 min at room temperature. Cells were imaged and DHT (10 nM) was added to the same cells without washing the antagonist to monitor the inhibitory effect of the antagonist on the DHT-induced receptor/coactivator interaction within ficaro. The results are the means ± S.D. of emission ratios from three different cells/experiments.

Procymidone and NP exhibited a weak inhibitory effect; the activity of DHT decreased by about 50% and 40%, respectively, with their highest concentration used in the experiment. From these results, it is concluded that flutamide is a strong AR antagonist followed by Gen and Bis-A, whereas procymidone and NP are weaker antagonists. Flutamide, Gen, and Bis-A, according to a receptor-binding assay,[8] showed high affinity for AR with potency almost equal to each other. The weak antagonistic activity of procymidone and NP is in agreement with previous reports in which both compounds showed very weak antagonist effects.[8,9]

The difference in the K_i values obtained by a binding assay and by the present method is most probably due to the fact that a binding assay represents the direct binding event of a ligand with a purified receptor, whereas the present FRET-based method represents the ability of a ligand, after penetrating through the cell membrane, to induce a distinct conformational change in the receptor that promotes/inhibits the interaction of the receptor with the coactivator. The receptor/coactivator interaction is a critical step for the transcription activation of the receptor. Therefore, the behavior of ficaro in response to a ligand, drug, or endocrine disruptor in the intact cells mimics endogenous functioning of the AR, which is present in various cells of a living body.

In conclusion, we have designed a sensitive fluorescent indicator to visualize, in real time, activities of the AR ligands in the physiological environment of single living cells. The indicator is capable of distinguishing ligands of different potencies for the AR. The present assay is not intended to read out the binding affinity of a drug but rather its efficacy as either an antagonist or partial agonist in vivo. The permeability of a drug into cells and the conformational changes induced in the AR all determine its efficacy, much more than a simple binding assay. Progesterone, glucocorticoid, and peroxisome proliferator activated receptors (PR, GR, and PPAR, respectively) also belong to the NR family and play important roles in the mediation of the actions of drugs for contraception (by PR), inflammation (by GR), and type-2 diabetes (by PPARγ). The present strategy of ficaro can be used to develop indicators for PR, GR, and PPARγ for screening and characterization of their ligands. The indicators would be helpful in the development of NR-based pharmaceutical drugs against different diseases.

Experimental Section

Materials: Fetal calf serum (FCS), Hank's balanced salt solution (HBSS), and LipofectAMIN 2000 reagents were purchased from Life Technologies (Rockville, MD). Minimum essential medium (MEM), trypsin-EDTA, DHT, testosterone, progesterone, cortisol, flutamide, Gen, Bis-A, procymidone, and NP were obtained from Sigma Chemicals Co. (St. Louis, MO). [1,2,4,5,6,7-^{3}H]DHT was supplied by Amersham Biosciences. Anti-GFP antibody was obtained from Clontech (Palo Alto, CA). All cloning enzymes were acquired from Takara Biomedical (Tokyo, Japan). The human AR cDNA plasmid was purchased from American Type Culture Collection (ATCC, VA, USA). A mammalian expression vector pcDNA3.1 (+) was obtained from Invitrogen Co. (Carlbad, CA). All other chemicals used were of analytical reagent grade. Human Tip60 in pcDNA 3.1 (+) under the

 © 2006 Wiley-VCH Verlag GmbH & Co. KGaA, Weinheim

control of CMV promoter was a kind gift from Dr. T. Suzuki (Graduate School of Pharmaceutical Sciences, Hokkaido University, Japan). LNCaP and PC-3 cells were kindly provided by Dr. Y. Hattori (Institute of Medicinal Chemistry, Hoshi University, Japan).

Plasmid construction: To prepare the cDNAs for the constructs shown in Figure 1b, fragment cDNAs of ECFP (1–238 amino acids), EYFP (1–238 amino acids), human AR LBD (672–910 amino acids), the flexible linker $(GGNGG)_3$, and Tip60 peptide (488–503 amino acids) were generated by standard polymerase chain reaction (PCR) to attach a Kozak sequence and restriction sites shown in constructs. In ficaro/3A, all the hydrophobic leucine residues of the LXXLL motif of the Tip60 peptide were replaced with alanine residues. To construct ficaro/mutLBD, Asn^{705} and Arg^{779} were replaced with alanine and glutamine, respectively[25] in the AR LBD of ficaro. The sequences of the pairs of complementary oligonucleotides used for generating these mutations are as following: (N705A) 5′TTGCTCTCTAGCCTCGCTGAACTGGGAGAGAGA3′ and 5′TCTCTCTCCCAGTTCAGCGAGGCTAGAGAGCAA3′; (R779Q) 5′GCATGCACAAGTCCCAGATGTACAGCCAGTG3′ and 5′CACTGGCTGTACATCTGGGACTTGTGCATGC3′. All PCR fragments were sequenced with an ABI310 genetic analyzer. The cDNAs were inserted at *Hind*III and *Xho*I sites of mammalian expression vector pcDNA3.1 (+).

Cell culture and transfection: PK-15 and CHO-K1 were cultured in MEM and F-12, respectively; HeLa, PC-3, and LNCaP cells were cultured in DMEM supplemented with FCS (10%), sodium pyruvate (1.0 mM) and nonessential amino acids (0.1 mM), respectively at 37°C in a humidified atmosphere of CO_2 (5%). Cells were transfected with an expression vector pcDNA3.1 (+) containing ficaro in the presence of LipofectAMIN 2000 reagent in 3.5-cm glass-bottomed dishes.

Immunoblot analysis for protein expression: The cell lysate of PK-15 transfected with pcDNA3.1 (+) encoding ficaro was subjected to SDS-PAGE by using 10% polyacryamide gel electrophoresis and electrophoretically transferred onto a nitrocellulose membrane. The membrane was probed with anti-GFP antibody (1:500 in skimmed milk (1%) in TBST (tris-HCl (50 mM; pH 8.0), NaCl (150 mM), tween 20 (0.05%))) and then with alkaline phosphatase-labeled anti-rabbit antibody (1:5000 in skimmed milk (1%) in TBST). The protein expression (Figure 1c) was analyzed with an image analyzer (LAS-1000 plus, Fujifilm Co., Tokyo, Japan) by using an ECL kit (Amersham Biosciences, UK).

Steroid-binding assay: Whole-cell binding assay[31] was performed to check the specificity of DHT binding with the AR LBD within ficaro. PK-15 cells were transfected with each expression vector encoding ficaro, ficaro/mutLBD, and CFP only (control). Cells were placed 24 h prior to the binding reaction in a medium free of serum and phenol red and incubated for 2 h at 37°C with [^{3}H]DHT (5 nM). Nonspecific binding of [^{3}H]DHT was assessed by adding a 100-fold excess of unlabeled DHT. Cells were washed twice in phosphate-buffered saline, harvested in a buffer containing SDS (2%), glycerol (10%), and tris (10 mM; pH 6.8), and the radioactivity was determined by a scintillation counter.

Cell imaging: The culture medium was replaced with HBSS for fluorescence imaging experiments. Within 12–24 h after transfection, the cells were imaged at room temperature on a Carl Zeiss Axiovert 135 microscope with a cooled charge-coupled device camera MicroMAX (Roper Scientific Inc, Tucson, AZ), controlled by MetaFluor (Universal Imaging, West Chester, PA). The exposure time at $440\pm$ 10-nm excitation was 100 ms. Fluorescence images were obtained through 480 ± 15 nm and 535 ± 12.5 nm filters with a $40\times$ oil-immersion objective (Carl Zeiss, Jena, Germany). Moderately bright cells were selected for imaging experiments.

Received: September 8, 2005
Revised: February 13, 2006
Published online: March 23, 2006

Keywords: agonists · antagonists · fluorescent probes · FRET (fluorescence resonant energy transfer) · receptors

[1] J. Gobinet, N. Poujol, C. Sultan, *Mol. Cell. Endocrinol.* **2002**, *198*, 15–24.
[2] A. Aranda, A. Pascual, *Phys. Rev. B* **2001**, *81*, 1269–1304.
[3] W. Bourguet, P. Germain, H. Gronemeyer, *Trends Pharmacol. Sci.* **2000**, *21*, 381–388.
[4] U. Fuhrmann, K. Parczyk, M. Klotzbucher, H. Klocker, A. C. B. Cato, *J. Mol. Med.* **1998**, *76*, 512–524.
[5] P. Iversen, I. Melezinek, A. Schmidt, *BJU Int.* **2001**, *87*, 47–56.
[6] J. S. Fisher, *Reproduction* **2004**, *127*, 305–315, and references therein.
[7] A. Freyberger, H. J. Ahr, *Toxicology* **2004**, *195*, 113–126.
[8] H. Fang, W. Tong, W. S. Branham, C. L. Moland, S. L. Dial, H. Hong, Q. Xie, R. Perkins, W. Owens, D. M. Sheehan, *Chem. Res. Toxicol.* **2003**, *16*, 1338–1358.
[9] P. Roy, H. Salminen, P. Koskimies, J. Simola, A. Smeds, P. Saukko, I. T. Huhtaniemi, *J. Steroid Biochem. Mol. Biol.* **2004**, *88*, 157–166.
[10] P. Sohoni, J. P. Sumpter, *J. Endocrinol.* **1998**, *158*, 327–339.
[11] K. W. Gaido, L. S. Leonard, S. Lovell, J. C. Gould, D. Babai, C. J. Portier, D. P. McDonnell, *Toxicol. Appl. Pharmacol.* **1997**, *143*, 205–212.
[12] M. E. Brady, D. M. Ozanne, L. Gaughan, I. Waite, S. Cook, D. E. Neal, C. N. Robson, *J. Biol. Chem.* **1999**, *274*, 17599–17604.
[13] L. Gaughan, M. E. Brady, S. Cook, D. E. Neal, C. N. Robson, *J. Biol. Chem.* **2001**, *276*, 46841–46848.
[14] A. Miyawaki, J. Llopis, R. Heim, J. M. McCaffery, J. A. Adams, M. Ikura, R. Y. Tsien, *Nature* **1997**, *388*, 882–887.
[15] M. Sato, Y. Ueda, T. Takagi, Y. Umezawa, *Nat. Cell. Biol.* **2003**, *5*, 1016–1022.
[16] M. Awais, M. Sato, K. Sasaki, Y. Umezawa, *Anal. Chem.* **2004**, *76*, 2181–2186.
[17] R. Michalides, A. Griekspoor, A. Balkenende, D. Verwoerd, L. Janssen, K. Jalink, A. Floore, A. Velds, L. V. Veer, J. Neefjes, *Cancer Cell* **2004**, *5*, 597–605.
[18] P. M. Matias, P. Donner, R. Coelho, M. Thomaz, C. Peixoto, S. Macedo, N. Otto, S. Joschko, P. Scholz, A. Wegg, S. Bäsler, M. Schäfer, U. Egner, M. A. Carrondo, *J. Biol. Chem.* **2000**, *275*, 26164–26171.
[19] A. K. Shiau, D. Barstad, P. M. Loria, L. Cheng, P. J. Kushner, A. D. Agard, G. L. Greene, *Cell* **1998**, *95*, 927–937.
[20] R. T. Nolte, G. B. Wisely, S. Westin, J. E. Cobb, M. H. Lambert, R. Kurokawa, M. G. Rosenfeld, T. M. Wilson, C. K. Glass, M. V. Milburn, *Nature* **1998**, *395*, 137–143.
[21] D. M. Herry, E. Kalkhoven, S. Hoare, M. G. Parker, *Nature* **1997**, *387*, 733–736.
[22] H. Ma, S. M. Huang, R. A. Irvin, P. Webb, P. J. Kushner, G. A. Coetzee, M. R. Stallcup, *Mol. Cell. Biol.* **1999**, *19*, 6164–6173.
[23] R. S. Savkur, T. P. Burris, *J. Pept. Res.* **2004**, *63*, 207–212.
[24] W. Bourguet, V. Vivat, J. M. Wurtz, P. Chambon, H. Gronemeyer, D. Moras, *Mol. Cell* **2000**, *5*, 289–298.
[25] N. Poujol, J. M. Wurtz, B. Tahiri, S. Lumbroso, J. C. Nicolas, D. Moras, C. Sulatan, *J. Biol. Chem.* **2000**, *275*, 24022–24031.
[26] B. He, J. A. Kemppainen, E. M. Wilson, *J. Biol. Chem.* **2000**, *275*, 22986–22994.
[27] H. C. Shen, G. Buchanan, L. M. Butler, J. Prescott, M. Henderson, W. D. Tilley, G. A. Coetzee, *Biol. Chem.* **2005**, *386*, 69–74.
[28] A. M. Vinggaard, E. C. B. Joergensen, J. C. Larsen, *Toxicol. Appl. Pharmacol.* **1999**, *155*, 150–160.
[29] R. S. R. Zand, D. J. A. Jenkins, T. J. Brown, E. P. Diamandis, *Clin. Chim. Acta* **2002**, *317*, 17–26.
[30] H. C. Cheng, *Pharmacol. Res.* **2004**, *50*, 21–40.
[31] H. J. Lee, S. Chattopadhyay, E. Y. Gong, R. S. Ahn, K. Lee, *Toxicol. Sci.* **2003**, *75*, 40–46.

 © 2006 Wiley-VCH Verlag GmbH & Co. KGaA, Weinheim

Self-Assembly

DOI: 10.1002/anie.200503632

Generating Isotropic Superparamagnetic Interconnectivity for the Two-Dimensional Organization of Nanostructured Building Blocks**

*Hao Ming Chen, Ru-Shi Liu, Hongliang Li, and Hua Chun Zeng**

Apart from materials synthesis, the development of methods for the organization of discrete nano-objects and nano-building blocks into larger configurations and conformations represents a challenging area in nanomaterials research.[1] A number of strategies which make use of various interaction forces among the assembling units have been developed. For example, chemical bonding,[2–5] van der Waals forces,[6–9] solvent adhesion and capillary forces,[10] hydrophilic and hydrophobic interactions,[11,12] electrostatic forces,[13] and magnetic attraction and repulsion have been employed in the self-organization of nanomaterials.[14–17] The major interactive forces involved in the organizing processes have been generated either through the utilization of intrinsic material properties, or through extrinsic modifications, such as introducing overlayers onto the surfaces of nano-objects,[6–10] or inserting functional segments into individual nano-building units.[15,16]

Among the various assembly strategies, surfactant mediation is a widely used approach for preparing 1D, 2D, and 3D assemblies and/or superlattices of monodisperse nanoparticles.[6–9] In this method, interconnectivity is generated through the van der Waals interactions of organic surfactants anchored on the external surfaces of the nanoparticles. Owing to the surface organic species, interparticulate spaces are always present in the assemblies, although these spaces can be tuned easily by varying the length and density of the chelated surfactants. Strictly speaking, the constructional units in such assemblies do not come into direct contact, and the included surfactants may alter the chemical nature of the organized material. Compared to the surfactant-mediated strategy, assembly using magnetic forces has received less attention, despite several important advancements in recent years.[14–17] For example, magnetic-moment alignment has been utilized in the head-to-tail or side-by-side organization, without surfactants, of 1D nanostructures (such as nanorods).[15,16] Although nonpermanent noncontact 2D lattices of magnetic particles have been obtained with the assistance of external magnetic fields,[18] stably ordered 2D assemblies of discrete nanostructures under both (external magnetic) field-free and surfactant-free conditions have remained unexplored.

Cubic structures are ideal building blocks for 2D construction and expansion. Herein, isotropic superparamagnetic interactions are used to assemble surface-reduced nanocubes of spinel cobalt oxide (Co_3O_4, an antiferromagnetic material) into ordered 2D arrays, in the absence of organic surfactants or external magnetic fields.

Figure 1 shows pristine Co_3O_4 nanocubes prepared using a modified surfactant-free method, in which Co_3O_4 was formed gradually from the reaction of cobalt hydroxides and dissolved oxygen in an aqueous medium.[19] The boundary planes of the as-prepared nanocubes are {100}, {010}, and {001}, with an average edge length of 33.8 ± 3.4 nm. Since Co_3O_4 is antiferromagnetic, the aggregation of the nanocubes on the transmission electron microscopy (TEM) sample grid is apparently random (Figure 1a–c). In some cases, however, close contacts between nanocubes are also observed, owing to the capillary effect of solvent trapped between the Co_3O_4 crystal planes during the drying of the suspension (Figure 1b,c). Structural and compositional characterization of the Co_3O_4 nanocubes was carried out by powder X-ray diffraction (XRD; JCPDS file no. 43-1003, $Fd\bar{3}m$, $a = 8.084$ Å), selected-area electron diffraction (SAED; Figure 1d), and energy dispersive X-ray spectroscopy (EDX; found Co/O atomic ratio $\approx 3/4$).

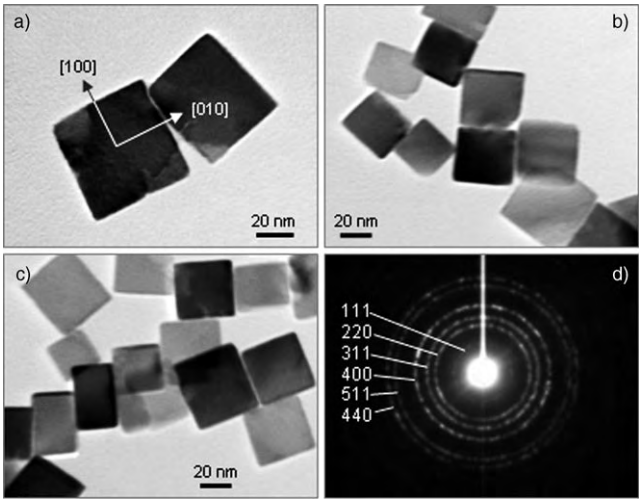

Figure 1. a)–c) TEM images and d) SAED pattern of the as-prepared Co_3O_4 nanocubes, which are randomly aggregated.

[*] Prof. Dr. H. C. Zeng
Department of Chemical and Biomolecular Engineering
Faculty of Engineering, National University of Singapore
10 Kent Ridge Crescent, Singapore 119260 (Singapore)
Fax: (+65) 6779-1936
E-mail: chezhc@nus.edu.sg
H. L. Li
Department of Electrical and Computer Engineering
Faculty of Engineering, National University of Singapore
10 Kent Ridge Crescent, Singapore 119260 (Singapore)
H. M. Chen, Prof. Dr. R.-S. Liu
Department of Chemistry
College of Science, National Taiwan University
No. 1, Sec. 4, Roosevelt Road
Taipei 106, Taiwan (Republic of China)

[**] The authors gratefully acknowledge the financial support of the Ministry of Education, Singapore.

Supporting information for this article is available on the WWW under http://www.angewandte.org or from the author.

 © 2006 Wiley-VCH Verlag GmbH & Co. KGaA, Weinheim

The pristine nanocubes were treated with N_2H_4 at room temperature, which led to the partial reduction of divalent and trivalent cobalt cations on the nanocube surfaces. This redox process was accompanied by the evolution of nitrogen gas from the suspension, and can be described by Equation (1). The formation of metallic cobalt on the surfaces of

$$Co_3O_4 + 2\,N_2H_4 \rightarrow 3\,Co + 2\,N_2 + 4\,H_2O \quad (1)$$

the nanocubes is also evident in the TEM images of the reduced product. In contrast to the as-prepared nanocubes (Figure 1, Figure 3a), the surface-reduced Co/Co_3O_4 nanocubes are aligned in 2D arrays (ordering range 250–600 nm; Figure 2, Figure 3b, and Supporting Information). Since no surfactants were used in our synthesis, the surfactant-assisted assembly mechanism can be ruled out.[6–9] Owing to the redox reaction in Equation (1), the observed organization can be attributed to a weak magnetic attraction among the metallic cobalt particles present on the nanocube surfaces. There is essentially no space between the smooth Co/Co_3O_4 nanocubes, in contrast to organic-surfactant-assisted assemblies of nonmagnetic or magnetic nanoparticles, in which interparticle spaces with sizes depending on the length and interpenetration of the surfactants are invariably observed. The Co/Co_3O_4 nanocubes of Figure 2 thus represent the first ordered 2D arrays of intimately connected nanoparticles assembled through the use of surface magnetic interactions, without organic surfactants or external magnetic fields.

The surface reduction of Co_3O_4 nanocubes with N_2H_4 was further investigated using both the bulk-phase analytical method XRD and the surface-sensitive technique X-ray photoelectron spectroscopy (XPS). The similarity of the XRD patterns of the nanocubes before (Co_3O_4) and after (Co/Co_3O_4) the reduction (Figure 4a) reveals that no phase change occurs in the bulk sample, and suggests that the reduction takes place primarily on the nanocube surfaces; note that the metallic cobalt surfaces are too thin to be detected by XRD. The XP spectrum of the Co/Co_3O_4 nanocubes after the reduction (Figure 4b) confirms the presence of metallic cobalt on the nanocube surfaces. In the XP spectrum of the as-prepared sample, Co $2p_{3/2}$ peaks at 779.9 and 781.7 eV can be assigned to Co_3O_4 and CoO phases,

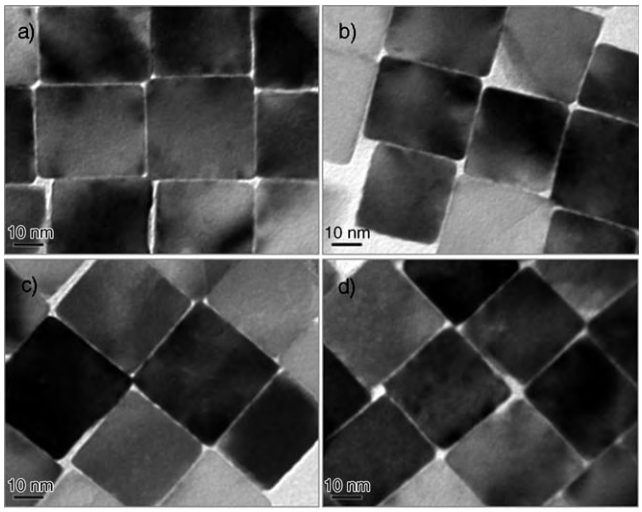

Figure 2. a)–d) TEM images of the surface-reduced Co/Co_3O_4 nanocubes, which are assembled in an ordered 2D array. Note that the nanocubes are in mutual contact.

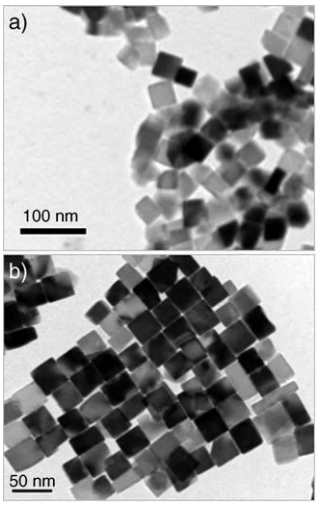

Figure 3. Comparison of TEM images of a) the as-prepared Co_3O_4 nanocubes, and b) the surface-reduced Co/Co_3O_4 nanocubes. The nanocubes in (a) are essentially randomly distributed, while those in (b) are assembled in a 2D array with long-range order.

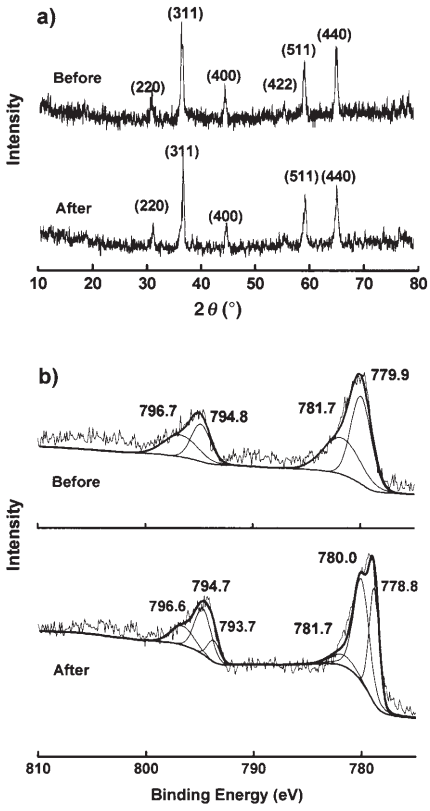

Figure 4. a) XRD patterns and b) XP spectra (Co 2p core level) of the nanocubes before (Co_3O_4) and after (Co/Co_3O_4) surface reduction. In (b), the fits (bold) to the experimental spectra are derived from curves for Co_3O_4, CoO, and in the case of the Co/Co_3O_4 nanocubes, Co. See text for discussion of spectral details.

 © 2006 Wiley-VCH Verlag GmbH & Co. KGaA, Weinheim

respectively (there is always an equilibrium of these two chemical species on the surfaces of air-handled Co_3O_4 samples).[20] In agreement with these assignments, deconvoluted Co $2p_{1/2}$ counterpart branches are observed for the Co_3O_4 and CoO phases at 794.8 and 796.7 eV, both approximately 15 eV higher in energy than the Co $2p_{3/2}$ branches.[20] In the XP spectrum of the surface-reduced Co/Co_3O_4 nanocubes, a pronounced new Co $2p_{3/2}$ peak corresponding to metallic cobalt appears at 778.8 eV, accompanied by its corresponding $2p_{1/2}$ peak at 793.7 eV.[19] Therefore, our complementary XRD and XPS investigations confirm unambiguously that the surfaces of the Co_3O_4 nanocubes have been partially reduced to metallic cobalt, while their bulk remains largely unmodified.

The interactions between the cobalt particles generated on the outer surfaces of the Co_3O_4 nanocubes were investigated by characterizing the magnetic properties of the reduced Co/Co_3O_4 sample. In Figure 5a, the zero-field-cooled (ZFC) and field-cooled (FC) magnetization of the pristine Co_3O_4 and reduced Co/Co_3O_4 nanocubes are reported as a function of temperature. The ZFC magnetization curves of both the as-prepared and surface-reduced nanocubes show a pronounced cusp at approximately 32–35 K (the Néel point T_N of Co_3O_4).[21] The dip on the lower-temperature side of the cusp is then followed by an increase in the sample magnetization at approximately 15 K, which is more dramatic for the surface-reduced nanocubes. Furthermore, the ZFC and FC curves of the as-prepared sample overlap at temperatures above T_N, while the curves of the surface-reduced nanocubes only merge above approximately 120 K. All these observations indicate a higher magnetization in the reduced sample. Hysteresis-loop measurements on the Co_3O_4 and Co/Co_3O_4 nanocubes at different temperatures (Figure 5b,c) are consistent with the ZFC–FC findings. In general, the magnetization of the as-prepared Co_3O_4 sample is less sensitive to temperature change. On the other hand, the surface-reduced Co/Co_3O_4 nanocubes show much higher magnetizations and a larger dependence on the measuring temperature. As detailed in Figure 5b, the magnetization of the two samples increases substantially at lower temperatures, and both remanence and coercivity (that is, ferromagnetic hysteresis) are noticeable at 5 K. The ferromagnetism is stronger in the reduced nanocubes (Figure 5a,b). At higher temperatures (for example, 280 K), both the Co_3O_4 and the Co/Co_3O_4 samples show superparamagnetic characteristics, especially the surface-reduced nanocubes, which have a higher magnetization.

The superparamagnetic behavior at higher temperatures arises from both the bulk and the surface components of the nanocubes. Though cobalt metal would be expected to exhibit ferromagnetic ordering, it has been shown that very small cobalt-metal domains appear to be superparamagnetic at room temperature.[22] The reduced Co/Co_3O_4 nanocubes also appear to be superparamagnetic (Figure 5b,c), as no magnetic hysteresis is observed for this sample at 280 K. Owing to the surface-reductive modification, superparamagnetic cobalt-metal domains on the nanocube surfaces could be responsible for generating the interconnectivity among the Co/Co_3O_4 nanocubes at room temperature, although more in-depth investigation of this aspect is required.

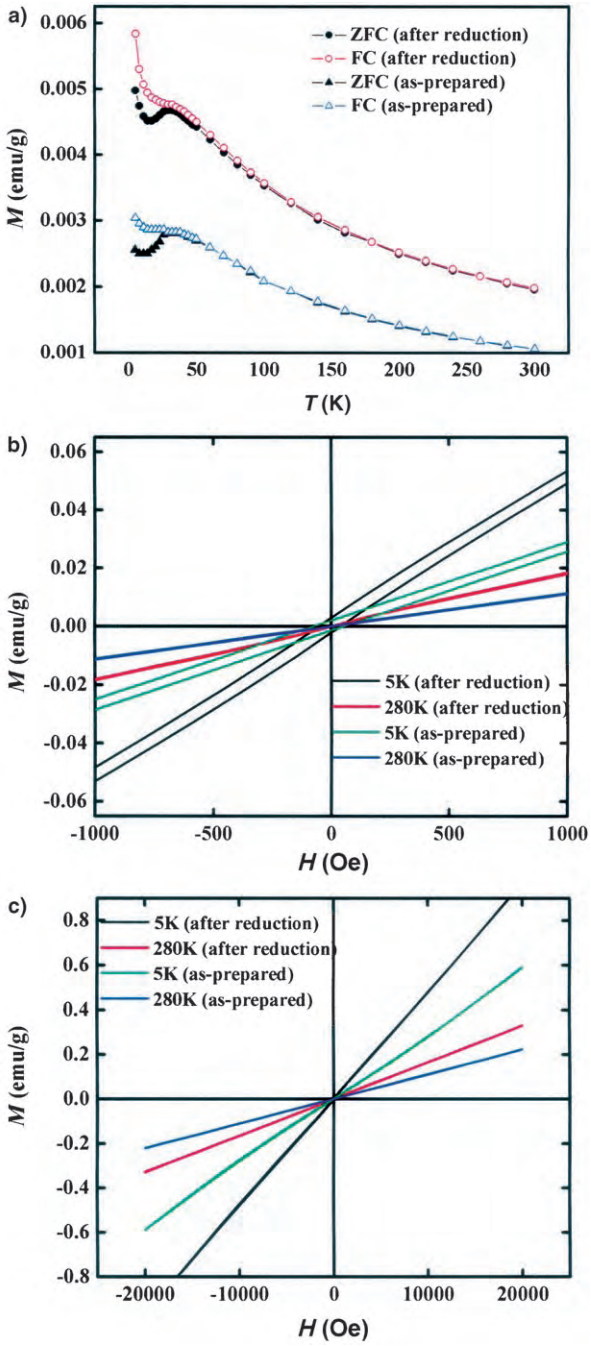

Figure 5. a) Temperature-dependence of the ZFC and FC magnetization of the nanocubes before (Co_3O_4) and after (Co/Co_3O_4) surface reduction, in an applied field of 100 Oe. b) Low-field section and c) complete measurement range of hysteresis loops (magnetization versus applied field) at 5 and 280 K for the nanocubes before (Co_3O_4) and after (Co/Co_3O_4) surface reduction. For visual clarity, the experimental data points are connected by lines.

Based on the above observations, we propose two different models for the organizing mechanism of the reduced Co/Co_3O_4 nanocubes in the absence of an external magnetic field (Figure 6). In model a, a net magnetic moment summed over a nanocube (as a basic building block) generates a linear assembly. Since the formation of such a 1D array is not observed, the superparamagnetic domains formed on the

 © 2006 Wiley-VCH Verlag GmbH & Co. KGaA, Weinheim

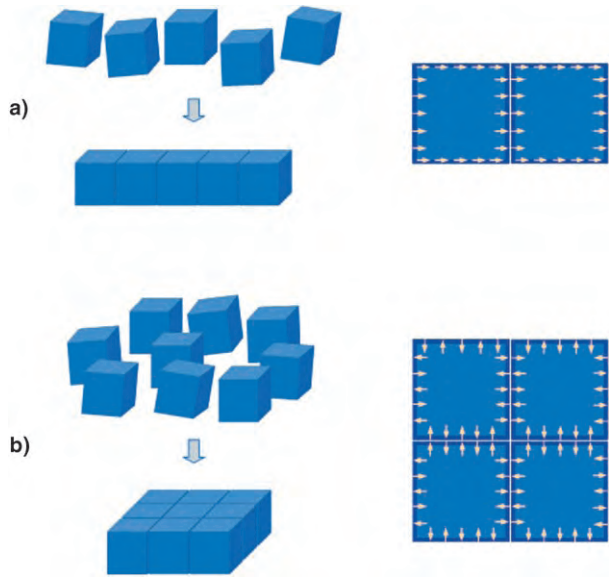

Figure 6. Assembly mechanisms: a) uniformly oriented magnetic domains (right, top view) on the surfaces of the Co/Co_3O_4 nanocubes generate a 1D array (left); b) randomly oriented magnetic domains (right, top view) generate a 2D array (left). The metallic cobalt surfaces formed on the nanocubes are shown in dark blue, and the individual magnetic domains are indicated by small arrows (domain walls are not shown).

surfaces of the nanocubes must be randomly distributed. In model b, the magnetic domains on the nanocube surfaces are assumed to be arranged randomly, producing no (or a very weak) global magnetic moment per nanocube. This model accounts well for the 2D aggregates observed in Figure 2. It seems that the liquid environment of the suspension provides excellent rotational freedom, which allows the surface domains on neighboring nanocubes to match up by aligning their magnetic moments during the drying process. Furthermore, owing to the observed superparamagnetic behavior of the reduced Co/Co_3O_4 nanocubes (Figure 5b,c), any mismatched domains present at the interfaces between the nanocubes may also be realigned easily. With superparamagnetic surface domains, for example, the cubes would not be required to have a great deal of rotational freedom in an aggregate state, as the magnetization direction of each surface domain is free to reorient to suit those of partner cubes. While giving no overall magnetic moments, these localized surface domains work like stitches, pinning neighboring Co/Co_3O_4 nanocubes together. In principle, other less-symmetrical building units can also be organized into 2D arrays, as long as nanoparticles with superparamagnetic surfaces can be prepared. In addition to the 2D organization observed herein, 3D assemblies of nano-building units should also be attainable if the drying process can be better controlled.

In summary, we have used the surface reduction of nanocubes of the antiferromagnetic spinel oxide Co_3O_4, to demonstrate that magnetic alignment can also be extended to higher dimensions by forming superparamagnetic surfaces on pristine nanostructures. This isotropic superparamagnetic interconnectivity provides an efficient means for generating intimate contact among the assembled nano-building units, including less symmetrical ones, without the assistance of organic surfactants or external magnetic fields.

Experimental Section

Nanocubes of the spinel oxide Co_3O_4 were prepared by a nitrate-salt-mediated synthesis at 120 °C in aqueous solution. An aqueous solution of NaOH (100.0 mL, 0.30 M; > 99 %, Merck) was mixed with $NaNO_3$ (35.0–60.0 g; > 99.5 %, Merck) in a three-necked round-bottom flask, which was mounted with a water-cooled reflux unit. The reaction mixture was kept at a temperature of 120 °C, stirred vigorously, and bubbled with purified air at 50 mL min^{-1}. While stirring, an aqueous solution of $Co(NO_3)_2 \cdot 6H_2O$ (20.0 mL, 1.0 M; > 98 %, Fluka) was added to the flask within 1 min, resulting in an instantaneous precipitation. Upon heating (12 h), the color of the precipitate slowly changed from purple to brown and finally to black. The resulting black colloid was centrifuged at 2500 rpm. The solid obtained was washed several times with HCl (2.0 M) and deionized water, and then vacuum dried at room temperature overnight. In the surface reduction experiments, Co_3O_4 nanocubes (0.030 g) were suspended in deionized water (5 mL) and placed in an ultrasonic water bath for 60 min. Then an aqueous solution of N_2H_4 (20.0 mL, up to 5.0 M) was added to the suspension, with magnetic stirring at room temperature. After 15 min, bubbles of nitrogen gas were observed in the reaction mixture as a result of the redox reaction between N_2H_4 and the Co_3O_4 surfaces. After 5 h, the solid product was separated from the solution by centrifuge, and then washed and dried.

In self-assembly investigations, a small amount of either the as-prepared Co_3O_4 nanocubes or the surface-reduced Co/Co_3O_4 nanocubes was suspended in ethanol (3.0 mL) and placed in an ultrasonic water bath for 5 min. Several drops of this suspension were placed onto a carbon-coated 200-mesh copper grid and then dried at room temperature for further investigation by TEM (JEM-2010, 200 kV). The as-prepared Co_3O_4 and surface-reduced Co/Co_3O_4 samples were investigated by XRD (Shimadzu XRD-6000, $Cu_{K\alpha}$ radiation, $\lambda = 1.5406$ Å).

The XPS measurements were performed with an AXIS-HSi spectrometer (Kratos Analytical) using a monochromated $Al_{K\alpha}$ X-ray source (1486.7 eV). The Co_3O_4 and Co/Co_3O_4 samples were mounted on double-sided adhesive tape on a sample stud. The XP spectra were measured with a constant analyzer pass energy of 40.0 eV. All binding energies were referred to the C 1s peak (284.5 eV) arising from surface hydrocarbons (or adventitious hydrocarbons). Prior to peak deconvolution, X-ray satellites and inelastic background (Shirley-type) were subtracted. In addition, all component peaks were set to be Gaussian-type.

The magnetic properties of the as-prepared Co_3O_4 and surface-reduced Co/Co_3O_4 nanocubes were studied at temperatures from 2–300 K and at magnetic field strengths up to 20 kOe using a Quantum Design MPMS-XL SQUID magnetometer. ZFC and FC measurements were carried out at 100 Oe.

Received: October 14, 2005
Revised: December 6, 2005
Published online: March 20, 2006

Keywords: cobalt · magnetic properties · nanostructures · oxides · self-assembly

[1] G. M. Whitesides, B. Grzybowski, *Science* **2002**, *295*, 2418–2421.
[2] D. S. Ginger, H. Zhang, C. A. Mirkin, *Angew. Chem.* **2004**, *116*, 30–46; *Angew. Chem. Int. Ed.* **2004**, *43*, 30–45.
[3] R. L. Penn, J. F. Banfield, *Science* **1998**, *281*, 969–971.
[4] C. Pacholski, A. Kornowski, H. Weller, *Angew. Chem.* **2002**, *114*, 1234–1237; *Angew. Chem. Int. Ed.* **2002**, *41*, 1188–1191.

 © 2006 Wiley-VCH Verlag GmbH & Co. KGaA, Weinheim

[5] a) B. Liu, H. C. Zeng, *Small* **2005**, *1*, 566 – 571; b) H. G. Yang, H. C. Zeng, *Angew. Chem.* **2004**, *116*, 6056 – 6059; *Angew. Chem. Int. Ed.* **2004**, *43*, 5930 – 5933.
[6] a) F. Dumestre, B. Chaudret, C. Amiens, P. Renaud, P. Fejes, *Science* **2004**, *303*, 821 – 823; b) F. Dumestre, B. Chaudret, C. Amiens, M. Respaud, P. Fejes, P. Renaud, P. Zurcher, *Angew. Chem.* **2003**, *115*, 5371 – 5374; *Angew. Chem. Int. Ed.* **2003**, *42*, 5213 – 5216.
[7] V. F. Puntes, D. Zanchet, C. K. Erdonmez, A. P. Alivisatos, *J. Am. Chem. Soc.* **2002**, *124*, 12874 – 12880.
[8] a) Z. L. Wang, Z. R. Dai, S. H. Sun, *Adv. Mater.* **2000**, *12*, 1944 – 1946; b) H. Zeng, J. Li, J. P. Liu, Z. L. Wang, S. H. Sun, *Nature* **2002**, *420*, 395 – 398.
[9] a) J. Park, K. An, Y. Hwang, J.-G. Park, H.-J. Noh, J.-Y. Kim, J.-H. Park, N.-M. Hwang, T. Hyeon, *Nat. Mater.* **2004**, *3*, 891 – 895; b) J. Park, E. Lee, N.-M. Hwang, M. Kang, S. C. Kim, Y. Hwang, J.-G. Park, H.-J. Noh, J.-Y. Kim, J.-H. Park, T. Hyeon, *Angew. Chem.* **2005**, *117*, 2932 – 2937; *Angew. Chem. Int. Ed.* **2005**, *44*, 2872 – 2877.
[10] T. D. Clark, R. Ferrigno, J. Tien, K. E. Paul, G. M. Whitesides, *J. Am. Chem. Soc.* **2002**, *124*, 5419 – 5426.
[11] S. Park, J.-H. Lim, S.-W. Chung, C. A. Mirkin, *Science* **2004**, *303*, 348 – 351.
[12] A. D. Dinsmore, M. F. Hsu, M. G. Nikolaides, M. Marquez, A. R. Bausch, D. A. Weitz, *Science* **2002**, *298*, 1006 – 1009.
[13] E. Katz, I. Willner, *Angew. Chem.* **2004**, *116*, 6166 – 6235; *Angew. Chem. Int. Ed.* **2004**, *43*, 6042 – 6108.
[14] P. A. Smith, C. D. Nordquist, T. N. Jackson, T. S. Mayer, B. R. Martin, J. Mbindyo, T. E. Mallouk, *Appl. Phys. Lett.* **2000**, *77*, 1399 – 1401.
[15] V. F. Puntes, K. M. Krishnan, A. P. Alivisatos, *Science* **2001**, *291*, 2115 – 2117.
[16] a) J. C. Love, A. R. Urbach, M. G. Prentiss, G. M. Whitesides, *J. Am. Chem. Soc.* **2003**, *125*, 12696 – 12697; b) A. R. Urbach, J. C. Love, M. G. Prentiss, G. M. Whitesides, *J. Am. Chem. Soc.* **2003**, *125*, 12704 – 12705.
[17] a) D. L. Huber, *Small* **2005**, *1*, 482 – 501; b) J. Gao, B. Zhang, X. Zhang, B. Xu, *Angew. Chem.* **2006**, *118*, 1242 – 1245; *Angew. Chem. Int. Ed.* **2006**, *45*, 1220 – 1223.
[18] a) T. Terao, T. Nakayama, *Phys. Rev. E* **1999**, *60*, 7157 – 7161; b) B. A. Grzybowski, H. A. Stone, G. M. Whitesides, *Nature* **2000**, *405*, 1033 – 1036; c) F. Assi, R. Jenks, J. Yang, C. Love, M. Prentiss, *J. Appl. Phys.* **2002**, *92*, 5584 – 5586.
[19] J. Feng, H. C. Zeng, *J. Phys. Chem. B* **2005**, *109*, 17113 – 17119.
[20] a) R. Xu, H. C. Zeng, *Chem. Mater.* **2003**, *15*, 2040 – 2048; b) M. Oku, Y. Sato, *Appl. Surf. Sci.* **1992**, *55*, 37 – 41.
[21] a) P. Cossee, *J. Inorg. Nucl. Chem.* **1958**, *8*, 483 – 488; b) W. L. Roth, *J. Phys. Chem. Solids* **1964**, *25*, 1 – 10; c) S. A. Makhlouf, *J. Magn. Magn. Mater.* **2002**, *246*, 184 – 190.
[22] a) S. I. Woods, J. R. Kirtley, S. H. Sun, R. H. Koch, *Phys. Rev. Lett.* **2001**, *87*, 137205; b) J. Espinosa, H. Shi, D. Lederman, *J. Appl. Phys.* **2005**, *97*, 10B310.

 © 2006 Wiley-VCH Verlag GmbH & Co. KGaA, Weinheim

DOI: 10.1002/anie.200503987

Flattened Cone 2,8,14,20-Tetrakis(L-valinamido)-[4]resorcinarene: An Enantioselective Allosteric Receptor in the Gas Phase**

Bruno Botta, Fabiana Caporuscio, Deborah Subissati, Andrea Tafi, Maurizio Botta, Antonello Filippi, and Maurizio Speranza**

Allosteric modulation of receptors is now recognized as a very plausible mechanism by which many pharmaceuticals exert their activity against a variety of diseases.[1–12] The majority of allosteric effects operate through noncovalent interactions in supramolecular systems, such as enzyme–substrate complexes, receptor–ligand complexes, oligomeric proteins, transcription complexes, and cellular structures. Established methods for studying these effects suffer from various difficulties such as large sample requirements (X-ray crystallography), limited mass range (NMR spectroscopy), and resolution (gel electrophoresis), as well as lack of specificity. In contrast, mass spectrometry (MS) is an intrinsically fast technique, endowed with high sensitivity, molecular specificity, and tolerance to impurities. Therefore, it is considered the technique of choice for the fast screening of putative inhibitors in combinatorial synthesis and other situations where large numbers of candidate drugs need to be examined. Its unparalleled ability to distinguish between species of different molecular mass means it has the potential to analyze supramolecular assemblies of multiple components and, thus, provide unique information on their formation and properties that is complementary to that obtained by more conventional methods. Indeed, MS has the potential to investigate inhibition mechanisms in the gas phase, where the molecule–

[*] Prof. B. Botta, Prof. A. Tafi
Dipartimento Farmaco Chimico Tecnologico
Università di Siena
53100 Siena (Italy)
Fax: (+39) 0577-834333
E-mail: taft@unisi.it

Dr. F. Caporuscio, Dr. D. Subissati, Prof. M. Botta, Dr. A. Filippi, Prof. M. Speranza
Dipartimento di Studi di Chimica e Tecnologia delle Sostanze Biologicamente Attive
Università "La Sapienza"
00185 Roma (Italy)
Fax: (+39) 06-4991-3602
E-mail: maurizio.speranza@uniroma1.it

[**] This work was supported by the Ministero dell'Istruzione dell'Università e della Ricerca (MIUR, COFIN), the Consiglio Nazionale delle Ricerche (CNR), and the Istituto Pasteur Fondazione Cenci Bolognetti. B.B. and A.T. gratefully acknowledge Project "FIRB 2003" from MIUR (Ministero della Università e della Ricerca). We are grateful to F. Angelelli for technical assistance.

Supporting information for this article (computational details and kinetic plots) is available on the WWW under http://www.angewandte.org or from the author.

 © 2006 Wiley-VCH Verlag GmbH & Co. KGaA, Weinheim InterScience

receptor interactions are not perturbed by effects of the medium.[13] However, despite its unique potential, MS has not yet provided even a single example of gas-phase allosteric effects.

We believe that we have identified the first case of an enantioselective allosteric effect during the kinetic investigation of the ligand displacement reaction of proton-bound diastereomeric complexes $[\mathbf{1_L}\cdot H\cdot\mathbf{2_D}]^+$ and $[\mathbf{1_L}\cdot H\cdot\mathbf{2_L}]^+$ ($\mathbf{1_L}$ = flattened cone 2,8,14,20-tetrakis(L-valinamido)[4]resorcinarene (Scheme 1); $\mathbf{2_D}$ = D-tryptophan; $\mathbf{2_L}$ = L-tryptophan) by (*S*)-(+)- and (*R*)-(−)-2-butylamine ($\mathbf{B_S}$ and $\mathbf{B_R}$, respectively) [Eq. (1)].[14–16]

$$[\mathbf{1_L}\cdot H\cdot\mathbf{2}]^+ + \mathbf{B} \rightarrow [\mathbf{1_L}\cdot H\cdot\mathbf{B}]^+ + \mathbf{2} \quad (1)$$

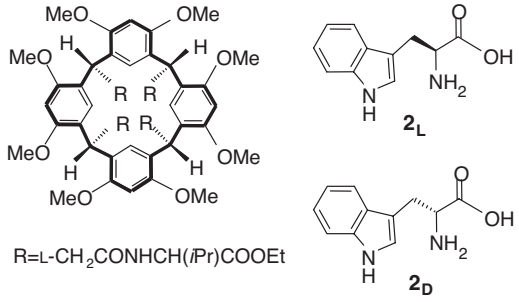

Scheme 1. Structures of the flattened-cone 2,8,14,20-tetrakis(L-valinamido)[4]resorcinarene ($\mathbf{1_L}$) and of L- ($\mathbf{2_L}$) and D-tryptophan ($\mathbf{2_D}$).

The reactions [Eq. (1)] were carried out in the cell of a Fourier transform ion cyclotron resonance (FT-ICR) mass spectrometer. The rate constants k' were obtained from the slopes of the pseudo-first-order rate plots ($\ln(I/I_0)$ versus t), where I is the abundance of complex $[\mathbf{1_L}\cdot H\cdot\mathbf{2}]^+$ at the delay time t and I_0 is the sum of the abundances of $[\mathbf{1_L}\cdot H\cdot\mathbf{2}]^+$ and $[\mathbf{1_L}\cdot H\cdot\mathbf{B}]^+$. Biexponential rate plots are invariably observed (Figure 1 and Supporting Information) irrespective of the configuration of **2** and **B**, which indicates the presence of several stable isomeric $[\mathbf{1_L}\cdot H\cdot\mathbf{2}]^+$ structures. The biexponential curve becomes linear ($r^2 = 0.996$) after a given reaction time (ca. 6 s in Figure 1), thus indicating that only the less-reactive isomer $[\mathbf{1_L}\cdot H\cdot\mathbf{2_D}]^+_{slow}$ is left at that time. The time-dependence of the more-reactive fraction $[\mathbf{1_L}\cdot H\cdot\mathbf{2_D}]^+_{fast}$ can be inferred from the overall decay of $[\mathbf{1_L}\cdot H\cdot\mathbf{2_D}]^+$ after subtracting the first-order decay of the $[\mathbf{1_L}\cdot H\cdot\mathbf{2_D}]^+_{slow}$ fraction.

The good linearity of the resulting curve ($r^2 = 0.993$) suggests that only a single isomer is present in the more-reactive $[\mathbf{1_L}\cdot H\cdot\mathbf{2_D}]^+_{fast}$ fraction. The value of the *y* intercept of this curve and that of the linear $[\mathbf{1_L}\cdot H\cdot\mathbf{2_D}]^+_{fast}$ decay curve provide an estimate of the relative distribution of $[\mathbf{1_L}\cdot H\cdot\mathbf{2_D}]^+_{fast}$ (27 %) and $[\mathbf{1}_{\mathbf{L}}\cdot H\cdot\mathbf{2_D}]^+_{slow}$ (73 %), respectively. Similar patterns were observed by changing the configuration of **2** and **B** (see Supporting Information).

The second-order rate constants k, calculated from the corresponding $k'/[\mathbf{B}]$ ratios, are listed in Table 1. Their values, compared with the relevant collision rate constants (k_{coll}),[17] provide a measure of the efficiency of the reaction (eff = k/k_{coll}). The enantioselectivity factor ρ is defined as the ratio between the k value for the reaction of a given **B** enantiomer with the $[\mathbf{1_L}\cdot H\cdot\mathbf{2_D}]^+$ complex and that with the $[\mathbf{1_L}\cdot H\cdot\mathbf{2_L}]^+$ complex. The enantioselectivity factor ξ is defined as the ratio between the k value for the reaction of a given $[\mathbf{1_L}\cdot H\cdot\mathbf{2}]^+$ complex with $\mathbf{B_R}$ and that with $\mathbf{B_S}$. The opposite ρ values obtained by changing the configuration of **B** demonstrate that the observed enantioselectivity is determined by a combination of kinetic and thermodynamic factors, that is, by the relative stability of the diastereomeric $[\mathbf{1_L}\cdot H\cdot\mathbf{2}]^+$ complexes and by the effects of the $[\mathbf{1_L}\cdot H]^+$ complex upon the transition structures involved in their displacement [Eq. (1)]. In this way, the interpretation of the kinetic results of Table 1 requires the structural and energetic analysis of the relevant proton-bound diastereomeric $[\mathbf{1_L}\cdot H\cdot\mathbf{2}]^+$ reactants. This task has been undertaken by using molecular mechanics (docking) calculations and molecular dynamics (MD) simulations.

Table 1: Exchange rate constants ($k \times 10^{-10}$ cm^3 molecule^{-1} s^{-1}).

Complex	$\mathbf{B_R}$ = (*R*)-(−)-$C_4H_9NH_2$			$\mathbf{B_S}$ = (*S*)-(+)-$C_4H_9NH_2$			
	k	eff	ρ	*k*	eff	ρ	ξ
$[\mathbf{1_L}\cdot H\cdot\mathbf{2_D}]^+_{fast}$	1.82 ± 0.04	0.16	1.60 ± 0.11	1.92 ± 0.04	0.12	0.82 ± 0.10	ξ_D = 0.95 ± 0.04
$[\mathbf{1_L}\cdot H\cdot\mathbf{2_L}]^+_{fast}$	1.14 ± 0.04	0.10		2.33 ± 0.20	0.16		ξ_L = 0.49 ± 0.06
$[\mathbf{1_L}\cdot H\cdot\mathbf{2_D}]^+_{slow}$	0.15 ± 0.01	0.01	1.07 ± 0.13	0.23 ± 0.01	0.02	0.62 ± 0.18	ξ_D = 0.65 ± 0.04
$[\mathbf{1_L}\cdot H\cdot\mathbf{2_L}]^+_{slow}$	0.14 ± 0.01	0.01		0.37 ± 0.07	0.03		ξ_L = 0.37 ± 0.09

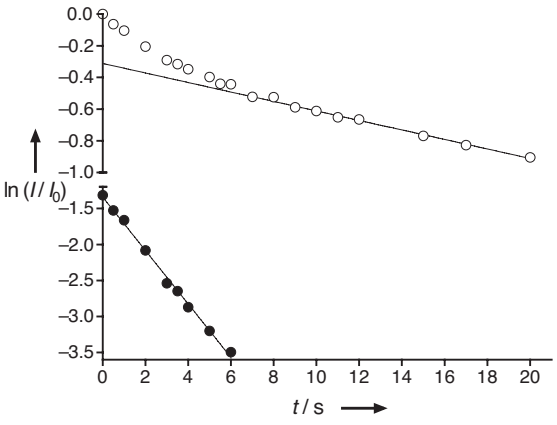

Figure 1. Kinetic plot for the gas-phase reaction between (*R*)-(−)-2-butylamine ($\mathbf{B_R}$; $P(\mathbf{B_R}) = 1.1 \times 10^{-7}$ mbar) and $[\mathbf{1_L}\cdot H\cdot\mathbf{2_D}]^+$.

The overall conformation of each resulting docking geometry was classified by the values taken by the ad hoc defined structural descriptor (SD) described in the Supporting Information. Accordingly, SD values around 0° correspond to the location of **2** at an external lower rim in proximity to the protonated pendant group of $[\mathbf{1_L}\cdot H]^+$ (henceforth denoted as *ext*). Values around −90° suggest location of the guest at the lower rim among the pendant groups of $[\mathbf{1_L}\cdot H]^+$ (henceforth denoted as *down*), and values of +90° its location in the achiral upper rim cavity (henceforth denoted as *up*).

 © 2006 Wiley-VCH Verlag GmbH & Co. KGaA, Weinheim

Figures 2 and 3 show the results of docking calculations on the homochiral $[\mathbf{1_L}\cdot H\cdot\mathbf{2_L}]^+$ and the heterochiral $[\mathbf{1_L}\cdot H\cdot\mathbf{2_D}]^+$ complexes, respectively. The distribution of the relevant SD values as a function of the energy of the resulting complexes

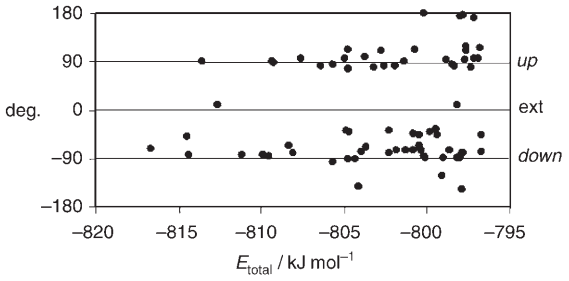

Figure 2. Docking of $[\mathbf{1_L}\cdot H\cdot\mathbf{2_L}]^+$.

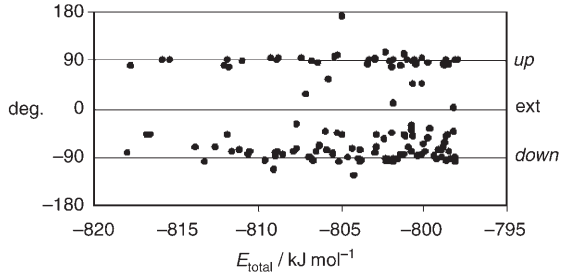

Figure 3. Docking of $[\mathbf{1_L}\cdot H\cdot\mathbf{2_D}]^+$.

(<20 kJ mol^{-1} over the global minimum) indicates both enantiomers of **2** residing preferentially at the *up* and *down* regions of the $[\mathbf{1_L}\cdot H]^+$ host. Molecular dynamics simulations starting from the global minimum of $[\mathbf{1_L}\cdot H\cdot\mathbf{2_L}]^+$ suggest that the guest can be permanently trapped in these two positions (Figure 4). Similar patterns were observed for $[\mathbf{1_L}\cdot H\cdot\mathbf{2_D}]^+$. The occurrence of stable *down* and *up* structures for the diastereomeric $[\mathbf{1_L}\cdot H\cdot\mathbf{2}]^+$ complexes accounts for their biexponential reaction kinetics (Figure 1 and Supporting Information). The average potential energy gaps, scaled to 300 K, between the *down* and *up* regioisomers of $[\mathbf{1_L}\cdot H\cdot\mathbf{2_D}]^+$ and $[\mathbf{1_L}\cdot H\cdot\mathbf{2_L}]^+$ amount to 3 and 8 kJ mol^{-1}, respectively, in favor of the *down* structures. Therefore, the more-stable *down* structures are associated with the most abundant $[\mathbf{1_L}\cdot H\cdot\mathbf{2}]^+_{slow}$ fractions (68–73%), while the less-stable *up* ones with the less-abundant $[\mathbf{1_L}\cdot H\cdot\mathbf{2}]^+_{fast}$ components (27–32%; Figure 5).

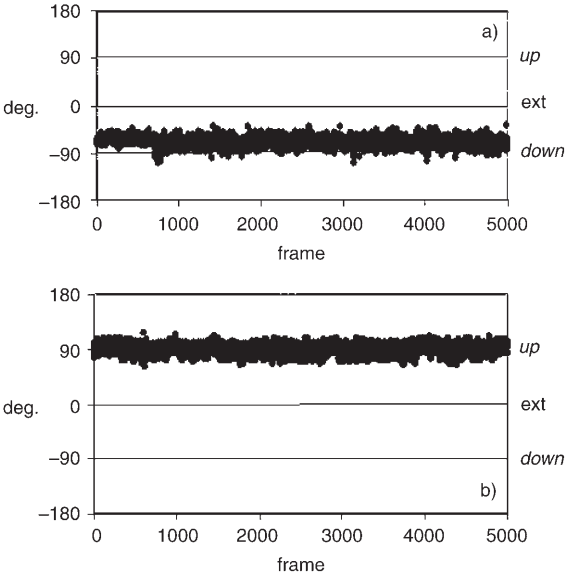

Figure 4. Molecular dynamics of *down* (a) and *up* (b) regioisomers of $[\mathbf{1_L}\cdot H\cdot\mathbf{2_L}]^+$.

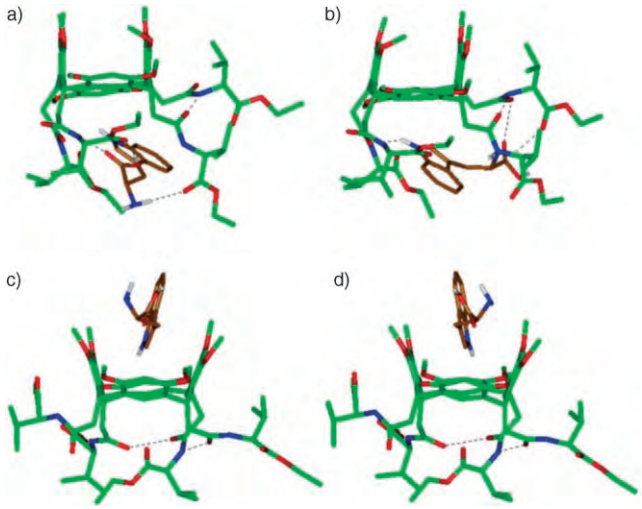

Figure 5. Front views of the fully minimized structures: *down* structures of complexes $[\mathbf{1_L}\cdot H\cdot\mathbf{2_D}]^+$ (a) and $[\mathbf{1_L}\cdot H\cdot\mathbf{2_L}]^+$(b) ; *up* structures of complexes $[\mathbf{1_L}\cdot H\cdot\mathbf{2_L}]^+$ (c) and $[\mathbf{1_L}\cdot H\cdot\mathbf{2_D}]^+$ (d). Hydrogen-bonding interactions are depicted as dotted lines.

Let us focus our attention on the *up* regioisomers (Figure 5c,d), which correspond to the diastereomeric $[\mathbf{1_L}\cdot H\cdot\mathbf{2}]^+_{fast}$ structures. Their formation can be certainly ascribed both to the low polarity of **2** and the structure of its side chain which allow **2** to establish a very effective π–π stacking interaction with the electron-rich cavity at the upper rim of the host. This interaction is strengthened by a dipolar interaction with the NH group properly located between the methoxy groups of two facing aromatic rings. According to Figure 5c,d, these cooperative interactions do not apparently perturb the lower-rim cavity of the host and, therefore, no appreciable enantioselectivity should be observed in the reaction of $[\mathbf{1_L}\cdot H\cdot\mathbf{2}]^+_{fast}$ with the enantiomers of **B**, that is, the value of ρ should be equal to unity and that of ξ_D should be equal to ξ_L. In contrast, $\rho = 1.60 \pm 0.11$ with $\mathbf{B_R}$ and $\rho = 0.82 \pm 0.10$ with $\mathbf{B_S}$ (Table 1). The opposite ρ factors are reflected in the corresponding ξ terms, which exhibit the largest variation ever measured for this kind of reaction ($\xi_D = 0.95 \pm 0.04$; $\xi_L = 0.49 \pm 0.06$; Table 1).[14–16] A rationale for this discrepancy is the fact that the $[\mathbf{1_L}\cdot H\cdot\mathbf{2}]^+$ *up* structures have a supramolecular chirality as a result of the bent position of the guest in the upper-rim cavity of the host (Figure 5c,d).

Therefore, interaction of amine **B** with the lower-rim cavity of the host[15] induces a conformational change which is transmitted to its upper-rim cavity so as to expel the guest at a rate which depends on both its configuration and that of **B**.

 © 2006 Wiley-VCH Verlag GmbH & Co. KGaA, Weinheim

This type of conformational coupling between the upper and lower cavities of $[\mathbf{1_L}\cdot H]^+$ can be regarded as the first example of heterotropic negative cooperativity in the gas phase. The fact that this kind of cooperativity: 1) is classified among the less-frequently observed allosteric effects even in natural and artificial systems;[18] 2) is potentially involved in important phenomena, such as liberation of toxins, catalysis, etc.;[18] and 3) is characterized by a significant enantioselectivity, gives more prominence to the present gas-phase observation.

Experimental Section

Eantiomerically pure $\mathbf{1_L}$ was synthesized from the $BF_3\cdot Et_2O$-catalyzed cyclization of the L enantiomer of (*E*)-*N*-[1-carboxyethyl)-2-methylpropyl]-2,4-dimethoxycinnamamide, and isolated according to established procedures.[19] The D and L enantiomers of tryptophan were obtained from Aldrich Co. and used without further purification. The (*R*)-(−) ($\mathbf{B_R}$) and (*S*)-(+) ($\mathbf{B_S}$) enantiomers of 2-butylamine were also obtained from Aldrich Co., and purified under vacuum with several freeze–thaw cycles. The experiments were performed at room temperature in an APEX 47e FT-ICR mass spectrometer equipped with an ESI source (Bruker Spectrospin) and a resonance cell ("infinity cell") situated between the poles of a superconducting magnet (4.7 T). Stock solutions of $\mathbf{1_L}$ (1×10^{-5} M) in H_2O/CH_3OH (1:3) containing a fivefold excess of the pure enantiomers of **2** were electrosprayed through a heated capillary (130 °C) into the external source of the FT-ICR mass spectrometer. The resulting ions were transferred into the resonance cell by a system of potentials and lenses, and quenched by collisions with methane pulsed into the cell through a magnetic valve. Abundant signals, corresponding to the natural isotopomers of the proton-bound complex $[\mathbf{1_L}\cdot H\cdot\mathbf{2}]^+$, were monitored and isolated by broad-band ejection of the accompanying ions. The $[\mathbf{1_L}\cdot H\cdot\mathbf{2}]^+$ family was then allowed to react with the chiral amine **B** present in the cell at a fixed pressure ($1.1–1.3\times10^{-7}$ mbar).

All the computational work was carried out on a SGI Origin300 server and visualized on a SGI Octane workstation. Molecular mechanics (MM) calculations (docking) and molecular dynamics simulations (MD) were performed using the AMBER* force field as implemented in MacroModel 5.5.[20] No cutoff was applied for the nonbonded interactions and the calculations were performed in the gas phase by selecting the constant dielectric treatment (dielectric constant $\varepsilon = 1.0$). Partial atomic charges to be used in the docking and MD simulations were obtained through quantum mechanics calculations performed with the semiempirical program MOPAC distributed by Accelrys Inc., and by using the AM1–Mulliken method. The atomic partial charges of tryptophan are specified in the last column of the three cartesian coordinate structures enclosed as Supporting Information (.pdb format generated by InsightII), which describe a low-energy conformation of the $\mathbf{2_L}$ enantiomer, whereas the partial charges used for $[\mathbf{1_L}\cdot H]^+$ have been already reported elsewhere.[15]

Received: November 9, 2005
Published online: February 27, 2006

Keywords: allosteric effect · enantioselectivity · enzyme models · gas-phase kinetics · host–guest systems

[1] A. Guidotti, J. Auta, J. M. Davis, E. Dong, D. R. Grayson, M. Veldic, X. Zhang, E. Costa, *Psychopharmacology* **2005**, *180*, 191.
[2] J. A. Schetz, *Mini-Rev. Med. Chem.* **2005**, *5*, 555.
[3] Z. G. Gao, S. K. Kim, A. P. Ijzerman, K. A. Jacobson, *Mini-Rev. Med. Chem.* **2005**, *5*, 545.
[4] C. Geserick, H. A. Meyer, B. Haendler, *Mol. Cell. Endocrinol.* **2005**, *236*, 1.
[5] B. M. Matata, M. M. Elahi, *Recent Res. Dev. Biophys.* **2004**, *3*, 93.
[6] R. G. Pertwee, *Life Sci.* **2005**, *76*, 1307.
[7] J. N. C. Kew, *Pharmacol. Ther.* **2004**, *104*, 233.
[8] J. P. Pin, J. Kniazeff, V. Binet, J. Liu, D. Maurel, T. Galvez, B. Duthey, M. Havlickova, J. Blahos, L. Prezeau, P. Rondard, *Biochem. Pharmacol.* **2004**, *68*, 1565.
[9] L. T. May, V. A. Avlani, P. M. Sexton, A. Christopoulos, *Curr. Pharm. Des.* **2004**, *10*, 2003.
[10] L. P. Henderson, J. C. Jorge, *Adv. Mol. Cell Biol.* **2004**, *32*, 219.
[11] D. S. Woodruff-Pak, *Drug Dev. Res.* **2002**, *56*, 335.
[12] M. Emre, *Int. J. Clin. Pract. Suppl.* **2002**, *127*, 64.
[13] For recent reviews on gas-phase enantioselectivity, see: a) M. Speranza, *Adv. Phys. Org. Chem.* **2004**, *39*, 147; b) M. Speranza, *Int. J. Mass Spectrom.* **2004**, *232*, 277.
[14] B. Botta, M. Botta, A. Filippi, A. Tafi, G. Delle Monache, M. Speranza, *J. Am. Chem. Soc.* **2002**, *124*, 7658.
[15] B. Botta, A. Tafi, M. Botta, G. Delle Monache, A. Filippi, M. Speranza, *Chem. Eur. J.* **2004**, *10*, 4126.
[16] B. Botta, D. Subissati, A. Tafi, G. Delle Monache, A. Filippi, M. Speranza, *Angew. Chem.* **2004**, *116*, 4871; *Angew. Chem. Int. Ed.* **2004**, *43*, 4767.
[17] T. Su, *J. Chem. Phys.* **1988**, *88*, 4102, 5355.
[18] H. J. Schneider, A. K. Yatsimirsky, *Principles and Methods in Supramolecular Chemistry*, Wiley, New York, **2000**.
[19] B. Botta, G. Delle Monache, P. Salvatore, F. Gasparrini, C. Villani, M. Botta, F. Corelli, A. Tafi, E. Gacs-Baitz, A. Santini, C. Carvalho, D. Misiti, *J. Org. Chem.* **1997**, *62*, 932.
[20] F. Mohamadi, N. G. J. Richards, W. C. Guida, R. Liskamp, M. Lipton, C. Caufield, G. Chang, T. Hendrickson, W. C. Still, *J. Comput. Chem.* **1990**, *11*, 440.

 © 2006 Wiley-VCH Verlag GmbH & Co. KGaA, Weinheim

Synthetic Methods

DOI: 10.1002/anie.200504555

Room-Temperature Nucleophilic Aromatic Fluorination: Experimental and Theoretical Studies**

*Haoran Sun and Stephen G. DiMagno**

Despite their rarity in nature,[1] organofluorine compounds play a leading role in the life sciences.[2–11] The high electronegativity and small atomic radius of the fluorine atom mean that its incorporation into biologically active compounds

[*] Dr. H. Sun, Prof. Dr. S. G. DiMagno
Department of Chemistry and
Center for Materials Research and Analysis
University of Nebraska–Lincoln
Lincoln, NE 68588-0304 (USA)
Fax: (+1) 402-472-9402
E-mail: sdimagno1@unl.edu

[**] We thank the Nebraska Research Initiative for financial support of this research, Rieke Metals Inc. for the gift of the substrates, and the Research Computing Facility at the University of Nebraska for supercomputer time.

Supporting information for this article is available on the WWW under http://www.angewandte.org or from the author.

WILEY InterScience DISCOVER SOMETHING GREAT
© 2006 Wiley-VCH Verlag GmbH & Co. KGaA, Weinheim

induces a relatively small structural perturbation, whereas drastically altering the electronic properties and bioavailability of the compounds.[9,12] Fluorine substitution is a particularly effective strategy for aromatic groups, as the electron-withdrawing nature of the fluorine atom reduces the susceptibility of an aryl ring to cytochrome P-450 catalyzed hydroxylation, a common step in drug catabolism.[8] The C–F dipole in fluoroaromatic groups can also lead to an increase in molecular recognition through favorable, though generally weak, electrostatic interactions.[3,6,10,11,13] Because of the medicinal importance of fluorinated aromatic compounds, mild and selective methods for their preparation are desirable.

We recently reported the preparation of a soluble, highly nucleophilic fluoride-ion source, anhydrous tetrabutylammonium fluoride ($TBAF_{anh}$).[14] $TBAF_{anh}$ can be dissolved in dimethyl sulfoxide (DMSO) and CH_3CN (2 M) and fluorinates primary alkyl halides and tosylates rapidly at low temperature (−35 °C, 5 min, THF). The rapid rate observed for S_N2 reactions that feature $TBAF_{anh}$ prompted us to investigate nucleophilic aromatic substitution (S_NAr) reactions with this reagent. Below we describe variants of the industrially important selective halogen exchange (Halex) and fluorodenitration processes for aromatic fluorination.[15–18] We show that $TBAF_{anh}$ permits these reactions to be performed under surprisingly mild conditions.

Electron-withdrawing substituents are typically required to activate chloroaromatic substrates toward Halex chemistry. The usual reagents employed to effect halogen exchange are spray-dried KF; a high-boiling-point polar aprotic solvent, such as sulfolane; and a phase-transfer catalyst to improve the solubility of the fluoride ion (Scheme 1). Prolonged and vigorous heating is often required. Such harsh conditions preclude syntheses in which the late introduction of fluorine substituents is desired. In contrast, many aromatic compounds undergo Halex reactions at room temperature in DMSO, CH_3CN, or THF upon exposure to $TBAF_{anh}$. In a typical preparation, $TBAF_{anh}$ (1.3 equiv) and the chloro- or nitroaromatic compound were simply stirred together in DMSO.[19] Representative fluorinations are shown in Table 1.

The scope of the room-temperature reactivity of $TBAF_{anh}$ with chloropyridines in DMSO is apparent from inspection of Table 1. If the pyridine ring has no electron-withdrawing groups, the nucleophilic substitution of chloride is sluggish for the *ortho* position and does not occur at all with *m*-chloropyridine. Smooth nucleophilic substitution occurs if mildly activating groups are present. A comparison of the mono- and dichloropyridine examples shows that a second electronegative substituent accelerates substitution: fluorination of 2-chloropyridine requires 14 days, whereas 2,6-dichloropyridine is exhaustively fluorinated in 90 minutes under identical conditions. In comparison, typical Halex fluorinations of 2,6-dichloropyridine require heating at 150 °C for ten hours.[20–23] Chloropyridine substrates bearing more strongly electron-withdrawing (trifluoromethyl or car-

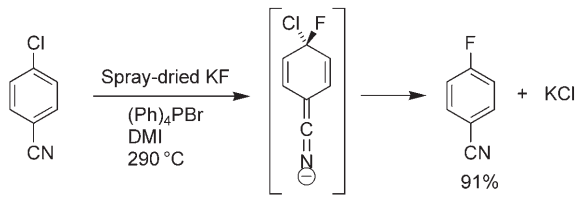

Scheme 1. A typical Halex reaction.[24] DMI = 1,3-dimethyl-2-imidazolidinone.

Table 1: Halex and fluorodenitration reactions of chloro- and nitroaromatic compounds by $TBAF_{anh}$.

Entries	Substrate	Conditions[a]	Product	Yield [%][b]
1		$TBAF_{anh}$ (4 equiv) 14 days	no reaction	0
2		$TBAF_{anh}$ (4 equiv) 14 days		80
3		$TBAF_{anh}$ (2.5 equiv) 1 h		> 95
4	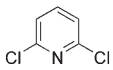	$TBAF_{anh}$ (2.5 equiv) 1.5 h	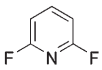	> 95
5	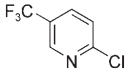	$TBAF_{anh}$ (1.3 equiv) 20 min	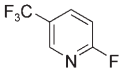	> 95
6	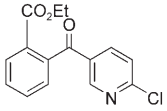	$TBAF_{anh}$ (1.3 equiv) 30 min	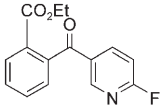	> 95
7		$TBAF_{anh}$ (1.3 equiv) 1 h		> 95
8	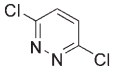	$TBAF_{anh}$ (2.5 equiv) 30 min	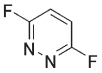	> 95
9	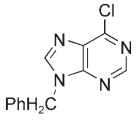	$TBAF_{anh}$ (1.3 equiv) 30 min	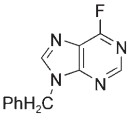	> 95
10	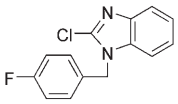	$TBAF_{anh}$ (1.4 equiv) ≈30 min	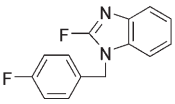	> 90
11	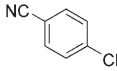	$TBAF_{anh}$ (1.5 equiv) 2 days	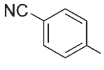	80
12	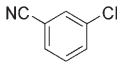	$TBAF_{anh}$ (1.5 equiv) 5 days	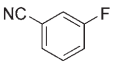	2
13	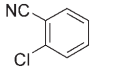	$TBAF_{anh}$ (1.5 equiv) 18 h	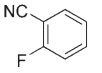	> 95
14	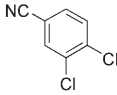	$TBAF_{anh}$ (2.5 equiv) 20 min	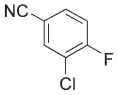	> 95
15	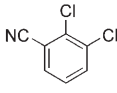	$TBAF_{anh}$ (1.4 equiv) 20 min	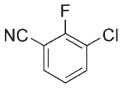	> 85

 © 2006 Wiley-VCH Verlag GmbH & Co. KGaA, Weinheim

Table 1: (Continued)

Entries	Substrate	Conditions[a]	Product	Yield [%][b]
16	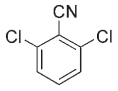	$TBAF_{anh}$ (2.5 equiv) 1 h	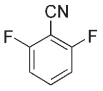	>90
17	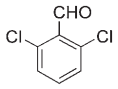	$TBAF_{anh}$ (2.5 equiv) 1.5 h	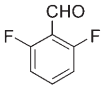	>90
18	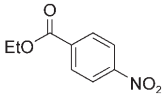	$TBAF_{anh}$ (1.3 equiv) 30 min	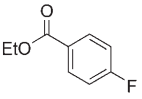	>95
19	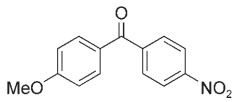	$TBAF_{anh}$ (1.3 equiv) 30 min	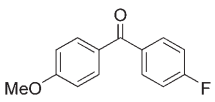	>95
20	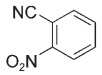	$TBAF_{anh}$ (1.3 equiv) 10 min		>95
21	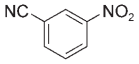	$TBAF_{anh}$ (1.3 equiv) 24 h	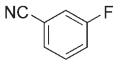	>95

[a] Reaction conditions: in an anhydrous solution of DMSO ([substrate] = 0.4 M) at 20 °C for the time indicated. [b] All yields are calculated from integration of ^{1}H and ^{19}F NMR signals relative to an added internal standard.

bonyl) substituents are also fluorinated rapidly, as are several other heterocyclic derivatives. It is noteworthy that N-benzyl-6-chloropurine is fluorinated quantitatively within 30 minutes. However, 6-chloropurine is deprotonated by $TBAF_{anh}$ if the amine is left unprotected, thus generating an equivalent of bifluoride ion. Fluorination of the 6-chloropurine anion requires excess $TBAF_{anh}$ (4 equiv) and an extended reaction time (14 days, 65% yield).

Heterocyclic substrates are much more reactive than simple arenes in Halex reactions. S_NAr reactions were attempted upon the three isomeric chlorobenzonitriles to gauge the reactivity of anhydrous $TBAF_{anh}$ toward substituted benzenes. Suzuki and Kimura synthesized fluorobenzonitriles from chlorobenzonitriles in a pressure reactor using spray-dried KF and tetraphenylphosphonium bromide in hot (290 °C) DMI (Scheme 1).[24] $TBAF_{anh}$ fluorinated 2- and 4-chlorobenzonitrile, albeit sluggishly, at room temperature in DMSO. The *meta* isomer was recovered under these conditions (Table 1). As in the case of pyridine, addition of a second chlorine atom accelerates substitution; 3,4-dichlorobenzonitrile and 2,3-dichlorobenzonitrile yield 3-chloro-4-fluorobenzonitrile and 2-fluoro-3-chlorobenzonitrile, respectively, within 20 minutes.

Adams and Clark reviewed aromatic fluorodenitration and reported that NO_2^- is superior to chloride as a leaving group in S_NAr;[15,18] thus, we assayed nitroaromatic compounds to expand the scope of room-temperature fluorination with $TBAF_{anh}$. The three isomeric mononitrobenzonitriles are fluorodenitrated readily with $TBAF_{anh}$; the nitrite leaving group even facilitates *m*-fluorination. $TBAF_{anh}$ performs fluorodenitration even on relatively weakly activated arenes; for example, ethyl 4-nitrobenzoate is fluorodenitrated within 30 minutes. Additional examples of fluorodenitration are summarized in Table 2. There are no reported examples of comparable, high-yielding fluorodenitration reactions performed under similarly mild conditions. Entries 6, 9, 10, and 17–19 (Table 2) show that various functional groups, including aryl esters, ethers, aldehydes, ketones, and N-benzyl protecting groups, are compatible with these fluorination conditions.

While our experimental studies show that electron-withdrawing groups are required for aromatic fluorodenitration with $TBAF_{anh}$ in DMSO, previous work has shown that the gas-phase reaction of nitrobenzene with fluoride ions is fairly favorable ($\Delta H° = -28.2$ kcal mol^{-1}) and has a very low activation barrier ($\Delta H^{\neq} = 3.5$ kcal mol^{-1}).[25] The reason for the attenuated solution-phase reactivity is that fluoride, the most densely charged monoanion, is tightly ion paired and

Table 2: Fluorodenitration of *para*-substituted nitrobenzenes

Entries	Substrate	Conditions[a]	Product	Yield [%][b]	σ^-	$\Delta G°$ [kcal mol^{-1}] (solution)	$\Delta G^{\neq}$ [kcal mol^{-1}] (solution)
1	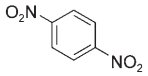	$TBAF_{anh}$ (1.3 equiv) <5 min	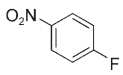	>95	1.27	−9.03	24.5
2	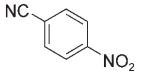	$TBAF_{anh}$ (1.3 equiv) 10 min	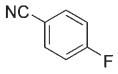	>95[c]	1.00	−8.00	29.8
3	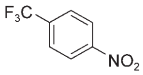	$TBAF_{anh}$ (1.3 equiv) 2 h	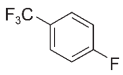	>90	0.65	−7.96	33.9
4	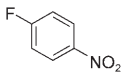	$TBAF_{anh}$ (2.5 equiv) >5 days	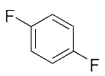	0	−0.03	−4.33	42.6
5	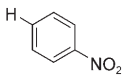	$TBAF_{anh}$ (2.5 equiv) >5 days	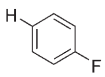	0	0	−5.01	42.5
6	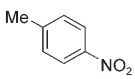	$TBAF_{anh}$ (2.5 equiv) >5 days	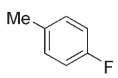	0	−0.17	−3.97	45.3

[a] Reaction conditions: in an anhydrous solution of DMSO ([substrate] = 0.4 M) at 20 °C for the time indicated. [b] All yields are calculated from integration of ^{1}H and ^{19}F NMR signals relative to an added internal standard. [c] Yield of the isolated product was 69%.

 © 2006 Wiley-VCH Verlag GmbH & Co. KGaA, Weinheim

strongly solvated.[15,26] Thus, we conducted computational studies to explore the impact of solvent upon the potential-energy surfaces of fluorodenitration reactions that feature a variety of 4-substituted nitrobenzenes (Scheme 2).

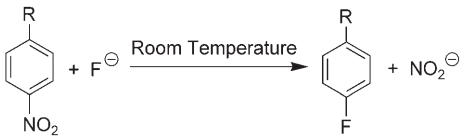

R = NO_2, CN, CF_3, F, H, Me

Scheme 2. The calculated fluorodenitration reactions.

Gas-phase structures and energies for all nitrobenzenes, fluorobenzenes, the nitrite ion, and the fluoride ion were calculated using density functional theory (B3LYP/6-311g++(d,p)/6-311g++(d,p)). Frequency calculations for all molecular species were also performed to provide thermal (298 K) and ZPE corrections for the thermochemical analysis. Polarizable continuum (PCM) and self-consistent isodensity polarizable continuum models (SCI-PCM) were employed to model the polar aprotic solvents used in the experiment. In practice, the two models gave comparable potential-energy diagrams and solvation energies.

The fluorodenitration reaction energies are shown in Figure 1, in which they are plotted against Hammet σ^- parameters. A comparison with the gas-phase experimental data shows that the DFT calculations correctly reproduce the experimentally determined thermodynamic enthalpy for the fluorodenitration of nitrobenzene;[25] thus, we deemed the basis set and method to be sufficient for the study of substituted nitrobenzenes. The gas-phase $\Delta G°$ and $\Delta H°$ values are large and negative for all fluorodenitration reactions of substituted nitrobenzenes, and an excellent linear free-energy relationship is produced. Extrapolation of this linear plot suggests that fluorodenitration is thermodynamically favorable for all *para*-substituted nitrobenzenes in the gas phase. In contrast, calculated solution-phase $\Delta G°$ and $\Delta H°$ values are only modestly negative for the free-ion reaction. Inclusion of ion pairing would further lessen the equilibrium constant for fluorodenitration as the fluoride ion is expected to ion pair to a greater extent than the nitrite ion. This suggests that the limitation of fluorodenitration to electron-poor nitroaromatic compounds in polar solvents at room temperature could arise from thermodynamic considerations.

For the transition-state (TS) search and activation-barrier calculations, basis-set superposition error (BSSE) was corrected by using the counterpoise method. It was found that BSSE correction resulted in very modest adjustments to the calculated activation barrier (0.7 kcal mol^{-1} for the gas-phase fluorination of nitrobenzene). In the gas-phase calculations, several stable fluoride–nitrobenzene complexes were found in our extensive search of the TS geometry and reaction-side local minima (RM), in agreement with previous theoretical studies.[25] Our focus was limited to the RM which led directly to transition states. Figure 2 shows typical structures of gas-phase RM and TS structures for the fluorodenitration of nitrobenzene and *p*-cyanonitrobenzene. If the *para* substituent is H or an electron-donating group, significant structural changes are observed between the RM and the TS. The RM has a weakly bound fluoride ion, little perturbation of the C–N bond length, and only a minor deflection of the nitro group from the plane of the aromatic ring, whereas the TS shows a "Meisenheimer-like" structure that indicates significant charge injection into the aromatic ring. In contrast, electron-withdrawing groups lead to Meisenheimer intermediates which require minimal structural reorganization to reach the TS. The calculations for the gas-phase reaction predict an excellent kinetic linear free-energy relationship; all gas-phase fluorodenitration reactions of *para*-substituted nitrobenzenes should be rapid at room temperature (Figure 1).

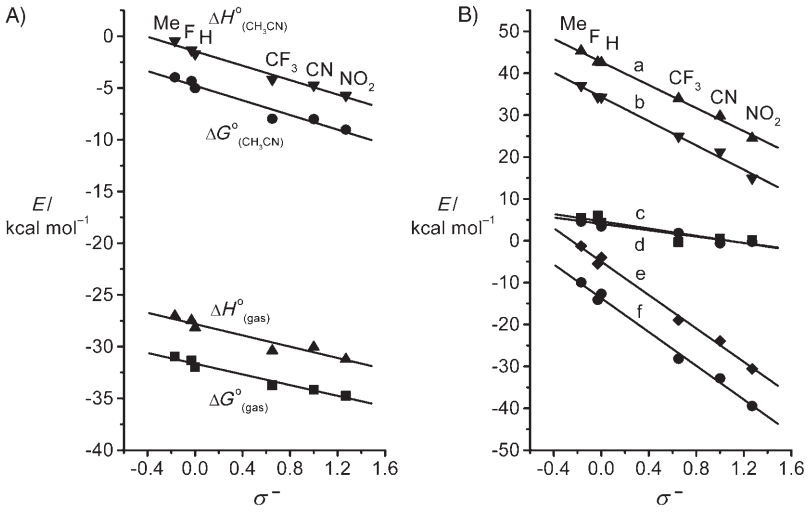

Figure 1. A) Calculated thermodynamic free-energy relationships for gas- and solution-phase fluorodenitration reactions. B) Calculated activation parameters for fluorodenitration reactions: a) $\Delta G^{\neq}$ in CH_3CN, b) $\Delta H^{\neq}$ in CH_3CN, c) $\Delta G^{\neq}$ for gas-phase RM to TS, d) $\Delta H^{\neq}$ for gas-phase RM to TS, e) $\Delta G^{\neq}$ for gas-phase dissociated reactants to TS, f) $\Delta H^{\neq}$ for gas-phase dissociated reactants to TS.

Solution-phase TS structures were located using potential-energy surface scans, in which optimizations were performed as the C–F length was stepped through several fixed values. The optimized solution-phase TS structures differ slightly from the gas-phase TS structures; the former exhibit longer C–F and C–N lengths. Removal of the solvent model and recalculation of the optimized solution-phase TS structures gave energies within 2 kcal mol^{-1} of the gas-phase TS energy for all of the substituted nitrobenzenes, thereby indicating that the impact of the solvent model upon the fluorodenitration TS geometries and internal energies is quite small. As strong solvation of the fluoride ion results in calculated RMs that feature free ions, activation energies (Table 2) were calculated directly from the energy difference between that of optimized TS structures and

 © 2006 Wiley-VCH Verlag GmbH & Co. KGaA, Weinheim

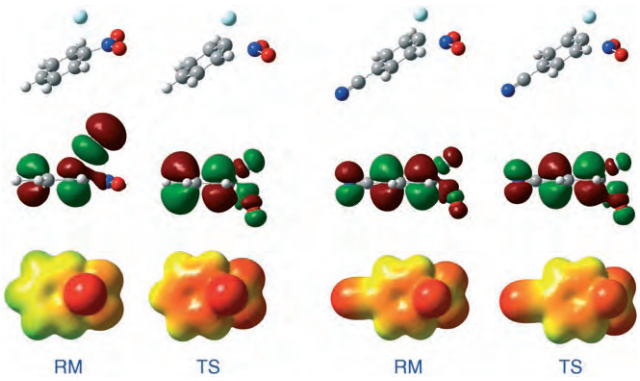

Figure 2. Optimized structures (top), highest occupied molecular orbitals (HOMO; middle) and electrostatic potential surfaces (ESP; bottom) for nitrobenzene (left) and *p*-cyanonitrobenzene (right) fluorodenitration reactions.

the sum of the energies of nitrobenzene and the fluoride ion. Preferential solvation of the fluoride ion is calculated to add 45–55 kcal mol^{-1} to the gas-phase free energy of activation. Activation energies for the fluorodenitration of nitrobenzene in cyclohexane, THF, and DMSO ($\Delta G^{\neq} = 20.5$, 37.5, and 42.5 kcal mol^{-1}, respectively) were also obtained using the PCM model; decreasing solvent polarity lowers the activation barrier substantially. Thus, if one can prepare soluble, more weakly ion-paired fluoride salts, it is expected that the scope of room-temperature fluorodenitration reactions can be expanded if nonpolar media are used.

A comparison of experimental and theoretical results shows that the calculated activation barriers for fluorodenitration in CH_3CN (or DMSO) are much too large. The experimental data indicate that $\Delta G^{\neq} = 20.5$ and 21.5 kcal mol^{-1} for the fluorodenitration of *p*-cyanonitrobenzene and *p*-trifluoromethylnitrobenzene, respectively, whereas the calculated values are $\Delta G^{\neq} = 29.8$ and 33.9 kcal mol^{-1}, respectively. Additionally, the Hammett plots (Figure 1) appear to be unrealistically steep ($\rho = -13$). Three sources of error in the PCM calculation are readily apparent. The calculated solvation energy for the fluoride ion is too large (−90.7 kcal mol^{-1}) relative to the experimental value (−82.6 kcal mol^{-1}), although it is in line with the stated error range of the solvent model.[27,28] Secondly, the overestimated steepness of the Hammett plot suggests that the solvent model cannot account accurately for the localization of negative charge in the less stable (more electron-rich) TS. The inadequacy of PCM to account for the strong electrostatic effects that arise from localized charge–solvent interactions has been highlighted by Truhlar and co-workers.[29] Thus, we would expect the experimental Hammett ρ value to be smaller than the PCM calculation indicates. Finally, ion pairing of the TBA cation to the fluoride anion and the TS have not been addressed herein, nor is the nature of the actual reactive species (contact ion pair, solvent-separated ion pair, free ion) known. Thus, this relatively simple fluorodenitration reaction constitutes an exceptionally challenging test case for computational solvent models.

In summary, $TBAF_{anh}$ in DMSO is a fluorinating reagent with unprecedented activity in room-temperature Halex and fluorodenitration reactions. The initial results suggest that ion pairing and solvation are the factors that limit the impressive nucleophilicity of the fluoride ion under conditions typically employed for nucleophilic aromatic substitution. Theoretical calculations show that gas-phase fluorodenitration reactions are both thermodynamically favorable and fast, whereas preferential solvation of the fluoride ion leads to the large activation barriers for the solution-phase reactions. It appears that a further expansion in the scope of room-temperature S_NAr fluorination is possible, provided one can prepare highly soluble, weakly ion-paired fluoride salts for use in relatively nonpolar media.

Received: December 22, 2005
Published online: March 20, 2006

Keywords: density functional calculations · fluorine · nucleophilic aromatic substitution · synthetic methods · tetrabutylammonium fluoride

[1] D. O'Hagan, C. Schaffrath, S. L. Cobb, J. T. G. Hamilton, C. D. Murphy, *Nature* **2002**, *416*, 279.
[2] G. Gerebtzoff, X. Li-Blatter, H. Fischer, A. Frentzel, A. Seelig, *ChemBioChem* **2004**, *5*, 676–684.
[3] F. Hof, D. M. Scofield, W. B. Schweizer, F. Diederich, *Angew. Chem.* **2004**, *116*, 5166–5169; *Angew. Chem. Int. Ed.* **2004**, *43*, 5056–5059.
[4] P. Jeschke, *ChemBioChem* **2004**, *5*, 570–589.
[5] I. Ojima, *ChemBioChem* **2004**, *5*, 628–635.
[6] J. A. Olsen, D. W. Banner, P. Seiler, U. O. Sander, A. D'Arcy, M. Stihle, K. Mueller, F. Diederich, *Angew. Chem.* **2003**, *115*, 2611–2615; *Angew. Chem. Int. Ed.* **2003**, *42*, 2507–2511.
[7] C. Pesenti, F. Viani, *ChemBioChem* **2004**, *5*, 590–613.
[8] H.-J. Bohm, D. Banner, S. Bendels, M. Kansy, B. Kuhn, K. Mueller, U. Obst-Sander, M. Stahl, *ChemBioChem* **2004**, *5*, 637–643.
[9] M. Schlosser, *Enantiocontrolled Synthesis of Fluoroorganic Compounds: Stereochemical Challenges and Biomedicinal Targets* (Ed.: V. A. Soloshonok), Wiley, Chichester, **1999**, 613 – 659.
[10] J. A. Olsen, D. W. Banner, P. Seiler, B. Wagner, T. Tschopp, U. Obst-Sander, M. Kansy, K. Mueller, F. Diederich, *ChemBioChem* **2004**, *5*, 666–675.
[11] J. C. Biffinger, H. W. Kim, S. G. DiMagno, *ChemBioChem* **2004**, *5*, 622–627.
[12] B. E. Smart, *J. Fluorine Chem.* **2001**, *109*, 3–11.
[13] H. W. Kim, P. Rossi, R. K. Shoemaker, S. G. DiMagno, *J. Am. Chem. Soc.* **1998**, *120*, 9082–9083.
[14] H. Sun, S. G. DiMagno, *J. Am. Chem. Soc.* **2005**, *127*, 2050–2051.
[15] D. J. Adams, J. H. Clark, *Chem. Soc. Rev.* **1999**, *28*, 225–231.
[16] M. Maggini, M. Passudetti, G. Gonzales-Trueba, M. Prato, U. Quintily, G. Scorrano, *J. Org. Chem.* **1991**, *56*, 6406–6411.
[17] S. D. Kuduk, R. M. DiPardo, M. G. Bock, *Org. Lett.* **2005**, *7*, 577–579.
[18] N. Boechat, J. H. Clark, *J. Chem. Soc. Chem. Commun.* **1993**, 921–922.
[19] Product characterization and reaction progress were assayed by ^1H, ^{19}F and ^{13}C NMR spectroscopic analysis; product purity and identity were confirmed by GC mass-spectroscopic analysis; commercially available fluoroaromatic compounds were used as GC standards; and the NMR data are reported in the Supporting Information.
[20] M. Darabantu, T. Lequeux, J. C. Pommelet, N. Ple, A. Turck, *Tetrahedron* **2001**, *57*, 739–750.

 © 2006 Wiley-VCH Verlag GmbH & Co. KGaA, Weinheim

[21] T. G. Muench (Dow Chemical Co., USA), US4071521, **1978**, p. 6.
[22] T. J. Giacobbe (Dow Chemical Co., USA), US4031100, **1977**, p. 7.
[23] M. M. Boudakian, *J. Heterocycl. Chem.* **1968**, *5*, 683 – 684.
[24] H. Suzuki, Y. Kimura, *J. Fluorine Chem.* **1991**, *52*, 341 – 351.
[25] T. Giroldo, L. A. Xavier, J. M. Riveros, *Angew. Chem.* **2004**, *116*, 3672 – 3674; *Angew. Chem. Int. Ed.* **2004**, *43*, 3588 – 3590.
[26] H. Plenio, *ChemBioChem* **2004**, *5*, 650 – 655.
[27] J. R. Pliego, Jr., J. M. Riveros, *J. Phys. Chem. A* **2001**, *105*, 7241 – 7247.
[28] J. R. Pliego, Jr., J. M. Riveros, *Phys. Chem. Chem. Phys.* **2002**, *4*, 1622 – 1627.
[29] C. P. Kelly, C. J. Cramer, D. G. Truhlar, *J. Chem. Theory Comput.* **2005**, *1*, 1133 – 1152.

 © 2006 Wiley-VCH Verlag GmbH & Co. KGaA, Weinheim

Protein Engineering

DOI: 10.1002/anie.200504018

Construction of a Ball-and-Spike Protein Supramolecule**

*Kenji Sugimoto, Shuji Kanamaru, Kenji Iwasaki, Fumio Arisaka, and Ichiro Yamashita**

In nature, symmetry is utilized in a wide range of ways to build large protein supramolecules, for example, viruses form very stable and symmetrical capsid structures. Viruses have a genome of nucleic acids enclosed by a protective protein shell. Short viral genomes code for only a few kinds of proteins and, as a result, they cannot efficiently prepare a large variety of proteins for the capsid. Instead, many copies of one or a few types of proteins are used efficiently to form the capsid. In other words, proteins are symmetrically arranged and form perfect spheres under the condition of limited types of proteins. Many types of spherical viruses have a capsid with icosahedral symmetry, such as the bean-pod mottle virus (BPMV).[1] The tubular structure of tobacco mosic virus (TMV) is composed of 2130 identical coat proteins that adopt a helical arrangement (49 subunits for every three turns[2]). This example demonstrates one type of protein subunit that can make 300×18 nm^2 tubular structures by using symmetry. The use of symmetry for the construction of larger nanostructures with less variety in the type of proteins used (smaller genome) is a common strategy in several life forms.

Proteins are produced by the information stored in DNA and, as a result, the synthesized proteins are usually chemically and structurally similar. The way in which tertiary structures are made is fascinating, and the role of protein folding, including the effect of primary, secondary, and higher order interactions in the protein structure and folding pathway of proteins, is becoming better known each day. However, even today, the design and synthesis of artificial proteins that can undergo symmetrical assembly is not an easy task. As a result, there is little work relating to the construction of large supramolecules made up of artificial proteins.[3] For example, Yeates et al. reported that chimera combined dimerization and trimerization interfaces can self-assemble to form complex spherical assemblies.[4]

Herein, we report a method to make novel protein architectures through the spontaneous self-assembly of two symmetric protein components, Dps protein[5–7] and cell-punctuating needles of the T4 bacteriophage.[8] The family of Dps proteins are DNA binding and are found in starved cells. They are induced in a variety of bacteria by oxidative or nutritional stress and protect DNA against oxidative damage mediated by H_2O_2.[9] The Dps from the bacterium *Listeria innocua* (LisDps) is similar in shape to ferritin, but the inner core and outer diameters are only about 5 nm and 8.5 nm, respectively. LisDps and has been shown to accommodate 500 atoms of Fe.[5–7] The cage protein is composed of 12 identical 18-kDa subunits that self-assemble to form a cage with 23-fold symmetry and four trimers distributed at the vertices of a tetrahedron (Figure 1 A). The amino acid sequence of LisDps shows no correspondence with that of a typical ferritin, but rather exhibits significant similarity with the sequences of the Dps family members.[6] The C-terminal β-helix domains of gp5 from the bacteriophage T4 (gp5C) are cell-punctuating needles.[8] The gp5 protein plays a very important role in the infection of *E. coli* by the bacteriophage. The crystal structure of gp5C was determined as the (gp5–gp27)$_3$ complex, with the three gp5C polypeptide chains winding around a central crystallographic threefold axis to create an equilateral triangular prism 7 nm in length and 2.8 nm in height (Figure 1 B). Furthermore, gp5C maintains a highly stable structure that is resistant to sodium dodecyl

[*] K. Sugimoto, Prof. I. Yamashita
CREST, Japan Science and Technology Agency
4-1-8 Honcho, Kawaguchi, Saitama 332-0012 (Japan)
and
Graduate School of Material Science
Nara Institute of Science and Technology
8916-5 Takayama-cho, Ikoma 630-0192 (Japan)
Fax: (+81) 743-72-6196
E-mail: ichiro@ms.naist.jp
Prof. K. Iwasaki[+]
Research Center for Ultra-High Voltage Electron Microscopy
Osaka University
7-1 Mihogaoka, Ibaraki, Osaka 567-0047 (Japan)
Prof. S. Kanamaru, Prof. F. Arisaka
Graduate School and School of Bioscience and Biotechnology
Tokyo Institute of Technology
4259 Nagatsuta-cho, Midori-ku, Yokohama-shi, Kanagawa 226-8501 (Japan)
[+] Current address: Institute for Protein Research
Laboratory of Protein Synthesis and Expression
Osaka University
3-2 Yamadaoka, Suita, Osaka 565-0871 (Japan)

[**] We are grateful to T. Douglas for a gift of the LisDps clone. A part of this work was supported by the Nanotechnology Support Project of the Ministry of Education, Culture, Sports, Science, and Technology (MEXT), Japan, at the Research Center for Ultrahigh Voltage Electron Microscopy, Osaka University.

Supporting information for this article is available on the WWW under http://www.angewandte.org or from the author.

 © 2006 Wiley-VCH Verlag GmbH & Co. KGaA, Weinheim

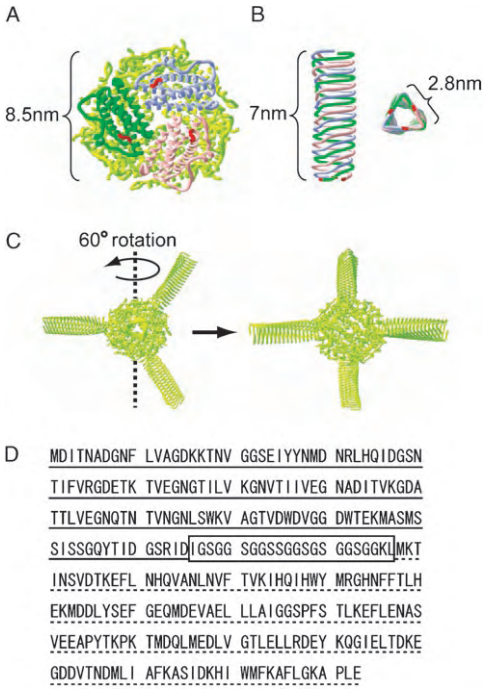

Figure 1. A) View of LisDps along the threefold axis. Each of the three monomers surrounding the threefold axis are colored differently (green, pink, and blue). The N-terminal residue of the LisDps monomer is colored red. B) Side view (left) and top view (right) of gp5C. The three gp5C monomers are colored green, pink, and blue. The C-terminal residue of the gp5C monomer is colored red. C) A model of BSPS after self-assembly. D) Amino acid sequence for BSPS. The gp5C segment (solid line) and the LisDps segment (dashed line) of BSPS are underlined. The flexible linker portion is boxed.

sulfate (SDS; 10%) and guanidine·HCl (2 M). The surface of gp5C is highly negatively charged. This negative charge plays an important role in repelling the phosphates of the lipid bilayer when the gp5C penetrates the outer cell membrane. These distinctive structures are known as "β-helix structures", and have been discovered in various proteins (for example, the phage P22 tailspike protein[10] and carbonic anhydrase[11]).

Both LisDps and gp5C have a threefold axis of symmetry (at the C terminus of gp5C and the N terminus of LisDps). Furthermore, the distance between the three C termini of gp5C is fairly similar to that between the three N termini of LisDps (1.8 nm and 3 nm, respectively). Thus, by fusing gp5C to the N terminus of LisDps through a flexible linker (Figure 1D), it is possible to construct a self-assembled fusion protein in which the tubelike gp5C protein is arrayed on the surface of the spherical LisDps. The flexible linker, which has 22 residues, is long enough to link LisDps with gp5C and not hinder the folding of individual proteins. Because LisDps has four threefold axes, four gp5C proteins can be attached to each LisDps, forming a ball-and-spike protein supramolecule (BSPS; Figure 1C).

LisDps, gp5C, and BSPS were expressed and self-assembled in the cytoplasm of *E. coli* BL21(DE3). A large amount of gp5C and LisDps was observed by using a T7 promoter system in the cell lysate. Although a high level of expression of BSPS by using the T7 promoter system resulted in the formation of considerable inclusion bodies, only a small amount of BSPS was observed in the cell lysate. The self-assembled gp5C, LisDps, and BSPS in the cell lysate were purified by anion-exchange and gel-filtration chromatographic techniques. The fractions from a Seperose 6 10/300GL column containing gp5C, LisDps, or BSPS were collected and applied to SDS–polyacrylamide. Figure 2A

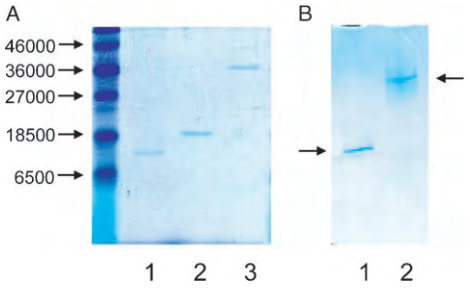

Figure 2. PAGE analysis of gp5C, LisDps, and BSPS. A) SDS gel electrophoresis (15% polyacrylamide) of gp5C (lane 1; $M_r = 14.4$ kD), LisDps (lane 2; $M_r = 18$ kD) and BSPS (lane 3; $M_r = 34.1$ kD). B) Non-denaturing gel electrophoresis (5–10% polyacrylamide) of LisDps (lane 1) and BSPS (lane 2). The arrows indicate the position of the assembled LisDps (lane 1) and assembled BSPS (lane 2).

shows that each fraction is pure and that each molecular weight corresponds to a specific subunit. Furthermore, size-exclusion HPLC analyses of all protein samples confirmed the purity of the proteins (gp5C; volume of elution (V_e) = 17.0 mL, LisDps; V_e = 15.6 mL, BSPS; V_e = 12.5 mL, see Supporting Information). It can be judged from the elution volume that LisDps maintains its native quaternary structure (V_e = 15.6 mL), whereas BSPS gives rise to a fast-moving component with V_e = 12.5 mL. The native polyacrylamide gel electrophoresis analysis (native-PAGE) also indicates that BSPS is less mobile than LisDps (Figure 2B). These results strongly suggest that, as expected, BSPS self-assembled to form a larger quaternary structure.

The structure of the self-assembled BSPS was visualized by TEM (Figure 3). The products formed were observed as spherical particles decorated with tubelike structures. Figure 3 shows TEM images of BSPS with four (top) and three (bottom) tubelike structures per spherical particle. The number of observed tubelike structures was derived from the direction of adsorption on the grid. The determined sizes were consistent with the known sizes of the individual proteins; however, the tubelike portions of BSPS were barely visible. This may be due to the extremely small size of gp5C (close to the limit observable for proteins by using TEM). The fact that it is hard to observe just gp5C by TEM (data not shown) supports this interpretation.

To determine whether both gp5C and LisDps portions in the BSPS are folded, we carried out not only the structural analysis of BSPS on the grid by TEM but also the structural analysis of BSPS in solution by a spectroscopic technique, such as dynamic light scattering (DLS) and circular dichroism (CD). The sizes of gp5C, LisDps, and BSPS were determined by DLS as shown in Table 1. The diameters of gp5C and LisDps are 7.2 and 9.2 nm, respectively, and the diameter of

 © 2006 Wiley-VCH Verlag GmbH & Co. KGaA, Weinheim

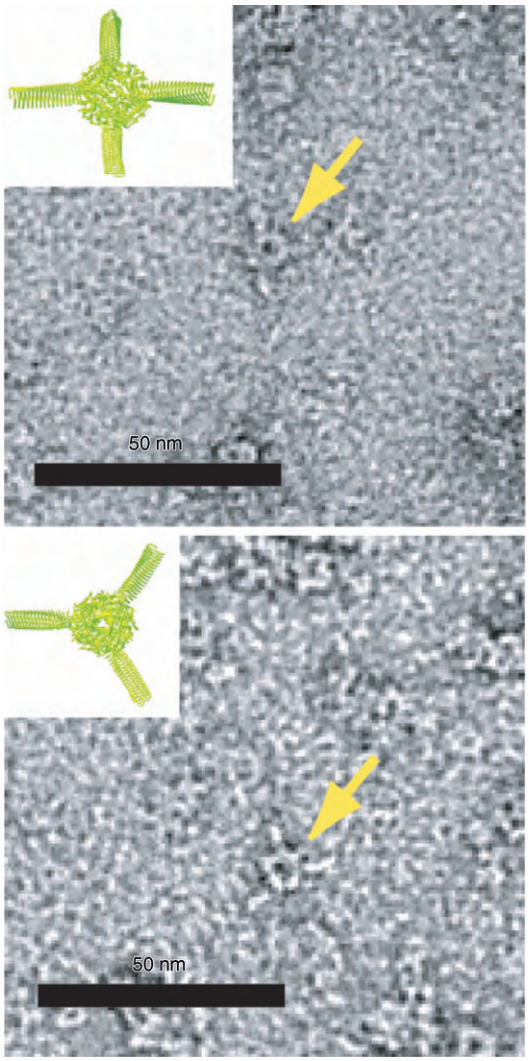

Figure 3. A negatively stained, self-assembled BSPS. The yellow arrows indicate self-assembled BSPS. The inset shows the theoretical model of the ball-and-spike protein supramolecule assembled from 12 copies of the BSPS.

Table 1: The sizes of gp5C, LisDps, and self-assembled BSPS as determined by dynamic light scattering studies.

Sample	Diameter [nm]	Polydispersity [nm][a]
gp5C	7.2	1.0
LisDps	9.2	0.7
BSPS	22.6	4.1

BSPS was determined to be 22.6 nm. This is comparable with the expected diameter of LisDps linked to two gp5C proteins (23.6 nm). The particle size agreed well with the measurements derived from TEM. From the CD spectra of gp5C, LisDps, and BSPS (Figure 4), the negative peaks of gp5C (216–218 nm) and LisDps (208 nm and 222 nm) suggest that the gp5C is predominantly in the β-sheet conformation, whereas LisDps is predominantly α-helical in conformation (Figure 4A). These spectra agree with previous data[12,13] and are consistent with the X-ray crystal structures.[5,8] The CD

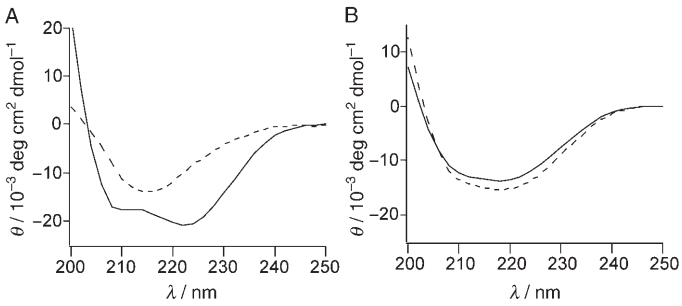

Figure 4. CD spectra of gp5C, LisDps, and self-assembled BSPS. A) Far-UV residue ellipticities of gp5C (dashed line) and LisDps (solid line). B) Far-UV residue ellipticities of self-assembled BSPS (solid line), and the calculated combined spectrum of LisDps with that of gp5C (dashed line). The protein concentration for all samples was 5 μM.

spectrum of BSPS is similar to that calculated by combining the spectrum of LisDps with that of gp5C (Figure 4B). This implies that BSPS formed the expected structure.

The results of native-PAGE, DLS, and size-exclusion HPLC analysis of BSPS indicate that BSPS subunits are self-assembled into a larger quaternary structure. Furthermore, the results of CD and TEM measurements suggest that both gp5C and LisDps portions in BSPS are correctly folded.

Unmodified LisDps can incorporate iron into its cavity and form an iron oxide core.[6,7,9] To investigate whether the biomineralization ability of BSPS was retained or not, ferrihydrite core formation by BSPS was studied in a solution containing BSPS (0.05 mg mL^{-1}), 2-[4-(2-hydroxyethyl)-1-piperazinyl]ethanesulfonic acid (HEPES) buffer solution (20 mM; pH 7.0), NaCl (150 mM), and ammonium iron(II) sulfate (0.5 mM). Iron-loaded BSPS was stained by aurothioglucose and observed by TEM (Figure 5). It is known that aurothioglucose does not stain the cavity because steric hindrance prevents it from entering the channels.[14] TEM images show that iron was incorporated in the cavity of BSPS. However, no iron was incorporated in the tubelike portions of BSPS (Figure 5A). This may be due to the extremely small pores of gp5C.[8] After the iron-incorporation experiment, BSPS was purified by gel-filtration chromatography, and energy-dispersive X-ray microanalysis (EDX) characteriza-

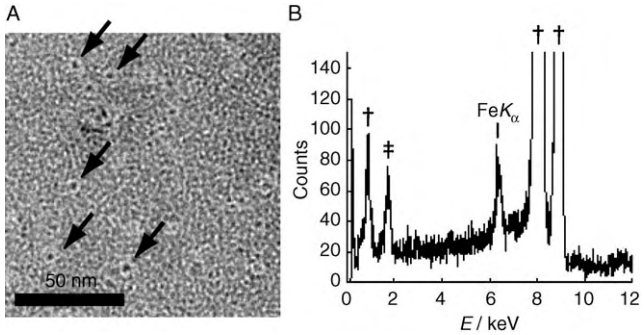

Figure 5. TEM image of iron-loaded BSPS. A) TEM image of iron-loaded BSPS stained by aurothioglucose. The black arrows indicate iron-loaded BSPS. B) EDX analysis of iron-loaded BSPS after purification by gel-filtration chromatography († indicates Cu from the supporting grid; ‡ indicates Si from the supporting grid).

 © 2006 Wiley-VCH Verlag GmbH & Co. KGaA, Weinheim

tion of the nanoparticle in BSPS was carried out. The EDX spectrum showed a peak for iron ($K_\alpha = 6.3$ keV) (Figure 5B). The three peaks at 0.9, 8.0, and 8.9 keV and a peak at 1.8 keV were assigned, to copper and silicon, respectively, from the supporting grid. This result demonstrates that BSPS maintains the natural potential to form inorganic nanoparticles at its center.

Many protein modules are driven to self-assemble through the natural oligomeric interfaces of their components by using symmetry, and thus inhibit the unnecessary aggregation. For example, virus capsids are highly symmetrical and allow the use of many copies of the same protein. Symmetry is the basic strategy of life and is essential to produce large structures with a only a small variety of protein types (equivalent to a smaller genome). More-complex protein structures also indispensably need symmetry to make up their structures. Herein, we demonstrated the concept of engineering a novel artificial protein supramolecule. By fusing gp5C to the N terminus of LisDps through a flexible linker, we constructed a ball-and-spike protein supramolecule. In further studies, the orientation of the spikes will be more precisely controlled through adjustment of the length of the linker. We anticipate that the concept of using such a novel pathway, based on the artificially designed self-assembly and biomineralization of protein supramolecules,[15] will be used to produce various nanometer-sized inorganic functional structures and electronic devices.

Received: November 11, 2005
Revised: December 8, 2005
Published online: March 23, 2006

Keywords: biomineralization · helical structures · protein structures · self-assembly · symmetry

[1] M. G. Rossmann, J. E. Johnson, *Annu. Rev. Biochem.* **1989**, *58*, 533 – 573.
[2] a) B. Bhyravbhatla, S. J. Watowich, D. L. D. Caspar, *Biophys. J.* **1998**, *74*, 604 – 615; b) R. Pattanayek, G. Stubbs, *J. Mol. Biol.* **1992**, *228*, 516 – 528.
[3] a) T. O. Yeates, J. E. Padilla, *Curr. Opin. Struct. Biol.* **2002**, *12*, 464 – 470; b) D. Moll, C. Huber, B. Schlegel, D. Pum, U. B. Sleytr, M. Sara, *Proc. Natl. Acad. Sci. USA* **2002**, *99*, 14646 – 14651; c) P. Ringler, G. E. Schulz, *Science* **2003**, *302*, 106 – 109.
[4] J. E. Padilla, C. Colovos, T. O. Yeates, *Proc. Natl. Acad. Sci. USA* **2001**, *98*, 2217 – 2221.
[5] A. Ilari, S. Stefanini, E. Chiancone, D. Tsernoglou, *Nat. Struct. Biol.* **2000**, *7*, 38 – 43.
[6] M. Bozzi, G. Mignogna, S. Stefanini, D. Barra, C. Longhi, P. Valenti, E. Chiancone, *J. Biol. Chem.* **1997**, *272*, 3259 – 3265.
[7] R. Chiaraluce, V. Consalvi, S. Cavallo, A. Ilari, S. Stefanini, E. Chiancone, *Eur. J. Biochem.* **2000**, *267*, 5733 – 5741.
[8] S. Kanamaru, P. G. Leiman, V. A. Kostyuchenko, P. R. Chipman, V. V. Mesyanzhinov, F. Arisaka, M. G. Rossmann, *Nature* **2002**, *415*, 553 – 557.
[9] M. Su, S. Cavallo, S. Stefanini, E. Chiancone, N. D. Chasteen, *Biochemistry* **2005**, *44*, 5572 – 5578.
[10] S. Steinbacher, R. Seckler, S. Miller, B. Steipe, R. Huber, P. Reinemer, *Science* **1994**, *265*, 383 – 386.
[11] C. Kisker, H. Schindelin, B. E. Alber, J. G. Ferry, D. C. Rees, *EMBO J.* **1996**, *15*, 2323 – 2330.
[12] S. Stefanini, S. Cavallo, B. Montagnini, E. Chiancone, *Biochem. J.* **1999**, *338*, 71 – 75.
[13] S. Kanamaru, N. C. Gassner, N. Ye, S. Takeda, F. Arisaka, *J. Bacteriol.* **1999**, *181*, 2739 – 2744.
[14] M. Okuda, K. Iwahori, I. Yamashita, H. Yoshimura, *Biotechnol. Bioeng.* **2003**, *84*, 187 – 194.
[15] a) M. Allen, D. Willits, M. Young, T. Douglas, *Inorg. Chem.* **2003**, *42*, 6300 – 6305; b) H. A. Hosein, D. R. Strongin, M. Allen, T. Douglas, *Langmuir* **2004**, *20*, 10283 – 10287; c) F. C. Meldrum, T. Douglas, S. Levi, P. Arosio, S. Mann, *J. Inorg. Biochem.* **1995**, *58*, 59 – 68; d) F. C. Meldrum, J. V. Wade, L. D. Nimmo, R. B. Heywood, S. Mann, *Nature* **1991**, *349*, 684 – 687; e) T. Douglas, P. E. D. Dickson, S. Betteridge, J. Charnock, D. C. Garner, S. Mann, *Science* **1995**, *269*, 54 – 56; f) D. J. Price, J. G. Joshi, *Toxicology* **1984**, *31*, 151 – 163; g) J. Fleming, J. G. Joshi, *Proc. Natl. Acad. Sci. USA* **1987**, *84*, 7866 – 7870; h) I. Yamashita, J. Hayashi, M. Hara, *Chem. Lett.* **2004**, *33*, 1158 – 1159.

 © 2006 Wiley-VCH Verlag GmbH & Co. KGaA, Weinheim

Non-natural Amino Acids

DOI: 10.1002/anie.200600264

A Genetically Encoded Photocaged Tyrosine**

*Alexander Deiters, Dan Groff, Youngha Ryu, Jianming Xie, and Peter G. Schultz**

"Photocaged proteins" are modified proteins in which biological activity can be controlled by light, usually by photolytic conversion from an inactive to an active form. This is particularly useful as irradiation is a relatively noninvasive method that allows both spatial and temporal control of protein activity in complex cellular systems.[1] The most common photocaging groups are *o*-nitrobenzyl groups and their derivatives,[2] which can be installed on hydroxy, carboxy, thio, or amino groups of proteins and are readily cleaved upon irradiation with 365-nm light. Caged proteins have been previously generated by chemical modification of isolated

[*] D. Groff,[+] Dr. Y. Ryu, J. Xie, Prof. P. G. Schultz
Department of Chemistry and
the Skaggs Institute for Chemical Biology
The Scripps Research Institute
10550 North Torrey Pines Road, La Jolla, CA 92037 (USA)
Fax: (+1) 858-784-9440
E-mail: schultz@scripps.edu
Prof. A. Deiters[+]
Department of Chemistry
North Carolina State University
Raleigh, NC 27695-8204 (USA)

[+] These authors contributed equally.

[**] A.D. gratefully acknowledges a postdoctoral fellowship from the Deutsche Forschungsgemeinschaft. This work was supported by funding from the National Institutes of Health (GM62159) and the Department of Energy (ER46051). This is manuscript 17952-CH of The Scripps Research Institute.

Supporting information for this article is available on the WWW under http://www.angewandte.org or from the author.

© 2006 Wiley-VCH Verlag GmbH & Co. KGaA, Weinheim

proteins,[3] and by the in vitro incorporation of caged amino acids with chemically aminoacylated tRNAs.[4] More recently, we demonstrated that *o*-nitrobenzyl-*S*-cysteine can be site-specifically incorporated into proteins (in yeast) by means of a unique suppressor tRNA/aminoacyl-tRNA synthetase pair.[5,6] Herein, we show that photocaged *o*-nitrobenzyl-*O*-tyrosine (ONBY)[7] can be genetically encoded in *E. coli* in response to an amber stop codon (TAG) with high fidelity and good efficiency (Scheme 1). Moreover, irradiation (365 nm)

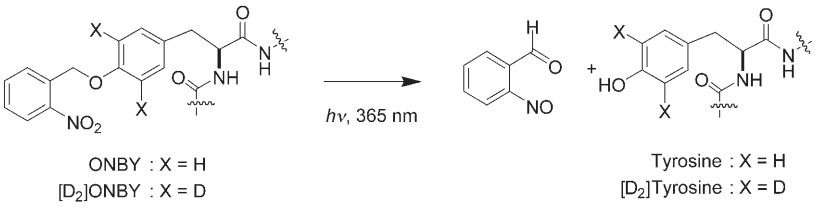

Scheme 1. Photodeprotection of *o*-nitrobenzyl adducts to yield the natural amino acid.

of *E. coli* that expresses a cytoplasmic photocaged β-galactosidase mutant resulted in the rapid and efficient restoration of enzyme activity. Because tyrosine is found in enzyme active sites (protein–ligand interfaces) and plays a major role in cellular signaling as a substrate for tyrosine kinases, the selective incorporation of ONBY into proteins should provide a useful tool for regulating protein function in vitro and in vivo.

A *Methanococcus jannaschii* $tRNA^{Tyr}_{CUA}$ ($Mj tRNA^{Tyr}_{CUA}$)/tyrosyl-tRNA synthetase (*Mj*TyrRS) pair was evolved that incorporates ONBY, but not any of the 20 common amino acids, into proteins in response to the amber stop codon TAG. To alter the specificity of the *Mj*TyrRS to selectively recognize ONBY, a library of $\approx 10^8$ *Mj*TyrRS mutants was generated by randomizing six residues (Tyr32, Leu65, Phe108, Gln109, Asp158, and Leu162) in the tyrosine binding pocket. The mutants were generated based on the crystal structure of the *Mj*TyrRS/$Mj tRNA^{Tyr}$ tyrosine complex.[8] These six residues include Tyr32 and Asp158, which form hydrogen bonds with the hydroxyl group of tyrosine. An active synthetase variant (ONBTyrRS) was identified by using chloramphenicol acetyl transferase (CAT) and barnase reporter systems for the positive and negative selections, respectively, as previously described.[6] *E. coli* expressing the ONBTyrRS/*Mj*tRNA pair survived on 100 $\mu g\,mL^{-1}$ chloramphenicol in the presence of ONBY (1 mM), and less than 10 $\mu g\,mL^{-1}$ in its absence. The large difference in chloramphenicol resistance suggests a substantial in vivo specificity for the selected synthetase/tRNA pair for ONBY over endogenous amino acids. The mutant synthetase contains the following mutations: Tyr32→Gly32, Leu65→Gly65, Phe108→Glu108, Asp158→Ser158, and Leu162→Glu162. The Asp158→Ser158 and Tyr32→Gly32 mutations likely result in the loss of hydrogen bonds with the natural substrate tyrosine, thereby disfavoring its binding. Furthermore, the Tyr32→Gly32 and Leu65→Gly65 mutations likely increase the size of the substrate-binding pocket to accommodate the bulky *o*-nitrobenzyl moiety.

To measure the fidelity and efficiency of ONBY incorporation into proteins, the amino acid was inserted at position four in a C-terminal hexahistidine-tagged mutant sperm-whale myoglobin gene. In the presence of both the ONB-TyrRS/$Mj tRNA^{Tyr}_{CUA}$ pair and ONBY (1 mM), full length myoglobin was produced in GMML (glycerol minimal media supplemented with leucine). Purified protein was obtained by nickel nitrilotriacetic acid (Ni-NTA) affinity chromatography with a yield of $\approx 2\,mg\,L^{-1}$ and judged to be >90% homogeneous by SDS-PAGE and gelcode blue staining. The yield is comparable to myoglobin expression by using the wild-type *Mj*TyrRS/$Mj tRNA^{Tyr}_{CUA}$ pair that suppresses the same amber codon. No myoglobin was detected if the non-natural amino acid was withheld or in the presence of tyrosine (1 mM). This reveals a very high selectivity of the mutant synthetase for ONBY.

To further characterize the fidelity with which ONBY is incorporated into proteins, a myoglobin mutant with an amber codon at Gly74 was coexpressed with ONBTyrRS and $Mj tRNA^{Tyr}_{CUA}$ in the presence of ONBY (1 mM). A tryptic digest of the protein was subjected to liquid chromatography and tandem MS. The precursor ions corresponding to the singly and doubly charged ions of the peptide HGVTVLTALGJILK containing the non-natural amino acid (denoted J; see the Supporting Information) were separated and fragmented with an ion-trap MS. The fragment-ion masses were consistent with the site-specific incorporation of tyrosine at position 74. The detection of Tyr74 is most likely owing to a fragmentation of the labile nitrobenzylether moiety during MS analysis. To confirm the incorporation of the caged amino acid, a deuterated derivative of ONBY ([D_2]ONBY) was synthesized and used to express the same myoglobin mutant under identical conditions. The protein was trypsinized and analyzed by mass spectrometry. An assignment of the fragment ion masses revealed [D_2]tyrosine incorporation at position 74 of myoglobin, confirming the incorporation of [D_2]ONBY.

The use of this photocaged tyrosine to noninvasively control protein function was demonstrated by the photochemical activation of β-galactosidase enzymatic activity upon irradiation both in vivo and in vitro. A photocaged β-galactosidase was previously generated by chemical modification of the enzyme with a thiol specific reagent, but this method can not precisely control the site of modification and is not applicable to the in vivo generation of photocaged proteins.[9] β-Galactosidase has an essential tyrosine at position 503, which, if mutated to Phe or Ile, results in a 10^4–10^6-fold loss in activity.[10] Consequently, the tyrosine codon (TAC) at residue 503 of the *lacZ* gene was mutated to an amber TAG codon, and ONBY was incorporated at this position by using the ONBTyrRS/$Mj tRNA^{Tyr}_{CUA}$ pair. β-Galactosidase activity was measured in vivo by using a modified Miller assay.[11] The enzymatic activity of the β-galactosidase that contained ONBY in place of Tyr503 (Y503ONBY) (Figure 1a) was comparable to the background activity in cells without the non-natural amino acid (approximately 5% of wild-type). After irradiating bacteria for 30 minutes with 365-nm monochromatic light, the β-galactosidase activity of the Y503ONBY mutant increased to roughly 67% of the

 © 2006 Wiley-VCH Verlag GmbH & Co. KGaA, Weinheim

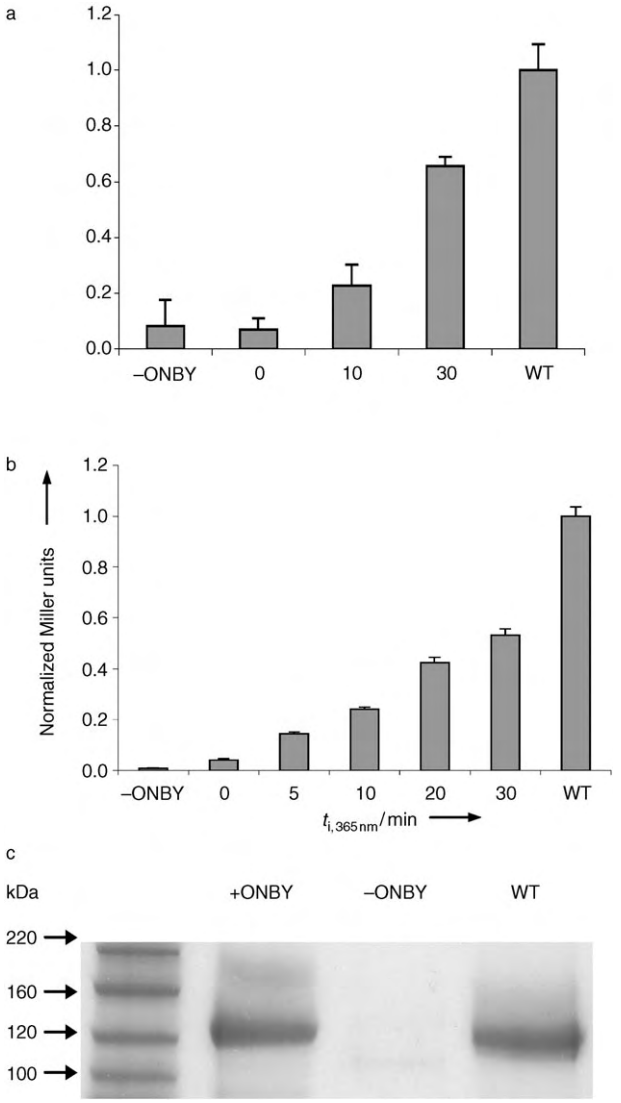

Figure 1. Expression and photoactivation of β-galactosidase Y503ONBY. Cells were cotransformed with pSUP-ONBY and either pBad*lacZ* or pBad*lacZ*503TAG and grown in 2YT to an OD_{600} of 1.8. a) Whole cell assay with photocleavage in vivo; b) photocleavage of purified protein in vitro; c) His_6 protein expressed in 2YT with ONBY-(5 mM) purified with Ni-NTA chromatography. $t_{i,365\,nm}$ = irradiation time at 365 nm, WT = wild-type.

wild-type level. These results demonstrate that it is feasible to decage an enzyme in living cells.

To further verify these results and assess the stability of the photocaged β-galactosidase, a sample of these cells was lysed and lacZ503ONBY was purified by using nickel-affinity chromatography. β-Galactosidase activity was absent once again in lysates from cultures with the 503TAG mutant in the absence of ONBY. The yield of the purified 503ONBY mutant was similar to that of the wild-type protein (Figure 1c); the activity of the caged protein was about 4% of that of wild-type β-galactosidase. Irradiation with 365-nm monochromatic light for 30 min resulted in an increase in the enzyme activity to 54% of wild-type β-galactosidase levels, (Figure 1b) consistent with the above results.

In conclusion, we have demonstrated a general method for photocaging tyrosine in any protein that can be expressed in *E. coli* including the 1024-residue β-galactosidase. By using this strategy, it should be possible to photoactivate a variety of enzymes, transcription factors, and integral membrane proteins that contain tyrosine residues that are essential for activity. We are currently extending these studies to other caged amino acids such as serine, threonine, lysine, and other organisms including yeast and mammalian cells.

Experimental Section

To express photocaged myoglobin, plasmid pBAD/JYAMB-4TAG (which encodes a mutant sperm-whale myoglobin gene with an araBAD promoter and a rrnB terminator, the *Mj*tRNA with a lpp promoter and a rrnC terminator, and a tetracycline resistance marker) was cotransformed with plasmid pBK-ONBTyrRS (which encodes the ONBTyrRS gene and a kanamycin resistance gene) into DH10B *E. coli*. Cells were amplified in Luria-Bertani (LB) media (5 mL), supplemented with tetracycline (25 mg L^{-1}) and kanamycin (30 mg L^{-1}), washed with phosphate-buffered saline (PBS), and used to innoculate 500 mL of liquid glycerol minimal media (supplemented with leucine (0.3 mM)) containing the appropriate antibiotics, ONBY (1 mM), and arabinose (0.02%). Cells were grown to saturation and then harvested by centrifugation. The protein was purified by using Ni-affinity chromatography, yielding 2–3 mg of mutant myoglobin.

β-Galactosidase containing ONBY substituted for Tyr503 was expressed from a single-plasmid system. Plasmid pSup-ONBTyrRS-6TRN (a p15A replicon that encodes six copies of the amber suppressor tRNA under control of the proK promoter and terminator, and ONBTyrRS under the control of a mutated form of the glnS promoter) was generated by inserting the ONBTyrRS gene from pBK-ONBTyrRS into the NdeI and PstI sites of pSup-BpaRS-6TRN plasmid. A single amino acid substitution of Asp268→Arg (D286R) was introduced into the ONBTyrRS gene by quickchange site-directed mutagenesis (Stratagene) to afford pSup-ONBTyrRS-6TRN(D268R).[12] The tyrosine codon (TAC) at residue 503 of the *lacZ* gene in pBAD/Myc-His/*LacZ* (Invitrogen) was mutated to an amber (TAG) codon by site-directed mutagenesis to generate pBAD/Myc-His/*LacZ*(Y503TAG). *E. coli* DH10B cells cotransformed with pBAD/Myc-His/*LacZ*(Y503TAG) and pSup-ONBTyrRS-6TRN-(D286R) were incubated overnight at 37°C in 2× yeast–tryptone (2YT) containing chloramphenicol (50 μg mL^{-1}) and carbenicillin (100 μg mL^{-1}). The fresh 2YT medium containing the antibiotics and ONBY (1 mM) was inoculated with the overnight culture (1:50 dilution) and incubated at 37°C. After one hour, cells were induced with arabinose (0.02%). After a two hour induction, the cells were harvested. For the uncaging experiments in vivo, cells were resuspended in Z buffer (sodium phosphate (0.1M), KCl (0.01M), $MgSO_4$ (0.001M), β-mercaptoethanol (0. 05M); pH 7) and irradiated with 365-nm light. At each time point, an aliquot of the cell suspension was taken and the β-galactosidase activity was measured according to the method described by Miller. [11] For the in vitro uncaging experiments, the protein was purified by using Ni-affinity chromatography to afford 0.8 mg of mutant β-galactosidase. The purified protein was then irradiated, and approximately 0.8 μg of protein was added to 700 μL of Z buffer and assayed again with the same protocol as for the assay in vivo with the omission of toluene and SDS.

Received: January 21, 2006
Published online: March 20, 2006

Keywords: amino acids · mutagenesis · photocaged tyrosine · proteins

 © 2006 Wiley-VCH Verlag GmbH & Co. KGaA, Weinheim

[1] S. R. Adams, R. Y. Tsien, *Annu. Rev. Physiol.* **1993**, *55*, 755; G. Marriott, J. Ottl, *Methods Enzymol.* **1998**, *291*, 155.
[2] R. S. Givens, J. F. Weber, A. H. Jung, C. H. Park, *Methods Enzymol.* **1998**, *291*, 1.
[3] C. H. Self, S. Thompson, *Nat. Med.* **1996**, *2*, 817.
[4] a) S. Cook, W. E. Jack, X. Xiong, L. E. Danley, J. A. Ellman, P. G. Schultz, C. J. Noren, *Angew. Chem.* **1995**, *107*, 1736; *Angew. Chem. Int. Ed. Engl.* **1995**, *34*, 1629; b) K. D. Philipson, J. P. Gallivan, G. S. Brandt, D. A. Dougherty, H. A. Lester, *Am. J. Physiol. Cell Physiol.* **2001**, *281*, C195.
[5] a) L. Wang, P. G. Schultz, *Angew. Chem.* **2005**, *117*, 34; *Angew. Chem. Int. Ed.* **2005**, *44*, 34; b) Z. Zhang, J. Gildersleeve, Y. Y. Yang, R. Xu, J. A. Loo, S. Uryu, C. H. Wong, P. G. Schultz, *Science* **2004**, *303*, 371; c) N. Wu, A. Deiters, T. A. Cropp, D. King, P. G. Schultz, *J. Am. Chem. Soc.* **2004**, *126*, 14306; d) J. W. Chin, T. A. Cropp, J. C. Anderson, M. Mukherji, Z. Zhang, P. G. Schultz, *Science* **2003**, *301*, 964.
[6] L. Wang, A. Brock, B. Herberich, P. G. Schultz, *Science* **2001**, *292*, 498.
[7] J. C. Miller, S. K. Silverman, P. M. England, D. A. Dougherty, H. A. Lester, *Neuron* **1998**, *20*, 619.
[8] a) T. Kobayashi, O. Nureki, R. Ishitani, A. Yaremchuk, M. Tukalo, S. Cusack, K. Sakamoto, S. Yokoyama, *Nat. Struct. Biol.* **2003**, *10*, 425; b) Y. Zhang, L. Wang, P. G. Schultz, I. A. Wilson, *Protein Sci.* **2005**, *14*, 1340.
[9] R. Golan, U. Zehavi, M. Naim, A. Patchornik, P. Smirnoff, M. Herchman, *J. Protein Chem.* **2000**, *19*, 123.
[10] R. M. Penner, N. J. Roth, B. Rob, H. Lay, R. E. Huber, *Biochem. Cell Biol.* **1999**, *77*, 229.
[11] J. H. Miller, *Experiments in Molecular Genetics*, Cold Springs Harbor Laboratory, Cold Springs Harbor, NY, **1972**.
[12] Y. Ryu, P. G. Schultz, *Nat. Meth.* **2006**, *3*, 263.

 © 2006 Wiley-VCH Verlag GmbH & Co. KGaA, Weinheim

Natural Product Synthesis

DOI: 10.1002/anie.200600210

Total Synthesis of (+)-β-Erythroidine**

*Hironori Fukumoto, Keisuke Takahashi, Jun Ishihara, and Susumi Hatakeyama**

The *Erythrina* alkaloids[1] have received considerable attention over the past few decades owing to their intriguing biological activity[2] and characteristic polycondensed structures, which provide an opportunity to develop a new ring-forming methodology.[3] This family of alkaloids are classified into two groups according to their structural features: those whose D rings are aromatic, and those whose D rings contain an unsaturated lactone. Although a wide variety of methods have already been developed for the synthesis of the group containing an aromatic D ring,[1,3] the synthesis of their counterparts with non-aromatic D rings is limited to that of (±)-cocculolidine by Kitahara and co-workers.[3p] Herein, we describe the first total synthesis of (+)-β-erythroidine (**1**), a non-aromatic dienoid-type *Erythrina* alkaloid isolated from several species of the *Erythrina* genus together with α-erythroidine.[4,5]

Recently, we developed an efficient method[3j,6] for the construction of the erythrinan skeleton which relies on ring-closing metathesis[7,8] of a dienyne. On the basis of this methodology, we envisaged dienyne **2** as a precursor of **1** and postulated that this intermediate could be accessed from β-keto ester **3**, which would be available from **5** through **4** by N-alkylation followed by Dieckmann condensation (Scheme 1). In this synthetic plan, another key issue which must be addressed is the enantiocontrolled construction of ethynylated amino acid fragment **5**, which contains a quaternary center.

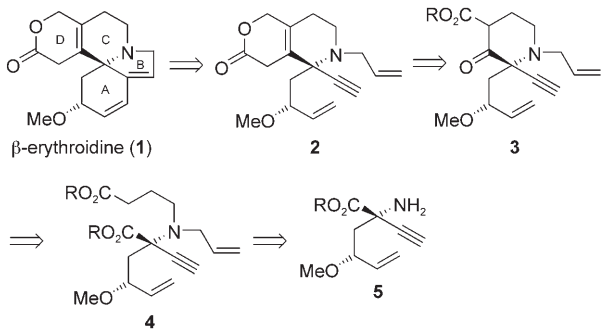

Scheme 1. Retrosynthetic analysis of β-erythroidine (**1**).

The required amino acid fragment was synthesized as **18** in enantiocontrolled manner by taking advantage of the method[9] that we previously developed for the construction of quaternary amino acids (Scheme 2). Thus, according to the procedure developed by Kotsuki et al.,[10] triflate **7**, which is readily available from 2,3-*O*-isopropylidene-D-threitol (**6**) through the corresponding monotosylate,[11] was treated with lithiated propargyl tetrahaydropyranyl ether to give tosylate **8**. Iodination of **8** followed by reductive cleavage of the resulting iodide gave alcohol **10**. Methylation of **10** and subsequent removal of the THP protecting group afforded propargyl alcohol **11**. Successive treatment[12] of **11** with $NaH_2Al(OCH_2CH_2OMe)_2$ and iodine allowed stereo- and regioselective formation of *Z*-iodoalkene **12**. Upon Sonogashira coupling[13] of **12** with trimethylsilylacetylene, the acetylene functionality was cleanly introduced and, after desilylation, *Z*-allylic alcohol **13** was obtained quantitatively. Although subsequent epoxidation of **13** proceeded with poor diastereoselectivity under Katsuki–Sharpless catalytic asym-

[*] H. Fukumoto, K. Takahashi, Dr. J. Ishihara, Prof. Dr. S. Hatakeyama
Graduate School of Biomedical Sciences
Nagasaki University
1-14 Bunkyo-machi, Nagasaki 852-8521 (Japan)
Fax: (+81) 95-819-2426
E-mail: susumi@net.nagasaki-u.ac.jp

[**] This work was partly supported by a Grant-in-Aid for Scientific Research on Priority Areas (16073213) from the Ministry of Education, Culture, Sports, Science, and Technology (MEXT). We thank Prof. Takanori Suzuki (Graduate School of Science, Hokkaido University) for the X-ray analysis of **16**.

Supporting information for this article is available on the WWW under http://www.angewandte.org or from the author.

 © 2006 Wiley-VCH Verlag GmbH & Co. KGaA, Weinheim

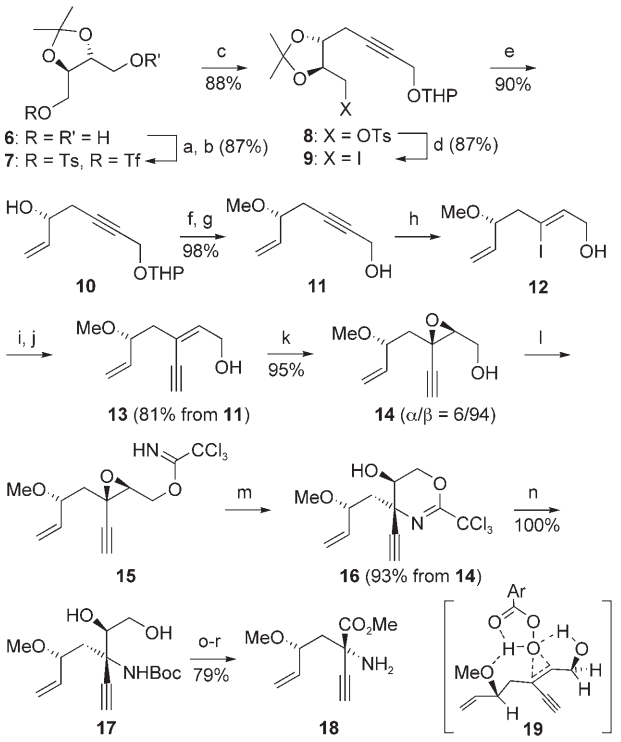

Scheme 2. Preparation of amino acid fragment **18**. Reagents and conditions: a) Ag_2O, TsCl, KI, CH_2Cl_2; b) Tf_2O, Et_3N, CH_2Cl_2, −15 °C; c) *n*BuLi, $CHCCH_2OTHP$, THF/DMPU, −20 °C; d) NaI, DMF, 70 °C; e) Zn, AcOH, EtOH, sonication; f) MeI, Ag_2O, Et_2O; g) PPTS, MeOH; h) $NaH_2Al(OCH_2CH_2OMe)_2$, Et_2O, 0 °C, then I_2; i) CHCTMS, [Pd-$(PPh_3)_2Cl_2$], CuI, iPr_2NH, THF, sonication; j) K_2CO_3, MeOH; k) *m*CPBA, $NaHCO_3$, CH_2Cl_2, −50 °C; l) Cl_3CCN, DBU, 4 Å M.S., CH_2Cl_2, 0 °C; m) $BF_3{\cdot}OEt_2$, CH_2Cl_2, −20 °C; n) 1 M HCl, THF, then Boc_2O, $NaHCO_3$; o) $NaIO_4$, THF/H_2O; p) $NaClO_2$, NaH_2PO_4, 2-methyl-2-butene, *t*BuOH/H_2O; q) CH_2N_2, MeOH; r) TFA, CH_2Cl_2. Ts = *p*-toluenesulfonyl; Tf = trifluoromethanesulfonyl; THP = tetrahydropyranyl; DMPU = *N,N′*-dimethyl-*N,N′*-propylene urea; DMF = *N,N*-dimethylformamide; PPTS = pyridinium *p*-toluenesulfonate; TMS = trimethylsilyl; *m*CPBA = *m*-chloroperoxybenzoic acid; DBU = 1,8-diazabicyclo-[5.4.0]undec-7-ene; Boc = *tert*-butoxycarbonyl; TFA = trifluoroacetic acid.

metric epoxidation conditions,[14] we were pleased to find that the epoxidation using *m*CPBA occurred with excellent diastereoselectivity to give epoxide **14** as an inseparable mixture of α and β diastereoisomers (6:94 ratio, respectively). The observed high diastereoselectivity can be explained through transition state **19** where the approach of *m*CPBA is restricted to the β-face by hydrogen bonding (Scheme 2).[15]

At this stage, stereoselective introduction of a nitrogen atom at the quaternary center was achieved by Lewis acid promoted cyclization of an epoxy-trichloroacetimidate.[9] Thus, the epoxy alcohol **14** was converted into imidate **15** by reaction with trichloroacetonitrile in the presence of DBU. Upon treatment of **15** with 0.5 equivalents of $BF_3{\cdot}OEt_2$ in CH_2Cl_2 at −20 °C, the cyclization took place selectively at the quaternary center of the epoxide with complete inversion of the stereochemistry to produce dihydrooxazine **16**. The stereochemical structure of **16** was unambiguously confirmed by X-ray analysis.[16] Acidic hydrolysis of **16** followed by *tert*-butoxycarbonylation afforded diol **17** quantitatively, which was successfully converted into the required ethynylated amino acid derivative **18** by a four-step sequence involving oxidation with $NaIO_4$, Pinnick oxidation,[17] esterification, and removal of the Boc protecting group.

Construction of the C,D ring system began with reductive alkylation of **18** (Scheme 3). Thus, reaction of **18** with methyl

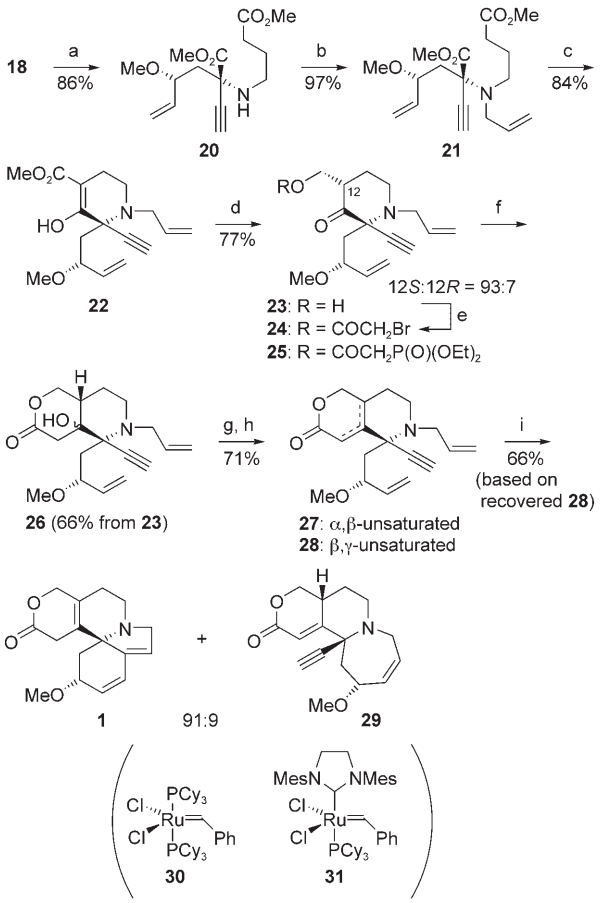

Scheme 3. Completion of the total synthesis of (+)-β-erythroidine (**1**). Reagents and conditions: a) $MeO_2C(CH_2)_2CHO$, $NaBH(OAc)_3$, 4 Å M.S., THF, 0 °C; b) allyl bromide, K_2CO_3, DMF; c) NaH, MeOH, toluene, reflux; d) NaH, THF, 0 °C, then AlH_3, −10 °C; e) $BrCH_2COCl$, pyridine, CH_2Cl_2, 0 °C; f) SmI_2, THF; g) $SOCl_2$, pyridine; h) 10% NaOH, dioxane, reflux, then acidified with conc. HCl; i) **30** (0.1 equiv), CH_2Cl_2. Cy = cyclohexyl; Mes = mesityl.

3-formylpropanoate in the presence of $NaBH(OAc)_3$[18] and molecular sieves gave **20**, which was then allylated to afford amine **21** in good yield. Upon treatment of **21** with NaOMe in boiling toluene, Dieckmann condensation cleanly occurred to give condensation product **22**, which adopts almost exclusively the enol form. After conversion of **22** into the corresponding sodium enolate, its reduction in situ with AlH_3[19] gave a mixture (93:7) of aldol **23** and its C12 epimer, the stereochemistry of which was determined by NOE experiments (Figure 1).

To construct the D ring by an intramolecular Horner–Emmons reaction,[20] we attempted to prepare **25** from **23** by using either diethyl phosphonoacetic acid or its chloride under various conditions. However, this acylation proved

 © 2006 Wiley-VCH Verlag GmbH & Co. KGaA, Weinheim

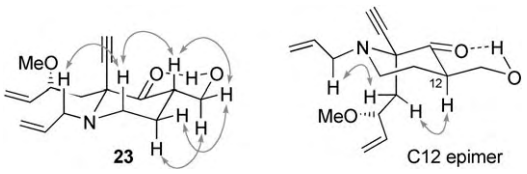

Figure 1. Significant NOE observed in the NOESY NMR spectra of aldol **23** and its C12 epimer.

troublesome because dehydration always took place predominantly. Therefore, we next investigated the approach based on an SmI_2-mediated intramolecular Reformatsky reaction.[21] In this case, acylation of **23** with bromoacetyl chloride in the presence of pyridine took place successfully to give bromoacetate **24** together with a small amount of the corresponding dehydrated product, although **24** was chromatographically unstable. Without purification, treatment of **24** with SmI_2 in THF at room temperature led to cyclization to give lactone **26** as a mixture of epimers (60:40). Treatment of **26** with thionyl chloride in pyridine caused dehydration to give an inseparable mixture of α,β-unsaturated lactone **27** and β,γ-unsaturated lactone **28** (74:26). Gratifyingly, in this particular case, saponification followed by acidification allowed highly selective production of the β,γ-lactone to give a mixture of **27** and **28** in a ratio of 6:94. Finally, treatment of this isomeric mixture with 0.1 equivalents of Grubbs' first-generation catalyst **30** in CH_2Cl_2 at room temperature for 6.5 h cleanly furnished (+)-β-erythroidine (**1**; $[\alpha]_D^{21} = +50.0°$ ($c = 0.21$, EtOH)),[22] in 42% yield together with **29** (4%), although an appreciable amount of unconverted **28** (31%) was recovered. In this particular case, Grubbs' second-generation catalyst **31** turned out to be less effective and gave **1** in less than 30% yield. The spectral data of **1** thus obtained show good agreement with those reported[4b,c] for the natural specimen.

In addition, we investigated the ring-closing metathesis of **20, 22, 26**, and **36** using catalysts **30** and **31** (Scheme 4). These results revealed that the mode of metathesis largely depends upon the structure of the substrate. Importantly, neither **32** nor **37** could be converted into **1** because of the extreme instability arising from their tetrahydroindole structures under basic conditions.

In conclusion, we have demosntrated the first total synthesis of (+)-β-erythroidine, a non-aromatic *Erythrina* alkaloid, in naturally occurring form by employing Lewis acid promoted cyclization of the epoxy-trichloroacetimidate and tandem ring-closing metathesis of the dienyne as key steps. The present work opens a new avenue for the enantioselective synthesis of *Erythrina* alkaloids.

Received: January 18, 2006
Published online: March 21, 2006

Keywords: alkaloids · erythroidine · natural products · ring-closing metathesis · total synthesis

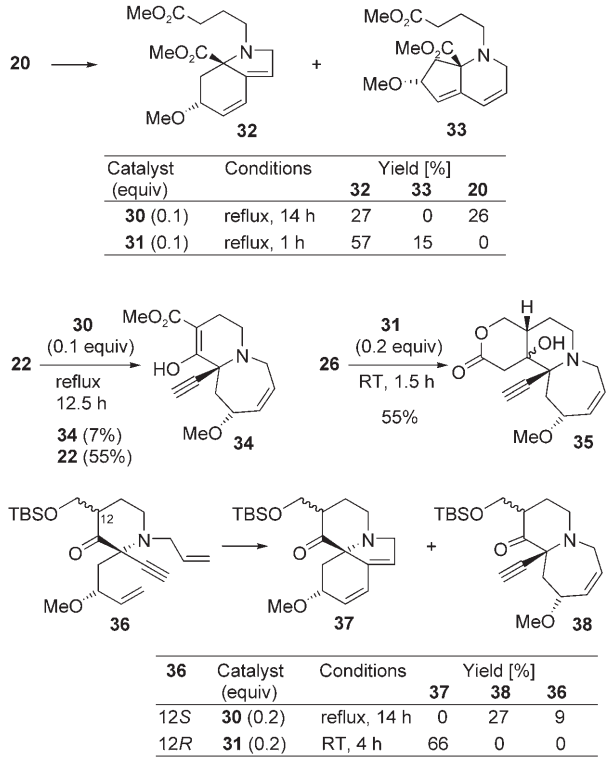

Catalyst (equiv)	Conditions	Yield [%] 32	33	20
30 (0.1)	reflux, 14 h	27	0	26
31 (0.1)	reflux, 1 h	57	15	0

36	Catalyst (equiv)	Conditions	Yield [%] 37	38	36
12*S*	**30** (0.2)	reflux, 14 h	0	27	9
12*R*	**31** (0.2)	RT, 4 h	66	0	0

Scheme 4. Ring-closing metathesis of dienynes. The reactions were carried out using Grubbs' catalysts **30** or **31** (0.1 or 0.2 equiv) in CH_2Cl_2 (0.05 M).

[1] For reviews, see: a) A. S. Chawla, V. K. Kapoor in *Alkaloids: Chemical and Biological Perspectives, Vol. 9* (Ed.: S. W. Pelletier), Pergamon, Oxford, **1993**, pp. 86–153; b) Y. Tsuda, T. Sano in *The Alkaloids, Vol. 48* (Ed.: G. A. Cordell), Academic Press, New York, **1996**, pp. 249–337.

[2] Members of the *Erythrina* family display curare-like and hypnoptic activity as well as a variety of pharmacological effects, such as sedative, hypotensive, neuromascular-blocking, and CNS activity. See: A. Padwa, R. Henning, C. O. Kappe, T. S. Roger, *J. Org. Chem.* **1998**, *63*, 1144–1155, and references therein.

[3] For recent reports on the construction of the erythrinane skeleton, see: a) A. J. Blake, C. Gill, D. A. Greenhalgh, N. S. Simpkins, F. Zhang, *Synthesis* **2005**, 3287–3292; b) A. Padwa, H. I. Lee, P. Rashatasakhon, M. Rose, *J. Org. Chem.* **2004**, *69*, 8209–8218; c) S. A. A. El Biary, H. Braun, L. F. Tietze, *Angew. Chem.* **2004**, *116*, 5505–5507; *Angew. Chem. Int. Ed.* **2004**, *43*, 5391–5393; d) S. M. Allin, G. B. Streetley, M. Slater, S. L. James, W. P. Martin, *Tetrahedron Lett.* **2004**, *45*, 5493–5496; e) Y. Yasui, K. Suzuki, T. Matsumoto, *Synlett* **2004**, 619–622; f) Y. Yasui, Y. Koga, K. Suzuki, T. Matsumoto, *Synlett* **2004**, 615–618; g) C. Gill, D. A. Greenhalgh, N. S. Simpkins, *Tetrahedron Lett.* **2003**, *44*, 7803–7807; h) M. M. Abelman, J. F. Curtis, D. R. James, *Tetrahedron Lett.* **2003**, *44*, 6527–6531; i) H. I. Lee, M. P. Cassidy, P. Rashatasakhon, A. Padwa, *Org. Lett.* **2003**, *5*, 5067–5070; j) M. A. Guerrero, R. Cruz-Almanza, L. D. Miranda, *Tetrahedron* **2003**, *59*, 4953–4958; k) H. Fukumoto, T. Esumi, J. Ishihara, S. Hatakeyama, *Tetrahedron Lett.* **2003**, *44*, 8047–8049; l) K. Shimizu, M. Takimoto, M. Mori, *Org. Lett.* **2003**, *5*, 2323–2325; m) S. Chikaoka, A. Toyao, M. Ogasawara, O. Tamura, H. Ishibashi, *J. Org. Chem.* **2003**, *68*, 312–318; n) S. M. Allin, S. L. James, M. R. J. Elsegood, W. P. Martin, *J. Org. Chem.* **2002**, *67*, 9464–9467; o) L. M. Miranda, S. Z. Zard, *Org. Lett.* **2002**, *4*, 1135–1138; p) T. Kawasaki, N. Onoda, H. Watanabe, T. Kitahara, *Tetrahedron lett.* **2001**, *42*, 8003–8006; q) C. Jousse-

 © 2006 Wiley-VCH Verlag GmbH & Co. KGaA, Weinheim

Karinthi, C. Riche, A. Chiaroni, D. Desmaële, *Eur. J. Org. Chem.* **2001**, 3631 – 3640; r) A. Toyao, S. Chikaoka, Y. Takeda, O. Tamura, O. Muraoka, G. Tanabe, H. Ishibashi, *Tetrahedron Lett.* **2001**, *42*, 1729 – 1732; s) S. Hosoi, M. Nagao, Y. Tsuda, K. Isobe, T. Sano, T. Ohta, *J. Chem. Soc. Perkin Trans. 1* **2000**, 1505 – 1511; t) A. Padwa, A. G. Waterson, *J. Org. Chem.* **2000**, *65*, 235 – 244.

[4] For isolation and structure determination, see: a) V. Boekelheide in *The Alkaloids, Vol. 7* (Ed.: R. H. F. Manske), Academic Press, New York, **1960**, pp. 201 – 227; b) M. I. Aguilar, F. Giral, O. Espejo, *Phytochemistry* **1981**, *20*, 2061 – 2062; c) A. S. Chawla, A. H. Jackson, P. Ludgate, *J. Chem. Soc. Perkin Trans. 1* **1982**, 2903 – 2907.

[5] For absolute configuration, see: a) G. R. Wenzinger, V. Boekelheide, *Proc. Chem. Soc. London* **1963**, 53; b) A. W. Hanson, *Acta Crystallogr.* **1963**, *16*, 939 – 942.

[6] Mori and co-workers also reported the same methodology for the construction of the erythrinane skeleton.[31]

[7] For tandem ring-closing metathesis, see: a) S. Randl, S. Blechert in *Handbook of Metathesis, Vol. 2* (Ed.: R. H. Grubbs), Wiley-VCH, Weinheim, **2003**, pp. 151 – 175.

[8] For related ring-closing metathesis of dieneynes, see: a) T. Honda, H. Namiki, M. Watanabe, H. Mizutani, *Tetrahedron Lett.* **2004**, *45*, 5211 – 5213; b) T. Honda, H. Namiki, K. Kaneda, H. Mizutani, *Org. Lett.* **2004**, *6*, 87 – 89; c) J. Huang, H. Xiong, R. P. Hsung, C. Rameshkumar, J. A. Mulder, T. P. Grebe, *Org. Lett.* **2002**, *4*, 2417 – 2420.

[9] S. Hatakeyama, H. Matsumoto, H. Fukuyama, Y. Mukugi, H. Irie, *J. Org. Chem.* **1997**, *62*, 2275 – 2279.

[10] H. Kotsuki, I. Kadota, M. Ochi, *Tetrahedron Lett.* **1990**, *31*, 4609 – 4612.

[11] A. Bouzide, G. Sauvé, *Org. Lett.* **2002**, *4*, 2329 – 2332.

[12] S. E. Denmark, T. K. Jones, *J. Org. Chem.* **1982**, *47*,4595 – 4597.

[13] K. Sonogashira in *Handbook of Organopalladium Chemistry for Organic Synthesis, Vol. 1* (Eds.: E. Negishi, A. De Meijere), Wiley-Interscience, **2002**, pp. 493 – 529.

[14] Y. Gao, R. M. Hanson, J. M. Klunder, S. Y. Ko, H. Masamune, K. B. Sharpless, *J. Am. Chem. Soc.* **1987**, *109*, 5765 – 5780.

[15] M. R. Johnson, Y. Kishi, *Tetrahedron Lett.* **1979**, *20*, 4347 – 4350.

[16] CCDC-292947 contains the supplementary crystallographic data for this paper. These data can be obtained free of charge from The Cambridge Crystallographic Data Centre via www.ccdc.cam.ac.uk/data_request/cif.

[17] B. S. Bal, W. E. Childers, H. W. Pinnick, *Tetrahedron* **1981**, *37*, 2091 – 2096.

[18] A. F. Abdel-Magid, K. G. Carson, B. D. Harris, C. A. Maryanoff, R. D. Shah, *J. Org. Chem.* **1996**, *61*, 3849 – 3862.

[19] a) G. Laval, G. Audran, J.-M. Galano, H. Monti, *J. Org. Chem.* **2000**, *65*, 3551 – 3554; b) K. Isobe, K. Mohri, H. Sano, J. Taga, Y. Tsuda, *Chem. Pharm. Bull.* **1986**, *34*, 3029 – 3032.

[20] a) A. Nangia, P. B. Rao, *Tetrahedron Lett.* **1992**, *33*, 2375 – 2378; b) Y. Tsuda, A. Ishiura, S. Hosoi, K. Isobe, *Chem. Pharm. Bull.* **1992**, *40*, 1697 – 1702.

[21] For a review, see: R. Ocampo, W. R. Dolbier, Jr., *Tetrahedron* **2004**, *60*, 9325 – 9374.

[22] The specific rotation of natural β-erythroidine was not reported.

 © 2006 Wiley-VCH Verlag GmbH & Co. KGaA, Weinheim

Cycloaddition

DOI: 10.1002/anie.200504470

Rh-Catalyzed [4+2] Annulation of 4-Alkynals with Isocyanates and Its Application to the Parallel Kinetic Resolution of Unfunctionalized 4-Alkynals**

Ken Tanaka, Yuji Hagiwara, and Masao Hirano*

Transition-metal-catalyzed carbocyclizations are useful methods for the construction of carbocycles and heterocycles.[1] In particular, cycloadditions that use isocyanates are efficient methods for the construction of nitrogen-containing heterocycles.[2] For example, transition-metal-catalyzed [2+2+2] cycloadditions of alkynes with isocyanates to prepare substituted 2-pyridones have been widely examined with Co,[3] Ni,[4] Ru,[5] and Rh[6,7] catalysts. However, to the best of our knowledge, transition-metal-catalyzed [4+2] cycloadditions that use isocyanates to prepare six-membered nitrogen-containing heterocycles have not been reported.

We recently reported the rhodium-catalyzed regio- and enantioselective intermolecular [4+2] carbocyclization of 4-alkynals with *N,N*-dialkyl acrylamides for the synthesis of enantioenriched cyclohexanones through five-membered acyl rhodium intermediates **A**, which are formed by the intramolecular hydroacylation of alkynes.[8–11] Herein, we establish a rhodium-catalyzed intermolecular [4+2] annulation of 4-alkynals with isocyanates for the preparation of 4-alkylideneglutarimides (Scheme 1), and its application to a parallel kinetic resolution of unfunctionalized 4-alkynals.[12]

The rhodium-catalyzed [4+2] annulation of 3-methyl-4-nonynal (**1a**) with *n*-butyl isocyanate (**2a**) was examined using various mono- or bidentate phosphine ligands. The

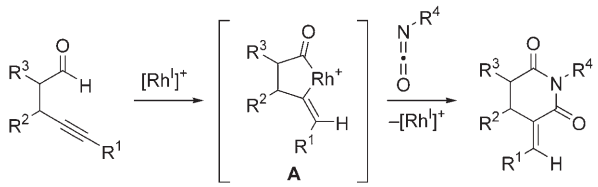

Scheme 1. Intermolecular [4+2] annulation of 4-alkynals with isocyanates.

[*] Prof. Dr. K. Tanaka, Y. Hagiwara, Dr. M. Hirano
Department of Applied Chemistry
Graduate School of Engineering
Tokyo University of Agriculture and Technology
Koganei, Tokyo 184-8588 (Japan)
Fax: (+81) 42-388-7037
E-mail: tanaka-k@cc.tuat.ac.jp

[**] We thank Takasago International Corporation for the gift of segphos and Prof. Gregory C. Fu (Massachusetts Institute of Technology, USA) for his helpful encouragement.

Supporting information for this article is available on the WWW under http://www.angewandte.org or from the author.

WILEY InterScience DISCOVER SOMETHING GREAT

© 2006 Wiley-VCH Verlag GmbH & Co. KGaA, Weinheim

study revealed that the use of bidentate phosphine ligands with large P-M-P natural bite angles (1,3-propanediylbis-[(diphenyl)phosphine] (dppp), 1,4-butanediylbis[(diphenyl)-phosphine] (dppb), 1,1′-bis(diphenylphosphino)ferrocene (dppf), and (1,1′-binaphthalene)-2,2′-diylbis(diphenylphosphine) (*rac*-BINAP)) gave glutarimide **3aa**, which was produced in the highest yield with dppp. The reactions of **1a** with a series of isocyanates **2a–f** were examined by using Rh^I/dppp as the catalyst (Table 1, entries 1–6). The reactions

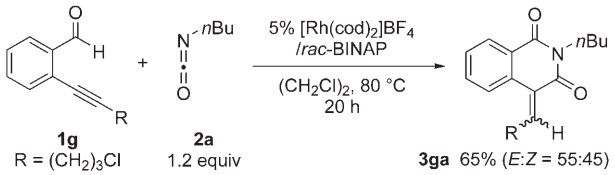

Scheme 2. Intermolecular [4+2] annulation of 2-alkynylbenzaldehyde **1g** with isocyanate **2a**. cod = 1,5-cyclooctadiene.

Table 1: Rhodium-catalyzed [4+2] annulation of 4-alkynals with isocyanates to give 2-alkylideneglutarimides.[a]

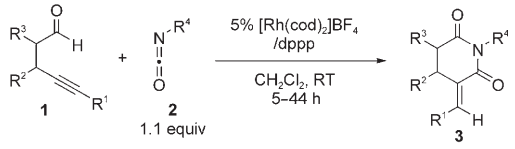

Entry	1	R^1	R^2	R^3	2	R^4	3	Yield [%][b]
1	**1a**	*n*Bu	Me	H	**2a**	*n*Bu	**3aa**	82
2	**1a**	*n*Bu	Me	H	**2b**	*n*Oct	**3ab**	75
3	**1a**	*n*Bu	Me	H	**2c**	Cy	**3ac**	67
4	**1a**	*n*Bu	Me	H	**2d**	Bn	**3ad**	79
5	**1a**	*n*Bu	Me	H	**2e**	4-MeOBn	**3ae**	75
6	**1a**	*n*Bu	Me	H	**2f**	Ph	**3af**	45
7[c,d]	**1b**	*n*Bu	H	Me	**2a**	*n*Bu	**3ba**	63
8	**1c**	Cy	Me	H	**2a**	*n*Bu	**3ca**	87
9[d]	**1d**	$SiMe_3$	Me	H	**2a**	*n*Bu	**3da**	91
10[e]	**1e**	1-cyclohexenyl	Me	H	**2a**	*n*Bu	**3ea**	83
11[e]	**1f**	Ph	Me	H	**2a**	*n*Bu	**3fa**	71

[a] Reactions were carried out with **1** (0.40 mmol), **2** (0.44 mmol), $[Rh(cod)_2]BF_4$ (0.020 mmol), dppp (0.020 mmol), and CH_2Cl_2 (1.0 mL). [b] Yields of the isolated products. [c] Ligand = dppb. [d] Catalyst = 10 mol%. [e] Ligand = *rac*-BINAP. Cy = cyclohexyl.

of **1a** with alkyl (entries 1–3), benzyl (entry 4), methoxybenzyl (entry 5), and aryl (entry 6) isocyanates afforded the corresponding glutarimides in moderate-to-high yields. We also explored the scope of this process in respect to 4-alkynals (entries 1 and 7–11). A variety of 4-alkynals were subjected to this process by employing appropriate bidentate phosphine ligands. The reactions tolerated substitutions at both the 3 and 2 positions (entries 1 and 7, respectively). 5-Alkyl-, 5-trimethylsilyl-, 5-alkenyl-, and 5-aryl-substituted 4-alkynals with **2a** afforded the corresponding glutarimides in high yields (entries 1 and 8–11, respectively). Importantly, a single olefin isomer described in Table 1 was produced for all of these annulations. On the other hand, the reaction of 2-alkynylbenzaldehyde **1g** with **2a** furnished a mixture of *E*/*Z* isomers of glutarimide **3ga** at an elevated temperature (80 °C) in the presence of 5 mol% Rh^I/*rac*-BINAP as the catalyst (Scheme 2).[13,14]

During the screening of ligands for the reaction of **1a** with **2a**, the use of *rac*-BINAP afforded a significant amount of the cyclopentenone **4a** as a by-product to the desired glutarimide **3aa**. We anticipated that parallel kinetic resolution of 4-alkynal **1a** for the preparation of the enantioenriched glutarimide **3aa** and cyclopentenone **4a** might proceed.[12] We were pleased to find that enantioenriched **3aa** and **4aa** were obtained in 58 and 24% yield with 49 and 81% *ee*, respectively, when the same reaction was conducted using 5% Rh^I/(*R*)-BINAP (Scheme 3).

After screening a variety of chiral bidentate phosphine ligands, (*S*)-segphos[15] was found to be the ligand of choice in terms of yield and enantioselectivity of the products. We therefore examined the scope of the Rh^I/(*S*)-segphos-catalyzed parallel kinetic resolution of 4-alkynals in the presence of 0.5 equivalents of isocyanates (Table 2).[16] Alkyl, benzyl, and aryl isocyanates could be employed for this resolution process (entries 1–4, respectively). We also extended the scope of this process with respect to 4-alkynals (entries 5–9). The reactions tolerated both alkyl and aryl substitutions at the 3-position (entries 1, 5, and 6) and alkyl, alkenyl, and aryl groups substitutions at the 5-position (entries 5 and 7–9).[17]

Interestingly, the reaction of 5-trimethylsilyl-4-alkynal **1j** with isocyanate **2a** using 20 mol% Rh^I/(*R*)-BINAP afforded enantioenriched glutarimide **3ja** and aziridine **5** in 17 and 16% yield with 62 and 7% *ee*, respectively (Scheme 4).

Scheme 5 shows a plausible mechanism for this reaction. The rhodium catalyst oxidatively inserts into the aldehyde C–H bond, thus affording a rhodium acyl hydride **B**. The *cis*

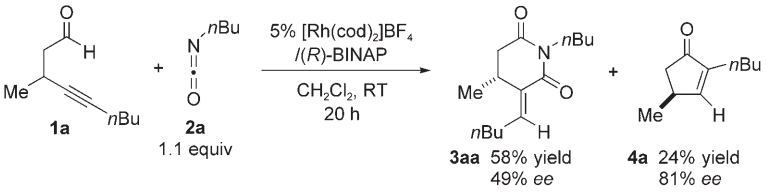

Scheme 3. The parallel kinetic resolution of 3-methyl-4-nonynal (**1a**), which leads to enantioenriched 2-alkylideneglutarimide **3aa** and cyclopentenone **4a**.

addition of the rhodium hydride to the metal-bound alkyne then provides the five-membered acyl rhodium intermediate **A**.[18] Complexation of the isocyanate is followed by insertion to form metallacycle **C**. Reductive elimination from **C** furnishes the glutarimide **3** and regenerates the Rh catalyst. The cyclopentenone **4** can be obtained through the rhodium-catalyzed *trans* hydroacylation of **1**.[19]

In conclusion, we have developed a rhodium-catalyzed intermolecular [4+2] annulation of 4-alkynals with isocyanates for the preparation of 2-alkylideneglutarimides and applied this approach to the parallel kinetic resolution of unfunctionalized 4-alkynals. This method serves as an attractive new route to enantioenriched 2-alkylideneglutarimides and cyclopentenones given the one-step access to 4-alkynals from readily available terminal alkynes.

 © 2006 Wiley-VCH Verlag GmbH & Co. KGaA, Weinheim

Table 2: Rhodium-catalyzed parallel kinetic resolution of 3-substituted 4-alkynals to yield enantioenriched 2-alkylideneglutarimides and cyclopentenones.[a]

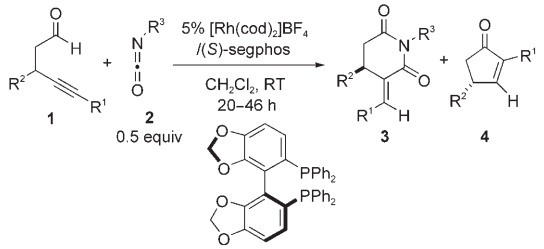

Entry	1	R^1	R^2	2	R^3	3		4	
						Yield [%][b]	*ee* [%][c]	Yield [%][b]	*ee* [%][c]
1	**1h**	*n*Bu	*n*Bu	**2a**	*n*Bu	34	91	28	92
2	**1h**	*n*Bu	*n*Bu	**2b**	Cy	30	81	38	94
3	**1h**	*n*Bu	*n*Bu	**2c**	Bn	36	88	26	91
4	**1h**	*n*Bu	*n*Bu	**2d**	Ph	20	52	38	94
5	**1a**	*n*Bu	Me	**2a**	*n*Bu	38	87	39	83
6[d]	**1i**	*n*Bu	Ph	**2a**	*n*Bu	22	97	36	78
7[d]	**1c**	Cy	Me	**2a**	*n*Bu	33	64	30	98
8	**1e**	1-cyclohexenyl	Me	**2a**	*n*Bu	49	56	26	85
9[d]	**1f**	Ph	Me	**2a**	*n*Bu	35	72	31	76

[a] Reactions were carried out with **1** (0.40 mmol), **2** (0.20 mmol), $[Rh(cod)_2]BF_4$ (0.020 mmol), (*S*)-segphos (0.020 mmol), and CH_2Cl_2 (2.0 mL). [b] Yields of the isolated products. [c] The *ee* values were determined by chiral HPLC or GC analysis. [d] Catalyst = 10 mol%.

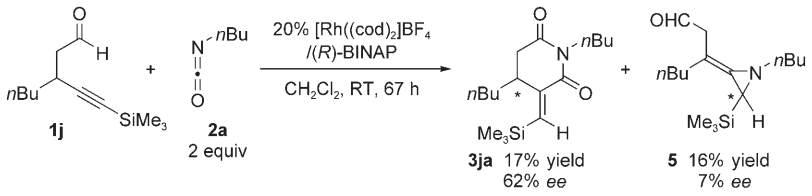

Scheme 4. Intermolecular [4+2] annulation of 5-trimethylsilyl-4-alkynal **1j** with isocyanate **2a**.

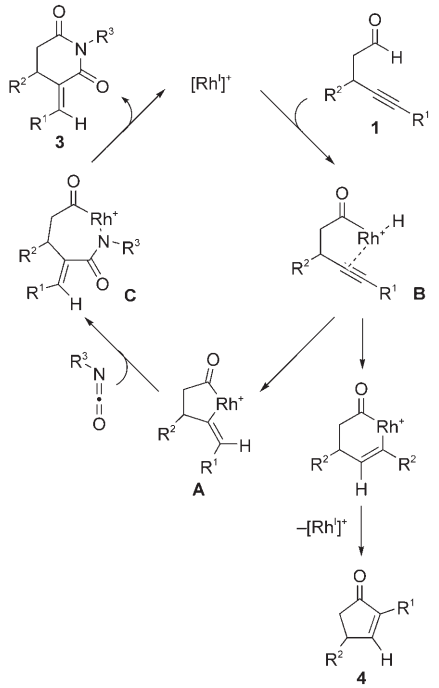

Scheme 5. Plausible reaction mechanism for the rhodium-catalyzed intermolecular [4+2] annulation of 4-alkynals with isocyanates.

Experimental Section

Representative procedure (Table 2, entry 5): In an Ar atmosphere, a solution of (*S*)-segphos (12.2 mg, 0.020 mmol) in CH_2Cl_2 (1.0 mL) was added to a solution of $[Rh(cod)_2]BF_4$ (8.1 mg, 0.020 mmol) in CH_2Cl_2 (1.0 mL), and the resulting mixture was stirred for 5 min. H_2 was introduced to the reaction solution in a Schlenk tube. The resulting solution was concentrated to dryness after stirring for 0.5 h at room temperature. 3-Methylnon-4-ynal (**1a**; 60.9 mg, 0.400 mmol) and *n*-butyl isocyanate (**2a**; 19.8 mg, 0.20 mmol) were added to the residue by using CH_2Cl_2 (2.0 mL), and the reaction mixture was stirred at room temperature for 20 h. The resulting solution was concentrated and purified by chromatography on silica gel (hexane/EtOAc 12:1), which furnished (*R*)-(+)-1-butyl-4-methyl-3-pentylidenepiperidine-2,6-dione ((*S*)-(+)-**3aa**; 38.5 mg, 0.153 mmol, 38% yield, 87% *ee*) as a pale-yellow oil and (*S*)-(+)-2-butyl-4-methylcyclopent-2-enone ((*R*)-(+)-**4a**; 23.9 mg, 0.157 mmol, 39% yield, 83% *ee*) as a colorless oil. (*S*)-(+)-**3aa**: $[\alpha]_D^{25}$ +56.3° ($CHCl_3$, $c = 1.625$, 87% *ee*); IR (neat) 2920, 2855, 1710, 1662, 1635, 1430, 1330, 1176, 1122, 728 cm^{-1}; ^1H NMR ($CDCl_3$, 300 MHz) $\delta = 6.92$ (t, $J = 7.8$ Hz, 1H), 3.70–3.93 (m, 2H), 3.06–3.20 (m, 1H), 2.71 (dd, $J = 16.2$ and 5.4 Hz, 1H), 2.62 (dd, $J = 16.2$ and 2.4 Hz, 1H), 2.10–2.33 (m, 2H), 1.24–1.59 (m, 8H), 1.10 (d, $J = 7.2$ Hz, 3H), 0.93 ppm (t, $J = 7.8$ Hz, 6H); ^{13}C NMR ($CDCl_3$, 75 MHz) $\delta = 171.5$, 165.9, 142.7, 131.8, 39.8, 39.3, 30.8, 30.1, 27.7, 26.2, 22.5, 20.3, 20.0, 13.82, 13.76 ppm; HRMS (EI) calcd for $C_{15}H_{25}NO_2$: $[M]^+$ 251.1885, found 251.1847; chiralpak AS, hexane/*i*PrOH (98:2), 1.0 mL min^{-1}, retention times: 4.9 min (minor isomer) and 5.6 min (major isomer). (*R*)-(+)-**4a**: $[\alpha]_D^{25}$ +84.6° ($CHCl_3$, $c = 0.950$, 83% *ee*); ^1H NMR ($CDCl_3$, 300 MHz) $\delta = 7.13$–7.21 (m, 1H), 2.81–2.94 (m, 1H), 2.63 (dd, $J = 18.9$ and 6.3 Hz, 1H), 2.08–2.19 (m, 2H), 1.96 (dd, $J = 18.9$ and 2.1 Hz, 1H), 1.26–1.52 (m, 4H), 1.17 (d, $J = 6.9$ Hz, 3H), 0.91 ppm (t, $J = 6.6$ Hz, 3H); ^{13}C NMR ($CDCl_3$, 75 MHz) $\delta = 209.8$, 162.5, 145.4, 43.3, 33.3, 29.8, 24.2, 22.4, 20.4, 13.8 ppm; chiraldex G-TA column, 90 °C isothermal, retention times: 19.5 min (major isomer) and 21.4 min (minor isomer).[20]

Received: December 16, 2005
Published online: March 20, 2006

Keywords: aldehydes · alkynes · annulation · asymmetric catalysis · parallel kinetic resolution

[1] For reviews of transition-metal-catalyzed cycloadditions, see: a) I. Ojima, M. Tzamarioudaki, Z. Li, R. J. Donovan, *Chem. Rev.* **1996**, *96*, 635–662; b) M. Lautens, W. Klute, W. Tam, *Chem. Rev.* **1996**, *96*, 49–92; c) J. E. Robinson in *Modern Rhodium-Catalyzed Organic Reactions* (Ed.: P. A. Evans), Wiley-VCH, **2005**, p. 241.

[2] For review, see: J. A. Varela, C. Saà, *Chem. Rev.* **2003**, *103*, 3787–3801.

[3] a) P. Hong, H. Yamazaki, *Tetrahedron Lett.* **1977**, *18*, 1333–1336; b) R. A. Earl, K. P. C. Vollhartd, *J. Org. Chem.* **1984**, *49*, 4786–4800; c) L. V. R. Bonaga, H.-C. Zhang, A. F. Moretto, H. Ye,

 © 2006 Wiley-VCH Verlag GmbH & Co. KGaA, Weinheim

D. A. Gauthier, J. Li, G. C. Leo, B. E. Maryanoff, *J. Am. Chem. Soc.* **2005**, *127*, 3473 – 3485.
[4] a) H. Hoberg, B. W. Oster, *Synthesis* **1982**, 324 – 325; b) H. A. Duong, M. J. Cross, J. Louie, *J. Am. Chem. Soc.* **2004**, *126*, 11438 – 11439.
[5] a) Y. Yamamoto, H. Takagishi, K. Itoh, *Org. Lett.* **2001**, *3*, 2117 – 2119; b) Y. Yamamoto, K. Kinpara, T. Saigoku, H. Takagishi, S. Okuda, H. Nishiyama, K. Itoh, *J. Am. Chem. Soc.* **2005**, *127*, 605 – 613.
[6] S. T. Flynn, S. E. Hasso-Henderson, A. W. Parkins, *J. Mol. Catal.* **1985**, *32*, 101 – 105.
[7] K. Tanaka, A. Wada, K. Noguchi, *Org. Lett.* **2005**, *7*, 4737 – 4739.
[8] K. Tanaka, Y. Hagiwara, K. Noguchi, *Angew. Chem.* **2005**, *117*, 7426 – 7429; *Angew. Chem. Int. Ed.* **2005**, *44*, 7260 – 7263.
[9] For rhodium-catalyzed [4+2] carbocyclization of 4-alkynals with alkynes to prepare cyclohexenones, see: K. Tanaka, G. C. Fu, *Org. Lett.* **2002**, *4*, 933 – 935.
[10] Murakami and co-workers reported that five-membered acyl rhodium intermediates, formed by the insertion of rhodium between the carbonyl carbon atom and the α-carbon atom of the cyclobutanones, react intramolecularly with alkenes, thus leading to bicyclic cyclohexanones; see: M. Murakami, T. Itahashi, Y. Ito, *J. Am. Chem. Soc.* **2002**, *124*, 13976 – 13977.
[11] For the synthesis of quinones through the reactions of maleoil cobalt complexes with alkynes, see: S. Iyer, L. S. Liebeskind, *J. Am. Chem. Soc.* **1987**, *109*, 2759 – 2770.
[12] For the rhodium-catalyzed parallel kinetic resolution of 3-methoxy-4-alkynals to prepare enantioenriched cyclopentenones and cyclobutanones, see: K. Tanaka, G. C. Fu, *J. Am. Chem. Soc.* **2003**, *125*, 8078 – 8079.
[13] For the rhodium-catalyzed enantioselective [4+2] carbocyclization of 2-alkynylbenzaldehydes with *N,N*-dialkyl acrylamides, see ref. [8].
[14] For the rhodium-catalyzed [4+2] dimerization of 2-vinylbenzaldehyde, see: K. Kundu, J. V. McCullagh, A. T. Morehead, Jr., *J. Am. Chem. Soc.* **2005**, *127*, 16042 – 16043.
[15] T. Saito, T. Yokozawa, T. Ishizaki, T. Moroi, N. Sayo, T. Miura, H. Kumobayashi, *Adv. Synth. Catal.* **2001**, *343*, 264 – 267.
[16] Dienals were generated as by-products to the desired 2-alkylideneglutarimides and cyclopentenones through the rhodium-catalyzed carbonyl migration, see: K. Tanaka, G. C. Fu, *Chem. Commun.* **2002**, 684 – 685.
[17] The absolute configurations of the major enantiomers (+)-**3aa** and (+)-**4a** were assigned to be *R* and *S*, respectively, through chemical correlation (see the Supporting Information).
[18] K. Tanaka, G. C. Fu, *Angew. Chem.* **2002**, *114*, 1677 – 1679; *Angew. Chem. Int. Ed.* **2002**, *41*, 1607 – 1609.
[19] K. Tanaka, G. C. Fu, *J. Am. Chem. Soc.* **2005**, *127*, 11492 – 11493.
[20] The full experimental procedures and characterization data are given in the Supporting Information.

 © 2006 Wiley-VCH Verlag GmbH & Co. KGaA, Weinheim

Oxidation

DOI: 10.1002/anie.200504605

Oxidative De-aromatization of *para*-Alkyl Phenols into *para*-Peroxyquinols and *para*-Quinols Mediated by Oxone as a Source of Singlet Oxygen**

M. Carmen Carreño, Marcos González-López, and Antonio Urbano**

The controlled oxidation of organic compounds is particularly important for aromatic derivatives bearing alkyl substituents that are prone to suffer over-oxidation. The search for selective methods to effect the oxidative de-aromatization of *para*-alkyl phenols into 4-alkyl-4-hydroperoxy-2,5-cyclohexadienones (*para*-peroxyquinols) and 4-alkyl-4-hydroxy-2,5-cyclohexadienones (*para*-quinols) is of huge interest because of the essential role played by such derivatives in the skeletons of many natural products,[1] as well as being valuable building blocks in organic synthesis[2] and novel therapeutic agents.[3] Although natural products with peroxy functional groups are relatively abundant,[4] there are only a few examples of natural derivatives possessing the *para*-hydroperoxy-2,5-cyclohexadienone structure.[5] In contrast, the *para*-quinol moiety is found in a great number of natural products (Scheme 1).[6]

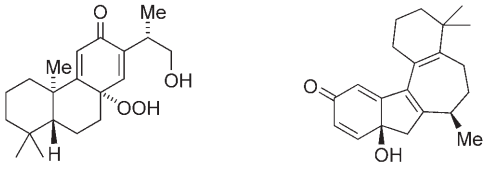

Scheme 1. Examples of natural *para*-peroxyquinol and *para*-quinol structures.

The synthesis of *para*-peroxyquinols[7] is usually achieved by the reaction of *para*-substituted phenols with singlet oxygen ($^1O_2$)[8] formed by irradiation of gaseous oxygen with ultraviolet light in the presence of sensitizers.[9] However,

[*] Prof. Dr. M. C. Carreño, M. González-López, Dr. A. Urbano
Departamento de Química Orgánica (C-I)
Universidad Autónoma de Madrid
Cantoblanco, 28049 Madrid (Spain)
Fax: (+34) 91-497-3966
E-mail: carmen.carrenno@uam.es
antonio.urbano@uam.es

[**] We thank the Ministerio de Ciencia y Tecnología (Grants BQU2002-03371 and CTQ2005-02095/BQU) and the Comunidad Autónoma de Madrid (Grant GR/MAT/0152/2004) for financial support. M.G.-L. thanks the Comunidad Autónoma de Madrid for a fellowship.

Supporting information for this article is available on the WWW under http://www.angewandte.org or from the author.

© 2006 Wiley-VCH Verlag GmbH & Co. KGaA, Weinheim

despite its efficiency, this method has not been applied extensively. Chemical sources of $^1O_2$ involve the use of transition-metal ions such as Cr^{VI}, Ti^{IV}, Mo^{VI}, or Ce^{IV} in the presence of H_2O_2, or Ru^{III} or I^{III} using *t*BuOOH as a cooxidant. Among the numerous methods described for the preparation of *para*-quinols,[7] hypervalent iodine(III) oxidants such as (diacetoxyiodo)benzene (PIDA) and [bis(trifluoroacetoxy)iodo]benzene (PIFA) have usually been the reagents of choice for the oxidation of *para*-alkyl phenols.[10] Very recently, Jacobs and co-workers reported the oxidation of *para*-substituted phenols to form *para*-quinol ethers in which H_2O_2 was used in the presence of a tungstate-exchanged layered double hydroxide catalyst.[11]

Oxone is an inexpensive and easily handled solid consisting of a 2:1:1 mixture of $KOSO_2OOH$, $KHSO_4$, and K_2SO_4. As a result of its nontoxic "green" nature, affordability, and safety profile, oxone is nowadays a popular reagent for different chemical oxidations,[12] and very commonly for the generation of dimethyldioxirane for selective epoxidations.[13]

During the course of our recent work on asymmetric synthesis based on *para*-(tolylsulfinyl)methyl-*para*-quinols,[14] we found that oxone is an efficient reagent for the practical and selective oxidative de-aromatization of several *para*-alkyl phenols. Herein, we describe that it is possible to gain direct access to *para*-peroxyquinols or the corresponding *para*-quinols, depending on the experimental conditions, in excellent yields under very mild conditions. The effectiveness of the method is illustrated with the synthesis of two natural products, hallerone and rengyolone which contain the *para*-quinol moiety.

The reaction of 3,4,5-trimethylphenol (**1a**) with oxone (8.0 equiv) in the presence of $NaHCO_3$ (24.8 equiv), in a mixture of CH_3CN/H_2O at room temperature, afforded *para*-peroxyquinol **2a** which was isolated pure in 93% yield (Scheme 2). The hydroperoxy structure of **2a** was initially established by spectroscopic methods and later confirmed by its reduction to *para*-quinol **3a** by treatment with an excess of PPh_3 (Scheme 2). Although the hydroperoxy function was cleanly reduced, separation of *para*-quinol **3a** from the generated triphenylphosphine oxide was troublesome. We then designed a one-pot procedure, in which water-soluble reducing agents were used, to simplify such a transformation. Thus, by adding $Na_2S_2O_3$ (10.0 equiv) to the reaction medium after completion of the oxidative de-aromatization step, we were pleased to observe the formation of *para*-quinol **3a** (Scheme 2), which was isolated in 83% yield, without further purification.

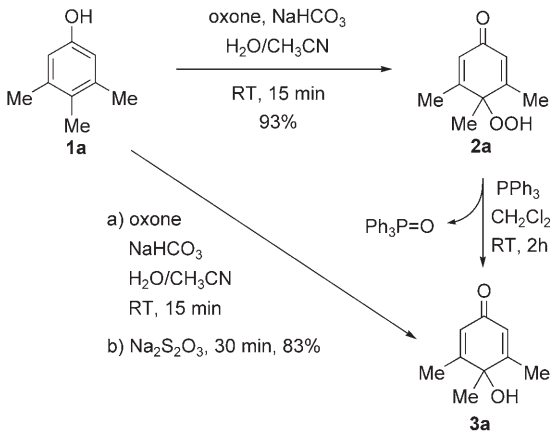

Scheme 2. Formation of *para*-peroxyquinols and *para*-quinols from *para*-alkyl phenols in the presence of oxone.

We later extended the scope of the method to the preparation of the *para*-peroxyquinols and *para*-quinols shown in Table 1, where we have also included, for comparison, the maximum yields reported for previous transformations of *para*-alkyl phenols **1** into *para*-peroxyquinols **2** or *para*-quinols **3**. The oxidative de-aromatization of *para*-alkyl phenols **1b–k** with oxone was performed as indicated before for **1a** (see also the Supporting Information). The reaction was very fast (15–140 min) and *para*-peroxyquinols **2b–k** were obtained in good to excellent yields (53–100%) when the crude mixture was quenched with water (Method A), without further purification in most cases. Direct access to *para*-quinols **3b–k** was also possible by adding solid $Na_2S_2O_3$ (10.0 equiv) to the crude reaction mixture after completion of the oxidative de-aromatization step (disappearance of phenols **1** as judged by thin-layer chromatography), and stirring for 30 min at room temperature (Method B). This route enabled the expected *para*-quinols **3** to be isolated in moderate to excellent yields (33–98%), without further purification in most cases.

The results compiled in Table 1 deserve some comment. As can be seen, phenols **1a–e** bearing methyl groups at different positions (entries 1–5) furnished, in very short times (25–50 min), exclusively *para*-peroxyquinols **2a–e** (Method A) in excellent yields (91–99%), which are higher than those reported for different sources of singlet oxygen. The *para*-quinols **3a–e** were obtained from phenols **1a–e** (Method B) in good to excellent yields (72–95%), which again improve upon those described using other oxidants, mainly I^{III} reagents. It is worth mentioning the excellent result achieved in the reaction of **1d** (entry 4), which gave rise to 4-hydroxy-2,4,6-trimethyl-2,5-cyclohexadienone (**3d**), a known drug and vitamin E precursor, in 95% yield.[15]

The reaction of **1f** (entry 6), bearing an *ortho*-OMe group, gave rise to *para*-peroxyquinol **2f** (53%) or *para*-quinol **3f** (33%). Although these yields are only moderate, our synthesis improved upon the yields previously obtained under different conditions (see Table 1). It is noteworthy that the reaction of **1f** with iodine(III) reagents exclusively furnished the corresponding *ortho*-quinone monoacetal.[16]

This oxone-mediated process was also extended to polycyclic phenols. Thus, the reaction of tetrahydronaphthol **1g** with oxone (entry 7) gave *para*-peroxyquinol **2g** (65%) or *para*-quinol **3g** (56%), whereas derivatives **2h** (100%) or **3h** (98%) were obtained in excellent yields from the oxidative de-aromatization of naphthol **1h** (entry 8).

With these results in hand, we decided to apply the methodology to the synthesis of some simple natural products based on a *para*-quinol structure such as hallerone (**3i**) or halleridone (rengyolone) (**3j**). These cyclohexylethanoids have been isolated from the plant *Halleria Lucida*,[6a] and were found to have interesting biological and therapeutic properties.[17] Both derivatives have been synthesized previ-

 © 2006 Wiley-VCH Verlag GmbH & Co. KGaA, Weinheim

Table 1: Oxidative de-aromatization of *para*-alkyl phenols **1** into *para*-peroxyquinols **2** or *para*-quinols **3** with oxone.[a]

Entry	Substrate	R^1	R^2	R^3	R^4	Product method A[b]	*t* [min][c]	Yield [%][d]	Product method B[e]	Yield [%][f]
	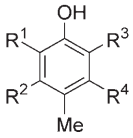					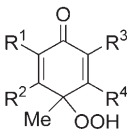			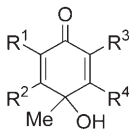	
1	**1a**	H	Me	H	Me	**2a**	35	93	**3a**	83 (63)[29]
2	**1b**	Me	H	H	H	**2b**	25	92 (75)[24]	**3b**	75 (60)[29]
3	**1c**	H	Me	H	H	**2c**	35	91 (68)[24]	**3c**	72 (67)[29]
4	**1d**	Me	H	Me	H	**2d**	50	99 (70)[25]	**3d**	95 (91)[11]
5	**1e**	H	H	H	H	**2e**	35	93 (87)[26]	**3e**	81 (61)[19]
6	**1f**	OMe	H	H	H	**2f**	20	53 (14)[27]	**3f**	33 (25)[30]
7	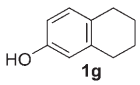 **1g**					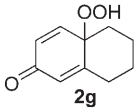 **2g**	40	65 (65)[28]	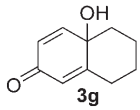 **3g**	56 (55)[31]
8	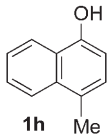 **1h**					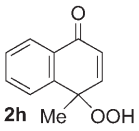 **2h**	20	100	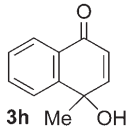 **3h**	98
9	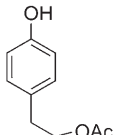 **1i**					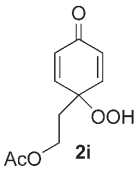 **2i**	140	62	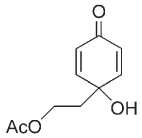 **3i: hallerone**	48 (38)[18a]
10[g]	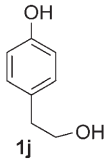 **1j**					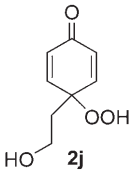 **2j**	25	80	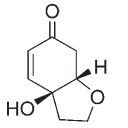 **3j: halleridone rengyolone**	50 (37)[18b]
11[g]	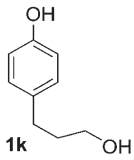 **1k**					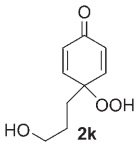 **2k**	15	74	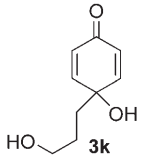 **3k**	50

[a] All reactions were typically performed on a 1 mmol scale by adding 8.0 equiv of oxone and 24.8 equiv of sodium bicarbonate to a solution of the *para*-alkyl phenol **1** in a mixture of CH_3CN/H_2O at 25 °C (see the Supporting Information). [b] The reaction was quenched with water. [c] Time required for disappearance of *para*-alkyl phenols **1** as judged by thin-layer chromatography. [d] The maximum reported yields for the transformation of *para*-alkyl phenols **1** into *para*-peroxyquinols **2**, with the corresponding reference yield given in parentheses. [e] The reaction was diluted with H_2O, then 10.0 mmol of solid sodium thiosulfate ($Na_2S_2O_3$) was added, and the resulting mixture was stirred at 25–28 °C until the corresponding hydroperoxide had been consumed (ca. 30 min). [f] The maximum reported yields for the transformation of *para*-alkyl phenols **1** into *para*-quinols **3**, with the corresponding reference are given in parentheses. [g] The reaction was carried out in H_2O as the sole solvent.

ously in yields of 38 and 37%, respectively, by sensitized photooxygenation of the corresponding phenols.[18] Thus, the oxidative de-aromatization of phenol **1i** under our typical reaction conditions (entry 9) afforded, *para*-peroxyquinol **2i** in 62% yield (Method A) or *para*-quinol **3i** in 48% yield (Method B). The physical and spectroscopic data of the latter compound were identical to those described for the natural product hallerone. The reaction of phenol **1j** with oxone (entry 10) took place in H_2O as the sole solvent and gave *para*-peroxyquinol **2j** (Method A) in 80% yield. The bicyclic *para*-quinol **3j**, identified as the natural product rengyolone, was obtained in 50% yield from phenol **1j** (Method B) in a one-pot three-reaction sequence comprising oxidative de-aromatization, reduction of the peroxy functionality, and intramolecular conjugate addition to the cyclohexadienone moiety which gave rise to the *cis*-fused tetrahydrofurane ring.

Finally, the reaction of phenol **1k**, bearing a C_3 chain at the *para* position, with oxone in H_2O (entry 11) gave rise to *para*-peroxyquinol **2k** (Method A) in 74% yield, or *para*-quinol **3k** (Method B) in 50% yield. It is also noteworthy that the reaction of phenol **1k** with hypervalent iodine reagents did not yield *para*-quinol **3k** but exclusively afforded, through intramolecular attack of the aliphatic OH on the *para* position of the phenolic OH, the corresponding oxa-spiro cyclohexadienone,[19] which was not detected in our case.

 © 2006 Wiley-VCH Verlag GmbH & Co. KGaA, Weinheim

Although it is known that the active ingredient of oxone, potassium peroxymonosulphate, decomposes in aqueous basic medium to generate singlet oxygen (Scheme 3),[20] to the best of our knowledge this process has not been exploited from a synthetic point of view. In our case, it could be assumed that the reactive $^1O_2$ species, which is generated from an excess of oxone in the presence of $NaHCO_3$, would be the species responsible for the oxidative de-aromatization of *para*-alkyl phenols to *para*-peroxyquinols (Scheme 3). The process involves a [4+2] cycloaddition[21] between $^1O_2$ and electron-rich *para*-alkyl phenols and gives rise initially to the formation of a 1,4-endoperoxide, which immediately evolves to the 4-hydroperoxy-2,5-cyclohexadienone as a result of its unstable peroxyhemiacetal structure. The presence of water seems to be essential for the success of this process, which is consistent with the well-documented enhanced rate of [4+2] cycloadditions involving $^1O_2$ in such solvents.[22] Moreover, water could accelerate or facilitate the opening of the peroxide–acetal intermediate to yield the required substrates. This mechanistic pathway also accounts for the exclusive formation of *para*-peroxyquinols, even when *ortho* analogues could be formed upon oxidative de-aromatization of the *ortho*-substituted phenols **1b**, **1d**, or **1f**. Finally, the presence of singlet oxygen in the base-mediated decomposition of oxone was confirmed by a trapping experiment with 9,10-dimethylanthracene (Scheme 3), which afforded known *endo*-peroxide **4** on reaction with oxone under the above-mentioned conditions.[23]

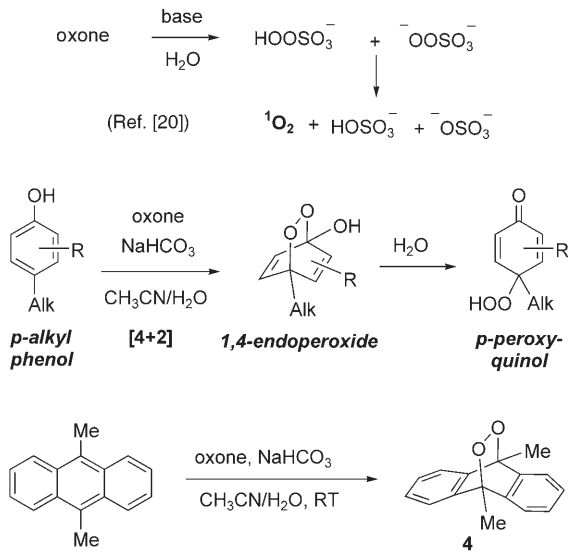

Scheme 3. Mechanism for the formation of *para*-peroxyquinols and evidence that $^1O_2$ is the reactive species from oxone.

In conclusion, easily handled oxone provides an eco-friendly, inexpensive and practical source of singlet oxygen for the selective one-pot oxidative de-aromatization of *para*-alkyl phenols to *para*-peroxy quinols and *para*-quinols in good to excellent yields under very mild conditions. The current method is experimentally simple, occurs in very short reaction times, and generally improves upon the yields obtained with other oxidants.

Received: December 28, 2005
Published online: March 20, 2006

Keywords: natural products · oxidation · oxone · singlet oxygen · synthetic methods

[1] For a recent example, see X. Wang, J. A. Porco, Jr., *Angew. Chem.* **2005**, *117*, 3127–3131; *Angew. Chem. Int. Ed.* **2005**, *44*, 3067–3071.
[2] For a recent example, see J. E. Baldwin, R. M. Adlington, V. W.-W. Sham, R. Márquez, P. G. Bulger, *Tetrahedron* **2005**, *61*, 2353–2363.
[3] J. M. Berry, T. D. Bradshaw, I. Fichtner, R. Ren, C. H. Schwalbe, G. Wells, E.-H. Chew, M. F. G. Stevens, A. D. Westwell, *J. Med. Chem.* **2005**, *48*, 639–644.
[4] D. A. Casteel, *Nat. Prod. Rep.* **1999**, *16*, 55–73.
[5] See for example, Glutinosin C: X. Niu, S. Li, Q. Zhao, Z. Lin, H. Sun, Y. Lu, L. Zhang, Q. Zheng, *Tetrahedron Lett.* **2002**, *43*, 5277–5280.
[6] See for example, halleridone and hallerone: a) V. Ravikanth, P. Ramesh, P. V. Diwan, Y. Venkateswarlu, *Biochem. Syst. Ecol.* **2000**, *28*, 905–906; frondosin C: b) A. D. Patil, A. J. Freyer, L. Killmer, P. Offen, B. Carte, A. J. Jurewiz, R. K. Johnson, *Tetrahedron* **1997**, *53*, 5047–5060; elisabethol: c) A. Ata, R. G. Kerr, C. E. Moya, R. S. Jacobs, *Tetrahedron* **2003**, *59*, 4215–4222.
[7] D. Magdziak, S. J. Meek, T. R. R. Pettus, *Chem. Rev.* **2004**, *104*, 1383–1429.
[8] For early studies, see a) T. Matsuura, K. Omura, R. Nakashima, *Bull. Chem. Soc. Jpn.* **1965**, *38*, 1358–1362; recent work: b) W. Adam, H. Kiliç, Ch. R. Saha-Möller, *Synlett* **2002**, 510–512.
[9] M. C. DeRosa, R. J. Crutchley, *Coord. Chem. Rev.* **2002**, 351–371.
[10] R. M. Moriarty, O. Prakash, *Org. React.* **2001**, *57*, 327–415.
[11] B. F. Sels, D. E. De Vos, P. A. Jacobs, *Angew. Chem.* **2005**, *117*, 314–317; *Angew. Chem. Int. Ed.* **2005**, *44*, 310–313.
[12] M. C. Marcotullio, F. Epifano, M. Curini, *Trends Org. Chem.* **2003**, *10*, 21–34.
[13] Y. Shi, *Acc. Chem. Res.* **2004**, *37*, 488–496.
[14] M. C. Carreño, M. Ribagorda, A. Somoza, A. Urbano, *Angew. Chem.* **2002**, *114*, 2879–2881; *Angew. Chem. Int. Ed.* **2002**, *41*, 2755–2757.
[15] M. Costantini, F. Igersheim, L. Krumenacker, US 4612401, **1986**; [*Chem. Abstr.* **1986**, *104*, 129540].
[16] S.-Y. Gao, S. Ko, Y.-L. Lin, R. K. Peddinti, C.-C. Liao, *Tetrahedron* **2001**, *57*, 297–308.
[17] a) A. Nagakura, M. Sato, M. Kikuchi, T. Nakatsu, JP 02200631, **1990**; b) W.-Ch. Hsu, S.-H. Keng, US 6063383, **2000**; [*Chem. Abstr.* **2000**, *132*, 352791].
[18] a) J. L. Bretón, L. D. Llera, E. Navarro, J. Trujillo, *Tetrahedron* **1987**, *43*, 4447–4451; b) E. Navarro, S. J. Alonso, J. Boada, J. Trujillo, M. J. Ayuso, A. Gutiérrez Navarro, *Fitoterapia* **1992**, *63*, 251–254.
[19] P. Wipf, Y. Kim, *J. Am. Chem. Soc.* **1994**, *116*, 11678–11688.
[20] a) W. Adam, D. V. Kazakov, V. P. Kazakov, *Chem. Rev.* **2005**, *105*, 3371–3387; b) D. F. Evans, M. W. Upton, *J. Chem. Soc. Dalton Trans.* **1985**, 1151–1153; c) D. L. Ball, J. O. Edwards, *J. Am. Chem. Soc.* **1956**, *78*, 1125–1129.
[21] a) J.-M. Aubry, Ch. Pierlot, J. Regaudy, R. Schmidt, *Acc. Chem. Res.* **2003**, *36*, 668–675; b) W. Adam, M. Prein, *Acc. Chem. Res.* **1996**, *29*, 275–283.
[22] J. M. Aubry, B. Mandard-Cazin, M. Rougee, R. V. Bensasson, *J. Am. Chem. Soc.* **1995**, *117*, 9159–9164.

 © 2006 Wiley-VCH Verlag GmbH & Co. KGaA, Weinheim

[23] a) H. Kotani, K. Ohkubo, S. Fukuzumi, *J. Am. Chem. Soc.* **2004**, *126*, 15999 – 16006; b) R. L. Donkers, M. S. Workentin, *J. Am. Chem. Soc.* **2004**, *126*, 1688 – 1698.
[24] L. Liu, D. Wang, X. Xiao, *Huaxue Xuebao* **1989**, *47*, 456 – 460.
[25] D. H. R. Barton, P. D. Magnus, *J. Chem. Soc. Perkin Trans. 1* **1975**, 1610 – 1614.
[26] W. Adam, P. Lupón, *Chem. Ber.* **1988**, *121*, 21 – 25.
[27] P. Fricko, M. Holocher-Ertl, K. Kratzl, *Monatsh. Chem.* **1980**, *111*, 1025 – 1041.
[28] E. C. McGoran, M. Wybomey, *Tetrahedron Lett.* **1989**, *30*, 783 – 786.
[29] A. McKillop, L. McLaren, R. J. K. Taylor, *J. Chem. Soc. Perkin Trans. 1* **1994**, 2047 – 2048.
[30] R. Saladino, V. Neri, E. Mincione, P. Filippone, *Tetrahedron* **2002**, *58*, 8493 – 8500.
[31] B. A. Solaja, D. R. Milic, M. J. Gasic, *Tetrahedron Lett.* **1996**, *37*, 3765 – 3768.

 © 2006 Wiley-VCH Verlag GmbH & Co. KGaA, Weinheim

Synthetic Methods

DOI: 10.1002/anie.200504164

Hydrosilylation of Alkenes with Early Main-Group Metal Catalysts**

*Frank Buch, Julie Brettar, and Sjoerd Harder**

The catalytical hydrosilylation of alkenes is of great importance in the production of silicon compounds.[1] There are numerous methods to initiate this highly atom-efficient key transformation. Classical thermal and radical-initiated reactions often lead to oligomers, especially when readily polymerizable alkenes (e.g., styrenes) are used.[2] The discovery of the Speier hydrosilylation catalyst $[H_2PtCl_6]\cdot 6H_2O$/*i*PrOH represented a major breakthrough in silicon chemistry.[3] This catalyst was later replaced by the more active and selective Karstedt catalyst.[4] Nevertheless, in some cases poor regiocontrol and side reactions, such as alkene isomerization and hydrogenation, are still an issue.[5] The last decade has seen the development of lanthanide-based catalysts.[6] Although these catalysts show poor regioselectivity in some cases, they certainly feature several advantages, such as 1) tunability of the regiochemistry by metal size and ligand choice and 2) enantioselective hydrosilylation. Hydrosilylation catalyzed by $LiAlH_4$ has been described but requires highly active SiH_4 and high pressure, which result in multiple hydrosilylation.[7] The only representative catalysts from the main-group elements are the Lewis acids $AlCl_3$ and $B(C_6F_5)_3$.[8]

As organometallic complexes of the heavier alkaline-earth metals (Ca, Sr, and Ba) show similarities with organolanthanides[9] and are increasingly used in catalysis,[10–12] they could be potential candidates for early main-group metal hydrosilylation catalysts. A possible catalytic cycle could be analogous to that established for the hydrosilylation with lanthanide catalysts (Scheme 1). This mechanism poses two tentative problems: the proposed catalytically active species, a heteroleptic metal hydride complex, is currently unknown for the heavier alkaline-earth metals. Our previous attempts to isolate well-defined soluble heteroleptic Ca hydrides resulted in the precipitation of insoluble CaH_2.[13] A highly reactive, short-lived Ca hydride complex as an intermediate in a catalytic cycle, however, remains feasible. The second problem is that early main-group metal alkyl complexes, and possibly also hydrides, only add to conjugated alkenes (e.g., styrene and butadiene), which also readily polymerize under these conditions.

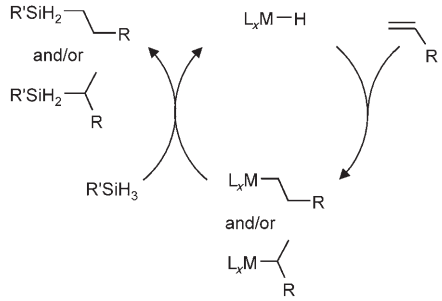

Scheme 1. Established catalytic cycle for hydrosilylation with lanthanide catalysts.

Calcium-mediated hydrosilylation was first attempted with 1,1-diphenylethylene (DPE), a substrate which does not polymerize. Addition of 5 mol% of the heteroleptic catalyst **1** to a mixture of DPE and $PhSiH_3$ at 50 °C resulted in

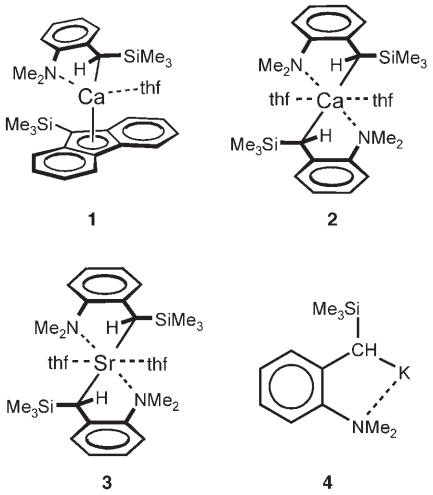

[*] F. Buch, Dr. J. Brettar, Prof. Dr. S. Harder
Anorganische Chemie
Universität Duisburg-Essen
Universitätsstrasse 5, 45117 Essen (Germany)
Fax: (+49) 201-183-2621
E-mail: sjoerd.harder@uni-due.de

[**] We kindly acknowledge H. Bandmann, Dr. T. Schaller, and W. Karow for measurement of the NMR (500 MHz) spectra, GCMS analyses, and many fruitful discussions.

Supporting information for this article is available on the WWW under http://www.angewandte.org or from the author.

 © 2006 Wiley-VCH Verlag GmbH & Co. KGaA, Weinheim

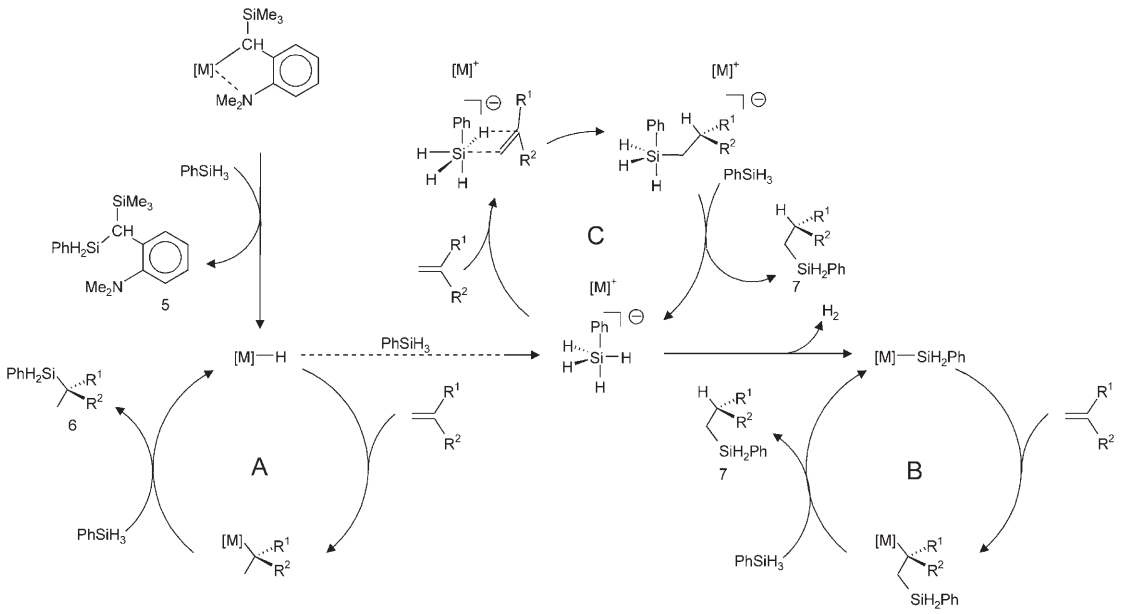

Scheme 2. Initiation and possible catalytic cycles for hydrosilylation with early main-group metal catalysts.

complete conversion of the α-Me_3Si-2-(Me_2N)-benzyl (DMAT) ligand into **5** (Scheme 2). The intense red color of the reaction mixture suggests addition of the resulting hydride to DPE and formation of $MePh_2C^-$, an intermediate in catalytic cycle A. However, an overnight reaction gave only 10% conversion into hydrosilylation product **6** ($R^1 = R^2 = Ph$; Table 1, entry 1).

As homoleptic **2** generally shows higher reactivity than heteroleptic **1**, this compound was also tested as a potential

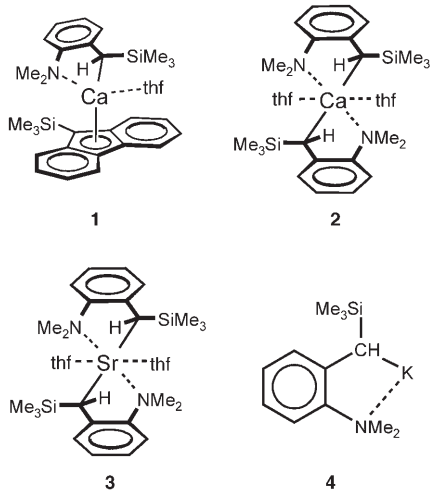

catalyst (Table 1, entries 2 and 3). Despite the possible formation of insoluble CaH_2 in the initiation step, a clean and complete conversion of DPE and $PhSiH_3$ into the expected silane **6** was observed overnight (catalyst loading: 2.5 mol%; no traces of the other regioisomer could be found). An increase in the catalyst loading to 10 mol% gave full conversion within 2 h. The more reactive Sr analogue **3** gave similar results with a catalyst loading of 2.5 mol% (Table 1, entry 4).

The cleanliness and speed of the reactions indicate that soluble heteroleptic R-M-H species play a role in the catalytic cycle. The attempted isolation of a heteroleptic [(DMAT)-CaH] complex was not successful, and there is evidence that hydride-rich clusters of $[\{(DMAT)_{<1}CaH_{>1}\}_n]$ exist in solution.[14] It is, however, not excluded that small amounts of CaH_2 precipitate in a very fine highly reactive form and, after a heterogeneous reaction, are reintroduced in the catalytic cycle (in some cases a fine precipitate was observed). Freshly ground, commercially available CaH_2 was found not to be active as a hydrosilylation catalyst (Table 1, entry 5).

The scope of hydrosilylation with polar early main-group catalysts was further investigated by probing different substrates. The hydrosilylation of α-Me-styrene with $PhSiH_3$ proceeded slowly with Ca catalyst **2**, but use of the Sr analogue **3** gave fast conversion (Table 1, entries 6 and 7). Runs with a bulkier secondary silane (Table 1, entry 8) also gave good conversion, albeit slower. As expected, no conversion was observed in the hydrosilylation of unactivated alkenes, such as allylbenzene and norbornene.

In contrast to our expectations, the hydrosilylation of styrene with $PhSiH_3$ did not give polystyrene by-products, but clean and very fast regioselective hydrosilylation was observed already at room temperature (Table 1, entries 9 and 10). A decrease in the catalyst loading to 0.5 mol% (Table 1, entry 11) and reaction with a secondary silane (Table 1, entry 12) both gave a good conversion; furthermore, the heteroleptic calcium catalyst **1** was found to be active (Table 1, entry 13). The hydrosilylation of styrene is apparently much faster than its polymerization.

The alkaline-earth-metal catalysts **2** and **3** also showed very high activity in the hydrosilylation of the conjugated double bond in hexadiene, thus exclusively yielding the

 © 2006 Wiley-VCH Verlag GmbH & Co. KGaA, Weinheim

Table 1: Summary of results for the hydrosilylation of alkenes with various main-group metal catalysts.

Entry	Substrates	Product	Catalyst	[cat.]/[alkene] [%]	*T* [°C]	*t* [h]	Conver. [%]
1	DPE $PhSiH_3$	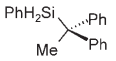	**1**	5	50	16	10
2	DPE $PhSiH_3$	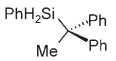	**2**	2.5	50	16	>98
3	DPE $PhSiH_3$	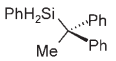	**2**	10	50	2	>98
4	DPE $PhSiH_3$	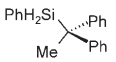	**3**	2.5	50	2	>98
5	DPE $PhSiH_3$	–	CaH_2[a]	25	50	48	0
6	$Ph(Me)C{=}CH_2$ $PhSiH_3$	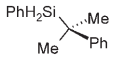	**2**	2.5	50	24	20
7	$Ph(Me)C{=}CH_2$ $PhSiH_3$	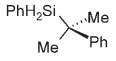	**3**	2.5	50	2.5	>98
8	$Ph(Me)C{=}CH_2$ $Ph(Me)SiH_2$	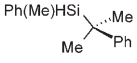	**3**	2.5	50	24	>98
9	styrene $PhSiH_3$	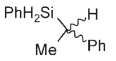	**2**	2.5	20	<0.1	>98
10	styrene $PhSiH_3$	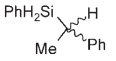	**3**	2.5	20	<0.1	>98
11	styrene $PhSiH_3$	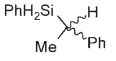	**2**	0.5	50	1.5	>98
12	styrene $Ph(Me)SiH_2$	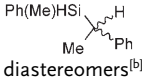 diastereomers[b]	**2**	2.5	20	<0.1	>98
13	styrene $PhSiH_3$	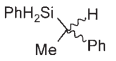	**1**	5	50	20	>98
14	cyclohexadiene $PhSiH_3$	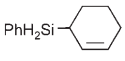	**2**	2.5	20	<0.1	>98
15	cyclohexadiene $PhSiH_3$	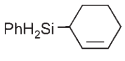	**3**	2.5	20	<0.1	>98
16	DPE $PhSiH_3$	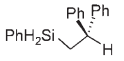	**4**	5	50	2	>98
17	DPE $PhSiH_3$	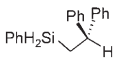	KH[c]	25	50	4[d]	>98
18	 $PhSiH_3$	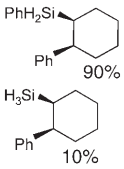 90% 10%	**4**	5	50	16	>98
19[e]	DPE $PhSiH_3$	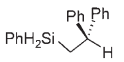	**2**	2.5	50	3	>98
20[e]	DPE $PhSiH_3$	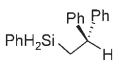	**3**	2.5	50	2	>98
21[e]	DPE $PhSiH_3$	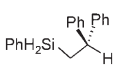	**4**	5	20	<0.1	>98

[a] Commercially obtained CaH_2 was freshly ground under nitrogen. [b] Both diastereomers were obtained in an approximate ratio of 1:1. [c] KH was isolated from a commercially available suspension in paraffin oil. [d] A 90-min induction period was observed. [e] Reaction in THF.

monosilylated product with a Si atom in the allylic position (Table 1, entries 14 and 15).

The "in situ" generation of highly reactive alkaline-earth-metal hydrides drew our attention to the use of organopotassium compounds as potential catalysts in alkene hydrosilylation. The reaction of 5 mol% of K(DMAT) **4** with DPE and $PhSiH_3$ immediately produced the initiation product **5**, and complete conversion of the substrates was reached within 2 h (Table 1, entry 16). Analysis, however, showed exclusive formation of the other regioisomer **7**. Interestingly, similar results were obtained with commercially available KH; however, a 90-min induction period was observed (Table 1, entry 17). Hydrosilylation of other alkenes with the potassium catalyst **4** either resulted in no reaction (allylbenzene, norbornene), a sluggish reaction (cyclohexadiene), or partial alkene polymerization (styrene and α-Me-styrene).

It is unlikely that regioisomer **7** is formed by the hydride cycle (cycle A) through a 1,2-insertion which produces the resonance-unstabilized $Ph_2CHCH_2^-$ ion. The fast and exclusive formation of hydrosilylation product **7** (no traces of **6** could be detected) indicates that the potassium-mediated hydrosilylation might operate through a different mechanism. A possible route could be the silanide pathway (cycle B), a mechanism that has been rejected for lanthanide-catalyzed hydrosilylation[6a] but has been proposed in transition-metal-catalyzed hydrosilylation.[15] The first step is well established: KH reacts with $PhSiH_3$ to form hypervalent $PhSiH_4^-K^+$, which yields $PhSiH_2^-K^+$ after the loss of H_2.[16] Addition of the silanide to DPE (cycle B) gives the resonance-stabilized intermediate $PhSiH_2CH_2CPh_2^-K^+$, which gives **7** after σ-bond metathesis with $PhSiH_3$.

A recently reported crystal structure of $Ph_3SiH_2^-K^+$[17] raises the possibility that potassium-mediated hydrosilylation could

 © 2006 Wiley-VCH Verlag GmbH & Co. KGaA, Weinheim

proceed through a concerted insertion reaction of the alkene with the pentavalent $PhSiH_4^-$ intermediate (Scheme 2, cycle C). Steric interactions between the Ph rings in DPE and the silanide anion would result in the exclusive formation of regioisomer **7**. This mechanism is analogous to the well-established mechanism for the KF-catalyzed hydrosilylation of ketones (Scheme 3).[18]

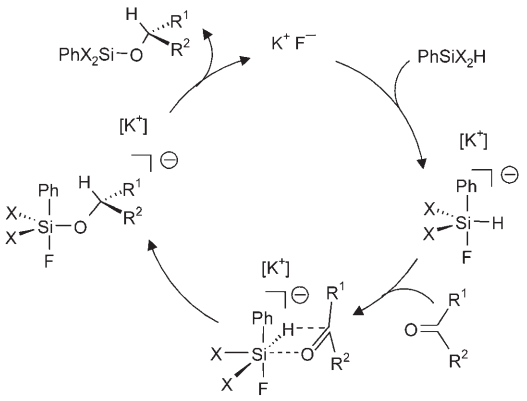

Scheme 3. Mechanism for the KF-catalyzed hydrosilylation of ketones.

Hydrosilylation of a cyclic alkene gave strong support for a silanide mechanism: overnight reaction of 1-Ph-cyclohexene with $PhSiH_3$ using potassium catalyst **4** (Table 1, entry 18) resulted in the formation of 1-Ph-2-$PhSiH_2$-cyclohexane exclusively as a *cis* diastereomer, from which a *trans* addition of the silane can be concluded. This result essentially rules out a concerted addition as in cycle C, but is in agreement with the two-step silanide mechanism in cycle B. Exclusive formation of the *cis* isomer can be explained by σ-bond metathesis in which $PhSiH_3$ approaches from the least-hindered side. This preferred stereochemistry is opposite to that in the hydroboration and therefore allows access to the complementary alcohols after a Tamao–Fleming oxidation. The additional formation of approximately 10% of *cis*-1-Ph-2-SiH_3-cyclohexane and even larger amounts of Ph_2SiH_2 also points to a concomitant disproportionation of the silane substrate during the overnight reaction ($2\,PhSiH_3 \rightarrow Ph_2SiH_2 + SiH_4$, etc.) and formation of $KSiH_3$. This base-catalyzed disproportionation,[19] which is proposed to proceed through a hypervalent intermediate,[16] could be reproduced by reaction of **4** with excess $PhSiH_3$ in the absence of an alkene.[20] The formation of $KSiH_3$ is in agreement with the recent finding that prolonged reaction of KH with $PhSiH_3$ yields $KSiH_3$.[21]

The complete change in regioselectivity observed in switching from Ca (or Sr) catalysts to the corresponding K catalyst indicates that metal–carbon bond polarity could be a decisive factor. For this reason, we also studied the effect of the solvent on the regioselectivity. Whereas hydrosilylation of DPE with Ca catalyst **2** in benzene gave essentially similar results as the solvent-free runs (that is, sole formation of product **6**), experiments in THF gave fast and exclusive formation of regioisomer **7** (Table 1, entry 19). The reaction in Et_2O produced a mixture of isomers **6** (75%) and **7** (25%), which shows that regioselectivity can be tuned by solvent polarity. The use of other styrenic substrates led to oligomeric products. A complete change in regioselectivity was also observed for the Sr catalyst **3** in THF (Table 1, entry 20). The reaction in Et_2O only gave regioisomer **7**, which is in agreement with the larger ionicity of the Sr–C bond. The addition of THF to the DPE/$PhSiH_3$/**4** system gave essentially the same product as found in the THF-free system; however, the conversion was much faster (Table 1, entry 21). Phenylcyclohexane could not be hydrosilylated using catalysts **2** and **3** in THF (also not without solvent). This behavior indicates that the metal plays an important role in the catalytic species and rules out the ion-pair mechanism (cycle C).

It is hitherto unclear how bond polarity redirects the catalytic reaction from the hydride cycle to the silanide cycle. The reaction is initiated in all cases by formation of **5** and a metal hydride, which either reacts with the alkene or the silane. A reasonable explanation could be that large cations and polar solvents favor the formation of the intermediate ion pair $[M^+][PhSiH_4^-]$, which converts into a silanide.[22]

In summary, the first hydrosilylation catalysts based on early main-group metals (Ca, Sr, and K) are very effective for the conversion of conjugated double bonds. The catalytic reactions are initiated in all cases by the formation of a highly reactive metal hydride, which either adds to an alkene or to the silane. The regiochemistry for the hydrosilylation of DPE can be completely controlled by either the polarity of the solvent or metal choice. Further research will be directed to the isolation of well-defined heteroleptic alkaline-earth-metal hydrides and other possible intermediates; therefore, better insight into the mechanisms involved may be gained. In addition, possible enantioselective hydrosilylation with these catalysts will be explored.

Experimental Section

All experiments were carried out using standard Schlenk techniques and freshly dried solvents. Alkene substrates were dried over CaH_2 and freshly distilled prior to use. The silanes $PhSiH_3$ (Fluka) and $Ph(Me)SiH_2$ (Aldrich) were used as received. The catalysts were prepared according to our previously reported methods: **1**,[10b] **2**,[10a] **3**,[23] and **4**.[23]

A typical hydrosilylation experiment: a dry Schlenk tube was charged with the alkene substrate (2.0 mmol) and the silane (2.0 mmol). After addition of the catalyst (generally 2.5 mol%) and heating of the solution to the required temperature (generally 50 °C), a color change to red was usually observed. In some cases, a fine material, presumably a metal hydride, was deposited. To follow the conversion, samples were taken at regular time intervals and analyzed by ^1H NMR spectroscopy and GC MS. In all cases (except entry 18 in Table 1), the crude reaction products consisted of essentially pure hydrosilylation product with traces of the product of initiation **5** and in some cases small amounts of one of the substrates. All hydrosilylation products and initiation products were isolated as pure compounds and completely characterized by ^1H, ^{13}C, and 2D NMR spectroscopy and by GC MS (see the Supporting Information). In a typical larger scale experiment (20 mmol of styrene and $PhSiH_3$; Ca catalyst **2**), product **6** ($R^1 = Ph$, $R^2 = H$) was obtained after isolation by column chromatography in 92% yield.

Received: November 22, 2005
Published online: March 20, 2006

 © 2006 Wiley-VCH Verlag GmbH & Co. KGaA, Weinheim

Keywords: alkaline-earth metals · homogeneous catalysis · hydrides · hydrosilylation · silanides

[1] I. Ojima, Z. Li, J. Zhu in *The Chemistry of Organosilicon Compounds*, *Vol. 2* (Eds.: Z. Rappoport, Y. Apeloig), Wiley, New York, **1998**, p. 1687.

[2] D. A. Armitage in *Comprehensive Organometallic Chemistry*, *Vol. 2* (Eds.: F. G. A. Stone, E. W. Abel), Pergamon, Oxford, **1982**, p. 115.

[3] J. L. Speier, *Adv. Organomet. Chem.* **1979**, *17*, 407.

[4] a) B. D. Karstedt, (General Electric), US Patent 3 715 334, **1973**; b) P. B. Hitchcock, M. F. Lappert, N. J. W. Warhurst, *Angew. Chem.* **1991**, *103*, 439; *Angew. Chem. Int. Ed. Engl.* **1991**, *30*, 438.

[5] It has been suggested that this is due to the formation of colloidal Pt species: a) J. Stein, L. N. Lewis, Y. Gao, R. A. Scott, *J. Am. Chem. Soc.* **1999**, *121*, 3693; b) I. E. Markó, S. Stérin, O. Buisine, G. Berthon, G. Michaud, B. Tinant, J.-P. Declercq, *Adv. Synth. Catal.* **2004**, *346*, 1429.

[6] a) P.-F. Lu, L. Brard, Y. Li, T. J. Marks, *J. Am. Chem. Soc.* **1995**, *117*, 7157; b) H. Schumann, M. R. Keitsch, J. Demtschuk, G. A. Molander, *J. Organomet. Chem.* **1999**, *582*, 70; c) T. I. Gountchev, T. D. Tilley, *Organometallics* **1999**, *18*, 5661; d) A. A. Trifonov, T. P. Spaniol, J. Okuda, *Organometallics* **2001**, *20*, 4869; e) O. Tardif, M. Nishiura, Z. Hou, *Tetrahedron* **2003**, *59*, 10525; f) Y. Horino, T. Livinghouse, *Organometallics* **2004**, *23*, 12.

[7] M. Kobayashi, M. Itoh, *Chem. Lett.* **1996**, 1013.

[8] a) K. Oertle, H. Wetter, *Tetrahedron Lett.* **1985**, *26*, 5511; b) M. Rubin, T. Schwier, V. Gevorgyan, *J. Org. Chem.* **2002**, *67*, 1936.

[9] a) R. A. Williams, T. P. Hanusa, J. C. Huffman, *Organometallics* **1990**, *9*, 1128; b) M. Rieckhoff, U. Pieper, D. Stalke, F. T. Edelmann, *Angew. Chem.* **1993**, *105*, 1102; *Angew. Chem. Int. Ed. Engl.* **1993**, *32*, 1079; c) C. Eaborn, P. B. Hitchcock, K. Izod, Z.-R. Lu, J. D. Smith, *Organometallics* **1996**, *15*, 4783; d) F. Weber, H. Sitzmann, M. Schultz, C. D. Sofield, R. A. Andersen, *Organometallics* **2002**, *21*, 3139; e) S. Harder, *Angew. Chem.* **2004**, *116*, 2768; *Angew. Chem. Int. Ed.* **2004**, *43*, 2714.

[10] a) S. Harder, F. Feil, A. Weeber, *Organometallics* **2001**, *20*, 1044; b) F. Feil, S. Harder, *Angew. Chem.* **2001**, *113*, 4391; *Angew. Chem. Int. Ed.* **2001**, *40*, 4261.

[11] Z. Zhong, P. J. Dijkstra, C. Birg, M. Westerhausen, J. Feijen, *Macromolecules* **2001**, *34*, 3863; M. H. Chisholm, J. C. Gallucci, K. Phomphrai, *Inorg. Chem.* **2004**, *43*, 6717.

[12] M. R. Crimmin, M. S. Hill, *J. Am. Chem. Soc.* **2005**, *127*, 2043.

[13] J. Brettar, F. Buch, S. Harder, unpublished results.

[14] Reaction of $[(DMAT)_2Ca]\cdot 2THF$ (**2**) with one equivalent of $PhSiH_3$ cleanly yields $PhH_2Si(DMAT)$ and a clear yellow solution presumably of [(DMAT)CaH]. Attempted crystallization of this product resulted in large yellow crystalline blocks which were determined to be **2**. The mother liquor was still largely clear at this stage and no fine CaH_2 precipitate could be detected. The mother liquor gave more well-defined crystals of **2** after repeated concentration and must have consisted of a soluble hydride-rich Ca cluster $[\{(DMAT)_{<1}CaH_{>1}\}_n]$ at this stage. At later stages, a fine white powder precipitated, which reacts vigorously with ethanol under gas evolution. Soluble hydride-rich clusters have been recently observed in lanthanide chemistry; for a review, see: Z. Hou, *Bull. Chem. Soc. Jpn.* **2003**, *76*, 2253.

[15] A. M. LaPointe, F. C. Rix, M. Brookhart, *J. Am. Chem. Soc.* **1997**, *119*, 906, and references therein.

[16] a) D. J. Hajdasz, R. R. Squires, *J. Am. Chem. Soc.* **1986**, *108*, 3139; b) J. L. Brefort, R. Corriu, C. Guérin, B. Henner, *J. Organomet. Chem.* **1989**, *370*, 9; c) B. Becker, R. Corriu, C. Guérin, B. J. L. Henner, Q. Wang, *J. Organomet. Chem.* **1989**, *359*, C33; d) B. Becker, R. Corriu, C. Guérin, B. J. L. Henner, *J. Organomet. Chem.* **1989**, *369*, 147.

[17] M. J. Bearpark, G. S. McGrady, P. D. Prince, J. W. Steed, *J. Am. Chem. Soc.* **2001**, *123*, 7737.

[18] a) J. Boyer, R. Corriu, R. Perz, C. Reye, *Tetrahedron* **1981**, *37*, 2165; b) J. Boyer, R. Corriu, R. Perz, M. Poirier, C. Reye, *Synthesis* **1981**, 558; c) R. Schiffers, H. B. Kagan, *Synlett* **1997**, *10*, 1175; d) C. Chuit, R. Corriu, C. Reye, C. Young, *Chem. Rev.* **1993**, *93*, 1371.

[19] a) J. A. Morrison, M. A. Ring, *Inorg. Chem.* **1967**, *6*, 100; b) M. Itoh, K. Inoue, J. Ishikawa, K. Iwata, *J. Organomet. Chem.* **2001**, *629*, 1.

[20] Reaction of **4** with neat $PhSiH_3$ (20-fold excess; 50 °C) gave the initiation product **5** and resulted in gas development. Analysis of the product showed Ph_2SiH_2 and minor amounts of Ph_3SiH. The evolved gas, which ignited spontaneously in air, was quenched in ethanol (with catalytical amounts of LiOEt) and gave $Si(OEt)_4$. No sign of dehydropolymerization reactions ($2\,PhSiH_3 \rightarrow PhSiH_2SiH_2Ph + H_2$) were observed.

[21] Z. Hou, Y. Zhang, M. Nishiura, Y. Wakatsuki, *Organometallics* **2003**, *22*, 129.

[22] The stability of $Ca^{2+}\cdot 6THF$ ions is well known: a) W. L. Driessen, M. Den Heijer, *Inorg. Chim. Acta* **1979**, *33*, 261; b) S. Harder, F. Feil, T. Repo, *Chem. Eur. J.* **2002**, *8*, 1991; c) S. Perruchas, F. Simon, S. Uriel, N. Avarvari, K. Boubekeur, P. Batail, *J. Organomet. Chem.* **2002**, *643–644*, 301; d) I. G. Fedushkin, A. N. Lukoyanov, S. Dechert, H. Schumann, *Eur. J. Inorg. Chem.* **2004**, *12*, 2421; e) S. Harder, S. Müller, E. Hübner, *Organometallics* **2004**, *23*, 178.

[23] F. Feil, S. Harder, *Organometallics* **2001**, *20*, 4616.

 © 2006 Wiley-VCH Verlag GmbH & Co. KGaA, Weinheim

Biosensors

DOI: 10.1002/anie.200503588

Polymethacrylates with a Covalently Linked Cu^{II}–Cyclen Complex for the In Situ Generation of Nitric Oxide from Nitrosothiols in Blood**

*Sangyeul Hwang, Wansik Cha, and Mark. E. Meyerhoff**

Nitric oxide produced by endothelial cells (EC) which line the walls of all blood vessels plays an important role in preventing platelet activation, adhesion, and, ultimately, thrombosis at the EC/blood interface.[1,2] We have reported previously that

[*] S. Hwang, W. Cha, Prof. M. E. Meyerhoff
Department of Chemistry
The University of Michigan
930 North University Avenue
Ann Arbor, MI, 48109-1055 (USA)
Fax: (+1) 734-647-4865
E-mail: mmeyerho@umich.edu

[**] We thank the NIH (EB-000783 and EB-004527) for the financial support of this research.

Supporting information for this article is available on the WWW under http://www.angewandte.org or from the author.

© 2006 Wiley-VCH Verlag GmbH & Co. KGaA, Weinheim
InterScience

plasticized polymeric films doped with a lipophilic copper(II) complex decompose *S*-nitrosothiols (RSNO), such as *S*-nitrosoglutathione (GSNO), to NO at their interface in the presence of naturally occurring reducing equivalents (e.g., glutathione (GSH)).[3] Indeed, it is well known that Cu^{II}/Cu^{I} ions can catalyze the generation of NO from RSNO species (see the Supporting Information).[4,5] Furthermore, it was reported that peptide- and protein-bound Cu^{II} can be reduced to Cu^{I} by a thiol to generate NO from RSNO.[6] It now appears that appropriate Cu^{II}/Cu^{I} organic ligand complexes can carry out similar redox chemistry.[3] Hence, it should be possible to utilize endogenous reducing equivalents (e.g., ascorbate, GSH, and cysteine (CySH)) and the endogenous NO precursors (e.g., GSNO, S-nitrosocysteine (CysNO), and S-nitrosoalbumin (AlbSNO)) in blood to generate locally enhanced NO levels at a polymer/blood interface by immobilizing catalytic Cu^{II}/Cu^{I} sites within the polymeric material. Although the exact concentrations of RSNOs in normal human blood are in debate,[7,8] the levels of RSNOs and required reducing equivalents are thought to be in the nanomolar to micromolar range.[9,10] As very low levels of NO (< 1 nM) can be effective in inhibiting platelet function,[11] even a small fractional conversion of endogenous RSNO species into NO at a polymer/blood interface could be beneficial in lowering the risk of thrombus formation at such interfaces.

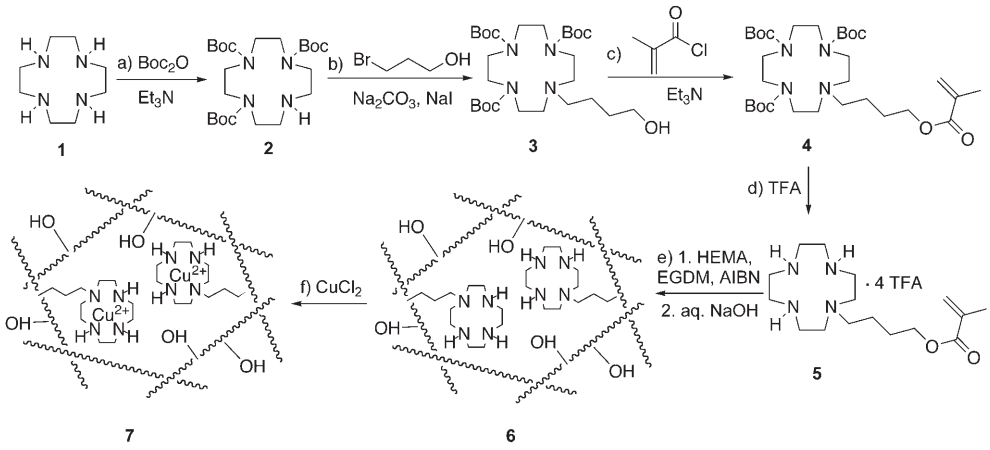

Scheme 1. The synthesis of the cross-linked hydrogel Cu^{II}–cyclen–pHEMA polymer **7**. a) Boc_2O (3 equiv), Et_3N (3 equiv), $CHCl_3$, RT, 12 h (76%); b) 3-bromopropanol (3.4 equiv), Na_2CO_3 (1.2 equiv), NaI (1.3 equiv), CH_3CN, 80 °C, 12 h (88%); c) methacryloyl chloride (5.4 equiv), Et_3N (9.5 equiv), THF, −20 °C, RT, 1 h (59%); d) trifluoroacetic acid (TFA), CH_2Cl_2, 0 °C, RT, 12 h (quantitative yield); e) 1. HEMA (66.0 wt%), ethyleneglycol dimethacrylate (EGDM; 2.1 wt%), azobisisobutyronitrile (AIBN; 0.4 wt%), 65 °C, 12 h; 2. soaked and washed with a solution of aqueous NaOH/EtOH (1:10, v/v, pH 11–12); f) $CuCl_2 \cdot 2H_2O$ (1 equiv vs **5**) in EtOH, 65 °C, 4 h.

Herein, we report the synthesis of a modified Cu^{II}–cyclen (cyclen = 1,4,7,10-tetraazacyclododecane) complex covalently attached to a cross-linked poly(2-hydroxyethyl methacrylate) (pHEMA) and demonstrate that this new material can catalytically generate NO from naturally occurring RSNOs at the physiological pH value. Further, it will be shown that spontaneous NO generation from RSNOs which exist in fresh sheep's blood can be achieved with this novel material.

Cyclen is known to have very high binding constant with Cu^{II} ($10^{23}\,M^{-1}$)[12] and square-pyramidal structure,[12,13] thus allowing this complex to possess an open site(s) at which interactions with reducing equivalents and RSNO species are possible. Herein, a propylmethacrylate derivative of cyclen was prepared for copolymerization with 2-hydroxyethyl methacrylate (HEMA; see Scheme 1). pHEMA is a high-water-uptake polymer network into which endogenous reducing agents (CySH, GSH, ascorbate, etc.) and low-molecular-weight RSNOs (CySNO and GSNO) can readily penetrate. Thus, in contrast to the system described previously,[3] potential NO generation by the resulting polymeric material could take place within the bulk of a polymer coating, not merely at the polymer/solution interface.

The film of Cu^{II}–cyclen–pHEMA **7** displayed a λ_{max} value in the range 621–644 nm in the visible region of the UV/Vis spectrum after being fully hydrated with deionized water or phosphate-buffered saline (PBS) (10 mM, pH 7.4). This absorption is within the range known for square-pyramidal Cu^{II} complexes (550–670 nm).[14] In addition, electron paramagnetic resonance (EPR) spectra of **7** in both frozen aqueous and PBS-buffered solutions exhibited the typical four-line patterns expected for a Cu^{II}–cyclen complex (see the Supporting Information).[15] Moreover, the extent of the blue color of **7** and the corresponding copper content, as determined by atomic absorption (AA) spectrophotometric analysis after dissolution of a given mass of film in a solution of sulfuric acid, correlated very closely with the molar ratio of the modified cyclen monomer **5**/HEMA used in the polymerization reaction and the theoretical amount of copper expected (see the Supporting Information). Taken together, the data suggest that most cyclen sites covalently linked to the polymer are complexed with Cu^{II} ions in the final cross-linked pHEMA films.

Figure 1 illustrates the NO generation that is achieved when a small piece of the Cu^{II}–cyclen–pHEMA film is placed in and then removed from a solution of GSNO and GSH in deoxygenated PBS buffer. The NO generated is monitored continuously with a chemiluminescence NO analyzer (NOA). As shown in Figure 1a, a blank experiment in which a hydrogel film of **6** (not treated with copper) was placed in the test solution did not generate any detectable NO. This experiment demonstrates that, as expected, copper ions are key for NO generation. In a second blank experiment, a cross-linked pHEMA film of the same size was prepared by the reaction of HEMA, EGDM, and AIBN, but without copolymerization of **5**, and further treated with copper ions by using

 © 2006 Wiley-VCH Verlag GmbH & Co. KGaA, Weinheim

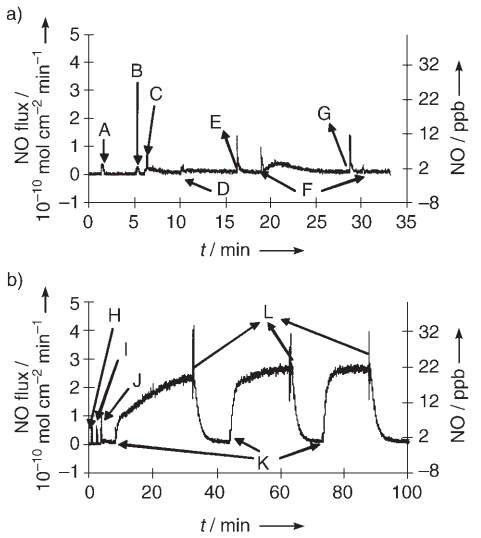

Figure 1. The profiles of NO generation for the following disk polymers (thickness: 0.3 mm; radius: 2.0 mm) in deoxgenated PBS buffer (2 mL, 10 mM; pH 7.4), monitored with a chemiluminescence NOA at room temperature after the following steps: a) A: Addition of EDTA (10 μM); B: addition of GSH (30 μM); C: addition of GSNO (10 μM); D: insertion of the cross-linked film **6**; E: removal of the cross-linked film **6**; F: insertion of pHEMA; G: removal of pHEMA. b) H: Addition of EDTA (10 μM); I: addition of GSH (5 μM); J: addition of GSNO (5 μM); K: insertion of Cu^{II}–cyclen–pHEMA **7**; L: removal of **7**.

the same method employed for the preparation of **7**; this film yielded only a small NO flux upon the very first immersion in the solution of GSNO. This behavior is due to nonspecifically adsorbed Cu^{II} ions adhered to the pHEMA matrix. Indeed, little or no NO generation was observed for subsequent immersions of the same blank films (see Figure 1a). In contrast, the first immersion of a similarly sized film of **7** into the solution of GSNO provided a slow increase in the NO flux which reached a steady state (see Figure 1b). The NO flux decreased to the baseline quickly after this film was removed from the reaction cell. Subsequent immersion/removal cycles of the same film showed that **7** could reversibly achieve nearly the same steady-state NO flux on sequential immersions into fresh solutions of GSNO/GSH. When CysNO was examined as the RSNO substrate, higher fluxes of NO generation were achieved over a relatively short time periods (see the Supporting Information), but the NO generation decreased quickly, as the bulk CysNO substrate was consumed by a rapid catalytic reaction. These observations might relate to the relative reaction rates of the two species with immobilized Cu^{II} sites. As the concentration of CySNO in blood is higher than GSNO,[10] CySNO is more likely to contribute toward a larger fraction of the potential NO-generating capability by the new Cu^{II}–cyclen–pHEMA polymers when they are in contact with fresh blood.

Several soaking experiments with the new polymeric films were conducted in the presence of excess amounts of solutions of GSH and/or GSNO in PBS buffer to investigate the potential leaching of copper ions and the deactivation of **7**. The extraction solutions were shaken continuously, and replaced with fresh solution daily. There was substantial leaching of copper ions, as measured by AA spectrophotometric analysis (the films soaked in the solutions still retained more than 64% of their original copper content after 15 days at 37.5°C; see the Supporting Information), and this leaching resulted in a decrease in the apparent level of NO generation (25–50% decrease) relative to a control of the same film (not soaked in solutions of GSH and/or GSNO). However, the λ_{max} value of the film, as shown by UV/Vis spectroscopic analysis, did not change in location before and after such soaking, thus suggesting that GSH (a reducing agent) and glutathione disulfide (GSSG, a by-product of the NO-generation reaction), both strong ligands for copper ions,[16,17] do not bind irreversibly as ligands for the covalently linked complex. A more critical test was the examination of NO generation by films of the new Cu^{II}–cyclen–pHEMA **7** material (radius: 2.8 mm; thickness: 0.2 mm; type: disk) from GSNO before and after the exposure to animal blood for a finite period. It was found that NO generation from GSNO is maintained after soaking such films in 10 mL of the sheep plasma for 3 days at 4°C or whole blood for 1 day at 4°C (see the Supporting Information). These results indicate that the deactivation of **7** caused by endogenous free thiols, proteins, and other blood components may not be a significant issue. Clearly, a large number of in vivo studies over varying time periods will be required to fully assess the true NO-generation ability and resultant thromboresistance of the new polymer under physiological conditions.

To further demonstrate that the Cu^{II}–cyclen–pHEMA polymer can generate NO spontaneously in fresh whole blood, an amperometric RSNO sensor was constructed using an interpenetrating network (IPN) film of **7** and hydrophilic polyurethane (HPU, Tecophilic, SP-93A-100) as an outer film on a NO-selective electrochemical sensor (see the Supporting Information). The response of a control NO sensor without the polymer containing the Cu^{II}–cyclen complex (but with an HPU outer membrane) was also monitored in the same blood samples. Each sensor was precalibrated for an intrinsic direct amperometric response to NO (see the Supporting Information), and then the NO and RSNO levels were measured, respectively, in the fresh sheep's blood diluted with PBS buffer at 37°C. Figure 2 shows that the NO sensor without the catalytic Cu^{II}–cyclen–pHEMA polymer site in the outer membrane has relatively little amperometric response when placed in the blood sample, whereas the difference in NO responses between the RSNO and NO sensors (equivalent to ≈25 nM NO, calculated from calibration curves) appears to be due to the decomposition of RSNO species in the sheep's blood by the IPN film of **7** and HPU. Therefore, this experiment confirms that the Cu^{II}–cyclen complex covalently attached to pHEMA generates NO from endogenous substrates in the sheep blood in vitro.

In conclusion, a Cu^{II}–cyclen complex was covalently to attached pHMEA, and the resulting material is capable of generating NO from naturally occurring RSNO species, both in buffer solution and directly when in contact with fresh whole blood. The presence of endogenous reducing equivalents is required for such catalytic chemistry to take place. Assessment of the stability of the new Cu^{II}–cyclen–pHEMA **7** material suggests that the slow leaching of copper ions from

 © 2006 Wiley-VCH Verlag GmbH & Co. KGaA, Weinheim

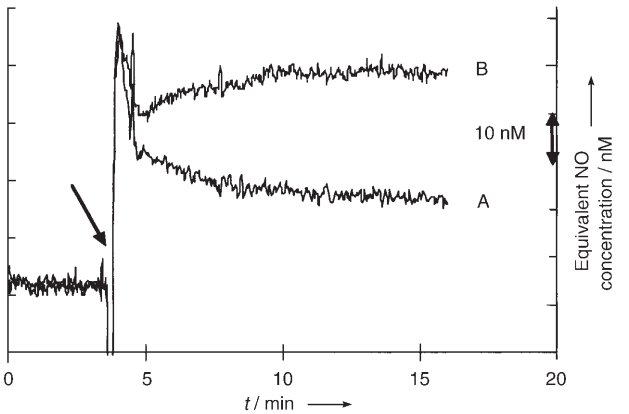

Figure 2. The direct amperometric detection of endogenous RSNOs in fresh sheep's blood by using a NO sensor A) as a control and a RSNO sensor and B) upon injection of 6 mL of fresh sheep's blood (→) into PBS buffer (30 mL, 10 mM; pH 7.4) at 37°C under a stream of nitrogen.

the polymer film may cause a measurable decrease in NO generation with time, but copper deactivation is not a significant problem. Although fundamental questions with respect to the exact mechanism by which **7** generates NO remain, the data presented herein suggest that this new material may prove beneficial as a potentially new thromboresistant blood-contacting material for biomedical applications with contact times of hours to several days. Experiments in vivo to demonstrate the effectiveness of this material in reducing thrombus formation will begin shortly.

Received: October 11, 2005
Revised: January 12, 2006
Published online: March 20, 2006

Keywords: biosensors · copper · N ligands · nitrogen oxides · polymers

[1] R. T. Mathie, T. M. Griffith, *The Haemodynamic Effects of Nitric Oxide*, Imperial College Press, Singapore, **1999**.
[2] A. O. Mateo, A. A. D. Artinano, *Pharmacol. Res.* **2000**, *42*, 421–427.
[3] B. K. Oh, M. E. Meyerhoff, *J. Am. Chem. Soc.* **2003**, *125*, 9552–9553.
[4] S. C. Askew, D. J. Barnett, J. McAninly, D. L. H. Williams, *J. Chem. Soc. Perkin Trans. 2* **1995**, 741–745.
[5] A. P. Dicks, P. H. Beloso, D. L. H. Williams, *J. Chem. Soc. Perkin Trans. 2* **1997**, 1429–1434.
[6] A. P. Dicks, D. L. H. Williams, *Chem. Biol.* **1996**, *3*, 655–659.
[7] R Rossi, D. Giustarini, A. Milzani, R. Colombo, I. Dalle-Donne, P. Di Simplicio, *Circ. Res.* **2001**, *89*, 47e.
[8] J. S. Stamler, *Circ. Res.* **2004**, *94*, 414–417.
[9] D. Giustarini, A. Milzani, R. Colombo, I. Dalle-Donne, R. Rossi, *Clin. Chim. Acta* **2003**, *330*, 85–98.
[10] M. Kelm, *Biochim. Biophys. Acta* **1999**, *1411*, 273–289.
[11] M. W. Vaughn, L. Kuo, J. C. Liao, *Am. J. Physiol.* **1998**, *274*, H2163–H2176.
[12] V. J. Thom, G. D. Hosken, R. D. Hancock, *Inorg. Chem.* **1985**, *24*, 3378–3381.
[13] V. J. Thom, C. C. Fox, J. C. A. Boeyens, R. D. Hancock, *J. Am. Chem. Soc.* **1984**, *106*, 5947–5955.
[14] M. C. Styka, R. C. Smierciak, E. L. Blinn, R. E. DeSimone, J. V. Passariello, *Inorg. Chem.* **1978**, *17*, 82–86.
[15] M. Soibinet, I. Dechamps-Olivier, E. Guillon, J.-P. Barbier, M. Aplincourt, F. Chuburu, M. L. Baccon, H. Handel, *Eur. J. Inorg. Chem.* **2003**, *10*, 1984–1994.
[16] H. K. Baek, R. L. Cooper, R. A. Holwerda, *Inorg. Chem.* **1985**, *24*, 1077–1081.
[17] B. C. Gilbert, S. Silvester, P. H. Walton, *J. Chem. Soc. Perkin Trans. 2* **1999**, 1115–1121.

 © 2006 Wiley-VCH Verlag GmbH & Co. KGaA, Weinheim

Glycosylations

DOI: 10.1002/anie.200503195

Substrate Specificity of the Macrolide-Glycosylating Enzyme Pair DesVII/DesVIII: Opportunities, Limitations, and Mechanistic Hypotheses**

*Svetlana A. Borisova, Changsheng Zhang, Haruko Takahashi, Hua Zhang, Alexander W. Wong, Jon S. Thorson, and Hung-wen Liu**

Macrolide antibiotics consist of a polyketide macrolactone with one or more deoxysugar residues attached. Macrolides target protein translation and are highly effective against gram-positive bacteria and represent an important class of compounds in our current antibiotic arsenal to treat pathogenic bacteria.[1] However, as with most broadly prescribed antibiotics, the rapid emergence of macrolide-resistant organisms dictates the continuous need for new macrolide analogues to help sustain our battery of effective agents against the constant onslaught of potentially lethal microbes.[2] The recent determination of the 3D structure of the 50S ribosomal subunit complexed with a variety of macrolides clearly reveals that the sugar substituents of these macrolides contribute to

[*] Dr. S. A. Borisova, Dr. H. Takahashi, Dr. H. Zhang, Dr. A. W. Wong, Prof. H.-w. Liu
Division of Medicinal Chemistry, College of Pharmacy
and Department of Chemistry and Biochemistry, University of Texas
Austin, TX 78712 (USA)
Fax: (+1) 512-471-2746
E-mail: h.w.liu@mail.utexas.edu
Dr. C. Zhang, Prof. J. S. Thorson
Laboratory for Biosynthetic Chemistry and
National Cooperative Drug Discovery Group
Pharmaceutical Sciences Division
School of Pharmacy, University of Wisconsin
Madison, WI 53705 (USA)

[**] This work was supported in part by the National Institutes of Health (grants GM 35906 and GM 54346 (H.-w.L.) and AI 52218, CA 84374 and GM 70637) and an NCDDG grant (U19 CA 113297) from the National Cancer Institute (J.S.T.).

Supporting information for this article is available on the WWW under http://www.angewandte.org or from the author.

WILEY InterScience DISCOVER SOMETHING GREAT
© 2006 Wiley-VCH Verlag GmbH & Co. KGaA, Weinheim

binding and sterically infringe upon the polypeptide exit tunnel—thereby preventing peptide-chain elongation.[3] Structural studies also show that the C5 disaccharide moieties of 16-membered macrolides, such as spiramycin and carbomycin, extend further into the exit tunnel toward the adjacent peptidyl transferase center. Moreover, a direct correlation between the length of truncated peptides released by a macrolide-bound ribosome and the length of the saccharide side chain of the macrolide has been established. Cumulatively, these studies clearly demonstrate the essential nature of interactions between rRNA and deoxy sugars of macrolide antibiotics and suggest that alterations of these appended carbohydrates may modulate binding and/or potentially circumvent certain resistance mechanisms.

Given the architectural and synthetic complexity of macrolides, pathway engineering has emerged as an attractive means for in vivo analogue production, presenting new derivatives with variant aglycones and/or sugars.[4] These in vivo studies have also revealed a relaxed specificity of the responsible macrolide glycosyltransferases toward both their sugar and aglycone substrates.[5] In 2004 we successfully demonstrated the first in vitro activity of a purified macrolide glycosyltransferase, DesVII,[6] which catalyzes the attachment of TDP-desosamine (**1**) to 10-deoxymethynolide (**2**) or narbonolide (**3**) in the biosynthesis of methymycin (**6**), neomethymycin (**7**), pikromycin (**8**), and narbomycin (**5**) in *Streptomyces venezuelae* (Scheme 1).

This in vitro study revealed an unusual requirement for DesVII activity: the need for an additional protein partner, DesVIII. Recently, a similar requirement for an auxiliary protein (EryCII) was also established for EryCIII, which catalyzes the attachment of desosamine (**1**) to the related erythronolide core.[7] Interestingly, among the growing number of in vitro studies of related glycosyltransferases—including those for nonribosomal peptides,[8] aminocoumarins,[9] enediynes,[10] macrolactams,[11] macrolides,[6,7,12] and aromatic polyketides[13]—only five, including DesVII and EryCIII, have been shown to depend on a DesVIII homologue.[14] Although their function remains unclear, the genes coding for DesVIII homologues are only found within biosynthetic loci encoding for aminosugar-bearing metabolite biosynthesis where they typically reside directly upstream to the aminosugar glycosyltransferase gene.[15] Thus, DesVIII was initially implicated as necessary for the incorporation of aminosugar moieties in these metabolites.[6]

In study reported herein, we extend the established in vitro DesVII/DesVIII assay to assess the level of aglycone and sugar substrate tolerance by this catalytic pair. In addition to providing a set of new macrolides, this work reveals a notably stringent 6-deoxysugar requirement for DesVII/DesVIII-catalyzed glycosylation. More importantly, this work also reveals that the DesVIII "boost" is not limited to aminosugars and thus vastly contrasts the earlier "aminosugar carrier" hypothesis.

The recombinant DesVII protein was overproduced in *E. coli* as a C-terminal His_6-tagged fusion protein and purified as previously described.[6] The DesVIII protein was produced in *E. coli* as a fusion with maltose-binding protein at its N terminus. The fusion protein was cleaved by treatment with protease and untagged DesVIII protein was used in the assays together with DesVII.[16] A number of TDP-sugars were tested as donor substrates for DesVII/DesVIII with the native macrolide aglycone **2** (Scheme 2) as the acceptor. These include TDP derivatives of glucose **9**, galactose **10**, mannose **11**, and a series of amino and acetamido hexoses **12**–**18**. TDP-sugars deoxygenated at C3 and C4, **19** and **20**, as well as TDP-xylose **21** were also examined. As the natural substrate desosamine (**1**) is a 6-deoxyhexose, a variety of 6-deoxy sugars **22**–**27** and 6-deoxyaminosugars **28**–**31** were also tested.

Of the sugar nucleotides employed, compound **9** was commercially available, compounds **1**,[17] **26**,[18] and **28**[17b] were previously synthesized chemically, compound **30** was prepared by a chemoenzymatic method,[17b] and compounds **23**, **25**,[16] and **27**[19] were obtained through enzymatic synthesis. The remaining 16 TDP-sugars **10**–**22**, **24**, **29**, **31** were generated in situ through an engineered nucleotidylyltransferase (E_p) catalyzed chemoenzymatic route from the respective sugar-1-phosphates as previously described.[20] For each assay, TDP-sugar formation in situ was assessed by HPLC, the reaction mixture subsequently adjusted to pH 9, and DesVII, DesVIII, and **2** added. The progress of the glycosylation reaction was monitored by TLC. The products from samples showing positive TLC results were subsequently isolated by preparative TLC or HPLC, and their identities established by high-resolution MS and/or NMR spectroscopic analysis.[16]

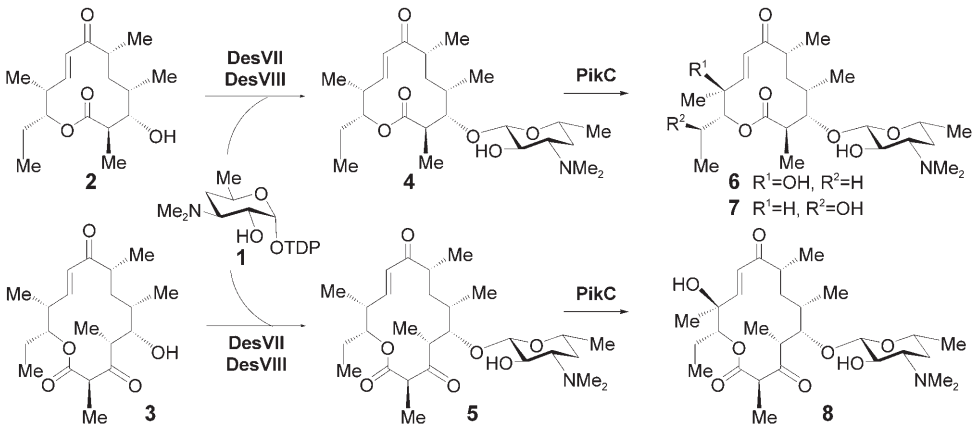

Scheme 1. Final steps of the biosynthesis of macrolide antibiotics methymycin (**6**), neomethymycin (**7**), narbomycin (**5**), and pikromycin (**8**) in *Streptomyces venezuelae*. PikC = cytochrome P450 hydroxylase; TDP = thymidine diphosphate.

Of the 23 activated sugars tested, only seven were accepted by DesVII/DesVIII to give products **4** and **32**–**37** (Scheme 2), of which **35**–**37** have never been reported. The in vitro production of macrolides **32** and **33**, previ-

 © 2006 Wiley-VCH Verlag GmbH & Co. KGaA, Weinheim

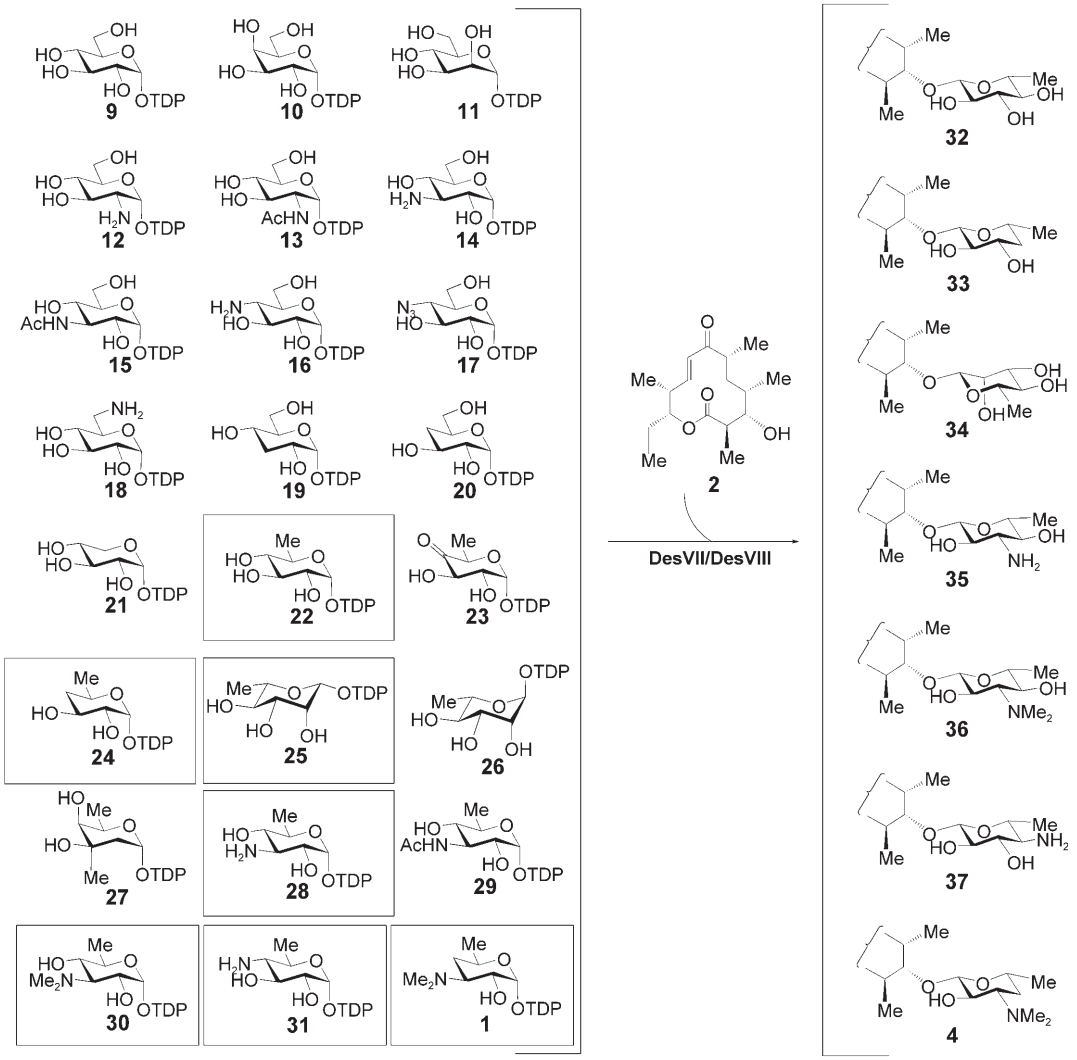

Scheme 2. Study of sugar nucleotide substrate specificity of DesVII/DesVIII using 10-deoxymethynolide (**2**) as acceptor.

ously identified shunt metabolites from *S. venezuelae* disruption mutants, suggests that reduction of the keto group of NDP-sugars **23** or **38** likely occurs prior to glycosylation (Scheme 3) in these engineered mutant strains.[5d,b] This order of events is further supported by the observation that **23** is not a substrate of DesVII/DesVIII.

Consistent with the early in vivo studies, a strict requirement for 6-deoxysugars was also observed in vitro. TDP-sugars bearing functional groups at C6 (e.g. **9**–**20**) or lacking C6 (e.g. **21**) failed as DesVII/DesVIII substrates, whereas fairly broad structural variation was tolerated among the 6-deoxyhexose substrates tested, including both D (e.g. **22, 24**) and L sugars (**25**). Aminosugars and *N*-alkyl aminosugars were found to be substrates (e.g., **1, 28, 30**, and **31**), but *N*-acyl aminosugars were not. The fact that aminosugar **28** is a substrate whereas *N*-acetamido sugar **29** is not supports our previous hypothesis that *N*-acetylation occurs after glycosylation in the production of **40** and **41** (Scheme 3).[5c,f,21]

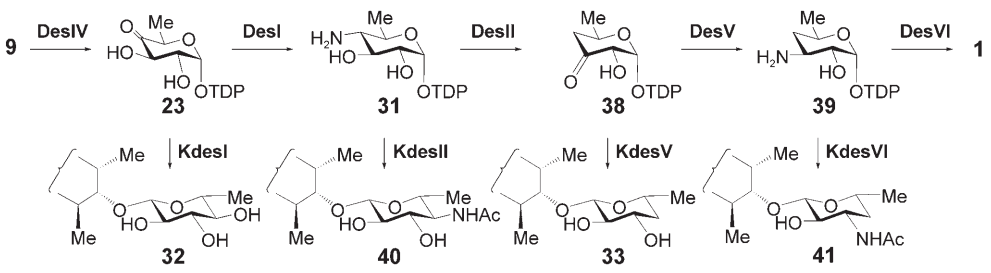

Scheme 3. Biosynthetic pathway to TDP-desosamine (**1**) from TDP-glucose (**9**). Also shown are macrolide products isolated from the fermentation broths of various gene-disruption mutants of *S. venezuelae*. Kdes = *S. venezuelae* mutants in which the respective des genes are inactivated.

Furthermore, C3 alkylation and/or C2 deoxygenation appear to be detrimental (e.g. **27**) whereas the correct anomeric configuration (e.g. **25** versus **26**) is essential for DesVII/DesVIII activity. Most importantly, parallel assays in the absence of DesVIII led to a dramatic decrease in DesVII activity (ranging from a

 © 2006 Wiley-VCH Verlag GmbH & Co. KGaA, Weinheim

more than 30-fold decrease in yield to no product at all), including those assays with substrates that lack amino functionality (e.g. **24** and **25**).[16] Clearly, the DesVIII augmentation effect is not limited to aminosugar substrates only.

Given the well-characterized in vivo aglycone tolerance of DesVII/DesVIII,[22] we next set out to explore this potential in vitro, particularly in the context of non-natural sugar donors. Consistent with earlier observations, we found DesVII/DesVIII to be capable of adding desosamine to the natural acceptors 10-deoxymethynolide (**2**) and narbonolide (**3**) to give **4** and **5**, respectively. Interestingly, the hydroxylated analogues of **2**, methynolide (**42**) and neomethynolide (**43**), can also be glycosylated to yield **6** and **7**, respectively. Remarkably, all six confirmed non-natural in vitro sugar substrates **22, 24, 25, 28, 30**, and **31** from the studies described above, were also successful DesVII/DesVIII substrates with aglycones **2, 3, 42**, and **43** (Scheme 4). In the context of the previous hypothesis that PikC-catalyzed aglycone hydroxylation (i.e. the conversions of **4** into **6**/**7** and **5** into **8**) is a postglycosylation event,[23] these results demonstrate a tolerance of DesVII/DesVIII towards the hydroxylation pattern of the aglycone and imply some flexibility in the glycosylation/hydroxylation sequence of biosynthetic steps. Many of the macrolides first identified through pathway engineering (**32**,[5d] **34, 50–52**,[5e] **45–46**,[14a] **61–62**,[5b] **63–66**[24]) were also identified in this study.

Interestingly, we found **1, 22, 24, 25, 28, 30**, and **31** to be substrates with the 16-membered tylactone (**44**) as well to give **48, 68, 67, 53, 59, 49**, and **60**, respectively (Scheme 4). Of these products, **48** and **49** had been previously identified in vi-

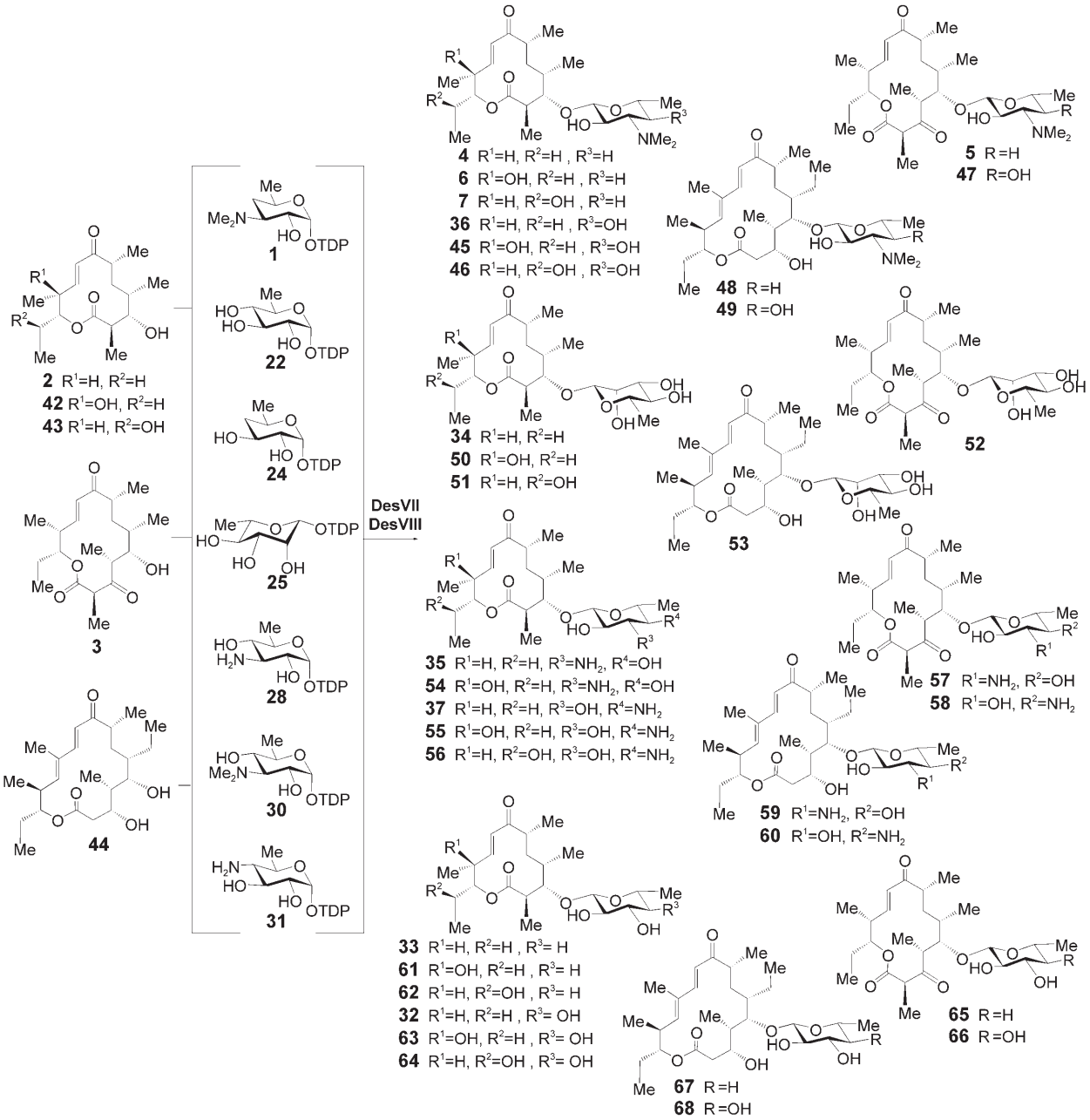

Scheme 4. Structures of macrolides identified in this study.

 © 2006 Wiley-VCH Verlag GmbH & Co. KGaA, Weinheim

vo,[25,14a] while others have not been reported. Also, although **44** contains two potential glycosylation sites, the DesVII/DesVIII system was regioselective for C5. Most importantly, parallel assays lacking DesVIII again led to a dramatic reduction in the yield of the glycosylated products. Such an ability to utilize a non-natural aglycone and a non-natural sugar in the coupling reaction is unusual for enzyme catalysis, but appears to be more common among glycosyltransferases involved in the biosynthesis of secondary metabolites.[4,5] The demonstrated aglycone as well as sugar promiscuity of this system presents an opportunity for macrolide glycodiversification.

In summary, the in vitro DesVII/DesVIII characterization described herein not only demonstrates its potential for macrolactone glycodiversification,[26] but also further expands our understanding of the DesVII/DesVIII glycosylation machinery. Based on these studies, DesVII/DesVIII exhibits a stringent 6-deoxysugar requirement but an otherwise relaxed substrate specificity toward both TDP-sugar donor and aglycone acceptor. The catalytic capabilities of DesVII/DesVIII, as indicated by the formation of 19 previously unreported macrolides in this limited exploration, hold high promise in biosynthetic application to construct new macrolide derivatives. More importantly, these results reveal that DesVIII equally augments DesVII activity toward both aminosugars and non-aminosugars. The lack of preferential aminosugar enhancement contrasts the previously proposed "aminosugar-carrier" role for this intriguing protein. DesVIII has also been speculated to play a role in the enhancement of the aglycone–glycosyltransferase interaction considering the high hydrophobic nature of the aglycones **2** and **3**. However, given the fact that the DesVIII augmentation effect holds for both hydrophobic (such as **2** and **3**) and more-hydrophilic aglycones (such as **42** and **43**), a specific "aglycone-carrier" role for DesVIII may also be called into question. Since DesVII shows good sequence homology to members of the glycosyltransferase GT-B superfamily, which contain two distinct domains for harboring the aglycone and TDP-sugar substrate, it is more likely that binding of DesVIII to DesVII may optimize a DesVII conformational change bringing these two domains to close proximity during coupling, or may simply facilitate the proper folding of DesVII and thereby improve its catalytic efficiency. In fact, our preliminary experiments showed that DesVIII is only required for initial activation of DesVII and the activated DesVII can catalyze the glycosyl transfer alone. Interestingly, a similar observation was recently reported for activation of glycosyltransferase EryCIII by DesVIII homologues EryCII and AknT.[7] The authors proposed that auxiliary proteins induce a one-time conformational change of glycosyltransferase to its active form. Experiments are in progress to investigate further the catalytic properties of DesVII and DesVIII.

Received: September 8, 2005
Revised: January 18, 2006
Published online: March 15, 2006

Keywords: antibiotics · biosynthesis · carbohydrates · glycosylation · macrolides

[1] a) H. Takashima, *Curr. Top. Med. Chem.* **2003**, *3*, 991; b) M. Gaynor, A. S. Mankin, *Front. Med. Chem.* **2005**, *2*, 21.
[2] a) A. Coates, Y. Hu, C. Page, *Nat. Rev. Drug Discovery* **2002**, *1*, 895; b) T. C. Henninger, *Expert Opin. Ther. Pat.* **2003**, *13*, 787.
[3] a) F. Schlünzen, R. Zarivach, J. Harms, A. Bashan, A. Tocilj, R. Albrecht, A. Yonath, F. Franceschi, *Nature* **2001**, *413*, 814; b) J. L. Hansen, J. A. Ippolito, N. Ban, P. Nissen, P. B. Moore, T. A. Steitz, *Mol. Cell* **2002**, *10*, 117; c) F. Schlünzen, J. M. Harms, F. Franceschi, H. A. S. Hansen, H. Bartels, R. Zarivach, A. Yonath, *Structure* **2003**, *11*, 329; d) R. Berisio, F. Schlünzen, J. Harms, A. Bashan, T. Auerbach, D. Baram, A. Yonath, *Nat. Struct. Biol.* **2003**, *10*, 366; e) R. Berisio, J. Harms, F. Schluenzen, R. Zarivach, H. A. S. Hansen, P. Fucini, A. Yonath, *J. Bacteriol.* **2003**, *185*, 4276; f) D. Tu, G. Blaha, P. B. Moore, T. A. Steitz, *Cell* **2005**, *121*, 257.
[4] a) C. Méndez, J. A. Salas, *Trends Biotechnol.* **2001**, *19*, 449; b) E. Rodriguez, R. McDaniel, *Curr. Opin. Microbiol.* **2001**, *4*, 526; c) J. S. Thorson, T. J. Hosted, Jr., J. Jiang, J. B. Biggins, J. Ahlert, *Curr. Org. Chem.* **2001**, *5*, 139; d) W. R. Strohl, *Metab. Eng.* **2001**, *3*, 4; e) U. Rix, C. Fischer, L. L. Remsing, J. Rohr, *Nat. Prod. Rep.* **2002**, *19*, 542; f) X. He, H.-w. Liu, *Annu. Rev. Biochem.* **2002**, *71*, 701; g) A. P. Salas, L. Zhu, C. Sánchez, A. F. Braña, J. Rohr, C. Méndez, J. A. Salas, *Mol. Microbiol.* **2005**, *58*, 17.
[5] a) L. Zhao, D. H. Sherman, H.-w. Liu, *J. Am. Chem. Soc.* **1998**, *120*, 10256; b) L. Zhao, N. L. S. Que, Y. Xue, D. H. Sherman, H.-w. Liu, *J. Am. Chem. Soc.* **1998**, *120*, 12159; c) L. Zhao, J. Ahlert, Y. Xue, J. S. Thorson, D. H. Sherman, H.-w. Liu, *J. Am. Chem. Soc.* **1999**, *121*, 9881; d) S. A. Borisova, L. Zhao, D. H. Sherman, H.-w. Liu, *Org. Lett.* **1999**, *1*, 133; e) H. Yamase, L. Zhao, H.-w. Liu, *J. Am. Chem. Soc.* **2000**, *122*, 12397; f) L. Zhao, S. Borisova, S.-M. Yeung, H.-w. Liu, *J. Am. Chem. Soc.* **2001**, *123*, 7909.
[6] S. A. Borisova, L. Zhao, C. E. Melançon III, C.-L. Kao, H.-w. Liu, *J. Am. Chem. Soc.* **2004**, *126*, 6534.
[7] Y. Yuan, H. S. Chung, C. Leimkuhler, C. T. Walsh, D. Kahne, S. Walker, *J. Am. Chem. Soc.* **2005**, *127*, 14128.
[8] a) H. C. Losey, M. W. Peczuh, Z. Chen, U. S. Eggert, S. D. Dong, I. Pelczer, D. Kahne, C. T. Walsh, *Biochemistry* **2001**, *40*, 4745; b) H. C. Losey, J. Jiang, J. B. Biggins, M. Oberthür, X. Y. Ye, S. D. Dong, D. Kahne, J. S. Thorson, C. T. Walsh, *Chem. Biol.* **2002**, *9*, 1305; c) X. Fu, C. Albermann, J. Jiang, J. Liao, C. Zhang, J. S. Thorson, *Nat. Biotechnol.* **2003**, *21*, 1467; d) T. L. Li, F. Huang, S. F. Haydock, T. Mironenko, P. F. Leadlay, J. B. Spencer, *Chem. Biol.* **2004**, *11*, 107; e) W. Lu, M. Oberthür, C. Leimkuhler, J. Tao, D. Kahne, C. T. Walsh, *Proc. Natl. Acad. Sci. USA* **2004**, *101*, 4390; f) X. Fu, C. Albermann, C. Zhang, J. S. Thorson, *Org. Lett.* **2005**, *7*, 1513.
[9] a) C. Albermann, A. Soriano, J. Jiang, H. Vollmer, J. B. Biggins, W. A. Barton, J. Lesniak, D. B. Nikolov, J. S. Thorson, *Org. Lett.* **2003**, *5*, 933; b) C. L. Freel Meyers, M. Oberthür, J. W. Anderson, D. Kahne, C. T. Walsh, *Biochemistry* **2003**, *42*, 4179.
[10] C. Zhang, J. S. Thorson, unpublished results.
[11] a) A. Minami, R. Uchida, T. Eguchi, K. Kakinuma, *J. Am. Chem. Soc.* **2005**, *127*, 6148; b) A. Minami, K. Kakinuma, T. Eguchi, *Tetrahedron Lett.* **2005**, *46*, 6187.
[12] a) L. M. Quirós, J. A. Salas, *J. Biol. Chem.* **1995**, *270*, 18234; b) L. M. Quirós, R. J. Carbajo, A. F. Braña, J. A. Salas, *J. Biol. Chem.* **2000**, *275*, 11713; c) H. Y. Lee, H. S. Chung, C. Hang, C. Khosla, C. T. Walsh, D. Kahne, S. Walker, *J. Am. Chem. Soc.* **2004**, *126*, 9924; d) M. Yang, M. R. Proctor, D. N. Bolam, J. C. Errey, R. A. Field, H. J. Gilbert, B. G. Davis, *J. Am. Chem. Soc.* **2005**, *127*, 9336.
[13] W. Lu, C. Leimkuhler, M. Oberthür, D. Kahne, C. T. Walsh, *Biochemistry* **2004**, *43*, 4548.
[14] a) C. E. Melançon III, H. Takahashi, H.-w. Liu, *J. Am. Chem. Soc.* **2004**, *126*, 16726; b) W. Lu, C. Leimkuhler, G. J. J. Gatto,

 © 2006 Wiley-VCH Verlag GmbH & Co. KGaA, Weinheim

R. G. Kruger, M. Oberthur, D. Kahne, C. T. Walsh, *Chem. Biol.* **2005**, *12*, 527.
[15] Examples of *desVIII* homologues include: a) doxorubicin: S. L. Otten, X. Liu, J. Ferguson, C. R. Hutchinson, *J. Bacteriol.* **1995**, *177*, 6688; b) tylosin: A. R. Gandecha, S. L. Large, E. Cundliffe, *Gene* **1997**, *184*, 197; c) erythromycin: R. G. Summers, S. Donadio, M. J. Staver, E. Wendt-Pienkowski, C. R. Hutchinson, L. Katz, *Microbiology* **1997**, *143*, 3251; d) oleandomycin: C. Olano, A. M. Rodriguez, J. M. Michel, C. Méndez, M. C. Raynal, J. A. Salas, *Mol. Gen. Genet.* **1998**, *259*, 299; e) megalomicin: Y. Volchegursky, Z. Hu, L. Katz, R. McDaniel, *Mol. Microbiol.* **2000**, *37*, 752; f) aclarubicin: K. Raty, T. Kunnari, J. Hakala, P. Mantsala, K. Ylihonko, *Mol. Gen. Genet.* **2000**, *264*, 164; g) nogalamycin: S. Torkkell, T. Kunnari, K. Palmu, P. Mantsala, J. Hakala, K. Ylihonko, *Mol. Genet. Genomics* **2001**, *266*, 276; h) β-rhodomycin: Y. Miyamoto, O. Johdo, Y. Nagamatsu, A. Yoshimoto, *FEMS Microbiol. Lett.* **2002**, *206*, 163; i) mycinamicin: Y. Anzai, N. Saito, M. Tanaka, K. Kinoshita, Y. Koyama, F. Kato, *FEMS Microbiol. Lett.* **2003**, *218*, 135.
[16] See Supporting Information for details.
[17] a) C.-w. Chang, L. Zhao, H. Yamase, H.-w. Liu, *Angew. Chem.* **2000**, *112*, 2244; *Angew. Chem. Int. Ed.* **2000**, *39*, 2160; b) H. Chen, H. Yamase, K. Murakami, C.-w. Chang, L. Zhao, Z. Zhao, H.-w. Liu, *Biochemistry* **2002**, *41*, 9165.
[18] Y. Zhao, J. S. Thorson, *J. Org. Chem.* **1998**, *63*, 7568.
[19] H. Takahashi, Y.-n. Liu, H. Chen, H.-w. Liu, *J. Am. Chem. Soc.* **2005**, *127*, 9340.
[20] a) J. Jiang, J. B. Biggins, J. S. Thorson, *J. Am. Chem. Soc.* **2000**, *122*, 6803; b) J. Jiang, J. B. Biggins, J. S. Thorson, *Angew. Chem.* **2001**, *113*, 1550; *Angew. Chem. Int. Ed.* **2001**, *40*, 1502; c) W. A. Barton, J. Lesniak, J. B. Biggins, P. D. Jeffrey, J. Jiang, K. R. Rajashankar, J. S. Thorson, D. B. Nikolov, *Nat. Struct. Biol.* **2001**, *8*, 545; d) W. A. Barton, J. B. Biggins, J. Jiang, J. S. Thorson, D. B. Nikolov, *Proc. Natl. Acad. Sci. USA* **2002**, *99*, 13397; e) J. Jiang, C. Albermann, J. S. Thorson, *ChemBioChem* **2003**, *4*, 443.
[21] The *N*-acetyl-substituted **31** is a poor E_p substrate and thus was not available in sufficient quantities for the in vitro studies.
[22] a) L. Tang, R. McDaniel, *Chem. Biol.* **2001**, *8*, 547; b) Y. J. Yoon, B. J. Beck, B. S. Kim, H.-Y. Kang, K. A. Reynolds, D. H. Sherman, *Chem. Biol.* **2002**, *9*, 203.
[23] a) M. C. Betlach, J. T. Kealey, G. W. Ashley, R. McDaniel, *Biochemistry* **1998**, *37*, 14937; b) D. E. Cane, E. I. Graziani, *J. Am. Chem. Soc.* **1998**, *120*, 2682; c) E. I. Graziani, D. E. Cane, M. C. Betlach, J. T. Kealey, R. McDaniel, *Bioorg. Med. Chem. Lett.* **1998**, *8*, 3117; d) Y. Xue, D. Wilson, L. Zhao, H.-w. Liu, D. H. Sherman, *Chem. Biol.* **1998**, *5*, 661.
[24] J. S. J. Hong, S. H. Park, C. Y. Choi, J. K. Sohng, Y. J. Yoon, *FEMS Microbiol. Lett.* **2004**, *238*, 391.
[25] S. Gaisser, J. Reather, G. Wirtz, L. Kellenberger, J. Staunton, P. F. Leadlay, *Mol. Microbiol.* **2000**, *36*, 391.
[26] a) J. Yang, D. Hoffmeister, L. Liu, X. Fu, J. S. Thorson, *Bioorg. Med. Chem.* **2004**, *12*, 1577; b) J. M. Langenhan, B. R. Griffith, J. S. Thorson, *J. Nat. Prod.* **2005**, *68*, 1696; c) B. R. Griffith, J. M. Langenhan, J. S. Thorson, *Curr. Opin. Biotechnol.* **2005**, *16*, 622.

 © 2006 Wiley-VCH Verlag GmbH & Co. KGaA, Weinheim

Synthesis Design

DOI: 10.1002/anie.200504067

Reactivity-Based One-Pot Synthesis of the Tumor-Associated Antigen N3 Minor Octasaccharide for the Development of a Photocleavable DIOS-MS Sugar Array**

*Jinq-Chyi Lee, Chung-Yi Wu, Junefredo V. Apon, Gary Siuzdak, and Chi-Huey Wong**

Human milk contains a variety of biologically important oligosaccharides which reflect the lactating mother's Lewis blood group.[1] Antigens N3, known as N3 major and N3 minor, are examples of such milk-derived octasaccharides (Scheme 1).[2] N3 major, difucosyllacto-*N*-hexose (**1**), is the major component of N3 antigens containing Le^a and Le^x moieties. N3 minor, difucosyllacto-*N*-neohexaose (**2**), contains two Le^x units and a lactose unit. The trisaccharide Le^x is one of the carbohydrate determinants of blood groups and is known to be a tumor-related antigen.[3] The N3 antigens containing one or two Le^x units were also overexpressed in various tumors, including gastrointestinal cancer cells. Although the synthesis of **1** and **2** has been reported,[4,5] little is know regarding the function of **2**. We describe here the synthesis of **2** by using the one-pot strategy based on anomeric reactivity,[6] and the use of this glycan as a model to develop photocleavable arrays on porous silicon suitable for direct characterization by mass spectrometry.

Carbohydrate arrays are becoming powerful tools in glycobiology and glycomics.[7] We have recently reported the formation of a covalent array of complex oligosaccharides on glass slides[8] and microtiter plates for high-throughput analysis of sugar–protein interactions.[9] The microplate

[*] Dr. J.-C. Lee, Dr. C.-Y. Wu, Prof. C.-H. Wong
Department of Chemistry and
The Skaggs Institute for Chemical Biology
The Scripps Research Institute
10550 North Torrey Pines Road, La Jolla, CA 92037 (USA)
Fax: (+1) 858-784-2409
E-mail: wong@scripps.edu
Dr. C.-Y. Wu, Prof. C.-H. Wong
The Genomics Research Center
Academia Sinica
No. 128 Academia Road Section 2, Nan-Kang
Taipei, 11529 (Taiwan)
J. V. Apon, Prof. G. Siuzdak
Department of Molecular Biology and Chemistry and
The Scripps Center for Mass Spectrometry
The Scripps Research Institute
10550 North Torrey Pines Road, La Jolla, CA 92037 (USA)

[**] J.-C.L. and C.-Y.W. contributed equally. This work was supported by the NIH. C.-Y.W. thanks the National Science Council of Taiwan and the Genomics Research Center, Academia Sinica for financial support. DIOS-MS = desorption/ionization on silicon mass spectrometry.

Supporting information for this article is available on the WWW under http://www.angewandte.org or from the author.

© 2006 Wiley-VCH Verlag GmbH & Co. KGaA, Weinheim

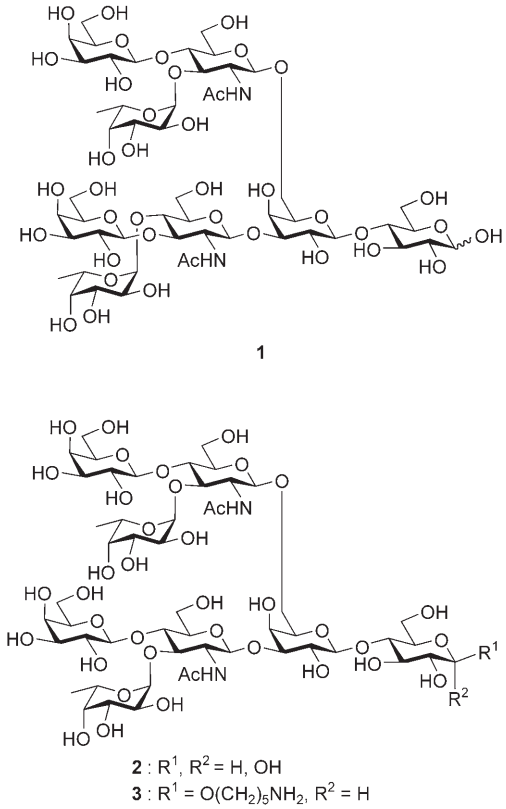

Scheme 1. The structures of antigens N3 **1**, **2**, and the amine-containing analogue **3**.

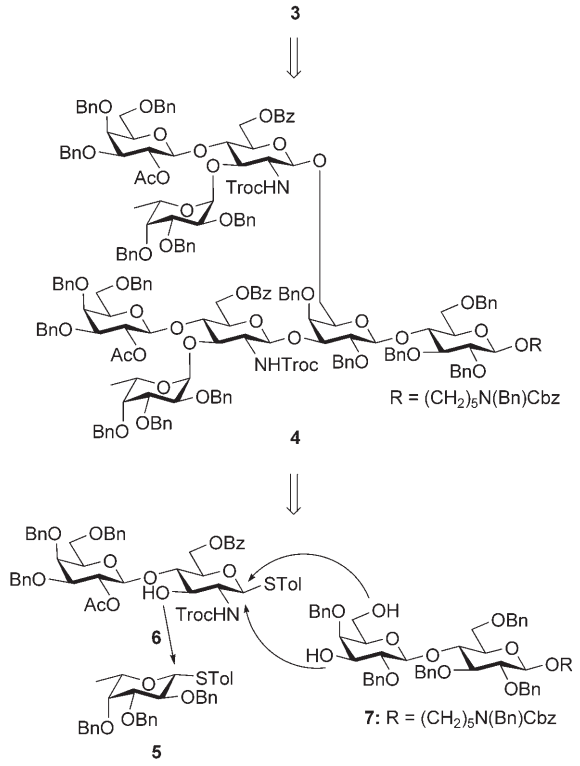

Scheme 2. Retrosynthetic analysis of the antigen N3 minor glycoside **3**. Bn = benzyl, Bz = benzoyl, Cbz = benzyloxycarbonyl, Tol = *p*-methylphenyl, Troc = 2,2,2-trichloroethoxycarbonyl.

methodology incorporates a cleavable disulfide linker which allows characterization and quantitative analysis of the array. However, chemical cleavage of the disulfide bonds is not ideal for the glass-slide format. Furthermore, microtiter plate arrays require larger amounts of glycans than glass-slide arrays do, although microtiter plate arrays have advantages in certain applications.

Desorption/ionization on silicon mass spectrometry (DIOS-MS) is an ionization method that uses a porous silicon surface to generate gas-phase ions of small molecules (<3000 Da) without a matrix.[10] With this technique, the process of sample manipulation is minimized and it only requires very small volumes for analysis. To test the feasibility of this system for sugar arrays, we prepared the amine-containing antigen N3 minor **3** and printed it on the surface of a modified porous silicon with a photocleavable linker, which could be cleaved by a laser ($\lambda = 337$ nm) in the mass spectrometric analysis to detect the carbohydrate on the porous silicon. A similar photocleavable linker on beads was used by Gerdes and Waldmann previously.[11]

We used the programmable one-pot synthesis strategy to prepare antigen N3 minor **3**, since the method is rapid and has been used in the synthesis of many complex oligosaccharides.[12–16] The methodology is based on the use of designer thioglycoside building blocks with defined relative reactivity values (RRVs) that are collected in the Optimer database.[6]

Our retrosynthetic plan of the antigen N3 minor octasaccharide **3** is shown in Scheme 2. The target molecule **3** can be prepared through a global deprotection of the fully protected oligosaccharide **4**, which could be assembled by one-pot glycosylation with three key building blocks: fucosyl unit **5**, lactosaminyl disaccharide unit **6**, and lactosyl unit **7**. Since the reactivities of these three building blocks decrease progressively, they can react sequentially in a single flask. The fucosyl building block **5** (RRV $= 7.2 \times 10^4$) and the reducing end unit **7** (RRV $= 0$) have the highest and the least reactivity, respectively. The lactosaminyl diasccharide **6** (RRV $= 41$), with a reactivity falling between **5** and **7**, was prepared from galactosyl donor **8** and acceptor **9** (Scheme 3).

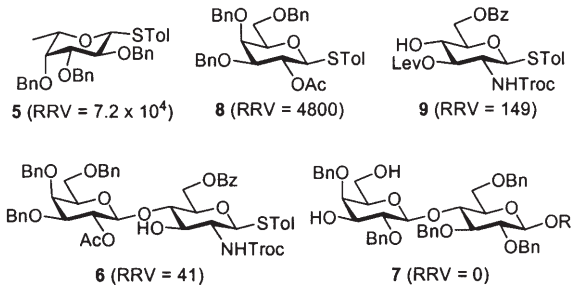

Scheme 3. Relative reactivity values (RRV) of building blocks **5**–**9**. Lev = levulinoyl.

The preparation of perbenzylated fucosyl thioglycoside **5** and galactosyl thioglycoside **8** followed literature procedures.[6,17] The synthesis of lactosaminyl disaccharide building block **6** is illustrated in Scheme 4. Thioglycoside **10**,[6]

 © 2006 Wiley-VCH Verlag GmbH & Co. KGaA, Weinheim

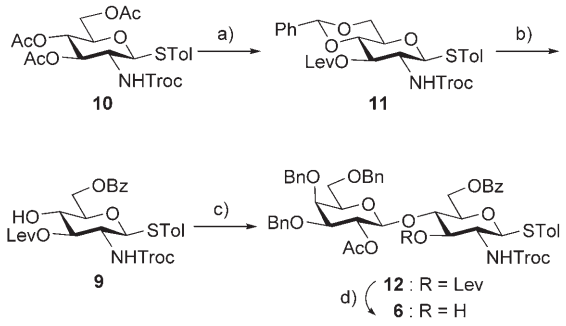

Scheme 4. Synthesis of lactosaminyl disaccharide building block **6**. a) 1. NaOMe, MeOH/CH_2Cl_2; 2. $PhCH(OMe)_2$, cat. CSA, CH_3CN; 3. levulinic acid, DCC, DMAP, 76% over 3 steps; b) 1. TFA/CH_2Cl_2/H_2O = 4:10:1; 2. BzCl, pyridine, CH_2Cl_2, 73% in 2 steps; c) 1. **8**, BSP, Tf_2O, AW-300 molecular sieves, CH_2Cl_2, 54%. d) H_2NNH_2/xH_2O, pyridine, AcOH, 88%. CSA = camphorsulfonic acid, DCC = 1,3-dicyclohexylcarbodiimide, DMAP = *N*,*N*′-dimethylaminopyridine, BSP = benzenesulfinyl piperidine, Tf_2O = trifluoromethanesulfonic anhydride, TFA = trifluoroacetic acid.

generated from D-glucosamine hydrochloride in three steps, underwent sequential deacetylation, benzylidenation, and levulinoylation at O3 to yield compound **11**. Hydrolysis of **11** gave the corresponding 4,6-diol intermediate, which upon subsequent selective O6-benzoylation with benzoyl chloride afforded the acceptor **9**. Coupling of the galactosyl thioglycoside **8** and **9**, with activation by benzenesulfinyl piperidine/trifluoromethanesulfonic anhydride (BSP/Tf_2O) gave the β-linked disaccharide **12** in 54% yield.[15] The levulinoate group was finally removed with hydrazine hydrate in an acetic acid/pyridine mixture and the disaccharide building block **6** was isolated in 88% yield.[18]

The lactosyl building block **7** was prepared from β-lactose octaacetate (Scheme 5), which was first transformed into the corresponding lactosyl bromide by using 33% hydrogen bromide in acetic acid and further coupled with *N*-(5-hydroxypentyl)carbamate in the presence of silver carbonate to provide an inseparable mixture of the expected β-lactoside and its orthoester by-product. The mixture was subjected to deacetylation to obtain the desired β-lactoside **13** in 46% yield over three steps. Regioselective allylation of compound **13** at O3′ with dibutyltin oxide and allyl bromide afforded the allyl ether product,[19] from which the fully protected lactoside **14** was obtained through 4,6-*O*-benzylidenation and perbenzylation (54% over 4 steps). The benzylidene acetal group of **14** was removed under acidic conditions and the primary hydroxy group of the generated diol was regioselectively silylated in excellent yield followed by benzylation at O4′ to yield **15**. The TBDPS group was cleaved by treatment with TBAF and the C3′ allyl ether was removed by using a two-step sequence. Isomerization of the terminal double bond with Wilkinson's catalyst ($[RhCl(PPh_3)_3]$) and DBU, with concomitant hydrolysis of the resulted enol ether using a mixture of aqueous HCl and acetone provided **7** in good yield.[20]

With the desired building blocks **5**–**7** in hand, we proceeded to synthesize the antigen N3 minor octasaccharide **3** by a reactivity-based one-pot strategy, as outlined in Scheme 6. Coupling of fucosyl thioglycoside **5** with the less reactive lactosaminyl disaccharide unit **6** using BSP/Tf_2O as a promoter proceeded cleanly to give the Le^x trisaccharide fragment. After completion of this reaction, without workup, the lactosyl building block **7** was added in the same pot, followed by addition of NIS and TfOH as activators to introduce two trisaccharide moieties at the same time. The

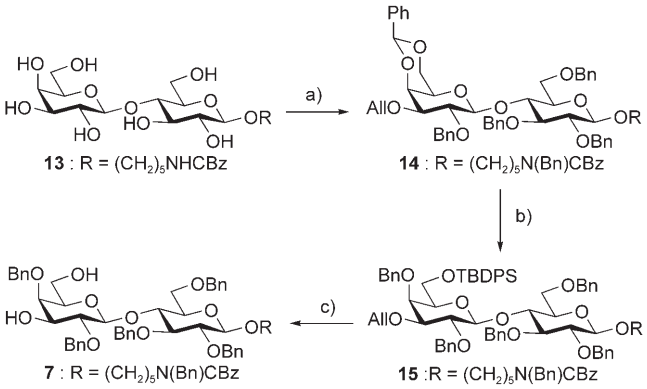

Scheme 5. Synthesis of lactosyl building block **7**. a) 1. Bu_2SnO, C_6H_6; 2. AllBr, TBAI, C_6H_6; 3. $PhCH(OMe)_2$, cat. CSA, CH_3CN; 4. BnBr, 60% NaH, DMF, 54% over 4 steps; b) 1. TFA/CH_2Cl_2/H_2O = 4:10:1; 2. TBDPSCl, Et_3N, CH_2Cl_2; 3. BnBr, 60% NaH, DMF, 52% over 3 steps; c) 1. TBAF,THF; 2. $Ph(PPh_3)_3Cl$, DBU, EtOH/$PhCH_3$/H_2O = 8:3:1; 3. 1 M HCl_{aq}/acetone = 1:9, 69% over 3 steps. All = allyl, TBDPS = *tert*-butyldiphenylsilyl, TBAI = tetrabutylammonium iodide, TBAF = tetrabutylammonium fluoride, DBU = 1,8-diazabicyclo-[5.4.0]undec-7-ene.

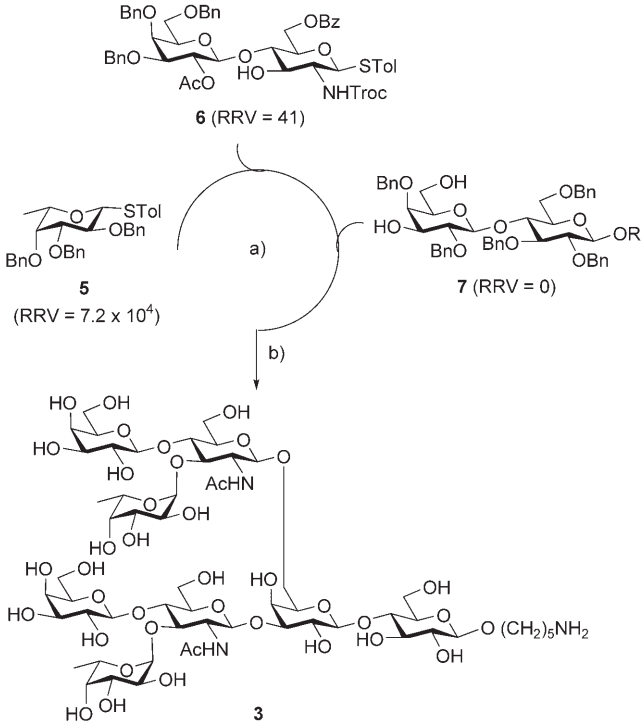

Scheme 6. One-pot synthesis of antigen N3 minor **3**. a) 1. BSP, Tf_2O, AW-300 molecular sieves, CH_2Cl_2, −70 to −10°C; 2. NIS, TfOH, 0°C to RT; b) 1. Zn, AcOH, RT; 2. Ac_2O, DMAP, pyridine, 0°C to RT; 3. NaOMe, MeOH, RT; 4. Pd-black, H_2 (1 atm), MeOH with 5% formic acid, 11% from (a). NIS = *N*-iodosuccinimide.

 © 2006 Wiley-VCH Verlag GmbH & Co. KGaA, Weinheim

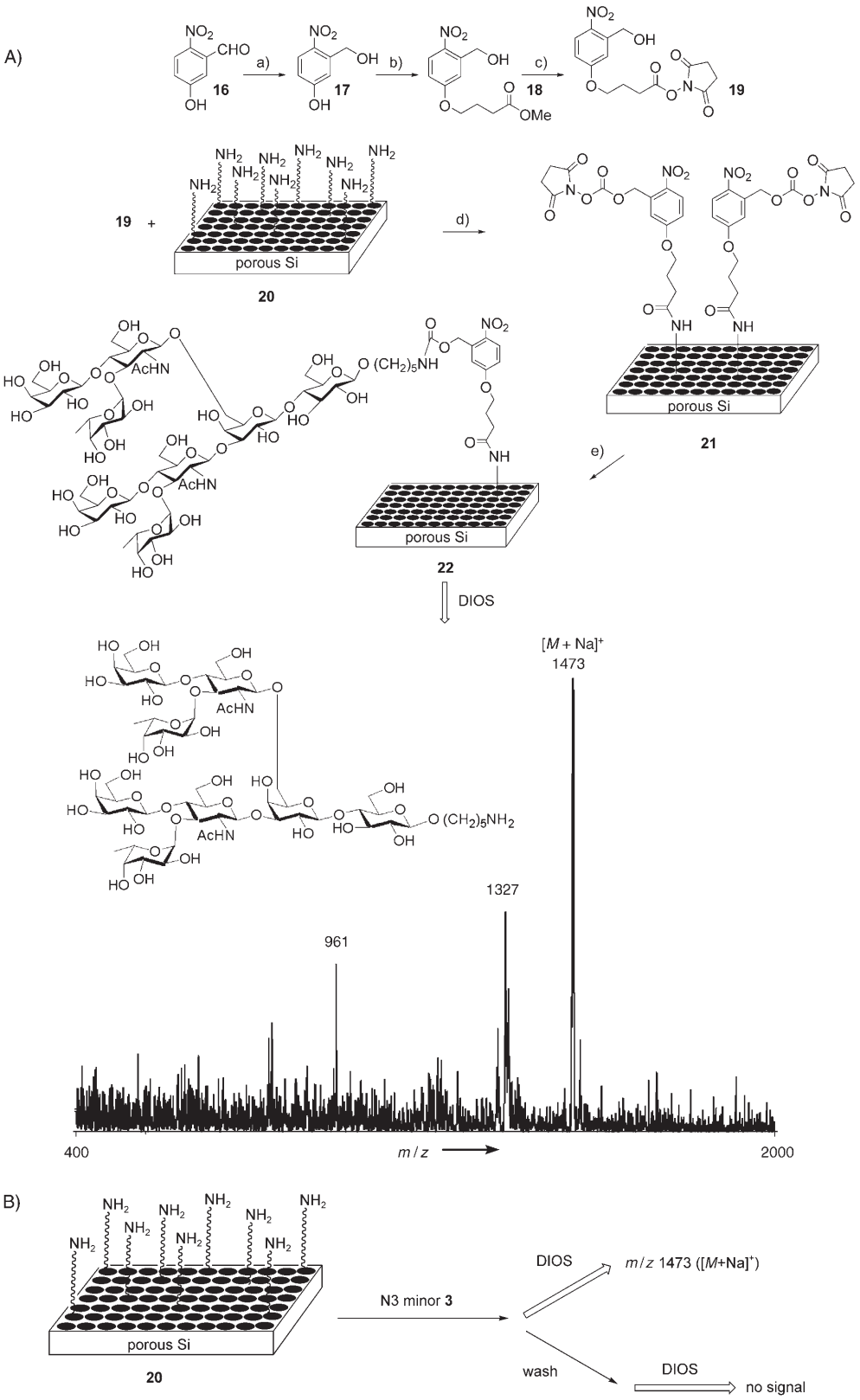

Scheme 7. A) Preparation of porous silicon sugar array and the resulting DIOS-MS spectrum of antigen N3 minor **3**. a) $NaBH_4$, MeOH, 0 °C to RT, 97%; b) methyl 4-bromobutyrate, TBAF, RT, 88%; c) 1. LiOH, MeOH, H_2O, 0 °C to RT; 2. DCC, *N*-hydroxysuccinimide, THF, RT, 82% over 2 steps; d) 1. Et_3N, toluene, RT; 2. *N*,*N*′-disuccinimidyl carbonate, Et_3N, CH_3CN, RT; e) 1. antigen N3 minor **3**, Et_3N; 2. wash with MeOH and H_2O.
B) Control experiment: N3 minor **3** was noncovalentaly deposited on the silylated amino surface **20**, and showed no signal by DIOS-MS after it had been washed.

 © 2006 Wiley-VCH Verlag GmbH & Co. KGaA, Weinheim

reaction was stirred at room temperature to obtain the octasaccharide **4**, which has the skeleton of N3 minor. The mixture of the desired octasaccharide and the inseparable unknown by-product was isolated after the one-pot glycosylation reaction. The by-product was removed after deprotection and chromatography to give pure N3 minor antigen (see the Supporting Information). The two trichloroethyl carbamate (Troc) functional groups were removed with activated Zn nanoparticles in acetic acid, followed by acetylation of the free amino groups with acetic anhydride and pyridine in the presence of catalytic amounts of DMAP to afford the corresponding NHAc derivative. Cleavage of the *O*-acyl groups under Zemplén conditions and deprotection of the benzyl ether and benzyl carbamate groups were accomplished by hydrogenolysis with palladium black in 5% formic acid/methanol solution. The target antigen N3 minor **3** was finally obtained in 11% yield based on the one-pot glycosylation of building blocks **5**–**7**. The characterization and configuration of **3** were confirmed by NMR spectroscopic and HRMS analysis.

The preparation of the photocleavable sugar array on porous silicon is shown in Scheme 7. 5-Hydroxyl-2-nitrobenzaldehyde (**16**) was reduced with sodium borohydride ($NaBH_4$) to give compound **17** (97%), which was subsequently subjected to regioselective alkylation with methyl 4-bromobutyrate and TBAF to provide **18** in 88% yield.[21] Hydrolysis of the methyl ester **18** using LiOH, followed by reaction with *N*-hydroxysuccinimide gave the succinic ester **19** (82% over 2 steps). Coupling of **19** with the silylated amino surface **20**[10] furnished the photocleavable linker with a free hydroxy group, which was transformed into the carbamate ester **21** in the presence of *N*,*N*′-disuccinimidyl carbonate and triethylamine. Finally, the N3 minor **3** was printed directly on the plate of **21**. Extensive washing of the plate with MeOH and H_2O resulted in the formation of the photocleavable sugar array on the porous silicon (for detailed experimental procedures, see the Supporting Information). DIOS-MS analysis showed a strong signal at *m*/*z* 1473 ($[M+Na]^+$) and a signal at *m*/*z* 1327 (corresponding to the defucosylated molecule). In the control experiment, we printed the N3 minor **3** on the silylated amino surface **20**, which showed no signal after it had been washed. A mannose array was also prepared for the binding study with ConA, and the result showed that nonspecific lectin-surface interactions are insignificant.

In summary, we have successfully synthesized the tumor-associated antigen N3 minor octasaccharide by using the reactivity-based one-pot strategy. The strategy proved that complex molecules can be rapidly assembled using readily available thioglycosides with defined relative reactivity values as building blocks. In addition, we have developed a novel strategy for arraying synthetic carbohydrates on porous silicon surface containing a photocleavable linker for direct characterization by mass spectrometry. This strategy should be useful for preparation of a large glycan array for high-throughput analysis.

Received: November 15, 2005
Revised: January 7, 2006
Published online: March 20, 2006

Keywords: carbohydrates · glycan array · glycosylation · mass spectrometry · synthesis design

[1] A. Kobata in *The Glycoconjugates*, *Vol. 1* (Eds.: M. I. Horowitz, W. Pigman), Academic Press, New York, **1977**, pp. 423–440.
[2] a) A. Kobata, *Methods Enzymol.* **1972**, *28*, 262–271; b) A. Kobata, V. Ginsburg, *Arch. Biochem. Biophys.* **1972**, *150*, 273–281.
[3] S. Hakomori, *Annu. Rev. Immunol.* **1984**, *2*, 103–126.
[4] S. J. Danishefsky, P. P. Deshpande, I. J. Kim, P. Livingston, J. K. Hyun, G. Ragupathi, T. K. Park, Pat. WO9830190, **1998**.
[5] H. M. Kim, I. J. Kim, S. J. Danishefsky, *J. Am. Chem. Soc.* **2001**, *123*, 35–48.
[6] Z. Zhang, I. R. Ollmann, X.-S. Ye, R. Wischnat, T. Baasov, C.-H. Wong, *J. Am. Chem. Soc.* **1999**, *121*, 734–753.
[7] For recent reviews: a) M. Mrksich, *Chem. Biol.* **2004**, *11*, 739–140; b) T. Feizi, F. Fazio, C. Wengang, C.-H. Wong, *Curr. Opin. Struct. Biol.* **2003**, *13*, 637–645; c) K. Drickamer, M. E. Taylor, *Genomebiology* **2002**, *3*, 1034.1–1034.4; d) K. R. Love, P. H. Seeberger, *Angew. Chem.* **2002**, *114*, 3733–3736; *Angew. Chem. Int. Ed.* **2002**, *41*, 3583–3586.
[8] a) M. C. Bryan, F. Fazio, H.-K. Lee, C.-Y. Huang, A. Y. Chang, M. D. Best, D. A. Calarese, O. Blixt, J. C. Paulson, D. Burton, I. A. Wilson, C.-H. Wong, *J. Am. Chem. Soc.* **2004**, *126*, 8640–8641; b) O. Blixt, S. Head, et al., *Proc. Natl. Acad. Sci. USA* **2004**, *109*, 17033–17038; c) C.-Y. Huang, D. A. Tharey, A. Y. Chang, M. D. Best, J. Hoffman, S. Head, C.-H. Wong, *Proc. Natl. Acad. Sci. USA* **2006**, *103*, 15–20.
[9] F. Fazio, M. C. Bryan, O. Blixt, J. C. Paulson, C.-H. Wong, *J. Am. Chem. Soc.* **2002**, *124*, 14397–14402.
[10] a) J. Wei, J. M. Buriak, G. Siuzdak, *Nature* **1999**, *399*, 243–246; b) Z. Shen, J. J. Thomas, C. Averbuj, K. M. Broo, M. Engelhard, J. E. Crowell, M. G. Finn, G. Siuzdak, *Anal. Chem.* **2001**, *73*, 4932–4937; c) S. A. Trauger, E. P. Go, Z. Shen, J. V. Apon, B. J. Compton, E. S. P. Bouvier, M. G. Finn, G. Siuzdak, *Anal. Chem.* **2004**, *76*, 4484–4489.
[11] J. M. Gerdes, H. Waldmann, *J. Comb. Chem.* **2003**, *5*, 814–820.
[12] F. Burkhart, Z. Zhang, S. Wacowich-Sgarbi, C.-H. Wong, *Angew. Chem.* **2001**, *113*, 1314; *Angew. Chem. Int. Ed.* **2001**, *40*, 1274–1277.
[13] T. K.-K. Mong, C.-H. Wong, *Angew. Chem.* **2002**, *114*, 4261; *Angew. Chem. Int. Ed.* **2002**, *41*, 4087–4090.
[14] T. K.-K. Mong, C.-Y. Huang, C.-H. Wong, *J. Org. Chem.* **2003**, *68*, 2135–2142.
[15] T. K.-K. Mong, H.-K. Lee, S. G. Durón, C.-H. Wong, *Proc. Natl. Acad. Sci. USA* **2003**, *100*, 797–802.
[16] H.-K. Lee, C. N. Scanlan, C.-Y. Huang, A. Y. Chang, D. A. Calarese, R. A. Dwek, P. M. Rudd, D. R. Burton, I. A. Wilson, C.-H. Wong, *Angew. Chem.* **2004**, *116*, 1018; *Angew. Chem. Int. Ed.* **2004**, *43*, 1000–1003.
[17] K. Chayajarus, D. J. Chambers, M. J. Chughtai, A. J. Fairbanks, *Org. Lett.* **2004**, *6*, 3797–3800.
[18] J. H. van Boom, P. M. J. Burgers, *Tetrahedron Lett.* **1976**, *17*, 4875–4878.
[19] X. Qian, K. Sujino, A. Otter, M. M. Palcic, O. Hindsgaul, *J. Am. Chem. Soc.* **1999**, *121*, 12063–12072.
[20] F. Roussel, M. Takhi, R. R. Schmidt, *J. Org. Chem.* **2001**, *66*, 8540–8548.
[21] C.-Y. Wu, A. Brik, S.-K. Wang, Y.-H. Chen, C.-H. Wong, *ChemBioChem* **2005**, *6*, 2176–2180.

 © 2006 Wiley-VCH Verlag GmbH & Co. KGaA, Weinheim

Bioinorganic Chemistry

DOI: 10.1002/anie.200600260

Short Oxo–Titanium(IV) Bond in Bacterial Transferrin: A Protein Target for Metalloantibiotics**

Maolin Guo, Ian Harvey, Dominic J. Campopiano, and Peter J. Sadler**

Titanium is becoming increasingly mobilized in the environment on account of its widespread use (as TiO_2) in white pigments. In medicine it is used in surgical and dental implants, and there is interest in the design of titanium complexes as drugs. Titanium enhances the effectiveness of antibiotics such as metronidazole,[1] and Ti^{IV} compounds also exhibit antibacterial and antiviral activity.[2] Titanocene dichloride has been on clinical trials as an anticancer agent.[3] However, little is known about the biological chemistry of titanium. We found recently that Ti^{IV} binds strongly to the human iron-transport protein transferrin (Tf; human transferrin hTf),[4] as well as to small phenolate ligands.[5] Ti^{IV} is selectively delivered into tumor tissues in vivo by Tf.[6] Now we have investigated reactions of Ti^{IV} with bacterial transferrin (ferric-ion-binding protein, FBP) with a view to exploring Ti^{IV} compounds as inhibitors of iron uptake by pathogenic bacteria. Novel antibiotics are urgently required to combat the rapid development of resistance to currently used drugs. Our work demonstrates that FBP can stabilize unusual configurations of Ti^{IV}, and that Ti^{IV} binding to FBP has promising characteristics for consideration as a candidate metalloantibiotic.

Iron is an essential and a limiting resource in most environments, and effective iron acquisition is critical for bacterial virulence.[7] Numerous pathogenic bacteria, such as *Haemophilus influenzae* and *Neisseria gonorrhoeae* have evolved a specific iron-uptake system, which can steal iron from the host Tf and lactoferrin (Lf).[8,9] The key to this iron-stealing system is a ferric ion-binding protein which shuttles Fe^{III} across the periplasmic space and is critical for virulence.[7,8] Structural data on FBPs reveal that the 3D-fold resembles that of each lobe of mammalian Tf, with Fe^{III} bound in a cleft between the two domains, although the iron site in FBP is much more solvent-exposed. Four classes of FBP Fe^{III} binding sites have been identified (Figure 1). All

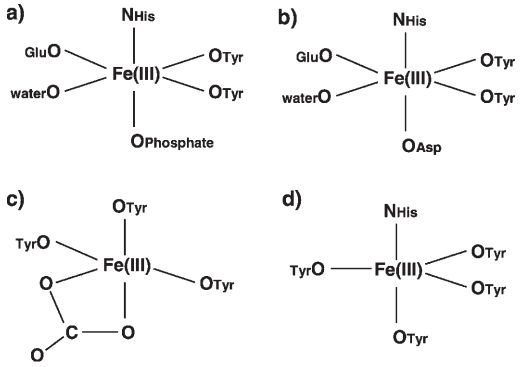

Figure 1. The Fe^{III} binding sites in four classes of bacterial transferrins (FBPs). a) *Neisseria gonorrhoeae or Haemophilus influenzae* (class 1). b) *Yersina enterocolitica* (class 2). c) *Mannheimia haemolytica* (class 3). d) *Campylobacter jejuni* (class 4).

FBPs contain a pair of highly conserved consecutive Tyr residues (Y195 and Y196 in *N. gonorrhoeae* FBP) at the active site. This pair is critical for tight metal binding, as revealed by site-directed mutagenesis[9b] and crystal structures of FBP complexes with Fe^{III}, Zr^{IV}, and Hf^{IV} in the metal-binding cleft.[10]

To explore the interaction of FBP with titanium complexes, we studied the binding of Ti^{IV} to apo-FBP (apo-FBP = metal-free FBP) under physiologically relevant conditions. Reactions of Ti^{IV}–citrate (Ti^{IV}–cit) with apo-FBP (26.8 μM, 1:1) in physiological buffer at 310 K produced a new broad band in the UV/Vis spectra, centered at around 323 nm (see Supporting Information). UV difference spectra obtained under similar conditions (Figure 2a) revealed two additional sharper bands at 247 nm and 294 nm. The reaction was complete in approximately 20 min. The stoichiometry of Ti^{IV} binding to apo-FBP was found to be 1:1 (Figure 2b), which was confirmed by inductively coupled plasma optical emission spectroscopy (ICP-AES) analysis of purified Ti–FBP (Ti/FBP ratio of 1.2(±0.1)/1).

We investigated the displacement of Ti^{IV} from Ti–FBP by Fe^{III}. The complex $[Fe(NTA)_2]$ (1.0 mol equiv, NTA = nitrilotriacetate) was added to Ti-FBP solution (28 μM in 10 mM 2-[4-(2-hydroxyethyl)-1-piperazinyl]ethane sulfonic acid (Hepes), 5 mM NaH_2PO_4, pH 7.4) and Fe^{III}-binding was monitored by the appearance of the Fe^{III}–FBP ligand-to-metal charge transfer (LMCT) band at around 481 nm. Over 3 h, there was a small increase in intensity at >420 nm accompanied by a smaller decrease in intensity at <420 nm with an isosbestic point at 420 nm (see Supporting Information). This result suggested that Fe^{III} partially displaced Ti^{IV} from Ti–FBP. However, the final increase in intensity at 481 nm ($\Delta A_{481} = 0.018$), suggested that only 26% of the Ti^{IV}

[*] Dr. M. Guo, Dr. D. J. Campopiano, Prof. Dr. P. J. Sadler
School of Chemistry
The University of Edinburgh
West Mains Road, Edinburgh, EH93JJ (UK)
Fax: (+44) 131-650-6452
E-mail: mguo@umassd.edu
p.j.sadler@ed.ac.uk
Dr. M. Guo
Department of Chemistry and Biochemistry
University of Massachusetts
Dartmouth, MA 02747 (USA)
Fax: (+1) 508-999-9167
Dr. I. Harvey
Synchrotron Radiation Department
CCLRC Daresbury Laboratory, Warrington WA4 4AD (UK)

[**] We thank the Wellcome Trust, Overseas Research Student Award, and University of Massachusetts Dartmouth for their support for this work.

Supporting information for this article is available on the WWW under http://www.angewandte.org or from the author.

© 2006 Wiley-VCH Verlag GmbH & Co. KGaA, Weinheim

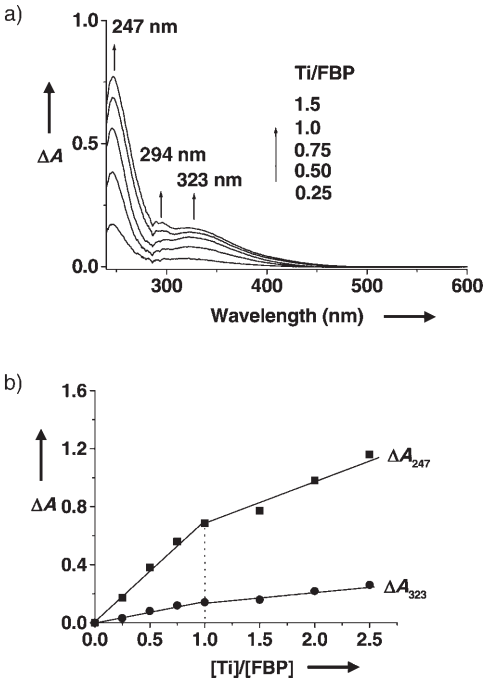

Figure 2. a) UV difference spectra for the titration of apo-FBP with Ti^{IV}–cit. Conditions: 40.4 μM apo-FBP in physiological buffer (100 mM NaCl, 25 mM HCO_3^-, 4 mM NaH_2PO_4, pH 7.4), 298 K. The ratio of Ti/FBP increases from bottom to top. b) Titration curve for the reaction in (a). The increase in intensities of the absorbance (*A*) at 323 nm and 247 nm are plotted against the ratio [Ti]/[FBP].

was displaced. This result shows that Ti^{IV} binding to FBP is competitive with that of Fe^{III}, and can be contrasted with Ti_2–hTf from which Ti^{IV} is readily and completely displaced by Fe^{III} from $[Fe(NTA)_2]$.[4]

Next, we investigated the displacement of Fe^{III} from holo-FBP (holo-FBP = as isolated, metal-loaded FBP) by Ti^{IV}. Holo-FBP contains Fe^{III} bound in a closed protein cleft with phosphate as the synergistic anion.[8,9] When 1.0 mol equiv of Ti^{IV}–cit was added to a solution of holo-FBP (51 μM) in physiological buffer at 298 K, there was no change to the LMCT band of Fe^{III}–FBP at 481 nm, but a very small increase in the absorbance at approximately 318 nm and 254 nm occurred over about 30 min (see Supporting Information). This situation implied formation of Ti–(O)Tyr bonds in the reaction. However, the increase in intensity of the CT band at 318 nm only accounted for about 26% of that for Ti^{IV}–FBP at similar concentrations. The perturbation of Tyr phenolate π–π* transition (increase at 254 nm) is also much weaker (only ca 4.8%) compared to that for Ti^{IV} binding to apo-FBP at similar concentrations. This data implied that Ti^{IV} can bind without Fe^{III} displacement, perhaps via formation of Fe-oxo/hydroxo/phosphate/tyrosinate-Ti bridges. Further Ti^{IV} was added and UV/Vis spectra were recorded after equilibration (see Supporting Information). When the Ti/Fe–FBP ratio increased to >4, the Tyr to Fe–FBP LMCT band at 481 nm decreased in intensity and almost completely disappeared in the presence of approximately 20 mol equiv Ti^{IV}, indicative of Fe^{III} displacement by Ti^{IV}.

The differences in Ti^{IV} uptake and metal-displacement reactions between bacterial FBP and the mammalian Tf are notable, despite their similar Fe^{III} ligands and high iron affinities ($K_a > 10^{18}$ M). In contrast to the slow uptake (>10 h at 310 K) of Ti^{IV} by apo-hTf from Ti^{IV}–cit,[4] the uptake of Ti^{IV} by apo-FBP is rapid and complete within 20 min at 310 K. Moreover, Ti^{IV} is readily and completely displaced by Fe^{III} from Ti_2–hTf on reaction with $[Fe(NTA)_2]$.[4] But this is not the case for Ti–FBP, for which Ti^{IV} is only partially displaced by Fe^{III}, and Ti^{IV} can rapidly displace Fe^{III} from native Fe-phosphate-FBP. These differences between bacterial and mammalian transferrins may be due to the differences in the location of the Fe^{III} sites: in Tf, Fe^{III} is buried within the protein core, whilst in FBP the active site lies nearer the protein surface and is solvent-exposed and accessible.[8,10] This arrangement may provide a more facile route for entry of Ti^{IV} into the binding cleft by attack on the metal-binding Tyr side-chains.

^{1}H NMR spectroscopic studies were carried out to investigate whether anticancer drug titanocene dichloride, $[Cp_2TiCl_2]$ ($Cp = C_5H_5$), also binds to FBP. ^{1}H NMR spectra of apo-FBP are complicated by the overlap of resonances, but Ti^{IV}-induced specific changes in the upfield region (0.5 to −1 ppm, see Supporting Information). These changes indicated that one Ti^{IV} ion binds specifically to apo-FBP and that Ti^{IV} binding induces characteristic structural changes in the protein. The ^{1}H NMR spectra also showed that the Cp ligands are displaced during the reaction (Figure 3).

^{31}P NMR spectroscopic studies suggested that Ti^{IV} binding to FBP is not accompanied by the binding of phosphate as a synergistic anion (See Supporting Information).

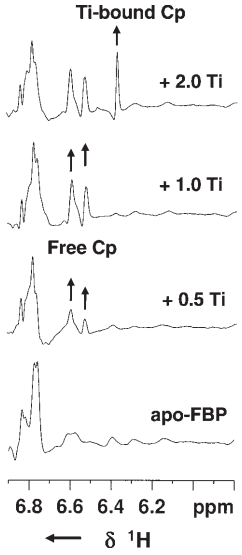

Figure 3. 500 MHz ^{1}H NMR spectra showing the displacement of Cp ligands from $[Cp_2TiCl_2]$(aq) on reaction with apo-FBP (1 mM in 0.1 M KCl, 3 mM NaH_2PO_4, pH 7.4, 298 K). Ti^{IV}-bound Cp gives a singlet at $\delta = 6.42$ ppm at neutral pH, while released Cp (CpH) shows multiplets at $\delta = 6.57$, 6.62 ppm, and 2.95 ppm. When 0.5 mol equiv $[Cp_2TiCl_2]$(aq) is added to apo-FBP, Cp (CpH) is released (two broad peaks at $\delta = 6.54$ and 6.60 ppm). These two peaks increased in intensity when 1.0 mol equiv of $[Cp_2TiCl_2]$(aq) was added, and no peak for Ti-bound Cp was observed at this stage. When a second mol equiv of $[Cp_2TiCl_2]$(aq) was added, no further change in the free CpH resonances occurred, but a strong singlet assignable to Ti^{IV}-bound Cp appeared at $\delta = 6.39$ ppm. This suggests that apo-FBP takes up only one mol equiv of Ti^{IV} from titanocene dichloride which results in the displacement of the Cp ligands.

 © 2006 Wiley-VCH Verlag GmbH & Co. KGaA, Weinheim

Our preliminary crystallographic data for Ti–FBP[11] at medium resolution (2.4 Å), suggest a model in which a highly hydrated Ti^{IV} center occupies the position which was occupied by iron and phosphate in native Fe–FBP and is bound to the protein by Tyr residues. However, the detail of the hydration is not yet clear. Thus Ti K-edge X-ray absorption near-edge structure (XANES) and extended X-ray absorption fine structure (EXAFS) studies (Figure 4) were carried out to

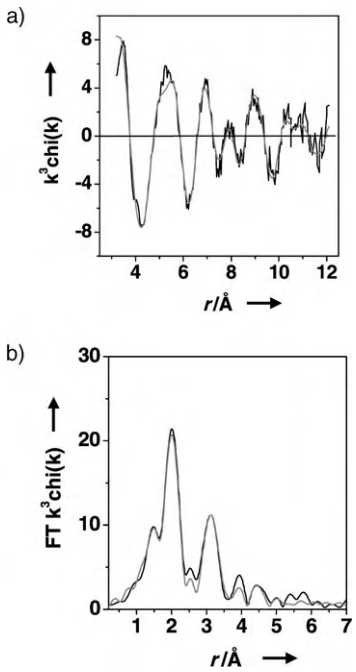

Figure 4. a) EXAFS spectrum of Ti–FBP. b) Fourier transform. Dark line experimental data; gray line calculated data.

investigate the environment of Ti in Ti–FBP, prepared by treating apo-FBP with Ti^{IV} citrate (see Experimental Section). The XANES edge position confirms the oxidation state of the Ti as 4+, as with Ti-loaded transferrin.[12] The Fourier transform shows two intense, overlapping peaks at approximately 1.64 Å and 1.97 Å, and a broader peak at 3.09 Å. The 1.64 Å and 1.97 Å peaks were simulated with six oxygen atoms as back-scatterers at three distances (1 atom at 1.64 Å, 2 atoms at 1.80 Å, and 3 atoms at 1.96 Å), and are due to scattering from the atoms directly coordinated to the Ti^{IV} center. In addition to this "inner sphere", eight additional oxygen atoms form an "outer sphere" (3 atoms at 2.95 Å and 5 atoms at 3.33 Å; for detailed refinement analysis see the Supporting Information).

The five longer inner-sphere Ti–O bonds in Ti–FBP (1.80 Å and 1.95 Å) are within the range of typical Ti–O single bonds. The short oxo–Ti bond (1.64 Å) is either an unusually short Ti–O single bond or, more likely, a Ti=O double bond.[13] Although Ti–O single bonds as short as 1.66 Å have been reported[14] for $[\{TiCl_2(MeCN)_2(\mu\text{-}O)\}_4]\cdot 2MeCN$, the Ti-O-Ti bonds in this cluster alternate between (averages of) 1.67 and 1.95 Å, and such a structure gave an unreasonable fit to our EXAFS data. Short Ti–O bonds of comparable length to that in Ti–FBP have been assigned to Ti=O double bonds in low-molecular-weight octahedral Ti^{IV} complexes, such as the macrocyclic complex $[(L)Ti(O)(X)_2]$ (L = 1,4,7-trimethyl-1,4,7-triazacyclononane; X = NCS or Cl; 1.64 Å).[15] Hydrogen-bonding to such a terminal oxo ligand tends to lengthen the bond slightly, for example, to 1.68 Å in the seven-coordinate pentagonal-bipyramidal carbonato complex $[C(NH_2)_3]_4[TiO(CO_3)_3]\cdot 2H_2O$.[16] Amongst the shortest Ti=O bonds reported in the Cambridge database (CCDC) are those for porphyrin complexes (ca. 1.62–1.64 Å). Steric hindrance around the Ti–O bond, as in $[\{Ti(O)(2,6\text{-}i Pr_2OAr\}_2(NC_5H_4\text{-}4NC_4H_8)_2]$ (2,6-iPr$_2$OAr = 2,6-diisopropylphenoxide, NC_5H_4-4NC_4H_8 = 4-pyrrolidinopyridine)[17] is effective in preventing Ti-O-Ti bridging which tends to lengthen the bond to approximately 1.66–1.72 Å. Titanyl groups can exert a strong *trans* influence, for example, lengthening a *trans* Ti–N bond by 0.2 Å.[15] The presence of a strong terminal oxo–Ti bond in Ti–FBP may explain the lack of a bound phosphate as a synergistic anion. A synergistic anion is crucial for Fe^{III} to bind to both Tf and FBP, however, the oxo atom may serve the role of synergistic anion for Ti^{IV} in Ti–FBP, that is, Ti^{IV} may bring its own synergistic anion as Ti=O. This unique property may allow Ti^{IV} to bind strongly to FBP under various environmental conditions. We noted previously[4] the lack of need for a synergistic anion for strong binding of Ti^{IV} to hTf.

Efficient iron acquisition is required for the virulence of pathogenic bacteria and iron-uptake genes are amongst the virulence genes.[18] There are at least 53 bacterial species containing the FBP gene, and the di-tyrosyl metal-binding motif is highly conserved amongst these species. FBP thus provides a potential target for the design of broad-spectrum antibacterial agents. Inhibitors of iron uptake by FBP could be active against diseases caused by these pathogens. Targeting this pathway may provide a means to overcome existing mechanisms of bacterial resistance and our findings encourage the exploration of Ti^{IV} complexes as potential novel metalloantibiotics.

Experimental Section

Solutions of $[Cp_2TiCl_2]$, Ti-citrate, and $[Fe(NTA)_2]$,[4] recombinant holo-FBP from *Neisseria gonorrhoeae*, and apo-FBP (purity > 95%) were prepared as described previously.[9]

UV/Vis spectra were recorded on a Shimadzu UV-1000 spectrometer at 298 K or 310 K. UV difference spectra after addition of metal complex to apo-FBP were recorded immediately and at different time intervals. For titration experiments, aliquots of Ti^{IV} complex (0.5–10.0 μL) were added and the solution was left to equilibrate at 298 K for 30 min.

ICP-AES was performed on a Thermo Jarrell Ash IRIS spectrometer.[4,9] Apo-FBP loaded with Ti using 3 mol equiv Ti-cit in 10 mM Tris-Cl buffer was purified by using Centricon 30 (Amicon) ultrafilters and washing three times with buffer with ultrafiltration after each washing. The final protein solution was diluted with Tris buffer, and Ti and Fe content was measured without digestion of the sample.

^1H and ^{31}P NMR spectra were recorded on a Bruker DMX 500 spectrometer. FBP samples were dissolved in 0.1M KCl in D_2O/H_2O (10%/90%) and the pH value was adjusted to 7.4 ± 0.1. Resolution enhancement was achieved by processing the free induction decays

 © 2006 Wiley-VCH Verlag GmbH & Co. KGaA, Weinheim

with a combination of unshifted sine-bell and exponential functions (line broadening of 1.5–20 Hz) using XWIN-NMR software.

X-ray spectra were recorded at the Ti K-edge (4.966 keV) on EXAFS station 8.1 at the Daresbury Laboratory Synchrotron Radiation Source, at 90 K in fluorescence mode using a 13-element Ge solid-state detector. Ti–FBP was prepared by loading apo-FBP with 2 mol equiv of $[Cp_2TiCl_2]$(aq) in 0.1 M KCl (pH 7.4) in the presence of 3 mM phosphate. The excess Ti was removed from the yellowish solution by ultrafiltration (Centricon 10) four times with KCl solution. Data were processed using EXCALIB, SPLINE (modified for use with EXCURV), and analyzed using the rapid curved-wave formalization in EXCURV98, as described in ref. [9a].

Received: January 20, 2006
Published online: March 20, 2006

Keywords: bioinorganic chemistry · EXAFS spectroscopy · iron · metalloproteins · titanium

[1] L. Bunetel, J. Guerin, G. Agnani, S. Piel, H. Pinsard, J. C. Corbel, M. Bonnaure-Mallet, *Biomaterials* **2001**, *22*, 3067 – 3072.
[2] a) H. Köpf, P. Köpf-Maier, *Angew. Chem.* **1979**, *18*, 509; *Angew. Chem. Int. Ed. Engl.* **1979**, *18*, 477 – 478; b) C. W. Schwietert, J. P. McCue, *Coord. Chem. Rev.* **1999**, *184*, 67 – 89.
[3] N. Kröger, U. R. Kleeberg, K. Mross, L. Edler, D. K. Hossfeld, *Onkologie* **2000**, *23*, 60 – 62.
[4] M. Guo, H. Sun, H. J. McArdle, L. Gambling, P. J. Sadler, *Biochemistry* **2000**, *39*, 10023 – 10033.
[5] M. Guo, H. Sun, S. Bihari, J. A. Parkinson, R. D. Gould, S. Parsons, P. J. Sadler, *Inorg. Chem.* **2000**, *39*, 206 – 215.
[6] A. L. Vavere, M. J. Welch, *J. Nucl. Med.* **2005**, *46*, 683 – 690.
[7] a) K. N. Raymond, E. A. Dertz, S. S. Kim, *Proc. Natl. Acad. Sci. USA.* **2003**, *100*, 3584 – 3588; b) V. Braun, *Int. J. Med. Microbiol.* **2001**, *291*, 67 – 79.
[8] a) T. A. Meitzner, S. B. Tencza, P. Adhikari, K. G. Vaughan, A. J. Nowalk, *Top. Microbiol. Immun.* **1998**, *225*, 113 – 135; b) S. A. L. Tom-Yew, D. T. Cui, E. G. Bekker, M. E. P. Murphy, *J. Biol. Chem.* **2005**, *280*, 9283 – 9290.
[9] a) M. Guo, I. Harvey, W. Yang, L. Coghill, D. J. Campopiano, J. A. Parkinson, R. T. A. MacGillivray, W. R. Harris, P. J. Sadler, *J. Biol. Chem.* **2003**, *278*, 2490 – 2502; b) M. Guo, PhD Thesis, University of Edinburgh, **2000**.
[10] a) D. Alexeev, H. Zhu, M. Guo, W. Zhong, D. J. B. Hunter, W. Yang, D. J. Campopiano, P. J. Sadler, *Nat. Struc. Biol.* **2003**, *10*, 297 – 302; b) H. Zhu, D. Alexeev, D. J. B. Hunter, D. J. Campopiano, P. J. Sadler, *Biochem. J.* **2003**, *376*, 35 – 41; c) W. Zhong, D. Alexeev, M. Guo, D. J. B. Hunter, D. J. Campopiano, P. J. Sadler, *Angew. Chem.* **2004**, *116*, 6040 – 6044; *Angew. Chem. Int. Ed.* **2004**, *43*, 5914 – 5918.
[11] M. Guo, D. Alexeev, D. J. Campopiano, P. J. Sadler, unpublished results.
[12] M. Guo, I. Harvey, P. J. Sadler, unpublished results.
[13] a) R. Guilard, J.-M. Latour, C. Lecomte, J.-C. Marchon, J. Protas, D. Ripoll, *Inorg. Chem.* **1978**, *17*, 1228 – 1237; b) M. R. Smith III, P. T. Matsunaga, R. A. Andersen, *J. Am. Chem. Soc.* **1993**, *115*, 1049 – 1050.
[14] G. R. Willey, J. Palin, M. G. B. Drew, *J. Chem. Soc. Dalton Trans.* **1994**, 1799 – 1804.
[15] P. Jeske, G. Haselhorst, T. Weyhermüller, K. Weighardt, B. Nuber, *Inorg. Chem.* **1994**, *33*, 2462 – 2471.
[16] P.-J. Li, S.-H. Huang, K.-Y. Huang, R.-J. Wang, T. C. W. Mak, *Inorg. Chim. Acta* **1990**, *175*, 105 – 110.
[17] J. E. Hill, P. E. Fanwick, I. P. Rothwell, *Inorg. Chem.* **1989**, *28*, 3602 – 3604.
[18] C. L. Kurz, S. Chauvet, E. Andres, J. J. Ewbank, *EMBO J.* **2003**, *22*, 1451 – 1460.

 © 2006 Wiley-VCH Verlag GmbH & Co. KGaA, Weinheim

Continuous-Flow Reactions

DOI: 10.1002/anie.200503600

Catalysis in Capillaries by Pd Thin Films Using Microwave-Assisted Continuous-Flow Organic Synthesis (MACOS)**

*Gjergji Shore, Sylvie Morin, and Michael G. Organ**

Microwave-assisted organic synthesis (MAOS) has blossomed over the last five years to become a presence in most academic and industrial labs.[1] At the same time, significant efforts have been made to develop flow methods for synthetic chemistry.[2,3] Both methodologies reduce the time required to conduct synthesis, but in different ways. MAOS greatly accelerates the rate of individual chemical transformations by direct and more effective heating of the reaction solution than that with conventional heating sources such as an oil bath or heating mantle. Flow techniques target handling and processing operations between transformations, often using solid-supported reagents/catalysts and chromatographic media to streamline reaction workup and purification by requiring only simple filtration. An optimal arrangement would be to combine MAOS with flow techniques to gain the powerful benefits of both, and this is the starting point for microwave-assisted continuous-flow organic synthesis (MACOS).[4–6] To fuel the development of this new area, new reagents and catalysts that are immobilized on surfaces must be developed that can withstand pressurized flow, microwave irradiation, and very high temperatures.

This report details the development of thin metal films that serve as catalysts for MACOS. There are two literature reports that describe the deposition of Pd black on the surface of glass reaction vessels where the metal films themselves proved suitable to catalyze Heck and Sonogashira couplings,[7] as well as C–P coupling.[8] In these cases, the reactions were run in batch mode; that is, the reactions were not flowed through the microwave chamber. These Pd-film-catalyzed reactions required anywhere from 3 min to 5 d of constant irradiation to achieve good conversion. Here we detail the methods to deposit Pd on the inner surface of capillaries, the complete characterization of these films including their morphology and elemental composition, and their use in Suzuki and Heck reactions using MACOS.

[*] G. Shore, Prof. S. Morin, Prof. M. G. Organ
The Department of Chemistry, York University
4700 Keele Street, Toronto, ON M3J1P3 (Canada)
Fax: (+1) 416-735-5936
E-mail: organ@yorku.ca

[**] This work was funded by the Ontario Research and Development Challenge Fund (ORDCF), Canada Foundation for Innovation (CFI), the Ontario Innovation Trust (OIT), NSERC, and York University. The authors are grateful to Biotage Inc. for the donation of a Smith Creator Synthesizer to develop this new methodology. We acknowledge Ross Davidson at Surface Science Western, University of Western Ontario, London, ON, for the SEM and EDX measurements.

© 2006 Wiley-VCH Verlag GmbH & Co. KGaA, Weinheim

The preparation of Pd films is based on methods for the preparation of palladium particles and sols by thermal decomposition of organometallic compounds in organic solvents.[9] It was reported that monodispersed Pd nanoparticles could be obtained by rapid heating of the solution.[9d] While the methodology for the preparation of Pd sols can be optimized carefully to prevent sedimentation and flocculation by using the appropriate organic solvent[9c–e] or by controlling the amount of water present,[10] we optimized sedimentation/flocculation in order to produce the metal film. Pd thin films were prepared by flowing a 0.1 mmol mL^{-1} solution of $Pd(OAc)_2$ into a 1150-μm capillary, capping the ends, and heating the capillary at 150 °C for 30 min. During this time, Pd^0 gradually plated out on the wall of the capillary producing a black film with a mat appearance. Closer inspection of the film morphology revealed that the films are highly porous and consist of nanometer-size Pd crystallites (see Figure 1).

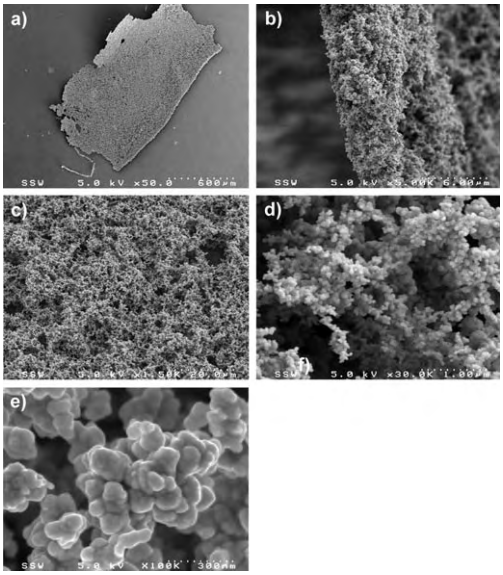

Figure 1. a) SEM image of the Pd films prepared inside a glass capillary and removed. (×50.0). b) Cross-section of the edge located on the lefthand side of sample shown in (a) (×5000). Image taken from the central portion of the sample in (a) at c) ×1500, d) ×30000, and e) ×100000.

Although the films formed quite uniformly around the entire glass surface, the capillaries were rotated during heating to promote an even film thickness and counter any possible role played by gravity in the deposition process. To drive off any residual organic matter and to improve Pd adherence to the glass wall, some capillaries were calcinated. In this procedure, the liquid solution was drained out of the capillary and it was placed back in the oven and heated at 400 °C for 1 min; this was repeated three times. This heat treatment resulted in a noticeable enhancement of the film porosity.

Film morphology was examined using scanning electron microscopy (SEM) and energy-dispersive X-ray (EDX) analysis. The images in Figure 1 a–e were obtained from a piece of the film removed from the capillary wall. Figure 1 b–e show the Pd film morphology with increasing magnification, and it is clear that the porosity is both extensive and regular. The higher magnification in Figure 1d,e reveals that the films are made of small grains of Pd that are in the range of 60 to 140 nm in diameter. The cross-sectional view in Figure 1 a illustrates that the Pd film is approximately 6 μm thick (evaluated from the edge on the lefthand side).

SEM analysis was also performed on Pd films prepared on glass slides to study the effect of high-temperature calcination on film morphology. After the film had been deposited and washed, it was heated three separate times (1 min each time) at 350–400 °C, and this vastly increased the porosity of the resulting film over that of noncalcinated films. This indicates that residual carbonaceous material is most likely located on surface of the Pd gains. (Note that calcination temperature is well below the Pd annealing temperature.) We also noted that the Pd film morphology is more compact when they are prepared on slides rather than in the capillaries. This could be because of the slower rate of metal deposition in the capillaries as there is less dissolved $Pd(OAc)_2$ there than in the larger flasks in which the glass plates are coated.

EDX analysis was performed on the film formed in the capillary as well as on films that were prepared on glass slides. Films on slides that were not calcinated were found to contain an average of 28.0 wt % of carbon, which dropped to 15.0 wt % for the calcinated samples. For calcinated capillary samples the amount of elemental carbon dropped further to 5.5 wt %. This could be the result of a slower, more controlled film deposition leading to larger and more regular pores. This is corroborated by the increase in porosity observed for films prepared in capillaries, which would allow trapped carbonaceous material to be removed more efficiently. The films prepared in capillaries consist primarily of Pd (94.0 wt %) and, other than carbon, only oxygen (0.3 wt %) was detected, which could be associated with the presence of a thin surface oxide on the Pd grains. The presence of such a small amount of carbon and oxygen indicates that the film is mostly metallic. Based on the weight change of the capillary before and after the film preparation, the film thickness as evaluated by SEM and the dimension of the capillary, we calculated the density of the porous Pd film to be around 3 g cm^{-3}. This corresponds to a porosity of about 75 %.

The Pd-coated capillaries were first put to use in Suzuki–Miyara coupling reactions, and the results are summarized in Table 1. Premixed solutions containing the aryl boronic acid, aryl bromide, base, and solvent were flowed through the metal-coated capillary while it was subjected to microwave irradiation (power setting ≈30 W) such that the IR sensor read a constant temperature of 200 °C (see Figure 2). In all cases, including the coupling of both electron-rich and electron-poor aryl halides with electron-poor boronic acids, good to excellent conversion was obtained. Perhaps most interestingly, the reaction with the highly hindered 2-bromo-1,3,5-trimethylbenzene (Table 1, entry 6) proceeded very well although the reaction presumably proceeds at the surface of the film (vide infra).

Two important control experiments were then performed. It has been proposed that when catalytic reactions, such as the Suzuki–Miyama coupling, are performed with heated metal

 © 2006 Wiley-VCH Verlag GmbH & Co. KGaA, Weinheim

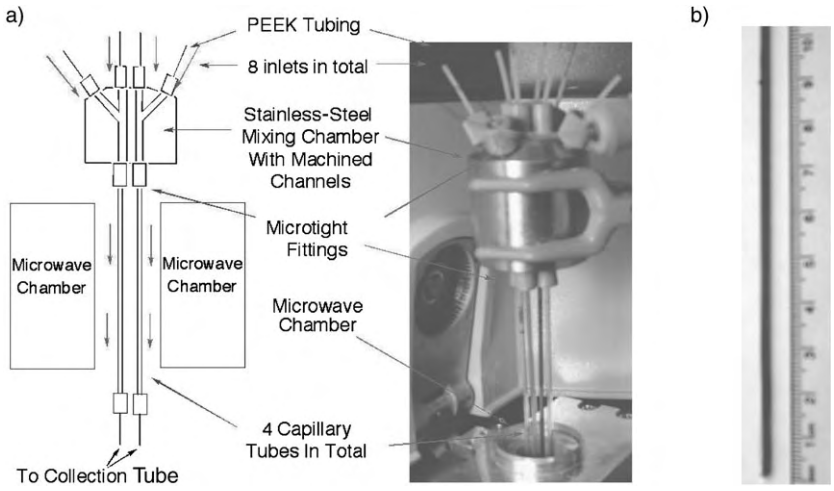

Figure 2. Capillary reactor system for MACOS. a) Schematic diagram and photograph of a four-capillary, parallel reactor system. During irradiation the reactor is lowered into the microwave chamber such that the mixing chamber is seated on top of the visible ring entering the chamber. b) A 10-cm-long capillary with a Pd film on the inner surface placed next to a ruler.

films that metal nanoclusters are liberated from the surface and in fact catalysis takes place with these clusters in solution. To probe this possibility, a Pd-coated capillary through which DMF was flowed was microwaved under identical conditions as those used during the typical coupling reactions (see Table 1, entry 4) until 2 mL of DMF was collected. Half of the capillary effluent was placed in a standard conical microwave vessel. The remaining reaction components were added (adjusted to provide the same concentrations) in analogy to the coupling detailed in entry 3 (Table 1). The mixture was then heated under batch-mode conditions for 20 min at the same temperature as that recorded during under flow conditions ($\approx$200 °C). Whereas the reaction under flow conditions gave quantitative conversion after being microwaved for literally a few seconds, the batch reaction scarcely pro-

Table 1: Suzuki–Miyara coupling of aryl boronic acids and bromides using MACOS with Pd-coated capillaries.

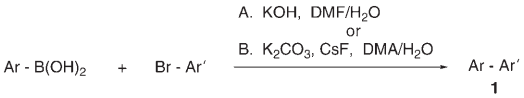

Entry	$ArB(OH)_2$	BrAr′	Cond.[a]	*T* [°C][b]	Product		Conv. [%][c] (yield [%])
1	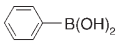	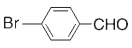	A	205	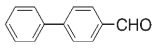	**1a**[10]	88
2	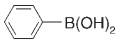	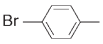	A	205	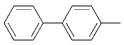	**1b**[10]	95
3			A	205			97
4	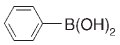	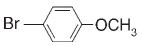	[d]	205	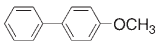	**1c**[2]	7
5			[e]	205			58
6	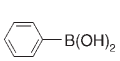	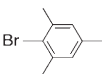	A	200	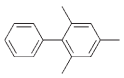	**1d**[10]	92
7	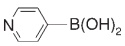	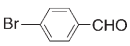	B	215	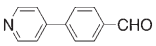	**1e**[2]	93
8[f]	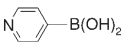		B	220	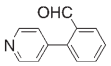	**1f**[2]	59
9[f]	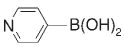		B	210	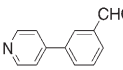	**1g**[2]	73
10	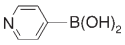		B	215	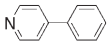	**1h**[2]	81 (74)[g]
11[f]	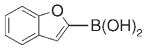	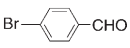	B	225	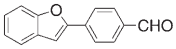	**1i**[10]	84 (76)[g]

[a] General reaction conditions: Reaction solutions were flowed through a single inlet into the Pd-coated 1150-μm (i.d.) capillary while being irradiated (see Figure 2) unless otherwise noted. [b] Temperature on the outer surface of the Pd-coated capillary as measured by the IR sensor of the Smith Creator microwave synthesizer. [c] Conversion was determined by withdrawing a crude sample directly from the effluent from the capillary and analyzing it by ^{1}H NMR spectroscopy. The ratio of starting material to product determined the percent conversion (there were no visible by-products present, only starting material and product in all cases). [d] DMF was flowed through a Pd-coated capillary while being irradiated as above. The eluent was pooled and split into two portions; half was analyzed by atomic emission spectrometry for Pd (see text), and to the other half was added the bromide, boronic acid, and base. This sample was then microwaved for 20 min at 180 °C. [e] The reaction conditions were identical to those in entry 3 except that the capillary was heated at 200 °C using an oil bath instead of using microwave heating. [f] Yield was determined by capturing a known volume of effluent from the capillary and purifying the product by silica gel chromatography. From the volume, the actual amount (mmol) of starting material could be calculated, and from this the theoretical yield was calculated. [g] In this case, 2.0 equiv aryl boronic acid was used.

 © 2006 Wiley-VCH Verlag GmbH & Co. KGaA, Weinheim

ceeded at all. Additionally, the other half of the effluent collected was analyzed for Pd content by atomic emission spectrometry (ICP-AES) to determine if Pd was liberated from the film during prolonged heating; no Pd could be detected (< 2 ppm). This strongly suggests that reaction at the metal surface is necessary to achieve the tremendous conversions observed under flow conditions and that little conversion results from solubilized Pd nanoclusters. Pd analysis of the crude cross-coupling product mixture did show slightly elevated levels of Pd (19.2 ppm). It is possible that oxidative addition, considered by some to be the rate-determining step of cross coupling, must take place at the surface and in doing so liberates Pd atoms and transmetalation and reductive elimination occur in solution away from the surface. In any case, routine purification removed these trace quantities providing clean products.

Table 2: Heck coupling of aryl iodides with acrolein derivatives using MACOS through Pd-coated capillaries.

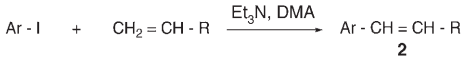

Entry	ArI[a]	R	*T* [°C][b]	Product		Conv. [%][c] (Yield [%])
1	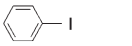	CO_2CH_3	205	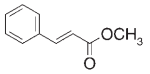	**2a**[10]	80
2	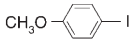	CO_2CH_3	200	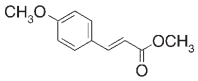	**2b**[1]	58
3		CO_2CH_3	205	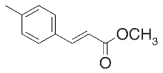	**2c**[1]	89
4		CO_2CH_3	200	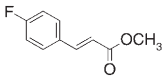	**2d**[10]	89 (79)[d]
5		$CO_2C(CH_3)_3$	215	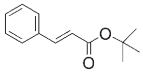	**2e**[10]	99
6		CN	220	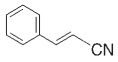	**2f**[10]	99 (82)[d]

[a] Reaction solutions containing aryl iodide (1.0 equiv), acrylate (1.3 equiv), and base (3.0 equiv) in DMA were premixed and flowed through a single inlet into the Pd-coated capillary while being irradiated. [b] Temperature on the outer surface of the Pd-coated capillary as measured by the IR sensor. [c] Conversion was determined by ^{1}H NMR spectroscopy relative to the residual starting material. [d] Yield was determined by capturing a known volume of effluent from the capillary and purifying the product by silica gel chromatography. From the volume, the actual amount (mmol) of starting material could be calculated, and from this the theoretical yield was calculated.

The need for microwave irradiation with such films has also been questioned. That is, if it is simply the heated film that is responsible for the conversions observed, then heating by any other method to reach the same temperature should result in identical conversion rate and yield. To this end, the reaction in entry 3 (Table 1) was repeated with the exception that the capillary was immersed in an oil bath set at 200 °C. The capillary was allowed to come to temperature, and the flow reaction carried out under otherwise identical conditions (Table 1, entry 5). The conversion obtained was just over half of that obtained by heating with microwave irradiation. Thus, in the absence of irradiation, the same conversion rate cannot be achieved, meaning that the microwave is essential for this process. This raises an interesting question then: How does irradiation cause these tremendous rate enhancements, which an apparent Arrhenius relationship cannot explain? With simple heat transfer, the highest temperature that the film can obtain is the same temperature as the heat source, 200 °C in this case with the oil bath. The origin of the "microwave effect" in reaction-rate enhancement has been debated, and many argue that it is just more effective heating and nothing to do with microwaves per se. It is possible that "hot spots" are being created in the metal film that are well above the averaged 200 °C temperature recorded by the IR sensor of the microwave, and it is these areas of the film that are responsible for the tremendous rate enhancements observed for these couplings.

Next we investigated the Heck coupling (Table 2) and found once again that the Pd film was very effective at promoting this transformation under continuous-flow conditions. If the conversion is in fact an accurate reflection of individual steps in the catalytic cycle, it is informative to note that conversions in entries 1–4 (Table 2) follow the general trend that electron-deficient aryl iodides are more reactive, suggesting that oxidative addition with the Pd film is rate limiting. Since this is the trend one would expect with homogeneous catalysis, a similar mechanism may be operational for the Pd film.

It is clear that continuous-flow reactors will receive more emphasis in organic synthesis in the future. Considerable advances have been made in multistep synthesis using flow methods through supported-reagent and scavenger columns.[3] Greater attention will be given to improving the practicality of flow methods to increase their implementation. Because residence time in the flow reactor is generally shorter than the reaction time of batch synthesis, conversion rates must be high. Microwave irradiation will most certainly help increase the variety of reactions that can be done in a flow format. In this work we have shown that metal-film-coated capillaries in conjunction with microwave irradiation do indeed lead to tremendous rate enhancements, and therefore MACOS holds great promise for the future of flow synthesis.

Capillaries as reaction vessels, while they are small, offer several advantages over other commercially available systems. They produce the small quantities required by modern biochemists for screening purposes very efficiently, quickly, and with very little waste. For example, 10 mg of product can be obtained from our flow reactor system within 1 min. Scale-up is achieved by simply flowing longer, and reaction

 © 2006 Wiley-VCH Verlag GmbH & Co. KGaA, Weinheim

conditions do not have to be optimized for different batch sizes. We have obtained gram quantities by flowing reaction mixtures through a single capillary for about 90 min; bundling capillaries together will produce much larger quantities in the same time period. Unlike expension chip-type reactors (e.g., US$3280 per chip from Microlyne Inc.), several capillaries can be purchased for US$0.01. Further, owing to simple, straight design of the capillary system developed in this report, and other systems from our group,[6] particulate matter cannot accumulate and block the reactor as is the case with more elaborate chip designs[11] and even large-bore spiral[4c] reactors designed specifically for microwave applications.

In summary, the Pd^0 films prepared in this report are highly porous and composed of nanometer-size grains (94.0 wt% Pd and 5.5 wt% carbon). The film thickness is approximately 6 μm and the film porosity is of the order of 75%. The films are robust and stand up well to the physical wear and tear of flow conditions and the high temperatures associated with microwave irradiation. The Pd film serves as an excellent catalyst for Suzuki–Miyama and Heck reactions, given the very short durations that the reaction mixture actually spends in the capillary, which is far less than one minute. In further investigations we are examining Pd and other metal films for metal-catalyzed reactions, as well as other reactions that are not specifically metal catalyzed.

Experimental Section

Pd film coating of capillaries: Borosilicate capillaries (1150 μm i.d.) were filled with a 0.1 mmol mL^{-1} solution of palladium acetate in DMF. The capillaries were then capped at both ends with septa and placed in a muffle furnace at room temperature, and the temperature was gradually increased up to 150 °C. After 10 min, metallic palladium was gradually released from the solution and deposited on the inner wall of the capillary. The capillaries were rotated a few times during deposition to encourage uniform film thickness, and heating was continued at 150 °C for a total of 30 min. Capillaries were calcinated by removing the plugs, pouring out the remaining solution, rinsing with fresh DMF, and heating (3 × 1 min each time) at 400 °C before use.

Preparation and analysis of Pd thin films: Capillaries were cleaved open and pieces of the films were fixed on carbon tape for analysis. Films were also prepared on 1-cm^2 flat borosilicate glass slides by dipping them in the same $Pd(OAc)_2$ solution described above. Sample imaging was carried out with a Hitachi S-4500 field emission scanning electron microscope (SEM) equipped with an EDAX Phoenix model energy-dispersive X-ray (EDX) analyzer. EDX analysis can detect all elements above atomic number 5 and has a minimum detection limit of 0.5 wt% for most elements. A 5-kV electron beam was used to obtain SEM images and EDX spectra. Both the lower and upper SE detectors were used for imaging purposes.

Microwave irradiation experiments: All microwave experiments were performed in a MACOS reactor designed and constructed in our laboratory (see Figure 2), operating at a frequency of 2.45 GHz with irradiation power from 0 to 300 W. The reactions were carried out in Pd-film-coated glass capillaries (1150 μm i.d.) that were placed in the cavity of the Biotage Smith Creator Synthesizer. The recorded temperature was measured by an IR sensor that was focused on the outer surface of the reaction capillaries.

General procedure for the Suzuki–Miyara coupling: Condition A: A stock solution containing the aryl halide (0.6 mmol, 1 equiv), arylboronic acid (1.2 equiv), base (2 M KOH, 0.9 mL, 3 equiv) in DMF (2 mL) was prepared. Condition B: In reactions with pyridineboronic acid, the stock solution contained aryl halide (0.6 mmol, 1 equiv), pyridine boronic acid (1.2 equiv), base (K_2CO_3, 120 mg, 1.5 equiv), and CsF (217 mg, 2.4 equiv) all dissolved in DMA/H_2O (2:1; 3 mL). The plumbing of the MACOS microreactor system was primed with the same solvent as the stock solution. A 1-mL aliquot from the homogenous stock solution was taken up in a Hamilton gas-tight syringe and connected to the microreactor by PEEK tubing with the aid of microtight fittings. The syringe was placed in a Harvard 22 syringe pump that was set to deliver 10 μL min^{-1}, and the single-mode microwave was programmed to heat constantly at the temperatures indicated in Table 1. The output from the reactor was fed into a collection tube and then analyzed by ^1H NMR spectroscopy immediately after the reaction. All products are known and their spectra were identical to those reported in the literature (see Table 1 for references).

General procedure for the Heck coupling: A stock solution containing the aryl halide (1.2 mmol, 1.2 equiv), acrylate (1 mmol, 1 equiv), and base (triethylamine, 3 mmol, 3 equiv) in 1.5 mL DMA was prepared. The MACOS reaction was performed using the same technique as that described above for the Suzuki–Miyama reaction. All products are known and their spectra were identical to that reported in the literature (see Table 2 for references).

Received: October 12, 2005
Revised: November 24, 2005
Published online: March 20, 2006

Keywords: cross-coupling · microwaves · palladium · synthetic methods · thin films

[1] a) J. P. Tierney, P. Lidstrom, *Microwave Assisted Organic Synthesis*, Blackwell, Oxford, **2005**; b) C. O. Kappe, *Angew. Chem.* **2004**, *116*, 6408; *Angew. Chem. Int. Ed.* **2004**, *43*, 6250; c) M. Nüchter, B. Ondruschka, W. Bonrath, A. Gum, *Green Chem.* **2004**, *6*, 128; d) K. M. K. Swamy, W.-B. Yeh, M.-J. Lin, C.-M. Sun, *Curr. Med. Chem.* **2003**, *10*, 2403; e) B. Wathey, J. Tierney, P. Lidstrom, J. Westman, *Drug Discovery Today* **2002**, *7*, 373; f) P. Lidstrom, J. Tierney, B. Wathey, J. Westman, *Tetrahedron* **2001**, *57*, 9225.

[2] For discussion of flow synthesis on a microscale, see: a) G. N. Doku, W. Verboom, D. N. Reinhoudt, A. van den Berg, *Tetrahedron* **2005**, *61*, 2733; b) H. R. Luckarift, L. J. Nadeau, J. C. Spain, *Chem. Commun.* **2005**, 383; c) G. Jas, A. Kirschning, *Chem. Eur. J.* **2003**, *9*, 5708; d) N. G. Anderson, *Org. Process Res. Dev.* **2001**, *5*, 613; e) M. Sands, S. J. Haswell, S. M. Kelly, V. Skelton, D. O. Morgan, P. Styring B. Warrington, *Lab Chip* **2001**, *1*, 64; f) W. Ehrfeld, V. Hessel, H. Löwe, *Microreactors: New Technology for Modern Chemistry*, Wiley-VCH, Weinheim, **2000**; g) A. M. Hafez, A. E. Taggi, H. Wack, W. J. Drury III, T. Lectka, *Org. Lett.* **2000**, *2*, 3963.

[3] For discussion of flow synthesis on a nonmicroscale, see: a) R. A. Kautz, W. K. Goetzinger, B. L. Karger, *J. Comb. Chem.* **2005**, *7*, 14; b) D. M. Ratner, E. R. Murphy, M. Jhunjhunwala, D. A. Snyder, K. F. Jensen, P. H. Seeberger, *Chem. Commun.* **2005**, 578; c) S. Saaby, K. R. Knudsen, M. Ladlow, S. V. Ley, *Chem. Commun.* **2005**, 2909.

[4] For reports dealing with the use of flow microwave approaches for preparative- or semipreparative-scale organic synthesis, see: a) M. C. Bagley, R. L. Jenkins, M. C. Lubinu, C. Mason, R. Wood, *J. Org. Chem.* **2005**, *70*, 7003; b) S. Saaby, I. R. Baxendale, S. V. Ley, *Org. Biomol. Chem.* **2005**, *3*, 3365; c) N. S. Wilson, C. R. Sarko, G. P. Roth, *Org. Process Res. Dev.* **2004**, *8*, 535; d) M. Fagrell PCT Int. Appl. (**2003**), 20 pp. CODEN: Continuous flow system with microwave heating for organic synthesis reactions: PIXXD2 WO 2003041856A1 20030522

 © 2006 Wiley-VCH Verlag GmbH & Co. KGaA, Weinheim

CAN 138:403615 AN 2003:396771; e) K. D. Raner, C. R. Strauss, R. W. Trainor, J. S. Thorn, *J. Org. Chem.* **1995**, *60*, 2456.
[5] For examples of the use of microwave-assisted microfluidic devices to prepare individual compounds, see: a) P. Watts, S. J. Haswell, *Chem. Eng. Technol.* **2005**, *28*, 290; b) P. He, S. J. Haswell, P. D. I. Fletcher, *Sens. Actuators B* **2005**, *105*, 516; c) P. He, S. J. Haswell, P. D. I. Fletcher, *Lab Chip* **2004**, *4*, 38.
[6] For previous reports from our laboratories outlining the development of a microscale continuous-flow microwave system utilizing capillaries as reaction vessels, see: a) E. Comer, M. G. Organ, *J. Am. Chem. Soc.* **2005**, *127*, 8160; b) E. Comer, M. G. Organ, *Chem. Eur. J.* **2005**, *11*, 7223.
[7] J. Li, A. W.-H. Ma, C. R. Strauss, *Chem. Commun.* **1997**, 1275.
[8] A, Stadler, C. A. Kappe, *Org. Lett.* **2002**, *4*, 3541.
[9] a) E. K. Esumi, O. Sadakane, K. Torigoe, K. Meguro, *Colloids Surf.* **1992**, *62*, 255; b) K. Esumi, M. Suzuki, T. Tano, K. Torigoe, K. Meguro, *Colloids Surf.* **1991**, *55*, 9; c) K. Esumi, T. Tano, K. Torigoe, K. Meguro, *Chem. Mater.* **1990**, *2*, 564; d) K. Esumi, K. Meguro, *Langmuir* **1989**, *5*, 268; e) T. Tano, K. Esumi, K. Meguro, *J. Colloid Interface Sci.* **1989**, *133*, 530.
[10] M. E. Labib, R. Williams, *J. Colloid Interface Sci.* **1987**, *115*, 330.
[11] G. Mueller, T. Gaup, *Aldrich ChemFiles Enabling Technologies: Microreactor Technology* **2005**, *5*, pp. 15–16.

 © 2006 Wiley-VCH Verlag GmbH & Co. KGaA, Weinheim

Annulation Reactions

DOI: 10.1002/anie.200503627

Rhenium- and Aniline-Catalyzed One-Pot Annulation of Aromatic Ketones and α,β-Unsaturated Esters Initiated by C–H Bond Activation**

Yoichiro Kuninobu, Yuta Nishina, Makoto Shouho, and Kazuhiko Takai**

Although there have been many reports on the synthesis of cyclic compounds, annulation methods from two molecules have been shown to be particularly effective. Two typical approaches are employed to construct cyclic frameworks by annulation: cycloaddition reactions[1] and sequential addition–cyclization reactions.[2] In the latter approach, a starting point such as a carbon–halogen bond is usually required to generate reactive species for the addition. If C–H bond activation can be used to start the sequential reaction, it is not necessary to prepare a halogen-containing compound, and the process does not form an inorganic by-product. Thus, the reaction process becomes more atom-economical. Most practical C–H bond-activation processes use ruthenium and rhodium catalysts.[3,4] These catalysts promote C–H bond activation of the *ortho* positions of aromatic ketones and successive insertion of nonpolar unsaturated bonds. However, the reaction terminates by reductive elimination after the insertion step. We recently found that a rhenium complex, $[\{ReBr(CO)_3(thf)\}_2]$, catalyzes the C–H bond activation of aromatic aldimines. Insertion of internal acetylenes or aryl isocyanates occurs at the carbon–rhenium bond, and more importantly, further intramolecular cyclization to the aldimine moiety proceeds to give indenes[5] or phthalimidines.[6] The difference could result from the fact that the rhenium–carbon bonds are more polar than rhodium– or ruthenium–carbon bonds. We disclose herein that the rhenium catalyst $[\{ReBr(CO)_3(thf)\}_2]$ and *p*-anisidine cocatalyst promoted the one-pot annulation of aromatic ketones with α,β-unsaturated esters to give indene derivatives. The reaction produces only water as a side product, and hence is environmentally benign.

The reaction of aromatic ketimine **1a** and ethyl acrylate (**2a**) in the presence of $[\{ReBr(CO)_3(thf)\}_2]$ as a catalyst gave indene derivative **3a** in 85% yield [Eq. (1)].[7,8] In this reaction, the imine moiety acted as a directing group for the C–H bond activation and also as an acceptor for the cyclization.[9] Acetophenone, which bears a ketone group, remained unchanged under similar reaction conditions. The formation of **3a** with the rhenium catalyst is in sharp contrast to the result with a rhodium complex, $[RhCl(PPh_3)_3]$, which catalyzes only C–H bond activation and insertion of an acrylate.[10]

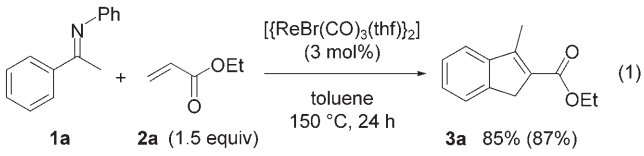

1a **2a** (1.5 equiv) **3a** 85% (87%) (1)

In the reaction shown in Equation (1), aniline was formed as a side product. This suggests the formation of indene derivative **3a** by the reaction of acetophenone with ethyl acrylate (**2a**) in the presence of a catalytic amount of the rhenium complex and aniline, because a ketimine is formed in situ by the reaction of acetophenone with aniline. We carried out the following reactions to examine this hypothesis. The reaction of acetophenone (**4a**) with ethyl acrylate (**2a**) in the presence of a catalytic amount of the rhenium complex $[\{ReBr(CO)_3(thf)\}_2]$ and aniline in toluene at 150 °C for 24 h gave the corresponding indene derivative **3a** in 56% yield. This result shows that aniline was regenerated after the formation of the indene derivative, and that the desired catalytic cycle was at play. The yield of **3a** increased to 86% when the reaction was carried out at 180 °C. The use of *p*-anisidine as a cocatalyst instead of aniline afforded **3a** in 93% yield (Table 1, entry 1).[8] In general, an effective synthesis of

[*] Dr. Y. Kuninobu, Y. Nishina, M. Shouho, Prof. Dr. K. Takai
Division of Chemistry and Biochemistry
Graduate School of Natural Science and Technology
Okayama University
Tsushima, Okayama 700-8530 (Japan)
Fax: (+81) 86-251-8094
E-mail: kuninobu@cc.okayama-u.ac.jp
ktakai@cc.okayama-u.ac.jp

[**] Financial support by a Grant-in-Aid for Scientific Research on Priority Areas (No. 14078219, "Reaction Control of Dynamic Complexes") from the Ministry of Education, Culture, Sports, Science, and Technology of Japan.

Supporting information for this article is available on the WWW under http://www.angewandte.org or from the author.

InterScience
© 2006 Wiley-VCH Verlag GmbH & Co. KGaA, Weinheim

Table 1: Rhenium- and aniline-catalyzed annulation of aromatic ketones with α,β-unsaturated esters.[a]

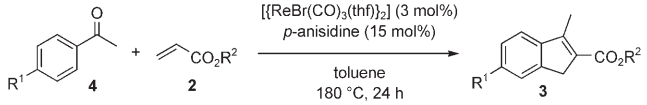

Entry	Ketone	Olefin	Product	Yield [%][b,c]
1	**4a** (R^1 = H)	**2a** (R^2 = Et)	**3a**	93 (99)
2	**4b** (R^1 = OMe)	**2a**	**3b** (R^1 = OMe; R^2 = Et)	80 (82)
3	**4c** (R^1 = Me)	**2a**	**3c** (R^1 = Me; R^2 = Et)	85 (89)
4	**4d** (R^1 = CF_3)	**2a**	**3d** (R^1 = CF_3; R^2 = Et)	37 (53)
5		**2a**	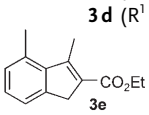	11 (16)
6	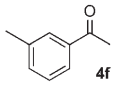	**2a**	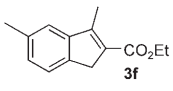 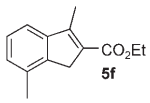	68 (69) [77:23]
7	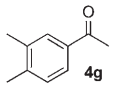	**2a**	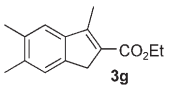 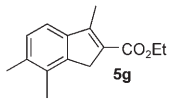	88 (93) [88:12]
8	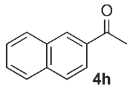	**2a**	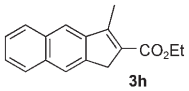 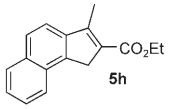	90 (93) [80:20]
9[d]	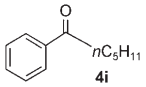	**2a**	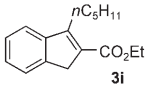	84 (86)
10	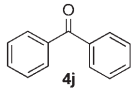	**2a**	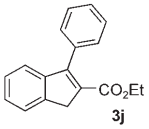	72 (74)
11	**4a**	**2b** (R^2 = Me)	**3k** (R^1 = H; R^2 = Me)	81 (90)
12	**4a**	**2c** (R^2 = Ph)	**3l** (R^1 = H; R^2 = Ph)	28 (29)

[a] Olefin: 1.5 equiv. [b] Yields of isolated product. Yields determined by ^{1}H NMR spectroscopy are reported in parentheses. [c] The ratios of **3** and **5** are given in square brackets. [d] 48 h.

aromatic ketimines is difficult because of the slow reaction rates and low yields owing to a side reaction.[11] From this viewpoint, the yield obtained in entry 1 deserves special mention.

After testing several solvents, we found that toluene gave the best result (Table 1, entry 1).[12] The concentration of the reaction mixture proved to affect the yield of **3a** markedly. In low concentrations (0.5 and 1.0 M) in toluene, the yields were low (29% and 60%, respectively). The yield improved to 93% at a higher concentration (2.5 M) in toluene, although the yield decreased to 82% in the solvent-free reaction.

The reactions of **2a** and acetophenone derivatives **4b**,**c**, which bear an electron-donating group at the *para* position, gave the corresponding indene derivatives **3b**,**c** in 80% and 85% yields, respectively (Table 1, entries 2 and 3). However, the yield decreased in the reaction of an acetophenone derivative bearing an electron-withdrawing group (Table 1, entry 4). To investigate the selectivity of nonsymmetric ketones, **2a** was treated with acetophenone derivatives that have methyl groups at the *ortho, meta* and/or *para* positions (Table 1, entries 5–7). Only the single product **3e** was obtained in 11 yield by using an aceotophenone derivative with a methyl group at the *ortho* position; however, acetophenone derivatives **4f** and **4g** afforded indene derivatives **3f** and **5f** (77:23) and **3g** and **5g** (88:12) in 68% and 88% yields, respectively. Similarly, **4h** gave **3h** and **5h** in good yields and selectivity (Table 1, entry 8). Indene derivative **3i** was obtained in 84% yield by treatment of ketone **4i** with **2a** (Table 1, entry 9). Benzophenone **4j** afforded indene derivative **3j** in 72% yield (Table 1, entry 10). The reactions of ketone **4a** and methyl acrylate (**2b**) or phenyl acrylate (**2c**) led to the corresponding indene derivatives **3k** and **3l** in 81% and 28% yields, respectively (Table 1, entries 11 and 12).[13] However, a bulky *tert*-butyl acrylate did not afford an indene derivative. Ethyl methacrylate and ethyl *trans*-crotonate did not give the indene derivatives either.

To investigate the compatibility of functional groups under the reaction conditions, we added several substrates in the reaction of acetophenone (**4a**) with ethyl acrylate (**2a**). When 1-dodecene was added, the indene derivative **3a** was obtained in 97% yield, and 1-dodecene was recovered quantitatively. Under similar conditions, 2-dodecanone and methyl laurate were recovered quantitatively, and **3a** was obtained in 77% and 84%, respectively.[14]

The proposed mechanism for the formation of indene derivatives is shown in Scheme 1.[15] A ketimine is formed by the reaction of acetophenone with aniline through dehydration. C–H bond activation is accelerated by the coordination of a nitrogen atom of the ketimine derivative to a rhenium center. After C–H bond activation, an α,β-unsaturated compound inserts into the rhenium–carbon bond of an aryl–rhenium intermediate. The intramolecular nucleophilic cyclization by attack of an alkyl rhenium moiety at the imine group followed by reductive elimination and the elimination of aniline affords an indene derivative. The elimination of aniline is important to promote the reaction catalytically.

In summary, we have developed a rhenium-catalyzed conjugate addition and cyclization through C–H bond activation in the reaction of an aromatic ketimine with an

 © 2006 Wiley-VCH Verlag GmbH & Co. KGaA, Weinheim

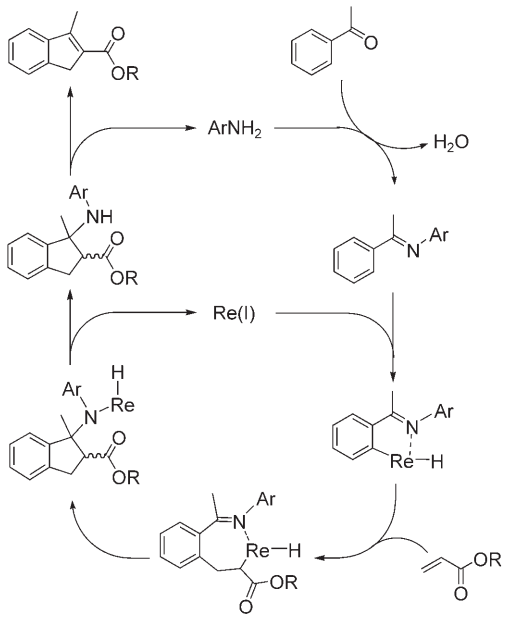

Scheme 1. Proposed mechanism for the formation of indene derivatives.

α,β-unsaturated ester. After the cyclization, the elimination of aniline gives the corresponding indene derivatives. The indene derivatives can also be obtained by the reaction of acetophenone with α,β-unsaturated esters in the presence of catalytic amounts of the rhenium complex and aniline. The latter [3+2] annulation reaction to give indene derivatives is efficient because the reaction proceeds with only loss of water. Further investigations of rhenium-catalyzed chemical transformations through C–H bond activation are now in progress.

Experimental Section

3a (rhenium-catalyzed): A mixture of phenyl-(1-phenyl-ethylidene)-amine (97.8 mg, 0.500 mmol), ethyl acrylate (75.1 mg, 0.750 mmol), and $[\{ReBr(CO)_3(thf)\}_2]$ (12.7 mg, 0.0150 mmol) was dissolved in toluene (1.0 mL) and stirred at 150 °C for 24 h. The crude product was purified by column chromatography on silica gel to give **3a** (85.9 mg, 85 % yield) as a pale yellow solid.

3a (rhenium- and aniline-catalyzed): A mixture of acetophenone (60.1 mg, 0.500 mmol), ethyl acrylate (75.1 mg, 0.750 mmol), *p*-anisidine (9.2 mg, 0.0750 mmol), and $[\{ReBr(CO)_3(thf)\}_2]$ (12.7 mg, 0.0150 mmol) was dissolved in toluene (0.2 mL) and stirred at 180 °C for 24 h. The crude product was purified by column chromatography on silica gel to give **3a** (96.0 mg, 95 % yield) as a pale yellow solid.

Received: October 13, 2005
Revised: January 27, 2006
Published online: March 23, 2006

Keywords: annulation · C–H activation · conjugate addition · cyclization · rhenium

[1] a) *Comprehensive Organic Synthesis*, *Vol. 5* (Ed.: L. A. Paquette), Pergamon, Oxford, **1991**; b) *Cycloaddition Reactions in Organic Synthesis* (Eds.: S. Kobayashi, K. A. Jørgensen), Wiley-VCH, Weinheim, **2002**.

[2] a) D. P. Curran, *Comprehensive Organic Synthesis*, *Vol. 4*, Pergamon, Oxford, **1991**, pp. 779–831; b) P. Knochel, *Comprehensive Organic Synthesis*, *Vol. 4*, Pergamon, Oxford, **1991**, pp. 865–911.

[3] a) F. Kakiuchi, S. Murai, *Top. Organomet. Chem.* **1999**, *3*, 47–79; b) Y. Guari, S. Sabo-Etienne, B. Chaudret, *Eur. J. Inorg. Chem.* **1999**, 1047–1055; c) G. Dyker, *Angew. Chem.* **1999**, *111*, 1808–1822; *Angew. Chem. Int. Ed.* **1999**, *38*, 1698–1712.

[4] For the synthesis of cyclic compounds through C–H bond activation, see: a) K. L. Tan, R. G. Bergman, J. A. Ellman, *J. Am. Chem. Soc.* **2001**, *123*, 2685–2686; b) R. K. Thalji, K. A. Ahrendt, R. G. Bergman, J. A. Ellman, *J. Am. Chem. Soc.* **2001**, *123*, 9692–9693; c) K. L. Tan, A. Vasudevan, R. G. Bergman, J. A. Ellman, A. J. Souers, *Org. Lett.* **2003**, *5*, 2131–2134; d) R. K. Thalji, J. A. Ellman, R. G. Bergman, *J. Am. Chem. Soc.* **2004**, *126*, 7192–7193.

[5] Y. Kuninobu, A. Kawata, K. Takai, *J. Am. Chem. Soc.* **2005**, *127*, 13498–13499.

[6] Y. Kuninobu, Y. Tokunaga, A. Kawata, K. Takai, *J. Am. Chem. Soc.* **2006**, *128*, 202–209.

[7] The yield determined by ^{1}H NMR spectroscopy with 1,1,2,2-tetrachloroethane as an internal standard is reported in parenthesis.

[8] The reactions between acetophenone and ethyl acrylate did not proceed when using ruthenium complexes $[Ru_3(CO)_{12}]$ or $[RuH_2(CO)(PPh_3)_3]$ or rhodium complex $[RhCl(PPh_3)_3]$ as catalysts.

[9] Ketimines bearing a methoxy group on a nitrogen atom of the imine moiety and hydrazone did not afford indene derivatives.

[10] S.-G. Lim, J.-A. Ahn, C.-H. Jun, *Org. Lett.* **2004**, *6*, 4687–4690.

[11] a) R. W. Layer, *Chem. Rev.* **1963**, *63*, 489–510; b) H. Heaney, M. T. Simcox, A. M. Z. Slawin, R. G. Giles, *Synlett* **1998**, 640–642.

[12] The yield of **3a** decreased when the reaction was conducted in octane (60 %). When polar solvents 1,4-dioxane, dimethoxyethane, or *N*,*N*-dimethylformamide were used, the yield of **3a** decreased to 34 %, 25 %, and 25 %, respectively. When 1,1,2,2-tetrachloroethane was used, the indene derivative **3a** was not obtained at all.

[13] Ethyl methacrylate, ethyl *trans*-crotonate, and *tert*-butyl acrylate did not afford the indene derivatives and most of the acrylates remained. Phenyl vinyl sulfone, *N*,*N*-dimethylacrylamide, and acrylonitrile also did not give the indene derivatives as a result of polymerization of these electrophiles under the conditions.

[14] Although the reactions were conducted in toluene (2.5 M), the amounts of the additives were similar to that of toluene; because the yield of the reaction decreases with a decrease in the concentration of acetophenone and ethyl acrylate, the yield of **3a** dropped to approximately 80 %.

[15] A referee suggested an alternative mechanism through the Baylis–Hilman reaction: 1) a tertiary alcohol is generated by the reaction between ethyl acrylate and acetophenone with aniline; 2) cyclization under the reaction conditions. To examine this possibility, we synthesized the tertiary alcohol and exposed the alcohol to the reaction conditions. However, the alcohol did not cyclize to the indene. Thus, we are tempted to assume that the indene derivatives are formed via C–H bond activation.

 © 2006 Wiley-VCH Verlag GmbH & Co. KGaA, Weinheim

Antimalarial Drugs

DOI: 10.1002/anie.200504033

Total Syntheses of Hexacyclinol, 5-*epi*-Hexacyclinol, and Desoxohexacyclinol Unveil an Antimalarial Prodrug Motif**

*James J. La Clair**

In memory of Udo Gräfe

Hexacyclinol (**1**) was isolated by Gräfe and co-workers from the basidiospores collected from *Panus rudis* growing on dead betula woods in Siberia.[1] In 1999, our exploration into German fungal cultures provided a strain of *P. rudis* 99-329 that was not only capable of the biosynthesis of **1** but also provided trace amounts of *epi*-5-hexacyclinol (**2**) and desoxohexacyclinol (**3**).[2] Further study indicated that the retrocycloaddition of **1** and **2** released oxygen to afford a mixture of trienes **3** (Scheme 1). Subsequent [2+2+2] cycloaddition of **3**

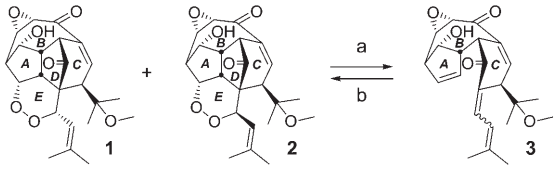

Scheme 1. Hexacyclinol interconversions: a) in vacuo, neat, 95%; b) O_2, rose bengal, MeOH, *hν*, 0°C, 89%.

with singlet oxygen returned a mixture of **1** and **2**. As this process could be cycled, it offered a key handle in expediting the synthesis of this family of terpenes.

The synthesis of **1** and **2** through **3** simplifies the complexity of the hexacyclinol ring system by removal of the D/E rings (Scheme 1). On the basis of this argument, a campaign to **3** was launched using the synthetic plan outlined in Scheme 2. The plan began with an intact A ring as shown in intermediate **A**. The first stage of this project sought a rapid appendage of C7 and C17 onto **A** followed by the installation of the lower half of the B ring as given by the conversion of **D** into **E**. From **E**, a series of three sequences (**E**→**F**, **F**→**G**, and **G**→**I**, Scheme 2) were used to stitch the molecule together, beginning with the insertion of C15–C16, followed by creation

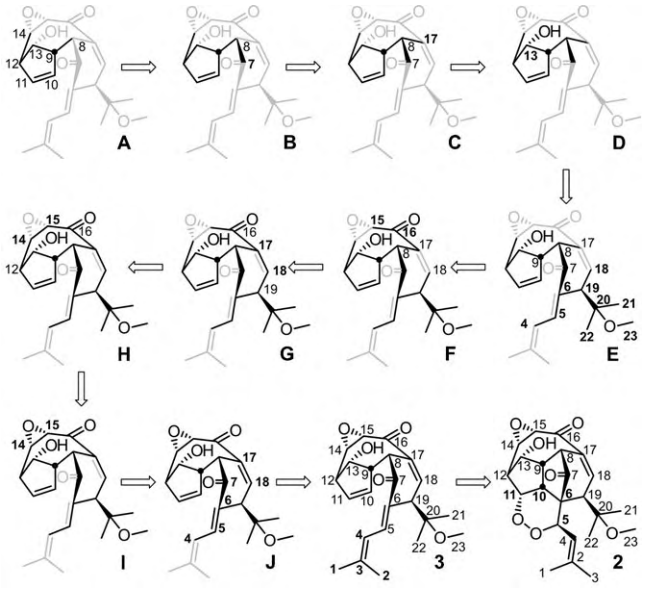

Scheme 2. Synthetic plan depicting the strategic intermediates **A**–**J**. Completed bonds are shown in black, and the skeleton is depicted in gray.

of the C17–C18 bond, and ending with installation of the C14–C15 epoxide.

Intermediate **A** was developed from bis(acetate) **4**.[3] Protection with TBS, deacetylation, and nosylation of the primary alcohol afforded **5** (Scheme 3). Under these conditions, nosylate **5** was obtained along with a bis(nosylate) derivative (3–5% yield), which was removed after treatment of the mixture with sodium cyanide in DMSO to convert **5** into **6**. This sequence was conducted on a multigram scale to provide **6** after a single chromatographic purification step. The synthesis of **6** completed the installation of C7 as indicated by the conversion of **A** into **B** (Scheme 2).

The next stage in this synthesis involved the installation of C17, as given by the conversion of **B** into **C** (Scheme 2). This operation was accomplished through the conversion of **6** into bromoacetal **7** by reaction with 1,2-dibromoethylmethyl ether (Scheme 3).[4] Treatment of crude **7** with NaHMDS at −78°C followed by warming to room temperature resulted in 3:2 mixture of **8a**/**8b**. Fortunately, protonation of the enolate of **8a**/**8b** with triphenylacetic acid afforded a mixture favoring the desired nitrile **8a** by 11:1. To increase the material throughput to **8a**, the cyclization and isomerization steps were conducted in a one-pot operation.

With intermediate **C** in hand, the next step required correction of the stereochemistry at C13. As provided by **4**, this center required inversion as illustrated by the conversion into **D** (Scheme 2). The process began by convertion of the nitrile of **8a** to dithiane **13** (Scheme 3). Slow addition of DIBAL-H at −20°C to **8a** at −78°C in toluene afforded **9** in high yield. The resulting aldehyde **9** was subsequently protected as dithiane **10**. The acetal ring of **10** was opened by treatment with dilute aqueous acid to provide **11**, which was in turn oxidized to the corresponding acid **12** through a buffered Tollens oxidation followed by hydrolysis of the incipient lactone. As noted by Smith et al.,[5] the oxidation of

[*] Dr. J. J. La Clair
Xenobe Research Institute
P.O. Box 4073, San Diego, CA 92164-4073 (USA)
Fax: (+1) 858-401-3083
E-mail: i@xenobe.org

[**] A considerable portion of this work was conducted during 1999–2002 at Bionic Bros GmbH, Germany. J.J.L.C. acknowledges the assistance of five technicians.

Supporting information for this article is available on the WWW under http://www.angewandte.org or from the author.

 © 2006 Wiley-VCH Verlag GmbH & Co. KGaA, Weinheim

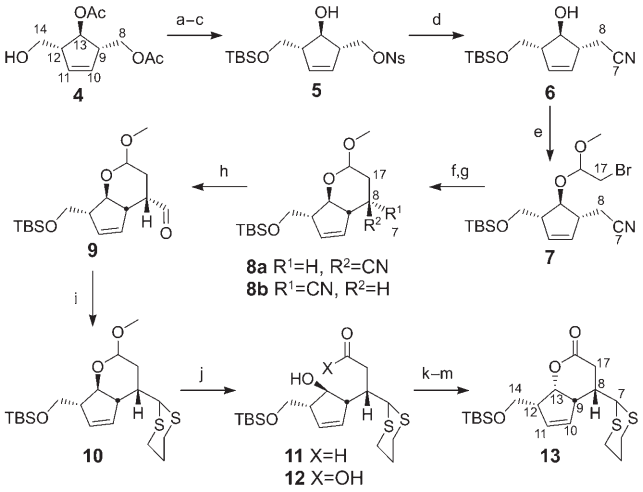

Scheme 3. Access to intermediate **D** through the synthesis of **13**. a) TBSCl, imidazole, DMAP (cat.), CH_2Cl_2; b) NH_3, MeOH, room temperature; c) NsCl, pyridine, 0 °C→RT; d) NaCN (1.5 equiv), DMSO, 85 °C, 32 h, 72% from **4**; e) methylvinyl ether, Br_2; then add to **6**, 2,6-lutidine (2 equiv), CH_2Cl_2, 0 °C→RT, 67%; f) NaHMDS, THF, −78 °C→RT; g) NaHMDS, THF, −78 °C→−40 °C; then Ph_3CO_2H, THF, 67% from **7**; h) DIBAL-H, toluene, −78 °C→RT; i) $(TMSSCH_2)_2CH_2$, $ZnBr_2$, CH_2Cl_2, 59% from **8a**; j) HCl in aq. THF; k) slow addition of Ag_2O in paraffin, CH_2Cl_2, room temperature; l) LiOH, aq. THF; m) PPh_3, DIAD, CH_2Cl_2, room temperature, 16 h, 68% from **10**. TBS = *tert*-butyldimethylsilyl, DMAP = 4-dimethylaminopyridine, Ns = 4-nitrobenzenesulfonyl, DMSO = dimethyl sulfoxide, HMDS = hexamethyldisilazane, DIBAL-H = diisobutylaluminum hydride, DIAD = diisopropyl azodicarboxylate.

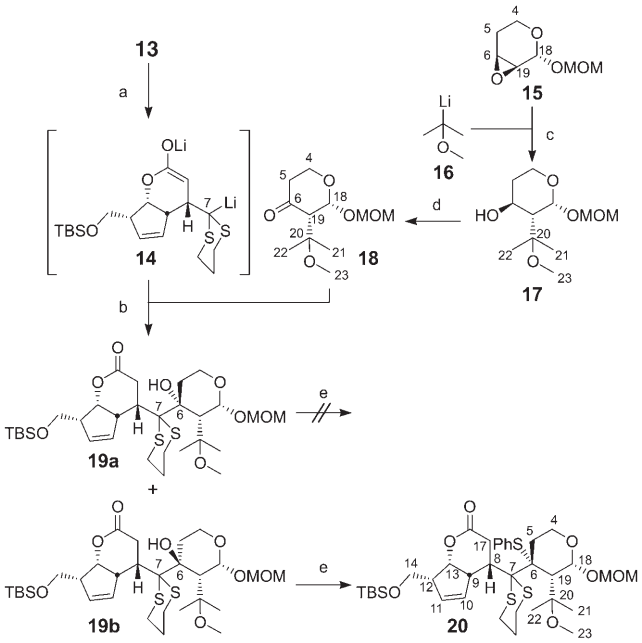

Scheme 4. Access to intermediate **E** through the synthesis of **20**. a) LDA (1.1 equiv), HMPA (3 equiv), THF; −78 °C then *n*BuLi (1.1 equiv) at −78 °C→−60 °C, 2 h; b) slow addition of **18** in THF to **14** in THF, −78 °C, 2 h; then −78 °C→RT, 62% of **19b** and 15% of **19a**; c) add **16** in Et_2O to **15** in Et_2O/pentane (8:1 v/v), −78 °C→0 °C, 12 h, 89%; d) TPAP (cat.), NMO, CH_2Cl_2, 92%; e) PhSH, PEt_3, DEAD, CH_2Cl_2, 45 °C, 24 h, 94%. LDA = lithium diisopropylamide, HMPA = hexamethylphosphoramide, MOM = methoxymethyl, TPAP = tetrapropylammonium perruthenate, NMO = *N*-methylmorpholine-*N*-oxide, DEAD = diethyl azodicarboxylate.

an aldehyde in the presence of a dithiane is a nontrivial operation. For this example, oxidation of **11** to **12** was achieved by delivering Ag_2O in wax (5% Ag_2O in paraffin).[6] Here, slow addition and transfer of Ag_2O to the reaction medium was optimal in favoring aldehyde oxidation. An intramolecular Mitsunobu inversion of **12** to lactone **13** was used to install the correct stereochemistry at C13.

With **13** in hand, the plan called for the simultaneous appendage of C4–C6 and C18–C23 as indicated by the conversion of **D** into **E** (Scheme 2). Ketone **18** provided an ideal match for the installation of these atoms as it was rapidly prepared from epoxide **15**[7] (Scheme 4). The process was facilitated through anchimeric-assisted addition of corresponding α-lithioether **16**, prepared by the methods of Cohen and Matz,[8] to **15** to yield **17**. Gram quantities of **18** were obtained after oxidation of **17** with either SO_3–pyridine, TPAP—NMO, or Dess–Martin periodinane.

Condensation of **13** with **18** was carried out by generation of dianion **14** by the stepwise addition of LDA and *n*BuLi to **13** (Scheme 4). A chromatographically separable mixture of **19a** and **19b** (1:4.5) was obtained after slow addition of **18** to **14** at −78 °C followed by gradual warming to room temperature. Separation of these diastereomers was enhanced by the selective inversion of **19b** to mercaptan **20**. Under these conditions, the inversion of **19a** was not observed. The fact that **19a** was returned after treatment with DEAD, PBu_3, and acetic acid suggested that the C6-carbinol was too hindered to form the required alkoxyphosphonium intermediate. Completion of **20** involved the installation of C4–C6 and C18–C23 with the appropriate stereochemistry at C6 and provided functional handles at C17 and C18 for fusion of the B and C rings.

The synthesis continued by a three-stage stitching sequence as depicted by the processing of **E** to **H** (Scheme 2). The operation began with the installation of C15–C16 bond as given by the conversion of **E** into **F**. Experimentally, this was conducted by *C*-acylation of **20** with pyruvonitrile (Scheme 5).[9] Oxidation of the resulting product **21** with mCPBA followed by treatment with a catalytic amount of CSA in methanol afforded ketosulfoxide **22**. Treatment of **22** with aqueous acid opened the MOM-protected acetal. Analysis of the mixture by NMR spectroscopy indicated that the resulting material existed in a complex equilibrium that contained residues attributable to **23a** and **23b**.

Treatment of this mixture **23a,b** with sulfene (MsCl, Et_3N) led to the formation of a single product **25** (Scheme 5), apparently through incipient generation of mesylate **24a** or chloride **24b**. The reversible nature of mesylation with sulfene was key to this process.[10] After screening conditions, an optimized 74–77% yield of **25** was obtained after adding an equivalent of MsCl and triethylamine once an hour for 5 h. Access to **25** completed the installation of the C17–C18 bond as shown by the conversion of intermediate **F** into **G**

 © 2006 Wiley-VCH Verlag GmbH & Co. KGaA, Weinheim

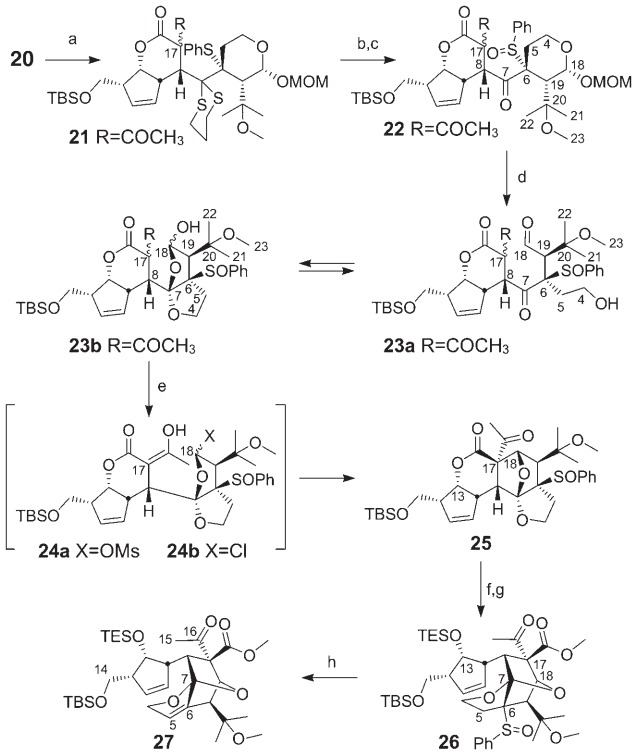

Scheme 5. Access to intermediate **G** through the synthesis of **27**. a) LDA (1.1 equiv), THF; −78 °C→−50 °C; then CH_3COCN, −78 °C; then −78 °C→0 °C,12 h, 92%; b) mCPBA (3.0 equiv), CH_2Cl_2; c) CSA (0.2 equiv), room temperature, wet *t*BuOMe, 6 h, 94% from **21**; d) TMSCl (1.2 equiv), H_2O (5.0 equiv), CH_2Cl_2, 0 °C, 97%; e) add MsCl (1 equiv) and Et_3N (1 equiv) in CH_2Cl_2 once an hour for 5 h at −10 °C; −10 °C→RT, 16 h, 76%; f) PhSNa (0.2 equiv), MeOH; g) TESOTf, 2,6-lutidine, CH_2Cl_2, −20 °C→RT, 82% from **25**; h) 60–70 °C, DMF, 16 h, 92%. mCPBA = *meta*-chloroperbenzoic acid, CSA = camphorsulfonic acid, TMS = trimethylsilyl, Ms = methanesulfonyl, TESOTf = triethylsilyl triflate, DMF = *N*,*N*-dimethylformamide.

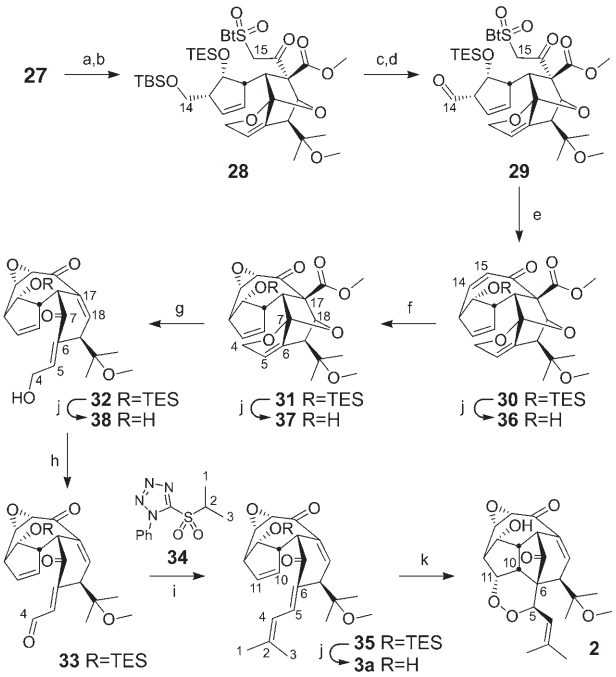

Scheme 6. Synthesis of desoxohexacyclinol (**3**). a) KHMDS (1.1 equiv), THF; −78 to −50 °C; then $(BtS)_2$, −78 °C; −78 °C→0 °C, 12 h; b) oxone, wet 1,4-dioxane, 87% from **27**; c) TBAF, wet THF, 0 °C→RT; d) Dess–Martin periodinane, CH_2Cl_2, 0 °C→RT; e) slow addition of DBU (1.2 equiv), DMAP (cat.), THF, −40 °C→RT, 10 h, 72% from **28**; f) Ph_3COOH, L-(+)-diisopropyltartrate, toluene, CH_2Cl_2 (3:1 v/v), 92%; g) KOTMS, THF, −10 °C→35 °C, 5 h, 69%; h) MnO_2, CH_2Cl_2, room temperature; i) **34**, KHMDS, −78 °C; −78 °C→−30 °C, 2 h; add **33** at −78 °C; −78 °C→RT, 3 h; then room temperature, 12 h, 76% from **32**; j) cat. aq. H_2SiF_6, CH_3CN/*t*BuOH (9:1 v/v), room temperature, 78% for **3a**; 81% for **36**; 72% for **37**; 84% for **38**; k) O_2, rose bengal, MeOH, *hν*, 0 °C, 82%. Bt = 1-benzothiazole, TBAF = tetra-*n*-butylammonium fluoride, DBU = 1,8-diazabicyclo[5.4.0]undec-7-ene.

(Scheme 2). The final stitch (**G** to **H**) called for the creation of the C14–C15 bond. This process began with methanolysis of the lactone in **25** by treatment with sodium thiophenoxide in methanol followed by protection of the secondary alcohol to afford **26** (Scheme 5). Thermolysis of **26** induced a regioselective *syn*-elimination to provide **27**. At this stage, the appropriate functionality was installed to address the formation of the C14–C15 epoxide.

A Julia–Kocienski reaction was selected for this process as the projected enone **30** was envisioned as a suitable precursor to the C14–C15 epoxide (Scheme 6). Sulfone **28** was prepared by α-thiolation of **27** with 2,2′-dithiobis(benzothiazole) followed by oxidation with oxone. Selective deprotection of the primary TBS-protected ether followed by oxidation with Dess–Martin periodinane provided the precursor to the Julia–Kocienski reaction **29**. Slow addition of DBU with a catalytic amount of DMAP to **29** in THF over 2 h at −40 °C followed by warming to room temperature over 10 h afforded the desired enone **30** in good yield. Epoxidation at C14–C15, as required by **H** to **I** (Scheme 2), was effected by using the tartrate-mediated nucleophilic epoxidation conditions developed by Porco and co-workers to yield a single epoxide **31**.[11]

The synthesis of desoxohexacyclinol (**3**) was accomplished by unveiling the 7-oxabicyclo[2.2.1]heptane and thereby completing the synthesis of the C ring (**I** to **J**, Scheme 2). Hydrolysis of **31** with TMSOK[12] or nBu$_3$SnOH[13] generated the corresponding acid, which underwent subsequent β-eliminative ring opening to provide **32** (Scheme 6). Hydrolysis of the C14–C15 epoxide was avoided by slow addition of TMSOK or nBu$_3$SnOH. At this point, the final carbon atoms C1–C3 were installed through a second Julia–Kocienski reaction (Scheme 6). Allylic oxidation with MnO_2 was effective at converting **32** into aldehyde **33**, which was in turn filtered through dry silica gel and immediately treated with the anion of **34** to afford **35**. Remarkably, this addition was achieved with less than 5% addition to the C14–C15 epoxide. Mild deprotection with fluorosilicic acid[14] completed the synthesis to provide **3a** in an overall yield of 0.8–1.3% from **4**. Confirmation of this yield was established by the most-recent campaign that provided 3.6 g of **3a** from 1 mol of **4**.

Exposure of **3a** to singlet oxygen[15] resulted in a [2+2+2] cycloaddition[16] that afforded a mixture of chromatographically separable **1** and **2** (8:1). Samples of synthetic hexacyclinol (**1**),[17] **2**,[18] and **3**[19] were identical in R_f, HPLC

 © 2006 Wiley-VCH Verlag GmbH & Co. KGaA, Weinheim

retention, physical properties, and spectral data to authentic samples of **1–3** isolated in our laboratories.[2] The optical rotation of synthetic **1** ($[\alpha]_D(4.0\,mg\,mL^{-1}) = +131.5°$) was comparable to that obtained in samples of isolated **1** ($[\alpha]_D(4.0\,mg\,mL^{-1}) = +132.2°$) as well as that reported by Gräfe and co-workers ($[\alpha]_D(4.03\,mg\,mL^{-1}) = +130.5°$),[1] thereby confirming the absolute stereochemistry of hexacyclinol (**1**).

While the yield and complexity of this synthesis may not be ideal for therapeutic use, the value of this synthetic route became apparent upon screening the activity of the late-stage intermediates. Intermediates **36–38**, prepared by deprotection of the precursors **30–32**, respectively, were analyzed for their inhibition of *Plasmodium berghei*.[2] Remarkably, **36, 37**, and **38** displayed IC_{50} values of 9.3 ± 2.6, 6.1 ± 1.5, and 2.1 ± 0.7 nM, respectively, against a chloroquine-sensitive *P. berghei*. In the same assay, artemisinin displayed an IC_{50} value of 2.5 ± 0.9 nM.[2,20] Comparable activity was also obtained in in vivo antimalarial assays, which indicated that **36, 37**, and **38** displayed ED_{50} values of 8.9, 1.6, and 5.2 $mg\,kg^{-1}$, respectively, against chloroquine-sensitive *P. berghei*. This activity was found to be comparable to sodium artesunate, which delivered an ED_{50} value of 4.3 $mg\,kg^{-1}$ when examined in parallel.[2,21] While the mode of action of these materials has yet to be verified,[2] prior observations on **3** suggest that these materials arise through a three-step prodrug-like motif (Scheme 7). Efforts are now underway to determine the

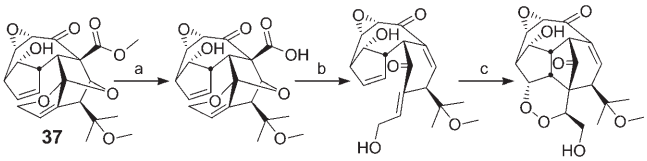

Scheme 7. Suggested mechanism supporting the in vivo activity of **37**. a) Hydrolysis; b) decarboxylative β-elimination; c) [2+2+2] cycloaddition with singlet oxygen.

validity of this mechanism as well as to identify a minimal pharmacophore.[22]

Received: November 14, 2005
Published online: February 9, 2006

Keywords: antimalarial agents · medicinal chemistry · natural products · terpenoids · total synthesis

[1] B. Schlegel, A. Hartl, H. M. Dahse, F. A. Gollmick, U. Gräfe, H. Dorfelt, B. Kappes, *J. Antibiot.* **2002**, *55*, 814.
[2] J. J. La Clair, unpublished results.
[3] Bis(acetate) **4** was prepared according to the procedure reported in: M. Tanaka, Y. Norimine, T. Fujita, H. Suemune, K. Sakai, *J. Org. Chem.* **1996**, *61*, 6952.
[4] G. Stork, M. Kahn, *J. Am. Chem. Soc.* **1985**, *107*, 500.
[5] A. B. Smith III, D. Lee, C. M. Adams, M. C. Kozlowski, *Org. Lett.* **2002**, *4*, 4539.
[6] SmI_2 as suggested by Smith et al.[5] also failed. An alternative synthesis using a triethylsilylcyanohydrin was used to alleviate concerns over the use of a dithiane. Details of this route shall be explained in forthcoming publications.
[7] Epoxide **15** was prepared using a method described in: G. Anker, J. Attaghrai, D. Picq, D. Anker, *Carbohydr. Res.* **1987**, *159*, 159.
[8] T. Cohen, J. R. Matz, *J. Am. Chem. Soc.* **1980**, *102*, 6900.
[9] G. A. Kraus, M. Shimagaki, *Tetrahedron Lett.* **1981**, *22*, 1171.
[10] The primary mesylate of **24c** was the major product obtained by treating **23a,b** with MsCl in pyridine. The reversibility of mesylation with sulfene was previously described for cyclization procedures: P. T. Lansbury, J. J. La Clair, *Tetrahedron Lett.* **1993**, *34*, 4431.

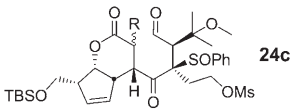

[11] C. Li, R. P. Johnson, J. A. Porco, Jr., *J. Am. Chem. Soc.* **2003**, *125*, 5095.
[12] D. E. Pearson, C. A. Buehler, A. Calvin, *Chem. Rev.* **1974**, *74*, 45.
[13] K. C. Nicolaou, A. A. Estrada, M. Zak, S. H. Lee, B. S. Safina, *Angew. Chem.* **2005**, *117*, 1402; *Angew. Chem. Int. Ed.* **2005**, *44*, 1378.
[14] D. R. Williams, D. C. Kammler, A. F. Donnell, W. R. F. Goundry, *Angew. Chem.* **2005**, *117*, 6873; *Angew. Chem. Int. Ed. Angew. Chem. Int. Ed. Engl.* **2005**, *44*, 6715.
[15] D. M. Nowak, P. T. Lansbury, *Tetrahedron* **1998**, *54*, 319.
[16] a) T. Tamai, K. Mizuno, I. Iiashida, Y. Otsuji, *Tetrahedron Lett.* **1993**, *34*, 2641; b) V.-H. Nguyen, H. Nishino, K. Kazu, *Tetrahedron Lett.* **1997**, *38*, 1773.
[17] Physical and spectral properties of **1**: Colorless solid; m.p.: 172–174 °C; $R_f = 0.83$ in CH_3Cl/MeOH (9:1 v/v); IR (film): $\tilde{\nu} = 3417$, 3018, 2985, 2935, 1699, 1625, 1382, 1214, 1009, 1132, 996, 982, 910 cm^{-1}; ^1H NMR (500 MHz, $CDCl_3 + 1\%$ CD_3OD, J [Hz]): $\delta = 6.73$ (dd, $J = 5.3$, 2.4, 1H), 5.46 (d, $J = 10.1$, 1H), 4.99 (br dd, $J = 5.2$, 1H), 4.81 (d, $J = 10.1$, 1H), 3.81 (dd, $J = 9.5$, 1.6, 1H), 3.64 (m, 1H), 3.59 (d, $J = 5.3$,1H), 3.55 (m, 1H), 3.51 (dd, $J = 2.8$, 0.5, 1H), 3.29 (d, $J = 3.0$, 1H), 3.24 (d, $J = 3.6$, 1H), 3.03 (s, 3H), 2.75 (dd, $J = 5.2$, 7.9, 1H), 1.77 (s, 3H), 1.73 (s, 3H), 1.27 (s, 3H), 1.15 ppm (s, 3H); HR-EIMS: calcd m/z: 416.1835; found: 416.1892. See Supporting Information for spectra.
[18] Physical and spectral properties of **2**: Colorless solid; m.p.: 165–169 °C; $R_f = 0.79$ in CH_3Cl/MeOH (9:1 v/v); IR (film): $\tilde{\nu} = 3418$, 3015, 2980, 2932, 1701, 1626, 1380, 1216, 1005, 1131, 995, 981, 912 cm^{-1}; ^1H NMR (500 MHz, $CDCl_3 + 1\%$ CD_3OD, J [Hz]): $\delta = 6.78$ (dd, $J = 5.4$, 2.2, 1H), 5.41 (d, $J = 10.6$, 1H), 5.01 (br dd, $J = 5.2$, 1H), 4.56 (d, $J = 8.2$, 1H), 3.76 (dd, $J = 9.5$, 1.6, 1H), 3.58 (m,1H), 3.52 (m, 1H), 3.51 (d, $J = 5.2$, 1H), 3.48 (dd, $J = 2.9$, 0.5, 1H), 3.32 (d, $J = 2.8$, 1H), 3.26 (d, $J = 3.4$, 1H), 3.08 (s, 3H), 2.78 (dd, $J = 5.1$, 7.8, 1H), 1.81 (s, 3H), 1.72 (s, 3H), 1.28 (s, 3H), 1.17 ppm (s, 3H); HR-EIMS: calcd m/z: 416.1835; found: 416.1881. See Supporting Information for spectra.
[19] Physical and spectral properties of **3** as a 1:1 mixture of olefin isomers: Waxy solid; $R_f = 0.68$ in CH_3Cl/MeOH (12:1 v/v); IR (film): $\tilde{\nu} = 3417$, 2965, 2955, 1695, 1624, 1422, 1272, 1104, 1002, 992, 972, 912 cm^{-1}; ^1H NMR (500 MHz, $CDCl_3 + 1\%$ CD_3OD, J [Hz]): $\delta = 6.90$ (d, $J = 9.2$, 1.3, 1H); 6.94 (d, $J = 10.5$, 0.7, 1H), 5.92 (d, $J = 9.3$, 1.2, 1H); 5.89 (d, $J = 10.5$, 0.7, 1H), 5.79 (dd, $J = 5.3$, 2.4, 1H), 5.56 (dd, $J = 9.3$, 2.4, 1H), 5.22 (dd, $J = 9.3$,1.8, 1H), 3.65 (dd, $J = 2.1$, 0.8, 1H), 3.51 (dd, $J = 2.3$, 1.8, 1H), 3.31 (m, 1H), 3.21 (dd, $J = 8.4$, 1.1, 1H), 3.16 (br d, $J = 2.6$, 1H), 3.16 (d, $J = 2.0$, 1H), 3.06 (m, 1H) , 2.82 (s, 3H), 1.76 (s, 3H), 1.75 (s, 3H), 1.21 (s, 3H), 1.18 ppm (s, 3H); HR-EIMS: calcd m/z: 384.1937; found: 384.1911. See Supporting Information for spectra.

 © 2006 Wiley-VCH Verlag GmbH & Co. KGaA, Weinheim

[20] W. Peters, B. L. Robinson, *Ann. Trop. Med. Parasitol.* **1999**, *93*, 325.
[21] A. M. Szpilman, E. E. Korshin, H. Rozenberg, M. D. Bachi, *J. Org. Chem.* **2005**, *70*, 3618.
[22] **Note added in proof**: The ^{1}H NMR spectra for this Communication were determined by contract services. The spectra provided in the Supporting Information were collected by N. Voss (Berlin, Germany). The operator added the peak for $CDCl_3$ to the spectrum of synthetic hexacyclinol (**1**), however, this was done incorrectly at $\delta \approx 7.5$ ppm and against the request of the author. Additionally, one spectrum was duplicated and a copy of the spectra for natural 5-*epi*-hexacyclinol was not provided.

 © 2006 Wiley-VCH Verlag GmbH & Co. KGaA, Weinheim

Host–Guest Complexes

DOI: 10.1002/anie.200504262

Cyclic Dimethylsiloxanes as Pseudo Crown Ethers: Syntheses and Characterization of $Li(Me_2SiO)_5[Al\{OC(CF_3)_3\}_4]$, $Li(Me_2SiO)_6[Al\{OC(CF_3)_3\}_4]$, and $Li(Me_2SiO)_6[Al\{OC(CF_3)_2Ph\}_4]$**

Andreas Decken, Jack Passmore, and Xinping Wang*

In memory of Chunying Liao

Although the chemistry of silicon is notably different from that of carbon,[1] parallels between the chemistry of the two elements continue to emerge, for example, the recent syntheses of a proposed Si≡Si triple bond,[2] persilaaromatic rings,[3] silylium ions,[4] and silaadamantane.[5] However, few stable adducts of silicon ethers (for example, $(Me_3Si)_2O$) have been prepared,[6] and there have been no reports of direct reactions of metal ions with cyclic dimethysiloxanes D_n ($D_n = (Me_2SiO)_n$, $n = 1$–40)[7] or related compounds, in contrast to the extensive and selective reaction of metal ions with the structurally similar crown ethers.[8] Silacrown ethers containing one or two Me_2SiO units have a drastically reduced ability to bind metal cations compared to crown ethers.[9] This observation has been attributed to the low basicity of oxygen in siloxane compounds,[10] the reasons for which are of continuing interest.[11] Nevertheless, two examples[12] of $[KD_7]^+$ ions were unexpectedly isolated from reactions in the presence of silicone grease,[13] although the mechanisms of the reactions are unclear. In a reaction designed to give $Se_6Ph_2[Al_F]_2$ ($[Al_F] = Al\{OC(CF_3)_3\}_4$) from $Se_4(AsF_6)_2$, 2 Li-$[Al_F]$, and Se_2Ph_2 in the presence of silicone grease, we unexpectedly obtained crystals of $LiD_6[Al_F]$. Subsequently, we prepared $LiD_5[Al_F]$, $LiD_6[Al_F]$, and $LiD_6[Al_{PhF}]$ ($[Al_{PhF}] = Al\{OC(CF_3)_2Ph\}_4$) in high yield by the reaction of $Li[Al_F]$ or $Li[Al_{PhF}]$ with D_5 or D_6 in CH_2Cl_2 solution [Eq. (1)].

$$LiX + D_n \xrightarrow[RT]{CH_2Cl_2} LiD_nX \quad (1)$$

$X = [Al_F]$ ($n = 5$ or 6) or $[Al_{PhF}]$ ($n = 6$)

These results, and the calculated energies of related reactions of alkali-metal cations with cyclic dimethysiloxanes imply the existence of a new class of host–guest complexes for the cyclic siloxanes that is similar to, but less extensive than, that for the crown ethers; for example, the reaction of $Li[Al_{PhF}]$ and D_5 in CH_2Cl_2 did not give the expected product $LiD_5[Al_{PhF}]$.[14] In addition, these findings imply that new classes of metal complexes of cyclosiloxane analogues (for example, cyclophosphazenes) may be prepared by using metal salts of large weakly coordinating anions, which minimize lattice-energy changes and cation–anion interactions.[15]

The IR and Raman spectra of the moisture-sensitive, thermally stable, colorless salts $LiD_5[Al_F]$, $LiD_6[Al_F]$, and $LiD_6[Al_{PhF}]$ showed the characteristic peaks of the anions, as well as peaks very similar to those of the siloxane reactants. Electron ionization mass spectrometry (EI-MS) and chemical analysis of the products were consistent with the given formulations. The $^{29}Si\{^1H\}$ NMR signals of $LiD_6[Al_{PhF}]$ ($\delta = -10.14$ ppm) and $LiD_6[Al_F]$ ($\delta = -9.22$ ppm) in liquid SO_2 were different from that of D_6 ($\delta = -22.69$ ppm), implying the presence of the $[LiD_6]^+$ ion, or an equilibrium mixture of $[LiD_6]^+$, Li^+, and D_6.[16] The $^{29}Si\{^1H\}$ NMR chemical shift of $LiD_5[Al_F]$ ($\delta = -21.28$ ppm) is similar to that of D_5 ($\delta = -21.67$ ppm), indicating complete dissociation of the complex into Li^+, $[Al_F]^-$, and D_5 in liquid SO_2. This observation is consistent with the less negative estimated energy ($\Delta E = -210$ kJ mol^{-1}, HF/6-31G*) for the reaction of $Li[Al_F]$ with D_5 [Eq. (2)] compared to that for the corresponding reaction with D_6 ($\Delta E = -242$ kJ mol^{-1}; Scheme 1).[17]

$$Li[Al_F]_{(s)} + D_{5(l)} \rightarrow LiD_5[Al_F]_{(s)} \quad (2)$$

A preliminary single-crystal X-ray diffraction (XRD) study of $LiD_5[Al_F]$[18] clearly showed that the structure of the $[LiD_5]^+$ ion is very similar to that calculated by ab initio and density functional theory (DFT) methods (Figure 1, Table 1). The solid-state structures of the $[LiD_6]^+$ ions (Figure 2) in both $LiD_6[Al_F]$ and $LiD_6[Al_{PhF}]$ are similar,[19,20] but the cation in $LiD_6[Al_F]$ more clearly resembles the ideal gas-phase structure, in which the Li^+ ion is in the plane of the Si_6O_6 ring. The distortion from the ideal structure results from $Li^+\cdots F^{\delta-}$ interactions between the cations and the anions. The strength of these interactions, which can be judged by calculating their

[*] Dr. A. Decken, Prof. J. Passmore, X. Wang
Department of Chemistry
University of New Brunswick
Fredericton, NB E3B 6E2 (Canada)
Fax: (+1) 506-453-4981
E-mail: passmore@unb.ca

[**] Acknowledgement is made to NSERC (Canada) for financial support of this research, Mikko Rautiainen for help with calculations, and Dr. Carsten Knapp for his helpful suggestions.

Supporting information for this article is available on the WWW under http://www.angewandte.org or from the author.

 © 2006 Wiley-VCH Verlag GmbH & Co. KGaA, Weinheim

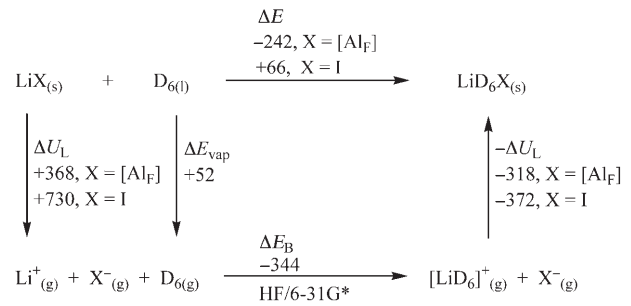

Scheme 1. Born–Haber cycle for the reaction of LiX (X = [Al_F] or I) with D_6. Lattice energies ΔU_L, energy of vaporization ΔE_{vap}, binding energies ΔE_B (calculated at the HF/6-31G* level of theory), and energies of formation ΔE are given in kJ mol^{-1}.

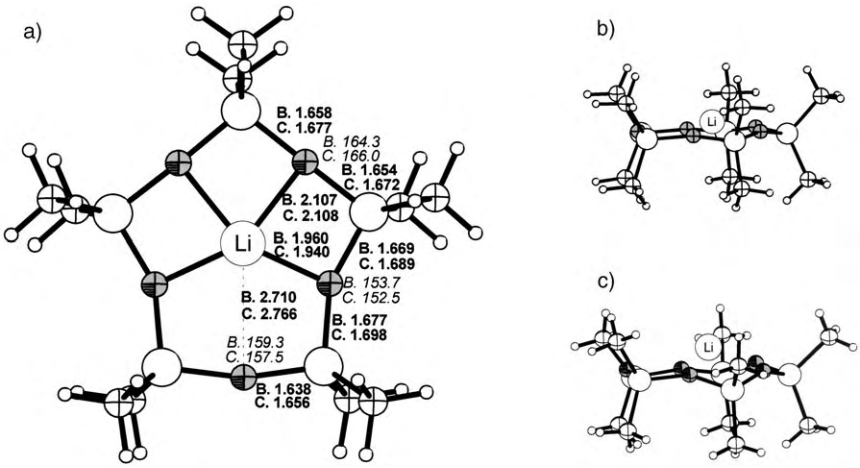

Figure 1. a) Top view and b) side view of the optimized C_s geometry of the $[LiD_5]^+$ ion; interatomic distances [Å] (bold) and angles [°] (italic) calculated at the HF/6-31G* (B) and B3LYP/6-31G* (C) levels of theory are indicated. c) Side view of the $[LiD_5]^+$ ion in the preliminary crystal structure of $LiD_5[Al_F]$. $D_5 = (Me_2SiO)_5$; $[Al_F] = Al\{OC(CF_3)_3\}_4$. Large open Si, filled crossed O, open crossed C, small open H.

bond valence s (in valence units vu),[21] is greater in the salt of the more basic $[Al_{PhF}]^-$ ion ($s = 0.125$ vu) than in $LiD_6[Al_F]$ ($s = 0.041$ vu), leading to a greater displacement of the Li^+ ion out of the Si_6O_6 plane in $LiD_6[Al_{PhF}]$ (0.423(3) Å) than in $LiD_6[Al_F]$ (0.13(1) Å), and to a slightly stronger coordination of four oxygen atoms to the Li^+ ion in $LiD_6[Al_F]$ (Li–O 2.03(2)–2.07(1) Å; $s = 0.81$ vu) than in $LiD_6[Al_{PhF}]$ (Li–O 2.059(3)–2.099(4) Å; $s = 0.77$ vu). Related compounds with five-coordinate Li^+ ions include Li([12]crown-4)Cl (Li–O 2.128(2) Å) and Li([12]crown-4)[$CF_3SO_2N(CH_2)_3OCH_3$] (Li–O 2.080(3)–2.187(3) Å).[22] The cyclohexaphosphonitrile ring, which is isoelectronic to cyclohexasiloxane, acts as a macrocyclic ligand to Cu^{2+} and Co^{2+} in the ions $[\{N_6P_6(NMe_2)_{12}\}MCl]^+$ (M = Cu, Co).[23] In these cations, the metal atoms are coordinated by four nitrogen atoms of the cyclohexaphosphazene ring and one chlorine atom, in a coordination geometry that is similar to that of the lithium atoms in $LiD_6[Al_{PhF}]$.

The average Si–O_{NC} bond lengths and Si-O_{NC}-Si angles involving the noncoordinating oxygen atoms (O_{NC}) in the $[LiD_6]^+$ ions of $LiD_6[Al_F]$ and $LiD_6[Al_{PhF}]$ (Figure 2c, Table 1) are similar to those found for the oxygen atoms in D_6 by electron diffraction (ED).[24] For the coordinating oxygen atoms, however, the average Si–O bond lengths are slightly longer, and the average Si-O-Si angles are smaller. The average Si–C bond lengths for the silicon atoms adjacent to two coordinating oxygen atoms are similar to those for the silicon atoms adjacent to only one coordinating oxygen atom. The average lengths of all the Si–C bonds in the $[LiD_6]^+$ ions are slightly shorter than that in D_6 (Table 1). These differences are consistent with a strong electrostatic interaction between the lithium and oxygen atoms,[25] and an induced polarization of the $p^2(O) \rightarrow \sigma^*(Si–CH_3)$ interactions, which leads to a slight weakening of the Si–O bonds and a slight strengthening of the Si–C bonds (Figure 3). The calculated natural bond orbital (NBO) charges support this picture: upon coordination of D_6 to the Li^+ ion, the charge on the coordinating oxygen atoms becomes more negative, the charge on the $SiMe_2$ fragments

Table 1: Experimental and calculated average distances [Å] and angles [°] for the $[LiD_5]^+$ and $[LiD_6]^+$ ions, and for the free D_5 and D_6 molecules.

	Symmetry	Method	Li–O	Si–O	Si–O_{NC}[a]	Si–C[b]	Si-O_{NC}-Si	Si-O-Si
D_5	C_s	HF/6-31G*			1.632	1.874	159.0	
	C_s	B3LYP/6-31G*			1.654	1.876	152.7	
	D_{5d}[c]	ED[d]			1.620(2)	1.845(4)	146.5(1)	
	C_s[c]	XRD[e]			1.629(1)	1.845(2)	148.0(1)	
$[LiD_5]^+$	C_s	HF/6-31G*	2.034	1.664	1.638	1.862	159.3	159.0
	C_s	B3LYP/6-31G*	2.023	1.684	1.656	1.863	157.5	159.2
D_6	C_2	HF/6-31G*			1.632	1.874	158.2	
	C_2	B3LYP/6-31G*			1.656	1.876	153.7	
	D_{3d}[c]	ED[d]			1.622(1)	1.846(1)	149.6(1)	
$[LiD_6]^+$	C_2	HF/6-31G*	2.042	1.671	1.631	1.865	151.5	143.5
	C_2	B3LYP/6-31G*	2.023	1.692	1.651	1.867	149.3	142.9
	C_2[c]	XRD ($[Al_F]^-$)	2.06(1)	1.661(6)	1.617(7)	1.837(1)	151.1(5)	141.1(4)
	C_2[c]	XRD ($[Al_{PhF}]^-$)	2.078(3)	1.655(1)	1.620(2)	1.836(2)	146.5(1)	141.7(1)

[a] The subscript NC denotes noncoordinating O atoms; O atoms without subscripts are coordinated to Li atoms. [b] Average length for all Si–C bonds. [c] Approximate symmetries. [d] The gas-phase structures of D_5 and D_6 were determined by electron diffraction (ED); the final structures are not well defined.[24] [e] The single-crystal structure of D_5 was determined by X-ray diffraction (XRD): S. Parson, D. Rankin, P. Wood, private communication to the Cambridge Structural Database, CCDC-247844, The Cambridge Crystallographic Data Centre, **2004**.

 © 2006 Wiley-VCH Verlag GmbH & Co. KGaA, Weinheim

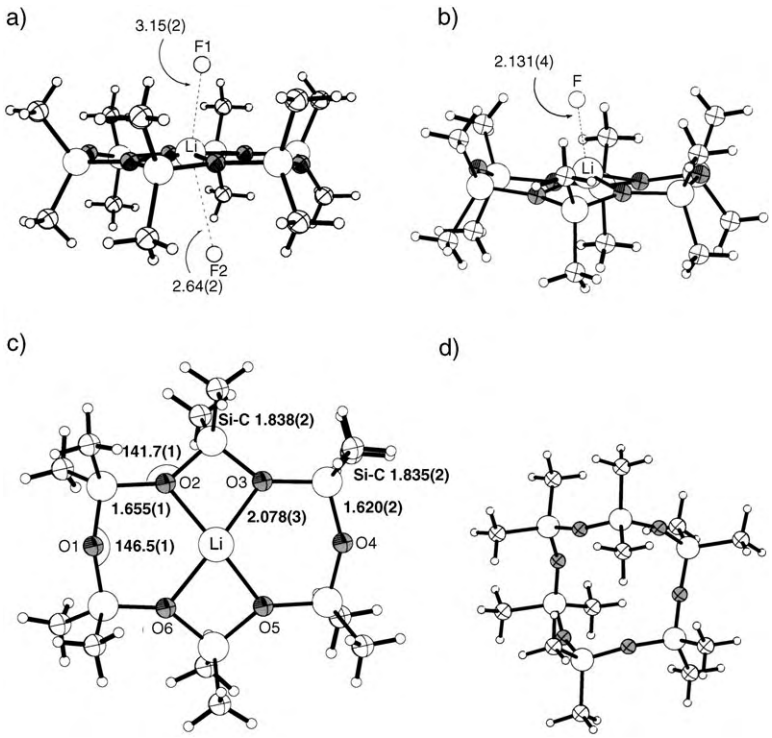

Figure 2. a) Side view of the $[LiD_6]^+$ ion in $LiD_6[Al_F]$. b) Side view and c) top view of the $[LiD_6]^+$ ion in $LiD_6[Al_{PhF}]$; average interatomic distances [Å] (Li–O, Si–O, Si–O_{NC}, O_2Si–C, and O(O_{NC})Si–C; the subscript NC denotes noncoordinating O atoms; O atoms without subscripts are coordinated to the Li atom) and angles [°] (Si-O-Si and Si-O_{NC}-Si) are indicated. d) Optimized C_2 geometry of D_6 at the HF/6-31G* level of theory. $D_6 = (Me_2SiO)_6$; $[Al_F] = Al\{OC(CF_3)_3\}_4$; $[Al_{PhF}] = Al\{OC(CF_3)_2Ph\}_4$. Large open Si, filled crossed O, open crossed C, small open H.

Table 2: Average atomic and fragment NBO charges (q) for D_6 and its alkali-metal complexes $[MD_6]^+$ (M = Li, Na, Rb), calculated at the B3LYP/6-31G* level of theory.

	D_6	$[LiD_6]^+$	$[NaD_6]^+$	$[KD_6]^+$
symmetry	C_2	C_2	D_{3h}	C_{6v}
$q(M^+)$		0.932	0.962	0.978
$q(O_{NC}$[a])	−1.275	−1.271		
q(O)		−1.316	−1.303	−1.297
$q(SiMe_2)$	1.275	1.313	1.309	1.301
$\Delta q(SiMe_2)$[b]	0	0.038	0.034	0.026

[a] The subscript NC denotes noncoordinating O atoms; O atoms without subscripts are coordinated to M atoms. In $[NaD_6]^+$ and $[KD_6]^+$, the M atoms are coordinated by all O atoms equally. See Supporting Information for details. [b] Difference between the average charges $q(SiMe_2)$ of $[MD_6]^+$ and of free D_6.

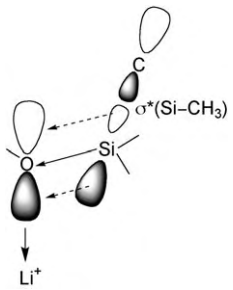

Figure 3. Schematic representation of the polarization of the O–Si bond and the $p^2(O) \rightarrow \sigma^*(Si\text{-}CH_3)$ interaction upon coordination of D_6 to Li^+ in the $[LiD_6]^+$ ion.

becomes more positive, and the charge on lithium becomes slightly less than 1, which implies a very small amount of Li–O covalent bonding (Table 2). Further calculations on $[MD_6]^+$ (M = Na, K) imply that replacement of the Li^+ ion by the less polarizing Na^+ and K^+ ions increases the positive charge on the metal atom, decreases the positive charge on the $SiMe_2$ fragments, and decreases the negative charge on the coordinating oxygen atoms. In contrast, there is little change in the C–O bond lengths and C-O-C angles in [18]crown-6 upon coordination to alkali-metal cations,[25] consistent with the absence of $p^2 \rightarrow \sigma^*$ hyperconjugation in the crown ether.

The structure of D_6 was determined in the gas phase by ED.[24] This study suggested that the D_6 ring is puckered, with some methyl groups pointing inward (see Figure 2d for the geometry of D_6 calculated at the HF/6-31G* level of theory). Rotation of the inner methyl groups outward produces a larger cavity at the center of the ring, which is occupied by Li^+ in the $[LiD_6]^+$ ion (the calculated geometry of $[LiD_6]^+$ is similar to that of the cation in $LiD_6[Al_F]$, Figure 2a). Upon coordination of the Li^+ ion, the Si_6O_6 framework of D_6 becomes nearly planar. However, in $LiD_6[Al_{PhF}]$, stronger Li···F and H···F contacts cause some deformation (bending) of the Si_6O_6 plane (Figure 2b).[26]

The syntheses of the $LiD_5[Al_F]$, $LiD_6[Al_F]$, and $LiD_6[Al_{PhF}]$ salts are the first examples of the preparation of host–guest complexes directly from cyclic dimethylsiloxanes, alkali-metal ions, and weakly coordinating anions. Their structures imply that the cyclic dimethylsiloxanes (D_5 and D_6) act as pseudo crown ethers and provide rare examples of silicon ethers behaving as Lewis bases. The counterpoise-corrected binding energies for the alkali-metal complexes $[MD_6]^+$ exhibit a remarkable similarity to that for [18]crown-6 (Figure 4):[27] for both sets of complexes (in the gas phase), the binding energies become less negative with increasing size of the alkali-metal cation. However, the binding affinity of D_6 calculated at the HF/3-21G level is approximately 100 kJ mol^{-1} less than that of [18]crown-6, reflecting the lower basicity of the siloxanes. Thus, the reaction of $D_{6(l)}$ with $LiI_{(s)}$ is thermodynamically unfavorable ($\Delta E = +66$ kJ mol^{-1}; Scheme 1).[28] However, replacement of I^- by the larger ion $[Al_F]^-$ reduces the unfavorable change in lattice energy on

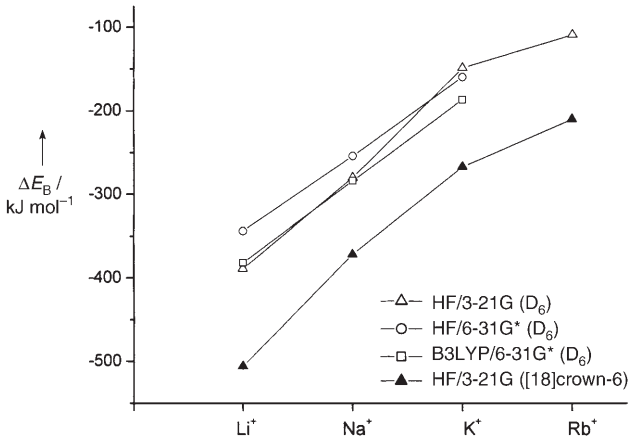

Figure 4. Binding energies ΔE_B (counterpoise corrected) of D_6 and [18]crown-6 with alkali-metal cations.

 © 2006 Wiley-VCH Verlag GmbH & Co. KGaA, Weinheim

going from LiX to LiD_6X ($\Delta U_L(LiX) - \Delta U_L(LiD_6X) = +358\ kJ\,mol^{-1}$ for X = I and $+50\ kJ\,mol^{-1}$ for $X = [Al_F]$), and the energy of formation of $LiD_6[Al_F]_{(s)}$ from $Li[Al_F]_{(s)}$ and $D_{6(l)}$ is $\Delta E = -242\ kJ\,mol^{-1}$ (Scheme 1). Thus, a new class of salts with cyclosiloxane–metal cations and weakly coordinating anions can be anticipated.

Experimental Section

$LiD_5[Al_F]$: CH_2Cl_2 (50 mL) was added to D_5 (0.45 mL, 1.16 mmol) over solid $Li[Al_F]$ (0.985 g, 1.01 mmol) in a 100-mL Schlenk flask. The resulting colorless, clear solution was concentrated to saturation by stirring overnight at room temperature. Large crystals were obtained after 1 day at −20 °C. The solvent was removed under vacuum, and the crystallized product was washed three times with *n*-hexane. Yield: 1.25 g (90 %, based on $Li[Al_F]$). $^{29}Si\{^1H\}$ NMR (79.4 MHz, SO_2, RT): $\delta = -21.28$ ppm (m, D_5); $^{13}C\{^1H\}$ NMR (100.6 MHz, SO_2, RT): $\delta =$ 0.893 ppm (s, D_5); ^1H NMR (400.0 MHz, SO_2, RT): $\delta = 0.125$ ppm (s, D_5); ^{19}F NMR (376.3 MHz, SO_2, RT): $\delta = -74.113$ ppm (s, $Li[Al_F]$); ^{27}Al NMR (104.2 MHz, SO_2, RT): $\delta = 35.107$ ppm (s, $Li[Al_F]$); ^7Li NMR (155.4 MHz, SO_2, RT): $\delta = -0.288$ ppm (s, $Li[Al_F]$). FT-IR (KBr, solid, RT, $\tilde{\nu}$ assigned to $[LiD_5]^+$ marked with *, e.g. 2972 (w),*): $\tilde{\nu} =$ 2972 (w),* 2907 (w),* 1626 (w), 1356 (s),* 1301 (s), 1275 (s),* 1236 (s), 1215 (vs), 1163 (m), 1026 (s; ϑ_{as}(SiOSi)),* 971 (vs), 855 (m),* 825 (s),* 808 (s),* 752 (m; ϑ_a(SiC2)),* 726 (s; ϑ_s(SiC2)),* 709 (m),* 666 (w; ϑ_s(SiOSi)),* 572 (w), 568 (m), 555 (m), 534 (m), 439 (m), 401 cm^{-1} (m). FT-Raman (RT, $\tilde{\nu}$ assigned to $[LiD_5]^+$ marked with *): $\tilde{\nu} =$ 2975 (m; ϑ_a(CH)),* 2914 (s; ϑ_s(CH)),* 1494 (w), 1402 (w), 1276 (w), 797 (w),* 745 (w),* 536 (m), 321 (w), 164 cm^{-1} (w). EI-MS (30 eV): *m*/*z* (%): 539 (20) $[M^+ - D_5 - OC(CF_3)_3 - C_2F_8O]$, 522 (33) $[M^+ - D_5 - C(CF_3)_3 - 3CF_3 - F]$, 354 (100) $[M^+ - Li[Al_F] - Me = D_5^+ - Me]$. Elemental analysis (%) calcd: C 23.24, H 2.25; found: C 23.37, H 2.47. M.p.: 216 °C (decomp).

$LiD_6[Al_F]$: The preparation of $LiD_6[Al_F]$ was similar to that of $LiD_5[Al_F]$ ($Li[Al_F]$ 0.808 g, 0.830 mmol; D_6 0.50 mL, 1.08 mmol; CH_2Cl_2 50 mL). Yield: 1.12 g (95 %, based on $Li[Al_F]$). $^{29}Si\{^1H\}$ NMR (79.4 MHz, SO_2, RT): $\delta = -9.22$ ppm (s, $SiMe_2$); $^{13}C\{^1H\}$ NMR (100.6 MHz, SO_2, RT): $\delta = 120.011$ (q, J(C,F) = 291 Hz, 3 C, CF_3), 79.219 (s, 1 C, $OCCF_3$), 0.202 ppm (s, 3 C, $SiMe_2$); ^1H NMR (400.0 MHz, SO_2, RT): $\delta = 0.296$ ppm (s, $SiMe_2$); ^{19}F NMR (376.3 MHz, SO_2, RT): $\delta = -75.193$ ppm (s, $[Al_F]$); ^{27}Al NMR (104.2 MHz, SO_2, RT): $\delta = 34.998$ ppm (s, $[Al_F]$); ^7Li NMR (155.4 MHz, SO_2, RT): $\delta = 0.190$ ppm (s). IR (KBr, neat, RT, $\tilde{\nu}$ assigned to $[LiD_6]^+$ marked with *): $\tilde{\nu} =$ 2965 (m),* 2916 (w),* 1537 (w), 1494 (w),* 1408 (m),* 1377 (w),* 1352 (s), 1300 (s), 1276 (s),* 1241 (s), 1216 (s), 1167 (s), 1132 (m), 1087 (s; ϑ_{as}(SiOSi)),* 1010 (s), 968 (s), 853 (s),* 822 (s),* 794 (s; ϑ_a(SiC2)),* 752 (m; ϑ_a(SiC2)),* 724 (s; ϑ_s(SiC2)),* 665 (w; ϑ_s(SiOSi)),* 619 (m; ϑ_s(SiOSi)),* 560 (m), 532 (m), 441 (m), 396 cm^{-1} (s). Raman (RT, $\tilde{\nu}$ assigned to $[LiD_6]^+$ marked with *): $\tilde{\nu} =$ 2975 (s; ϑ_a(CH)),* 2915 (vs; ϑ_s(CH)),* 1495 (w), 797 (w),* 745 (w),* 542 (m), 320 (w), 168 cm^{-1} (w). EI-MS (30 eV): *m*/*z* (%): 539 (15) $[M^+ - D_6 - OC(CF_3)_3 - C_2F_8O]$, 522 (31) $[M^+ - D_6 - C(CF_3)_3 - 3CF_3 - F]$, 354 (100) $[M^+ - Li[Al_F] - Me = D_6^+ - Me]$. Elemental analysis (%) calcd: C 23.72, H 2.56; found C 23.77, H 2.60. M.p. 286 °C (decomp).

$LiD_6[Al_{PhF}]$: CH_2Cl_2 (20 mL) was transferred onto D_6 (0.45 mL, 0.97 mmol) over solid $Li[Al_{PhF}]$ (0.956 g, 0.95 mmol) in a 100-mL Schlenk flask. The resulting yellowish, clear solution was stirred overnight at room temperature. *n*-Hexane (40 mL) was added to the solution, and a large amount of crystals was obtained after 1 day at −20 °C. The crystals were separated by filtration, and the filtrate was further concentrated to one third, producing more crystals, which were washed with *n*-hexane. Total yield: 1.17 g (85 %, based on $Li[Al_{PhF}]$). $^{29}Si\{^1H\}$ NMR (79.4 MHz, SO_2, RT): $\delta = -10.14$ ppm (s, $SiMe_2$); $^{13}C\{^1H\}$ NMR (100.6 MHz, SO_2, RT): $\delta = 0.454$ (s, $SiMe_2$), 80.085 (s, $OC(CF_3)_2Ph$), 125.763 (q, J(C,F) = 291 Hz, CF_3), 128.186 (s, *ortho*-C_6H_5), 128.688(s, *meta*-C_6H_5), 129.206 (s, *para*-C_6H_5), 136.069 ppm (s, *ipso*-C_6H_5); ^1H NMR (400.0 MHz, SO_2, RT): $\delta =$ 0.288 (s, 36 H, $SiMe_2$), 7.898 (m, 8 H, *meta*-C_6H_5), 7.330 (m, 4 H, *para*-C_6H_5), 7.233 ppm (m, 8 H, *ortho*-C_6H_5); ^{19}F NMR (376.3 MHz, SO_2, RT): $\delta = -74.119$ ppm (s, $[Al_{PhF}]$); ^{27}Al NMR (104.2 MHz, SO_2, RT): $\delta = 29.552$ ppm (s, $[Al_{PhF}]$); ^7Li NMR (155.4 MHz, SO_2, RT): $\delta =$ 0.180 ppm (s). FT-IR (KBr, neat, RT, $\tilde{\nu}$ assigned to $[LiD_6]^+$ marked with *): $\tilde{\nu} =$ 3666 (w), 3576 (w), 3062 (vw), 2963 (w),* 2899 (vw),* 1622 (m), 1502 (w), 1485 (w), 1446 (m),* 1412 (w),* 1331 (m), 1305 (s), 1266 (vs),* 1223 (s), 1193 (vs), 1198 (vs), 1133 (s), 1078 (s; ϑ_{as}(SiOSi)),* 1026 (s), 1001 (s; ϑ_{as}(SiOSi)),* 996 (vs), 966 (vs), 932 (s), 915 (m), 855 (s),* 821 (s),* 795 (s; ϑ_a(SiC2)),* 761 (m), 743 (m), 713 (vs), 688 (m),* 658 (m; ϑ_s(SiOSi)),* 619 (w), 559 (w), 538 (w), 495 (w), 435 (m), 396 cm^{-1} (m). FT-Raman (RT, $\tilde{\nu}$ assigned to $[LiD_6]^+$ marked with *): $\tilde{\nu} =$ 3084 (s), 2967 (s; ϑ_a(CH)),* 2909 (vs; ϑ_s(CH)),* 1604 (w), 1495 (w), 1171 (w), 1038 (m), 1005 (m),* 786 (w), 735 (w), 619 (w),* 542 cm^{-1} (m). EI-Ms (30 eV): *m*/*z* (%): 918 (92) $[M^+ - D_6 - CF_3 - F]$, 901 (100) $[M^+ - D_6 - CF_3 - 2F]$, 429 (40) $[M^+ - Li[Al_{PhF}] - Me = D_6^+ - Me]$. Elemental analysis (%) calcd: C 39.72, H 3.89; found: C 39.70, H 3.84. M.p.: 132 °C (decomp).

The following are given in the Supporting Information: general experimental techniques; a description of the reaction designed to produce $Se_6Ph_2[Al_F]_2$, from which crystals of $LiD_6[Al_F]$ were isolated; a comparison of the FT-IR, FT-Raman, and NMR spectra of $LiD_5[Al_F]$, $LiD_6[Al_F]$, and $LiD_6[Al_{PhF}]$ with those of the reactants; different views of the crystal structures of $LiD_5[Al_F]$, $LiD_6[Al_F]$, and $LiD_6[Al_{PhF}]$; and details of the calculations.

Received: November 30, 2005
Published online: March 20, 2006

Keywords: crown compounds · host–guest systems · lithium · siloxanes · weakly coordinating anions

[1] N. N. Greenwood, A. Earnshaw, *Chemistry of the Elements*, 2nd ed. Butterworth-Heinemann, Oxford, **1997**, p. 328.
[2] A. Sekiguchi, R. Kinjo, M. Ichinohe, *Science* **2004**, *305*, 1755.
[3] M. Ichinohe, M. Igarashi, K. Sanuki, A. Sekiguchi, *J. Am. Chem. Soc.* **2005**, *127*, 9978.
[4] C. Kim, C. A. Reed, D. W. Elliott, L. J. Mueller, F. Tham, L. Lin, J. B. Lambert, *Science* **2002**, *297*, 5582, and references therein.
[5] J. Fischer, J. Baumgartner, C. Marschner, *Science* **2005**, *310*, 825.
[6] There is no definite evidence for the existence of neutral BF_3 adducts of silicon ethers: H. J. Emeléus, M. Onyszchuk, *J. Chem. Soc.* **1958**, 604. A protonated silanol that is stable at room temperature occurs in the salt $tBu_3Si(OH_2)[Br_6CB_{11}H_6]$, which has been isolated and crystallographically characterized: Z. Xie, R. Bau, C. A. Reed, *J. Chem. Soc. Chem. Commun.* **1994**, 2519. For siloxonium ions unstable above −30 °C, see: a) G. A. Olah, H. Doggweiler, J. D. Felberg, S. Frohlich, *J. Org. Chem.* **1985**, *50*, 4847; b) M. Kira, T. Hino, H. Sakurai, *J. Am. Chem. Soc.* **1992**, *114*, 6697; c) G. A. Olah, X. Li, Q. Wang, G. Rasul, G. K. S. Prakash, *J. Am. Chem. Soc.* **1995**, *117*, 8962.
[7] a) M. J. Hunter, J. F. Hyde, E. L. Warrick, H. J. Fletchers, *J. Am. Chem. Soc.* **1946**, *68*, 667; b) W. Patnode, D. F. Wilcock, *J. Am. Chem. Soc.* **1946**, *68*, 358; c) J. F. Hyde, R. C. Delong, *J. Am. Chem. Soc.* **1941**, *63*, 1194; d) T. Alvik, J. Dale, *Acta. Chem. Scand.* **1971**, *25*, 2131, and references therein.
[8] C. J. Pedersen, *J. Am. Chem. Soc.* **1967**, *89*, 7017.
[9] O. Mikio, I. Yoshihisa, K. Takashi, H. Tadao, *Bull. Chem. Soc. Jpn.* **1984**, *57*, 887.
[10] a) R. West, L. Whatley, K. Lake, *J. Am. Chem. Soc.* **1961**, *83*, 761; b) B. D. Shepherd, *J. Am. Chem. Soc.* **1991**, *113*, 5581, and references therein. The lower basicity of siloxanes is also reflected in their higher ionization energy E_i compared to

 © 2006 Wiley-VCH Verlag GmbH & Co. KGaA, Weinheim

carbon analogues; for example, the E_i for $(Me_3Si)_2O$ (9.64 eV) is 0.83 eV higher than that for $(Me_3C)_2O$ (8.81 eV).

[11] The nature of the Si–O bonding in siloxanes has been attributed to strong $Si^{\delta+}\cdots O^{\delta-}$ electrostatic interactions, dπ–pπ bonding, or $p^2\rightarrow\sigma^*$ negative hyperconjugation, and is still under debate: a) R. J. Gillespie, E. A. Robinson, *Chem. Soc. Rev.* **2005**, *34*, 396; b) H. Oberhammer, J. E. Boggs, *J. Am. Chem. Soc.* **1980**, *102*, 7241; c) S. Shambayati, J. F. Blake, S. G. Wierschke, W. L. Jorgensen, S. L. Schreiber, *J. Am. Chem. Soc.* **1990**, *112*, 697; d) Y. Mo, Y. Zhang, J. Gao, *J. Am. Chem. Soc.* **1999**, *121*, 5737, and references therein.

[12] $(KD_7)K_3[InH(CH_2tBu)_3]_4$ and $(KD_7)[K\{C(SiMe_3)_2[SiMe_2(CH=CH_2)]\}_2]$ were obtained accidentally upon crystallization of $K[InH(CH_2tBu)_3]$ from heptane or during the metallation of $HC(SiMe_3)_2[SiMe_2(CH=CH_2)]$ with methylpotassium, respectively, both in the presence of silicone grease: a) M. R. Churchill, C. H. Lake, S. H. Chao, J. O. T. Beachley, *J. Chem. Soc. Chem. Commun.* **1993**, 1577; b) C. Eaborn, P. B. Hitchcock, K. Izod, J. D. Smith, *Angew. Chem.* **1995**, *107*, 2936; *Angew. Chem. Int. Ed. Engl.* **1995**, *34*, 2679.

[13] Silicone grease consists principally of polydimethylsiloxane (>80%), dimethylcyclosiloxane (<1%, ring size unknown), and hydroxy-terminated dimethylsiloxane (ca. 5–10%).[12a] For silicone grease as a serendipitous reagent, see: I. Haidue, *Organometallics* **2004**, *23*, 3.

[14] Single-crystal XRD and FT-IR spectroscopic analysis of the product showed it to be a new polymorph of the starting material $Li[Al_{PhF}]$. See Supporting Information for details.

[15] a) S. H. Strauss, *Chem. Rev.* **1993**, *93*, 927; b) C. Reed, *Acc. Chem. Res.* **1998**, *31*, 133; c) I. Krossing, I. Raabe, *Angew. Chem.* **2004**, *116*, 2116; *Angew. Chem. Int. Ed.* **2004**, *43*, 2066; d) T. S. Cameron, A. Decken, I. Dionne, M. Fang, I. Krossing, J. Passmore, *Chem. Eur. J.* **2002**, *8*, 3386; e) T. S. Cameron, J. Passmore, X. Wang, *Angew. Chem.* **2004**, *116*, 2029; *Angew. Chem. Int. Ed.* **2004**, *43*, 1995.

[16] The associative–dissociative process of metal cation/crown ether complexes in solution has been well determined: M. K. Amini, M. Shamsipur, *J. Phys. Chem.* **1991**, *95*, 9601, and references therein.

[17] For details of reaction-energy calculations, see Supporting Information. Gaussian 03, Revision C.02, J. A. Pople, et al. Gaussian, Inc., Wallingford CT, PA, **2004**.

[18] $LiD_5[Al_F]$ crystallizes in the monoclinic space group $P2_1/c$, with $a=10.9596(9)$, $b=28.564(2)$, $c=17.028(1)$ Å, $\beta=97.324(2)^\circ$, $V=5302(2)$ Å^3, and $Z=4$. The structure was not completely determined, because of disorder in the anion.

[19] Structure determination of $LiD_6[Al_F]$: Bruker AXS P4/SMART 1000 diffractometer, graphite-monochromatized $Mo_{K\alpha}$ radiation ($\lambda=0.71073$ Å), $T=173(1)$ K, $P\bar{1}$, $Z=4$, $a=11.0053(19)$, $b=22.828(4)$, $c=24.398(5)$ Å, $\alpha=101.660(4)$, $\beta=102.974(3)$, $\gamma=103.558(3)^\circ$, $V=5592.7(18)$ Å^3, $\rho_{calcd}=1.664$ mg m^{-3}, $2\theta_{max}=50.0^\circ$, 26311 reflections collected, 17449 independent reflections, 1485 parameters, $R1(I>2\sigma)=0.1049$, $R1$(all data) = 0.1422. There are two symmetry-independent $[LiD_6]^+$ ions in $LiD_6[Al_F]$, one of which is shown in Figure 2a. The main difference between the two cations is the differing strength of their Li···F contacts (3.02(2) and 3.19(2) Å for the $[LiD_6]^+$ ion not shown in Figure 2a). The structure of $LiD_6[Al_F]$ was not well determined, owing to severe rotational disorder in the anion, which prevents precise comparison with that of $LiD_6[Al_{PhF}]$.

[20] Structure determination of $LiD_6[Al_{PhF}]$: Bruker AXS P4/SMART 1000 diffractometer, graphite-monochromatized $Mo_{K\alpha}$ radiation ($\lambda=0.71073$ Å), $T=173(1)$ K, $P\bar{1}$, $Z=2$, $a=11.9673(9)$, $b=15.9362(12)$, $c=17.7554(12)$ Å, $\alpha=88.198(2)$, $\beta=87.127(2)$, $\gamma=72.045(1)^\circ$, $V=3216.8(4)$ Å^3, $\rho_{calcd}=1.498$ mg m^{-3}, $2\theta_{max}=55.0^\circ$, 22472 reflections collected, 14017 independent reflections, 823 parameters, $R1(I>2\sigma)=0.0416$, $R1$(all data) = 0.0667. CCDC-291338 ($LiD_6[Al_F]$) and CCDC-291339 ($LiD_6[Al_{PhF}]$)contain the supplementary crystallographic data for this paper. These data can be obtained free of charge from The Cambridge Crystallographic Data Centre via www.ccdc.cam.ac.uk/data_request/cif.

[21] The bond valences s (in valence units vu) are defined as $s=\exp[(R_o-R)/B]$, where R is the observed distance, R_o is the covalent bond length of the bond (bond order = 1; for Li–F, $R_o=1.36$ Å; for Li–O, $R_o=1.466$ Å), and B is an empirical parameter set to 0.37. a) I. D. Brown *in Structure and Bonding in Crystals, Vol. 2* (Eds.: M. O'Keefe, A. Navrotsky), Academic Press, London, **1981**; b) I. D. Brown, *The Chemical Bond in Inorganic Chemistry (The Bond Valence Model)*, Oxford University Press, Oxford, **2002**.

[22] a) F. Gingl, W. Hiller, J. Strahle, H. Borgholte, K. Dehnicke, *Z. Anorg. Allg. Chem.* **1991**, *606*, 91; b) R. E. A. Dillon, C. L. Stern, D. F. Shriver, *Chem. Mater.* **2000**, *12*, 1122.

[23] a) W. C. Marsh, N. L. Paddock, C. J. Stewart, J. Trotter, *J. Chem. Soc. D* **1970**, 1190; b) W. C. Marsh, J. Trotter, *J. Chem. Soc. A* **1971**, 1482; c) W. Harrison, J. Trotter, *J. Chem. Soc. Dalton.* **1973**, 61.

[24] H. Oberhammer, W. Zeil, *J. Mol. Struct.* **1973**, *18*, 309.

[25] NBO and natural energy decomposition analysis of alkali-metal complexes of [18]crown-6 indicated that electrostatic interactions and polarization are the dominant bonding forces between the host and guest; the contribution of charge transfer is much less important: E. D. Glending, D. Feller, M. A. Thompson, *J. Am. Chem. Soc.* **1994**, *116*, 10657.

[26] The angle between the O1-O2-O6 and O3-O4-O5 planes in $LiD_6[Al_{PhF}]$ is 144.4(1)°. To investigate the influence of the Li···F and H···F contacts in $LiD_6[Al_{PhF}]$ on the geometry of $[LiD_6]^+$ ion, we calculated the optimized geometry for the hypothetical complex LiD_6F. The initial geometry of LiD_6F contained a planar $[LiD_6]^+$ ion, with a F^- ion bonded to the lithium atom. Optimization led to a bent geometry, confirming that the geometry of the $[LiD_6]^+$ ion in $LiD_6[Al_{PhF}]$ is remarkably affected by strong Li···F and H···F contacts. See Supporting Information for details.

[27] The binding affinity for [18]crown-6 with the alkali-metal cations Li^+, Na^+, K^+, and Rb^+ was taken from ref. [25].

[28] For the vaporization energy ΔE_{vap}, see: D. F. Wilcock, *J. Am. Chem. Soc.* **1946**, *68*, 691. The lattice energies U_L for LiX and LiD_6X (X = $[Al_F]$, I) were estimated using Jenkins and Passmore's volume-based relationship $U_L=2I[(\alpha/V^{1/3})+\beta]$ [kJ mol^{-1}], where $\alpha=117.3$ kJ mol^{-1} nm, $\beta=51.9$ kJ mol^{-1}, V [nm^3] is the volume of the corresponding salt, and I is the sum of the ionic strength: H. D. B. Jenkins, H. K. Roobottom, J. Passmore, L. Glasser, *Inorg. Chem.* **1999**, *38*, 3609.

 © 2006 Wiley-VCH Verlag GmbH & Co. KGaA, Weinheim

Photoelectrochemistry

DOI: 10.1002/anie.200504454

An Organic Photoelectrode Working in the Water Phase: Visible-Light-Induced Dioxygen Evolution by a Perylene Derivative/Cobalt Phthalocyanine Bilayer**

Toshiyuki Abe, Keiji Nagai,* Satoko Kabutomori, Masao Kaneko, Akio Tajiri, and Takayoshi Norimatsu*

Photochemical conversion is one of the most promising renewable energy resources.[1] Great efforts have been made to create a photochemical energy conversion system ever since Fujishima and Honda reported the photoelectrochemical water splitting by the UV-responsive TiO_2 electrode.[2] To increase the efficiency of solar energy conversion, it is desirable to create a photoenergy conversion system that is responsive to visible light across the entire solar spectral region. Inorganic semiconductors have been used as effective photocatalysts for the photolysis water into O_2 and H_2 with visible light at wavelengths under around 500 nm.[3] However, there have been no examples to date of organic photocatalysts as these are susceptible to oxidative decomposition.

Photoelectrochemistry is a promising method to investigate and establish photoenergy conversion systems. Highly ordered molecule-based photoelectrodes have been fabricated by means of self-assembled monolayers (SAMs) and Langmuir–Blodgett (LB) films.[4] We recently reported that the organic bilayer composed of 3,4,9,10-perylenetetracarboxylic acid bisbenzimidazole (PTCBI, an n-type semiconductor) and 29*H*,31*H*-phthalocyanine (H_2Pc, a p-type semiconductor) can act as a photoanode owing to the photophysical character of the bilayer, whereby oxidation of an aqueous thiol was efficiently induced at the H_2Pc/water interface.[5] Although it has been postulated that organic bilayers are not sufficiently stable for application in water,[6] we have shown the PTCBI/H_2Pc bilayer to function as a stable photoanode in the water phase. However, SAMs, LB films, and the PTCBI/H_2Pc bilayer have not been able to be coupled with electron donation from water (or OH^- ions) even though the oxidation of water molecules (or OH^- ions) into O_2 is a most important process in the production of H_2 in a water photolysis system. Herein we show that an organic bilayer of PTCBI and cobalt(II) phthalocyanine (CoPc, (Figure 1)) can act as a photoanode that is capable of evolving O_2 at the CoPc/water interface. This bilayer could form the basis of a stable and efficient photoelectrochemical water-splitting system.

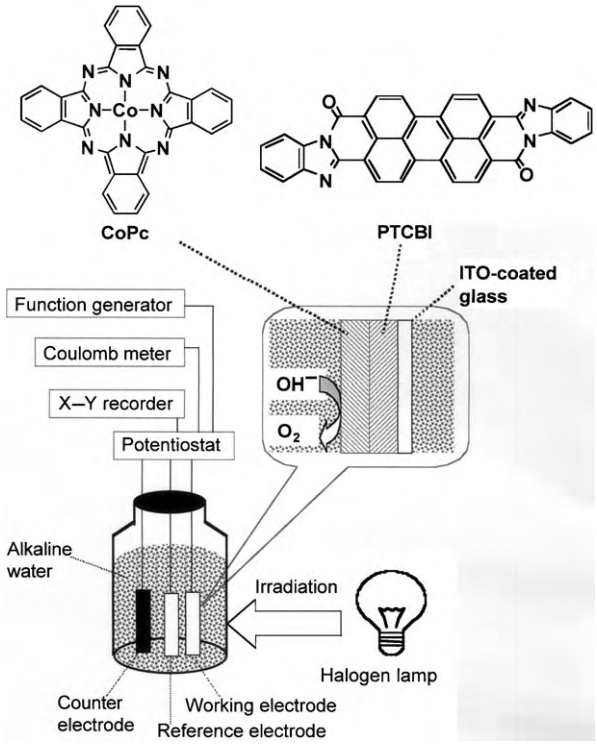

Figure 1. Chemical structures of the perylene derivative PTCBI and cobalt phthalocyanine (CoPc), and schematic illustration of the apparatus for photoelectrochemical measurements.

The photoelectrochemical characteristics of an ITO/PTCBI/CoPc electrode (ITO = indium–tin oxide) that had been soaked in water were investigated first in the presence of a sacrificial electron donor (triethylamine, TEA). The cyclic voltammogram (CV; Figure 2a) showed a large photoanodic current on the order of $\mu A\,cm^{-2}$ at about 0 V (vs. Ag/AgCl), which is attributable to TEA oxidation. However, no anodic current was observed in the dark; moreover, there was almost no photoelectrochemical response at the ITO coated with a single layer of CoPc (denoted as ITO/CoPc). The bilayer composed of perylene and phthalocyanine is known to function as a photovoltaic cell in the dry state;[7,8] moreover, an electrochemical photovoltaic cell consisting of a single-layered perylene photoanode and a Zn–phthalocyanine photocathode in the liquid phase, which also contains a redox couple, has also been constructed.[9] In a separate

[*] Prof. T. Abe, S. Kabutomori, Prof. A. Tajiri
Department of Materials Science and Technology
Hirosaki University
Hirosaki 036-8561 (Japan)
Fax: (+81) 172-39-3580
E-mail: tabe@cc.hirosaki-u.ac.jp
Dr. K. Nagai, Prof. T. Norimatsu
Institute of Laser Engineering (ILE)
Osaka University, Suita 565-0871 (Japan)
Fax: (+81) 6-6877-4799
E-mail: knagai@ile.osaka-u.ac.jp
Prof. M. Kaneko
Faculty of Science
Ibaraki University
Mito 310-8512 (Japan)

[**] This work was partially supported by Grant-in-Aid for Scientific Research (No. 15750110 (T.A.)) and for Scientific Research in Priority Areas (Fundamental Science and Technology of Photofunctional Interfaces, No. 417 (T.A., K.N., and M.K.)) from the Ministry of Education, Culture, Sports, Science, and Technology (MEXT), Japan.

InterScience
© 2006 Wiley-VCH Verlag GmbH & Co. KGaA, Weinheim

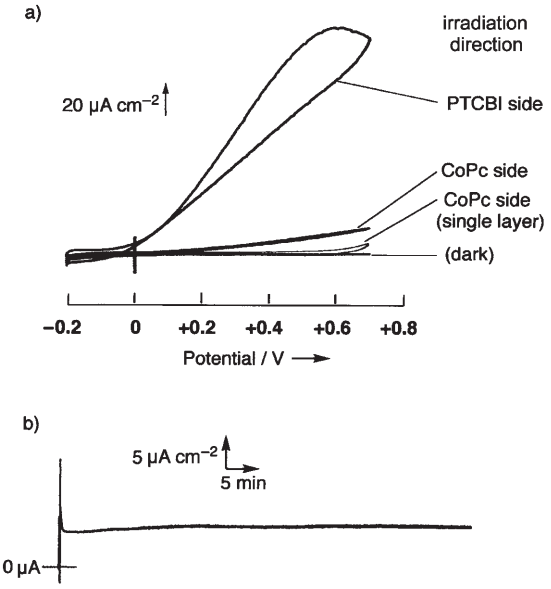

Figure 2. a) Typical CVs at both ITO/PTCBI/CoPc and ITO/CoPc under illumination. Conditions: aqueous NaOH electrolyte with TEA (1.0×10^{-3} mol L^{-1}; pH ≈ 11); film thickness: bilayer 600 nm (PTCBI) and 190 nm (CoPc); CoPc single layer 120 nm; scan rate 20 mV s^{-1}; reference electrode Ag/AgCl. b) Time course of photoanodic current at ITO/PTCBI/CoPc, irradiated from the PTCBI side. Conditions: aqueous NaOH electrolyte with TEA (1.0×10^{-3} mol L^{-1}; pH ≈ 11); film thickness: 600 nm (PTCBI)/190 nm (CoPc); applied potential +0.3 V.

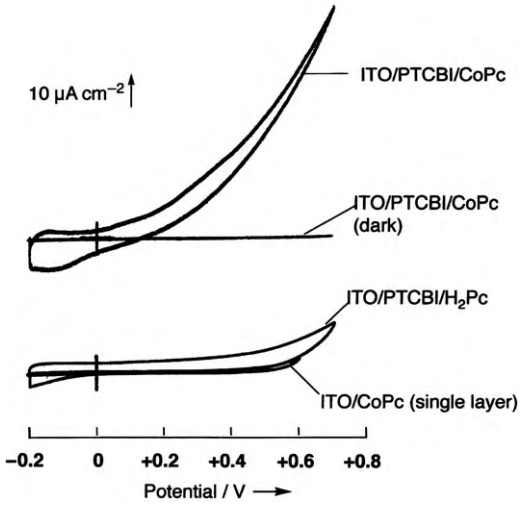

Figure 3. Typical CVs at ITO/PTCBI/CoPc, ITO/CoPc, and ITO/PTCBI/H_2Pc in an aqueous NaOH solution (pH ≈ 11). Conditions: film thickness: PTCBI/CoPc bilayer 350 nm (PTCBI)/190 nm (CoPc); CoPc single layer 70 nm; PTCBI/H_2Pc bilayer 470 nm (PTCBI)/130 nm (H_2Pc); scan rate 20 mV s^{-1}; reference electrode Ag/AgCl.

Table 1: Data for the photoelectrochemical photolysis of water at a ITO/PTCBI/CoPc electrode.[a]

Run	Bias Potential [V vs. Ag/AgCl]	*t* [h]	O_2 [μL]	H_2 [μL]	TON [h^{-1}]
1	+0.3	3	9.65	20.8	2.0×10^3
2	+0.4	3	17.0	32.6	3.5×10^3
3[b]	+0.4	3	0	0	

[a] Conditions: film thickness 160 nm (PTCBI)/90 nm (CoPc); alkaline (NaOH) electrolyte (pH 11). [b] The potentiostatic electrolysis was carried out in the dark.

experiment, we also observed a photovoltage of approximately 0.5 V in a dry cell of the PTCBI/CoPc bilayer; thus, it appears that a p–n junction is formed at the interface of this bilayer. Therefore, the generation of a photoanodic current at the CoPc/water interface (shown in Figure 2a) may be coupled with hole conduction by the CoPc layer. CVs were also measured with different directions of the incident irradiation, and this showed that only a small photocurrent is generated when the cell is irradiated on the CoPc side. The dependence of the CV on the irradiation direction suggests that the photoanodic current generation cannot be induced by absorption of the whole layer of PTCBI/CoPc. The origin of the photocurrent generated at the ITO/PTCBI/CoPc electrode is discussed below. The time course of the photocurrent at the photoanode was measured in the presence of TEA (Figure 2b). It shows that the present organic bilayer can exhibit a stable photoelectrochemical response as a photoelectrode even in the water phase.

In the absence of TEA in the water phase, the photoanodic current is coupled with electron donation from the conversion of OH^- into O_2; however, a noticeable photoelectrochemical response could not be seen at either ITO/CoPc or ITO/PTCBI/H_2Pc (Figure 3). Potentiostatic electrolysis at the ITO/PTCBI/CoPc electrode was conducted in alkaline water free of the sacrificial reagent (pH 11). Table 1 shows the results of the potentiostatic electrolysis. The stoichiometric photoelectrochemical splitting of water into O_2 and H_2 took place at an applied bias potential lower than the formal potential (ca. +0.38 V vs. Ag/AgCl for the O_2/OH^- couple); that is, O_2 was generated by highly efficient photocatalysis by CoPc at the photoanode and H_2 was yielded concurrently at the counter electrode. In determining the turnover number (TON) for the photocatalytic ability of CoPc for O_2 evolution, the number of CoPc molecules exposed on the electrode surface (area 1 cm^2) was calculated by considering the size of a CoPc molecule.[10] The TON was increased by applying a higher bias potential to the bilayer. This increase is attributed to the increase of photogenerated carriers coupled with O_2 evolution at the CoPc/water interface. Moreover, the amount of O_2 generated increased with electrolysis time for a constant applied potential of +0.4 V at the bilayer (Figure 4), which shows that continual water photolysis involving O_2 evolution takes place at the CoPc/water interface. The slight deviation from a linear relationship between the amount of generated O_2 with time in Figure 4 may be ascribed to adsorption of O_2 to the CoPc surface or its dissolution into the water phase, especially in the initial stage of the electrolysis. Potentiostatic electrolysis was also carried out in >95% $H_2{}^{18}O$ (pH 11).[11a] Mass spectrometry after electrolysis confirmed the formation of $^{18}O^{18}O$ from $H_2{}^{18}O$ (there was almost no formation of $^{16}O^{18}O$ (<1% w.r.t. $^{18}O^{18}O$) and $^{16}O^{16}O$ (<1% w.r.t. $^{18}O^{18}O$)),[11b] which shows that the evolved O_2 originates from water. To our knowledge, this is the first example of visible-light-induced O_2 evolution by CoPc. Figure 5 presents a schematic energy diagram for

 © 2006 Wiley-VCH Verlag GmbH & Co. KGaA, Weinheim

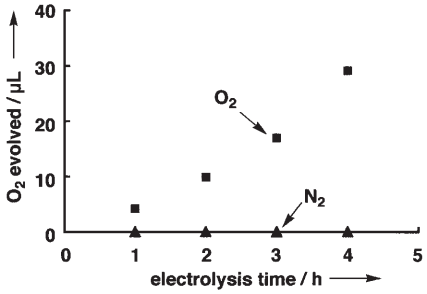

Figure 4. Time course of the amount of O_2 evolved at ITO/PTCBI/CoPc in an aqueous NaOH solution (pH ≈ 11). Conditions: applied potential +0.4 V; film thickness: 160 nm (PTCBI)/90 nm (CoPc); irradiated from the PTCBI side.

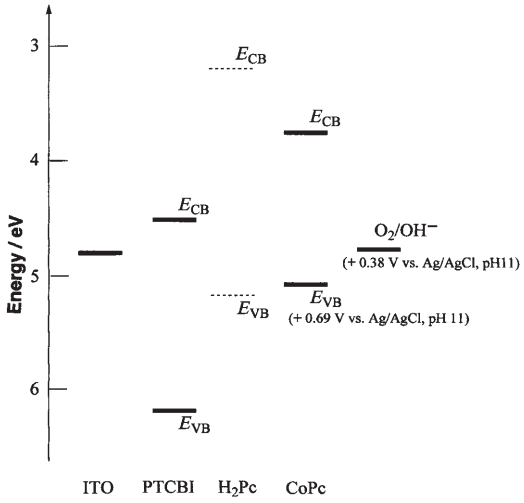

Figure 5. Schematic energy diagram for O_2 evolution at the CoPc/water interface. E_{VB} and E_{CB} denote the energy levels of the valence and conduction bands, respectively.

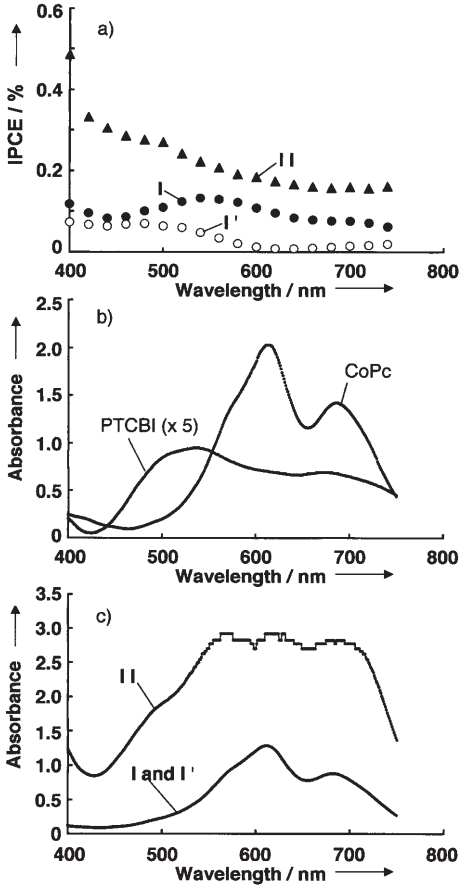

Figure 6. a) Action spectra for photocurrent generated at ITO/PTCBI/CoPc (● for I, ○ for I′, and ▲ for II). Conditions: film thickness: I and I′ 55 nm (PTCBI)/105 nm (CoPc); II 605 nm (PTCBI)/190 nm (CoPc); applied potential +0.3 V; aqueous NaOH electrolyte containing TEA (5×10^{-3} mol L^{-1}; pH ≈ 11). b) Absorption spectra of PTCBI and CoPc. Film thickness: PTCBI 60 nm; CoPc 190 nm. c) Absorption spectra of PTCBI/CoPc bilayer for I, I′, and II. IPCE = incident photon-to-current conversion efficiency.

the O_2 evolution at the CoPc/water interface. In view of the energy levels for ITO,[12] PTCBI,[12] CoPc,[13] and the O_2/OH^- redox couple, the oxidative power photogenerated at the CoPc/water interface is high enough to evolve O_2 from OH^-. Although the energy level of the valence band (E_{VB}) for H_2Pc is close to that of CoPc,[13a] no evolution of O_2 has been confirmed at the photoanode of the PTCBI/H_2Pc bilayer.[5] In the present bilayer, an inner-sphere interaction between the OH^- and Co^{III} ions can be expected, especially at the pH employed,[13b] and this may be a crucial factor in enabling O_2 evolution.

To investigate the origin of the photocurrent generated at the CoPc/water interface, action spectra for the photocurrent were measured with respect to both the direction of the incident light and the thickness of the film; these are compared with the absorption spectra of PTCBI, CoPc, and the bilayer in Figure 6. First, the PTCBI side was irradiated with monochromatic light (I and II in Figure 6a). A photocurrent was found to be generated for a thin PTCBI layer (I) over the wavelength range employed, and the resulting action spectrum resembled the absorption spectrum of PTCBI (Figure 6b). The action spectrum was also measured for a thick PTCBI layer (II), and the photocurrent was larger than for I. However, the action spectrum for irradiation from the CoPc side of I, (I′; Figure 6a) differed noticeably from that of I. At wavelengths longer than 550 nm, where the absorption of CoPc (Figure 6b) is large, only a small photocurrent was generated, which suggests that absorption by CoPc does not result in photocurrent generation. The action spectra shown in Figure 6a do not correspond with the absorption spectrum of the PTCBI/CoPc bilayer (Figure 6c). Thus, the photocurrent is not generated by visible-light absorption by the whole PTCBI/CoPc bilayer, but rather by absorption by only the PTCBI layer, in accord with the case for the PTCBI/H_2Pc photoanode.[5]

The role of CoPc is of note in comparing the present photoanodic characteristics with the conventional ones. Firstly, oxidative power can be generated at the CoPc/water interface through p-type photoconduction by CoPc; that is, the photoelectrode characteristic of the PTCBI/CoPc bilayer differs from that of the CoPc single layer, in which photoreduction can be induced at the solid/liquid interface.[14] Secondly, the hole-doped CoPc (Co^{III}Pc) can efficiently

 © 2006 Wiley-VCH Verlag GmbH & Co. KGaA, Weinheim

activate OH^- for O_2 evolution through an inner-sphere interaction; this differs from the PTCBI/H_2Pc bilayer, which does not lead to evolution of O_2 at the solid/liquid interface. The organic PTCBI/CoPc bilayer acts as a stable photocatalyst for multiple-electron oxidation that is responsive to visible light over a wide range of wavelengths and could constitute an essential part of an artificial photosynthetic system.

Experimental Section

PTCBI was prepared and purified by a previously described method.[15] CoPc was purchased from Tokyo Kasei Kogyo Co., Ltd. ITO-coated glass (sheet resistance 13 $\Omega\,cm^{-2}$; transmittance 85%; thickness of the coated indium–tin oxide 110 nm) was obtained from the Nippon Sheet Glass Co., Ltd. The PTCBI/CoPc bilayer was prepared by vapor deposition (degree of the vacuum $< 1\times10^{-3}$ Pa; deposition speed 0.05 $nm\,s^{-1}$) and consisted of PTCBI coated on an ITO glass plate with CoPc coated on top of the PTCBI layer (denoted as ITO/PTCBI/CoPc). The temperature at the ITO plate was not controlled during the vapor deposition. Absorption spectra were measured with a Hitachi U-2010 spectrophotometer. The resulting absorption spectra of both PTCBI and CoPc were identical to those reported earlier,[7,16] and their absorption coefficients indicated the thickness of the film employed (the aggregation structure of the CoPc single layer can also be identified from the absorption spectrum; that is, the polymorph of CoPc is assignable to the alpha phase, which is also supported by an earlier study[16]). Since the additivity of the absorption coefficients is considered to be held on the visible absorption spectrum of the bilayer, the thickness of each layer was estimated by the solving simultaneous equations for the absorbance at two distinct wavelengths.

An electrochemical glass cell was equipped with the modified ITO working electrode (effective area 1 cm^2), a spiral Pt counter electrode, and an Ag/AgCl (in saturated KCl electrolyte) reference electrode. The complete photoelectrochemical study was carried out in alkaline water (pH 11) under an Ar atmosphere by using a potentiostat (Hokuto Denko, HA-301) with a function generator (Hokuto Denko, HB-104), a coulomb meter (Hokuto Denko, HF-201), and an X–Y recorder (GRAPHTEC, WX-4000) under illumination. A 150-W halogen lamp (light intensity ca. 70 $mW\,cm^{-2}$) was used as a light source under typical conditions. The procedure of the photoelectrochemical measurement is shown schematically in Figure 1. The action spectra for the photocurrent were measured by using a halogen lamp (300 W) as the light source in combination with a monochromator (SOMA OPTICS, LTD., S-10). The light intensity was measured by using a power meter (type 2A, OPHIR JAPAN, LTD.). The IPCE value was calculated with Equation (1), in which I is

$$\text{IPCE}\ (\%) = ([I/e]/[W/\varepsilon])\,100 \qquad (1)$$

the photocurrent density (measured in $A\,cm^{-2}$), e is the elementary electric charge (in C), W is the light intensity (in $W\,cm^{-2}$), and ε is the photon energy. In the present study, the effect of the reflection of the incident light from the glass surface was not considered (i.e., the light intensity was not corrected).

The production of O_2 and H_2 was analyzed with a thermal conductivity detector (TCD) gas chromatograph (Shimadzu, GC-8A) with a 5-Å molecular sieve column and Ar carrier gas. The gaseous products were quantified by a chromatogram analyzer (Shimadzu, C-R8A). The Supporting Information contains details of the quantification of O_2 and shows that there was no contamination of O_2 from air in the present work.

Received: December 15, 2005
Published online: March 20, 2006

Keywords: dioxygen evolution · photocatalysis · photoelectrochemistry · phthalocyanines · semiconductors

[1] a) M. Kaneko, I. Okura in *Photocatalysis* (Eds.: M. Kaneko, I. Okura), Kohdansha-Springer, Tokyo, **2002**, pp. 1–5; b) T. Abe, M. Kaneko, *Prog. Polym. Sci.* **2003**, *28*, 1441–1488.
[2] A. Fujishima, K. Honda, *Nature* **1972**, *238*, 37–40.
[3] a) Z. Zou, J. Ye, K. Sayama, H. Arakawa, *Nature* **2001**, *414*, 625–627; b) S. U. M. Khan, M. Al-Shahry, W. B. Ingler, Jr., *Science* **2002**, *297*, 2243–2245.
[4] a) G. R. Torres, E. Dupart, C. Mingotaud, S. Ravaine, *J. Phys. Chem. B* **2000**, *104*, 9487–9490; b) E. Soto, J. C. MacDonald, C. G. F. Cooper, W. G. McGimpsey, *J. Am. Chem. Soc.* **2003**, *125*, 2838–2839; c) T. Hasobe, H. Imahori, P. V. Kamat, T.-K. Ahn, S.-K. Kim, D. Kim, A. Fujimoto, T. Hirakawa, S. Fukuzumi, *J. Am. Chem. Soc.* ***2005****, 127*, 1216–1228; d) S. Yang, L. Fan, S. Yang, *J. Phys. Chem. B* **2004**, *108*, 4394–4404.
[5] T. Abe, K. Nagai, M. Kaneko, T. Okubo, K. Sekimoto, A. Tajiri, T. Norimatsu, *ChemPhysChem* **2004**, *5*, 716–720.
[6] S. R. Forrest, *Chem. Rev.* **1997**, *97*, 1793–1896.
[7] T. Morikawa, C. Adachi, T. Tsutsui, S. Saito, *Nippon Kagaku Kaishi* **1990**, 962–967.
[8] a) C. W. Tang, *Appl. Phys. Lett.* **1986**, *48*, 183–185; b) D. Wöhrle, L. Kreienhoop, G. Schnurpfeil, J. Elbe, B. Tennigkeit, S. Hiller, D. Schlettwein, *J. Mater. Chem.* **1995**, *5*, 1819–1824; c) D. Wöhrle, L. Kreienhoop, D. Schlettwein in *Phthalocyanines, Properties and Applications* (Eds.: C. C. Leznoff, A. B. P. Lever), VCH, New York, **1996**, pp. 219–284.
[9] T. Oekermann, D. Schlettwein, D. Wöhrle, *J. Appl. Electrochem.* **1997**, *27*, 1172–1178.
[10] B. Böttger, U. Schindewolf, D. Möbius, J. L. Ávila, M. T. Martín, R. Rodríguez-Amaro, *Langmuir* **1998**, *14*, 5188–5194.
[11] a) For the ^{18}O-isotopic labeling study, >95% ^{18}O-labeled water ($H_2{}^{18}O$) was purchased from Cambridge Isotope Laboratories, Inc. Potentiostatic electrolysis was run by applying a bias potential of +0.4 V to ITO/PTCBI/CoPc under illumination for 3 h in a He atmosphere. The gaseous products were analyzed by a mass spectrograph (Shimadzu, QP2010) operated in the electron-ionization mode; b) In a control experiment in which an electrochemical cell was allowed to stand for 3 h in the dark under a He atmosphere, no $^{18}O^{18}O$ was detected.
[12] A. Yakimov, S. R. Forrest, *Appl. Phys. Lett.* **2002**, *80*, 1667–1669.
[13] a) R. O. Loutfy, Y. C. Cheng, *J. Chem. Phys.* **1980**, *73*, 2902–2910; b) J. H. Zagal, M. A. Gulppi, C. Depretz, D. Lelièvre, *J. Porphyrins Phthalocyanines* **1999**, *3*, 355–363.
[14] J. R. Premkumar, R. Ramaraj, *Chem. Commun.* **1997**, 343–344.
[15] T. Maki, H. Hashimoto, *Bull. Chem. Soc. Jpn.* **1952**, *25*, 411–413.
[16] N. Ohta, M. Gomi, *Jpn. J. Appl. Phys.* **2000**, *39(7A)*, 4195–4197.

 © 2006 Wiley-VCH Verlag GmbH & Co. KGaA, Weinheim

Polymer Chemistry

DOI: 10.1002/anie.200600058

Highly Active, Productive, and Syndiospecific Yttrium Initiators for the Polymerization of Racemic β-Butyrolactone**

Abderramane Amgoune, Christophe M. Thomas, Simona Ilinca, Thierry Roisnel, and Jean-François Carpentier**

Biodegradable polymers have recently gained great attention as a replacement for conventional synthetic materials.[1] Among the new biodegradable polymers that have been developed during the last decade,[2] polyhydroxyalkanoates (PHAs) are of particular interest.[3] These materials combine the film-barrier properties of polyesters with the mechanical performance properties of petroleum-based polyethylene and polypropylene. The most common PHA is poly(3-hydroxybutyrate) (PHB), which is an isotactic, highly crystalline thermoplastic polyester produced by various bacteria and algae. One of the most convenient and promising synthetic routes to PHAs uses metal initiators to effect the ring-opening polymerization (ROP) of β-butyrolactone (BBL), where the relief of ring strain is the driving force for polymerization.[2a] Highly isotactic (*R*)- or (*S*)-PHB can be obtained when optically pure (*R*)- or (*S*)-BBL is involved,[4] while use of a racemic (*rac*) mixture of BBL gives rise to atactic PHB[5] and PHB enriched in isotactic[6] or syndiotactic[7] diads. However, most initiators are extremely slow and produce low-molecular-weight PHB. Although some initiators polymerize BBL with excellent rates,[8] stereospecific polymerization of *rac*-BBL remains a challenge. Recently, we reported that well-defined single-site bis(phenolate) complexes of Group 3 metals are highly active initiators in the synthesis of heterotactic and syndiotactic poly(lactic acid) from *rac*-lactide and *meso*-lactide, respectively.[9] Herein, we report a highly active and stereoselective initiator for the polymerization of *rac*-BBL, generating highly syndiotactic PHB.

The high lactide polymerization activities observed with the yttrium initiators **1a,b** and **2a,b** led us to investigate these complexes for the ROP of *rac*-BBL (Scheme 1 and Scheme 2).[9b] The solution-state structures of **1a** and **2a** were recently reported,[9b] and these structures are now supported by the X-ray crystal structure of **1a** (Figure 1).[10] Complex **1a**

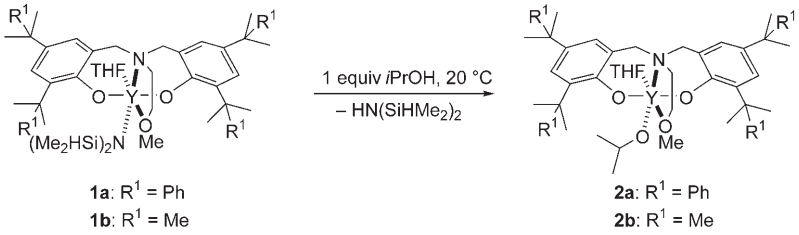

Scheme 1. Synthesis of complexes **1** and **2**.

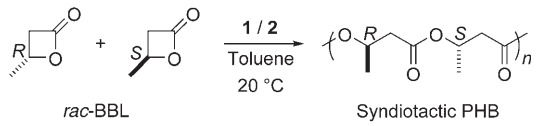

Scheme 2. Synthesis of syndiotactic PHB.

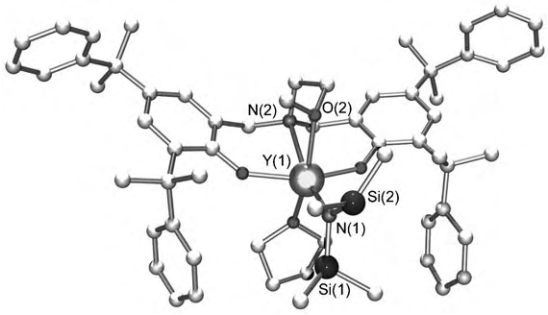

Figure 1. Crystal structure of complex **1a**; all hydrogen atoms and solvent molecules are omitted for clarity.

adopts a distorted octahedral coordination geometry about the yttrium atom with all four donors of the bis(phenolate) ligand bound to the metal center. One THF ligand and one bis(dimethylsilyl)amido group occupy the remaining *cis* positions.

Initial polymerizations were performed using 0.5 mol% of **1a,b** or in situ generated **2a,b** with commercially available *rac*-BBL. Complexes **1a,b** and **2a,b** are active initiators for the controlled ROP of *rac*-BBL under mild conditions. However, as polymerizations of *rac*-BBL with **2a,b** proceed more rapidly than with **1a,b**, we decided to explore this reaction by using the former complexes (Table 1).[11] We observed a strong influence of the solvent. For [BBL]/[**2a**] = 200, polymerization in toluene and chlorobenzene reached 97% conversion in less than 1 minute (Table 1, entries 1, 2),

[*] A. Amgoune, Dr. C. M. Thomas, S. Ilinca, Prof. Dr. J.-F. Carpentier
Organométalliques et Catalyse
Institut de Chimie de Rennes
Université de Rennes 1
35042 Rennes (France)
Fax: (+33) 2-2323-6939
E-mail: christophe.thomas@univ-rennes1.fr
jean-francois.carpentier@univ-rennes1.fr
Dr. T. Roisnel
Centre de Diffractométrie X
Institut de Chimie de Rennes
Université de Rennes 1
35042 Rennes (France)

[**] This research was financially supported in part by the Region Bretagne (grant-in-aid COPOBIO to A.A.). We thank A. Bondon (University of Rennes 1) for NMR experiments.

Supporting information for this article is available on the WWW under http://www.angewandte.org or from the author.

InterScience © 2006 Wiley-VCH Verlag GmbH & Co. KGaA, Weinheim

Table 1: Syndiospecific polymerization of *rac*-butyrolactone.[a]

Entry	Complex	[BBL]/[Y]	[BBL] [M]	Solvent	t [min]	Yield [%][b]	M_n [g mol^{-1}][c]	PDI[c]	P_r[d]	T_m [°C][e]
1	**2a**	200	2.44	Toluene	1	98	22600	1.15	0.88	154
2	**2a**	200	2.44	C_6H_5Cl	1	95	24600	1.15	0.84	158
3	**2a**	200	2.44	THF	120	98	27400	1.03	0.83	133
4	**2a**	400	2.44	Toluene	1	98	26100	1.06	0.89	157
5	**2a**	400	1.00	Toluene	10	98	37400	1.14	0.90	167
6	**2a**	400	4.80	Toluene	4	95	36100	1.08	0.87	150
7[f]	**2a**	400	1.00	Toluene	720	98	37100	1.10	0.94	178
8	**2a**	600	2.44	Toluene	5	98	47200	1.10	0.88	155
9	**2a**	1000	neat	–	5	95	48600	1.16	0.81	142
10	**2a**	2000	8.80	Toluene	18	87	39900	1.18	0.87	156
11	$Y[N(SiHMe_2)_2]_3(THF)_2$	400	2.44	Toluene	4320	94	27700	1.22	0.55	95
12	"$Y(OiPr)_3$"	400	2.44	Toluene	120	95	26400	1.27	0.51	91
13	**2b**	400	2.44	Toluene	2	95	33900	1.10	0.81	138

[a] All reactions were performed at 20 °C (except for Entry 7). [b] As determined by the integration of methine ^{1}H NMR resonances of *rac*-BBL and PHB. [c] M_n and M_w/M_n of polymer determined by size-exclusion chromatography in $CHCl_3$ at room temperature using polystyrene standards. PDI = polydispersity index. [d] P_r is the probability of racemic linkages between monomer units and is determined from the carbonyl region of the $^{13}C\{^1H\}$ NMR spectrum. [e] Determined by differential scanning calorimetry (DSC; second scan). [f] Reaction run at −20 °C.

while polymerization in THF led to 98% conversion within 2 h (Table 1, entry 3). Decreasing the concentration of monomer resulted in a substantial decrease in the rate of polymerization (Table 1, entries 4, 5). All other polymerization reactions were therefore preferably conducted in toluene at a concentration of *rac*-BBL of 2.44 M. Several reactions were also performed by changing the monomer-to-metal ratio. For instance, complete conversion of 400 equivalents of *rac*-BBL was achieved within 1 minute at room temperature (turnover frequency, TOF = 24000 h^{-1}; Table 1, entry 4). The activity of this system is thus more than one order of magnitude higher than that of yttrium 2-methoxyethoxide as previously reported by Spassky and co-workers under similar conditions.[12] To confirm the influence of the bis(phenolate) ligand on the activity, control experiments were carried out with $Y[N(SiHMe_2)_2]_3(THF)_2$ and "$Y(OiPr)_3$" (generated in situ) as initiators (Table 1, entries 11, 12). The results show that **2a** indeed displays a significantly higher activity than the two reference systems when polymerizations are carried out in toluene. The yttrium alkoxide **2a** can polymerize 1000 equivalents of monomer within 5 minutes at 20 °C in neat BBL resulting in TOF = 12000 h^{-1} (Table 1, entry 9), and 2000 equivalents at high concentrations of monomer in less than 20 minutes (TOF = 6000 h^{-1}; Table 1, entry 10).

For [BBL]/[**2a**] < 1000, the resultant polymers reveal narrow molecular-weight distributions and experimental number-average molecular masses (M_n) close to the theoretical ones. However, for higher ratios, experimental M_n values do not correspond well with calculated M_n values. This mismatch possibly arises from chain-transfer processes or poor correlation between the polystyrene calibration of the gel permeation chromatograph and the actual molecular weights of the PHB chains, as already reported by Coates and co-workers.[8]

Microstructural analysis by ^{13}C NMR spectroscopy of the different PHBs formed from *rac*-BBL revealed that complexes **2** exert a significant influence at room temperature on the tacticity of the polymer formed (Scheme 2). On the basis of prior ^{13}C NMR assignments of the carbonyl region of PHB, the upfield and downfield signals in the carbonyl region correspond to the *meso* (*m*) diad sequences, *R*–*R* and *S*–*S*, and the racemic (*r*) diad sequences, *R*–*S* and *S*–*R*, respectively.[13] Our PHBs feature a strong contribution correlating to *r*-centered diads ($\delta = 169.16$ ppm), indicative of syndiotactic PHB (Figure 2). Expansion of the methylene region shows

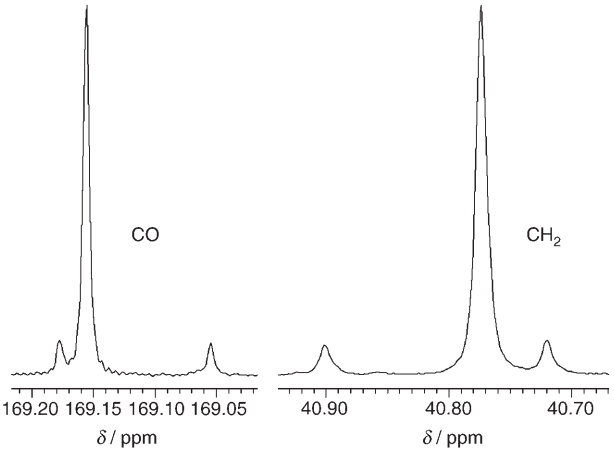

Figure 2. Carbonyl and methylene regions of the ^{13}C NMR spectrum (125 MHz, $CDCl_3$, 40 °C) of PHB prepared by polymerization of *rac*-BBL using complex **2a** (see Table 1, entry 7).

four peaks that correspond to triad sensitivity (Figure 2). We correlated the most intense resonance at $\delta = 40.77$ ppm to the *rr* triad, and we attributed the resonances at $\delta = 40.72$ and 40.90 ppm to the *mr* and the *rm* triads, respectively. The remaining *mm* triad at $\delta = 40.85$ ppm is almost negligible.[14] Statistical analysis confirms a chain-end control mechanism (See Supporting Information). We observed differences in the microstructure of the PHBs depending on the nature of the solvent. While polymerization of *rac*-BBL in toluene gave PHB with nearly 90% of syndiotactic enchainment (Table 1, entry 1), polymerizations in THF and chlorobenzene gave

 © 2006 Wiley-VCH Verlag GmbH & Co. KGaA, Weinheim

83% and 84%, respectively, of syndiotacticity (Table 1, entries 2 and 3). At −20°C, polymerization proceeded slowly but the resulting PHB revealed a higher degree of syndiotacticity ($P_r = 0.94$; Table 1, entry 7). As already observed for the polymerization of *rac*-lactide,[9b] complex **2b**, which bears *tert*-butyl groups at the phenolate rings, reveals a lower selectivity for syndiotactic PHB ($P_r = 0.81$; Table 1, entry 13). This decrease in tacticity is consistent with previous observations that ligand substituents are primordial for stereochemical control through a chain-end control mechanism.[15]

DSC measurements of selected PHB samples showed the strong influence of the stereochemistry on the melting temperature (T_m), which increases with the degree of syndiotacticity (Table 1, entries 2, 7, 9, 10). For the most syndiotactic polymer, T_m is around 178°C, that is, the highest melting temperature reported so far for syndiotactic PHB.[13,16] The DSC traces display a single, sharp transition endotherm at high temperature, demonstrating the formation of a uniform crystalline ordering in the solid state, which may indicate a narrower dispersion of stereochemical chain sequences.

It is well established that the ring opening of BBL by metal alkoxides can proceed by a coordination–insertion mechanism or an anionic mechanism.[8] To determine the route involved in the ROP of BBL with **2a**, reactions were conducted with [BBL]/[Y] ratios of less than 10. The unambiguous identification by ^{1}H NMR spectroscopy of the -O*CH*$(CH_3)_2$ end group at $\delta = 5.00$ ppm confirmed that the BBL ring is cleaved at the acyl–oxygen bond and inserted into the metal–isopropoxide bond. Furthermore, *trans*-crotonate (and carboxy) groups were not observed in the ^{1}H NMR spectrum, confirming the coordination–insertion mechanism. Indeed an anionic mechanism leads generally to a high concentration of crotonate.[8]

In conclusion, the yttrium alkoxide complex **2a** exhibits the highest activity and greatest stereoselectivity for syndiospecific polymerization of *rac*-BBL to date. These results suggest a number of new avenues for biodegradable polymers.

Received: January 6, 2006
Published online: March 20, 2006

Keywords: homogeneous catalysis · polymers · ring-opening polymerization · tacticity · yttrium

[1] R. E. Drumright, P. R. Gruber, D. E. Henton, *Adv. Mater.* **2000**, *12*, 1841–1846.
[2] a) M. Okada, *Prog. Polym. Sci.* **2002**, *27*, 87–133; b) O. Dechy-Cabaret, B. Martin-Vaca, D. Bourissou, *Chem. Rev.* **2004**, *104*, 6147–6176; c) J. Wu, T.-L. Yu, C.-T. Chen, C.-C. Lin, *Coord. Chem. Rev.* **2006**, *250*, 602–626.
[3] a) K. E. Ulrich, S. M. Cannizzaro, R. S. Langer, K. M. Shakesheff, *Chem. Rev.* **1999**, *99*, 3181–3198; b) H.-M. Müller, D. Seebach, *Angew. Chem.* **1993**, *105*, 483–509; *Angew. Chem. Int. Ed. Engl.* **1993**, *32*, 477–502; c) K. Sudesh, H. Abe, Y. Doi, *Progr. Polym. Sci.* **2000**, *25*, 1503–1555.
[4] Y. Yori, M. Suzuki, A. Yamaguchi, T. Nishishita, *Macromolecules* **1993**, *26*, 5533–5534.
[5] a) N. C. Billingham, M. G. Proctor, J. D. Smith, *J. Organomet. Chem.* **1988**, *341*, 83–93; b) M. Moeller, R. Kånge, J. L. Hedrick, *J. Polym. Sci. Part A* **2000**, *38*, 2067–2074.
[6] a) B. Wu, R. W. Lenz, *Macromolecules* **1998**, *31*, 3473–3477; b) S. Bloembergen, D. A. Holden, T. L. Bluhm, G. K. Hamer, R. H. Marchessault, *Macromolecules* **1989**, *22*, 1656–1663.
[7] a) Y. Hori, T. Hagiwara, *Int. J. Biol. Macromol.* **1999**, *25*, 237–245; b) H. R. Kricheldorf, S. Eggerstedt, *Macromolecules* **1997**, *30*, 5693–5697.
[8] L. R. Rieth, D. R. Moore, E. B. Lobkovsky, G. W. Coates, *J. Am. Chem. Soc.* **2002**, *124*, 15239–15248.
[9] a) C.-X. Cai, A. Amgoune, C. W. Lehmann, J.-F. Carpentier, *Chem. Commun.* **2004**, 330–331; b) A. Amgoune, C. M. Thomas, T. Roisnel, J.-F. Carpentier, *Chem. Eur. J.* **2006**, *12*, 169–179.
[10] Diffraction data were collected at 100 K using an APEX 2 AXS-Bruker diffractometer with graphite-monochromatized $Mo_{K\alpha}$ radiation ($\lambda = 0.71073$ Å). The value of R_{int} was found to be greater than 0.15 because the crystal was weakly diffracting, so that a large proportion of essentially "non-observed" reflections were used in the refinement. Crystal data for **1a**: $C_{61}H_{77}N_2O_4Si_2Y \cdot C_7H_8$, $M_r = 1139.47$, white blocks, $0.25 \times 0.05 \times 0.05$ mm^3, monoclinic, space group $P2_1/c$, $a = 15.4649(12)$, $b = 20.1003(16)$, $c = 19.7728(14)$ Å, $\alpha = 90$, $\beta = 98.426(3)$, $\gamma = 90°$, $V = 6080.0(8)$ Å^3, $Z = 4$, $\rho_{calcd} = 1.245$ g cm^{-3}, $\mu = 1.048$ mm^{-1}, $F(000) = 2424$, $T = 100(2)$ K, $R_1 = 0.0975$, w$R_2 = 0.3101$, 5286 independent reflections [$2\theta \leq 51.00°$] and 695 parameters. CCDC-294486 (**1a**) contains the supplementary crystallographic data for this paper. These data can be obtained free of charge from The Cambridge Crystallographic Data Centre via www.ccdc.cam.ac.uk/data_request/cif.
[11] Polymerizations with complex **2a** were found to proceed five times faster than with complex **1a**.
[12] A. Le Borgne, C. Pluta, N. Spassky, *Macromol. Rapid Commun.* **1994**, *15*, 955–960.
[13] J. E. Kemnitzer, S. P. McCarthy, R. A. Gross, *Macromolecules* **1993**, *26*, 1221–1229.
[14] For the methyl and methine carbon signals, diad and triad sequences, respectively, were assigned and were in good agreement with the carbonyl and methylene carbon signals. See Supporting Information.
[15] a) B. M. Chamberlain, M. Cheng, D. R. Moore, E. B. Lobkovsky, T. M. Ovitt, G. W. Coates, *J. Am. Chem. Soc.* **2001**, *123*, 3229–3238; b) M. Mitani, R. Furuyama, J.-I. Mohri, J. Saito, S. Ishii, H. Terao, T. Nakano, H. Tanaka, T. Fujita, *J. Am. Chem. Soc.* **2003**, *125*, 4293–4305; c) B. L. Small, M. Brookhart, *Macromolecules* **1999**, *32*, 2120–2130.
[16] a) H. R. Kricheldorf, S.-R. Lee, N. Scharnagi, *Macromolecules* **1994**, *27*, 3139–3146; b) R. A. Gross, Y. Zhang, G. Konrad, R. W. Lenz, *Macromolecules* **1988**, *21*, 2657–2668.

 © 2006 Wiley-VCH Verlag GmbH & Co. KGaA, Weinheim

Reduction

DOI: 10.1002/anie.200600184

Highly Enantioselective Conjugate Reduction of β,β-Disubstituted α,β-Unsaturated Nitriles**

*Daehyung Lee, Daesung Kim, and Jaesook Yun**

Optically active nitrile compounds with a β-stereocenter are versatile synthetic intermediates for a number of biologically active compounds.[1] The nitrile group is a very useful synthetic group that can be transformed into other useful functionalities, such as amine, aldehyde, and carboxylic acid groups; furthermore, the isolation of nitrile-containing natural products continues to increase.[2] Despite recent advances in metal-catalyzed conjugate reductions, the development of asymmetric reductions of conjugated nitriles still remains challenging because of their intrinsic low reactivity[3] and the linearity of the CN group. The two asymmetric examples that we are aware of are the Co-catalyzed conjugate reduction of α,β-unsaturated nitriles[4] and the Rh-catalyzed hydrogenation of α,β-unsaturated nitriles.[5] However, the enantioselectivities achieved by these catalyst systems were significantly lower than those for analogous esters and amides, presumably because of the steric and coordinating environment exerted by the linear nitrile group (Scheme 1).

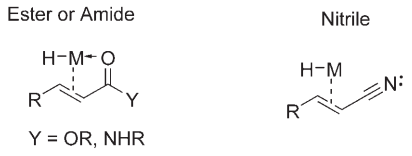

Scheme 1. Comparison of the coordinating environments of α,β-unsaturated esters, amides, and nitriles.

Copper hydride ligated by non-racemic ligands has been used for effecting the asymmetric hydrosilylation of aromatic ketones,[6] imines,[7] enones,[8] α,β-unsaturated esters,[9] and nitroalkenes[10] in the presence of excess hydrosilane. However, an enantioselective asymmetric conjugate reduction method of α,β-unsaturated nitriles catalyzed by copper hydride has not been reported yet. Herein, we report a highly enantioselective conjugation reduction of α,β-unsaturated nitriles employing a $Cu(OAc)_2$/josiphos catalyst.

Recently, we described the first use of air-stable Cu^{II} precursors $Cu(OAc)_2$ and $Cu(OAc)_2{\cdot}H_2O$ for the reproducible generation of copper(I) hydride in copper-catalyzed reduction methodology.[6b,11] In contrast to previous reports of reductions catalyzed by copper hydride by others,[12] an inhibitory effect by the CN functional group on the activity of copper(I) hydride was not observed under our reduction conditions,[6b,13] in which a chelating bisphosphine ligand was used in combination with the copper precursors. On the basis of these results, we started to investigate asymmetric reductions of β-substituted cinnamonitrile (**1a**) using $Cu(OAc)_2$ as the catalytic precursor and a chiral bisphosphine ligand in the presence of polymethylhydrosiloxane (PMHS; Table 1). In initial experiments, C_2-symmetric binaphthyl-based bisphosphine ligands, such as (1,1'-binaphthalene)-2,2'-diylbis(diphenylphosphine)((*S*)-BINAP) and (*R*)-*p*-tol-BINAP, were investigated. The catalyst system prepared from $Cu(OAc)_2$/BINAP was not effective for the reduction of (*E*)-**1a**, as it lost its catalytic activity before the completion of the reaction (Table 1, entry 1). Although the reaction progressed smoothly to completion in 11 h with (*R*)-*p*-tol-BINAP, the saturated nitrile **2a** was produced with only moderate enantiomeric excess (65% *ee*; Table 1, entry 2). This level of enantioselectivity is considerably lower than that achieved for the reduction of analogous esters and enones with copper(I) hydride and the same ligand.[8a,9a] Moreover, when we applied this system to (*Z*)-**1a**, an almost racemic mixture of product (2% *ee*) was obtained (Table 1, entry 3).

Table 1: Asymmetric conjugate reduction of **1a**.[a]

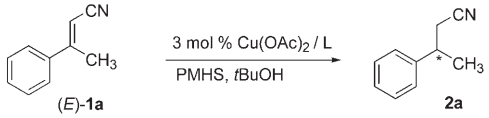

(*E*)-**1a** **2a**

Entry	Substrate	Ligand	*t* [h]	*T* [°C]	Yield [%][b]	*ee* [%][c]
1	(*E*)-**1a**	(*S*)-BINAP	>24[d]	RT	25	65 (*S*)
2	(*E*)-**1a**	(*R*)-*p*-tol-BINAP	11	RT	92	65 (*R*)
3	(*Z*)-**1a**	(*R*)-*p*-tol-BINAP	11	RT	65	2 (*S*)
4	(*E*)-**1a**	(*S,R*)-**3**	**5**	**0**	**92**	**97** (*S*)
5	(*E*)-**1a**	(*R,S*)-**4**	24	0	90	65 (*R*)
6	(*E*)-**1a**	(*R,S*)-**5**	4.5	0	81	96 (*R*)
7[e]	(*E*)-**1a**	(*R,S*)-**5**	12.5	RT	80	95 (*R*)
8[f]	(*Z*)-**1a**	(*R,S*)-**3**	**4.5**	**0**	**91**	**99** (*S*)
9	(*Z*)-**1a**	(*R,S*)-**5**	4.5	RT	87	89 (*S*)

[a] Reaction conditions: $Cu(OAc)_2$ (3 mol%), ligand (3 mol%), PMHS (4 equiv), and *t*BuOH (4 equiv) were used unless otherwise noted. [b] Yield of the isolated product. [c] Determined by chiral HPLC. [d] Incomplete conversion. [e] Catalyst = 1.5 mol%. [f] Ligand = (*R,S*)-josiphos.

We continued our investigation with screening of the commercially available josiphos family of ligands **3**–**5**, which were found to be effective in a number of asymmetric reactions (Scheme 2).[14] Gratifyingly, the use of josiphos ligand **3** dramatically enhanced the enantioselectivity of the reduction of (*E*)-**1a**, thus providing **2a** in 97% *ee* (Table 1, entry 4). Ligand **4** proved to be inferior to the other

[*] D. Lee, D. Kim, Prof. J. Yun
Department of Chemistry and Institute of Basic Science
Sungkyunkwan University
Suwon 440-746 (Korea)
Fax: (+82) 31-290-7075
E-mail: jaesook@skku.edu

[**] This work was supported by a Korea Research Foundation grant funded by the Korean Government (R08-2004-000-10429-0). The LC and GC equipment was supported by the Faculty Research Fund 2005, Sungkyunkwan University. Prof. C. Song and E. Kwon at SKKU are acknowledged for valuable advice and assistance with the chiral analysis.

Supporting information for this article is available on the WWW under http://www.angewandte.org or from the author.

 © 2006 Wiley-VCH Verlag GmbH & Co. KGaA, Weinheim

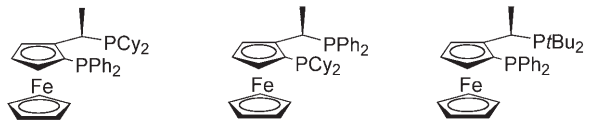

Scheme 2. Chiral ferrocenyl-based bisphosphines.

structurally related bisphosphine ligands in terms of reactivity and enantioselectivity (Table 1, entry 5). Ligand **5**, which possesses *tert*-butyl groups instead of the cyclohexyl groups of the original josiphos ligand **3**, displayed a similar reactivity but yielded the product **2a** with a lower enantiomeric excess (Table 1, entry 6). It is of note that ligand **3** was also highly effective for the reduction of (*Z*)-**1a**, thus affording **2a** in 91% yield and with 99% *ee* (Table 1, entry 8). The reduction of the *E* and *Z* isomers resulted in the formation of opposite enantiomers.

With an established, optimal protocol using ligand **3**, the conjugate reduction of different β-aryl-substituted α,β-unsaturated nitriles was examined, and the results are summarized in Table 2. In general, the reduction of the substrates occurred smoothly at 0°C to give the corresponding chiral saturated nitriles in good yields and with high enantioselectivities. The reduction of Cl- and CH_3-substituted aromatic unsaturated nitriles provides the respective saturated nitrile products in good yield and with high enantiomeric excess (Table 2, entries 1–3). Bulky alkyl substituents (Et, *i*Pr) at the β-position of the nitrile did not affect the efficiency of the process, thus affording reduced products **2d** and **2e** in 98 and 99% *ee*, respectively (Table 2, entries 4 and 5). The substrate **1f** with the phenyl ring substituted at the *ortho* position was reduced with high enantioselectivity as well (Table 2, entry 6). However, the level of enantioselectivity (65% *ee*) obtained with a heteroaromatic pyridyl substrate **1g** was significantly lower than that of the analogous phenyl derivative (Table 2, entry 7). It is presumed that the steric change at the *ortho* position of the aromatic counterpart is the main reason for the lower enantiomeric excess.

Table 2: Enantioselective conjugate reduction of α,β-unsaturated nitriles.[a]

Entry	Substrate	Ligand	*t* [h]	Yield [%][b]	*ee* [%][c]
1	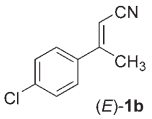 (*E*)-**1b**	(*S*,*R*)-**3**	23	92	97
2	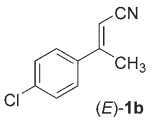 (*E*)-**1b**	(*R*,*S*)-**5**	23	98	94
3	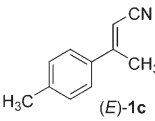 (*E*)-**1c**	(*S*,*R*)-**3**	21	91	95 (*S*)
4	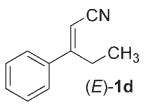 (*E*)-**1d**	(*S*,*R*)-**3**	12	88	98
5	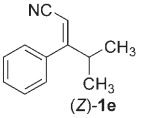 (*Z*)-**1e**	(*S*,*R*)-**3**	10	81	99
6	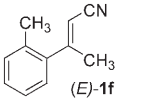 (*E*)-**1f**	(*R*,*S*)-**3**	10	92	98
7	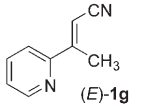 (*E*)-**1g**	(*S*,*R*)-**3**	8.5	96	65

[a] Reaction conditions: $Cu(OAc)_2$ (3 mol%), ligand (3 mol%), PMHS (4 equiv), and *t*BuOH (4 equiv) in toluene at 0°C. [b] Yield of the isolated product. [c] Determined by chiral HPLC.

Currently, we presume that a bisphosphine-ligated copper(I) hydride species is the active catalytic species and that silanes[15] effect the generation of copper(I) hydride from the Cu^{II} precursor. The active copper hydride species reacts with a α,β-unsaturated nitrile to form a new organocopper species, and the intermediate undergoes rapid deprotonation by *t*BuOH to yield the chiral protonated product and a copper alkoxide. The latter then regenerates the active copper hydride catalyst with PMHS.

In summary, we have shown that a highly enantioselective reduction of α,β-unsaturated nitriles can be conducted by using a $Cu(OAc)_2$/josiphos complex as the catalyst under hydrosilylation conditions. This reaction provides access to valuable β-aryl-substituted chiral nitriles in good yields and with excellent enantioselectivities by employing a bench-top stable catalytic precursor and a readily available, commercial bisphosphine ligand. Studies are underway to establish the full scope of this methodology.

Experimental Section

General procedure for the conjugate reduction of α,β-unsaturated nitriles: $Cu(OAc)_2$ (2.72 mg, 0.015 mmol) and ligand (0.015 mmol) were placed in an oven-dried Schlenk tube, and PMHS (0.12 mL, 2 mmol) and toluene (0.5 mL) were added under nitrogen. The reaction mixture was stirred for 5 min at 0°C and then α,β-unsaturated nitrile (0.5 mmol) was added, followed by *t*BuOH (0.19 mL, 2.0 mmol). The reaction tube was washed with toluene (0.5 mL) and sealed, and the reaction mixture was stirred until no starting material was detected by TLC analysis. The reaction mixture was quenched with water and transferred into a round-bottom flask with the aid of Et_2O (10 mL), and then NaOH (2.5 M, 1.2 mL) was added. The biphasic mixture was stirred vigorously for 0.5 h. The layers were separated and the aqueous layer was extracted with Et_2O (3 × 20 mL). The combined organic layers were washed with brine, dried over $MgSO_4$, and concentrated. The product was purified by chromatography on silica gel or Kugelrohr distillation.

Received: January 17, 2006
Published online: March 20, 2006

Keywords: asymmetric catalysis · copper · enantioselectivity · nitriles · reduction

 © 2006 Wiley-VCH Verlag GmbH & Co. KGaA, Weinheim

[1] a) D. C. Harrowven, D. D. Pascoe, D. Demurtas, H. O. Bourne, *Angew. Chem.* **2005**, *117*, 1247 – 1248; *Angew. Chem. Int. Ed.* **2005**, *44*, 1221 – 1222; b) L. Banfi, A. Basso, V. Gandolfo, G. Guanti, R. Riva, *Tetrahedron Lett.* **2004**, *45*, 4221 – 4223; c) K. Mori, *Tetrahedron: Asymmetry* **2005**, *16*, 685 – 692; d) M. B. Andrus, E. L. Meredith, E. J. Hicken, B. L. Simmons, R. R. Glancey, W. Ma, *J. Org. Chem.* **2003**, *68*, 8162 – 8169; e) A. Abate, E. Brenna, C. D. Negri, C. Fuganti, S. Serra, *Tetrahedron: Asymmetry* **2002**, *13*, 899 – 904.

[2] F. F. Fleming, *Nat. Prod. Rep.* **1999**, *16*, 597 – 606.

[3] a) E. Keinan, D. Perez, *J. Org. Chem.* **1987**, *52*, 2576 – 2580; b) E. Keinan, N. Greenspoon, *J. Am. Chem. Soc.* **1986**, *108*, 7314 – 7325; c) G. Blay, L. Cardona, B. Garcia, L. Lahoz, J. R. Pedro, *Tetrahedron* **1996**, *52*, 8611 – 8618; d) S. Matsunaga, T. Kinoshita, S. Okada, S. Harada, M. Shibasaki, *J. Am. Chem. Soc.* **2004**, *126*, 7559 – 7570.

[4] M. Misun, A. Pfaltz, *Helv. Chim. Acta.* **1996**, *79*, 961 – 972.

[5] D. Saylik, E. M. Campi, A. C. Donohue, W. R. Jackson, A. J. Robinson, *Tetrahedron: Asymmetry* **2001**, *12*, 657 – 667.

[6] a) B. H. Lipshutz, K. Noson, W. Chrisman, *J. Am. Chem. Soc.* **2001**, *123*, 12917 – 12918; b) D. Lee, J. Yun, *Tetrahedron Lett.* **2004**, *45*, 5415 – 5417.

[7] B. H. Lipshutz, H. Shimizu, *Angew. Chem.* **2004**, *43*, 2228 – 2230; *Angew. Chem. Int. Ed.* **2004**, *43*, 2228 – 2230.

[8] a) Y. Moritani, D. H. Appella, V. Jurkauskas, S. L. Buchwald, *J. Am. Chem. Soc.* **2000**, *122*, 6797 – 6798; b) B. H. Lipshutz, J. M. Servesko, *Angew. Chem.* **2003**, *115*, 4937 – 4940; *Angew. Chem. Int. Ed.* **2003**, *42*, 4789 – 4792.

[9] a) D. H. Appella, Y. Moritani, R. Shintani, E. M. Ferreira, S. L. Buchwald, *J. Am. Chem. Soc.* **1999**, *121*, 9473 – 9474; b) B. H. Lipshutz, J. M. Servesko, B. R. Taft, *J. Am. Chem. Soc.* **2004**, *126*, 8352 – 8353.

[10] a) C. Czekelius, E. M. Carreira, *Angew. Chem.* **2003**, *115*, 4941 – 4943; *Angew. Chem. Int. Ed.* **2003**, *42*, 4793 – 4795; b) C. Czekelius, E. M. Carreira, *Org. Lett.* **2004**, *6*, 4575 – 4577.

[11] D. Lee, J. Yun, *Tetrahedron Lett.* **2005**, *46*, 2037 – 2039.

[12] a) B. H. Lipshutz, K. Noson, W. Chrisman, A. Lower, *J. Am. Chem. Soc.* **2003**, *125*, 8779 – 8789; b) J.-X. Chen, J. F. Daeuble, D. M. Brestensky, J. M. Stryker, *Tetrahedron* **2000**, *56*, 2153 – 2166.

[13] a) D. Kim, B.-M. Park, J. Yun, *Chem. Commun.* **2005**, 1755 – 1757; b) J. Yun, D. Kim, H. Yun, *Chem. Commun.* **2005**, 5181 – 5183.

[14] For brief reviews, see: a) H.-U. Blaser, W. Brieden, B. Pugin, F. Spindler, M. Studer, A. Togni, *Top. Catal.* **2002**, *19*, 3 – 16; b) S. Woodward, *Angew. Chem.* **2005**, *44*, 5696 – 5698; *Angew. Chem. Int. Ed.* **2005**, *44*, 5560 – 5562.

[15] Silanes, such as $PhSiH_3$, Ph_2SiH_2, and PMHS, were effective for the activation of the copper precursor, although alkyl silanes were less effective.

 © 2006 Wiley-VCH Verlag GmbH & Co. KGaA, Weinheim

Homogeneous Catalysis

DOI: 10.1002/anie.200504309

A Ligand-Library Approach to the Highly Efficient Rhodium/Phosphoramidite-Catalyzed Asymmetric Arylation of *N,N*-Dimethylsulfamoyl-Protected Aldimines**

Richard B. C. Jagt, Patrick Y. Toullec, Danny Geerdink, Johannes G. de Vries, Ben L. Feringa,* and Adriaan J. Minnaard**

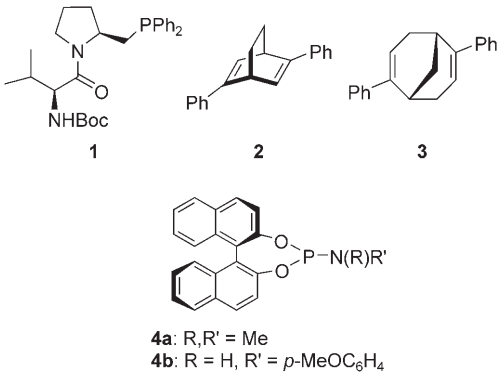

1 2 3

4a: R,R' = Me
4b: R = H, R' = *p*-MeOC$_6$H$_4$

The asymmetric synthesis of diarylmethyl amines is of great importance because they are present in a variety of pharmacologically active structures.[1] Among other methods for performing the catalytic asymmetric synthesis of diarylmethyl amines,[2] the recently developed rhodium-catalyzed asymmetric arylation of aldimines is an important strategy.[3] Excellent enantioselectivities have been reported for the addition of aryl stannane[4] and aryl titanium[5] reagents. Aryl boronic acids have received increasing attention as arylating reagents because they are readily available, stable, and compatible with a large variety of functional groups, and they produce nontoxic by-products.[6,7] So far, three groups have reported on the rhodium(I)-catalyzed asymmetric addition of aryl boron reagents to aldimines. Tomioka and co-workers described the first enantioselective addition of aryl boronic acids and their boroxine trimers to benzaldimines using the chiral amidophosphane ligand **1** (Boc = *tert*-butyloxycarbonyl).[8] Enantioselectivities above 90% were obtained through steric tuning of substituents on both the substrate and the boron reagent. Hayashi and co-workers reported excellent enantioselectivities for the addition of aryl boroxines to *N*-tosyl- and *N*-nosylbenzaldimines employing chiral diene ligands (i.e. **2** and **3**).[9] Recently, Ellman and co-workers reported an example of high enantioselectivity for the addition of aryl boronic acids to *N*-diphenylphosphinoyl benzaldimine using deguphos as a chiral ligand.[10]

From a synthetic point of view, the current methodology still presents some major drawbacks. Often large amounts of boronic acid (2–5 equiv) and catalyst (at least 3 mol%) are required to obtain full conversion. Moreover, the removal of the protecting groups is either not straightforward,[10,11] or requires environmentally unfriendly reagents.[9b]

We envisioned a more efficient and versatile synthetic method for this transformation that relies on the combination of a new catalyst and protecting group. Herein we report the development of a highly active rhodium(I) catalyst that allows the efficient asymmetric synthesis of diarylmethyl amines under mild conditions without extensive hydrolysis of the aryl boronic acid (Scheme 1). Furthermore, we present *N,N*-dimethylsulfamoyl as an inexpensive, low-molecular-weight protecting/activating group for this reaction and describe an efficient method for its removal.[12]

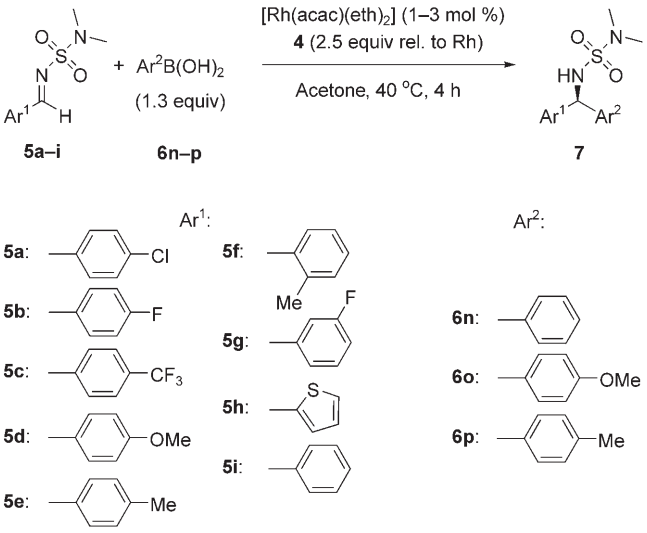

Scheme 1. Rhodium/phosphoramidite-catalyzed addition of aryl boronic acids **6** to *N,N*-dimethylsulfamoyl-protected aldimines **5.** acac = acetylacetonate, eth = ethylene.

We focused on monodentate phosphoramidites **4**,[13] a class of low-cost, readily available chiral ligands, which have been applied successfully in the related rhodium-catalyzed asymmetric conjugate addition of aryl boronic acids to enones.[14] Although it has been observed that the two reactions have different ligand requirements,[9a] phosphoramidites are easily tunable because of their modular composition and are therefore well suited to a combinatorial approach in the design of asymmetric catalysts.[15]

[*] R. B. C. Jagt, Dr. P. Y. Toullec, D. Geerdink, Prof. Dr. J. G. de Vries, Prof. Dr. B. L. Feringa, Dr. A. J. Minnaard
Department of Organic and Molecular Inorganic Chemistry
Stratingh Institute, University of Groningen
Nijenborgh 4, 9747 AG, Groningen (The Netherlands)
Fax: (+31) 50-363-4296
E-mail: j.g.de.vries@rug.nl
b.l.feringa@rug.nl
a.j.minnaard@rug.nl

[**] Financial support from DSM, the Ministry of Economic Affairs, and the Dutch Science Foundation NWO/CW, administered through the CW/Combichem program, is gratefully acknowledged. We thank E. P. Schudde and T. D. Tiemersma-Wegman for technical support.

Supporting information for this article is available on the WWW under http://www.angewandte.org or from the author.

 © 2006 Wiley-VCH Verlag GmbH & Co. KGaA, Weinheim

Dimethylsulfamoyl aldimines can be prepared through the reaction of an aldehyde with *N,N*-dimethylsulfamide by azeotropic removal of water in similar or greater yields than for the corresponding tosylimines.[16] Initial studies were carried out with *para*-chlorobenzaldimine **5a** and a slight excess (1.3 equiv) of phenylboronic acid (**6n**). We found that dioxane, which is generally used as a solvent in this reaction,[8,9] could be replaced by the nontoxic solvent acetone. When the substrate and reagent were added to a solution of a rhodium catalyst generated from 3 mol% [Rh(acac)(eth)$_2$] and 7.5 mol% **4a** in acetone at 40 °C, full conversion was obtained within 4 h, and **7an** could be isolated in 94% yield (Table 1, entry 1) with a promising enantioselectivy of 82% *ee*.

Table 1: Enantioselective rhodium/phosphoramidite-catalyzed asymmetric arylation of imines **5** with aryl boronic acids **6**.[a]

Entry	Imine	$Ar^2B(OH)_2$	Ligand	Yield [%][b]	*ee* [%][c]
1	**5a**	**6n**	(*S*)-**4a**	94	82 (*S*)
2	**5a**	**6n**	(*R*)-**4b**	95	95 (*R*)
3	**5b**	**6n**	(*R*)-**4b**	81	93 (*R*)
4	**5c**	**6n**	(*R*)-**4b**	98	94 (*R*)
5	**5d**	**6n**	(*R*)-**4b**	72	90 (*R*)
6	**5e**	**6n**	(*R*)-**4b**	77	92 (*R*)
7	**5i**	**6o**	(*R*)-**4b**	97	92 (*S*)
8	**5i**	**6p**	(*R*)-**4b**	81	94 (*S*)
9	**5f**	**6n**	(*R*)-**4b**	91	87 (*R*)
10	**5g**	**6n**	(*R*)-**4b**	81	93 (*R*)
11	**5h**	**6n**	(*R*)-**4b**	81	91 (*R*)
12[d]	**5a**	**6n**	(*R*)-**4b**	92	94 (*R*)

[a] Reactions were carried out on a 0.2-mmol scale in acetone at 40 °C for 4 h with 1.3 equiv of boronic acid **6** in the presence of a catalyst generated from 3 mol% [Rh(acac)(eth)$_2$] and 7.5 mol% monodentate phosphoramidite **4**. [b] Yield of isolated product after column chromatography on silica gel (heptane/EtOAc 80:20). [c] Determined by chiral HPLC. The absolute configuration of **7an** was established by comparison of its optical rotation after deprotection with literature values; the configurations of the other products were deduced by analogy. [d] Reaction was carried out overnight on a 1-g scale in acetone at 45 °C with a catalyst generated from 1 mol% [Rh(acac)(eth)$_2$] and 2.5 mol% **4b**.

In situ screening of a diverse ligand library generated by parallel synthesis (see the Supporting Information) revealed aniline-based phosphoramidites as efficient ligands for this reaction. Further screening of a more focused, 24-membered ligand library provided the *para*-methoxyaniline-derived phosphoramidite **4b** as the most efficient ligand for this reaction. Full conversion was reached within 4 h with an excellent enantioselectivity of 95% *ee* (Table 1, entry 2).

The rhodium-catalyzed asymmetric arylation of **5** using **4b** as a chiral ligand is compatible with a wide range of functional groups. Phenylation of benzaldimines with electron-withdrawing chloro, fluoro, and trifluoromethyl substituents (**5a**–**c**; Table 1, entries 2–4) at the *para* position gave the corresponding amines in high yields with 92–95% *ee*. As already observed for the addition of aryl boronic acids to aldehydes,[17] this 1,2-addition reaction is influenced by the electronic substitution pattern of both reaction partners. For substrates with electron-donating methoxy (**5d**) and methyl (**5e**) substituents at the *para* position, the conversion was not complete after 4 h (Table 1, entries 5 and 6). The alternative arylation of the unsubstituted benzaldimine **5i** with *para*-methoxy- (**6o**) and *para*-methylphenylboronic acid (**6p**; Table 1, entries 7 and 8), however, proceeds with high yields and enantioselectivities (92% and 94% *ee*, respectively). A slightly lower *ee* value is observed for *ortho*-methyl-substituted **5f** (87% *ee*), but addition to *meta*-fluoro-substituted **5g** proceeds with 93% *ee*. Addition of **6n** to (2-thienyl)carboxaldimine **5h** proceeds with 91% *ee*, which demonstrates that this methodology is not limited to substituted benzaldimines.

In contrast to 1,4-addition processes, in which water or an alcohol additive has been proven essential to protonate the oxa-π-allyl intermediate,[18] the reaction described herein requires no added protic solvent. This suggests an alternative pathway in which the amide functionality of intermediate **D** induces the transmetalation between the aryl boronic acid and the rhodium center (Scheme 2).[19] However, the direct

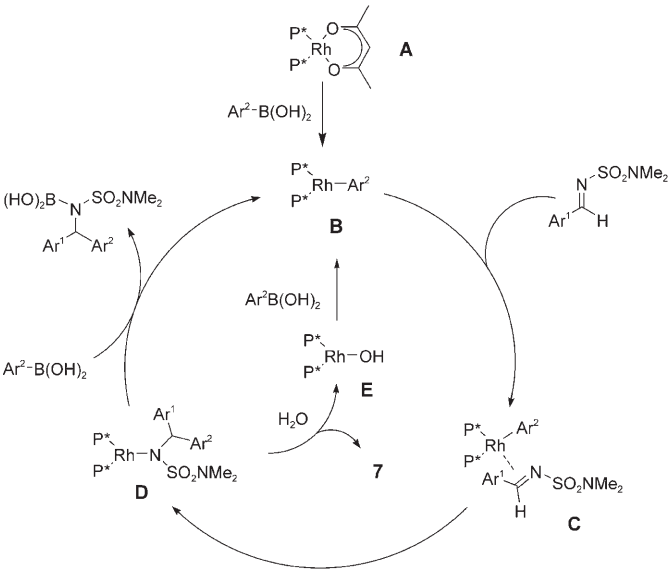

Scheme 2. Proposed mechanism. **A** catalyst precursor, **B** rhodium aryl complex, **C** catalyst substrate species, **D** catalyst product species, **E** rhodium hydroxy complex.

protonation by traces of water originating from the aryl boronic acid remains possible. The aryl boronic acid loading can be lowered considerably because the major side reaction, the hydrolysis of aryl boronic acid through protonolysis of intermediate **B**, is suppressed.

Synthesis of **7an** on a gram scale with only 1 mol% catalyst gave the product in 92% yield and 94% *ee* (Table 1, entry 12). The removal of the *N,N*-dimethylsulfamoyl protecting group has been reported several times to proceed by hydrolysis under harsh conditions.[20] We envisioned that the protecting groups could be removed under milder, more environmentally benign conditions through transamination.[21] Deprotection of **7an** proceeded cleanly after prolonged heating in 1,3-diaminopropane. The reaction rate could be increased considerably by using microwave-assisted heating.[22] The deprotection was complete within 2 h, and the

 © 2006 Wiley-VCH Verlag GmbH & Co. KGaA, Weinheim

amine **8an** was isolated in 96% yield with retention of configuration (Scheme 3).

In summary, the catalytic asymmetric synthesis of diarylmethyl amines by means of a rhodium/phosphoramidite system gave high enantioselectivities (up to 95% *ee*) and

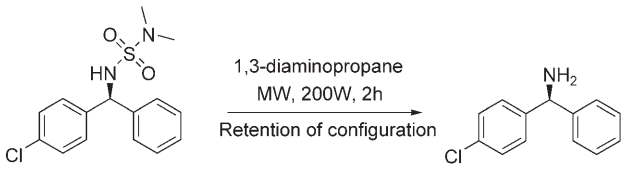

Scheme 3. Removal of the *N,N*-dimethylsulfamoyl protecting group. MW = microwave.

high yields (up to 98%). Along with the introduction of the small and cheap *N,N*-dimethylsulfamoyl protecting group, which was easily removed by microwave-assisted transamination, this method represents a highly versatile and selective transformation.

Received: December 4, 2005
Published online: March 23, 2006

Keywords: arylation · arylboronic acids · asymmetric catalysis · diarylmethylamines · phosphoramidites

[1] For examples of such pharmacophores, see: a) N. Plobeck, D. Delorme, Z.-Y. Wei, H. Yang, F. Zhou, P. Schwarz, L. Gawell, H. Gagnon, B. Pelcman, R. Schmidt, S.-Y. Sue, C. Walpole, W. Brown, E. Zhou, M. Labarre, K. Payza, S. St-Onge, A. Kamassah, P.-E. Morin, D. Projean, *J. Med. Chem.* **2000**, *43*, 3878; b) C. J. Opalka, T. E. D'Ambra, J. J. Faccone, G. Bodxon, E. Cossement, *Synthesis* **1995**, 766.

[2] a) E. J. Corey, C. J. Helal, *Tetrahedron Lett.* **1996**, *37*, 4837; b) N. Hermanns, S. Dahmen, C. Bolm, S. Bräse, *Angew. Chem.* **2002**, *114*, 3844; *Angew. Chem. Int. Ed.* **2002**, *41*, 3692; c) N. Cabello, J.-C. Kizirian, A. Alexakis, *Tetrahedron Lett.* **2004**, *45*, 4639.

[3] For a review on catalytic enantioselective addition to imines, see: a) S. Kobayashi, H. Ishitani, *Chem. Rev.* **1999**, *99*, 1069; for a review on catalytic asymmetric arylations, see: b) C. Bolm, J. P. Hildebrand, K. Muniz, N. Hermanns, *Angew. Chem.* **2001**, *113*, 3382; *Angew. Chem. Int. Ed.* **2001**, *40*, 3284; for a review on rhodium-catalyzed carbon–carbon-bond-forming reactions, see: c) T. Hayashi, K. Yamasaki, *Chem. Rev.* **2003**, *103*, 169; d) K. Fagnou, M. Lautens, *Chem. Rev.* **2003**, *103*, 169; e) *Modern Rhodium-Catalyzed Organic Reactions* (Ed.: P. A. Evans), Wiley-VCH, Weinheim, **2005**.

[4] a) T. Hayashi, M. Ishigedani, *J. Am. Chem. Soc.* **2000**, *122*, 976; b) M. Ueda, N. Miyaura, *J. Organomet. Chem.* **2000**, *595*, 31.

[5] T. Hayashi, M. Kawai, N. Tokunaga, *Angew. Chem.* **2004**, *116*, 6251; *Angew. Chem. Int. Ed.* **2004**, *43*, 6125.

[6] N. Miyaura, A. Suzuki, *Chem. Rev.* **1995**, *95*, 2457.

[7] For the first non-enantioselective addition of arylboronic acids to imines, see reference [4b] and: M. Ueda, A. Saito, N. Miyaura, *Synlett* **2000**, *11*, 1637.

[8] M. Kuriyama, T. Soeta, X. Hao, Q. Chen, K. Tomioka, *J. Am. Chem. Soc.* **2004**, *126*, 8128.

[9] a) N. Tokunaga, Y. Otomaru, K. Okamoto, K. Ueyama, R. Shintani, T. Hayashi, *J. Am. Chem. Soc.* **2004**, *126*, 13584; b) Y. Otomaru, N. Tokunaga, R. Shintani, T. Hayashi, *Org. Lett.* **2005**, *7*, 307.

[10] D. J. Weix, Y. Shi, J. A. Ellman, *J. Am. Chem. Soc.* **2005**, *127*, 1092. The authors of this paper also mention the problematic removal of the *N*-tosyl activating/protecting group and use the *N*-diphenylphosphinoyl group as an alternative.

[11] For difficulties concerning the removal of the *N*-tosyl protecting group in this system, see reference [9], R. R. Milburn, V. Snieckus, *Angew. Chem.* **2004**, *116*, 910; *Angew. Chem. Int. Ed.* **2004**, *43*, 892, and references therein.

[12] For the synthesis of *N,N*-dimethylsulfamoyl-protected benzaldimines, see: a) M. Huisman, R. ten Have, A. M. van Leusen, *Synth. Commun.* **1997**, *27*, 945; b) R. ten Have, M. Huisman, A. Meetsma, A. M. van Leusen, *Tetrahedron* **1997**, *53*, 11355.

[13] B. L. Feringa, *Acc. Chem. Res.* **2000**, *33*, 346.

[14] a) J.-G. Boiteau, R. Imbos, A. J. Minnaard, B. L. Feringa, *Org. Lett.* **2003**, *5*, 681; see also: J.-G. Boiteau, R. Imbos, A. J. Minnaard, B. L. Feringa, *Org. Lett.* **2003**, *5*, 1385; b) J.-G. Boiteau, A. J. Minnaard, B. L. Feringa, *J. Org. Chem.* **2003**, *68*, 9481; c) A. Duursma, R. Hoen, J. Schuppan, R. Hulst, A. J. Minnaard, B. L. Feringa, *Org. Lett.* **2003**, *5*, 3111; d) R. B. C. Jagt, J. G. de Vries, B. L. Feringa, A. J. Minnaard, *Org. Lett.* **2005**, *7*, 2433.

[15] a) L. Lefort, J. A. F. Boogers, A. H. M. de Vries, J. G. de Vries, *Org. Lett.* **2004**, *6*, 1733; b) A. Duursma, L. Lefort, J. A. F. Boogers, A. H. M. de Vries, J. G. de Vries, A. J. Minnaard, B. L. Feringa, *Org. Biomol. Chem.* **2004**, *2*, 1682.

[16] B. E. Love, P. S. Raje, T. C. Williams, *Synlett* **1994**, 493.

[17] a) M. Sakai, M. Ueda, N. Miyaura, *Angew. Chem.* **1998**, *110*, 3475; *Angew. Chem. Int. Ed.* **1998**, *37*, 3279; b) C. Moreau, C. Hague, A. S. Weller, C. G. Frost, *Tetrahedron Lett.* **2001**, *42*, 6957.

[18] T. Hayashi, M. Takahashi, Y. Takaya, M. Ogasawara, *J. Am. Chem. Soc.* **2002**, *124*, 5052.

[19] For a previous example of 1,2-addition to benzaldimines in aprotic media, see reference [10].

[20] a) L. V. Kudzma, S. P. Turnbull, *Synthesis* **1991**, 1021; b) J. Hine, H.-M. Tsay, *J. Org. Chem.* **1983**, *48*, 3797; c) R. Adams, W. P. Samuels, *J. Am. Chem. Soc.* **1955**, *77*, 5375.

[21] For references concerning transamination reactions of sulfamide and derivatives thereof, see: a) S. D. McDermott, W. J. Spillane, *Synthesis* **1983**, 192; b) M. Preiss, *Chem. Ber.* **1978**, *111*, 1915.

[22] C. O. Kappe, *Angew. Chem.* **2004**, *116*, 6408; *Angew. Chem. Int. Ed.* **2004**, *43*, 6250.

 © 2006 Wiley-VCH Verlag GmbH & Co. KGaA, Weinheim

Helical Structures

DOI: 10.1002/anie.200600123

A Nonanuclear Gallium(III) Cluster: An Intermediate in the Formation of Dinuclear Triple-Stranded Helicates?**

Markus Albrecht, Sabrina Dehn, and Roland Fröhlich*

Dedicated to Professor Hansgeorg Schnöckel on the occasion of his 65th birthday

During the last 20 years the chemistry of helicates has been thoroughly investigated and many fundamental mechanistic principles of metallo-supramolecular chemistry have been understood (such as, stereochemistry, orientation of ligands, and self-recognition).[1] However, owing to the complexity of the kinetic and thermodynamic factors which are involved in the self-assembly of helicates, only preliminary results were obtained regarding the mechanisms of helicate formation (Figure 1).[2,3]

In many cases the self-assembly of the helicates is assumed to proceed in a cooperative process or at least by strict self-assembly. Therefore, investigations focused mainly on structural aspects of the coordination compounds but not on possible intermediates of their formation.[4] Only in few cases intermediates were observed.[5]

Recently we described that the bis-β-diketonate ligand H_2**1** (Figure 1) forms dinuclear triple-stranded helicates $[(\mathbf{1})_3M_2]$ with gallium(III) and iron(III), regardless of the metal:ligand ratio indicating a strict self-assembly.[6] Whereas with nickel(II) ions, different di- or trinuclear complexes can be obtained at different ligand:metal ratios.[7]

The strict self-assembly of the gallium complex $[(\mathbf{1})_3Ga_2]$ is assumed to be due to the high predisposition of **1** for helicate formation.[6] To show this feature, we have now prepared the related ligand H_2**2** (Figure 1) which has a six-membered central ring and thus with a slightly different relative orientation of the metal binding sites compared to H_2**1**.

Upon treating two equivalents of gallium(III) with three equivalents of H_2**2** (approximately 50 mg) in the presence of 3.3 equivalents of potassium carbonate as base in methanol (10 mL) the triple-stranded helicate $[(\mathbf{2})_3Ga_2]$ could be detected by ESI MS, but is only formed in a mixture with other complexes and could not be isolated in pure form. This observation is supported by NMR spectroscopy experiments in $CDCl_3$ (with $[Ga(acac)_3]$ as the gallium source). This study indicated, that the complex formation with H_2**2** did not proceed with strict self-assembly.

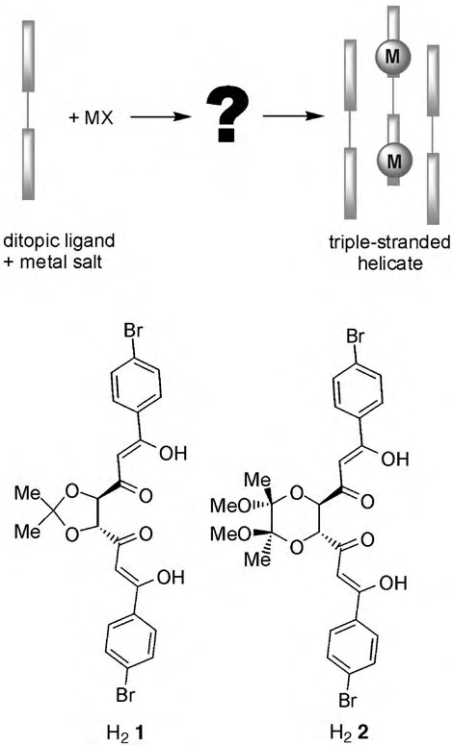

Figure 1. Schematic representation of the assembly of homoleptic helicates from ditopic ligands (e.g. H_2**1** or H_2**2**) and metal salts MX. Usually only the resulting helicates are observed, while intermediates remain unknown.

To obtain possible intermediate structures of the helicate formation we performed the reaction between gallium nitrate and H_2**2** in (wet) methanol in a 1:1 ratio in the presence of potassium carbonate as base. The crude material was extracted with chloroform to obtain a yellow solid which was investigated by mass spectrometry (ESI-MS). We observed in the positive detection mode the base peak at m/z 1405 ($[(\mathbf{2})_2Ga_2OH)]^+$), but again, no clear set of signals could be observed by NMR spectroscopy.

Crystallization of the material from dichloromethane/hexane afforded crystals of the nonanuclear cluster $[(\mathbf{2})_8Ga_9(OH)_{10}]NO_3$.[8] Figure 2a shows the molecular structure of the cation $[(\mathbf{2})_8Ga_9(OH)_{10}]^+$ revealing the efficient shielding of the inner nonanuclear gallium hydroxide cluster by eight of the ditopic ligands **2**. However, the structure of the compound and the arrangement of the ligands can be more easily understood from the reduced representation shown in Figure 2b (the ligands are only indicated). $[(\mathbf{2})_8Ga_9(OH)_{10}]^+$ bears four double-stranded homochiral Δ,Δ-configured "pre-helicate subunits", in which two gallium(III) ions are wrapped by only two ligands **2**. In addition a hydroxy group is bridging those metals. The fragment $[(\mathbf{2})_2(\mu\text{-}OH)Ga_2]^+$ (Figure 2c) is also detected by positive ESI-MS to be a dominate species in solution (m/z 1405). The double-stranded dinuclear unit

[*] Prof. Dr. M. Albrecht, S. Dehn
Institut für Organische Chemie
RWTH-Aachen
Landoltweg 1, 52074 Aachen (Germany)
Fax: (+49) 241-80-92385
E-mail: markus.albrecht@oc.rwth-aachen.de
Dr. R. Fröhlich
Organisch-Chemisches Institut
Universität Münster
Corrensstrasse 40, 48149 Münster (Germany)

[**] This work was supported by the Deutsche Forschungsgemeinschaft (GK 440 "Methoden der asymmetrischen Synthese").

InterScience
© 2006 Wiley-VCH Verlag GmbH & Co. KGaA, Weinheim

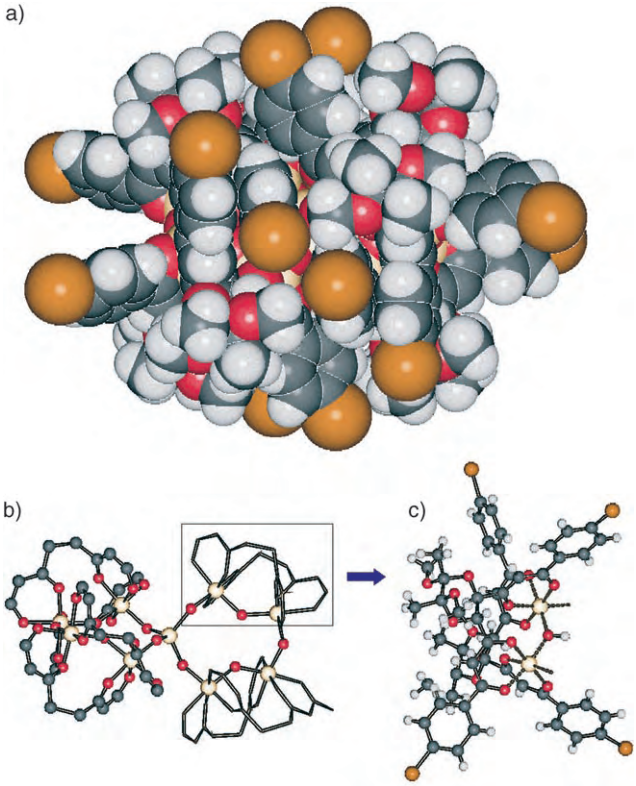

Figure 2. a) The structure of the cluster cation $[(\mathbf{2})_8Ga_9(OH)_{10}]^+$, b) representation of the central $\{Ga_9(OH)_{10}\}$ cluster unit (ligands are only indicated), and c) the dinuclear pre-helicate moiety $[(\mathbf{2})_2(\mu\text{-}OH)Ga_2]^+$ which is found four times in the cluster and is detected in solution by ESI-MS. H: white; C: gray; O: red; Br: orange; Ga: beige.

$\{(\mathbf{2})_2Ga_2\}$ is structurally very similar to the analogous part $\{(\mathbf{1})_2Ga_2\}$ of the triple-stranded helicate $[(\mathbf{1})_3Ga_2]$.[6] In the units of the cluster of ligand **2**, the place of the third bridging ligand is taken by OH groups.

In the cluster, two $[(\mathbf{2})_2(\mu\text{-}OH)Ga_2]^+$ ions are connected by a Ga-OH-Ga linkage. The two resulting tetranuclear units are bound to a central gallium atom through hydroxide groups. The central gallium is tetracoordinate, while the other eight Ga^{3+} centers are hexacoordinate and have a distorted octahedral coordination environment (Figure 2b).[9]

Gallium hydroxide clusters are rare.[10] An interesting 13-nuclear gallium(III) complex $[Ga_{13}[\mu_3\text{-}OH)_6(\mu_2\text{-}OH)_{18}(H_2O)_{24}]^{15+}$ was recently described by Johnson et al.[11] For our compound $[(\mathbf{2})_8Ga_9(OH)_{10}]^+$, the cluster unit is more effectively shielded owing to the eight ditopic ligands **2**, which wrap it up. The use of the enantiomerically pure ligand **2** results in the diastereoselective formation of the oligonuclear coordination compound in enantiomerically pure form.

The cluster compound $[(\mathbf{2})_8Ga_9(OH)_{10}]NO_3$ probably represents an intermediate in the formation of the helicate $[(\mathbf{2})_3Ga_2]$. The fragments $[(\mathbf{2})_2(\mu\text{-}OH)Ga_2]^+$ are precursors for the triple-stranded complex. In the present case, the isolation of the cluster was possible because of the structure of the ligand which disfavors helicate formation. The use of ligand geometries and/or metal coordination geometries that are unsuitable for helix formation, such as those as described herein, should offer an easy method to obtain similar cluster compounds which are wrapped by linear oligotopic ligands. As an alternative, linear "helicating" ligands should also be able to stabilize cluster compounds if the ligands have a denticity which is incommensurate to the metal coordination number.[12] Currently we are searching for examples for the latter case. Following this concept, we expect the formation of new cluster compounds with linear wrapping ligands, for which we can not predict the structure.[13,14]

Received: January 11, 2006
Published online: March 20, 2006

Keywords: cluster compounds · gallium · helical structures · self-assembly

[1] For reviews see: a) C. Piguet, G. Bernardinelli, G. Hopfgartner, *Chem. Rev.* **1997**, *97*, 2005–2062; b) M. Albrecht, *Chem. Rev.* **2001**, *101*, 3457–3498; c) M. J. Hannon, L. J. Childs, *Supramol. Chem.* **2004**, *16*, 7–22.

[2] a) A. Pfeil, J.-M. Lehn, *J. Chem. Soc. Chem. Commun.* **1992**, 838–840; b) N. Fatin-Rouge, S. Blanc, E. Leize, A. Van Dorsselaer, P. Baret, J.-L. Pierre, A.-M. Albrecht-Gary, *Inorg. Chem.* **2000**, *39*, 5771–5778; c) N. Fatin-Rouge, S. Blanc, A. Pfeil, A. Rigault, A.-M. Albrecht-Gary, J. M. Lehn, *Helv. Chim. Acta* **2001**, *84*, 1694–1711; d) J. Hamacek, S. Blanc, M. Elhabiri, E. Leize, A. Van Dorsselaer, C. Piguet, A.-M. Albrecht-Gary, *J. Am. Chem. Soc.* **2003**, *125*, 1541–1550; e) M. Elhabiri, J. Hamacek, J.-C. G. Bünzli, A.-M. Albrecht-Gary, *Eur. J. Inorg. Chem.* **2004**, 51–62.

[3] K. Zeckert, J. Hamacek, J.-P. Rivera, S. Floquet, A. Pinto, M. Borkovec, C. Piguet, *J. Am. Chem. Soc.* **2004**, *126*, 11589–11601.

[4] a) C. Piguet, M. Borkovec, J. Hamacek, K. Zeckert, *Coord. Chem. Rev.* **2005**, *249*, 705–726; b) for strict self-assembly see: J. S. Lindsey, *New J. Chem.* **1991**, *15*, 153–180.

[5] a) N. Martin, J.-C. G. Bünzli, V. McKee, C. Piguet, G. Hopfgartner, *Inorg. Chem.* **1998**, *37*, 577–589; b) E. J. Enemark, T. D. P. Stack, *Inorg. Chem.* **1996**, *35*, 2719–2720; c) J.-M. Senegas, S. Koeller, G. Bernardinelli, C. Piguet, *Chem. Commun.* **2005**, 2235–2237.

[6] M. Albrecht, S. Schmid, M. deGroot, P. Weis, R. Fröhlich, *Chem. Commun.* **2003**, 2526–2527.

[7] M. Albrecht, S. Dehn, G. Raabe, R. Fröhlich, *Chem. Commun.* **2005**, 5690–5692.

[8] X-ray crystal structure analysis for $[(\mathbf{2})_8Ga_9(OH)_{10}]NO_3$: formula $[(C_{26}H_{24}O_8Br_2)_8Ga_9(OH_{10})]NO_3$, $M_r = 5853.75$, light green crystal $0.20 \times 0.20 \times 0.10$ mm, $a = 29.017(1)$ Å, $V = 24431.9(15)$ Å^3, $\rho_{calcd} = 1.194$ g cm^{-3}, $\mu = 3.634$ mm^{-1}, empirical absorption correction ($0.530 \le T \le 0.713$), $Z = 1$, cubic, space group $P23$ (no. 195), $\lambda = 1.54178$ Å, $T = 223$ K, ω and ϕ scans, 52009 reflections collected ($\pm h$, $\pm k$, $\pm l$), $[(\sin\theta)/\lambda] = 0.60$ Å^{-1}, 12979 independent ($R_{int} = 0.081$) and 7889 observed reflections [$I \ge 2\sigma(I)$], 695 refined parameters, $R = 0.097$, $wR^2 = 0.328$, Flack parameter 0.00(5), max. (min.) residual electron density 0.72 (−0.86) e Å^{-3}, hydrogen atoms are calculated and refined riding, analysis of limited accuracy owing to low crystal quality and strong absorption. Data set was collected with a Nonius KappaCCD diffractometer. Programs used: data collection COLLECT (Nonius B. V., 1998), data reduction Denzo-SMN (Z. Otwinowski, W. Minor, *Methods Enzymol.* **1997**, *276*, 307–326), absorption correction Denzo (Z. Otwinowski, D. Borek, W. Majewski, W. Minor, *Acta Crystallogr. Sect. A* **2003**, *59*, 228–234), structure solution SHELXS-97 (G. M. Sheldrick, *Acta Crystallogr. Sect. A* **1990**, *46*, 467–473), structure refinement

 © 2006 Wiley-VCH Verlag GmbH & Co. KGaA, Weinheim

SHELXL-97 (G. M. Sheldrick, Universität Göttingen, **1997**), graphics SCHAKAL (E. Keller, Universität Freiburg, **1997**). CCDC 294885 contains the supplementary crystallographic data for this paper. These data can be obtained free of charge from The Cambridge Crystallographic Data Centre via www.ccdc.cam.ac.uk/data_request/cif.

[9] The cluster also can be discussed as an aggregate of double-stranded helicates. For selected examples of helicate aggregation see: a) L. J. Childs, N. W. Alcock, M. J. Hannon, *Angew. Chem.* **2001**, *113*, 1113 – 1115; *Angew. Chem. Int. Ed. Engl.* **2001**, *40*, 1079 – 1081; b) L. J. Childs, N. W. Alcock, M. J. Hannon, *Angew. Chem.* **2002**, *114*, 4418 – 4421; *Angew. Chem. Int. Ed.* **2002**, *41*, 4244 – 4247; c) M. Vázquez, A. Taglietti, D. Gatteschi, L. Sorace, C. Sangregorio, A. M. González, M. Maneiro, R. M. Pedrido, M. R. Bermelo, *Chem. Commun.* **2002**, 1840 – 1841.

[10] For example, a) N. Wiberg, K. Amelunxen, H.-W. Lerner, H. Nöth, W. Ponikwar, H. Schwenk, *J. Organomet. Chem.* **1999**, *574*, 246 – 251; b) F. J. Feher, T. A. Budzichowski, J. W. Ziller, *Inorg. Chem.* **1997**, *36*, 4082 – 4086; c) M. V. Capparelli, P. Hodge, B. Piggott, *Chem. Commun.* **1997**, 937 – 938.

[11] E. Rather, J. T. Gatlin, P. G. Nixon, T. Tsukamoto, V. Kravtsov, D. W. Johnson, *J. Am. Chem. Soc.* **2005**, *127*, 3242 – 3243.

[12] A related "incommensurate strategy" was introduced earlier for the formation of metallosupramolecular aggregates, e.g.: a) T. Beissel, R. E. Powers, K. N. Raymond, *Angew. Chem.* **1996**, *108*, 1166 – 1168; *Angew. Chem. Int. Ed. Engl.* **1996**, *35*, 1084 – 1086; b) C. Brückner, R. E. Powers, K. N. Raymond, *Angew. Chem.* **1998**, *110*, 1937 – 1940; *Angew. Chem. Int. Ed.* **1998**, *37*, 1837 – 1839; c) M. Scherer, D. Caulder, D. W. Johnson, K. N. Raymond, *Angew. Chem.* **1999**, *111*, 1689 – 1694; *Angew. Chem. Int. Ed.* **1999**, *38*, 1588 – 1592.

[13] For an example see: J. Sanmartin, M. R. Bermejo, A. M. Garcia-Deibe, O. Piro, E. E. Castellano, *Chem. Commun.* **1999**, 1953 – 1954.

[14] R. E. P. Winpenny, *J. Chem. Soc. Dalton Trans.* **2002**, 1 – 10.

 © 2006 Wiley-VCH Verlag GmbH & Co. KGaA, Weinheim

Cluster Compounds

DOI: 10.1002/anie.200504406

A Hexanuclear Iron(III) Carboxylate with an $[Fe_6(\mu_3\text{-}O)_3(\mu_2\text{-}OH)]^{11+}$ Core as an Efficient Catalyst for Cycloalkane Oxidation**

Günter Trettenhahn, Michael Nagl, Norbert Neuwirth, Vladimir B. Arion, Walther Jary, Peter Pöchlauer, and Walther Schmid**

Catalytic alkane functionalization continues to attract the attention of researchers.[1] Starting with the discovery of the platinum(II)-catalyzed activation of unfunctionalized alkanes,[2] a variety of activating systems involving organometallic species[3,4] have been developed. In addition numerous catalytic systems based on high-valent metal complexes, such as metal-oxo complexes,[1i,5] peroxo complexes,[6] and metal-catalyzed (Ru^{III}, Fe^{III} Mn^{IV}, V^{IV},V^{V}) systems using H_2O_2,[1f,j,7,10c] organic peroxides,[8,10c] or dioxygen (catalyzed by Co^{II},Co^{III} or polyoxometalates[9]) as oxidizing agents were investigated. In the Gif systems,[10] developed by Barton and co-workers, and in the iron picolinate systems, introduced by Sawyer and Sobkowiak,[11] peroxo radicals are thought to be generated in situ from dioxygen by means of a reducing agent (Fe^0, Zn^0, Fe^{II} carboxylates). The development of synthetic, biomimetic model compounds[12] for non-heme iron proteins, such as methane monooxygenase (MMO), has opened up a new approach in alkane activation chemistry.[1c,e,g,13,14b,c,d]

[*] Prof. V. B. Arion
Institute of Inorganic Chemistry
Faculty of Chemistry
University of Vienna
Waehringerstrasse 42, 1090 Vienna (Austria)
Fax: (+43) 1-4277-52680
E-mail: vladimir.arion@univie.ac.at

Dr. M. Nagl, Mag. N. Neuwirth, Prof. W. Schmid
Institute of Organic Chemistry
Faculty of Chemistry
University of Vienna
Waehringerstrasse 38, 1090 Vienna (Austria)
Fax: (+43) 1-4277-9521
E-mail: walther.schmid@univie.ac.at

Dr. G. Trettenhahn
Institute of Physical Chemistry
Faculty of Chemistry, University of Vienna
Waehringerstrasse 42, 1090 Vienna (Austria)

Dr. W. Jary, Dr. P. Pöchlauer
DSM Fine Chemicals Austria Nfg GmbH & Co KG
St.-Peter-Strasse 25, 4021 Linz (Austria)

[**] This work was supported by DSM Fine Chemicals Austria and the University of Vienna. Mr. B. Mienert (Max-Planck-Institute for Bioinorganic Chemistry, Mülheim an der Ruhr (Germany)) is kindly acknowledged for carrying out the Mössbauer spectra measurements. We also thank Prof. Ya. D. Lampeka, Dr. S. Shova and Mr. N. A. Sheddan for valuable discussions.

Supporting information for this article is available on the WWW under http://www.angewandte.org or from the author.

WILEY InterScience DISCOVER SOMETHING GREAT

© 2006 Wiley-VCH Verlag GmbH & Co. KGaA, Weinheim

Some of these compounds were shown to be valuable model precursors for high-valent μ-oxo diiron species.[12b,d,14] Iron acetate, pivalinate, and picolinate species present in alkane activating systems of the Gif^{III} and Gif^{IV} and GoAgg^{III} types have been extensively characterized.[15,16]

Although basic iron salts of benzoic acid derivatives were reported by Weinland almost one century ago,[17] they continue to provide examples of unusual chemical transformations leading to multinuclear architectures.[18] Perhaps the most evident structural feature of polynuclear iron complexes (Fe_n where $n>3$) is their highly symmetrical core structure. Recently, a series of novel oligonuclear iron complexes has been reported, including a 4-nitrobenzoato-Schiff base complex with an irregular pentanuclear iron core.[19]

In search of new catalytic systems for low-temperature industrial liquid-phase alkane oxidations, we have been screening a number of Fe^{II} and Fe^{III} carboxylates; in these tests the iron nitrobenzoate $[Fe_3O(p\text{-}NO_2C_6H_4COO)_6](p\text{-}NO_2C_6H_4COO)\cdot H_2O$ (**1**),[20] was quite successful which inspired us to investigate the structure and spectroscopic properties of this promising type of compound.

Herein we report the synthesis of the hexanuclear iron *p*-nitrobenzoate $[Fe_6O_3(OH)(p\text{-}NO_2C_6H_4COO)_{11}(dmf)_4]$ (**2**) with an unprecedented $[Fe_6(\mu_3\text{-}O)_3(\mu_2\text{-}OH)]^{11+}$ core. The complex exhibited remarkable catalytic activity in the oxidation of cyclohexane with H_2O_2, thus being a rare example (apart from polyoxometalates) of a metal complex with a nuclearity greater than three that has catalytic potential in an alkane oxidation process.[1a,21]

Complex **2**, resulting from dissolution of **1** in dimethylformamide (DMF), crystallized with 4.5 molecules of DMF and 2.7 molecules of H_2O per formula unit in the triclinic space group $P\bar{1}$.[22] The six Fe atoms are distributed within three linked triangular $[Fe_3(\mu_3\text{-}O)]$ units Fe1-Fe2-Fe3, Fe2-Fe3-Fe4, and Fe4-Fe5-Fe6 (Figure 1). While the first and second triangular units share an edge, the second and third share an apex. This arrangement leads to the formation of the fourth triangle unit Fe3-Fe4-Fe5, where the atoms Fe3 and Fe5 are bridged by a hydroxo group with the Fe3-O(H)-Fe5 angle at 139.3(2)°. The dihedral angle between the planes through Fe1, Fe2, Fe3 and Fe2, Fe3, Fe4 is 12.7°, between the planes through Fe2, Fe3, Fe4 and Fe3, Fe4, Fe5 it is only 0.5°, whereas between the planes through Fe3, Fe4, Fe5 and Fe4, Fe5, Fe6 it is 56.3°. All four triangles are scalene. The central μ_3-oxo atom in each Fe_3 subunit deviates slightly out from the corresponding Fe_3 plane; the atom O1 by 0.268, O2 by −0.294 and O3 by −0.062 Å. The pairs of atoms Fe1 and Fe2, Fe4 and Fe6, and Fe5 and Fe6 are bridged by two μ-carboxylate groups, while Fe1 and Fe3, Fe2 and Fe3, and Fe4 and Fe5 are bridged by one carboxylate group. All the Fe atoms are six-coordinate. The coordination geometry of Fe1 is completed by two terminal DMF ligands, that of Fe3 and Fe6 by one DMF ligand and that of Fe5 by a carboxylate ligand coordinated in a monodentate manner, which, in addition is involved in a strong intramolecular hydrogen bonding with the μ-hydroxo group [O4···O41 2.704 Å] (Figure 2) by the second oxygen atom. There are no other reported examples of Fe_6 compounds containing a unit in which an $[Fe_2O_2]$ rhombus is edge fused to an $[Fe_3O_2(OH)]$ irregular hexagon to which two additional Fe atoms are attached (Fe1 and Fe6 in Figure 1). The discovered structural motif can also be regarded as a combination of a "butterfly" $\{Fe_4O_2\}$ core and an $\{Fe_3O\}$ core which share an apex and in addition are bridged by a hydroxo group.

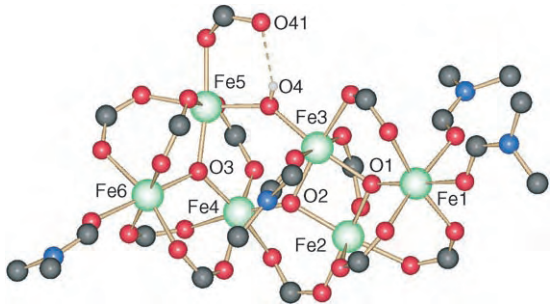

Figure 2. The molecular structure of **2** (SCHAKAL Plot).[23] *p*-Nitrophenyl rings and hydrogen atoms (except that attached to O4) are omitted for clarity; Fe: green, O: red, N: blue, C: gray. Selected bond lengths [Å] and angles [°]: Fe1–O1 1.826(3), Fe2–O1 1.923(3), Fe3–O1 1.957(3), Fe2–O2 1.973(3), Fe3–O2 1.915(4), Fe4–O2 1.875(3), Fe4–O3 1.952(3), Fe5–O3 1.940(3), Fe6–O3 1.883(3), Fe3–O4 1.935(4), Fe5–O4 1.938(4); Fe1-O1-Fe2 125.91(18), Fe1-O1-Fe3 132.85(19), Fe2-O1-Fe3 94.90(15), Fe2-O2-Fe3 94.64(14), Fe3-O2-Fe4 129.28(18), Fe2-O2-Fe4 128.66(18), Fe4-O3-Fe5 120.07(17), Fe4-O3-Fe6 119.29(18), Fe5-O3-Fe6 120.33(17), Fe3-O4-Fe5 139.3(2).

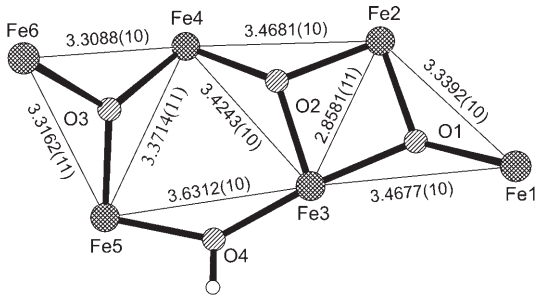

Figure 1. The topology of the $[Fe_6O_3(OH)]^{11+}$ core of complex **2**, showing interatomic distances; other relevant geometric parameters are quoted in the legend to Figure 2.

The Mössbauer spectrum of **2** (Figure 3) recorded at 80 K shows a quadrupole doublet with an isomer shift $\delta = 0.53\ mm\,s^{-1}$ and a splitting $\Delta E_Q = 0.96\ mm\,s^{-1}$ typical of octahedral, high-spin Fe^{III} complexes in an environment of hard donor atoms.[24,25] These values are also in accordance with those of model compounds for carboxylate bridged diiron proteins (δ values of 0.41 to 0.52 $mm\,s^{-1}$ and ΔE_Q values of 0.61 to 1.93 $mm\,s^{-1}$).[12b] Bond valence sum (BVS) analysis for Fe3 and Fe5 gave BVS values of 3.10 and 3.06 in agreement with a formal oxidation state +III for these hydroxo-bridged iron centers.[26]

Addition of H_2O_2 to the solution of **2** in MeCN:DMF (10:1) at 6.5 °C resulted in the growth of two bands in the visible region of the UV/Vis spectra, with maxima at 436 and

 © 2006 Wiley-VCH Verlag GmbH & Co. KGaA, Weinheim

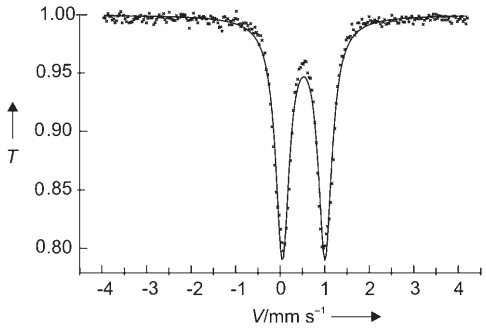

Figure 3. Zero-field Mössbauer spectrum of the solid sample of **2** at 80 K. The isomer shift, δ, is referenced against α-Fe at 298 K.

478 nm and extinction coefficients of $\varepsilon = 2290$ and $1740\,\text{M}^{-1}\,\text{cm}^{-1}$, respectively, implying the formation of a peroxo species.[27] The ε values were calculated by using the molar concentration of the starting compound **2**. The bands of the μ-peroxo hexairon complex are shifted to higher energies compared to those of μ-peroxo mono- and diiron complexes.[27] The presence of additional bridging oxo and hydroxo groups is known to significantly influence the spectroscopic properties of peroxo complexes. The significant blue shift and low intensity of the charge-transfer (CT) bands of peroxo species were attributed to the increase of the energy gap between interacting d_π orbitals of Fe^{III} centers and π^* orbitals of the peroxide, thus decreasing the overlap between them.[28] Figure 4 shows the evolution of the electronic spectra during the formation of the peroxo complex from **2**.

Kinetic studies indicated that the stability of the peroxo intermediate arising from **2** is temperature dependent. At temperatures $\geq 15.4\,^\circ\text{C}$ the peroxo complex decomposed after its concentration passed through a maximum. The initial increase of the electronic absorption up to its maximum value follows a first-order kinetics. At 6.5 °C the intermediate peroxo species is more stable and no maximum is reached during the first 1000 s. The rate constant at this temperature is $0.017\,\text{s}^{-1}$ (calculated for the first 100 s). This data was examined by an Arrhenius plot which led to an activation energy of $E_A = 48\,\text{kJ mol}^{-1}$ and a frequency factor of $A = 1.9 \times 10^7\,\text{s}^{-1}$ for the formation of the peroxo complex.[29] The decrease of the absorption bands, especially at higher temperature, indicates the instability of the peroxo species (see Supporting Information).

Complex **2** exhibited remarkable catalytic activity in the oxidation of cyclohexane in solution. In our model reaction we converted cyclohexane into cyclohexanol (OL) and cyclohexanone (ON) in MeCN using a molar excess of aqueous H_2O_2 as the oxidizing agent. Total yields from 20–30 mol % of alcohol and ketone with turnover numbers (TON) of 100 were observed when the molar ratio of catalyst **2**:cyclohexane was approximately 1:320 (Table 1). These results are comparable with those of analogous high-performing systems.[1]

Table 1: Oxidation of cyclohexane catalyzed by **2**.[a]

Entry	Cat.	$n(C_6H_{12})$ [mmol]	$n(H_2O_2)$ [mmol]	$n(H_2O_2)$ [mmol h^{-1}]	Yield[b] [mol %] (±0.4 mol %) OL	ON	OL+ON
1	**2**	10	55	24	9.9	13.3	23.2
2[c]	**2**	10	55	12	8.0	12.0	20.0
3	**2**	10	80	40	15.0	14.7	29.7
4	**2**	10	120	70	9.6	15.7	25.3
5	**2**	20	3	–[d]	0.7	0.8	1.5
6	**1**[e]	10	80	40	8.3	9.0	17.3
7[f]	**1**[e]	10	80	40	4.3	6.3	10.6

[a] Reaction conditions: 0.03 mmol of **2** were dissolved in MeCN (20 mL), cyclohexane (10 or 20 mmol), 50% w/w H_2O_2 solution added (syringe pump). [b] Yield [mol %] based on substrate (cyclohexane). [c] 30% w/w H_2O_2 added. [d] H_2O_2 added at once. [e] 0.06 mmol iron *p*-nitrobenzoate (**1**) prepared by precipitation from aqueous solution. [f] 0.42 mmol DMF added.

By applying commercially available 50 % H_2O_2 solution, we reached a total yield of 29.7 mol % of alcohol and ketone (Table 1, entry 3). In experiments varying the concentration of H_2O_2, comparable yields were obtained (entries 1 and 2). However, further increase of both the amount and the addition rate of the oxidant, led to a decrease in yield (entry 4). The molar ratio of the products OL:ON obtained by using complex **2**, was between 1:1 and 1:1.5, and did not change significantly when applying lower amounts of oxidant to the substrate (Table 1, entry 5). These results may suggest a radical type oxidation mechanism, assuming a Haber–Weiss process.[13] However, treatment of the reaction mixture with triphenylphosphine prior to GC analysis significantly decreases the ON:OL ratio, as reported by Shul'pin and coworkers for other catalytic systems,[1k,30] indicating a cyclohexyl hydroperoxide as the primary oxidation product. Significantly lower yields were obtained (Table 1, entry 6) when using **1** as catalyst instead of **2**. Addition of DMF up to a molar ratio of DMF:**1** of 7:1 lead to even lower values (entry 7).

In conclusion, we have developed an efficient procedure for metal-catalyzed liquid-phase oxidation of cycloalkanes by using a hexanuclear iron complex with an unprecedented core

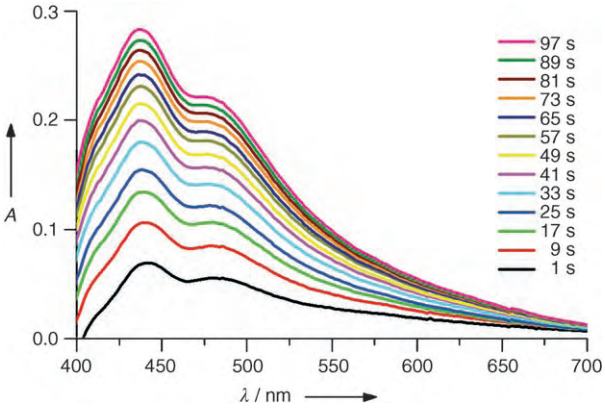

Figure 4. Formation of the peroxo intermediate from **2**·4.5 DMF·2.7 H_2O ($c = 2.07 \times 10^{-4}$ M) at 6.5 °C in MeCN:DMF (10:1).

 © 2006 Wiley-VCH Verlag GmbH & Co. KGaA, Weinheim

structure. Some key structural features of this complex show similarity to biomimetic diiron complexes, such as the Fe–Fe distances and the Mössbauer parameters δ and ΔE_Q. The easy accessibility of this hexanuclear iron complex and its catalytic potency makes it a suitable candidate for large-scale oxidations of various alkanes.

Experimental Section

Acetonitrile (analytical grade from Riedel de Haën) was dried over CaH_2 before use. Hydrogen peroxide (50% solution) was purchased from Acros. Other reagents were purchased from Aldrich.

1: A solution of iron(III) chloride hexahydrate (3.38 g, 12.5 mmol) in water (15 mL) was added, under stirring, to an aqueous solution (60 mL) of *p*-nitrobenzoic acid (6.26 g, 37.5 mmol) and sodium hydrogencarbonate (3.15 g, 37.5 mmol) at room temperature. The flesh-colored precipitate formed was collected by filtration, washed thoroughly with water, and dried for 8 h under vacuum at 60 °C. Yield: 5.60 g, 98.4%. Elemental analysis (%) calcd for $C_{49}H_{30}Fe_3N_7O_{30}$: C 43.14, H 2.22, N 7.19; found: C 43.39, H 2.67, N 7.15; UV/Vis absorption (in CH_3CN): λ_{max} (ε_{max} [$M^{-1}cm^{-1}$]) = 264 (69600), 344sh (8750), 460sh (650) nm; IR (CsI): $\tilde{\nu}$ = 1701 (C=O), 1587, 1542, 1524 (NO_2), 1420, 1349 (NO_2), 725 cm^{-1}; ESI-MS: *m*/*z* 1180 $[Fe_3O(p\text{-}NO_2C_6H_4COO)_6]^+$.

2: Complex **1** (0.30 g, 0.1 mmol) was dissolved in DMF (1.5 mL) and diethyl ether was allowed to diffuse into this solution at 10 °C. After four days dark red-brown crystals were separated by filtration, washed several times with a mixture of diethyl ether and DMF (13:1) to remove the co-precipitated colorless needles of *p*-nitrobenzoic acid, and dried in the air. Yield: 0.27 g, 96.0% (based on Fe). Elemental analysis (%) calcd for $C_{89}H_{73}Fe_6N_{15}O_{52}$: C 42.42, H 2.92, N 8.34; found: C 42.31, H 2.64, N 8.20; UV/Vis absorption (in CH_3CN): λ_{max} (ε_{max} [$M^{-1}cm^{-1}$]) = 268 (129000), 344sh (18600), 460sh (1670) nm; IR (CsI): $\tilde{\nu}$ = 1657, 1622, 1585, 1525 (NO_2), 1419, 1348 (NO_2), 726 cm^{-1}.

Alkane oxidation experiments; general procedure: cyclohexane (10.0 mmol) was added to a clear orange-red solution of **2**·4.5 DMF·2.7 H_2O (0.03 mmol) in dry acetonitrile (MeCN; 20 mL), After thermal equilibration (55 °C), H_2O_2 (50% aqueous solution) was added by syringe pump (1.3–3.5 mL h^{-1}). The reaction mixture was stirred for another 30 min. After addition of internal standards (*n*-heptane, 2-ethyl-1-butanol, 5-methyl-2-hexanone) and dichloromethane, extraction and filtration through silica, the amounts of residual cyclohexane and of the oxidation products (cyclohexanol and cyclohexanone) were determined using capillary gas chromatography-FID detection (column: carbowax, T-gradient 45–210 °C, carrier gas: H_2).

IR spectra were recorded on a Bruker FT-IR VERTEX70 instrument in the region of 4000–400 cm^{-1}. UV/Vis spectra were recorded using a Hewlett-Packard 8452 A spectrometer in the spectral range 190–800 nm with 2 nm spectral resolution. The sample (about 2 mg) was dissolved in CH_3CN:DMF (10:1) as solvent. This solution was measured as reference/background spectrum. Then H_2O_2 (25 μL; 30% aqueous solution, analytical grade) was added and the recording of spectra was started immediately. All experiments were carried out under temperature control (6.5, 15.4, 25.4, and 38.8 °C). Electrospray ionization mass spectrometry was carried out with a Bruker Esquire 3000 instrument (Bruker Daltonic, Germany).

Received: December 12, 2005
Published online: March 20, 2006

Keywords: alkanes · cluster compounds · iron · nitrobenzoate · oxidations

[1] a) A. M. Kirillov, M. N. Kopylovich, M. V. Kirillova, M. Haukka, M. Fatima, C. Guedes da Silva, A. J. L. Pombeiro, *Angew. Chem.* **2005**, *117*, 4419–4423; *Angew. Chem. Int. Ed.* **2005**, *44*, 4345–4349; b) M. D. Hughes, Y.-J. Xu, P. Jenkins, P. McMorn, P. Landon, D. I. Enache, A. F. Carley, G. A. Attard, G. J. Hutchings, F. King, E. H. Stitt, P. Johnston, K. Griffin, C. J. Kiely, *Nature* **2005**, *437*, 1132–1135; c) M. C. Esmelindro, E. G. Oestreicher, H. Marquez-Alvarez, C. Dariva, S. M. S. Egues, C Fernandes, A. J. Bortoluzzi, V. Drago, O. A. C. Antunes, *J. Inorg. Biochem.* **2005**, *99*, 2054–2061; d) G. B. Shul'pin, G. V. Nizova, Y. N. Kozlov, V. S. Arutyunov, A. C. M. Dos Santos, A. C. T. Ferreira, D. Mandelli, *J. Organomet. Chem.* **2005**, *690*, 4498–4504; e) G. J. P. Britovsek, J. England, A. J. P. White, *Inorg. Chem.* **2005**, *44*, 8125–8134; f) C. Pavan, J. Legros, C. Bolm, *Adv. Synth. Catal.* **2005**, *347*, 703–705; g) R. H. Fish, A. Rabion, K. Neimann, R. Neumann, J.-M. Vincent, M. Contel, C. Izuel, P. R. Villuendas, P. J. Alonso, *Top. Catal.* **2005**, *32*, 185–196; h) J. Tong, Z. Li, C. Xia, *J. Mol. Catal. A* **2005**, *231*, 197–203; i) B. C. Bales, P. Brown, A. Dehestani, J. M. Mayer, *J. Am. Chem. Soc.* **2005**, *127*, 2832–2833; j) Y. N. Kozlov, G. V. Nizova, G. B. Shul'pin, *J. Mol. Catal. A* **2005**, *227*, 247–253; k) G. B. Shul'pin, C. C. Golfeto, G. Süss-Fink, L. S. Shul'pina, D. Mandelli, *Tetrahedron Lett.* **2005**, *46*, 4563–4567; l) S. Tanase, C. Foltz, R. de Gelder, R. Hage, E. Bouwman, J. Reedijk, *J. Mol. Catal. A* **2005**, *225*, 161–167; m) C. Limberg, *Angew. Chem.* **2005**, *117*, 6256–6258; *Angew. Chem. Int. Ed.* **2005**, *44*, 6102–6104; n) G. B. Shul'pin, *Transition Metals for Organic Synthesis, Vol. 2*, Wiley-VCH, Weinheim, 2nd ed., **2004**, pp. 215–241; o) J. A. Labinger, *J. Mol. Catal. A* **2004**, *220*, 27–35.

[2] N. F. Gol'dshleger, M. B. Tyabin, A. E. Shilov, A. A. Shteinman, *Zh. Fiz. Khim.* **1969**, *43*, 2174–2175; N. F. Gol'dshleger, M. B. Tyabin, A. E. Shilov, A. A. Shteinman, *Russ. J. Phys. Chem.* **1969**, *43*, 1222–1223.

[3] A. E. Shilov, G. B. Shul'pin, *Chem. Rev.* **1997**, *97*, 2879–2932.

[4] a) M. Lersch, M. Tilset, *Chem. Rev.* **2005**, *105*, 2471–2526; b) R. H. Crabtree, *J. Organomet. Chem.* **2004**, *689*, 4083–4091; c) R. A. Periana, G. Bhalla, W. J. Tenn, K. J. H. Young, X. Y. Liu, O. Mironov, C. Jones, V. R. Ziatdinov, *J. Mol. Catal. A* **2004**, *220*, 7–25.

[5] a) G. K. Cook, J. M. Mayer, *J. Am. Chem. Soc.* **1994**, *116*, 1855–1868; b) T. C. Lau, C. K. Mak, *J. Chem. Soc. Chem. Commun.* **1995**, 943–944.

[6] a) H. Mimoun, L. Saussine, E. Daire, M. Postel, J. Fischer, R. Weiss, *J. Am. Chem. Soc.* **1983**, *105*, 3101–3110; b) E. Daire, H. Mimoun, L. Saussine, *Nouv. J. Chim.* **1984**, *8*, 271–274.

[7] a) A. S. Goldstein, R. S. Drago, *J. Chem. Soc. Chem. Commun.* **1991**, 21–22; b) G. V. Nizova, Y. N. Kozlov, G. B. Shul'pin, *Russ. Chem. Bull.* **2004**, *53*, 2330–2333; c) G. B. Shul'pin, G. V. Nizova, Y. N. Kozlov, L. G. Cuervo, G. Süss-Fink, *Adv. Synth. Catal.* **2004**, *346*, 317–332; d) G. V. Nizova, C. Bolm, S. Ceccarelli, C. Pavan, G. B. Shul'pin, *Adv. Synth. Catal.* **2002**, *344*, 899–905; e) R. H. Fish, M. S. Konings, K. J. Oberhausen, R. H. Fong, W. M. Yu, G. Christou, J. B. Vincent, D. K. Coggin, R. M. Buchanan, *Inorg. Chem.* **1991**, *30*, 3002–3006.

[8] a) S. Menage, M. N. Collomb-Dunand-Sauthier, C. Lambeaux, M. Fontecave, *J. Chem. Soc. Chem. Commun.* **1994**, 1885–1886; b) J. Kim, R. G. Harrison, C. Kim, L. Que, Jr., *J. Am. Chem. Soc.* **1996**, *118*, 4373–4379; c) R. H. Fish, R. H. Fong, K. J. Oberhausen, M. S. Konings, M. C. Vega, G. Christou, J. B. Vincent, R. M. Buchanan, *New J. Chem.* **1992**, *16*, 727–733.

[9] a) A. S. Goldstein, R. S. Drago, *Inorg. Chem.* **1991**, *30*, 4506–4510; b) Y. Ishii, T. Iwahama, S. Sakaguchi, K. Nakayama, Y. Nishiyama, *J. Org. Chem.* **1996**, *61*, 4520–4526; c) X. Baucherel, I. W. C. E. Arends, S. Ellwood, R. A. Sheldon, *Org. Process Res. Dev.* **2003**, *7*, 426–428; d) X. Baucherel, L. Gonsalvi, I. W. C. E. Arends, S. Ellwood, R. A. Sheldon, *Adv. Synth. Catal.* **2004**, *346*,

 © 2006 Wiley-VCH Verlag GmbH & Co. KGaA, Weinheim

286 – 296; e) N. Mizuno, M. Tateishi, T. Hirose, M. Iwamoto, *Chem. Lett.* **1993**, 2137 – 2140.

[10] a) D. H. R. Barton, M. J. Gastiger, W. B. Motherwell, *J. Chem. Soc. Chem. Commun.* **1983**, 41 – 43; b) D. H. R. Barton, D. Doller, *Acc. Chem. Res.* **1992**, *25*, 504 – 512; c) D. H. R. Barton, F. Halley, N. Ozbalik, M. Schmitt, E. Young, G. Balavoine, *J. Am. Chem. Soc.* **1989**, *111*, 7144 – 7149.

[11] a) C. Sheu, S. A. Richert, P. Cofre, B. Ross, Jr., A. Sobkowiak, D. T. Sawyer, J. R. Kanofsky, *J. Am. Chem. Soc.* **1990**, *112*, 1936 – 1942; b) D. T. Sawyer, A. Sobkowiak, T. Matsushita, *Acc. Chem. Res.* **1996**, *29*, 409 – 416.

[12] a) S. J. Lippard, *Angew. Chem.* **1988**, *100*, 353 – 371; *Angew. Chem. Int. Ed. Engl.* **1988**, *27*, 344 – 361; b) E. Y. Tshuva, S. J. Lippard, *Chem. Rev.* **2004**, *104*, 987 – 1012; c) D. M. Kurtz, *Chem. Rev.* **1990**, *90*, 585 – 606; d) M. Costas, M. P. Mehn, M. P. Jensen, L. Que, Jr., *Chem. Rev.* **2004**, *104*, 939 – 986.

[13] M. Costas, K. Chen, L. Que, Jr., *Coord. Chem. Rev.* **2000**, *200–202*, 517 – 544.

[14] a) J. U. Rohde, J. H. In, M. H. Lim, W. W. Brennessel, M. R. Bukowski, A. Stubna, E. Muenck, W. Nam, L. Que, Jr., *Science* **2003**, *299*, 1037 – 1039; b) G. B. Shul'pin, H. Stoeckli-Evans, D. Mandelli, Y. N. Kozlov, A. T. Vallina, C. B. Woitiski, R. S. Jimenez, W. A. Carvalho, *J. Mol. Catal. A* **2004**, *219*, 255 – 264; c) T. A. van den Berg, J. W. de Boer, W. R. Browne, G. Roelfes, B. L. Feringa, *Chem. Commun.* **2004**, 2550 – 2551; d) J. Kaizer, E. J. Klinker, N. Y. Oh, J. U. Rohde, W. J. Song, A. Stubna, J. Kim, E. Muenck, W. Nam, L. Que, Jr., *J. Am. Chem. Soc.* **2004**, *126*, 472 – 473; e) R. H. Fish, M. S. Konings, K. J. Oberhausen, R. H. Fong, W. M. Yu, G. Christou, J. B. Vincent, D. K. Coggin, R. M. Buchanan, *Inorg. Chem.* **1991**, *30*, 3002 – 3006; f) R. A. Leising, B. A. Brennan, L. Que, Jr., B. G. Fox, E. Muenck, *J. Am. Chem. Soc.* **1991**, *113*, 3988 – 3990.

[15] D. H. R. Barton, M. J. Gastiger, W. B. Motherwell, *J. Chem. Soc. Chem. Commun.* **1983**, 731 – 733.

[16] a) A. E. Tapper, J. R. Long, R. J. Staples, P. Stavropoulos, *Angew. Chem.* **2000**, *112*, 2433 – 2436; *Angew. Chem. Int. Ed.* **2000**, *39*, 2343 – 2346; b) B. Singh, J. R. Long, G. C. Papaefthymiou, P. Stavropoulos, *J. Am. Chem. Soc.* **1996**, *118*, 5824 – 5825.

[17] a) R. F. Weinland, L. Herget, *Arch. Pharm.* **1924**, *262*, 163 – 182; b) R. F. Weinland, A. Herz, *Ber. Dtsch. Chem. Ges.* **1913**, *45*, 2662 – 2680.

[18] a) W. Micklitz, S. J. Lippard, *J. Am. Chem. Soc.* **1989**, *111*, 6856 – 6858; b) W. Micklitz, V. McKee, R. L. Rardin, L. E. Pence, G. C. Papaefthymiou, S. G. Bott, S. J. Lippard, *J. Am. Chem. Soc.* **1994**, *116*, 8061 – 8069; c) S. M. Gorun, G. C. Papaefthymiou, R. B. Frankel, S. J. Lippard, *J. Am. Chem. Soc.* **1987**, *109*, 3337 – 3348; d) E. J. Seddon, J. C. Huffman, G. Christou, *J. Chem. Soc. Dalton Trans.* **2000**, 4446 – 4452.

[19] C. Boskovic, A. Sieber, G. Chaboussant, H. U. Guedel, J. Ensling, W. Wernsdorfer, A. Neels, G. Labat, H. Stoeckli-Evans, S. Janssen, *Inorg. Chem.* **2004**, *43*, 5053 – 5068.

[20] W. Jary, P. Poechlauer, N. Neuwirth, M. Nagl, W. Schmid, PTC Int. Appl. WO2005063385, **2005**, [*Chem. Abstr.* **2005**, 143, 133822].

[21] a) R. H. Fish, R. H. Fong, K. J. Oberhausen, M. S. Konings, M. C. Vega, G. Christou, J. B. Vincent, R. M. Buchanan, *New J. Chem.* **1992**, *16*, 727 – 733; b) M. M. Kats, G. B. Shul'pin, *Izv. Akad. Nauk SSSR Ser. Khim.* **1990**, *10*, 2461; c) E. Libby, H. Vogel Guillen, *Ing. Cienc. Quim.* **1997**, *17*, 54 – 57.

[22] Crystal data for $[Fe_6O_3(OH)(p\text{-}NO_2C_6H_4COO)_{11}(dmf)_4]\cdot 4.5\,DMF\cdot 2.7\,H_2O$: $C_{102.5}H_{109.95}Fe_6N_{19.5}O_{59.23}$, $M_r = 2897.75$, triclinic, space group $P\bar{1}$, $a = 16.8181(6)$, $b = 17.1254(6)$, $c = 26.4339(9)$ Å, $\alpha = 82.955(2)$, $\beta = 73.785(2)$, $\gamma = 62.640(2)°$, $V = 6492.6(4)$ Å^3, $Z = 2$, $\rho_{calcd} = 1.482$ g cm^{-3}, $Mo_{K\alpha}$ radiation ($\lambda = 0.71073$ Å, $\mu = 0.755$ mm^{-1}), $T = 100$ K, $R = 0.0605$ ($F^2 > 2\sigma$), $R_w = 0.1860$ (for 126824 data and 1732 refined parameters). A single crystal of suitable size was attached to a glass fiber using acrylic resin and mounted on a goniometer head at 40 mm from the detector. Data were collected on a Bruker X8APEX II CCD diffractometer. 1476 frames were measured, each for 25 s over 1° scan width. The data were processed using Denzo-SMN software.[31] The structure was solved by direct methods and refined by full-matrix least-squares techniques using the SHELX-97 program. Non-hydrogen atoms were refined with anisotropic displacement parameters. H atoms were placed in calculated positions and refined as riding atoms. CCDC-292546 contains the supplementary crystallographic data for this paper. These data can be obtained free of charge from The Cambridge Crystallographic Data Centre via www.ccdc.cam.ac.uk/data_request/cif.

[23] E. Keller, A Computer Program for the Graphic Representation of Molecular and Crystallographic Models, Universität Freiburg, **1999**.

[24] M. D. Snodin, L. Ould-Moussa, U. Wallmann, V. Bachler, E. Bill, H. Hummel, T. Weyhermüller, P. Hildebrandt, K. Wieghardt, *Chem. Eur. J.* **1999**, *5*, 2554 – 2565.

[25] S. Kimura, E. Bill, E. Bothe, T. Weyhermüller, Wieghardt, *J. Am. Chem. Soc.* **2001**, *123*, 6025 – 6039.

[26] a) N. E. Brese, M. O'Keefe, *Acta Crystallogr. Sect. B* **1991**, *47*, 192 – 197; b) H. H. Thorp, *Inorg. Chem.* **1992**, *31*, 1585 – 1588.

[27] a) X. Zhang, H. Furutachi, S. Fujinami, S. Nagamoto, Y. Maeda, Y. Watanabe, T. Kitagawa, M. Suzuki, *J. Am. Chem. Soc.* **2005**, *127*, 826 – 827; b) M. R. Bukowski, P. Comba, C. Limberg, M. Merz, L. Que, Jr., T. Wistuba, *Angew. Chem.* **2004**, *116*, 1303 – 1307; *Angew. Chem. Int. Ed.* **2004**, *43*, 1283 – 1287; c) D. T. Sawyer, M. S. McDowell, L. Spencer, P. K. S. Tsang, *Inorg. Chem.* **1989**, *28*, 1166 – 1170; d) I. Shweky, L. E. Pence, G. C. Papaefthymiou, R. Sessoli, J. W. Yun, A. Bino, S. J. Lippard, *J. Am. Chem. Soc.* **1997**, *119*, 1037 – 1042.

[28] X. Zhang, H. Furutachi, S. Fujinami, S. Nagatomo, Y. Maeda, Y. Watanabe, T. Kitagawa, M. Suzuki, *J. Am. Chem. Soc.* **2005**, *127*, 826 – 827.

[29] M. Torrent, D. G. Musaev, K. Morokuma, H. Basch, *J. Phys. Chem. B* **2001**, *105*, 4453 – 4463.

[30] a) G. B. Shul'pin, *J. Mol. Catal. A* **2002**, *189*, 39 – 66; b) G. V. Nizova, B. Krebs, G. Süss-Fink, S. Schindler, L. Westerheide, L. Gonzalez Cuervo, G. B. Shul'pin, *Tetrahedron* **2002**, *58*, 9231 – 9237.

[31] Z. Otwinowski, W. Minor, *Processing of X-ray Diffraction Data Collected in Oscillation Mode* in *Methods in Enzymology, Vol. 276: Macromolecular Crystallography, Part A* (Eds.: C. W. Carter, Jr., R. M. Sweet), Academic Press, **1997**, pp. 307 – 326.

 © 2006 Wiley-VCH Verlag GmbH & Co. KGaA, Weinheim

N_2 Activation

DOI: 10.1002/anie.200503709

Cleavage of the N_2 Triple Bond by the Ti Dimer: A Route to Molecular Materials for Dinitrogen Activation?**

Hans-Jörg Himmel, Olaf Hübner, Wim Klopper, and Laurent Manceron*

Dinitrogen activation is still a very lively field of research that has witnessed some major advances in recent years.[1] One important direction of this research is the search for new transition- and rare-earth-metal complexes that coordinate N_2 and allow its reduction or oxidation; for example, an Mo complex has been reported as being capable of reducing N_2 to NH_3 under mild conditions.[2] The associated catalytic cycle was investigated with the aid of quantum chemical calculations and compared with catalysis by biological systems involving nitrogenase.[3] This cycle includes a sequence of steps in which the formal oxidation state of the Mo atom varies between III and VI.

We and other research groups have generated and characterized the Ti dimer with the aid of the matrix isolation technique. On the basis of resonance Raman measurements,[4] the Ti–Ti bond energy has been estimated to be approximately 120 kJ mol^{-1}, although quantum chemical calculations[5] suggest a somewhat higher value of 150 kJ mol^{-1}. We have also characterized several electronically excited states of this interesting molecule by using absorption spectroscopy and quantum chemical calculations. Such excited states are very important in relation to the unusual reactivity of metal dimers such as Ti_2 as well as small clusters.[6] The unusually high reactivity of Ti_2 has already been observed in the complex it forms with Xe.[4] Herein, we report the reaction with N_2, which proceeds in a single step without a significant activation barrier to result in complete cleavage of the strong N≡N triple bond and the formation of a cyclic Ti(μ-N)$_2$Ti molecule. By contrast, a Ti atom in its electronic ground state does not react with N_2; matrix-isolation experiments give no spectroscopic evidence to suggest the formation of even a loosely bound complex. The behavior of Ti_2 thus provides a textbook example of the remarkable differences in reactivity between metal atoms, dimers, and small clusters. Our results pave the way to new catalytically active, Ti-nanoparticle-containing materials for dinitrogen activation.

Figure 1 shows the IR spectrum of an Ne matrix containing Ti_2 and 0.05 % $^{14}N_2$.[7] The IR spectrum is characterized by intense bands which can be assigned to a single product of the

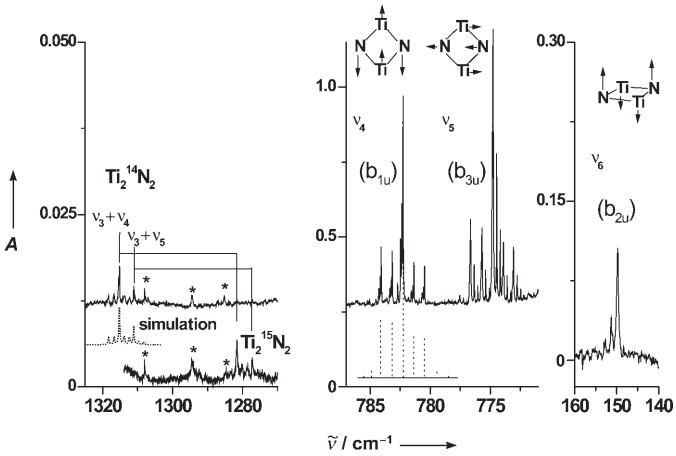

Figure 1. Infrared spectrum of Ti_2N_2 isolated in solid neon at 3 K in the fundamental and combination regions. Left (top and bottom): spectra observed with $^{14}N_2$ or $^{15}N_2$ precursors; insert: the dotted line presents a simulation for two bands centered at 1315.2 and 1311.1 cm^{-1} for the expected Ti_2 natural isotopic distribution. The asterisks designate CH_4 and N_2O impurity bands. Center and right: spectrum observed with $Ti_2{}^{14}N_2$ and a comparison with a stick spectrum (•••••) representing the expected Ti_2 natural isotopic distribution.

spontaneous reaction between Ti_2 and N_2. The most intense band occurs at 774.77 cm^{-1}, and a second feature that also exhibits a marked Ti isotopic pattern characteristic of the presence of two equivalent Ti atoms is observed at slightly higher energy (Table 1). This second band has its central component at 782.25 cm^{-1} and exhibits fine structure at a resolution of 0.02 cm^{-1}. Since the relative intensities change when the reaction conditions are altered, a matrix effect is judged to be responsible for this fine structure. In the low-wavenumber region, there is a third, less intense band of the same product at 149.72 cm^{-1}. Three additional bands showing isotopic patterns characteristic of two equivalent Ti atoms are also observed with central components at 1315.2, 1311.1, and 1246.15 cm^{-1}, and a fourth band is observed at 1238.7 cm^{-1}. Subsequent analysis shows that these bands are associated not with fundamental wavenumbers, but rather with combination

[*] Dr. H.-J. Himmel
Inorganic Chemistry Laboratory
University of Oxford
South Parks Road, Oxford OX1 3QR (UK)
Fax: (+44) 1865-272-690
E-mail: hans-jorg.himmel@chem.ox.ac.uk
Dr. O. Hübner
Institut für Nanotechnologie
Forschungszentrum Karlsruhe
Postfach 3640, 76021 Karlsruhe (Germany)
Prof. Dr. W. Klopper
Institut für Physikalische Chemie
Universität Karlsruhe (TH)
76128 Karlsruhe (Germany)
Dr. L. Manceron
LADIR-Laboratoire de Dynamique
Interactions et Réactivité, UMR 7075
Université Pierre et Marie Curie-CNRS
case 49, 4, Place Jussieu, 75252 Cedex, Paris (France)

[**] H.-J.H. gratefully acknowledges financial support by the Deutsche Forschungsgemeinschaft (DFG) and the German Academic Exchange Service (DAAD PROCOPE grant). W.K. acknowledges support by the DFG through the Center for Functional Nanostructures (CFN, Project No. C3.3). L.M. acknowledges support by the Centre National de la Recherche Scientifique (PICS3032) and Ministère des Affaires Etrangères (PROCOPE09643SG).

 © 2006 Wiley-VCH Verlag GmbH & Co. KGaA, Weinheim

Table 1: Observed wavenumbers ([cm^{-1}], relative intensities in parentheses) of the bands of different isotopomers of Ti_2N_2 in solid neon.

$Ti_2{}^{14}N_2$	$Ti_2{}^{15}N_2$	$Ti_2{}^{14}N^{15}N$
1315.2	1281.6	1298.5
1311.1	1277.2	
1246.15	1223.7	1235.7
1238.7	1216.4	
		801.2 (0.08)
782.25 (0.53)	762.20	772.52 (0.50)
774.77 (1.00)	754.77	761.54 (1.00)
149.72 (0.18)	145.85	147.78 (0.2)

modes. Experiments in which the concentration of titanium and dinitrogen were altered, as well as annealing experiments, confirm that all these bands belong to a single product.

The experiments were repeated with $^{15}N_2$, equimolar mixtures of $^{14}N_2$ and $^{15}N_2$, as well as 1:2:1 mixtures of $^{14}N_2$/$^{14}N^{15}N$/$^{15}N_2$. In the experiments with $^{15}N_2$, all the bands were shifted, as anticipated, to lower wavenumbers. The spectrum obtained in the experiments using equimolar mixtures of $^{14}N_2$ and $^{15}N_2$ is essentially a superposition of the spectra recorded with $^{14}N_2$ and $^{15}N_2$ separately. This result indicates that the product contains no more than two N atoms and that the reaction proceeds by cleavage of a single N_2 molecule. In diffusion experiments at 9 K in the dark, the Ti_2 absorption bands are observed to decrease concomitantly with the growth of Ti_2N_2 absorption bands. It appears therefore that the reaction of Ti_2 with N_2 under matrix conditions leads without activation energy to a molecule with the overall formula Ti_2N_2. Additional bands are observed in the experiments with 1:2:1 mixtures of $^{14}N_2$/$^{14}N^{15}N$/$^{15}N_2$ that are not present in the experiments with $^{14}N_2$ or $^{15}N_2$ alone, which results in a triplet pattern for each of the absorption bands. The strongest band now appears at 761.54 cm^{-1}, which is not quite midway between the corresponding bands in the $^{14}N_2$ (774.77 cm^{-1}) and $^{15}N_2$ experiments (754.77 cm^{-1}). The patterns imply that the two N atoms in the Ti_2N_2 product are equivalent. The spectra from the experiments with $^{14}N^{15}N$ show a fourth fundamental band, located at 801.2 cm^{-1}. The fact that this absorption is observed only if the symmetry is reduced by the presence of ^{14}N and ^{15}N in the product molecule argues for a point group with a center of inversion.

Most fitting with these observations is the inference that Ti_2N_2 exhibits D_{2h} symmetry, and that the symmetry is reduced to C_{2v} in the $Ti_2{}^{14}N^{15}N$ isotopomer. Only three of the six fundamental vibrations are IR active in the D_{2h} point group. The band at low wavenumber (149.72 cm^{-1} for $Ti_2{}^{14}N_2$) can thus be assigned to the out-of-plane deformation [$\nu_6(b_{2u})$], and the bands at 782.25 and 774.77 cm^{-1} for $Ti_2{}^{14}N_2$ can be assigned to the stretching modes $\nu_4(b_{1u})$ and $\nu_5(b_{3u})$, respectively. Finally, the band at 801.2 cm^{-1} observed for the $Ti_2{}^{14}N^{15}N$ isotopomer corresponds to the $\nu_1(a_1)$ mode of the C_{2v}-symmetric molecule; the corresponding stretching mode in D_{2h} symmetry has a_g symmetry and is therefore IR silent. If the symmetry is reduced from D_{2h} to C_{2v}, the b_{3u} mode (ν_5) transforms to the a_1 representation. This mode appears at 761.54 cm^{-1} for $Ti_2{}^{14}N^{15}N$. As a result of coupling with the other a_1 mode at 801.2 cm^{-1}, the wavenumber of this mode is red-shifted with respect to the mean of the wavenumbers observed for the $\nu_5(b_{3u})$ mode of $Ti_2{}^{14}N_2$ and $Ti_2{}^{15}N_2$. The bands at 1315.2, 1311.1, 1246.15, and 1238.7 cm^{-1} of $Ti_2{}^{14}N_2$ can be assigned to the combinations $\nu_3(b_{2g}) + \nu_4(b_{1u})$, $\nu_3(b_{2g}) + \nu_5(b_{3u})$, $\nu_2(a_g) + \nu_4(b_{1u})$, and $\nu_2(a_g) + \nu_5(b_{3u})$. Hence the wavenumbers of the gerade modes can be estimated, and thus a relatively complete vibrational analysis of the molecule in its electronic ground state can be carried out. Unfortunately it was not possible to obtain Raman spectra of this species.

In summary, the experimental results show that Ti_2 reacts with N_2 without any significant reaction barrier to give the D_{2h}-symmetric Ti_2N_2 molecule [Eq. (1)]. This molecule has a planar, cyclic structure with alternating Ti and N atoms. A

(1)

normal-coordinate analysis yields an N-Ti-N bond angle of $(90 \pm 5)°$ and a Ti–N stretching force constant of 322 $N\,m^{-1}$. The Ti–N bond length can be estimated by using an empirical correlation[8] to be (175 ± 3) pm. The N···N separation is estimated to be approximately 247 pm, which indicates that there is no significant direct interaction between the two N atoms. The strong N≡N bond is thus completely cleaved in an exothermic reaction.

Quantum-chemical calculations were carried out to obtain more information about the reaction product and the thermodynamics of this unusual change. In contrast to an earlier calculation, which predicted a $^3B_{1u}$ electronic ground state,[9] the present calculations with the multireference configuration interaction (MRCI) method based on multiconfigurational self-consistent field calculations with natural atomic orbital basis sets (Ti: [7s6p4d3f2g]; N: [5s4p3d2f])[10] yield a ^1A_g electronic ground state, whereas the $^3B_{1u}$ state is 22.4 $kJ\,mol^{-1}$ higher in energy.

Figure 2 shows isodensity surfaces of the molecular valence orbitals of the ^1A_g state. The two lowest orbitals comprise essentially the nitrogen lone pairs. Following these are six N(p)–Ti(d) bonding orbitals (about 1.95 electrons per orbital), all of which are polarized towards the nitrogen atoms. The two highest orbitals (1.5 and 0.5 electrons) are the bonding and antibonding combinations of Ti d orbitals. A bond order of 1.5 per Ti–N bond is obtained from the six approximately doubly occupied Ti–N bonding orbitals. The N···N and Ti···Ti separations in the ground state are calculated according to MRCI to be 251.0 and 255.4 pm, respectively, without Davidson corrections, and 251.9 and 256.1 pm, respectively, with Davidson corrections. These values are pleasingly close to the experimental estimates. For computational efficiency, we rely on density functional calculations (BP86/def2-TZVP)[11] for the vibrational frequencies. Table 2 compares the experimentally observed vibrational wavenumbers with the calculated values. The agreement is highly satisfactory and lends strong support to our assignment.

We found that Ti atoms under similar conditions do not react with N_2. Thus, the Ti dimer, although featuring a relatively weak Ti–Ti bond, shows a reactivity completely

 © 2006 Wiley-VCH Verlag GmbH & Co. KGaA, Weinheim

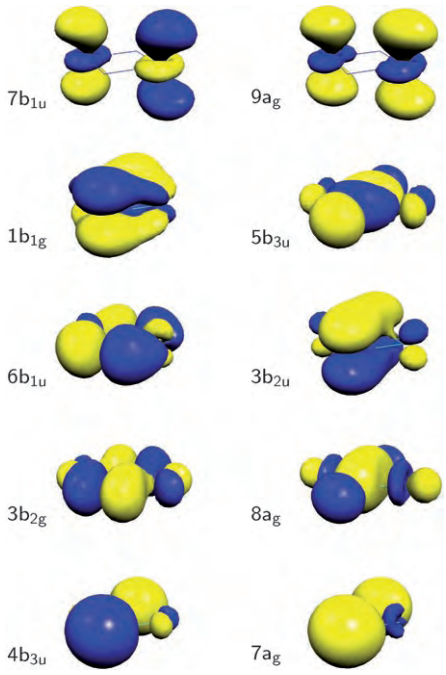

Figure 2. Isodensity surfaces of the valence orbitals of the ^1A_g ground state of Ti_2N_2.

Table 2: Comparison of the wavenumbers [cm^{-1}] observed and calculated for $^{48}Ti(\mu\text{-}^{14}N)_2{}^{48}Ti$.

Obsd	Calcd[a]	Assignment
811[b]	836.9	$\nu_1(a_g)$
464 ± 5[c]	471.2	$\nu_2(a_g)$
538 ± 5[c]	551.0	$\nu_3(b_{2g})$
782.25	829.0	$\nu_4(b_{1u})$
774.77	780.7	$\nu_5(b_{3u})$
149.72	212.2	$\nu_6(b_{2u})$

[a] Harmonic frequencies calculated by using the BP86 functional and polarized triple-zeta valence basis sets (def2-TZVP) for the ^1A_g ground state in the broken-symmetry approximation. $R_{N\text{-}N} = 249.9$ pm, $R_{Ti\text{-}Ti} = 256.0$ pm. Alignment of the Ti atoms along the *z*-axis and N atoms along the *x*-axis. [b] Estimated on the basis of a normal coordinate analysis, considering also the wavenumber observed for this mode for $Ti_2{}^{14}N^{15}N$. [c] Estimated from the wavenumbers observed for the combination bands.

different from Ti atoms. Although the ground state of Ti_2 shows one dominant configuration, the contribution of excited valence configurations is not negligible. Therefore we do not have much confidence in the density functional calculations of the reaction enthalpy. We decided to estimate the standard enthalpy for the formation ($\Delta H_f°$) of Ti_2N_2 through isodesmic reactions based on the hypothetical reaction $2\,TiCl_4 + Si_2N_2 \rightarrow 2\,SiCl_4 + Ti_2N_2$. This reaction enthalpy was calculated (BP86/def2-TZVP)[11] to be 170 kJ mol^{-1}, and thus the reaction is endothermic. Si_2N_2 has already been characterized in matrix-isolation experiments.[12] To calculate its enthalpy of formation, we first estimated the enthalpy change for the reaction $2\,Si_{(g)} + N_{2(g)} \rightarrow Si_2N_{2(g)}$ (-433 kJ mol^{-1}) by quantum chemical calculations. From the $\Delta H_f°$ of $Si_{(g)}$ ($+450$ kJ mol^{-1}),[9] the $\Delta H_f°$ of Si_2N_2 is calculated to be about 467 kJ mol^{-1}. The $\Delta H_f°$ of $Ti_2N_{2(g)}$ can thus be estimated to be approximately 437 kJ mol^{-1} ($\Delta H_f°$ values for $TiCl_4$ and $SiCl_4$: -763.2 and -662.8 kJ mol^{-1}, respectively[13]). In view of the larger $\Delta H_f°$ value for two single N atoms (945.4 kJ mol^{-1}), this value for the $\Delta H_f°$ of $Ti_2N_{2(g)}$ demonstrates the high affinity of titanium for nitrogen.[14]

This value also implies that the reaction between $Ti_{2(g)}$ (for which $\Delta H_f°$ is ca. 833 kJ mol^{-1}) and N_2 is highly exothermic ($\Delta H_f°$ estimated to be ca. -396 kJ mol^{-1}).[15] The enthalpy change for the reaction $2\,Ti_{(s)} + N_2 \rightarrow 2\,TiN_{(s)}$ (double the enthalpy of formation) amounts to -675.4 kJ mol^{-1}. These considerations, together with the fact that crystalline titanium is inert toward nitrogen up to elevated temperatures[16] (the nitride is formed by direct reaction above 1000–1400 °C), are in line with the view that the barrier to the formation of solid TiN from solid Ti and N_2 is caused by the thermal energy required to form Ti_2 or other small clusters from solid Ti. According to these calculations, Ti_2N_2 could very well be an intermediate in the formation of solid titanium nitride (Figure 3). We are presently not able to give a detailed

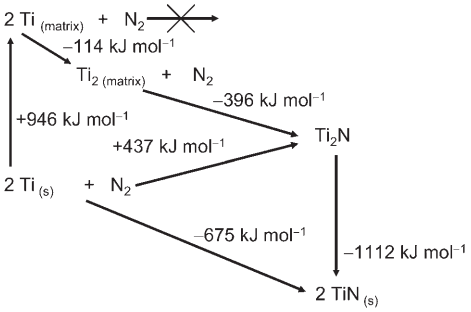

Figure 3. Thermodynamics of the reactions leading to Ti_2N_2 and solid TiN.

mechanism for the spontaneous reaction of Ti_2 with N_2, but it is probable that the relatively large number of low-lying electronic states of Ti_2 facilitates the reaction. Our quantum chemical calculations on Ti_2[5] reveal at least 15 different electronic terms with energies up to 1 eV, the lowest at about 0.2 eV. In contrast, the Ti atom has only two excited terms below 1 eV (^5F, ^1D), the lower at 0.8 eV.

We are currently extending our work to host systems other than noble-gas matrices, namely microporous materials, which allow the stabilization of Ti_2 or Ti nanoparticles at ambient temperature. These Ti-loaded materials may be able to be used for industrial processes involving the reduction or oxidation of N_2. Our current research also highlights the difference in reactivity between a metal atom M and an aggregate M_n.

Received: October 19, 2005
Published online: March 21, 2006

Keywords: cluster compounds · matrix isolation · N–N activation · nitrides · reaction mechanisms

 © 2006 Wiley-VCH Verlag GmbH & Co. KGaA, Weinheim

[1] See, for example: a) R. R. Schrock, *Philos. Trans. R. Soc. London Ser. A* **2005**, *363*, 959; b) D. C. Rees, F. A. Tezcan, C. A. Haynes, M. Y. Walton, S. Andrade, O. Einsle, J. B. Howard, *Philos. Trans. R. Soc. London Ser. A* **2005**, *363*, 971, and references therein.

[2] D. V. Yandulov, R. R. Schrock, *Science* **2003**, *301*, 76.

[3] a) F. Studt, F. Tuczek, *Angew. Chem.* **2005**, *117*, 5783; *Angew. Chem. Int. Ed.* **2005**, *44*, 5639; b) J. Kästner, P. E. Blöchl, *ChemPhysChem* **2005**, *6*, 1724.

[4] H.-J. Himmel, A. Bihlmeier, *Chem. Eur. J.* **2003**, *9*, 627.

[5] O. Hübner, H.-J. Himmel, L. Manceron, W. Klopper, *J. Chem. Phys.* **2004**, *121*, 7195.

[6] a) H.-J. Himmel in *Inorganic Chemistry in Focus II*, Wiley-VCH, Weinheim, **2005**, pp. 1–13; b) A. Köhn, B. Gaertner, H.-J. Himmel, *Chem. Eur. J.* **2003**, *9*, 3909.

[7] Titanium vapor was generated by heating a Ti–Mo filament (Godfellow, 85% Ti, 15% Mo) to 1400–1600 °C. The metal deposition rate was monitored with a quartz crystal microbalance and varied from 1.5 to 20 nmol min^{-1}. Ne and N_2 were obtained from Air Liquide, France (99.9995% and 99.998% purities, respectively), and $^{15}N_2$ was obtained from Isotec, USA (99.0% ^{15}N). $^{14}N^{15}N$ was generated from an equimolar mixture of $^{14}N_2$ and $^{15}N_2$ in a high-voltage, 100-mA DC discharge. See reference [5] for details of the matrix apparatus.

[8] H.-J. Himmel, O. Hübner, W. Klopper, L. Manceron, *Phys. Chem. Chem. Phys.*, submitted.

[9] G. P. Kushto, P. F. Souter, G. V. Chertihin, L. Andrews, *J. Chem. Phys.* **1999**, *110*, 9020.

[10] a) MOLPRO, a package of ab initio programs designed by H.-J. Werner and P. J. Knowles, Version 2002.6, R. D. Amos, A. Bernhardsson, A. Berning, P. Celani, D. L. Cooper, M. J. O. Deegan, A. J. Dobbyn, F. Eckert, C. Hampel, G. Hetzer, P. J. Knowles, T. Korona, R. Lindh, A. W. Lloyd, S. J. McNicholas, F. R. Manby, W. Meyer, M. E. Mura, A. Nicklass, P. Palmieri, R. Pitzer, G. Rauhut, M. Schütz, U. Schumann, H. Stoll, A. J. Stone, R. Tarroni, T. Thorsteinsson, and H.-J. Werner; b) P.-O. Widmark, P.-Å. Malmqvist, B. O. Roos, *Theor. Chim. Acta* **1990**, *77*, 291; c) P. Amérigo, M. Merchán, I. Nebot-Gil, P.-O. Widmark, B. O. Roos, *Theor. Chim. Acta* **1995**, *92*, 149.

[11] a) R. Ahlrichs, M. Bär, M. Häser, H. Horn, C. Kölmel, *Chem. Phys. Lett.* **1989**, *162*, 165; b) O. Treutler, R. Ahlrichs, *J. Chem. Phys.* **1995**, *102*, 346; c) F. Weigend, R. Ahlrichs, *Phys. Chem. Chem. Phys.* **2005**, *7*, 3297.

[12] G. Maier, H. P. Reisenauer, J. Glatthaar, *Organometallics* **2000**, *19*, 4775. Si_2N_2 exhibits a butterfly structure (C_{2v} symmetry).

[13] M. W. Chase, Jr., NIST-JANAF Thermochemical Tables, 4th Edition, *J. Phys. Chem. Ref. Data*, Monograph 9, ACS and AIP, Washington DC, **1998**.

[14] Ti sponge heated to 1000 °C can be used to free Ar gas from traces of N_2.

[15] The compound $[\{V(Me_3SiN\{CH_2CH_2NSiMe_3\}_2)(\mu\text{-}N)\}_2]$ is another example of a bis(μ-nitrido)-bridged complex (G. K. B. Clentsmith, V. M. E. Bates, P. B. Hitchcock, F. G. N. Colke, *J. Am. Chem. Soc.* **1999**, *121*, 10444). The reaction between two moieties of the model complex $[HN(CH_2CH_2NH)_2V]$ and N_2 was also calculated to be highly exothermic (V. M. E. Bates, G. K. B. Clentsmith, F. G. N. Cloke, J. C. Greene, H. D. Ll. Jenkin, *Chem. Commun.* **2000**, 927).

[16] *Comprehensive Inorganic Chemistry, Vol. 3* (Eds.: J. C. Bailar, H. J. Emelens, R. Nyholm, A. F. Trotman-Dickinson), Pergamon, Oxford, **1973**, p. 381.

 © 2006 Wiley-VCH Verlag GmbH & Co. KGaA, Weinheim

Upconversion

DOI: 10.1002/anie.200503966

Structural and Spectroscopic Characterization of Active Sites in a Family of Light-Emitting Sodium Lanthanide Tetrafluorides**

Annina Aebischer, Marc Hostettler, Jürg Hauser, Karl Krämer, Thomas Weber, Hans Ulrich Güdel, and Hans-Beat Bürgi**

Hexagonal β-$NaYF_4$ co-doped with Yb^{3+} and Er^{3+}, which was first studied more than 30 years ago,[1–3] is extremely efficient in converting near infrared (NIR) radiation into visible (VIS) light in a so-called upconversion (UC) process.[4–6] Such UC phosphors can be applied in display devices[7] and as labels in immunoassays.[8] Efficient UC has also been reported for β-$NaYF_4$ doped with Pr^{3+}.[9] Intense light emission was found in β-$NaEuF_4$[10] and β-$NaGdF_4$ doped with Ce^{3+} and Eu^{3+}.[11] Evidence of a multiple-site character of the emission was found by site-selective spectroscopy, and the high efficiency of the light emission was vaguely ascribed to it.[9–13] To date, all reported spectroscopic studies on doped β-$NaLnF_4$ (Ln = Y, La–Lu) have been done on powder samples.[6,9–13] The number of crystallographic sites occupied by the dopant Ln^{3+} is controversially given as two[11,13] or three.[10,12] Burns has found that crystals of hexagonal β-$NaNdF_4$ are disordered and has reported an average structure in space group $P\bar{6}$.[14] More recent X-ray powder data of the related phase β-$Na_{1.34(1)}(Y_{0.747}Yb_{0.25}Tm_{0.003})_{1.555(4)}F_6$ have been interpreted in terms of space group $P6_3/m$.[5] An unambiguous structural characterization of the spectroscopic sites, one of the prerequisites for understanding the energy-transfer processes underlying the light emission, has not been provided to date. Herein we report the first polarized absorption spectra from single crystals of β-$NaGdF_4$ doped with Er^{3+}, interpret the

[*] A. Aebischer, Dr. K. Krämer, Prof. H. U. Güdel
Department of Chemistry and Biochemistry
University of Bern
Freiestrasse 3, 3012 Bern (Switzerland)
Fax: (+41) 31-631-4399
E-mail: guedel@iac.unibe.ch
Dr. M. Hostettler, Dr. J. Hauser, Prof. H.-B. Bürgi
Laboratory of Crystallography
University of Bern
Freiestrasse 3, 3012 Bern (Switzerland)
Fax: (+41) 31-631-3996
E-mail: hans-beat.buergi@krist.unibe.ch
Dr. T. Weber
Laboratory of Crystallography
ETH Zurich
Wolfgang-Pauli-Strasse 10, 8093 Zürich (Switzerland)

[**] We thank Prof. R. B. Neder for help with the DISCUS software and D. Biner for assistance in the syntheses. This work was financially supported by the Swiss National Science Foundation.

Supporting information for this article is available on the WWW under http://www.angewandte.org or from the author.

WILEY InterScience DISCOVER SOMETHING GREAT
© 2006 Wiley-VCH Verlag GmbH & Co. KGaA, Weinheim

spectra on the basis of a microscopic model of the structural disorder as derived from diffuse X-ray scattering experiments, and show that standard single-crystal X-ray methods produce misleading results.

Thoma et al. reported the phase diagrams for the compounds discussed herein (β-$NaLaF_4$ and undoped as well as Er^{3+}-doped β-$NaGdF_4$).[15] The hexagonal β-form of $NaLnF_4$ is stable at room temperature for the whole series of lanthanides and yttrium. Both β-$NaLaF_4$ and β-$NaGdF_4$ melt incongruently: β-$NaLaF_4$ decomposes to an NaF enriched melt and LaF_3, and β-$NaGdF_4$ to an NaF enriched melt and cubic α-NaF-GdF_3, the latter being a disordered fluorite-related phase of variable composition and is one to two orders of magnitude less UC efficient than the β-phase.[2]. Phase purity is an important factor for the UC efficiency of Yb^{3+}/Er^{3+} and Yb^{3+}/Tm^{3+} co-doped $NaYF_4$ powders.[1,5] To obtain pure hexagonal powders and large single crystals the molar ratio of the starting materials NaF and LnF_3 has to be adjusted very carefully according to the appropriate phase diagrams.[15]

Our single-crystal diffraction study shows that the Laue symmetry of the total scattering of β-$NaLaF_4$ and β-$NaGdF_4$ is $\bar{6}$ and $6/m$. Structure refinements against the Bragg data in all space groups compatible with the Laue class unambiguously indicate space group $P\bar{6}$. Cell constants, atomic coordinates, and anisotropic displacement parameters are given in the Experimental Section and in the Supporting Information. The discrepancy between the space groups $P6_3/m$ from powder[5] and $P\bar{6}$ from single-crystal work[15] is attributed to the reduced information content in a powder diagram. The reflections (hkl) and (khl) have the same scattering angle but generally different intensities in the two space groups $\bar{6}$ and $6/m$. The intensities of these reflections cannot be determined separately from powder experiments, which yield only their sum, but are determined individually from a single-crystal experiment, thus allowing an unambiguous space group determination.

The average structure of the β-$NaLnF_4$ family of compounds shows three different columns of cations (Figure 1a). The site at (0,0,0), subsequently called B, as well as the site at (2/3, 1/3, 1/2), called A, are coordinated by nine F^- ions forming tricapped trigonal prisms with crystallographic C_{3h} symmetry. Site B is fully occupied by Ln^{3+}, whereas site A shows occupational disorder involving a 1:1 ratio of Na^+ and Ln^{3+} ions. The third cation site, with irregular octahedral coordination, is half vacant and half occupied by Na^+. The crystal structure of $LaCl_3$, needed for comparison later, is very similar: Cl^- ions take the positions of the F^- ions; the two C_{3h} symmetric, tricapped trigonal-prismatic sites are fully occupied by La^{3+} and crystallographically equivalent whereas the half-occupied Na^+ sites are empty.[16] Contrary to the β-$NaLnF_4$ structure type the $LaCl_3$ structure is ordered.

Disorder in the structure of β-$NaLaF_4$ was characterized from measurements of the diffuse scattering and reconstructions of undistorted planes of reciprocal space from the raw diffraction data of β-$NaLaF_4$. The relevant information is found in the a^*, b^* planes at $l=(2n+1)/2$. Three main features characterize these planes: 1) along c^*, diffuse scattering is as sharp as the Bragg reflections (Figure 1b); 2) within the planes a honeycomb pattern with webs at h and/or $k=(2n+1)/2$ is found; 3) consecutive planes, for example, $(hk-1.5)$ and $(hk-2.5)$, reveal different radial modulations of the honeycomb pattern (Figure 2c and d).

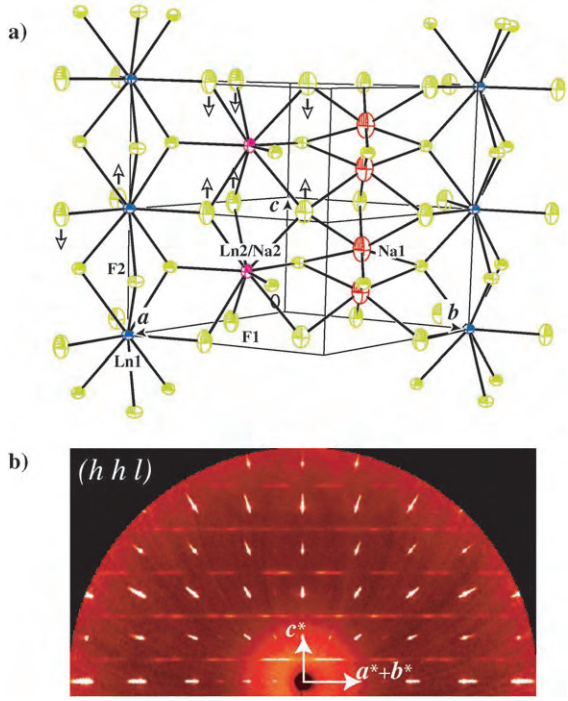

Figure 1. a) Average structure of β-$NaLnF_4$ (Ln = Y, La–Lu) showing the three different columns of metal sites along c: Site A with a 1:1 mixture of Na2 and Ln2 (pink), site B with Ln1 (blue), both with C_{3h} symmetric, tricapped trigonal-prismatic coordination geometry, and the Na1 site (red) with C_3 symmetric, distorted octahedral coordination geometry. Local distortions owing to the disorder in the crystal are indicated by arrows. b) (hhl) reciprocal layer showing the traces of the planes of diffuse scattering parallel to a^*+b^* at $l=(2n+1)/2$ between a regular array of Bragg reflections at integer l. Note the sharpness of the diffuse planes along c^* and that the diffuse intensities are orders of magnitude weaker than the Bragg intensities.

The three features, which complement fragmentary observations by Burns,[14] can be assigned to three aspects of disorder. 1) The sharpness of the honeycomb layers along c^* implies a real structure with translational order along c, that is, within the column of site A the Na2 and Ln2 atoms alternate with a translation distance $c'=2c$ corresponding to a reciprocal repeat distance $c^{*\prime}=c^*/2$ (Figure 1a). 2) The continuous honeycomb pattern in the a^*,b^* plane requires a disordered arrangement of the ordered Na2/Ln2 columns along a and b. A column with a Ln2 atom at a given z value will have three neighboring columns with either Ln2 or Na2 atoms at the same z value, corresponding to positive or negative correlation. Model crystals consisting of $100\times100\times1$ unit cells and a 1:1 mixture of Na2 and La2 atoms on site A have been generated for a range of correlations with the Monte Carlo method implemented in the DISCUS software.[17] Negative correlation between neighboring Na/Ln columns produces a honeycomb pattern (Figure 2a) as observed experimentally (Figure 2c and d); zero correlation produces continuous diffuse intensity (not shown); positive

 © 2006 Wiley-VCH Verlag GmbH & Co. KGaA, Weinheim

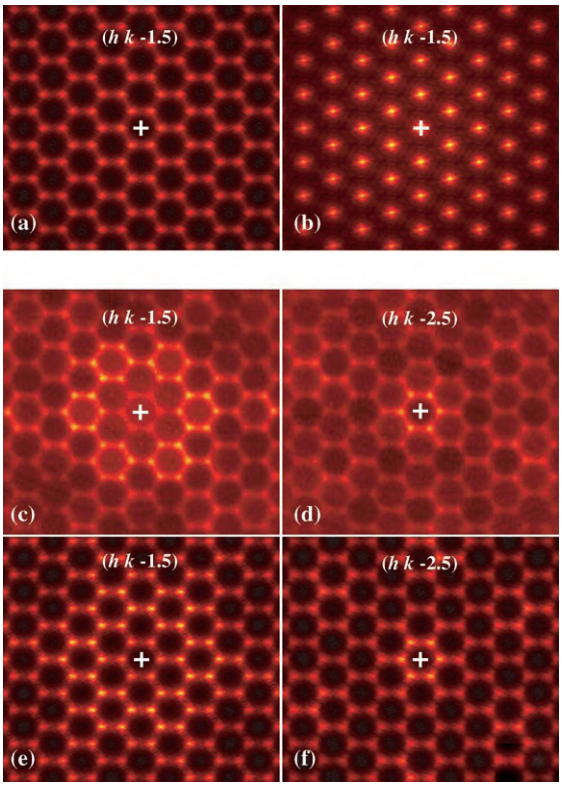

Figure 2. Diffuse scattering of β-$NaLaF_4$. Top: simulation of the reciprocal layer (*hk*−1.5) for Na2···Ln2 columns ordered along *c*, but disordered in the *a,b* plane a) with a negative correlation of −0.26 and b) with a positive correlation of +0.26. Middle: Observed reciprocal layers c) (*hk*−1.5) and d) (*hk*−2.5). Bottom: Simulation taking into account both the disorder of the Na2···Ln2 columns and a displacements of F1 atoms towards Ln2 by 0.07 Å for the reciprocal layers e) (*hk*−1.5) and f) (*hk*−2.5).

correlation produces broad maxima at integer values of *h* and *k* (Figure 2b). Thus Na2···Ln2 columns tend to be next to Ln2···Na2 columns. Note that this arrangement is analogous to that of an antiferromagnetic frustration on a 2D hexagonal Ising lattice.[18] 3) In the average structures the mean-square displacement of the F1 atom along *c*, U_{33}, is at least two-times larger than any other U_{ii} of F1 or F2, indicating positional disorder of F1 along *c* (Figure 1a and Supporting Information). Indeed, given the strict alternation of Ln2 and Na2 atoms along *c*, consideration of Coulomb interactions and bond-order calculations[19] suggest that F1 is displaced away from $Na2^+$ towards $Ln2^{3+}$. Such a displacement enhances the intensity on a ring of six hexagons around the origin in the (*hk*−1.5) layer (Figure 2e) and of the central hexagon in the (*hk*−2.5) layer (Figure 2f), as observed experimentally (Figure 2c and d, respectively). A displacement of F1 towards Na2 would interchange the patterns in Figure 2e and f, contrary to experimental observation. We have adjusted the values of the correlation and of the displacement of F1 by visually comparing the simulated intensities with the observed ones. The best match was obtained with a correlation of −0.26 and a displacement of F1 by 0.07 Å towards Ln2 (Figure 2e and f).

The average structures of β-$NaLaF_4$, β-$NaNdF_4$,[14] and β-$NaGdF_4$ are very similar: atomic positions are almost identical and the mean-square displacement parameters show analogous trends (see Supporting Information). The features in the raw and the reconstructed diffraction images of β-$NaLaF_4$ and β-$NaGdF_4$ are closely similar and consistent with the partial diffuse scattering data reported by Burns for β-$NaNdF_4$.[14] These similarities led us to conclude that the three compounds are isostructural with respect to both their average and disordered structures.

High-resolution absorption and emission spectra of the f–f multiplets of β-$NaGdF_4$:Er^{3+} show approximately twice as many lines as $LaCl_3$:Er^{3+}.[20] This doubling is illustrated in Figure 3a for the $^4I_{15/2}\rightarrow{}^4S_{3/2}$ region of the low-temperature,

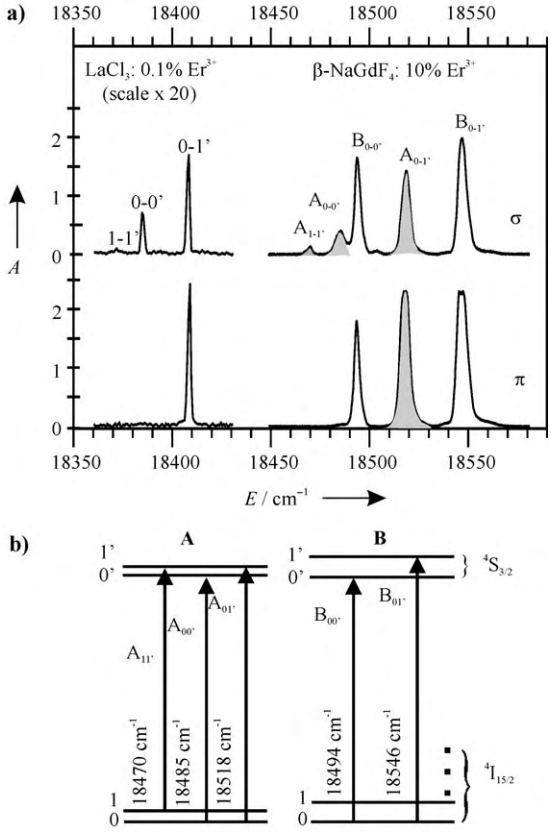

Figure 3. a) Polarized single-crystal absorption spectra of $LaCl_3$:0.1% Er^{3+} at 15 K (from Ref.[20]) and of β-$NaGdF_4$:10% Er^{3+} at 20 K in the $^4I_{15/2}\rightarrow{}^4S_{3/2}$ region. The light is polarized with the electric vector perpendicular (σ) and parallel (π) to the crystal *c* axis. The labels A (shaded bands) and B (unshaded bands) refer to the two sets of Er^{3+} ions, and the labels 0, 0′, 1, 1′ to the ligand-field levels defined in Figure 3b. b) Relevant crystal-field components of the Er^{3+} $^4I_{15/2}$ and $^4S_{3/2}$ states for the two sets A and B, respectively. The arrows and labels refer to Figure 3a.

polarized single-crystal absorption spectra. The lines of β-$NaGdF_4$:Er^{3+} are blue-shifted by about 120 cm^{-1} relative to the lines of $LaCl_3$:Er^{3+}. In a crystal field with C_{3h} point symmetry the $^4I_{15/2}$ ground-state multiplet of Er^{3+} splits into eight Kramers doublets. In our low-temperature experiment only the lowest two, labeled 0 and 1 in Figure 3b, are relevant.

 © 2006 Wiley-VCH Verlag GmbH & Co. KGaA, Weinheim

The $^4S_{3/2}$ excited state splits into two components labeled 0′ and 1′. Given the crystal structure of $LaCl_3$ described above, the interpretation of the Er^{3+}-doped $LaCl_3$ spectrum is straightforward.[20] The dopant Er^{3+}, as well as the La^{3+} ions, occupy a single site with tricapped trigonal-prismatic coordination geometry and symmetry C_{3h}.[16] The selection rules applicable to this symmetry require two lines to be observed in σ polarization (0→0′ and 0→1′), but only one in π polarization (0→1′), as found experimentally (Figure 3a). A weak σ-allowed hotband, 1→1′, is also observed.

The $^4I_{15/2}\rightarrow{}^4S_{3/2}$ absorption lines of β-$NaGdF_4$:Er^{3+} can be divided into two sets A and B, shown as shaded and unshaded bands, respectively, in Figure 3a. Spectrum A follows the C_{3h} selection rules described for $LaCl_3$:Er^{3+},[20] whereas spectrum B does not and must therefore arise from an ion in a site of lower symmetry. The assignment of the A and B spectra in Figure 3a to two crystallographically independent Er^{3+} sets is corroborated by the results of site-selective excitation experiments (not shown). The energy-level splittings derived from the experimental data are generally larger for set B (Figure 3b). The total absorption intensity of set B is about twice that of set A (Figure 3a).

The results described for β-$NaGdF_4$:Er^{3+}, β-$NaGdF_4$, and β-$NaLaF_4$ appear contradictory: the X-ray data indicate an average structure with two different, but C_{3h} symmetric Ln^{3+} sites, whereas the spectral data indicate only one such site and another one lacking C_{3h} symmetry. The contradiction is resolved, if the structural implications of the microscopic model of disorder are taken into account. The six F1 atoms forming the trigonal prism around site A (Na2/Ln2 columns) are displaced in unison along *c* towards Ln2 and away from Na2 (arrows in Figure 1a), implying that locally, site A (Na2/Ln2 columns) preserves C_{3h} symmetry. Not so for site B (Ln1 columns): the displacement of the three F1 atoms capping the F2 prism will depend on the three surrounding Na2/Ln2 columns. There are two possibilities: if all three F1 atoms are displaced in the same direction, the local symmetry of site B is reduced to C_3. Alternatively, if two F1 atoms are displaced in one direction and the third F1 in the opposite one (arrows in Figure 1a), the local symmetry is reduced to C_1. In our model crystals with 10000 unit cells, the C_3 symmetric situation is found in 5–7% of the cases, the asymmetric one in 93–95%. This statistic reflects the negative correlation implying that neighboring Na2/Ln2 columns tend to be different. The displacement of the F1 atoms by 0.07 Å induces changes up to 2° in the $F2_{prism}$-Ln-$F1_{capping}$ angles. It is amusing to note that site A, which shows occupational disorder in the average structure, maintains a symmetric inner-sphere coordination geometry, whereas for the fully occupied site B the first coordination shell is mostly asymmetric.

It is now straightforward to assign the crystallographic sites A and B to the spectroscopic sets A and B, respectively. The observation of C_{3h} selection rules for spectrum A is in agreement with the symmetric coordination of site A, while the violation of C_{3h} selection rules and the larger energy splittings of spectrum B reflect the distortion of the coordination geometry of site B to C_1 symmetry. The spectroscopic intensity ratio A/B in Figure 3a is about 0.5, in agreement with the structural site occupancies by Ln of 0.5 and 1, respectively, for sites A and B (see Supporting Information). This result also shows that the distribution of Er^{3+} onto the two Ln^{3+} sites is statistical. Spectra obtained from powders sometimes appear to indicate three sites containing optically active ions.[10,12] Since our single-crystal spectra can be interpreted unambiguously in terms of two spectroscopic sets, which in turn can be assigned unequivocally to two crystallographic sites, the observation of a third set is probably due to contamination of the powders by the cubic α-NaF-LnF_3 form.[1,15]

In summary, the first polarized absorption spectra of single crystals of β-$NaGdF_4$:Er^{3+}, a member of an important family of upconversion materials, have been measured. To elucidate the structural nature of the photoactive sites and to correlate them unambiguously with the spectroscopic data, it was necessary to interpret the diffuse X-ray scattering in terms of a microscopic model of disorder. The relevance of correlating structural and spectroscopic sites for light-emitting materials, Yb^{3+} and Er^{3+} co-doped β-$NaYF_4$ in particular, is significant. The UC process in this compound has been shown to involve successive energy-transfer steps from Yb^{3+} to Er^{3+}.[3] The presence of two independent sites for both Yb^{3+} and Er^{3+} ions in the most efficient UC material β-$NaYF_4$: 18% Yb^{3+}, 2% Er^{3+}[5–6] quadruples the number of possible $Yb^{3+}\rightarrow Er^{3+}$ energy-transfer processes and thus significantly increases the probability of an extremely efficient resonant or near resonant process. The presence of multiple active sites has been correlated with high light yield also in other phosphors.[21] The present single-crystal study lends strong support to the idea that the generally high emission intensities, and in particular, the high NIR→green/red and NIR→blue UC emission intensities in β-$NaYF_4$: 18% Yb^{3+}, 2% Er^{3+} and β-$NaYF_4$: 25% Yb^{3+}, 0.3% Tm^{3+}, respectively,[5] originate from the interplay of the ions on the two sites.

Experimental Section

Single crystals of β-$NaLaF_4$, β-$NaGdF_4$, and β-$NaGdF_4$:10% Er^{3+} were grown by the Bridgman technique in glassy carbon ampoules under an Ar atmosphere. A mixture of the starting materials NaF and LnF_3 (Ln = La, Gd, Er) was synthesized according to Ref. [5] The NaF:LnF_3 ratio was chosen to be 0.38:0.62. The single-crystalline part of the material was found in the tip of the ampoules, well separated from the polycrystalline NaF/β-$NaLnF_4$ eutectic mixture.

Low-temperature polarized absorption spectra were recorded on a Cary 6000i (Varian) spectrophotometer using a closed-cycle helium cryostat (Air Products, Displex) and calcite polarizers.

Crystal-structure determination for $NaLaF_4$ ($NaGdF_4$): Crystals of globular shape, size $0.02\times0.035\times0.05\,mm^3$ ($0.02\times0.023\times0.03\,mm^3$), hexagonal, $P\bar{6}$, $a=6.1863(9)$ (6.0304(9)), $c=3.8338(8)$ Å (3.6111(7) Å), $V=127.06(4)$ Å^3 (113.73(3) Å^3), $\rho_{calcd}=4.664\,g\,cm^{-3}$ ($5.612\,g\,cm^{-3}$), $T=298$ K; Bruker Smart 1 K area detector diffractometer with graphite-monochromated $Mo_{K\alpha}$ radiation, $\lambda=0.71073$ Å, 0.3° ω-scans, SMART and SAINT software;[22] 1335 (1612) reflections measured, 219 (191) unique, $R_{int}=0.0321$ (0.0126), $2\theta_{max}=55.08°$ (54.62°), empirical absorption correction with SADABS,[23] $\mu=12.657\,mm^{-1}$ ($21.924\,mm^{-1}$), $T_{min}=0.510$ (0.491), $T_{max}=0.776$ (0.645); full-matrix least-squares refinement against F^2 with SHELXL97[24] using 219 (191) reflections ($I>2\sigma(I)$) and 22 parameters, $R1=0.0130$ (0.0094) ($I>2\sigma(I)$), $wR2=0.0307$ (0.0238) (all data), inversion twinning ratio 0.32(4) (no twinning), residual electron density $+0.603/-0.82\,e\,Å^{-3}$ ($+0.340/-0.374\,e\,Å^{-3}$).

 © 2006 Wiley-VCH Verlag GmbH & Co. KGaA, Weinheim

Further details on the crystal structure investigation may be obtained from the Fachinformationszentrum Karlsruhe, 76344 Eggenstein-Leopoldshafen, Germany (fax: (+49) 7247-808-666; e-mail: crysdata@fiz-karlsruhe.de), on quoting the depository numbers CSD-415869 and -415868).

Single-crystal diffuse scattering data of β-$NaLaF_4$ were collected at room temperature on the sample used to measure Bragg diffraction (MAR345 image-plate detector, $Ag_{K\alpha}$ radiation, $\lambda = 0.561$ Å, ϕ scans of 0.5°). The Bragg reflections were indexed and the crystal orientation determined with the program XDS.[25] Undistorted layers of reciprocal space were reconstructed from the raw images using XCAVATE.[26]

Received: November 8, 2005
Published online: March 20, 2006

Keywords: diffuse X-ray scattering · disorder · lanthanides · optical spectroscopy · upconversion

[1] T. Kano, H. Yamamoto, Y. Otomo, *J. Electrochem. Soc.* **1972**, *119*, 1561.
[2] J. L. Sommerdijk, *J. Lumin.* **1973**, *6*, 61.
[3] V. J. Rao, P. B. Bakare, *Indian J. Pure Appl. Phys.* **1973**, *11*, 442.
[4] F. Auzel, *Chem. Rev.* **2004**, *104*, 139.
[5] K. W. Krämer, D. Biner, G. Frei, H. U. Güdel, M. P. Hehlen, S. R. Lüthi, *Chem. Mater.* **2004**, *16*, 1244.
[6] J. F. Suyver, J. Grimm, K. W. Krämer, H. U. Güdel, *J. Lumin.* **2005**, *114*, 53.
[7] M. L. F. Phillips, M. P. Hehlen, K. Nguyen, J. M. Sheldon, N. J. Cockroft, *Proc. Electrochem. Soc.* **2000**, *99–40*, 123.
[8] R. S. Niedbala, H. Feindt, K. Kardos, T. Vail, J. Burton, B. Bielka, S. Li, D. Milunic, P. Bourdelle, R. Vallejo, *Anal. Biochem.* **2001**, *293*, 22.
[9] P. Boutinaud, R. Mahiou, N. Martin, M. Malinowski, *J. Lumin.* **1997**, *72–74*, 809.
[10] D. Zakaria, R. Mahiou, D. Avignant, M. Zahir, *J. Alloys Compd.* **1997**, *257*, 65.
[11] H. S. Kiliaan, J. F. A. K. Kotte, G. Blasse, *Chem. Phys. Lett.* **1987**, *133*, 425.
[12] N. Martin, P. Boutinaud, M. Malinowski, R. Mahiou, J. C. Cousseins, *J. Alloys Compd.* **1998**, *275–277*, 304.
[13] R. Mahiou, A. Arbus, J. C. Cousseins, M. T. Fournier, *J. Less-Common Met.* **1987**, *136*, 9.
[14] J. H. Burns, *Inorg. Chem.* **1965**, *4*, 881.
[15] R. E. Thoma, H. Insley, G. M. Herbert, *Inorg. Chem.* **1966**, *5*, 1222.
[16] W. H. Zachariasen, *J. Chem. Phys.* **1948**, *16*, 254.
[17] Th. Proffen, R. B. Neder, *J. Appl. Crystallogr.* **1997**, *30*, 171.
[18] U. Steinbrenner, A. Simon, *Z. Kristallogr.* **1997**, *212*, 428.
[19] I. D. Brown, *The Chemical Bond in Inorganic Chemistry*, Oxford University Press, Oxford, **2002**.
[20] K. W. Krämer, H. U. Güdel, R. N. Schwartz, *Phys. Rev. B* **1997**, *56*, 13830.
[21] G. Blasse, B. C. Grabmaier, *Luminescent Materials*, Springer, Berlin, **1994**, p. 123.
[22] SMART, Version 5.059 & SAINT, Version 6.02a Bruker AXS Inc., Madison (Wisconsin, USA), **2001**.
[23] G. M. Sheldrick, SADABS, Version 2.06, Empirical Absorption Correction Program, University of Göttingen (Germany), **2002**.
[24] G. M. Sheldrick, SHELXS97 and SHELXL97, University of Göttingen (Germany), **1997**.
[25] W. Kabsch, *J. Appl. Crystallogr.* **1993**, *26*, 795.
[26] M. A. Estermann, W. Steurer, *Phase Transitions* **1998**, *67*, 165.

 © 2006 Wiley-VCH Verlag GmbH & Co. KGaA, Weinheim

Cover Picture

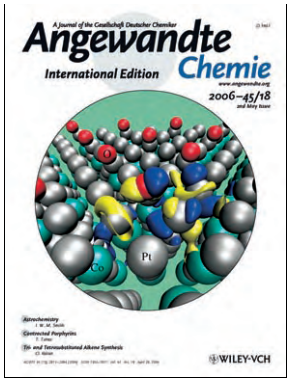

Vojislav Stamenkovic, Bongjin Simon Mun, Karl J. J. Mayrhofer, Philip N. Ross, Nenad M. Markovic, Jan Rossmeisl, Jeff Greeley, and Jens K. Nørskov*

Alloying platinum surfaces with 3d transition metals makes better cathodes for fuel cells. In their Communication on page 2897 ff., J. K. Nørskov and co-workers show that this process results in a tuning of the electronic structure of the surface and increases its catalytic activity for the oxygen reduction reaction. The cover picture shows how a wave function involving oxygen p and surface platinum d states in Pt_3Co is influenced by cobalt atoms in the second layer.

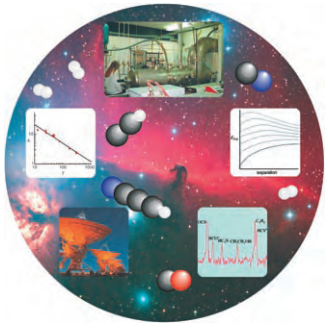

Gas-Phase Reactions
About 135 types of molecules have already been identified in space, especially in interstellar clouds. In his Review on page 2842 ff., I. W. M. Smith discusses gas-phase reactions at very low temperatures which contribute to an understanding of astrochemistry.

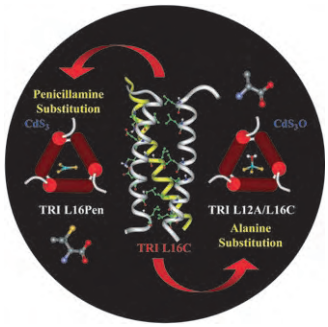

Metalloproteins
In their Communication on page 2864 ff. V. L. Pecoraro and co-workers describe how changing only one of the amino acids in the primary sequence of TRI peptides can result in selective control over the coordination number of a metal center.

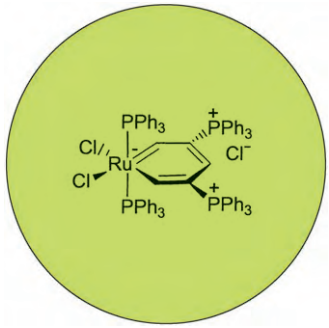

Metallabenzenes
The isolation and characterization of air-stable metallabenzenes with a transition metal of the second transition series is described by G. C. Jia, H. P. Xia, and co-workers in their Communication on page 2920 ff.

Contents

VIP *The following Communications have been judged by at least two referees to be "very important papers" and will be published online at www.angewandte.org soon:*

*V. Lavallo, Y. Canac, B. Donnadieu, W. Schoeller, G. Bertrand**
CO Fixation to Stable Acyclic and Cyclic Alkyl Amino Carbenes: Stable Amino Ketenes with a Small HOMO–LUMO Gap

*D. Rohde, C.-J. Yan, H.-J. Yan, L.-J. Wan**
From Lamellar to Hexagonal Self-Assembly of Bis(dioxaborin) Molecules

*T. Adler, N. Borho, M. Reiher, M. Suhm**
Chirality-Induced Hydrogen-Bond Topology Switch: Tetrameric Methyl Lactate Clusters in the Gas Phase

*D. Bang, B. Pentelute, S. H. Kent**
Kinetically Controlled Ligation for the Convergent Chemical Synthesis of Proteins

*H. Chen, Z. Ouyang, R. G. Cooks**
Thermal Production and Reactions of Organic Ions at Atmospheric Pressure

*Y. Sawada, K. Matsumoto, S. Kondo, H. Watanabe, T. Ozawa, K. Suzuki, B. Saito, T. Katsuki**
Titanium/Salan-Catalyzed Asymmetric Epoxidation with Aqueous Hydrogen Peroxide as the Oxidant

News

Organic Chemistry: Danishefsky Honored ____ **2830**

Biochemistry: Prize to Carell ____ **2830**

Polymer Chemistry: Rieger and Luinstra Awarded ____ **2830**

Books

Citation Analysis in Research Evaluation — Henk F. Moed — *reviewed by W. Marx* ____ **2831**

Highlights

Contracted Porphyrins

T. Torres* ____ **2834 – 2837**

From Subphthalocyanines to Subporphyrins

Contracting porphyrins: An important step on the way to the as-yet unrealized contracted porphyrin, the so-called subporphyrin, is a tribenzosubporphyrin (see structure). The new system, which is closely related to boronsubphthalocyanines, comprises a 14-π-electron aromatic core and adopts a nonplanar bowl-shaped conformation.

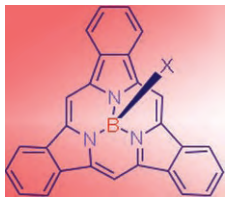

Homogeneous Catalysis

O. Reiser* ____ **2838 – 2840**

Palladium-Catalyzed Coupling Reactions for the Stereoselective Synthesis of Tri- and Tetrasubstituted Alkenes

Making advances: Efficient strategies relying on palladium-catalyzed cross-coupling reactions are now available for the assembly of tri- and tetrasubstituted alkenes with excellent stereocontrol (see scheme; Y = Hal, X = ZnHal or MgHal; other variants: Y = BR_2, X = I).

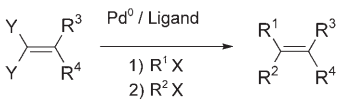

InterScience

© 2006 Wiley-VCH Verlag GmbH & Co. KGaA, Weinheim

Reviews

It's amongst the stars: Over the past two decades, it has become possible to measure rate constants for elementary gas-phase reactions at temperatures as low as 10 K, largely by using the CRESU (Cinétique de Réaction en Ecoulement Supersonique Uniforme) technique (experimental setup shown). The factors that determine the reaction rates and the implications in the chemistry of interstellar clouds are reviewed.

Gas-Phase Reactions

I. W. M. Smith* _____ **2842 – 2861**

Reactions at Very Low Temperatures: Gas Kinetics at a New Frontier

Communications

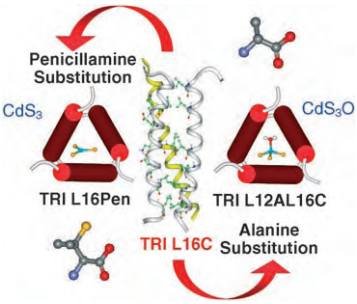

It isn't natural: TRI peptides can selectively control the coordination number of a metal center by changing only one of the amino acids in the primary sequence. Replacement of the cysteine residue with penicillamine leads to a three-coordinate complex $Cd^{II}S_3$, whereas substitution of alanine for leucine gives four-coordinate CdS_3O (see scheme).

Metalloproteins

K.-H. Lee, C. Cabello, L. Hemmingsen, E. N. G. Marsh, V. L. Pecoraro* _____ **2864 – 2868**

Using Nonnatural Amino Acids to Control Metal-Coordination Number in Three-Stranded Coiled Coils

A highly polar micro-environment, which is suitable for efficient metal scavenging and heterogeneous catalyst preparation, is provided by polyionic gel beads **1** (see scheme). These heterogeneous media enable easy product isolation and catalyst recycling. As an example, a Pd-soaked ionic gel **2** is shown to transform into a highly efficient and recyclable catalyst **3** in the Suzuki cross-coupling reaction.

Ionic Resins

C. Thiot, M. Schmutz, A. Wagner,* C. Mioskowski* _____ **2868 – 2871**

Polyionic Gels: Efficient Heterogeneous Media for Metal Scavenging and Catalysis

For the USA and Canada:
ANGEWANDTE CHEMIE International Edition (ISSN 1433-7851) is published weekly by Wiley-VCH PO Box 191161, D 69451 Weinheim, Germany. Air freight and mailing in the USA by Publications Expediting Inc. 200 Meacham Ave., Elmont, NY 11003. Periodicals postage paid at Jamaica NY 11431. US POSTMASTER: send address changes to *Angewandte Chemie*, Wiley-VCH, 111 River Street, Hoboken, NJ 07030. Annual subscription price for institutions: US$ 5685/5168 (valid for print and electronic / print or electronic delivery); for individuals who are personal members of a national chemical society prices are available on request. Postage and handling charges included. All prices are subject to local VAT/sales tax.

© 2006 Wiley-VCH Verlag GmbH & Co. KGaA, Weinheim

The best in chemistry –

for more than a hundred years

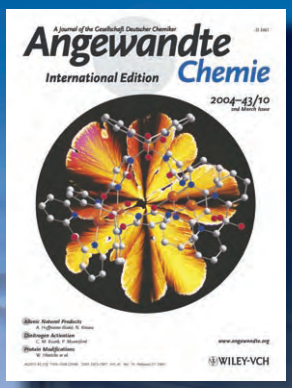

A Journal of the Gesellschaft Deutscher Chemiker

Angewandte International Edition Chemie

www.angewandte.org

1888: ***The beginning of a success story***

Constant Innovations

1962: *First issue of the International Edition*
1976: *Graphical abstracts*
1979: *Cover pictures*
1988: *Centenary of Angewandte*
1989: *Routine use of color*
1991: *New section: Highlights*
1992: *Computerized editorial tracking system*
1995: *Internet service for readers*
1998: *Regular press service; full-text online*
2000: *New section: Essays; EarlyView: Communications available online ahead of the printed version*
2001: *New section: Minireviews*
2002: *Online submission of manuscripts*
2003: *Weekly publication; new section: News; new layout*
2004: *Backfiles (1962-1997); ManuscriptXpress: Online system for authors and referees*

Angewandte's advisors...

Rolf Thauer
MPI für terrestrische Mikrobiologie, Marburg

» *In 1970 Karl Decker, Kurt Jungermann, and I published a review on "Energy Production in Anaerobic Organisms" in* ***Angewandte Chemie****. We were soon surprised how many scientists from all over the world had read the article. Ever since then I have admired the broad scope, the high impact, and internationality of this Journal and I am therefore very proud, as a "chemical microbiologist", to be a member of its Editorial Board.* «

Angewandte Chemie International Edition *is a journal of the German Chemical Society (GDCh)*

GDCh

WILEY InterScience® DISCOVER SOMETHING GREAT

WILEY-VCH

11991404_gu

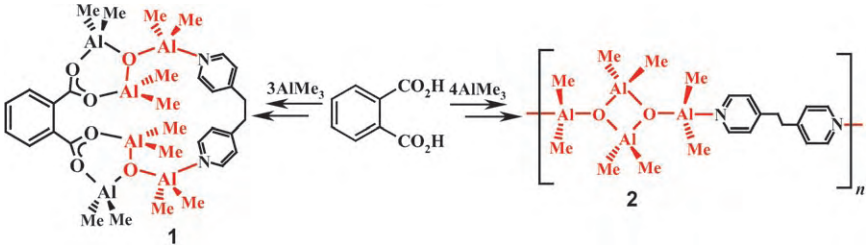

Alumoxanes

J. Lewiński,* W. Bury, I. Justyniak,* J. Lipkowski ——— **2872 – 2875**

Efficient Route to Tetramethylalumoxane and Carboxylate Alumoxanes through the Alkylation of Phthalic Acid

Spaced out: The macrocyclic carboxylate-substituted alumoxane **1** and coordination polymer **2** were obtained by stepwise treatment of phthalic acid with $AlMe_3$ and 1,2-bis(4-pyridyl)ethane. In this non-hydrolytic route to alumoxane derivatives, the selective formation of **1** or **2** is determined by the stoichiometric amount of $AlMe_3$ employed.

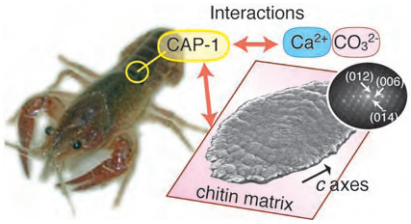

Gone fishing: Unidirectionally oriented $CaCO_3$ crystalline films have been prepared on chitin matrices in the presence of calcification-associated peptide (CAP-1), which was isolated from the exoskeleton of the red swamp crayfish. The interactions of CAP-1 with the matrix and the acidic nature of the peptide lead to a filmlike assembly of $CaCO_3$ nanocrystals through transformation of amorphous calcium carbonate (see picture).

Biomineralization

A. Sugawara, T. Nishimura, Y. Yamamoto, H. Inoue, H. Nagasawa, T. Kato* ——— **2876 – 2879**

Self-Organization of Oriented Calcium Carbonate/Polymer Composites: Effects of a Matrix Peptide Isolated from the Exoskeleton of a Crayfish

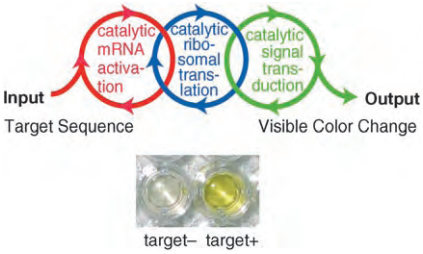

Sensing DNA with RNA: Simple and sensitive DNA sensing was achieved by using an RNA probe which is composed of a molecular-beacon-like *cis*-repressing sequence and a gene for the reporter protein. The RNase H activity coupled molecular-beacon–mRNA system enabled visible sensing of the target nucleotide sequence in a cell-free translation solution (see picture).

DNA Sensing

A. Narita, K. Ogawa, S. Sando,* Y. Aoyama* ——— **2879 – 2883**

Visible Sensing of Nucleic Acid Sequences with a Genetically Encodable Unmodified RNA Probe

Natural cellulose sheets can be used as substrates for protein immobilization. Individual cellulose nanofibers are first coated with ultrathin titania layers to enable the chemisorption of biotin, and then streptavidin is anchored. The sheets have a high binding capacity for biomolecules (see the fluorescence micrographs) without deterioration of their mechanical and water-absorbing properties.

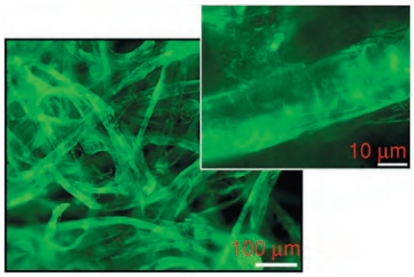

Protein Immobilization

J. Huang, I. Ichinose,* T. Kunitake ——— **2883 – 2886**

Biomolecular Modification of Hierarchical Cellulose Fibers through Titania Nanocoating

© 2006 Wiley-VCH Verlag GmbH & Co. KGaA, Weinheim

Contents

Cluster Catalysis

M. B. Thathagar, J. E. ten Elshof, G. Rothenberg* ——— **2886 – 2890**

Pd Nanoclusters in C–C Coupling Reactions: Proof of Leaching

A simple experiment based on exclusion of Pd nanoclusters was used to identify the true catalytic species in cluster-catalyzed Heck cross-couplings. A special reactor was used in which two compartments are separated by a nanoporous membrane that allows the passage of Pd atoms and ions but not of Pd nanoclusters (see picture). The results show that the real catalysts in the Heck coupling of *n*-butyl acrylate with iodobenzene are species leached from the Pd nanoclusters.

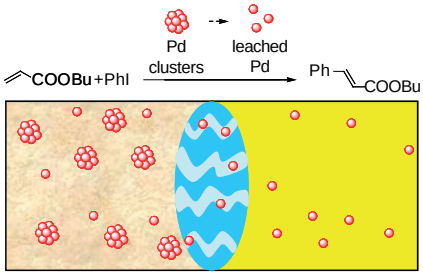

Anion Binding

M. Mascal* ——— **2890 – 2893**

Precedent and Theory Unite in the Hypothesis of a Highly Selective Fluoride Receptor

Room for a small one: A series of [1,3,5]cyclophane-based receptors incorporating triazine, cyanuric acid, or boroxine rings are predicted to strongly complex fluoride ions by a combination of anion–π interactions and ion-pair reinforced hydrogen bonding, while size-excluding the larger chloride anion. The top view of a calculated structure of the triazine cage with an included fluoride ion is shown.

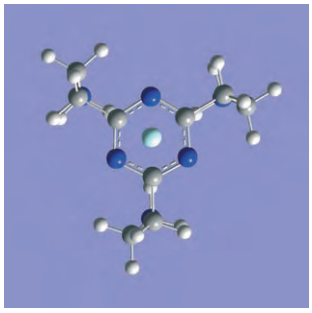

Formamide Hydrolysis

J. Blumberger,* B. Ensing, M. L. Klein ——— **2893 – 2897**

Formamide Hydrolysis in Alkaline Aqueous Solution: Insight from Ab Initio Metadynamics Calculations

What is the active nucleophile in the alkaline hydrolysis of formamide: the hydroxide ion or a water molecule in its first solvation shell? To allow the two mechanisms in question to be distinguished, a 2D free-energy surface was computed (see picture) using Car–Parrinello metadynamics simulation. The results show that direct nucleophilic attack by a hydroxide ion is the preferred mechanism.

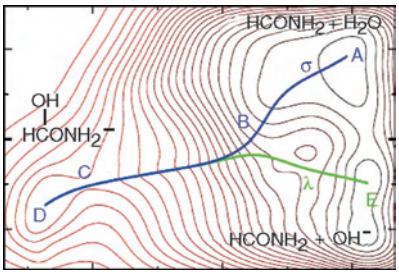

Oxygen Reduction Reaction

V. Stamenkovic, B. S. Mun, K. J. J. Mayrhofer, P. N. Ross, N. M. Markovic, J. Rossmeisl, J. Greeley, J. K. Nørskov* ——— **2897 – 2901**

Changing the Activity of Electrocatalysts for Oxygen Reduction by Tuning the Surface Electronic Structure

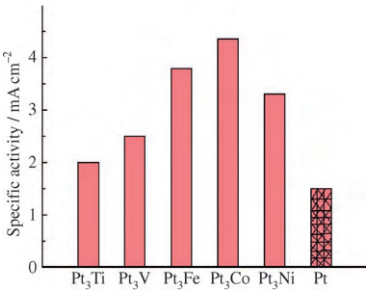

Going platinum: The theoretical description of electrocatalytic phenomena is extremely challenging. A simple, density functional theory based model has been developed that is able to give a semi-quantitative description of the reaction kinetics for the electrocatalytic oxygen reduction on several platinum binary alloys, Pt_3M (see graph).

© 2006 Wiley-VCH Verlag GmbH & Co. KGaA, Weinheim

Facing facts: Control of the configuration of the propargylic center in **1** is essential for the facial selectivity observed in the Pt-, Au-, or Cu-catalyzed enyne cycloisomerization. This route has been used for the stereoselective synthesis of the naturally occurring sesquiterpene (−)-cubebol (**2**).

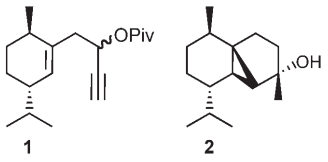

Synthetic Methods

C. Fehr,* J. Galindo ——— **2901 – 2904**

Synthesis of (−)-Cubebol by Face-Selective Platinum-, Gold-, or Copper-Catalyzed Cycloisomerization: Evidence for Chirality Transfer

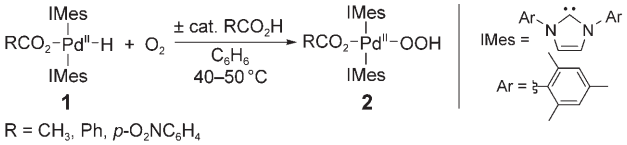

A critical step: The reaction of molecular oxygen with a reduced palladium species represents the key step in Pd-catalyzed aerobic oxidation reactions. New Pd^{II}–hydride complexes **1** have been prepared which react with molecular oxygen to produce Pd^{II}–hydroperoxide adducts **2**. Carboxylic acid catalysis of this reaction has important implications for Pd-catalyzed aerobic oxidation reactions.

Palladium Catalysis

M. M. Konnick, B. A. Gandhi, I. A. Guzei, S. S. Stahl* ——— **2904 – 2907**

Reaction of Molecular Oxygen with a Pd^{II}–Hydride To Produce a Pd^{II}–Hydroperoxide: Acid Catalysis and Implications for Pd-Catalyzed Aerobic Oxidation Reactions

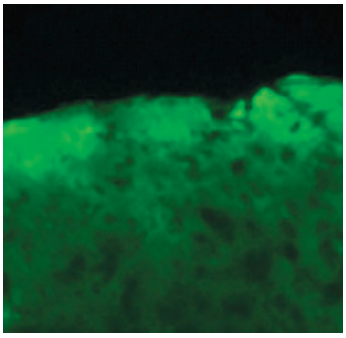

Delivery vehicles: Novel guanidine-containing "transporters" constructed on a dimeric inositol scaffold show significant translocation across the cell membrane and the blood–brain barrier, as well as unique in vitro and in vivo distributions. Doxorubicin was efficiently delivered to mouse-brain tissue by conjugating the compound with such a transporter (see the fluorescence microscopy image).

Cell-Penetrating Molecules

K. K. Maiti, O.-Y. Jeon, W. S. Lee, D.-C. Kim, K.-T. Kim, T. Takeuchi, S. Futaki, S.-K. Chung* ——— **2907 – 2912**

Design, Synthesis, and Membrane-Translocation Studies of Inositol-Based Transporters

The final synthetic challenges associated with sarain A have been overcome, thus leading to its first total synthesis. Critical to success was a late-stage intramolecular Stille coupling to construct the unsaturated macrocyclic ring and introduce the skipped triene functionality of the natural product.

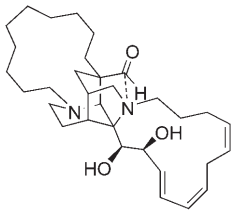

sarain A

Alkaloids

N. K. Garg, S. Hiebert, L. E. Overman* ——— **2912 – 2915**

Total Synthesis of (−)-Sarain A

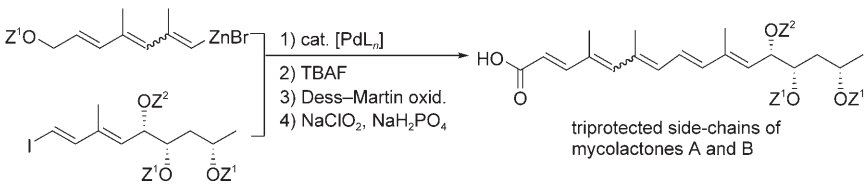

triprotected side-chains of mycolactones A and B

Piecing them together: The side chains of mycolactones A and B are synthesized with a high degree of stereoselectivity. The components of the side chains are prepared separately, then combined through Pd-catalyzed cross-coupling (see scheme; Z^1 = *tert*-butyldimethylsilyl, Z^2 = methoxymethyl, TBAF = tetra-*n*-butylammonium fluoride).

Organic Synthesis

N. Yin, G. Wang, M. Qian, E. Negishi* ——— **2916 – 2920**

Stereoselective Synthesis of the Side Chains of Mycolactones A and B Featuring Stepwise Double Substitutions of 1,1-Dibromo-1-alkenes

© 2006 Wiley-VCH Verlag GmbH & Co. KGaA, Weinheim

Contents

Metallabenzenes

H. Zhang, H. P. Xia,* G. M. He, T. B. Wen, L. Gong, G. C. Jia* ——— **2920 – 2923**

Synthesis and Characterization of Stable Ruthenabenzenes

A rare breed: Although many stable metallabenzene derivatives with a metal atom from the third transition series are known, those with a metal atom from the first and the second transition series are rare. Air-stable ruthenabenzenes (e.g. **1** and **2**) have now been isolated and characterized.

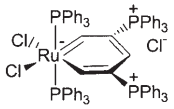

1

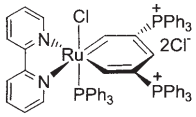

2

Helicene Synthesis

S. K. Collins,* A. Grandbois, M. P. Vachon, J. Côté ——— **2923 – 2926**

Preparation of Helicenes through Olefin Metathesis

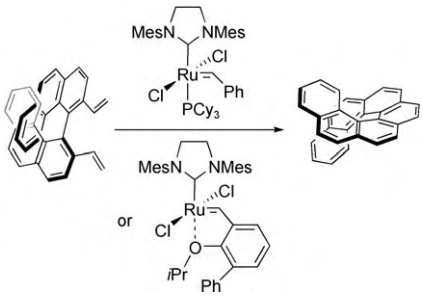

Metathesis with a twist! A ring-closing-metathesis strategy has been developed for the preparation of various substituted [5]helicene motifs and [6]- and [7]helicenes. The two optimized protocols include one method that utilizes the Grubbs second-generation catalyst under microwave-irradiation conditions and another that employs a modified Grubbs–Hoveyda catalyst at 40 °C in a sealed reaction vessel. (Mes = mesityl)

Dehydrocoupling

R. Waterman, T. D. Tilley* ——— **2926 – 2929**

Catalytic Antimony–Antimony Bond Formation through Stibinidene Elimination from Zirconocene and Hafnocene Complexes

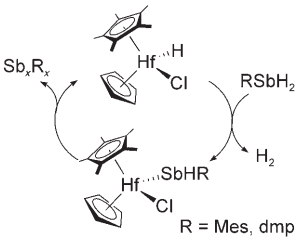

Bringing together: Zirconium and hafnium d^0 metallocene complexes catalyze the dehydrocoupling of the stibines $MesSbH_2$ (Mes = mesityl) and $dmpSbH_2$ (dmp = 2,6-dimesitylphenyl) to Sb_4Mes_4 and (dmp)Sb=Sb(dmp), respectively, with liberation of H_2. Kinetic analysis shows that thermal decomposition of hafnium stibide complexes proceeds through α-hydrogen migration and stibinidene elimination.

Organic Oxidants

M. J. Gallen, R. Goumont, T. Clark, F. Terrier, C. M. Williams* ——— **2929 – 2934**

o-Iodoxybenzoic Acid (IBX): pK_a and Proton-Affinity Analysis

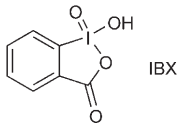

Not just a pretty oxidant! IBX (1-Hydroxy-1,2-benziodoxol-3(1*H*)-on-1-oxide), an important oxidant in organic synthesis, is shown to be relatively acidic on the organic scale. The pK_a value and proton affinity of IBX were determined both in silico and in vitro. This acidity could explain the non-oxidation processes mediated by IBX.

Nanocomposites

S. Bhattacharya,* A. Srivastava, A. Pal ——— **2934 – 2937**

Modulation of Viscoelastic Properties of Physical Gels by Nanoparticle Doping: Influence of the Nanoparticle Capping Agent

Cap in hand: The viscoelastic properties of low-molecular-mass organogelator–gold nanoparticle (LMOG–Au NP) composites can be modulated by the capping agent on the nanoparticle. The interactions between the LMOG and Au NP depend on the ability of ligands to interdigitate within the gel aggregates (see picture).

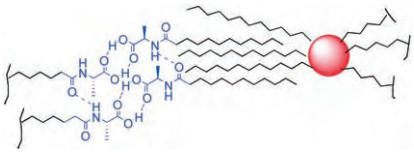

© 2006 Wiley-VCH Verlag GmbH & Co. KGaA, Weinheim

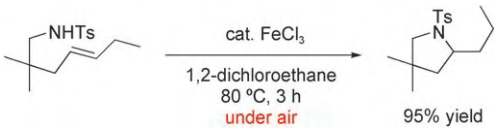

A new catalytic activity of iron salts for intramolecular hydroamination is revealed. A number of aminoolefins underwent the reaction under mild conditions to form the corresponding pyrrolidine derivatives in good yield. The reaction displayed good functional-group compatibility and resistance to air and moisture. (Ts = e-toluenesulfonyl)

Cyclizations

K. Komeyama,* T. Morimoto, K. Takaki* ——— **2938 – 2941**

A Simple and Efficient Iron-Catalyzed Intramolecular Hydroamination of Unactivated Olefins

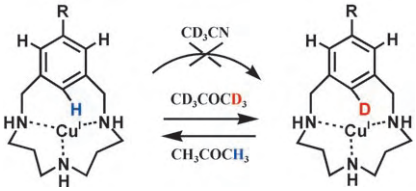

The first reversible and regiospecific H/D exchange promoted by Cu^I proceeds in weakly coordinating deuterated "acidic" solvents, such as [D_6]acetone or [D_4]methanol (see scheme). The kinetics of the reaction have been studied in both directions (H/D and D/H exchange) by ^1H and ^2H NMR spectroscopy, and a molecular mechanism is proposed that is in accordance with all experimental and theoretical data.

Isotope Exchange

X. Ribas,* R. Xifra, T. Parella, A. Poater, M. Solà,* A. Llobet* ——— **2941 – 2944**

Regiospecific C–H Bond Activation: Reversible H/D Exchange Promoted by Cu^I Complexes with Triazamacrocyclic Ligands

A rare twist: A new class of mixed γ-peptides, derived from dipeptide repeats with alternating C-linked carbo-γ^4-amino acids and γ-aminobutyric acid have shown the presence of left-handed 9-helices in solution with $CDCl_3$ (see superimposition of 15 minimum-energy structures of a hexapeptide).

Peptide Structures

G. V. M. Sharma,* P. Jayaprakash, K. Narsimulu, A. Ravi Sankar, K. Ravinder Reddy, P. Radha Krishna, A. C. Kunwar* ——— **2944 – 2947**

A Left-Handed 9-Helix in γ-Peptides: Synthesis and Conformational Studies of Oligomers with Dipeptide Repeats of C-Linked Carbo-γ^4-amino Acids and γ-Aminobutyric Acid

Remember this: The conjugated copolymer PFOxPy, which contains both electron-donor and -acceptor groups, exhibits dynamic random access memory behavior in the sandwich structure ITO/PFOxPy/Al (see picture). The device is characterized by low read, write, and erase voltages, a high ON/OFF current ratio (up to 10^6), stable ON and OFF states under a constant stress of −1 V, and up to 10^8 read cycles at a read voltage of −1 V.

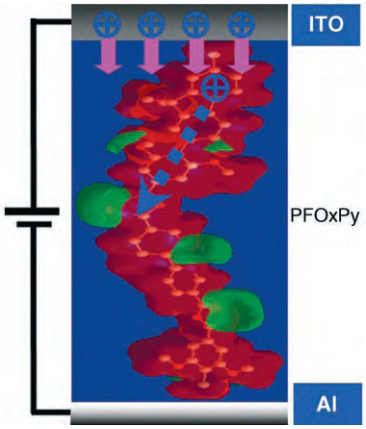

Polymer-Based Dynamic Memory

Q.-D. Ling, Y. Song, S.-L. Lim, E. Y.-H. Teo, Y.-P. Tan, C. Zhu, D. S. H. Chan, D.-L. Kwong, E.-T. Kang,* K.-G. Neoh ——— **2947 – 2951**

A Dynamic Random Access Memory Based on a Conjugated Copolymer Containing Electron-Donor and -Acceptor Moieties

© 2006 Wiley-VCH Verlag GmbH & Co. KGaA, Weinheim

Contents

β-Hydroxy Esters

P. G. Cozzi* ——— 2951 – 2954

A Catalytic, Me_2Zn-Mediated, Enantioselective Reformatsky Reaction with Ketones

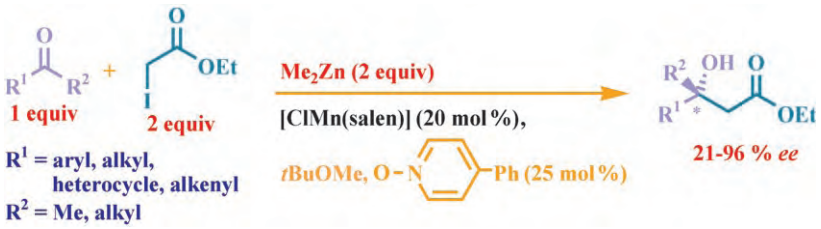

Kill two birds with one ... Salen! A catalytic and practical Me_2Zn-mediated enantioselective Reformatsky reaction promoted by [ClMn(salen)] with a ketone as the electrophile is presented (see scheme). The broad scope and simple nature of this procedure, which allows the use of commercially available starting materials and leads to useful building blocks containing quaternary stereocenters, make it extremely attractive. (salen = *N*,*N*′-ethylenebis(salicylideneamine).)

Nanogels

G. Wulff,* B.-O. Chong, U. Kolb ——— 2955 – 2958

Soluble Single-Molecule Nanogels of Controlled Structure as a Matrix for Efficient Artificial Enzymes

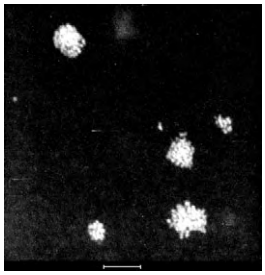

Copy cats! Soluble single-molecule nanogels (see STEM micrograph; scale-bar = 20 nm) with a densely packed structure are prepared by a new method, and for the first time efficient molecular imprinting is possible. These nanogels with defined molecular weights of, for example, 40000 Da, low polydispersities, and on average one active site per particle proved to be catalytically active enzyme mimics.

Metalation

A. Krasovskiy, V. Krasovskaya, P. Knochel* ——— 2958 – 2961

Mixed Mg/Li Amides of the Type $R_2NMgCl{\cdot}LiCl$ as Highly Efficient Bases for the Regioselective Generation of Functionalized Aryl and Heteroaryl Magnesium Compounds

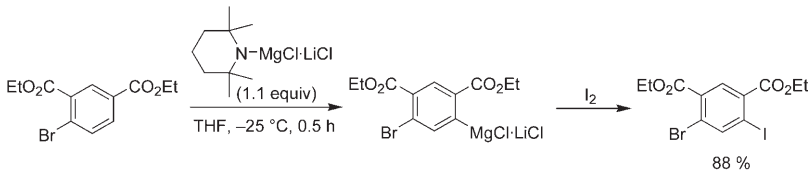

Two are better than one: Mixed lithium-magnesium complexes of the type $R_2NMgCl{\cdot}LiCl$ are kinetically highly active bases that convert a range of polyfunctional aromatic and heteroaromatic substrates into the corresponding magnesiated derivatives with high regioselectivity.

Quantum Dynamics

I. Barth, J. Manz* ——— 2962 – 2965

Periodic Electron Circulation Induced by Circularly Polarized Laser Pulses: Quantum Model Simulations for Mg Porphyrin

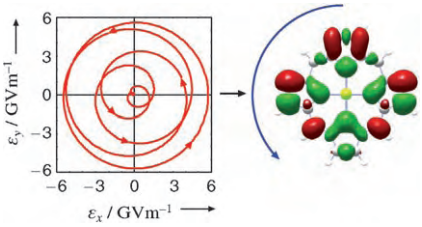

What goes round comes round! Quantum dynamical simulations predict that ultrashort circularly polarized laser pulses can selectively induce the circulation of electrons in a ring-shaped molecule—with near equal laser and electron periods below one femtosecond (see figure).

© 2006 Wiley-VCH Verlag GmbH & Co. KGaA, Weinheim

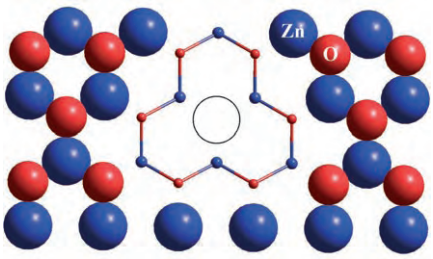

"**Systematic errors**", namely, oxygen vacancy sites in ZnO, are the active centers for the hydrogenation of CO to give methanol. Nanocrystalline ZnO with a high density of oxygen vacancies was prepared from special organometallic precursors, and its catalytic properties for methanol synthesis were studied.

Heterogeneous Catalysis

S. Polarz,* J. Strunk, V. Ischenko, M. W. E. van den Berg, O. Hinrichsen,* M. Muhler, M. Driess ——— **2965 – 2969**

On the Role of Oxygen Defects in the Catalytic Performance of Zinc Oxide

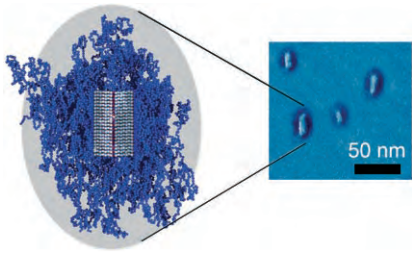

Hard-core visualization: Bilayer hockey-puck micelles are formed in nonpolar solvents from "sticky" rod–coil block copolymers based on oligo(*p*-benzamide)s. Images obtained by scanning force microscopy (SFM) give insight into the structure of the anisotropic micellar core. The picture shows a model (left) and an SFM image (right) of the micelle consisting of an aramide core and a poly(ethylene glycol) corona.

Block Copolymers

T. W. Schleuss, R. Abbel, M. Gross, D. Schollmeyer, H. Frey, M. Maskos, R. Berger, A. F. M. Kilbinger* ——— **2969 – 2975**

Hockey-Puck Micelles from Oligo(*p*-benzamide)-*b*-PEG Rod–Coil Block Copolymers

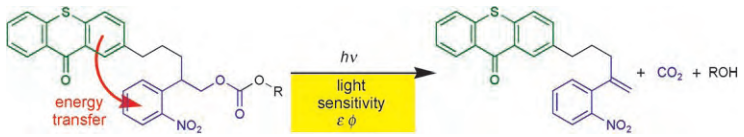

Brought to light: The light sensitivity of photolabile protecting groups of the nitrophenylpropoxycarbonyl (NPPOC) type was enhanced by up to a factor of 25. This was achieved by covalently linking the protecting group to a sensitizer with a much better absorptivity and the ability to transfer its electronic excitation to the protecting group (see scheme).

Intramolecular Sensitization

D. Wöll, J. Smirnova, W. Pfleiderer, U. E. Steiner* ——— **2975 – 2978**

Highly Efficient Photolabile Protecting Groups with Intramolecular Energy Transfer

Sources

Product and Company Directory

You can start the entry for your company in "Sources" in any issue of *Angewandte Chemie*.

If you would like more information, please do not hesitate to contact us.

Wiley-VCH Verlag – Advertising Department
Tel.: 0 62 01 - 60 65 65
Fax: 0 62 01 - 60 65 50
E-Mail: MSchulz@wiley-vch.de

Service

Keywords ——— ***2980***

Authors ——— ***2981***

Preview ——— ***2983***

© 2006 Wiley-VCH Verlag GmbH & Co. KGaA, Weinheim

Corrigendum

A Highly Enantio- and Diastereoselective Cu-Catalyzed 1,3-Dipolar Cycloaddition of Azomethine Ylides with Nitroalkenes

X.-X. Yan, Q. Peng, Y. Zhang,
K. Zhang, W. Hong, X.-L. Hou,*
Y.-D. Wu **1979—1983**

Angew. Chem. Int. Ed. **2006**, *45*

DOI 10.1002/anie.200503672

In this Communication, the structures of (S,R_{phos},R)-**3g** and (S,S_{phos},R)-**3h** given in Equation (1) should be as follows:

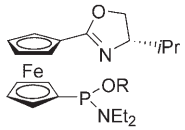

(S,R_{phos},R)-**3g**
(S,S_{phos},R)-**3h**
R=(*R*)-2-(2'-hydroxy-1,1'-binaphthyl)

Additionally, in Figure 1 the upper structure is that of *endo*-**4k** while the lower structure is that of *exo*-**4k**. The authors apologize for the oversight.

For more information on ChemMedChem see www.chemmedchem.org

 © 2006 Wiley-VCH Verlag GmbH & Co. KGaA, Weinheim

Awarded...

S. J. Danishefsky Honored by US Academy

The US National Academy of Science has honored Samuel J. Danishefsky with the Award in Chemical Sciences. Danishefsky obtained his PhD in 1962 at Harvard University under the direction of P. Yates. From 1961 to 1963, he was a Postdoctoral Fellow at Columbia University (New York) in the group of G. Stork. He then joined the faculty at the University of Pittsburgh before moving to Yale University in 1980. In 1993, he returned to Columbia University as a Professor of Chemistry and is currently Head of Bioorganic Chemistry at the Memorial Sloan–Kettering Cancer Center in Manhattan.

S. J. Danishefsky

Danishefsky's research interests focus on the development of strategies and methods for organic synthesis and its application to problems of biological importance. In particular, his group works on the syntheses of antitumor and antiinfective natural products, and their analogues, as well as the syntheses of fully synthetic carbohydrate epitope vaccines. He has recently reported on tetrahydroisoquinoline alkaloids[1a] and the stereospecific formal total synthesis of the cytotoxic natural product ecteinascidin 743.[1b] Danishefsky serves on the editorial board of *ChemBioChem*.

T. Carell, B. Rieger, and G. A. Luinstra receive Philip Morris Prizes

Thomas Carell has been awarded a Philip Morris Research Prize for his work on DNA repair. Carrel's research group at the Ludwig-Maximilians-Universität (LMU) in Munich (Germany) investigates the function of repair enzymes by systematically incorporating lesions into artificial DNA strands. Carell studied chemistry in Münster and Heidelberg (Germany), obtained his doctorate in 1993 under H. A. Staab at the Max Planck Institute for Medical Research in Heidelberg, and then went as a postdoctoral researcher to J. Rebek at MIT (Cambridge, USA). He completed his habilitation with F. Diederich at the ETH Zürich (Switzerland). In 2000 he became a full professor at the University of Marburg (Germany) and moved to the LMU Munich in December 2003. Besides DNA repair, Carell is also interested in the biophysical properties of DNA and hybrid compounds based on DNA or inspired by its structure. His latest Communication in *Angewandte Chemie* reports on the transport of excess electrons through DNA with different strength electron acceptors.[2]

T. Carell

A further prize was awarded to **Bernhard Rieger** (Universität Ulm, Germany) and **Gerrit A. Luinstra** (BASF, Ludwigshafen, Germany) for their work on the catalysis of hydroxybutyrate polymerization with the goal of obtaining biodegradable synthetic materials. Their article about the generation of aliphatic polycarbonates from epoxides with the help of Cr^{III} and Al^{III} salen complexes was featured on the cover of Issue 21, 2005 of *Chemistry—A European Journal*.[3]

B. Rieger

Rieger completed his PhD in asymmetric catalysis in 1988 at the LMU Munich under W. Beck, and then was a postdoctoral researcher with J. C. W. Chien at the University of Massachusetts at Amherst (USA). From 1989 to 1991 he worked at BASF on metallocene-catalyzed polymerization. He returned to academia and finished his habilitation in 1995 at the Eberhard-Karls-Universität Tübingen (Germany). In the same year, he became a professor in Ulm, and has led the Department for Materials and Catalysis there since 1997.

Luinstra obtained his doctorate in organotitanium chemistry in 1991 at the Universität Groningen (The Netherlands) under J. H. Teuben. He undertook postdoctoral research with J. A. Labinger and J. E. Bercaw from 1991 to 1993 at Caltech (Pasadena, USA) on the topic of methane oxidation with Pt^{II}/Pt^{IV}. Afterwards, he researched at the Universität Konstanz (Germany), where he completed his habilitation on organometallic chemistry and homogeneous catalysis in 1999. In the same year he joined BASF.

G. A. Luinstra

Research Prizes were also awarded to Hannah Moyer (Universität Heidelberg) for her work on the adaptability of the brain, as well as to the nuclear physicists Joachim Ullrich and Robert Moshammer (MPI Heidelberg) for their work on the reaction microscope.

[1] a) C. Chan, S. Zheng, B. Zhou, J. Guo, R. M. Heid, B. J. D. Wright, S. J. Danishefsky, *Angew. Chem.* **2006**, *118*, 1781; *Angew. Chem. Int. Ed.* **2006**, *45*, 1749; b) S. Zheng, C. Chan, T. Furuuchi, B. J. D. Wright, B. Zhou, J. Guo, S. J. Danishefsky, *Angew. Chem.* **2006**, *118*, 1786; *Angew. Chem. Int. Ed.* **2006**, *45*, 1754.

[2] A. Manetto, S. Breeger, C. Chatgilialoglu, T. Carell, *Angew. Chem.* **2006**, *118*, 325; *Angew. Chem. Int. Ed.* **2006**, *45*, 318.

[3] G. A. Luinstra, G. R. Haas, F. Molnar, V. Bernhart, R. Eberhardt, B. Rieger, *Chem. Eur. J.* **2005**, *11*, 6298.

DOI: 10.1002/anie.200601262

WILEY InterScience DISCOVER SOMETHING GREAT
© 2006 Wiley-VCH Verlag GmbH & Co. KGaA, Weinheim

Contracted Porphyrins

DOI: 10.1002/anie.200504265

From Subphthalocyanines to Subporphyrins**

*Tomás Torres**

Keywords:
aromaticity · boron · porphyrinoids · subphthalocyanines · subporphyrins

Dedicated to Professor Wolfram Schäfer on the occasion of his 75th birthday

Porphyrins (**1**; Figure 1) represent one of the most widely studied macrocyclic ring systems.[1] One of their best-known synthetic analogues are the phthalocyanines (Pcs, **2**), also known as tetrabenzotetraazaporphyrins,[2] which are two-dimensional 18-π-electron aromatic systems that consist of four isoindole subunits linked together through nitrogen atoms. Their electronic delocalization gives rise to numerous properties that make phthalocyanines interesting in different fields of science and technology.[3] Other analogues, such as tetrabenzoporphyrins (**3**)[4] and porphyrazines (**4**),[5] are structurally closely related to both **1** and **2**. However, whereas the synthesis of porphyrins and phthalocyanines is well established, the preparation of new congeners remains an expanding topic.

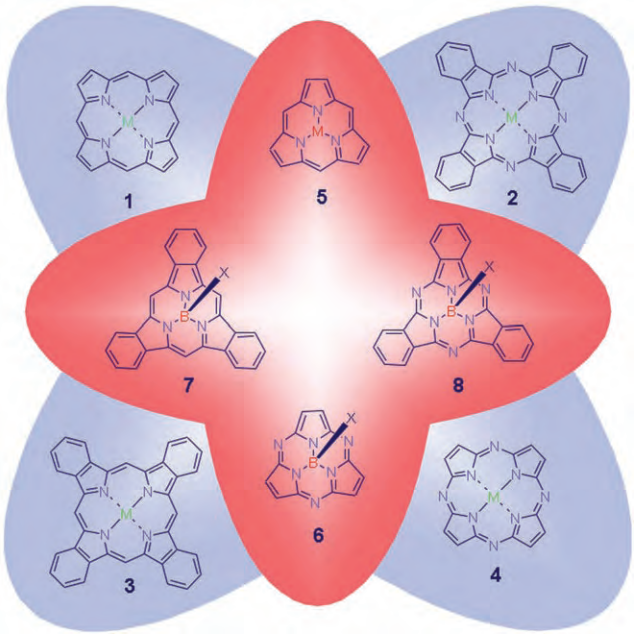

Figure 1. Porphyrin analogues.

Expanded porphyrins and phthalocyanines[6] differ from other porphyrinoids in terms of their larger central core, while they retain an extended electron conjugation. Sapphyrin and superphthalocyanine are particularly interesting examples among the many different expanded systems reported to date (Figure 2). Indeed, the beginnings of expanded porphyrin chemistry can be traced back to Woodward and co-workers, with their serendipitous discovery of sapphyrin.[6c]

However, much less synthetic effort has been devoted to preparing contracted porphyrinoids, such as the subporphyrins (**5**), subporphyrazines (**6**), tribenzosubporphyrins (**7**), and subphthalocyanines (**8**), each of which contain three pyrrole or three isoindole units (Figure 1).[7] Compounds **6**, **7**, and **8** have only been reported in the form of their boron complexes, whereas examples of **5** are still unknown. Another key feature of these macrocycles is that they comprise a 14-π-electron aromatic core but nonetheless adopt a nonplanar cone-shaped conformation. Thus, they represent fascinating examples of nonplanar aromaticity and, not surprisingly, reveal rather unique spectral and electronic features.

By far, the best known of these contracted porphyrinoid species are the

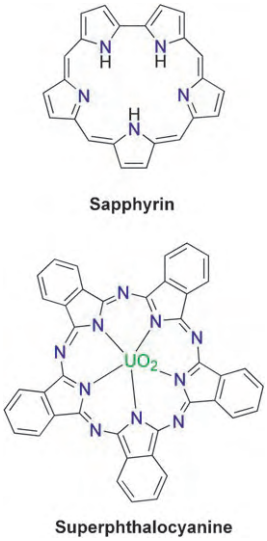

Figure 2. Expanded porphyrin systems.

[*] Prof. T. Torres
Departamento de Química Orgánica (C-I)
Facultad de Ciencias
Universidad Autónoma de Madrid
Cantoblanco, 28049 Madrid (Spain)
Fax: (+34) 91-497-3966
E-mail: tomas.torres@uam.es

[**] The author thanks Dr. M. S. Rodríguez-Morgade, Dr. C. G. Claessens, Dr. D. González-Rodríguez, and Prof. J. L. Sessler for their constructive comments.

InterScience
© 2006 Wiley-VCH Verlag GmbH & Co. KGaA, Weinheim

subphthalocyanines (SubPcs, **8**),[8] which were discovered serendipitously by Meller and Ossko in 1972.[9] They consist of three N-fused diiminoisoindoline units arranged around a central boron atom. While they are relatively new, subphthalocyanines have already proved promising for applications in chemistry, physics, and materials sciences.[8] What makes SubPcs particularly attractive is that their optoelectronic features may be fine-tuned by varying their axial X ligands or by functionalizing the various peripheral positions.[8] The intrinsic chirality of subphthalocyanines with C_3 or C_1 symmetries[10] is an additional aspect that promises to enhance their potential utility as building blocks for the construction of complex molecules. The chemistry of subphthalocyanines has blossomed in the last decade as a result of dedicated efforts of the groups of Kobayashi,[11] Hanack,[12] and Torres,[13] among others.[14]

The next member of the subporpyrinoid family, the subporphyrazine (SubPz), was only recently unambiguously described.[15] Subporphyrazines were prepared in about 20% yield by treating disubstituted maleonitriles with boron trichloride. The easier axial substitution by nucleophiles in subporphyrazines, in comparison with subphthalocyanines, is thought to reflect the stronger interaction of the peripheral substituents with the macrocyclic core.

Recently, in a remarkable paper, Kim, Osuka, and co-workers described for the first time a subporphyrinoid of the type **7**.[16] The authors described therein the first synthesis of a subporphyrin as its tribenzo-substituted boron complex, **7** (X = OH, OMe, O*i*Pr, OCOPh, $OCOCF_3$, OCOMe). The synthesis of tribenzosubporphyrins such as **7** can be performed by the thermal self-condensation of isoindolinone-3-acetic acid in the presence of a boron(III) template, in this case boric acid (Scheme 1). The method is a modification of a protocol developed by Gouterman and co-workers[17] for the synthesis of tetrabenzoporphyrin, which also started from isoindolinone-3-acetic acid but relied on Zn^{II} as the templating cation. Although the reaction conditions were quite harsh (heating at 350°C or use of microwave enhancement) and the yields were rather low at approximately

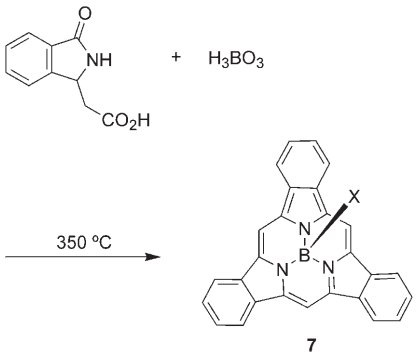

Scheme 1. Preparation of a tribenzosubporphyrin **7** (X = OH).

1.5%, the isolation and characterization of compound **7** represents a significant contribution to the chemistry of porphyrinoids.

Employing less-aggressive boron(III) reagents, such as boric or phenylboronic acids, rather than the boron(III) halides that are commonly used in the preparation of subphthalocyanines **8**[8] should provide greater compatibility with many common functional groups. Nonetheless, by using other boron reagents, including trialkyl borates or more-reactive boronic acid derivatives, it may be possible to increase the yield of the reaction.

X-ray crystal structural analyses revealed that the tribenzosubporphyrins **7** have bowl-shaped structures, whose curvatures depend on the nature of the axial group.[16] The degree of curvature of the tribenzosubporphyrins is lower than that of the subphthalocyanines **8**. However, in both cases spectroscopic features associated with aromaticity (e.g., strong diatropic ring-current effects) are observed in the NMR spectrum. These findings suggest, as in the case of the SubPcs and SubPzs, the presence of a 14-π-electron aromatic core.

The aromatic character of nonplanar macrocyclic or fused-ring systems has long fascinated chemists. The nonplanar structure seen in **7**, as well as in other subporphyrinoids such as **6** and **8**, provides a clear testing ground for advanced models of aromaticity (Figure 3). From an experimental perspective, it is clear that the marked deviation from planarity of subphthalocyanines and, to a lesser extent, of tribenzosubporphyrins, has an important effect on

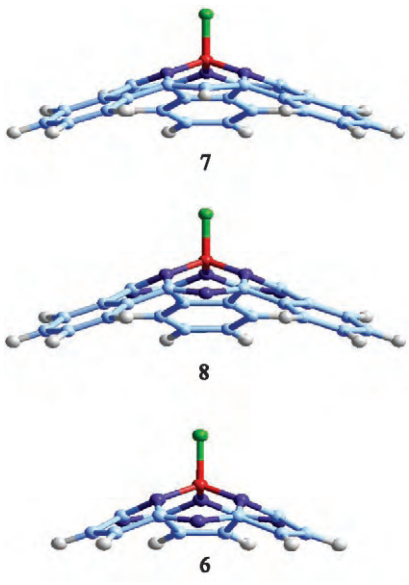

Figure 3. Ball-and-stick representations of a tribenzosubporphyrin (**7**), subphthalocyanine (**8**), and subazaporphyrin (**6**), based on AM1 calculations. The curvature increases from **7**→**8**→**6**. B red, N dark blue, X green, C pale blue, H white.

the chemical and electronic properties of the systems as a whole. An understanding of this on an empirical level is critical to the application of these kinds of materials.

The curved nature of the subporphyrinoids makes these molecules particularly interesting as building blocks in supramolecular systems, as the concave and convex π surfaces can interact in different ways with other electroactive moieties. This possibility was already explored in the field of subphthalocyanines.[18] Moreover, fused binuclear subphthalocyanine systems were also reported.[19] These dimers and related trimers[19a] reveal interesting spectroscopic features, including strongly red-shifted Q bands, and they also represent a first step towards the stepwise synthesis of larger systems with well-defined curved, fully conjugated π surfaces. Similar chemistry is anticipated in the case of the subporphyrins, and novel mixed systems can be envisaged, wherein different porphyrinoid subunits are combined.

The optical properties of tribenzosubporphyrins, subporphyrazines, and subphthalocyanines can be regarded as being analogous to those of their corresponding four-membered partners, por-

© 2006 Wiley-VCH Verlag GmbH & Co. KGaA, Weinheim

phyrins, porphyrazines, and phthalocyanines, respectively, even though there are obviously important differences with regards molecular symmetry and molecular size. Generally, the subporphyrinoids display absorbance bands in the UV/Vis spectral region that are considerably blue-shifted with respect to those of their corresponding partners, mainly as a result of their smaller π-conjugated cores. They are intensively colored, from orange to deep red. It is these characteristics that make them potentially applicable in high-density optical data storage.[8a]

The tribenzosubporphyrins **7** are chemically stable, in contrast to the subporphyrazines **6** and subphthalocyanines **8**, which are relatively unstable as a result of their iminic double bonds. The central macrocyclic core in **7** seems to be robust enough to allow chemical modifications of the peripheral substituents, thus facilitating chemical functionalization of this prototypical system. Further work needs to be done to find alternative synthetic pathways to not only improve the reaction yields but also produce functionalized systems or systems with lower overall symmetry. In this context, important targets are subporphyrins, subporphyrazines, and subphthalocyanines that either do not contain boron (i.e., free-base forms) or incorporate another different central cation.[20] It is also important to explore the extent to which appropriate peripheral and axial substituents may be introduced, and to what extent will heteroatom replacements in the pyrrole or isoindole subunits be tolerated. Another parameter that may be varied is the number and nature of the bridging *meso* linkages.

Although most of these ideas hold promise for the future, some opportunities can already be envisioned. The resolution of appropriately substituted intrinsically chiral nonplanar subporphyrinoids **6**, **7**, and **8** on a preparative scale would open up a number of opportunities in molecular recognition chemistry. Likewise, the bowl shape of these compounds makes them ideal building blocks for constructing nonplanar nanometer-sized fully aromatic molecular architectures. Indeed, molecular cages constructed by supramolecular self-assembly of two or more adequately functionalized macrocyclic subunits have already been described.[21]

Detailed studies of the photophysical and electrochemical properties of tribenzosubporphyrins **7** and subporphyrazines **6** are also called for. Comparisons between these systems and better studied congeners, such as subphthalocyanines, in conjunction with supporting theoretical studies will provide a deeper understanding of the electronic properties of these subporphyrinoids. Such information is not only of intrinsic interest, it will set the stage for the use of these subporphyrinoid systems in the fields of nanotechnology and molecular materials.

The accomplishments achieved so far in the subporphyrinoid area are remarkable. However, it is clear that much more remains to be done and that, more than likely, the best is yet to come. In such a context, an intriguing question remains: Can the modified Gouterman strategy reported by Kim, Osuka, and co-workers be used to prepare the most obvious missing member of the series, namely subporphyrin **5**? Or, will a totally new method need to be developed? The answer is simply not known at present, but the challenge and opportunity that such a target presents is sure to attract great efforts to develop this important area of porphyrin-related chemistry.[22]

[1] a) *The Porphyrin Handbook*, *Vols. 1–10* (Eds.: K. M. Kadish, K. M. Smith, R. Guilard), Academic Press, San Diego, CA, **2000**; b) *The Porphyrin Handbook*, *Vols. 11–14* (Eds.: K. M. Kadish, K. M. Smith, R. Guilard), Academic Press, San Diego, CA, **2003**.

[2] *The Porphyrin Handbook*, *Vols. 15–20* (Eds.: K. M. Kadish, K. M. Smith, R. Guilard), Academic Press, San Diego, CA, **2003**.

[3] a) N. B. McKeown, *Phthalocyanines Materials: Synthesis, Structure and Function*, Cambridge University Press, Cambridge, **1998**; b) G. de la Torre, P. Vázquez, F. Agulló-López, T. Torres, *Chem. Rev.* **2004**, *104*, 3723.

[4] T. D. Lash, *J. Porphyrins Phthalocyanines* **2001**, *5*, 267.

[5] a) M. S. Rodríguez-Morgade, P. V. Stuzhin, *J. Porphyrins Phthalocyanines* **2004**, *8*, 1129; b) S. L. J. Michel, B. M. Hoffman, S. M. Baum, A. G. M. Barrett, *Prog. Inorg. Chem.* **2001**, *50*, 473.

[6] a) A. Jasat, D. Dolphin, *Chem. Rev.* **1997**, *97*, 2267; b) J. L. Sessler, D. Seidel, *Angew. Chem.* **2003**, *115*, 42, 5292; *Angew. Chem. Int. Ed.* **2003**, *42*, 5134; c) R. B. Woodward in *Aromaticity: An International Symposium* (Sheffield, UK), Special Publication No. 21, The Chemical Society, London, **1966**.

[7] Corroles and related systems are not discussed in the present Highlight because their "contraction" does not imply a reduction in the number of pyrrole or isoindole moieties.

[8] a) C. G. Claessens, D. González-Rodríguez, T. Torres, *Chem. Rev.* **2002**, *102*, 835; b) "Synthesis and Spectroscopic Properties of Phthalocyanine Analogs": N. Kobayashi in *The Porphyrin Handbook*, *Vols. 15* (Eds.: K. M. Kadish, K. M. Smith, R. Guilard), Academic Press, San Diego, CA, **2003**, pp. 161–262.

[9] A. Meller, A. Ossko, *Monatsh. Chem.* **1972**, *103*, 150.

[10] a) C. G. Claessens, T. Torres, *Tetrahedron Lett.* **2000**, *41*, 6361; b) N. Kobayashi, *Coord. Chem. Rev.* **2001**, *219–221*, 99.

[11] a) N. Kobayashi, R. Kondo, S.-I. Nakajima, T. Osa, *J. Am. Chem. Soc.* **1990**, *112*, 9640; b) N. Kobayashi, T. Ishizaki, K. Ishii, K. Konami, *J. Am. Chem. Soc.* **1999**, *121*, 9096.

[12] M. Hanack, M. Geyer, *J. Chem. Soc. Chem. Commun.* **1994**, 2253.

[13] A. Sastre, B. del Rey, T. Torres, *J. Org. Chem.* **1996**, *61*, 8591.

[14] a) E. Musluoglu, A. Gürek, V. Ahsen, A. Gül, Ö. Bekaroglu, *Chem. Ber.* **1992**, *125*, 2337; b) A. Weitemeyer, H. Kliesch, D. Wöhrle, *J. Org. Chem.* **1995**, *60*, 4900; c) K. Kasuga, T. Idehara, M. Handa, Y. Ueda, T. Fujiwara, K. Isa, *Bull. Chem. Soc. Jpn.* **1996**, *69*, 2559; d) S. V. Kudrevich, S. Gilbert, J. E. van Lier, *J. Org. Chem.* **1996**, *61*, 5706; e) J. R. Stork, R. J. Potucek, W. S. Durfee, B. C. Noll, *Tetrahedron Lett.* **1999**, *40*, 8055; f) R. Potz, M. Göldner, H. Hückstädt, U. Cornelissen, A. Tutaß, H. Homborg, *Z. Anorg. Allg. Chem.* **2000**, *626*, 588.

[15] M. S. Rodríguez-Morgade, S. Esperanza, T. Torres, J. Barberá, *Chem. Eur. J.* **2005**, *11*, 354.

[16] Y. Inokuma, J. H. Kwon, T. K. Ahn, M.-C. Yoo, D. Kim, A. Osuka, *Angew. Chem.* **2006**, *118*, 975; *Angew. Chem. Int. Ed.* **2006**, *45*, 961.

[17] L. Edwards, M. Gouterman, C. B. Rose, *J. Am. Chem. Soc.* **1976**, *98*, 7638.

[18] D. González-Rodríguez, T. Torres, D. M. Guldi, J. Rivera, M. A. Herranz, L. Echegoyen, *J. Am. Chem. Soc.* **2002**, *126*, 6301.

[19] a) C. G. Claessens, T. Torres, *Angew. Chem.* **2002**, *114*, 2673; *Angew. Chem. Int. Ed.* **2002**, *41*, 2561; b) T. Fukuda,

 © 2006 Wiley-VCH Verlag GmbH & Co. KGaA, Weinheim

J. R. Stork, R. J. Potucek, M. M. Olmstead, B. C. Noll, N. Kobayashi, W. S. Durfee, *Angew. Chem.* **2002**, *114*, 2677; *Angew. Chem. Int. Ed.* **2002**, *41*, 2565.

[20] A patent including an aluminum subphthalocyanine has been issued, however, no proofs about the structure of the compound are given therein; see: A. Zafirov, S. Rakovski, J. Bakardjieva-Eneva, L. Prahov, L. Assenova, F. Marrandino, PCT Int. Appl. WO-2002080158, **2002**.

[21] C. G. Claessens, T. Torres, *J. Am. Chem. Soc.* **2002**, *124*, 14522.

[22] **Note added in proof**: Latos-Grażyński and co-workers have recently reported the synthesis and characterization of subpyriporphyrin, a free-base [14]triphyrin(1.1.1) homologue with an embedded pyridine moiety. The new macrocycle introduces a unique structural pattern of free-base triphyrin distinguished by location of three nitrogen atoms at corners of an approximately equilateral triangle, approaching a limit of porphyrin contraction. The free-base macrocycle is slightly ruffled and is nonaromatic as a result of the cross-conjugation imposed by the pyridine ring. However, it reacts with $PhBCl_2$ to yield a 14-π-electron aromatic σ-phenyl boron(III) complex. For details, see: R. Myslinborski, L. Latos-Grażyński, L. Szterenberg, T. Lis, *Angew. Chem.* DOI: 10.1002/ange.200600589; *Angew. Chem. Int. Ed.* DOI: 10.1002/anie.200600589.

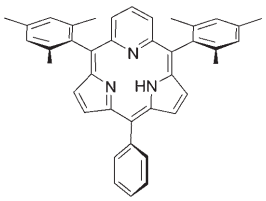

Comprehensive Coverage of Nanotechnology

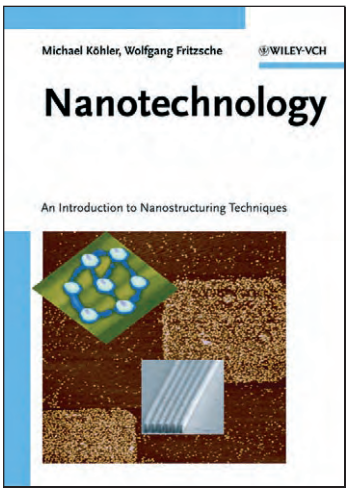

2004. XII, 272 pages, 143 figures, 9 tables. Hardcover.
ISBN 3-527-30750-8
€ 119.- /£ 85.- /US$ 160.-

MICHAEL KÖHLER and WOLFGANG FRITZSCHE

Nanotechnology
An Introduction to Nanostructuring Techniques

Nanotechnology - the generation, modification and utilization of objects with tiniest dimensions - enjoys great success due to its purposeful combination of physical, mechanical and molecular techniques.

Written for both scientists and engineers, this book offers fascinating insight into nanotechnology, starting out with the fundamentals of microtechnology and chemistry necessary for understanding the shaping of nanoscale structures, then illustrating the fabrication of nanostructures from different materials through a variety of examples and finally presenting methods for characterization of the generated structures to the reader.

"...comprehensive coverage of all underlying principles..."
Chemistry & Industry

23600511_kn

Register now for the free
WILEY-VCH Newsletter!
www.wiley-vch.de/home/pas

WILEY-VCH • P.O. Box 10 11 61 • D-69451 Weinheim, Germany
Fax: +49 (0) 62 01 - 60 61 84
e-mail: service@wiley-vch.de • http://www.wiley-vch.de

WILEY-VCH

© 2006 Wiley-VCH Verlag GmbH & Co. KGaA, Weinheim

Homogeneous Catalysis

DOI: 10.1002/anie.200600025

Palladium-Catalyzed Coupling Reactions for the Stereoselective Synthesis of Tri- and Tetrasubstituted Alkenes**

*Oliver Reiser**

Keywords:
alkenes · boron · C–C coupling · palladium · zinc

Ever since Georg Wittig developed the first olefination of a ketone back in 1953,[1] the synthesis of alkenes has become an indispensable strategic tool for the construction of complex molecules.[2] The award of the Nobel Prize in Chemistry in 2005 for the development of olefin metathesis[3] ("alkene olefination") to Y. Caulvin, R. Grubbs, and R. Schrock marks the current apex of a half-century of successful developments in alkene synthesis. Nevertheless, the stereoselective synthesis of tri- and tetrasubstituted alkenes, which are important constituents in many natural products and drugs such as ratjadone (**1**)[4] and (*Z*)-tamoxifen (**2**)[5], is still a challenge. Palladium- or nickel-catalyzed cross coupling reactions,[6,7] often preceded by hydrometalation of alkynes,[8] offer an attractive alternative to carbonyl olefinations[9] and cross-metathesis reactions[10] for the stereoselective synthesis of acyclic alkenes (Scheme 1).

In particular, the coupling of 1,1- or 1,2-dihalogenated or the corresponding dimetalated substrates such as **8** and **9** could open an efficient route to tri- and tetrasubstituted alkenes. While such reactions with substrates of type **9** have met with some success,[11] problems are encountered in controlling the chemo- and regioselectivity in sequential couplings as well as preparing the starting alkenes in geometrically pure form. 1,1-Dihalo-1-alkenes **8** (Y = Cl, Br, I), which are readily prepared from aldehydes or ketones, can further be directly converted into 1,1-dimetalated alkenes **8** (e.g. Y = BR_2, SnR_3). Consequently, a broad range of starting materials of type **8** are available that appear to be suitable for a variety of transition-metal-catalyzed coupling reactions.

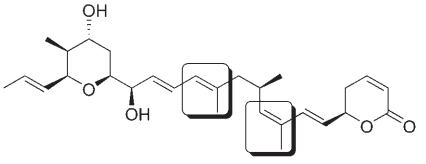

Ratjadone (**1**)

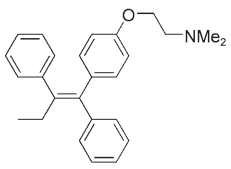

(*Z*)-Tamoxifen (**2**)

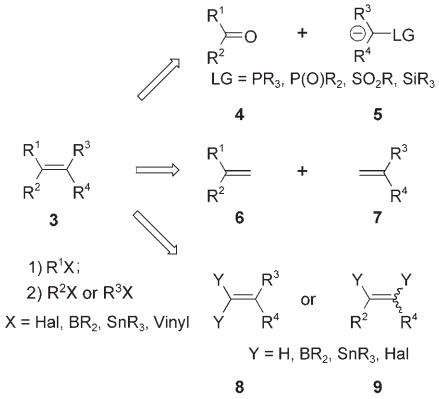

Scheme 1. Common strategies for the synthesis of alkenes. LG = leaving group.

The palladium- or nickel-catalyzed, sequential cross-coupling of 1,1-dihalo-1-alkenes has been established as an efficient method for the synthesis of trisubstituted alkenes.[12] However, this approach was mainly limited to aryl-, alkenyl-, and alkynylmetals, while stepwise alkylation remained problematic[13] and generally resulted in twofold substituted products. The only exception was the palladium-catalyzed sequential alkylation of β,β-dichlorostyrene (**10**), which was treated first with *n*BuZnCl followed by *n*HexMgBr to give rise to **11** in 62% overall yield (Scheme 2). The

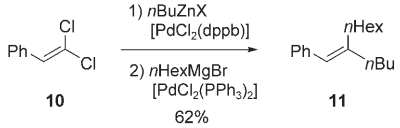

Scheme 2. Sequential palladium-catalyzed dialkylation of β,β-dichlorostyrene (**10**).

obstacle to alkylation reactions seems to have been overcome with new catalysts and reaction conditions, and generally applicable protocols to stereoselectively construct tri- and tetrasubstituted alkenes are within sight.[14]

Several key issues, exemplified for the dibromoalkene **12**, had to be recognized in the course of the development of this methodology (Scheme 3): The initial oxidative addition of palladium(0) takes place selectively *trans* to the R group regardless of the palladium–ligand complex employed, leading to diene **13** upon coupling with the alkenylzinc reagent. Subsequent coupling of

[*] Prof. Dr. O. Reiser
Institut für Organische Chemie
Universität Regensburg
Universitätsstrasse 31
93053 Regensburg (Germany)
Fax: (+49) 941-943-4121
E-mail: oliver.reiser@chemie.uni-regensburg.de

[**] This work was supported by the Fonds der Chemischen Industrie.

InterScience
© 2006 Wiley-VCH Verlag GmbH & Co. KGaA, Weinheim

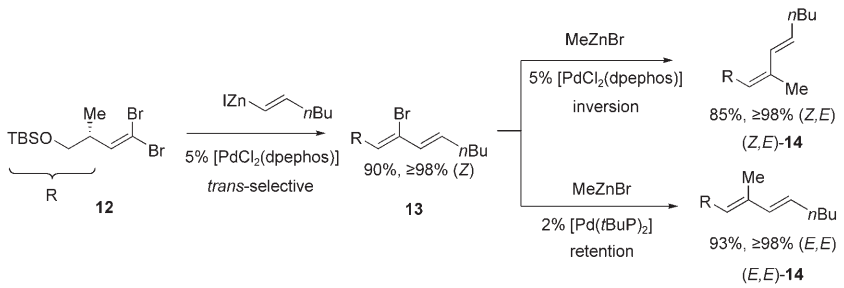

Scheme 3. Stereoselective synthesis of (*Z*,*E*)- and (*E*,*E*)-1,3-butadienes **14**. TBS = *tert*-butyldimethylsilyl.

13 with a second organozinc reagent can be achieved with control of the double-bond geometry depending on the palladium–ligand complex employed. While with Pd–phosphane catalysts such as $[Pd(PPh_3)_4]$ and $[PdCl_2(dpephos)]$[15] complete inversion at the Br-bearing C–C double bond is observed resulting in (*Z*,*E*)-**14**, the use of tBu_3P or N-heterocyclic carbene ligands (NHCs) leads to (*E*,*E*)-**14** and the original double-bond geometry is conserved.

It is plausible that steric hindrance in an intermediate like **15** (Scheme 4)

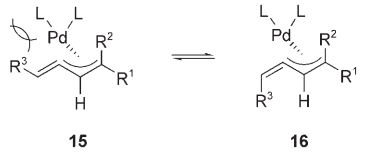

Scheme 4. Isomerization of alkyenylidene-substituted π-allylpalladium complexes. L = ligand.

between the palladium–ligand fragment and R^3 might favor inversion, but the usual mechanistic rational invoking the π–σ–π mechanism commonly encountered in the isomerization of π-allylpalladium complexes[16] cannot operate since it also would involve inversion of R^1 and R^2. Moreover, the remarkable ligand control cannot be rationalized in an obvious way, since bulkier ligands seem to favor retention of the double-bond geometry.

While the alkenylation/alkylation sequence allows the selective assembly of alkenes **14**, the development of an alkylation/alkylation sequence proved to be more challenging as the undesired twofold alkylation leading to **21** can dominate (Scheme 5). This undesired side reaction can be largely suppressed

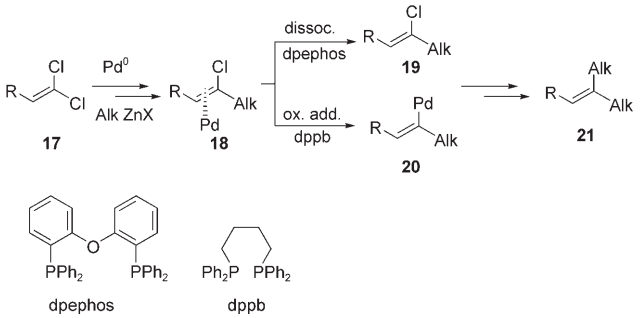

Scheme 5. Competitive mono- and dialkylation of 1,1-dichloro-1-alkenes **17**. Alk = Alkyl.

if 1,1-dichloroalkenes **17** instead of the corresponding dibromoalkenes and if dpephos[15] instead of dppb[15] are used. In some cases, the addition of one equivalent of *N*-methylimidazole (NMI) further improved the ratio in favor of the monoalkylated product **19** over the dialkylated alkene **21**. The ability of the oxygen atom in dpephos to coordinate with palladium might facilitate the dissociation of the catalyst from the intermediate **18**. Likewise, the role of the additive NMI could be explained.

The subsequent cross-coupling of **19** with retention of double-bond configuration was best carried out with Pd^0/tricyclohexylphosphine (PCy_3) or Pd^0/tricyclopentylphosphine ($PCyp_3$), while Pd/$PtBu_3$ or nickel–phosphine catalysts led to isomerization of the products. In this way, readily available Grignard reagents could be employed to yield trisubstituted alkenes in excellent yields and selectivity, as exemplified in Scheme 6.

The "reversed" approach, that is, the coupling of 1,1-dimetalated 1-alkenes[17] **8** (Y = metal) with electrophiles offers a complimentary route to tetrasubstituted alkenes. In early examples *gem*-1,1-di-

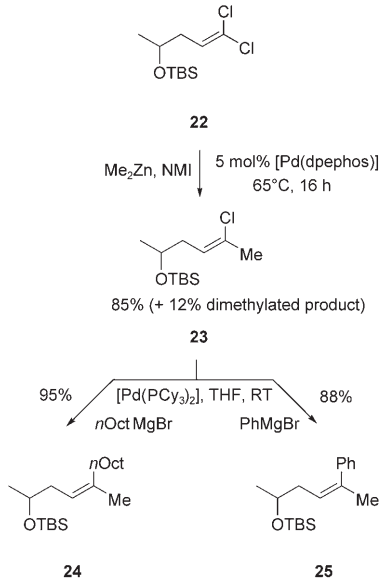

Scheme 6. Sequential alkylation–alkylation or alkylation–arylation of 1,1-dichloro-1-alkenes.

zincio and 1,1-distannyl reagents were employed,[18] while more recently 1,1-diboryl-1-alkenes **28**, readily available[19] from 1,1-dibromo-1-alkenes **26** or from ketones **27**, have been used (Scheme 7).[20] Again, a key requirement for the sequential introduction of the two coupling partners is the that the reaction is stereoselective as well as a monosubstitution. Remarkably, the first palladium-catalyzed cross-coupling (arylation or vinylation) of **28** to give rise to **29** takes place already at room temperature exclusively *trans* to the aryl group Ar even in the presence of sterically demanding alkyl groups R such as *i*Pr or *t*Bu in *cis* position, pointing to an electronic activation of the reacting carbon–boron bond. Consequently, a second cross-coupling reaction (aryla-

© 2006 Wiley-VCH Verlag GmbH & Co. KGaA, Weinheim

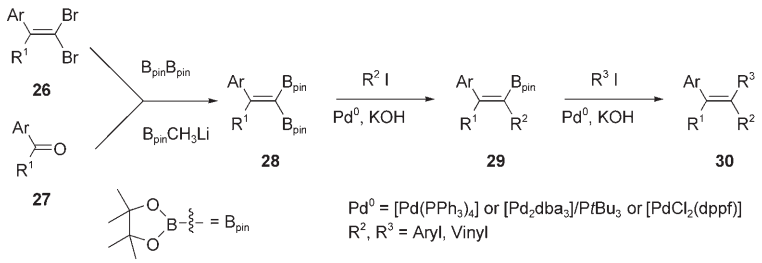

Scheme 7. 1,1-Diboryl-1-alkenes as starting materials for the synthesis of highly substituted alkenes.

tion or vinylation), which requires elevated temperatures, can follow to effectively yield a broad variety of alkenes **30**.

This strategy was used to accomplish a one-pot synthesis of (*Z*)-tamoxifen (**2**) from **31** by the sequential addition of stoichiometric amounts of the coupling partners to the reaction mixture (Scheme 8). By reversal of the addition

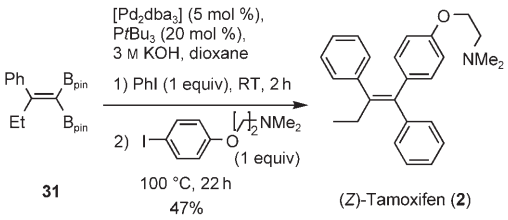

Scheme 8. One-pot synthesis of (*Z*)-tamoxifen (**2**).

of the coupling partners—carried out in two separate steps—(*E*)-tamoxifene is also available.

The remarkable influence on the course of palladium-catalyzed cross-coupling reactions by steric and electronic variations of the ligands or the substrates, especially by the choice of metal of the species undergoing transmetalation, continues to open up ample possibility for the discovery of new processes. The approaches discussed here are among the most efficient strategies for the synthesis of tri- and tetrasubstituted alkenes with high geometrical control.

Published online: April 3, 2006

[1] G. Wittig, G. Geissler, *Justus Liebigs Ann. Chem.* **1953**, 44; see also H. Staudinger, J. Meyer, *Helv. Chim. Acta* **1919**, *2*, 619.

[2] *Modern Carbonyl Olefination* (Ed.: T. Takeda), Wiley-VCH, Weinheim, **2004**.

[3] *Handbook of Metathesis*, *Vol. 1–3* (Ed.: R. H. Grubbs), Wiley-VCH, Weinheim, **1993**.

[4] a) D. Schummer, K. Gerth, H. Reichenbach, G. Höfle, *Liebigs Ann.* **1995**, 685; b) U. Bhatt, M. Christmann, M. Quitschalle, E. Claus, M. Kalesse, *J. Org. Chem.* **2001**, *66*, 1885; c) D. R. Williams, D. C. Ihle, S. V. Plummer, *Org. Lett.* **2001**, *3*, 1383.

[5] H. Wiseman, *Tamoxifen: Molecular Basis of Use in Cancer Treatment and Prevention*, Wiley, Chichester, **1994**.

[6] *Metal-Catalyzed Cross Coupling Reactions*, *Vols. 1 and 2* (Eds.: A. de Meijere, F. Diederic), Wiley-VCH, Weinheim, **2004**.

[7] Leading reviews for applications in natural product synthesis: a) Z. Tan, E.-i. Negichi *in Handbook of Organopalladium Chemistry for Organic Synthesis*, *Vol. 1* (Ed.: E.-i. Negishi), Wiley, New York, **2002**, p. 863; b) S. R. Chemler, D. Trauner, S. Danishefsky, *Angew. Chem.* **2001**, *113*, 4676; *Angew. Chem. Int. Ed.* **2001**, *40*, 4544.

[8] Representative examples: a) P. Dimopoulos, A. Athlan, S. Manaviazar, K. J. Hale, *Org. Lett.* **2005**, *7*, 5373; b) C. Zhou, D. E. Emrich, R. C. Larock, *Org. Lett.* **2003**, *5*, 1579; c) J. i. Uenishi, R. Kawahama, O. Yonemitsu, A. Wada, M. Ito, *Angew. Chem.* **1998**, *110*, 334; *Angew. Chem. Int. Ed.* **1998**, *37*, 320; d) W. R. Roush, R. J. Sciotti, *J. Org. Chem.* **1998**, *63*, 5473; e) W. R. Roush, R. J. Sciotti, *J. Am. Chem. Soc.* **1998**, *120*, 7411.

[9] Leading review for applications in natural product synthesis: K. C. Nicolaou, M. W. Harter, J. L. Gunzner, A. Nadin, *Liebigs Ann.* **1997**, 1283.

[10] Representative examples in natural product synthesis: a) C. A. Verbicky, C. K. Zercher, *Tetrahedron Lett.* **2000**, *41*, 8723; b) R. B. Chhor, B. Nosse, S. Soergel, C. Böhm, M. Seitz, O. Reiser, *Chem. Eur. J.* **2003**, *9*, 260; c) C. Böhm, O. Reiser, *Org. Lett.* **2001**, *3*, 1315.

[11] a) S. D. Brown, R. W. Armstrong, *J. Am. Chem. Soc.* **1996**, *118*, 6331; b) S. D. Brown, R. W. Armstrong, *J. Org. Chem.* **1997**, *62*, 7076; c) K. Voigt, P. v. Zezschwitz, K. Rosauer, A. Lansky, A. Adams, O. Reiser, A. de Meijere, *Eur. J. Org. Chem.* **1998**, 1521; d) A. Lansky, O. Reiser, A. de Meijere, *Synlett* **1990**, 405; e) O. Reiser, S. Reichow, A. de Meijere, *Angew. Chem.* **1987**, *99*, 1285; *Angew. Chem. Int. Ed. Engl.* **1987**, *26*, 1277.

[12] T. Sugihara in *Handbook of Organopalladium Chemistry for Organic Synthesis*, *Vol. 1* (Ed.: E.-i. Negishi), Wiley, New York, **2002**, p. 649.

[13] A. Minato, K. Suzuki, K. Tamao, *J. Am. Chem. Soc.* **1987**, *109*, 1257.

[14] Z. Tan, E.-i. Negishi, *Angew. Chem.* **2006**, *118*, 776; *Angew. Chem. Int. Ed.* **2006**, *45*, 762.

[15] Abbreviations: dpephos = bis(2-diphenylphosphinophenyl) ether, dppb = bis-(diphenylphosphino)-1,4-butane; cf. also Scheme 5.

[16] a) B. M. Trost, D. L. Vanvranken, *Chem. Rev.* **1996**, *96*, 395; b) O. Reiser, *Angew. Chem.* **1993**, *105*, 576; *Angew. Chem. Int. Ed. Engl.* **1993**, *32*, 547.

[17] I. Marek, *Chem. Rev.* **2000**, *100*, 2887.

[18] a) I. Creton, I. Marek, J. F. Normant, *Synthesis* **1996**, 1499; b) E.-i. Negishi, H. Sawada, J. M. Tour, Y. Wei, *J. Org. Chem.* **1988**, *53*, 913; c) P. Quayle, J. Wang, J. Xu, C. J. Urch, *Tetrahedron Lett.* **1998**, *39*, 485; d) J. G. Duboudin, B. Jousseaume, *J. Organomet. Chem.* **1979**, *168*, 1; e) I. Creton, I. Marek, J. F. Normant, *Tetrahedron Lett.* **1999**, *40*, 1899.

[19] M. Shimizu, C. Nakamaki, K. Shimono, M. Schelper, T. Kurahashi, T. Hiyama, *J. Am. Chem. Soc.* **2005**, *127*, 12506.

[20] a) T. Hata, H. Kitagawa, H. Masai, T. Kurahashi, M. Shimizu, T. Hiyama, *Angew. Chem.* **2001**, *113*, 812; *Angew. Chem. Int. Ed.* **2001**, *40*, 790; b) T. Kurahashi, T. Hata, H. Masai, H. Kitagawa, M. Shimizu, T. Hiyama, *Tetrahedron* **2002**, *58*, 6381; c) D. S. Matteson, P. B. Tripathy, *J. Organomet. Chem.* **1970**, *21*, P6; d) D. S. Matteson, P. B. Tripathy, *J. Organomet. Chem.* **1974**, *69*, 53.

 © 2006 Wiley-VCH Verlag GmbH & Co. KGaA, Weinheim

DOI: 10.1002/anie.200502747

Gas-Phase Reactions

Reactions at Very Low Temperatures: Gas Kinetics at a New Frontier

*Ian W. M. Smith**

Keywords:
astrochemistry · capture theories · gas-phase reactions · low-temperature reactions · reaction kinetics

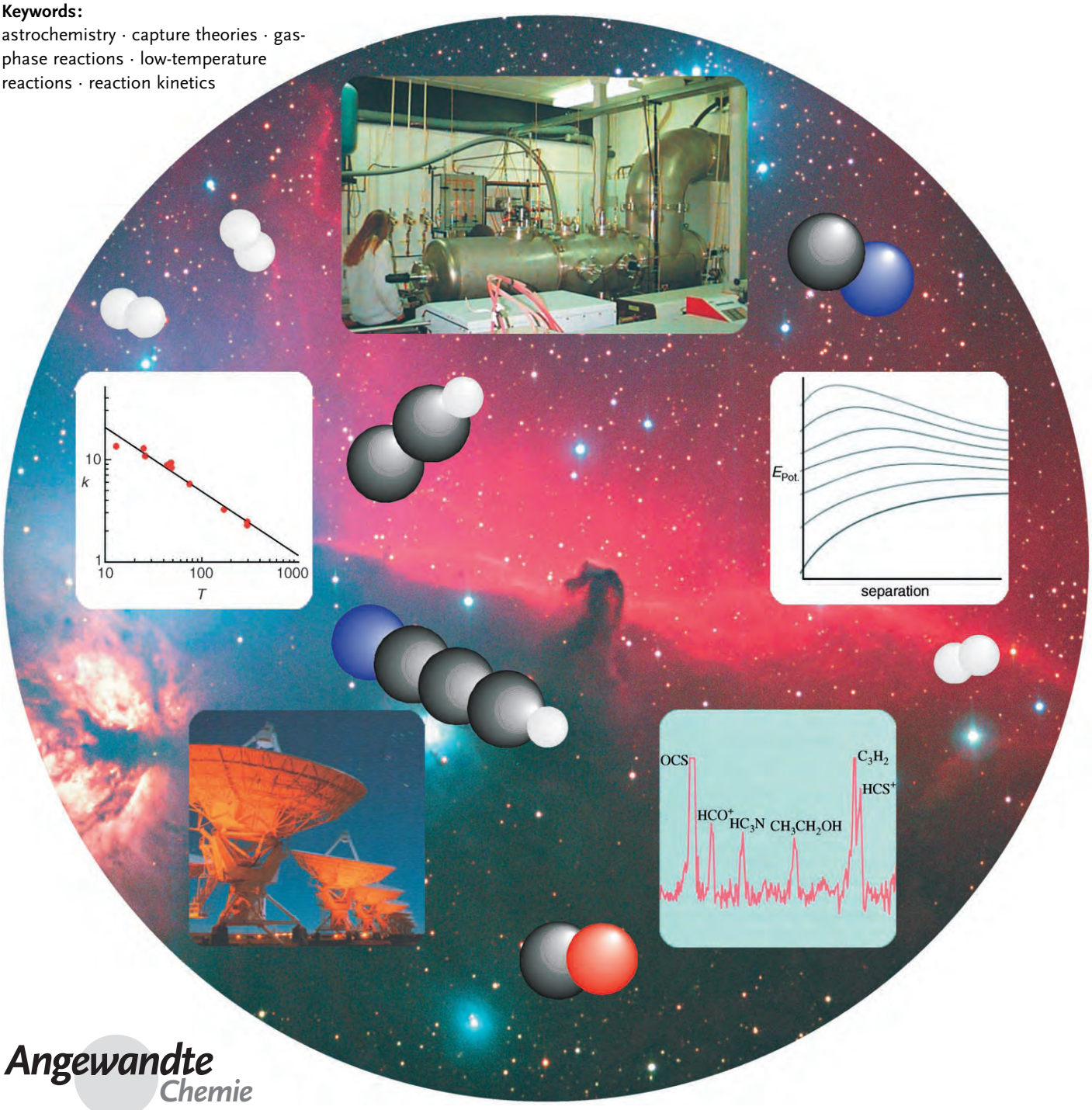

© 2006 Wiley-VCH Verlag GmbH & Co. KGaA, Weinheim

Advances in experimental techniques, especially the development of the CRESU (Cinétique de Réaction en Ecoulement Supersonique Uniforme) method, allow many gas-phase molecular processes to be studied at very low temperatures. This Review focuses on the reactions of molecular and atomic radicals with neutral molecules. Rate constants for almost 50 such reactions have been measured at temperatures as low as 13 K by using the CRESU method. The surprising demonstration that so many reactions between electrically neutral species can be extremely rapid at these very low temperatures has excited interest both from theoreticians and from those seeking to understand the chemistry that gives rise to the 135 or so molecules that are present in low-temperature molecular clouds in the interstellar medium. Theoretical treatments of these reactions are based on the idea that a reaction occurs when the long-range potential between the reagent species brings them into close contact. The astrochemical context, theoretical studies, and the determination of the rate constants of these low-temperature reactions are critically discussed.

From the Contents

1. Introduction 2843
2. Astrochemistry: Molecules in Space[7] 2844
3. The CRESU Method for Studying Neutral–Neutral Reactions at Ultralow Temperatures 2846
4. Rate Constants for Neutral–Neutral Reactions and their Temperature Dependence 2849
5. Understanding and Predicting the Rate Constants for Fast Reactions at Ultralow Temperatures 2852
6. Estimating Rate Constants for Astrochemical Modeling 2858
7. Summary and Outlook 2859

1. Introduction

A new era in chemical kinetics was heralded 20 years ago by the results reported by Bertrand Rowe, then at the Laboratoire d'Aérothermique in Meudon.[1] Using an apparatus that incorporated a shaped Laval nozzle, he generated a jet of moderately dense and strongly cooled gas. This technique, which is referred to by the acronym CRESU (cinétique de réaction en ecoulement supersonique uniforme; reaction kinetics in uniform supersonic flows), was initially deployed to study the kinetics of ion–molecule reactions at temperatures as low as 20 K. Later, by precooling the gas prior to its expansion through the nozzle, this range was extended down to 8 K.[2]

These original, groundbreaking CRESU experiments made use of the 20-m-long wind tunnel in the Meudon laboratory that was made available for kinetic measurements when it was not being used to perform experiments in aerodynamics. In 1990, the Rowe group moved to the Université de Rennes I, where they built a CRESU apparatus specifically designed to study molecular processes at low temperatures.[3] A fruitful collaboration was started with my own group (which still continues today) and led to a second CRESU apparatus[4] being built at the University of Birmingham. Since 1992, these twin apparatuses have been employed to study the rates of a wide variety of gas-phase molecular processes: ion–molecule reactions, energy transfer in molecular collisions, including transfer between rotational, vibrational, and spin-orbit states, dimer formation, electron attachment, and, perhaps most importantly, the kinetics of reactions between electrically neutral species.

This Review concentrates on what has been learnt from these CRESU experiments about neutral–neutral reactions.[++] Before the deployment of the CRESU method, there were very few kinetic measurements on such reactions below 200 K and none at all below 77 K, the temperature of liquid N_2. As other methods are developed for cooling molecules still further towards absolute zero,[5] we can expect the lowest temperatures at which the rates of reactions are measured to be lowered still further. Until then, the "very low temperatures" of the title refer to those temperatures accessed by the CRESU method, that is, down to about 7 K.

Although this Review describes the CRESU method and surveys the results that have been obtained with it, in contrast to other recent and earlier reviews,[6] it places some emphasis on the theoretical understanding of fast reactions at low temperatures and how what has been learnt for a limited number of reactions (about 50 neutral–neutral reactions in all) can help us estimate the rate constants for reactions that have not been studied, and may never be studied, in the laboratory. This last aim is important because of the relevance of low temperature reactions to the production and destruction of molecules in extremely cold regions of the interstellar medium (ISM).

[*] I. W. M. Smith[+]
Department of Chemistry
The University of Birmingham
Edgbaston, Birmingham B15 2TT (UK)
E-mail: i.w.m.smith@bham.ac.uk
[+] Present address:
University Chemical Laboratories
Lensfield Road, Cambridge CB2 1EW (UK)
Fax: (+44) 01223-336-362

[++] The term neutral–neutral reaction is used to designate a reaction between an atomic or a molecular free radical and a neutral molecule as co-reagent.

© 2006 Wiley-VCH Verlag GmbH & Co. KGaA, Weinheim

The Review is organized as follows: Section 2 provides a brief survey of those aspects of astrophysical chemistry that are relevant to low-temperature chemical reactions. This section includes an up-to-date list of molecules that have been definitively identified in the ISM through the use of spectroscopic techniques, and the physical conditions in those regions of the ISM in which most molecules have been found is discussed. Section 3 covers the CRESU method, including its strengths and limitations, and indicates how some of the limitations might be overcome. Section 4 briefly reviews the results obtained on neutral–neutral reactions, particularly with respect to the temperature dependence of the rate constants. However, this section is brief, and the interested reader can consult the original papers or more-comprehensive reviews to learn more about the details of measurements on any particular reaction or set of reactions.

In some respects, Sections 5 and 6 form the main thrust of this Review. Section 5 is my personal view of the present state of our understanding of fast, low-temperature reactions. There are now many reactions, both ion–molecule and neutral–neutral reactions, whose rate constants do not vary or increase as the temperature is lowered and approach values, at low temperatures, that might be expected on the basis of simple collision theories. It is clear that these reactions cannot have significant activation energies (E_{act}) relative to RT, for example, at 20 K, and that therefore they must proceed along a minimum-energy path that has no maximum or barrier higher than the asymptotic energy associated with the separated reagents. Instead, the rate of reaction must be controlled by the ability of the long-range potential between the reagents to bring them into intimate contact.

The understanding of interstellar chemistry, or at least of the chemistry in cold, dense, interstellar clouds (ISCs), where the bulk of molecular species have been observed, requires computer modeling that, in turn, requires as input low-temperature rate constants for many chemical reactions—many more than have been measured in laboratory experiments. Section 6 explains how such rate constants might be rationally estimated in the many cases in which experimental values are not available.

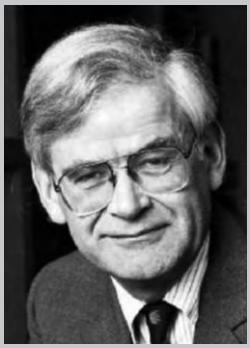

Ian Smith obtained his BA and PhD from the University of Cambridge. From 1966 to 1985, he was on the academic staff of the Department of Physical Chemistry in Cambridge, before moving in 1985 to the University of Birmingham, where he became Mason Professor of Chemistry in 1991. He has received several awards from the RSC and in 1995 he was elected a Fellow of the Royal Society. With his collaborators, he was awarded one of the first Descartes Prizes of the European Union in 2000. Although retired from his position in Birmingham, he remains active in research and teaching in the Cambridge Chemistry Department.

2. Astrochemistry: Molecules in Space[7]

Our personal vision of the cosmos is strongly influenced by what we see in the night sky on a cloudless night well away from the glare of city lights. Such a picture is, of course, biased by the fact that our eyes are sensitive only to the visible part of the electromagnetic spectrum, and hence we preferentially observe those objects (stars) with surface temperatures of at least a few thousand degrees and which therefore emit strongly in the visible region. Such an environment is not promising for the survival of molecules. Under the conditions found close to stars, molecules readily dissociate and ionize.

Molecules are found by peering into much colder and darker regions of interstellar space. To conduct this search one must employ instruments that detect radiation of longer wavelengths than visible light. The majority of the molecules whose presence in the ISM has been definitely confirmed have been identified by their spectroscopic signatures in the millimeter wave region of the spectrum, where radiative transitions between rotational levels occur. Observations in this region, by what are conventionally called "radio telescopes", have two important advantages. First, the Earth's atmosphere is essentially transparent at these wavelengths, so the instruments can be based on the ground (fortunately, in view of their size). Second, the particles of interstellar dust, which are always found with molecules in the ISM (see below), are small enough that millimeter wave radiation is not scattered but can escape from the ISCs.

Within the context of astrochemistry, a radio telescope (or, more usually, an array of radio telescopes) can be deployed in two related ways to provide complementary information. First, the detectors can be tuned to a particular molecular frequency; for example, 115.24 GHz (equivalent to a wavelength of 2.60 mm), which is associated with the $J=1\rightarrow J=0$ rotational transition in $^{12}C^{16}O$, and a scan of the sky performed to find those regions that are rich in this emission frequency. Figure 1 shows the results of such a scan within the Orion constellation. Clearly, there are two regions, or "giant molecular clouds", that are particularly strong in this emission. CO can be used as the marker for at least three reasons: a) CO is a moderately strong mm-wave emitter, b) CO is, after H_2, the second-most-abundant molecule in the ISM,[*] and c) CO appears always to be found in conjunction with other molecules.

Once a line-of-sight with strong emission from CO has been found, the radio telescopes can be operated in their second mode, which allows spectroscopic measurements. That is, the telescopes can be pointed at a region identified as having a high CO concentration, and the frequency to which the detectors are sensitive can be scanned in order to search for emission frequencies from other molecules. Figure 2 shows the result of one such experiment. It shows a rather large number of molecular transitions over a relatively small range of frequencies (only 500 MHz in 85 000 MHz), and these emission frequencies (except for one indicated with a question mark) can be assigned by comparison with labo-

[*] In ISCs, He atoms are present at ≈10% of the concentration of H_2; the abundance of CO molecules relative to that of H_2 is $\approx 10^{-4}$.

 © 2006 Wiley-VCH Verlag GmbH & Co. KGaA, Weinheim

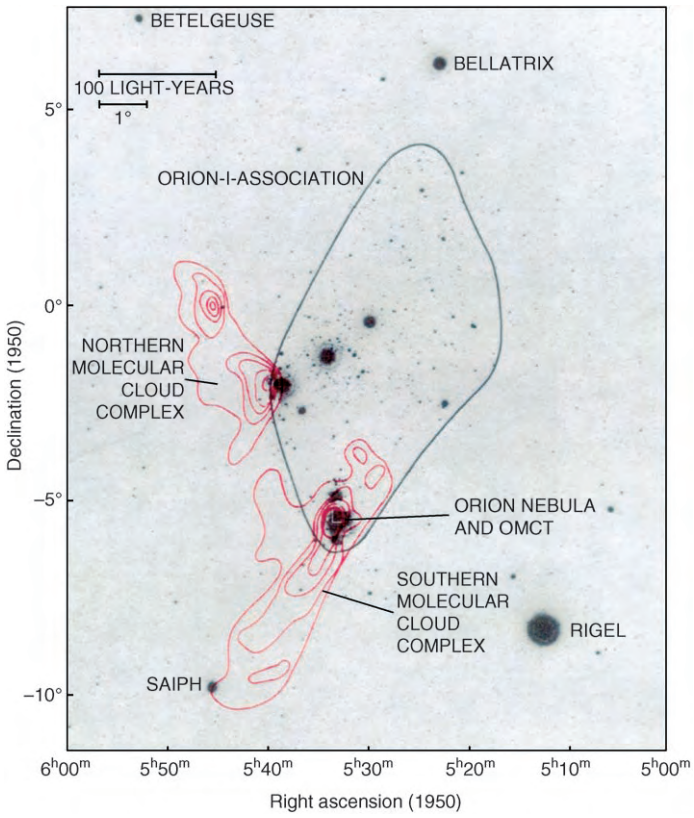

Figure 1. "Radio map" of the giant molecular clouds in Orion (the three black images in line are the three stars in Orion's belt). The red contour lines show the intensity of emission in the $J=1\rightarrow J=0$ rotational transition in carbon monoxide. The enormous size of these clouds can be gauged by the scale in the top left of the diagram. (Reproduced, with permission, from reference [62].)

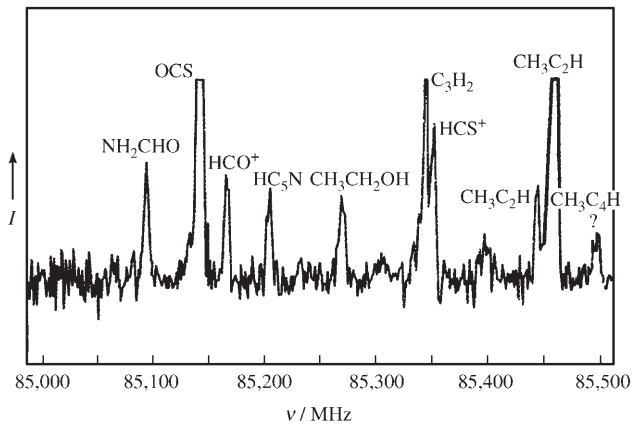

Figure 2. Part of a millimeter-wave spectrum (85 650 MHz is equivalent to a wavelength of 3.5 mm) recorded from the molecular cloud Sagittarius B2 displaying the presence of both neutral and charged molecules and the predominance of C-containing species. (Reproduced, with permission, from reference [63].)

ratory spectra. (In practice, this is easier said than done. Many of the "unstable" species observed in the ISM are difficult to make in sufficient concentrations in the laboratory for their spectra to be recorded.)

The application of mm-wave spectroscopy has been responsible for the positive identification of most molecules known to exist in the ISM. Of course, a fundamental requirement for a strong electric-dipole-induced transition between the rotational levels of a molecule is that the molecule has a permanent electric dipole. This means that the method is "blind" to a number of possibly important molecules, such as N_2, O_2, CO_2, C_2H_2, and above all H_2. Molecular hydrogen, which is 10 000 times more abundant in dense molecular clouds than any other molecule, can, however, be detected by its very weak quadrupole-induced rotational and rotational–vibrational spectra. Nonpolar molecules that contain more than two atoms, for example, CO_2 and C_2H_2, give rise to infrared-active vibrations. However, the observation of such transitions requires that, as far as possible, the effects of IR absorption in the Earth's atmosphere be minimized. In this respect, ISO, the infrared space observatory, has made vital observations, not only on gas-phase molecules but also on the composition of interstellar dust grains.[8]

Table 1 lists the 135 molecules that have been identified so far in the ISM by the application of mm-wave and infrared spectroscopy. The molecules are arranged in columns according to the number of atoms (N) that they contain. Diatomic and triatomic molecules are the most common, and the number of molecules in each column decreases as N increases. Although both ionic and neutral species are observed, there are many more neutral than ionic species. The table is rich in carbon-containing species. However, and despite the fact that the elemental abundance of hydrogen exceeds that of any other element, except helium, by four orders of magnitude, many of the observed species are highly unsaturated: there are many free radicals (e.g. CH, OH, HCO, C_2H, etc.) and many species with carbon chains, both radicals (e.g. C_3H, C_4H, C_5, C_5H, etc.) and unsaturated molecules (C_2H_2, C_2H_4, $HC_{10}CN$, etc.). Table 1 also records the very recent (but controversial) observation of the simplest amino acid, glycine (H_2NCH_2COOH).[9]

To be sure of molecular assignments, it is vital that more than one spectroscopic transition from a particular species is observed. In addition, the observation of more than one molecular frequency can, through careful interpretation of the relative intensities, reveal the physical conditions—that is, the temperature and pressure—in the environment of the molecule. Temperatures between 10 and 50 K and molecular densities of $\approx 10^4\ cm^{-3}$ are typical in the quiescent cores of dense molecular clouds. The use of the word "dense" requires some explanation, as a density of $10^4\ cm^{-3}$ corresponds to a super-high vacuum in a laboratory experiment. However, in the ISM, this density must be compared with an average interstellar density of $\approx 1\ cm^{-3}$ and a "background density" (that is, outside the molecular clouds) of approximately $0.1\ cm^{-3}$. Both the density and the temperature rise in those regions of ISCs where stars are starting to form, as gravity pulls together the molecules and dust particles in the cloud. Infrared observations are particularly useful in the study of these warmer star-forming regions of ISCs.

It is interesting to translate the physical conditions in dense ISCs into gas kinetic properties. Simple estimates based on the temperature and density given in the previous paragraph indicate that a CO molecule travels for approximately

 © 2006 Wiley-VCH Verlag GmbH & Co. KGaA, Weinheim

Table 1: Reported interstellar and circumstellar molecules.[a]

$N=2$		$N=3$		$N=4$	$N=5$	$N=6$	$N=7$	$N=8$	$N=9$	$N=10$	$N=11$	$N=12$	$N=13$
H_2	AlCl	H_3^+	OCS	NH_3	CH_4	CH_3OH	CH_3NH_2	$HCOOCH_3$	$(CH_3)_2O$	$(CH_3)CO$	HC_8CN	C_6H_6	$HC_{10}CN$
CH	PN	CH_2	MgCN	H_3O^+	SiH_4	CH_3SH	CH_3CCH	CH_3C_2CN	C_2H_5OH	CH_3C_4CN			
CH^+	SiN	NH_2	MgNC	H_2CO	CH_2NH	C_2H_4	CH_3CHO	HC_6H	C_2H_5CN	H_2NCH_2COOH ?			
NH	SiO	H_2O	NaCN	H_2CS	H_2C_3	CH_3CN	*c*-CH_2OCH_2	C_7H	CH_3C_4H	CH_3CH_2CHO			
OH	SiS	H_2S	SO_2	*l*-C_3H	*c*-C_3H_2	CH_3NC	CH_2CHCN	$HOCH_2CHO$	C_8H	$(CH_2OH)_2$			
HF	CO^+	C_2H	N_2O	*c*-C_3H	H_2CCN	H_2CCHO	HC_4CN	CH_3COOH	HC_6CN				
C_2	SO^+	HCN	SiCN	HCCH	H_2CCN	NH_2CHO	C_6H	$H_2CCCHCN$					
CN	PO	HNC	CO_2	$HCNH^+$	CH_2CO	HC_3NH^+	H_2CCHOH	H_2C_6					
CO	SH	HCO	*c*-SiC_2	H_2CN	HCOOH	H_2C_4		CH_2CHCHO					
CS	AlF	HCO^+	SiNC	HCCN	C_4H	C_5H							
CP	FeO	HOC^+	AlNC	HNCO	HC_2CN	C_5N							
NO	SiC	HN_2^+		$HOCO^+$	HC_2NC	HC_4H							
NS	CF^+	HNO		HNCS	C_4Si	HC_3CN							
SO	N_2 ?	HCS^+		C_2CN	C_5								
HCl		C_3		C_3O	HNC_3								
NaCl		C_2O		C_3S	H_2COH^+								
KCl		C_2S		SiC_3									
				CH_3									

[a] see http://www.cv.nrao.edu/~awootten/allmols.html. Formulae given in **blue** represent molecular ions. Formulae given in **red** represent neutral molecules containing carbon. Different isotopomers of the same species are not listed.

7 days between successive collisions with H_2 and during that time it will travel about 75 000 km. Huge as these values seem to those used to conditions in an earthly laboratory, they are, of course, quite small on astronomical scales of time and length.

As already mentioned, regions where molecules are found are rich in particulate matter: variously referred to as interstellar grains or interstellar dust. These particles are believed to be carbon- or silicon-based with a covering of molecules condensed from the cloud.[10] They are thought to have a diameter of about 0.1 μm. As well as allowing astronomers to record spectacular photographs of dense interstellar clouds, dust particles undoubtedly perform at least two crucial functions. First, they provide a catalyst on which H atoms can combine to form molecular H_2. The gas density is far too low for this to occur by the three-body mechanism, $H + H + H_2 \rightarrow H_2 + H_2$, familiar to laboratory gas kineticists. Second, the dust grains shield molecules that are formed in ISCs from the dissociation and ionization effects of short-wavelength stellar radiation.

The clouds in which most molecules are found are "dark" as well as "dense". The particles, whose number density is thought to be about 1 m^{-3}, may perform other roles in the chemistry of ISCs. It is possible, but as yet unproven, that they might catalyze chemical reactions other than the combination of H atoms, with the products released from the ultracold surface as a result of the heat released in the reaction. In addition, the relative and absolute rates of condensation onto, and evaporation from, dust grains may influence the relative and absolute abundances of gas-phase species in different regions of ISCs.[11]

The extremely low temperatures found in dark, dense ISCs pose two questions. First, are the molecules that are observed there actually formed in these ISCs? Second, if they are, what chemical reactions can occur under these extreme conditions and hence contribute to the overall chemistry?

Other mechanisms that might explain the presence of molecules include the possibilities that: a) the molecules are the products of chemistry that occurs elsewhere (for example, in warmer regions of the ISM) and then accumulate in the ISCs, and b) the observed molecules are produced in the breakdown of particles formed in higher-temperature regions. The former hypothesis is rejected on the basis that any molecules formed outside the clouds would be subjected to harsh interstellar radiation and would therefore not survive journeys across vast regions of space. Evidence against the latter possibility, besides the lack of a suitable mechanism for fragmentation, is the predominance of small molecules amongst those that have been identified in dense ISCs.

Therefore, it appears that, despite their very low temperatures, dark, dense ISCs support a rich chemistry in situ. The knowledge that many ion–molecule reactions proceed rapidly, with rate constants that either show no temperature dependence or accelerate as the temperature is lowered, led to the first generation of chemical models strongly emphasizing ion–molecule reactions.[12] Although it is generally accepted that the first steps to the formation of many molecules involve the ionization of H_2 by cosmic rays and the subsequent reaction of H_2^+ with H_2 to yield H_3^+, on the basis of the experiments reviewed herein, it is also now generally accepted that many neutral–neutral reactions should be included in chemical models of ISCs.

3. The CRESU Method for Studying Neutral–Neutral Reactions at Ultralow Temperatures

3.1. Attaining Very Low Temperatures

The uniqueness of experiments performed in a CRESU apparatus lies in the ability to establish very low temperatures, without significant condensation or even clustering of the molecular species included in the gas. The crucial process

 © 2006 Wiley-VCH Verlag GmbH & Co. KGaA, Weinheim

is the isentropic expansion of gas from a gas reservoir through a carefully designed, convergent–divergent Laval nozzle into a large chamber. This process provides a jet of gas moving at supersonic speed. The density of gas in the jet is quite high (typically 10^{16}–2×10^{17} cm^{-3}), so collisions are frequent and maintain thermal equilibrium; that is, there is a defined gas temperature, which is, of course, related to the distribution of relative speeds in the molecular collisions that occur in the gas. The gas in the jet remains uniform in density and temperature for several decimeters; a typical flow velocity of Mach 5, corresponds to a time of at least 150 μs but rarely greater than 1 ms.

The conditions in the gas jet produced in a CRESU apparatus are determined principally by the design of the Laval nozzle. Each nozzle provides a particular combination of temperature and molecular density for the carrier gas being used. Consequently, one needs a number of nozzles to cover a range of temperatures. The nozzles are mounted on the front of the gas reservoir in such a way that they are relatively easy to remove when one wishes to carry out kinetic measurements at a new temperature. Experiments can be performed with N_2 or Ar as the carrier gas; however, at the lowest temperatures, helium must be employed to prevent the formation of complexes, either between pairs of atoms of the carrier gas or between an atom of the carrier gas and any molecular gas added to the flow to make the kinetic measurements. Figure 3 shows how a CRESU apparatus is configured for experiments on the kinetics of reactions of $C(^3P)$ atoms.[13]

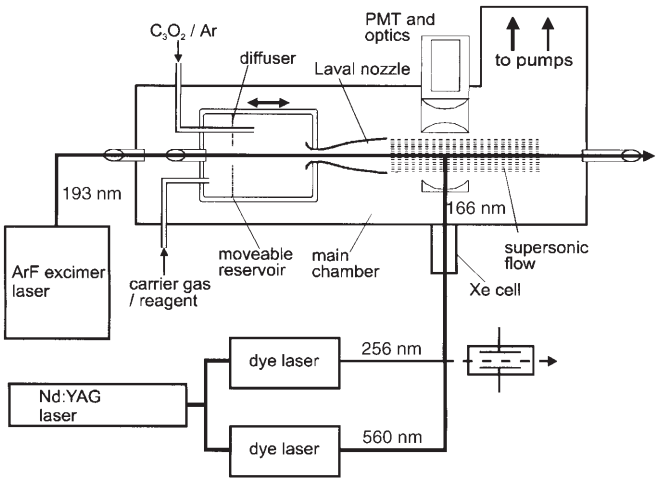

Figure 3. Plan of a CRESU apparatus configured to measure rate constants for reactions of $C(^3P)$ atoms. PMT = photomultiplier tube. The atoms were created by photolysis of C_3O_2 at 193 nm and observed by LIF in the vacuum ultraviolet (VUV). Tunable radiation at about 166 nm was generated in a four-wave-mixing process in Xe by using dye laser radiation at 256 nm and tunable dye laser radiation at about 560 nm. (Reproduced, with permission, from reference [64].)

The pressure in the gas reservoir, upstream of the Laval nozzle and where any molecular gases are mixed with the carrier gas, is usually a few tens of mbar. The reservoir is normally maintained at room temperature, but it can be cooled in liquid N_2 if temperatures below 10 K are required in the jet.[2,4] Of course, such cooling is only possible in those cases in which the vapor pressure at 77 K of any molecular gas present in the gas mixture is higher than the partial pressure of that gas in the reservoir. The reservoir can also be heated if species are being used which have low vapor pressures at room temperature.[14] Expansion through the Laval nozzle then provides cooling, albeit not, of course, to temperatures as low as those attained when the reservoir is at ambient temperature or below.

At their "throats" or narrowest points, the diameters of the Laval nozzles used in a CRESU apparatus vary between 3 mm, to generate a temperature in a He flow of 15 K, to 50 mm, in a nozzle that produces only moderate cooling and a temperature of 149 K, again using He as the carrier. These nozzles do not serve as severe constraints on the gas flow, so the continuous volume flow through the chamber is considerable (of the order of 3×10^4 m^3h^{-1}), and a rather massive pumping system is required to cope with it.

3.2. Measuring Rate Constants

In the original experiments of Rowe and co-workers on ion–molecule reactions,[1,2] the CRESU apparatus was used, in effect, as a wall-less flow tube. That is, changes in the concentration of ions formed in an early part of the flow were measured downstream as the concentration of a molecular reagent was changed. The distance between the points at which ions were formed and observed was kept constant and could be converted into a "reaction time" from a knowledge of the flow velocity in the jet. Mass spectrometric techniques allowed the observation of both product and reagent ions.

By contrast, nearly all measurements on neutral–neutral reactions have employed a time-resolved mode, in which atomic or molecular radicals are generated by pulsed laser photolysis (PLP) of a suitable precursor and the decay in their subsequent concentration is monitored by a suitable spectroscopic technique, usually laser-induced fluorescence (LIF), as shown in Figure 3. To create an even concentration of radicals along the longitudinal axis of the flow, the photolysis laser is invariably directed along this axis of the gas jet, whereas the "probe" laser may be directed either along the same axis or perpendicular to it. Where LIF is used, the probe laser, like the photolysis laser, is pulsed, but, in contrast to the photolysis laser, the probe laser must be tunable so that its frequency can be adjusted to promote the free radical to an excited, fluorescing state. Table 2 summarizes the photochemical sources of the atoms and radicals for which kinetic studies in CRESU experiments have been carried out, along with the LIF transitions or other methods used in their observation.

Information about how the relative concentration of the radical species varies with time in a particular experiment is obtained by recording the intensity of the LIF signal as the time delay between the pulses from the photolysis and probe lasers is varied systematically. An example of such a result is shown in Figure 4a. As the concentration of atomic or molecular radicals is always very much less than that of the co-reagent, the kinetics of decay are pseudo-first-order and the decaying LIF signals are fitted to an exponential to yield a

© 2006 Wiley-VCH Verlag GmbH & Co. KGaA, Weinheim

Table 2: Formation and observation of free radicals in CRESU experiments.

Radical	Method of formation	Method of observation
$CN(^2\Sigma^+)$	a) PLP of NCNO at 583 nm; b) PLP of ICN at 266 nm	LIF excited in the (0,0) band of the ($B^2\Sigma^+$-$X^2\Sigma^+$) system at 388 nm
$OH(^2\Pi)$	PLP of H_2O_2 at 266 nm	LIF excited in the (0,0) band of the ($A^2\Sigma^+$-$X^2\Pi$) system at 308 nm
C_2H	PLP of C_2H_2 at 193 nm	time-resolved chemiluminescence from $CH(A^2\Delta)$ formed in the $C_2H + O_2$ reaction
CH	multiphoton PLP of $CHBr_3$ at 266 nm	LIF excited in the (0,0) band of the ($A^2\Delta$-$X^2\Pi$) system at 430 nm
$C(^3P_J)$	PLP of C_3O_2 at 193 nm	a) time-resolved chemiluminescence from $NO(B^2\Pi)$ formed in the $C(^3P) + NO_2$ reaction; b) LIF on the $^3P_1$–$^3P_0$ line at 165.69 nm
$Al(^2P_J)$	multiphoton PLP of $Al(CH_3)_3$ at 266 nm	LIF on the $^2S_{1/2}$–^2P_J lines at 394.40 and 396.15 nm
$Si(^3P_J)$	multiphoton PLP of $Si(CH_3)_4$ at 266 nm	LIF on the $^3P_1$–$^3P_0$ line at 251.43 nm
$B(^2P_J)$	PLP of $B(CH_3O)_3$ at 266 nm	LIF on the $^2S_{1/2}$–^2P_J lines at 249.7 nm

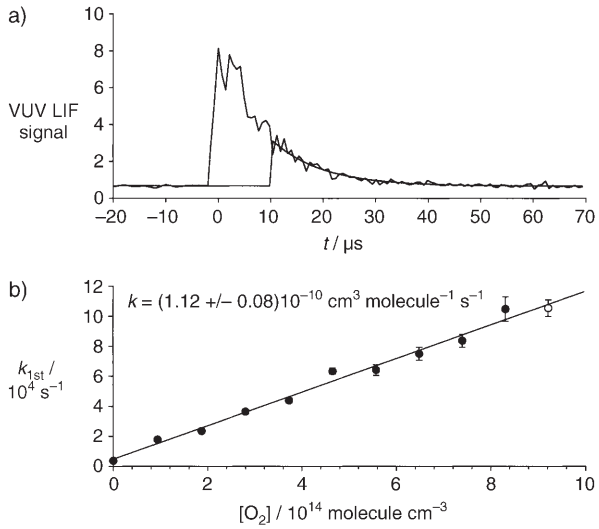

Figure 4. Kinetic data on the reaction of $C(^3P_J)$ atoms with O_2 at 15 K. a) Decay in the VUV LIF signal from $C(^3P)$ atoms in the presence of 9.2×10^{14} molecules cm^{-3} of O_2. The signal decay is fitted to an exponential curve after a 10-μs delay to allow relaxation among the spin-orbit levels of the ^3P_J state. b) Variation of the first-order constants obtained at 15 K from experiments with the concentration of O_2 like that in a). The open point shows the value derived from the decay shown in a). The slope of the line yields the second-order rate constant for $C(^3P_J) + O_2$ at 15 K. (Reproduced, with permission, from reference [64].)

first-order constant (k_{1st}). The second-order rate constant (k_{2nd}) for the reaction is then found by measuring how k_{1st} varies as the concentration of co-reagent, [Reag], is varied in a series of experiments (Figure 4b).

It should be noted that the exponential fit in Figure 4a is only started after 10 μs have elapsed from the creation of the $C(^3P_J)$ atoms. This allows the non-Boltzmann distribution over the spin-orbit states of the $C(^3P_J)$ atoms that are produced in the photolysis of C_3O_2 time to relax through collisions with the carrier gas. In general, the photolytic process used to create the atomic or molecular radicals will not produce them in thermal equilibrium with the surrounding gas in the supersonic flow. Excess translational energy will be accommodated rapidly by collisions. However, atoms such as $C(^3P_J)$ or molecules such as $OH(^2\Pi_\Omega)$ with L or $\Lambda > 0$ will usually be created with a non-Boltzmann distribution over spin-orbit levels. In general, such distributions and how they evolve with time can be observed spectroscopically by recording an LIF spectrum as the frequency of the probe laser is scanned. One can thus assess what time must be allowed for the initial distribution to relax to the Boltzmann distribution at the temperature of the experiment.

An example of this procedure for $C(^3P_J)$ atoms formed by photolysis of C_3O_2 is shown in Figure 5. The spectrum taken with a 0.1-μs delay shows that the atoms are initially distributed over the three spin-orbit levels, $J = 0$, 1, and 2, roughly according to their statistical degeneracies, but after a 10-μs delay a Boltzmann distribution over the J levels for 15 K has been established. A similar situation with respect to rotational distributions arises in molecular radicals formed by photodissociation. The need to allow rotational relaxation is exemplified by the LIF spectra of $OH(^2\Pi)$ recorded at different delays following the photodissociation of H_2O_2.[15]

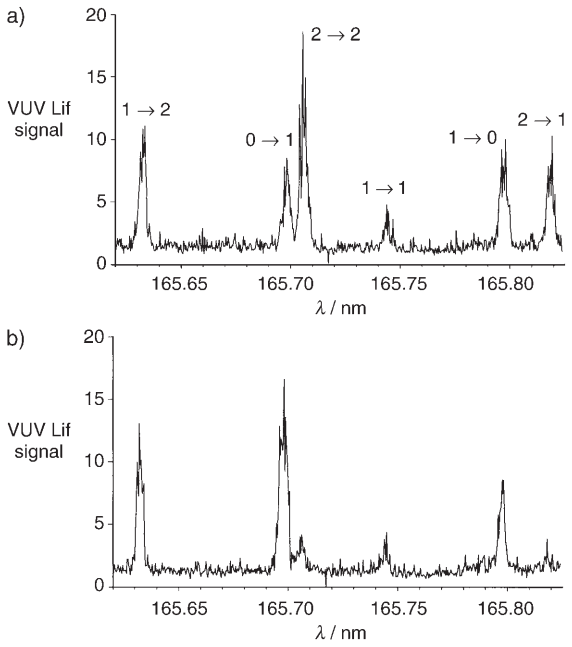

Figure 5. LIF spectra of atomic carbon, $C(^3P_J)$, recorded in a CRESU flow at 15 K in helium but with different delays between a) $\Delta t = 0.1$ μs and b) $\Delta t = 10$ μs. In a), the lines are assigned according to the values of J in the lower and upper levels. (Reproduced, with permission, from reference [64].)

 © 2006 Wiley-VCH Verlag GmbH & Co. KGaA, Weinheim

In general, spin-orbit and rotational relaxation occurs readily in collisions of the radicals with atoms or molecules of the carrier gas. Consequently, it is possible to decouple the rates of relaxation and reaction. On the other hand, vibrational relaxation of simple species by nonreactive collision partners is generally rather slow. In practice, the photodissociation processes used to prepare CN and OH radicals (see Table 2) produce only very small fractions of the radicals in vibrational levels $v > 0$. However, in the case of $CH(^2\Pi)$ formed from the sequential multiphoton dissociation of $CHBr_3$, vibrational levels above $v = 0$ are significantly populated. Independent kinetic measurements of $CH(^2\Pi, v{=}0)$ and $CH(^2\Pi, v{=}1)$ were made and provided useful information about the relaxation of vibrationally excited CH radicals in collisions with species such as H_2[16] CO[17] and N_2,[17] for which both relaxation and association proceed through the initial formation of a strongly bound complex.[18]

Because the sample of radicals produced along the core of the flow is moving rapidly, the reaction under investigation must perturb the radical concentration in the time (150 μs–1 ms) that it takes the gas to flow from the exit of the Laval nozzle to the point from which LIF is observed. Furthermore, as there are limits to how much co-reagent can be added to the flow, without either destroying the integrity of the flow or causing dimers to form, only second-order rate constants that exceed $\approx 10^{-12}$ cm^3 molecule^{-1} s^{-1} can be measured by using the CRESU technique.

3.3. Strengths and Limitations of the CRESU Method

Although a few efforts have been made to employ free jets as a medium for kinetic measurements,[19] at the present time it can be said that the CRESU experiment provides essentially the only method for obtaining temperatures much lower than 100 K and down to about 10 K in a manner that then allows one to measure the rates of molecular processes in gases involving electrically neutral species. The frequency of collisions with the carrier gas means that it provides a thermally equilibrated sample. The temperature can be calculated from the design of the Laval nozzle and the conditions under which it is operated, and this temperature can be checked by recording spectra, for example, of CN[3] OH[15] and NO,[4] and estimating the temperature from the relative intensities of rotational lines within a particular vibrational band, either one within an electronic band system[3,15] or an overtone band within the electronic ground state.[4]

The rapid expansion of gas and the fact that molecules in the jet do not collide with any surfaces makes it possible to maintain a high level of supersaturation, especially with respect to the co-reagent. Nevertheless, one must guard against the formation of dimers and higher oligomers. In general, this only becomes a problem at the lowest temperatures and the highest reagent concentrations. It can frequently be identified by nonlinearity in the plot of k_{1st} versus [Reag].[3]

Nevertheless, the CRESU method does have its limitations and it is important to be aware of them. One that the method shares with most direct kinetic experiments is that, in experiments on neutral–neutral reactions, changes in concentration are observed in only one species—the radical reagent. Consequently, no information is obtained directly about the products of the reaction. In some cases, these can be inferred reliably. However, in others, more than one set of products might be allowed thermochemically. A problem is that there is not really any universal way of determining branching ratios. Nevertheless, some methods being applied in experiments at higher temperatures should be transferable to the CRESU environment. One such technique would involve the observation of H atom products by VUV-LIF.[20] A second, more-general method could be the determination of product branching ratios by the absorption of tunable IR diode laser radiation.[21]

A second difficulty arises because of the huge continuous gas flows in a CRESU experiment. Of course, most of the gas flow is provided by the inert (and relatively inexpensive) carrier gas. Nevertheless, the flows of co-reagent gas are substantial and inhibit the use of, for example, deuterated species or other species that need special synthesis. The use of pulsed Laval nozzles has been pioneered by Smith and coworkers,[22]and the method has been adopted in a number of other laboratories.[23] Apparatuses incorporating pulsed Laval nozzles have time-averaged flows that are lower by factors of 10–100 than those employed in continuous-flow CRESU experiments. However, as yet, pulsed Laval nozzle experiments have not accessed the very low temperatures that have been reached in CRESU experiments, the lowest temperature reported being 58 K.[23d]

4. Rate Constants for Neutral–Neutral Reactions and their Temperature Dependence

Rate constants for about 50 neutral–neutral reactions have now been measured at temperatures as low as 13 K by one or other of the two continuous-flow CRESU apparatuses in existence. Table 3 displays the lowest temperatures at which these rate constants were measured in CRESU apparatuses. In considering these results, it is important to recall (see Section 3) that it is impossible to measure rate constants with values less than 10^{-12} cm^3 molecule^{-1} s^{-1} by using the CRESU method, unless the co-reagent is also the carrier gas, as in the case of CH radicals reacting with N_2.[17b] Therefore, an entry in Table 3 implies that the reaction to which the entry refers proceeds rapidly at very low temperatures. In general, the measurement of rate constants at temperatures even lower than those recorded is restricted by the tendency of the co-reagent to form dimers in the cold environment of the supersonic jet. Table 3 is color-coded to indicate the magnitude of the rate constant for individual metatheses[*] at 298 K. For all of these reactions, the rate constant exceeds 10^{-11} cm^3 molecule^{-1} s^{-1} at 298 K.

[*] The term metatheses is used for bimolecular reactions that yield two product species, distinct from association reactions in which two reagents combine to yield a single molecular product.

© 2006 Wiley-VCH Verlag GmbH & Co. KGaA, Weinheim

Table 3: Lowest temperatures at which rate constants have been measured.[a]

Radical → Co-reagent ↓	CN($X^2\Sigma^+$)	OH($X^2\Pi$)	C_2H($X^2\Sigma^+$)	CH($^2\Pi$) $\nu=1$	CH($^2\Pi$) $\nu=0$	C(^3P)[b] (b)	C(^3P)[b] (a)	Al(^2P)	Si(^3P)	B(^2P)
CH_4					23					
C_2H_6	25				23					
NH_3	25				23					
H_2				23	53					
D_2					23					
HBr		23								
N_2				23	53					
CO				23	53					
C_2H_2	25		15		23	15	15		15	23
C_2H_4	25		15		23	15	15		15	23
C_3H_6			15			15				
$CH_3C{\equiv}CH$	15		27			15				
$CH_2{=}C{=}CH_2$	15		27				15			
butenes		23			23					
benzene					25					
anthracene		58								
O(^3P)		38								
NO		23			13	15			15	
NO_2		53								
O_2	13		15		13	15	15	23	15	23

[a] **Violet print** indicates reactions that have rate constants $\geq 10^{-10}$ cm^3 molecule^{-1} s^{-1} at 298 K; **light blue print** indicates reactions that have rate constants between 10^{-10} and 5×10^{-11} cm^3 molecule^{-1} s^{-1} at 298 K; **dark blue print** indicates reactions that have rate constants between 5×10^{-11} and 1×10^{-11} cm^3 molecule^{-1} s^{-1} at 298 K; **orange print** indicates reactions that proceed by pressure-dependent association; **red print** indicates reactions that probably proceed by association in the high-pressure limit. [b] carbon atoms observed by: a) time-resolved chemiluminescence from NO($B^2\Pi$) formed in the C(^3P) + NO_2 reaction; b) LIF on the $^3P_1$–$^3P_0$ line at 165.69 nm.

The order in which the co-reagents are listed in the first column of Table 3 reflects their chemical nature. Thus, the first six molecules, from CH_4 to HBr, are saturated; that is, they only contain single chemical bonds, and no unpaired electrons. The next group, from N_2 to anthracene, are unsaturated; that is, they are aromatic or contain at least one double or triple bond, but no unpaired electrons. Finally, the last four species are radicals as they contain one or more unpaired electrons.

Some species from all three classes undergo fast reactions with neutral radicals at low temperatures and, therefore, in all these cases the reaction must proceed over a potential-energy surface with no barrier. This is to be expected for reactions between two free radicals, such as CN and O_2, but not when one of the species is a saturated molecule, as in the reaction of CN with C_2H_6. In most cases, it seems likely that there is initial formation of an energized adduct, which corresponds to a significant potential-energy minimum on the potential-energy surface, and that this adduct then decomposes by one or more exothermic pathways to yield two products. One example is that shown in Equation (1).

$$CN + C_2H_2 \rightarrow (C_2H_2CN)^* \rightarrow C_2HCN + H \quad (1)$$

In general, the second-order rate constants (k_{2nd}) for the reactions in Table 3 increase as the temperature is lowered from room temperature to the lowest temperature at which measurements can be made. However, the form and magnitude of the change varies quite widely. Figure 6 shows four examples of how rate constants vary with temperature. Although these examples are all reactions of the CN radical, they illustrate the wide range of behavior that has been found. In some cases, $\ln k_{2nd}$ varies linearly with $\ln T$ over quite a wide range of temperature, indicating that k_{2nd} varies as T^{-n} where $n > 0$.

For a limited number of reactions, indicated by orange shading in Table 3, the adduct formed by association of the reagents may have no exothermic dissociation pathway. The reaction can then proceed by collisional stabilization of the adduct and the rate of reaction will be pressure-dependent, unless the kinetics are in the high-pressure limit.[*]. Examples of such reactions that have been studied in CRESU experiments include those of CH radicals with H_2,[16] N_2,[17] and CO,[17] and those of OH radicals with NO,[24] and NO_2[25] For most of these association reactions, the pressure dependence of the second-order rate constant has been studied in CRESU experiments and five nozzles were constructed to yield a temperature of 53 ± 1 K with densities of the carrier gas (Ar) in the gas jet ranging from 5.15×10^{16} to 8.21×10^{17} molecules cm^{-3}. Results for the Equations (2) and (3) are shown in Figure 7. The rate constants for

$$CH + N_2\,(+M) \rightarrow HCN_2\,(+M);\ \Delta H^\circ_{298} = -97\ \text{kJ mol}^{-1} \quad (2)$$

$$CH + CO\,(+M) \rightarrow HCCO\,(+M);\ \Delta H^\circ_{298} = -306\ \text{kJ mol}^{-1} \quad (3)$$

[Eq. (2)] are lower than those for [Eq. (3)] on account of its lower exothermicity and are in the low-pressure limit, where the second-order rate constants are directly proportional to the total gas density. The rate constants for [Eq. (3)] are higher and show evidence of "fall-off" behavior.[29] The reactions between OH radicals and butenes[15] and OH and anthracene,[14] and probably those between CH and butenes and CH and benzene (red in Table 3) are presumed to occur by association: but now the adducts are sufficiently large that the kinetics are in the high-pressure limit, even at the relatively low pressures found in a CRESU expansion.

[*] Some aspects of association reactions are considered in Section 5.4. Further discussion can be found in reference [29]. In the high-pressure limit, the rate of stabilizing collisions is so rapid that the initial formation of the energized adduct becomes rate-determining and the rate of association is independent of the total pressure. In the low-pressure limit, only a small fraction of the energized adducts are collisionally stabilized, and the rate of association is proportional to the total pressure. The 'fall-off' regime covers the range of pressure between these two limits.

 © 2006 Wiley-VCH Verlag GmbH & Co. KGaA, Weinheim

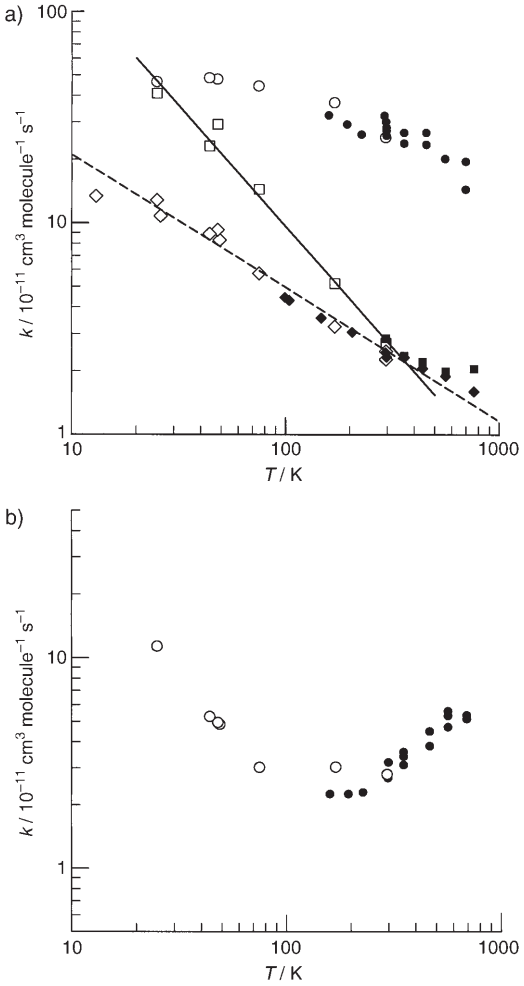

Figure 6. a) Rate constants for the reactions of CN radicals with C_2H_2 (○, ●), O_2 (◇, ◆), and NH_3 (□, ■). The lines show fits to the rate constants of the form $k = A\,(T/298)^{-n}$. For CN + O_2 between 13 K and 761 K, $n = 0.63 \pm 0.04$; for CN + NH_3 between 25 K and 298 K, $n = 1.14 \pm 0.15$. (Data from: references [3b, 26, 65]) b) Rate constants for the reactions of CN radicals with C_2H_6. Open symbols represent results obtained in a CRESU apparatus, closed symbols those obtained in conventional heated or cooled cells. (Data from: references [26, 65c].)

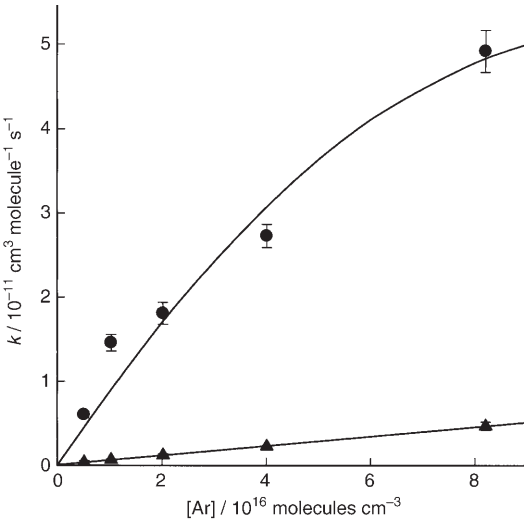

Figure 7. Experimental second-order rate constants for the association reaction of CH with N_2 (▲) and CO (●) at 53 K, plotted as a function of the argon buffer-gas density. (Adapted from Figure 1 in reference [17c].

In Table 3, violet print indicates those reactions that have particularly large rate constants ($k \geq 10^{-10}$ cm^3 molecule^{-1} s^{-1}) even at 298 K. Almost all the reactions of radicals with unsaturated molecules (i.e., alkenes and alkynes) that have been studied in CRESU experiments fall into this category and probably proceed by addition of the radical followed by elimination of an H atom. In a number of instances, as exemplified by the data for [Eq. (1)] plotted in Figure 6a,[26] the rate constants rise to some high and limiting value as the temperature is lowered, but then remain constant (or even fall slightly) as the temperature is lowered still further. In all these cases, the limiting value is close to the rate constant (here termed Z^o) that one would estimate on the simplistic basis of capture by a long-range potential arising from dispersion forces (see Section 5).

Figure 6a shows rate constants for the reactions between a) CN radicals and O_2, and b) CN and NH_3, which vary as T^{-n} with $n = 0.63$ and 1.14, respectively.[3] The rate of the reaction CN + NH_3 shows the strongest negative dependence on temperature of any neutral–neutral metathesis yet studied by the CRESU technique. For a number of other reactions, such as that between C(^{3}P) atoms and C_2H_2[27] the decrease in k_{2nd} as the temperature is lowered may be fitted to a power law expression, but with a much smaller value of n than those found for CN + O_2 and CN + NH_3. In some of these cases, experiments with crossed molecular beams showed that this form of T dependence of the thermal rate constants is consistent with a reaction cross-section that varies as $(E_{trans})^{-(n+1/2)}$.[13b,c]

Figure 6b shows perhaps the most puzzling data that have been obtained in any CRESU experiment on neutral–neutral reactions. For CN + C_2H_6, the rate constant has a minimum value at about room temperature but increases to both higher and lower temperatures.[26] Given the high value of the rate constant at low temperatures, it seems that there can be no barrier on the potential-energy surface for this reaction between a free radical and an alkane, but unfortunately there have been no ab initio calculations of the potential-energy surface or minimum-energy path for this reaction. Further discussion is postponed to Section 5.2.2.

Most of the radicals identified in Table 3 exhibit spin-orbit splitting of their electronic ground state, as the total electronic spin (S) and the electronic angular momentum (L or Λ) are both greater than zero. Furthermore, the spin-orbit splitting is of the order of, or less than, k_BT at room temperature. A consequence is that the relative equilibrium populations in different spin-orbit levels may change markedly over the temperature ranges covered in CRESU experiments and one might ask whether this change is reflected in the temperature dependence of the rate constants.

A case illustrating this point is provided by the reactions of C(^3P_J) atoms.[13,27] The $^3P_2$ and $^3P_1$ levels are 43.4 and 16.4 cm^{-1} above the $^3P_0$ ground term, respectively—equiv-

 © 2006 Wiley-VCH Verlag GmbH & Co. KGaA, Weinheim

alent to ε/k_B values of 62.4 and 23.6 K. At room temperature, the Boltzmann distribution over different J levels is dominated by the respective statistical degeneracies: the relative populations are: $^3P_2/^3P_1/^3P_0$ 4.04:2.77:1.00. However, at 15 K, the lowest temperature at which CRESU experiments have been carried out on reactions of $C(^3P_J)$ atoms, the relative populations are $^3P_2/^3P_1/^3P_0$ 0.08:0.62:1.00. The high values of the rate constants for the reactions of $C(^3P_J)$ atoms with alkenes and alkynes and their very slight dependence on temperature provide strong empirical evidence that a reaction can occur with equal facility from all the spin-orbit levels of the $C(^3P_J)$ atom.

In the reactions of radicals with singlet ($S=0$) molecules, such as $C(^3P_J)$ atoms with alkenes and alkynes,[27] any potential-energy surfaces that correlate with the separated reagents have the same spin multiplicity as the radical. For example, in the case of $C(^3P_J) + C_2H_2$ there will be three triplet surfaces ($2\,^3A' + {}^3A''$). However, if the electronic state of the co-reagent has a nonzero value of the spin quantum number, then potential-energy surfaces of different spin multiplicity arise. This situation is exemplified by the interaction of the atomic and molecular radicals listed in Table 3 with the radicals $O(^3P)$, $NO(X^2\Pi_J)$, $NO_2(X^2A_1)$, and $O_2(X^3\Sigma_g^-)$.

For example, in the case of $CN(^2\Sigma^+) + O_2(^3\Sigma_g^-)$, in which there are no complications introduced by spin-orbit effects, one doublet $^2A'$ surface and one $^4A'$ quartet surface arise. A reaction will only occur at the lower doublet surface, which arises when one electron from O_2 and the unpaired electron from CN "pair up", but only a third of the CN + O_2 collisions will occur on this surface. In general, radical–radical reactions will only occur on the surface or surfaces that correlate with the reagents and which have the lowest spin multiplicity consistent with the adiabatic correlation rules.[29] Consequently, the values of their rate constants at low temperatures are likely to be lower than those for reactions between radicals and unsaturated molecules.

Finally, and in preparation for a more detailed discussion, in Section 5, of efforts to understand what factors control the rates of rapid low-temperature reactions, it is notable that the distribution of reagent molecules over rotational levels, like those over spin-orbit levels, will change considerably over the temperature range covered in CRESU experiments. If the rate of any reaction is dependent on the initial rotational levels of the reagents, then this will be reflected in the variation of the thermal rate constant with temperature.

5. Understanding and Predicting the Rate Constants for Fast Reactions at Ultralow Temperatures

The observation of second-order rate constants that, at ultra-low temperatures, approach the "collision-determined limit" (i.e. Z^o as defined in Section 4) is clear evidence that such reactions proceed over potential-energy surfaces with no significant barrier on the minimum electronic energy path leading from reagents to products. In such cases, it is likely that the rate constant, or more fundamentally the cross-section, for the reaction will be determined by the ability of the attractive potential between the reagents to bring them into close contact. Efforts to model reactions on this basis frequently refer to "capture". Capture theories[28] usually suppose that the important part of the intermolecular potential is sufficiently "long-range" that it can be expressed as the sum of various electrostatic terms: for example, ion-induced dipole, ion–dipole, dipole–dipole, dispersion, etc. However, and especially in reactions between neutral species, this is clearly not the case and we examine this assumption in the first part of this section.

5.1. Two-Body Capture

It is useful to begin by considering a two-body system, A + B, in which the attractive, long-range part of the intermolecular potential (V) can be expressed simply in terms of one or more terms of the type CR_{AB}^{-n} (n is an integer and R_{AB} is the separation between the centers of the particles A and B). The cases of $n=4$ and $n=6$ correspond to the attractions resulting from ion-induced dipole and dispersion forces, respectively.

Because of the need to preserve orbital angular momentum in a two-body collision, the dynamics of collisions between A and B at a particular collision energy (ε_{tr}) and impact parameter (b) are best discussed in terms of an effective potential [Eq. (4)].[29] Differentiating $V_{eff}(R_{AB})$ with

$$V_{eff}(R_{AB}) = \varepsilon_{tr}\, b^2/R_{AB}{}^2 - C\, R_{AB}{}^{-n} \tag{4}$$

respect to R_{AB} and setting the result equal to zero allows one to determine the value of R_{AB} at which there is a maximum in the effective potential-energy curve and the height of this centrifugal barrier [Eq. (5a, b)].

$$R_{AB,max} = \left(\frac{n\,C}{2\varepsilon_{tr}\,b^2}\right)^{1/(n-2)} \tag{5a}$$

$$V_{eff}(R_{AB,max}) = \varepsilon_{tr}\, b^2 \left(\frac{2\,\varepsilon_{tr}\,b^2}{n\,C}\right)^{2/(n-2)} (1-2/n) \tag{5b}$$

By equating ε_{tr} to $V_{eff}(R_{AB,max})$, [Eq. (6)] shows, for a given collision energy, the maximum value of b at which capture,

$$b_{max} = \left(\frac{n\,C}{2\varepsilon_{tr}}\right)^{1/n} \left(\frac{n}{n-2}\right)^{(n-2)/2n} \tag{6}$$

and therefore "core" collisions, can occur. Consequently, the cross-section for capture can be written as [Eq. (7)] Integra-

$$S_{capture} = \pi\, b_{max}{}^2 = \pi \left(\frac{n\,C}{2\varepsilon_{tr}}\right)^{2/n} \left(\frac{n}{n-2}\right)^{(n-2)/n} \tag{7}$$

tion of this expression over a thermal distribution of collision energies then yields an expression for the rate constant according to this highly simplified model. This simple treatment forms the basis of more-sophisticated capture theories[28] in which the potential is no longer assumed to depend solely on the separation of the two species.

 © 2006 Wiley-VCH Verlag GmbH & Co. KGaA, Weinheim

The treatment that has just been outlined for two-body capture is of greatest relevance and value for ion–molecule reactions. When the reagents A and B are, respectively, an ion carrying unit charge e and a polarizable molecule, which does not have a permanent electric dipole moment, but in which a dipole can be induced, then the long-range potential can be expressed as [Eq. (8)] (α and α'

$$V = -(^1/_2\alpha e^2)R_{AB}{}^{-4} \text{ in cgs units and}$$
$$V = -\{^1/_2\alpha' e^2/(4\pi\varepsilon_0)^2\}\ R_{AB}{}^{-4} \text{ in SI units} \quad (8)$$

represent the polarizability of the neutral molecule in cgs and SI units, respectively, and $(4\pi\varepsilon_0)$ allows for the permittivity of a vacuum).

Substitution of $n=4$ in Equation (7) yields [Eq. (9)], an

$$S_{capture} = \pi\left(\frac{2\alpha e^2}{\varepsilon_{tr}}\right)^{1/2} \text{ in cgs units, and}$$
$$S_{capture} = \pi\left(\frac{2\alpha' e^2}{(4\pi\varepsilon_0)^2\varepsilon_{tr}}\right)^{1/2} \text{ in SI units} \quad (9)$$

expression for the capture cross-section. After integration over a thermal distribution of collision energies, one obtains extraordinarily simple, and temperature-independent, expressions for the rate constants for reactions between species with collision mass μ [Eq. (10)]. This model, normally

$$k(T)_{capture} = \left(\frac{4\pi^2\alpha e^2}{\mu}\right)^{1/2} \text{ in cgs units, and}$$
$$k(T)_{capture} = \left(\frac{4\pi^2\alpha' e^2}{(4\pi\varepsilon_0)^2\mu}\right)^{1/2} \text{ in SI units} \quad (10)$$

referred to as the Langevin model,[30] rests on two main assumptions: 1) the only important part of the intermolecular potential is that arising at long-range from the interaction between the charge on the ion and the induced dipole on the molecule; 2) this potential is isotropic, that is, independent of the orientation of the molecule to the line joining the center of the molecule to that of the ion.

For reasonable values of α and μ, it can be shown that the centrifugal maxima do indeed occur at large internuclear separations at which chemical forces are unlikely to be significant. Thus with $\alpha = 2.6$ Å^3 and $\mu = 14$ amu, substitution in [Eq. (10)] yields $k(T)_{capture} = 1.0\times10^{-9}$ cm^3 molecule^{-1} s^{-1}, a value that is, of course, independent of temperature. Other quantities that can be estimated from Equations (4)–(10), are listed in Table 4 for two collision energies, $\varepsilon_{tr} = (30\text{ K})\,k_B$, and $\varepsilon_{tr} = (300\text{ K})\,k_B$.

Even at a collision energy of $300\,k_B$, the separation at which centrifugal maxima appear on the effective potentials are $R_{AB,max} \geq 4.3$ Å. At lower temperatures, these separations are greater still and the description of the intermolecular forces just in terms of the interaction between the charge on the ion and the induced dipole on the molecule would appear to be very reasonable. Chemical forces arising from the sharing of electrons will play little role, and any anisotropy in the intermolecular potential is likely to be small. Consequently, at $R_{AB,max}$, the separation of reagent rotational-energy levels will not be significantly perturbed from those in the isolated molecules, and the rate constants for capture are unlikely to depend significantly on the rotational states of the reagents.

Table 4: Values of quantities derived from two-body treatments of molecular collisions.

1) Properties of potential with $V = -(^1/_2\alpha e^2)R_{AB}{}^{-4}$.[a]

	b_{max} [Å]	$R_{AB,max}$ [Å]		$\{V(R_{AB,max})/k_B\}$/K	
		For $b=b_{max}$	For $b=b_{max}/2^{1/2}$	For $b=b_{max}$	For $b=b_{max}/2^{1/2}$
$\varepsilon_{tr}=(30\text{ K})\,k_B$	10.9	7.7	10.9	−30	−7.5
$\varepsilon_{tr}=(300\text{ K})\,k_B$	6.1	4.3	6.1	−300	−75

2) Properties of potential with $V = -C R_{AB}{}^{-6}$.[b]

	b_{max} [Å]	$R_{AB,max}$ [Å]		$\{V(R_{AB,max})/k_B\}$/K	
		For $b=b_{max}$	For $b=b_{max}/2^{1/2}$	For $b=b_{max}$	For $b=b_{max}/2^{1/2}$
$\varepsilon_{tr}=(30\text{ K})\,k_B$	6.4	4.7	5.6	−27.5	−9.75
$\varepsilon_{tr}=(300\text{ K})\,k_B$	4.4	3.2	3.8	−276	−97.4

[a] The polarizability α of the molecule is 2.6×10^{-24} cm^{-3}, and the charge e on the electron is 3.333×10^{-10} esu. [b] C arises from dispersion forces and is put equal to $^2/_3\ \alpha_1\alpha_2\{I_1 I_2/(I_1 + I_2)\}$ with $\alpha_1=\alpha_2=2.6\times10^{-24}$ cm^{-3} and $I_1=I_2=6$ eV.

The Langevin model makes two important predictions: 1) the formulae for the cross-sections and rate constants contain nothing about the two reagents other than the values of the charge on the ion, the polarizability of the neutral molecule, and the collisional reduced mass; 2) the thermal rate constants for ion–molecule reactions, involving nonpolar molecules, should be independent of temperature. A comparison between experimental data for the reactions between He^+ and N_2 and between N^+ and O_2[31] and the corresponding Langevin predictions are shown in Figure 8. The agreement is

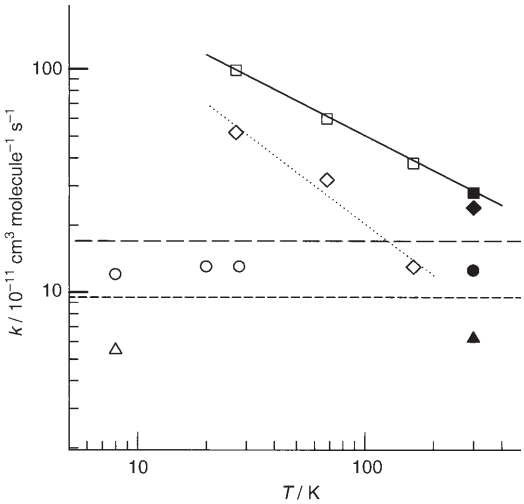

Figure 8. Examples of rate constants for ion–molecule reactions at low temperatures. Experimental data for $He^+ + N_2$ (○, ●) and $N^+ + O_2$ (△, ▲) are compared with estimates of the respective Langevin rate constants: ––– and -----. The rate constants for $N^+ + H_2O$ (□, ■) and $N^+ + NH_3$ (◇, ◆) are fitted to expressions of the form: $k = A\ (T/298)^{-n}$. For $N^+ + H_2O$ between 27 K and 300 K, $n=0.52$; for $N^+ + NH_3$ between 27 K and 163 K, $n=0.77$. Open and closed symbols are consistent with Figure 6. (Data from references [31, 35].)

© 2006 Wiley-VCH Verlag GmbH & Co. KGaA, Weinheim

remarkably good. The Langevin formula may predict too high a rate constant when more than one potential-energy surface correlates with the separated reagents, as some of these surfaces may exhibit barriers to reaction. Consequently, at least in these cases, the simple Langevin treatment should be viewed as providing an upper estimate to the actual rate constant for capture—and hence for reaction.[27b,32]

When the long-range attraction arises from dispersion forces, the long-range potential varies as CR_{AB}^{-6}. Substitution of $n=6$ into Equation (7) yields [Eq. (11)]. Two findings of

$$S_{\text{capture}} = \pi\left(\frac{27\,C}{8\varepsilon_{\text{tr}}}\right)^{1/3} \text{ and}$$
$$k(T)_{\text{capture}} = \pi\left(\frac{8\,k_B\,T}{\pi\mu}\right)^{1/2}\left(\frac{2\,C}{k_B\,T}\right)^{1/3}\Gamma(^2/_3) \qquad (11)$$

this simplistic treatment are worthy of note. First, the model predicts a slight positive dependence of $k(T)_{\text{capture}}$ on temperature: the decrease in the cross-section with ε_{tr} is more than compensated by the increased frequency of collisions at higher temperature. The second finding emerges from the results of calculations that are given in the second part of Table 4. Compared with the results reported for ions plus polarizable molecules, the maxima on the effective potentials occur at significantly smaller internuclear separations. This latter finding suggests that estimates of cross-sections or rate constants for neutral–neutral reactions, which are based merely on a long-range representation of the intermolecular potential, are questionable except, perhaps, at very low collision energies and temperatures.

5.2. Capture in the Presence of Directional Forces

5.2.1. Ion–Molecule Reactions

For most chemical reactions, two-body models are too simplistic, not least because they assume that the intermolecular potential depends only on the separation (R_{AB}) of the two reagents. With the single exception of the reaction between an ion and a nonpolar but polarizable molecule, the intermolecular potential will also depend on one or more coordinates describing the relative orientation of the reagents. Such directional forces may arise through the presence of electric dipole (or higher multipoles) on one or both of the reagents, or when chemical forces are significant.

The simplest case to treat is the reaction between an ion and a polar molecule, and such reactions have been the focus of a number of theoretical treatments.[27b] The long-range electronic potential depends both on R, the separation between the charge (here assumed to be the electronic charge e) and the (point) dipole (μ_D), and θ, the angle that the charge-dipole vector ($\mathbf{R}$) makes with the direction of the dipole ($\boldsymbol{\mu}_D$) [Eq. (12)].

$$V(R) = -(^1/_2\alpha e^2)R^{-4} - e\mu_D\cos\theta R^{-2} \text{ in cgs units and}$$
$$V(R) = -\{^1/_2\alpha' e^2/(4\pi\varepsilon_0)^2\}R^{-4} - \{e\mu_D\cos\theta/(4\pi\varepsilon_0)\}R^{-2} \text{ in SI units} \qquad (12)$$

The rotationally adiabatic capture theory[*] of Clary and co-workers,[27] which is very like the statistical adiabatic capture model (SACM) of Troe and co-workers,[33] and not unlike the long-range microcanonical transition-state theory of Georgievskii and Klippenstein,[34] treats the problem by calculating rotationally specific rate constants—that is, rate constants for capture (assumed to be those for reaction) for reagents in specific rotational levels.

Figure 9 shows the form of rotationally adiabatic potentials for the $C^+ + HCl$ reaction. In all the examples shown,

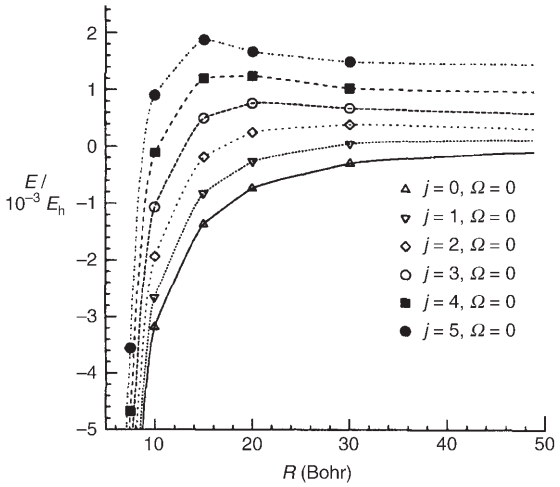

Figure 9. Rotationally adiabatic potential-energy curves for the $C^+ + HCl$ reaction with zero total angular momentum ($J=0$) but different values of the rotational angular momentum (j) in HCl. (Reproduced, with permission, from reference [32].)

the total angular momentum is the same, $J=0$, but the contributions to J from the orbital angular momentum and the rotational angular momentum (j) are different. The maxima in these curves arise from two effects: 1) the centrifugal maximum that limits the capture cross-section in the two-body case, and 2) the increasing separation of rotational levels as R decreases and free rotation becomes restricted rotation (and eventually a bending vibration in the complex that is formed). Clary and co-workers[27b] used quantum mechanics to represent the relative motion of the two reagents. However, this is scarcely necessary, as tunneling effects have been shown to be slight. To a good approximation classical mechanics will provide a satisfactory answer to the problem of finding the maximum value of J for which capture is possible for collisions at a given ε_{tr} and a selected value of j,

[*] The basic idea of the rotationally adiabatic capture theory and the statistical adiabatic channel model is that reaction proceeds adiabatically—–that is, without change of state—–along effective potential-energy curves that incorporate the electronic potential energy, the centrifugal energy, and the energy associated with particular quantum states of the reacting species. When the reagents are far apart, the last term simply corresponds to quantum states (e.g., rotational levels or combinations of rotational levels) of the isolated reagents. As the reagents approach, the energies of these states evolve, as, for example, free rotations become hindered rotations.

 © 2006 Wiley-VCH Verlag GmbH & Co. KGaA, Weinheim

the rotational level of the molecule. As before, the calculated cross-sections for capture must then be integrated over thermal distributions of ε_{tr} in order to find state-selected rate constants (k_j) for capture.

Figure 10 shows the values of k_j for the reaction between the N^+ ion and the strongly polar NH_3 molecule. It can be clearly seen that the values of k_j for all j values from 0 to 3

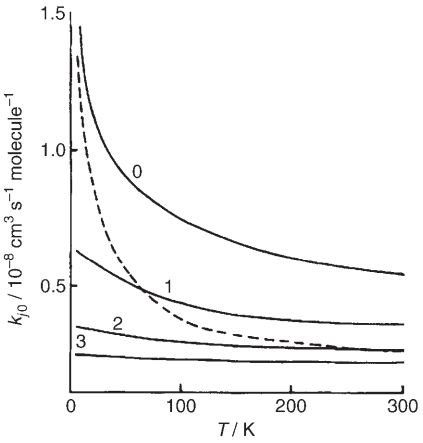

Figure 10. Rotationally selected rate constants k_{j0} for the reaction $N^+ + NH_3$ (j, $k=0$) calculated by using rotationally adiabatic capture theory. -----: Thermally averaged rate constant $k(T)$. (Reproduced, with permission, from reference [66].)

increase as the temperature is lowered. However, both the values of k_j and their rate of increase at lower temperatures are largest for the low j levels. Consequently, the variation of the thermally averaged rate constant, $k(T)$, with temperature is stronger than of any of the individual k_j values. It is also apparent that the rate constants for reactions between ions and polar molecules are appreciably larger than the values predicted by the simple Langevin treatment, especially at the low temperatures of ISCs. Thermal rate constants for the reactions of the N^+ ion with the strongly polar molecules H_2O and NH_3[35] are compared in Figure 8 with those for some reactions of the ions with nonpolar molecules. The effect of the ion–(permanent) dipole forces in enhancing the rate constants at low temperatures is clearly apparent.

It is clear that rate constants for ion–molecule reactions predicted on the basis of "capture" by the long-range electrostatic forces between the charge on the ion and the dipole (induced and permanent) on the molecule are very effective. Where the rate constant for such a reaction at room temperature is of the order of the Langevin value, then its value at lower temperatures can now be predicted with confidence. The only exception to this generalization may arise when the size of the reagents is large, so that the internuclear separations on the simple intermolecular potential are of the same order as the combined size of the reagents.[27b]

5.2.2. *Neutral–neutral Reactions*

Section 4 summarized the kinetic data for neutral–neutral reactions that have been obtained at low temperatures in CRESU experiments and included some discussion of possible effects on the rate constants of the electronic states of the reagents. Further theoretical attempts to explain and predict the values of rate constants for reactions between neutral species that remain rapid at very low temperatures start from two fundamental premises: 1) there must be no barrier along the minimum energy path leading from reagents to products on one (or possibly more) potential-energy surface(s) that correlate with reagents and products, and 2) as with ion–molecule reactions, it is the form of the interactions between reagents at long and medium range that is crucial in determining whether the reagents will come into close contact and hence react. Given this fundamental similarity with fast ion–molecule reactions, it is not surprising that all the methods that have been used to treat ion–molecule reactions have also been applied to neutral–neutral reactions.

However, as already pointed out, there are two crucial differences between neutral–neutral reactions and reactions of ions and neutral molecules. First, the long-range interactions between neutral species, which arise from electric multipole interactions and dispersion forces, are much weaker than those between ions and molecules. Consequently, the maxima on the adiabatic potential curves, which include both centrifugal effects and changes in quantum-state spacing as the reagents approach, occur at smaller reagent separations, at which chemical forces may contribute significantly to the intermolecular potential. Second, there are subtle differences in the potentials for different rapid neutral–neutral reactions.

Despite the reservations just expressed, capture treatments based on the consideration of only the long-range potential, resulting from multipolar interactions and dispersion forces, have met with some success.[13b,36] In general, they have succeeded for reactions that, even at room temperature, have rate constants close to values that would be estimated on a simple collision basis. For such reactions, violet print in Table 3, the rate constant shows only a mild negative temperature dependence and, in some cases, may even pass through a shallow maximum at low temperatures. It seems that the potential arising from the formation of a new chemical bond plays a small role: the range and directionality of such forces are insufficient to influence the probability of capture. It may be significant that such behavior is common when the radical reagent is an atom and strong directional forces are less likely.

Very recently, Georgievskii and Klippenstein[34] carried out a comprehensive comparison between experimental low-temperature rate constants and microcanonical transition-state-theory calculations based on complete, if approximate, representations of the long-range potential. In general, their estimated rate constants are somewhat larger than those found experimentally, though in many cases the difference amounts to less than a factor of 2.

In contrast to the kinetic data discussed so far, the rate constants shown in Figure 6a for the reactions of CN radicals with O_2 and with NH_3 show marked negative dependences on temperature, reminiscent of the temperature dependence of reactions between ions and polar molecules in which there are rather strong directional forces between the reagents. Both reactions were the subject of theoretical studies designed to

 © 2006 Wiley-VCH Verlag GmbH & Co. KGaA, Weinheim

explain the strong negative dependence of the rate constants on temperature.

The influence of the spin correlation rules on the reaction of $CN(X^2\Sigma^+)$ with $O_2(X^3\Sigma_g^-)$ was considered in Section 4, where it was argued that only one third of CN + O_2 collisions occur on the doublet surface and lead to reaction. As a result, any estimate of the rate constant on this surface alone must be lowered by a factor of 3. The $T^{-0.63}$ dependence of the rate constant for this reaction cannot be explained by simple capture theories based only on the long-range potential,[33,37] even when taking into account the dipole–quadrupole interaction, which introduces an element of directionality into the long-range potential. Rather, it seems that in this case the medium-range potential due to strong chemical forces (the NCO_2 transitory intermediate is bound by about 189 kJ mol^{-1})[38] must play a decisive role. The resultant directionality in the potential between the reagents probably explains why the rate constant at 298 K is appreciably lower than that estimated by simple capture theories.[33,37] Moreover, by analogy with reactions between ions and dipolar molecules, the negative dependence of the reaction rate may, at least in part, be due to a rotational-state dependence of the rate constants and the increasing fraction of the two reagents that occupy low rotational states as the temperature is lowered.

The mechanism for the CN + NH_3 reaction is more problematic. Among other reasons, it is not known whether the reaction leads to HCN + NH_2 or H + $NCNH_2$. Despite the presence of strong dipole–dipole forces, estimates of the rate constants by capture methods[39] do not reproduce either the magnitude of the rate constant or its temperature dependence. The lack of agreement between theory and experiment prompted Faure et al.[40] to use a three-atom-model system with quasi-classical trajectories to investigate the effect of introducing a submerged barrier (or "reef") in the intermolecular potential at medium range. The introduction of this submerged barrier at a separation of 2.5 Å between the center of mass of CN and the third species X, and with an energy of 54 meV below the asymptotic energy of CN + X leads to estimated rate constants that decrease with temperature in a manner not dissimilar to that found for CN + NH_3 and CN + O_2. Moreover, the trajectory calculations of Faure et al.[39] revealed that the rate constant strongly depends on the initial rotational state of the CN: the lower j states react faster than the high j states. It should be stressed that these features of the estimated rates are most probably the result of the increasing directionality of the potential-energy surface, when it was modified to introduce the submerged barrier in the entrance valley of the surface. The temperature dependence of the rate constant for the reaction between CN radicals and C_2H_6, which is shown in Figure 6b, is one of the most intriguing results obtained so far with a CRESU apparatus.[25] Indeed, the mild, but positive, T dependence found at room temperature and above suggested that the reaction rates at the low temperatures reached by the CRESU method might be too low to measure. In practice, the rate constant was found to increase as the temperature was lowered below 200 K and to reach its maximum measured value at 25 K—the lowest temperature at which experiments were performed. A possible explanation for this unusual temperature dependence is that, in simplistic terms, the location of the transition state changes as the temperature changes. The form of the lowest adiabatic channels (that is, including centrifugal effects and quantum state energies) may show no maxima, or only slight maxima at rather long range, and flux through these channels could dominate and determine the kinetics at the lowest temperatures. At higher temperatures, flux along higher adiabatic channels will become more important. These channels may exhibit maxima and (at closer range) more-widely spaced maxima, associated with a submerged barrier in the minimum-energy path. Flux along these adiabatic surfaces will be more important at higher temperatures, as the average energies of the reagents increase, and could explain the increase in rate as the temperature is raised above room temperature.

As a final example, Equation (13) is considered briefly. The recent measurements on this reaction in a CRESU

$$O(^3P_J) + OH(X^2\Pi_\Omega) \rightarrow O_2(X^3\Sigma_g^-) + H(^2S) \quad (13)$$

apparatus[41] have broken new ground, since both reagents are unstable radicals and had to be created by pulsed-laser photolysis at 157 nm with an F_2 excimer laser. Measurements were made at 142, 83, 47, and 39 K, using N_2 as the carrier gas to ensure rapid quenching of the $O(^1D)$ atoms created in the photolysis of O_2. These experiments suggest that the rate constant through this temperature range has a value of $(3.5 \pm 1) \times 10^{-11}$ cm^3 molecule^{-1} s^{-1}—although simpler experiments at temperatures as low as 158 K[42] suggest somewhat higher values. From the standpoint of astrochemistry, these measurements all suggest that the reaction between OH and oxygen atoms must be quite rapid within the cold (10–20 K) dense cores of ISCs so that the surprisingly low levels of O_2 in ISCs cannot be ascribed to the slowness of this reaction.[43]

From a theoretical standpoint, the reaction provides an extreme example of the influence of spin-orbit correlations on the rate of a reaction, as $O(^3P_J)$ + $OH(X^2\Pi_\Omega)$ correlate with no fewer than 12 potential-energy surfaces, ($3^2A' + 3^2A'' + 3^4A' + 3^4A''$). However, there is strong theoretical evidence[44] that rapid reaction can only occur across the lowest $^2A'$ surface, which corresponds to the ground electronic state of the HO_2 radical. Consequently, the rate constant for reaction is lowered because only a small proportion of collisions occur on the barrierless surface leading to products.

5.3. Evidence for Effects of Reagent Rotation on Reactivity; Comparison of Excitation Functions and Rate Constants

Direct experimental evidence for the effects of reagent rotational energy/states on fast low-temperature reactions is almost entirely lacking.[45] One reason for this is that the collisional transfer of molecules between different rotational levels is extremely facile (occurs with every collision) making the measurement of rotationally selected reaction rates very difficult. Experimentalists must not only devise a method of preparing molecules in defined rotational levels, they must

 © 2006 Wiley-VCH Verlag GmbH & Co. KGaA, Weinheim

also find a method to distinguish between reactive and inelastic states of the prepared level.

In the case of ion–molecule reactions, the excellent agreement between measured rate constants and those predicted on the basis of rates that depend on the initial rotational level of the dipolar molecular reagent is, in itself, convincing evidence for the effects of the reagent rotation on the reaction rate. Although methods exist for preparing molecular ions in selected rotational levels,[46] indications are that it is the dipole of the molecular reagent that is crucial.[47] No method appears to have been devised for the selection of the rotational level of neutral molecules under conditions in which the rate of an ion–molecule reaction can be measured.

As already pointed out, the influence of reagent rotation on the rates of neutral–neutral reactions is less firmly established by the comparison between experimental rate constants and those predicted on the basis of capture theories that use only the long-range intermolecular potential arising from dipole–dipole forces, dispersion forces, etc. One circumstantial piece of evidence against the importance of the rotational states of the reagents arises from a comparison between the measured temperature dependence of thermal rate constants, especially those obtained in a CRESU apparatus, and those deduced from simple treatments of excitation functions obtained in crossed-beam experiments at low collision energy.

As an example,[13b] the reaction between $C(^3P_J)$ atoms and O_2 has been studied both 1) over the temperature range 15–295 K, and 2) in the collisional energy (ε_{tr}) range 4–100 meV ($\varepsilon_{tr}/k_B = 46$–1160 K). Within this range of collision energy, the reaction cross-section varies linearly with $(\varepsilon_{tr})^{-0.94}$. The integration of such an excitation function over distributions of thermal energy leads to a prediction of a rate constant that varies as $T^{-0.44}$, in fair agreement with the experimentally determined variation of $T^{-0.34\pm0.08}$. The rotational distribution in O_2 and the spin-orbit populations in $C(P_J)$ are not the same in the two experiments; therefore, because of the good agreement between the two temperature dependences it is assumed that there is at least no strong dependence of the reaction cross-section on these distributions. However, it has to be said that such comparisons have, as yet, been made for only a limited number of reactions: CN + O_2,[48] Al + O_2,[49] and $C(P_J)$ + O_2,[13b] as well as $C(P_J)$ + NO,[13b] $C(P_J)$ + $CH_3C{\equiv}CH$[13c] and $C(P_J)$ + $CH_2{=}C{=}CH_2$.[13c] Apart from the first reaction, none of the rate constants for these reactions show very marked negative temperature dependences.

One promising experimental method for investigating the rotational-state dependence of fast, low-temperature reactions is being pursued in our laboratory, and a preliminary account of such experiments has been published.[50] In these experiments, CN radicals are prepared in a selected rotational level (N_i) in the $v = 2$ vibrational level of the $X^2\Sigma^+$ electronic ground state. Two kinds of experiment are then performed: 1) Kinetic measurements: the rate constant for total (reaction + rotational energy transfer) loss from N_i is measured. 2) Spectroscopic experiments: state-to-state rate coefficients for transfer to other N levels in $X^2\Sigma^+(v{=}2)$ are determined. The sum of these state-to-state rate coefficients corresponds to the rotational-transfer component of the rate coefficient for total removal from the specified level N_i, so the difference between this total rate coefficient and the sum of the state-to-state rate coefficients is the rate constant for the reaction from level N_i. Results have been reported for the reaction between $CN(X^2\Sigma^+, v{=}2, N_i = 0)$ and C_2H_2. Further work is in progress.

5.4. Association Reactions

As stated earlier, although the majority of neutral–neutral reactions whose low-temperature kinetics have been observed by using the CRESU technique proceed through the initial formation of a transient complex. Most, like Equation (1), yield two products. However, there are a few instances of association reactions (orange print in Table 3). These systems differ from the metatheses that proceed via a transient complex in that the lowest-energy pathway for dissociation of the complex is redissociation back to the reagents, rather than dissociation forward to a new pair of species.

Under most laboratory conditions, including those in CRESU experiments, association only occurs if the initially formed complex, which contains energy released in the formation of the new chemical bond, is stabilized by a collision in which internal energy is removed. The mechanism can therefore be written as Equation (14)[29] and the second-

$$A + B \underset{k_a}{\overset{k_d}{\rightleftharpoons}} (AB)^* \xrightarrow{k_M[M]} AB \qquad (14)$$

order rate constant, at a total pressures or gas density [M] such that $k_M[M] \ll k_d$, is given by Equation (15). $(AB)^*$

$$k^\circ_{2nd} = k_M\,(k_a/k_d)[M] \qquad (15)$$

represents a molecule formed by association with sufficient energy to redissociate, whereas AB is a molecule that does not have sufficient energy to redissociate and that will eventually be fully thermalized; $k_M(k_a/k_d)$ corresponds to the third-order rate constant (k°_{3rd}) that is usually quoted as the limiting low-pressure rate constant. The data for Equation (2) between CH radicals and N_2 shown in Figure 7 conforms to this analysis. The linearity of the plot of k°_{2nd} versus [M] confirms that the kinetics are in the low-pressure regime.

As [M] is increased and the value of $k_M[M]$ approaches that of k_d, the rate constant defined by $k_{2nd} = -\{d[AB]/dt\}/[A][B]$ shows a more-complex dependence on the total gas density [M]. The pressure-dependence in this fall-off region is difficult to study in CRESU experiments, as the range of total gas density that can be achieved is strictly limited and because experiments at different gas densities but the same temperature each require the construction of a different Laval nozzle. Nevertheless, as explained in Section 4, some such measurements have been performed (see Figure 7) and confirm that an associative mechanism is operative in the reactions of CH radicals with N_2 [Eq. (2)] and with CO [Eq. (3)].

© 2006 Wiley-VCH Verlag GmbH & Co. KGaA, Weinheim

At the gas densities of ISCs, the mechanism of association in which collisions remove energy from the initially formed, energy-rich complex becomes negligibly slow. Consequently, the only mechanism for stabilization is radiative association [Eq. (16)]. If $k_{rad} \ll k_d$, the overall rate constant is given by [Eq. (17)]. The role that such reactions may play in the

$$A + B \underset{k_a}{\overset{k_d}{\rightleftharpoons}} (AB)^* \xrightarrow{k_{rad}} AB + h\nu \quad (16)$$

$$k_{RA} = k_{rad}\,(k_a/k_d) \quad (17)$$

chemistry of ISCs, especially in the synthesis of larger molecules, has been appreciated for many years,[12a,b] and a number of broadly similar methods[51] have been applied to estimate values of k_{RA} for potentially important association reactions between ions and neutral molecules.

The direct measurement of rate constants for radiative association is generally very difficult as the total pressure in the system must be low enough to satisfy the criterion $k_M[M] < k_{rad}$. However, such measurements have been achieved for a number of ion–molecule systems, mainly by using various kinds of cryogenically cooled "ion traps". The first direct measurements were made by Dunn and co-workers on the reactions of C^+ and CH_3^+ with H_2 in a liquid-helium-cooled Penning trap.[52] More recently, several kinds of radio-frequency ion traps have been developed to study radiative association, and the methods and results have been expertly reviewed by Gerlich and Horning.[53] One limitation in these methods is that the neutral gas must be kept at a pressure lower than its saturated vapor pressure at the temperature of the walls of the apparatus.

Of course, such methods rely on the presence of a charge on the ion, so that this species can be trapped in a specially designed electromagnetic field, and they are therefore not applicable to neutral–neutral systems. On the other hand, rate constants for such systems and for ion–molecule systems that do not lend themselves to the trapping experiments are relatively easy to estimate, either ab initio[51,54,55] or by making use of experimental information on the low-pressure rate constant for collisionally stabilized association. It is clear that the expressions given above for k°_{2nd} and k_{RA} [Eqs. (15) and (17)] lead to Equation (18). Hence, if k°_{3rd} is experimentally

$$k_{RA} = k_{rad}\,k^\circ_{2nd}/k_M[M] = k^\circ_{3rd}\,(k_{rad}/k_M) \quad (18)$$

known, estimating k_{RA} only requires k_{rad} and k_M to be calculated and this is relatively straightforward. In most cases k_{rad} values of about $10^3\ s^{-1}$ have been estimated.[51,54,55]

Evidently neither k_{rad} nor k_M are likely to depend strongly on temperature, that is, on the distributions of translational and internal energies in the colliding species that form the energized complexes. Consequently, the effect of temperature on the values of k°_{3rd} and k_{RA} is likely to be similar, as both depend largely on the temperature dependence of (k_a/k_d). Experimental evidence[56] and theoretical treatments[57] of the temperature dependence of rate constants of association reactions at low-pressure limits show that k°_{3rd} frequently varies as T^{-n} ($n = 1$–3).

For small AB, the values of k_{RA} are much smaller than the rate constants for binary collisions of A and B, because the complex $(AB)^*$ redissociates to A + B much faster than it emits a photon and becomes stable AB; that is, $k_d \gg k_{rad}$. Consequently, radiative association reactions are likely to play a significant role in the chemistry of ISCs only when: 1) one of the reagents is the relatively abundant molecule H_2, as in the reactions $C^+ + H_2$,[50] $CH_3^+ + H_2$,[50] and possibly $CH + H_2$;[16b] or 2) when AB is large so that the redissociation of $(AB)^*$ is slow ($k_d \leq 10^4\ s^{-1}$).[55] The ion–molecule associations $C^+ + H_2$ and $CH_3^+ + H_2$ are thought to be important because the metathesis reactions $C^+ + H_2 \rightarrow CH^+ + H$ and $CH_3^+ + H_2 \rightarrow CH_4^+ + H$ are endothermic and therefore very slow at the temperatures found in the cold cores of ISCs.

6. Estimating Rate Constants for Astrochemical Modeling

A major motivation for the experimental and theoretical investigation of fast low-temperature reactions is the wish to understand and, if possible, to model the synthesis of those molecules that have been observed in the distant, low-temperature environments of dense ISCs. The earliest chemical models[12] of ISCs strongly emphasized the role of ion–molecule chemistry, and this feature of models has survived until quite recently. In cases in which neutral–neutral reactions were included in models, their rate constants were usually estimated from the room-temperature value (k-(300 K)) and the simplistic "hard-sphere" relationship [Eq. (19)].[29] However, the CRESU measurements summarized herein clearly show that the rate constants for those neutral–neutral reactions that remain fast at low temperatures generally increase as the temperature is lowered; they do not decrease as suggested by the "hard-sphere" treatment.

$$k(T) = k(300\ K)\ (T/300)^{+0.5} \quad (19)$$

Current models of cold dense ISCs include about 400 species and around 4000 reactions. Databases are held at the University of Manchester[58] and at the University of Ohio.[59] Of course, low-temperature rate constants have only been measured for a small fraction of these reactions, and the reaction products have been measured for even fewer. For ion–molecule reactions that occur rapidly at room temperature—that is, that have rate constants of about $10^{-9}\ cm^3\ molecule^{-1}\ s^{-1}$—the methods outlined above can be used to estimate the low-temperature rate constants with some confidence. However, as has already been emphasized, the position is different for neutral–neutral reactions since there are no simple "universal" models that describe the temperature dependence of fast neutral–neutral reactions.

In the model recently described by Smith et al.,[60] 317 neutral–neutral reactions are included. For about 80% of these, one reagent is an atom H, C, O, N, S or Si. There have been direct experiments at low temperatures on the rates of fewer than 20 of the neutral–neutral reactions included in the model. For about 50 reactions, rate constants could be

 © 2006 Wiley-VCH Verlag GmbH & Co. KGaA, Weinheim

estimated on the basis of "chemical similarity". For instance, as CN radicals, C_2H radicals, and $C(^3P_J)$ atoms are known to react rapidly with C_2H_2 and C_2H_4, it is safe to assume that they react with similar rate constants with larger alkynes and alkenes. In addition, parallels were drawn between families of reaction such as: $O(^3P_J) + OH$, $S(^3P_J) + OH$, $O(^3P_J) + SH$, and $S(^3P_J) + SH$.

For other proposed reactions, rate constants were estimated by using "chemical intuition". The first test that a reaction had to pass for inclusion in the model was that it is exothermic, as reactions that are even slightly endothermic will be slow at the low temperatures associated with dense ISCs. The second test was that, at room temperature, it has a rate constant $\geq 10^{-11}\,cm^3\,molecule^{-1}\,s^{-1}$. If it does, there is unlikely to be a significant barrier on the minimum-energy path leading from reagents to products and it was assumed that the rate constant would increase, rather than decrease, at low temperatures.

Reactions between two free radicals (that is, species with open electron shells) needed special consideration. In the case of reactions without barriers, the limited evidence suggests that the rate constants for radical–radical reactions are somewhat lower than those for reactions between one radical and one closed-shell molecule, on account of the multiplicity of potential-energy surfaces that correlate with the reagents of radical–radical reactions. In general, the slight evidence is that reactions will only occur over potential-energy surfaces whose total spin corresponds to a pairing of electrons as the reagents approach. On the other hand, it seems as if reactions can occur with similar ease from all spin-orbit components of an atomic radical with $L > 0$ or a molecular radical with $\Lambda > 0$, as long as the spin-orbit splitting is not too great.

Two final comments are in order. The first concerns the limited nature of the kinetic information that is available, even for those reactions that have been studied at low temperature by the CRESU technique. Nearly all these measurements, especially those on neutral–neutral reactions, provide values of the rate constants for the disappearance of a selected reagent. Thus, the measurements on Equation (1) between CN radicals and C_2H_2 molecules provide a rate constant defined in terms of the consumption of CN radicals; no information is provided about the identity of the products. In certain cases, such as Equation (1), thermochemistry and chemical intuition can be used to infer the products with at least a fair degree of certainty, but this is not always so. Secondly, it must be stressed that the agreement between the abundances observed in ISCs and those currently predicted by chemical models leaves a lot to be desired. The reasons for this discrepancy remain a very active area of research involving astrochemists, laboratory chemists, and theoreticians.

7. Summary and Outlook

This Review has described the CRESU method for measuring the rate constants of gas-phase reactions between electrically neutral species and the results that this method has yielded. These unique measurements have been set in context:

- first, in relation to understanding the chemistry that occurs in the interstellar medium and, in particular, that leads to the abundances of molecules that are observed in the very cold environment of dense interstellar clouds, and
- second, with respect to how we might understand the factors that control the rates of these reactions and the dependence of their rate constants on temperature.

Part of the reason for wishing to understand what controls the rates of these reactions is that such an understanding is a necessary prerequisite to predicting the rate constants for other reactions that might play a role in the chemistry of interstellar clouds—but whose rate constants at very low temperatures are unlikely to be measured, at least in the foreseeable future. Examination of the low-temperature data obtained so far suggests that any bimolecular reaction that has a rate constant in excess of $10^{-11}\,cm^3\,molecule^{-1}\,s^{-1}$ at 298 K has no significant activation energy and may, therefore, have a rate constant at 10–20 K at or close to the "gas kinetic collision limit". This observation can help with the prediction of approximate rate constants for those reactions whose kinetics have been studied at room temperature. That leaves many reactions—especially those between unstable radicals—that may be important in the chemistry of interstellar clouds, but for which rate constants are not available at any temperature.

This Review has not provided much detail about quantum-chemical calculations and their relevance in deciding a) what reactions may proceed rapidly at very low temperatures, and b) what the products of particular reactions are when simple thermochemical arguments cannot decide between alternative channels. Theory can play, and is playing, its part here. In encouraging the participation of theoreticians in this field, it may be worth stressing that, at the present stage of its development, astrochemistry does not need to know the values of the rate constants for particular reactions to 10 or 20 percent. It seems likely that individual reactions either have rate constants that are a) negligibly small, as the reactions are inhibited by a barrier on the minimum-energy path that is much larger than RT at the low temperatures of interstellar clouds, or b) close to $10^{-10}\,cm^3\,molecule^{-1}\,s^{-1}$ at the temperatures of ISCs, because there is no barrier along the path of minimum potential energy. Quantum chemistry can also play an important role in predicting the products of particular low-temperature reactions. As emphasized earlier, virtually no CRESU experiments have led to the identification of the products of neutral–neutral reactions. This is likely to be an area for future experimental endeavor. Furthermore, because full ab initio, quantum-mechanical calculations are time-consuming, one can expect the development of semiempirical methods that might make it possible to predict which reactions have significant barriers and which do not, so that approximate estimates of the low-temperature rate constants can be made.[67]

The massive pumping requirements and the large consumption of gases may have inhibited the development of

© 2006 Wiley-VCH Verlag GmbH & Co. KGaA, Weinheim

more than two continuous flow CRESU apparatuses. As stated in Section 3.3, a number of laboratories are now employing pulsed Laval nozzles to generate uniform supersonic flows that currently reach temperatures as low as to 58 K. Moreover, during the final preparation of this Review, a miniaturized CRESU apparatus was reported[61] in which the overall pumping speed is only a small fraction of those in the continuous CRESU apparatuses operated at Rennes and Birmingham. At present, the lowest temperature achieved is 77 K. Further decreases in the lowest temperatures that can be achieved in these smaller apparatuses is to be expected. Both should enable low-temperature experiments to be performed that use co-reagents that cannot be employed in the large, continuous-flow, CRESU apparatuses because of cost or availability.

I am greatly indebted to all the people who have contributed to the success of the CRESU experiments in Rennes and Birmingham. Many of these can be identified in the references given in this article, but we have also benefited greatly from skilled technical help. I am especially grateful to Bertrand Rowe, the inventor of the continuous-flow CRESU techniques. The work on processes involving neutral–neutral species has been carried out in a collaborative project that has been as enjoyable as it has been successful. Ian Sims was responsible for performing the first experiments on neutral–neutral reactions in what was then the only CRESU apparatus in the world—in Rennes. He also jointly directed the efforts on low-temperature processes in Birmingham. Eric Herbst taught me most of the astrochemistry that I know. I also thank David Clary for useful discussions regarding the theoretical understanding of rapid low-temperature reactions. Finally, I am grateful to Dr Delphine Chastaing for permission to reproduce some diagrams from her thesis. I also gratefully acknowledge long-term support from the U.K. Engineering and Physical Sciences Research Council (EPSRC) and from the European Union through a number of programs.

Received: August 4, 2005

[1] a) B. R. Rowe, G. Dupeyrat, J. B. Marquette, P. Gaucheral, *J. Chem. Phys.* **1984**, *80*, 4915–4921; b) G. Dupeyrat, J. B. Marquette, B. R. Rowe, *Phys. Fluids* **1985**, *28*, 1273–1279; c) B. R. Rowe, J. B. Marquette, *Int. J. Mass Spectrom. Ion Proc.* **1987**, *80*, 239–254.

[2] a) J. B. Marquette, B. R. Rowe, G. Dupeyrat, E. Roueff, *Astron. Astrophys.* **1985**, *147*, 115–120; b) B. R. Rowe, J. B. Marquette, G. Dupeyrat, E. E. Ferguson, *Chem. Phys. Lett.* **1985**, *113*, 403–406; c) P. Gaucheral, J. B. Marquette, C. Rebrion, G. Poissant, G. Dupeyrat, B. R. Rowe, *Chem. Phys. Lett.* **1986**, *132*, 63–66.

[3] a) I. R. Sims, J.-L. Queffelec, A. Defrance, C. Rebrion-Rowe, D. Travers, B. R. Rowe, I. W. M. Smith, *J. Chem. Phys.* **1992**, *97*, 8798–8800; b) I. R. Sims, J.-L. Queffelec, A. Defrance, C. Rebrion-Rowe, D. Travers, P. Bocherel, B. R. Rowe, I. W. M. Smith, *J. Chem. Phys.* **1994**, *100*, 4229–4241.

[4] P. L. James, I. R. Sims, I. W. M. Smith, M. H. Alexander, M. Yang, *J. Chem. Phys.* **1998**, *109*, 3882–3897.

[5] H. L. Bethlem, G. Meijer, *Int. Rev. Phys. Chem.* **2003**, *22*, 73–128.

[6] a) I. R. Sims, I. W. M. Smith, *Annu. Rev. Phys. Chem.* **1995**, *46*, 109–137; b) I. W. M. Smith, B. R. Rowe, *Acc. Chem. Res.* **2000**, *33*, 261–268; c) I. W. M. Smith, *Chem. Soc. Rev.* **2001**, *30*, 137–146.

[7] a) E. Herbst, *Annu. Rev. Phys. Chem.* **1995**, *46*, 27–53; b) E. Herbst, *Chem. Soc. Rev.* **2001**, *30*, 168–176.

[8] The Web page http://www.iso.vilspa.esa.es/science/publications.html lists the numerous scientific publications arising from the deployment of ISO.

[9] a) Y. J. Kuan, S. B. Charnley, H. C. Huang, W. L. Tseng, Z. Kisiel, *Astrophys. J.* **2003**, *593*, 848–867; b) L. E. Snyder, F. J. Lovas, J. M. Hollis, D. N. Friedel, P. R. Jewell, A. Remijan, V. V. Hyushin, *Astrophys. J.* **2005**, *619*, 914–930.

[10] T. Henning in *IAU Sympos. 178 Molecules in Astrophysics: Probes and Processes* (Ed.: E. F. van Dishoeck), Kluwer Academic Publishers, Dordrecht, **1997**.

[11] S. Viti, M. P. Collings, J. W. Dever, M. R. S. McCoustra, D. A. Williams, *Mon. Not. R. Astron. Soc.* **2004**, *354*, 1141–1145.

[12] a) E. Herbst, W. Klemperer, *Astrophys. J.* **1973**, *185*, 505–533; b) J. H. Black, A. Dalgarno, *Astrophys. Lett.* **1973**, *15*, 79–82; c) S. S. Prasad, W. T. Huntress, Jr., *Astrophys. J. Suppl. Ser.* **1980**, *43*, 1–35; d) Y. P. Viala, *Astrophys. J. Suppl. Ser.* **1986**, *64*, 391–437; e) A. Dalgarno, *Int. J. Mass Spectrom. Ion Proc.* **1987**, *81*, 1–13.

[13] a) D. Chastaing, S. D. Le Picard, I. R. Sims, *J. Chem. Phys.* **2000**, *112*, 8466–8469; b) W. D. Geppert, D. Reigneur, T. Stoecklin, C. Naulin, M. Costes, D. Chastaing, S. D. LePicard, I. R. Sims, I. W. M. Smith, *Phys. Chem. Chem. Phys.* **2000**, *2*, 2873–2881; c) D. Chastaing, S. D. Le Picard, I. R. Sims, I. W. M. Smith, W. D. Geppert, C. Naulin, M. Costes, *Chem. Phys. Lett.* **2000**, *331*, 170–176.

[14] F. Goulay, C. Rebrion-Rowe, J. L. Le Garrec, S. D. Le Picard, A. Canosa, B. R. Rowe, *J. Chem. Phys.* **2005**, *122*, 104308.

[15] I. R. Sims, I. W. M. Smith, P. Bocherel, A. Defrance, D. Travers, B. R. Rowe, *J. Chem. Soc. Faraday Trans.* **1994**, *90*, 1473–1478.

[16] a) R. A. Brownsword, A. Canosa, B. R. Rowe, I. R. Sims, I. W. M. Smith, D. W. A. Stewart, A. C. Symonds, D. Travers, *J. Chem. Phys.* **1997**, *106*, 7662–7677; b) R. A. Brownsword, I. R. Sims, I. W. M. Smith, D. W. A. Stewart, A. Canosa, B. R. Rowe, *Astrophys. J.* **1997**, *485*, 195–202.

[17] a) R. A. Brownsword, L. B. Herbert, I. W. M Smith, D. W. A. Stewart, *J. Chem. Soc. Faraday Trans.* **1996**, *92*, 1087–1094; b) L. Herbert, I. R. Sims, I. W. M. Smith, D. W. A. Stewart, A. Canosa, B. R. Rowe, *J. Phys. Chem.* **1996**, *100*, 14928–14935; c) S. D. Le Picard, A. Canosa, B. R. Rowe, R. A. Brownsword, I. W. M. Smith, *J. Chem. Soc. Faraday Trans.* **1998**, *94*, 2889–2993.

[18] I. W. M. Smith, *J. Chem. Soc. Faraday Trans.* **1997**, *93*, 3741–3750.

[19] M. Hawley, M. A. Smith, *J. Chem. Phys.* **1991**, *95*, 8862–8864.

[20] N. Choi. M. A. Blitz, K. McKee, M. J. Pilling, P. W. Seakins, *Chem. Phys. Lett.* **2004**, *384*, 68–72.

[21] C. A. Taatjes and J. F. Hershberger, *Annu. Rev. Phys. Chem.* **2001**, *52*, 41–70.

[22] a) D. B. Atkinson, M. A. Smith, *Rev. Sci. Instrum.* **1995**, *66*, 4434; b) C. Mullen, M. A. Smith, *J. Phys. Chem. A* **2005**, *109*, 1391–1399; c) C. Mullen, M. A. Smith, *J. Phys. Chem. A* **2005**, *109*, 3893–3902.

[23] for example: a) A. B. Vakhtin, S. Lee, D. E. Heard, I. W. M. Smith, S. R. Leone, *J. Phys. Chem. A* **2001**, *105*, 7889–7895; b) A. B. Vakhtin, J. E. Murphy, S. R. Leone, *J. Phys. Chem. A* **2003**, *107*, 10055–10062; c) B. Nizamov, S. R. Leone, *J. Phys. Chem. A* **2004**, *108*, 3766–3771; d) T. Spangenberg, S. Kohler, B. Hansmann, U. Wachsmuth, B. Abel, M. A. Smith, *J. Phys. Chem. A* **2004**, *108*, 7527–7534.

[24] P. Sharkey, I. R. Sims, I. W. M. Smith, P. Bocherel, B. R. Rowe, *J. Chem. Soc. Faraday Trans.* **1994**, *90*, 3609–3616.

[25] A. Canosa, personal communication.

 © 2006 Wiley-VCH Verlag GmbH & Co. KGaA, Weinheim

[26] I. R. Sims, J.-L. Queffelec, A. Defrance, D. Travers, B. R. Rowe, L. Herbert, J. Karthauser, I. W. M. Smith, *Chem. Phys. Lett.* **1993**, *211*, 461 – 468.
[27] a) D. Chastaing, P. L. James, I. R. Sims, I. W. M. Smith, *Phys. Chem. Chem. Phys.* **1999**, *1*, 2247 – 2256; b) D. Chastaing, S. D. Le Picard, I. R. Sims, I. W. M. Smith, *Astron. Astrophys.* **2001**, *365*, 241 – 247; c) D. C. Clary, E. Buonomo, I. R. Sims, I. W. M. Smith, W. D. Geppert, C. Naulin, M. Costes, L. Cartechini, P. Casavecchia, *J. Phys. Chem. A* **2002**, *106*, 5541 – 5552.
[28] a) D. C. Clary, *Mol. Phys.* **1984**, *53*, 3 – 21; b) D. C. Clary, *Annu. Rev. Phys. Chem.***1990**, *41*, 61 – 90.
[29] I. W. M. Smith, *Kinetics and Dynamics of Elementary Gas Reactions*, **1980**, Butterworths, London.
[30] G. Gioumousis, D. P. Stevenson, *J. Chem. Phys.* **1958**, *29*, 294 – 299.
[31] B. R. Rowe, J. B. Marquette, G. Dupeyrat, E. E. Ferguson, *Chem. Phys. Lett.* **1985**, *113*, 403 – 406.
[32] C. E. Dateo, D. C. Clary, *J. Chem. Phys.* **1989**, *90*, 7216 – 7228.
[33] a) M. Quack, J. Troe, *Ber. Bunsen-Ges.* **1974**, *78*, 240 – 252; b) J. Troe, *Chem. Phys. Lett.* **1985**, *122*, 425 – 430.
[34] Y. Georgievskii, S. J. Klippenstein, *J. Chem. Phys.* **2005**, *122*, 194103 – 1–17.
[35] J. B. Marquette, B. R. Rowe, G. Dupeyrat, G. Poissant, C. Rebrion, *Chem. Phys. Lett.* **1985**, *122*, 431 – 435.
[36] For example, see: a) S. D. Le Picard, A. Canosa, D. Travers, D. Chastaing, B. R. Rowe, T. Stoecklin, *J. Phys. Chem. A* **1997**, *101*, 9988 – 9992; b) D. Reignier, T. Stoecklin, S. D. Le Picard, A. Canosa, B. R. Rowe, *J. Chem. Soc. Faraday Trans.* **1998**, *94*, 1681 – 1686.
[37] T. Stoecklin, C. E. Dateo, D. C. Clary, *J. Chem. Soc. Faraday Trans.* **1991**, *87*, 1667 – 1679.
[38] S. J. Klippenstein, Y.-W. Kim, *J. Chem. Phys.* **1993**, *99*, 5790 – 5799.
[39] a) A. Faure, C. Rist, P. Valiron, *Chem. Phys.* **1999**, *241*, 29 – 42; b) A. Faure, C. Rist, P. Valiron, *Astron. Astrophys.* **1999**, *248*, 972 – 977.
[40] A. Faure, L. Wiesenfeld, P. Valiron, *Chem. Phys.* **2000**, *254*, 49 – 67.
[41] D. Carty, A. Goddard, S. V. Kohler, I. R. Sims, I. W. M. Smith, *J. Phys. Chem. A* **2006**, *110*, 3101 – 3109.
[42] I. W. M. Smith, D. W. A. Stewart, *J. Chem. Soc. Faraday Trans.* **1994**, *90*, 3221 – 3227.
[43] S. Viti, E. Roueff, T. W. Hartquist, G. P. des Forets, D. A. Williams, *Astron. Astrophys.* **2001**, *370*, 557 – 569.
[44] a) J. Troe, *J. Phys. Chem.* **1986**, *90*, 3485 – 3492; b) L. B. Harding, A. I. Maergoiz, J. Troe, V. G. Ushakov, *J. Chem. Phys.* **2000**, *113*, 11019 – 11034; c) J. Troe, V. G. Ushakov, *J. Chem. Phys.* **2001**, *115*, 3621 – 3628.
[45] S. Schlemmer, E. Lescop, J. von Richthofen, D. Gerlich, *J. Chem. Phys.* **2002**, *117*, 2068 – 2075. This article describes elegant experiments on the ion–molecule reaction $C_2H_2^+ + H_2 \rightarrow C_2H_3^+ + H$ and includes measurements of the effect of the rotational state of $C_2H_2^+$ in its $v_3 = 1$ vibrational level on the reaction rate. However, this reaction is endothermic, and therefore the observations cannot lead to any general conclusions about the effects of reagent rotation on fast exothermic ion–molecule reactions.
[46] a) F. Merkt, S. R. Mackenzie, T. P. Softley, *J. Chem. Phys.* **1993**, *99*, 4213 – 4214; b) S. R. Mackenzie, T. P. Softley, *J. Chem. Phys.* **1994**, *101*, 10609 – 10617.
[47] D. C. Clary, *Chem. Phys. Lett.* **1995**, 232, 267 – 272.
[48] a) D. M. Sonnehfroh, R. G. Macdonald, K. Liu, *J. Chem. Phys.* **1990**, *93*, 1478 – 1479; b) R. G. Macdonald, D. M. Sonnehfroh, D.-J. Liu, K. Liu, *Can. J. Chem.* **1994**, *72*, 660 – 672.
[49] C.Naulin and M. Costes, *Chem. Phys. Lett.* **1999**, *310*, 231 – 239.
[50] K. M. Hickson, C. M. Sadowski, I. W. M. Smith, *Chem. Phys. Lett.* **2003**, *372*, 443 – 450.
[51] a) D. R. Bates, E. Herbst in *Rate Coefficients in Astrochemistry* (Ed.: T. J. Millar, D. A. Williams), Kluwer, Dordrecht, **1988**; b) R. C. Dunbar, *Int. J. Mass Spectrom. Ion Proc.* **1997**, *160*, 1 – 16; c) S. J. Klippenstein, Y. C. Yang, V. Ryzhov, R. C. Dunbar, *J. Chem. Phys.* **1996**, *104*, 4502 – 4516.
[52] a) S. E. Barlow, G. H. Dunn, M. Schauer, *Phys. Rev. Lett.* **1984**, *52*, 902 – 905; b) S. E. Barlow, J. A. Luine, G. H. Dunn, *Int. J. Mass Spectrom. Ion Proc.* **1986**, *74*, 97 – 128.
[53] D. Gerlich, S. Horning, *Chem. Rev.* **1992**, *92*, 1509 – 1539.
[54] I. W. M. Smith, *Chem. Phys.* **1989**, *131*, 391 – 401.
[55] J. R. Barker, *J. Phys. Chem.* **1992**, *96*, 7361 – 7367.
[56] M. J. Howard, I. W. M. Smith, *Prog. React. Kinet.* **1983**, *21*, 55 – 200.
[57] a) J. Troe, *J. Chem. Phys.* **1977**, *66*, 4745 – 4757; b) J. Troe, *J. Chem. Phys.* **1977**, *66*, 4758 – 4775.
[58] Y. H. Le Teuff, T. J. Millar, A. J. Markwick, *Astron. Astrophys. Suppl.* **2000**, *146*, 157 – 168; see also: http://www.rate99.co.uk.
[59] http://www.physics.ohio-state.edu/≈eric/research.html.
[60] I. W. M. Smith, E. Herbst, Qiang Chang, *Mon. Not. R. Astron. Soc.* **2004**, *350*, 323 – 330.
[61] N. Daugey, P. Caubet, B. Retail, M. Costes, A. Bergeat, G. Dorthe, *Phys. Chem. Chem. Phys.* **2005**, *7*, 2921 – 2927.
[62] C. G. Wynn-Williams, *Sci. Am.* **1981**, *245*, 31.
[63] J. B. Kaler, *Cosmic Clouds: Birth, Death, and Recycling in the Galaxy*, Scientific American Library, **1997**.
[64] D. Chastaing, PhD thesis, University of Birmingham, **1999**.
[65] a) I. R. Sims, I. W. M. Smith, *J. Chem. Soc.* **1988**, *84*, 527 – 539; b) I. R. Sims, I. W. M. Smith, *Chem. Phys. Lett.* **1988**, *151*, 481 – 484; c) L. Herbert, I. W. M. Smith, R. Spencer-Smith, *Int. J. Chem. Kinet.* **1992**, *24*, 791 – 802.
[66] D. C. Clary, *J. Chem. Soc. Faraday Trans. 2* **1987**, *83*, 139 – 148.
[67] I. W. M. Smith, A. M. Sage, N. M. Donahue, E. Herbst, I. H. Park, *Faraday Discuss.* **2006**, *133*, in press.

© 2006 Wiley-VCH Verlag GmbH & Co. KGaA, Weinheim

Communications

DOI: 10.1002/anie.200504548

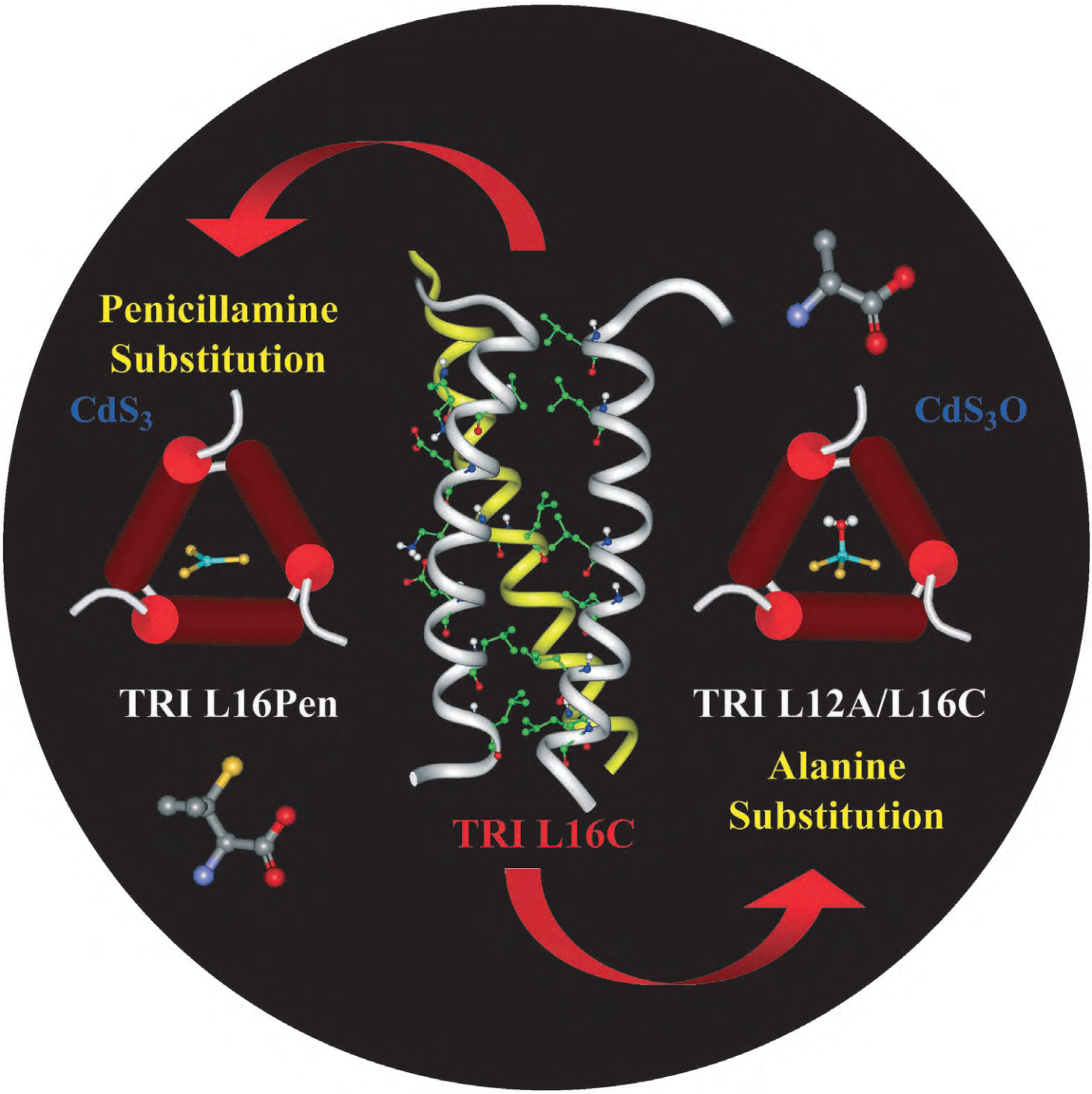

Controlling the coordination geometry of a metal center is the first step in preparing proteins capable of catalysis. Substitution of a single amino acid can shift an equilibrium of 3- and 4-coordinate Cd^{II}–peptide complexes to proteins containing exclusively 3- or 4-coordinate metal sites. For details, see the communication by V. L. Pecoraro and co-workers on the following pages.

WILEY InterScience DISCOVER SOMETHING GREAT
© 2006 Wiley-VCH Verlag GmbH & Co. KGaA, Weinheim

Metalloproteins

DOI: 10.1002/anie.200504548

Using Nonnatural Amino Acids to Control Metal-Coordination Number in Three-Stranded Coiled Coils**

*Kyung-Hoon Lee, Chris Cabello, Lars Hemmingsen, E. Neil G. Marsh, and Vincent L. Pecoraro**

Proteins are remarkably adept at controlling the geometry and the type and number of ligands bound to a metal center. A single protein may contain two or more metal ions in very different coordination environments.[1,2] For example, 5-aminolevulinic acid dehydratase, which is found in mammals and yeast and is involved in the biosynthesis of heme, contains two Zn^{II} ions, one bound in a five-coordinate geometry with oxygen and nitrogen atoms as ligands and the other bound in a pseudo-tetrahedral geometry with three cysteine sulfur atoms and an exogenous water molecule.[1,2] Lead toxicity results in part from the displacement of the Zn^{II} ion by Pb^{II} from the tetrahedral site (but not from the pentacoordinate site), thus rendering the enzyme inactive.[3] Such exquisite control of ion recognition by proteins is difficult to reproduce with small molecules under most synthetic conditions.

We have been exploring how subtle changes in small, de novo designed peptides can produce even stronger control of metal-coordination number and ligand type.[4] In particular, we have asked whether the same metal can be bound to structurally related peptides with identical first-coordination-sphere ligands derived from the protein, but in one case form a trigonal structure and in a second case form a four-coordinate pseudo-tetrahedral environment.[4] The relative importance of a metal's geometric preference and the inherent protein structure is fundamental to understanding the folding,[5–8] stability,[9,10] and conformational changes[4,5,11] of metalloproteins, and hence the control of such site discrimination has been an important objective of protein design studies.

The peptides described herein are variants of the TRI family of peptides shown in Table 1. The sequence of the TRI peptide is Ac-G(LKALEEK)$_4$G-NH_2.[12] A leucine residue at the hydrophobic layers is replaced by a cysteine residue at position 16 (TRI L16C) for generating a metal-binding site.[12] According to previous studies of Cd^{II} binding to TRI L16C by ^{113}Cd NMR spectroscopy,[13] ^{111m}Cd perturbed angular correlation (PAC) spectroscopy,[14,15] and X-ray absorption spectroscopy (XAS),[16] two cadmium species were present at pH 8.5.[17] The PAC results on the Cd complex of TRI L16C indicated that 41% of the Cd^{II} centers had a trigonal planar geometry ($\omega_o = 0.438$; $\eta = 0.20$) and 59% the tetrahedral ($\omega_o = 0.337$; $\eta = 0.22$) cadmium structure.[17] In contrast, ^{113}Cd NMR spectroscopy exhibited a single resonance at 625 ppm. These observations indicate that the two structures interconvert rapidly on the NMR timescale (0.01–10 ms), but are in the slow exchange regime on the PAC timescale (0.1–100 ns).[4,17,18] The observed Cd–S bond distance of 2.49 Å for the TRI L16C peptide is in good agreement with an equilibrium distribution of three- and four-coordinate Cd^{II} complexes (CdS_3: Cd–S 2.45 Å; CdS_4: Cd–S 2.54 Å).[17,19–22]

Our objective was to prepare peptides with minimal sequence changes that would bind Cd^{II} exclusively in either three- or four-coordinate geometries. The goal is particularly challenging because three-coordinate Cd^{II} structures have never been observed in biological molecules or in small-molecule complexes in water. Our strategy was to modify steric bulk around the metal-binding site in an effort to either allow or exclude exogenous water ligands from approaching the metal. Hodges had previously estimated that replacing leucine with alanine could allow as many as five water molecules to enter the hydrophobic interior of a four-stranded α-helical bundle.[34] As shown by the data in Figures 1 and 2 and Table 2, decreasing the steric bulk above the metal-binding site by substitution of a leucine with an alanine

Table 1: Sequences of the peptides used in this study.

Peptide	Sequence[a]
TRI L16C	Ac-G LKALEEK LKALEEK **C**KALEEK LKALEEK G-NH_2
TRI L12A/L16C	Ac-G LKALEEK LK**A**AEEK **C**KALEEK LKALEEK G-NH_2
TRI L12Hfl/L16C	Ac-G LKALEEK LK**X$_1$**EEK **C**KALEEK LKALEEK G-NH_2
TRI L16Pen	Ac-G LKALEEK LKALEEK **X$_2$**KALEEK LKALEEK G-NH_2

[a] X_1 = L-5,5,5,5′,5′,5′-hexafluoroleucine, X_2 = Penicillamine.

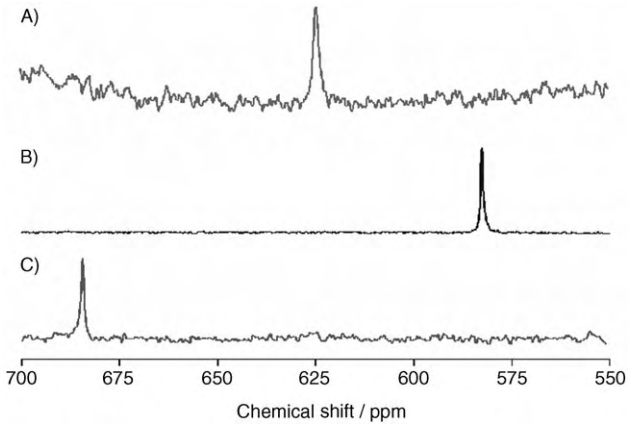

Figure 1. ^{113}Cd NMR spectra of the TRI family of peptides studied. A) $[Cd(TRI\ L16C)_3]^-$; B) $[Cd(TRI\ L12A/L16C)_3]^-$; C) $[Cd(TRI\ L16Pen)_3]^-$.

[*] Dr. K.-H. Lee, C. Cabello, Prof. E. N. G. Marsh, Prof. V. L. Pecoraro
Department of Chemistry
University of Michigan
Ann Arbor, MI 48109 (USA)
Fax: (+1) 734-615-3790
E-mail: vlpec@umich.edu
Prof. L. Hemmingsen
Department of Mathematics and Physics
Royal Veterinary and Agricultural University
Thorvaldsensvej 40, 1871 Frederiksberg D (Denmark)

[**] V.L.P. thanks the National Institutes of Health for support of this research (ES012236), C.C. thanks the Chemistry/Biology Interface Training Program for a Fellowship (TG32 GM008597), and L.H. thanks the EU for support within the network on "Metallo-beta-lactamases as model zinc enzymes".

 © 2006 Wiley-VCH Verlag GmbH & Co. KGaA, Weinheim

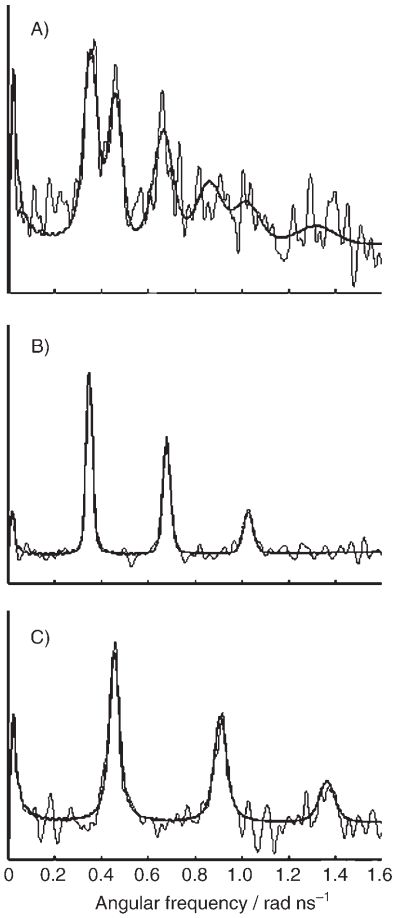

Figure 2. PAC spectra of A) $[Cd(TRI\ L16C)_3]^-$, B) $[Cd(TRI\ L12A/L16C)_3]^-$, and C) $[Cd(TRI\ L16Pen)_3]^-$.

Table 2: Physical parameters for $[Cd^{II}(TRI)_3]^-$ peptides.

Peptide[a]	λ_{max} ($\Delta\varepsilon$)[b]	^{113}Cd NMR[c]	^{111m}Cd PAC (ω_o, η, %)[d]
L16C[17]	232 (22600)	625	0.438(4), 0.20(3), 41% 0.337(2), 0.22(1), 59%
L12A/L16C	231 (21200)	574	0.3405(3), 0.141(4), 100%
L12Hfl/L16C	231 (19400)	607	–
L16Pen	231 (21600)	684	0.4540(9), 0.02(10), 100%

[a] All complexes correspond to $[Cd^{II}(TRI\ derivative)_3]^-$. [b] λ_{max} given in nm and $\Delta\varepsilon$ given as $M^{-1}cm^{-1}$. [c] Given in ppm versus the standard $Cd(ClO_4)_2$ in D_2O. Data collected at pH 8.5. [d] ω_o given in rad ns^{-1}; η is a unitless quantity. Percentage values of species are based on best fit to PAC. Calculated values for pure trigonal planar $Cd^{II}S_3$ are $\omega_o = 0.450$ and $\eta = 0$.

residue in the hydrophobic core provided 100% of the four-coordinate structure $[Cd(TRI\ L12A/L16C)_3]$.[4] Thus, the pure four-coordinate complex could be prepared straightforwardly by hydrating the metal-binding cavity.

By using the ^{113}Cd NMR chemical shifts for $[Cd(TRI\ L16C)_3]^-$ and $[Cd(TRI\ L12A/L16C)_3]^-$ together with the quantification of the percentages of three- and four-coordinate species from PAC spectroscopy, we are now able to calculate the theoretical ^{113}Cd NMR chemical shift of a complete three-coordinate cadmium species ($Cd^{II}S_3$) to be approximately 698 ppm. This value, as well as that of the $Cd^{II}S_3O$ species (574 ppm), differs from previously used[22,23] assignments for three- and four-coordinate Cd^{II} and leads to the reassessment of earlier reports of pure three-coordinate Cd^{II}.[4,23]

The more challenging objective was to dehydrate the Cd^{II} core environment. We reasoned that if decreasing the substituent bulk above the metal site allowed the access of more water, and hence a higher metal-coordination number, then increasing the steric constraints might yield a less hydrated environment that could provide the desired adduct with a lower coordination number. To this end, we synthesized the nonnatural amino acid L-5,5,5,5′,5′,5′-hexafluoroleucine,[24] and incorporated this residue into the layer above the metal-binding site (TRI L12Hfl/L16C) by manual peptide synthesis.[25] To ensure that the aggregation state and metal-binding properties of this peptide were unperturbed by the fluoro groups, we completed guanidinium chloride denaturation titrations of the system as well as metal-binding titrations with Hg^{II} and Cd^{II} solutions. As expected on the basis of previous literature precedent,[26–29] there was a slight stabilization of the three-stranded coiled coil ($\Delta G_{bind} = -0.4$ kcal mol^{-1} per peptide) as a result of the increased hydrophobicity of the hexafluoroleucine side chain. The metal-binding titrations with Hg^{II} and Cd^{II} ions gave similar results to those of other peptide derivatives, and metal-binding association constants were determined which showed that the $[Hg^{II}(TRI\ L12Hfl/L16C)_3]^-$ complex followed the free-energy correlation reported for numerous other derivatives in the TRI peptide family.[30] Based on these results, we concluded that the fluorinated peptides behaved as other members of this series. The ^{113}Cd NMR chemical shift for this peptide corresponds to a mixture of CdS_3 and CdS_3O complexes (Figure 1 and Table 2). Furthermore, relative to TRI L16C, the distribution was shifted away from the desired three-coordinate complex. These observations demonstrate that obtaining the elusive CdS_3 geometry requires more than simply increasing the side-chain bulk above the metal.

An alternative strategy was to provide more steric bulk within the trigonal plane of the Cd^{II} ion. This was achieved by replacement of a cysteine with a penicillamine residue[31] (TRI L16Pen), which has two methyl groups replacing the β-methylene hydrogen atoms of cysteine. We reasoned that these two methyl groups could affect both the conformation of the sulfur donors to Cd, while enhancing the local bulk directly around the metal center. As shown in Figure 1 and Table 2, the ^{113}Cd NMR spectrum of $[Cd(TRI\ L16Pen)_3]^-$ was markedly different from those of all other TRI derivatives. The value of 684 ppm in Table 2 is very close to the predicted fully three-coordinate chemical shift of 698 ppm. Conclusive proof for the assignment of this derivative as a CdS_3 species comes from the PAC measurements shown in Figure 2. Only one species is observed with $\omega_o = 0.4540$ and $\eta = 0.02$. Thus, we have prepared for the first time a water-stable, three-coordinate CdS_3 structure.

In conclusion, we have shown that it is possible to control the coordination number of a metal ion in a model protein of $M_r \approx 10200$ Da by changing only one of the amino acid residues in the primary sequence. By starting with the TRI L16C peptide, simple replacement of the cysteine

 © 2006 Wiley-VCH Verlag GmbH & Co. KGaA, Weinheim

residue with penicillamine can shift a 41:59 equilibrium of three- and four-coordinate structures to fully three-coordinate. Alternatively, by substituting an alanine residue for leucine in the layer above the metal, TRI L16C can be converted to a peptide that binds Cd^{II} exclusively as a four-coordinate CdS_3O complex. Clearly, small changes, even in such simple systems, can profoundly alter the energy landscape for a metalloprotein. As an example, further structural studies are required to understand why additional bulk from hexafluoroleucine above the metal leads to more water binding, whereas bulk within the plane of the metal fully excludes water from the center. Furthermore, these studies underscore an advantage of de novo design methods, as this technique allows us to employ nonnatural amino acids in our protein sequence readily. We expect that future studies with these peptides will help to unravel the mechanism of heavy-metal insertion into proteins, and may provide insight into metal trafficking in cells by metallochaperones.

Experimental Section

Peptide synthesis and purification: All the peptides of the TRI family except the fluorinated one were synthesized with Fmoc-protected (Fmoc = 9-fluorenylmethoxycarbonyl) amino acids by standard protocols on an ABI 433A automated synthesizer. Peptides were cleaved from the resin by stirring the mixture of trifluoroacetic acid (TFA), ethanedithiol, thioanisole, and anisole (90:3:5:2) at room temperature for 2 h. Peptide TRI L12Hfl/L16C was synthesized by using *t*Boc-protected (*t*Boc = *t*-butoxycarbonyl) amino acids for Merrifield solid-phase synthesis on 4-methylbenzhydrylamine (MBHA) resin. Coupling reactions were carried out manually with the in situ neutralization/HBTU protocol[25] on a 0.25 mM scale. The peptide was cleaved from the resin under vigorous HF conditions. The nonnatural fluorinated amino acid L-5,5,5,5′,5′,5′-hexafluoroleucine was synthesized as reported previously[23] and converted to *t*Boc-protected derivatives by standard procedures for *t*Boc solid-phase peptide synthesis. Peptides were dissolved in 10% acetic acid and purified by reversed-phase HPLC on a preparative C_{18} column, with a linear gradient from 0 to 90% acetonitrile containing 0.1% TFA. The identity of the peptides was proved by matrix-assisted laser desorption/ionization time-of-flight (MALDI-TOF) mass spectrometry and the purity was determined by analytical HPLC. The peptide concentrations were determined by Ellman's test.[32]

^{113}Cd NMR spectroscopy: ^{113}Cd NMR spectra were collected on a Varian UnityINOVA 500-MHz NMR spectrophotometer equipped with a 5-mm tunable broadband probe. $Cd(ClO_4)_2$ (0.1M) in D_2O was used as an external reference. All spectra were recorded at room temperature for 3 h. The ^{113}Cd–TRI peptide complexes were prepared by using $^{113}CdCl_2$ (95% enriched, Cambridge Isotopes). The complex solutions ($\approx$6 mM) were prepared in 10% D_2O without using a buffer solution. The pH values of the solutions were adjusted to 8.5 with KOH solution. All the spectra were generated from the free induction decays with the software MestRe-C.[33]

^{111m}Cd PAC spectroscopy: PAC experiments were carried out at a temperature of 1 ± 2 °C. The radioactive ^{111m}Cd solution (10–40 μL) was mixed with nonradioactive cadmium acetate and Tris buffer. The TRI family of peptides was then added to the ^{111m}Cd solution and the sample was left to equilibrate for 10 min to allow metal binding. Sucrose was added to produce a 55% (w/w) solution to reduce the Brownian tumbling of the molecules, and the pH was adjusted to 8.7 with H_2SO_4 and KOH. All buffers were purged with argon and treated to prevent metal contamination. The final volumes of the samples were from 0.05 to 0.5 mL with a concentration of 300 μM peptide and 20 mM Tris and a Cd^{II}/peptide ratio of 1:12. All fits were carried out with 400 data points, but the first three points were disregarded because of systematic errors.

Received: December 21, 2005
Published online: April 5, 2006

Keywords: amino acids · cadmium · coordination modes · metalloproteins · peptides

[1] P. T. Erskine, N. Senior, S. Awan, R. Lambert, G. Lewis, I. J. Tickle, M. Sarwar, P. Spencer, P. Thomas, M. J. Warren, P. M. Shoolingin-Jordan, S. P. Wood, J. B. Cooper, *J. Struct. Biol.* **1997**, *4*, 1025.
[2] P. T. Erskine, E. Norton, J. B. Cooper, R. Lambert, A. Coker, G. Lewis, P. Spencer, M. Sarwar, S. P. Wood, M. J. Warren, P. M. Shoolingin-Jordan, *Biochemistry* **1999**, *38*, 4266.
[3] M. J. Warren, J. B. Cooper, S. P. Wood, P. M. Shoolingin-Jordan, *Trends Biochem. Sci.* **1998**, *23*, 217.
[4] K.-H. Lee, M. Matzapetakis, S. Mitra, E. N. G. Marsh, V. L. Pecoraro, *J. Am. Chem. Soc.* **2004**, *126*, 9178.
[5] D. Ghosh, V. L. Pecoraro, *Inorg. Chem.* **2004**, *43*, 7902.
[6] M. R. Ghadiri, C. Soares, C. Choi, *J. Am. Chem. Soc.* **1992**, *114*, 825.
[7] D. R. Benson, B. R. Hart, X. Zhu, M. B. Doughty, *J. Am. Chem. Soc.* **1995**, *117*, 8502.
[8] B. T. Farrer, V. L. Pecoraro, *Proc. Natl. Acad. Sci. USA* **2003**, *100*, 3760.
[9] L. Regan, N. D. Clarke, *Biochemistry* **1990**, *29*, 10878.
[10] B. T. Farrer, C. McClure, J. E. Penner-Hahn, V. L. Pecoraro, *Inorg. Chem.* **2000**, *39*, 5422.
[11] S. Geremia, L. D. Costanzo, L. Randaccio, D. E. Engel, A. Lombardi, F. Nastri, W. F. DeGrado, *J. Am. Chem. Soc.* **2005**, *127*, 17266.
[12] G. Dieckmann, D. McRorie, J. D. Lear, K. A. Sharp, W. F. DeGrado, V. L. Pecoraro, *J. Mol. Biol.* **1998**, *280*, 897.
[13] M. F. Summers, *Coord. Chem. Rev.* **1988**, *86*, 43.
[14] L. Hemmingsen, K. N. Sas, E. Danielsen, *Chem. Rev.* **2004**, *104*, 4027.
[15] L. Hemmingsen, L. Olsen, J. Antony, S. P. A. Sauer, *J. Biol. Inorg. Chem.* **2004**, *9*, 591.
[16] S. P. Cramer, K. O. Hodgson, *Prog. Inorg. Chem.* **1979**, *26*, 1.
[17] M. Matzapetakis, B. T. Farrer, T.-C. Weng, L. Hemmingsen, J. E. Penner-Hahn, V. L. Pecoraro, *J. Am. Chem. Soc.* **2002**, *124*, 8042.
[18] L. Hemmingsen, C. Damblon, J. Antony, M. Jensen, H. W. Adoph, S. Wommer, G. C. K. Roberts, R. Bauer, *J. Am. Chem. Soc.* **2001**, *123*, 10329.
[19] C. E. Holloway, M. Melnik, *Main Group Met. Chem.* **1995**, *18*, 451.
[20] A.-K. Duhme, H. Strasdeit, *Z. Anorg. Allg. Chem.* **1999**, *625*, 6.
[21] K. Tang, X. Jin, S. Li, Z. Li, Y. Tang, *J. Coord. Chem.* **1994**, *31*, 305.
[22] E. S. Gruff, S. A. Koch, *J. Am. Chem. Soc.* **1990**, *112*, 1245.
[23] X. Q. Li, K. Suzuki, K. Kanaori, K. Tajima, A. Kashiwada, H. Hiroaki, D. Kohda, T. Tanaka, *Protein Sci.* **2000**, *9*, 1327.
[24] J. T. Anderson, P. L. Toogood, E. N. G. Marsh, *Org. Lett.* **2002**, *4*, 4281.
[25] M. Schnolzer, P. Alewood, A. Jones, D. Alewood, S. B. H. Kent, *Int. J. Pept. Protein Res.* **1992**, *40*, 180.
[26] K.-H. Lee, H.-Y. Lee, M. M. Slutsky, J. T. Anderson, E. N. G. Marsh, *Biochemistry* **2004**, *43*, 16277.
[27] Y. Tang, D. A. Tirrell, *J. Am. Chem. Soc.* **2001**, *123*, 11089.
[28] Y. Tang, G. Ghirlanda, W. A. Petka, T. Nakajima, W. F. DeGrado, D. A. Tirrell, *Angew. Chem.* **2001**, *113*, 1542; *Angew. Chem. Int. Ed.* **2001**, *40*, 1494.
[29] B. Bilgicer, X. Xing, K. Kumar, *J. Am. Chem. Soc.* **2001**, *123*, 11815.

 © 2006 Wiley-VCH Verlag GmbH & Co. KGaA, Weinheim

[30] D. Ghosh, K.-H. Lee, B. Demeler, V. L. Pecoraro, *Biochemistry* **2005**, *44*, 10732.
[31] A. K. Petros, S. E. Shaner, A. L. Costello, D. L. Tierney, B. R. Gibney, *Inorg. Chem.* **2004**, *43*, 4793.
[32] G. L. Ellman, *Arch. Biochem. Biophys.* **1959**, *82*, 70.
[33] C. Cobas, J. Cruces, F. J. Sardina, MestRe-C version 2.3, Universidad de Santiago de Compostela, Spain, **2000**.
[34] O. D. Monera, F. D Sonnichsen, L. Hicks, C. M. Kay, R. S. Hodges, *Protein Eng.* **1996**, *9*, 353.

 © 2006 Wiley-VCH Verlag GmbH & Co. KGaA, Weinheim

Ionic Resins

DOI: 10.1002/anie.200504580

Polyionic Gels: Efficient Heterogeneous Media for Metal Scavenging and Catalysis**

Carine Thiot, Marc Schmutz, Alain Wagner, and Charles Mioskowski**

Ionic liquids have attracted great attention as alternative reaction media in organic synthesis. These highly polar solvents often lead to enhanced reaction kinetics and product selectivity.[1] Comprehensive information about this field may be found in the excellent reviews by Welton,[2] Seddon,[3] and Keim.[4] However, despite promising and sometimes spectacular results, practical drawbacks, such as product isolation and recovery of the catalyst, are still important barriers to their widespread use in research and process chemistry. To benefit from the reactivity advantages offered by the polar ionic environments without suffering from the drawbacks, we investigated insoluble polyionic gels. Herein, we show that polyionic gel beads constitute a highly polar microenvironment, suitable for both efficient metal scavenging and active heterogeneous catalyst preparation.

[*] Dr. A. Wagner
Novalyst Discovery
23 Rue de Loess
67037 Strasbourg Cedex (France)
Fax: (+33) 3-8810-7226
E-mail: aw@novalyst.com
Dr. C. Thiot, Dr. C. Mioskowski
Université Louis Pasteur
Faculté de Pharmacie
74 Route du Rhin
67401 Illkirch-Graffenstaden (France)
Dr. M. Schmutz
ICS-CNRS UPR22
6 Rue de Boussingault
67083 Strasbourg Cedex (France)

[**] We thank the MENRT and the EEC network IBAAC for financial support, Polymer Laboratories Ltd. for the resins as gifts, and Prof. M. Reetz for helpful discussions.

Supporting information for this article is available on the WWW under http://www.angewandte.org or from the author.

A suspension of ionic gel **1**[5] was gently stirred at 30 °C in a solution (orange color) of $Pd(OAc)_2$ in dimethylformamide (DMF; 50 mg of $Pd(OAc)_2$ (20 μmol); 0.1 equivalent of Pd per ammonium unit in 0.5 mL of DMF). The orange supernatant became totally colorless after 30 min, whereas the polyionic resin became remarkably dark orange (Scheme 1). Bleaching of the supernatant did not occur in the control experiments using polystyrene (PS) and Merrifield resins **4** and **5**, respectively. This first observation clearly illustrates the high affinity of ionic gels for metal precursors.

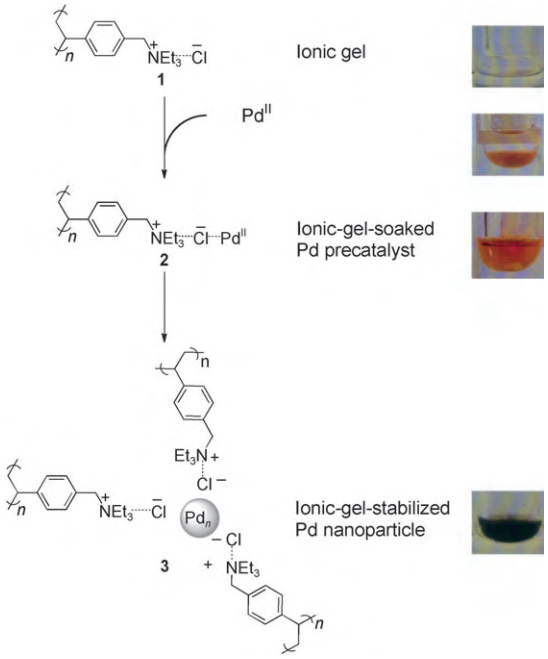

Scheme 1. Preparation of ionic-gel-stabilized Pd nanoparticles **3**.

The exact Pd content was determined for gels **4**, **5**, and the ionic gel **1**. The measured data are consistent with the qualitative observations. Gels that result from **4** and **5** showed a very low Pd content (0.01 and 0.07 mmol g^{-1}, respectively), whereas ionic gel **2** was found to have a significant Pd content. Indeed, the use of a 1:1 molar ratio of Pd/N^+ during the soaking process resulted in a high Pd content (1.25 mmol g^{-1}) for ionic gel **1**. In addition, a 1:10 ratio gave a loading of 0.13 mmol g^{-1}, which roughly corresponds to the total absorption of Pd in solution. Indeed, only traces of Pd were detected by inductively coupled plasma atomic emission spectrometric (ICP-AES) analysis of the supernatant (<0.5% of the initial Pd concentration in solution).

In the next step, the efficiency of the three gels as catalysts in a model Suzuki coupling reaction was evaluated.[6–8] Gels that resulted from **4** and **5** did not display any catalytic activity, whereas a high catalytic activity was observed (79% yield) for ionic gel **2**. Interestingly, during the coupling reaction, a color change of the polyionic gel from orange to black was observed after 30 minutes. Transmission electron microscopy (TEM) analysis of the gel after the reaction indicated the presence of colloidal Pd particles **3** (Figure 1a). The size of the particles ranged from 3 to 10 nm, with a mean

InterScience
© 2006 Wiley-VCH Verlag GmbH & Co. KGaA, Weinheim

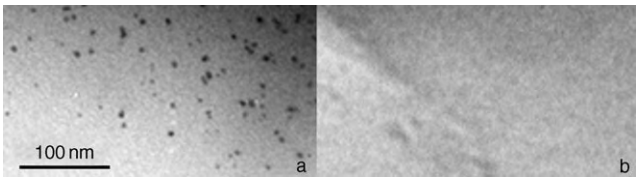

Figure 1. Representative TEM images. a) Ionic-gel-stabilized Pd nanoparticles **3** and b) ionic-gel-soaked Pd precatalyst **2** before reaction.

value of 4 ± 1 nm. No Pd nanoparticles were detected in resin **2** prior to the reaction (Figure 1b).

It appears that insoluble polyionic gels promote the formation of stabilized Pd nanoparticles during the Suzuki reaction. A similar phenomenon has already been described for homogeneous catalysts in the presence of ammonium salts. Indeed, chemical or electrochemical reduction of transition-metal salts leads to $R_4N^+X^-$-stabilized colloids. In addition, the formation of stabilized metal colloids in the presence of soluble ammonium salts was also observed in cross-coupling reactions.[9] Thus, these results confirm the similar behavior between the ionic gels and ionic solvents.

The gel-embedded Pd colloids, **3** which were preformed by heating resin **2** at 85 °C, showed a similar catalytic activity when engaged in the Suzuki coupling reaction. Heterogeneity tests were performed[10,11] to determine whether the Pd nanoparticles are actually the catalytically active species or they are a reservoir for more active soluble forms of Pd. Both a hot-filtration test and a three-phase test indicated that the catalysis is carried out by a heterogeneous Pd catalyst.[12] The catalyst was recycled for five cycles in the model Suzuki reaction. As expected, the catalytic activity of these preformed gel-embedded colloidal catalysts proved to be almost constant, as conversion starts at 77% and reaches 68% after five runs. ICP-AES analysis of the supernatant after the first run indicated the level of Pd to be 2 ppm, which corresponds to an original metal loss of less than 2%.

Interestingly, Kirschning and co-workers previously reported that Pd nanoparticles formed inside a monolithic glass/polymer composite by ion-exchange followed by a subsequent reduction are very active catalysts in hydrogenation and cross-coupling reactions.[13] In our case, it thus appears that strong non-covalent metal–ion interactions account for both very efficient metal scavenging and stabilization of catalytically active Pd colloids in the polyionic gel phase, as with the ionic liquids. In addition, such gels lead to stable catalysts of straightforward preparation and use. Indeed, these gels allow product isolation after the reaction by simple filtration and recovery of the ionic catalyst after washing. The pioneering work of Kirschning and co-workers and our results seem to indicate that the formation of dispersed and stabilized colloidal particles in an inert matrix could be a general approach to form highly active catalytic species.

Catalyst **2** was compared to standard homogeneous Pd catalytic systems and the commercially available polyurea-microencapsulated Pd catalysts (Pd EnCat), which were developed by Ley and co-workers[14] for the coupling of 1-bromo-4-butylbenzene and benzeneboronic acid (Table 1). A

Table 1: Comparison of catalytic activity.[a]

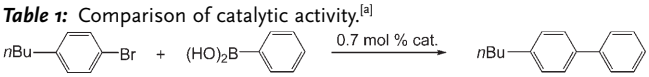

Entry	Catalyst	Yield [%][b]
1	$Pd(OAc)_2$	46
2	$Pd(OAc)_2/PPh_3$[c]	50
3	Pd EnCat TPP30	62
4	Pd^0 EnCat 30NP	48
5	$Pd(OAc)_2/NBu_4Cl$[d]	65
6	Pd **2**	79

[a] A solution of *n*BuPhBr (0.149 mmol), $PhB(OH)_2$ (0.179 mmol), and iPr_2NH (0.372 mmol) in $MeCN/H_2O$ (3:1 v/v; 4 mL) was heated at 85 °C for 6.5 h under argon. [b] Determined by GC-MS (internal standard: *trans*-decahydronaphthalene). [c] PPh_3 (2.1 mol%) was added. [d] NBu_4Cl (7.0 mol%) was added.

low yield (46%) of the coupling product was observed with homogeneous $Pd(OAc)_2$ (Table 1, entry 1) under our conditions (0.7 mol% Pd, $MeCN/H_2O$ (3:1 v/v), 85 °C, 6.5 h). The addition of PPh_3 (2.1 mol%) in the reaction media did not improve the yield significantly (Table 1, entry 2). The Pd EnCat catalyst with coencapsulated phosphine mediates a satisfactory yield (Table 1, entry 3), whereas, as described by Jeffery and David,[15] the presence of soluble ammonium salts (7.0 mol% NBu_4Cl) increased the yield (65%, Table 1, entry 5). The coupling reaction carried out with soaked Pd **2** occurred in 79% yield, thus confirming that polyionic gels provide a particularly appropriate environment for organometallic catalysis.

The soaking ability and catalytic activity of ionic gels should depend on both the strength of the ionic environment and the metal–ion interactions. Therefore, a series of ionic gels with various loadings, counteranions, and alkyl ammonium units were prepared (Table 2). To compare resins, we

Table 2: Structural variations in the ionic gels.[a]

Entry	R_3N	X	Pd [mmol g^{-1}]	Yield [%][b,c]	TOF [h^{-1}][d]
1	Et_3N	Cl	0.13	79	526
2	Et_3N	Br	0.10	75	554
3	Et_3N	F	0.10	67	530
4	Et_3N	AcO	0.09	78	590
5	Et_3N	PF_6	0.04	45	349
6	Oct_3N	Cl	0.08	86	612

[a] A solution of *n*BuPhBr (0.149 mmol), $PhB(OH)_2$ (0.179 mmol), and iPr_2NH (0.372 mmol) in $MeCN/H_2O$ (3:1 v/v; 4 mL) was heated in the presence of catalyst (0.7 mol% of Pd) at 85 °C for 6.5 h under argon. [b] Determined by GC-MS (internal standard: *trans*-decahydronaphthalene). [c] The reactions were carried out in triplicate, with a standard deviation of ± 2%. [d] TOF was measured at a 25% mean yield.

defined their metal-soaking ability as the capacity of the resins to absorb a metal in solution. This metal-soaking ability is given in units of mmol g^{-1} and is determined by elemental analysis. The Pd/N^+ molar ratio used for the soaking process was maintained at 1:10 and the standard amount of Pd in catalytic reactions at 0.7 mol%.

All the halide counteranions showed a very similar scavenging abilities and catalytic activities (Table 2,

 © 2006 Wiley-VCH Verlag GmbH & Co. KGaA, Weinheim

entries 1–3). As expected, a non-coordinating anion, such as hexafluorophosphate, led to a weaker metal absorption (Pd content was 0.04 mmol g^{-1}, relative to the theoretical value of 0.09 mmol g^{-1}) and a lower catalytic activity (turnover frequency (TOF) = 349 h^{-1}, Table 2, entry 5). The catalytic activity was affected by both the structure of the ammonium unit and the strength of the ionic environment. A lipophilic ammonium group (Table 2, entry 6) displayed both a very good soaking ability (Pd content = 0.08 mmol g^{-1}, which corresponds to a total absorption of Pd) and an enhanced catalytic activity (TOF = 612 h^{-1}). Increasing the loading of the ammonium group led to improved soaking ability, yield of coupling product, and TOF (when starting from a highly loaded Merrifield resin of 4.30 mmol g^{-1}, the Pd content was found to be 0.24 mmol g^{-1}, thus affording a yield of 84% and a TOF of 724 h^{-1}). These results indicate that as expected the catalyst reactivity can be fine-tuned by adjusting the structure and the loading of the ionic gel.

Finally, a series of aryl halides and boronic acids were employed to investigate the scope of the reaction (Table 3). In all cases, after completion of the reaction according to TLC analysis, (6.5 h, 85 °C) the catalyst was removed by filtration, the filtrate was concentrated under reduced pressure, and the crude product purified by chromatography on silica gel. The catalytic system **2** proved to be effective for a wide combination of aryl bromides and boronic acids (electron-rich, electron-deficient, and highly functionalized bromoarenes and boronic acids). In particular, the primary amine function is compatible with the coupling conditions (Table 3, entries 4 and 7).

Table 3: Pd^{II}-catalyzed Suzuki cross-coupling reactions of aryl bromides.[a]

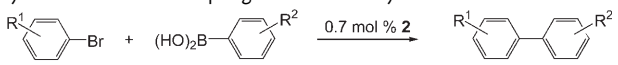

Entry	(Hetero)aryl bromide	(Hetero)aryl boronic acid	Product	Yield [%][b]
1	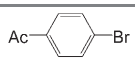	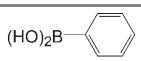	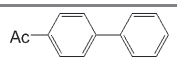	95
2	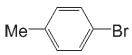	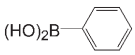	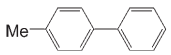	95
3	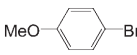	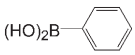	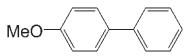	80
4	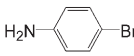	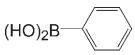	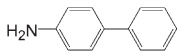	95
5	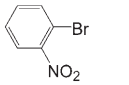	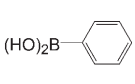	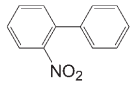	90
6	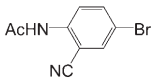	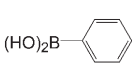	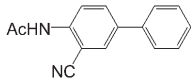	85
7	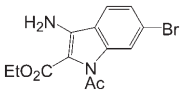	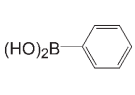	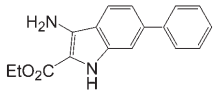	76
8	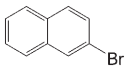	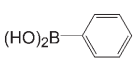	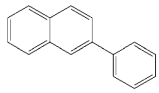	90
9	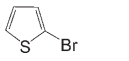	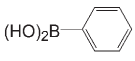	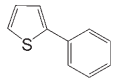	95
10	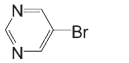	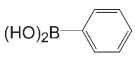	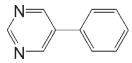	96
11	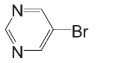	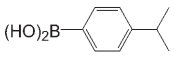	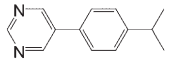	96
12	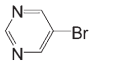	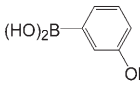	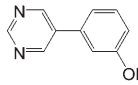	95
13	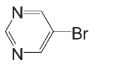	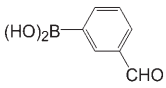	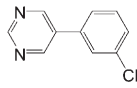	77
14	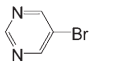	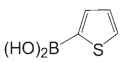	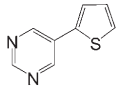	92

[a] A solution of aryl bromide (0.149 mmol), boronic acid (0.179 mmol), and iPr_2NH (0.372 mmol) in $MeCN/H_2O$ (1:3 v/v; 4 mL) was heated in the presence of **2** (Pd content = 0.7 mol%) at 85 °C for 6.5 h under argon. [b] Yield of the isolated product.

To further investigate the scope of the scavenging ability and catalytic efficiency of polyionic gels, Rh-soaked catalyst **6** was prepared from the ionic gel **1** and the Wilkinson precursor, using the straightforward procedure described above (Rh/N^+ = 1:10). The resulting gel (Rh content = 0.11 mmol g^{-1}) was tested in the hydrosilylation of phenylacetylene (**7**) with diethoxymethylsilane. The reaction proceeded with regio- and stereoselectivities to afford the (*E*)-1-silyl-1-alkene **8** in 89% yield, no *Z* isomer was observed by ^1H NMR spectroscopic analysis of the crude reaction mixture (Scheme 2). Our ionic gel-soaked catalyst proved to be almost as active and selective as its homogeneous counterpart, which afforded the *E* isomer **8** in 98% yield.[16] It thus indicated that catalyst preparation by metal soaking into an ionic gel can be extended to other classes of organometallic complexes.

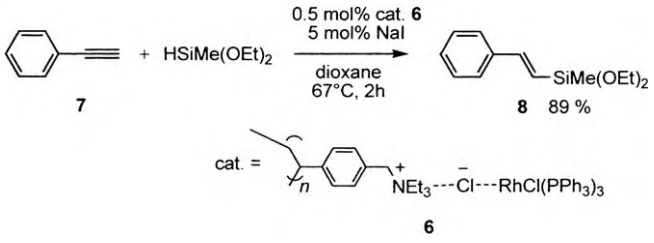

Scheme 2. Rhodium-catalyzed hydrosilylation of phenylacetylene **7**.

 © 2006 Wiley-VCH Verlag GmbH & Co. KGaA, Weinheim

In summary, we have shown that polyionic gels represent a viable alternative to ionic liquids as reaction media for recyclable heterogeneous catalytic systems. They display an efficient metal-soaking ability, which relies on strong non-covalent interactions between metal and ions within the polyionic gel. They provide a favorable and stabilizing environment for the generation of active heterogeneous metal-based catalytic systems. Further studies for the preparation of other catalytic systems and selective metal sponges are currently under investigation.

Experimental Section

Preparation of polyionic gel **1**: A Merrifield-type resin (5 g, 7.91 mmol, 1.58 mmol Cl g^{-1}) was placed into a 100-mL scintillation vial followed by toluene/MeCN (50 mL, 1:1 v/v). The vial was shaken for 15 min, triethylamine (11 mL, 79.82 mmol, 10 equiv) was added, and the reaction mixture was agitated at 80 °C for 3 days. The reaction mixture was poured into a fritted funnel, and the resin was washed successively with MeOH/CH_2Cl_2 (3 × 50 mL) and Et_2O (2 × 50 mL). The resin was transferred into a vial and dried under vacuum to give polyionic gel **1** (5.47 g). The loading was determined to be 1.37 mmol g^{-1} by microanalysis.

Preparation of polyionic gel precatalyst **2**: Polyionic gel **1** (500 mg, 0.681 mmol, 1.37 mmol g^{-1}) and DMF (4 mL) were added to a 10-mL reaction vessel with a stir bar. After the resin had been mixed for 10 min (agitation conditions: mix every 3.5 s, upstroke = 2.2 s, upward = 65 %), a solution of $Pd(OAc)_2$ (15.3 mg, 0.068 mmol, 0.1 equiv) in DMF (8 mL) was added. The resulting mixture was then mixed for 20.5 h at 30 °C. The solution was drained, and the orange beads were successively washed with DMF (2 × 4 mL), EtOH/CH_2Cl_2 (3 × 4 mL), and Et_2O (2 × 4 mL). Air was used to dry the beads before they were transferred to a vial and dried under vacuum to afford the ionic-gel precatalyst **2** (390 mg, 0.15 mmol Pd g^{-1} by microanalysis).

A representative Suzuki-type coupling reaction with the polyionic gel precatalyst **2**: 1-Bromo-4-butylbenzene (26.3 μL, 0.149 mmol, 1 equiv) was added to an agitating mixture (agitation conditions: mix every 3.5 s, upstroke = 2.2 s, upward = 65 %) of precatalyst **2** (7 mg, 1.05 μmol, 0.15 mmol Pd g^{-1}), benzeneboronic acid (21.8 mg, 0.179 mmol, 1.2 equiv), and *i*Pr_2NH (54.6 μL, 0.372 mmol, 2.5 equiv) in a MeCN/H_2O (4 mL, 3:1 v/v). After the addition, the reaction mixture was allowed to agitate for 6.5 h at 85 °C. The reaction mixture was then drained, the resin washed with acetonitrile (2 × 4 mL), and the filtrate washed with brine. The organic layer was extracted with EtOAc (3 × 4 mL), dried over Na_2SO_4, and concentrated under reduced pressure. A 79 % yield was determined by GC mass-spectroscopic analysis using *trans*-decahydronaphthalene as the internal standard.

Received: December 23, 2005
Published online: March 28, 2006

Keywords: C–C coupling · heterogeneous catalysis · ionic resins · metal scavengers · palladium

[1] a) R. Sheldon, *Chem. Commun.* **2001**, 2399; b) J. Dupont, R. F. De Souza, P. A. Z. Suarez, *Chem. Rev.* **2002**, *102*, 3667.
[2] T. Welton, *Chem. Rev.* **1999**, *99*, 2071.
[3] J. D. Holbrey, K. R. Seddon, *Clean Prod. Process.* **1999**, *1*, 223.
[4] P. Wasserscheid, W. Keim, *Angew. Chem.* **2000**, *112*, 3926; *Angew. Chem. Int. Ed.* **2000**, *39*, 3772.
[5] Some ammonium resins are commercially available from Polymer Laboratories Ltd., Senn Chemicals, or other suppliers; however to access a wider range of loading, cross-linking, resin type, and ammonium groups, we preferred to prepare them from commercially available Merrifield resins. A typical polymeric ammonium gel **1** was prepared by heating a chloromethyl resin **5** (1.58 mmol g^{-1}) with an excess of triethylamine (10 equiv) at 80 °C for 3 days in toluene/MeCN (1:1).
[6] a) N. Miyaura, A. Suzuki, *Chem. Rev.* **1995**, *95*, 2457, and references therein; b) A. Suzuki, *J. Organomet. Chem.* **1999**, *576*, 147.
[7] For Suzuki reactions in ionic liquids, see: a) W. Miao, T. H. Chan, *Org. Lett.* **2003**, *5*, 5003; b) C. J. Mathews, P. J. Smith, T. Welton, *J. Mol. Catal. A* **2004**, *214*, 27.
[8] In MeCN/H_2O (3:1 v/v), *n*BuPhBr (1 equiv), $PhB(OH)_2$ (1.2 equiv), *i*Pr_2NH (2.5 equiv), and **2** (0.7 mol %) under Ar at 85 °C for 6.5 h.
[9] a) J. Kiwi M. Grätzel, *J. Am. Chem. Soc.* **1979**, *101*, 7214; b) M. T. Reetz, E. Westermann, *Angew. Chem.* **2000**, *112*, 170; *Angew. Chem. Int. Ed.* **2000**, *39*, 165; c) X.-D. Mu, J.-Q. Meng, Z.-C. Li, Y. Kou, *J. Am. Chem. Soc.* **2005**, *127*, 9694.
[10] a) Y. Li, X. M. Hong, D. M. Collard, M. A. El Sayed, *Org. Lett.* **2000**, *2*, 2385; b) B. M. Choudary, S. Madhi, N. S. Chowdary, M. L. Kantam, B. Sreedhar, *J. Am. Chem. Soc.* **2002**, *124*, 14127; c) C. M. Crudden, M. Sateesh, R. Lewis, *J. Am. Chem. Soc.* **2005**, *127*, 10045.
[11] a) M. T. Reetz, G. Lohmer, *Chem. Commun.* **1996**, 1921; b) A. H. M. De Vries, J. M. C. A. Mulders, J. H. M. Mommers, H. J. W. Henderickx, J. G. De Vries, *Org. Lett.* **2003**, *5*, 3285; c) C. C. Cassol, A. P. Umpierre, G. Machado, S. I. Wolke, J. Dupont, *J. Am. Chem. Soc.* **2005**, *127*, 3298; d) V. Calo, A. Nacci, A. Monopoli, F. Montingelli, *J. Org. Chem.* **2005**, *70*, 6040.
[12] a) R. A. Sheldon, M. Wallau, I. W. C. E. Arends, U. Schuchardt, *Acc. Chem. Res.* **1998**, *31*, 485; b) J. Rebek, F. Gavina, *J. Am. Chem. Soc.* **1974**, *96*, 7112; c) J. Rebek, D. Brown, S. Zimmerman, *J. Am. Chem. Soc.* **1975**, *97*, 454.
[13] a) A. Kirschning, G. Jas, *Top. Curr. Chem.* **2004**, *242*, 209; b) G. Jas, A. Kirschning, *Chem. Eur. J.* **2003**, *9*, 5708; c) U. Kunz, H. Schönfeld, A. Kirschning, W. Solodenko, *J. Chromatogr. A.* **2003**, 1006, 241; d) W. Solodenko, H. Wen, S. Leue, F. Stuhlmann, G. Argirusi, H. Jas, H. Schönfeld, U. Kunz, A. Kirschning, *Eur. J. Org. Chem.* **2004**, 3601.
[14] a) C. Ramarao, S. V. Ley, S. C. Smith, I. M. Shirley, N. De Almerda, *Chem. Commun.* **2002**, 1132; b) N. Bremeyer, S. V. Ley, C. Ramarao, M. Shirley, S. C. Smith, *Synlett* **2002**, 1843; c) J. Q. Yu, H. C. Wu, C. Ramarao, J. B. Spencer, S. V. Ley, *Chem. Commun.* **2003**, 678; d) S. V. Ley, C. Mitchell, D. Pears, C. Ramarao, J. Q. Yu, W. Zhou, *Org. Lett.* **2003**, *5*, 4665.
[15] a) T. Jeffery, *Tetrahedron* **1996**, *52*, 10113; b) T. Jeffery, M. David, *Tetrahedron Lett.* **1998**, *39*, 5751.
[16] a) A. Mori, E. Takahisa, H. Kajiro, K. Hirabayashi, Y. Nishihara, T. Hiyama, *Chem. Lett.* **1998**, 443.

 © 2006 Wiley-VCH Verlag GmbH & Co. KGaA, Weinheim

Alumoxanes

DOI: 10.1002/anie.200504414

Efficient Route to Tetramethylalumoxane and Carboxylate Alumoxanes through the Alkylation of Phthalic Acid**

Janusz Lewiński, Wojciech Bury, Iwona Justyniak,* and Janusz Lipkowski*

Dedicated to Professor Herbert W. Roesky on the occasion of his 70th birthday

The chemistry of alumoxanes and organoaluminum carboxylates has been under investigation in the last few decades, and in some ways, studies on these two quite different entities have often overlapped. Alumoxanes are attracting attention as highly active catalysts or co-catalysts as a result of their importance for the polymerization of a wide range of organic monomers, and initial studies into these systems trace back to the end of the 1950s.[1] Renewed interest in alkylalumoxanes was generated in the 1980s primarily from the work of Kaminsky and co-workers.[2] Most commonly, alumoxanes of general formula $(R_2AlOAlR_2)_n$ or $(RAlO)_n$ are formed by the controlled hydrolysis of alkylaluminum compounds.[3] However, a number of alternative routes have also been investigated which are essentially based on reactions of trialkylaluminum compounds with oxygen-containing inorganic or organic compounds,[4] including preparation by the alkylation of aluminum carboxylates.[5] Organoaluminum carboxylates and particularly carboxylate alumoxanes are very useful precursors in materials science.[6] The synthesis of well-defined carboxylate-substituted alumoxanes has been nicely developed by Barron and co-workers, who employed the traditional synthetic route from alumoxanes and carboxylic acids as well as a "top-down" approach from boehmite and carboxylic acids.[6c,7]

Despite long-lasting studies, there is a relative paucity of structural data for both classes of compounds. The exact composition and structure of alumoxanes featuring short-chain alkyl substituents are still not entirely clear because of the presence of multiple equilibria and rapid exchange reactions. The reported structures for simple systems are limited only to the anionic species $[Al_7O_6Me_{16}]^-$[4a] and $[(Me_2AlOAlMe_3)_2]^{2-}$.[4b] The significant steps in determining the structure of alumoxane species have been achieved by Barron and co-workers. The authors, by employing sterically demanding *tert*-butylaluminum derivatives, structurally authenticated the first tetraalkylalumoxane $[(tBu_2AlOAltBu_2)_2]$, its Lewis acid/base adduct with pyridine $[tBu_2(py)AlOAltBu_2(py)]$ (structure **I**), and a series of

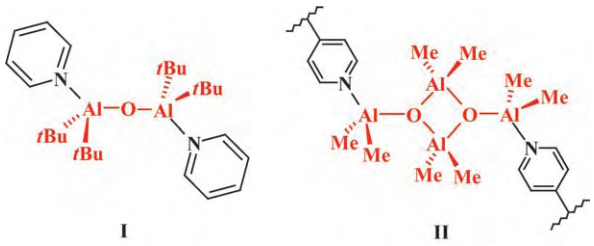

I II

$[(tBuAlO)_n]$ cage clusters.[3b,8] With regard to the study described herein, it is also pertinent to note that Pasynkiewicz and co-workers extensively studied the solution structures of tetramethylalumoxane and its adducts with monodentate and bidentate Lewis bases. Based on spectroscopic data, the authors postulated the formation of various monomeric or oligomeric alumoxane species supported by benzonitrile or *N,N,N′N′*-tetramethylethylenediamine ligands.[9] More recently, in the course of numerous investigations of the hydrolysis of alkylaluminum compounds and other reaction systems, several interesting alumoxanes (or alumoxane units involved in organometallic cluster backbones) have been isolated and structurally characterized.[4b,e,f,h] Particularly noteworthy are the achievements of Roesky and co-workers, whereby sterically encumbering β-diketiminates were used as supporting ligands for alumoxane units.[10] The first crystallographic evidence for organoaluminum carboxylate species was given by Atwood and co-workers with the structural determination of $[MeCO_2(AlMe_3)_2]^-$.[11] More recently, dialkylaluminum monocarboxylates[12] and a series of alkylaluminum compounds that were derived from bifunctional carboxylic acids have been crystallographically characterized.[5b,13] The latter studies by several research groups have provided a variety of novel multinuclear clusters, and subsequent discoveries indicate that the chemistry of aluminum carboxylates remains largely unexplored.

In the course of our investigations on the effect of both the metal-bound alkyl group and the organic residue on the structure of Group 13 carboxylates, we have revealed an alkylation of the carboxylate group of glycine with concomitant methylalumoxane $(MAO)_n$ formation in the reaction with $AlMe_3$.[5b] However, in the analogous reaction system involving anthranilic acid, the carboxylate group of the aromatic acid appeared resistant to C-alkylation.[5b] These findings have prompted our study on the reaction of phthalic acid with an excess of $AlMe_3$, and herein we report on the effective non-hydrolytic synthesis of tetramethylalumoxane and novel carboxylate-substituted alumoxanes. In addition, we demonstrate that alumoxanes and carboxylate alumox-

[*] Dr. J. Lewiński, W. Bury
Department of Chemistry
Warsaw University of Technology
Noakowskiego 3, 00-664 Warsaw (Poland)
Fax: (+48) 22-6607-279
E-mail: lewin@ch.pw.edu.pl
Dr. I. Justyniak, Prof. Dr. J. Lipkowski
Institute of Physical Chemistry
Polish Academy of Sciences
Kasprzaka 44/52, 01-224 Warsaw (Poland)
Fax: (+48) 22-343-3333
E-mail: iwonaj@ichf.edu.pl

[**] This work was supported by the State Committee for Scientific Research (Grant No. 3T08E05327).

InterScience
© 2006 Wiley-VCH Verlag GmbH & Co. KGaA, Weinheim

anes can be successfully utilized as secondary building units in the construction of extended assemblies (structural motif **II**).

Addition of two equivalents of $AlMe_3$ to phthalic acid resulted in the quantitative formation of the tetranuclear adduct $[\{(AlMe_2)_2(\mu\text{-}O_2C)_2\text{-}1,2\text{-}C_6H_4\}_2]$ (**1**).[13b] However, an excess of $AlMe_3$ dramatically changes the distribution and structure of the products, as depicted in Scheme 1. The reaction of phthalic acid with three equivalents of $AlMe_3$ proceeded with a color change of the solution from colorless to yellow after four hours, which was accompanied by the appearance of signals attributed to carbon-bound methyl groups in the aliphatic region of the ^1H NMR spectrum of the reaction mixture. These new resonances are indicative of C-methylation of the carboxylate group. Subsequent addition of 0.5 equivalents of 1,2-bis(4-pyridyl)ethane to the reaction mixture at ambient temperature resulted in slow deposition of colorless crystals of the novel carboxylate alumoxane **2** (path a, Scheme 1). Interestingly, analysis of the reaction mixture confirmed the conversion of approximately half of an equivalent of phthalic acid into 3,3-dimethyl-2-benzofuran-1(3*H*)-one (**A**).[14] Thus, the additional equivalent of $AlMe_3$ leads to C-alkylation of the carboxylate group with the concomitant formation of the cyclic ester **A** and tetramethylalumoxane, and the latter alumoxane species is subsequently trapped by unreacted **1**. The ^1H NMR spectrum of **2** supports this formulation (see Experimental Section).

Compound **2** crystallized as a monomer with C_1 symmetry (Figure 1). The structure consists of a hexanuclear cluster in which two tetramethylalumoxane moieties are entrapped by the monomeric subunit of the alkylaluminumphthalate **1**, and is completed by the 1,2-bis(4-pyridyl)ethane ligand, which links the alumoxane Al centers to afford a 22-membered macrocyclic ring system. An alternative view of the composition of **2** is as a carboxylate alumoxane consisting of two tetramethylalumoxane moieties which are mounted on the phthalic acid carboxylate group and bridged by the dicationic $\{Me_2Al{-}NC_5H_4(CH_2CH_2)C_5H_4N{-}AlMe_2\}^{2+}$ spacer. Thus, the carboxylate groups act as bridging ligands between the two dimethylaluminum units of each alumoxane moiety, and the observed coordination mode confirms a high affinity of the carboxylate group toward the {AlOAl} unit.[7] The geometry of the $\{Al_3(\mu_3\text{-}O)\}$ moiety deviates slightly from planarity, with the oxygen atoms positioned above the plane defined by the aluminum atoms (average distance from the O atom to the Al_3 plane: 0.157 Å). The Al–O bond lengths involving the oxo oxygen atom are essentially equal (average: 1.808 Å) and are slightly shorter than the carboxylate Al–O bond lengths (average: 1.867 Å). The 1,2-bis(4-pyridyl)ethane ligand adopts a *gauche* conformation with a dihedral angle of 48.74° between the phenyl rings.

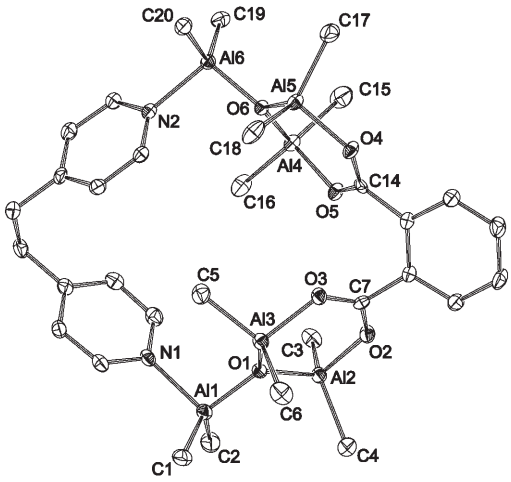

Figure 1. Molecular structure of **2** with thermal ellipsoids drawn at the 30% probability level. Hydrogen atoms are omitted for clarity. Selected bond lengths [Å] and angles [°]: Al1-O1 1.801(2), Al2-O1 1.809(2), Al3-O1 1.810(2), Al1-N1 1.988(3), Al2-O2 1.871(2), Al3-O3 1.863(2), Al4-O6 1.810(2), Al4-O5 1.864(2), Al5-O6 1.810(2), Al5-O4 1.867(2), Al6-O6 1.803(2), Al6-N2 1.984(2); Al1-O1-Al2 117.69(11), Al1-O1-Al3 119.09(10), Al2-O1-Al3 121.05(11), Al6-O6-Al4 120.63(10), Al6-O6-Al5 116.43(11), Al4-O6-Al5 120.60(11).

Similar treatment of phthalic acid with four equivalents of $AlMe_3$ in CH_2Cl_2 for 24 hours followed by addition of one equivalent of 1,2-bis(4-pyridyl)ethane afforded the crystalline Lewis acid/base tetramethylalumoxane/bipyridine adduct **3** and the cyclic ester **A** in good yield (path b,

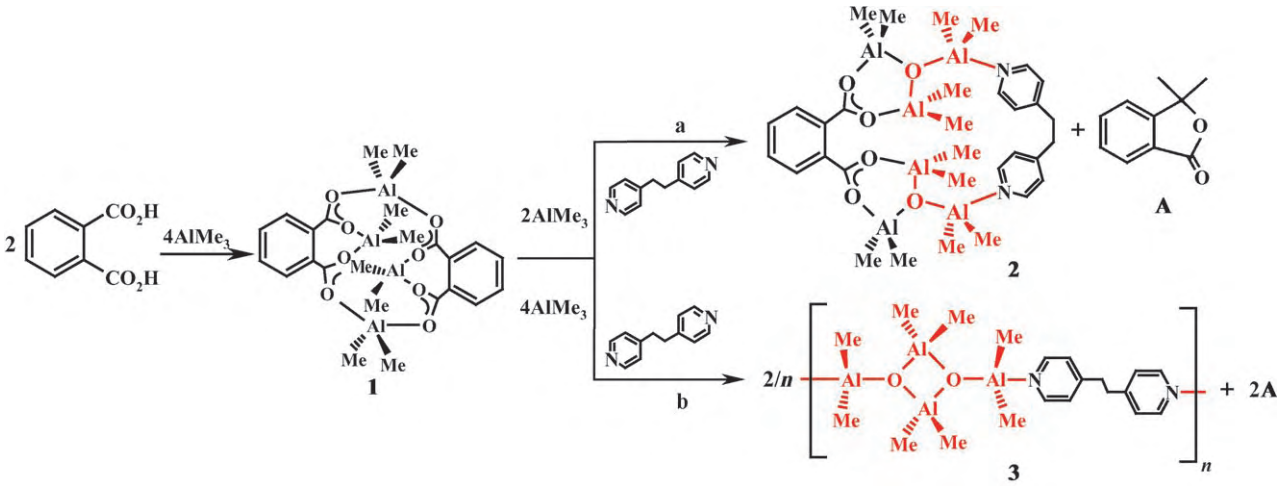

Scheme 1. Synthesis of **2** (path a) and **3** (path b).

© 2006 Wiley-VCH Verlag GmbH & Co. KGaA, Weinheim

Scheme 1). Strikingly, when phthalic acid was treated with more than four equivalents of $AlMe_3$ under similar conditions, the alkylation of the second carboxylic group was not observed. Moreover, our attempts to convert **2** into **3** failed; the addition of one equivalent of $AlMe_3$ to **2** in CH_2Cl_2 resulted in the formation of the Lewis acid adduct [{1,2-bis(4-pyridyl)ethane}$(AlMe_3)_2$], which retarded further transformations.[15] Compound **3** was characterized spectroscopically, and its molecular structure was determined by X-ray crystallography. The structural analysis of **3** revealed an unprecedented zigzag coordination polymer resulting from self-assembly of the dimeric $\{Me_2Al(\mu\text{-}O)AlMe_2\}_2$ alumoxane units with the bipyridine spacer in an *anti* conformation (Figures 2 and 3). Thus, 1,2-bis(4-pyridyl)ethane is a very flexible ligand that may act as a spacer in both an intra- and intermolecular fashion. The $\{Al_3(\mu_3\text{-}O)\}$ alumoxane moieties in **3**, in contrast to those in **2**, are planar. The Al–O bond lengths (average: 1.828 Å) are slightly longer than those observed in **2**, and the Al–N bond lengths are comparable to those in **2**. Compound **3** represents the first example of a structurally characterized tetramethylalumoxane species.

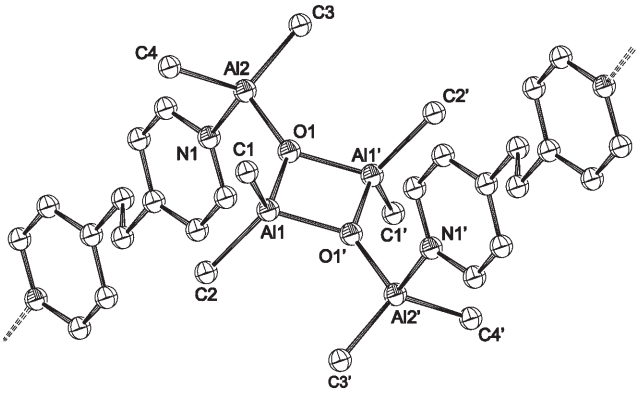

Figure 2. Molecular structure of **3** with thermal ellipsoids drawn at the 30% probability level. Hydrogen atoms are omitted for clarity. The atoms which are labeled with a prime (′) are at symmetry-equivalent positions ($-x$, $-y$, $-z+1$). Selected bond lengths [Å] and angles [°]: Al1-O1 1.831(5), Al1-O1′ 1.828(5), Al1-C1 1.966(7), Al1-C2 1.985(7), Al2-O1 1.761(5), Al2-C3 1.954(8), Al2-C4 1.946(7), Al2-N1 2.001(6); O1-Al1-O1′ 85.6(2), Al1-O1-Al1′ 94.4(2), C1-Al1-C2 113.3(3), O1-Al2-N1 101.7(2), C4-Al2-C3 119.2(3), Al2-O1-Al1′ 132.4(3), Al2-O1-Al1 133.1(3).

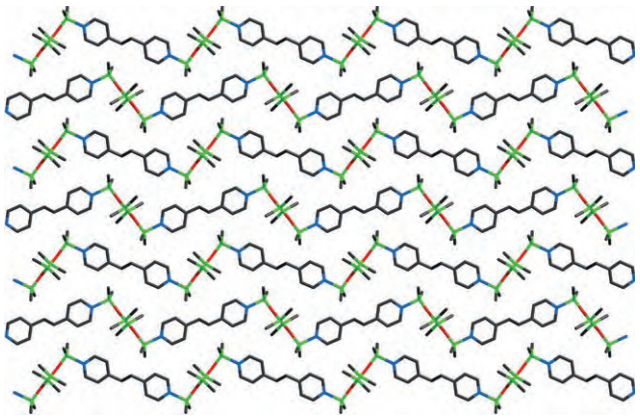

Figure 3. Crystal structure of **3** viewed along the *a* axis. The solvent molecules and hydrogen atoms are omitted for clarity.

In conclusion, we have provided an efficient route to tetramethylalumoxane moieties and carboxylate-substituted alumoxanes by the reaction of phthalic acid with $AlMe_3$. This simple method for accessing these important classes of compounds opens new opportunities to probe their reaction chemistry. In addition, we have demonstrated that alumoxanes can act as secondary building units in the construction of extended macrocyclic assemblies or functional coordination networks, which would be of interest in catalysis and materials science.

Experimental Section

2: $AlMe_3$ (0.216 g, 3.00 mmol) was added to a solution of phthalic acid (0.166 g, 1.00 mmol) in CH_2Cl_2 (7 mL) at −78 °C. The reaction mixture was allowed to warm to room temperature with stirring. After 24 h, a solution of 1,2-bis(4-pyridyl)ethane (0.092 g, 0.50 mmol) in toluene (4 mL) was added. The solution was concentrated, and small block-shaped crystals were obtained upon overnight storage at 0 °C. Compound **2** is insoluble in aromatic solvents and THF, and is sparingly soluble in CH_2Cl_2. Yield: 0.275 g (76%); ^{1}H NMR (400 MHz, CD_2Cl_2): $\delta = -0.99$ (s, 24H, $AlCH_3$), −0.57 (s, 12H, $AlCH_3$), 3.17 (s, 4H, CH_2), 7.21 (d, $J = 5.9$ Hz, 4H, Ar), 7.65 (q, $J = 2.9$ Hz, 2H, Ar), 7.81 (q, $J = 2.9$ Hz, 2H, Ar), 8.47 ppm (d, $J = 6.6$ Hz, 4H, Ar); ^{27}Al NMR: no signals could be observed; IR (nujol): $\tilde{\nu} =$ 1625(m), 1602(m), 1575(s), 1507(m), 1495(m), 1457(s), 1378(s), 1194(m), 1068(m), 1043(m), 826(m), 727(s), 696(s), 655(m). Elemental analysis (%) calcd for $C_{32}H_{52}Al_6N_2O_6$: C 53.18, H 7.25, N 3.88; found: C 53.23, H 7.31, N 3.84 (sample was dried in vacuo for 10 h).

3: The reaction was carried out according to the same procedure as described for **2** by using $AlMe_3$ (0.288 g, 4.00 mmol) and phthalic acid (0.166 g, 1.00 mmol) in CH_2Cl_2 (7 mL). After 24 h, a solution of 1,2-bis(4-pyridyl)ethane (0.184 g, 1.00 mmol) in CH_2Cl_2 (4 mL) was added, and the solution was stirred for an additional 30 minutes. The volatiles were then removed under reduced pressure, and the amorphous residue was dissolved in hot THF (7 mL). After the solution had stood overnight at 0 °C, colorless square-shaped crystals were formed. Yield: 0.387 g (87%); ^{1}H NMR (400 MHz, [D$_8$]THF): $\delta = -1.03$ (s, 12H, $AlCH_3$), −0.81 (s, 12H, $AlCH_3$), 2.98 (s, 4H, CH_2), 7.19 (d, $J = 5.1$ Hz, 4H, Ar), 8.44 ppm (d, $J = 5.9$ Hz, 4H, Ar); ^{27}Al NMR: no signal could be observed; IR (nujol): $\tilde{\nu} =$ 1622(m), 1606(m), 1559(m), 1461(s), 1377(s), 1193(m), 1068(m), 1036(m), 836(m br), 790(m br), 720(m br). Elemental analysis (%) calcd for $C_{20}H_{36}Al_4N_2O_2$: C 54.05, H 8.16, N 6.30; found: C 54.01, H 8.21, N 6.28 (sample was dried in vacuo for 10 h).

Crystal data for **2**·toluene, $C_{39}H_{60}Al_6N_2O_6$: $M_r = 814.77$, crystal dimensions $0.50 \times 0.30 \times 0.20$ mm^3, monoclinic, space group $P2_1/c$ (no. 14), $a = 12.6314(3)$, $b = 22.0489(6)$, $c = 20.1576(3)$ Å, $\beta = 123.911(2)°$, $V = 4659.15(19)$ Å^3, $Z = 4$, $F(000) = 1736$, $\rho_{calcd} = 1.162$ g cm^{-3}, $\theta_{max} = 21°$, $R_1 = 0.0427$, $wR_2 = 0.0896$ for 4191 reflections with $I_o > 2\sigma(I_o)$. The structure was solved by direct methods by using the program SHELXS-97[16] and was refined by full-matrix least squares on F^2 with the program SHELXL-97.[17] H atoms were included in idealized positions and refined isotropically. Crystal data for **3**·2THF, $C_{28}H_{52}Al_4N_2O_4$: $M_r = 588.76$, crystal dimensions $0.40 \times 0.30 \times 0.25$ mm^3, monoclinic, space group $P2_1/n$ (no. 14), $a = 9.0731(18)$, $b = 11.6608(13)$, $c = 16.172(3)$ Å, $\beta = 96.752(6)°$, $V = 1702.1(5)$ Å^3, $Z = 2$, $F(000) = 636$, $\rho_{calcd} = 1.149$ g cm^{-3}, $\theta_{max} = 22.71°$. Several attempts to isolate suitable single crystals resulted only in twinned crystals. The structure was solved by direct methods by using the program SHELXS-97[16] and was refined by full-matrix least squares on F^2, including intensities of superimposed reflections of the

 © 2006 Wiley-VCH Verlag GmbH & Co. KGaA, Weinheim

twin, with the program SHELXL-97.[17] The refined fractional contribution of the minor twin component was 0.365(2). H atoms were included in idealized positions and refined isotropically. Final R indices: $R_1 = 0.0912$, $wR_2 = 0.2350$ for 1569 reflections with $I_o > 2\sigma(I_o)$. CCDC-292582 (**2**) and CCDC-292583 (**3**) contain the supplementary crystallographic data for this paper. These data can be obtained free of charge from The Cambridge Crystallographic Data Centre via www.ccdc.cam.ac.uk/data_request/cif.

Received: December 12, 2005
Revised: January 12, 2006

Keywords: alkylation · aluminum · alumoxanes · carboxylate ligands · coordination polymers

[1] a) R. O. Colclough, *J. Polym. Sci.* **1959**, *34*, 178; b) R. O. Colclough, G. Gee, A. H. Jagger, *J. Polym. Sci.* **1960**, *48*, 273; c) E. J. Vandenberg, *J. Polym. Sci.* **1960**, *47*, 489; d) T. Saegusa, Y. Fujii, H. Fujii, J. Furukawa, *Makromol. Chem.* **1962**, *55*, 232; e) S. I. Ishida, *J. Polym. Sci.* **1962**, *62*, 1; f) C. Longiave, R. Castelli, *J. Polym. Sci. Part C* **1963**, *4*, 387; g) G. B. Sakharovskaya, *Zh. Obshch. Khim.* **1969**, *39*, 788.

[2] a) H. Sinn, W. Kaminsky, H. J. Vollmer, R. Woldt, *Angew. Chem.* **1980**, *92*, 396; *Angew. Chem. Int. Ed. Engl.* **1980**, *19*, 390; b) W. Kaminsky, H. Sinn, *Adv. Organomet. Chem.* **1980**, *18*, 99.

[3] See, for example: a) S. Pasynkiewicz, *Polyhedron* **1990**, *9*, 429; b) M. R. Mason, J. M. Smith, S. G. Bott, A. R. Barron, *J. Am. Chem. Soc.* **1993**, *115*, 4971; c) J. Storre, C. Schnitter, H. W. Roesky, H. G. Schmidt, M. Noltemeyer, R. Fleischer, D. Stalke, *J. Am. Chem. Soc.* **1997**, *119*, 7505.

[4] a) J. L. Atwood, D. C. Hrncir, R. D. Priester, R. D. Rogers, *Organometallics* **1983**, *2*, 985; b) J. L. Atwood, M. J. Zaworotko, *J. Chem. Soc. Chem. Commun.* **1983**, 302; c) W. Uhl, M. Koch, W. Hiller, M. Heckel, *Angew. Chem.* **1995**, *107*, 1122; *Angew. Chem. Int. Ed. Engl.* **1995**, *34*, 989; d) W. Uhl, M. Koch, S. Pohl, W. Saak, W. Hiller, M. Heckel, *Z. Naturforsch. B* **1995**, *50*, 635; e) R. J. Wehmschulte, P. P. Power, *J. Am. Chem. Soc.* **1997**, *119*, 8387; f) P. Sobota, J. Utko, J. Ejfler, L. B. Jerzykiewicz, *Organometallics* **2000**, *19*, 4929; g) K. Kasprzak, J. Serwatowski, *Appl. Organometal. Chem.* **2004**, *18*, 394; h) Ł. John, J. Utko, L. B. Jerzykiewicz, P. Sobota, *Inorg. Chem.* **2005**, *44*, 9131.

[5] a) V. C. Gibson, C. Redshaw, A. J. P. White, D. J. Williams, *Chem. Commun.* **2001**, 79; b) J. Lewiński, I. Justyniak, J. Zachara, E. Tratkiewicz, *Organometallics* **2003**, *22*, 4151; c) T. Dalet, H. Cramail, A. Deffieux, *Macromol. Chem. Phys.* **2004**, *205*, 1394.

[6] For selected examples, see: a) H. Yamane, Y. Kimura, *Polymeric Materials Encyclopedia*, *Vol. 1* (Ed.: J. C. Salamone), CRC Press, Boca Raton, New York, **1996**, p. 202, and references therein; b) C. C. Landry, N. Pappe, M. R. Mason, A. W. Apblett, A. N. Tyler, A. N. MacInnes, A. R. Barron, *J. Mater. Chem.* **1995**, *5*, 331; c) A. Kareiva, C. J. Harlan, D. B. MacQueen, R. L. Cook, A. R. Barron, *Chem. Mater.* **1996**, *8*, 2331; d) T. Loiseau, C. Serre, C. Huguenard, G. Fink, F. Taulelle, M. Henry, T. Bataille, G. Ferey, *Chem. Eur. J.* **2004**, *10*, 1373; e) S. Bourrelly, P. L. Llewellyn, C. Serre, F. Millange, T. Loiseau, G. Ferey, *J. Am. Chem. Soc.* **2005**, *127*, 13519.

[7] a) C. C. Landry, J. A. Davis, A. W. Apblett, A. R. Barron, *J. Mater. Chem.* **1993**, *3*, 597; b) Y. Koide, A. R. Barron, *Organometallics* **1995**, *14*, 4026; c) Y. Koide, S. G. Bott, A. R. Barron, *Organometallics* **1996**, *15*, 2213.

[8] a) C. C. Landry, C. J. Harlan, S. G. Bott, A. R. Barron, *Angew. Chem.* **1995**, *107*, 1315; *Angew. Chem. Int. Ed. Engl.* **1995**, *34*, 1201; b) C. N. McMahon, A. R. Barron, *J. Chem. Soc. Dalton Trans.* **1998**, 3703; c) S. J. Obrey, A. R. Barron, *J. Chem. Soc. Dalton Trans.* **2001**, 2456.

[9] a) M. Bolesławski, S. Pasynkiewicz, A. Minorska, W. Hryniów, *J. Organomet. Chem.* **1974**, *65*, 165; b) A. Kunicki, J. Serwatowski, S. Pasynkiewicz, M. Bolesławski, *J. Organomet. Chem.* **1977**, *128*, 21; c) A. Piotrowski, A. Kunicki, S. Pasynkiewicz, *J. Organomet. Chem.* **1980**, *201*, 105; d) A. Sadownik, S. Pasynkiewicz, M. Bolesławski, H. Szachnowska, *J. Organomet. Chem.* **1978**, *152*, C49.

[10] a) G. Bai, H. W. Roesky, J. Li, M. Noltemeyer, H. G. Schmidt, *Angew. Chem.* **2003**, *115*, 5660; *Angew. Chem. Int. Ed.* **2003**, *42*, 5502; b) G. Bai, Y. Peng, H. W. Roesky, J. Li, H. G. Schmidt, M. Noltemeyer, *Angew. Chem.* **2003**, *115*, 1164; *Angew. Chem. Int. Ed.* **2003**, *42*, 1132; c) Y. Peng, G. Bai, H. Fan, D. Vidovic, H. W. Roesky, J. Magull, *Inorg. Chem.* **2004**, *43*, 1217; d) G. Bai, S. Singh, H. W. Roesky, M. Noltemeyer, H. G. Schmidt, *J. Am. Chem. Soc.* **2005**, *127*, 3449; e) J. Chai, V. Jancik, S. Singh, H. Zhu, C. He, H. W. Roesky, H. G. Schmidt, M. Noltemeyer, N. S. Hosmane, *J. Am. Chem. Soc.* **2005**, *127*, 7521.

[11] S. G. Bott, A. W. Coleman, J. L. Atwood, *J. Am. Chem. Soc.* **1986**, *108*, 1709.

[12] a) C. E. Bethley, C. L. Aitken, C. J. Harlan, Y. Koide, S. G. Bott, A. R. Barron, *Organometallics* **1997**, *16*, 329; b) D. A. Dickie, D. D. Choytun, M. C. Jennings, H. A. Jenkins, J. A. C. Clyburne, *J. Organomet. Chem.* **2004**, *689*, 2186.

[13] a) J. Lewiński, J. Zachara, I. Justyniak, *Organometallics* **1997**, *16*, 3859; b) J. Lewiński, J. Zachara, I. Justyniak, *Inorg. Chem.* **1998**, *37*, 2575; c) C. S. Branch, J. Lewiński, I. Justyniak, S. G. Bott, J. Lipkowski, A. R. Barron, *J. Chem. Soc. Dalton Trans.* **2001**, 1253; d) C. Redshaw, M. R. J. Elsegood, *Chem. Commun.* **2001**, 2016; e) C. Redshaw, M. R. J. Elsegood, K. E. Holmes, *Angew. Chem.* **2005**, *117*, 1884; *Angew. Chem. Int. Ed.* **2005**, *44*, 1850.

[14] The organic residue was analyzed by GC as well as by ^{1}H NMR and IR spectroscopy. Both the ^{1}H NMR ($CDCl_3$) and IR spectra of 3,3-dimethyl-2-benzofuran-1(3*H*)-one (**A**) were consistent with the literature data: T. R. Beebe, R. Adkins, R. Baldridge, V. Hensley, D. McMillen, D. Morris, R. Noe, F. Weng Ng, G. Powell, C. Spielberger, M. Stolte, *J. Org. Chem.* **1987**, *52*, 5472.

[15] The adduct [{1,2-bis(4-pyridyl)ethane}($AlMe_3$)$_2$] was isolated from the reaction mixture by crystallization, and the spectroscopic data were consistent with the literature data: D. Ogrin, L. H. van Poppel, S. G. Bott, A. R. Barron, *Dalton Trans.* **2004**, 3689.

[16] G. M. Sheldrick, *Acta Crystallogr.* **1990**, *46*, 467.

[17] G. M. Sheldrick, SHELXL-97, University of Göttingen, Germany, **1997**.

 © 2006 Wiley-VCH Verlag GmbH & Co. KGaA, Weinheim

Biomineralization

DOI: 10.1002/anie.200503800

Self-Organization of Oriented Calcium Carbonate/Polymer Composites: Effects of a Matrix Peptide Isolated from the Exoskeleton of a Crayfish**

*Ayae Sugawara, Tatsuya Nishimura, Yuya Yamamoto, Hirotaka Inoue, Hiromichi Nagasawa, and Takashi Kato**

Biological minerals are inorganic/organic composites that function as structural supports, protection, and mineral stores.[1] The cooperation of biomacromolecules such as proteins and polysaccharides plays a determining role in morphological control in the formation of biominerals.[1] A number of in vitro experiments for the nucleation and growth of biominerals demonstrated that their morphologies are influenced by the extracted organic biomacromolecules of bone and dentin,[2] mollusk shells,[3] skeletons,[4] and larval spicules[5] of sea urchin, ascidian spicules,[6] and coralline alga skeletons.[7] However, studies on individual proteins are limited because of difficulties in the isolation and purification of these biomacromolecules.[3g] An understanding of the structure–function relationships of individual proteins for biomineralization would offer not only deeper insight into biomineralization, but also ideas for the design of novel inorganic/organic composite materials.[1a,8] Our strategy is to develop new inorganic/organic composites that exhibit controlled morphologies and properties. We have prepared thin-film $CaCO_3$ crystals by using a combination of polymer thin films and simpler acidic polymers such as poly(acrylic acid) and poly(glutamic acid).[9] For further control of the morphologies of such composite materials, more careful design of the organic matrix is essential.

[*] Dr. A. Sugawara, Dr. T. Nishimura, Y. Yamamoto, Prof. Dr. T. Kato
Department of Chemistry and Biotechnology
School of Engineering
The University of Tokyo
Hongo, Bunkyo-ku, Tokyo 113-8656 (Japan)
Fax: (+81) 3-5841-8661
E-mail: kato@chiral.t.u-tokyo.ac.jp
Dr. H. Inoue, Prof. Dr. H. Nagasawa
Department of Applied Biological Chemistry
Graduate School of Agricultural and Life Sciences
The University of Tokyo
Yayoi, Bunkyo-ku, Tokyo 113-8657 (Japan)

[**] This study was partially supported by a Grant-in-Aid for the 21st Century COE Program for Frontiers in Fundamental Chemistry (T.K. and A.S.) and for Exploratory Research (17655048; T.K.) from the Ministry of Education, Culture, Sports, Science, and Technology. T.N. expresses thanks for a JSPS Research Fellowship for Young Scientists (No. 10624).

Supporting information for this article is available on the WWW under http://www.angewandte.org or from the author.

The exoskeletons of crustaceans[10] are fascinating biominerals in the view of materials science, because they are ductile, tough, and lightweight. The exoskeleton of crayfish mainly consists of frameworks of α-chitin/protein microfibrils and calcium carbonate that is closely associated with the fibrils. Figure 1a shows the scanning electron microscopy

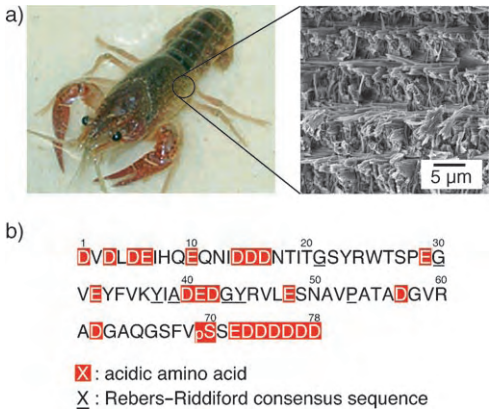

Figure 1. a) Photograph of *Procambarus clarkii* and SEM image of the fractured surface of its exoskeleton. b) Amino acid sequence of CAP-1. pS = phosphoserine.

(SEM) image of a fracture surface of the exoskeleton of a crayfish, *Procambarus clarkii*. X-ray studies revealed that both calcite and amorphous calcium carbonate are present in crayfish exoskeletons.[10a] If we could prepare biomineralization-inspired materials with self-organized structures similar to that of the exoskeleton, new soft composite synthetic materials that are environmentally friendly would be obtained. For this purpose, it is important to examine the role of natural peptides in the formation of biominerals.

In 2001, Inoue et al.[11a] isolated a peptide named calcification-associated peptide (CAP-1) from the exoskeleton of a crayfish (Figure 1a). They showed that CAP-1 has calcium-binding ability and it inhibits the precipitation of calcium carbonate. They also showed that CAP-1 interacts with chitin.[11] CAP-1 is expressed in the epidermal tissue during the postmolt stage where and when calcification takes place,[12] which indicates that CAP-1 is involved in the formation of the exoskeleton. CAP-1 has three specific features (Figure 1b): 1) it is a highly acidic peptide—in particular, it has a hexameric aspartic acid sequence in the C-terminal section; 2) it has a "Rebers–Riddiford (R&R) consensus sequence", which is conserved in cuticle proteins of many arthropods[13]—it was postulated that this motif might be involved in the protein–chitin interaction;[14] and 3) it has a phosphoserine residue at the 70th position.

Herein, we report the formation of oriented thin-film crystals of calcium carbonate by the specific combination of chitin and CAP-1 as the matrix for crystallization. We also describe the effects of the recombinant peptide rCAP-1 (Scheme 1a) and synthetic peptides (Scheme 1b and c) on the morphologies of calcium carbonate. These peptides have been designed and prepared based on the chemical structure of CAP-1 to understand the specific function of organic components.

InterScience
© 2006 Wiley-VCH Verlag GmbH & Co. KGaA, Weinheim

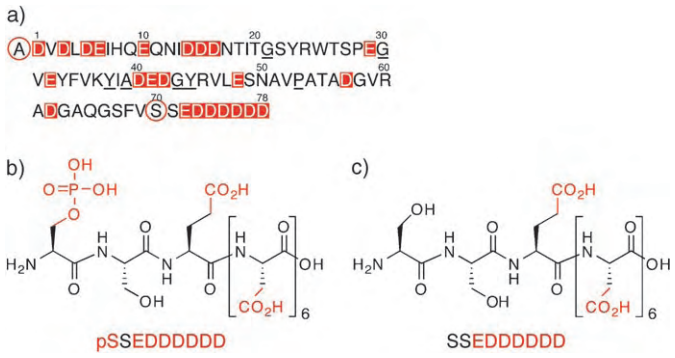

Scheme 1. a) Amino acid sequence of the recombinant peptide rCAP-1. Red circles indicate the amino acids that are different from those of CAP-1. b, c) Chemical structures of the synthetic peptides $pSSED_6$ and S_2ED_6.

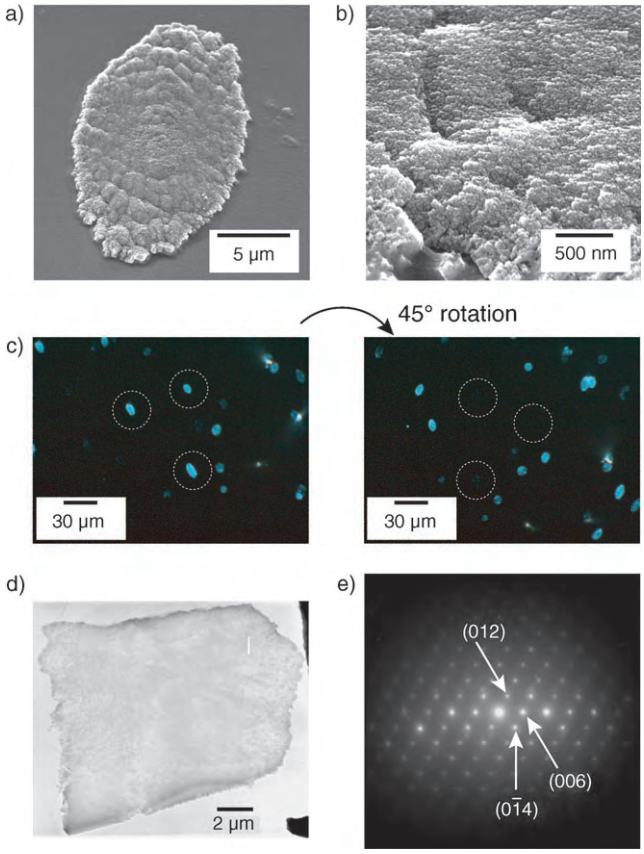

Figure 2. a) SEM image of $CaCO_3$ crystals grown on a chitin matrix in the presence of CAP-1 (3.0×10^{-3} wt%). b) Magnified image of the crystal surface in (a). c) Polarizing optical microscopic images of the uniaxially oriented crystals. The right-hand image is a 45° rotation of the sample in the image on the left. d) TEM image and e) the corresponding selected-area electron diffraction image of the uniaxially oriented crystal grown on a chitin matrix in the presence of CAP-1.

The $CaCO_3$ crystallization from a supersaturated solution of calcium carbonate was conducted on a chitin substrate in the presence of CAP-1 for 20 hours. The chitin matrix for the crystallization was prepared by spin-coating the solution onto glass substrates. SEM observation of the matrix revealed that microfibrils of about 10-nm diameter are formed (see Supporting Information). The X-ray diffraction (XRD) pattern of the matrix shows that its crystalline structure is assigned to α-chitin, the same crystalline form as that in the exoskeleton of the crayfish (see Supporting Information).[15] In the absence of CAP-1, rhombohedral calcite crystals form on the chitin matrix, which shows that the matrix alone has no significant effect on the crystallization of calcium carbonate. In the presence of 3.0×10^{-3} wt% of CAP-1, thin crystalline films of calcium carbonate grow on the chitin matrix. The size of these crystals is about 10 μm and the thickness is about 1 μm (Figure 2a). The detailed observation of these crystalline films by SEM has clarified that they are composed of assemblies of nanocrystals (Figure 2b). The crystals intimately associate with chitin fibrils through CAP-1, and form calcium carbonate/chitin nanocomposites.

Observations by polarizing optical microscopy revealed that the chitin surface is not fully covered with $CaCO_3$ thin films (Figure 2c). This observation suggests that CAP-1 has an inhibitory effect on $CaCO_3$ crystallization. Figure 2c shows that when the samples are rotated under crossed polarizers at 45°, the optical images of some crystals change from bright to dark. This switching is observed for all crystals on 45° rotation from a proper angle. The fact that such optical change is observed for all of these crystals indicates that each film is uniaxially oriented (Figure 2c). The direction of the orientation of each film is random on the chitin matrix. Transmission electron microscopy (TEM) and electron diffraction studies of these films showed that they have single-crystallographic orientation such that the *c* axis is unidirectionally oriented in these calcite films (Figure 2d and e). The same electron diffraction pattern was observed for the whole of one calcite film (see Supporting Information).

To understand the formation process of the unidirectionally oriented calcite films, we performed a real-time observation of calcium carbonate deposition by using polarizing optical microscopy under crossed polarizers. About 5 minutes after mixing the solutions of CAP-1 and calcium carbonate, oriented crystalline films 10 μm in size suddenly appeared on the chitin matrix. No further growth was observed during incubation for 20 hours. The sudden appearance of the crystalline films can be attributed to the transformation from the amorphous to the crystalline state of calcium carbonate. It is expected that CAP-1, which was isolated from the exoskeleton of crayfish containing amorphous calcium carbonate (ACC), can interact with the ACC and lead to its stabilization.[5,6,16]

We consider the process of formation of the unidirectionally oriented crystals over 10 μm in size to be as follows (see Supporting Information). ACC interacting with CAP-1 may initially form on the chitin matrix. Then nucleation starts on the nanoscale region of the ACC on the oriented crystalline chitin fibril that is 10 nm in width. This transformation might be induced by the aligned functional groups of CAP-1 that bind to the chitin fibril with the R&R consensus sequence. For cuticle proteins of insects containing this sequence, it was proposed that they bind to α-chitin with the R&R consensus sequence, which adopts an antiparallel β-pleated sheet conformation.[14] Amorphous-to-crystalline transformation of calcium carbonate has often been observed in biomine-

 © 2006 Wiley-VCH Verlag GmbH & Co. KGaA, Weinheim

alization[16] and in crystal growth in biologically inspired systems.[17a,18] Our assumption on the formation process is also supported by some work on single-crystalline films obtained through ACC precursors.[17,18]

One of the characteristics of the chemical structure of CAP-1 is the phosphoserine residue at the 70th position. To examine the role of this residue, we performed $CaCO_3$ crystallization in the presence of rCAP-1 in which the phosphate group is absent from the 70th position (Scheme 1a). rCAP-1 was expressed in *Escherichia coli* cells as reported previously.[12] Figure 3a shows the SEM image of the

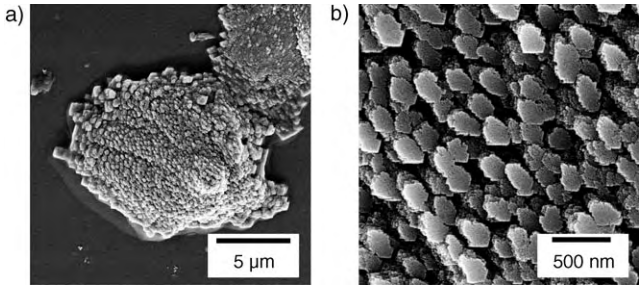

Figure 3. a) SEM image of $CaCO_3$ crystals grown on a chitin matrix in the presence of rCAP-1. b) Magnified image of the crystal surface in (a).

$CaCO_3$ crystals formed on the chitin matrix in the presence of rCAP-1 (3.0×10^{-3} wt%). Although the surface of the crystals is not as flat as those obtained in the presence of CAP-1, uniaxially oriented crystals are also formed in the presence of rCAP-1 (see Supporting Information). Figure 3b reveals that the surface of the oriented crystals is composed of an assembly of block-shaped calcite crystals about 0.2 μm in size, unlike the crystals formed in the presence of CAP-1 which are finer (tens of nanometers; Figure 2b). Phosphate groups at serine residues were reported to have calcium-binding ability.[19] CAP-1 may also bind to calcium ions more strongly than rCAP-1 because of the existence of the phosphate group, which leads to disturbance of the crystal growth and to the stabilization of the amorphous state. Such effects of CAP-1 on the crystallization may give rise to the smaller size of crystals.

To examine the effects of the size of acidic molecules and of the R&R consensus sequence on the crystallization, we prepared peptides $pSSED_6$ and S_2ED_6 (Scheme 1b) by solid-phase synthesis. These synthetic peptides are the C-terminal acidic domains of CAP-1 and rCAP-1, respectively. No thin-film crystals were obtained by using these synthetic peptides (Figure 4). Half-dome structures are formed in the presence of $pSSED_6$ (Figure 4a), while peanut-shaped crystals are observed with S_2ED_6 (Figure 4c). Crystallographic orientation is not unidirectional for these crystals, while oriented crystals are obtained in the presence of CAP-1 and rCAP-1. These results demonstrate that the R&R consensus sequence interacts with chitin and affects the crystallographic orientation of $CaCO_3$ on the chitin matrix. The phosphate group of $pSSED_6$ also exerts effects on the surface morphology of the crystals. The size of the block-shaped crystals formed with

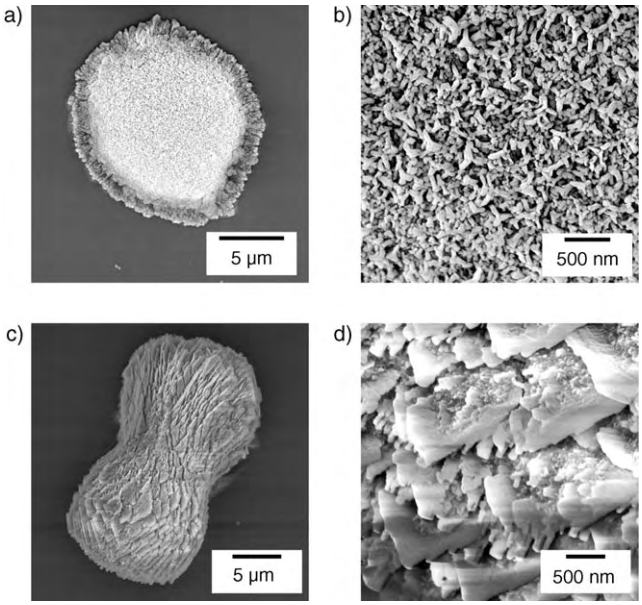

Figure 4. SEM images of $CaCO_3$ crystals grown on chitin matrices in the presence of the synthetic peptides a, b) $pSSED_6$ and c, d) S_2ED_6. b, d) Magnified images of the crystal surface in (a) and (c), respectively.

$pSSED_6$ is much smaller than that of the crystals formed with S_2ED_6, which has no phosphate group (Figure 4b and d). The observation that no thin films are formed in the presence of the shorter peptides reveals that longer chains of acidic structures may be needed for thin-film formation of $CaCO_3$ crystals.

In conclusion, we have succeeded in preparing uniaxially oriented $CaCO_3$ thin-film crystals on chitin matrices by using a natural peptide (CAP-1) isolated from the exoskeleton of a crayfish. The peptide exhibits several functions: 1) deposition of $CaCO_3$ on the surface; 2) arrangement of its acidic groups by specific interaction with chitin; and 3) stabilization of amorphous $CaCO_3$. The combination of these functions has led to the formation of the uniaxially oriented $CaCO_3$ films. The structure–function relationship of CAP-1 has been examined by comparison with the functions of analogous synthetic peptides. These results have provided us with important information on the design of organic matrices for the preparation of inorganic/organic hybrid materials that exhibit highly controlled morphologies and significant properties.

Received: October 27, 2005
Revised: January 24, 2006

Keywords: biomineralization · calcium · crystal growth · materials science · peptides

[1] a) S. Mann in *Biomineralization* (Eds: R. G. Compton, S. G. Davies, J. Evans), Oxford University Press, Oxford, **2001**; b) L. Addadi, S. Weiner, *Angew. Chem.* **1992**, *104*, 159–176; *Angew. Chem. Int. Ed. Engl.* **1992**, *31*, 153–169.
[2] a) G. He, T. Dahl, A. Veis, A. George, *Nat. Mater.* **2003**, *2*, 552–558; b) P. H. Tartaix, M. Doulaverakis, A. George, L. W. Fisher,

 © 2006 Wiley-VCH Verlag GmbH & Co. KGaA, Weinheim

W. T. Butler, C. Qin, E. Salih, M. Tan, Y. Fujimoto, L. Spevak, A. L. Boskey, *J. Biol. Chem.* **2004**, *279*, 18115 – 18120.
[3] a) A. P. Wheeler, J. W. George, C. A. Evans, *Science* **1981**, *212*, 1397 – 1398; b) L. Addadi, S. Weiner, *Proc. Natl. Acad. Sci. USA* **1985**, *82*, 4110 – 4114; c) G. Falini, S. Albeck, S. Weiner, L. Addadi, *Science* **1996**, *271*, 67 – 69; d) A. M. Belcher, X. H. Wu, R. J. Christensen, P. K. Hansma, G. D. Stucky, D. E. Morse, *Nature* **1996**, *381*, 56 – 58; e) X. Shen, A. M. Belcher, P. K. Hansma, G. D. Stucky, D. E. Morse, *J. Biol. Chem.* **1997**, *272*, 32472 – 32481; f) T. Samata, N. Hayashi, M. Kono, K. Hasegawa, C. Horita, S. Akera, *FEBS Lett.* **1999**, *462*, 225 – 229; g) B.-A. Gotliv, L. Addadi, S. Weiner, *ChemBioChem* **2003**, *4*, 522 – 529; h) M. Michenfelder, G. Fu, C. Lawrence, J. C. Weaver, B. A. Wustman, L. Taranto, J. S. Evans, D. E. Morse, *Biopolymers* **2003**, *70*, 522 – 533.
[4] A. Berman, L. Addadi, S. Weiner, *Nature* **1988**, *331*, 546 – 548.
[5] S. Raz, P. C. Hamilton, F. H. Wilt, S. Weiner, L. Addadi, *Adv. Funct. Mater.* **2003**, *13*, 480 – 486.
[6] a) J. Aizenberg, G. Lambert, L. Addadi, S. Weiner, *Adv. Mater.* **1996**, *8*, 222 – 226; b) J. Aizenberg, G. Lambert, S. Weiner, L. Addadi, *J. Am. Chem. Soc.* **2002**, *124*, 32 – 39.
[7] S. Raz, S. Weiner, L. Addadi, *Adv. Mater.* **2000**, *12*, 38 – 42.
[8] a) T. Kato, A. Sugawara, N. Hosoda, *Adv. Mater.* **2002**, *14*, 869 – 877; b) H. Cölfen, *Curr. Opin. Colloid Interface Sci.* **2003**, *8*, 23 – 31; c) F. C. Meldrum, *Int. Mater. Rev.* **2003**, *48*, 187 – 224.
[9] a) T. Kato, *Adv. Mater.* **2000**, *12*, 1543 – 1546; b) T. Kato, T. Suzuki, T. Amamiya, T. Irie, M. Komiyama, H. Yui, *Supramol. Sci.* **1998**, *5*, 411 – 415; c) T. Kato, T. Suzuki, T. Irie, *Chem. Lett.* **2000**, 186 – 187; d) A. Sugawara, T. Kato, *Chem. Commun.* **2000**, 487 – 488; e) N. Hosoda, T. Kato, *Chem. Mater.* **2001**, *13*, 688 – 693; f) A. Sugawara, T. Ishii, T. Kato, *Angew. Chem.* **2003**, *115*, 5457 – 5461; *Angew. Chem. Int. Ed.* **2003**, *42*, 5299 – 5303; g) A. Sugawara, T. Kato, *Compos. Interfaces* **2004**, *11*, 287 – 295.
[10] a) D. F. Travis, *Ann. N. Y. Acad. Sci.* **1963**, *109*, 177 – 245; b) D. Raabe, P. Romano, C. Sachs, A. Al-Sawalmih, H.-G. Brokmeier, S.-B. Yi, G. Servos, H. G. Hartwig, *J. Cryst. Growth* **2005**, *283*, 1 – 7; c) D. Raabe, C. Sachs, P. Romano, *Acta Mater.* **2005**, *53*, 4281 – 4292; d) A. Becker, A. Ziegler, M. Epple, *J. Chem. Soc. Dalton Trans.* **2005**, 1814 – 1820.
[11] a) H. Inoue, N. Ozaki, H. Nagasawa, *Biosci. Biotechnol. Biochem.* **2001**, *65*, 1840 – 1848; b) H. Inoue, T. Ohira, N. Ozaki, H. Nagasawa, *Biochem. Biophys. Res. Commun.* **2004**, *318*, 649 – 654.
[12] H. Inoue, T. Ohira, N. Ozaki, H. Nagasawa, *Comp. Biochem. Physiol. Part B* **2003**, *136*, 755 – 765.
[13] J. E. Rebers, L. M. Riddiford, *J. Mol. Biol.* **1988**, *203*, 411 – 423.
[14] a) S. O. Andersen, P. Hojrup, P. Roepstorff, *Insect Biochem. Mol. Biol.* **1995**, *25*, 153 – 176; b) V. A. Iconomidou, G. D. Chryssikos, V. Gionis, J. H. Willis, S. J. Hamodrakas, *Insect Biochem. Mol. Biol.* **2001**, *31*, 877 – 885.
[15] C. T. Andrade, K. M. P. Silva, M. I. Tavares, R. A. Simão, C. Achete, C. A. Pérez, *J. Appl. Polym. Sci.* **2002**, *83*, 151 – 159.
[16] a) Y. Levi-Kalisman, S. Raz, S. Weiner, L. Addadi, I. Sagi, *Adv. Funct. Mater.* **2002**, *12*, 43 – 48; b) L. Addadi, S. Raz, S. Weiner, *Adv. Mater.* **2003**, *15*, 959 – 970.
[17] a) J. Aizenberg, D. A. Muller, J. L. Grazul, D. R. Hamann, *Science* **2003**, *299*, 1205 – 1208; b) J. T. Han, X. Xu, D. H. Kim, K. Cho, *Adv. Funct. Mater.* **2005**, *15*, 475 – 480.
[18] a) E. Loste, F. C. Meldrum, *Chem. Commun.* **2001**, 901 – 902; b) M. Li, S. Mann, *Adv. Funct. Mater.* **2002**, *12*, 773 – 779; c) L. B. Gower, D. J. Odom, *J. Cryst. Growth* **2000**, *210*, 719 – 734.
[19] A. Hecker, O. Testenière, F. Marin, G. Luquet, *FEBS Lett.* **2003**, *535*, 49 – 54.

 © 2006 Wiley-VCH Verlag GmbH & Co. KGaA, Weinheim

DNA Sensing

DOI: 10.1002/anie.200503836

Visible Sensing of Nucleic Acid Sequences with a Genetically Encodable Unmodified RNA Probe**

Atsushi Narita, Kazumasa Ogawa, Shinsuke Sando, and Yasuhiro Aoyama**

As the amount of identified genetic information continues to grow, there has been much current interest in rapid and simple gene sensing with high sequence selectivity.[1] Among various types of homogeneous sensing methods,[1,2] such as the use of molecular beacons (MBs; Figure 1a),[2a,b] several new strategies have enabled catalytic sensing of a target sequence over the equivalent stoichiometry of the target molecule through a signal-amplifying process.[3–12] These strategies include DNA/RNAzyme-[3–5] or enzyme-coupled[6,7] approaches, template-directed catalytic chemical reaction probes,[8,9] and a method with electrochemical catalysis[10] or mechanistically controllable magnetic particles.[11] Recently, we reported a new strategy with MB–mRNA systems for sensitive genotyping.[12] The strategy was based on the system of naturally occurring[13] or engineered[14] hairpin-shaped RNAs for conformation-induced control of translation frequency, so that the sensing can be conducted by using genetically encodable unmodified RNA as a probe in a typical prokaryotic translation system.

The artificial translation regulation system is composed of a *cis*-acting MB-like RNA structure, wherein the loop region (green in Figure 1a) is complementary to the target and the stem is composed of sequences for a RBS (red) and the anti-RBS or RBS-docking domain complementary thereto (pink).[12] Target binding is designed to result in the opening of the MB structure, thereby making the RBS domain accessible by the ribosome and hence initiating the translation of a reporter gene, such as luciferase. Although the MB–mRNA system actually realized the sensitive detection of nucleic acids through the double signal-amplifying process of catalytic translation and catalytic signal transduction through enzymatic reaction of the translated reporter protein, the

[*] A. Narita, K. Ogawa, Dr. S. Sando, Prof. Dr. Y. Aoyama
Department of Synthetic Chemistry and Biological Chemistry
Graduate School of Engineering
Kyoto University
Katsura, Nishikyo-ku, Kyoto 615-8510 (Japan)
Fax: (+81) 75-383-2767
E-mail: ssando@sbchem.kyoto-u.ac.jp
aoyamay@sbchem.kyoto-u.ac.jp

[**] This work was supported by an Industrial Technology Research Grant Program from the New Energy and Industrial Technology Development Organization (NEDO) of Japan and also partly by Grants-in-Aid (Grant nos.: 16350087 and 17034026) from the Japanese Government. A.N. acknowledges a fellowship from JSPS.

Supporting information for this article is available on the WWW under http://www.angewandte.org or from the author.

© 2006 Wiley-VCH Verlag GmbH & Co. KGaA, Weinheim

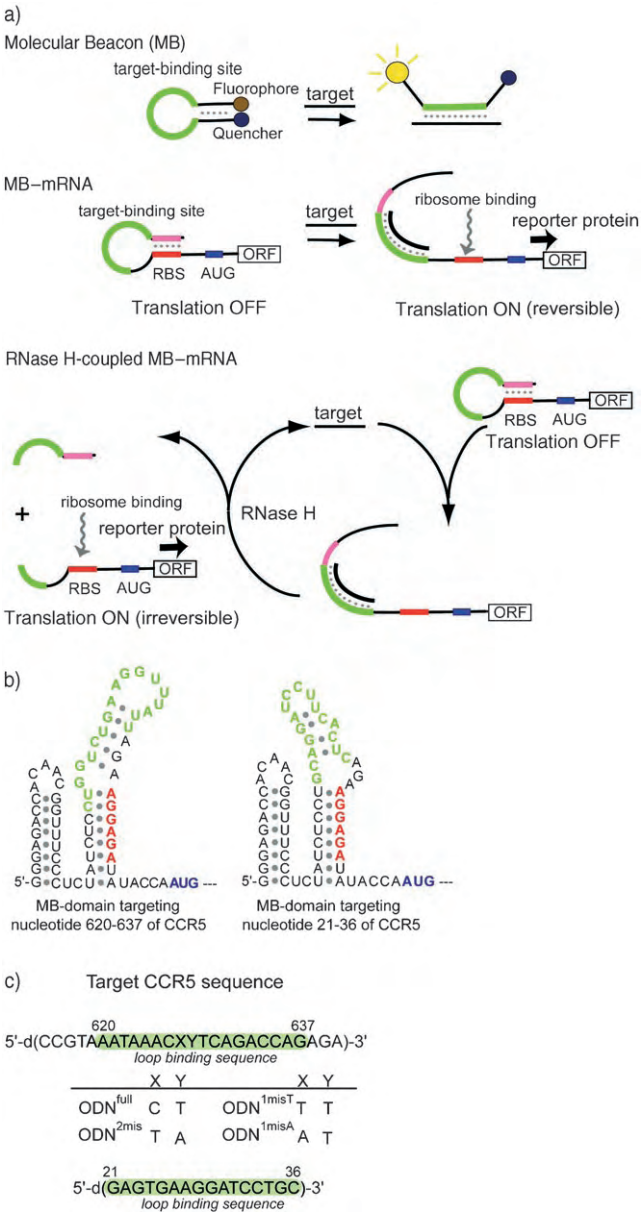

Figure 1. a) Illustration of MB, MB–mRNA, and RNase H activity coupled MB–mRNA systems. The ribosome-binding site (RBS), anti-RBS or RBS-locking site, start codon, and target-binding domain are colored red, pink, blue, and green, respectively. b) Predicted secondary structures of the 5′-end region of MB–mRNA targeting the nucleotide 620–637 or 21–36 regions of the human CCR5 gene sequence. c) Sequences of the 620–637 and 21–36 regions of the target human CCR5 gene.

method still has two major shortcomings. The first is sequence selectivity. The target-binding domain should be sufficiently long to open the MB (hairpin) structure, so that the probe fails to discriminate single nucleotide differences, for example, the C to T transition that forms a relatively stable GT mismatch in the target/probe heteroduplex. The second is sensitivity. As stoichiometric binding of the target to the probe is required for continuous translation of a reporter protein, the translation-activated mRNA probe is, at best, equimolar to the target; this typically leads to low signal intensity, especially when the target is present in a tiny amount.

The present work is concerned with an RNase H activity coupled MB–mRNA system. The RNase H activity coupled approach allows triple catalytic sensing of target nucleic acids with improved selectivity and enhanced sensitivity. In addition, we report herein an application for the visible sensing of nucleic acids with an unmodified RNA probe in this RNase H activity coupled system.

RNase H is an endoribonuclease that specifically hydrolyzes the phosphodiester bonds of RNA in the DNA/RNA heteroduplex.[15] Therefore, an MB–mRNA system coupled with the RNase H activity could drive an additional process for catalytic production of a translation-activated mRNA probe, wherein the target-bound loop region (target = oligodeoxynucleotide (ODN)) is digested by coexisting RNase H to release an anti-RBS stem domain away from the mRNA body, thus allowing catalytic use of target DNA (Figure 1a).

To demonstrate the designed triply catalytic gene sensing, we first used an mRNA probe composed of the MB domain targeting the nucleotide 620–637 site (18 nucleotides (nts)) of the human CC chemokine receptor 5 (CCR5) gene sequence (Figure 1b),[16] downstream of which is a codon-optimized luciferase reporter gene, derived from pBESTluc vector (Promega). The sensing of target CCR5 ODNs (Figure 1c) with the MB–mRNA probe ($\approx$1.8 pmol in 10 μL solution, 0.1 μg μL^{-1}) was carried out at 37 °C for 1 h in a reconstituted prokaryotic translation system (Pure System)[17,18] in the presence or absence of additional *Tth* RNase H (typically 0.01 U μL^{-1}); this was followed by a chemiluminescence (CL) assay of the luciferase expressed with a 96-well microplate reader (Wallac 1420 system; Figure 2). In the absence of RNase H, an equimolar amount of fully matched target ODN^{full} afforded a moderately enhanced CL (I_{on}/I_{off} = 314%) relative to that in the absence of the target (lane 1 versus lane 2 in Figure 2a). An RNase H activity coupled (0.01 U μL^{-1}) translation system, under otherwise identical conditions, resulted in an enhanced translation activation that reached 615% CL enhancement (lane 3 versus lane 4 in Figure 2a).

Control runs indicated that RNase H indeed catalyzed the target-assisted cleavage of the probe.[19,20] The probe can also be provided in the form of double-stranded (ds) DNA, from which the MB–mRNA will be transcribed in situ. Under the RNase H coupled T7-transcription/translation conditions, the precursor dsDNA (0.2 pmol) gave a further enhanced value of I_{on}/I_{off} = 1320% for an equimolar amount of target ODN^{full} (lane 1 versus lane 2 in Figure 2b). Nucleic acid sensing for a different CCR5 sequence was further conducted by using a newly designed MB-type *cis*-repressing domain targeting nucleotides 21–36 of CCR5 (Figure 1b). As seen in Figure 3, the presence of a fully matched sequence afforded highly enhanced CL under the RNase H activity coupled conditions, with I_{on}/I_{off} = 953% (lane 2 versus lane 3 in Figure 3), thus partly revealing the generality of the target sequence for this triple catalytic sensing system.

The sensitivity-enhanced RNase H activity coupled system still retained a low selectivity for single-nucleotide differences in the 18-nt binding site (lanes 5–7 in Figure 2a).

 © 2006 Wiley-VCH Verlag GmbH & Co. KGaA, Weinheim

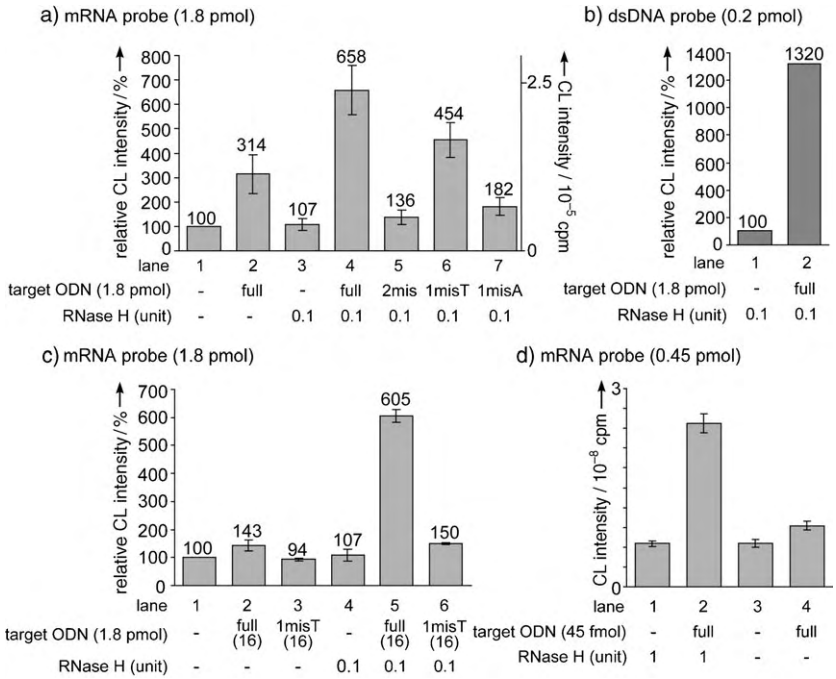

Figure 2. RNase H activity coupled sensing of the human CCR5 sequence by CL assay for a 2.5-μL aliquot of the RNase H activity coupled or noncoupled translation system (10 μL) after treatment with luciferase assay solution (100 μL; Promega). a) and b) Relative CL intensities in the presence or absence of target ODNs (1.8 pmol, target site 620–637) with a) MB–mRNA (1.8 pmol) or b) dsDNA template (0.2 pmol) as a probe. c) Relative CL intensities in the presence of target ODN(16) (1.8 pmol, target site 620–635) with MB–mRNA probe (1.8 pmol). d) Relative CL intensities in the presence of target ODNs (45 fmol; target site: 620–637) with MB–mRNA probe (0.45 pmol).

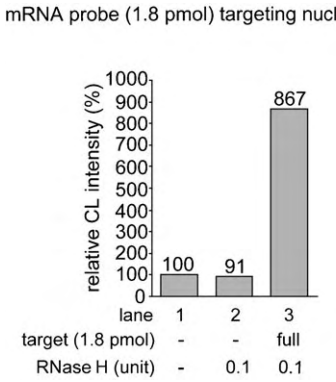

Figure 3. Detection of the nucleotide 21–36 region of the CCR5 sequence with the designed MB–mRNA probe (1.8 pmol) by a CL assay.

Two-base-mismatched ODN^{2mis} (T for C and A for T at positions 627 and 628) and one-base-mismatched ODN^{1misA} (C to A transversion at position 627) gave no notable enhancement ($I_{on}/I_{off} = 127\%$ for lane 3 versus lane 5 and 170% for lane 3 versus lane 7, respectively, in Figure 2a). However, nonnegligible CL enhancement was observed for the one-base-mismatched target ODN^{1misT} (C to T transition at position 627), perhaps due to the stable GT mismatch base pair in the resulting heteroduplex ($I_{on}/I_{off} = 424\%$ for lane 3 versus lane 6 in Figure 2a).

One-nucleotide selectivity was further investigated by using the shorter target of 16 nts (the nucleotide 620–635 region of the CCR5 gene sequence in Figure 1c). The shorter target length could lead to higher sequence selectivity; however, the target/probe hybridization of 16 nts seems to be too short to invade into the hairpin domain (a total of 13 internal base pairings) and open the MB structure by the presence of only one equivalent of a target with no external support, as revealed by the design of the conventional MB probe. This was the case. As shown in Figure 2c (lanes 2 and 3), the original system that was not RNase H activity coupled could not detect even a fully matched target of 16 nt (ODN$^{full(16)}$). However, in marked contrast, the RNase H activity coupled system allowed the 16-nt target to activate the translation of the MB-riboregulator mRNA ($I_{on}/I_{off} = 565\%$ for lane 5 versus lane 4 in Figure 2c) by concomitant catalytic cleavage of the hybridized MB–mRNA probe. Importantly, as expected, the shorter 16-nt-targeting MB–mRNA system, coupled with RNase H activity, succeeded in discriminating even the C to T transition at position 627 (ODN$^{1misT(16)}$, lane 5 versus lane 6 in Figure 2c).

The advantage of the present RNase H activity coupled system is greatly emphasized when we detect a small amount of target DNA.[19,20] The sensitivity or detection limit related to the I_{on}/I_{off} value was enhanced by the RNase H activity coupled MB–mRNA system, wherein the translation-activated mRNA probe could be catalytically amplified above the equivalent stoichiometry of the target through the third catalytic process. While the RNase H free system failed to detect 45 fmol (18 nM, 2.5 μL) of target ODN^{full} (lane 3 versus lane 4 in Figure 2d),[21] the RNase H activity coupled system enabled clear detection of the same amount of target with a CL enhancement of about 400% ($I_{on} = 24.7 \times 10^7$ cpm (counts per minute), $I_{off} = 6.5 \times 10^7$ cpm) in combination with a sensitive luminometer (Lumat LB 9507; lane 1 versus lane 2 in Figure 2d). This triple catalytic system allows detection of ≥ 9 fmol (3.6 nM, 2.5 μL) of target with repetitively reproducible results in the CL enhancement ($I_{on}/I_{off} = 1.7$; data not shown).

Finally, we achieved visible sensing of the target sequence by an unmodified but functional RNA probe. To visualize the sensing signal, we prepared a color-reporting MB–mRNA probe by exchanging the gene encoding luciferase with that for β-galactosidase (β-Gal; target: nucleotide 620–637 region of the CCR5 gene sequence). The expressed β-Gal could convert the substrate *ortho*-nitrophenyl-β-D-galactopyranoside (ONPG) into *ortho*-nitrophenol (ONP), hence leading to a visible color change to light yellow. Transcription/translation of the dsDNA template for the MB-controlled mRNA for β-Gal (0.2 pmol) was carried out in the presence of

 © 2006 Wiley-VCH Verlag GmbH & Co. KGaA, Weinheim

RNase H (0.1 U μL^{-1}) and target ODN^{full} (1.8 pmol). Enzymatic conversion of ONPG into ONP was quantitatively evaluated by measuring the absorbance increase at 405 nm (Figure 4a). In a similar manner to that described above, the remarkably high absorbance increase ($I_{off} = 0.04$ for lane 3, $I_{on} = 0.59$ for lane 4) was obtained, as expected, only for the RNase H coupled translation system; I_{on}/I_{off} reached 1475% (Figure 4a, lane 4 versus lane 3). Detection could be readily achieved with the naked eye. The presence of target ODN^{full} was easily distinguished by the visible yellow color of the solution (Figure 4b, lane 3 versus lane 2).

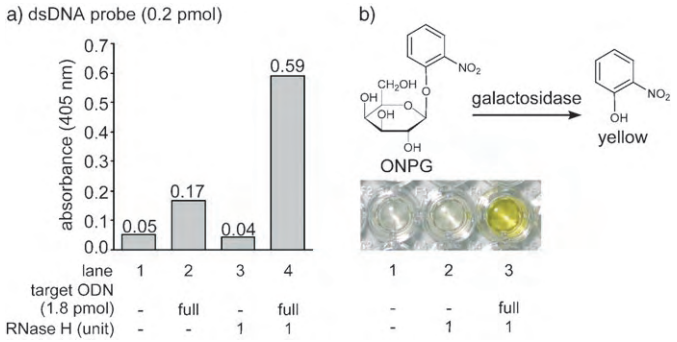

Figure 4. Visible sensing of the CCR5 gene sequence (region 620–637) by a β-galactosidase-encoding MB–mRNA probe. a) Absorbance (405 nm) of β-galactosidase assay solution with ONPG as a substrate (100 μL) containing an 11-μL aliquot of RNase H (0.1 U μL^{-1}) activity coupled MB–mRNA system (0.2 pmol of dsDNA template) translated in the presence of target ODN^{full} (1.8 pmol; target site: nucleotide 620–637 region of the human CCR5 gene). b) Reaction scheme and photographic images of the assay solutions.

In summary, we have demonstrated catalytic sensing of nucleic acids by using an unmodified RNA probe in an RNase H activity coupled cell-free translation system. The combination with RNase H activity, which induces the third signal-amplifying process of catalytic and irreversible activation of an mRNA probe, achieves an improved sequence selectivity (1-nucleotide selectivity in a target ODN of 16 nts in length) and an enhanced sensitivity (≥ 9 fmol of target). The observed sensitivity is comparable with that of the previously reported isothermal sensing system with an RNase H activity coupled, cleavable, fluorescence resonance-energy transfer (FRET) probe,[15c] but should also be compared with much higher sensitivities developed recently.[2f] Nevertheless, the characteristic aspect of the present system that simple/unmodified RNAs or even dsDNAs can be used as probes is something that can not be mimicked readily by other methods.

In particular, the present RNase H activity coupled system also allowed visible sensing of the target sequence under isothermal conditions. It is remarkable that the target sequence can be color-visualized without fluorophore/quencher molecules or inorganic nanoparticles such as quantum dots. What is needed for this color-based sensing is simply a genetically encodable unmodified RNA that works in a prokaryotic translation system. Since, in principle, any type of reporter proteins can be generated, the present method may facilitate high-throughput multiplex screening of genetic sequences (by using fluorescent proteins with different emission properties) or be applicable in electrochemical sensing devices (by using electrochemically sensible redox proteins). Nucleic acid based nanomachines or nanodevices may also be a potential application of this approach.[22] Further work is now under way along these lines.

Received: October 31, 2005
Revised: January 16, 2006
Published online: March 21, 2006

Keywords: DNA recognition · molecular beacons · nucleic acids · RNA · sensors

[1] K. Nakatani, *ChemBioChem* **2004**, *5*, 1623, and references therein.
[2] For examples of homogeneous gene sensing, see: a) S. Tyagi, F. R. Kramer, *Nat. Biotechnol.* **1996**, *14*, 303; b) S. Tyagi, D. P. Bratu, F. R. Kramer, *Nat. Biotechnol.* **1998**, *16*, 49; c) R. T. Ranasinghe, L. J. Brown, T. Brown, *Chem. Commun.* **2001**, 1480; d) S. Sando, E. T. Kool, *J. Am. Chem. Soc.* **2002**, *124*, 2096; e) J. Brunner, R. Kraemer, *J. Am. Chem. Soc.* **2004**, *126*, 13626; f) N. L. Rosi, C. A. Mirkin, *Chem. Rev.* **2005**, *105*, 1547; g) C. J. Yang, H. Lin, W. Tan, *J. Am. Chem. Soc.* **2005**, *127*, 12772.
[3] a) M. N. Stojanovic, P. de Prada, D. W. Landry, *ChemBioChem* **2001**, *2*, 411; b) M. N. Stojanovic, D. Stefanovic, *Nat. Biotechnol.* **2003**, *21*, 1069; c) Y. Tian, C. Mao, *Talanta* **2005**, *67*, 532.
[4] a) J. S. Hartig, I. Grüne, S. H. Najafi-Shoushtari, M. Famulok, *J. Am. Chem. Soc.* **2004**, *126*, 722; b) S. H. Najafi-Shoushtari, G. Mayer, M. Famulok, *Nucleic Acids Res.* **2004**, *32*, 3212.
[5] S. Sando, T. Sasaki, K. Kanatani, Y. Aoyama, *J. Am. Chem. Soc.* **2003**, *125*, 15720.
[6] A. Saghatelian, K. M. Guckian, D. A. Thayer, M. R. Ghadiri, *J. Am. Chem. Soc.* **2003**, *125*, 344.
[7] V. Pavlov, B. Shlyahovsky, I. Willner, *J. Am. Chem. Soc.* **2005**, *127*, 6522.
[8] H. Abe, E. T. Kool, *J. Am. Chem. Soc.* **2004**, *126*, 13980.
[9] J. Cai, X. Li, X. Yue, J. S. Taylor, *J. Am. Chem. Soc.* **2004**, *126*, 16324.
[10] C. Fan, K. W. Plaxco, A. J. Heeger, *Proc. Natl. Acad. Sci. USA* **2003**, *100*, 9134.
[11] F. Patolsky, Y. Weizmann, E. Katz, I. Willner, *Angew. Chem.* **2003**, *115*, 2474; *Angew. Chem. Int. Ed.* **2003**, *42*, 2372.
[12] S. Sando, A. Narita, K. Abe, Y. Aoyama, *J. Am. Chem. Soc.* **2005**, *127*, 5300.
[13] S. Brantl, *Biochim. Biophys. Acta* **2002**, *1575*, 15.
[14] F. J. Isaacs, D. J. Dwyer, C. Ding, D. D. Pervouchine, C. R. Cantor, J. J. Collins, *Nat. Biotechnol.* **2004**, *22*, 841.
[15] For an example of a nucleic acid detection system that utilizes RNase H, see: a) P. Duck, G. Alvarado-Urbina, B. Burdick, B. Collier, *BioTechniques* **1990**, *9*, 142; b) L. Cloney, C. Marlowe, A. Wong, R. Chow, R. Bryan, *Mol. Cell. Probes* **1999**, *13*, 191; c) J. J. Harvey, S. P. Lee, E. K. Chan, J. H. Kim, E.-S. Hwang, C.-Y. Cha, J. R. Knutson, M. K. Han, *Anal. Biochem.* **2004**, *333*, 246.
[16] For details on nucleotide numbering, see: S. Mummidi, S. S. Ahuja, B. L. McDaniel, S. K. Ahuja, *J. Biol. Chem.* **1997**, *272*, 30662.
[17] Y. Shimizu, A. Inoue, Y. Tomari, T. Suzuki, T. Yokogawa, K. Nishikawa, T. Ueda, *Nat. Biotechnol.* **2001**, *19*, 751.
[18] We independently confirmed that MB–mRNA-based nucleic acid sensing can also be carried out in a normal *Eschericha coli* S30 extract system (RTS HY100, Roche; 10 μL): intensity of luminescence with translation on/intensity of luminescence with translation off (I_{on}/I_{off}) = 400–600% for the MB–mRNA probe

 © 2006 Wiley-VCH Verlag GmbH & Co. KGaA, Weinheim

(1.8 pmol) with fully matched target ODN^{full} (20 pmol). However, addition of *Tth* RNase H induced no signal enhancement in this non-reconstituted cell-extract system.

[19] We carried out RNase H induced cleavage reactions of an MB domain with the 1–92 nucleotide sequence of the MB–mRNA probe used here. Gel analysis (see Supporting Information) indicated that cleavage occurred only after incubation in the copresence of the RNase H and target ODN, a result indicating that RNase H indeed catalyzed the target-assisted cleavage of the RNA probe with a turnover number of ≤ 50 with respect to the target ODN.

[20] A [target-]dependence study (see Supporting Information) revealed that the RNase H assisted MB–mRNA probe was $\approx 70\,\%$ fully activated even in the presence of 0.1 equiv of target ODN (probe/target = 10), in contrast to the activity of a stem-free control probe which existed in an open or translation-on state constantly in the absence of the target. This over-stoichiometric activation of the probe may be most reasonably explained in terms of target-assisted catalytic cleavage of the probe by RNase H.

[21] As described in our previous report,[12] the original MB–luciferase mRNA probe (4.5 fmol) allowed detection of 50 fmol of target. However, the signal intensity obtained is quite low compared with that of the present RNase H activity coupled system, due to the absence of the third signal-amplifying process of catalytic activation of the mRNA probe.

[22] N. C. Seeman, *Trends Biochem. Sci.* **2005**, *30*, 119, and references therein.

 © 2006 Wiley-VCH Verlag GmbH & Co. KGaA, Weinheim

Protein Immobilization

DOI: 10.1002/anie.200503867

Biomolecular Modification of Hierarchical Cellulose Fibers through Titania Nanocoating**

Jianguo Huang, Izumi Ichinose, and Toyoki Kunitake*

The immobilization of proteins on solid surfaces is a key step in the development of medical diagnostics, biomaterials, and cell and tissue engineering, as well as biochips and biosensors.[1–7] The proteins are generally anchored on solid substrates, such as gold, silicon, and glass, mediated by an organic adhesive layer, for example, through a self-assembled monolayer (SAM), lipid bilayer, or thin polymer film. Recently, even diamond became available for protein immobilization after suitable surface modification.[8] In addition to these two-dimensional flat surfaces, immobilization on morphologically complex surfaces has attracted increasing attention. Nanomaterials such as silicon nanowires,[9] silica nanoparticles,[10,11] and carbon nanotubes[12–14] were coated with proteins and converted into novel biomaterials useful for drug-delivery systems and biosensors. Rodlike micelles are expected to be suitable scaffolds for protein immobilization in the context of biofunctional hydrogels and soft nanotechnology.[15] Herein, we focused on a cellulosic substance with a hierarchical structure ranging from the macroscopic down to the nanometer scale. Protein molecules (streptavidin) were abundantly immobilized onto individual cellulose nanofibers. The resulting soft, water-absorbing, fibrous material fully retained the molecular recognition property of streptavidin.

Cellulose is a linear polymer of β-D-glucose. The polymer chains assemble into a nanofiber through multiple hydrogen bonding, and the nanofibers are further organized to give a network of microfibers. We have developed a method to uniformly coat individual nanofibers of cellulosic substance with ultrathin metal oxide gel layers by using a surface sol–gel process.[16–19] This process is a layer-by-layer deposition technique based on the adsorption of metal alkoxides from solution and the subsequent hydrolysis of the chemisorbed alkoxides.[20–22] If applied to the cellulosic substances, the surfaces of the nanofibers can be coated with sub-nanometer-thick metal oxide gel layers.

To coat the nanofibers with titania gel layers, a piece of filter paper (Advantec, quantitative ashless, 5A type) was placed in a suction filtering unit, washed with ethanol, and dried by aspirating the air. A solution of $Ti(OnBu)_4$ in toluene/ethanol (1:1 by volume; 100 mM, 10 mL) was then passed through the filter paper in 2 min. Ethanol (2×20 mL) was immediately passed through the filter paper to remove the unreacted metal alkoxides, followed by water (20 mL) to promote hydrolysis and condensation. Finally, the filter paper was dried with a flow of air. By repeating these procedures, the surfaces of the individual cellulose nanofibers were coated with ultrathin titania gel. To verify the uniform coating, we calcined the filter paper and examined it by electron microscopy. As shown in Figure 1a and b, complete calcination at 450 °C resulted in slight shrinkage. However, the pure titania sheet retained the morphological features of the initial cellulose nanofibers (Figure 1c). The transmission electron microscopy (TEM) image of an isolated titania nanotube (Figure 1d) demonstrated how uniformly the cellulose nanofibers were modified with ultrathin titania gel layers.

Such a nanocoating process made it possible to convert the cellulose fibers into biofunctional materials (Figure 2). For protein immobilization, a 5-nm-thick titania layer was deposited by ten cycles of the surface sol–gel process. The titania-coated surfaces were then biotinylated by immersing the filter paper (5×5 mm^2) in a solution of biotin (1.0 mL, 2 mg mL^{-1}) in phosphate-buffered saline (PBS, pH 7.4) for 3 h

[*] Dr. J. Huang, Dr. I. Ichinose
Advanced Materials Laboratory
National Institute for Materials Science
1-1 Namiki, Tsukuba, Ibaraki 305-0044 (Japan)
Fax: (+81) 29-852-7449
E-mail: ichinose.izumi@nims.go.jp
Prof. Dr. T. Kunitake
Topochemical Design Laboratory, Frontier Research System
The Institute of Physical and Chemical Research (RIKEN)
Wako, Saitama 351-0198 (Japan)

[**] This work was supported in part by a Grant-in-Aid for the Encouragement of Young Scientists from the Ministry of Education, Culture, Sports, Science, and Technology of Japan (Grant No. 16710095 to J.H.).

Supporting information for this article is available on the WWW under http://www.angewandte.org or from the author.

 © 2006 Wiley-VCH Verlag GmbH & Co. KGaA, Weinheim

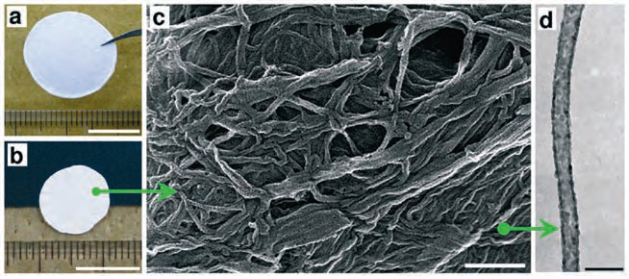

Figure 1. Titania nanocoating on individual cellulose nanofibers. a) Photograph of a piece of filter paper after deposition of a 10-nm-thick titania layer. b) Photograph of the pure titania sheet obtained by calcination of the filter paper shown in (a). c) Field-emission scanning electron microscopy (SEM) image of the sheet shown in (b). d) TEM image of a titania nanotube as a replica of the initial cellulose nanofiber. Scale bars: a) and b) 1 cm; c) 400 nm; d) 100 nm.

on a gold-coated QCM electrode (9 MHz) has been reported in our previous publications.[20–22] The amount of biotin adsorbed on a 5-nm-thick titania layer was estimated to give a QCM frequency change of 57 Hz (Figure 3a). This frequency shift corresponds to a mass increase of 51 ng and an adsorption thickness of 1.3 nm.[24] It is apparent that the surface of the thin titania layer can be fully covered by a biotin monolayer. The BSA used for blocking nonspecific adsorption sites gave a frequency shift of 7 Hz. The subsequent adsorption of streptavidin showed a frequency shift of 13 Hz. This frequency shift increased to 24 Hz without BSA treatment and 52 Hz when streptavidin was directly adsorbed on a titania layer. Adsorption of biotin and BSA are necessary for preventing strong nonspecific adsorption of streptavidin. From the frequency shift of 13 Hz, we estimated that the surface coverage of streptavidin was around 20%.[25] Uniform growth of a titania/biotin/BSA/streptavidin multilayer was confirmed by high-resolution SEM (see Supporting Information). We assumed that the surface of cellulose nanofibers coated with a 5-nm-thick titania layer would be similarly modified by the multilayer. In fact, we successfully verified such modification by fluorescence microscopy.

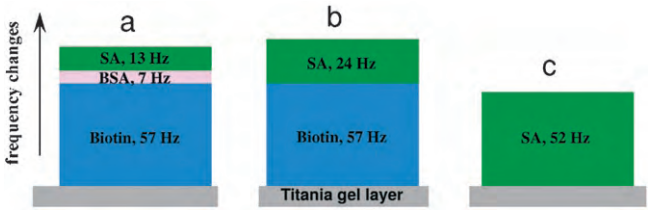

Figure 3. QCM frequency changes resulting from the adsorption of streptavidin on titania gel surfaces. a) Adsorption on a BSA-treated biotin layer; b) adsorption on a biotin layer; c) adsorption on a titania gel layer. SA = streptavidin.

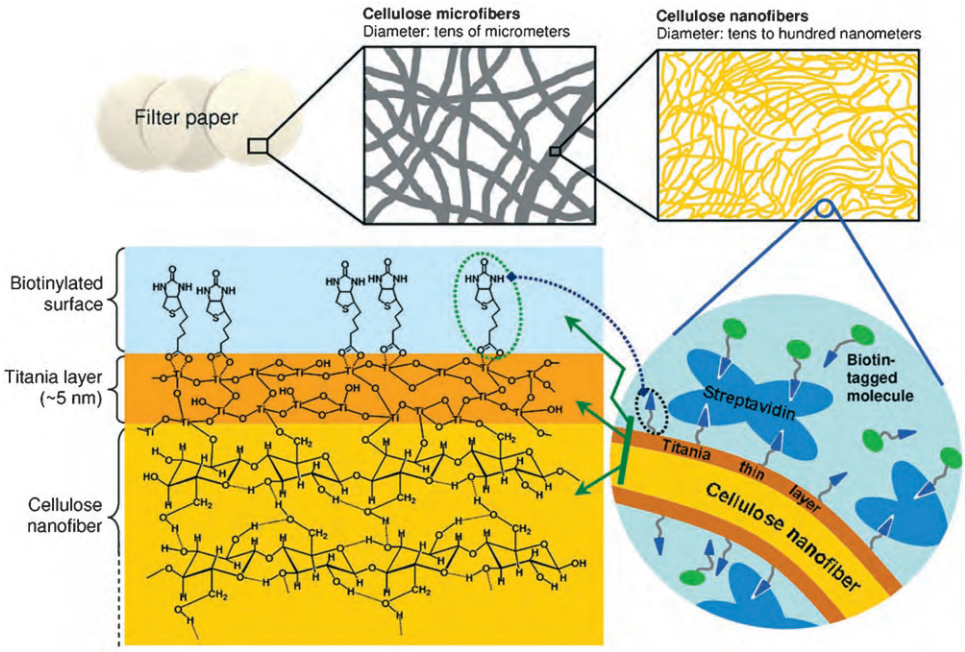

Figure 2. Protein (streptavidin) immobilization on individual cellulose nanofibers and binding of fluorescence-labeled biotin. The bottom-left panel shows the formation of a biotinylated surface on a cellulose nanofiber. The thickness of the titania layer is ≈5 nm.

at 4°C, followed by thorough rinsing with PBS and pure water, and drying under a stream of argon. A biotin monolayer remained on each nanofiber by coordination of the carboxy group. The resulting cellulose sheet was then placed in Denhardt's solution for 30 min to adsorb bovine serum albumin (BSA), to prevent nonspecific adsorption of streptavidin. The sheet was immersed in a solution of fluoresceinated streptavidin (Fluoro Alexa 488- or Alexa 546-labeled streptavidin, 0.1 mg mL^{-1} (≈1.5 μM) in PBS) for 30 min in the dark to immobilize the protein molecules through biotin–streptavidin interaction.[23]

The immobilization of multilayer assemblies was independently monitored by quartz-crystal microbalance (QCM) measurements. The preparation of an ultrathin titania layer

The filter paper that was modified with titania/biotin/BSA layers and then with Alexa 488- or Alexa 546-labeled streptavidin showed the characteristic green or red fluorescence of the fluoresceinated streptavidin (see Figure 4a and b). Streptavidin has two pairs of binding sites for biotin on opposite faces of the molecule. When immobilized on a cellulose nanofiber with one pair, the other pair is available for further attachment of biotinylated species (Figure 2). A native streptavidin-immobilized cellulose sheet bound biotin-4-fluorescein after immersion in the solution (0.1 mg mL^{-1} in PBS) for 30 min in the dark, and gave strong fluorescence (Figure 4c). Recently, it has been reported that proteins

 © 2006 Wiley-VCH Verlag GmbH & Co. KGaA, Weinheim

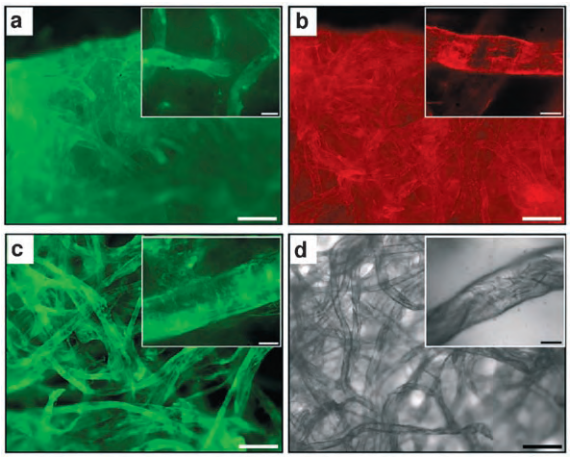

Figure 4. Fluorescence micrographs of cellulose microfibers modified with a) Alexa 488-labeled streptavidin, b) Alexa 546-labeled streptavidin, and c) native streptavidin. d) Transmitted bright-field micrograph of pure cellulose microfibers. Image (c) was obtained after binding of biotin-4-fluorescein. The insets show enlarged images. Scale bars: a)–d) 100 μm; inset of a) 20 μm; insets of b)–d) 10 μm. The false-color micrographic images were obtained by AxioVision LE.

immobilized on nanocurved surfaces were apt to retain their native structures and functions.[10,11] The same was true in our case. Control experiments on cellulose sheets without a titania coating revealed that streptavidin was not adsorbed at all (see Supporting Information). This finding indicates that the titania layer provides an activated surface for the formation of a biotin monolayer, which is essential for the immobilization of streptavidin.

Figure 5 shows fluorescence micrographs of the biotinylated cellulose sheets after binding Alexa 488-labeled streptavidin from solutions with different concentrations. The fluorescence intensity gradually decreased with decreasing protein concentration. Even at a concentration of 1.0×10^{-10} M, the cellulose microfibers were directly visible under the fluorescence microscope. This observation is attributed to the strong fluorescence arising from the large surface area of the hierarchical structure. In fact, the amount of immobilized

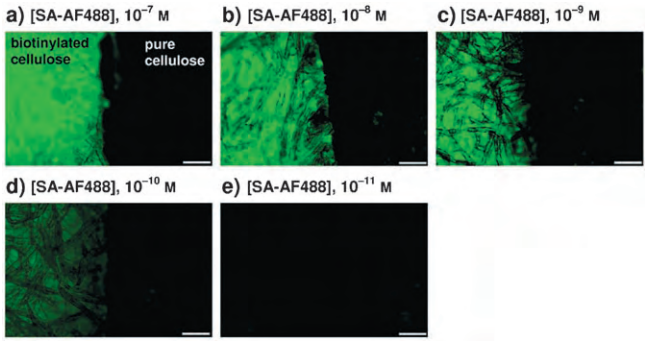

Figure 5. Fluorescence micrographs of a series of biotinylated cellulose microfibers after binding Alexa 488-labeled streptavidin. In each micrograph, the streptavidin-bound cellulose sheet was placed on the left-hand side. A pure cellulose sheet placed on the right-hand side for comparison appeared black, even after the same treatment procedures. Scale bars: 100 μm. SA-AF488 = Alexa 488-labeled streptavidin.

streptavidin was extremely high compared with the amount on a quartz substrate.

Figure 6 shows fluorescence micrographs of the native streptavidin-immobilized cellulose sheets after immersion in

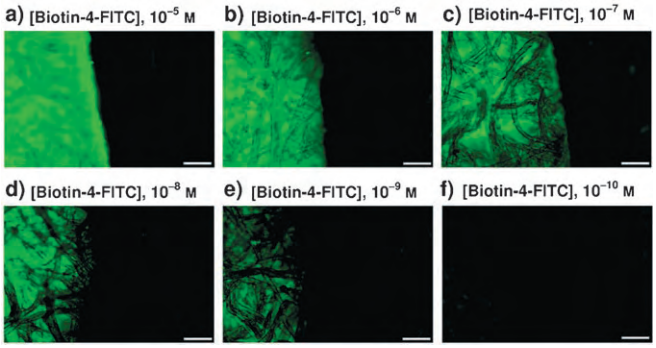

Figure 6. Fluorescence micrographs of a series of native streptavidin-immobilized cellulose microfibers after binding biotin-4-fluorescein from solutions of different concentrations. In each micrograph, the sample was placed on the left-hand side, and a piece of pure cellulose sheet was placed on the right-hand side for comparison. Scale bars: 100 μm. FITC = fluorescein isothiocyanate.

biotin-4-fluorescein solutions. The fluorescence decreased with the concentration of biotin-4-fluorescein. The lowest concentration detectable was 1.0×10^{-9} M, which was ten times lower than the aforementioned detection limit for fluoresceinated streptavidin. Here, we should be reminded that the dissociation constant of streptavidin for biotin is about 10^{-14} M. By assuming that this constant is applicable in our heterogeneous system, and that the detection limit is close to the fluorescence intensity from half of the maximum adsorption of streptavidin, the apparent concentration on a cellulose sheet could be estimated as 10^{-5} M. However, the apparent concentration of biotin on a titania-modified cellulose sheet is calculated to be 10^{-4} M from the detection limit (10^{-10} M) for Alexa 488-labeled streptavidin. These apparent concentrations should correspond to the molar ratio of active binding sites for biotin and streptavidin on cellulose nanofibers. We conclude that most of the natural streptavidin immobilized on biotinylated cellulose nanofibers was not denatured, as the fibers showed a strong binding property in spite of the extremely small number against immobilized biotin.

The nanomolar sensitivity achieved is comparable to that of the biosensors fabricated by using silicon nanowires,[9] carbon nanotubes,[12] or biologically functionalized nanowires of conducting polymer.[26] The cellulose sheet is composed of numerous nanofibers with a width of tens to hundred nanometers, which gives a large surface area. If we could increase the amount of anchored streptavidin, it would be possible to detect biotin-tagged molecules at picomolar concentrations. Our strategy, the use of a high surface area, enables us to capture biomolecules at a concentration near the dissociation constant. Moreover, the protein-functionalized cellulose sheet provides high affinity for water and mechanical strength, which is important for various practical applications. The titania nanocoating process converts cellulosic substances into promising scaffolds for various biomac-

 © 2006 Wiley-VCH Verlag GmbH & Co. KGaA, Weinheim

romolecules, and should be applicable to other natural cellulosic substances such as cotton and cloth. These cellulosic materials will be important for separation and extraction techniques, and future biological defense systems.

Received: November 2, 2005
Revised: February 1, 2006
Published online: March 23, 2006

Keywords: cellulose fibers · fluorescence · nanostructures · proteins · sol–gel processes

[1] D. R. Baselt, G. U. Lee, K. M. Hansen, L. A. Chrisey, R. J. Colton, *Proc. IEEE* **1997**, *85*, 672 – 680.
[2] Z. Yang, A. Chilkoti, *Adv. Mater.* **2000**, *12*, 413 – 417.
[3] K.-B. Lee, S.-J. Park, C. A. Mirkin, J. C. Smith, M. Mrksich, *Science* **2002**, *295*, 1702 – 1705.
[4] H. Baley, P. S. Cremer, *Nature* **2001**, *413*, 226 – 230.
[5] R. Bashir, R. Gomez, A. Sarikaya, M. R. Ladisch, J. Sturgis, J. P. Robinson, *Biotechnol. Bioeng.* **2001**, *73*, 324 – 328.
[6] G.-Y. Liu, N. A. Amro, *Proc. Natl. Acad. Sci. USA* **2002**, *99*, 5165 – 5170.
[7] Y. Lvov, K. Ariga, I. Ichinose, T. Kunitake, *J. Am. Chem. Soc.* **1995**, *117*, 6117 – 6123.
[8] A. Härtl, E. Schmich, J. A. Garrido, J. Hernando, S. C. R. Catharino, S. Walter, P. Feulner, A. Kromka, D. Steinmüller, M. Stutzmann, *Nat. Mater.* **2004**, *3*, 736 – 742.
[9] Y. Cui, Q. Wei, H. Park, C. M. Lieber, *Science* **2001**, *293*, 1289 – 1292.
[10] A. A. Vertegel, R. W. Siegel, J. S. Dordick, *Langmuir* **2004**, *20*, 6800 – 6807.
[11] M. Lundqvist, I. Sethson, B.-H. Jonsson, *Langmuir* **2004**, *20*, 10639 – 10647.
[12] R. J. Chen, S. Bangsaruntip, K. A. Drouvalakis, N. W. S. Kam, M. Shim, Y. Li, W. Kim, P. J. Utz, H. Dai, *Proc. Natl. Acad. Sci. USA* **2003**, *100*, 4984 – 4989.
[13] N. W. S. Kam, T. C. Jessop, P. A. Wender, H. Dai, *J. Am. Chem. Soc.* **2004**, *126*, 6850 – 6851.
[14] N. W. S. Kam, H. Dai, *J. Am. Chem. Soc.* **2005**, *127*, 6021 – 6026.
[15] J. D. Hartgerink, E. Beniash, S. I. Stupp, *Science* **2001**, *294*, 1684 – 1688.
[16] J. Huang, T. Kunitake, *J. Am. Chem. Soc.* **2003**, *125*, 11834 – 11835.
[17] J. Huang, T. Kunitake, S. Onoue, *Chem. Commun.* **2004**, 1008 – 1009.
[18] J. Huang, N. Matsunaga, K. Shimanoe, N. Yamazoe, T. Kunitake, *Chem. Mater.* **2005**, *17*, 3513 – 3518.
[19] R. A. Caruso, *Angew. Chem.* **2004**, *116*, 2802 – 2804; *Angew. Chem. Int. Ed.* **2004**, *43*, 2746 – 2748.
[20] I. Ichinose, H. Senzu, T. Kunitake, *Chem. Mater.* **1997**, *9*, 1296 – 1298.
[21] I. Ichinose, S.-W. Lee, T. Kunitake in *Supramolecular Organization and Materials Design* (Eds.: W. Jones, C. N. R. Rao), Cambridge University Press, Cambridge, **2002**, pp. 172 – 213, and references therein.
[22] J. Huang, I. Ichinose, T. Kunitake, *Chem. Commun.* **2002**, 2070 – 2071.
[23] W. Müller, H. Ringsdorf, E. Rump, G. Wildburg, X. Zhang, L. Angermaier, W. Knoll, M. Liley, J. Spinke, *Science* **1993**, *262*, 1706 – 1708.
[24] We assumed that the density of the biotin layer was 1.2 $g\,cm^{-3}$.
[25] N. Xia, J. S. Shumaker-Parry, M. H. Zareie, C. T. Campbell, D. G. Castner, *Langmuir* **2004**, *20*, 3710 – 3716.
[26] K. Ramanathan, M. A. Bangar, M. Yun, W. Chen, N. V. Myung, A. Mulchandani, *J. Am. Chem. Soc.* **2005**, *127*, 496 – 497.

 © 2006 Wiley-VCH Verlag GmbH & Co. KGaA, Weinheim

Cluster Catalysis

DOI: 10.1002/anie.200504321

Pd Nanoclusters in C–C Coupling Reactions: Proof of Leaching

*Mehul B. Thathagar, Johan E. ten Elshof, and Gadi Rothenberg**

Carbon–carbon coupling reactions are ubiquitous in organic synthesis. Heck,[1,2] Suzuki,[3,4] and Sonogashira couplings[5,6] occupy a special place among such reactions due to their mild reaction conditions. The coupling products are mostly used as intermediates for polymers, natural products, and bioactive compounds.[7,8]

The most common catalyst precursors for these reactions are palladium(II) complexes,[7,9,10] usually with phosphane ligands.[11] However, most of these ligands are air- and moisture-sensitive, involve multistep syntheses, and are difficult to separate from the final product. This makes "ligand-free" Pd catalysis an attractive option.[12–20] Pd^{II} salts form Pd^0 clusters under the reaction conditions, and these can catalyze coupling reactions. However, the "naked" Pd clusters aggregate to inactive Pd black.[15,19,21,22] To prevent this aggregation, stabilized Pd clusters[23] are increasingly being used as C–C coupling catalysts.[20,21,24–32] These clusters may be good catalysts, but we still do not know (in contrast to heterogeneous Pd[33]) whether catalysis occurs on the cluster surface or by leached[34] Pd species.[15,19,22,35,36]

Although much work has been done in this area, there is no single definitive experiment that reveals the detailed mechanism of cluster catalysis in the liquid phase.[35] From studies of cluster-size effects in Heck and Suzuki reactions, it was proposed that catalysis occurs at defect sites on the cluster surface.[27,37,38] Conversely, de Vries et al.[15] suggested an equilibrium between Pd clusters and a monomeric or dimeric moiety which is the actual active species. Recently, using transmission electron microscopy (TEM) and kinetic studies, we[39] and others[26,40] also demonstrated that species leached from the cluster surface are probably responsible for catalysis in these types of reactions. However, the conclusions were based on circumstantial evidence. Here we report the first direct and unambiguous test proving that leached Pd species are the true catalysts in Pd-cluster-catalyzed C–C coupling reactions.

[*] Dr. M. B. Thathagar, Dr. G. Rothenberg
van't Hoff Institute for Molecular Sciences
University of Amsterdam
Nieuwe Achtergracht 166, 1018 WV Amsterdam (The Netherlands)
Fax: (+31) 20-525-5604
E-mail: gadi@science.uva.nl

Dr. J. E. ten Elshof
Faculty of Science and Technology
University of Twente
P.O. Box 217, 7500 AE Enschede (The Netherlands)

Supporting information for this article is available on the WWW under http://www.angewandte.org or from the author.

WILEY InterScience DISCOVER SOMETHING GREAT
© 2006 Wiley-VCH Verlag GmbH & Co. KGaA, Weinheim

For this experiment, we built a special U-tube permeation cell[41] membrane reactor (Figure 1, top) consisting of two stainless steel compartments separated by a membrane (henceforth referred to as sides **A** and **B**). The membrane

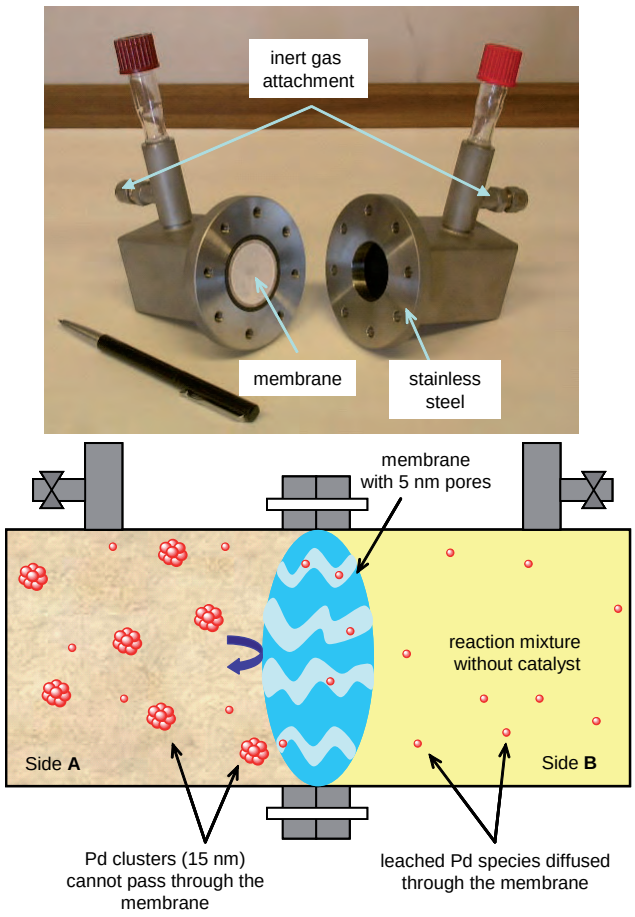

Figure 1. Photograph (top) and schematic (bottom) of the two-compartment membrane reactor and the cluster-exclusion concept.

physically separates the Pd clusters and the reaction mixture in the reactor. The concept is simple: the suspension of Pd clusters is placed on one side of the membrane, and the reaction mixture on the other (Figure 1, bottom). The membrane is designed[42] with 5-nm pores that allow the diffusion of leached Pd species, but not of Pd clusters. The clusters cannot pass through the membrane because they are too large (14.5 ± 2.5 nm, see below). Thus, monitoring the reaction over time on both sides gives direct information on the true catalyst.

The Pd clusters were synthesized by reducing $Pd(NO_3)_2$ with tetraoctylammonium glycolate (TOAG), used both as reducing and stabilizing agent.[43] This method gives clusters with an average size of 14.5 nm and a narrow particle size distribution (Figure 2). An α-alumina-supported nanoporous γ-alumina membrane was synthesized according to the reported procedure.[42] The pore size distribution of the membrane was determined by permporometry.[44,45] Most of the pores were around 4.9 nm and few pores were larger than 5 nm, with a maximum size of 11 nm. The minimum Pd cluster

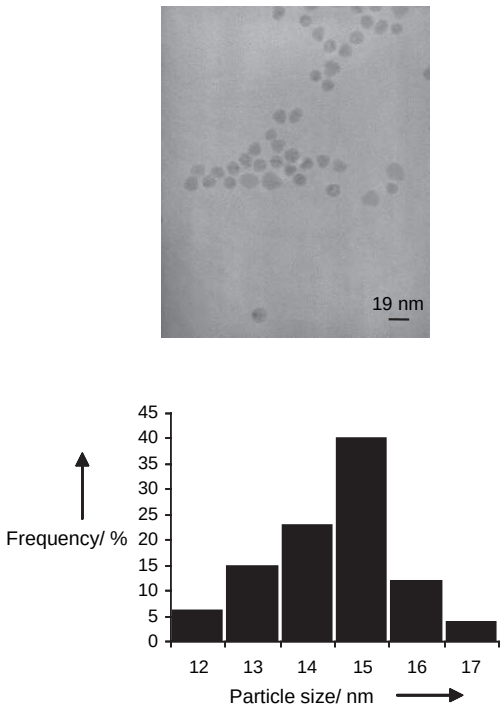

Figure 2. Transmission electron micrograph (top) and corresponding size distribution of the Pd clusters (bottom, based on 85 particles counted).

size was 12 nm. Moreover, due to the amorphous structure of the membrane, all the paths through it are tortuous wormholes, and no path consists of only maximum-size pores. Thus, this membrane also retains particles smaller than 11 nm.

In the first test reactions, we carried out Sonogashira coupling of phenylacetylene (**1**) with iodobenzene (**2**) [Eq. (1)]. We placed the Pd cluster suspension on side **A**,

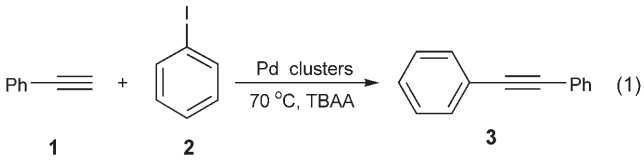

(1)

and **1, 2**, and tetrabutylammonium acetate (TBAA) as base on side **B**. The experiments were performed in DMF at 70 °C. Note that the base is soluble in this case. After 3 days, we observed 72% yield of coupling product **3** on side **B**, where there was originally no catalyst. However, as the reactants and base were not evenly distributed on both sides, they may have diffused from side **B** to the lower concentration on side **A**. It cannot be excluded that the reaction occurred in compartment **A** and the product then diffused from side **A** to side **B**. We did observe 9% yield of **3** on side **A**, which could be attributed to the product coming from side **B** or forming on side **A**. Consequently, this experiment did not give a clear answer to our question.

To reveal the actual catalytic species, it was necessary to prevent diffusion of the reactants through the membrane and

 © 2006 Wiley-VCH Verlag GmbH & Co. KGaA, Weinheim

to use an insoluble base. We therefore investigated the Heck reaction in the presence of NaOAc, which is insoluble in DMF. The coupling of *n*-butyl acrylate (**4**) with iodobenzene (**2**) to give *n*-butyl cinnamate (**6**) was used as a model reaction [Eq. (2)].

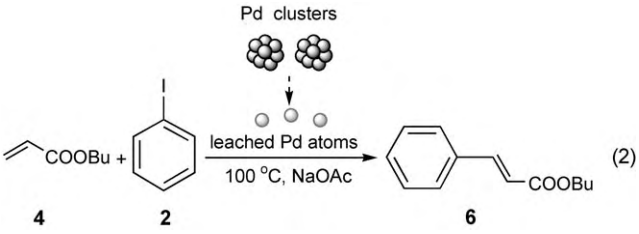

Before performing the coupling reaction, we examined the time-dependent transport of **4, 2**, and **6** through the membrane. Pure **4, 2**, and **6** in DMF were placed on side **B**, and only DMF on side **A**. Figure 3 shows that indeed all three

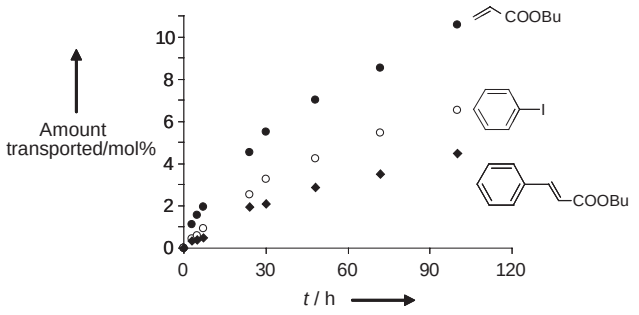

Figure 3. Time-dependent transport of molecules through the membrane from side **B** to side **A**.

compounds were transported from side **B** to side **A**. Note that no pressure was applied to the system; transport was purely due to concentration gradients. The transport rate was size-dependent: **4** > **2** > **6**. After 100 h, 10.5 mol% of **4**, 6.5 mol% of **2**, and 4.5 mol% of **6** were transported to side **A**. This blank experiment gives a measure of the background diffusion of these specific compounds through the membrane. Similar transport behavior can be expected during the reaction.

We then ran the Heck reaction using 1.5:1 molar mixtures of **4** and **2** on both sides of the membrane to avoid concentration gradients. NaOAc (1.5 equiv) was then added to side **B**, and the suspension of Pd clusters (0.01 equiv) was introduced into side **A** at 100 °C. Note that the base is necessary for closing the catalytic cycle. As there is no base on side **A**, no product can form there. Thus, any product observed on side **A** must come from side **B**.[46]

Figure 4 shows the yield of *n*-butyl cinnamate (**6**) versus time. No reaction was observed for the first 5 h because the released Pd species from side **A** must first diffuse through the nanoporous membrane to initiate the catalytic cycle on side **B**. When the leached Pd species reach side **B** the reaction rate increases and then slows as **2** is consumed. After 120 h, the yield of **6** on side **B** was 88%. We did not observe any diffused product **6** during the first 12 h on side **A**. However, after 120 h

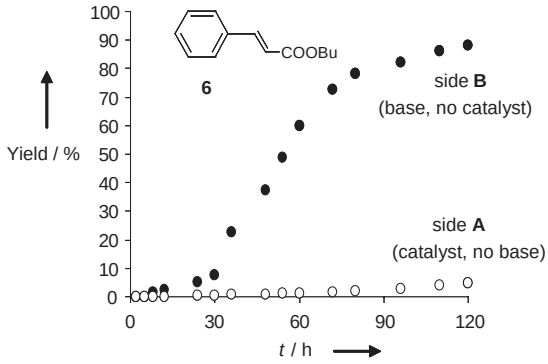

Figure 4. Time-resolved profile for the yield of **6**. The product observed on side **A** has diffused from side **B**.

4.9% of the product was observed that may have diffused from side **B**. Duplicate experiments showed good reproducibility. No aggregation was observed after the reaction on either side of the reactor.

X-ray photoelectron spectroscopy was performed on the membrane after the reaction to determine whether Pd enters the pores (see Supporting Information for details). There were no significant differences between the elemental compositions of the surface and subsurface layers. Traces of Pd were found on all spots on or below the membrane surface, but the concentration was in all cases within the range of 0.02–0.07 atom%. As the specific surface area[47] of this γ-alumina is about 285 $m^2 g^{-1}$, this is equivalent to a surface concentration of roughly one Pd atom per 20 nm^2.

The above results prove that the reaction involves leached Pd species, for which the nanosized Pd clusters act as reservoirs. We still do not know whether these species are Pd^0 atoms released from the defect sites or soluble Pd^{II} species formed after oxidative addition of PhI.[36,39] In theory, the Pd^0 and Pd^{II} species could "recluster" on the other side of the membrane, but in practice there is no stabilizer or reducing agent, both of which are crucial for cluster formation, so this option is extremely unlikely. In any event, these experiments prove the hypothesis of de Vries et al. regarding ligand-free Pd catalysts in Heck reactions.[15,48]

In summary, using a simple approach based on physical exclusion, we prove here that the Pd-cluster-catalyzed Heck reaction between *n*-butyl acrylate and iodobenzene (and probably also other Heck and Sonogashira reactions)[39] involves soluble Pd species released from the surface of the clusters. Moreover, the general new technique we described here permits the testing of many individual reactions. Further investigations into the mechanism of other cross-coupling reactions will be the subject of future research.

Experimental Section

Membrane preparation: The alumina membrane consists of a macroporous α-alumina support and a thin nanoporous γ-alumina layer. The α-alumina supports were made by colloidal filtration of well-dispersed 0.3-μm α-alumina particles (AKP-30, Sumitomo) in demineralized water. The 50-wt% dispersion was stabilized by peptizing with 0.02 M HNO_3. After drying at 25 °C for 24 h, the filter compact

 © 2006 Wiley-VCH Verlag GmbH & Co. KGaA, Weinheim

was sintered at 1100 °C in air for 2 h. Flat disks (∅ 39 mm, 2.0 mm thickness) were obtained by machining and polishing. The final porosity of these supports is about 30 %, and the average pore size 80–120 nm.[49] The nanoporous γ-alumina layer was prepared by dip-coating the α-alumina supports in a boehmite-based dip sol. The boehmite sol was prepared by heating 70.0 mol of double-distilled water to 95 °C, and then adding 0.50 mol of $Al(OsBu)_3$ (97 % purity, Acros) dropwise under a nitrogen flow to avoid premature hydrolysis. The mixture was stirred vigorously throughout the synthesis. After all the $Al(OsBu)_3$ was added, the mixture was kept at 95 °C for 3 h to evaporate the butanol. The mixture was cooled to 60 °C, peptized with HNO_3 (65 %, Merck) to pH 2.5, and then heated at reflux at 90 °C for 20 h (pH increases to 3.5) to yield a homogeneous and stable 0.5 M boehmite sol. The dip sol was prepared by mixing 30 mL of the boehmite sol with 20.0 mL of a solution of poly(vinyl alcohol) (PVA, Fluka, 98 % purity, $M = 72000\ g\,mol^{-1}$) made by adding 150 g of 0.05 M HNO_3 in water to 4.5 g of PVA and stirring for 2 h at 80 °C. The α-alumina supports were dip-coated with the γ-alumina sol under class 1000 clean-room conditions at a dip-coating speed of $1.1\ cm\,s^{-1}$. The coated supports were dried for 3 h (25 °C, relative humidity 40 %), and then calcined for 1 h (600 °C, air, heating/cooling rates $0.5\ °C\,min^{-1}$). The deposition/calcination cycle was repeated. This resulted in a flat nanoporous γ-alumina layer with a layer thickness of about 3 μm.

Heck coupling: Identical 1.5:1 mixtures of **4** (3.0 mmol, 0.38 g) and **2** (2.0 mmol, 0.40 g) in 50 mL of DMF were placed on both sides of the membrane reactor. NaOAc (3.0 mmol, 0.41 g) was then added to side **B**, and the Pd cluster suspension (3 mL, 10 mM, 1.0 mol %) was added to side **A**. The reactor was heated to 100 °C, and samples were taken from both compartments and analyzed by GC (pentadecane internal standard). After each experiment, the membrane was washed with acetone (4 × 10 mL) and extracted for 24 h with EtOH.

Received: December 5, 2005
Revised: February 3, 2006
Published online: March 23, 2006

Keywords: cross-coupling · Heck reaction · homogeneous catalysis · nanoparticles · palladium

[1] T. Mizoroki, K. Mori, A. Ozaki, *Bull. Chem. Soc. Jpn.* **1971**, *44*, 581.
[2] V. Farina, *Adv. Synth. Catal.* **2004**, *346*, 1553.
[3] N. Miyaura, T. Yanagi, A. Suzuki, *Synth. Commun.* **1981**, *11*, 513.
[4] F. Bellina, A. Carpita, R. Rossi, *Synthesis* **2004**, 2419.
[5] K. Sonogashira, Y. Tohda, N. Hagihara, *Tetrahedron Lett.* **1975**, *16*, 4467.
[6] P. Siemsen, R. C. Livingston, F. Diederich, *Angew. Chem.* **2000**, *112*, 2740; *Angew. Chem. Int. Ed.* **2000**, *39*, 2633.
[7] *Metal-Catalyzed Cross-Coupling Reactions* (Eds.: F. Diederich, P. J. Stang), Wiley-VCH, Weinheim, **1997**.
[8] *Transition Metals for Organic Synthesis; Building Blocks and Fine Chemicals* (Ed.: M. Beller), Wiley-VCH, Weinheim, **2004**.
[9] A. Zapf, M. Beller, *Top. Catal.* **2002**, *19*, 101.
[10] R. B. Bedford, C. S. J. Cazin, D. Holder, *Coord. Chem. Rev.* **2004**, *248*, 2283.
[11] D. H. Valentine, J. H. Hillhouse, *Synthesis* **2003**, 2437.
[12] Q. W. Yao, E. P. Kinney, Z. Yang, *J. Org. Chem.* **2003**, *68*, 7528.
[13] Y. Mori, M. Seki, *J. Org. Chem.* **2003**, *68*, 1571.
[14] A. Alimardanov, L. Schmieder-van de Vondervoort, A. H. M. de Vries, J. G. de Vries, *Adv. Synth. Catal.* **2004**, *346*, 1812.
[15] A. H. M. de Vries, J. Mulders, J. H. M. Mommers, H. J. W. Henderickx, J. G. de Vries, *Org. Lett.* **2003**, *5*, 3285.
[16] A. H. M. de Vries, F. J. Parlevliet, L. Schmieder-van de Vondervoort, J. H. M. Mommers, H. J. W. Henderickx, M. A. M. Walet, J. G. de Vries, *Adv. Synth. Catal.* **2002**, *344*, 996.
[17] B. M. Choudary, S. Madhi, N. S. Chowdari, M. L. Kantam, B. Sreedhar, *J. Am. Chem. Soc.* **2002**, *124*, 14127.
[18] M. B. Thathagar, J. Beckers, G. Rothenberg, *Green Chem.* **2004**, *6*, 215.
[19] M. T. Reetz, J. G. de Vries, *Chem. Commun.* **2004**, 1559.
[20] M. T. Reetz, E. Westermann, *Angew. Chem.* **2000**, *112*, 170; *Angew. Chem. Int. Ed.* **2000**, *39*, 165.
[21] M. B. Thathagar, J. Beckers, G. Rothenberg, *Adv. Synth. Catal.* **2003**, *345*, 979.
[22] A. Biffis, M. Zecca, M. Basato, *J. Mol. Catal. A* **2001**, *173*, 249.
[23] For a general overview on metal nanoclusters and their applications in catalysis, see: a) J. D. Aiken III, R. G. Finke, *J. Mol. Catal. A* **1999**, *145*, 1; b) J. S. Bradley, E. Hill, M. E. Leonowicz, H. Witzke, *J. Mol. Catal.* **1987**, *41*, 59; c) H. Bönnemann, R. M. Richards, *Eur. J. Org. Chem.* **2001**, 2455.
[24] For a recent review on the application of metal nanoclusters in C–C bond-formation reactions, see: M. Moreno-Mañas, R. Pleixats, *Acc. Chem. Res.* **2003**, *36*, 638.
[25] M. B. Thathagar, J. Beckers, G. Rothenberg, *J. Am. Chem. Soc.* **2002**, *124*, 11858.
[26] A. Gniewek, A. M. Trzeciak, J. J. Ziolkowski, L. Kepinski, J. Wrzyszcz, W. Tylus, *J. Catal.* **2005**, *229*, 332.
[27] R. Narayanan, M. A. El-Sayed, *Langmuir* **2005**, *21*, 2027.
[28] M. Beller, H. Fischer, K. Kuhlein, C. P. Reisinger, W. A. Herrmann, *J. Organomet. Chem.* **1996**, *520*, 257.
[29] M. T. Reetz, G. Lohmer, *Chem. Commun.* **1996**, 1921.
[30] M. T. Reetz, R. Breinbauer, K. Wanninger, *Tetrahedron Lett.* **1996**, *37*, 4499.
[31] Y. Li, X. M. Hong, D. M. Collard, M. A. El-Sayed, *Org. Lett.* **2000**, *2*, 2385.
[32] A. R. Gholap, K. Venkatesan, R. Pasricha, T. Daniel, R. J. Lahoti, K. V. Srinivasan, *J. Org. Chem.* **2005**, *70*, 4869.
[33] a) F. Y. Zhao, B. M. Bhanage, M. Shirai, M. Arai, *Chem. Eur. J.* **2000**, *6*, 843; b) R. L. Augustine, S. T. Oleary, *J. Mol. Catal. A* **1995**, *95*, 277; c) A. Biffis, M. Zecca, M. Basato, *J. Mol. Catal. A* **2001**, *173*, 249; d) B. M. Choudary, S. Madhi, N. S. Chowdari, M. L. Kantam, B. Sreedhar, *J. Am. Chem. Soc.* **2002**, *124*, 14127; e) S. S. Prockl, W. Kleist, M. A. Gruber, K. Köhler, *Angew. Chem.* **2004**, *116*, 1917; *Angew. Chem. Int. Ed.* **2004**, *43*, 1881; f) K. Köhler, R. G. Heidenreich, J. G. E. Krauter, M. Pietsch, *Chem. Eur. J.* **2002**, *8*, 622.
[34] For clarity, we use here the term "leaching", which is common in this context. In practice, oxidative addition is most likely the first event leading to detachment of Pd^{II} ions from the cluster.
[35] J. A. Widegren, R. G. Finke, *J. Mol. Catal. A* **2003**, *198*, 317.
[36] A. Biffis, M. Zecca, M. Basato, *Eur. J. Inorg. Chem.* **2001**, 1131.
[37] Y. Li, E. Boone, M. A. El-Sayed, *Langmuir* **2002**, *18*, 4921.
[38] J. Le Bars, U. Specht, J. S. Bradley, D. G. Blackmond, *Langmuir* **1999**, *15*, 7621.
[39] M. B. Thathagar, P. J. Kooyman, R. Boerleider, E. Jansen, C. J. Elsevier, G. Rothenberg, *Adv. Synth. Catal.* **2005**, *347*, 1965.
[40] C. C. Cassol, A. P. Umpierre, G. Machado, S. I. Wolke, J. Dupont, *J. Am. Chem. Soc.* **2005**, *127*, 3298.
[41] K. B. Jirage, J. C. Hulteen, C. R. Martin, *Science* **1997**, *278*, 655.
[42] S. R. Chowdhury, J. E. ten Elshof, N. E. Benes, K. Keizer, *Desalination* **2002**, *144*, 41.
[43] J. S. Bradley, B. Tesche, W. Busser, M. Maase, M. T. Reetz, *J. Am. Chem. Soc.* **2000**, *122*, 4631.
[44] Permporometry is a characterization technique for determining pore size distributions in membranes. It is based on the controlled blocking of the pores by capillary condensation and the simultaneous measurement of the inert-gas diffusion flux through the remaining open pores. When a condensable vapor (e.g., cyclohexane) is introduced at low vapor pressure, first a molecular adsorption layer (the t layer) is formed on the inner surface of the pores. The pore size (d [nm]) is defined by $d = 2(r_K + t)$, where r_K is the Kelvin radius, and t the layer thickness

 © 2006 Wiley-VCH Verlag GmbH & Co. KGaA, Weinheim

(ca. 0.3 nm). For more details, see: a) A. Mey-Marom, M. G. Katz, *J. Memb. Sci.* **1986**, *27*, 119; b) M. G. Katz, G. Baruch, *Desalination* **1986**, *58*, 199.
[45] N. Benes, A. Nijmeijer, H. Verweij in *Recent Advances in Gas Separation by Microporous Ceramic Membranes* (Ed.: N. K. Kanellopoulos), Elsevier, Amsterdam, **2000**.
[46] One can quantify the number of moles of diffused **6** on the clusters side by comparing the diffusion rates. However, very small amounts of **6** form since in the initial stage of the Heck reaction the concentration gradient is very low. This results in lower diffusion rates of **6** (3.5 mol% after 100 h) compared to those observed in the control experiments with pure **6** (4.5 mol% after 100 h, see Figure 3).
[47] S. R. Chowdhury, K. Keizer, J. E. ten Elshof, D. H. A. Blank, *Langmuir* **2004**, *20*, 4548.
[48] J. G. de Vries, *Dalton Trans.* **2006**, 421.
[49] For a detailed overview of this type of synthesis, see: N. Benes, A. Nijmeijer, H. Verweij in *Recent Advances in Gas Separation by Microporous Ceramic Membranes* (Ed.: N. K. Kanellopoulos), Elsevier, Amsterdam, **2000**, pp. 335–372.

 © 2006 Wiley-VCH Verlag GmbH & Co. KGaA, Weinheim

Anion Binding

DOI: 10.1002/anie.200504417

Precedent and Theory Unite in the Hypothesis of a Highly Selective Fluoride Receptor**

*Mark Mascal**

The concept of the metal-ion-sandwiching cylindrophane was advanced in 1998[1] and realized the following year.[2] The idea was straightforward, that is, that a trigonal-planar heteroatom ligand set could be built into a [1,3,5]cyclophane (**1**), wherein the two benzene rings would act as a barrier to any metals which could not penetrate the aromatic van der Waals space.

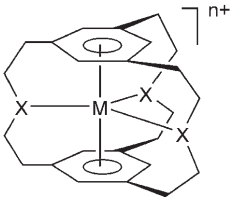

1, X = NH, O, S

Macrocycles such as **1**, which have chains with odd numbers of atoms between the aromatic rings, are known to show exceptional conformational stability.[3] In practice, this led to selective inclusion of Ag^{I} and Cu^{I}, two metal ions whose interactions with π systems are known to be unusually favorable.[4]

[*] Professor M. Mascal
Department of Chemistry
University of California, Davis
Davis, CA 95616 (USA)
Fax: (+1) 530-752-8995
E-mail: mascal@chem.ucdavis.edu

[**] This research was supported in part by the National Science Foundation through the San Diego Supercomputer Center under the SDSC/UC Academic Associates Program using DataStar, and by the National Center for Supercomputing Applications under grant number CHE040035N using the NCSA IBM p690.

It is a fact that the selective complexation of anions has been the focus of very substantial interest in recent times.[5] In principle at least, cylindrophane-type discrimination should be equally applicable to anion inclusion, assuming the electronic nature of the heteroatom ligands could be inverted, as shown for example in **2**.[6] Not surprisingly, modeling

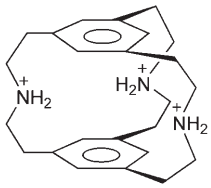

2

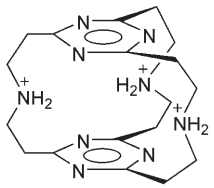

3

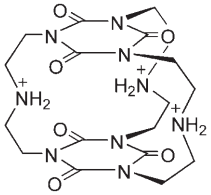

4

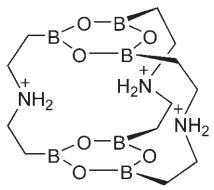

5

studies indicated that the repulsive interaction between anions and the benzene rings would make **2** a poor host. An apparent solution to this problem would be to also invert the electronic character of the aromatic rings, that is, from π-basic to π-acidic, which, it was proposed, could actually lead to a favorable interaction with anions. Indeed, detailed modeling studies by Frontera, Deyà, and co-workers,[7] Tarakeshwar, Kim, and co-workers,[8] and ourselves,[9] of anion–π interactions with triazines have revealed a bonding energy comparable to that of the well known cation–π complexation with benzene rings. Recently, examples of anion–π complexes have been observed experimentally,[10] thus adding substance to the emerging conclusion that a system such as **3** could act as a selective anion receptor. We now substantiate this hypothesis by integrating the above experimental precedent with a detailed theoretical study of the association of triazine cage **3** and its cyanuric acid (**4**) and boroxine (**5**) analogues with the fluoride and chloride ions.

The interaction between halide anions and the *s*-triazine ring has been previously modeled at various levels of theory and in all cases the $F^{-}\cdots Ar$ distance is considerably shorter than the corresponding $Cl^{-}\cdots Ar$ distance.[7–9] A recent investigation of cyanuric acid–anion bonding reaches the same conclusion.[11] To our knowledge, no such studies have yet been performed on the boroxine ring, but examination of its electrostatic potential map alongside those of *s*-triazine and cyanuric acid clearly indicated a substantial area of positive charge concentrated on the C_3 axis (Figure 1). The current study employs the density functional B3LYP method,[12] which is known to give acceptable agreement with noncovalent anion–π bond energies and distances calculated by the more expensive MP2 method.[13] Since the issue at stake here is the "fit" of the halide anions in the cavities of **3**–**5**, the

 InterScience © 2006 Wiley-VCH Verlag GmbH & Co. KGaA, Weinheim

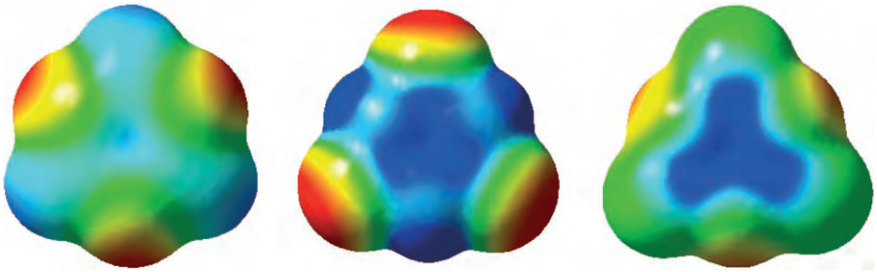

Figure 1. Calculated HF/6-31 + G(d,p) electrostatic potential surfaces for *s*-triazine (left), cyanuric acid (center), and boroxine (right), with surface energies ranging from −20 (red) to +20 (blue) kcal mol^{-1}.

empty receptors were first modeled to determine the bisector of the C_3 axis connecting the two Ar rings. This then could be compared to the preferred Ar···X$^-$ bond distances. Finally, the chloride and fluoride complexes of **3–5** were themselves modeled and the respective interaction energies determined.

All calculations were performed with the Gaussian03 program[14] with default SCF convergence criteria. Geometry optimizations were carried out using the Becke 3-parameter hybrid functional (B3LYP)[12] and the 6-31 + G(d,p) basis set. Frequency calculations were performed at the same level of theory to determine zero-point energy corrections, which were applied unscaled. Interaction energies were corrected for basis set superposition error using the counterpoise (CP) method of Boys and Bernardi.[15] In some optimizations the imposition of molecular symmetry led to the characterization of stationary points which were not true energy minima. These cases are discussed individually below.

The optimized distances between the center of the cavity of **3, 4**, and **5** and the mean plane of the aromatic ring are calculated to be 2.37, 2.20, and 2.34 Å, respectively. This is consistent with the distance of 2.46 Å found in the crystal structure of **1** (X = NH),[16] which shows the effect of repulsion between the electron-rich cavity and the benzene rings not present in **3–5**. When the above values are compared to the modeled equilibrium distances between free chloride or fluoride ions and the respective ring centroid (Table 1), a case for discrimination between the two halides based on the Ar–Ar distance emerges. The energetics of Ar···X$^-$ bonding are also significantly more favorable for fluoride than chloride, particularly for the cyanuric acid and boroxine ring systems. Here it must be noted that, with the exception of the triazine–chloride (TZ···Cl$^-$) and cyanuric acid–chloride (CA···Cl$^-$) cases, the simple Ar···X$^-$ complexes are not energy minima, but involve two imaginary vibrational frequencies, the animation of which corresponds to nucleophilic attack on the aromatic ring along two orthogonal trajectories. The problematic nature of fluoride in anion–π modeling has been described elsewhere.[11,13,17] To evaluate the anion–π interaction in halide complexes of the boroxine ring, C_{3v} symmetry was imposed during the geometry optimizations. In the absence of this constraint, the minimizations led to structures with boron–halide bonding. All other Ar···X$^-$ complexes could however be minimized without the condition of symmetry.

The geometry and energies of Ar···X$^-$···Ar sandwich complexes, which may be more relevant to the present inclusion study than the simple complexes, are also given in Table 1. Recent work by Frontera and co-workers has established that the interaction energies in complexes such as these are approximately additive, that is, E(Ar···X$^-$···Ar) ≈ E(2×Ar···X$^-$),[17] which is also supported here. In all Ar···X$^-$···Ar complexes the stationary points are not found to be minima, with imaginary vibrational frequency counts ranging from 1–5, although again the imposition of molecular symmetry was only necessary in the case of the boroxine sandwiches.

Table 1: Interaction energies [kcal mol^{-1}] and noncovalent bond distances [Å] for the complexes of *s*-triazine (TZ), cyanuric acid (CA), and boroxine (BX) with chloride and fluoride ions.

Complex	E[a]	E_{cp}[a]	$\Delta E_{F\text{-}Cl}$[b]	r[c]
TZ···Cl$^-$	−4.2	−4.0		3.48
TZ···F$^-$	−10.4	−9.0	−5.0	2.66
CA···Cl$^-$	−13.8	−13.5		3.06
CA···F$^-$	−27.4	−25.8	−12.3	2.25
BX···Cl$^-$	−12.9	−12.5		2.94
BX···F$^-$	−31.9	−29.6	−17.1	1.93
TZ···Cl$^-$···TZ	−8.1	−7.6		3.49
TZ···F$^-$···TZ	−18.9	−16.5	−8.9	2.70
CA···Cl$^-$···CA	−25.0	−24.2		3.12
CA···F$^-$···CA	−44.4	−41.7	−17.5	2.43
BX···Cl$^-$···BX	−23.1	−22.1		3.02
BX···F$^-$···BX	−47.2	−43.9	−21.8	2.23

[a] B3LYP/6-31 + G(d,p) interaction energies without (E) and with (E_{cp}) counterpoise correction. [b] Difference between the E_{cp} values of the fluoride and chloride complexes. [c] Noncovalent bond distances (r) for simple (Ar···X$^-$) and sandwich (Ar···X$^-$···Ar) complexes.

Table 2 compares the Ar–Ar bisector distances for empty receptors **3–5** with the ring centroid···anion distances of the halide sandwich complexes from Table 1. Examination of the numbers suggests that both chloride and fluoride are too large for the triazine-based receptor **3**, the former by 1.12 Å, but the latter by only 0.33 Å. This is likewise the case for the cyanuric acid receptor **4**, where the chloride ion is 0.92 Å and the fluoride ion 0.23 Å larger than the cavity. For boroxine analogue **5**, the chloride ion is 0.68 Å too large while the optimal fluoride bonding distance is actually slightly less than the dimension of the empty cavity by 0.11 Å.

Table 2: Comparison of the Ar–Ar bisector distances [Å] for empty receptors **3, 4**, and **5** with the ring centroid···anion distances [Å] of the Ar···X$^-$···Ar complexes from Table 1.

Ring system	Ar–Ar/2	Ar···Cl$^-$	Ar···F$^-$
s-triazine	2.37	3.49	2.70
cyanuric acid	2.20	3.12	2.43
boroxine	2.34	3.02	2.23

© 2006 Wiley-VCH Verlag GmbH & Co. KGaA, Weinheim

With the numbers both in Table 1 and Table 2 pointing to significant differences in the ability of **3–5** to accommodate fluoride versus chloride, it only remained to model the halide complexes of **3–5** themselves and evaluate the respective binding energies. Importantly, all six complexes listed in Table 3 are confirmed to be true energy minima, with no imaginary vibrational frequencies as determined by Hessian analysis. Optimizations were carried out in the gas phase and solution energies were then determined using the conductor-like polarizable continuum model (CPCM) for water ($\varepsilon = 78.39$),[18] with the molecular cavity specified by the United Atom Topological Model applied on radii optimized for the PBE0/6-31G(d) level of theory. Both gas- and solution-phase interaction energies are given in Table 3.

Table 3: Interaction energies [kcal mol^{-1}] for the complexes of **3, 4**, and **5** with fluoride and chloride ions.

Complex	E[a]	$\Delta E_{F\text{-}Cl}$[b]	E_{H_2O}[a]	$\Delta E_{F\text{-}Cl\ (H_2O)}$[b]
3·Cl$^-$	−237.5		−1.1	
4·Cl$^-$	−245.0		−13.4	
5·Cl$^-$	−254.8		−21.8	
3·F$^-$	−292.6	−55.1	−30.0	−28.9
4·F$^-$	−296.3	−51.4	−36.9	−23.5
5·F$^-$	−295.6	−40.7	−35.7	−13.9

[a] Counterpoise-corrected B3LYP/6-31 + G(d,p) interaction energies in the gas phase (E) and in an aqueous solvent model (E_{H_2O}). [b] Differences between the energy values of the fluoride and chloride complexes.

In agreement with predictions based on Ar···X$^-$ distances, complexation of fluoride in **3–5** is calculated to be more energetically favorable than chloride by > 40 kcal mol^{-1} in the gas phase. While the complexation energies for the F$^-$ ion in Table 3 are about three times the experimental enthalpy of F$^-$ hydration,[19] raw comparison of these values is of limited predictive significance in regard to the potential of **3–5** to extract fluoride from water, given the absence of activation parameters and entropy values, as well as the assumptions inherent in nonexplicit, polarized continuum models of water. However, comparison of the *relative* energetics of complexation points to a virtually exclusive preference for fluoride over chloride, from the gas phase to water, in all three receptors.

Since the principal interaction in these complexes is the ion-pair-reinforced hydrogen bonding of the ammonium groups with the anions, it may be supposed that the intrinsically stronger ammonium···F$^-$ interaction could actually form the basis for the difference in binding energy. To isolate the relative contributions of these interactions, we have also modeled the association of three NH_4^+ ions in a trigonal plane around the chloride and fluoride ions (Table 4). The difference between these energies and the much larger overall complexation energies in Table 3 are due for the most part to the fact that the three ammonium sites in **3–5** are in enforced proximity to each other, and this electrostatic repulsion term is not present for the simple NH_4^+ ion model. Attempting to reproduce an analogous proximity between three NH_4^+ ions is however unnecessary, since raising the energy of the starting point does not affect the comparison of the interaction energies. Even given that the contribution of three NH$^+$···F$^-$ bonds to the stabilization of the fluoride complexes of **3–5** is about 11 kcal mol^{-1} greater than that of three NH$^+$···Cl$^-$ bonds in the analogous chloride complexes (Table 4), there is still > 10 kcal mol^{-1} "additional" stability in the fluoride complexes of **3** and **4** in aqueous solution. This observation suggests that the discrimination is due, at least in these two cases, to the better steric fit of fluoride in the receptors. The fact that the fit of chloride in boroxine receptor **5** was predicted from the data in Table 2 to be the best of the three is consistent with the diminished stabilization of its fluoride complex (3 kcal mol^{-1}) above and beyond the stronger NH$^+$···F$^-$ hydrogen bonding.

Table 4: Interaction energies [kcal mol^{-1}] for $(NH_4^+)_3$···X$^-$ complexes.

Aggregate	E[a]	$\Delta E_{F\text{-}Cl}$[b]	E_{H_2O}[a]	$\Delta E_{F\text{-}Cl\ (H_2O)}$[b]
$(NH_4^+)_3$···Cl$^-$	−130.0		−10.8	
$(NH_4^+)_3$···F$^-$	−161.9	−31.9	−21.6	−10.8

[a] Counterpoise-corrected B3LYP/6-31 + G(d,p) interaction energies in the gas phase (E) and in an aqueous solvent model (E_{H_2O}). [b] Difference between the energy values of the fluoride and chloride complexes.

Finally, the angle of the intracavity NH···X$^-$ hydrogen bonds in the halide complexes of **3–5** lends further insights into the above complementarity argument. The N···Cl$^-$ distances in the chloride complexes of **3–5** are 0.06–0.17 Å shorter than those in the $(NH_4^+)_3$···Cl$^-$ model, thus leading to suboptimal NH···Cl$^-$ angles of 162–166°. On the other hand, the analogous N···F$^-$ distances are 0.08–0.18 Å longer than those of the $(NH_4^+)_3$···F$^-$ complex, with attendant angles of 176–177°. The optimized angle in both the fluoride and chloride $(NH_4^+)_3$···X$^-$ models is 179°.

Although in all three cases examined above, fluoride complexation benefits from stronger Ar···X$^-$···Ar interactions, stronger $^+$NH···X$^-$ bonding, and a better fit in the cyclophane cavity, the order of complementarity is clearly **3** > **4** > **5**, since the triazine ring shows the lowest energetic discrimination between the two halide ions while **3** shows the largest $\Delta E_{F\text{-}Cl}$ values, and vice-versa for boroxine and **5**.

Having thus established a basis for a fluoride-selective complexing agent, the synthesis of **3–5** is highly recommended. Benzene-based cyclophanes **1** have been prepared by joining two hemispheres of the cage using the intuitive S_N2 approach or by cyclotrimerization of the appropriately substituted triyne.[1,2,16] The synthesis of substituted *s*-triazines and cyanuric acids is well-described in the literature, so sufficient opportunity may exist for the preparation of these cages by analogous methods using materials derived from published sources. Trialkyl boroxines on the other hand can be prepared by the dehydration of alkyl boronic acids by azeotropic distillation with benzene.[20]

In summary, novel receptors are proposed that take advantage of the high conformational stability of the cylindrophane framework, which effectively discriminates guests by size. Based on the electron-deficient *s*-triazine, cyanuric acid, and boroxine ring systems, theoretical analysis of the binding energies of chloride and fluoride ions in macrocycles **3–5** suggests, in all three cases, a high level of selectivity for fluoride both in the gas phase and in a water solvent model.

 © 2006 Wiley-VCH Verlag GmbH & Co. KGaA, Weinheim

Although selective sensing of fluoride has been shown to be feasible because of its marked differences in chemical properties to those of chloride,[21] we are aware of few organic hosts which selectively encapsulate fluoride.[22] Such receptors may find applications both in sensing and in the ^{18}F labeling of targeted tracer probes in nuclear medicine.[23]

Received: December 12, 2005
Published online: March 21, 2006
Delayed at author's request

Keywords: ab initio calculations · anions · cyclophanes · host–guest systems · hydrogen bonding

[1] M. Mascal, J. Hansen, A. J. Blake, W.-S. Li, *Chem. Commun.* **1998**, 355. It could be argued that the very concept of the cylindrophane was introduced by Vögtle in 1973 (R. G. Lichtenthaler, F. Vögtle, *Chem. Ber.* **1973**, *106*, 1319), wherein a trioxo analogue of **1** was prepared (namely, $COCH_2SCH_2CH_2$-bridged), alongside a series of related cyclophanes. Although some of the macrocycles in that work appeared to form complexes with metal ions (but not the analogue of **1** above), no characterization of the products was possible. Later, Japanese workers reported the synthesis of a triester analogue of **1** (namely, $CH_2CO_2CH_2CH_2$-bridged; M. Kanishi, J. Kunizaki, J. Inanaga, M. Yamaguchi, *Bull. Chem. Soc. Jpn.* **1981**, *54*, 3828). No mention of the binding of metal ions was made.

[2] M. Mascal, J.-L. Kerdelhué, A. J. Blake, P. A. Cooke, *Angew. Chem.* **1999**, *111*, 2094; *Angew. Chem. Int. Ed.* **1999**, *38*, 1968.

[3] J. Dale, *Angew. Chem.* **1966**, *78*, 1070; *Angew. Chem. Int. Ed. Engl.* **1966**, *5*, 1000.

[4] M. Mascal, J.-L. Kerdelhué, A. J. Blake, P. A. Cooke, R. J. Mortimer, S. J. Teat, *Eur. J. Inorg. Chem.* **2000**, 485.

[5] a) J. W. Steed, J. L. Atwood in *Supramolecular Chemistry*, Wiley, New York, **2000**, pp. 198–249; b) *Supramolecular Chemistry of Anions* (Eds.: A. Bianchi, K. Bowman-James, E. Garcia-España), Wiley-VCH, New York, **1997**; c) P. D. Beer, P. A. Gale, *Angew. Chem.* **2001**, *113*, 502; *Angew. Chem. Int. Ed.* **2001**, *40*, 486.

[6] It should be noted here that a study (F. Hettche, P. Rei, R. W. Hoffmann, *Chem. Eur. J.* **2002**, *8*, 4946) has been published on a related trigonal design for anion recognition involving a cyanuric acid platform which may involve the ring in the binding of anions, although this is not commented upon in the paper. Although some selectivity between chloride, bromide, and nitrate ions was achieved, the work involved podand-like H-bonding hosts with a large degree of conformational flexibility, which is essentially the opposite of the emphasis of the present work.

[7] C. Garau, A. Frontera, P. Ballester, D. Quiñonero, A. Costa, P. M. Deyà, *Eur. J. Org. Chem.* **2005**, 179, and references therein.

[8] D. Kim, P. Tarakeshwar, K. S. Kim, *J. Phys. Chem. A* **2004**, *108*, 1250.

[9] M. Mascal, A. Armstrong, M. D. Bartberger, *J. Am. Chem. Soc.* **2002**, *124*, 6274.

[10] a) P. de Hoog, P. Gamez, I. Mutikainen, U. Turpeinen, J. Reedijk, *Angew. Chem.* **2004**, *116*, 5939; *Angew. Chem. Int. Ed.* **2004**, *43*, 5815; b) S. Demeshko, S. Dechert, F. Meyer, *J. Am. Chem. Soc.* **2004**, *126*, 4508; c) Y. S. Rosokha, S. V. Lindeman, S. V. Rosokha, J. K. Kochi, *Angew. Chem.* **2004**, *116*, 4750; *Angew. Chem. Int. Ed.* **2004**, *43*, 4650; d) R. M. Fairchild, K. Travis Holman, *J. Am. Chem. Soc.* **2005**, *127*, 16364.

[11] A. Frontera, F. Saczewski, M. Gdaniec, E. Dziemidowicz-Borys, A. Kurland, P. M. Deyà, D. Quiñonero, C. Garau, *Chem. Eur. J.* **2005**, *11*, 6560.

[12] a) A. D. Becke, *J. Chem. Phys.* **1993**, *98*, 5648; b) A. D. Becke, *J. Chem. Phys.* **1993**, *98*, 1372; c) C. Lee, W. Yang, R. G. Parr, *Phys. Rev. B* **1988**, *37*, 785; d) P. J. Stephens, F. J. Devlin, C. F. Chabalowski, M. J. Frisch, *J. Phys. Chem.* **1994**, *98*, 11623.

[13] D. Quiñonero, C. Garau, A. Frontera, P. Ballester, A. Costa, P. M. Deyà, *J. Phys. Chem. A* **2005**, *109*, 4632.

[14] Gaussian 03, Revision B.04: M. J. Frisch, et al., see Supporting Information.

[15] S. F. Boys, F. Bernardi, *Mol. Phys.* **1970**, *19*, 553.

[16] J. Hansen, A. J. Blake, W.-S. Li, M. Mascal, *J. Chem. Soc. Perkin Trans. 1* **1998**, 3371.

[17] C. Garau, D. Quiñonero, A. Frontera, P. Ballester, A. Costa, P. M. Deyà, *J. Phys. Chem. A* **2005**, *109*, 9341.

[18] V. Barone, M. Cossi, *J. Phys. Chem. A* **1998**, *102*, 1995.

[19] $\Delta H° =$ ca. 110 kcal mol^{-1}: M. D. Tissandier, K. A. Cowen, W. Y. Feng, E. Gundlach, M. H. Cohen, A. D. Earhart, J. V. Coe, *J. Phys. Chem. A* **1998**, *102*, 7787.

[20] The hydrolytic sensitivity of boroxines may limit the use of **5** to organic environments; P. K. McCusker, E. C. Asby, H. S. Makowski, *J. Am. Chem. Soc.* **1957**, *79*, 5179.

[21] Examples: a) M. Melaimi, F. P. Gabbaï, *J. Am. Chem. Soc.* **2005**, *127*, 9680; b) S. Aldridge, C. Bresner, I. A. Fallis, S. J. Coles, M. B. Hursthouse, *Chem. Commun.* **2002**, 740; c) G. Xu, M. A. Tarr, *Chem. Commun.* **2004**, 1050; d) S. Arimori, M. G. Davidson, T. M. Fyles, T. G. Hibbert, T. D. James, G. I. Kociok-Köhn, *Chem. Commun.* **2004**, 1640, and references therein.

[22] For a survey of macrocyclic and macrobicyclic amine-, ammonium-, and amide-based receptors which complex fluoride ions, see: K. Bowman-James, *Acc. Chem. Res.* **2005**, *38*, 671.

[23] S. S. Gambhir, *Nat. Rev. Cancer* **2002**, *2*, 683.

 © 2006 Wiley-VCH Verlag GmbH & Co. KGaA, Weinheim

Formamide Hydrolysis

DOI: 10.1002/anie.200600283

Formamide Hydrolysis in Alkaline Aqueous Solution: Insight from Ab Initio Metadynamics Calculations**

Jochen Blumberger, Bernd Ensing, and Michael L. Klein*

The nucleophilic attack of an amide bond by hydroxide is probably one of the best illustrations of solvent effects in chemistry (see Scheme 1). While barrierless and highly exothermic in the gas phase,[1] formation of the tetrahedral intermediate (**TI**) is the rate-determining step in the hydrol-

[*] Dr. J. Blumberger, Dr. B. Ensing, Prof. Dr. M. L. Klein
Center for Molecular Modeling and Department of Chemistry
University of Pennsylvania
231 S. 34th Street, Philadelphia, PA 19104-6323 (USA)
Fax: (+1) 215-573-6233
E-mail: jochen@cmm.upenn.edu

[**] We acknowledge the NIH for financial support and the Pittsburgh Supercomputing Center for providing high-performance computing facilities.

Supporting information for this article is available on the WWW under http://www.angewandte.org or from the author.

© 2006 Wiley-VCH Verlag GmbH & Co. KGaA, Weinheim

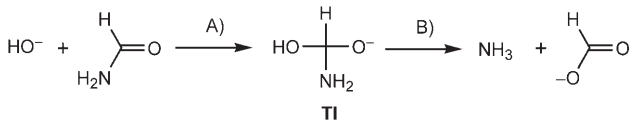

Scheme 1. Alkaline hydrolysis of formamide: 1) Formation of the tetrahedral intermediate (**TI**); 2) dissociation of **TI** into the products.

ysis of formamide in alkaline aqueous solution, with a free energy of activation of about 21 kcal mol^{-1}.[2] For this reason the barrier has often been referred to as "solvent induced".[1,3,4] The inverted energy profile for the reaction in solution is usually attributed to the large free energy of solvation of the hydroxide ion which has to be partly overcome to reach the transition-state region. Although free energies of activation have been calculated in reasonable[1,4,5] and somewhat better agreement with experiment,[3,6] a detailed understanding of the transport of hydroxide to the carbonyl bond has not been achieved yet. Motivated by the successful prediction of the solvation structure of aqueous hydroxide,[7] which was confirmed by recent neutron diffraction data,[8] we report herein the mechanism of the nucleophilic attack of formamide using Car–Parrinello molecular dynamics (CPMD) simulation.[9]

In the generally accepted picture, formation of **TI** proceeds through a direct nucleophilic attack of the hydroxide ion as illustrated in Figure 1 A. However, measurements of the heavy-atom kinetic isotope effect (KIE) by Marlier et al.[10] challenged this traditional view and they suggested that the formation of **TI** proceeds through a general-base mechanism (Figure 1 B). In this alternative mechanism, the nucleophile is a water molecule coordinated to hydroxide, separating it from formamide. The oxygen atom of water attacks the carbonyl bond under concerted donation of a proton to hydroxide, which merely acts as a general base. The mechanism shown in Figure 1 B reminds one of the structural diffusion process of aqueous hydroxide which proceeds through hydrogen transfer and subsequent change of the identity of the oxygen atom of hydroxide.[7] To date, the situation remains unclear because both mechanisms could be accommodated by the most recent KIE experiments and proton inventory analysis.[11] However, preference was given to direct nucleophilic attack, which was also the preferred view in a recent semi-continuum ab initio study.[6]

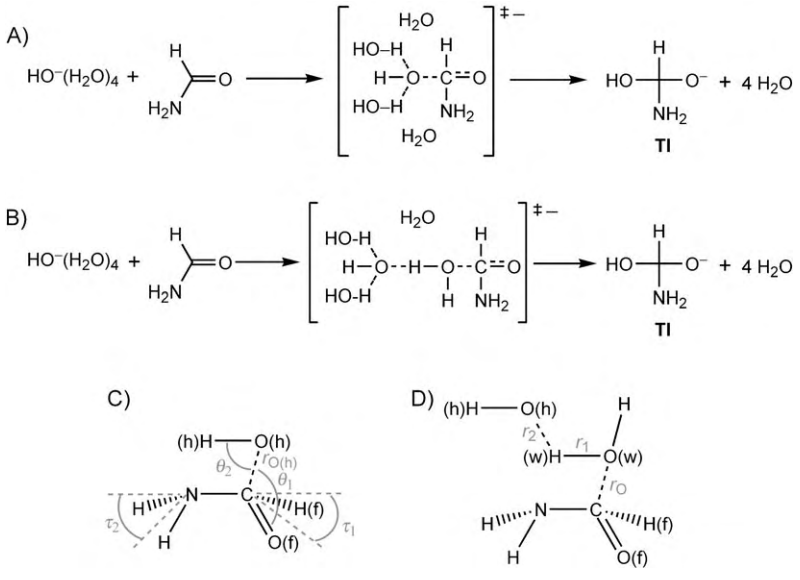

Figure 1. Two mechanisms for the first step of formamide hydrolysis in alkaline aqueous solution: A) Direct nucleophilic attack of formamide by hydroxide and B) general-base mechanism. C, D) Labeling of atoms and bonds in the umbrella-sampling (C) and 2D metadynamics (D) simulations, respectively (f = formamide, h = hydroxide, w = water).

Prompted by this controversy, we investigated the mechanism of formation of **TI** using metadynamics simulation[12] combined with CPMD.[13–15] As opposed to more conventional sampling methods, the metadynamics technique allows us to map out the relevant two-dimensional free-energy surface, $A(r_O,r_H)$, which describes the concerted general-base mechanism in question. The first order parameter was chosen to be the distance r_O between the carbon atom of formamide and the oxygen atom of the water molecule, O(w), that separates hydroxide and formamide.[16] The second order parameter measures the progress of transfer of the hydrogen atom of water, H(w), to hydroxide, $r_H = r_2 - r_1$ (Figure 1 D). In addition, we computed the one-dimensional free-energy profile $A(r_{O(h)})$ for the direct nucleophilic attack using umbrella sampling of the C–O(h) distance, $r_{O(h)}$ (Figure 1 C; see Ref. [17] for technical details).

The 2D free-energy landscape thus obtained is shown in Figure 2. We validated the free-energy surface by comparing $A(r_O)$ [Eq. (1); $\beta = 1/k_B T$] to $A(r_{O(h)})$, which are formally equal potentials of mean force (PMF).[18] We found that $A(r_O)$ approximates $A(r_{O(h)})$ fairly well, underestimating the barrier obtained from umbrella sampling by only 1.1 kcal mol^{-1}. The free-energy barrier obtained from the PMF $A(r_O)$, 17.9 kcal mol^{-1}, can be related to the experimental free enthalpy of activation only approximately by adding three additional free-energy terms, one of them accounting for standard concentrations of the solutes. These additional free-energy contributions were estimated in Ref. [17] to be 5.0 kcal mol^{-1}. Correcting for the error of the BLYP density functional (overestimation of the free-energy barrier by 1.7 kcal mol^{-1} relative to MP2, see Supporting Information), we obtained an estimate of 17.9 + 5.0 − 1.7 = 21.2 kcal mol^{-1} for the free energy of activation, which is virtually identical with the experimental free enthalpy of activation for formation of **TI**, $\Delta G^{\pm}_{25} =$ 21.2 kcal mol^{-1}.[2] The exact agreement with experiment is rather fortuitous because the uncertainty of the metadynamics simulation is about 2 kcal mol^{-1} (see Supporting Information) and the uncertainty associated with the estimation of the additional free-energy terms is 2–3 kcal mol^{-1}.[17]

$$A(r_O) = \int_{-1.5}^{1.5} dr_H \exp[-\beta(A(r_O;r_H))] \qquad (1)$$

Having validated the accuracy of our free-energy calculation, we next discuss the mechanism of forma-

 © 2006 Wiley-VCH Verlag GmbH & Co. KGaA, Weinheim

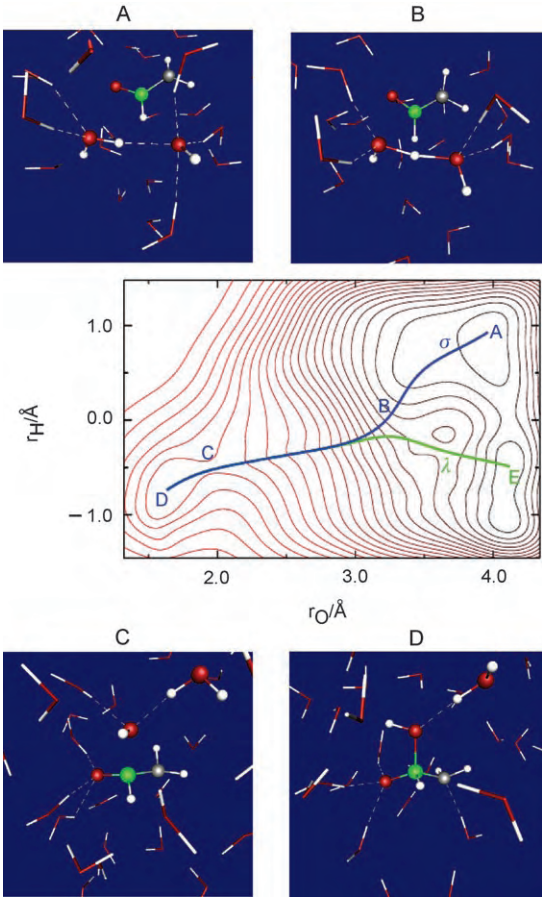

Figure 2. The center panel shows the 2D free-energy surface, $A(r_O,r_H)$, for the formation of the tetrahedral intermediate (**TI**) as obtained from Car–Parrinello metadynamics simulation. The minimum free-energy paths connecting A (formamide + hydroxide) with D (**TI**), and E (formamide + hydroxide) with D, are denoted paths σ and λ, respectively. The free energy of A is set equal to zero and increases monotonously along σ. The spacing between contour lines is equidistant and equal to 1 kcal mol^{-1}. The two distances (order parameters) are defined in Figure 1 D, $r_H = r_2 - r_1$. Snapshots of a reactive metadynamics trajectory along σ are shown for the reactant (A), hydrogen transfer (B), the transition state (C), and the tetrahedral intermediate (D). O red; N green; C gray; H white. Solute atoms and solvent molecules are depicted as spheres and sticks, respectively. Relevant hydrogen bonds are depicted in dashed lines.

tion of **TI**. The 2D free-energy surface exhibits two minima for the reactant state, one in which the nucleophile is initially a water molecule (A) and one in which it is the hydroxide ion (E; Figure 2). The corresponding minimum free-energy paths σ and λ, which connect A and E with the product **TI** (D) lead through the same transition state, C, that was also obtained by one-dimensional umbrella sampling of the distance $r_{O(h)}$. Upon analyzing the metadynamics trajectory along σ (snapshots A–D in Figure 2), we found clear separation between hydrogen transfer and formation of the carbon–oxygen bond for both directions, that is, for formation and dissociation of **TI**. At a separation distance $r_O = 2.8 \pm 0.2$ Å the hydrogen transfer is completed (up to $r_H = -0.3$ Å), and it is the fully restored hydroxide ion that participates in the transition state at $r_O = 1.95$ Å (snapshot C). Therefore, on the basis of the concept of the minimum free-energy path, we do not find evidence for concerted hydrogen transfer and nucleophilic attack, which makes the general-base mechanism less likely.

The mechanism described by the path σ can be considered as lying in between the general-base mechanism and the path λ, which describes direct nucleophilic attack. The difference between paths σ and λ is that in the former hydroxide is transported from a separation distance of 4 Å to the transition-state region (1.8–2.2 Å) by structural diffusion, while in the latter transport occurs through self-diffusion. Although the transition state is the same for both σ and λ, the two paths are distinct by the dynamics of desolvation prior to formation of the transition state. Figure 3 A and C show the solvent hydrogen coordination numbers for the oxygen atom of hydroxide, O(h) (direct nucleophilic attack), and for the water molecule that transforms into hydroxide along path σ. In Figure 3 A, the coordination number of hydroxide decreases from four to three at $r_{O(h)} = 3.3$ Å and from three to two at $r_{O(h)} = 2.0$ Å, shortly before the transition state is

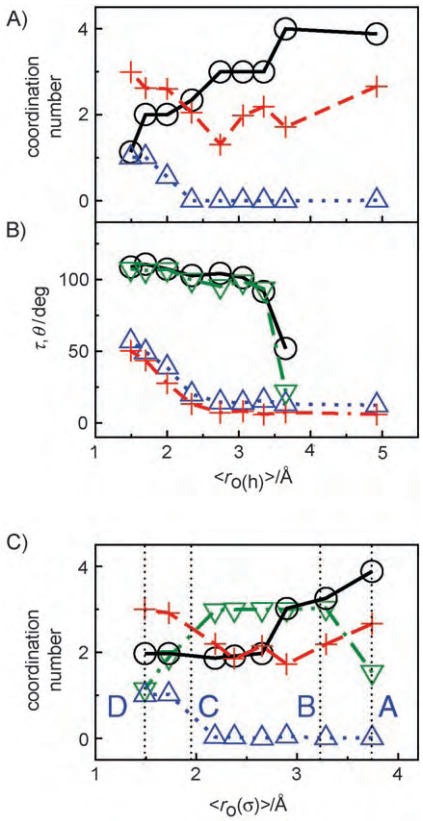

Figure 3. A) Solvent hydrogen coordination numbers of O(h) (○), O(f) (+), and N (△) for the direct nucleophilic attack of hydroxide. The data were obtained from umbrella sampling of the reaction coordinate $r_{O(h)}$. The coordination numbers were computed for each window by spherical integration of the radial distributions up to a distance of 2.5 Å and are plotted as a function of the average distance $\langle r_{O(h)} \rangle$. B) Average tilt angles τ_1 (+) and τ_2 (△) and bending angles θ_1 (○) and θ_2 (▽; see Figure 1 C for definitions). C) Solvent hydrogen coordination numbers of O(h) (○), O(w) (▽), O(f) (+), and N (△) along the minimum free-energy path σ shown in Figure 2. σ was sampled using nine windows with restraining potentials applied to r_O and r_H. Averages were computed from trajectories of length 8–10 ps.

 © 2006 Wiley-VCH Verlag GmbH & Co. KGaA, Weinheim

reached. The desolvation process is strikingly different along σ. The loss of a first-shell water molecule bonded to hydroxide initiates proton transfer. Upon completion of the transfer at $r_O = 2.7$ Å, the hydrogen coordination numbers for hydroxide and water generated at that instant are three and two, respectively. On the way to the transition state, a hydrogen bond between hydroxide and a solvent molecule is broken, generating the reactive twofold coordination.

In response to the accumulating negative charge density on formamide, the solvent hydrogen coordination number of the carbonyl oxygen atom, O(f), increases from about two for the reactant state to 2.6 for the transition state. Similarly, the coordination number of nitrogen increases from zero to 0.6. In parallel, the tilt angles measuring the tetrahedral character of carbon and nitrogen atoms increase from $\tau_1 = 6°$ and $\tau_2 = 12°$ to $\tau_1 = 28°$ and $\tau_2 = 39°$, respectively (Figure 3 B; see also Figure 1 C for a definition of the angles). At the transition state, both bending angles θ_1 (O(h)-C-O(f)) and θ_2 (H(h)-O(h)-C) are on average 107° to facilitate optimal interaction between the lone pair of hydroxide and the π* orbital of formamide. The change of solvation structure and intramolecular reorganization of formamide described here along the coordinate $r_{O(h)}$ is very similar to that along the path σ.

Upon analyzing the solvent dynamics in the transition-state region, we found that an additional hydrogen bond is formed either with oxygen atom Of or with nitrogen, that is, the coordination numbers of O(f) and N are either three and zero or two and one, giving on average 2.6 and 0.6, respectively. The formation of one hydrogen bond alternating at the transition state between O(f) and N cannot compensate for the loss of two strong hydrogen bonds formed with hydroxide. According to our results, this is the solvent contribution to the activation barrier for the formation of **TI**. However, as the tetrahedral character of carbon and nitrogen atoms is significantly increased at the transition state, a considerable contribution to the barrier comes from partial breaking of the π bond. At an average separation of 2.3 Å, a second hydrogen bond formed with hydroxide breaks (average hydrogen coordination number: 2.35), although the free energy increases to only two-thirds (12.4 kcal mol^{-1}) of the full barrier (19.0 kcal mol^{-1}). Both the increase in the tetrahedral angles from $\tau_1 = 13°$, $\tau_2 = 20°$ at 2.3 Å to $\tau_1 = 28°$, $\tau_2 = 39°$ at 2.0 Å and completion of the breaking of the second hydrogen bond make up the remaining third of the energy barrier. Hence, although the free energy of activation is entirely induced by the solvent[1,3,4,19] (because there is no barrier in the gas phase), desolvation of hydroxide is not the sole source for the activation barrier; electronic reorganization of formamide also provides a significant contribution.

Our results contrast the interpretation of a recent Car–Parrinello simulation study of the same reaction.[4] The authors reported a very early transition state located at $r_{O(h)} = 2.2$ Å, a distance that is larger by 0.34 Å compared to our value. At this separation, the π bond is still intact which led to the conclusion that the activation barrier is entirely due to desolvation of hydroxide. However, the numerical results in Reference [4] are somewhat uncertain (see Ref. [17] for a detailed discussion), while the two independent approaches presented here (extensive umbrella sampling and metadynamics) converge to the same result and predict a transition state at about 1.9 Å in good agreement with two previous computational studies.[1,6]

In summary, we have found two possible mechanisms for the nucleophilic attack of formamide by solvated hydroxide. Separated from the substrate by one layer of water molecules, hydroxide either attacks the carbonyl bond directly (path λ in Figure 2) or accepts a proton and transforms one of the water molecules into the reactive hydroxide ion (path σ, snapshots A–D in Figure 2). However, for the latter mechanism we find that hydrogen transfer is completed well before the transition state is reached. Thus, our theoretical picture of the first step of formamide hydrolysis supports the mechanistic interpretation of KIE studies of Slebocka-Tilk et al.[11] and is in line with the results of a recent semi-continuum study.[6]

We conclude that the electrophilic character of formamide is not strong enough for reaction with a first-shell water molecule of aqueous hydroxide. By contrast, a transition state related to a general-base mechanism was found for the more powerful electrophile, methyl formate.[20] Our simulation shows that the free-energy barrier for formation of the tetrahedral intermediate (**TI**) is, although not entirely, due to the breaking of two strong hydrogen bonds formed between the solvent and hydroxide. Such an unfavorable activation process of the nucleophile is effectively circumvented in an enzyme active site, where OH groups of amino acid side chains or OH groups bound to Zn ions are the nucleophile rather than solvated hydroxide. The electrophilic character of the substrate is usually increased at the active site and considerably higher than in aqueous solution, which could make the general-base mechanism more competitive. In future investigations, we will address this issue by studying the reaction mechanisms of Zn-containing peptidases.

Experimental Section

Computational methods: Metadynamics simulation was performed using the plane wave implementation[21] of Car–Parrinello molecular dynamics.[9] The reaction system was modeled by a periodically repeated cubic unit cell of length 10.032 Å containing one formamide molecule, one hydroxide ion, and 29 water molecules. The valence orbitals were expanded in plane waves with a reciprocal space kinetic energy cutoff of 70 Ry. Core electrons were described by pseudopotentials generated according to the Troullier–Martins scheme,[22] and the exchange correlation energy was calculated using the Becke–Lee–Yang–Parr (BLYP) density functional.[23,24] The metadynamics of the collective variables r_O,r_H were coupled to the dynamics of the physical system through an extended Car–Parrinello Lagrangian.[13] After equilibration of the reactant at 300 K, the 2D free-energy surface was explored using spherical gaussian potentials consecutively added to the metadynamics biasing potential. The minimum free-energy path connecting the reactant and product wells was located using the trace_irc program.[14] The detailed simulation protocol can be found in the Supporting Information.

Received: January 23, 2006
Published online: March 28, 2006

Keywords: ab initio calculations · hydrolysis · reaction mechanisms · solvent effects · thermodynamics

 © 2006 Wiley-VCH Verlag GmbH & Co. KGaA, Weinheim

[1] D. Bakowies, P. A. Kollman, *J. Am. Chem. Soc.* **1999**, *121*, 5712.
[2] H. Slebocka-Tilk, F. Sauriol, M. Monette, R. S. Brown, *Can. J. Chem.* **2002**, *80*, 1343.
[3] M. Štrajbl, J. Florián, A. Warshel, *J. Am. Chem. Soc.* **2000**, *122*, 5354.
[4] M. Cascella, S. Raugei, P. Carloni, *J. Phys. Chem. B* **2004**, *108*, 369.
[5] D. Zahn, *Chem. Phys. Lett.* **2004**, *383*, 134.
[6] J. R. Pliego, Jr., *Chem. Phys.* **2004**, *306*, 273.
[7] M. E. Tuckerman, D. Marx, M. Parrinello, *Nature* **2002**, *417*, 925.
[8] A. Botti, F. Bruni, S. Imberti, M. A. Ricci, A. K. Soper, *J. Mol. Liq.* **2005**, *117*, 81.
[9] R. Car, M. Parrinello, *Phys. Rev. Lett.* **1985**, *55*, 2471.
[10] J. F. Marlier, N. Carter Dopke, K. R. Johnstone, T. J. Wirdzig, *J. Am. Chem. Soc.* **1999**, *121*, 4356.
[11] H. Slebocka-Tilk, A. A. Neverov, R. S. Brown, *J. Am. Chem. Soc.* **2003**, *125*, 1851.
[12] A. Laio, M. Parrinello, *Proc. Natl. Acad. Sci. USA* **2002**, *99*, 12562.
[13] M. Iannuzzi, A. Laio, M. Parrinello, *Phys. Rev. Lett.* **2003**, *90*, 238302.
[14] B. Ensing, A. Laio, M. Parrinello, M. L. Klein, *J. Phys. Chem. B* **2005**, *109*, 6676.
[15] B. Ensing, M. L. Klein, *Proc. Natl. Acad. Sci. USA* **2005**, *102*, 6755.
[16] Equilibrium simulations show that the hydroxide ion, which undergoes structural diffusion in the bulk, is for most of the time separated from formamide by more than 5 Å. At the closest approach observed within 15 ps of dynamics (3.9 Å), the hydroxide ion was separated from formamide by one layer of water molecules.
[17] J. Blumberger, M. L. Klein, *Chem. Phys. Lett.*, **2006**, in press.
[18] See Supporting Information for a summary of data characterizing the 2D free-energy surface. Therein, we also discuss more technical aspects such as the accuracy of the metadynamics simulation and electronic structure method used, and possible uncertainties due to nuclear quantum effects.
[19] S. J. Weiner, U. Chandra Singh, P. A. Kollman, *J. Am. Chem. Soc.* **1985**, *107*, 2219.
[20] J. R. Pliego, Jr., J. M. Riveros, *Chem. Eur. J.* **2002**, *8*, 1945.
[21] CPMD Version 3.10.0, The CPMD consortium, http://www.cpmd.org, MPI für Festkörperforschung and the IBM Zurich Research Laboratory, **2005**.
[22] N. Troullier, J. Martins, *Phys. Rev. B* **1991**, *43*, 1993.
[23] A. D. Becke, *Phys. Rev. A* **1988**, *38*, 3098.
[24] C. Lee, W. Yang, R. Parr, *Phys. Rev. B* **1988**, *37*, 785.

 © 2006 Wiley-VCH Verlag GmbH & Co. KGaA, Weinheim

DOI: 10.1002/anie.200504386

Changing the Activity of Electrocatalysts for Oxygen Reduction by Tuning the Surface Electronic Structure**

*Vojislav Stamenkovic, Bongjin Simon Mun, Karl J. J. Mayrhofer, Philip N. Ross, Nenad M. Markovic, Jan Rossmeisl, Jeff Greeley, and Jens K. Nørskov**

The fuel cell is a promising alternative to environmentally unfriendly devices that are currently powered by fossil fuels. In the polymer electrolyte membrane fuel cell (PEMFC), the main fuel is hydrogen, which through its reaction with oxygen produces electricity with water as the only by-product. To make PEMFCs economically viable, there are several problems that should be solved; the main one is to find more effective catalysts than Pt for the oxygen reduction reaction (ORR), $1/2\,O_2 + 2\,H^+ + 2\,e^- = H_2O$. The design of inexpensive, stable, and catalytically active materials for the ORR will require fundamental breakthroughs, and to this end it is important to develop a fundamental understanding of the catalytic process on different materials. Herein, we describe how variations in the electronic structure determine trends in the catalytic activity of the ORR across the periodic table. We show that Pt alloys involving 3d metals are better catalysts than Pt because the electronic structure of the Pt atoms in the surface of these alloys has been modified slightly. With this understanding, we hope that electrocatalysts can begin to be designed on the basis of fundamental insight.

[*] Dr. J. Rossmeisl, Dr. J. Greeley, Prof. J. K. Nørskov
Center for Atomic-Scale Materials Physics, NanoDTU
Department of Physics
Technical University of Denmark
2800 Lyngby (Denmark)
Fax: (+45) 4593-2399
E-mail: norskov@fysik.dtu.dk

Dr. V. Stamenkovic, Dr. B. S. Mun, Dr. K. J. J. Mayrhofer, Dr. P. N. Ross
Materials Sciences Division
Lawrence Berkeley National Laboratory
University of California
Berkeley, CA 94720 (USA)

Dr. N. M. Markovic
Materials Science Division
Argonne National Laboratory
Argonne, IL 60439 (USA)

[**] This work was supported by the Director, Office of Science, Office of Basic Energy Sciences, Division of Materials Sciences, US Department of Energy (contract no. DE-AC03–76SF00098), by The Danish Research Council through the NABIIT program, and by the Danish Center for Scientific Computing (grant no. HDW-1103-06). J.G. acknowledges a H. C. Ørsted Postdoctoral Fellowship from the Technical University of Denmark. N.M.M. acknowledges support from the US Department of Energy under contract W-31-109-ENG-38.

 © 2006 Wiley-VCH Verlag GmbH & Co. KGaA, Weinheim InterScience

We studied polycrystalline alloy films of the type Pt_3M (M = Ni, Co, Fe, and Ti). Although such alloys have already been considered,[1–4] the role of the 3d metals in electrocatalytic activity of Pt for the ORR remains elusive. In previous work,[1,3] one of the difficulties in illuminating the effect of alloying components was that the kinetics of the ORR was determined on poorly characterized Pt_3M electrodes. However, we have recently studied Pt_3M alloys that were then annealed to 1000 K under ultrahigh-vacuum (UHV) conditions and subsequently characterized in detail.[5] From the analysis of low-energy ion-scattering spectra, we found that the first surface layer of these alloys consists of pure Pt. The surface enrichment of Pt atoms occurs as a result of a surface segregation phenomenon, whereby one of the alloy components (in this case Pt) enriches the surface region.[6] UHV experimental and theoretical analysis revealed that a strong enrichment of Pt in Pt_3M alloy systems is counterbalanced by the depletion of Pt in the first two or three layers, resulting in a concentration profile that oscillates around the bulk value.[7–11]

Subsequent testing of these Pt overlayers in electrochemical environments showed significant differences in the activity for the ORR. For the purpose of demonstrating catalytic enhancement by alloying Pt with the 3d elements, two representative sets of polarization curves for the ORR on Pt and Pt_3Co, along with data on the corresponding production of peroxide, are summarized in Figure 1. Note that after these samples were removed from the electrochemical cell they were again characterized in the UHV chamber, and the Pt overlayer structure was found to be essentially unchanged. Although the rate of the ORR is significantly enhanced on Pt_3Co (Figure 1 a,b), equally small amounts of peroxide are detected on the ring electrode on both surfaces, in agreement with previous studies.[5] The rate of the ORR on Pt alloyed by the 3d metals is dependent on the nature of the alloying component (see Figure 1 c). While the Ni, Co, and Fe alloys show a large improvement in activity compared to pure Pt, the enhancement is smaller for the earlier 3d metals. We thus have a series of well-characterized alloys showing an interesting volcano-shaped variation in the electrocatalytic activity. As such, this result is an excellent basis for developing an understanding of the factors that control the kinetics of the ORR.

A model of the ORR developed previously[12] was used as the starting point for the analysis of the experimentally observed volcano-shaped dependence as the 3d metal changes from Ni to Ti. By using density functional theory (DFT) calculations, the free energies of all intermediates of the ORR were calculated as a function of the cell potential (see Experimental Section). On this basis, a kinetic model was developed that gives the rate of the ORR at a given potential as a function of a single parameter characterizing the catalyst surface—the oxygen chemisorption energy, ΔE_O. Figure 2 shows how this model leads to a volcano-shaped dependence of the rate on ΔE_O. For metals that bind oxygen too strongly (to the left of the maximum), the rate is limited by the removal of adsorbed O and OH species; that is, the surface is oxidized and thus unreactive, as also suggested by Ross and co-workers.[13,14] For metal surfaces that bind oxygen too weakly, the rate is limited by the dissociation of O_2, or more likely, the transfer of electrons and protons to adsorbed O_2. These different rate-limiting steps are associated with different oxygen reduction mechanisms. Two such mechanisms, involving either O_2 dissociation or proton and electron transfer to molecular O_2, were considered in our analysis. The mechanisms are both characterized by ΔE_O, but they give rise to different slopes on the right side of the volcano-shaped plot (Figure 2). The volcano shape thus illustrates very well the Sabatier principle,[15] with the important new viewpoint that it is quantitative; thus, we know which bond energy gives the maximum of the "volcano".

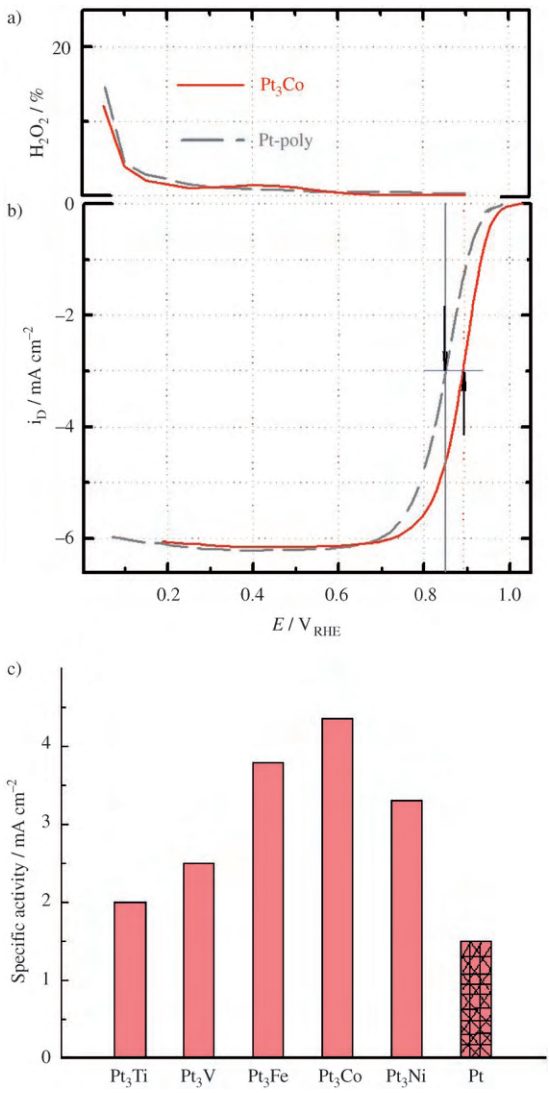

Figure 1. a) Production of peroxide from the oxygen reduction reaction (ORR) detected on a ring electrode and b) polarization curves (kinetic current density vs potential) for the ORR on Pt and Pt_3Co alloy surfaces on the disc electrode in 0.1 M $HClO_4$ recorded at 50 mV s^{-1} at 333 K (1600 rpm; RHE = reversible hydrogen electrode). Arrows indicate the values of the half-wave potential, which on Pt_3Co is shifted positively by about 50 mV. c) Specific activity of Pt and Pt_3M electrodes expressed as a kinetic current density for the ORR at 0.9 V (0.1 M $HClO_4$, 333 K).

 © 2006 Wiley-VCH Verlag GmbH & Co. KGaA, Weinheim

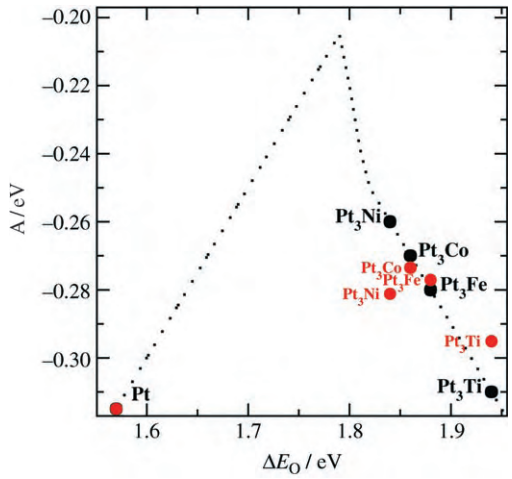

Figure 2. Model of the activity ($A = k_B T \ln(r)$, where r is the rate per surface atom per second) at a cell potential of 0.9 V shown (•••••, ●) as a function of the adsorption energy of oxygen, ΔE_O. On the left side of the plot, the rate is limited by removal of adsorbed O and OH species; immediately to the right of the maximum, the rate is limited by O_2 dissociation; and on the extreme right, the limiting step is protonation of adsorbed O_2. Also shown in red are the measured activities relative to that of Pt. The activity of the experiment is $A = k_B T \ln(i/i_{Pt}) + A_{Pt}$, where i/i_{Pt} is the current density relative to Pt, and A_{Pt} is the theoretical value for the activity of Pt. It is assumed that the number of active sites per surface area is the same for Pt and all the alloys. A factor of two in the preexponential factor would give rise to a difference of only ± 0.02 eV ($k_B T \ln 2$) in the activity. Changes in coverage for the different alloys are not considered. See text for details. The predictions of the model for Pt_3M (M = Ni, Co, Fe, Ti) alloys are shown relative to the predictions for Pt at the DFT-calculated values of ΔE_O.

One prediction of the model is that Pt binds oxygen a little too strongly, and finding a better electrocatalyst for the ORR thus amounts to finding a surface that binds oxygen more weakly than Pt does by about 0.2 eV. To test this prediction, we calculated ΔE_O for the (111) surfaces of a series of Pt_3M alloys with pure Pt in the first layer and only 50% Pt in the second layer to model the enrichment of Pt in the surface layer and the depletion of Pt in the next layer (the slabs thus retain bulk Pt_3M stoichiometry). The composition of the second layer can vary modestly from one alloy to the next for the different metals (see Reference [16] for a discussion of Pt–Fe, Pt–Co, and Pt–Ni alloy segregation). However, the calculated binding energies are not highly sensitive to such changes; changing the composition of M in the second layer from 50% to 25%, for example, changes binding energies by only approximately 0.05 eV for M = Fe, Co, and Ni. Thus, our simple stoichiometric model should be accurate for determining the trends in activities. These data, plus the corresponding activity predictions of the model, are shown in Figure 2. Clearly, the alloy surfaces form weaker bonds to oxygen than pure Pt, and the predicted activities (relative to pure Pt) are compatible with the experimental measurements that are also included in the figure. Experiment and theory agree almost quantitatively, but this excellent agreement in the relative rates is not the most significant point. Rather, we stress that we have a model of the ORR that accurately predicts trends in the catalytic activity; when appropriate models are employed, DFT calculations are known to be capable of reproducing such trends quite well.[17]

As ΔE_O is a good descriptor of the ORR activity of a given surface, the question arises as to which property of the catalyst determines it. It is well-established in the literature of surface science and heterogeneous catalysis that surface bond energies correlate with the average energy of the d states on the surface atoms to which the adsorbate binds (the d-band center).[18–25] This conclusion also holds for bonding of oxygen to the Pt_3M alloys, as illustrated in Figure 3. Similar effects

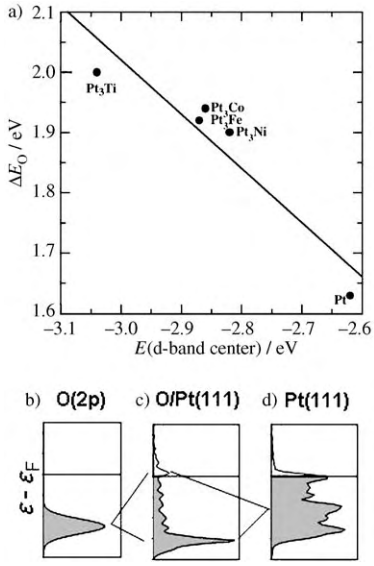

Figure 3. a) The correlation between the d-band center and the oxygen adsorption energy. The d-band center was calculated (DFT) as the average for the Pt atoms in the two top layers. b) sp-broadened 2p orbital for O(g), c) projected p density of states of oxygen atoms on Pt(111), and d) projected d density of states of Pt(111).

have been observed for Pt(111) with a 3d transition metal in the second layer, or for Pt(111) overlayers on 3d metals.[26,27]

The origin of this relationship is as follows: The variation in the oxygen–metal bond from one transition-metal surface to the next depends to a large extent on the strength of the coupling between the oxygen 2p states and the metal d states. This coupling forms bonding and antibonding states as illustrated in Figure 3b–d. The bonding states are filled, and the filling of the antibonding states, and thus the strength of the interaction, varies from surface to surface. In a metallic environment the filling depends on the position of the states relative to the Fermi level. An upward shift of the d states relative to the Fermi level must therefore result in an upward shift of the antibonding states, leading to less filling and thus to a stronger bond. For Pt overlayers or other structures involving bonding of oxygen to Pt, in which other factors that determine the coupling strength are approximately the same, this effect leads to the relationship shown in Figure 3.

Unlike the oxygen bond energy, which is hard to measure, the d-band center is accessible experimentally. We measured it for all of the alloys by using synchrotron-based high-resolution photoemission spectroscopy, a methodology pre-

 © 2006 Wiley-VCH Verlag GmbH & Co. KGaA, Weinheim

viously described.[28] Measurement of the d-band centers allows us to directly correlate the variations in the catalytic activity for the ORR with the variations in the surface electronic structure. As summarized in Figure 4, the activity

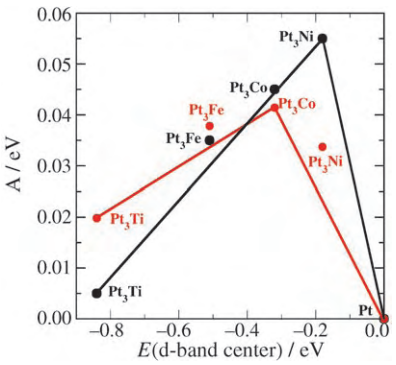

Figure 4. Activity versus the experimentally measured d-band center relative to platinum. The activity predicted from DFT simulations is shown in black, and the measured activity is shown in red.

(A) versus d-band center position at 0.9 V exhibits a classical volcano-shaped dependence, which agrees very well with the activity predicted from DFT calculations. For catalysts that bind oxygen too strongly, the rate is limited by the removal of surface oxide, while for catalysts that bind oxygen too weakly, the rate is limited by the transfer of electrons and protons to adsorbed O_2.

Note that a shift in the d states can also often be measured as a core-level shift, as the d states and the core levels shift together.[20] This effect can explain the correlations between ORR activity and the surface core-level shifts observed by Watanabe and co-workers.[29]

In summary, we have established how alloying Pt with 3d transition metals tunes the electronic structure to change the performance of an alloy for the ORR, and we have thus developed a model for the electrocatalytic activity of a metal surface for this process. The activity is given by the strength of the oxygen–metal bond interaction, which in turn depends on the position of the metal d states relative to the Fermi level. In this way we have established a new approach for the screening of new catalysts for the ORR, by looking for surfaces that bind oxygen a little weaker than Pt or, specifically for Pt skins, by looking for surfaces with a down shift of the Pt d states relative to the Fermi level.

Experimental Section

DACAPO, the total energy calculation code,[30] was used in this study. For all calculations, a four-layer slab, periodically repeated in a supercell geometry with six equivalent layers of vacuum between any two successive metal slabs, was used. A 2×2-unit cell was employed, and the top two layers of the slab were allowed to relax. Adsorption was allowed on only one of the two surfaces exposed, and the associated dipole was corrected for electrostatically.[31] Ionic cores were described by ultrasoft pseudopotentials,[32] and the Kohn–Sham one-electron valence states were expanded in a basis of plane waves with kinetic energy below 340 eV; a density cutoff of 500 eV was used. The surface Brillouin zone of close-packed metal surfaces was sampled at 18 special Chadi–Cohen **k** points. In all cases, convergence of the total energy was confirmed with respect to the **k** point set and with respect to the number of metal layers included. The exchange-correlation energy and potential were described self-consistently within the generalized gradient approximation (GGA-RPBE).[30] The self-consistent RPBE density was determined by iterative diagonalization of the Kohn–Sham Hamiltonian, Fermi population of the Kohn–Sham states ($k_BT=0.1$ eV), and Pulay mixing of the resulting electronic density.[33] All total energies were extrapolated to $k_BT=0$ eV. The d-band centers were calculated with an infinite cutoff radius.

On all metals and alloys (composition Pt_3M) investigated in this study, oxygen was found to adsorb at face-centered cubic (fcc) sites. Owing to the limited size of the unit cell, only two different fcc sites were present, one of which is close to one of the M atoms in the second layer, while the other is close to two M atoms. The latter was the most stable for all the considered alloys.

Solvent and potential effects were treated with the same model as used in our previous study.[12] In that work, it was confirmed that a bilayer of water has no effect on the binding energy of atomic oxygen. For the other species in the full model (not explicitly involved in the present calculations), the binding energies were corrected by the interaction of a water bilayer with the appropriate species on Pt(111). Potential effects were included by adjusting the free energies of adsorption (per transferred electron) by $-eU$. Electric-field effects were not explicitly included, but these effects were found to change the adsorption energies by less than 0.05 eV, and the effect was essentially constant from one metal to the next.

Received: December 9, 2005
Revised: February 6, 2006
Published online: April 5, 2006

Keywords: alloys · density functional calculations · electrochemistry · oxygen · platinum

[1] A. J. Appleby, *Catal. Rev.* **1970**, *4*, 221–244.
[2] P. Stonehart, *Chem. Ber.* **1990**, *94*, 913–921.
[3] K. Kinoshita, *Electrochemical Oxygen Technology*, Wiley, New York, **1992**.
[4] N. M. Markovic, P. N. Ross, *Surf. Sci. Rep.* **2002**, *45*, 121–229.
[5] V. Stamenkovic, T. J. Schmidt, P. N. Ross, N. M. Markovic, *J. Phys. Chem. B* **2002**, *106*, 11970–11979.
[6] A. V. Ruban, H. L. Skriver, J. K. Nørskov, *Phys. Rev. B* **1999**, *59*, 15990–16000.
[7] Y. Gauthier, Y. Joly, R. Baudoing, J. Rundgren, *Phys. Rev. B* **1985**, *31*, 6216–6218.
[8] U. Bardi, A. Atrei, E. Zanazzi, G. Rovida, P. N. Ross, *Vacuum* **1990**, *41*, 437–440.
[9] Y. Gauthier, *Surf. Rev. Lett.* **1996**, *3*, 1663–1689.
[10] M. A. Vasiliev, *J. Phys. D* **1997**, *30*, 3037–3070.
[11] M. Lundberg, *Phys. Rev. B* **1987**, *36*, 4692–4699.
[12] J. K. Nørskov, J. Rossmeisl, A. Logadottir, L. Lindqvist, J. R. Kitchin, T. Bligaard, H. Jonsson, *J. Phys. Chem. B* **2004**, *108*, 17886–17892.
[13] N. M. Markovic, H. A. Gasteiger, P. N. Ross, *J. Phys. Chem.* **1996**, *100*, 6715–6721.
[14] N. M. Markovic, T. A. Schmidt, V. Stamenkovic, P. N. Ross, *Fuel Cells* **2001**, *1*, 105–116.
[15] T. Bligaard, J. K. Nørskov, S. Dahl, J. Matthiesen, C. H. Chistensen, J. Sehested, *J. Catal.* **2004**, *224*, 206–217.
[16] Y. Gauthier, R. Baduoingsavois, J. M. Bugnard, U. Bardi, A. Atrei, *Surf. Sci.* **1992**, *276*, 1–11.
[17] B. Hammer, J. K. Nørskov, *Adv. Catal.* **2000**, *45*, 71–129.
[18] B. Hammer, J. K. Nørskov, *Nature* **1995**, *376*, 238–240.

 © 2006 Wiley-VCH Verlag GmbH & Co. KGaA, Weinheim

[19] J. Greeley, J. K. Nørskov, M. Mavrikakis, *Annu. Rev. Phys. Chem.* **2002**, *53*, 319 – 348.
[20] B. Hammer, Y. Morikawa, J. K. Nørskov, *Phys. Rev. Lett.* **1996**, *76*, 2141 – 2144.
[21] D. R. Alfonso, A. V. Cugini, D. S. Sholl, *Surf. Sci.* **2003**, *546*, 12 – 26.
[22] L. A. Kibler, A. M. El-Aziz, R. Hoyer, D. M. Kolb, *Angew. Chem.* **2005**, *117*, 2116 – 2120; *Angew. Chem. Int. Ed.* **2005**, *44*, 2080 – 2084.
[23] V. Pallassana, M. Neurock, *J. Catal.* **2000**, *191*, 301 – 317.
[24] A. Roudgar, A. Gross, *Phys. Rev. B* **2003**, *67*, 033409.
[25] M. Gajdos, A. Eichler, J. Hafner, *J. Phys. Condens. Matter* **2004**, *16*, 1141 – 1164.
[26] J. Zhang, M. B. Vukmirovic, Y. Xu, M. Mavrikakis, R. R. Adzic, *Angew. Chem.* **2005**, *117*, 2170 – 2173; *Angew. Chem. Int. Ed.* **2005**, *44*, 2132 – 2135.
[27] J. R. Kitchin, J. K. Nørskov, M. A. Barteau, J. G. Chen, *J. Chem. Phys.* **2004**, *120*, 10240 – 10246.
[28] B. S. Mun, C. Lee, V. Stamenkovic, N. M. Markovic, P. N. Ross, *Phys. Rev. B* **2005**, *71*, 115420.
[29] T. Toda, H. Igarashi, H. Uchida, M. Watanabe, *J. Electrochem. Soc.* **1999**, *146*, 3750 – 3756.
[30] B. Hammer, L. B. Hansen, J. K. Nørskov, *Phys. Rev. B* **1999**, *59*, 7413 – 7421.
[31] L. Bengtsson, *Phys. Rev. B* **1999**, *59*, 12301 – 12304.
[32] D. Vanderbilt, *Phys. Rev. B* **1990**, *41*, 7892 – 7895.
[33] G. Kresse, J. Furthmuller, *Comput. Mater. Sci.* **1996**, *6*, 15 – 50.

 © 2006 Wiley-VCH Verlag GmbH & Co. KGaA, Weinheim

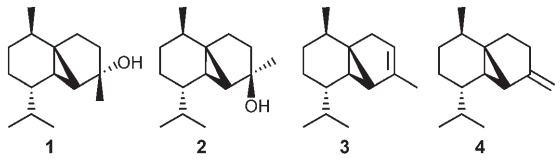

Scheme 1. Constituants of *Piper cubeba*.

Shortly after the discovery of this new skeleton, a synthesis of the racemic cubebenes **3** and **4** was reported by Piers et al., and a synthesis of **1**–**4** was reported by Yoshikoshi and coworkers.[7] Both syntheses are based on a cyclopropanation of diazoketone **5** (or the analogous isopropenyl compound, Scheme 2). Unfortunately, this route is not diastereoface-

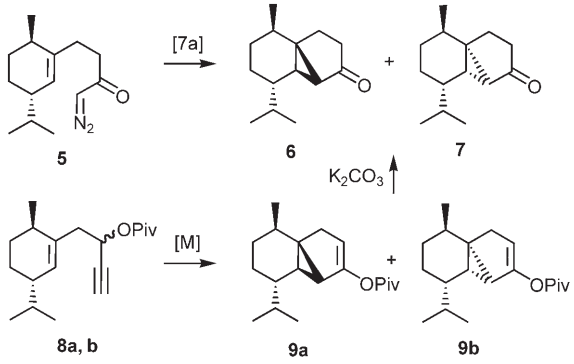

Scheme 2. Reported and planned synthesis of **6**.

DOI: 10.1002/anie.200504543

Synthesis of (−)-Cubebol by Face-Selective Platinum-, Gold-, or Copper-Catalyzed Cycloisomerization: Evidence for Chirality Transfer**

Charles Fehr and José Galindo*

Herein we describe a direct, stereoselective synthesis of (−)-cubebol,[1] based on Pt-,[2,3] Au-,[4] and Cu-catalyzed[5] enyne cycloisomerizations.

(−)-Cubebol (**1**), 4-epicubebol (**2**), and α- and β-cubebenes **3** and **4**, respectively, are naturally occurring sesquiterpenes, isolated from the berries of *Piper cubeba* (Scheme 1).[1] Whereas **2** has a very bitter taste, the almost odorless (−)-cubebol (**1**) has a pronounced cooling effect and lends itself to diverse applications in the field of flavors.[6] selective and affords the desired ketone **6** as the minor isomer in only moderate yield. We realized that a Pt-[2,3] or Au-catalyzed[4] cycloisomerization of enynol esters[8] would represent a direct and efficient access to cubebol.

The key precursors **8a** and **8b** (1:2 diastereomeric mixture) were readily prepared from (+)-(*R*,*R*)-tetrahydrocarvone (**10**) in an overall yield of 55% (Scheme 3). A Wittig–

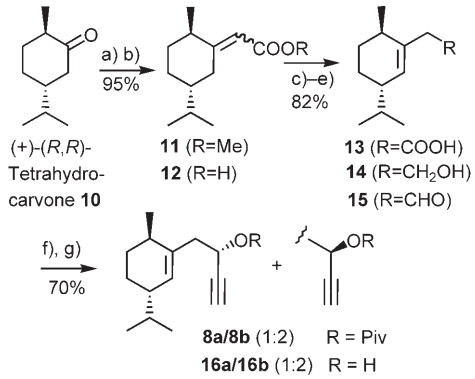

Scheme 3. Reagents and conditions: a) trimethyl phosphonoacetate (1.2 equiv), NaH (1.1 equiv), THF, reflux, 15 h; b) KOH (1.7 equiv), EtOH, 60 °C, 24 h; c) BuLi (3.0 equiv), 2,2,6,6-tetramethylpiperidine (TMP, 3.15 equiv), THF, −5 °C, 30 min, then **11**, −25 °C to RT, 16 h; then 5% HCl; d) $LiAlH_4$ (2 mol equiv), Et_2O, reflux, 45 min; e) Swern oxidation; f) HCCMgBr (1.2 equiv), THF, 25–28 °C, 45 min; g) PivCl (1.1 equiv), NEt_3 (1.2 equiv), DMAP (0.12 equiv), CH_2Cl_2 0 °C, 2 h. Piv = pivaloyl, DMAP = *N*,*N*-dimethylaminopyridine.

[*] Dr. C. Fehr, J. Galindo
Firmenich SA
Corporate R&D Division
P.O. Box 239, CH-1211 Genève 8 (Switzerland)
Fax: (+41) 22-780-3334
E-mail: charles.fehr@firmenich.com

[**] We thank Dr. Jean-Yves de Saint Laumer, Firmenich SA, Geneva, for the energy calculations.

 © 2006 Wiley-VCH Verlag GmbH & Co. KGaA, Weinheim

Horner reaction and saponification afforded the acid **12**. Whereas base-catalyzed deconjugation of the ester **11** proved to be unselective, and afforded (*Z*)-**11** and substantial amounts of the isomeric ester with a tetrasubstituted double bond, deprotonation of **12** using excess Li-TMP, followed by protonation of the dianion with 5% HCl, readily furnished **13**. $LiAlH_4$ reduction and Swern oxidation afforded the β,γ-unsaturated aldehyde **15**. Addition of ethynyl-MgBr and esterification with pivaloyl chloride produced **8a** and **8b** as a 1:2 diastereomeric mixture.

Chromatographic purification of the alcohols **16a**,**b** and esterification of the fractions enriched in **16a** or **16b** gave access to the pivalates **8a**,**b**, enriched in **8a** and **8b**, respectively. These were then submitted separately to the Pt- or Au-catalyzed cycloisomerization reaction (Table 1, entries 1–3). When a mixture of **8a** and **8b** (1:9) was treated with 2 mol% of $PtCl_2$, the expected tricyclic enol pivalates **9a** and **9b** were formed in a ratio of 3:2 in 80% yield (entry 1), and the Au-catalyzed reaction gave, in a less clean reaction, a 47:53 mixture of **9a** and **9b** (entry 2). In contrast, the reaction of a mixture of **8a** and **8b** (7:3) with $PtCl_2$ afforded mainly the desired **9a** (**9a**/**9b** = 86:14; entry 3).

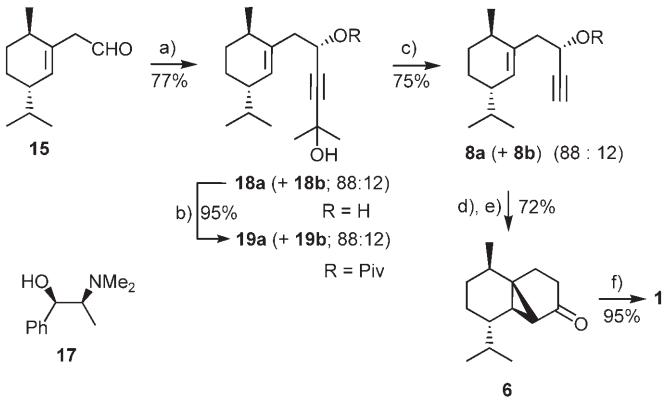

Scheme 4. Reagents and conditions: a) $Zn(OTf)_2$ (2.0 equiv), **17** (2.1 equiv), NEt_3, toluene, RT, 2 h; then 2-methyl-3-butyn-2-ol (2.1 equiv), RT, 15 min; then slow addition of **15** in toluene at RT (15 h + 9 h after introduction); b) PivCl (2.2 equiv), NEt_3 (1.1 equiv), DMAP (0.12 equiv), 0°C to RT, 15 h; c) K_2CO_3 (1.2 equiv), [18]crown-6 (0.4 + 0.4 equiv), toluene, reflux, 19 h + 5 h; d) see Table 1; e) K_2CO_3 (1.2 equiv), MeOH, RT, 90 min; f) $CeCl_3$ (2.0 equiv), MeLi (2.0 equiv), THF, −78°C, 1 h; then **6**, −78°C to RT, 2 h.

Table 1: Cycloisomerization of **8a** and **8b**.

Entry	**8a**/**8b**	Conditions	**9a**/**9b**	Yield [%]
1	10:90	$PtCl_2$ (2 mol%), DCE[a], 70°C, 9 h	60:40	80
2	10:90	$AgSbF_6/Ph_3PAuCl$ (2 mol%), CH_2Cl_2, 20°C, 40 min	47:53	65
3	70:30	$PtCl_2$ (2 mol%), DCE[a], 70°C, 9 h	86:14	–
4	88:12	$PtCl_2$ (2 mol%), DCE[a], 70°C, 9 h	94:6	81
5	98:2	$PtCl_2$ (2 mol%), DCE[a], 70°C, 9 h	99:1	–
6	98:2	$[Cu(CH_3CN)_4](BF_4)$ (2 mol%), DCE[a], 60°C, 9 h	99:1	77[b]

[a] DCE = 1,2-dichloroethane. [b] 90% conversion.

From the results shown in entries 1 and 3 it was anticipated that **8a** would afford **9a** with an excellent facial selectivity. We therefore addressed the question of a diastereoselective synthesis of **8a**, which was accomplished by a reagent-controlled diastereoselective addition (88:12) of 2-methyl-3-butyn-2-ol to aldehyde **15** using the Zn reagent obtained from (−)-*N*-methylephedrine (**17**) and $Zn(OTf)_2$, followed by esterification of a mixture of **18a** and **18b** and base-catalyzed cleavage of the carbinol fragment of **19a** and **19b**, according to the procedure of Carreira and co-workers (Scheme 4).[9,10] The *S* configuration of the newly formed stereogenic center is in accord with the above-cited work of Carreira and co-workers. A mixture of pivalates **8a** and **8b** (88:12) was used for the cycloisomerization step.

Indeed, $PtCl_2$-catalyzed cycloisomerization of a mixture of **8a** and **8b** (88:12) afforded **9a** with a 94:6 selectivity (Table 1, entry 4), and chromatographically enriched **8a** (**8a**/**8b** 98:2) afforded **9a** with excellent facial selectivity (99:1; entry 5). Interestingly, inexpensive $[Cu(CH_3CN)_4](BF_4)$ (2 mol%) also efficiently catalyzed the cycloisomerization (99:1; 77% yield after 90% conversion).[5] Prolonged reaction times or higher temperatures (70°C) favored the formation of by-products.

Hydrolysis of **9a** afforded the known ketone **6**, and diastereoselective (97:3) addition of MeLi/$CeCl_3$ furnished (−)-cubebol in 95% yield, identical in all respects with an authentic sample.[6]

The different diastereoface selectivities observed for the cycloisomerizations of **8a** and **8b** prompted us to examine the chirality transfer from the enantioenriched propargyl pivalates **21** and **25**, which are readily accessible from the aldehydes **20** and **24**.[11] Pt- or Cu-catalyzed rearrangement of **21** (95% *ee*) afforded **22**, which gave, after hydrolysis, ketone **23** with 57–61% *ee* (Scheme 5).[12] The *ee* value of **21** and **22** remained unaltered throughout the course of the reaction, as shown by measurements taken after 50% conversion.

Surprisingly, Pt-catalyzed cycloisomerization of **25** (69% *ee*) afforded, in addition to the expected rearranged enol pivalate **26** (10–20% *ee*, unknown absolute configuration), the isomeric non-rearranged enol pivalate **27** (60–67% *ee*, unknown absolute configuration), as evidenced by conversion of **26** and **27** into the ketones **28** and **29**, respectively.

The Pt- or Au-catalyzed cycloisomerizations of secondary enynol esters are believed to proceed by an initial [1,2] O shift of the metal-complexed acetylene **A** and subsequent cyclopropanation of the achiral transient vinyl carbene **C** (pathway (a); Scheme 6).[2] On the basis of the chirality transfer we observed, pathway (a) can be dismissed.[13] Alternatively, cyclopropanation of the electron-rich olefin with the metal-complexed acetylene **A**, followed by [1,2]-O-migration of **E** (pathway (b)),[14] the presumed reaction course for the formation of the non-rearranged enol pivalate **27** by a [1,2] H shift of **E** or **F**,[15] is also not operative for **26**, as the rearranged and non-rearranged cycloisomerization products **26** and **27** exhibit different enantiomeric excess values. This leads us to propose a new mechanism for the cycloisomerization with [1,2]-acyl shift (pathway (c)). Intramolecular addition of the ester carbonyl to the metal-complexed acetylene **A**

 © 2006 Wiley-VCH Verlag GmbH & Co. KGaA, Weinheim

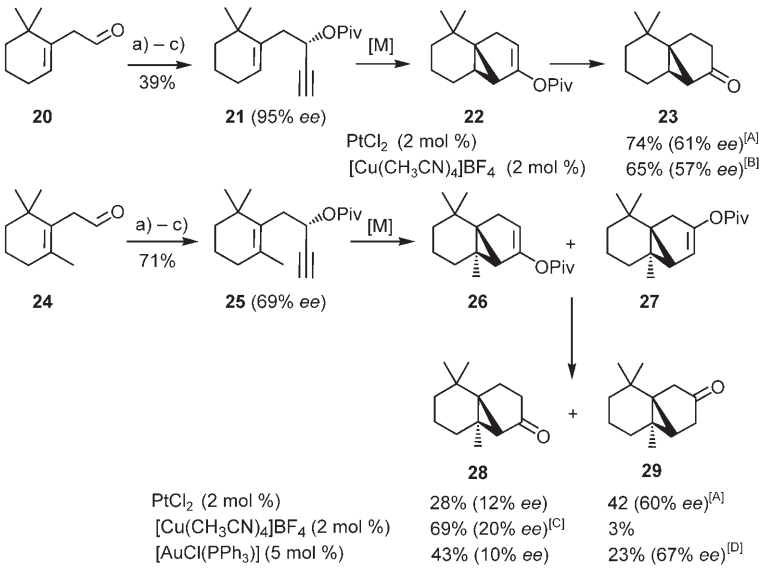

Scheme 5. Reagents and conditions: a)–c) see Scheme 3 a)–c); [A] DCE, 70 °C, 8 h; [B] toluene, 50 °C, 9 h, 73% conversion; [C] toluene, 50 °C, 4 h, 50% conversion; [D] DCE, 70 °C, 90 min; GC yields.

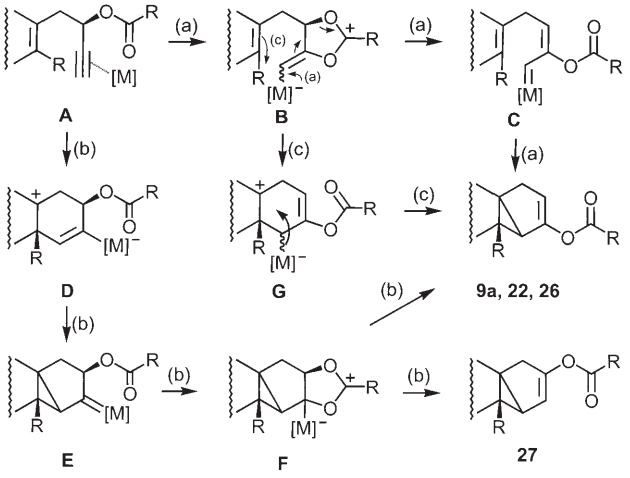

Scheme 6. Proposed mechanism for the cycloisomerizations.

leads to the vinyl metal species **B**, followed by nucleophilic attack of the C–C double bond to the oxy-allyl system and cyclopropane ring closure in **G**.[16,17]

In conclusion, we have succeeded in a direct, stereoselective synthesis of (−)-cubebol, based on a Pt-, Au-, or Cu-catalyzed cycloisomerization in which control of the configuration of the propargylic center is essential for the facial selectivity. In addition, complementary cycloisomerization studies of enantioenriched propargyl pivalates suggests that the cyclization occurs on a "half-rearranged" species **B** (Scheme 6).

Experimental Section

(−)-**6**: A solution of **8a** and **8b** (**8a**/**8b** = 88:12; 1.98 g; 6.80 mmol) in 1,2-dichloroethane (30 mL) was treated with $PtCl_2$ (36 mg; 0.136 mmol) and heated for 9 h at 70 °C. The solution was cooled and poured into saturated aqueous $NaHCO_3$. Extraction (Et_2O), washing (H_2O, then saturated aqueous NaCl), drying (Na_2SO_4), concentration, and bulb-to-bulb distillation (100–120 °C/0.01 mbar) afforded 1.60 g of **9a** and **9b** (**9a**/**9b** = 94:6; 81%). A solution of **9a** and **9b** (**9a**/**9b** = 94:6; 1.50 g; 5.17 mmol) in MeOH (25 mL) was treated with K_2CO_3 (861 mg; 6.24 mmol) and stirred for 90 min at RT. After partial concentration, the product was extracted (Et_2O/H_2O), washed (H_2O, then saturated aqueous NaCl), dried (Na_2SO_4), concentrated, and bulb-to-bulb distilled (100–125 °C/0.01 mbar) to afford 1.13 g of **6** (86% pure, 91%). Purification by chromatography on SiO_2 (150 g) with an eluent of cyclohexane/AcOEt (7:3), followed by crystallization in pentane at −78 °C afforded 680 mg of pure **6**. M.p. 60–60.5 °C (lit. 58.5–59.5 °C[7b]),$[\alpha]_D^{20}$ ($CHCl_3$; $c = 1.30$) −20.1 (lit. $[\alpha]_D^{20} = -23.9$ (isooctane)[7b]); ^{1}H NMR (400 MHz, $CDCl_3$): $\delta = 0.59$ (m, 1H), 0.90–1.00 (m, 1H), 0.91 (d, J = 7.0 Hz, 3H), 0.95 (d, $J = 6.5$ Hz, 3H), 0.99 (d, $J = 6.0$ Hz, 3H), 1.19 (m, 1H), 1.27 (t, $J = 2.5$ Hz, 1H), 1.45–1.52 (m, 2H), 1.58–1.70 (m, 2H), 1.78–1.90 (m, 2H), 1.98–2.21 ppm (m, 3H); ^{13}C NMR (100 MHz, $CDCl_3$): δ = 214.6 (s), 43.4 (d), 40.3 (s), 39.7 (d), 33.3 (t), 33.2 (d), 32.5 (d), 31.3 (d), 30.8 (t), 26.6 (t), 26.0 (t), 19.9 (q), 19.4 (q), 18.9 ppm (q); MS: m/z (%): 206 [M^+] (65), 191 (24), 164 (88), 149 (45), 135 (35), 122 (100), 107 (55), 93 (64), 91 (65), 79 (75), 69 (40), 55 (41), 41 (46).

23: $[\alpha]_D^{20}$ ($CHCl_3$; $c = 0.56$) + 24.8 (61% *ee* by chiral GC[18] (major enantiomer: first peak)); ^{1}H NMR (400 MHz, $CDCl_3$): $\delta = 0.92$–1.02 (m, 1H); 0.96 (s, 3H), 1.09 (s, 3H), 1.20–1.30 (m, 2H), 1.35–1.55 (m, 2H), 1.51 (d, $J = 2.5$ Hz, 1H), 1.59 (ddd, $J = 8.0$, 2.5, 2.1 Hz, 1H), 1.80–1.90 (m, 1H), 1.95–2.12 ppm (m, 4H); ^{13}C NMR (100 MHz, $CDCl_3$): $\delta = 214.8$ (s), 43.2 (s), 41.1 (d), 37.3 (t), 33.2 (t), 29.9 (s), 28.4 (d), 27.9 (q), 24.9 (q), 24.6 (t), 23.3 (t), 18.0 ppm (t); MS: m/z (%): 178 [M^+] (26), 163 (9), 136 (16), 135 (16), 121 (30), 110 (100), 107 (25), 93 (28), 91 (22), 79 (33), 69 (40).

28: 12% *ee* by chiral GC[18] (major enantiomer: first peak); ^{1}H NMR (400 MHz, $CDCl_3$): $\delta = 0.90$ (s, 3H), 0.99 (s, 3H), 1.00 (s, 3H), 1.07–1.30 (m, 4H), 1.34–1.48 (m, 1H), 1.60–1.70 (m, 2H), 2.15 (d, $J = 19.5$ Hz, 1H), 2.24 (d, $J = 19.5$ Hz, 1H), 2.51 (d, $J = 19.5$ Hz, 1H), 2.52 ppm (m, 1H); ^{13}C NMR (100 MHz, $CDCl_3$): $\delta = 220.2$ (s), 40.5 (t), 39.5 (t), 37.5 (t), 36.8 (s), 33.8 (t), 30.2 (s), 27.6 (2q), 25.6 (d), 24.4 (s), 18.1 (t); 17.1 ppm (q); MS: m/z (%): 192 [M^+] (51), 177 (57), 149 (63), 136 (64), 107 (73), 93 (100), 79 (97), 69 (71), 67 (38), 55 (39), 41 (48).

29: 60% *ee* by chiral GC[18] (major enantiomer: first peak); ^{1}H NMR (400 MHz, $CDCl_3$): $\delta = 0.95$ (s, 3H), 1.05–1.10 (m, 1H), 1.06 (s, 3H), 1.15–1.25 (m, 2H), 1.19 (s, 3H), 1.42 (m, 1H), 1.65 (s, 1H), 1.65–1.87 (m, 3H), 1.96–2.04 (m, 1H), 2.15–2.28 ppm (m, 2H); ^{13}C NMR (100 MHz, $CDCl_3$): $\delta = 215.9$ (s), 49.3 (s), 44.5 (d), 37.8 (2t), 34.2 (t), 31.8 (s), 30.9 (s), 27.6 (q), 26.2 (q), 21.9 (t), 18.8 (q); 18.0 ppm (t); MS: m/z (%): 192 [M^+] (43), 177 (27), 150 (58), 136 (71), 135 (100), 123 (60), 121 (55), 107 (64), 93 (59), 79 (57), 69 (38), 55 (30), 41 (38).

Received: December 21, 2005
Published online: March 23, 2006

Keywords: cycloisomerization · cyclopropanes · diastereoselectivity · homogeneous catalysis · natural products

[1] F. Vanasek, V. Herout, F. Sorm, *Collect. Czech. Chem. Commun.* **1960**, *56*, 919; Y. Ohta, K. Ohara, Y. Hirose, *Tetrahedron Lett.* **1968**, *9*, 4181, and references therein.

[2] Pt catalysis: a) Y. Harrak, C. Blaszykowski, M. Bernard, K. Cariou, E. Mainetti, V. Mouriès, A.-L. Dhimane, L. Fensterbank,

 © 2006 Wiley-VCH Verlag GmbH & Co. KGaA, Weinheim

M. Malacria, *J. Am. Chem. Soc.* **2004**, *126*, 8656; C. Blaszykowski, Y. Harrak, M.-H. Gonçalves, J.-M. Cloarec, A.-L. Dhimane, L. Fensterbank, M. Malacria, *Org. Lett.* **2004**, *6*, 3771; b) S. Anjum, J. Marco-Contelles, *Tetrahedron* **2005**, *61*, 4793; c) V. Mamane, T. Gress, H. Krause, A. Fürstner, *J. Am. Chem. Soc.* **2004**, *126*, 8654.

[3] a) E. Soriano, P. Ballesteros, J. Marco-Contelles, *Organometallics* **2005**, *24*, 3182; b) E. Soriano, J. Marco-Contelles, *J. Org. Chem.* **2005**, *70*, 9345.

[4] Au catalysis: A. Fürstner, P. Hannen, *Chem. Commun.* **2004**, 2546; F. Gagosz, *Org. Lett.* **2005**, *7*, 4129 and Ref. [2c].

[5] $[Cu(CH_3CN)_4](BF_4)$ efficiently catalyzes the cycloisomerization of certain unsaturated tertiary propargylic alcohols: C. Fehr, I. Farris, H. Sommer.

[6] M. I. Velazco, L. Wuensche, P. Deladoey (Firmenich SA), US 6214788 (prior. 31.03.1999), **1999**; [*Chem. Abstr.* **2000**, *133*, 265959].

[7] a) E. Piers, R. W. Britton, W. de Waal, *Tetrahedron Lett.* **1969**, *10*, 1251; E. Piers, R. W. Britton, W. de Waal, *Can. J. Chem.* **1971**, *49*, 12; b) A. Tanaka, R. Tanaka, H. Uda, A. Yoshikoshi, *J. Chem. Soc. Perkin 1* **1972**, 1721; A. Tanaka, H. Uda, A. Yoshikoshi, *Chem. Commun.* **1969**, 308; c) see also: S. Torii, T. Okamoto, *Bull. Chem. Soc. Jpn.* **1976**, *49*, 771.

[8] Reviews: S. Ma, S. Yu, Z. Gu, *Angew. Chem.* **2006**, *118*, 261; *Angew. Chem. Int. Ed.* **2006**, *45*, 200; C. Bruneau, *Angew. Chem.* **2005**, *117*, 2380; *Angew. Chem. Int. Ed.* **2005**, *44*, 2328; A. M. Echavarren, C. Nevado, *Chem. Soc. Rev.* **2004**, *33*, 431; M. Méndez, V. Mamane, A. Fürstner, *Chemtracts: Org. Chem.* **2003**, *16*, 397; C. Aubert, O. Buisine, M. Malacria, *Chem. Rev.* **2002**, *102*, 813.

[9] D. Boyall, F. Lopez, H. Sasaki, D. Frantz, E. M. Carreira, *Org. Lett.* **2000**, *2*, 4233; J. W. Bode, E. M. Carreira, *J. Org. Chem.* **2001**, *66*, 6410.

[10] Despite the slow addition of **15**, it accumulates during the reaction. Diminishing the amount of reagents leads to a slower reaction and to the formation of by-products.

[11] Synthesis of **20**: a) 2,2-dimethylcyclohexanone, triethyl phosphonoacetate (1.2 equiv), NaOEt (1.1 equiv), pentane, reflux, 24 h (100%); b) lithium diisopropylamide (LDA, 1.05 equiv), THF, −25°C to RT, 30 min (80%); c) $LiAlH_4$ (1.50 mol equiv), Et_2O, reflux, 45 min (93%); d) Swern oxidation (92%); for the synthesis of **21**, see: O. Isler, M. Montavon, R. Rüegg, P. Zeller, *Helv. Chim. Acta* **1956**, *39*, 259; G. L. Olson, H.-C. Cheung, K. D. Morgan, R. Borer, G. Saucy, *Helv. Chim. Acta* **1976**, *59*, 567.

[12] The indicated absolute configuration of **23** is based on the stereoselectivity observed in the cycloisomerization of **8a** (cubebol synthesis).

[13] The lower *ee* values of the rearrangement products when compared to the substrates reflect an imperfect stereocontrol and not a racemization, as the *ee* values of **21** and **22** remained constant during the reaction.

[14] This mechanism has recently been proposed on the basis of a DFT computational study: see Ref. [3].

[15] For the related cycloisomerization of propargylic alcohols or ethers, see E. Soriano, P. Ballesteros, J. Marco-Contelles, *Organometallics* **2005**, *24*, 3172 and Refs. [2a, 2c, 3b, 4, and 5].

[16] Incidentally, this mechanism is closely related to the mechanism proposed for the Rautenstrauch rearrangement: X. Shi, D. J. Gorin, F. D. Toste, *J. Am. Chem. Soc.* **2005**, *127*, 5802; we cannot exclude that, depending on the substrate, the reaction pathways (a) or (b) compete with pathway (c).

[17] A referee pointed out that the vinyl metal species **B** would most likely possess the *E* configuration. However, the formation of the *Z* isomer by anchimeric assistance[3b] is also plausible and would allow the cyclization **B**→**G** to occur with minimal steric interactions. The stereoselectivity of the cycloisomerization **8a**→**9a** can be rationalized by invoking minimal steric interactions. Placing the side chain above the cyclohexene ring orients the dioxolane and $PtCl_2$ (in (*Z*)-**B**, Scheme 6) away from the cyclohexene and the isopropyl groups. A preliminary calculation of the two possible reactive conformers (with OAc instead of OPiv) with an imposed distance of 3 Å shows that **B1** is more stable than **B2** by ca. 2.9 kcal mol^{-1}. Calculations were performed at the DFT level (B3LYP/LACVP**), using Jaguar 5.5; Schrödinger, Inc., Portland, OR, 1991–2005. Most probably the same diastereoface selectivity is observed in the cyclization **21**→**22**. The lower selectivity is certainly caused by the missing

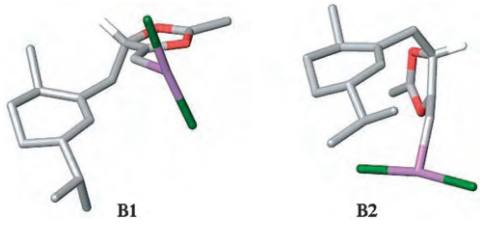

isopropyl group. Surprisingly, the cycloisomerization **25**→**26** is much less selective. This may be due to steric interactions between the methyl group and the metal. The cyclization **25**→**27** is highly selective. Probably the reaction conformer **A** (Scheme 6) in which the acetylene group is above the cyclohexene ring minimizes the steric interactions between the pivalate and the cyclohexene ring.

[18] Chiral capillary column: CP-Chirasil-DEX CB (25 m × 0.25 mm) (Chrompack).

 © 2006 Wiley-VCH Verlag GmbH & Co. KGaA, Weinheim

Palladium Catalysis

DOI: 10.1002/anie.200600532

Reaction of Molecular Oxygen with a Pd^{II}–Hydride To Produce a Pd^{II}–Hydroperoxide: Acid Catalysis and Implications for Pd-Catalyzed Aerobic Oxidation Reactions**

*Michael M. Konnick, Bhavesh A. Gandhi, Ilia A. Guzei, and Shannon S. Stahl**

Palladium-catalyzed reactions are among the most versatile methods for the selective aerobic oxidation of organic molecules.[1] These reactions are generally thought to proceed by a two-stage "oxidase" pathway that consists of Pd^{II}-mediated oxidation of the organic substrate followed by

[*] M. M. Konnick, B. A. Gandhi, I. A. Guzei, Prof. S. S. Stahl
Department of Chemistry
University of Wisconsin-Madison
1101 University Avenue, Madison, WI 53706 (USA)
Fax: (+1) 608-262-6143
E-mail: stahl@chem.wisc.edu

[**] Financial support from the following agencies is gratefully acknowledged: NSF (CHE-0094344) and the Dreyfus Foundation (Teacher-Scholar Award).

WILEY InterScience DISCOVER SOMETHING GREAT
© 2006 Wiley-VCH Verlag GmbH & Co. KGaA, Weinheim

dioxygen-coupled oxidation of the Pd^0 center. Oxidation of the reduced catalyst must be efficient because Pd^0 tends to decompose by aggregation into inactive metallic palladium. Understanding the fundamental reactivity of palladium with molecular oxygen can play an important role in the development of improved catalytic reactions. Two principle mechanisms have been proposed for the dioxygen-coupled oxidation of the reduced catalyst: 1) oxygenation of Pd^0 to form an η^2-peroxo species (Scheme 1, **C**→**D**)[2] and 2) direct reaction of molecular oxygen with a Pd^{II}–hydride intermediate (Scheme 1, **B**→**E**).[3] The reaction of Pd^0 with molecular

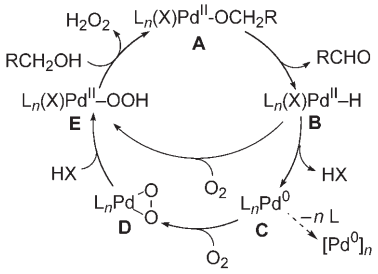

Scheme 1. Catalytic cycle of the Pd-catalyzed aerobic oxidation of alcohols.

oxygen has substantial precedent;[2,4] however, when we began our study, no examples of reactions of Pd^{II}–hydrides with molecular oxygen to produce Pd–hydroperoxides were known.[5,6] Herein, we report the synthesis and characterization of N-heterocyclic-carbene (NHC)-coordinated Pd^{II}–hydrides of the type *trans*-[Pd(H)(O_2CR)(IMes)$_2$] (IMes = mesityl), and their reaction with molecular oxygen to produce Pd^{II}–hydroperoxides. We find that the oxygenation reaction is significantly accelerated by the presence of exogenous carboxylic acids. Further study will be necessary to establish the precise mechanism of this transformation; however, the present results have important implications for catalyst reoxidation in Pd-catalyzed aerobic oxidation reactions.

We recently reported the isolation and characterization of the Pd^{II}–hydroperoxide complex *trans*-[Pd(OOH)(OAc)-(IMes)$_2$] (**3a**; Scheme 2).[2c] This complex and the corresponding benzoate derivatives **3b** and **3c** were prepared by oxygenation of [Pd^0(IMes)$_2$] (**1**) to form the η^2-peroxo complex [Pd(O_2)(IMes)$_2$] (**2**), followed by addition of one equivalent of carboxylic acid (Scheme 2, top pathway). This sequence (namely, **1**→**2**→**3**) reproduces the proposed Pd^0 catalyst-reoxidation pathway shown in Scheme 1 (**C**→**D**→**E**). The formation of Pd^0 under catalytic conditions is thought

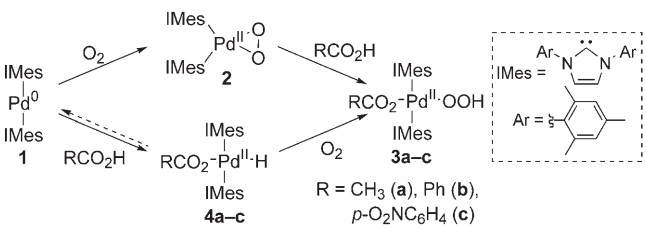

Scheme 2. Reactions of [Pd(IMes)$_2$] complexes with acetic acid and dioxygen.

to arise from reductive elimination of HX from a Pd^{II}–hydride intermediate **B**. Several groups have proposed that catalyst reoxidation may occur by dioxygen insertion into a Pd^{II}–hydride species.[3] Therefore, we sought to test whether the hydroperoxide adducts **3a–c** could arise from oxygenation of the corresponding Pd–H species (Scheme 2, bottom pathway).

To initiate this study, we prepared the requisite Pd^{II}–hydride complexes *trans*-[Pd(H)(O_2CR)(IMes)$_2$] **4a–c** (Scheme 2).[7] One equivalent of carboxylic acid reacts quantitatively with [Pd^0(IMes)$_2$] to produce **4a–c**. These complexes exhibit diagnostic IR stretching frequencies ($\tilde{\nu}$ = 2025 (**4a**), 2036 (**4b**), and 2089 cm^{-1} (**4c**)) and ^{1}H NMR chemical shifts (C_6D_6, $\delta = -17.86$ (**4a**), −17.77 (**4b**), and −18.03 ppm (**4c**)) associated with the Pd^{II}–H fragment. The benzoate analogue **4b** was also characterized by X-ray crystallography (Figure 1).[8]

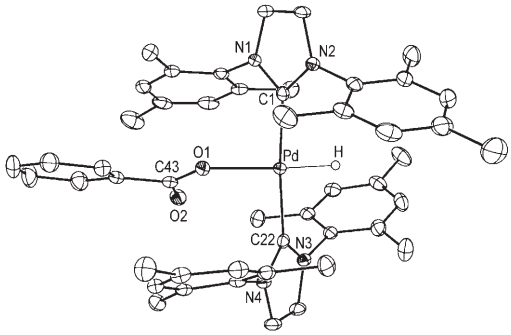

Figure 1. Molecular structure of **4b**, with 30% probability ellipsoids. Most of the hydrogen atoms are omitted for clarity. Selected bond lengths [Å]: Pd-H: 1.54(2), Pd-C1: 2.0159(17), Pd-C22: 2.0218(17), Pd-O1: 2.1343(13).

These Pd–hydride complexes react cleanly with molecular oxygen to produce Pd^{II}–hydroperoxides. Exposure of solutions of the Pd^{II}–hydrides **4a–c** in benzene to an atmosphere of dioxygen at moderate temperatures (40–50 °C) yields hydroperoxide complexes that are spectroscopically identical to the products obtained by protonation of the η^2-peroxo adducts **3a–c** (Scheme 2). The oxygenation reactions of the benzoate- and 4-nitrobenzoate-ligated Pd^{II}–hydride complexes **4b** and **4c** were monitored by ^{1}H NMR spectroscopy. The reaction rate exhibits a clean first-order dependence on [Pd−H], as revealed by the exponential time-course of the reactions (Figure 2). The presence of an electron-withdrawing nitro group on the benzoate ligand significantly enhances the oxygenation rate; the oxygenation of **4c** is nearly eightfold faster than that of **4b** at 51 °C ($k_{4b} = 2.21(0.14) \times 10^{-4}\ s^{-1}$ versus $k_{4c} = 16.6(1.1) \times 10^{-4}\ s^{-1}$).

The established precedent for the facile oxygenation of [Pd^0(IMes)$_2$] (Scheme 2, top pathway) suggests that the reaction of **4a–c** with molecular oxygen might proceed by reductive elimination of the carboxylic acid (Scheme 2, **4**→**1**) followed by oxygenation of Pd^0.[9] However, several alternative mechanisms are also possible. In particular, hydrides of other late transition metals (Rh and Pt) have been shown to undergo radical chain autoxidation to produce the corre-

 © 2006 Wiley-VCH Verlag GmbH & Co. KGaA, Weinheim

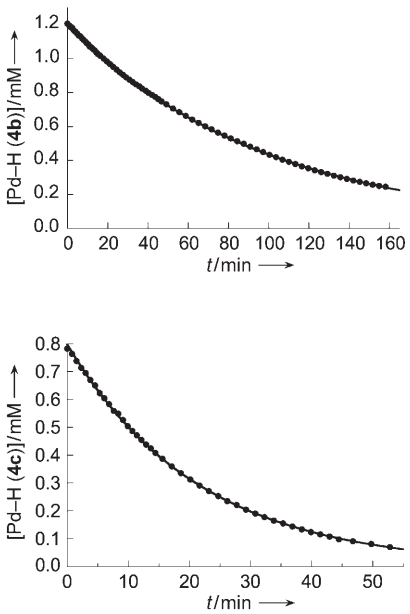

Figure 2. A representative time-course and exponential fit for the oxygenation of **4b** and **4c**. Reaction conditions: a) 1.1 atm O_2, 51 °C, C_6D_6; b) 1.1 atm O_2, 44 °C, C_6D_6.

sponding metal–hydroperoxide.[10] A homolytic, non-radical-chain oxygenation pathway[6a] and direct insertion of O_2 into a Pd–H bond[5] have also been proposed. Current efforts are focused on differentiating these pathways.

In the course of our ongoing mechanistic studies, we discovered that exogenous carboxylic acid catalyzes the oxygenation of **4a–c**. The presence of 10 mol% $PhCO_2H$ increases the rate of the oxygenation of **4b** 2–3-fold, and the rate continues to increase linearly with respect to $[PhCO_2H]$ (Figure 3). This observation was unexpected because, if the

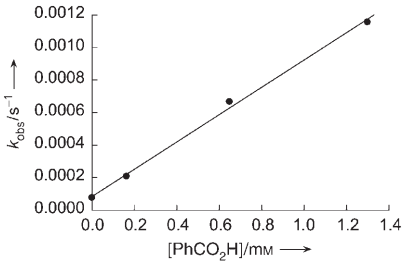

Figure 3. Effect of benzoic acid on the rate of oxygenation of **4b**. Reaction conditions: $[\mathbf{4b}]_0 = 1.5$ mM, 1.1 atm O_2, C_6D_6, 40 °C.

oxygenation of **4b** is initiated by pre-equilibrium reductive elimination of benzoic acid (**4b** ⇌ **1** + $PhCO_2H$), the presence of exogenous benzoic acid should inhibit the formation of $[Pd^0(IMes)_2]$ (**1**). Further studies will be necessary to elucidate the mechanistic origin of this result,[11] but this observation has important implications for aerobic oxidation catalysis.

A significant problem in homogeneous Pd-catalyzed oxidation reactions is catalyst decomposition by aggregation into inactive metallic Pd. This problem can be addressed, in part, by minimizing the steady-state concentration of Pd^0 during the catalytic reaction (e.g., **C**; Scheme 1). Carboxylic acids can react with Pd^0 to form Pd^{II}–hydride species that are less susceptible to decomposition.[12] The results outlined above, however, suggest that carboxylic acids not only provide a means to minimize Pd^0 concentration, but they also can promote oxygenation of the Pd^{II}–hydride intermediate. This dual role indicates that carboxylic acids can enhance both the stability and activity of homogeneous Pd oxidation catalysts.

Sigman and co-workers recently reported an important new class of NHC-coordinated Pd catalysts for the aerobic oxidation of alcohols,[13] and they demonstrated that carboxylic acid co-catalysts increase both the turnover rate and catalyst lifetime. The catalyst-stabilizing effect was attributed to the formation of Pd^{II}–hydride intermediates, and the rate acceleration was proposed to arise from partial-rate-limiting protonolysis of an η^2-peroxo intermediate (Scheme 1, **D** → **E**). Acid-catalyzed oxygenation of a Pd^{II}–hydride species, as described above, provides an alternative possible explanation for the rate enhancement. Separately, Jacobs and co-workers reported oxidative Heck reactions that undergo direct dioxygen-coupled turnover,[14] and the use of carboxylic acid co-catalysts resulted in unprecedented catalytic turnover numbers and activity. The results described above suggest that oxygenation of Pd^{II}–hydride intermediates, which undoubtedly form in the catalytic reactions, might contribute to the results.

In conclusion, we have prepared a new class of NHC-coordinated Pd^{II}–hydride complexes that undergo facile conversion to Pd^{II}–hydroperoxides in the presence of molecular oxygen. Future studies will seek to establish whether this formal dioxygen-insertion reaction proceeds by a direct or stepwise mechanism; in particular, they will assess whether Pd^0 intermediates are involved. The ability of carboxylic acids to catalyze the oxygenation of Pd^{II}–hydrides has important implications for improving the lifetime and activity of homogeneous Pd catalysts in aerobic oxidation reactions.

Received: February 9, 2006
Published online: March 28, 2006

Keywords: catalysis · molecular oxygen · oxidation · palladium

[1] a) S. S. Stahl, *Science* **2005**, *309*, 1824; b) S. S. Stahl, *Angew. Chem.* **2004**, *116*, 3480; *Angew. Chem. Int. Ed.* **2004**, *43*, 3400; c) M. S. Sigman, M. J. Schultz, *Org. Biomol. Chem.* **2004**, *2*, 2551; d) B. M. Stoltz, *Chem. Lett.* **2004**, *33*, 362; e) T. Nishimura, S. Uemura, *Synlett* **2004**, 201; f) R. A. Sheldon, I. W. C. E. Arends, G.-J. ten Brink, A. Dijksman, *Acc. Chem. Res.* **2002**, *35*, 774; g) M. Toyota, M. Ihara, *Synlett* **2002**, 1211.

[2] a) W. R. Thiel, *Angew. Chem.* **1999**, *111*, 3349; *Angew. Chem. Int. Ed.* **1999**, *38*, 3157; b) S. S. Stahl, J. L. Thorman, R. C. Nelson, M. A. Kozee, *J. Am. Chem. Soc.* **2001**, *123*, 7188; c) M. M. Konnick, I. A. Guzei, S. S. Stahl, *J. Am. Chem. Soc.* **2004**, *126*, 10212.

[3] a) T. Hosokawa, S.-I. Murahashi, *Acc. Chem. Res.* **1990**, *23*, 49; b) T. Nishimura, T. Onoue, K. Ohe, S. Uemura, *J. Org. Chem.* **1999**, *64*, 6750; c) J. Muzart, J. P. Pete, *J. Mol. Catal.* **1982**, *15*, 373.

[4] For additional examples of η^2-peroxo–palladium(II) species, see: a) G. Wilke, H. Schott, P. Heimbach, *Angew. Chem.* **1967**, *79*, 62;

 © 2006 Wiley-VCH Verlag GmbH & Co. KGaA, Weinheim

Angew. Chem. Int. Ed. Engl. **1967**, *6*, 92; b) C. J. Nyman, C. E. Wymore, G. Wilkinson, *J. Chem. Soc. A* **1968**, 561; c) S. Otsuka, A. Nakamura, Y. Tatsuno, *J. Am. Chem. Soc.* **1969**, *91*, 6994; d) T. Yoshida, S. Otsuka, *J. Am. Chem. Soc.* **1977**, *99*, 2134; e) T. Yoshida, K. Tatsumi, M. Matsumoto, K. Nakatsu, A. Nakamura, T. Fueno, S. Otsuka, *Nouv. J. Chim.* **1979**, *3*, 761; f) W. Clegg, G. R. Eastham, M. R. J. Elsegood, B. T. Heaton, J. A. Iggo, R. P. Tooze, R. Whyman, S. Zacchini, *J. Chem. Soc. Dalton Trans.* **2002**, 3300; g) G. Adjabeng, T. Brenstrum, C. S. Frampton, A. J. Robertson, J. Hillhouse, J. McNulty, A. Capretta, *J. Org. Chem.* **2004**, *69*, 5082; h) M. Yamashita, K. Goto, T. Kawashima, *J. Am. Chem. Soc.* **2005**, *127*, 7294.

[5] The first such example appeared recently: M. C. Denney, N. A. Smythe, K. L. Cetto, R. A. Kemp, K. I. Goldberg, *J. Am. Chem. Soc.* **2006**, *128*, 2508.

[6] For computational studies of dioxygen insertion into a Pd^{II}–hydride bond, see: a) J. M. Keith, R. J. Nielsen, J. Oxgaard, W. A. Goddard, III, *J. Am. Chem. Soc.* **2005**, *127*, 13172; b) T. Privalov, C. Linde, K. Zetterberg, C. Moberg, *Organometallics* **2005**, *24*, 885.

[7] N. D. Clement, K. J. Cavell, C. Jones, C. J. Elsevier, *Angew. Chem.* **2004**, *116*, 1297; *Angew. Chem. Int. Ed.* **2004**, *43*, 1277.

[8] Data for the X-Ray structure analysis of **4b**: $C_{49}H_{54}N_4O_2Pd$, $M_r = 837.36$, monoclinic, space group $P2_1/n$, $a = 12.5543(5)$, $b = 18.6672(7)$, $c = 18.4970(7)$ Å, $b = 92.7600(10)°$, $V = 4329.8(3)$ Å^3, $Z = 4$, $T = 100(2)$ K, $F_{000} = 1752$, $\mu = 0.471$ mm^{-1}, $\Theta = 1.92$–26.38, reflections collected 35721, independent reflections 8859 ($R_{int} = 0.0587$), GoF = 1.030, $R = 0.0276$, $wR_2 = 0.0788$, largest diffraction peak and hole 0.555/−0.237 e Å^{-3}. The data were collected on a Bruker CCD-1000 diffractometer using $Mo_{K\alpha}$ radiation, $\lambda = 0.71073$ Å. A successful solution by direct methods[15] provided most non-hydrogen atoms from the *E*-map. The remaining non-hydrogen atoms were located in an alternating series of least-squares cycles and difference Fourier maps. All non-hydrogen atoms were refined versus F^2[15] with anisotropic displacement coefficients. All hydrogen atoms except H were included in the structure factor calculation at idealized positions and were allowed to ride on the neighboring atoms with relative isotropic displacement coefficients. The H istrotropic displacement coefficient was refined independently. CCDC-297730 contains the supplementary crystallographic data for this paper. These data can be obtained free of charge from The Cambridge Crystallographic Data Centre by www.ccdc.cam.ac.uk/data_request/cif.

[9] For analogous mechanistic proposals for Rh^{III}- and Ir^{III}–hydride complexes, see: a) R. D. Gillard, B. T. Heaton, D. H. Vaughan, *J. Chem. Soc. A* **1970**, 3126; b) M. T. Atlay, M. Preece, G. Strukul, B. R. James, *Can. J. Chem.* **1983**, *61*, 1332.

[10] a) J. F. Endicott, C.-L. Wong, T. Inoue, P. Natarajan, *Inorg. Chem.* **1979**, *18*, 450; b) A. Bakac, *J. Am. Chem. Soc.* **1997**, *119*, 10726; c) A. Bakac, *J. Photochem. Photobiol. A* **2000**, *132*, 87; d) T. T. Wenzel, *Stud. Surf. Sci. Catal.* **1991**, *66*, 545; e) D. D. Wick, K. I. Goldberg, *J. Am. Chem. Soc.* **1999**, *121*, 11900.

[11] Preliminary ^{1}H NMR spectroscopic studies reveal that resonances associated with the coordinated benzoate ligand in **4b** broaden upon addition of sub-stoichiometric quantities of benzoic acid. This observation implies a fluxional process which involves an interaction between the free carboxylic acid and bound carboxylate ligand in **4b**. The mechanistic implications of these observations are the subject of ongoing study.

[12] For studies of reversible Pd^{II}–hydride formation, see: a) C. Amatore, A. Jutand, G. Meyer, I. Carelli, I. Chiarotto, *Eur. J. Inorg. Chem.* **2000**, 1855; b) I. D. Hills, G. C. Fu, *J. Am. Chem. Soc.* **2004**, *126*, 13178.

[13] a) D. R. Jensen, M. J. Schultz, J. A. Mueller, M. S. Sigman, *Angew. Chem.* **2003**, *115*, 3940; *Angew. Chem. Int. Ed.* **2003**, *42*, 3810; b) J. A. Mueller, C. P. Goller, M. S. Sigman, *J. Am. Chem. Soc.* **2004**, *126*, 9724; c) M. J. Schultz, S. S. Hamilton, D. R. Jensen, M. S. Sigman, *J. Org. Chem.* **2005**, *70*, 3343.

[14] M. Dams, D. E. De Vos, S. Celen, P. A. Jacobs, *Angew. Chem.* **2003**, *115*, 3636; *Angew. Chem. Int. Ed.* **2003**, *42*, 3512.

[15] Bruker-AXS (2000–2003) SADABS V.2.05, SAINT V.6.22, SHELXTL V.6.10 & SMART 5.622 Software Reference Manuals. Bruker-AXS, Madison, Wisconsin, USA.

 © 2006 Wiley-VCH Verlag GmbH & Co. KGaA, Weinheim

Cell-Penetrating Molecules

DOI: 10.1002/anie.200600312

Design, Synthesis, and Membrane-Translocation Studies of Inositol-Based Transporters**

*Kaustabh K. Maiti, Ock-Youm Jeon, Woo Sirl Lee, Dong-Chan Kim, Kyong-Tai Kim, Toshihide Takeuchi, Shiroh Futaki, and Sung-Kee Chung**

Cell membrane systems represent formidable physical barriers for the trafficking of unintended molecules. Only those molecules with an appropriate range of molecular size, polarity, and charge are allowed to pass through cell membranes. Many potential drug molecules have to overcome these barriers, and a variety of chemical and physical methods have been proposed as means of accomplishing this challenging task. A number of peptides have been reported to

[*] Dr. K. K. Maiti, O.-Y. Jeon, W. S. Lee, Prof. Dr. S.-K. Chung
Department of Chemistry
Pohang University of Science and Technology
Pohang 790-784 (Korea)
Fax: (+82) 54-279-3399
E-mail: skchung@postech.ac.kr

D.-C. Kim, Prof. Dr. K.-T. Kim
Department of Life Science
Pohang University of Science and Technology
Pohang 790-784 (Korea)

T. Takeuchi, Prof. Dr. S. Futaki
Department of Biofunctional Chemistry
Institute for Chemical Research
Kyoto University
Uji, Kyoto 611-0011 (Japan)
and
PRESTO
Japan Science and Technology Corporation (JST)
Kawaguchi, Saitama 332-0012 (Japan)

[**] We thank Dr. Hyun Soo Kim for technical assistance with cell cultures, MTT tests, and operation of the confocal laser scanning microscope at Postech. Financial support from Postech, Posco (Postech Biotech Center), BK-21, and MOST (National Frontier Research Program administered through KRICT/CBM), and Grants-in Aid for Scientific Research from the Ministry of Education, Culture, Sports, Science, and Technology of Japan is gratefully acknowledged.

Supporting information for this article is available on the WWW under http://www.angewandte.org or from the author.

© 2006 Wiley-VCH Verlag GmbH & Co. KGaA, Weinheim

translocate themselves across cell membranes. They are known as cell-penetrating peptides or protein transduction domains, and are capable of delivering exogenous molecules into cells. The first cell-membrane-penetrating property was observed with HIV-1 Tat protein (Tat-86) and then with the antennapedia (Antp) protein of *Drosophila* and others. Subsequent studies have demonstrated that the membrane-penetrating ability is clearly associated with relatively short peptide sequences in these proteins; for example, nine basic amino acid residues for the Tat protein (residues 49–57), 16 amino acids for the Antp protein (residues 43–58) that have a potentially amphipathic and basic helical structure, and 12 hydrophobic amino acids from Kaposi's sarcoma fibroblast growth factor membrane-translocating sequence (KFGF-MTS).[1–4] Despite the lack of a clear understanding of the membrane-translocation mechanisms, many research efforts have been extended toward their applications as delivery vectors in order to improve the pharmacology of poorly bioavailable drugs, such as, small molecules,[5] proteins,[6–10] nucleotides, and genes.[11–13] Reports have also appeared on the development of membrane-translocating transporter molecules that mimic natural and non-natural amino acids and their structural analogues, especially in the area of polycationic peptide mimetics.[14–23]

Although these peptides commonly share a high efficiency as molecular transporters, the structural motifs and physicochemical properties of these cell-penetrating peptides are quite diverse. It appears likely that different peptides may use variant mechanisms of translocation and that even the same peptide can use alternative pathways depending on conditions of administration and the nature of cargo, as was previously suggested.[10] Therefore, the modifications of the structures and physicochemical properties of even the known molecular transporters may yield novel transporters that exhibit different spectra in vivo and in vitro, as well as different translocation efficiencies. In addition, the in vivo efficacy, stability to various endogenous enzymes, processing cost, and long-term safety still remain practical concerns. With these considerations in mind, we have developed a novel class of molecular transporters as a potential delivery vector which consist of multiple units of the guanidine residue attached to the dimeric inositol molecule as a scaffold. Carbohydrate and inositol structures reveal the highest density of functionality among organic compounds per unit weight in the form of multiple hydroxy groups with diverse stereochemical variations. Also, they occur naturally and are largely devoid of any noticeable toxicity. Carbohydrates and inositols may provide an excellent platform to build a molecular diversity by appending desired structural residues around the scaffold. A number of research groups have previously attempted to design various peptidomimetics on the carbohydrate scaffolds.[24]

We prepared a number of synthetic transporter molecules by utilizing *myo*- and *scyllo*-inositol dimers as the scaffolds (Figure 1). Although *myo*-inositol is most abundant in nature and readily available, substitution at sites other than the C2 and C5 positions tends to generate a diastereomeric mixture, whereas *scyllo*-inositol, albeit less readily available, has a higher degree of symmetry with all equatorial hydroxy groups. We initially developed synthetic protocols with *myo*-inositol as the scaffold to give **1**, and then prepared the transporter **2** based on the *scyllo*-inositol scaffold (see Supporting Information for details of the syntheses of **1** and **2**).[25,26] Compounds **3a–c** were prepared as shown in Scheme 1. Compound **5**, prepared from 1-*O*-Bz-2,3:5,6-di-*O*-isopropylidene-*scyllo*-inositol[26] (see Supporting Information), was converted into **6** and **7**, and these two components were coupled using EDC, HOBT, and DMAP in DMF to give **8** in 65% yield. The compound **9**, obtained from **8** by removal of the isopropylidene protecting groups, was exhaustively acylated with *N*-Boc-protected 4-aminobutyric ($n=3$), 6-aminocaproic ($n=5$), and 8-aminocaprylic ($n=7$) acids, respectively, under EDC coupling conditions to give three dimeric products, **10a–c**, with varying chain lengths (see Scheme 1). Removal of the *N*-Boc protecting groups of **10a–c** exposed the terminal amino groups, which were guanidiny-

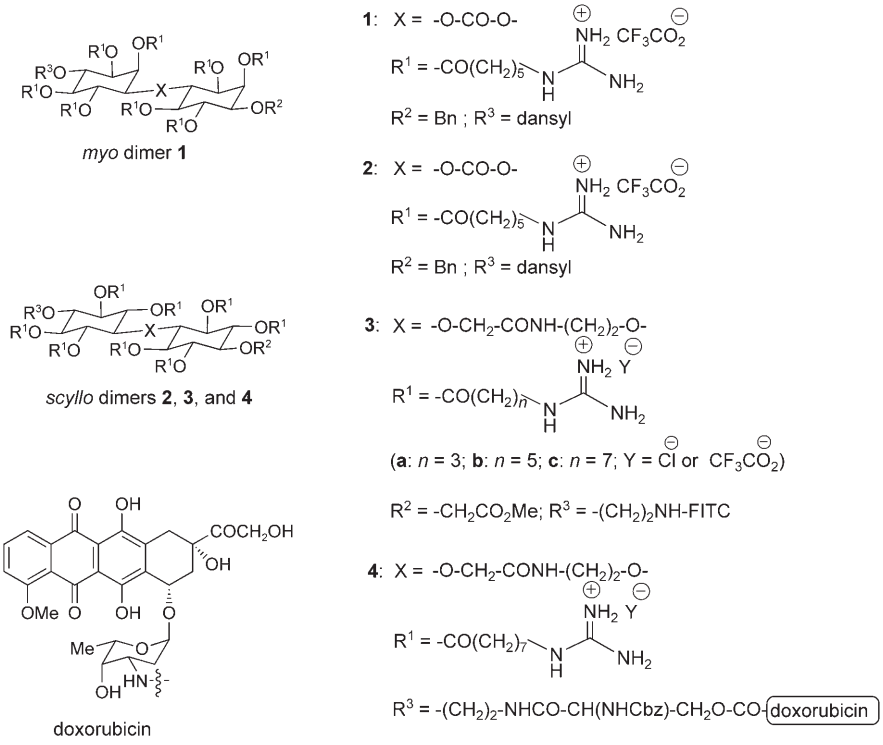

Figure 1. Structures of the synthetic molecular transporters **1–3** and a covalent conjugate of **3c** with doxorubicin, **4**. Cbz = carbobenzyloxy.

 © 2006 Wiley-VCH Verlag GmbH & Co. KGaA, Weinheim

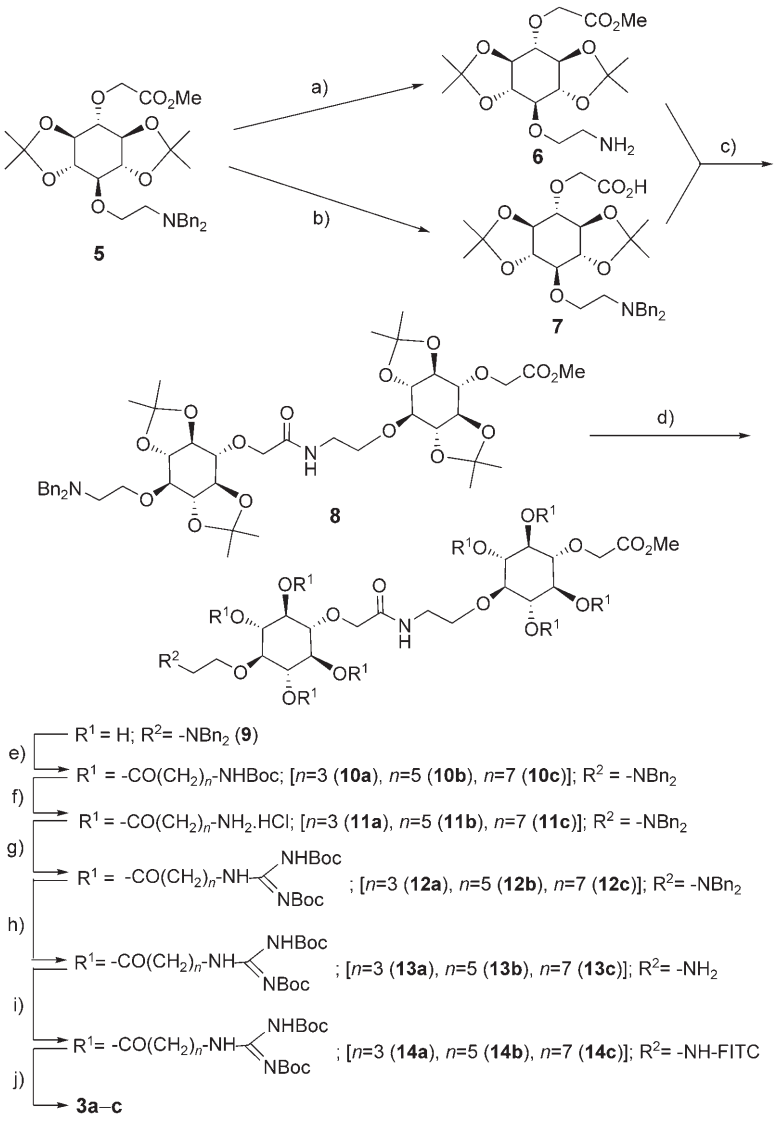

Scheme 1. Synthetic route to compounds **3a–c**. Reagents and conditions: a) 10% Pd/C, H_2 (1 atm), CH_2Cl_2/MeOH (1:9), quant.; b) NaOH, MeOH, then AcOH, 92%; c) **6**, **7**, EDC, HOBT, DMAP, DMF, 65%; d) *p*-TSA, CH_2Cl_2/MeOH (9:1), quant.; e) EDC, DMAP, *N*-Boc-protected acids: 4-aminobutyric acid ($n=3$), 6-aminocaproic acid ($n=5$), or 8-aminocaprylic acid ($n=7$), DMF, 65–80%; f) HCl(g), EtOAc, quant.; g) *N*,*N*′-di-Boc-*N*″-triflylguanidine, Et_3N, dioxane/H_2O (5:1), 55–76%; h) 10% Pd/C, H_2 (1 atm), MeOH/CH_2Cl_2 (9:1), 75–80%; i) FITC-I, Et_3N, THF, absolute EtOH, 52–65%; j) HCl(g), EtOAc, 76–80%; or TFA/CH_2Cl_2 (1:1), 86–94%. Bn = benzyl; EDC = 1-ethyl-3-(3-dimethylaminopropyl)-carbodiimide; HOBT = hydroxybenzotriazole; DMAP = 4-(dimethylamino)pyridine; DMF = *N*,*N*-dimethylformamide; *p*-TSA = *p*-toluenesulfonic acid; Boc = *tert*-butoxycarbonyl; FITC = fluorescein isothiocyanate; TFA = trifluoroacetic acid.

lated with a large excess of *N*,*N*′-di-Boc-*N*″-trifluoromethanesulfonylguanidine and triethylamine to give three target molecules, **12a–c**, with the Boc-protected guanidine moiety. After removal of the *N*-benzyl protecting group in the side chain of **12a–c**, the fluorescein tag was attached to the primary amino group of **13a–c** using fluorescein-5-isothiocyanate (FITC-I) and triethylamine to give **14a–c**. The Boc groups at the guanidine moieties in compounds **14** were removed with either trifluoroacetic acid or gaseous HCl to yield three molecular transporters, **3a–c**, as salts after purification by medium-pressure liquid chromatography (MPLC) on reverse-phase (C_8) silica gel.

For the preparation of a transporter–cargo conjugate, Cbz-protected L-serine was attached through an amide bond to the primary amine of compound **13c** under the EDC coupling conditions. The hydroxy group of the serine moiety was then coupled with the primary amino group of doxorubicin through a carbamate bond.[27] Finally the *N*-Boc protecting groups of the guanidine moieties were removed with gaseous HCl to yield the covalent conjugate **4** as its HCl salt (see Figure 1). All key synthetic intermediates as well as the final target compounds were satisfactorily characterized by NMR spectroscopy and MALDI-TOF mass spectrometry.

Preliminary evaluations of the synthetic transporters were carried out for their ability to translocate into the cytoplasm with three cell lines: COS-7, RAW264.7, and HeLa cells. After exposure of the cultured cells to the transporters for 3–5 minutes, cellular uptake of the four compounds **1**, **2**, **3b**, and **3c**, without fixing, was found to be more efficient than with the reference compounds, dansyl- and fluorescein-labeled nona-arginine (R9-Fl), on the basis of confocal laser scanning microscopy observations; compound **3a** appeared to be approximately as efficient as the reference standard. Thus, more detailed studies were carried out on HeLa cells with the more stable amide compounds **3a–c**. The internalization efficiencies of the transporters **3a–c** were compared with that of fluorescein-labeled octaarginine (R8-Fl), a representative cell-penetrating peptide. The HeLa cells were treated with the respective transporter (10 μM) at 37 °C for 1 h. Fluorescence-activated cell sorter (FACS) analysis of the transporters demonstrated that **3b** and **3c** were internalized 1.8 and 2.5 times as much as R8-Fl, whereas the amount of **3a** internalized was about half that of R8-Fl under the same conditions (Figure 2A). A more precise kinetics study of internalization was performed with the most efficient transporter **3c** in comparison with R8-Fl (Figure 2B). In contrast to the observation that the amount of R8-Fl internalized reached a plateau in 3 h, the internalization of **3c** kept increasing and did not reach a plateau in 6 h. The total cellular uptake of **3c** was almost three times higher than that of R8-Fl. However, no significant toxicity was evident for these cells.

The cellular (organellar) localizations of the transporter **3c** were examined next without fixing. First, HeLa cells were treated with **3c** (10 μM) at 37 °C for 1 h in the presence of tetramethylrhodamine-labeled transferrin (Rho-Tf) as a marker of clathrin endocytosis (25 $\mu g\,mL^{-1}$). Considerable fractions of both labels in punctate structures showed a

 © 2006 Wiley-VCH Verlag GmbH & Co. KGaA, Weinheim

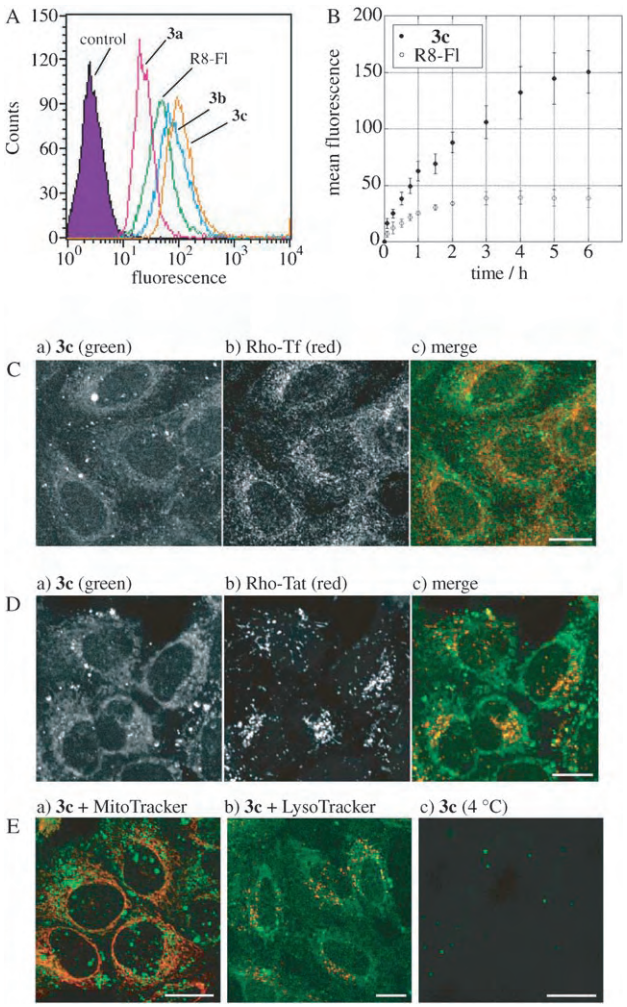

Figure 2. Cellular uptake studies of compound **3c** using HeLa cells. A) FACS analysis of the compounds **3a–c** taken up by HeLa cells. The cells were treated with compounds **3a–c** (10 μM each) in serum-containing minimum essential medium (MEM) at 37 °C for 1 h and were analyzed by FACS. B) Kinetics study of the amount of compound **3c** taken up by the cells in comparison with that of the fluorescein-labeled octaarginine (R8-Fl). The cells were incubated with compound **3c** or R8-Fl (10 μM each) at 37 °C for different time intervals and analyzed by FACS. C) Observation by confocal microscopy of the cells treated with **3c** (10 μM) in the presence of tetramethylrhodamine-labeled transferrin (Rho-Tf; 25 $\mu g\,mL^{-1}$) at 37 °C for 1 h. D) The cells were treated with **3c** and tetramethylrhodamine-labeled Tat peptide (Rho-Tat; 10 μM each) at 37 °C for 1 h. E): a) No significant colocalization of the signals of **3c** with MitoTracker (250 nM) is seen; b) the majority of **3c** did not reach the lysosome in 1 h (lysosomes were stained with 50 nM LysoTracker); c) no significant internalization was observed either for the cells treated with **3c** (10 μM) for 1 h at 4 °C. Scale bars: 20 μm. See text for details.

distinct localization pattern under the experimental conditions (Figure 2C). When the cells were similarly treated with **3c** at 4 °C, no significant internalization was observed (Figure 2E, part c). These results suggest that **3c** internalizes through an endocytic route that is different from the well-characterized clathrin-dependent pathway. Interestingly, **3c** may possibly internalize using pathways that are different even from those of the Tat peptide, another representative arginine-rich transporter. HeLa cells were treated with **3c** in the presence of tetramethylrhodamine-labeled Tat peptide (Rho-Tat; 10 μM each) at 37 °C for 3 h. Also, little colocalization of the signals of **3c** and Rho-Tat was observed. The majority of the signals from Rho-Tat were observed in the peripheries of the nucleus, whereas the wider spread signals of **3c** were observed in the cytosolic region. Moreover, as was previously observed, the Tat-positive structures were often considerably larger than those for **3c** (Figure 2D). We further examined whether **3c** was delivered into lysosomes or mitochondria by co-staining with specific dyes for lysosomes (LysoTracker) and mitochondria (MitoTracker), respectively (Figure 2E). No significant colocalization of the signals of **3c** with MitoTracker (250 nM) was observed (Figure 2E, part a), and the majority of **3c** did not reach the lysosome in 1 h (lysosomes were stained with 50 nM LysoTracker; see Figure 2E, part b). These results strongly suggest that **3c** may use different mechanisms of internalization and cellular localization from those transporters reported to date, even though it comprises a cluster of guanidinium moieties albeit on a dimeric inositol scaffold.

Next, we examined if compound **3c** also showed a unique in vivo biodistribution pattern. Thus, **3c** (HCl salt, 77 $mg\,kg^{-1}$) was dissolved in sterile distilled water and injected into 8-week-old mice (C57BL/6) intraperitoneally. After 20 minutes, the treated mice were perfused with 4% paraformaldehyde in phosphate buffer solution (PBS; pH 7.4), and the organs, including the heart, spleen, liver, kidneys, and lungs, cut into 15 μm sections, were incubated overnight in a solution of 0.5 M sucrose in PBS. After drying at 37 °C, the sections were washed with PBS and treated with 0.3% Triton X-100 at room temperature and analyzed by fluorescence microscopy. The Tat peptides were previously reported to show predominant tissue distribution in the liver, kidneys, lungs, heart muscle, and spleen.[23,28] In contrast to these observations, significantly lower extents of internalization of **3c** into the liver, kidney, and spleen were observed; **3c** was located only in the peripheries of these organs. However, much higher distributions of **3c** were seen in heart, lung, and brain tissues (Figure 3). Because of its potential implications on the possible selective delivery into the central nervous system, we specifically repeated the tissue distribution experiment of compound **3c** in the mouse brain at a dosage level of 57 $mg\,kg^{-1}$ for 20 minutes. The brain cortex region showed strong fluorescence, suggesting that the transporter indeed

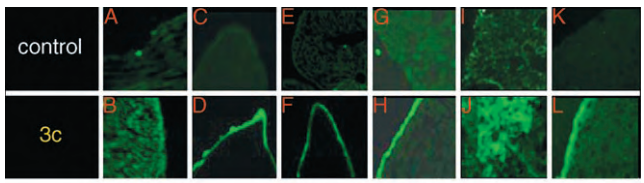

Figure 3. Distribution of **3c** (HCl salt) into mouse tissues. Fluorescence microscopy images (green fluorescence from FITC) of heart muscle (A, B), spleen (C, D), liver (E, F), kidney (G, H), and lung (I, J) tissue sections, and coronal brain sections (K, L) isolated from mice 20 minutes after intraperitoneal injection. Exposure time: 14000 ms (A, B); 500 ms (C, D); 300 ms (E, F); 500 ms (G, H); 1200 ms (I, J); 1000 ms (K, L); $\lambda_{em} = 488$ nm.

 © 2006 Wiley-VCH Verlag GmbH & Co. KGaA, Weinheim

crossed the blood–brain barrier (BBB) rapidly and efficiently (see Supporting Information). Development of vectors to help cross the BBB is one of the major challenges in drug delivery, and these observations should be useful in the development of organ-selective delivery technologies.

Last, we investigated the in vitro and in vivo distribution of the transporter **3c**–doxorubicin conjugate **4**. Doxorubicin hydrochloride (adriamycin) is extensively used clinically for the treatment of a variety of neoplastic diseases, including leukaemia and breast, ovarian, and solid cancers, but not brain cancer, as it does not overcome the BBB.[29] Doxorubicin reveals strong UV/Vis absorption bands and is also highly fluorescent. Compound **4** was examined for its cell-penetrating ability with HeLa cells without fixing. The conjugate **4** at concentrations of 10 and 30 μM showed much-enhanced translocation into the cytoplasm when compared with doxorubicin itself (Figure 4 A). However, the cells

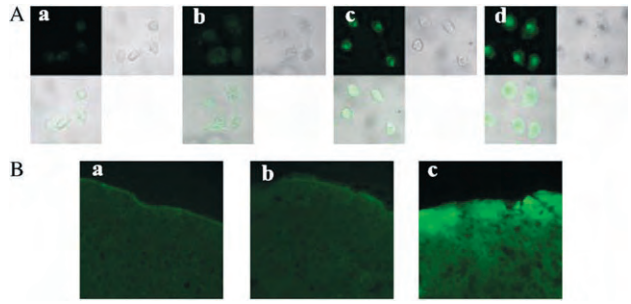

Figure 4. A) Fluorescence microscopy images of doxorubicin (green fluorescent emission) and doxorubicin–**3c** conjugate, **4**: a) doxorubicin (10 μM), b) doxorubicin–**3c** conjugate, **4** (HCl salt, 10 μM), c) doxorubicin (30 μM), and d) conjugate **4** (30 μM) in HeLa cells incubated for 15 minutes at 37 °C. B) Fluorescence microscopy images of mouse brain sections (cortex region): a) control (water), b) doxorubicin (21.3 mg kg^{-1}; M_r = 580 g mol^{-1}), and c) conjugate **4** (HCl salt, 115.8 mg kg^{-1}; M_r = 4452 g mol^{-1}). For part (B), sample treatment time: 20 minutes; exposure time: 9000 ms; λ_{em} = 488 nm.

treated with compound **4** showed changed morphologies, perhaps due to extensive cell death. Cell viability tests indeed indicated that the majority of the cells died at the dosage level of 10 μM of **4** after 24 h, whereas the same concentration of either doxorubicin or transporter **3c** alone caused no significant cell damage. This observation suggests that compound **4** was much more efficiently delivered into the cells compared to doxorubicin itself.

We further examined the uptake of free doxorubicin and the transporter–doxorubicin conjugate **4** into the brain. Thus, three mice (C57BL/6) were injected intraperitoneally with either sterile distilled water (0.5 mL, control), doxorubicin (21.3 mg kg^{-1}), or compound **4** (115.8 mg kg^{-1}) in the same volume of water. After 20 minutes, the mice were perfused with 4% paraformaldehyde in PBS (pH 7.4), and the brains were cut into 15 μm sections with a cryostat and incubated overnight in a solution of 0.5 M sucrose in PBS. After drying at 37 °C, the sections were washed with PBS and treated with 0.3% Triton X-100 at room temperature and analyzed by fluorescence microscopy. The fluorescence micrographs in Figure 4 B clearly show that a substantial amount of **4** is extensively distributed in the cortex region of the mouse brain (Figure 4 B, image c), whereas a very small amount of doxorubicin translocated into the brain cortex in the same timeframe (Figure 4 B, image b). These in vivo results suggest that the uptake of doxorubicin into the brain across the BBB is very inefficient, as expected, and that conjugation to the transporter **3c** significantly increases the uptake as well as the intercellular permeation of doxorubicin in the brain tissue.

In summary, the novel transporter structures based on dimeric inositol scaffolds reported here display unique spectra of distribution in vitro and in vivo. The lack of cell/organ specificities has generally been considered as one of the shortcomings of the Tat and oligoarginine-mediated delivery methods. However, the results shown here strongly suggest a possibility of designing highly sophisticated transporters by varying the structure of the backbone scaffold, charge densities, and perhaps other parameters. Thus, it is suggested that the structural diversity of sugars may be beneficial as scaffolds in the design of transporters in terms of not only aqueous solubility but also selective tissue and organellar distributions. Why the transporter **3c** shows these unique properties is not clear at this stage. Studies designed to provide additional information on these issues are in progress.

Received: January 24, 2006
Published online: March 23, 2006

Keywords: bioorganic chemistry · carbohydrates · drug delivery · fluorescence · membranes

[1] S. Futaki, *Adv. Drug Delivery Rev.* **2005**, *57*, 547.
[2] P. Ludberg, U. Langel, *J. Mol. Recognit.* **2003**, *16*, 227.
[3] A. Jolit, A. Prochiantz, *Nat. Cell Biol.* **2004**, *6*, 189.
[4] J. J. Schwartz, S. Zhang, *Curr. Opin. Mol. Ther.* **2000**, *2*, 162.
[5] J. B. Rothbard, S. Garlington, O. Lin, T. Kirschberg, E. Kreider, P. L. McGrane, P. A. Wender, P. A. Khavari, *Nat. Med.* **2000**, *11*, 1253.
[6] J. S. Wadia, S. F. Dowdy, *Curr. Protein Pept. Sci.* **2003**, *4*, 97.
[7] J. S. Wadia, R. V. Stan, S. F. Dowdy, *Nat. Med.* **2004**, *10*, 310.
[8] D. Jo, A. Nashabi, C. Doxsee, Q. Lin, D. Unutmaz, J. Chen, H. E. Ruley, *Nat. Biotechnol.* **2001**, *19*, 929.
[9] D. Jo, D. Liu, S. Yao, R. D. Collins, J. Hawiger, *Nat. Med.* **2005**, *11*, 892.
[10] I. Nakase, M. Niwa, T. Takeuchi, K. Sonomura, N. Kawabata, Y. Koike, M. Takehashi, S. Tanaka, K. Ueda, J. C. Simpson, A. T. Jones, Y. Sugiura, S. Futaki, *Mol. Ther.* **2004**, *10*, 1011.
[11] V. P. Tochilin, R. Rammohan, V. Weissig, T. S. Levchenko, *Proc. Natl. Acad. Sci. USA* **2001**, *98*, 8786.
[12] U. Krauss, M. Muller, M. Stahl, A. Beck-Sickinger, *Bioorg. Med. Chem. Lett.* **2004**, *14*, 51.
[13] K. Kogure, R. Moriguchi, K. Sasaki, M. Ueno, S. Futaki, H. Harashima, *J. Controlled Release* **2004**, *98*, 317.
[14] P. A. Wender, D. J. Mitchell, K. Pattabiraman, E. T. Pelkey, L. Steinman, J. B. Rothbard, *Proc. Natl. Acad. Sci. USA* **2000**, *97*, 13003.
[15] P. A. Wender, J. B. Rothbard, T. C. Jessop, E. L. Kreider, B. L. Wylie, *J. Am. Chem. Soc.* **2002**, *124*, 13382.
[16] J. B. Rothbard, E. Kreider, C. L. VanDeusen, L. Wright, B. L. Wylie, P. A. Wender, *J. Med. Chem.* **2002**, *45*, 3612.
[17] S. Futaki, T. Suzuki, W. Ohashi, T. Yagami, S. Tanaka, K. Ueda, Y. Sugiura, *J. Biol. Chem.* **2001**, *276*, 5836.

 © 2006 Wiley-VCH Verlag GmbH & Co. KGaA, Weinheim

[18] S. Futaki, I. Nakase, T. Suzuki, Y. Zhang, Y. Sugiura, *Biochemistry* **2002**, *41*, 7925.
[19] N. Umezawa, M. A. Gelman, M. C. Haigis, R. T. Raines, S. H. Gellman, *J. Am. Chem. Soc.* **2002**, *124*, 368.
[20] N. Rueping, Y. Mahajan, M. Sauer, D. Seebach, *ChemBioChem* **2002**, *3*, 257.
[21] P. Zhou, M. Wang, L. Du, G. W. Fisher, A. Waggoner, D. H. Ly, *J. Am. Chem. Soc.* **2003**, *125*, 6878.
[22] N. W. Luedtke, P. Carmichael, Y. Tor, *J. Am. Chem. Soc.* **2003**, *125*, 12374.
[23] J. Fernandez-Carneado, M. Van Gool, V. Martos, S. Castel, P. Prados, J. de Mendoza, E. Giralt, *J. Am. Chem. Soc.* **2005**, *127*, 869.
[24] G. T. Le, G. Abbenante, B. Becker, M. Grathwohl, J. Halliday, G. Tometzki, J. Zuegg, W. Meutermans, *Drug Discovery Today* **2003**, *8*, 701.
[25] S. K. Chung, Y. H. Ryu, *Carbohydr. Res.* **1994**, *258*, 145.
[26] S. K. Chung, Y. U. Kwon, Y. T. Chang, K. H. Sohn, J. H. Shin, B. J. Hong, I. H. Chung, *Bioorg. Med. Chem.* **1999**, *7*, 2577.
[27] S. Sengupta, D. Eavarone, I. Capila, G. Zhao, N. Watson, T. Kiziltepe, R. Sasisekharan, *Nature* **2005**, *436*, 568.
[28] S. R. Schwarze, A. Ho, A. Vocero-Akbani, S. F. Dowdy, *Science* **1999**, *285*, 1569.
[29] C. R. Rousselle, M. Smirnova, P. Clair, J.-M. Lefauconnier, A. Chavanieu, B. Calas, J.-M. Scherrmann, J. Temsamani, *J. Pharmacol. Exp. Ther.* **2001**, *296*, 124.

 © 2006 Wiley-VCH Verlag GmbH & Co. KGaA, Weinheim

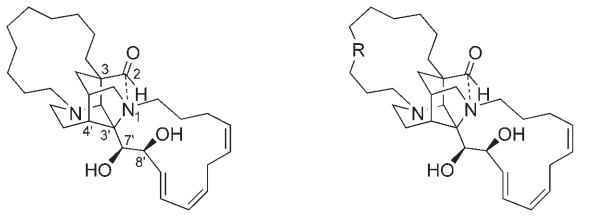

sarain A (**1**)

sarain B (**2**): R = –(*Z*)-CH=CH–
sarain C (**3**): R = –(*Z*)-CH=CHCH$_2$–

Scheme 1. Sarains A–C (**1**–**3**).

Alkaloids

DOI: 10.1002/anie.200600417

Total Synthesis of (−)-Sarain A**

*Neil K. Garg, Sheldon Hiebert, and Larry E. Overman**

The Mediterranean sponge *Reniera sarai* is a rich source of structurally unique alkaloids. The most remarkable of these, sarains A–C (**1**–**3**; Scheme 1), were isolated by Cimino and co-workers in 1986 and fully characterized three years later.[1–3] These alkaloids contain a unique diazatricycloundecane core, which is flanked by two macrocyclic rings. Of these large rings, the 14-membered ring is especially intricate, with both vicinal diol and skipped triene functionalities. Sarains A–C (**1**–**3**) possess a total of seven stereocenters, including a quaternary carbon atom at C3. In addition, the spatial proximity of the tertiary amine N1 atom and aldehyde functional group in **1**–**3** results in a proximity interaction, which is sensitive to the pH and solvent environment.[4] This interaction significantly complicates both the purification and characterization of these alkaloids.[1] Sarains A–C display antibacterial, insecticidal, and antitumor activities.[5]

Soon after the isolation of sarains A–C two decades ago, their unprecedented, intricate structures stimulated synthetic efforts in many laboratories worldwide. Significant progress towards sarain A (**1**) has been registered by Weinreb,[6] Heathcock,[7] Cha,[8] and Marazano,[9] in addition to us.[10] Although successful preparations of the diazatricycloundecane core and the saturated macrocycle of **1** have been described,[7d,6c,8b,c] assembly of the highly functionalized 14-membered ring has been reported only in a simple model system.[11] Likewise, chemistry associated with the introduction of the proximal tertiary amine and aldehyde groups has not been described. To date a completed total synthesis of **1** has remained an elusive goal. Herein, we describe our development of chemistry that addresses the final synthetic challenges associated with **1**, thus leading to the first total synthesis of this intriguing natural product.

An optimized route to access the tricyclic core and saturated macrocyclic ring of sarain A in enantiomerically pure form had been developed previously by our research group.[10] D-Diethyl tartrate (**4**) is first converted into oxazoline **5** in five straightforward steps (Scheme 2). The C4′-C3′-C7′ stereotriad of **1** then is established by stereoselective Michael addition of the lithium enolate of **5** to α,β-unsaturated ester **6** to provide adduct **7**,[12] which, in turn, is elaborated to enoxysilane **8**. In a critical transformation, exposure of intermediate **8** to BCl_3 facilitates intramolecular enoxysilane/*N*-sulfonyliminium ion cyclization to install the C3 quaternary carbon stereocenter and construct the core of **1**.[13] Subsequent conversion of tetracyclic aldehyde **9** into diene **10** allows the saturated macrocycle to be formed by ring-closing metathesis followed by hydrogenation.[6c,8b,14] Using this synthetic sequence, tetracyclic diamine diol **11** was prepared on a multigram scale.

Our initial attempts to advance intermediate **11** to **1** are summarized in Scheme 3. With the aim of ultimately fashioning the final macrocyclic ring by an intramolecular Stille

[*] Dr. N. K. Garg, Dr. S. Hiebert, Prof. L. E. Overman
Department of Chemistry
University of California—Irvine
1102 Natural Sciences 2, Irvine, CA 92697-2025 (USA)
Fax: (+1) 949-824-3866
E-mail: leoverma@uci.edu

[**] This research was supported by the NIH Heart, Lung, and Blood Institute (HL-25854). Postdoctoral fellowship support of N.K.G. from the NIH Heart, Lung, and Blood Institute (HL-80901) and of S.H. from the Natural Science and Engineering Research Council of Canada is gratefully acknowledged. The authors thank Dr. Christopher Douglas for helpful discussions and Dr. John Greaves, John Huckins, and Joy Middleton for experimental assistance. Professor Jin Cha is acknowledged for providing a sample of natural sarain A, obtained originally from Professor Cimino. The early stages of our sarain A synthesis were developed by Dr. Michael Becker, Dr. Peter Chua, Dr. Christopher Douglas, Dr. Robert Downham, Dr. Stephan Jaroch, Dr. Richard Matsuoka, and Dr. Fay Ng.

 InterScience © 2006 Wiley-VCH Verlag GmbH & Co. KGaA, Weinheim

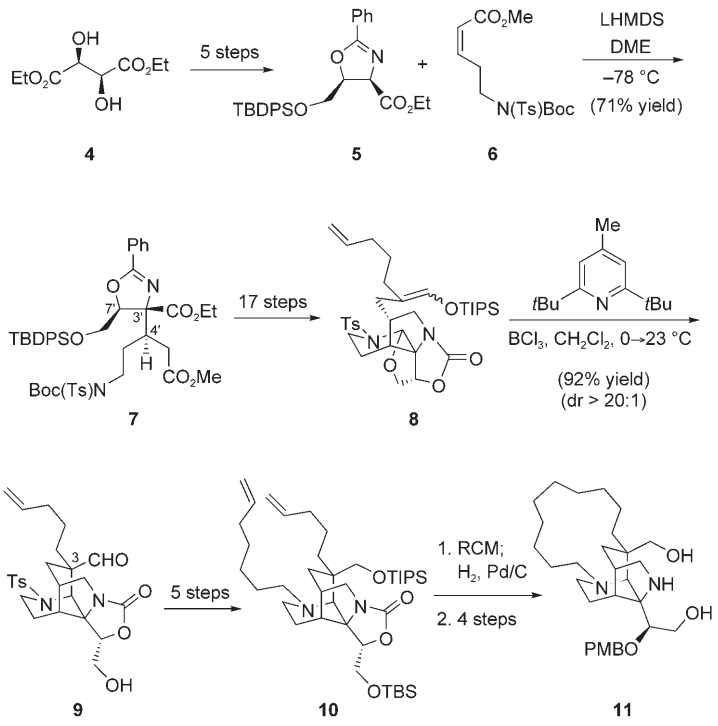

Scheme 2. Summary of the synthesis of tetracyclic diamine diol **11**. TBDPS = *tert*-butyldiphenylsilyl, LHMDS = lithium hexamethyldisilazanide, DME = 1,2-dimethoxyethane, Boc = *tert*-butoxycarbonyl, Ts = *p*-toluenesulfonyl, TIPS = triisopropylsilyl, TBS = *tert*-butyldimethylsilyl, RCM = ring-closing metathesis, PMB = *p*-methoxybenzyl.

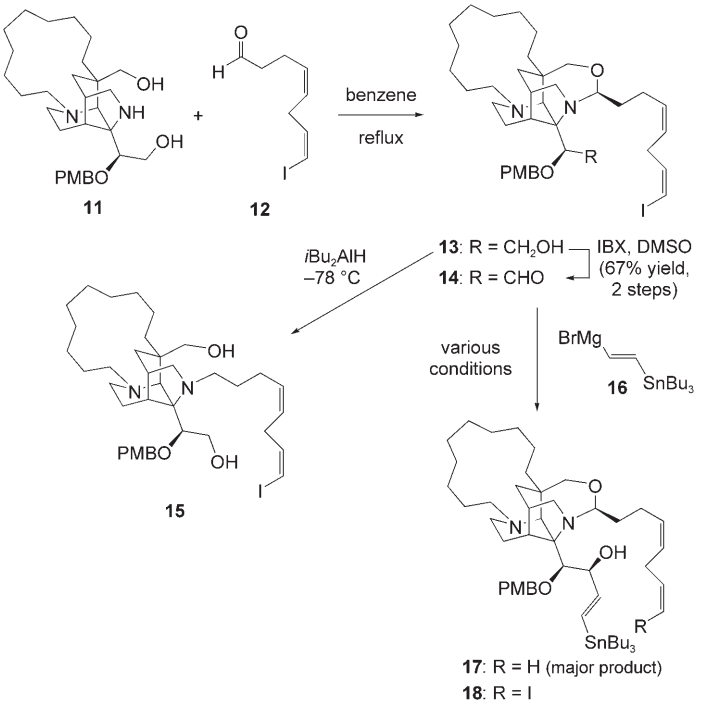

Scheme 3. Initial attempts to elaborate diamine diol **11**. IBX = iodoxybenzoic acid, DMSO = dimethyl sulfoxide.

reaction,[15] we first condensed diamine diol **11** with aldehyde **12**, thus generating the pentacyclic [1,3]oxazocane derivative **13** as a single stereoisomer (Scheme 3).[10c,16] Reduction of this intermediate with iBu_2AlH at −78 °C provided tertiary amine **15**, which to our surprise, was quite labile, thus undergoing extensive skeletal rearrangement when exposed to acetic acid at room temperature.[10c] As [1,3]oxazocane **13** did not exhibit this proclivity for skeletal reorganization, we decided to defer reduction of the *N*,*O*-acetal until the final macrocyclic ring was in place.

To fashion precursors of the macrocyclic triene ring from [1,3]oxazocane **13**, this intermediate was oxidized with IBX in DMSO to provide aldehyde **14** (Scheme 3).[17] Reaction of this α-alkoxy aldehyde with β-stannylvinylmagnesium bromide **16**[18] under a variety of conditions led to an inseparable mixture of two products. After inspection, it became apparent that although stereocontrolled addition of the Grignard reagent had occurred to generate the *syn* β-alkoxy alcohol,[19] the major product produced in this reaction, **17**, had lost the vinyl iodide functionality. In spite of extensive experimentation, we were unable to minimize the halogen–magnesium exchange that likely gave rise to triene **17**.

Given the difficulty associated with installing the vinyl stannane segment in the presence of the vinyl iodide, an alternative stepwise approach for accessing a Stille macrocyclization precursor was developed. In this strategy, diamine diol **11** was first condensed with siloxy butanal **19**[20] to give [1,3]oxazocane **20** (Scheme 4).[16,21] Oxidation of this alcohol with IBX generated aldehyde **21**, which reacted smoothly with Grignard reagent **16** to provide stannane **22** as a 3–4:1 mixture of stereoisomers. Although this mixture of epimers could not be separated, it was presumed that the major allylic alcohol product had an *S* configuration at C8′ as a result of chelation between the carbonyl oxygen atom and adjacent alkoxy substituent in the addition step.[22] Cleavage of the primary TBS ether of **22** with TBAF provided the corresponding mixture of diol epimers **23** in high yield.

We next explored several strategies for elaborating the primary alcohol group of **23** in the presence of the secondary allylic alcohol moiety. Selective oxidation of the primary alcohol proved impossible. Thus, diol **23** was converted under standard conditions into the bis(triethylsilyl) derivative **24**, at which point the C8′ epimers fortuitously could be separated by conventional column chromatography.[23] Isomerically pure **24** was then allowed to react with K_2CO_3 in methanol at room temperature to selectively cleave the primary TES ether. Dess–Martin oxidation of alcohol **25**,[24] followed by Wittig reaction with phosphonium salt **26**[25] in the presence of NaHMDS, provided Stille coupling substrate **27** in a straightforward manner.[26]

The critical macrocyclization and final steps to reach **1** are summarized in Scheme 5. In the presence of catalytic $[Pd(PPh_3)_4]$ and excess LiCl at ambient temperatures in THF, stannane iodide **27** cyclized in good yield to assemble the 14-membered triene ring. After reduction of the *N*,*O*-acetal functionality of this hexacyclic

 © 2006 Wiley-VCH Verlag GmbH & Co. KGaA, Weinheim

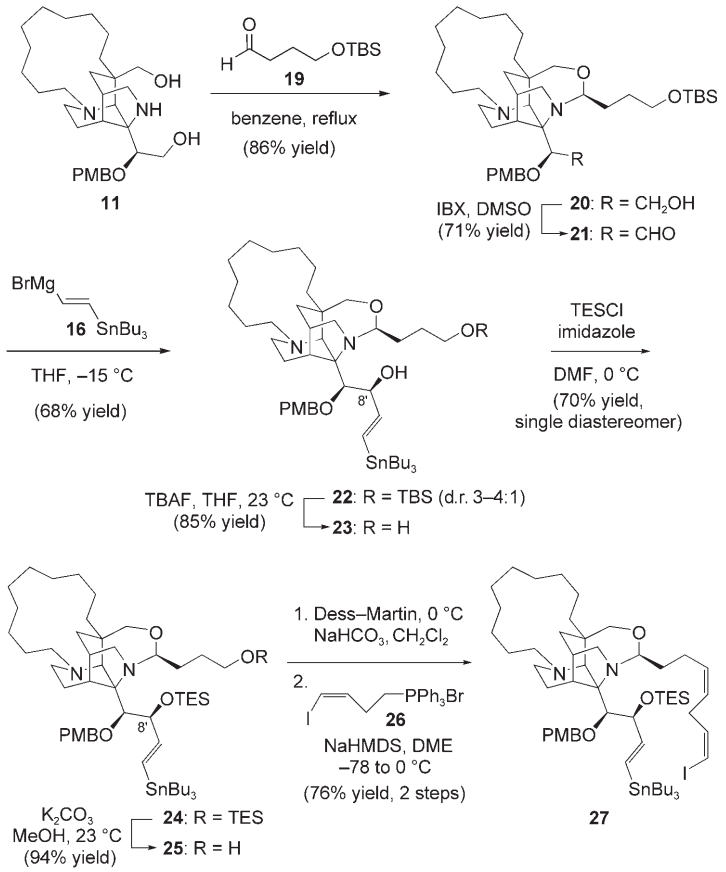

Scheme 4. Synthesis of Stille cyclization precursor **27**. TBAF = tetrabutylammonium fluoride, TES = triethylsilyl, DMF = *N*,*N*-dimethylformamide, Dess–Martin = 1,1,1-triacetoxy-1,1-dihydro-1,2-benziodoxol-3(1*H*)-one, NaHMDS = sodium hexamethyldisilazanide.

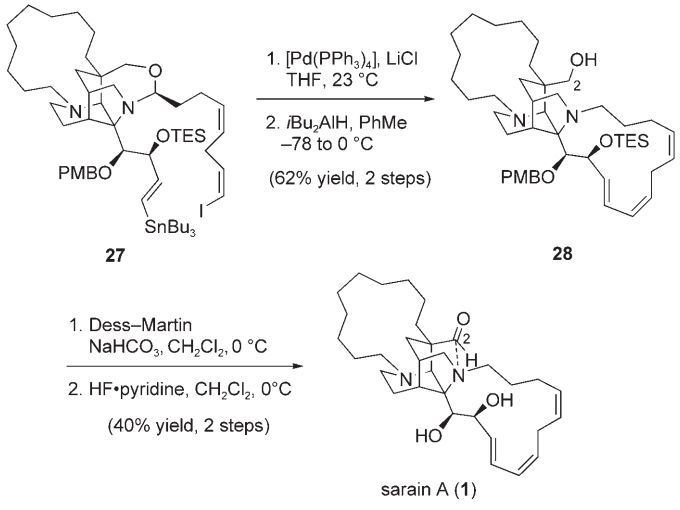

Scheme 5. Completion of the total synthesis of **1**.

product with *i*Bu$_2$AlH, pentacyclic alcohol **28** was obtained in 62% yield for the two steps.[27] In principle, all that remained to complete the synthesis of **1** was oxidation of the primary alcohol to the aldehyde and cleavage of the protecting groups that mask the C7′,C8′-diol. As a result of the proximity of the tertiary amine, we anticipated that the former conversion would be particularly challenging. Several mild oxidation procedures were screened, which ultimately identified bicarbonate-buffered, freshly prepared Dess–Martin periodinane[28] as the most effective reagent for introducing the correct oxidation state at C2. Because isolation and purification of intermediates containing the proximal aldehyde/tertiary amine unit proved to be difficult,[3] the subsequent diol deprotection was carried out directly. We were pleased to find that exposure of the crude oxidized product to excess HF·pyridine in CH_2Cl_2 at room temperature for one hour removed both protecting groups to provide **1** in 40% yield, after purification on silica gel. Synthetic sarain A was indistinguishable from an authentic sample of the natural product by NMR, mass-spectrometric, CD, and chromatographic comparisons.[29]

In summary, the first total synthesis of the structurally novel alkaloid sarain A (**1**) has been completed. Late stages of the synthesis feature the use of an intramolecular Stille reaction to fashion the 14-membered ring and introduce the skipped triene functionality of sarain A. The final steps of the synthesis involve an oxidation/deprotection sequence, in which careful handling of zwitterionic intermediates that display a tertiary amine/aldehyde proximity interaction was required.

Received: January 31, 2006
Published online: March 27, 2006

Keywords: alkaloids · macrocycles · natural products · Stille coupling · total synthesis

[1] a) G. Cimino, S. De Stefano, G. Scognamiglio, G. Sodano, E. Trivellone, *Bull. Soc. Chim. Belg.* **1986**, *95*, 783–800; b) G. Cimino, C. A. Mattia, L. Mazzarella, R. Puliti, G. Scognamiglio, A. Spinella, E. Trivellone, *Tetrahedron* **1989**, *45*, 3863–3872; c) G. Cimino, G. Scognamiglio, A. Spinella, E. Trivellone, *J. Nat. Prod.* **1990**, *53*, 1519–1525; d) Y. Guo, A. Madaio, E. Trivellone, G. Scognamiglio, G. Cimino, *Tetrahedron* **1996**, *52*, 8341–8348.

[2] Although referred to as sarains A–C in an initial report,[1b] these alkaloids were called saraines A–C by the Cimino group; these alkaloids have most commonly been termed sarain in the literature.

[3] Chromatographic purifications of sarains A–C were described by Cimino and co-workers as seldom being reproducible, possibly because of the zwitterionic character of these natural products; see reference [1b].

[4] For examples of proximity interactions of this type, see: a) N. J. Leonard, M. Oki, S. Chiavarelli, *J. Am. Chem. Soc.* **1955**, *77*, 6234–6237; b) A. J. Kirby, I. V. Komarov, V. A. Bilenko, J. E. Davies, J. M. Rawson, *Chem. Commun.* **2002**, 2106–2107.

[5] V. Caprioli, G. Cimino, A. De Guilio, A. Madaio, G. Scognamiglio, E. Trivellone, *Comp. Biochem. Physiol. B* **1992**, *103*, 293–296.

[6] a) J. Sisko, S. M. Weinreb, *J. Org. Chem.* **1991**, *56*, 3210–3211; b) J. Sisko, J. R. Henry, S. M. Weinreb, *J. Org. Chem.* **1993**, *58*, 4945–4951; c) O. Irie, K. Samizu, J. R. Henry, S. M. Weinreb, *J. Org. Chem.* **1999**, *64*, 587–595; d) S. Hong, J. Yang, S. M. Weinreb, *J. Org. Chem.* **2006**, *71*, 2078–2089.

[7] a) B. R. Henke, A. J. Kouklis, C. H. Heathcock, *J. Org. Chem.* **1992**, *57*, 7056–7066; b) D. A. Griffith, C. H. Heathcock, *Tetrahedron Lett.* **1995**, *36*, 2381–2384; c) C. H. Heathcock, M.

 © 2006 Wiley-VCH Verlag GmbH & Co. KGaA, Weinheim

Clasby, D. A. Griffith, B. R. Henke, M. J. Sharp, *Synlett* **1995**, 467–474; d) D. J. Denhart, D. A. Griffith, C. H. Heathcock, *J. Org. Chem.* **1998**, *63*, 9616–9617.

[8] a) M. J. Sung, H. I. Lee, Y. Chong, J. K. Cha, *Org. Lett.* **1999**, *1*, 2017–2019; b) M. J. Sung, H. I. Lee, H. B. Lee, J. K. Cha, *J. Org. Chem.* **2003**, *68*, 2205–2208; c) H. I. Lee, M. J. Sung, H. B. Lee, J. K. Cha, *Heterocycles* **2004**, *62*, 407–422.

[9] S. Hourcade, A. Ferdenzi, P. Retailleau, S. Mons, C. Marazano, *Eur. J. Org. Chem.* **2005**, 1302–1310.

[10] a) R. Downham, F. W. Ng, L. E. Overman, *J. Org. Chem.* **1998**, *63*, 8096–8097; b) S. Jaroch, R. T. Matsuoka, L. E. Overman, *Tetrahedron Lett.* **1999**, *40*, 1273–1276; c) C. J. Douglas, S. Hiebert, L. E. Overman, *Org. Lett.* **2005**, *7*, 933–936.

[11] An intramolecular Sonogashira coupling was used in the model studies of Heathcock and co-workers; see reference [7c].

[12] For the early use of enantiopure chiral oxazolidines in asymmetric synthesis, see: a) D. Seebach, J. D. Aebi, *Tetrahedron Lett.* **1983**, *24*, 3311–3314; b) G. Calderari, D. Seebach, *Helv. Chim. Acta* **1985**, *68*, 1592–1604.

[13] For a review of the chemistry of *N*-sulfonyliminium ions, see: S. M. Weinreb, *Top. Curr. Chem.* **1997**, *190*, 131–184.

[14] For a recent review of metathesis reactions in total synthesis, see: K. C. Nicolaou, P. G. Bulger, D. Sarlah, *Angew. Chem.* **2005**, *117*, 4564–4601; *Angew. Chem. Int. Ed.* **2005**, *44*, 4490–4527.

[15] For reviews of the intramolecular Stille coupling, see: a) M. A. J. Duncton, G. Pattenden, *J. Chem. Soc. Perkin Trans. 1* **1999**, 1235–1246; b) G. Pattenden, D. J. Sinclair, *J. Organomet. Chem.* **2002**, *653*, 261–268.

[16] The relative configuration at the aminal stereocenter was determined by ^{1}H–^{1}H NOESY and ROESY spectroscopic experiments.

[17] For a review of oxidations with IBX, see: H. Tohma, Y. Kita, *Adv. Synth. Catal.* **2004**, *346*, 111–124.

[18] Grignard reagent **16** was prepared by treating the corresponding lithium reagent with $MgBr_2$; for the preparation of this lithium reagent, see: D. Seyferth, S. C. Vick, *J. Organomet. Chem.* **1978**, *144*, 1–12.

[19] The diastereoselectivity in the addition of Grignard reagent **16** to aldehyde **14** was approximately 3:1.

[20] C. Taillier, B. Gille, V. Bellosta, J. Cossy, *J. Org. Chem.* **2005**, *70*, 2097–2108.

[21] Characterization data for **20**: $R_f = 0.24$ (4:1 hexanes/EtOAc containing 2% Et_3N); ^{1}H NMR (500 MHz, $CDCl_3$): $\delta = 7.30$ (d, $J = 8.6$ Hz, 2H), 6.87 (d, $J = 8.6$ Hz, 2H), 4.70 (d, $J = 11.1$ Hz, 1H), 4.41 (d, $J = 11.1$ Hz, 1H), 4.19–4.15 (m, 1H), 3.92 (dd, $J =$ 11.9, 3.3 Hz, 1H), 3.81 (s, 3H), 3.69–3.62 (m, 2H), 3.62–3.54 (m, 2H), 3.28 (s, 2H), 3.13 (d, $J = 9.2$ Hz, 1H), 3.10 (s, 1H), 3.08–3.02 (m, 1H), 2.76–2.66 (m, 3H), 2.64–2.58 (m, 1H), 2.13–2.08 (m, 1H), 2.08–2.00 (m, 1H), 1.96–1.92 (m, 1H), 1.75–1.66 (m, 3H), 1.60–1.10 (m, 23H), 0.88 (s, 9H), 0.03 ppm (s, 6H); ^{13}C NMR (125 MHz, $CDCl_3$): $\delta = 158.9$, 131.2, 129.2, 113.7, 87.8, 85.8, 80.1, 70.5, 68.5, 65.5, 63.2, 59.1, 59.0, 55.2, 49.9, 43.8, 42.5, 41.0, 39.3, 38.6, 38.4, 33.2, 29.6, 27.7, 26.8, 26.0, 25.7, 25.2, 25.1, 24.2, 23.7, 22.4, 21.6, 18.3, −5.3 ppm; IR (film): $\tilde{\nu} = 3400$ (br), 2928, 2854, 1613, 1514, 1471, 1388, 1361, 1302, 1248, 1097, 906 cm^{-1}; HRMS (ESI): m/z calcd for $C_{40}H_{69}N_2O_5Si$ $[M+H]^+$: 685.4976; found: 685.4988.

[22] For a pertinent review, see: M. T. Reetz, *Acc. Chem. Res.* **1993**, *26*, 462–468.

[23] Characterization data for **24**: $R_f = 0.62$ (4:1 hexanes/EtOAc containing 2% Et_3N); ^{1}H NMR (500 MHz, $CDCl_3$): $\delta = 7.29$ (d, $J = 8.7$ Hz, 2H), 6.85 (d, $J = 8.7$ Hz, 2H), 6.31–6.14 (m, 2H), 4.99 (d, $J = 11.5$ Hz, 1H), 4.54 (d, $J = 11.5$ Hz, 1H), 4.30 (t, $J = 6.8$ Hz, 1H), 4.16–4.09 (m, 1H), 3.81 (s, 3H), 3.72 (d, $J = 8.0$ Hz, 1H), 3.68–3.58 (m, 2H), 3.28 (d, $J = 11.7$ Hz, 1H), 3.17–3.03 (m, 3H), 2.97–2.88 (m, 1H), 2.87–2.76 (m, 1H), 2.75–2.68 (m, 1H), 2.68–2.55 (m, 2H), 2.49–2.42 (m, 1H), 2.11–1.99 (m, 2H), 1.86–1.76 (m, 2H), 1.75–1.16 (m, 32H), 1.05–0.85 (m, 36H) 0.66–0.53 ppm (m, 12H); ^{13}C NMR (125 MHz, $CDCl_3$): $\delta = 158.9$, 151.3, 132.7, 131.9, 128.4, 113.6, 88.4, 83.8, 80.7, 79.7, 74.5, 69.4, 68.9, 63.5, 60.5, 55.4, 50.8, 44.5, 42.2, 41.1, 38.8, 38.1, 37.5, 33.8, 30.5, 29.9, 29.5, 27.7, 25.3, 25.1, 24.9, 24.4, 23.3, 23.1, 21.6, 13.9, 9.4, 7.2, 7.1, 5.5, 4.6 ppm; IR (film): $\tilde{\nu} = 2956$, 2929, 2875, 1615, 1528, 1463, 1254, 1094, 1032 cm^{-1}; LRMS (ESI): m/z calcd for $C_{60}H_{111}N_2O_5Si_2Sn$ $[M+H]^+$: 1115.7; found: 1115.8.

[24] Attempts to achieve sequential deprotection of the primary TES ether and oxidation by use of Swern oxidation conditions were unsuccessful; for this procedure, see: A. Rodriguez, M. Nomen, B. W. Spur, J. J. Godfroid, *Tetrahedron Lett.* **1999**, *40*, 5161–5164.

[25] K. C. Nicolaou, J. Y. Ramphal, Y. Abe, *Synthesis* **1989**, 898–901.

[26] Characterization data for **27**: $R_f = 0.41$ (9:1 hexanes/EtOAc containing 2% Et_3N); ^{1}H NMR (500 MHz, $CDCl_3$): $\delta = 7.29$ (d, $J = 8.5$ Hz, 2H), 6.85 (d, $J = 8.5$ Hz, 2H), 6.41–6.11 (m, 4H), 5.58–5.49 (m, 1H), 5.42–5.33 (m, 1H), 4.99 (d, $J = 11.5$ Hz, 1H), 4.54 (d, $J = 11.5$ Hz, 1H), 4.29 (t, $J = 8.0$ Hz, 1H), 4.17–4.10 (m, 1H), 3.81 (s, 3H), 3.73 (d, $J = 8.0$ Hz, 1H), 3.31 (d, $J = 11.7$ Hz, 1H), 3.16–3.01 (m, 3H), 3.00–2.85 (m, 3H), 2.84–2.71 (m, 2H), 2.68–2.54 (m, 2H), 2.50–2.43 (m, 1H), 2.33–2.13 (m, 2H), 1.86–1.78 (m, 2H), 1.77–0.80 (m, 59H), 0.66–0.49 ppm (q, $J = 7.9$ Hz, 6H); ^{13}C NMR (125 MHz, $CDCl_3$): $\delta = 158.6$, 151.4, 139.9, 132.7, 132.1, 131.8, 128.4, 125.1, 113.6, 87.7, 83.4, 82.6, 79.8, 74.6, 69.3, 68.9, 60.4, 55.5, 51.0, 44.5, 42.2, 41.1, 38.8, 38.2, 37.6, 37.0, 33.5, 29.5, 27.7, 25.3, 25.1, 25.0, 24.8, 24.4, 23.4, 23.2, 21.6, 14.0, 9.5, 7.3, 5.6 ppm; IR (film): $\tilde{\nu} = 2931$, 2875, 1615, 1515, 1463, 1248, 1175, 1119, 1102, 1077, 1044, 1007 cm^{-1}; LRMS (ESI): m/z calcd for $C_{58}H_{100}IN_2O_4SiSn$ $[M+H]^+$: 1163.6; found: 1163.6.

[27] Characterization data for **28**: $R_f = 0.43$ (3:1 hexanes/EtOAc containing 2% Et_3N); ^{1}H NMR (500 MHz, $CDCl_3$): $\delta = 7.30$ (d, $J = 8.6$ Hz, 2H), 6.91 (d, $J = 8.6$ Hz, 2H), 6.80–6.68 (m, 1H), 6.16–6.06 (m, 2H), 5.65–5.48 (m, 3H), 4.94 (d, $J = 11.5$ Hz, 1H), 4.87 (d, $J = 9.7$ Hz, 1H), 4.64 (s, 1H), 4.52 (d, $J = 11.5$ Hz, 1H), 4.23–4.15 (m, 1H), 3.83 (s, 3H), 3.59–3.45 (m, 3H), 3.25–2.98 (m, 5H), 2.82–2.71 (m, 1H), 2.58–2.48 (m, 1H), 2.46–2.30 (m, 4H), 2.22–2.11 (m, 2H), 1.84–0.79 (m, 34H), 0.63 ppm (q, $J = 7.7$ Hz, 6H); ^{13}C NMR (125 MHz, $CDCl_3$): $\delta = 159.1$, 133.5, 131.9, 131.8, 128.9, 128.8, 126.6, 126.5, 113.8, 88.5, 84.4, 73.0, 72.0, 71.5, 64.5, 63.6, 61.3, 59.7, 55.5, 43.3, 43.2, 42.8, 39.5, 38.9, 29.9, 28.3, 27.1, 26.7, 26.5, 25.8, 24.4, 23.7, 23.1, 22.8, 21.8, 7.3, 5.6 ppm; IR (film): 3250 (br), 2931, 2875, 1615, 1517, 1465, 1250, 1042 cm^{-1}; HRMS (ESI): m/z calcd for $C_{46}H_{75}N_2O_4Si$ $[M+H]^+$: 747.5496; found: 747.5492.

[28] Dess–Martin periodinane was prepared using the procedure of Schreiber; see: S. D. Meyer, S. L. Schreiber, *J. Org. Chem.* **1994**, *59*, 7549–7552.

[29] Comparisons were made after adding CD_3CO_2D.[1c]

 © 2006 Wiley-VCH Verlag GmbH & Co. KGaA, Weinheim

Organic Synthesis

DOI: 10.1002/anie.200600012

Stereoselective Synthesis of the Side Chains of Mycolactones A and B Featuring Stepwise Double Substitutions of 1,1-Dibromo-1-alkenes**

*Ning Yin, Guangwei Wang, Mingxing Qian, and Eiichi Negishi**

We report herein a stereoselective synthesis of the side chains of mycolactones A (**1A**) and B (**1B**). These side chains **2A** and **2B**, respectively, are protected as a methoxymethyl (MOM) ether at C12 and *tert*-butyldimethylsilyl (TBS) derivatives at C13 and C15, and are thus ready to be used as intermediates for the synthesis of **1A** and **1B** (Scheme 1).

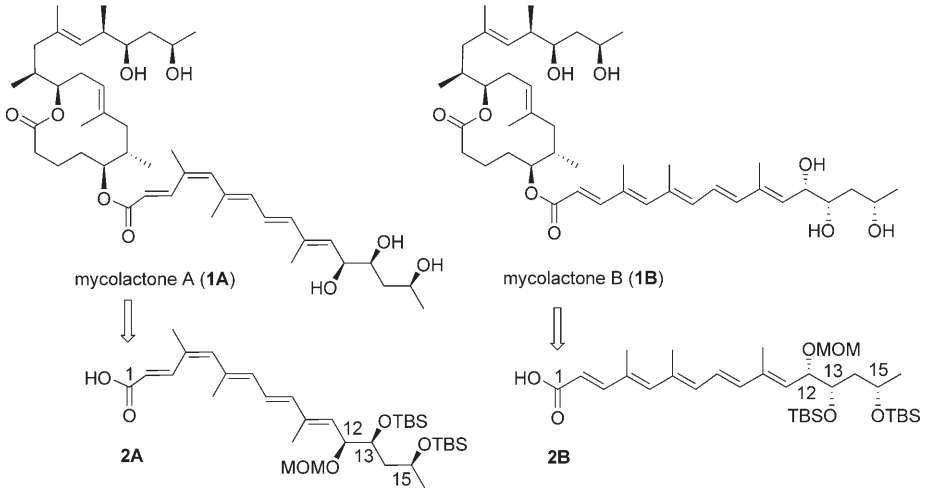

Scheme 1. Mycolactones A and B and their triprotected side chains.

Mycolactones A (**1A**) and B (**1B**) were isolated in 1999 by Small and co-workers[1] from *Mycobacterium ulcerans*, the causative pathogen of Buruli ulcer. Although their gross structures (atom connectivities) were elucidated through 2D NMR spectroscopic analysis,[1b] the finer stereochemical details were established by comparative NMR spectroscopic analysis of various stereoisomers of the molecular core[2] and the side chains as well as the entire compound,[3] prepared through stereodivergent syntheses.[4,5]

Apart from their biological and medicinal significance, both **1A** and **1B** contain conjugated pentaenes that display a rare and synthetically difficult methyl-substitution pattern, as well as two adjacent oxygenated asymmetric carbon centers; these compounds thus caught our attention as attractive and challenging synthetic targets. Although the head-to-tail (H-to-T; Scheme 2) construction of the pentaene fragment

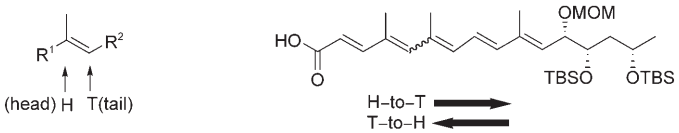

Scheme 2. Definition of the H (head) and T (tail) of trisubstitued alkenes and H-to-T and T-to-H constructions of **2A** and **2B**.

through the combined use of hydrozirconation–Pd-catalyzed cross-coupling[6] and carboalumination–Pd-catalyzed cross-coupling[6a–c,7] appears eminently feasible, most of the widely employed methods for the asymmetric synthesis of trisubstituted alkenes with an α-chiral substituent at the tail end, including those cited above,[2–5] involve tail-to-head (T-to-H; Scheme 2) construction. The synthesis of at least part of the desired pentaene fragments of **2A** and **2B** thus calls for the use of the same T-to-H construction protocol (Scheme 2).

It then occurred to us that the stereoselective T-to-H construction of trisubstituted alkenes by stepwise double substitution of 1,1-dihalo-1-alkenes[8–10] could be combined with the H-to-T construction of an appropriate head side fragment to produce **2A** and **2B**. Accordingly, the C1–C7 segment of **2B**, that is, **3B**, was synthesized in six steps from propargyl alcohol in 23% overall yield with >98% stereoselectivity (Scheme 3). Throughout its synthesis no other stereoisomer was detected. Although the Pd-catalyzed cross-coupling generally proceeds in higher yields with protected alcohol derivatives, the Zr-catalyzed carboalumination of unprotected allyl and propargyl alcohol derivatives proceeds in higher yields than that of their protected derivatives. Thus, the synthesis of **3B** (Scheme 3) may represent a compromise that favors efficiency, but no further efforts were made to optimize the yield of **3B**. The hydrozirconation reaction in the first step makes use of a recently developed in situ generation of $[HZrCp_2Cl]$ by the treatment of iBu_2AlH with $[Cp_2ZrCl_2]$ (Cp = cyclopentadienyl).[11] The use of ethynylzinc reagents in Pd-catalyzed alkynylation[12,13] permits the direct synthesis of terminal alkynes that would otherwise require two additional steps for protection and deprotection, such as with the Sonogashira alkynylation.[13,14]

The T-to-H synthesis of **4**, which can serve as a key intermediate corresponding to the C8–C16 segment of either

[*] Dr. N. Yin, G. Wang, Dr. M. Qian, Prof. E. Negishi
Herbert C. Brown Laboratories of Chemistry
Purdue University
560 Oval Dr., West Lafayette, IN 47907-2084 (USA)
Fax: (+1) 765-494-0239
E-mail: negishi@purdue.edu

[**] We thank the National Science Foundation (grant: CHE-0309613), the National Institutes of Heath (grant: GM36792), and Purdue University for supporting this research.

Supporting information for this article is available on the WWW under http://www.angewandte.org or from the author.

InterScience
© 2006 Wiley-VCH Verlag GmbH & Co. KGaA, Weinheim

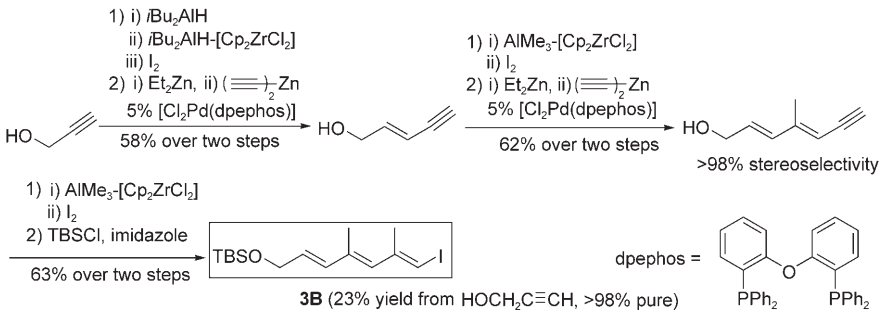

Scheme 3. H-to-T construction of the C1–C7 segment of the mycolactone B side-chain.

2A or **2B**, is summarized in Scheme 4. Commercially available and stereoisomerically pure (>98%) ethyl (*S*)-3-hydroxybutyrate was converted into TBS-protected (*S*)-3-hydroxybutyraldehyde **5**[3,15] in 82% yield over two steps. This aldehyde was subjected to allylboration with (*Z*)-MOMOCH=CHCH$_2$BIpc$_2$ (Ipc = isopinocampheyl)[16] and $BF_3{\cdot}OEt_2$ first at −90 °C for 3 h followed by slow warming to 0 °C and stirring at this temperature for 12 h. After oxidation of the boranes with H_2O_2/$NaHCO_3$ (30%) and chromatographic purification, **6** was obtained in 91% yield as a single stereoisomer. Its protection with TBSOTf (1.2 equiv; Tf = trifluoromethanesulfonyl) and 2,6-lutidine (2.5 equiv) in CH_2Cl_2 in quantitative yield, followed by Os-catalyzed dihydroxylation with *N*-methylmorpholine *N*-oxide (NMO) in THF/H_2O (4:1) in 98% yield, then oxidative cleavage with $NaIO_4$ (1.8 equiv) in quantitative yield, provided **7**, which was immediately subjected to the Corey–Fuchs reaction[17] to give **8** in 96% yield with >99% stereoisomeric purity. The crucial two-step Pd-catalyzed ethynylation–methylation[8a,d] followed by deprotection of the Me_3Si group proceeded in 61% overall yield with ≥98% stereoselectivity, with ^{13}C NMR spectroscopic analysis providing no indication of the presence of any other isomer. The overall yield of **4** prepared in 11 steps from ethyl (*S*)-3-hydroxybutyrate was 35%.

The Pd-catalyzed cross-coupling between the alkenyl zinc derivative, generated in situ by treating **3B** with *t*BuLi (2 equiv) followed by dry $ZnBr_2$ (1 equiv), and **4** (1.3:1) in the presence of [Pd(dpephos)Cl$_2$] (5%) in THF/DMF (1:1) at 23 °C for 8 h proceeded smoothly to give the desired pentaene **10B** in 73% yield with >98% stereoselectivity (Scheme 5). The *E* geometry of the two disubstituted alkenyl groups was confirmed by the ^{1}H NMR coupling constants for the two adjacent alkenyl protons (15.2–15.8 Hz); that of the three trisubstituted alkenyl groups was established by the measurements of NOE enhancements (Scheme 5). Removal of the TBS group with tetra-*n*-butylammonium fluoride (TBAF) in THF at 0 °C proceeded in 82% yield. The resulting alcohol was oxidized with Dess–Martin periodinane followed by $NaClO_2$/NaH_2PO_4 and *t*BuOH/H_2O/$CH_3C(CH_3)$=$CHCH_3$ (2:1:1) to provide, after chromatographic purification (silica gel, EtOAc/hexanes), **2B** in 77% yield over two steps. In summary, **2B** (>98% pure) was synthesized in 16% overall yield in 15 steps from ethyl (*S*)-3-hydroxybutyrate.

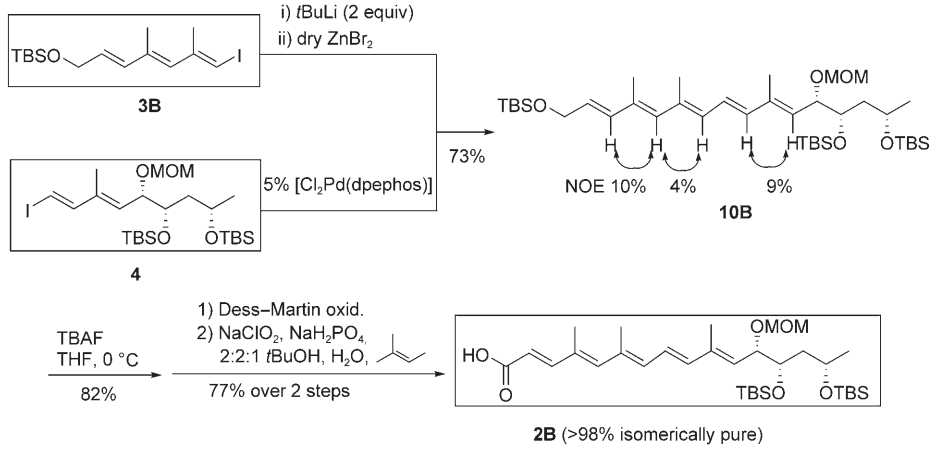

Scheme 5. Synthesis of a triprotected side chain **2B** of mycolactone B via Pd-catalyzed cross-coupling.

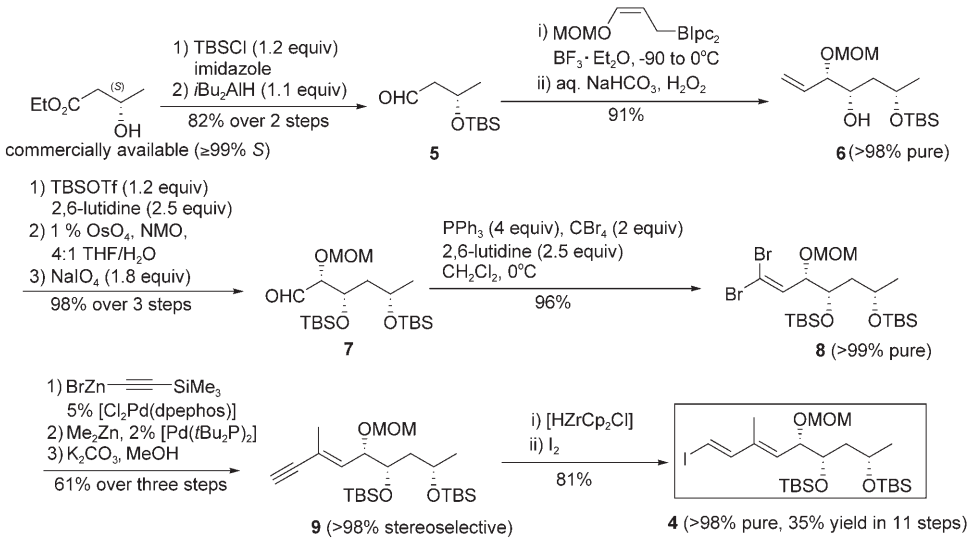

Scheme 4. T-to-H synthesis of the C8–C16 segment of **4**.

Despite these successful results (Scheme 5), the syn-

 © 2006 Wiley-VCH Verlag GmbH & Co. KGaA, Weinheim

thesis of **10** by Pd-catalyzed alkenyl–alkenyl coupling proved to be generally difficult. For instance, hydrozirconation of **9** with [$HZrCp_2Cl$] in THF followed by addition of **3B**, [$Pd(dpephos)Cl_2$] (5 mol%), and dry $ZnBr_2$ (1 mol equiv) led to the formation of the desired **10B** in less than 10% yield. Similarly disappointing were unsuccessful attempts to transform **8** into **10B** directly by Pd-catalyzed stepwise double substitution with the tetraenyl iodide prepared by Pd-catalyzed ethynylation of **3B** with bis(ethynyl)zinc followed by hydrozirconation with [$HZrCp_2Cl$] and iodinolysis. The yield of **10B** in this case was less than 5%. Even though the precise nature of these difficulties is not clear, it is possible that oligoenes of high coordinating ability can serve as catalyst poisons, and that the desired cross-coupling may have to overcome such difficulties. Clearly, further delineation of the critical factors involved in these reactions and the development of improved procedures are desired. In the meantime, it is gratifying that the Pd-catalyzed alkenyl–alkenyl coupling with alkenyl zinc derivatives can be successfully applied to obtain what appears to be the first stereoselective synthesis of a triprotected mycolactone B side chain.

The synthesis of the mycolactone A side chain (Scheme 6) required the 4*Z* isomer of **3B**, that is, **3A**, to be cross-coupled with the C8–C16 intermediate **4** in a manner similar to the synthesis of **2B**. It was then found that the 1,1-dibromoalkene **11** prepared in three steps from propargyl alcohol in 90% overall yield can be *trans*-selectively (>98%) monomethylated with Me_2Zn in the presence of [$Pd(dpephos)Cl_2$] (5 mol%) in THF/DMF (1:1; DMF = *N*,*N*-dimethylformamide) to provide (*Z*)-1-trimethylsilyl-4-bromo-3-penten-1-yne (**12**) in 70% yield, even though the same reaction with most of the other 1,1-dibromo-1-alkenes would produce mainly 1,1-dimethylated products.[18] As such, this access to **12** appears to represent the first successful *trans*-selective monoalkylation of a 1,1-dibromo-1-alkene, albeit with limited scope.[8e,9a] This result adds to the growing body of data pointing to the significant effects of proximal π bonds on the course of Pd-catalyzed cross-coupling of 1,1-dibromo-1-alkenes. Conversion of **12** into **3A** (43% overall yield) was done in four steps: Pd-catalyzed alkenylation, desilylation, Zr-catalyzed carboalumination and iodinolysis, and protection with TBSCl. The Pd-catalyzed cross-coupling of the zinc derivative of **3A** generated in situ with **4** was performed as in the corresponding reaction of **3B** (Scheme 5). The reaction proceeded smoothly and selectively to provide **10A** in 71% yield, which was then converted into **2A** in three steps in 64% combined yield. Overall, **2A** (>98% pure) was synthesized in 16% yield in 15 steps from ethyl (*S*)-3-hydroxybutyrate.

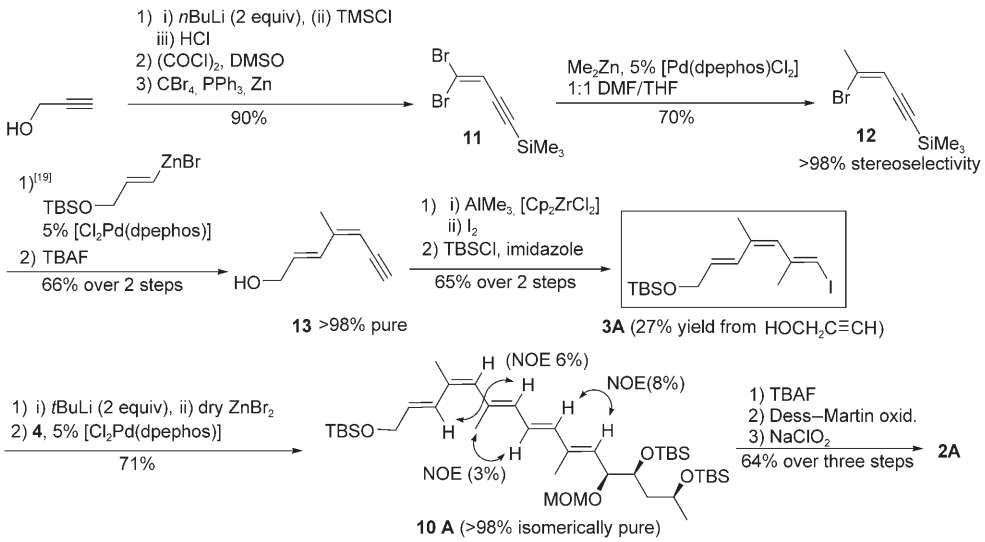

Scheme 6. Synthesis of a triprotected side chain **2A** of mycolactone A.

Experimental Section

12: Me_2Zn (1.70 mL, 2.0 M in toluene, 3.4 mmol) was added to a mixture of **11** (1.49 g, 5.3 mmol) and [$Cl_2Pd(dpephos)$] (189 mg, 0.26 mmol) in THF/DMF (1:1, 30 mL) at 23 °C. The resulting mixture was stirred at 23 °C for 2 h. After aqueous workup, the residue was purified by flash chromatography to give **12** (805 mg, 70%).

13: *t*BuLi (8.6 mL, 1.7 M in pentane, 14.6 mmol) was added slowly to a solution of (*E*)-1-(*tert*-butyldimethylsiloxy)-3-iodo-2-propene (2.23 g, 7.5 mmol) in Et_2O (7.5 mL) at −78 °C. The resulting solution was stirred at −78 °C for 30 min. A solution of $ZnBr_2$ (1.69 g, 7.5 mmol) in THF (7.5 mL) was added to the mixture. The mixture obtained was stirred at −78 °C for 15 min and then warmed to 23 °C over 30 min. A solution of **12** (805 mg, 3.7 mmol) and [$Cl_2Pd(dpephos)$] (134 mg, 0.19 mmol) in DMF (7.5 mL) was then added to the flask containing the alkenyl zinc obtained above by using a cannula at 23 °C. The reaction mixture was warmed to 45 °C and stirred for 8 h. After aqueous workup, the residue was purified by flash chromatography to afford (3*Z*,5*E*)-7-(*tert*-butyldimethylsiloxy)-1-trimethylsilyl-3,5-heptadien-1-yne (941 mg, 82%). This intermediate was then treated with TBAF (6.2 mL, 1.0 M in THF, 6.2 mmol) to afford **13** (305 mg, 81%, stereoisomeric purity ≥ 98% as examined by ^{13}C NMR spectroscopy). The stereochemistry of the trisubstituted alkene was established by measurements of NOE enhancements.

The Zr-catalyzed carboalumination and iodinolysis was performed by the reaction of [Cp_2ZrCl_2] (213 mg, 0.73 mmol), Me_3Al (0.60 mL, 6.2 mmol), and I_2 (945 mg, 3.7 mmol) to afford (2*E*,4*Z*,6*E*)-4,6-dimethyl-7-iodo-2,4,6-heptatrien-1-ol (455 mg, 69%), which was then treated with imidazole (351 mg, 5.2 mmol) and TBSCl (517 mg, 3.4 mmol) to give **3A** (612 mg, 94%). ^1H NMR (300 MHz, [D_6]benzene): $\delta = 0.03$ (s, 6H), 0.96 (s, 9H), 1.69 (s, 3H), 1.78 (s, 3H), 4.08 (d, $J = 4.3$ Hz, 2H), 5.50 (s, 1H), 5.70 (dt, $J = 4.4$, 15.7 Hz, 1H), 6.04 (s, 1H), 6.80 ppm (d, $J = 15.7$ Hz, 1H); ^{13}C NMR (75 MHz, [D_6]benzene): $\delta =$ −4.7, 19.0, 21.2, 25.6, 26.6, 64.0, 81.5, 127.6, 130.1, 131.8, 134.8, 144.8 ppm; HRMS (EI): calcd. for $C_{15}H_{27}IOSi$: $[M]^+$ 378.0876; found: 378.0870.

10A: *t*BuLi (0.78 mL, 1.7 M in pentane, 1.3 mmol) was added slowly to a solution of **3A** (250 mg, 0.66 mmol) in Et_2O (2 mL) at −78 °C. The resulting solution was stirred at −78 °C for 30 min, after which a solution of $ZnBr_2$ (149 mg, 0.66 mmol) in THF (2 mL) was introduced. The mixture obtained was stirred at −78 °C for 15 min and then warmed to 23 °C over 30 min. A solution of **4** (270 mg, 0.46 mmol) and [$Cl_2Pd(dpephos)$] (16 mg, 0.022 mmol) in DMF (2 mL) was added to the reaction mixture through a cannula at 23 °C, and the mixture was stirred for 8 h. After aqueous

 © 2006 Wiley-VCH Verlag GmbH & Co. KGaA, Weinheim

workup, the residue was purified by flash chromatography to afford **10A** (231 mg, 71%). $[\alpha]_D^{23} = +35°$ ($c = 2.8$, CH_2Cl_2); ^{1}H NMR (300 MHz, [D$_6$]benzene): $\delta = 0.07$ (s, 6H), 0.14 (s, 3H), 0.16 (s, 3H), 0.19 (s, 3H), 0.23 (s, 3H), 1.00 (s, 9H), 1.01 (s, 9H), 1.04 (s, 9H), 1.23 (d, $J = 5.9$ Hz, 3H), 1.87 (s, 6H, 4-CH_3 and 6-CH_3), 1.82 (s, 3H, 10-CH_3), 1.95–2.05 (m, 2H), 3.21 (s, 3H), 3.95–4.0 (m, 1H), 4.2–4.25 (m, 3H), 4.45 (d, $J = 6.4$ Hz, 1H), 4.61 (dd, $J = 5.3$, 9.4 Hz, 1H), 4.71 (d, $J = 6.4$ Hz, 1H), 5.55 (d, $J = 10.0$ Hz, 1H, 11-H), 5.80 (dt, $J = 4.7$, 15.8 Hz, 1H, 2-H), 5.88 (s, 1H, 5-H), 6.3–6.4 (m, 2H, 7-H and 9-H), 6.61 (dd, $J = 11.1$, 14.6 Hz, 1H, 8-H), 7.17 ppm (d, $J = 15.8$ Hz, 1H, 3-H); ^{13}C NMR (75 MHz, [D$_6$]benzene): $\delta = -4.7$, -4.0, -3.7, -3.4, 13.8, 18.2, 18.7, 18.8, 22.2, 24.6, 26.5, 26.7, 44.9, 55.7, 64.3, 66.5, 73.3, 75.1, 94.2, 125.9, 128.6, 129.7, 130.8, 132.0, 133.5, 134.2, 135.6, 137.5, 139.7 ppm; HRMS (ESI): calcd. for $C_{39}H_{76}O_5Si_3Na$: $[M+Na]^+$ 731.4898; found: 731.4884.

2A: $[\alpha]_D^{23} = +26°$ ($c = 3.5$, CH_2Cl_2); ^{1}H NMR (300 MHz, [D$_6$]benzene): $\delta = 0.14$ (s, 3H), 0.17 (s, 3H), 0.20 (s, 3H), 0.24 (s, 3H), 1.01 (s, 9H), 1.05 (s, 9H), 1.23 (d, $J = 6.4$ Hz, 3H), 1.63 (s, 3H), 1.78 (s, 3H), 1.87 (s, 3H), 1.9–2.0 (m, 2H), 3.32 (s, 3H), 3.97 (sext., $J = 5.9$ Hz, 1H), 4.00 (q, $J = 6.5$ Hz, 1H), 4.39 (dd, $J = 4.6$, 10.0 Hz, 1H), 4.49 (d, $J = 6.5$ Hz, 1H), 4.60 (d, $J = 7.0$ Hz, 1H), 5.58 (d, $J = 9.4$ Hz, 1H), 5.95–6.0 (m, 2H), 6.13 (d, $J = 10.6$ Hz, 1H), 6.35 (d, $J = 15.2$ Hz, 1H), 6.47 (dd, $J = 10.5$, 15.2 Hz, 1H), 8.29 ppm (d, $J = 15.8$ Hz, 1H); ^{13}C NMR (75 MHz, [D$_6$]benzene): $\delta = -4.0$, -3.7, -3.5, 13.7, 17.7, 18.7, 18.8, 21.3, 24.6, 26.5, 26.6, 45.0, 55.7, 66.5, 73.2, 75.2, 94.5, 118.7, 125.4, 131.4, 131.7, 135.0, 135.5, 139.3, 139.5, 142.8, 145.3, 173.5 ppm; HRMS (ESI): calcd. for $C_{33}H_{60}O_6Si_2Na$: $[M+Na]^+$ 631.3826; found: 631.3848.

2B: $[\alpha]_D^{23} = +33°$ ($c = 6.6$, CH_2Cl_2); ^{1}H NMR (300 MHz, [D$_6$]benzene): $\delta = 0.17$ (s, 3H), 0.19 (s, 3H), 0.22 (s, 3H), 0.26 (s, 3H), 1.04 (s, 9H), 1.08 (s, 9H), 1.26 (d, $J = 6.0$ Hz, 3H), 1.67 (s, 3H), 1.73 (s, 3H), 1.92 (s, 3H), 1.9–2.1 (m, 2H), 3.24 (s, 3H), 4.05 (q, $J = 6.1$ Hz, 1H), 4.22 (sext., $J = 6.0$ Hz, 1H), 4.49 (d, $J = 6.6$ Hz, 1H), 4.64 (dd, $J = 5.3$, 9.8 Hz, 1H), 4.72 (d, $J = 6.6$ Hz, 1H), 5.68 (d, $J = 9.8$ Hz, 1H), 6.48 (d, $J = 15.4$ Hz, 1H), 6.10–6.15 (m, 2H), 6.40 (d, $J = 15.2$ Hz, 1H), 6.52 (dd, $J = 10.9$, 15.1 Hz, 1H), 7.68 ppm (d, $J = 15.4$ Hz, 1H); ^{13}C NMR (75 MHz, [D$_6$]benzene): $\delta = -4.0$, -3.7, -3.5, 13.7, 14.3, 17.2, 18.7, 18.8, 24.5, 26.5, 26.6, 44.9, 55.7, 66.5, 73.2, 75.2, 94.4, 116.6, 125.3, 131.5, 133.1, 135.2, 136.1, 139.4, 139.7, 145.1, 153.5, 173.6 ppm; HRMS (ESI): calcd. for $C_{33}H_{60}O_6Si_2Na$: $[M+Na]^+$ 631.3826; found: 631.3828.

Received: January 3, 2006
Published online: March 24, 2006

Keywords: asymmetric synthesis · cross-coupling · haloalkenes · natural products · palladium

[1] a) K. M. George, D. Chatterjee, G. Gunawardana, D. Welty, J. Hayman, R. Lee, P. L. C. Small, *Science* **1999**, *283*, 854–857; b) G. Gunawardana, D. Chatterjee, K. M. George, P. Brennan, D. Whittern, P. L. C. Small, *J. Am. Chem. Soc.* **1999**, *121*, 6092–6093.

[2] A. B. Benowitz, S. Fidanze, P. L. C. Small, Y. Kishi, *J. Am. Chem. Soc.* **2001**, *123*, 5128–5129.

[3] F. Song, S. Fidanze, A. B. Benowitz, Y. Kishi, *Org. Lett.* **2002**, *4*, 647–650.

[4] For a nonstereoselective synthesis of tribenzyl-protected ethyl esters of the C15 epimers of the mycolactone A and B side chains, see: M. K. Gurjar, J. Cherian, *Heterocycles* **2001**, *55*, 1095–1103.

[5] For a recent report on attempts to synthesize the side chains of mycolactones A and B, see: R. P. van Summeren, B. L. Feringa, A. J. Minnaard, *Org. Biomol. Chem.* **2005**, *3*, 2524–2533.

[6] For recent reviews, see: a) S. Huo, E. Negishi in *Handbook of Organopalladium Chemistry for Organic Synthesis*, (Eds.: E. Negishi, A. de Meijere), Wiley-Interscience, New York, **2002**, chap. III.2.6, pp. 335–408; b) B. H. Lipshutz in *Handbook of Organopalladium Chemistry for Organic Synthesis* (Eds.: E. Negishi, A. de Meijere), Wiley-Interscience, New York, **2002**, chap.III.2.17.1, pp. 807–823; c) E. Negishi, Q. Hu, Z. Huang, M. Qian, G. Wang, *Aldrichimica Acta* **2005**, *38*, 71–88; for our recent paper on oligoene synthesis, see: d) F. Zeng, E. Negishi, *Org. Lett.* **2002**, *4*, 703–706.

[7] F. Zeng, E. Negishi, *Org. Lett.* **2001**, *3*, 719–722.

[8] a) J.-C. Shi, X. Zeng, E. Negishi, *Org. Lett.* **2003**, *5*, 1825–1828; b) X. Zeng, Q. Hu, M. Qian, E. Negishi, *J. Am. Chem. Soc.* **2003**, *125*, 13636–13637; c) J.-C. Shi, E. Negishi, *J. Organomet. Chem.* **2003**, *687*, 518–524; d) X. Zeng, M. Qian, Q. Hu, E. Negishi, *Angew. Chem.* **2004**, *116*, 2309–2313; *Angew. Chem. Int. Ed.* **2004**, *43*, 2259–2263; e) Z. Tan, E. Negishi, *Angew. Chem.* **2006**, *118*, 776–779; *Angew. Chem. Int. Ed.* **2006**, *45*, 762–765.

[9] a) A. Minato, K. Suzuki, K. Tamao, *J. Am. Chem. Soc.* **1987**, *109*, 1257–1258; b) A. Minato, *J. Org. Chem.* **1991**, *56*, 4052–4056; c) W. Shen, L. Wang, *J. Org. Chem.* **1999**, *64*, 8873–8879; d) J. Uenishi, K. Matsui, *Tetrahedron Lett.* **2001**, *42*, 4353–4355; e) J. Uenishi, K. Matsui, H. Ohmiya, *J. Organomet. Chem.* **2002**, *653*, 141–149; f) J. Uenishi, M. Ohmi, K. Matsui, M. Iwano, *Tetrahedron* **2005**, *61*, 1971–1979; g) J. Uenishi, K. Matsui, M. Ohmi, *Tetrahedron Lett.* **2005**, *46*, 225–228; h) J. Uenishi, K. Matsui, *Tetrahedron Lett.* **2005**, *46*, 359.

[10] Before we conducted a series of recent investigations,[8] the two-stage double substitution of 1,1-dihalo-1-alkenes with two different organometals had been reported only in a few papers.[9a–d] Moreover, there was just one successful example of the first-stage *trans*-selective monoalkylation of β, β-dichlorostyrene with *n*-butylzinc chloride in the presence of [Cl_2Pd(dppb)] (1 mol%; dppb = 1,4-bis(diphenylphosphino)butane) in 81% yield.[9a] This reaction was followed by second-stage alkylation with *n*-hexylmagnesium bromide in the presence of [Cl_2Ni(dppp)] (dppp = 1,3-bis(diphenylphosphino)propane) in 77% yield.[9a] However, it was recently shown that the high stereoselectivity observed in the second-stage alkylation is due to the presence of the Ph group in the β position, as the use of an alkyl group such as *n*-octyl in place of Ph under comparable conditions leads to a mixture of the *E* and *Z* isomers.[8e] Fortunately, the use of [Pd(tBu$_3$P)$_2$] in place of [Cl_2Ni(dppp)] suppressed the extent of isomerization to ≤ 3–4%.[8e] A second-stage alkylation that represents the only prior example of methylation was performed with a bromostilbene derivative.[9c] A few additional examples of the second-stage alkylation of (*Z*)-2-bromo-1-en-3-ynes were also reported.[9d] However, the details of the stereochemical results obtained in their case were questionable in view of recent related results reported by us.[8a–d] Despite subsequent publications[9f–h] from that same group, including one corrigendum[9h] that came to our attention after the submission of this paper, the stereochemical details remain to be fully clarified. No other Pd- or Ni-catalyzed second-stage alkylation with alkyl metals that produces trisubstituted alkenes appears to have been reported prior to our development of the Pd-catalyzed stereoselective method with essentially full retention[8a,c,d] or inversion[8b] of configuration.

[11] Z. Huang, E. Negishi, unpublished results.

[12] a) A. O. King, N. Okukado, E. Negishi, *J. Chem. Soc. Chem. Commun.* **1977**, *683*; b) E. Negishi, M. Kotora, C. Xu, *J. Org. Chem.* **1997**, *62*, 8957–8960.

[13] For a recent review of Pd-catalyzed alkynylation, see: E. Negishi, L. Anastasia, *Chem. Rev.* **2003**, *103*, 1979–2017.

[14] For a recent review of the Sonogashira alkynylation, see: K. Sonogashira in *Handbook of Organopalladium Chemistry for Organic Synthesis* (Eds.: E. Negishi, A. de Meijere), Wiley-Interscience, New York, **2002**, chap. III.2.8.1, pp. 494–529.

[15] I. Paterson, P. A. Craw, *Tetrahedron Lett.* **1989**, *30*, 5799–5802.

 © 2006 Wiley-VCH Verlag GmbH & Co. KGaA, Weinheim

[16] H. C. Brown, P. K. Jadhav, K. S. Bhat, *J. Am. Chem. Soc.* **1988**, *110*, 1535 – 1538; the (*Z*)-MOMOCH=CHCH$_2$BIpc$_2$ used in this work was derived from (+)-MeOBIpc$_2$.
[17] E. J. Corey, P. L. Fuchs, *Tetrahedron Lett.* **1972**, *13*, 3769 – 3772.
[18] A. Arefolov, N. F. Langille, J. S. Panek, *Org. Lett.* **2001**, *3*, 3281 – 3284.
[19] C. Xu, E. Negishi, *Tetrahedron Lett.* **1999**, *40*, 431 – 434.

 © 2006 Wiley-VCH Verlag GmbH & Co. KGaA, Weinheim

Metallabenzenes

DOI: 10.1002/anie.200600055

Synthesis and Characterization of Stable Ruthenabenzenes**

Hong Zhang, Haiping Xia, Guomei He, Ting Bin Wen, Lei Gong, and Guochen Jia**

Transition-metal-containing metallabenzenes[1–3] are an interesting class of compounds because they exhibit chemical properties of both organometallic compounds[1] and aromatic organic compounds.[1,4] The first stable transition-metal-containing metallabenzenes were reported in 1982 by Roper et al.[5] Since then a number of stable metallabenzenes have been successfully isolated and characterized. Most of the well-characterized stable metallabenzenes are those with a transition metal atom from the third transition series, especially osmium,[4–7] iridium,[2a–d,g–h,8] and platinum.[2e,9] In contrast, well-characterized metallabenzenes with a metal atom from the first or the second transition series are still very rare, although such species was predicted theoretically as early as 1979.[10] Although coordinated metallabenzenes with metal atoms from the first[11] and the second[12,13] transition series and 1,3-dimetallabenzenes[14] of Nb and Ta were isolated and well characterized, free metallabenzenes with a metal atom from the first or the second transition series have been isolated rarely. The ruthenabenzene [CpRu{C(Ph)CHCHC(Ph)C(OEt)}(CO)] (Cp = cyclopentadienyl), and related ruthenaphenoxide and ruthenaphenanthrene oxide reported by Jones and co-workers represent rare examples (and the only reported examples, to the best our knowledge) of spectroscopically characterized metallabenzenes with a metal from the second transition series.[15a] However, these species are thermally unstable at ambient temperature. Other metallabenzenes such as ferrobenzene,[16a] ruthenaphenanthrene,[15a] ruthenaphenol,[15b] and chromobenzene[16b] have been proposed as reactive intermediates, but no direct observation of such species have been made. Herein we report the isolation and characterization of thermally stable ruthenabenzenes.

We recently reported a convenient method for the preparation of osmabenzenes starting from the reactions of $[OsCl_2(PPh_3)_3]$ with HC≡CCH(OH)C≡CH.[7] We found that the method can also be used to prepare ruthenabenzenes. Treatment of $[RuCl_2(PPh_3)_3]$ (**1**)[17] with HC≡CCH(OH)C≡CH, PPh_3, and Bu_4NCl in THF produced cationic ruthenabenzene **2**, which was isolated as a green solid in 55% yield (Scheme 1). Interestingly, **2** can even be obtained from the one-pot reaction of $RuCl_3$, PPh_3, and HC≡CCH(OH)C≡CH in $CHCl_3$, although the yield is lower.

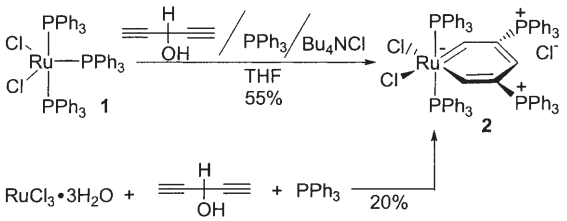

Scheme 1. Preparation of the stable ruthenabenzene **2**.

Complex **2** was characterized by solution NMR spectroscopy and elemental analysis. The $^{31}P\{^1H\}$ NMR spectrum in $CDCl_3$ showed two singlets at $\delta = 18.2$ and 8.1 ppm ($CPPh_3$ and $RuPPh_3$, respectively). The presence of the metallacycle is clearly indicated by the ^1H and ^{13}C NMR data. In particular, the ^1H NMR spectrum in $CDCl_3$ showed the characteristic signal for RuCH at $\delta = 17.5$ ppm and for γ-CH at $\delta = 8.2$ ppm. The ^1H NMR chemical shift for RuCH ($\delta = 17.5$ ppm) is significantly downfield relative to that for the vinyl complex $[Ru\{CH{=}CH(C_6H_4\text{-}p\text{-}OMe)\}Cl(CO)(PPh_3)_2]$ ($\delta = 8.13$ ppm),[18] but is close to those for ruthenium carbene complexes, for example, $[(PCy_3)(RO)_2Ru{=}CHPh]$ (Cy = cyclohexyl; R = *t*Bu: $\delta = 15.5$ ppm; $R = C(CF_3)_2(CH_3)$: $\delta = 17.5$ ppm; $R = C(CF_3)_3$: $\delta = 19.2$ ppm).[19] The $^{13}C\{^1H\}$ NMR spectrum (in CD_2Cl_2) showed the signals for RuCH, *C*PPh_3, and γ-CH at $\delta = 284.3$, 108.3, and 146.0 ppm, respectively. The NMR data suggest that the metallacycle of **2** has a delocalized symmetrical structure.

Unambiguous confirmation for the structure of **2** was provided by X-ray diffraction (Figure 1).[20] The complex contains an essentially planar six-membered metallacycle with two PPh_3 substituents. The coplanarity is reflected by the small deviations (0.0426 Å) from the RMS planes of the best fit through the six atoms Ru1, C1, C2, C3, C4, and C5. Within the metallacycle, the C–C bond lengths are in the range 1.378(7)–1.395(7) Å, and there is no significant C–C bond-

[*] H. Zhang, Prof. Dr. H. P. Xia, G. M. He, L. Gong
College of Chemistry and Chemical Engineering
State Key Laboratory for Physical Chemistry of Solid Surfaces
Xiamen University
Xiamen 361005 (P.R. China)
Fax: (+86) 592-218-6628
E-mail: hpxia@xmu.edu.cn
Dr. T. B. Wen, Prof. Dr. G. C. Jia
Department of Chemistry
The Hong Kong University of Science and Technology
Clear Water Bay, Kowloon (Hong Kong)
Fax: (+852) 2358-1594
E-mail: chjiag@ust.hk

[**] This work was supported by the program New Century Excellent Talents in Universities of China (NCET-04-0603), the National Science Foundation of China (20572089), and the Hong Kong Research Grant Council (HKUST6090/02P).

© 2006 Wiley-VCH Verlag GmbH & Co. KGaA, Weinheim

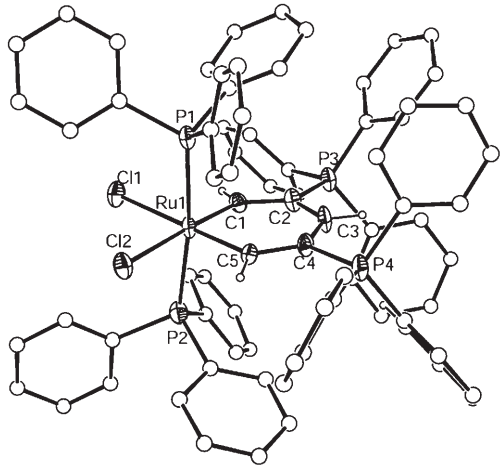

Figure 1. Molecular structure of **2** (thermal ellipsoids set at 50% probability). Selected bond lengths [Å] and angles [°]: Ru1–C1 1.922(5), C1–C2 1.382(7), C2–C3 1.395(7), C3–C4 1.378(7), C4–C5 1.391(7), C5–Ru1 1.911(5), C2–P3 1.790(5), C4–P4 1.792(5), Ru1–P1 2.4148(15), Ru1–P2 2.3926(15), Ru1–Cl1 2.5046(13), Ru1–Cl2 2.5196(13); C1-Ru1-C5 90.4(2), C1-Ru1-P1 92.25(15), C1-Ru1-P2 93.10(15), C5-Ru1-P1 93.17(15), C5-Ru1-P2 91.63(15), P1-Ru1-P2 172.78(5), Cl1-Ru1-Cl2 94.85(5), C2-C1-Ru1 129.5(4), C4-C5-Ru1 128.6(4), C1-C2-P3 123.3(4), C3-C4-P4 114.6(4), C3-C2-P3 114.3(4), C5-C4-P4 122.2(4), C1-C2-C3 122.2(5), C2-C3-C4 125.2(5), C3-C4-C5 123.2(4).

length alternation, as one might expect for a delocalized structure. To the best of our knowledge, this is the first structurally characterized uncomplexed metallabenzene with a metal atom from the second transition series.

In the solid state, ruthenabenzene **2** is air-stable. Its thermal stability is also remarkable, and **2** remains nearly unchanged when heated at 100 °C in air for 5 h. The higher thermal and air stability of ruthenabenzene **2** is probably related to the protecting effect of the bulky phosphine substituents and/or ligands. The electronic properties may also play an important role in the stability of **2**. To our knowledge, no metallabenzenes with a metal of the first or second transition series that are stable at room temperature have been reported previously. Thus, **2** is a rare example of thermally stable metallabenzenes with a transition metal atom from the second transition series.

Other thermally stable ruthenabenzenes can be obtained by substitution reactions of **2**. Treatment of **2** with PMe_3 produced complex **3**, which can be isolated as a green solid (Scheme 2). The structure of **3** is supported by NMR spectroscopic data. The $^{31}P\{^1H\}$ NMR spectrum showed a signal for $CPPh_3$ at $\delta = 18.1$ ppm and for $RuPMe_3$ at $\delta = -13.9$ ppm. Two signals for the metallacycle in the ^1H NMR spectrum ($\delta = 17.0$ (RuCH) and 7.9 ppm (γ-CH)) and three in the $^{13}C\{^1H\}$ NMR spectrum ($\delta = 279.6$ (RuCH), 143.3 (CH), and 107.3 ppm ($CPPh_3$)) verifies the symmetrical structure of **3**.

Addition of *t*BuNC to a solution of **2** in dichloromethane led to the formation of the isocyanide-containing complex **4**. The structure of ruthenabenzene **4** was readily assigned on the basis of the NMR spectroscopic data. In particular, the $^{31}P\{^1H\}$ NMR spectrum showed three singlets at $\delta = 25.1$

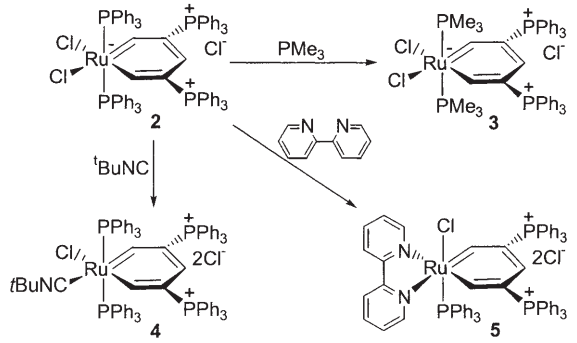

Scheme 2. Ligand-substitution reactions of ruthenabenzene **2**.

($RuPPh_3$), 23.3 ($CPPh_3$), and 18.3 ppm ($CPPh_3$). In the ^1H NMR spectrum, the two signals for RuCH appeared at $\delta = 15.6$ and 15.5 ppm. In the $^{13}C\{^1H\}$ NMR spectrum, the five signals for the metallacycle appeared at $\delta = 286.1$ (RuCH), 280.6 (RuCH), 149.1 (γ-*C*H), 113.7 ($CPPh_3$), and 113.6 ppm ($C(PPh_3)$).

Treatment of **2** with 2, 2′-dipyridyl led to the replacement of one chloride and one PPh_3 ligand by 2,2′-dipyridyl to give ruthenabenzene **5** (Scheme 2). The $^{31}P\{^1H\}$ NMR spectrum in $CDCl_3$ showed the signal for $CPPh_3$ at $\delta = 19.0$ ppm and for $RuPPh_3$ at $\delta = 45.6$ ppm. The ^1H NMR spectrum in $CDCl_3$ showed characteristic signals for RuCH at $\delta = 15.6$ and for γ-CH at $\delta = 8.2$ ppm. The $^{13}C\{^1H\}$ NMR spectrum showed three signals for the metallacycle at $\delta = 293.6$ (RuCH), 147.7 (γ-CH), and 120.2 ppm ($CPPh_3$), thus indicating that the metallacycle has a delocalized symmetrical structure.

The structure of **5** was also determined by X-ray diffraction (Figure 2).[20] Unlike complex **2**, the metallaben-

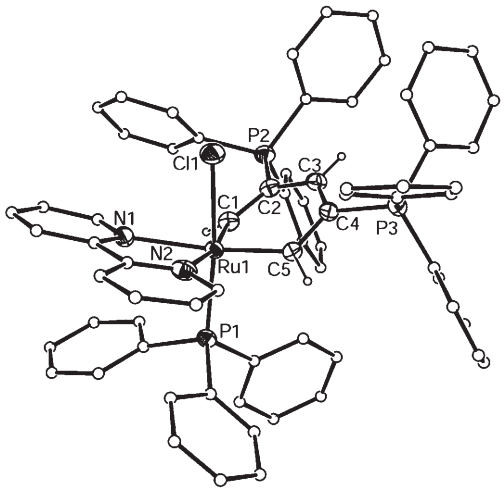

Figure 2. Molecular structure of **5** (thermal ellipsoids set at 50% probability). Selected bond lengths [Å] and angles [°]: Ru1–C1 1.935(4), C1–C2 1.382(6), C2–C3 1.387(7), C3–C4 1.396(7), C4–C5 1.407(6), C5–Ru1 1.914(4), C2–P2 1.793(5), C4–P3 1.790(5), Ru1–P1 2.3178(12), Ru1–Cl1 2.4407(13), Ru1–N1 2.210(4), Ru1–N2 2.189(4); C1-Ru1-C5 89.43(19), C1-Ru1-P1 94.23(14), C1-Ru1-Cl1 89.00(14), C5-Ru1-P1 96.47(14), C5-Ru1-Cl1 88.76(14), P1-Ru1-Cl1 173.87(4), N1-Ru1-N2 74.51(16), C2-C1-Ru1 123.9(3), C4-C5-Ru1 123.5(3), C1-C2-P2 117.2(4), C3-C4-P3 118.3(3), C3-C2-P2 118.8(4), C5-C4-P3 118.4(3), C1-C2-C3 123.9(4), C2-C3-C4 123.6(4), C3-C4-C5 122.8(4).

 © 2006 Wiley-VCH Verlag GmbH & Co. KGaA, Weinheim

zene ring of **5** is, unexpectedly, distorted with the ruthenium center tilted out of the plane of the C_5 backbone. Atoms C1–C5 are coplanar, with a maximum deviation from the least-squares plane of 0.0207 (32) Å for C2. The C–C bond lengths of the C1–C5 chain are in the range 1.382(6)–1.407(6) Å, and there is no C–C bond-length alternation. The ruthenium center lies −0.6722 (56) Å out of the plane of the ring carbon atoms (C1, C2, C3, C4, C5). The dihedral angle between this plane and the C1/Ru/C5 plane is 29.3°. The tilt angle is even larger than that in the coordinated ruthenabenzene $[(C_5H_5)Ru(\mu\text{-}C_7H_9)Ru(C_5Me_5)(CH_3CN)]PF_6$ (27.2°).[12a] It is not very clear why the metallabenzene ring of **5** deviates significantly from planarity, whereas that of the closely related ruthenabenzene **2** is essentially planar. Although not common, other nonplanar metallabenzenes are known. For example, in iridabenzenes supported by Tp ligand, the iridium metal is also bent by 0.57 to 0.76 Å out of the plane of the metallacyclic carbon atoms.[2a,h]

In summary, we have prepared and structurally characterized several ruthenabenzenes. Ruthenabenzenes **2**–**5** are rare examples of stable metallabenzenes with a transition metal of the second transition series.

Experimental Section

2: Method A: A mixture of $[RuCl_2(PPh_3)_3]$ (0.60 g, 0.63 mmol), HC≡CCH(OH)C≡CH (55 mg, 0.69 mmol), PPh_3 (0.83 g, 3.2 mmol), and Bu_4NCl (0.40 g, 5.4 mmol) in THF (10 mL) was stirred at room temperature for about 10 h to give a brownish-green suspension. The green solid was collected by filtration, washed with THF (5 × 2 mL), and then dried under vacuum (0.45 g, 55 %). Method B: A mixture of $[RuCl_3{\cdot}3H_2O]$ (0.10 g, 0.38 mmol), PPh_3 (0.60 g, 2.3 mmol), and HC≡CCH(OH)C≡CH (34 mg, 0.42 mmol) in $CHCl_3$ (15 mL) was stirred at room temperature for about 20 h to give a brownish-black solution. The volume of the mixture was reduced to approximately 3 mL under vacuum. Addition of diethyl ether (20 mL) to the residue produced a brown solid, which was collected by filtration, washed with THF (2 × 5 mL) and diethyl ether (2 × 5 mL), and dried under vacuum (0.10 g, 20 %). ^{1}H NMR (300.1 MHz, $CDCl_3$): $\delta = 17.5$ (d, $^3J(PH) = 18.9$ Hz, 2H; RuCH), 8.2 (t, $^3J(PH) = 14.0$ Hz, 1H; RuCHC(PPh$_3$)C*H*), 7.9–6.6 ppm (m, 60H; PPh$_3$); ^{31}P{^{1}H} NMR (121.5 MHz, $CDCl_3$): $\delta = 18.2$ (s; CPPh$_3$), 8.1 ppm (s, RuPPh$_3$); ^{13}C{^{1}H} NMR (125.7 MHz, CD_2Cl_2): $\delta = 284.3$ (d, $^2J(PC) = 11.6$ Hz; Ru*C*H), 146.0 (t, $^2J(PC) = 21.4$ Hz; RuCHC(PPh$_3$)*C*H), 137.3–126.8 (m, PPh$_3$), 108.3 ppm (dd, $^1J(PC) = 73.2$ Hz, $^3J(PC) = 12.1$ Hz; RuCH*C*(PPh$_3$)); elemental analysis: calcd for $C_{77}H_{63}Cl_3P_4Ru$ (%): C 70.08, H 4.81; found: C 69.65, H 4.88.

3: A solution of PMe_3 in THF (1.0 M; 4.5 mL, 4.5 mmol) was added to a solution of **2** (0.40 g, 0.31 mmol) in CH_2Cl_2 (10 mL). The reaction mixture was stirred at room temperature for about 12 h to give a brown solution. The volume of the mixture was reduced to approximately 1 mL under vacuum. The residue was purified by column chromatography (neutral alumina, eluent: acetone/methanol 5:1) to give **3** as a green solid (0.17 g, 58 %). ^{1}H NMR (500.4 MHz, $CDCl_3$): $\delta = 17.0$ (d, $^3J(PH) = 16.5$ Hz, 2H; RuCH), 7.9 (t, $^3J(PH) = 14.5$ Hz, 1H; RuCHC(PPh$_3$)C*H*), 7.8–7.2 ppm (m, 30H; PPh$_3$), 0.88 (t, $J(PH) = 4.1$ Hz, 18H; RuPMe$_3$); ^{31}P{^{1}H} NMR (202.4 MHz, $CDCl_3$): $\delta = 18.1$ (s; CPPh$_3$), −13.9 ppm (s; RuPMe$_3$); ^{13}C{^{1}H} NMR (125.7 MHz, $CDCl_3$): $\delta = 279.6$ (d, $^2J(PC) = 12.7$ Hz; RuCH), 143.3 (t, $^2J(PC) = 23.0$; RuCHC(PPh$_3$)*C*H), 134.9–128.4 (m; PPh$_3$), 107.3 (dd, ^{1}J(PC) = 75.2 Hz, $^3J(PC) = 12.0$ Hz; RuCH*C*(PPh$_3$)), 15.7 ppm (t, $J(PC) = 15.4$ Hz; PMe$_3$); elemental analysis: calcd for $C_{47}H_{51}Cl_3P_4Ru$ (%): C 59.60, H 5.43; found: C 59.79, H 4.96.

4: *t*BuNC (0.53 mL, 4.5 mmol) was added to a solution of **2** (0.40 g, 0.31 mmol) in CH_2Cl_2 (10 mL). The reaction mixture was stirred at room temperature for about 1 h to give a brown solution. The volume of the mixture was reduced to approximately 1 mL under vacuum. The residue was purified by column chromatography (neutral alumina, eluent: acetone/methanol 5:1) to give **4** as a green solid (0.23 g, 52 %). ^{1}H NMR (500.4 MHz, $CDCl_3$): $\delta = 15.6$ (d, $^3J(PH) = 23.3$ Hz, 1H; RuCH), 15.5 (d, $^3J(PH) = 19.0$ Hz, 1H, RuCH), 8.0 (t, $^3J(PH) = 13.5$ Hz, 1H; RuCHC(PPh$_3$)C*H*), 7.8–6.7 (m, 60H; PPh$_3$), 1.1 ppm (s, 9H; (CH$_3$)$_3$CNC); ^{31}P{^{1}H} NMR (202.4 MHz, $CDCl_3$): $\delta = 25.1$ (s; RuPPh$_3$), 23.3 ppm (s; CPPh$_3$), 18.3 ppm (s; CPPh$_3$); ^{13}C{^{1}H} NMR (125.7 MHz, CD_2Cl_2): $\delta = 286.1$ (d, $^2J(PC) = 9.8$ Hz; RuCH), 280.6 (d, $^2J(PC) = 10.2$ Hz; RuCH), 149.1 (t, $^2J(PC) = 22.1$; RuCHC(PPh$_3$)*C*H), 136.3–128.4 (m; PPh$_3$), 123.3 (s; (CH$_3$)$_3$CN*C*), 113.7 (d, $^1J(PC) = 72.3$ Hz; RuCH*C*(PPh$_3$)), 113.6 (d, $^1J(PC) = 72.8$ Hz; RuCH*C*(PPh$_3$)), 58.7 (s; (CH$_3$)$_3$*C*NC), 29.2 ppm (s; (*C*H$_3$)$_3$CNC); elemental analysis: calcd for $C_{82}H_{72}NP_4Cl_3Ru$ (%): N 1.00, C 70.21, H 5.17; found: N 1.35, C 70.24, H, 5.51.

5: 2,2′-Dipyridyl (94 mg, 0.60 mmol) was added to a solution of **2** (0.40 g, 0.31 mmol) in CH_2Cl_2 (10 mL). The reaction mixture was stirred at room temperature for about 5 h to give a brown-green solution. The volume of the mixture was reduced to approximately 1 mL under vacuum. The residue was purified by column chromatography (neutral alumina, eluent: acetone/methanol 5:1) to give **5** as a green solid (0.21 g, 49 %). ^{1}H NMR (500.4 MHz $CDCl_3$,): $\delta = 15.6$ (dd, $^3J(PH) = 16.0$ Hz, $^3J(PH) = 8.0$ Hz, 2H; RuCH), 9.0 (d, $^3J(HH) = 8.0$ Hz, 2H; NCH), 8.2 (t, $^3J(PH) = 8.0$ Hz, 1H; RuCHC(PPh$_3$)C*H*), 7.8–6.7 ppm (m, 51H; PPh$_3$, 2,2′-dipyridyl); ^{31}P{^{1}H} NMR (202.4 MHz, $CDCl_3$): $\delta = 45.6$ (t, $^4J(PP) = 2.6$ Hz; Ru(PPh$_3$)), 19.0 ppm (d, $^4J(PP) = 2.6$ Hz; CPPh$_3$); ^{13}C{^{1}H} NMR (125.7 MHz, CD_2Cl_2): $\delta = 293.6$ (d, $^2J(PC) = 12.6$ Hz; RuCH), 154.0 (s; N(CH)$_4$*C*C(CH)$_4$N), 147.7 (t, $^2J(PC) = 22.8$ Hz; RuCHC(PPh$_3$)*C*H), 147.5 (s; N(*C*H)(CH)(CH)(CH)C), 140.0 (s; N(CH)(*C*H)(CH)(CH)C), 136.3–128.4 (m; PPh$_3$), 126.0 (s; N(CH)(CH)(*C*H)(CH)C), 124.9 (s; N(CH)(CH)(CH)(*C*H)C), 120.2 ppm (dd, $^1J(PC) = 75.8$ Hz, $^3J(PC) = 13.1$ Hz; RuCH*C*(PPh$_3$)); elemental analysis: calcd for $C_{69}H_{56}N_2P_3Cl_3Ru$ (%): N 2.31, C 68.29, H 4.65; found: N 2.06, C 68.13, H 4.87.

Received: January 6, 2006
Published online: March 27, 2006

Keywords: alkynes · aromaticity · metallabenzenes · metallacycles · ruthenium

[1] J. R. Bleeke, *Chem. Rev.* **2001**, *101*, 1205.
[2] For examples of recent experimental work, see: a) E. Alvarez, M. Paneque, M. L. Poveda, N. Rendon, *Angew. Chem.* **2006**, *118*, 488; *Angew. Chem. Int. Ed.* **2006**, *45*, 474; b) H. P. Wu, T. J. R. Weakley, M. M. Haley, *Chem. Eur. J.* **2005**, *11*, 1191; c) C. S. Chin, H. Lee, M. S. Eum, *Organometallics* **2005**, *24*, 4849; d) C. S. Chin, H. Lee, *Chem. Eur. J.* **2004**, *10*, 4518; e) C. W. Landorf, V. Jacob, T. J. R. Weakley, M. M. Haley, *Organometallics* **2004**, *23*, 1174; f) P. Barrio, M. A. Esteruelas, E. Onate, *J. Am. Chem. Soc.* **2004**, *126*, 1946; g) R. D. Gilbertson, T. L. S. Lau, S. Lanza, H. P. Wu, T. J. R. Weakley, M. M. Haley, *Organometallics* **2003**, *22*, 3279; h) M. Paneque, C. M. Posadas, M. L. Poveda, N. Rendón, V. Salazar, E. Oñate, K. Mereiter, *J. Am. Chem. Soc.* **2003**, *125*, 9898.
[3] For examples of recent theoretical work, see: a) A. Karton, M. A. Iron, M. E. van der Boom, J. M. L. Martin, *J. Phys. Chem. A* **2005**, *109*, 5454; b) M. A. Iron, A. C. B. Lucassen, H. Cohen, M. E. van der Boom, J. M. L. Martin, *J. Am. Chem. Soc.* **2004**, *126*, 11699; c) M. A. Iron, J. M. L. Martin, M. E. van der Boom, *Chem. Commun.* **2003**, 132; d) M. A. Iron, J. M. L. Martin, M. E. van der Boom, *J. Am. Chem. Soc.* **2003**, *125*, 13020; e) M. A.

 © 2006 Wiley-VCH Verlag GmbH & Co. KGaA, Weinheim

Iron, J. M. L. Martin, M. E. van der Boom, *J. Am. Chem. Soc.* **2003**, *125*, 11702.
[4] C. E. F. Rickard, W. R. Roper, S. D. Woodgate, L. J. Wright, *Angew. Chem.* **2000**, *112*, 766; *Angew. Chem. Int. Ed.* **2000**, *39*, 750.
[5] G. P. Elliott, W. R. Roper, J. M. Waters, *J. Chem. Soc. Chem. Commun.* **1982**, 811.
[6] C. E. F. Rickard, W. R. Roper, S. D. Woodgate, L. J. Wright, *J. Organomet. Chem.* **2001**, *623*, 109.
[7] H. Xia, G. He, H. Zhang, T. B. Wen, H. H. Y. Sung, I. D. Williams, G. Jia, *J. Am. Chem. Soc.* **2004**, *126*, 6862.
[8] For an additional example, see: a) H. P. Wu, S. Lanza, T. J. R. Weakley, M. M. Haley, *Organometallics* **2002**, *21*, 2824; b) R. D. Gilbertson, T. J. R. Weakley, M. M. Haley, *J. Am. Chem. Soc.* **1999**, *121*, 2597; c) J. R. Bleeke, Y. F. Xie, W. J. Peng, M. Chiang, *J. Am. Chem. Soc.* **1989**, *111*, 4118; d) J. R. Bleeke, R. Behm, *J. Am. Chem. Soc.* **1997**, *119*, 8503; e) J. R. Bleeke, R. Behm, Y. F. Xie, M. Y. Chiang, K. D. Robinson, A. M. Beatty, *Organometallics* **1997**, *16*, 606, and references therein.
[9] For an example, see: V. Jacob, T. J. R. Weakley, M. M. Haley, *Angew. Chem.* **2002**, *114*, 3620; *Angew. Chem. Int. Ed.* **2002**, *41*, 3470.
[10] D. L. Thorn, R. Hoffman, *Nouv. J. Chim.* **1979**, *3*, 39.
[11] For coordinated metallabenzenes with a metal atom from the first transition series, see: a) J. Hein, J. C. Jeffery, P. Scherwood, F. G. A. Stone, *J. Chem. Soc. Dalton Trans.* **1987**, 2211; b) U. Bertling, U. Englert, A. Salzer, *Angew. Chem.* **1994**, *106*, 1026; *Angew. Chem. Int. Ed. Engl.* **1994**, *33*, 1003.
[12] For coordinated ruthenabenzene, see: a) H. W. Bosch, H.-U. Hund, D. Nietlispach, A. Salzer, *Organometallics* **1992**, *11*, 2087; b) W. Lin, S. R. Wilson, G. S. Girolami, *J. Chem. Soc. Chem. Commun.* **1993**, 284; c) W. Lin, S. R. Wilson, G. S. Girolami, *Organometallics* **1997**, *16*, 2356; d) U. Englert, F. Podewils, I. Schiffers, A. Salzer, *Angew. Chem.* **1998**, *110*, 2196; *Angew. Chem. Int. Ed.* **1998**, *37*, 2134; e) S. H. Liu, W. S. Ng, H. S. Chu, T. B. Wen, H. P. Xia, Z. Y. Zhou, C. P. Lau, G. Jia, *Angew. Chem.* **2002**, *114*, 1659; *Angew. Chem. Int. Ed.* **2002**, *41*, 1589; f) M. I. Bruce, N. N. Zaitseva, B. W. Skelton, A. H. White, *J. Chem. Soc. Dalton Trans.* **2002**, 1678; g) U. Effertz, U. Englert, F. Podewils, A. Salzer, T. Wagner, M. Kaupp, *Organometallics* **2003**, *22*, 264.
[13] For other coordinated metallabenzenes with a metal atom from the second transition series, see: a) M. S. Kralik, A. L. Rheingold, R. D. Ernst, *Organometallics* **1987**, *6*, 2612; b) M. S. Kralick, A. L. Rheingold, J. P. Hutchinson, J. W. Freeman, R. D. Ernst, *Organometallics* **1996**, *15*, 551.
[14] a) R. D. Profilet, P. E. Fanwick, I. P. Rothwell, *Angew. Chem.* **1992**, *104*, 1277; *Angew. Chem. Int. Ed. Engl.* **1992**, *31*, 1261; b) P. N. Riley, R. D. Profilet, M. M. Salberg, P. E. Fanwick, I. P. Rothwell, *Polyhedron* **1998**, *17*, 773.
[15] a) J. Yand, W. M. Jones, J. K. Dixon, N. T. Allison, *J. Am. Chem. Soc.* **1995**, *117*, 9776; b) J. Yang, J. Yin, K. A. Abboud, W. M. Jones, *Organometallics* **1994**, *13*, 971.
[16] a) R. Ferede, N. T. Allison, *Organometallics* **1983**, *2*, 463; b) T. M. Sivavec, T. J. Katz, *Tetrahedron Lett.* **1985**, *26*, 2159.
[17] P. S. Hallman, T. A. Stephenson, G. Wilkinson, *Inorg. Synth.* **1970**, *12*, 237.
[18] Y. Maruyama, K. Yamamura, T. Sagawa, H. Katayama, F. Ozawa, *Organometallics* **2000**, *19*, 1308.
[19] M. S. Sanford, L. M. Henling, M. W. Day, R. H. Grubbs, *Angew. Chem.* **2000**, *112*, 3593; *Angew. Chem. Int. Ed.* **2000**, *39*, 3451.
[20] Crystal data for **2**: $C_{77.50}H_{71}Cl_4O_{3.50}P_4Ru$, $M_r = 1425.09$, monoclinic, $P2(1)/n$, $Z = 4$, $a = 17.580(2)$, $b = 24.385(3)$, $c = 18.446(3)$ Å, $\alpha = 90$, $\beta = 110.948(2)$, $\gamma = 90°$, $V = 7385.3(17)$ Å^3; 53143 reflections, 12954 independent reflections ($R_{int} = 0.0705$); $R_1 = 0.0757$, $wR_2 = 0.1916$ for 847 parameters and 10129 reflections with $[I > 2\sigma(I)]$. Crystal data for **5**: $C_{70.50}H_{65}Cl_6N_2O_3P_3Ru$, $M_r = 1394.92$, triclinic, $P\bar{1}$, $Z = 2$, $a = 13.915(2)$, $b = 14.921(2)$, $c = 18.165(3)$ Å, $\alpha = 104.201(2)$, $\beta = 106.209(3)$, $\gamma = 102.962(3)°$, $V = 3332.6(9)$ Å^3; 33450 reflections, 12344 independent reflections ($R_{int} = 0.0357$); $R_1 = 0.0699$, $wR_2 = 0.1776$ for 784 parameters and 11133 reflections with $[I > 2\sigma(I)]$. Crystals of **2** and **5** suitable for X-ray diffraction were grown from a solution in CH_2Cl_2 layered with diethyl ether. Intensity data were collected on a Bruker SMART CCD Area Detector with graphite-monochromated $Mo_{K\alpha}$ radiation at temperature of 223 K. The structures were solved by direct methods, expanded by difference Fourier syntheses, and refined by full-matrix least-squares methods on F^2 by using the Bruker SHELXTL (Version 6.10) program package. All non-hydrogen atoms were refined anisotropically. CCDC-294492, and CCDC-294494 contain the supplementary crystallographic data for this paper. These data can be obtained free of charge from The Cambridge Crystallographic Data Centre via www.ccdc.cam.ac.uk/data_request/cif.

 © 2006 Wiley-VCH Verlag GmbH & Co. KGaA, Weinheim

Helicene Synthesis

DOI: 10.1002/anie.200504150

Preparation of Helicenes through Olefin Metathesis**

Shawn K. Collins, Alain Grandbois, Martin P. Vachon, and Julie Côté*

The last decade has seen the interest in helicenes and helical-type molecules undergo a significant renaissance. Although the [*n*]helicenes were long considered academic curiosities,[1] their helically chiral, conjugated structures afford fascinating optical[2] and electronic properties,[3] thus recently finding application in the field of medicinal chemistry.[4] Consequently, methods for the preparation of helicenes have advanced in tandem.[5] The need for more highly substituted and structurally varied helicenes has led to the development of new methods as replacements of the classical synthesis by the photocyclization of stilbenes.[6] These methods include successive Diels–Alder reactions,[7] cyclotrimerizations of

[*] Prof. Dr. S. K. Collins, A. Grandbois, M. P. Vachon, J. Côté
Department of Chemistry
Université de Montréal
C.P. 6128 Succursale Centre-ville
Montréal, Québec, H3C 3J7 (Canada)
Fax: (+1) 514-343-7586
E-mail: shawn.collins@umontreal.ca

[**] We are grateful to the National Sciences and Engineering Research Council of Canada (NSERC), Fonds Québecois de la Recherche sous la Nature et les Technologies (FQRNT), the Canadian Foundation for Innovation and the Université de Montréal for generous financial support of this research. We thank the laboratories of Prof. A. Charette and Prof. H. Lebel (Université de Montréal) for sharing of equipment, chemicals, and fruitful discussions.

Supporting information for this article is available on the WWW under http://www.angewandte.org or from the author.

© 2006 Wiley-VCH Verlag GmbH & Co. KGaA, Weinheim

acetylenes,[8] carbenoid couplings,[9] Pd-mediated techniques,[10] and radical cyclizations.[11] In general, each of the above methods is used to form a benzene ring within the helicene framework. Herein, we describe a preparation of helicenes using olefin metathesis for the formation of a benzene ring. It is quite surprising that despite the power of ring-closing olefin metathesis to prepare a variety of cyclic structures, so few examples have been documented for the formation of benzenes, undoubtedly one of the most important cycles in all of organic chemistry. Only three examples have been reported, all in the last two years.[12,13,14] Notably, King and co-workers clearly demonstrated by density functional theory calculations that the formation of an aromatic ring through olefin metathesis should act as a thermodynamic sink and an exergonic reaction is predicted by -28 kcal mol^{-1}.[13] However, there is no precedent that indicates whether olefin metathesis will be feasible to form the strained [5]helicene structure, although the normally competing reverse ring-opening reaction will not be possible. An added benefit of our strategy is the use of 1,1′-binaphthyls as precursors. The modification and alteration of this skeleton has been extensively studied with regards to the preparation of chiral ligands.[15] A short series of elementary transformations would prepare the 1,1′-binaphthyl framework for transformation into the helicene motif by a ring-closing metathesis reaction.[16]

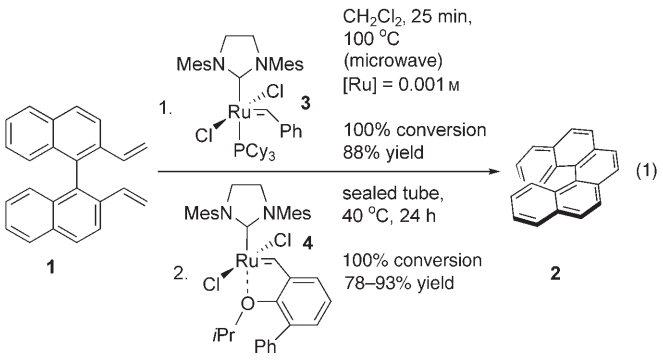

(1)

2,2′-Binaphthol was first converted into its corresponding divinyl precursor **1**.[17] Following extensive optimization,[18] two optimal protocols for the conversion of **1** into [5]helicene were identified [Eq. (1); Mes = mesityl, Cy = cyclohexyl]. The first utilizes catalyst **3** and resulted in a reproducible yield of 88% of the isolated product, [5]helicene, after 25 min in CH_2Cl_2 at 100 °C under microwave irradiation.[19] Although this protocol is extremely rapid, we sought to decrease the reaction temperature. Consequently, a second protocol was developed using catalyst **4**, whereby yields of 78–93% of the isolated [5]helicene could be obtained at 40 °C in a sealed-tube vessel.

Table 1: Preparation of helicenes by olefin metathesis.[a]

Entry	Precursor		Helicene		Cat.	*t*	Conversion [%][b]	Yield [%][c]
1	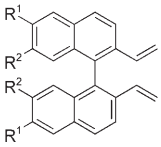	**5**	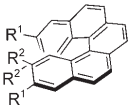	**6**	**3**	25 min	100	(90)
	$R^1 = p$-tol, $R^2 = H$,		$R^1 = p$-tol, $R^2 = H$,		**4**	24 h	55	87 (52)
2	$R^1 = H$, $R^2 = OMe$,	**7**	$R^1 = H$, $R^2 = OMe$,	**8**	**3**	120 min	95	57
					4	24 h	40	55 (25)
3	$R^1 = H$, $R^2 = OBn$,	**9**	$R^1 = H$, $R^2 = OBn$,	**10**	**3**	25 min	100	(61)
					4	24 h	41	49 (22)
4	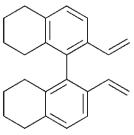	**11**	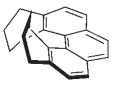	**12**	**3**	140 min	100	(80)
					4	24 h	50	(45)
5	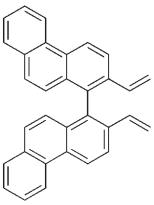	**13**	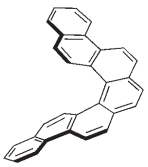	**14**	**3**	25 min	100	(75)
					4	24 h	45	55 (31)
6	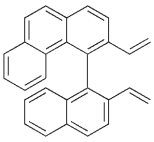	**15**	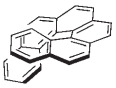	**16**	**3**	60 min	100	(80)
					4	24 h	100	(70)
7	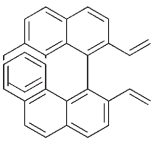	**17**	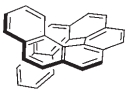	**18**	**3**	60 min	100	(81)
					4	24 h	100	(80)

[a] The reaction conditions: for catalyst **2**: [Ru] = 0.001 M in CH_2Cl_2, sealed tube, microwave heating in 5-min pulses at 100 °C, 10 mol% catalyst; for catalyst **5**: sealed tube, [Ru] = 0.001 M in PhH at 40 °C, 10 mol% catalyst. [b] Conversion measured by ^{1}H NMR spectroscopic analysis. [c] Yields calculated based on ^{1}H NMR spectroscopic analysis; yields of the isolated products were determined by flash column chromatography on silica gel and are indicated in brackets.

Following these studies, the two protocols outlined above were chosen for further examination (Table 1). Subsequently, the 6,6′-di-*p*-tolyl derivative **5** (using binaphthyl numbering) underwent smooth conversion into the corresponding helicene **6** when subjected to the microwave heating protocol (entry 1). A conversion of 100% was observed with ^{1}H NMR

 © 2006 Wiley-VCH Verlag GmbH & Co. KGaA, Weinheim

spectroscopic analysis and a yield of 90% of the isolated product **6** was obtained in just 25 min. Heating with catalyst **4** at 40°C for 24 h provided a yield of 52% of the isolated product (55% conversion; entry 1). These results for the two metathesis protocols are quite general in that the microwave protocol tends to give excellent conversions and yields, whereas the protocol which employs **4** at 40°C is gentler, albeit giving generally lower yields. Substituents at the 7,7′-positions of the binaphthyl skeleton also had little affect on the outcome of the ring-closing event (entries 2 and 3). The ring closure of dimethyl ether **7** was performed on the largest scale possible (which was limited because of the volume of the microwave vessel; scale: ≈350 mg of **7**; entry 2). The microwave could reach a maximum temperature of 120°C on this scale. Following irradiation for 120 min, **7** underwent 95% conversion, and 57% yield of the isolated helicene **8** was obtained. Treatment of **7** with **4** at 40°C in a sealed tube resulted in a conversion of 40% and a similar yield of 22% for the isolated product **8** (55% yield based on the recovered starting material). The dibenzyl ether **9** also provided a conversion of 100% after 25 min under microwave heating conditions (entry 3). However, some benzyl deprotection was observed and a yield of 61% was obtained for the isolated product **10**. The milder cyclization using **4** resulted in only 41% conversion, but cleavage of the benzyl group was not observed and the yield of the isolated product **10** (22% vs 49% yield based on the recovered starting material) was nearly identical to that observed for the methoxy derivative **8**. To improve the efficiency of the reaction, the microwave protocol was repeated, but catalyst **3** was replaced with **4**. As expected 100% conversion was observed after 25 min; however, some cleavage of the benzyl group was again observed, although the yield of the isolated product was slightly higher than the previous run with **3** (68 vs 61%).

Substituents at the 8,8′-positions were expected to be problematic, as they result in increased ring strain in the helicene products. Consequently, the first substrate investigated possessed the smallest substituent possible, an extra hydrogen atom (entry 4). 5,5′-6,6′-7,7′-8,8′-Octahydro-1,1′-bi-2-naphthol was transformed into **11** and subjected to microwave irradiation with **3**; although 100% conversion of **11** was obtained, 140 minutes were required for complete conversion. Surprisingly, 50% conversion (45% yield of the isolated product) was obtained with catalyst **4**, thus prompting a second trial with **4** under microwave irradiation. Gratifyingly, 75% conversion was obtained after only 25 min, and the saturated helicene **12** was isolated in 68% yield (86% yield based on recovered **11**).

Higher helicenes were also accessible using the above protocols. The first attempt involved the conversion of 2-phenanthrol into the corresponding divinyl precursor **13** through the same series of transformations used for **1** (entry 5).[15] The resulting helicene **14** was expected to form readily under conditions optimized for [5]helicene. Indeed, following microwave irradiation for 25 min in the presence **3**, 100% conversion of **13** was observed and 75% yield of the helicene product **14** was obtained. Strangely, heating **13** in a sealed tube with **4** gave a conversion of 45% and a yield of 55% (based on the recovered starting material) for **14**.

Subsequent experiments sought to further investigate the effect of the substituents which would result in increased strain in the helicene products. Consequently, the [6]helicene precursor **15** underwent smooth conversion (100%) to the corresponding [6]helicene **16** after 60 min under microwave irradiation, which was isolated in 80% yield (entry 6). Treatment with catalyst **4** at 40°C in a sealed tube resulted in 100% conversion and 70% yield of the isolated product. Similar results were obtained for the preparation of [7]helicene (entry 7). For example, substrate **17** required 60 min of microwave irradiation with **2** to undergo complete conversion into **18** (81% yield of isolated product). Milder conditions with catalyst **4** also resulted in 100% conversion and 80% yield of isolated [7]helicene.

In summary, we have developed a novel synthesis of substituted [5]helicenes and [6]- and [7]helicenes through ring-closing olefin metathesis. Conditions have been optimized using two separate protocols: catalyst **3**/CH_2Cl_2 under microwave irradiation or catalyst **4**/PhH at 40°C, when a sensitive functionality may be present. A highlight of this method is the facile formation of various substituted [5]helicenes and [6]- and [7]helicenes from the readily modifiable 1,1′-binaphthyls. For example, substituted [6]helicenes could be formed from mixed oxidative couplings between 3-phenanthrol and various 2-naphthols. This ease of functionalization suggests that these methods should be of significant interest in the fields of materials science and medicinal chemistry. These studies reinforce that olefin metathesis catalysts can be remarkably effective in generating strained molecular architectures and emphasize that ring-closing olefin metathesis can be a powerful route to the preparation of aromatic compounds. In contrast to other methods for helicene formation which utilize reactive radical or carbene intermediates, these olefin-metathesis conditions are gentle and the possibility of an asymmetric route to helicenes through a kinetic-resolution route is currently being pursued.

Received: November 21, 2005
Published online: March 28, 2006

Keywords: arenes · helical structures · helicenes · microwave irradiation · olefin metathesis

[1] a) C. Schmuck, *Angew. Chem.* **2003**, *115*, 2552–2556; *Angew. Chem. Int. Ed.* **2003**, *42*, 2448–2452; b) H. Hopf, *Classics in Hydrocarbon Chemistry*, Wiler-VCH, Weinheim, **2000**, pp. 321–330; c) F. Vögtle, *Fascinating Molecules in Organic Chemistry*, Wiley, New York, **1992**, pp. 156–180; d) K. P. Meurer, F. Vögtle, *Top. Curr. Chem.* **1985**, *127*, 1–76; e) R. H. Martin, *Angew. Chem.* **197**4, 86, 727–738; *Angew. Chem. Int. Ed. Engl.* **1974**, *13*, 649–658.

[2] T. J. Katz, *Angew. Chem.* **2000**, *112*, 1997–1999; *Angew. Chem. Int. Ed.* **2000**, *39*, 1921–1923.

[3] S. Grimme, L. Harren, A. Sobanski, F. Vögtle, *Eur. J. Org. Chem.* **1998**, 1491–1509.

[4] a) S. Honzawa, H. Okubo, S. Anzai, M. Yamaguchi, K. Tsumoto, I. Kumagai, *Bioorg. Med. Chem.* **2002**, *10*, 3213; b) Y. Xu, X. Y. Zhang, H. Sugiyama, T. Umano, H. Osuga, K. Tanaka, K. *J. Am. Chem. Soc.* **2004**, *126*, 6566–6567.

 © 2006 Wiley-VCH Verlag GmbH & Co. KGaA, Weinheim

[5] A. Urbano, *Angew. Chem.* **2003**, *115*, 4116 – 4119; *Angew. Chem. Int. Ed.* **2003**, *42*, 3986 – 3989.
[6] a) W. H. Laarhoven, W. J. C. Prinsen, *Top. Curr. Chem.* **1984**, *125*, 63 – 130; b) L. Liu, B. Yang, T. J. Katz, M. K. Poindexter, *J. Org. Chem.* **1991**, *56*, 3769 – 3775.
[7] a) M. C. Carreno, S. Garcia-Cerrada, A. Urbano, *J. Am. Chem. Soc.* **2001**, *123*, 7929; b) M. C. Carreno, S. Garcia-Cerrada, A. Urbano, *Chem. Eur. J.* **2003**, *9*, 4118 – 4131; c) M. C. Carreno, M. Gonzalez-Lopez, A. Urbano, *Chem. Commun.* **2005**, 611 – 613.
[8] a) I. G. Stara, I. Stary, A. Kollarovic, F. Teply, S. Vyskocil, D. Saman, *Tetrahedron Lett.* **1999**, *40*, 1993; b) F. Teply, I. G. Stara, I. Stary, A. Kollarovic, D. Saman, L. Rulisek, P. Fiedler, *J. Am. Chem. Soc.* **2002**, *124*, 9175 – 9180; c) I. G. Stara, Z. Alexandrova, F. Teply, P. Sehnal, I. Stary, D. Saman, M. Budesinsky, J. Cvacka, *Org. Lett.* **2005**, *7*, 2547 – 2550.
[9] a) F. Dubois, M. Gingras, *Tetrahedron Lett.* **1998**, *39*, 5039 – 5040; b) M. Gingras, F. Dubois, *Tetrahedron Lett.* **1999**, *40*, 1309 – 1312.
[10] K. Nakano, Y. Hidehira, K. Takahashi, T. Hiyama, K. Nozaki, *Angew. Chem.* **2005**, *117*, 7298 – 7300; *Angew. Chem. Int. Ed.* **2005**, *44*, 7136 – 7138.
[11] a) D. C. Harrowven, M. I. T. Nunn, D. R. Fenwick, *Tetrahedron Lett.* **2002**, *43*, 7345 – 7347; b) D. C. Harrowven, M. I. T. Nunn, D. R. Fenwick, *Tetrahedron Lett.* **2002**, *43*, 3189 – 3191.
[12] A. Iuliano, P. Piccioli, D. Fabbri, *Org. Lett.* **2004**, *6*, 3711 – 3714.
[13] M. C. Bonifacio, C. R. Robertson, J.-Y. Jung, B. T. King, *J. Org. Chem.* **2005**, *70*, 8522 – 8526.
[14] S. C. Pelly, C. J. Parkinson, W. A. L. van Otterlo, C. B. de Koning, *J. Org. Chem.* **2005**, *70*, 10474 – 10481.
[15] Y. Chen, S. Yekta, A. K. Yudin, *Chem. Rev.* **2003**, *103*, 3155 – 3212.
[16] a) R. H. Grubbs, *Tetrahedron* **2004**, *60*, 7117 – 7140; b) C. W. Lee, R. H. Grubbs, *J. Org. Chem.* **2001**, *66*, 7155 – 7158.
[17] Binaphthol ditriflate is carboxymethylated using an established protocol; see: M. Seki, S.-I. Yamada, T. Kuroda, R. Imashiro, T. Shimizu, *Synthesis* **2000**, 1677 – 1680; subsequent reduction (lithium aluminum hydride, Et_2O), oxidation (pyridinium chlorochromate, CH_2Cl_2), and the Wittig reaction (*t*BuOK, $CH_2{=}PPh_3$, THF) yields the divinyl precursor.
[18] See the Supporting Information for the experimental procedures and further details concerning catalyst optimization.
[19] Higher temperatures can be used, but did not affect the rate or yield of [5]helicene significantly.

 © 2006 Wiley-VCH Verlag GmbH & Co. KGaA, Weinheim

Dehydrocoupling

DOI: 10.1002/anie.200600318

Catalytic Antimony–Antimony Bond Formation through Stibinidene Elimination from Zirconocene and Hafnocene Complexes**

*Rory Waterman and T. Don Tilley**

Metal-catalyzed dehydrocoupling reactions have emerged as an important synthetic method for the generation of element–element bonds and the production of new types of inorganic oligomers and polymers.[1] Current information indicates that these coupling reactions occur by a number of different mechanisms. For silane couplings catalyzed by d^0-metal complexes, σ-bond metathesis reactions appear to be important.[2] However, related catalysts mediate similar Sn–Sn bond formations and dehydropolymerizations by a mechanism that involves α-hydrogen migration and stannylene elimination, followed by rapid insertion of stannylene units into Sn–H or M–Sn bonds (Scheme 1).[3] The latter mecha-

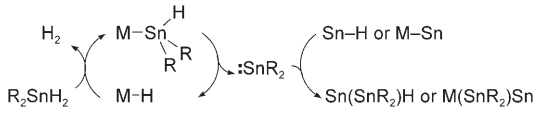

Scheme 1. Possible mechanism for stannane dehydrocoupling.

nism represents an unusual pathway in transition-metal chemistry and is of interest in determining how generally useful this process might be. This elimination mechanism is expected to be most favored for the heavier main-group elements, which readily form stable low-valent species. These elements should also possess weak element–hydrogen bonds which could additionally promote α-hydrogen migration. To explore the possible utility of this unusual reaction type, we investigated the dehydrocoupling of stibines. Herein, we provide two examples of metal-catalyzed Sb–Sb bond formation and evidence that these reactions occur through α-hydrogen migration with stibinidene (:SbR) elimination from d^0-metal–SbHR derivatives. For Group 15 elements, catalytic dehydrocouplings have been reported for primary phosphines[4] and Lewis acid/phosphine adducts.[5]

[*] Dr. R. Waterman, Prof. Dr. T. D. Tilley
Department of Chemistry
University of California, Berkeley
Berkeley, CA 94720-1460 (USA)
Fax: (+1) 510-642-8940
E-mail: tdtilley@berkeley.edu

[**] This work was supported by the US National Science Foundation (Grant no. 0132099). The authors acknowledge the Miller Institute for Basic Research in Science for a Research Fellowship (R.W.) and Professorship (T.D.T.).

Supporting information for this article is available on the WWW under http://www.angewandte.org or from the author.

WILEY InterScience DISCOVER SOMETHING GREAT
© 2006 Wiley-VCH Verlag GmbH & Co. KGaA, Weinheim

The stibines $MesSbH_2$ (**1**; Mes = mesityl) and $dmpSbH_2$ (**2**; dmp = 2,6-dimesitylphenyl) were readily prepared by reduction of the dichloro precursors using $LiAlH_4$ to afford analytically pure colorless crystals in 53 and 81% yield, respectively [Eq. (1)].[6] As with $(2,6\text{-}Trip_2C_6H_3)SbH_2$ (Trip = 2,4,6-iPr$_3$C$_6$H$_2$),[6c] stibine **2** (m.p. 174–176 °C) shows considerably greater thermal stability than **1**, which decomposes in the solid state over a period of hours at ambient temperature to insoluble products. The deuterated stibine $MesSbD_2$ ([D$_2$]**1**) was similarly prepared by reduction of $MesSbCl_2$ using $LiAlD_4$ in 43% yield of the isolated product. The IR spectrum of [D$_2$]**1** exhibits a ν_{Sb-D} stretch (1341 cm^{-1}) that is shifted with respect to the ν_{Sb-H} stretch of **1** (1873 cm^{-1}) by the expected amount.

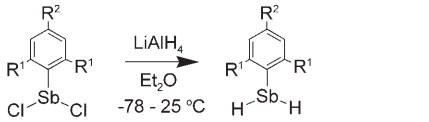

(1)

1: R^1 = R^2 = Me, 53%
2: R^1 = Mes, R^2 = H, 81%

Zirconocene complexes [$Cp_2Zr(H)Cl$] and [Cp_2ZrMe_2] (Cp = cyclopentadienyl) react with 20 equivalents of stibine **1** in C_6D_6 to liberate H_2 and produce the known tetrastibene Sb_4Mes_4 (**3**) in high yield [> 95%; Eq. (2)].[6b] It is noteworthy

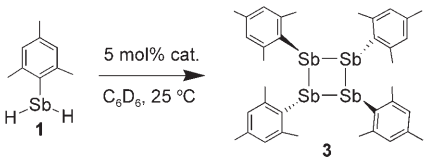

(2)

cat. (reaction time) =[$Cp_2Zr(H)Cl$] (<0.5 h), [Cp_2ZrMe_2] (16 h), [CpCp*Hf(H)Cl](8 h)

that these reactions occur in the dark, but ambient lighting accelerates the dehydrocoupling. Qualitatively, [$Cp_2Zr(H)Cl$] (< 0.5 h) is a much faster catalyst than [Cp_2ZrMe_2] (≈ 16 h), likely a result of a slower initial reaction of **1** with dimethyl zirconocene.[2] Intermediate species were not observed by ^{1}H NMR spectroscopy during the course of these reactions. Stiochiometric dehydrocoupling of phenylstibine ($PhSbH_2$) has been reported by reaction with alkyllithium reagents, sodium metal, or hydrogen traps (styrene or phenylacetylene).[7]

The hafnium hydride [CpCp*Hf(H)Cl] (**4**; Cp* = pentamethylcyclopentadienyl) is a much slower catalyst than [$Cp_2Zr(H)Cl$] for the dehydrocoupling of Equation (2) (≈ 8 h), and addition of one equivalent of **1** to a solution of **4** in C_6D_6 resulted in rapid evolution of H_2 and near-quantitative formation of [CpCp*HfCl{Sb(H)Mes}] (**5**), as identified by ^{1}H and ^{13}C NMR spectroscopy [Eq. (3)]. The Sb–H proton of **5** resonates at $\delta = 2.46$ ppm, an upfield shift from the Sb–H resonance of **1** ($\delta = 3.12$ ppm). Installation of the stibide ligand presumably occurs through σ-bond metathesis to form H_2. The σ-bond metathesis reaction that forms stibide complex **5** is fast ($t_{1/2} < 2$ min) relative to the reaction of [$Sn(H)_2Mes_2$] with **4** to form [CpCp*HfCl{$Sn(H)Mes_2$}] ($t_{1/2} \approx 75$ min). The facile activation of an Sb–H bond is consistent with the known, small bond-dissociation energy for SbH_3 (61 kcal mol^{-1}).[8] The isotope effect associated with the Sb–H bond activation ($k_H/k_D = 1.2(2)$) was determined by a competition experiment that involved treatment of **4** with an excess of **1** and [D$_2$]**1** (1:1) in C_6D_6. This isotope effect is small relative to that expected for a σ-bond metathesis mechanism;[2] however, pre-equilibrium coordination of the stibine to the Hf center could explain the observed isotope effect.[3a]

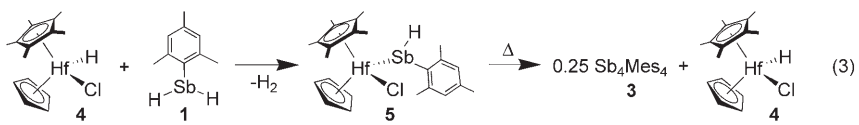

(3)

Compound **5** exhibits limited thermal stability in solution and could not be isolated as a pure solid. Thermal decomposition of **5** led to quantitative formation of tetrastibene **3** and hafnium hydride **4** [Eq. (3)], as determined by ^{1}H and ^{13}C NMR spectroscopy. Reaction of a solution of **4** in C_6D_6 with [D$_2$]**1** resulted in evolution of HD and quantitative formation of [CpCp*HfCl{Sb(D)Mes}] ([D$_1$]**5**), as determined by NMR spectroscopy. The thermal decomposition of [D$_1$]**5** provided **3** and hafnium deuteride [CpCp*Hf(D)Cl] in nearly quantitative yields.

The sequence of stoichiometric reactions in Equation (3) appears to involve elementary steps that account for the catalytic dehydrocoupling of $MesSbH_2$ by **4**. Thus, the Sb–Sb bond-forming process was investigated in more detail. The decomposition of **5** follows first-order kinetics ($k = 1.02(6) \times 10^{-4}$ s^{-1}) over approximately five half-lives, as evaluated by ^{1}H NMR spectroscopy. Decomposition of [D$_1$]**5** proceeds at a rate of $k = 2.53(5) \times 10^{-5}$ s^{-1}, which gives a kinetic isotope effect (k_H/k_D) of 4.0 for this reaction. This relatively large isotope effect is consistent with significant Sb–H bond cleavage in the transition state. Additional evidence for an α-hydrogen migration/stibinidene elimination pathway comes from an Eyring analysis, which provided the activation parameters $\Delta H^{\ddagger} = 27.3(1)$ kcal mol^{-1} and $\Delta S^{\ddagger} = -20.0(1)$ eu (for $T = 2.2$–46.9 °C). These values are similar to those obtained for the α-stannylene elimination reaction of [CpCp*HfCl($SnPh_3$)], which results in the formation of [CpCp*HfClPh] and diphenylstannylene,[3c] and are consistent with an ordered transition state [Eq. (4)].

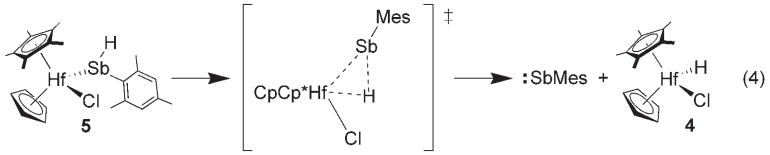

(4)

Presumably, the reaction shown in Equation (4) involves the elimination of mesitylstibinidene (:SbMes), which condenses to form the observed tetrastibene **4**. An attempt to trap free :SbMes was made by addition of 2,3-dimethyl-1,3-butadiene (10–60 equiv), an effective trap for free stibinidene,[9] to solutions of **5** in C_6D_6. However, the presence of the added

 © 2006 Wiley-VCH Verlag GmbH & Co. KGaA, Weinheim

diene had no effect on the rates of decomposition or formation of Sb_4Mes_4 as the exclusive Sb-containing product. The inability to trap free stibinidene is consistent with a rapid Sb–Sb bond-forming event. In d^0-metal-catalyzed dehydrocoupling of secondary stannanes, stannylene fragments are difficult to trap and appear to rapidly insert into metal–hydride and metal–tin bonds.[3]

The treatment of solutions of **4** in hexane with $dmpSbH_2$ resulted in the evolution of H_2 and the formation of a red solution, from which analytically pure red crystals of [CpCp*HfCl{Sb(H)dmp}] (**6**) were obtained in 89% yield [Eq. (5)]. Complex **6** was characterized by NMR and IR spectroscopic analysis and a single-crystal X-ray diffraction study. Diagnostic spectroscopic features for **6** include a ^{1}H NMR resonance at $\delta = 2.49$ ppm for the stibide ligand proton (cf. $\delta = 2.46$ ppm for **5**) and a IR

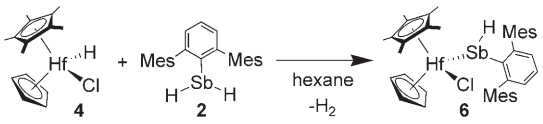

(5)

stretch at $\nu_{SbH} = 1830\ cm^{-1}$, a value 41 cm^{-1} lower in energy than that for $dmpSbH_2$. The latter observation is consistent with a metal-bound stibide ligand.[10]

The solid-state structure of **6** is shown in Figure 1.[11] The Hf–Sb bond length is 3.0035(8) Å; a search of the Cambridge Structural Database provided no examples of Group 4 metals with stibine or stibide ligands. The structurally characterized complex most closely related to **6** is $[Cp_2Nb(H)_2(SbPh_2)]$, which features a Nb–Sb bond length of 2.8929(4) Å and a pyramidal Sb center (angles at Sb: $\Sigma = 306.3°$).[12] The Sb–C(11) bond of **6** is roughly coplanar with the Hf–Cp centroid vector—an arrangement likely to reduce steric interactions. However, such a geometry also allows for donation from the lone pair on the antimony center to a vacant orbital on Hf.[13] Current evidence prohibits definitive assignment of such an interaction.

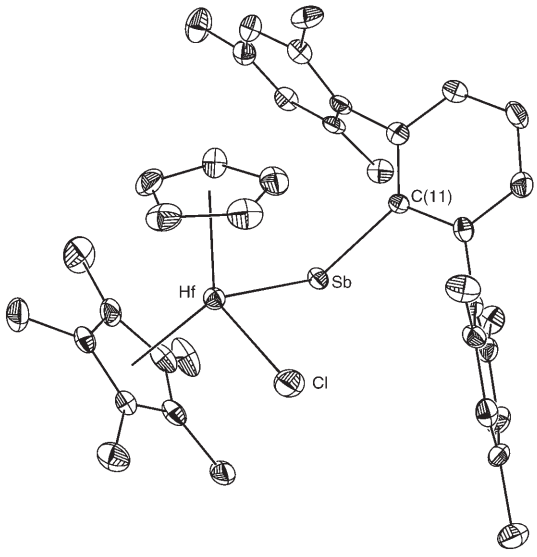

Figure 1. Perspective view of one enantiomer of [CpCp*HfCl{Sb(H)dmp}] (**6**), with thermal ellipsoids drawn at the 35% probability level. Hydrogen atoms have been omitted for clarity. Select bond lengths [Å] and angles [°]: Hf–Sb 3.0035(8), Hf–Cl 2.407(2), Sb–C(11) 2.180(8); Cl-Hf-Sb 96.62(6), C(11)-Sb-Hf 112.2(2).

Thermal decomposition of **6** proceeded smoothly in C_6D_6 to give **4** and the reported distibene (dmp)Sb=Sb(dmp) [**7**; Eq. (6)].[6b] Furthermore, **4** catalyzed the dehydrocoupling of $dmpSbH_2$ in C_6D_6 solution to form H_2 and **7** in > 95% yield, as

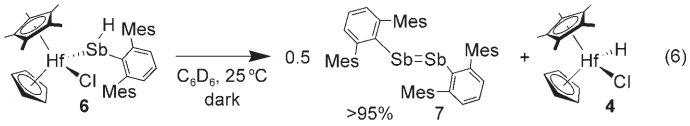

(6)

determined by ^{1}H NMR spectroscopy. A preliminary kinetic investigation indicates that thermal decomposition proceeds with a first-order dependence on the concentration of **6** ($k = 1.29(5) \times 10^{-5}\ s^{-1}$), which is consistent with an α-hydrogen migration/stibinidene extrusion mechanism.

In summary, Group 4 metal complexes have been shown to catalytically dehydrocouple stibines. These dehydrocoupling reactions with the hafnium catalyst [CpCp*Hf(H)Cl] show first-order dependence on the hafnium stibide species, a large primary kinetic isotope effect, and activation parameters that are consistent with a mechanism that involves α-hydrogen migration and elimination of a stibinidene fragment (α-stibinidene elimination). Efforts to extend this chemistry, which involves elimination of low-valent fragments, to catalytic reactions of additional stibines, other elements, and new processes are ongoing.

Received: January 25, 2006
Published online: March 23, 2006

Keywords: antimony · dehydrocoupling · elimination · hafnium · stibinidenes

[1] a) F. Gauvin, J. F. Harrod, H. G. Woo, *Adv. Organomet. Chem.* **1998**, *42*, 363–405; b) J. Y. Corey, *Adv. Organomet. Chem.* **2004**, *51*, 1–52; c) T. D. Tilley, *Comments Inorg. Chem.* **1990**, *10*, 37–46.
[2] T. D. Tilley, *Acc. Chem. Res.* **1993**, *26*, 22–29.
[3] a) N. R. Neale, T. D. Tilley, *J. Am. Chem. Soc.* **2002**, *124*, 3802–3803; b) N. R. Neale, T. D. Tilley, *Tetrahedron* **2004**, *60*, 7247–7260; c) N. R. Neale, T. D. Tilley, *J. Am. Chem. Soc.* **2005**, *127*, 14745–14755.
[4] a) N. Etkin, M. C. Fermin, D. W. Stephan, *J. Am. Chem. Soc.* **1997**, *119*, 2954–2955; b) M. C. Fermin, D. W. Stephan, *J. Am. Chem. Soc.* **1995**, *117*, 12645–12646; c) V. P. W. Böhm, M. Brookhart, *Angew. Chem.* **2001**, *113*, 4832–4834; *Angew. Chem. Int. Ed.* **2001**, *40*, 4694–4696.
[5] C. A. Jaska, I. Manners in *Inorganic Chemistry in Focus II* (Eds: G. Meyer, D. Naumann, L. Wesemann), Wiley-VCH, Weinheim, **2005**, pp. 53–64.
[6] a) Primary stibine $dmpSbH_2$ is novel; synthesis of $MesSbH_2$ has been reported recently: H. J. Breunig, M. E. Ghesner, E. Lork,

 © 2006 Wiley-VCH Verlag GmbH & Co. KGaA, Weinheim

Z. Anorg. Allg. Chem. **2005**, *631*, 851 – 856; b) M. Ates, H. J. Breunig, A. Soltani-Neshan, M. Z. Tegeler, *Z. Naturforsch. B* **1986**, *41*, 321 – 326; c) B. Twamley, C. D. Sofield, M. M. Olmstead, P. P. Power, *J. Am. Chem. Soc.* **1999**, *121*, 3357 – 3367.

[7] a) K. Issleib, A. Balszuweit, *Z. Anorg. Allg. Chem.* **1975**, *418*, 158 – 166; b) K. Issleib, A. Balszuweit, *Z. Anorg. Allg. Chem.* **1976**, *419*, 87 – 91.

[8] F. A. Cotton, G. Wilkinson, C. A. Murillo, M. Bochmann, *Advanced Inorganic Chemistry*, 6th ed., Wiley, New York, **1999**, p. 88.

[9] T. Sasamori, Y. Arai, N. Takeda, R. Okazaki, N. Tokitoh, *Chem. Lett.* **2001**, 42 – 43.

[10] H.-G. Woo, J. F. Walzer, T. D. Tilley, *J. Am. Chem. Soc.* **1992**, *114*, 7047 – 7055.

[11] Crystal structure analysis of **6**: $C_{39}H_{45}ClHfSb$, $M_r = 849.44$, triclinic, $P\bar{1}$, $a = 9.070(2)$, $b = 11.309(2)$, $c = 18.282(3)$ Å, $\alpha = 83.691(4)$, $\beta = 80.809(3)$, $\gamma = 71.477(3)°$, $V = 1751.7(5)$ Å^3, $Z = 2$, $\rho = 1.611$ g cm^{-3}, $\mu = 3.833$ mm^{-1}, $F(000) = 838$, $\theta = 1.13$–$26.39°$. Final $R1 = 5.20\,\%$, $wR2 = 11.55\,\%$, GOF = 0.963 for 379 parameters and 11 448 reflections (of which 6913 with $I > 2\sigma(I)$), max positive and negative peaks in DF map 3.777 and -1.298 e Å^{-3}. Data were collected at 163(2) K Bruker Platform goniometer ($Mo_{K\alpha}$ radiation, 0.71073 Å) equipped with a CCD detector (Smart Apex). A Patterson search was used to locate the Hf and Sb atoms; all non-H atoms were converted and refined anisotropically. Hydrogen atoms were refined isotropically, fixed at calculated positions. Despite large residual electron density proximal to the Sb center, a stable hydrogen atom could not be refined at that location. CCDC-285852 contains the supplementary crystallographic data for this paper. These data can be obtained free of charge from The Cambridge Crystallographic Data Centre via www.ccdc.cam.ac.uk/data_request/cif.

[12] G. I. Nikonov, L. G. Kuzmina, J. A. K. Howard, *Organometallics* **1997**, *16*, 3723 – 3725.

[13] R. T. Baker, J. F. Whitney, S. S. Wreford, *Organometallics* **1983**, *2*, 1049 – 1051.

 © 2006 Wiley-VCH Verlag GmbH & Co. KGaA, Weinheim

Organic Oxidants

DOI: 10.1002/anie.200504156

o-Iodoxybenzoic Acid (IBX): pK_a and Proton-Affinity Analysis **

*Michael J. Gallen, Régis Goumont, Timothy Clark, François Terrier, and Craig M. Williams**

o-Iodoxybenzoic acid (IBX; **1**)[1,2] is an important oxidant in organic synthesis owing to the landmark contributions by

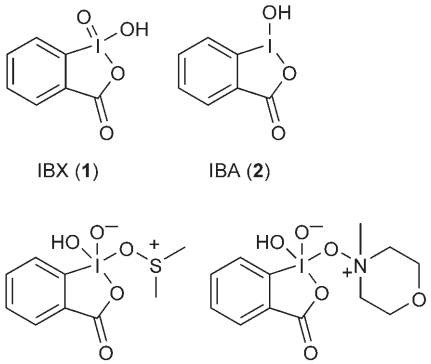

Nicolaou et al.[3–11] Some stunning examples include benzylic oxidation,[7,8] dehydrogenation of carbonyls and alcohols to α,β-unsaturated enones,[3,4,7] and cyclic amination.[6,9–11] Since then, the synthetic community has witnessed many new oxidation-based applications of this reagent by the Nicolaou group and others; examples include the conversions of amines into imines,[12,13] of dithioketals,[12–14] dithioacetals,[12–14] and oximes[15] into ketones and aldehydes, of alcohols into esters,[16] as well as oxidative 1,3-transpositions,[17] aromatizations,[18] and demethylations.[19]

[*] M. J. Gallen, Dr. C. M. Williams
School of Molecular and Microbial Sciences
University of Queensland
Brisbane, 4072, Queensland (Australia)
Fax: (+61) 733-654-299
E-mail: c.williams3@uq.edu.au
R. Goumont, Prof. F. Terrier
Institut Lavoisier-Franklin
Université de Versailles
45 avenue des Etats Unis, 78035 Versailles cedex (France)
Prof. T. Clark
Computer-Chemie-Centrum
Friedrich-Alexander-Universität Erlangen-Nürnberg
Nägelsbachstrasse 25, 91052 Erlangen (Germany)

[**] We thank the University of Queensland and the Université de Versailles for financial support.

Supporting information for this article is available on the WWW under http://www.angewandte.org or from the author.

© 2006 Wiley-VCH Verlag GmbH & Co. KGaA, Weinheim

There are other IBX-mediated processes, however, that are oxidative transformations only in part, for example, the one-pot conversion of tetrahydropyranyl (THP) ethers **5** into aldehydes/ketones **6**[20] and of silyl enol ethers **7** into enones **8**[5] (Scheme 1). Considering these processes and the observation in our own laboratories that IBX unexpectedly converted ketone **9** into bicycle **10**[21] (Scheme 1), we investigated the possibility that IBX may exhibit physical properties of note (other than oxidant and explosive[1b,13,22]).

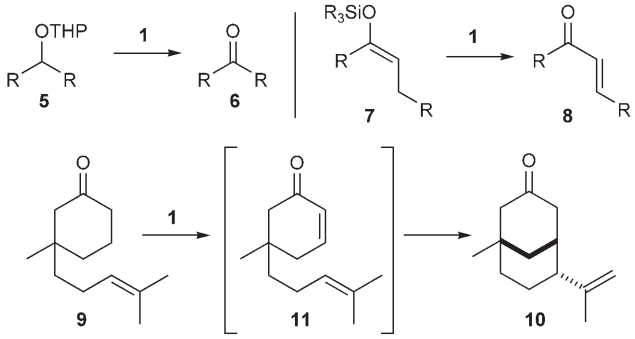

Scheme 1. IBX-mediated processes that are oxidative transformations only in part.

Given that both **5** and **7** are acid-sensitive, and that the formation of **10** can be prevented by using IBX·NMO (**4**; NMO = *N*-methylmorpholine *N*-oxide), which instead affords **11**,[23] we investigated the acidity of IBX. Even though its chemical name *o*-iodoxybenzoic acid implies that this molecule must display a certain level of Brønsted acidity, in fact no such information has been reported or considered in the literature.[24]

A computational study of acidity (proton affinity) at the PW91/dnp and B3LYP/LANL2dz + p levels[25] were performed on IBX in the first instance, although the oxidative by-product 2-iodosobenzoic acid (IBA; **2**) (from the one-step reduction of **1**) and the more active oxidant **4** were also compared. Furthermore, because both IBX and IBA can exist in two tautomeric forms (**12** and **13** (IBX), **14** and **15** (IBA); Scheme 2), an understanding of their operating structures was required.

Geometry optimizations were performed starting from deprotonated forms derived from the optimized structures of the two tautomers **12**–**15**, and this led to a single anion for both IBX and IBA (**16** and **17**, respectively), both of which have a partially opened five-membered ring at the I–O3 bond (Supporting Information). The calculated gas-phase proton affinity for deprotonated IBX **16** (337 kcal mol^{-1}) is quite close to the experimental value for dichloroactetate (328 kcal mol^{-1}).[26–28] Deprotonated IBA **17** has an almost identical calculated gas-phase proton affinity to **16** at the B3LYP/LANL2dz + p level, but IBA is calculated to be a weaker acid than IBX at the PW91/dnp level. The acidities in aqueous solution were estimated by using standard SCRF-PCM calculations[30] with default settings for Gaussian 03. They gave a calculated energy change in aqueous solution for the proton-exchange reaction $CHCl_2COO^- + \mathbf{1} \rightarrow CHCl_2COOH + \mathbf{16}$ of only 0.52 kcal mol^{-1}, which, when combined with the pK_a value of dichloroacetate in water (1.26), gave an estimated aqueous pK_a value for IBX of roughly 1.6.

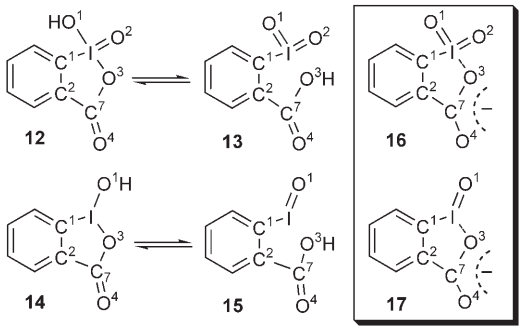

Scheme 2. Calculated structures for deprotonated IBX and IBA.

Complexation of IBX (e.g. **3**) or IBA with dimethyl sulfoxide (DMSO) (gas-phase proton affinities of **16**·DMSO and **17**·DMSO are both 327 kcal mol^{-1}) makes both compounds stronger acids, as does complexation with NMO, although the latter has a larger effect for IBX (gas-phase proton affinity of **16**·NMO = 326 kcal mol^{-1}) than for IBA (**17**·NMO 328 kcal mol^{-1}). Notably, the COOH tautomers of both IBX and IBA (**13** and **15**, respectively) are stabilized by complexation with DMSO and to a lesser extent with NMO, but in both cases this stabilization is not large enough to make them the more stable of the two tautomers.

Solution-phase acidity determinations were performed in both aqueous media and DMSO. An aqueous pK_a value of 2.40 for IBX was obtained by using standard potentiometric titration methods. Determining a pK_a value for IBX in DMSO (i.e. **3**) was much more difficult as potentiometric measurements[31] proved unsuitable. Furthermore, as the ionization of IBX does not induce absorbance changes in the UV/Vis spectral region, buffers formed from the appropriate colorless amine, carboxylic acid, or phenol were not used to determine pK_a values spectrophotometrically because an excessively large number of potential buffers could be envisioned.[32,33] However, in keeping with the indicator strategy, the alternative approach of measuring the pH value of IBX buffer solutions with reference to suitable indicators of known $pK_a^{Me_2SO}$ values was pursued.

Considering the acidity of IBX in water ($pK_a^{H_2O} = 2.40$) and the well-known fact that the acidity of oxygen acids[34–37] strongly decrease on going from water to DMSO (e.g. the pK_a value of acetic acid is 4.75 in water and 12.3 in DMSO[33]), we anticipated that the change in solvent would increase the $pK_a^{Me_2SO}$ value of IBX by at least 5 pK_a units.[34–37] The ionization of 2,4-dinitrophenol (**18**; Scheme 3) ($pK_a^{Me_2SO} = 5.12$)[33] in a 1:1 IBX buffer ([IBX] = [IBX$^-$] = 0.012 M) was therefore investigated.

The resulting UV/Vis spectrum was identical to that obtained in a 1:1 1,4-diazabicyclo[2.2.2]octane (DABCO) buffer ([DABCO] = [DABCOH$^+$] = 0.012 M; pH = 9.06), leaving no doubt that the 1:1 IBX buffer is sufficiently basic to allow complete ionization of **18**, that is, $pK_a^{IBX} \geq 6.6$. 4-Nitrobenzyltriflone (**19**; pK = 9.46)[37a] was similarly studied in a 1:1 IBX buffer to obtain an upper limit for pK_a^{IBX}. In this

 © 2006 Wiley-VCH Verlag GmbH & Co. KGaA, Weinheim

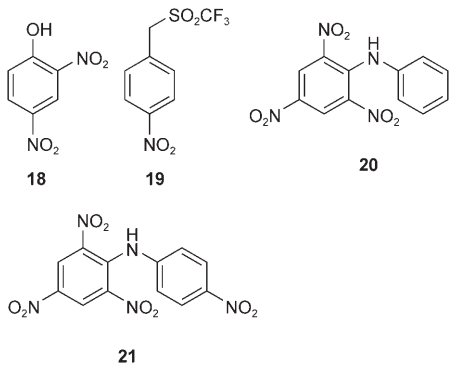

Scheme 3. UV/Vis spectral indicators used herein.

case, no appreciable development of the absorbance of the carbanion of **19** ($\lambda_{max} = 475$ nm) was observed, suggesting that $pK_a^{IBX} \leq 8$. Based on the two limits above, two indicators were selected to determine accurately the $pK_a^{Me_2SO}$ value of IBX, namely, 2,4,6-trinitrodiphenylamine (**20**; $pK_a^{Me_2SO} = 8.01$) (Figure 1) and 4′,2,4,6-tetranitrodiphenylamine (**21**; $pK_a^{Me_2SO} = 6.07$) (Figure 2).[32]

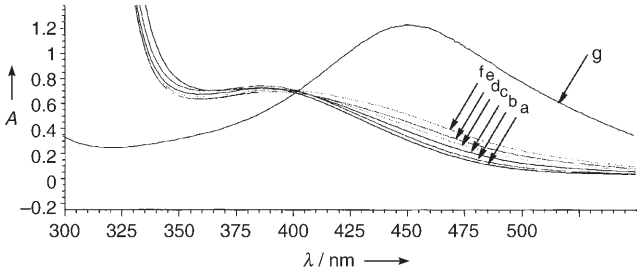

Figure 1. Ionization of **20** ($pK_a = 8.01$) in DMSO:[38] a) to f) refer successively to 1:2, 1:1, 2:1, 3:1, 4:1, and 5:1 IBX buffers; g) 1:1 butylamine buffer ($pK_a = 11.12$).

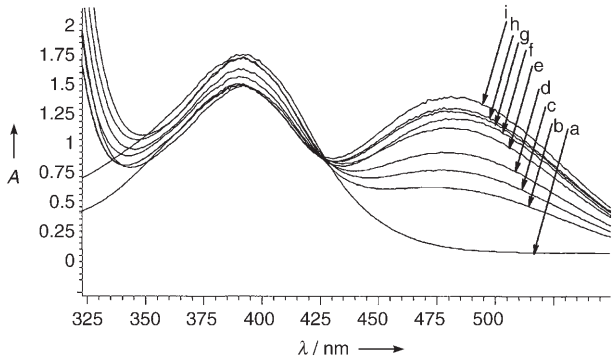

Figure 2. Ionization of **21** ($pK_a = 6.07$) in DMSO:[38] a) 0.1 M CF_3SO_3H; b) to h) refer successively to 1:4, 1:3, 1:2, 1:1, 2:1, 3:1, and 4:1 IBX buffers; i) 1:1 DABCO buffer ($pK_a = 9.06$).

Pronounced variations in the visible absorption of **21** (Figure 2) were observed in progressing along the buffer series with a nearly complete conversion of this substrate into the conjugate base of **21** in the most basic buffer used. The absorbance of the conjugate base of **21** in its pure form (A_{21^-}) was measured with a 1:1 DABCO buffer (pH = 9.06). From the pK_a value of **21** and the observed variations in the $\frac{[21^-]}{[21]}$ ratio calculated as $\frac{A-A_{21}}{A_{21^-}-A}$, the pH values of each of the IBX buffer solutions were readily obtained [Eq. (1)]. From these pH

$$pH = pK_a^{21} + \log\frac{[21^-]}{[21]} = pK_a^{5} + \log\frac{A-A_{21}}{A_{21^-}-A} \quad (1)$$

values, the pK_a of IBX·DMSO was then calculated at each pH value [Eq. (2)]. This resulted in an average pK_a^{IBX} of 6.65 ± 0.05 (Supporting Information). Even though the ionization of **20** was far from complete in the most basic IBX buffer employed, a similar p*K*a value (6.78 ± 0.1) was derived from the analysis of the absorbance variations observed for this indicator along the IBX buffer series (Figure 1 and Supporting Information). However, the observed consistency between the two pK_a^{IBX} values obtained provides evidence that the measurements in DMSO are not appreciably affected by side phenomena such as homoconjugation.[34,39,40]

$$pK_a^{IBX} = pH - \log\frac{[IBX^-]}{[IBX]} \quad (2)$$

Extensive studies of solvent effects on the acidity of common oxygen acids such as carboxylic acids, phenols, oximes, or nitronic acids have shown that the transition from water to DMSO decreases the acidity markedly.[32–37,41,42] The pK_a values of acetic acid and benzoic acid are 4.75 and 4.19, respectively, in water at 25 °C,[43] but 12.3 and 11, respectively, in pure DMSO.[33] Similarly, the pK_a of phenol increases from 9.89 in water to 18.0 in DMSO.[33,43] This effect of changing from water to DMSO has long been attributed to a decrease in the stability of the conjugate oxyanionic structures owing to the loss of favorable hydrogen-bonding solvation.[33,35–37,41,42] In this context, the increase observed in the pK_a value of IBX from water to DMSO was to be expected. However, this increase amounts to ≈4 p*K* units, which represents a rather moderate change relative to a common reference such as acetic acid ($\Delta pK_a = 7.5$). Within a family of structurally similar oxyacids, the solvent effect has been found to be a function of the acidity in aqueous solution.[37,41] For example, the pK_a value of dichloroacetic acid is 1.48 in water[43] and 6.4 in DMSO,[33] that is, $\Delta pK_a = 4.9$, versus $\Delta pK_a = 7.5$ for acetic acid. Similar increases in $\Delta pK_a = pK_a^{Me_2SO} - pK_a^{H_2O}$ with increasing $pK_a^{H_2O}$ values have been found in phenol and oxime systems and accounted for in terms of an increased hydrogen-bonding solvation of the oxyanions with increasing basicity.[37,44] The greater the $pK_a^{H_2O}$, the greater will be the stabilization of the oxyanions by hydrogen-bonding solvation in aqueous solution, and hence the greater will be the destabilization of these species on going to DMSO. Based on these arguments, the 4-p*K*-unit decrease in acidity of IBX from water to DMSO seems in order, especially in comparison to that of similarly acidic systems (i.e. dichloroacetic acid) in aqueous solution.

What impact does the acidity of IBX have on the currently accepted mechanism of oxidation reactions? In direct one-step oxidation processes the current mechanism is unaltered. However, in stepwise processes (one-pot, two or more steps)

 © 2006 Wiley-VCH Verlag GmbH & Co. KGaA, Weinheim

such as the conversion of THP ethers **5** into aldehydes/ketones **6**, an acid-catalyzed conversion into the alcohol **22** followed by oxidation to the aldehyde/ketone **6** is now very likely the case. In fact, THP ether hydrolysis (acid cat.) in the presence of IBX (i.e. **23**→**24**; Scheme 4) was observed by Rao and co-workers,[20] but was, we believe, incorrectly attributed to the presence of β-cyclodextrin.

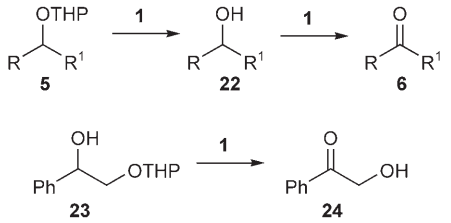

Scheme 4. IBX-catalyzed THP deprotection.

In our case it would seem that IBX performs the expected dehydrogenation of ketone **9** to give enone **11**, which then undergoes an acid-catalyzed ene reaction to afford **10** (Scheme 5). However, in the case of **7**→**8** (Scheme 6), it is very difficult to appreciate the effect that IBX acidity has on this reaction, for example, protolysis to ketone **25**, mainly because silyl enol ethers are so notoriously susceptible to protolysis by strong or weak acids.

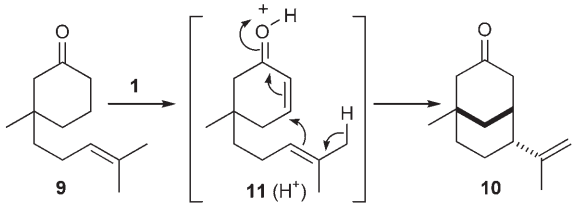

Scheme 5. IBX-catalyzed ene reaction.

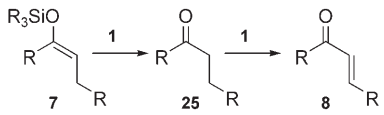

Scheme 6. IBX dehydrogenation of silylenol ethers.

What impact does the acidity of IBX have on synthetic utility? In most cases the acidity of IBX (or IBA) has no adverse effects on substrate or product as demonstrated in the current literature. Considering, however, that **4** prevents the ene reaction (Scheme 5; giving **11** as the sole product) in cases in which the substrate or product may be acid-sensitive, for example, when certain protecting groups are present, we would recommend the use of **4** instead of **1** or **3**.[45]

In conclusion, the pK_a value and proton affinity of IBX has been determined by in silico (337 kcal mol^{-1}) and in vitro ($pK_a^{H_2O} = 2.40$, $pK_a^{Me_2SO} = 6.65$) methods, which suggest that IBX has an acidity in water similar to that of 2-nitrobenzoic acid ($pK_a^{H_2O} = 2.18$) and an acidity in DMSO similar to that of dichloroacetic acid ($pK_a^{Me_2SO} = 6.4$), thus implying that **1** and **3** are relatively acidic on the organic scale. This knowledge should aid those wishing to utilize this important suite of hyperiodine reagents **1**–**4** in future synthetic transformations.

Experimental Section

Calculations: Geometries were initially optimized[46] with Dmol^3 using the dnp basis set[47] with DFT semi-core pseudopotentials[47,48] and the Perdew 91 (P91) exchange and correlation functionals.[49] The geometries thus obtained were employed as starting points for optimizations with Gaussian 03[50] using the LANL2dz basis set[51] and Los Alamos pseudopotentials[52] augmented with a set of polarization functions.[53] All LANL2dz calculations used the hybrid B3LYP functional,[54] which includes contributions from Hartree–Fock exchange with Becke[55] and Vosko, Wilk, and Nusair (VWN)[56] exchange functionals and the Lee, Yang, Parr (LYP) correlation functional.[57] The structures obtained at the B3LYP/LANL2dz + p level were confirmed to be local minima by the calculation of their normal vibrations within the harmonic approximation.

Aqueous titrations of IBX[1b] (**1**) were carried out on a Metrohm 796 Titroprocessor with an Ionode IJ44 pH electrode containing a saturated KCl gel. The pH potentiometric titrations were made on solutions in a double-walled glass vessel maintained at 25.1 ± 0.1 °C with an external water heater. Nitrogen was bubbled through the solution to maintain an inert atmosphere. Efficient stirring of the solution was obtained with a magnetic stirrer. The instrument was standardized against standard buffers of pH 4.00, 7.00, and 10.00 from Biolab with adjustments made for temperature. This standardization procedure was repeated before each experiment, and a slope of 0.95–1.00 was required from the Metrohm program for the Nernstian plot before titration could proceed. Calibration was performed by titration of Et_4NClO_4 (0.1 M) in $HClO_4$ (6 mM) with Et_4NOH (0.096 M). A plot of potential against pH provided a slope of −58.9 mV, close to the expected theoretical value of −59.1 mV. The $E°$ and pK_w values were obtained for each aqueous titration and used in the pK_a calculations, as they deviated from those of pure water. The titration curves were fitted with the TITFIT program.[58]

Titrations of IBX in DMSO: The procedure described by Bordwell[33] and Crampton and Robotham[32] was used to determine spectrophotometrically the pK_a of IBX with reference to the various selected indicators. UV/Vis spectra were taken on an HP 8453 spectrophotometer at 25 ± 0.2 °C. DABCO and **18** of the highest quality available commercially were used and were not purified. Butylamine was distilled prior to use, whereas **21**,[59] **19**,[37a] and **20**[60] were prepared as reported. DMSO was heated at reflux over calcium hydride, distilled, and the fractions at 32–35 °C (under 2-mmHg pressure) were collected and stored under argon. All solutions of indicators and IBX were freshly prepared in a glove box under argon. We generated all the IBX buffers by adding DABCO to the appropriate parent IBX solution, such that the molarity of the base component (IBX^-) was always 0.012 M. Butylamine and DABCO buffers (1:1) were made by the introduction of trifluoromethanesulfonic acid to generate the required concentration (0.012 M) of the acid forms.

Received: November 22, 2005
Published online: March 27, 2006

Keywords: acidity · density functional calculations · *o*-iodoxybenzoic acid · oxidation · proton affinity

 © 2006 Wiley-VCH Verlag GmbH & Co. KGaA, Weinheim

[1] a) C. Hartman, V. Meyer, *Ber. Dtsch. Chem. Ges.* **1893**, *26*, 1727; b) M. Frigerio, M. Santagostino, S. Sputore, *J. Org. Chem.* **1999**, *64*, 4537; c) A. R. Katrizky, B. L. Duell, J. K. Gallos, *Magn. Reson. Chem.* **1989**, *27*, 1007.

[2] For selected reviews, see: a) T. Wirth, U. H. Hirt, *Synthesis* **1999**, 1271; b) T. Wirth, *Angew. Chem.* **2001**, *113*, 2893; *Angew. Chem. Int. Ed.* **2001**, *40*, 2812; c) A. Varvoglis, S. Spyroudis, *Synlett* **1998**, 221; d) T. Kitamura, Y. Fujiwara, *Org. Prep. Proced. Int.* **1997**, *29*, 409; e) P. J. Stang, V. V. Zhdankin, *Chem. Rev.* **1996**, *96*, 1123; f) R. M. Moriarty, R. K. Vaid, *Synthesis* **1990**, 431; g) *Hypervalent Iodine in Organic Synthesis* (Ed.: A. Varvoglis), Academic Press, San Diego, **1996**, p. 256.

[3] K. C. Nicolaou, Y.-L. Zhong, P. S. Baran, *J. Am. Chem. Soc.* **2000**, *122*, 7596.

[4] K. C. Nicolaou, T. Montagnon, P. S. Baran, *Angew. Chem.* **2002**, *114*, 1035; *Angew. Chem. Int. Ed.* **2002**, *41*, 993.

[5] K. C. Nicolaou, D. L. F. Gray, T. Montagnon, S. T. Harrison, *Angew. Chem.* **2002**, *114*, 1038; *Angew. Chem. Int. Ed.* **2002**, *41*, 996.

[6] K. C. Nicolaou, P. S. Baran, Y.-L. Zhong, S. Barluenga, K. W. Hunt, R. Kranich, J. A. Vega, *J. Am. Chem. Soc.* **2002**, *124*, 2233.

[7] K. C. Nicolaou, T. Montagnon, P. S. Baran, Y.-L. Zhong, *J. Am. Chem. Soc.* **2002**, *124*, 2245.

[8] K. C. Nicolaou, P. S. Baran, Y.-L. Zhong, *J. Am. Chem. Soc.* **2001**, *123*, 3183.

[9] K. C. Nicolaou, Y.-L. Zhong, P. S. Baran, *Angew. Chem.* **2000**, *112*, 639; *Angew. Chem. Int. Ed.* **2000**, *39*, 625.

[10] K. C. Nicolaou, P. S. Baran, R. Kranich, Y.-L. Zhong, K. Sugita, N. Zou, *Angew. Chem.* **2001**, *113*, 208; *Angew. Chem. Int. Ed.* **2001**, *40*, 202.

[11] K. C. Nicolaou, P. S. Baran, Y.-L. Zhong, J. A. Vega, *Angew. Chem.* **2000**, *112*, 2625; *Angew. Chem. Int. Ed.* **2000**, *39*, 2525.

[12] K. C. Nicolaou, C. J. N. Mathison, T. Montagnon, *Angew. Chem.* **2003**, *115*, 4211; *Angew. Chem. Int. Ed.* **2003**, *42*, 4077.

[13] K. C. Nicolaou, C. J. N. Mathison, T. Montagnon, *J. Am. Chem. Soc.* **2004**, *126*, 5192.

[14] N. S. Krishnaveni, K. Surendra, Y. V. D. Nageswar, K. R. Rao, *Synthesis* **2003**, 2295.

[15] N. S. Krishnaveni, K. Surendra, Y. V. D. Nageswar, K. R. Rao, *Synthesis* **2003**, 1968.

[16] A. Giannis, A. Schultz, *Adv. Synth. Catal.* **2004**, *346*, 252.

[17] M. Shibuya, S. Ito, M. Takahashi, Y. Iwabuchi, *Org. Lett.* **2004**, *6*, 4303.

[18] S. Kotha, S. Banerjee, K. Mandal, *Synlett* **2004**, 2043.

[19] A. Ozanne, L. Pouységu, D. Depernet, B. François, S. Quideau, *Org. Lett.* **2003**, *5*, 2903.

[20] M. Narender, M. S. Reddy, V. P. Kumar, Y. V. D. Nageswar, K. R. Rao, *Tetrahedron Lett.* **2005**, *46*, 1971.

[21] Bicycle **10** is structurally similar to the core of spirovibsanin A: M. Kubo, T. Fujii, H. Hioki, M. Tanaka, K. Kawazu, Y. Fukuyama, *Tetrahedron Lett.* **2001**, *42*, 1081; our work towards the total synthesis of spirovibsanin A will be reported in due course.

[22] a) J. B. Plumb, D. J. Harper, *Chem. Eng. News* **1990**, *68*, 3; b) R. E. Ireland, L. Liu, *J. Org. Chem.* **1993**, *58*, 2899.

[23] a) R. Heim, S. Wiedemann, C. M. Williams, P. V. Bernhardt, *Org. Lett.* **2005**, *7*, 1327; b) D. P. Tilly, C. M. Williams, P. V. Bernhardt, *Org. Lett.* **2005**, *7*, 5155.

[24] The structure and acidity of IBA have been discussed in reference [2e]; see also: R. A. Moss, K. W. Alwis, G. O. Bizzigotti, *J. Am. Chem. Soc.* **1983**, *105*, 681; IBX ligand-exchange calculations were recently reported: J. T. Su, W. A. Goddard III, *J. Am. Chem. Soc.* **2005**, *127*, 14146.

[25] The suitability of this level of theory was tested by the calculation of the gas-phase proton affinity of dichloroacetate. The calculated value (328.2 kcal mol^{-1}, including zero-point energy correction) is remarkably close to the experimental values of 328.4 ± 2.1,[26] 327.3 ± 2.1,[27] and 328.4 ± 2.6 kcal mol^{-1}.[28] As expected, the calculated value decreases to 318.6 kcal mol^{-1} upon inclusion of standard diffuse functions[29] in the basis set. Thus, although diffuse functions clearly help describe the anion better, results similar to experimental values can be obtained without them. In the following discussion, the B3LYP/LANL2dz + p results with zero-point energy corrections will be used. The PW91 calculations for the DMSO and NMO complexes suffer from the known weakness of PW91 in describing hydrogen bonds and overestimate the stability of direct interactions with the iodine.

[26] J. B. Cumming, P. Kebarle, *Can. J. Chem.* **1978**, *56*, 1.

[27] M. Fujio, R. T. McIver, Jr., R. W. Taft, *J. Am. Chem. Soc.* **1981**, *103*, 4017.

[28] G. W. Caldwell, R. Renneboog, P. Kebarle, *Can. J. Chem.* **1989**, *67*, 611–618.

[29] T. Clark, J. Chandrasekhar, G. W. Spitznagel, P. von R. Schleyer, *J. Comput. Chem.* **1983**, *4*, 294.

[30] V. Barone, M. Cossi, J. Tomasi, *J. Chem. Phys.* **1997**, *107*, 3210.

[31] a) C. D. Ritchie, R. E. Uschold, *J. Am. Chem. Soc.* **1967**, *89*, 1721; b) W. S. Matthews, J. E. Bares, J. E. Bartmess, F. G. Bordwell, F. J. Cornforth, G. E. Drucker, Z. Margolin, R. J. McCallum, G. J. McCollum, N. R. Vanier, *J. Am. Chem. Soc.* **1975**, *97*, 7006.

[32] M. R. Crampton, I. A. Robotham, *J. Chem. Res. (S)* **1997**, 22.

[33] F. G. Bordwell, *Acc. Chem. Res.* **1988**, *21*, 456.

[34] J. C. Hallé, R. Gaboriaud, R. Schaal, *Bull. Soc. Chim. Fr.* **1970**, 2047.

[35] a) A. J. Parker, *Chem. Rev.* **1969**, *69*, 1; b) E. Buncel, H. Wilson, *Adv. Phys. Org. Chem.* **1977**, *14*, 133; c) C. D. Ritchie in *Solute–Solvent Interactions* (Eds.: J. F. Coetzee, C. D. Ritchie), Dekker, New-York, **1966**, p. 216; d) C. Reichardt, *Solvents and Solvent Effects in Organic Chemistry*, VCH, Weinheim, **1988**, chap. 4.

[36] F. Terrier, G. Moutiers, L. Xiao, E. Le Guével, F. Guir, *J. Org. Chem.* **1995**, *60*, 1748.

[37] a) F. Terrier, E. Kizilian, R. Goumont, N. Faucher, C. Wakselman, *J. Am. Chem. Soc.* **1998**, *120*, 9496; b) R. Goumont, E. Magnier, E. Kizilian, F. Terrier, *J. Org. Chem.* **2003**, *68*, 6566; c) F. Terrier, E. Magnier, E. Kizilian, C. Wakselman, E. Buncel, *J. Am. Chem. Soc.* **2005**, *127*, 5563.

[38] For the UV/Vis spectra in Figures 1 and 2, the observed variations at $\lambda < 350$–380 nm have no significance as they reflect the absorbance of the IBX buffer.

[39] a) F. G. Bordwell, R. J. McCallum, W. N. Olmstead, *J. Org. Chem.* **1984**, *49*, 1424–1427; b) I. M. Kolthoff, M. K. Chantooni, Jr., S. Bhowmik, *J. Am. Chem. Soc.* **1968**, *90*, 23–28.

[40] Although homoconjugation (i.e. homohydrogen bonding of the type AH + A$^-$ → AHA$^-$) can complicate acidity measurements of oxygen or nitrogen acids in dipolar aprotic solvents,[31–35,39] the impact of this association depends on the solvent; for example, homoconjugation is weaker in DMSO than in acetonitrile. Conversely, the phenomenon is strongly related to the acidity of the AH/A$^-$ pair; it occurs, for example, to a much greater extent for weakly acidic carboxylic acids or phenols (association constants of 11000 and 4000 have been measured for phenol ($pK_a = 18$) and benzoic acid ($pK_a = 11.1$) in DMSO) than for relatively acidic oxygen acids. As there is no such association detected for phenols (i.e. 2,6-dinitrophenol ($pK_a = 4.9$) or 4-chloro-2,6-dinitrophenol ($pK_a = 3.6$)) in DMSO,[39b] the contribution of homoconjugation to the IBX system can only be minor.

[41] a) C. F. Bernasconi, P. Paschalis, *J. Am. Chem. Soc.* **1986**, *108*, 2969; b) C. F. Bernasconi, *Adv. Phys. Org. Chem.* **1992**, *27*, 119; c) C. F. Bernasconi, D. A. V. Kliner, A. S. Mullin, J. X. Ni, *J. Org. Chem.* **1988**, *53*, 3342.

[42] M. Laloi-Diard, J. F. Verchère, P. Gosselin, F. Terrier, *Tetrahedron Lett.* **1984**, *25*, 1267.

 © 2006 Wiley-VCH Verlag GmbH & Co. KGaA, Weinheim

[43] Data taken from: Handbook of Chemistry and Physics, 51st ed., CRC, Cleveland, **1970–1971**, p. D120.
[44] F. Terrier, P. Rodriguez-Dafonte, E. Le Guével, G. Moutiers, unpublished results.
[45] Iodic acid, a close relative of IBX, was not investigated; however, it has a reported aqueous pK_a value of 0.8. For iodic acid as a reagent, see: K. C. Nicolaou, T. Montagnon, P. S. Baran, *Angew. Chem.* **2002**, *114*, 1444; *Angew. Chem. Int. Ed.* **2002**, *41*, 1386; for the pK_a of iodic acid see: Kolthoff, *Treatise on Analytical Chemistry*, Interscience Encyclopedia, Inc., New York, **1959**.
[46] B. Delley in *Modern Density Functional Theory: A Tool for Chemistry* (Eds.: J. M. Seminario, P. Politzer), Elsevier Science, Amsterdam, **1995**.
[47] B. Delley, *J. Chem. Phys.* **1990**, *92*, 508.
[48] The DSPP pseudopotentials are norm-conserving; D. R. Hamann, M. Schlüter, C. Chiang, *Phys. Rev. Lett.* **1979**, *43*, 1494.
[49] J. P. Perdew, Y. Wang, *Phys. Rev. B* **1992**, *45*, 13244.
[50] Gaussian 03 (Revision A.1), M. J. Frisch, G. W. Trucks, H. B. Schlegel, G. E. Scuseria, M. A. Robb, J. R. Cheeseman, J. A. Montgomery, Jr., T. Vreven, K. N. Kudin, J. C. Burant, J. M. Millam, S. S. Iyengar, J. Tomasi, V. Barone, B. Mennucci, M. Cossi, G. Scalmani, N. Rega, G. A. Petersson, H. Nakatsuji, M. Hada, M. Ehara, K. Toyota, R. Fukuda, J. Hasegawa, M. Ishida, T. Nakajima, Y. Honda, O. Kitao, H. Nakai, M. Klene, X. Li, J. E. Knox, H. P. Hratchian, J. B. Cross, C. Adamo, J. Jaramillo, R. Gomperts, R. E. Stratmann, O. Yazyev, A. J. Austin, R. Cammi, C. Pomelli, J. W. Ochterski, P. Y. Ayala, K. Morokuma, G. A. Voth, P. Salvador, J. J. Dannenberg, V. G. Zakrzewski, S. Dapprich, A. D. Daniels, M. C. Strain, O. Farkas, D. K. Malick, A. D. Rabuck, K. Raghavachari, J. B. Foresman, J. V. Ortiz, Q. Cui, A. G. Baboul, S. Clifford, J. Cioslowski, B. B. Stefanov, G. Liu, A. Liashenko, P. Piskorz, I. Komaromi, R. L. Martin, D. J. Fox, T. Keith, M. A. Al-Laham, C. Y. Peng, A. Nanayakkara, M. Challacombe, P. M. W. Gill, B. Johnson, W. Chen, M. W. Wong, C. Gonzalez, J. A. Pople, Gaussian, Inc., Pittsburgh, PA, **2003**.
[51] T. H. Dunning, Jr., P. J. Hay in *Modern Theoretical Chemistry, Vol. 3* (Ed.: H. F. Schaefer III), Plenum, New York, **1976**, pp. 1–28.
[52] a) P. J. Hay, W. R. Wadt, *J. Chem. Phys.* **1985**, *82*, 270; b) W. R. Wadt, P. J. Hay, *J. Chem. Phys.* **1985**, *82*, 284; c) P. J. Hay, W. R. Wadt, *J. Chem. Phys.* **1985**, *82*, 299.
[53] M. J. Frisch, J. A. Pople, J. S. Binkley, *J. Chem. Phys.* **1984**, *80*, 3265.
[54] A. D. Becke, *J. Chem. Phys.* **1993**, *98*, 5648.
[55] A. D. Becke in *The Challenge of d- and f-Electrons: Theory and Computation* (Eds.: D. R. Salahub, M. C. Zerner), American Chemical Society, Washington, D.C., **1989**, chap. 12, pp. 165–179.
[56] S. H. Vosko, L. Wilk, M. Nusait, *Can. J. Phys.* **1980**, *58*, 1200.
[57] C. Lee, W. Yang, R. G. Parr, *Phys. Rev. B* **1988**, *37*, 785.
[58] A. D. Zuberbühler, T. A. Kaden, *Talanta* **1982**, *29*, 201.
[59] C. F. van Duin, *Recl. Trav. Chim. Pays-Bas* **1919**, *38*, 359.
[60] R. J. W. Le Fèvre, *J. Chem. Soc.* **1931**, 813.

 © 2006 Wiley-VCH Verlag GmbH & Co. KGaA, Weinheim

Nanocomposites

DOI: 10.1002/anie.200504461

Modulation of Viscoelastic Properties of Physical Gels by Nanoparticle Doping: Influence of the Nanoparticle Capping Agent**

Santanu Bhattacharya, Aasheesh Srivastava, and Asish Pal*

Materials in the nanometer regime are of great contemporary interest because of their numerous properties and the various applications envisaged for them.[1] In real-life or high-end applications, these materials are often mixed with other systems to yield new composites that have superior properties compared to those of the constituents. For example, novel composites engineered from polymers and carbon nanotubes (CNTs) offer the promise of plastics with enhanced thermal, electronic, and mechanical properties.[2] Similarly, there are reports of studies on nanoparticles (NPs) embedded in polymers and polymeric gels.[3a] These mixtures exhibit interesting optoelectronic properties, such as temperature-dependent reversible UV/Vis spectral changes, as a result of the controlled and reversible aggregation of the NPs in polymer–NP and dendrimer–NP ensembles.[3b–d] The electron–phonon dynamics of NPs entrapped in polymeric gels have also been studied. Compared to NPs in the solution phase, NPs in such confined media display quite different behavior.[3e] Thus, the design and investigation of these materials is highly important and of significant technological relevance.

Despite the intense interest in composites of polymers and nanotubes, the effects of nanomaterial incorporation into gels based on low-molecular-mass organogelators (LMOGs) have not been explored. Also, the ability to control and quantify particle dispersion in such gels is an unresolved issue of fundamental importance. A molecular-level understanding of the interaction of NPs with molecular gels would be useful for the design of new materials. Hence, we sought to examine whether incorporation of NPs into LMOG-based gels is feasible without disturbing the gelation, and if so, whether the resulting gels have any advantages.

Gels exhibit properties intermediate to those of a Newtonian liquid and a Hookean solid, and hence gels are described as viscoelastic materials. In contrast to polymeric gels, where suitable solvents are retained by the polymer network, the LMOGs self-assemble into fibrous aggregates,

[*] Prof. Dr. S. Bhattacharya, A. Srivastava, A. Pal
Department of Organic Chemistry
Indian Institute of Science
Bangalore 560012 (India)
Fax: (+91) 80-2360-0529
E-mail: sb@orgchem.iisc.ernet.in

[**] This work was supported by DBT and DST. We thank G. Rajesh and Dr. A. K. Sood for access to the rheology facility, and the Materials Research Center and the Institute Nanotechnology Initiative for the TEM and SEM experiments, respectively.

WILEY InterScience DISCOVER SOMETHING GREAT
© 2006 Wiley-VCH Verlag GmbH & Co. KGaA, Weinheim

which results in a meshlike organization that holds the solvent molecules by interfacial tension and supramolecular interaction effects.[4] The self-assembly of fibrillar networks is predominantly through hydrogen-bonding, π–π stacking, or van der Waals interactions.[5] In a few cases charge transfer and ion pairing are also involved.[6] A large variety of sugar and amino acid derivatives are known to rigidify solvents at very low concentrations, sometimes gelling both organic and aqueous media.[7] In rare cases, the gelator molecules may crystallize too, thus giving an insight into the interaction between the gelator and the solvent.[8]

Recently, a thiol-containing organogelator has been synthesized and gold NPs were prepared with this gelator as the capping agent.[9a] Upon solvent evaporation it spontaneously gave fibrous NP assemblies. In another report McPherson et al. described the spatial compartmentalization of CdS NPs into strands of an organogel assembly.[9b] The above findings indicate that the interesting properties of LMOGs can be successfully applied toward templating novel NP composites. Herein, we show the utility of supramolecular gel aggregates for assembling Au NPs, and also discover for the first time the profound influence of the NP capping agent on achieving control over the viscoelastic properties of the resultant composites.

We have previously reported the synthesis and characterization of an efficient gelator based on a fatty acid amide of L-alanine (**1**).[10] Gelator **1** produced stable gels in both aromatic

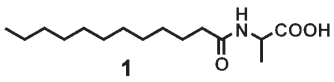

1

and aliphatic hydrocarbons. It also exhibited important properties, such as phase-selective, thermoreversible gelation of a variety of organic solvents, even in the presence of water. We wanted to examine whether monolayer-protected Au NPs can be incorporated in such gels without compromising the gelation manifested by **1**.

To investigate the gel–NP interaction, we selected different kinds of Au NPs. The first set was based on capping agents, for example, *n*-alkanethiols (AuC_{m+2}) where $m = 4$, 6, and 10. The other NPs were coated with either a cholesterol-based thiol (AuChol) or *p*-thiocresol (AuPhMe). These NPs were prepared by a two-phase method.[11] The resulting NPs had an average diameter of (4.5 ± 0.5) to (5.5 ± 0.5) nm for AuC_{m+2}, (6 ± 1) nm for AuPhMe, and (3 ± 0.8) nm for

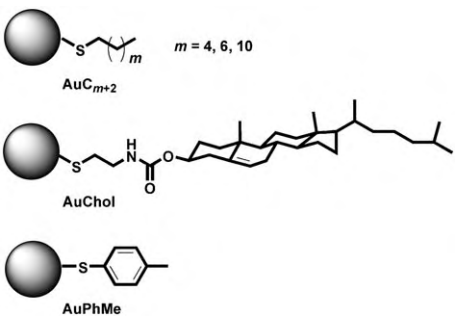

AuChol, as observed by TEM (not shown). Thus, there was a small variation of the NP size with the molecular structure and bulkiness of the capping agent under comparable conditions of NP synthesis. The capping agents also gave structural diversity to the NPs.

We found that even in the presence of the Au NPs, **1** still formed stable gels in both toluene and heptane. It was observed that even at a NP/gelator ratio of 1:1 (w/w), gelation was achievable in a thermoreversible manner. Presumably, this is because the NPs are very small as compared to the gel fibers. X-ray diffraction studies on the gel and gel–NP composites indicate that the gel arrangement is not affected by NP incorporation. The diffraction peaks overlap in all cases (not shown).

TEM images of the Au NPs in toluene (Figure 1a) and in the gel–NP composite indicate that **1** forms onion-like aggregates in toluene. The NPs are embedded on the surface of the gel assembly (Figure 1b), which is clear evidence of NP incorporation into the aggregates formed by **1**.

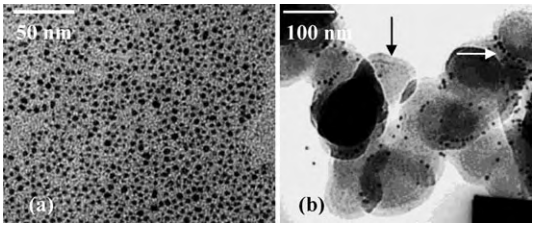

Figure 1. TEM images of AuC_{12} a) as a solution in toluene and b) upon incorporation into gels of **1** in toluene. The black arrow shows the gel aggregate and the white arrow indicates the localization of AuC_{12} on the gel assembly.

Scanning electron microscopy (SEM) of the xerogel and the corresponding gel–NP composites, however, revealed that there was a striking morphological transformation of the gel microstructure on incorporating NPs. Interestingly, the microstructures of the gel–NP composites were dependent on the capping agent on the NPs. The gel in its native state had fibrous assemblies (Figure 2a). When AuC_{12} (2.17 wt%) was incorporated into it, the fibers appeared to coalesce (Figure 2b). This finding is probably a result of interdigitation of the long chains on the NP surface with the gelator molecules within the gel assemblies, which brings the fibers together. Incorporation of AuChol resulted in the formation of "rolled-tubular"-type aggregates (Figure 2c). These aggregates were much larger than the fibers of the native gel, which indicates that the NPs induce further aggregation of the gel fibers. Incorporation of AuPhMe into gels of **1** led to the formation of platelet-like aggregates with a thickness in the range of 1–2 μm (Figure 2d). This result suggests that the interactions of **1** with AuPhMe are not as strong as they are in the case of **1**–AuChol or **1**–AuC_{12} composites.

Long hydrocarbon and cholesteryl moieties are known to stabilize supramolecular aggregates by interdigitation through van der Waals interactions.[12] However, this type of stabilization is not effective when a small, rigid aromatic capping agent is anchored on the NP surface. This is reflected

 © 2006 Wiley-VCH Verlag GmbH & Co. KGaA, Weinheim

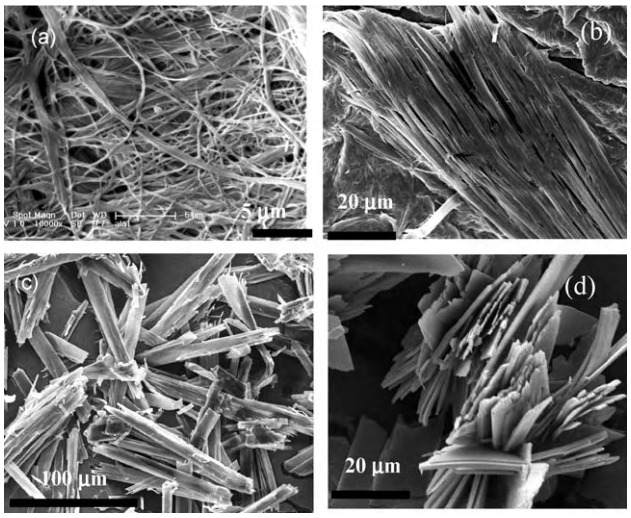

Figure 2. SEM images of xerogels of a) **1**, b) **1**–AuC_{12} composite, c) **1**–AuChol composite, and d) **1**–AuPhMe composite.

in the lower rigidity of the **1**–AuPhMe composite as compared to the other two composites (see below).

The results obtained from TEM and SEM clearly indicate that NPs interact intimately with the gelator molecules inside gels. This finding prompted us to investigate whether the rheology of the gel–NP composites would also be influenced by NP incorporation. Such studies give information about the flow behavior and the rigidity of gels.[13,14] The rheology also indicates the yield stress σ_y, which is the critical applied stress after which the gel starts to flow.[14] Accordingly, the viscoelastic behavior of the native gel and the gel–NP composites was measured. We observed that the gel made in toluene succumbs to the applied stress and begins to flow at about 160 Pa (Figure 3, inset). Incorporation of various NPs into the gel results in the rigidification of the resulting composites (Figure 3). For AuC_{12} the yield stress of the gel–NP composite reaches a maximum at 2.17 wt% of NPs. The maximum yield stress obtained in this case was about 430 Pa. Further incorporation of NPs lowered the yield stress of the composite. Thus, an optimum level of NP incorporation gives the gel maximum rigidity, after which the gel organization becomes perturbed in the accommodation of NPs, and gel rigidity decreases.

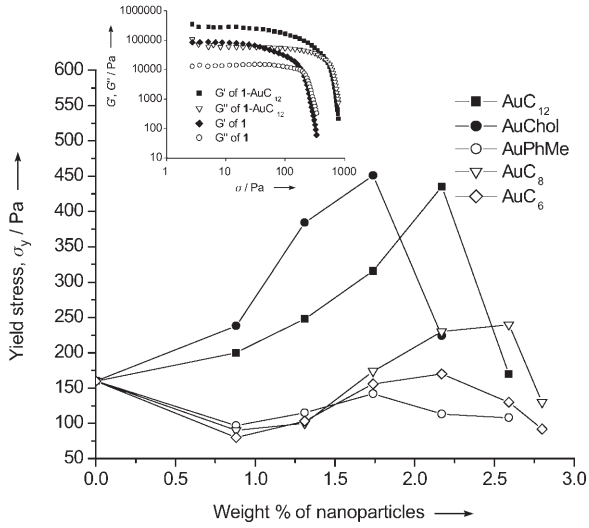

Figure 3. Plots of yield stress versus NP concentration. Inset: plots of storage modulus G' and loss modulus G'' versus stress for a gel of **1** in toluene and a **1**–AuC_{12} composite containing 2.17 wt% of NPs.

Incorporation of NPs coated with smaller chain (hexane and octane) thiols also rigidified the gel, albeit with yield stresses considerably lower than that in the AuC_{12} case. Also, the rigidification achieved by AuC_8 incorporation was greater than that for AuC_6. Clearly the gel rigidity depends critically on the chain length of the alkanethiols attached to the gold surface. In the homologous series of *n*-alkanethiol-based capping agents, the rigidity of AuC_{m+2}–NP composites increases steadily as the chain lengths are increased. This finding suggests chain interdigitation as a possible mechanism of attaining mechanical stability of the resulting composites. In the case of AuChol incorporation, the composite possessed the highest rigidity (ca. 450 Pa) amongst the five **1**–Au NP composites examined. This is probably a consequence of the greater van der Waals interaction area of the inflexible cholesteryl group of AuChol as compared to the *n*-alkyl groups of AuC_{m+2}. This composite also achieved maximal rigidity at a lower weight percentage of NPs (1.74 wt%).

In contrast, when the capping agent on the NPs was changed to a rigid aromatic system like thiocresol, we observed a completely different behavior. The incorporation of even a small amount (0.8 wt%) of AuPhMe made the composite less rigid (140 Pa) than the native gel. An increase in the number of NPs endowed some rigidity to the composite, although even at its maximal rigidity, this composite was still less rigid than the native gel itself. This increase in rigidity is probably a result of incorporation of the hard nanoparticulate material in the sample. A further increase of the NP loading led to a decreased rigidity of the composite, similar to the decrease observed in other cases. In control experiments, inclusion of the corresponding thiols (up to 2.7 wt%) did not lead to any noticeable increase in the gel rigidity. This could be because of random distribution of the thiols in the gel matrix. The chemisorption of thiols on the Au NP surface, however, impacts the gel rigidity quite remarkably. Thus, the capping agent present on the NP surface dictates the interactions of the NPs with the gelator aggregates. Enhanced van der Waals interactions of the gel fibers with sufficiently long alkyl-chain or cholesteryl units on the surface of the NPs collated the gel fibers into close-packed aggregates, which resulted in their greater rigidity as compared to that of the native gel.

It is clear that Au NPs can be very effectively incorporated into LMOG-based gels of **1** without disturbing the gelation properties. The interaction of NPs with **1** is intimately related to the molecular structure of the capping agent anchored on the NP surface. Incorporation of NPs altered the microstructure of the gel aggregate, although gelation was not compromised. The gel fibers became more compact upon incorporation of Au NPs coated with capping agents capable of interdigitation (Scheme 1). This was reflected in the increased mechanical strength of the gel assembly. The

 © 2006 Wiley-VCH Verlag GmbH & Co. KGaA, Weinheim

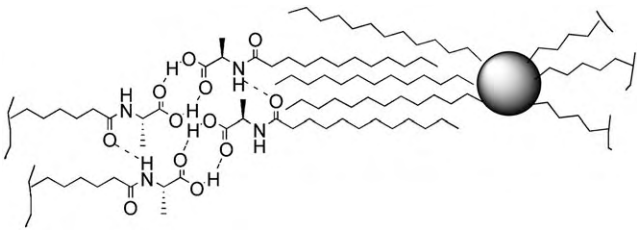

Scheme 1. Schematic illustration of the interaction of AuC_{12} with the gelator assembly.

changes exhibited by these NP additives for relatively low NP concentrations ($\approx$2 wt%) are impressive. We were able to define a relationship between materials and molecular properties by manipulation of the molecular structures of the NP capping agents. Therefore, this method opens up a convenient new path to modulating the properties of such composites.

Experimental Section

Gelation: The resistance of the solvent–gelator mixture toward flow under gravity was used as the test of gelation. Gelator **1** was heated in a water bath at 60°C in a test tube containing a toluene solution of NPs to form a clear sol, which, upon cooling under ambient conditions for 30 min, formed a gel that was stable to inversion of the test tube.

TEM: A toluene solution of NPs (0.1 mg mL^{-1}) was drop-coated on a carbon-coated Cu grid and allowed to dry under ambient conditions. The coating was analyzed in a JEOL 200CX TEM operated at 120 kV. For gel–NP composites, the sample also contained **1** (1 mg mL^{-1}) along with the NPs at same concentration.

SEM: The gel–NP composites were carefully scooped on the brass stubs and were allowed to dry overnight in air. The samples were further dried in a vacuum for 1 h, then coated with gold vapor to make them conducting and analyzed on a Quanta 200 SEM operated at 20 kV.

Rheology: An Anton Paar 100 rheometer with a cone–plate geometry (CP 25-2) was used. The gap distance between the cone and the plate was fixed at 0.05 mm. The native gel in toluene (prepared from 20 mg mL^{-1} of **1**) or composite (containing the requisite number of NPs in addition to **1**) was scooped on the plate of the rheometer. A stress–amplitude sweep experiment was performed at a constant oscillation frequency of 1 Hz for the strain range 0.001 to 100 at 20°C. The rheometer had a built-in computer which converted the torque measurements into either G' (storage modulus) or G'' (loss modulus) in oscillatory shear experiments.

Received: December 15, 2005
Revised: January 20, 2006

Keywords: gels · gold · nanostructures · rheology · supramolecular chemistry

[1] a) M.-C. Daniel, D. Astruc, *Chem. Rev.* **2004**, *104*, 293; b) C.-C. Chen, C.-Y. Tsai, F.-H. Ko, C.-C. Pun, H.-L. Chen, P.-H. Chen, *Jpn. J. Appl. Phys. 1* **2004**, *43*, 3843; c) H. Ahn, A. Chandekar, B. Kang, C. Sung, J. E. Whitten, *Chem. Mater.* **2004**, *16*, 3274; d) C. R. Yonzon, E. Jeoung, S. Zou, G. C. Schatz, M. Mrksich, R. P. Van Duyne, *J. Am. Chem. Soc.* **2004**, *126*, 12669; e) S. Wang, S. Sato, K. Kimura, *Chem. Lett.* **2003**, *32*, 520.

[2] W. C. Yount, D. M. Loveless, S. L. Craig, *Angew. Chem.* **2005**, *117*, 2806; *Angew. Chem. Int. Ed.* **2005**, *44*, 2746.

[3] a) J.-H. Kim, T. R. Lee, *Chem. Mater.* **2004**, *16*, 3647; b) A. K. Boal, B. L. Frankamp, O. Uzun, M. T. Tuominen, V. M. Rotello, *Polym. Prepr.* **2003**, *44*, 699; c) O. Uzun, B. L. Frankamp, V. M. Rotello, *Polym. Prepr.* **2002**, *43*, 419; d) S. Srivastava, B. L. Frankamp, V. M. Rotello, *Chem. Mater.* **2005**, *17*, 487; e) M. Mohammad, T. Ahmadi, S. Link, M. Braun, M. A. El-Sayed, *Chem. Phys. Lett.* **2001**, *343*, 55.

[4] a) F. Fages, F. Vögtle, M. Zinic, *Top. Curr. Chem.* **2005**, *256*, 77; b) M. de Loos, B. L. Feringa, J. H. van Esch, *Eur. J. Org. Chem.* **2005**, 3615; c) J. H. van Esch, B. L. Feringa, *Angew. Chem.* **2000**, *112*, 2351; *Angew. Chem. Int. Ed.* **2000**, *39*, 2263; d) P. Terech, R. G. Weiss, *Chem. Rev.* **1997**, *97*, 3133; e) S. Bhattacharya, U. Maitra, S. Mukhopadhyay, A. Srivastava in *Molecular Gels: Materials with Self-Assembled Fibrillar Networks* (Eds.: R. G. Weiss, P. Terech), Springer, Dordrecht, **2005**.

[5] a) N. Diaz, F.-X. Simon, M. Schmutz, M. Rawiso, G. Decher, J. Jestin, P. J. Mesini, *Angew. Chem.* **2005**, *117*, 3324; *Angew. Chem. Int. Ed.* **2005**, *44*, 3260; b) X. Huang, P. Terech, S. R. Raghavan, R. G. Weiss, *J. Am. Chem. Soc.* **2005**, *127*, 4336; c) H. Ihara, M. Takafuji, T. Sakurai, *Encycl. Nanosci. Nanotechnol.* **2004**, *9*, 473.

[6] a) N. M. Sangeetha, U. Maitra, *Chem. Soc. Rev.* **2005**, *34*, 821; b) A. Srivastava, S. Ghorai, A. Bhattacharjya, S. Bhattacharya, *J. Org. Chem.* **2005**, *70*, 6574; c) F. Camerel, C. F. J. Faul, *Chem. Commun.* **2003**, 1958; d) J. H. Jung, S. J. Lee, J. A. Rim, H. Lee, T.-S. Bae, S. S. Lee, S. Shinkai, *Chem. Mater.* **2005**, *17*, 459; e) U. Beginn, M. Möller, S. Keinath, *Chem. Eng. Commun.* **2005**, *192*, 1116; f) S. J. George, A. Ajoyaghosh, *Chem. Eur. J.* **2005**, *11*, 3217; g) S. Bhattacharya, S. N. G. Acharya, *Chem. Mater.* **1999**, *11*, 3504.

[7] a) D. Inoue, M. Suzuki, H. Shirai, K. Hanabusa, *Bull. Chem. Soc. Jpn.* **2005**, *78*, 721; b) Y. Ji, Y.-F. Luo, X.-R. Jia, E.-Q. Chen, Y. Huang, C. Ye, B.-B. Wang, Q.-F. Zhou, Y. Wei, *Angew. Chem.* **2005**, *117*, 6179; *Angew. Chem. Int. Ed.* **2005**, *44*, 6025; c) S. Bhuniya, S. M. Park, B. H. Kim, *Org. Lett.* **2005**, *7*, 1741; d) N. Brosse, D. Barth, B. Jamart-Gregoire, *Tetrahedron Lett.* **2004**, *45*, 9521; e) V. Caplar, M. Zinic, J.-L. Pozzo, F. Fages, G. Mieden-Gundert, F. Vögtle, *Eur. J. Org. Chem.* **2004**, 4048; f) S. Tamaru, M. Nakamura, M. Takeuchi, S. Shinkai, *Org. Lett.* **2001**, *3*, 3631; g) O. Gronwald, S. Shinkai, *Chem. Eur. J.* **2001**, *7*, 4329.

[8] D. K. Kumar, D. A. Jose, A. Das, P. Dastidar, *Chem. Commun.* **2005**, 4059.

[9] a) M. Kimura, S. Kobayashi, T. Kuroda, K. Hanabusa, H. Shirai, *Adv. Mater.* **2004**, *16*, 335; b) B. Simmons, S. Li, V. T. John, G. L. McPherson, C. Taylor, D. K. Schwartz, K. Maskos, *Nano Lett.* **2002**, *2*, 1037.

[10] a) S. Bhattacharya, Y. K. Ghosh, *Chem. Commun.* **2001**, 185; b) S. Bhattacharya, Y. K. Ghosh, *Chem. Eng. News* **2001**, *79*, 12.

[11] a) M. Brust, M. Walker, D. Bethell, D. J. Schiffrin, R. Whyman, *J. Chem. Soc. Chem. Commun.* **1994**, 801; b) S. Bhattacharya, A. Srivastava, *Langmuir* **2003**, *19*, 4439.

[12] a) M. Giersig, P. Mulvaney, *Langmuir* **1993**, *9*, 3408; b) L. O. Brown, J. E. Hutchison, *J. Phys. Chem. B* **2001**, *105*, 8911; c) R. H. Terrill, T. A. Postlethwaite, C.-H. Chen, C.-D. Poon, A. Terzis, A. Chen, J. E. Hutchison, M. R. Clark, G. Wignall, J. D. Londono, R. Superfine, M. Falvo, C. E. Johnson, Jr., E. T. Samulski, R. W. Murray, *J. Am. Chem. Soc.* **1995**, *117*, 12537; d) Y. K. Ghosh, S. S. Indi, S. Bhattacharya, *J. Phys. Chem. B* **2001**, *105*, 10257.

[13] a) O. Bychuk, B. O'Shaughnessy, *Phys. Rev. Lett.* **1995**, *74*, 1795; b) H. Rehage, H. Hoffmann, *Mol. Phys.* **1991**, *74*, 933; c) H. Rehage, H. Hoffmann, *J. Phys. Chem.* **1988**, *92*, 4712; d) J. Haldar, V. K. Aswal, P. S. Goyal, S. Bhattacharya, *Angew. Chem.* **2001**, *113*, 1278; *Angew. Chem. Int. Ed.* **2001**, *40*, 1228.

[14] F. M. Menger, A. V. Peresypkin, *J. Am. Chem. Soc.* **2003**, *125*, 5340.

 © 2006 Wiley-VCH Verlag GmbH & Co. KGaA, Weinheim

Cyclizations

DOI: 10.1002/anie.200503789

A Simple and Efficient Iron-Catalyzed Intramolecular Hydroamination of Unactivated Olefins

Kimihiro Komeyama, Takayuki Morimoto, and Ken Takaki**

Nitrogen heterocycles have attracted significant interest among synthetic and medicinal chemists over the years, because they form the core structures and are key synthetic intermediates of natural products.[1] The importance of intramolecular hydroamination in the synthesis of these heterocycles has been widely recognized, and much effort has been made towards exploiting this technique.[2] The most promising hydroamination ever reported includes two distinctive metal-catalyzed processes: amine activation and olefin activation. In the former process, the transformation takes place with early transition metals through amido and imido species.[3] Although the catalysts reveal good reactivity towards unactivated olefins, high compatibility of the substrates would not be expected because of the extreme sensitivity of the metals to heteroatom functional groups.[4] In the latter process, late-transition-metal complexes are the catalysts of choice, but they have been used only for allenes[5] and alkynes,[6] not alkenes. Moreover, the reaction is often accompanied by olefin isomerization[7] and oxidative amination.[8] Recently, a platinum catalyst with a high capacity for intramolecular hydroamination of *N*-alkylaminoolefins was reported by Widenhoefer et al.[9] However, this procedure requires proper loading of the expensive catalyst and high temperature (120 °C). Therefore, the development of a more practical catalyst system that can be used for hydroamination with fewer limitations under mild conditions is desired.

Although the high affinity of iron for olefins was proved by many reactions with the cyclopentadienyliron dicarbonyl (Fp) species,[10,11] as well as by recent examples with iron salts,[12] it has, surprisingly, not hitherto been applied in catalytic hydroamination. Herein we report our investigations into $FeCl_3$-catalyzed intramolecular hydroamination, in which we found that the iron activity was superior to that of conventional transition-metal catalysts.

When 2,2-dimethyl-1-(4-toluenesulfonylamino)pent-4-ene (**1a**) was treated with $FeCl_3$ (10 mol%) in 1,2-dichloroethane (DCE) at 80 °C for 2 h, 2,4,4-trimethyl-1-(4-toluenesulfonyl)pyrrolidine (**2a**) was isolated in quantitative yield without any by-products [Eq. (1)].

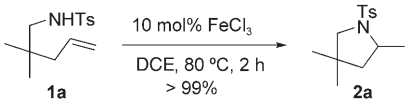

(1)

Notably, the presence of water did not prevent the reaction, that is, the same results were obtained with $FeCl_3 \cdot 6H_2O$ under air. Although $FeCl_2 \cdot 4H_2O$ gave a moderate yield of **2a** (73%), no reaction occurred in the presence of other iron salts such as $Fe(NO_3)_3$, $Fe_2(SO_4)_3$, and $Fe(acac)_3$ (acac = acetylacetonate). For comparison with these results, the reaction was carried out with many transition-metal chlorides and triflates (OTf) under similar conditions but under a nitrogen atmosphere.[13] Of the catalysts tested, $Cu(OTf)_2$ and AgOTf gave **2a** in quantitative and 78% yields, respectively, but longer reaction times ($\approx$16 h) were necessary for the reaction to be complete.

The reaction yield depended on the solvent used (Table 1). DCE and hexane were the most suitable for the transformation (Table 1, entries 1 and 2), whereas little or no **2a** was obtained with coordinative solvents such as benzene, 1,4-dioxane, tetrahydrofuran, 2-propanol, dimethyl sulfoxide, and *N*,*N*-dimethylformamide (Table 1, entries 3–8).

Table 1: Effect of solvent on the intramolecular hydroamination of **1a** with $FeCl_3 \cdot 6H_2O$.[a]

Entry	Solvent	**2a** [%][b]
1	DCE[c]	56
2	hexane	52
3	benzene	19
4	1,4-dioxane	9
5	THF[d]	<1
6	2-propanol	<1
7	DMSO[e]	0
8	DMF[f]	0

[a] Reaction conditions: **1a** (0.5 mmol), $FeCl_3 \cdot 6H_2O$ (10 mol%), solvent (5 mL), 80 °C, 1 h under air. [b] NMR spectroscopic yield based on internal standard. [c] DCE = 1,2-dichloroethane. [d] THF = tetrahydrofuran. [e] DMSO = dimethyl sulfoxide. [f] DMF = *N*,*N*-dimethylformamide.

Next, the compatibility of $FeCl_3$ with various types of aminoolefins **1a**–**1i** was investigated under the optimized conditions in air (Table 2). As in the case of **1a** (Table 2, entry 1), the 2,2-disubstituted aminoolefin **1b** was smoothly transformed into the corresponding pyrrolidine **2b** in quantitative yield (Table 2, entry 2). Although 1,2-disubstituted aminoolefins are known to be the least reactive substrates toward intramolecular hydroamination,[14] **1c** and **1d** were completely converted by $FeCl_3 \cdot 6H_2O$ (10 mol%) into **2c** and **2d**, respectively, within 3 h (Table 2, entries 3 and 4). The high reactivity did not require dialkyl substituents β to the amino group, that is, **2e** was produced from **1e** in excellent yield, albeit with low diastereoselectivity (3.8:1) (Table 2, entry 5).

[*] K. Komeyama, T. Morimoto, Dr. K. Takaki
Department of Chemistry and Chemical Engineering
Graduate School of Engineering, Hiroshima University
Kagamiyama, Higashi-Hiroshima 739-8527 (Japan)
Fax: (+81) 82-424-5494
E-mail: kkome@hiroshima-u.ac.jp
ktakaki@hiroshima-u.ac.jp

Supporting information for this article is available on the WWW under http://www.angewandte.org or from the author.

WILEY InterScience DISCOVER SOMETHING GREAT
© 2006 Wiley-VCH Verlag GmbH & Co. KGaA, Weinheim

Table 2: Intramolecular hydroamination of various aminoolefins.[a]

Entry	Substrate	Product	*t* [h]	Yield [%][b] (d.r.)[c]
1	**1a**	**2a**	2	97
2	**1b**	**2b**	2	>99
3	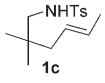 **1c**	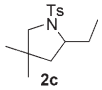 **2c**	3	95
4	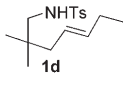 **1d**	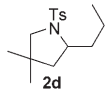 **2d**	3	95
5	**1e**	**2e**	2	97 (3.8:1)
	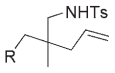	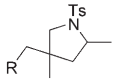		
6	**1f** R = OMe	**2f**	9	96 (1.1:1)
7	**1g** R = OTs	**2g**	21	81 (1.3:1)
8	**1h** R = I	**2h**	4	93 (2.1:1)
9	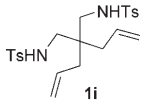 **1i**	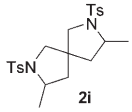 **2i**	38	82 (2:2:1:1)

[a] Reaction conditions: aminoolefin **1** (1 mmol), $FeCl_3 \cdot 6H_2O$ (10 mol%), 1,2-dichloroethane (10 mL), 80 °C under air. [b] Yield of isolated product. [c] Determined by ^1H or ^{13}C NMR spectroscopy. Ts = *p*-toluenesulfonyl.

Functional groups such as ether, tosylate, and iodide were also permitted in the reaction (Table 2, entries 6–8). In particular, the iodide-substituted aminoolefin **1h** gave the corresponding pyrrolidine **2h** in high yield (93%) without the elimination of iodide (Table 2, entry 8), which is uncommon in late-transition-metal chemistry. Furthermore, the system was also applicable to the synthesis of the 2,7-diazaspirobicyclic compound **2i** (Table 2, entry 9).

We also found that a suitably positioned hydroxy group resulted in competition with the sulfonamide functional group (Scheme 1). Thus, reaction of **3** at 80 °C for 2 h gave a mixture of tetrahydrofurylsulfonamide **4** and pyrrolidinoalcohol **5** (≈ 4:1) in 96% total yield (Scheme 1, Equation (2)), whereas a longer reaction time provided the 2-aza-7-oxospirobicyclic compound **6** in excellent yield with a diastereomer ratio of 4:3:2:1 (Scheme 1, Equation (3)).

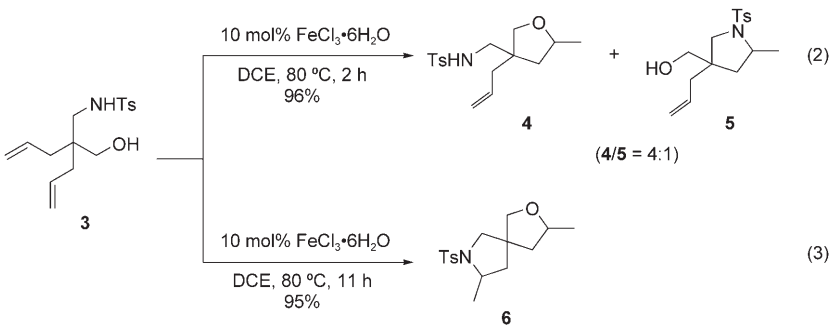

Scheme 1. Intramolecular hydroamination of **3** with different reaction times.

Finally, we attempted to extend our methodology to the synthesis of piperidine and azepane derivatives. Surprisingly, we found that the construction of five-membered rings was more favorable than that of six- and seven-membered rings under the present conditions (Scheme 2).[15] For example,

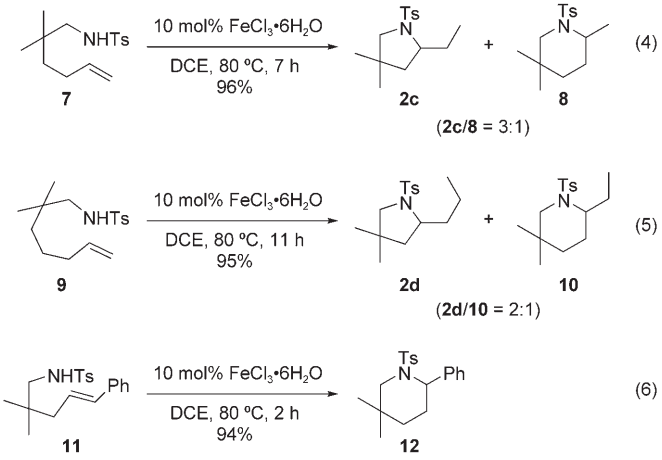

Scheme 2. Intramolecular hydroamination of aminoolefins with various carbon-chain lengths.

treatment of 2,2-dimethyl-1-(4-toluenesulfonylamino)hex-5-ene (**7**) with $FeCl_3 \cdot 6H_2O$ gave **2c** in 72% yield together with 2-methylpiperidine **8** (24%) (Scheme 2, Equation (4)). Similarly, exposure of 2,2-dimethyl-1-(4-toluenesulfonylamino)-hept-6-ene (**9**) to iron(III) chloride did not provide a seven-membered ring; instead, **2d** and 2-ethylpiperidine **10** were formed in 63% and 32% yield, respectively (Scheme 2, Equation (5)). Because the **2c**/**8** and **2d**/**10** ratios did not change further upon separate treatment with the catalyst under the reaction conditions, the above results would be caused by an isomerization process, probably of the starting substrates, during the reaction. On the other hand, 2,2-dimethyl-5-phenyl-1-(4-toluenesulfonylamino)pent-4-ene (**11**) produced 2-phenylpiperidine **12** in 94% yield through 6-*endo*-trig cyclization, and no 2-benzylpyrrolidine was detected (Scheme 2, Equation (6)).

In conclusion, we have demonstrated a simple iron-salt-catalyzed intramolecular hydroamination of unactivated olefins. The reaction proceeds under mild conditions, and it is not necessary to exclude air and moisture. Of special importance is the tolerance of aminoolefins containing halide moieties, which is rarely observed with Group 9 and 10 metals. Moreover, 1,2-disubstituted aminoolefins readily react in the present system. With regard to the $FeCl_3$-catalyzed reaction suggested herein, we must clarify whether the reaction pro-

 © 2006 Wiley-VCH Verlag GmbH & Co. KGaA, Weinheim

ceeds through the action of an acid catalyst, particularly HCl, which may be generated from the iron salt under the reaction conditions. Treatment of **1e** with $FeCl_3$ (10 mol%) in the presence of 2,6-di-*tert*-butylpyridine (10 mol%) at 80°C for 2 h did not provide **2e**.[16] However, no reaction took place with only HCl (30 mol%) under similar conditions.[17] Based on these experiments, we concluded that the simple acid-catalyzed pathway does not contribute to the present reaction. In further studies, we found that the activity of the catalyst could be much improved by a silver-salt additive, which allows the reaction of **1a** to be completed within 1 h. Studies on other mechanistic aspects and the scope and limitation of the iron-catalyzed reaction are in progress.

Experimental Section

Hydroamination of **1a**: A mixture of **1a** (267 mg, 1 mmol) and $FeCl_3{\cdot}6H_2O$ (27 mg, 0.1 mmol) in DCE (10 mL) was heated at 80°C for 2 h while being monitored by silica-gel TLC. The reaction was allowed to cool and quenched with water (10 mL). The aqueous phase was extracted with diethyl ether (20 mL). The combined organic layer was washed with brine (10 mL), dried over $MgSO_4$, filtered, and evaporated. The crude product was purified by column chromatography on silica gel (60–230 mesh) with a hexane/ethyl acetate (3:1) eluent to provide **2a** (259 mg, 0.97 mmol, 97%) as a white solid. M.p.: 82–83°C; ^{1}H NMR ($CDCl_3$): $\delta = 0.53$ (3H, s), 1.02 (3H, s), 1.34–1.42 (1H, m), 1.41 (3H, d, $J = 6.3$ Hz), 1.72 (1H, dd, $J = 12.6$, 7.3 Hz), 2.41 (3H, s), 3.05 (1H, d, $J = 10.6$ Hz), 3.15 (1H, d, $J = 10.6$ Hz), 3.56–3.69 (1H, m), 7.30 (2H, $J = 7.9$ Hz), 7.72 ppm (2H, $J = 8.3$ Hz); ^{13}C NMR ($CDCl_3$): $\delta = 21.5$, 22.7, 25.8, 26.5, 37.1, 48.8, 55.9, 61.4, 127.4, 129.4, 135.2, 143.0 ppm; MS: *m/z* (%): 267 ([M^+] 5), 252 (100), 155 (51), 91 (86), 56 (98); elemental analysis: calcd (%) for $C_{14}H_{21}NO_2S$: C 62.89, H 7.92, N 5.24; found: C 63.04, H 7.85, N 5.22.

Received: October 26, 2005
Revised: January 11, 2006
Published online: March 23, 2006

Keywords: alkenes · homogeneous catalysis · hydroamination · iron · nitrogen heterocycles

[1] D. O'Hagan, *Nat. Prod. Rep.* **2000**, *17*, 435–446.
[2] For reviews on inter- and intramolecular hydroaminations, see: a) F. Alonso, I. P. Beletskaya, M. Yus, *Chem. Rev.* **2004**, *104*, 3079–3159; b) F. Pohlki, S. Doye, *Chem. Soc. Rev.* **2003**, *32*, 104–114; c) T. E. Müller, M. Beller, *Chem. Rev.* **1998**, *98*, 675–703; for a selected example of *o*-iodoxybenzoic acid (IBX) mediated hydroamination, see: d) K. C. Nicolaou, P. S. Baran, Y.-L. Zhong, J. A. Vega, *Angew. Chem.* **2000**, *112*, 2625–2629; *Angew. Chem. Int. Ed.* **2000**, *39*, 2525–2529; for recent examples of Brønsted acid catalyzed hydroamination, see: e) B. Schlummer, J. F. Hartwig, *Org. Lett.* **2002**, *4*, 1471–1474; f) C. M. Haskins, D. W. Knight, *Chem. Commun.* **2002**, 2724–2725; for a selected example of *N*-bromosuccinimide-catalyzed hydroamination, see: g) S. K. Talluri, A. Sudalai, *Org. Lett.* **2005**, *7*, 855–857.
[3] Ca: a) M. R. Crimmin, I. J. Casely, M. S. Hill, *J. Am. Chem. Soc.* **2005**, *127*, 2042–2043; lanthanides: b) K. C. Hultzsch, *Org. Biomol. Chem.* **2005**, *3*, 1819–1824; c) T. K. Panda, A. Zulys, M. T. Gamer, P. W. Roesky, *Organometallics* **2005**, *24*, 2197–2202; d) J. Collin, J.-C. Daran, O. Jacquet, E. Schulz, A. Trifonov, *Chem. Eur. J.* **2005**, *11*, 3455–3462; e) S. Hong, T. J. Marks, *Acc. Chem. Res.* **2004**, *37*, 673–686; f) Y. K. Kim, T. Livinghouse, Y. Horino, *J. Am. Chem. Soc.* **2003**, *125*, 9560–9561; g) Y. K. Kim, T. Livinghouse, *Angew. Chem.* **2002**, *114*, 3797–3799; *Angew. Chem. Int. Ed.* **2002**, *41*, 3645–3647; actinides: h) T. Straub, A. Haskel, T. G. Neyroud, M. Kapon, M. Botoshansky, M. S. Eisen, *Organometallics* **2001**, *20*, 5017–5035; i) A. Haskel, T. Straub, M. S. Eisen, *J. Am. Chem. Soc.* **1996**, *118*, 3773–3775; Sc: j) J. Y. Kim, T. Livinghouse, *Org. Lett.* **2005**, *7*, 4391–4393; Group 4 metals: k) J. A. Bexrud, J. D. Beard, D. C. Leitch, L. L. Schafer, *Org. Lett.* **2005**, *7*, 1959–1962; l) D. V. Gribkov, K. C. Hultzsch, *Angew. Chem.* **2004**, *116*, 5659–5663; *Angew. Chem. Int. Ed.* **2004**, *43*, 5542–5546; m) A. Tillack, H. Jiao, I. G. Castro, C. G. Hartung, M. Beller, *Chem. Eur. J.* **2004**, *10*, 2409–2420; n) L. Ackermann, R. G. Bergman, R. N. Roy, *J. Am. Chem. Soc.* **2003**, *125*, 11956–11963; o) F. Pohlki, S. Doye, *Angew. Chem.* **2001**, *113*, 2361–2364; *Angew. Chem. Int. Ed.* **2001**, *40*, 2305–2308; p) B. F. Straub, R. G. Bergman, *Angew. Chem.* **2001**, *113*, 4768–4771; *Angew. Chem. Int. Ed.* **2001**, *40*, 4632–4635; q) P. L. McGrane, M. Jensen, T. Livinghouse, *J. Am. Chem. Soc.* **1992**, *114*, 5459–5460; r) P. J. Walsh, A. M. Baranger, R. G. Bergman, *J. Am. Chem. Soc.* **1992**, *114*, 1708–1719.
[4] R. Anwander in *Lanthanides: Chemistry and Use in Organic Synthesis* (Ed.: S. Kobayashi), Springer, New York, **1999**, pp. 1–61.
[5] Pd: a) M. Meguro, Y. Yamamoto, *Tetrahedron Lett.* **1998**, *39*, 5421–5424; Ag: b) T. Gallagher, S, W. Jones, M. F. Mahon, K. C. Molloy, *J. Chem. Soc. Perkin Trans. 1* **1991**, 2193–2198; c) J. S. Prasad, L. S. Liebeskind, *Tetrahedron Lett.* **1988**, *29*, 4253–4256; d) R. Kinsman, D. Lathbury, P. Vernon, T. Gallagher, *J. Chem. Soc. Chem. Commun.* **1987**, 243–244; e) D. Lathbury, T. Gallagher, *J. Chem. Soc. Chem. Commun.* **1986**, 114–115; f) S. Arseniyadis, J. Sartoretti, *Tetrahedron Lett.* **1985**, *26*, 729–732; g) S. Arseniyadis, J, Gore, *Tetrahedron Lett.* **1983**, *37*, 3997–4000; h) A. Claesson, C. Sahlberg, K. Luthman, *Acta Chem. Scand. Ser. B* **1979**, *33*, 309–310.
[6] Pd: a) G. B. Bajracharya, Z. Huo, Y. Yamamoto, *J. Org. Chem.* **2005**, *70*, 4883–4886; b) N. T. Patil, N. K. Pahadi, Y. Yamamoto, *Tetrahedron Lett.* **2005**, *46*, 2101–2103; c) L. M. Letete, I. Kadota, Y. Yamamoto, *J. Am. Chem. Soc.* **2004**, *126*, 1622–1623; d) T. E. Müller, M. Berger, M. Grosche, E. Herdtweck, F. P. Schmidtchen, *Organometallics* **2001**, *20*, 4384–4393; e) T. E. Müller, A.-K. Pleier, *J. Chem. Soc. Dalton Trans.* **1999**, 583–587; f) T. E. Müller, *Tetrahedron Lett.* **1998**, *39*, 5961–5962; Rh and Ir: g) L. D. Field, B. A. Messerle, K. Q. Vuong, P. Turner, *Organometallics* **2005**, *24*, 4241–4250; Re: h) L. L. Ouh, T. E. Müller, Y. K. Yan, *J. Organomet. Chem.* **2005**, *690*, 3774–3782; Cu: i) Y. Tamaru, M. Kimura, S. Tanaka, S. Kure, Z.-I. Yoshida, *Bull. Chem. Soc. Jpn.* **1994**, *67*, 2838–2849.
[7] L. S. Hegedus, J. M. McKearin, *J. Am. Chem. Soc.* **1982**, *104*, 2444–2451.
[8] a) R. F. Shannon, L. B. Jodie, S. S. Stahl, *Angew. Chem.* **2002**, *114*, 172–174; *Angew. Chem. Int. Ed.* **2002**, *41*, 164–166; b) P. J. Harrington, L. S. Hegedus, K. F. McDaniel, *J. Am. Chem. Soc.* **1987**, *109*, 4335–4338; c) L. S. Hegedus, B. Akermark, K. Zetterberg, L. F. Olsson, *J. Am. Chem. Soc.* **1984**, *106*, 7122–7126; d) L. S. Hegedus, J. M. McKearin, *J. Am. Chem. Soc.* **1982**, *104*, 2444–2451; e) L. S. Hegedus, G. F. Allen, D. J. Olsen, *J. Am. Chem. Soc.* **1980**, *102*, 3583–3587; f) L. S. Hegedus, G. F. Allen, J. J. Bozell, E. L. Waterman, *J. Am. Chem. Soc.* **1978**, *100*, 5800–5807; g) L. S. Hegedus, G. F. Allen, E. L. Waterman, *J. Am. Chem. Soc.* **1976**, *98*, 2674–2676.
[9] C. F. Bender, R. A. Widenhoefer, *J. Am. Chem. Soc.* **2005**, *127*, 1070–1071.
[10] a) L. S. Hegedus in *Comprehensive Organic Synthesis*, *Vol. 4* (Eds.: B. M. Trost, I. Fleming), Pergamon, New York, **1991**, pp. 551–569; b) A. J. Pearson in *Comprehensive Organic Synthesis*, *Vol. 4* (Eds.: B. M. Trost, I. Fleming), Pergamon, New

 © 2006 Wiley-VCH Verlag GmbH & Co. KGaA, Weinheim

York, **1991**, pp. 663 – 714; c) A. Rosan, M. J. Rosenblum, *J. Org. Chem.* **1975**, *40*, 3621 – 3622.
[11] a) S. R. Berryhill, T. Price, M. Rosan, *J. Org. Chem.* **1983**, *48*, 158 – 162; b) P. Lennon, M. Madhavarao, A. Rosan, *J. Organomet. Chem.* **1976**, *108*, 93 – 109.
[12] For a review on iron-catalyzed reactions, see: C. Bolm, J. Legros, J. L. Paih, L. Zani, *Chem. Rev.* **2004**, *104*, 6217 – 6254.
[13] No reaction took place with other metal chlorides ($CoCl_2$, $NiCl_2$, $CuCl_2$, $ZnCl_2$) and triflates of La and Sc. With $PdCl_2$, the terminal olefinic moiety of **1a** was isomerized to an internal one.
[14] a) J.-S. Ryu, T. J. Marks, *Org. Lett.* **2001**, *3*, 3091 – 3094; b) B. Åkermark, K. Zetterberg, *J. Am. Chem. Soc.* **1984**, *106*, 5560 – 5561; c) B. Åkermark, J.-E. Bäckvall, *Tetrahedron Lett.* **1975**, *16*, 819 – 822.
[15] Similar selectivity was reported by Haskins and Knight.[2f]
[16] a) T. C. Wabnitz, J.-Q. Yu, J. B. Spencer, *Chem. Eur. J.* **2004**, *10*, 484 – 493; b) P. V. Bonnesen, C. L. Puckett, R. V. Honeychuck, W. H. Hersh, *J. Am. Chem. Soc.* **1989**, *111*, 6070 – 6081.
[17] No reaction was observed with other acid catalysts such as *p*-toluenesulfinic acid and phenylacetic acid.

 © 2006 Wiley-VCH Verlag GmbH & Co. KGaA, Weinheim

Isotope Exchange

DOI: 10.1002/anie.200504222

Regiospecific C–H Bond Activation: Reversible H/D Exchange Promoted by Cu^{I} Complexes with Triazamacrocyclic Ligands**

Xavi Ribas, Raül Xifra, Teodor Parella, Albert Poater, Miquel Solà,* and Antoni Llobet**

Selective C–H bond activation by metals under mild conditions is a major subject of research targeting the final functionalization of organic substrates.[1] The characterization of the usually unstable intermediates of the C–H bond activation prior to functionalization is crucial for the mechanistic comprehension of the reaction.[2] Different mechanisms, such as oxidative addition, electrophilic metalation, or agostic bonding, have been proposed in extensive work published on the C–H activation of aromatic or aliphatic compounds catalyzed by second- and third-row transition metals (TMs; i.e., Pd and Pt,[3] and Ru, Rh, and Ir[4]). However, much less work is found with first row TMs (i.e., Ni,[4c,5] Co,[6] Fe,[7] and Mn[8]) and even less for the biologically relevant metal copper.[9] We have already reported an example of intramolecular aromatic C–H activation by Cu^{II} in a disproportionation reaction and characterized an aryl copper(III) species as a reaction product.[10] Herein, we report on the reactivity of five triazamacrocyclic ligands with Cu^{I} and the study of these reactions by ^{1}H and ^{2}H NMR spectroscopy, ESI mass spectrometry, and density functional computations.

The reaction of the ligands H-H33m, pMe-H33m, and pNO_2-H33m (Scheme 1) with one equivalent of $[Cu^{I}(CH_3CN)_4]PF_6$ in CD_3CN under N_2 afforded the corresponding $[Cu^{I}(R^{1}\text{-H33m})]^{+}$ complexes (Scheme 2). The ^{1}H NMR spectra of these complexes are very similar to those of the free ligands. However, when performing the reaction in $[D_6]$acetone, we observed a gradual decay of the singlet corresponding to H_a in the ^{1}H NMR spectra, with no other integration changes in the rest of the signals. The ESI mass spectra of deuterated acetone solutions show a peak corresponding to $[Cu^{I}(R^{1}\text{-H33m})]^{+}+1$, compared to the peak for $[Cu^{I}(R^{1}\text{-H33m})]^{+}$ in the case of CD_3CN solutions, which clearly suggests the substitution of H_a by a deuterium atom (Scheme 2). This result was confirmed by demetalation of the deuterated complex by adding an excess of 1,10-phenanthro-

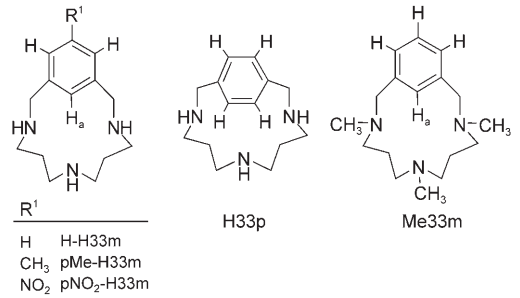

Scheme 1. Ligands used for Cu^{I} complexation.

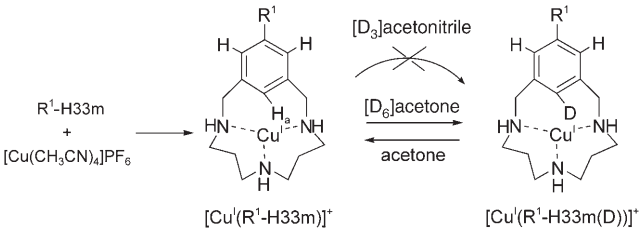

Scheme 2. Synthesis of the copper complexes and their solvent-dependent reversible isotope exchange.

[*] Dr. X. Ribas, Dr. R. Xifra, A. Poater, Prof. M. Solà
Institut de Química Computacional and
Departament de Química
Universitat de Girona
Campus Montilivi, 17071 Girona (Spain)
Fax: (+34) 972-418-150
E-mail: xavi.ribas@udg.es
miquel.sola@udg.es
Prof. A. Llobet
Departament de Química
Universitat Autònoma de Barcelona
08193 Bellaterra (Spain)
Fax: (+34) 935-813-101
E-mail: antoni.llobet@uab.es
Dr. T. Parella
Servei de RMN
Universitat Autònoma de Barcelona
08193 Bellaterra (Spain)

[**] This research was supported by the MEC (Spain; projects BQU2003-02884, BQU2003-01677, and CTQ2005-08797-C02-01). X.R. is grateful for a Juan de la Cierva contract from MEC.

Supporting Information for this article is available on the WWW under http://www.angewandte.org or from the author.

 © 2006 Wiley-VCH Verlag GmbH & Co. KGaA, Weinheim

line (phen) to form the highly stable complex $[Cu^{I}(phen)_2]PF_6$, the free deuterated ligand remaining in solution. Chromatographic purification afforded the deuterated ligands H-H33m(D), pMe-H33m(D), and pNO_2-H33m(D), which were characterized by ^1H and ^2H NMR spectroscopy and ESI mass spectrometry to confirm the regiospecific deuteration at the inner-macrocyclic aromatic position.

We studied the kinetics of this H/D exchange reaction in the R^1-H33m systems by following the decay of the H_a NMR signal. The three ligands were chosen in order to study the influence of the electronic effect exerted by the R^1 substituents on the isotopic exchange. The decay of the signal intensity was fitted by pseudo-first-order kinetics, and the reaction rates ($k_{obs,H/D}$) are listed in Table 1. The deuterium atom comes from [D_6]acetone (see discussion below), so the pseudo-first-order kinetics are explained by the large excess of the deuterium source. In order to extract kinetic information we measured kinetic isotope effects (KIE). We prepared the Cu^{I} complexes of the pure monodeuterated ligands ($[Cu^{I}(R^1\text{-H33m(D)})]^+$), which allowed us to follow the decay of the deuterium signal by performing ^2H NMR experiments in nondeuterated acetone. We noticed that, apart from the gradual disappearance of the aromatic-deuterium singlet, a triplet corresponding to monodeuterated acetone (CDH_2COCH_3) at $\delta = 2.05$ ppm gradually increased in intensity, also following first-order kinetics, with the same rates (Figure 1 and Table 1), to finally give the complexes with the original nondeuterated ligands (see Supporting Information).

Table 1: Kinetic data for the H/D ($k_{obs,H/D}$) and D/H ($k_{obs,D/H}$) isotopic substitution at 300 K obtained for a first-order rate law.

	$[Cu^{I}(H\text{-}H33m)]^+$	$[Cu^{I}(pMe\text{-}H33m)]^+$	$[Cu^{I}(pNO_2\text{-}H33m]^+$
$k_{obs,H/D}$ [min^{-1}][a]	0.0144(5)	0.0134(2)	0.00033(1)
$k_{obs,D/H}$ [min^{-1}][b]	0.0164(4)	0.0165(8)	0.000054(5)
overall KIE	0.88	0.81	6.1

[a] From ^1H NMR studies in CD_3COCD_3. [b] From ^2H NMR studies in CH_3COCH_3 for monodeuterated $[Cu^{I}(R^1\text{-H33m(D)})]^+$ complexes.

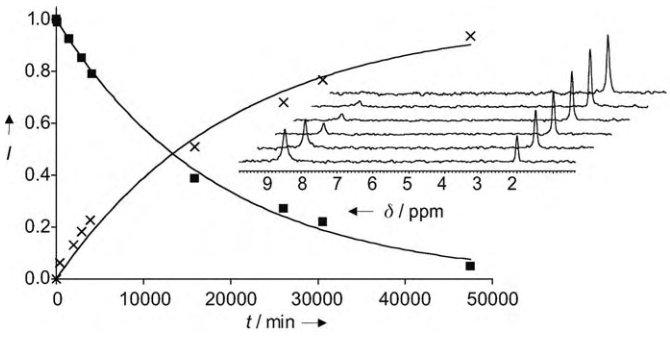

Figure 1. Plot of normalized signal intensity versus time for the decay of the aromatic-deuterium signal at $\delta = 8.45$ ppm (■) and the growth of the CDH_2COCH_3 signal at $\delta = 2.05$ ppm (×) in the ^2H NMR spectrum of the $[Cu^{I}(pNO_2\text{-H33m(D)})]^+$ complex in CH_3COCH_3 (inset: evolution of the ^2H NMR spectrum with time).

In order to gain more insight into the nature of this C–H activation, we studied the isotopic exchange reaction for the H-H33m system in different deuterated solvents. The reaction proceeds in CD_3OD[11] but does not proceed in CD_3CN or CD_2Cl_2, thus clearly manifesting the need for an acidic deuterium atom. We also performed theoretical studies, and DFT geometry optimizations in the gas phase were carried out for the free H-H33m ligand, the $[Cu^{I}(H\text{-H33m})]^+$ complex, and the same Cu^{I} complex starting with two axially coordinated molecules of acetonitrile, acetone, or methanol.[12] We found an agostic interaction between Cu^{I} and the C–H_a bond for $[Cu^{I}(H\text{-H33m})]^+$, with a lengthening of the C–H_a bond (1.098 Å) compared to that in the free ligand (1.092 Å) and an angle of 11.8° between this bond and the plane of the aromatic ring (Figure 2a).

When introducing acetone and methanol molecules both axial molecules remain mostly uncoordinated ($d_{Cu\text{-}O} > 2.9$ Å) and the copper center remains in the macrocyclic plane (defined as the best fitted plane that contains the nitrogen atoms of the ligand, Figure 2b and Supporting Information), thus enabling formation of the agostic interaction between Cu^{I} and the C–H_a bond (the aromatic C–H_a bond is elongated by 0.006 and 0.004 Å with respect to the free ligand in the presence of acetone and

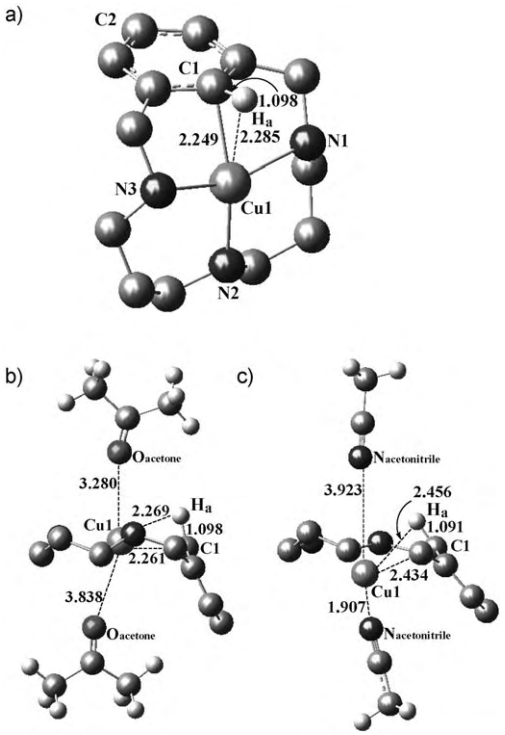

Figure 2. DFT geometry optimizations of a) the $[Cu^{I}(H\text{-H33m})]^+$ complex in the absence of solvent molecules (showing the Cu···C–H_a agostic bond), b) the complex with two axially coordinated CH_3COCH_3 molecules (the agostic interaction with C–H_a persists), and c) the complex with one coordinated CH_3CN molecule and a second uncoordinated CH_3CN (no agostic interaction observed). Ligand hydrogen atoms other than H_a are omitted. All distances are given in Å.

 © 2006 Wiley-VCH Verlag GmbH & Co. KGaA, Weinheim

methanol molecules, respectively). In the case of CH_3CN, the Cu^I center is forced out of the macrocyclic plane and the metal adopts a distorted tetrahedral coordination geometry by binding to one CH_3CN molecule; the other axial solvent molecule remains mainly uncoordinated with a very weak contact (Figure 2c). Indeed, the C–H_a bond length and C2-C1-H_a angle are the same as in the free ligand, therefore no agostic interaction is found.[13]

With all these theoretical data at hand, we followed the H/D exchange for complex $[Cu^I(pMe\text{-}H33m)]^+$ by ^1H NMR spectroscopy at different concentrations of $[D_6]$acetone in an innocent solvent such as CD_2Cl_2—the concentration of the complex was kept constant—and also found first-order kinetics with respect to acetone (see Supporting Information).

The kinetics in pure $[D_6]$acetone indicate a pseudo-first-order reaction for all systems that is roughly two orders of magnitude faster ($k_{obs,H/D}$) for H-H33m and pMe-H33m than for pNO_2-H33m (see Table 1). However, when we studied the D/H exchange for the respective deuterated ligands in pure nondeuterated acetone, the $k_{obs,D/H}$ values were about three orders of magnitude higher (Table 1). These data suggest an inverse KIE for H-H33m and pMe-H33m and a direct KIE for pNO_2-H33m (Table 1), and indicate the presence of radically different rate-determining steps (rds) for these systems. It is important to note here that the addition of H^- to our previous $[Cu^{III}L]^{2+}$ complex (L: H-H33m acting as an organometallic aryl ligand) gives the corresponding $[Cu^I(H\text{-}H33m)]^+$ complex quantitatively.[14] Furthermore, the existence of inverse isotope effects for the breaking of Rh^{III}–H bonds has been well documented.[15] The presence of free D^+ caused the decomposition of the complex.[16]

Consistent with all the data reported, and taking into account the first-order kinetics with respect to complex and acetone, the mechanism outlined in Scheme 3 can be proposed. Initially, $[D_6]$acetone in its enolic form coordinates to the metal center (species **A**).[17] It then follows an oxidative type of addition to yield a formal H^- bonded to a Cu^{III} center (species **B**;[18] rds for pNO_2-H33m in agreement with a direct KIE), followed by the H/D exchange (species **C**; rds for H-H33m and pMe-H33m, in agreement with an inverse KIE) to finally generate the acetone-coordinated $[Cu^I(H\text{-}H33m(D))]^+$ complex (**D**) with an incorporated deuterium atom. Indeed, the difficulty of reaching the Cu^{III} oxidation state for the complex with the strongly electron-withdrawing NO_2 group with regard to the complexes containing pMe-H33m and H-H33m has been shown recently by ourselves[10b] and agrees with the mechanism proposed. In addition, the higher stability of the Cu^{III} complex **B** containing the pMe-H33m ligand with an electron-donating group with regard to the H-H33m complex (stronger Cu–H bond in the former) results in lower rates for the former (see Table 1). However, the stronger Cu–H bond generates a slightly larger inverse isotope effect for the H/D exchange process and thus leads to a lower KIE for the pMe-H33m system.

The precise macrocyclic coordination environment is essential for the reaction to take place, and this is evidenced by the absence of H/D exchange in the sterically hindered $[Cu^I(H33p)]^+$ system (in H33p, the aromatic ring is *para*-substituted instead of *meta*-substituted as in H-H33m), where, despite there being two inner-macrocycle aromatic C–H bonds, no reaction takes place (see Supporting Information). The $[Cu^IMe33m]^+$ system also does not undergo isotopic exchange in $[D_6]$acetone. Here, the reason is the stabilization of low copper oxidation states due to N-methylation, as described by Meyerstein et al. and Bernhardt,[19] which prevents the formation of high-oxidation-state intermediates and is therefore in line with our mechanistic proposal.

In conclusion, we have presented the first example of a reversible intramolecular H/D exchange promoted by Cu^I. The process is finely controlled by the precise coordination distance required to form the agostic interaction between Cu^I and the aromatic C–H_a bond, and thus the reactivity is sharply modified by the coordination effect exerted by the solvent used. The reactivity can also be tuned by the electronic effects of the aromatic ring and the amine substitution. The reaction is regiospecific and allows us to isolate the corresponding monodeuterated free ligands, which, in turn, have permitted us to gain insight into the isotopic exchange mechanism. Kinetic studies at different temperatures and in different solvents, as well as theoretical calculations, are currently in progress to gain further mechanistic insight into this exciting reaction.

Received: November 28, 2005
Published online: March 28, 2006

Keywords: agostic interactions · C–H activation · copper · density functional calculations · isotopic labeling

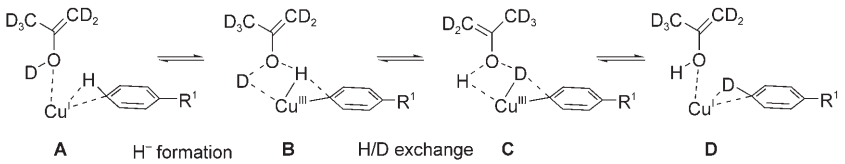

Scheme 3. Proposed H/D exchange mechanism.

[1] J. M. Thomas, R. Raja, G. Sankar, R. G. Bell, *Acc. Chem. Res.* **2001**, *34*, 191–200.
[2] S. S. Stahl, J. A. Labinger, J. E. Bercaw, *Angew. Chem.* **1998**, *110*, 2298–2311; *Angew. Chem. Int. Ed.* **1998**, *37*, 2180–2192.
[3] a) A. E. Shilov, G. B. Shul'pin, *Chem. Rev.* **1997**, *97*, 2879–2932; b) M. Q. Slagt, G. Rodríguez, M. M. P. Grutters, R. J. M. Klein Gebbink, W. Klopper, L. W. Jenneskens, M. Lutz, A. L. Spek, G. van Koten, *Chem. Eur. J.* **2004**, *10*, 1331–1344.
[4] a) M. Gozin, A. Weisman, Y. Ben-David, D. Milstein, *Nature* **1993**, *364*, 699–701; b) M. E. van der Boom, D. Milstein, *Chem. Rev.* **2003**, *103*, 1759–1792; c) M. Albrecht, G. van Koten, *Angew. Chem.* **2001**, *113*, 3866–3898; *Angew. Chem. Int. Ed.* **2001**, *40*, 3750–3781.
[5] a) M. Stepien, L. Latos-Grażyński, *Acc. Chem. Res.* **2005**, *38*, 88–98; b) J. Cámpora, P. Palma, D. Río, M. M. Conejo, E. Álvarez, *Organometallics* **2004**, *23*, 5653–5655.
[6] J. D. Harvey, C. J. Ziegler, *Chem. Commun.* **2004**, 1666–1667.

 © 2006 Wiley-VCH Verlag GmbH & Co. KGaA, Weinheim

[7] K. Rachlewicz, S.-L. Wang, J.-L. Ko, C.-H. Hung, L. Latos-Grażyński, *J. Am. Chem. Soc.* **2004**, *126*, 4420 – 4431.
[8] D. S. Bohle, W.-C. Chen, C.-H. Hung, *Inorg. Chem.* **2002**, *41*, 3334 – 3336.
[9] a) P. J. Chmielewski, L. Latos-Grażyński, I. Schmidt, *Inorg. Chem.* **2000**, *39*, 5475 – 5482; b) A. Srinivasan, H. Furuta, *Acc. Chem. Res.* **2005**, *38*, 10 – 20; c) M. Castro, J. Cruz, H. López-Sandoval, N. Barba-Behrens, *Chem. Commun.* **2005**, 3779 – 3781.
[10] a) X. Ribas, D. A. Jackson, B. Donnadieu, J. Mahía, T. Parella, R. Xifra, B. Hedman, K. O. Hodgson, A. Llobet, T. D. P. Stack, *Angew. Chem.* **2002**, *114*, 3117 – 3120; *Angew. Chem. Int. Ed.* **2002**, *41*, 2991 – 2994; b) R. Xifra, X. Ribas, A. Llobet, A. Poater, M. Duran, M. Solà, T. D. P. Stack, J. Benet-Buchholz, B. Donnadieu, J. Mahía, T. Parella, *Chem. Eur. J.* **2005**, *11*, 5146 – 5156.
[11] Similar reactivity is found when using CD_3OD with the systems H-H33m and pMe-H33m, although with bigger reaction rates than in [D_6]acetone. In the case of CD_3OH no disappearance of the H_a signal is observed because the exchange occurs between the protons of the alcohol groups.
[12] Calculations were performed with the ADF program using the BP86 functional combined with a DZP basis set for C, N, O, and H, and a TZP basis set for Cu. See Supporting Information for further details.
[13] Several attempts to crystallize the Cu^I complexes from different solvent mixtures were performed, although crystallographic characterization was only achieved with a CH_3CN/diethyl ether mixture for a related ligand with the same R-H33m macrocyclic skeleton. The structure analysis confirmed the release of the Cu^I center out of the macrocyclic plane, due to coordination to one CH_3CN molecule, and formation of a coordination polymer (these results will be published elsewhere).
[14] The addition of 1.5 equiv of $NaBH_4$ to the corresponding organometallic $[Cu^{III}L]^{2+}$ compound (reference [10a]) leads to the Cu^I complex bearing the H_a aromatic proton (as monitored by ^{1}H NMR spectroscopy), which gives support to the formation of a transient aryl copper(III) hydride.
[15] a) W. D. Jones, *Acc. Chem. Res.* **2003**, *36*, 140 – 146; b) W. D. Jones, F. J. Feher, *J. Am. Chem. Soc.* **1984**, *106*, 1650 – 1663.
[16] The addition of 0.5 equiv of CF_3COOD to a solution of $[Cu^I$(H-H33m)$]^+$ in CD_2Cl_2 (noncoordinating solvent) gives a species with broad ^{1}H NMR signals (probably partial decomplexation and oligomerization due to protonation of the amine moiety).
[17] The direct coordination of acetone to a metal center has been reported, along with the description of the keto–enol equilibrium; see: M. A. Henderson, *Langmuir* **2005**, *21*, 3451 – 3458; J. Ruiz, M. T. Martínez, V. Rodríguez, G. López, J. Pérez, P. A. Chaloner, P. B. Hitchcock, *Dalton Trans.* **2004**, 3521 – 3527).
[18] DFT calculations failed to locate the postulated hydride intermediate **B**. We are currently investigating the possibility of a solvent-assisted stabilization of this intermediate species.
[19] a) G. Golub, H. Cohen, P. Paoletti, A. Bencini, L. Messori, I. Bertini, D. Meyerstein, *J. Am. Chem. Soc.* **1995**, *117*, 8353 – 8361; b) D. Meyerstein, *Coord. Chem. Rev.* **1999**, *185–186*, 141 – 147; c) P. V. Bernhardt, *J. Am. Chem. Soc.* **1997**, *119*, 771 – 774; d) P. V. Bernhardt, *Inorg. Chem.* **2001**, *40*, 1086 – 1092.

 © 2006 Wiley-VCH Verlag GmbH & Co. KGaA, Weinheim

Peptide Structures

DOI: 10.1002/anie.200504380

A Left-Handed 9-Helix in γ-Peptides: Synthesis and Conformational Studies of Oligomers with Dipeptide Repeats of C-Linked Carbo-γ⁴-amino Acids and γ-Aminobutyric Acid**

Gangavaram V. M. Sharma, Pagadala Jayaprakash, Kongari Narsimulu, Ampapathi Ravi Sankar, Kondreddy Ravinder Reddy, Palakodety Radha Krishna, and Ajit C. Kunwar**

The design of nonnatural oligomers that form diversified secondary structures is an active area of research.[1] An extensive search of the β-peptide class of foldamers has provided several new secondary structures, while the γ-peptides, despite the possibility of having and traversing a larger conformational space, have received less attention. Dado and Gellman[2] identified the H-bonding of the nearest neighbor in γ-amino acid derivatives by FTIR and NMR studies. Seebach and co-workers[3] and Hanessian et al.[4] reported 14-helices in γ-peptides, while a 9-membered H-bonded ring was also observed by Seebach et al.[3b] in the crystal structure of a dipeptide. Recently, Farrera-Sinfreu et al.[5] reported 9-membered sheets in γ-peptides from cyclic γ-amino acids, while Balaram and co-workers[6] reported 9-helices and ribbons in γ-peptides from constrained acyclic γ-amino acids. Theoretical predictions by Hofmann and co-workers[7] for γ-peptides revealed that structures with 14- and 9-helices are most stable. Herein, we report a left-handed 9-helix in a novel class of mixed γ-peptides, derived from dipeptide repeats with alternating C-linked carbo-γ⁴-amino acids (γ-Caas) and γ-aminobutyric acid (GABA), in $CDCl_3$.

Our earlier findings[8] on mixed β-peptides derived from alternating C-linked carbo-β³-amino acids (β-Caas) and β-homoglycine (β-hGly) revealed a switching of the handed-

[*] Dr. G. V. M. Sharma, P. Jayaprakash, Dr. K. Ravinder Reddy, Dr. P. Radha Krishna
D-211, Discovery Laboratory
Organic Chemistry Division III
Indian Institute of Chemical Technology
Hyderabad 500 007 (India)
Fax: (+91) 40-2716-0387/2719-3108
E-mail: esmvee@iict.res.in

K. Narsimulu, Dr. A. Ravi Sankar, Dr. A. C. Kunwar
Centre for Nuclear Magnetic Resonance
Indian Institute of Chemical Technology
Hyderabad 500 007 (India)
Fax: (+91)-040-2719-3108
E-mail: kunwar@iict.res.in

[**] IICT Communication No. 050802. J.P., K.R.R., and A.R.S. are thankful to CSIR, New Delhi, for financial support. We thank Prof. N. Shamala and P. G. Vasudev for helpful discussions.

Supporting information for this article (NMR details, solvent titration plots, and distance constraints used in molecular dynamics calculations) is available on the WWW under http://www.angewandte.org or from the author.

WILEY InterScience DISCOVER SOMETHING GREAT
© 2006 Wiley-VCH Verlag GmbH & Co. KGaA, Weinheim

ness, to result in left- as well as right-handed 10/12-mixed helices, which are facilitated by the conformational freedom provided by the β-hGly moiety. Based on these results and previous theoretical predictions about the nearest-neighbor H-bonds, we envisaged that mixed γ-peptides may adopt novel and interesting secondary structures. Hence, the requisite γ-Caa **1** (Scheme 1), prepared from the corresponding β-Caa,[9] was subsequently used to prepare the γ-peptides **2** and **3** by conventional peptide-coupling methods and was thoroughly investigated by NMR and circular dichroism (CD) spectroscopy and molecular dynamics (MD) analysis.[10]

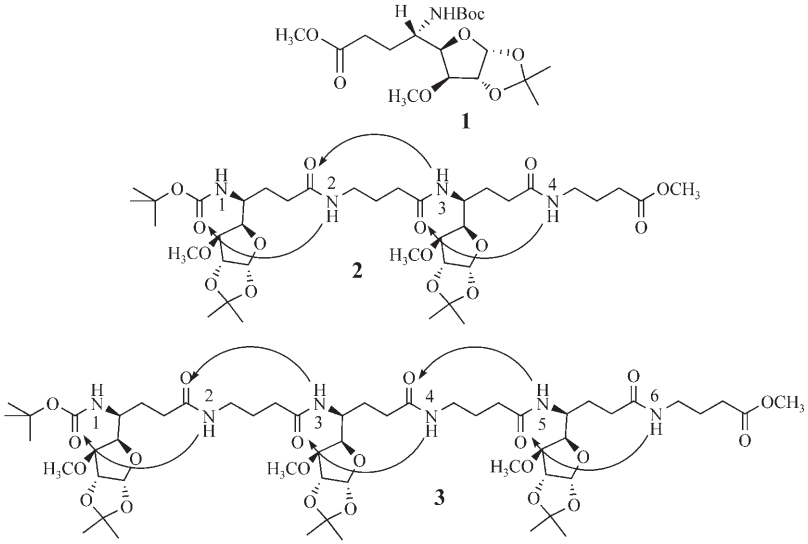

Scheme 1. Structures of **1** and γ-peptides **2** and **3** with the hydrogen bonding indicated. Boc = *tert*-butoxycarbonyl.

In the ^{1}H NMR spectrum of **2** in $CDCl_3$, the NH(2), NH(3), and NH(4) amide proton resonances appeared at $\delta =$ 6.92, 7.00, and 7.60 ppm, respectively; the participation of these moieties in H-bonding was confirmed from solvent titration studies.[11] For the γ-Caas, the values of $^3J_{NH,C_\gamma H} \approx 9.0$–9.5 Hz indicated that the NH and C_γH protons are antiperiplanar (*ap*) and imply a value for C(O)-N-C_γ-C_β (ϕ) of about 120°. The values of $^3J_{C_\beta H,C_\gamma H} < 5.0$ and > 10.0 Hz supported N-C_γ-C_β-C_α (θ_1) values of about −60° or 180°, while a strong NOE for NH/C_βH (the one *ap* with respect to C_γH) confirms $\theta_1 \approx -60°$. Stereospecific assignments for C_αH protons were possible only for C_αH(3) protons, where one of the protons showed values of $^3J_{C_\alpha H,C_\beta H} = 10.5$ and 5.0 Hz, a fact suggesting C_γ-C_β-C_α-C(O) (θ_2) values of about −60° or 180°. The same proton also displayed NOEs with NH(3), NH(4), and C_γH(2), which is possible only for $\theta_2 \approx -60°$ and C_β-C_α-C(O)-N (ψ) $\approx \pm 100°$. Similarly, for GABA residues, the values of $^3J_{NH,C_\gamma H} \approx 5$ and 7 Hz support $\phi \approx 120°$. The observation of strong NH(i+1)/C_αH(i) NOE correlations suggests that $|\psi|$ may have a value of about 100°.

In the ROESY experiments, several long-range NOEs, such as NH(i+1)/C_γH(i), C_γH(i)/C_αH(i+1), NH(i+1)/C_αH(i), NH(i)/C_βH(i), NH(i)/C_αH(i), and C_γH(i)/C_αH(i), were observed. However, it was difficult to get more definitive structural information, especially for the GABA residues, partly due to fraying at the termini and partly due to spectral overlap. Therefore, a study was undertaken with hexapeptide **3** for structure confirmation.

In **3**, participation of all the amide protons, except NH(1), in H-bonding was indicated by their low-field shifts and was confirmed by solvent titration studies.[11] For γ-Caa residues, $^3J_{NH,C_\gamma H} \approx 9$ Hz, which is consistent with *trans* disposition (*ap*) of the NH and C_γH protons and supports a ϕ value of about 120°. The stereospecific assignments for the C_βH protons of γ-Caas were made based on the coupling constants and NOEs (Figure 1). The values of $^3J_{C_\beta H,C_\gamma H} < 5.0$ and > 10.0 Hz imply that $\theta_1 \approx -60°$ or 180° and the strong NOE for NH/$C_\beta H_{(pro\text{-}R)}$ (which is *ap* with respect to C_γH) confirms that $\theta_1 \approx -60°$. Stereospecific assignment of the C_αH protons of γ-Caas was only possible for C_αH(3). The values of $^3J_{C_\alpha H,C_\beta H}$ of 11.3 and 2.8 Hz, as well as the strong NOE correlation with $C_\gamma H_{(pro\text{-}S)}$(2) (assigned as discussed below), allowed the assignment of the C_αH proton signal at $\delta = 2.11$ ppm as $C_\alpha H_{(pro\text{-}S)}$. Furthermore,the NH/$C_\alpha$H NOE ruled out structures with $\theta_2 \approx 60°$. The NOE correlations NH(i)/C_αH(i), NH(i+1)/C_αH(i), and C_γH(i−1)/C_αH(i) are possible only for $\theta_2 \approx -60°$ ($\theta_2 \approx 180°$ gives an extended structure) and $|\psi| \approx 100°$. Thus, for the γ-Caa residues, the backbone dihedral angles are $\phi \approx 120°$, $\theta_1 \approx -60°$, $\theta_2 \approx -60°$, and $|\psi| \approx 100°$.

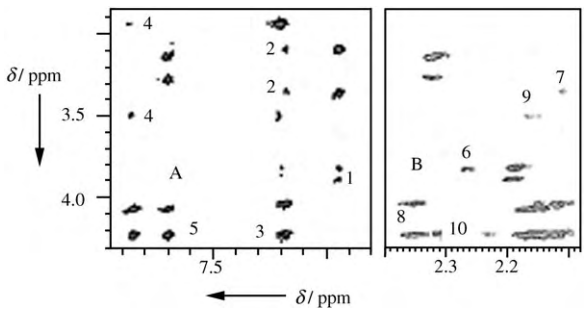

Figure 1. ROESY spectrum of **3**. The NOEs for C_γH(i)/NH(i+1) (i = 1–5) are marked as 1–5 (A) and those for C_γH(i)/$C_\alpha H_{(pro\text{-}S)}$($i$+1) ($i$ = 1–5) are marked as 6–10 (B).

For GABA residues, the values of $^3J_{NH,C_\gamma H} \approx 5$ and 7 Hz correspond to $\phi \approx 120°$. By using the difference in the strength of the interresidue NH/C_γH NOEs, the up-field-shifted C_γH proton was assigned as $C_\gamma H_{(pro\text{-}R)}$, which is also approximately in an *ap* arrangement with respect to NH; this allowed us to fix the ϕ value as ≈120°. The NOE correlations, NH(i)/C_βH(i) and $C_\gamma H_{(pro\text{-}S)}$($i$)/$C_\alpha$H($i$+1), for the GABA residues support $\theta_1 \approx -60°$. For the C_αH protons of the GABA residues, due to severe spectral overlap in the C_αH region, spectral parameters and stereospecific assignments could be obtained only for C_αH(4) protons, which resonate at $\delta = 2.35$ and 2.24 ppm. For the C_αH signal at $\delta = 2.35$ ppm, $^3J_{C_\alpha H,C_\beta H} = 10.5$ and 5.5 Hz and

 © 2006 Wiley-VCH Verlag GmbH & Co. KGaA, Weinheim

it has a strong NOE correlation, $C_\gamma H(3)/C_\alpha H$, which allowed the assignment of this proton as $C_\alpha H_{(pro\text{-}S)}$, thereby supporting $\theta_2 \approx -60°$. Based on the strong $C_\alpha H(2)/C_\gamma H(1)$ NOE correlation, the down-field $C_\alpha H$ signal of GABA(2) was also assigned as $C_\alpha H_{(pro\text{-}S)}$. Strong NOEs for $NH(5)/C_\alpha H_{(pro\text{-}S)}(4)$ and $NH(3)/C_\alpha H_{(pro\text{-}S)}(2)$ suggest $|\psi| \approx 100°$. Since the signs of some of the dihedral angles could not be derived, all sign combinations were considered and it was found that all the NOEs, including $NH(i)/C_\gamma H_{(pro\text{-}S)}(i-1)$, $C_\gamma H_{(pro\text{-}S)}(i)/C_\alpha H_{(pro\text{-}S)}(i+1)$, and $NH(i)/NH(i+1)$, are satisfied for $\phi \approx 120°$, $\theta_1 \approx -60°$, $\theta_2 \approx -60°$, and $\psi \approx 100°$.

Thus, from the above data, a 9-membered H-bond involving $NH(i)\cdots CO(i-2)$ is inferred and the distinct presence of a left-handed 9-helix in **3** was obtained. The finding for **3** very strongly supports a 9-helix in **2**.

The observation of weak NOEs for $NH(3)/C_\gamma H(1)$ and $NH(5)/C_\gamma H(3)$ in **3**, however, indicates the presence of another minor structure in addition to the predominant left-handed 9-helix. Based on the predictions by Hofmann and co-workers[7] and the NOEs mentioned above, the minor structure was presumed to be a 14-helix, although careful scrutiny of the NMR evidence ruled out the presence of any other helix type.

The CD spectra (Figure 2) of **2** and **3** in CH_3OH show maxima at about 200 nm, zero-crossing at 208 nm, and minima at about 215 nm. However, for γ-peptides, fingerprints of well-defined structures in the CD spectra have so far not been recognized.

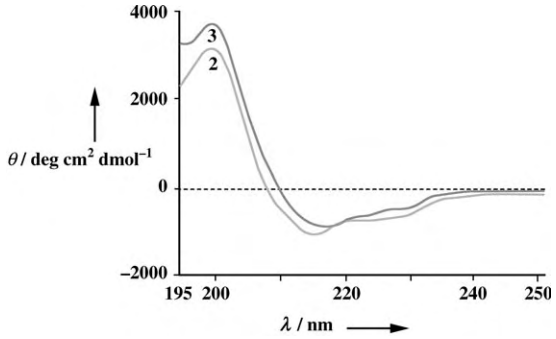

Figure 2. CD spectra of 200 μM solutions of **2** and **3** in CH_3OH.

Restrained MD calculations conclusively confirmed the presence of the 9-helical structure in peptides **2** and **3**. A large number of distance constraints, derived from the volume integrals from the ROESY experiments by using a two-spin approximation, were used quantitatively. Figure 3 depicts a superimposition of 15 of the lowest-energy structures calculated for **2** and **3**, which have left-handed 9-helical structures. For clarity, all the protons have been removed and the sugar units were replaced by methyl groups after the MD calculations. The root mean square deviation (RMSD) values for the backbone and the maximum NOE violations for **2** are 0.91 and 0.57 Å, respectively, while the corresponding values for **3** are 1.18 and 0.42 Å, respectively. The average values of the dihedral angles (excluding the terminal residues) for **3** are $\phi = (125 \pm 20)°$, $\theta_1 = -(68 \pm 5)°$, $\theta_2 = -(65 \pm 4)°$, and $\psi = (97 \pm 10)°$. These helices have about 2.3 residues per turn and a height-per-residue value of about 3.3 Å. The helices reported by Balaram and co-workers[6] have values of $\phi = 109°$, $\theta_1 = -63°$, $\theta_2 = -77°$, and $\psi = 88°$, 2.7 residues per turn, and a height-per-residue value of 3.4 Å, while the dihedral angle

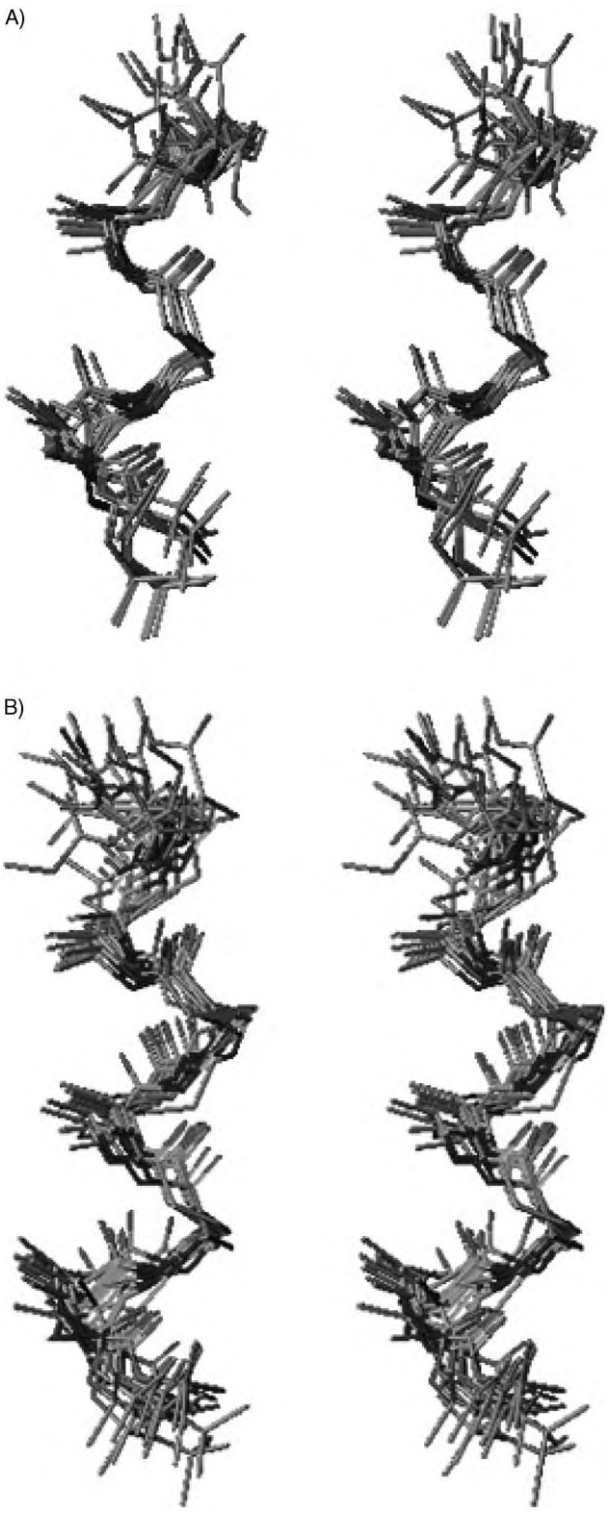

Figure 3. Stereoviews of the superimposition of 15 minimum-energy structures of A) tetrapeptide **2** and B) hexapeptide **3**.

 © 2006 Wiley-VCH Verlag GmbH & Co. KGaA, Weinheim

values predicted theoretically[7] are $\phi = 97°$, $\theta_1 = -70°$, $\theta_2 = -75°$, and $\psi = 97°$.

This study thus presents the identification of a novel left-handed 9-helix in mixed γ-peptides derived from alternating γ-Caa and GABA residues. The new design, besides being an example of the formation of left-handed helical structures, may provide an opportunity to understand the functions of such systems. Furthermore, information about the conformational preferences of Caas with carbohydrate side chains would help in the design and the synthesis of a variety of γ-peptides with novel and diversified secondary-structure alternatives and useful functions.

Received: December 9, 2005
Revised: January 19, 2006
Published online: March 23, 2006

Keywords: amino acids · aminobutyric acid · conformation analysis · helical structures · peptides

[1] a) D. J. Hill, M. J. Mio, R. B. Prince, T. S. Hughes, J. S. Moore, *Chem. Rev.* **2001**, *101*, 3893 – 4011; b) D. Seebach, A. K. Beck, D. J. Bierbaum, *Chem. Biodiversity* **2004**, *1*, 1111 – 1239; c) R. P. Cheng, S. H. Gellman, W. F. DeGrado, *Chem. Rev.* **2001**, *101*, 3219 – 3232.

[2] G. P. Dado, S. H. Gellman, *J. Am. Chem. Soc.* **1994**, *116*, 1054 – 1062.

[3] a) T. Hintermann, K. Gademann, B. Jaun, D. Seebach, *Helv. Chim. Acta* **1998**, *81*, 983 – 1002; b) D. Seebach, M. Brenner, M. Rueping, B. Jaun, *Chem. Eur. J.* **2002**, *8*, 573 – 584; c) D. Seebach, M. Brenner, M. Rueping, B. Schweizer, B. Jaun, *Chem. Commun.* **2001**, 207 – 208; d) M. Brenner, D. Seebach, *Helv. Chim. Acta* **2001**, *84*, 1181 – 1189.

[4] S. Hanessian, X. Luo, R. Schaum, S. Michnick, *J. Am. Chem. Soc.* **1998**, *120*, 8569 – 8570.

[5] J. Farrera-Sinfreu, L. Zaccaro, D. Vidal, X. Salvatella, E. Giralt, M. Pons, F. Albericio, M. Royo, *J. Am. Chem. Soc.* **2004**, *126*, 6048 – 6057.

[6] P. G. Vasudev, N. Shamala, K. Ananda, P. Balaram, *Angew. Chem.* **2005**, *117*, 5052 – 5055; *Angew. Chem. Int. Ed.* **2005**, *44*, 4972 – 4975.

[7] C. Baldauf, R. Gunther, H.-J. Hofmann, *Helv. Chim. Acta* **2003**, *86*, 2573 – 2588.

[8] a) G. V. M. Sharma, K. Ravinder Reddy, P. Radha Krishna, A. Ravi Sankar, K. Narsimulu, S. Kiran Kumar, P. Jayaprakash, B. Jagannadh, A. C. Kunwar, *J. Am. Chem. Soc.* **2003**, *125*, 13670 – 13671; b) G. V. M. Sharma, K. Ravinder Reddy, P. Radha Krishna, A. Ravi Sankar, P. Jayaprakash, B. Jagannadh, A. C. Kunwar, *Angew. Chem.* **2004**, *116*, 4051 – 4055; *Angew. Chem. Int. Ed.* **2004**, *43*, 3961 – 3965; c) G. V. M. Sharma, P. Nagender, P. Radha Krishna, P. Jayaprakash, K. V. S. Ramakrishna, A. C. Kunwar, *Angew. Chem.* **2005**, *117*, 6028 – 6032; *Angew. Chem. Int. Ed.* **2005**, *44*, 5878 – 5882.

[9] G. V. M. Sharma, V. Goverdhan Reddy, A. Subhash Chander, K. Ravinder Reddy, *Tetrahedron: Asymmetry* **2002**, *13*, 21 – 24.

[10] See the Supporting Information.

[11] Solvent titration studies were carried out by sequentially adding up to 33% of [D_6]DMSO to $CDCl_3$ solutions of the peptides.

 © 2006 Wiley-VCH Verlag GmbH & Co. KGaA, Weinheim

Polymer-Based Dynamic Memory

DOI: 10.1002/anie.200504365

A Dynamic Random Access Memory Based on a Conjugated Copolymer Containing Electron-Donor and -Acceptor Moieties

Qi-Dan Ling, Yan Song, Siew-Lay Lim, Eric Yeow-Hwee Teo, Yoke-Ping Tan, Chunxiang Zhu, Daniel Siu Hhung Chan, Dim-Lee Kwong, En-Tang Kang, and Koon-Gee Neoh*

Electroactive organic and polymeric materials are alternatives to traditional Si, Ge, and GaAs semiconductors that have to face the problem of scaling-down in cell size.[1,2] Several types of organic electronics and devices,[3] including light-emitting diodes,[4] transistors,[5] lasers,[6] photovoltaic cells,[7] switches,[8] and memories,[9] have been realized. Recently, flash (rewritable) memory[10] and write-once read-many-times (WORM) memory[11] based on polymeric materials has been demonstrated.

Polymer memories exhibit simple structures, good scalability, low-cost potential, 3D stacking capability, and a large capacity for data storage.[12] Rather than encoding "0" and "1" as the amount of charge stored in a cell, as in silicon-based devices, polymer memory stores data, for instance, based on the high and low conductivity response to an applied voltage.[13,14] In the pioneering work, the polymers were used as polyelectrolytes[15] and as matrices for dyes,[16] gold nano-particles,[17] or organic donor–acceptor (DA) systems,[18] and we have demonstrated a flash memory and a WORM memory based on a nonconjugated and a conjugated copolymer, respectively, containing lanthanide complexes.[19,20]

In this work, we report a novel memory device based on a conjugated copolymer (PFOxPy, structure shown in Figure 1a) that contains both electron-donor and -acceptor groups but no metal complex. In contrast to the nonvolatile flash and WORM memory devices based on polymers containing metal complexes, the device based on PFOxPy is

[*] Dr. Q.-D. Ling, S.-L. Lim, Prof. E.-T. Kang, Prof. K.-G. Neoh
Department of Chemical and Biomolecular Engineering
National University of Singapore
10 Kent Ridge
119260 Singapore (Singapore)
Fax: (+65) 6779-1936
E-mail: cheket@nus.edu.sg

Y. Song, E. Y.-H. Teo, Y.-P. Tan, Prof. C. Zhu, Prof. D. S. H. Chan
SNDL
Department of Electrical and Computer Engineering
National University of Singapore
119260 Singapore (Singapore)

Prof. D.-L. Kwong
Institute of Microelectronics
11 Science Park Road, Singapore Science Park II
117685 Singapore (Singapore)

Supporting Information for this article is available on the WWW under http://www.angewandte.org or from the author.

© 2006 Wiley-VCH Verlag GmbH & Co. KGaA, Weinheim

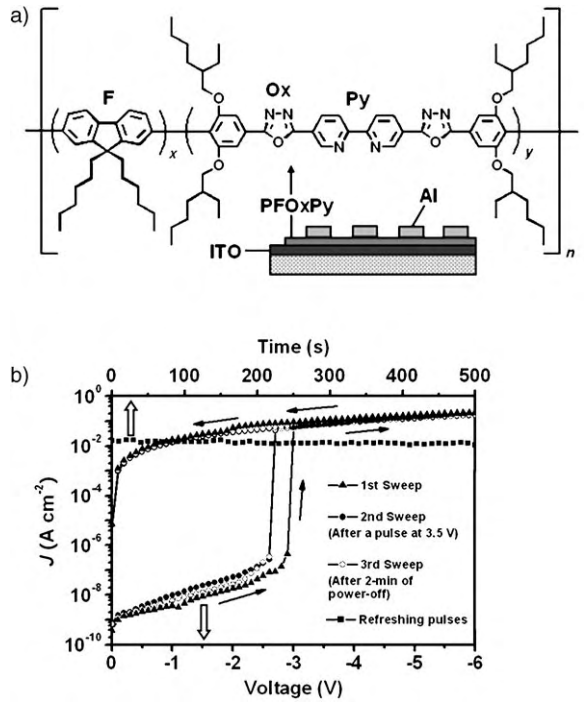

Figure 1. a) Molecular structure of the conjugated copolymer PFOxPy ($x/y = 0.81:0.19$). The inset shows a schematic of the memory device. b) Typical *J*–*V* characteristics of the ITO/PFOxPy/Al device in the ON and OFF states whilst maintaining the ON state by refreshing at −1 V every 10 s.

a volatile memory. However, the ON state can be electrically sustained by a refreshing pulse and reset to the initial OFF state by a reverse pulse. Thus, the device behaves as a dynamic random access memory (DRAM). This polymer-based DRAM device exhibits fairly good reliability and performance: 1) a high ON/OFF current ratio of up to 10^6 promises a low misreading rate, 2) both the ON and OFF states are stable up to 10^8 read cycles at a read voltage of −1.0 V, and 3) both states are stable at a constant voltage stress of −1.0 V.

PFOxPy was synthesized by the Suzuki coupling copolymerization of the monomers 9,9-dihexyl-9*H*-fluorene-2,7-bis(trimethylene boronate) (**M1**), 2,7-dibromo-9,9-dihexyl-9*H*-fluorene (**M2**), and 5,5′-bis(5-(4-bromo-3,5-bis(2-ethylhexyloxy)phenyl)-1,3,4-oxadiazol-2-yl)-2,2′-bipyridine (**M3**). The number-average molecular weight of PFOxPy is 26649, with a polydispersity index of 1.39. Because of its long alkyl and alkoxy substituents, PFOxPy is soluble in common organic solvents, such as THF, toluene and chloroform, and it can be spin-cast into uniform thin films from a toluene solution (10 mg mL^{-1}).

The memory device has the simple structure of a PFOxPy film (approx. 50 nm thick) sandwiched between an indium-tin-oxide (ITO) bottom electrode and an aluminium top electrode (about 0.5 μm thick; see inset of Figure 1a). The device has an active area of 0.4×0.4 mm^2, as dictated by the shadow-mask used for electrode deposition. The memory effect of PFOxPy is shown by the current density–voltage (*J*–*V*) characteristics in Figure 1b. The device was swept negatively, with the sweep direction indicated by the arrows. Initially, the device was at its low-conductivity state (OFF state). The current density in this state is quite low (on the order of 10^{-9}–10^{-7} A cm^{-2}). When a switching threshold voltage of about −2.8 V (onset) was applied, an abrupt increase in *J* from 10^{-7} to 10^{-2} A cm^{-2} was observed, indicating the transition from a low-conductivity state to a high-conductivity state (ON state). This electrical transition serves as the "writing" process for the memory device. Subsequent forward and backward sweeps showed that the device remains in its high-conductivity state. The distinct bi-electrical states in the voltage range of about 0 to −2 V allow a voltage (e.g., −1.0 V) to read the "0" or "OFF" signal (before writing) and "1" or "ON" (after writing) signal of the memory. As indicated in the second sweep, a reverse voltage pulse of about 3.5 V resets the memory device to the initial low-conductivity state ("0" or OFF state), which corresponds to the "erasing" process for the memory device. The erased state ("0") can be further written to the stored state ("1") when the switching threshold voltage is applied, thereby indicating that the memory device is rewritable. The slightly higher turn-on voltage for the first sweep might be caused by an initial delay in conformational change of the polymer chain under the electric field.

The third sweep was carried out after turning off the power for about two minutes. It was found that the ON state had relaxed to the steady OFF state. However, the device could be reprogrammed to the ON state. The short retention time of the ON state indicates that the memory device is volatile. However, the ON state can be electrically sustained by a refreshing voltage pulse of −1 V every 10 s (Figure 1b). The above characteristics are repeatable with high accuracy, and device degradation was not observed. This ability to write, read, erase, and refresh the electronic states of the device fulfils the functionality of a DRAM.

In order to understand the memory behavior of the present PFOxPy device, the electronic properties of PFOxPy were studied by density functional theory (DFT). Calculations of the optimized geometry, total charge density, electrostatic potentials (ESP), and molecular orbitals of the basic unit (BU), which includes all the functional moieties and segments, namely the fluorene oligomer (four repeat units; F), the 2,2′-bipyridine moiety (Py), and the 1,3,4-oxadiazole moiety (Ox) of PFOxPy, were carried out at the B3LYP/6-31G(d) level with the Gaussian 03 program package.[21] The alkyl groups of PFOxPy were not included in the calculation since they do not significantly affect the equilibrium geometry and thus the electronic properties. The energy levels of the HOMO and LUMO for the BU and functional fragments of PFOxPy are summarized in Figure 2a, along with the work functions (Φ) of the ITO and Al electrodes. In comparison with the energy levels of the F fragment, the introduction of electron-withdrawing 2,2′-bipyridine and 1,3,4-oxadiazole units lowers slightly the HOMO and LUMO energy levels of Py and Ox, respectively. The lowest energy barrier is between the Φ of ITO and the HOMO (0.40 eV) of the F fragment, which suggests that hole injection from ITO into the HOMO of PFOxPy (corresponding to a negative bias or with ITO as the anode) is the favored process; electron

 © 2006 Wiley-VCH Verlag GmbH & Co. KGaA, Weinheim

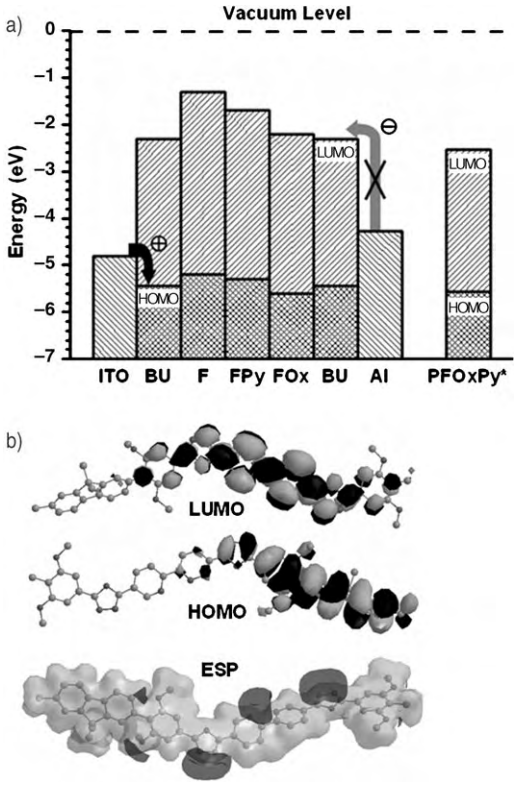

Figure 2. DFT molecular simulation results (B3LYP/6-31G(d) level): a) LUMO and HOMO energy levels for the basic unit (BU) and functional segments of PFOxPy along with the work function of the electrodes. The energy levels of the copolymer measured by cyclic voltammetry are indicated with an asterisk. b) LUMO, HOMO, and molecular electrostatic potential (ESP) surfaces of the BU of PFOxPy.

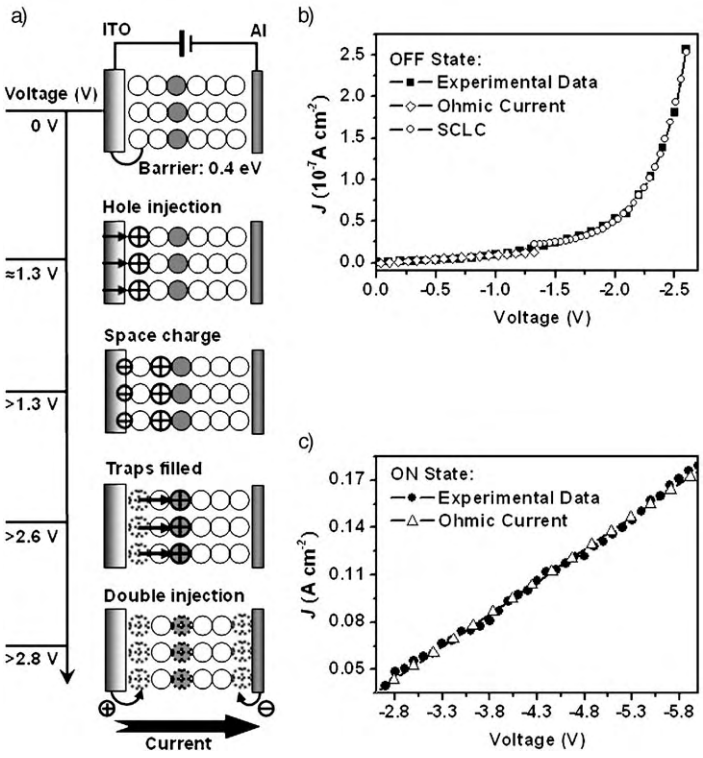

Figure 3. a) Operational mechanism of the memory. Experimental and fitted *J*–*V* curves of the ITO/PFOxPy/Al device: b) OFF state with the Ohmic current (< 1.3 V) and SCLC (≈ 1.3–2.6 V) models, and c) ON state with the Ohmic current model (> 2.8 V).

injection from Al into the LUMO of PFOxPy will be much more difficult due the high energy barrier (1.97 eV). Thus, PFOxPy is a p-type material and holes dominate the conduction process. The LUMO and HOMO of BU show the delocalization in PFOxPy (Figure 2b). The molecular surface with continuous positive ESP (in grey) along the conjugated backbone indicates that charge carriers can migrate through this open channel. However, there are some negative ESP regions (dark) which arise from the electron-acceptor groups. These negative regions can serve as "traps" to block the mobility of charge carriers. The depth of these traps, which arise from the 1,3,4-oxadiazole electron-acceptor moieties, is about 0.6 eV (Figure 2a). However, in the presence of incorporated 2,2′-bipyridine groups the depth of the traps is reduced to 0.3 eV. The traps are shallow, and filled traps can easily be detrapped. These shallow traps lead to low write/erase voltages and volatility of memory devices based on PFOxPy.

The operational mechanism of the memory is depicted in Figure 3a. Under a low negative bias voltage (0 to 1.3 V, with ITO as the anode), the *J*–*V* curve is linear and can be fitted with the Ohmic model, corresponding to a room-temperature resistance on the order of $10^9\ \Omega$ (Figure 3b). At this stage the material is insulating and the device is in its OFF state. A Schottky barrier (0.4 eV) forms under bias. Since the material is p-type in the OFF state, this barrier will be located near the anode. When the field exceeds the Schottky barrier, carrier generation (hole injection) occurs near the anode, leading to an accumulation of space charges and a redistribution of the electric field. The ohmic current changes to a space-charge-limited current (SCLC; bias ≈ 1.3–2.6 V) of the form of Equation (1).[22]

$$J \propto \frac{9\,\varepsilon_i \mu V^2}{8\,d^3} \qquad (1)$$

Herein, μ is the carriers' mobility, c is a positive constant independent of V or T, ε_i is the dynamic permittivity of the insulator, and d is the film thickness. Figure 3b shows that the *J*–*V* curve can be fitted rather well by this model. Close to the turn-on voltage the generated carriers fill some of the charge traps and the Al cathode also becomes an electron-injecting contact (to the charged HOMOs or radical cations), which leads to double injection and thus enhanced carrier concentration and mobility; the current increases rapidly to switch the device to the high-conductivity state (ON state). In the ON state (> 2.8 V), the *J*–*V* curve again follows the Ohmic model, with a room-temperature resistance on the order of $10^3\ \Omega$ (Figure 3c). The conductivity in the ON state is about 10^6 times that in the OFF state and can be retained as long as the current flow is maintained. As indicated by the theoretical results, the traps in PFOxPy are shallow. This feature defines the volatile characteristic of the present memory device. A reversed voltage pulse causes detrapping of the filled traps;

 © 2006 Wiley-VCH Verlag GmbH & Co. KGaA, Weinheim

turning off the power for a few minutes will have a similar effect. However, a refreshing pulse of −1 V every 10 s can replenish the traps and sustain the ON state.

The performance of the DRAM device based on PFOxPy was evaluated under ambient conditions. Figure 4a shows the

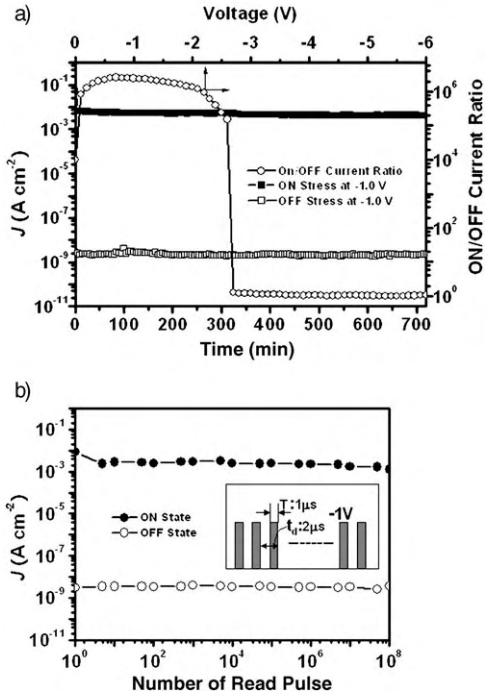

Figure 4. a) Stability of the ITO/PFOxPy/Al device in either ON or OFF state under a constant stress (−1 V) and the ON/OFF current ratio for the same sweep. b) Effect of read cycles on the ON and OFF states. The inset shows the pulses used for this measurement.

ratio of the ON- to OFF-state current as a function of the applied voltage for the same sweep. An ON/OFF current ratio of more than 10^6 is achieved for this memory device. This feature promises a low misreading rate due to the precise control of the ON and OFF states. In addition to a low misreading rate, stability is always an important issue in memory device performance. The stability of the device under a constant stress of −1.0 V is displayed by Figure 4a. No degradation in current density for the ON and OFF states was observed during the test.

The effect of continuous read pulses (with a read voltage of −1.0 V) on the ON and OFF states was also investigated (Figure 4b). The inset in Figure 4b shows the pulses used for the measurements. No resistance degradation was observed for the ON and OFF states after more than one hundred million (10^8) read cycles. Neither the voltage stress nor the read pulses cause the state transition since the applied voltage (−1 V) is lower than the switching threshold voltage (about −2.8 V) and can maintain the current flow in the ON state. Thus, both states are stable under the voltage stress and are insensitive to read pulses. The performance of the present polymer memory device compares favorably with that of current single-layer molecular (non-polymeric) memory devices.[23]

In summary, a polymer memory device based on the conjugated copolymer PFOxPy, which contains both electron-donor and -acceptor groups and with the sandwich structure ITO/PFOxPy/Al, allows us to write, read, erase, and refresh its electronic states. It fulfils the functionality of a dynamic random access memory (DRAM). After the device has been transformed to the ON state, it can be reset to the OFF state simply by turning off the power or by applying a reverse voltage pulse. The device also exhibits low reading, writing, and erasing voltages and a high ON/OFF current ratio of more than 10^6. Both the ON and OFF states are stable under a constant voltage stress of −1.0 V and survive up to 10^8 read cycles at a read voltage of −1.0 V. In this as-yet unoptimized single-layer architecture, the switching speed is about an order of magnitude slower than that (approx. 1 μs) of a NAND (NOT/AND) memory based on traditional semiconductors. However, the polymer DRAM distinguishes itself from the conventional silicon-based memory technologies by its solution processability and potential for high-density data storage through 3D stacking.

Experimental Section

M1 and **M2** were prepared as described in the literature.[24] **M3** was synthesized by reaction of methyl 4-bromo-3,5-bis(2-ethylhexyloxy)-benzoate[25] with hydrazine in the presence of methanol to form the corresponding hydrazide compound,[26] which was subsequently treated with 5,5′-bis(chlorocarbonyl)-2,2′-bipyridine.[27] The resulting compound was refluxed in excess phosphorus oxychloride to give **M3** as a light-yellow powder. Yield: 67.2%. M.p. ≈ 188.5 °C. C,H,N analysis (%) for $C_{58}H_{78}Br_2N_6O_6$: calcd. C 62.47, H 7.05, N 7.54; found C 62.85, H 6.87, N 7.20. MS (EI): m/z: 1115 $[M]^+$, 1003, 890, 778, 666 (100%), 586, 437, 357, 112, 70, 55. ^{1}H NMR ($CDCl_3$, 300 MHz): δ = 9.48 (s, 2H, Py-H), 8.74 (d, J = 8.2 Hz, 2H, Py-H), 8.61 (d, J = 2.1 Hz, 2H, Py-H), 8.58 (s, 4H, Ar-H), 4.06 (d, J = 5.6 Hz, 8H, OCH_2), 1.89–1.81 (m, 4H, CH), 1.67–1.49 (m, 12H, CH_2), 1.40–1.35 (m, 12H, CH_2), 1.01–0.91 ppm (m, 24H, CH_3). FT-IR (KBr pellet): $\tilde{\nu}$ = 2960, 2931, 2872, 2855, 1602, 1585, 1539, 1460, 1428, 1383, 1353, 1317, 1238, 1113, 1034, 1014, 846, 741 cm^{-1}.

PFOxPy: Monomers **M2** (0.39 g, 0.8 mmol) and **M3** (0.45 g, 0.4 mmol) were dissolved in degassed toluene (3 mL) in a small Schlenk flask under argon. **M1** (0.60 g, 1.2 mmol) was mixed with 1.0–1.5 mol% of $[Pd(PPh_3)_4]$ and added to the flask. A degassed aqueous solution of potassium carbonate (3 mL, 2.0 M) and toluene (2 mL) were added to the reactor. The mixture was stirred vigorously at 80–90 °C for 72 h under argon. The resulting solution was added dropwise, with stirring, to excess methanol to precipitate the polymer. The fibrous solid was collected by filtration and washed with methanol and water. The material was washed by Soxhlet extraction with acetone for 2 d to remove oligomers and catalyst residues. The product was dried overnight at room temperature under reduced pressure. Yield: 0.87 g (83.4%). $M_n = 2.66 \times 10^4$, $M_w = 3.71 \times 10^4$, PDI (polydispersity index) = 1.39. x = 0.81, y = 0.19 (calculated from the XPS composition data). ^{1}H NMR ($CDCl_3$, 300 MHz): δ = 9.44 (s, Py-H), 8.72 (d, J = 8.4 Hz, Py-H), 8.61 (d, J = 2.1 Hz, Py-H), 8.59 (d, J = 2.3 Hz, Ar-H), 8.55 (d, J = 2.1 Hz, Ar-H), 7.20 (s, Ar-H), 4.04 (d, J = 5.6 Hz, OCH_2), 1.89–1.81 (m, CH), 1.69–1.47 (m, CH_2), 1.39–1.35 (m, CH_2), 1.01–0.91 ppm (m, CH_3). FT-IR (KBr pellet): $\tilde{\nu}$ = 2960, 2928, 2876, 2859, 1600, 1584, 1538, 1457, 1426, 1383, 1352, 1313, 1236, 1109, 1092, 1013, 973, 870, 840, 739, 645, 594 cm^{-1}. XPS (binding energy, eV): C1s: 284.6 (C-H/C-C), 285.6 (C=N-C in pyridyl), 286.1 (*C*-O, alkoxy), 287.4 (O-C=N in oxadiazole); N1s: 399.0 (C=N-C in pyridyl), 399.5 (C=N-N in oxadiazole). Cyclic voltammetry (0.1 M nBu$_4$NPF$_6$ in MeCN, Pt counter electrode, Ag/AgCl):

 © 2006 Wiley-VCH Verlag GmbH & Co. KGaA, Weinheim

$E_{Red}(onset) = -1.76$ V, $E_{Ox}(onset) = +1.27$ V; $E_{LUMO} = -2.54$ eV, $E_{HOMO} = -5.57$ eV.

Calculations of the molecular orbitals and electronic properties for the basic unit and functional fragments of PFOxPy were carried out using the Gaussian 03 program package on a Compaq GS320 alpha sever with 8 CPUs and up to 4 GB memory. The molecular orbitals and static electronic properties were calculated using density functional theory (DFT) at the B3LYP/6-31G(d) level.[21]

Fabrication and characterization of the memory device: The indium-tin-oxide (ITO)/glass substrate was cleaned with water, acetone, and then 2-propanol in an ultrasonic bath (15 min each). A toluene solution of PFOxPy (10 mg mL^{-1}) was spin-coated onto ITO, followed by solvent removal in a vacuum chamber at 10^{-5} Torr and 50 °C for 12 h. The thickness of the polymer layer was about 50 nm. Aluminum top electrodes (for needle contacts) with an area of 0.4×0.4 mm^2 and a thickness of 0.5 μm were thermally evaporated onto the polymer surface at about 10^{-7} Torr through a shadow mask. The devices were characterized, under ambient conditions, using a Hewlett–Packard 4156A semiconductor parameter analyzer equipped with an Agilent 16440A SMU/pulse generator.

Received: December 8, 2005
Published online: March 27, 2006

Keywords: conjugation · dynamic memory · materials science · polymers

[1] F. M. Raymo, *Adv. Mater.* **2002**, *14*, 401.
[2] C. Li, D. H. Zhang, X. L. Liu, S. Han, T. Tang, C. W. Zhou, W. Fan, J. Koehne, J. Han, M. Meyyappan, A. M. Rawlett, D. W. Price, J. M. Tour, *Appl. Phys. Lett.* **2003**, *82*, 645.
[3] S. R. Forrest, *Nature* **2004**, *428*, 911.
[4] J. H. Burroughes, D. D. C. Bradley, A. R. Brown, R. N. Marks, K. Mackay, R. H. Friend, P. L. Burns, A. B. Holmes, *Nature* **1990**, *347*, 539.
[5] F. Garnier, R. Hajlaoui, A. Yassar, P. Srivastava, *Science* **1994**, *265*, 1684.
[6] N. Tessler, G. J. Denton, R. H. Friend, *Nature* **1996**, *382*, 695.
[7] M. Granstrom, K. Petritsch, A. C. Arias, A. Lux, M. R. Andersson, R. H. Friend, *Nature* **1998**, *395*, 257.
[8] H. Goto, E. Yashima, *J. Am. Chem. Soc.* **2002**, *124*, 7943.
[9] Q. Li, G. Mathur, S. Gowda, S. Surthi, Q. Zhao, L. Yu, J. S. Lindsey, D. F. Bocian, V. Misra, *Adv. Mater.* **2004**, *16*, 133.
[10] J. Ouyang, C. W. Chu, C. R. Szmanda, L. P. Ma, Y. Yang, *Nat. Mater.* **2004**, *3*, 918.
[11] S. Moller, C. Perlov, W. Jackson, C. Taussig, S. R. Forrest, *Nature* **2003**, *426*, 166.
[12] A. Stikeman, *Technol. Rev.* **2002**, *105*, 31.
[13] Z. M. Liu, A. A. Yasseri, J. S. Lindsey, D. F. Bocian, *Science* **2003**, *302*, 1543.
[14] D. M. Taylor, C. A. Mills, *J. Appl. Phys.* **2001**, *90*, 306.
[15] S. Moller, S. R. Forrest, C. Perlov, W. Jackson, C. Taussig, *J. Appl. Phys.* **2003**, *94*, 7811.
[16] A. Bandyopadhyay, A. J. Pal, *Adv. Mater.* **2003**, *15*, 1949.
[17] R. J. Tseng, J. X. Huang, J. Ouyang, R. B. Kaner, Y. Yang, *Nano Lett.* **2005**, *5*, 1077.
[18] C. W. Chu, J. Ouyang, J. H. Tseng, Y. Yang, *Adv. Mater.* **2005**, *17*, 1440.
[19] Q. D. Ling, Y. Song, S. J. Ding, C. X. Zhu, D. S. H. Chan, D. L. Kwong, E. T. Kang, K. G. Neoh, *Adv. Mater.* **2005**, *17*, 455.
[20] Y. Song, Q. D. Ling, C. X. Zhu, E. T. Kang, D. S. H. Chan, Y. H. Wang, D. L. Kwong, *IEEE Electron Device Lett.*, **2006**, *27*, 154..
[21] Gaussian 03 (Revision C.02): M. J. Frisch et al., see Supporting Information.
[22] C. A. Mills, D. M. Taylor, A. Riul, A. P. Lee, *J. Appl. Phys.* **2002**, *91*, 5182.
[23] A. Bandyopadhyay, A. J. Pal, *Appl. Phys. Lett.* **2003**, *82*, 1215, and references therein.
[24] Q. D. Ling, E. T. Kang, K. G. Neoh, W. Huang, *Macromolecules* **2003**, *36*, 6995.
[25] A. Fürstner, F. Stelzer, A. Rumbo, H. Krause, *Chem. Eur. J.* **2002**, *8*, 1856.
[26] X. W. Zhan, Y. Q. Liu, X. Wu, S. Wang, D. B. Zhu, *Macromolecules* **2002**, *35*, 2529.
[27] L. S. Tan, J. L. Burkett, S. R. Simko, M. D. Alexander, Jr., *Macromol. Rapid Commun.* **1999**, *20*, 16.

 © 2006 Wiley-VCH Verlag GmbH & Co. KGaA, Weinheim

β-Hydroxy Esters

DOI: 10.1002/anie.200504239

A Catalytic, Me_2Zn-Mediated, Enantioselective Reformatsky Reaction With Ketones**

*Pier Giorgio Cozzi**

Dedicated to Professor Achille Umani-Ronchi on the occasion of his 70th birthday

The Reformatsky reaction,[1] one of the classic "named" reactions, was discovered almost 120 years ago and is still widely used in synthesis.[2] It consists of the zinc-induced formation of β-hydroxyalkanoates from α-halocarbonyl compounds and aldehydes or ketones. Its excellent functional group tolerance and the possibility of preparing the reagent in situ, by activation of zinc metal following a variety of different methods,[3] have contributed to its success. In the last six years, homogeneous Reformatsky-type reactions based on the use of Me_2Zn or Et_2Zn in the presence of nickel[4] or rhodium[5] have been described.

Although progress has been made on an asymmetric version of the Reformatsky reaction with the introduction of chiral auxiliaries[6] or ligands,[7] a truly catalytic version has still not been achieved. Very few methods have been reported

[*] Prof. Dr. P. G. Cozzi
Dipartimento di Chimica "G. Ciamician"
Università di Bologna
Via Selmi, 2, 40126 Bologna (Italy)
Fax: (+39) 051-209-9456
E-mail: piergiorgio.cozzi@unibo.it

[**] Dr. Eleonora Rivalta is acknowledged for her experimental help. Professor Giuseppe Bartoli and Dr. Paolo Melchiorre are acknowledged for allowing use of their chiral GC instruments. The European Commission (project FP6-505267-1(LIGBANK)), MIUR (Progetto Nazionale Stereoselezioni in Chimica Organica: Metodologie ed Applicazioni), and FIRB (Progettazione, preparazione e valutazione biologica e farmacologica di nuove molecole organiche quali potenziali farmaci innovativi) are acknowledged for their financial support of this research.

Supporting Information for this article is available on the WWW under http://www.angewandte.org or from the author.

© 2006 Wiley-VCH Verlag GmbH & Co. KGaA, Weinheim

for the catalytic aldol reaction of ketones,[8] although the stereocontrolled addition of Reformatsky-type reagents to ketones has received increased attention for the preparation of quaternary stereocenters.[9]

Herein, we disclose the first practical catalytic enantioselective Reformatsky reaction with ketones, which is based on the use of [ClMn(salen)] as the chiral catalyst. Recently, we reported a highly efficient, enantioselective,[10] one-pot three-component imino-Reformatsky reaction that gives β-amino esters in moderate to good yields. We therefore tried to use this protocol with ketones, and obtained good conversions but only low *ee* values. We reasoned that a controlled and mild formation of the zinc reagent, using the less reactive Me_2Zn in the presence of a chiral zinc complex, should lead to the first catalytic version of this important reaction.

Zinc enolates can be prepared by direct exchange of iodo esters with Et_2Zn[11] or iPr_2Zn.[12] Enantioselective variants based on the exchange between an iodoacetate and Et_2Zn have also been developed.[13] We therefore tested several chiral ligands in the presence of Me_2Zn and iodoacetate[14] in a model reaction with acetophenone, and observed the desired conversion only in the presence of the salen ligand (Scheme 1;

Scheme 1. The Me_2Zn-mediated Reformatsky reaction promoted by [ClMn(salen)] that was chosen as the model reaction.

see Supporting Information for further details).[15,16] Among the M(salen) complexes tested, [ClMn(salen)][17] emerged as

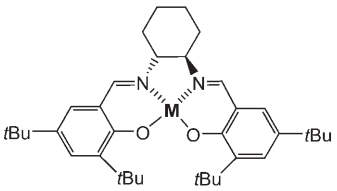

the most promising catalyst, and the effect of changing various reaction parameters (solvent, temperature, mode of addition) was therefore evaluated with this complex (see Supporting Information). Complete conversion and a good level of *ee* values were obtained when performing the reaction at reflux temperature in *t*BuOMe. The enantiomeric excess improved slightly (up to 66% *ee*) upon performing the reaction in the presence of 4-phenylpyridine *N*-oxide, an additive that is often used in enantioselective [ClMn(salen)]-catalyzed epoxidations,[18] although we observed lower reactivity at room temperature or under reflux conditions.

Different esters were also evaluated during the optimization of the process (Scheme 2, Table 1). As can be seen from these data, increasing the steric hindrance of the ester caused a drop in enantiomeric excess, with the ethyl ester giving the

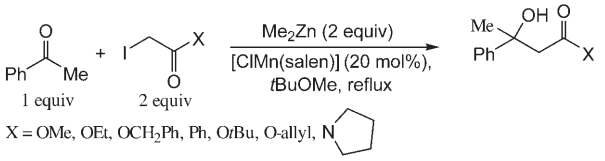

Scheme 2. Iodo derivatives used in the Me_2Zn-mediated Reformatsky reaction promoted by [ClMn(salen)].

Table 1: Results of the enantioselective Reformatsky reactions shown in Scheme 2.

Entry[a]	Iodo derivative[b]	Conversion [%][c]	*ee* [%][d]
1	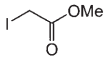	85	46
2	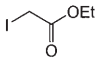	95 (90)	63
3	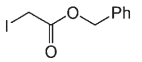	60	44
4	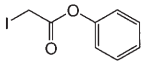	50	16
5	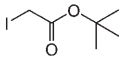	90	0
6	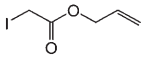	90	40
7	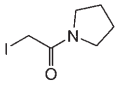	84	10

[a] All the reactions were performed as shown in Scheme 2 (for experimental details see Supporting Information). [b] All iodo derivatives were prepared by an exchange reaction with the corresponding bromoacetate using NaI in acetone at room temperature. [c] Conversion evaluated by HPLC analysis of the crude reaction mixture; yield of isolated product in parentheses. [d] Determined by chiral HPLC analysis (Chiralcel OD column).

highest *ee* value. Different Mn(salen) complexes were also prepared (see Supporting Information) and used in the model reaction, although they proved to be no better.[19] Since the best conversion with acetophenone was obtained in refluxing *t*BuOMe for a short reaction time,[20] we tested other ketones using this protocol. Unfortunately, although conversion was good, the enantiomeric excesses obtained were only moderate. However, to our delight, when the reaction was performed at room temperature in the presence of 4-phenylpyridine *N*-oxide (Scheme 3) the enantiomeric excesses were substantially improved.

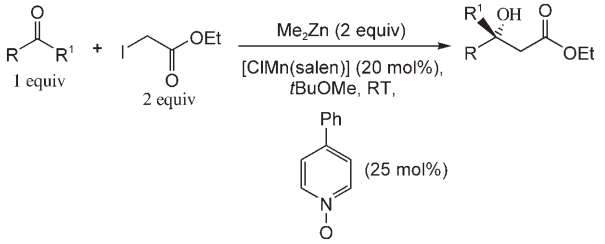

Scheme 3. Catalytic enantioselective Reformatsky reactions promoted by [ClMn(salen)] and 4-phenylpyridine *N*-oxide.

 © 2006 Wiley-VCH Verlag GmbH & Co. KGaA, Weinheim

The reaction shows broad scope, since aromatic, aliphatic, heterocyclic, and α,β-unsaturated ketones all react to give the desired products in moderate yields (Table 2). Aromatic ketones gave enantioselectivities in the range 69–86%;

Table 2: Catalytic enantioselective Reformatsky reaction with a variety of ketones.

Entry[a]	Ketone	Yield [%][b]	*t* [h]	*ee* [%][c]
1[d]	1-tetralone	65	3	69
2	1-tetralone	45	48	86
3[d,e]	1-indanone	75	1.50	72 (*R*)
4[f]	1-indanone	40	1.50	78 (*R*)
5	1-indanone	64	40	84 (*R*)
6	2-chloroacetophenone	53	30	84
7	2-chloroacetophenone	73	120	80
8	4-chloroacetophenone	55	72	85
9	1-acetonaphthone	53	80	82
10[e]	4-bromoacetophenone	46	30	80 (*R*)
11[e]	3-methylacetophenone	48	100	81 (*R*)
12	acetylferrocene	70	20	57
13	2-furylacetone	51	120	40
14[g]	propiophenone	60	48	53 (*R*)
15	(*E*)-4-phenyl-3-buten-2-one	54	24	49
16[h]	(*E*)-3-penten-2-one	30	24	75 (*R*)
17	2,2-dimethylcyclopentanone	70	120	96
18	4-phenylbutan-2-one	77	24	23
19[i]	4-phenylbutan-2-one	57	18	26
20[j]	6-methyl-5-hepten-2-one	40	24	21 (*S*)
21	3-methylbutan-2-one	63	72	28
22	cyclopropylacetone	78	72	86

[a] All the reactions were performed in duplicate, at room temperature, using 2 equiv of ethyl iodoacetate and 2 equiv of Me_2Zn. The catalyst was prepared by stirring [Cl(Mn(salen)] (20 mol%) and 4-phenylpyridine *N*-oxide (25 mol%) in *t*BuOMe for 1 h (for experimental details see Supporting Information). [b] Yield of product after purification by column chromatography. [c] Determined by chiral HPLC (Chiralcel OD column) or GC analysis. The enantiomeric excesses given are the averages of two runs. [d] The reaction was performed at reflux without the presence of 4-phenylpyridine *N*-oxide.[e] The absolute configuration was established by chemical correlation (see Supporting Information for details). [f] The reaction was performed at reflux in the presence of 25 mol% of 4-phenylpyridine *N*-oxide. [g] The absolute configuration was determined based on the sign of optical rotation of the corresponding diol.[24] [h] The absolute configuration was determined based on the comparison of the sign of optical rotation with the reported value.[25] [i] The reaction was performed in the presence of 80 mol% [ClMn(salen)]. [j] The absolute configuration was determined based on the comparison of the sign of optical rotation with the reported value.[26]

electron-poor and electron-rich ketones behaved similarly. As noted previously by Denmark et al.,[8a,b] the reactivity of furylacetone was again modest as the coordination of the furan oxygen atom to the metal probably diminishes the enantiomeric excess. Unlike the catalytic system described by Denmark et al., however, α,β-unsaturated ketones gave enantiomeric excesses of up to 75%. Aliphatic linear ketones gave synthetically useless results (Table 2, entries 18–20), but the results obtained with 2,2-dimethylcyclopentanone (Table 2, entry 17) represent the highest enantiomeric excess reported to date for a simple aliphatic ketone.[8d,g] In general, steric hindrance seems to control selectivity in the present reaction. Although we are unable to suggest a mechanism for this reaction, the clean reaction obtained with allyl iodoacetate (Table 1, entry 6) seems to rule out the formation of radical intermediates.[21]

In conclusion, we have developed the first effective, catalytic, enantioselective Reformatsky reaction based on the use of inexpensive and readily available [ClMn(salen)][22] as the catalyst with an iodo ester as reaction partner. The formation of a reactive zinc enolate under mild conditions, which is able to react in a stereoselective manner with a rather unreactive ketone, has been realized whilst avoiding the use of strong bases, sensitive enolates, and expensive ligands. We believe that several interesting reactions of this Reformatsky-type reagent with other electrophiles could be possible.[23]

Received: November 29, 2005
Revised: January 30, 2006
Published online: March 23, 2006

Keywords: enantioselectivity · homogeneous catalysis · ketones · manganese · N ligands

[1] S. Reformatsky, *Ber. Dtsch. Chem. Ges.* **1887**, *20*, 1210–1211; for a review, see: R. Ocampo, W. R. Dolbier, Jr., *Tetrahedron* **2004**, *60*, 9325–9374; see also: S. A. Babu, M. Yasuda, I. Shibata, A. Baba, *J. Org. Chem.* **2005**, *70*, 10408–10419, and references therein.

[2] a) A. Fürstner, *Synthesis* **1989**, 571–590; b) A. Fürstner in *Organozinc Reagents* (Eds.: P. Knochel, P. Jones), Oxford University Press, New York, **1999**, pp. 287–305; c) J. A. Marshall, *Chemtracts* **2000**, *13*, 705–707; d) J. Podlech, T. C. Maier, *Synthesis* **2003**, 633–655; e) F. Orsini, G. Sello, *Curr. Org. Synth.* **2004**, *1*, 111–135; f) E. Nakamura in *Organometallics in Synthesis: A Manual* (Ed.: M. Schlosser), Wiley, New York, **2002**, pp. 579–664.

[3] a) Rieke-Zn: R. D. Rieke, S. J. Uhm, *Synthesis* **1975**, 452–453; b) Zn/Cu couple: E. Santaniello, A. Manzocchi, *Synthesis* **1977**, 698–699; Zn/Ag on graphite: R. Csuk, A. Fürstner, H. J. Weidmann, Jr., *J. Chem. Soc. Chem. Commun.* **1986**, 775–776.

[4] a) J. C. Adrian, Jr., M. L. Snapper, *J. Org. Chem.* **2003**, *68*, 2143–2150; b) A. Dondoni, A. Massi, S. Sabbatini, *Chem. Eur. J.* **2005**, *11*, 7110–7125.

[5] a) K. Kanai, H. Wakabayashi, T. Honda, *Org. Lett.* **2000**, *2*, 2549–2551; b) K. Kanai, H. Wakabayashi, T. Honda, *Heterocycles* **2002**, *58*, 47–51.

[6] a) J. D. Clark, G. A. Weisenburger, D. K. Anderson, P.-J. Colson, A. D. Edney, D. J. Gallagher, H. P. Kleine, C. M. Knable, M. K. Lantz, C. M. V. Moore, J. B. Murphy, T. E. Rogers, P. G. Ruminski, A. S. Shah, N. Storer, B. E. Wise, *Org. Proc. Res. Dev.* **2004**, *8*, 51–61; b) S. Marcotte, X. Pannecoucke, C. Feasson, J.-C. Quirion, *J. Org. Chem.* **1999**, *64*, 8461–8464.

[7] a) K. Sorger, H. Petersen, J. Stohrer, *Eur. Pat. Appl.* **2004**, EP 1394140; b) D. H. Park, H. J. Choi, S.-G. Lee, *J. Korean Chem. Soc.* **2003**, *47*, 597–600; c) Y. Fujiwara, T. Katagiri, K. Uneyama, *Tetrahedron Lett.* **2003**, *44*, 6161–6163; d) J. M. Andres, R. Pedrosa, A. Perez-Encabo, *Tetrahedron* **2000**, *56*, 1217–1223; e) J. M. Andres, Y. Martin, R. Pedrosa, A. Perez-Encabo, *Tetrahedron* **1997**, *53*, 3787–3794; f) A. Mi, Z. Wang, Z. Chen, Y. Jiang, A. S. C. Chan, T.-K. Yang, *Tetrahedron: Asymmetry* **1995**, *6*, 2641–2642; g) D. Pini, A. Mastantuono, P. Salvadori, *Tetrahedron: Asymmetry* **1994**, *5*, 1875–1876; h) K. Soai, A. Oshio, T. Saito, *J. Chem. Soc. Chem. Commun.* **1993**, 811–812; i) P. S. Johar, S. Araki, Y. Butsugan, *J. Chem. Soc. Perkin Trans.* **1992**, 711–713.

 © 2006 Wiley-VCH Verlag GmbH & Co. KGaA, Weinheim

[8] a) S. E. Denmark, Y. Fan, M. D. Eastgate, *J. Org. Chem.* **2005**, *70*, 5235 – 5248; b) S. E. Denmark, Y. Fan, *J. Am. Chem. Soc.* **2002**, *124*, 4233 – 4235; c) K. Oisaki, Y. Suto, M. Kanai, M. Shibasaki, *J. Am. Chem. Soc.* **2003**, *125*, 5644 – 5645; d) K. Oisaki, D. Zhao, Y. Suto, M. Kanai, M. Shibasaki, *Tetrahedron Lett.* **2005**, *46*, 4325 – 4329; e) N. Gathergood, K. Juhl, T. B. Poulsen, K. Thordrup, K. A. Jørgensen, *Org. Biomol. Chem.* **2004**, *2*, 1077 – 1085; f) D. A. Evans, S. W. Tregay, C. S. Burgey, N. A. Paras, T. Vojkovsky, *J. Am. Chem. Soc.* **2000**, *122*, 7936 – 7943; g) D. A. Evans, C. S. Burgey, M. C. Kozlowski, S. W. Tregay, *J. Am. Chem. Soc.* **1999**, *121*, 686 – 699; h) Riant et al. have recently described a highly enantioselective and diastereoselective addition of enolates to aryl ketones: J. Deschamp, O. Chuzel, J. Hannedouche, O. Riant, *Angew. Chem.* **2006**, *118*, 1314 – 1319; *Angew. Chem. Int. Ed.* **2006**, *45*, 1292 – 1297.

[9] A. Ojida, T. Yamano, N. Taya, A. Tasaka, *Org. Lett.* **2002**, *4*, 3051 – 3054.

[10] P. G. Cozzi, E. Rivalta, *Angew. Chem.* **2005**, *117*, 3666 – 3669; *Angew. Chem. Int. Ed.* **2005**, *44*, 3600 – 3603.

[11] a) S. Ito, H. Shinokubo, K. Oshima, *Tetrahedron Lett.* **1998**, *39*, 5235 – 5236; b) K. Maruoka, N. Hirayama, H. Yamamoto, *Polyhedron* **1990**, *9*, 223 – 226.

[12] I. Sato, Y. Takizawa, K. Soai, *Bull. Chem. Soc. Jpn.* **2000**, *73*, 2825 – 2826.

[13] Y. Ukaji, S. Takenaka, Y. Horita, K. Inomata, *Chem. Lett.* **2001**, 254 – 255.

[14] Binol, *N*-methylephedrine, pybox, sparteine, bis-sulfonamides, bis-imines, taddol, box, binap, and hydroxyphenyloxazoline employed in a model reaction in Et_2O as the reaction solvent with PhCOMe, iodoacetate, and Me_2Zn gave no conversion after 24 h.

[15] Different chiral or achiral salen-type ligands (0.1 equiv) were tested in the presence of PhCOMe (1 equiv) and Me_2Zn (2 equiv) in Et_2O as the solvent.

[16] The absolute configuration of the product was established by comparing the optical rotation with that of a known product, see: M. Guetté, J. Capillon, J.-P. Guettè, *Tetrahedron* **1973**, *29*, 3659 – 3667.

[17] [ClMn(salen)] was prepared according to: M. Palucki, N. S. Finney, P. J. Pospisil, M. L. Guler, T. Ishida, E. N. Jacobsen, *J. Am. Chem. Soc.* **1998**, *120*, 948 – 954, and references therein. Commercially available [ClMn(salen)] shows higher reactivity but slightly lower enantioselectivity (see Supporting Information (Table 3, entry 5)). Differences in performance for catalytic epoxidation with commercially available [ClMn(salen)] have also been observed and are probably due to the presence of oxo compounds, see: J. R. Chipperfield, J. Clayton, K. A. Siraj, S. Woodward, *J. Chem. Soc. Dalton Trans.* **2000**, 1087 – 1094, and references therein.

[18] E. McGarrigle, D. G. Gilheany, *Chem. Rev.* **2005**, *105*, 1563 – 1602.

[19] Schiff bases with hindered groups in positions 2 and 2′ give better results. This could be related to the stability of Mn(salen) in the presence of an excess of Me_2Zn. For the relative stability of metal–Schiff base complexes in the presence of other metal complexes, see: E. Solari, F. Corazza, C. Floriani, A. Chiesi-Villa, C. Guastini, *J. Chem. Soc. Dalton Trans.* **1990**, 1345 – 1355.

[20] Increasing the reaction time at reflux gave a lower yield and complete conversion of the ketone.

[21] For radical reactions mediated by Mn^{III}, see: a) T. Linker, *J. Organomet. Chem.* **2002**, *661*, 159 – 167; b) K. Narasaka, *Pure Appl. Chem.* **1997**, *69*, 601 – 604; c) D. Yang, X.-Y. Ye, S. Gu, M. Xu, *J. Am. Chem. Soc.* **1999**, *121*, 5579 – 5580.

[22] For the use of [ClMn(salen)] as a Lewis acid, see: a) S. S. Kim, S. H. Lee, *Synth. Commun.* **2005**, *35*, 751 – 759.

[23] The reaction with benzaldehyde following the optimized protocol afforded the desired product with 40 % *ee*. We are now studying different salen ligands in order to improve the enantiomeric excess with aldehydes.

[24] S. Mitsui, Y. Kudo, *Tetrahedron* **1967**, *23*, 4271 – 4277.

[25] I. Dyong, D. Glittemberg, *Chem. Ber.* **1977**, *110*, 2721 – 2728.

[26] K. Y.-K. Chow, J. Bode, *J. Am. Chem. Soc.* **2004**, *126*, 8126 – 8127.

 © 2006 Wiley-VCH Verlag GmbH & Co. KGaA, Weinheim

Nanogels

DOI: 10.1002/anie.200503926

Soluble Single-Molecule Nanogels of Controlled Structure as a Matrix for Efficient Artificial Enzymes**

Günter Wulff, Byong-Oh Chong, and Ute Kolb*

Dedicated to Professor David C. Sherrington on the occasion of his 60th birthday

For years, the construction of efficient artificial mimics of natural enzymes has been a challenging topic for scientists from a variety of disciplines.[1] Macrocyclic compounds, polymers, micelles, and others have been used as matrices for the construction of these mimics.[2] More recently, inspired by the concept of transition-state stabilization in enzyme catalysis[3] researchers have raised catalytically quite active antibodies against stable transition-state analogues of the reaction of interest.[4] Similarly, molecularly imprinted polymers[5] offer excellent possibilities for mimicking the active sites of enzymes since not only the shape of the transition state can be mimicked by imprinting but also suitable catalytic groups and binding sites can be introduced in a predetermined orientation.[6] However, only recently have compounds with strong catalytic activity clearly surpassing that of the corresponding catalytic antibodies been prepared.[7] The disadvantage of these molecularly imprinted model systems is their insolubility and the heterogeneity of the active sites.

Here we report on a new procedure to obtain molecularly imprinted catalysts in the form of soluble, single-molecule nanogels of defined structure. As they contain just one active site per particle, they are very similar to natural enzymes. More homogeneous imprinting has already been achieved by Zimmerman et al.,[8] who performed molecular imprinting inside dendrimers. But this method requires elaborate syntheses, and the selectivity in molecular recognition was modest. A more general method should be the synthesis of highly cross-linked, soluble nanogels. In this case it is crucial to avoid macrogelation during the polymerization and to produce separated, intramolecularly cross-linked macromolecules. Such polymers can be obtained, for example, by emulsion polymerization.[9] An elegant approach avoiding aqueous solutions during preparation has been described by Graham et al.[10] The polymerization is conducted in homogeneous solution at higher dilution in solvents with a solubility parameter δ similar to that of the corresponding polymer. Earlier work in our group[11] has shown that it is indeed possible to obtain molecularly imprinted, soluble, highly cross-linked nanogels by this method; however, the selectivity was rather low. Similar results were obtained by Resmini et al.;[12] the catalytic activity of their nanogels was also low with only 1 % of the prepared sites being catalytically active. They also did not control the size and the molecular weight of the nanoparticles. In general, nanogels of this type seem to be unsuitable for molecular imprinting because they possess a noncompact "fractal"[13] structure.

During the development of more efficient nanogels we used a rather simple catalytic system that was already employed with insoluble, molecularly imprinted polymers.[14] Imprinted nanogels were thus prepared by polymerization and cross-linking of complex **1**, which consists of a diphenyl

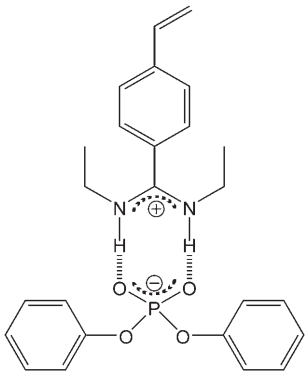

1

phosphate template as the stable transition-state analogue of the carbonate hydrolysis and *N*,*N*′-diethyl-4-vinylbenzamidine as the functional monomer. Removal of the template leads to active sites with a shape corresponding to the shape of the transition state and with one amidine group each. The ratio of the monomers and the content of cross-linker were the same as that in the preparation of insoluble macroporous polymers[14] (see Table 1). Radical polymerization was performed in dilute solution in cyclopentanone (0.1–1.5 wt %). (Cyclopentanone proved to be the best solvent for this purpose.) The resultant nanogels could be isolated from the completely transparent solution by precipitation with petroleum ether or by ultracentrifugation. The template was removed afterwards. Since the nanogels are completely soluble in THF, $CHCl_3$, DMF, CH_2Cl_2, DMSO, and in mixtures of water and acetonitrile, they could be investigated by typical analytical methods for polymers, such as gel permeation chromatography (GPC) and membrane osmometry, and kinetic experiments could be conducted in homogeneous solution.

[*] Prof. Dr. G. Wulff, Dr. B.-O. Chong
Institute of Organic and Macromolecular Chemistry
Heinrich Heine University Düsseldorf
Universitätsstrasse 1, 40225 Düsseldorf (Germany)
Fax: (+49) 211-811-5840
E-mail: wulffg@uni-duesseldorf.de
Dr. U. Kolb
Institute of Physical Chemistry
University of Mainz
Welderweg 11, 55099 Mainz (Germany)

[**] We thank Dr. P. Casper for the GPC measurements. This work was supported by the Deutsche Forschungsgemeinschaft and the Fonds der Chemischen Industrie. B.-O.C. acknowledges a scholarship from the DFG Graduierten-Kolleg "Molecular physiology: Substance and energy transformation".

Supporting information for this article is available on the WWW under http://www.angewandte.org or from the author.

 © 2006 Wiley-VCH Verlag GmbH & Co. KGaA, Weinheim

Table 1: Preparation and molecular weights of imprinted nanogels **ING1**–**ING7**.[a]

Nanogel	$c_{monomer}$ [%]	Method[b]	Yield [%]	M_n ($\times 10^3$)	M_w/M_n	$M_{n,abs.}$ ($\times 10^4$)	$M_{n,abs.}/M_n$
ING1	1.0	standard	53.6	23.1	8.5	38.1	16.5
ING2	1.0	A	81.3	29.5	10.4	49.2	16.7
ING3	1.0	B, C	83.7	24.5	6.0	62.4	25.5
ING4	1.5	A, B, C, D	99.5	42.2	18.6	92.4	21.9
ING5	0.5	B, C	61.1	8.91	3.6	26.1	29.3
ING6	0.1	B, C	27.6	1.34	1.54	4.43	33.0
ING7	0.1	B, C, E	31.4	1.30	1.54	3.90	30.1

[a] Standard conditions: The monomer mixture consists of 80 wt% of ethylene dimethacrylate, 11 wt% of methyl methacrylate, 9 wt% of **1**; addition of azobis(isobutyronitrile) (3 wt% of the monomer mixture). The mixture was heated in cyclopentanone at the stated concentration under nitrogen to 80 °C for 4 d. After evaporation to one-third of the volume, the product was isolated by precipitation by adding to of five times the volume of petroleum ether (b.p. 60–80 °C), ultrafiltration, and drying. The template was removed by dissolving the nanogel in chloroform and shaking the solution three times with aqueous 0.05 N NaOH solution. The organic layer was washed with neutral water, and the nanogel was isolated as before by precipitation. Apparent molecular weights (M_n, M_w) were determined in THF by GPC using linear polystyrenes as standards (for details see the Supporting Information). $M_{n,abs.}$ values were obtained by membrane osmometry in chloroform using regenerated cellulose membranes with pore sizes of 5 to 10 nm. [b] Variations: A) cross-linking content 90%. B) Stepwise polymerization at 60 °C (144 h), 70 °C (96 h), and 80 °C (96 h) with additional 1% initiator at 70 °C and 80 °C. C) In the "postdilution method" the monomer mixture was dissolved in the same volume of cyclopentanone and heated to 60 °C for 120 min. (This time was determined in advance from heating experiments until macrogelation occurred.) The mixture was then diluted with cyclopentanone to the desired monomer concentration (0.1–1.5%) and polymerized further in the stepwise temperature mode. D) Cross-linker trimethylolpropane trimethacrylate (TRIM). E) Template monomer **1** at half concentration (4.5%).

The preparation of the first nanogel (**ING1**, Table 1) was analogous to previous syntheses.[10,11] **ING1** has an apparent number-average molecular weight M_n of 23100 (by GPC) and a high polydispersity of $M_w/M_n = 8.5$. The GPC analysis clearly shows that the nanogels are completely soluble. Membrane osmometry was employed to obtain information on the absolute number-average molecular weight ($M_{n,abs.}$) of the nanogel. It can be seen that $M_{n,abs.}$ is 16 times greater than M_n (GPC). This is not surprising since highly cross-linked nanogels dissolved in good solvents possess a much more densely packed structure than the linear polystyrenes with the same molecular weight used as standards in GPC. The ratio $M_{n,abs.}/M_n$ therefore gives a good indication of the density of the nanogels.

The catalytic activity of the nanogels was determined by investigating the rate of hydrolysis of **2** [Eq. (1)] in HEPES buffer (pH 7.3)/acetonitrile (1:1). The kinetic data is given in Table 2. The kinetics were studied at low conversion, and pseudo-first-order rate constants ($k_{impr.}$) were calculated. The efficiency of the catalyst was expressed by the ratio of the rate constant in the presence of the nanogel catalyst to that in HEPES–AcCN solution ($k_{impr.}/k_{sol.}$). The ratio of the rate constants in the presence of the imprinted nanogel to that of a corresponding control nanogel ($k_{impr.}/k_{contr.}$) reflects effects connected to the imprinting in the nanogel (the imprinting effect[6a]).

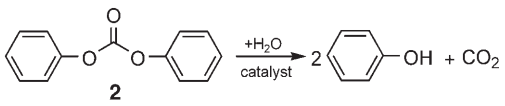

2 (1)

Table 2: Catalytic activity of the imprinted nanogels **ING1**–**ING7**.

Nanogel	$k_{impr.}$[a] ($\times 10^{-7}$) [min^{-1}]	$k_{impr.}/k_{sol.}$[b]	$k_{impr.}/k_{contr.}$[c]	Available cavities [$mmol\,g^{-1}$][d]	Cavities per particle
ING1	3.59	14.8	1.42	0.067	25.5
ING2	6.16	25.3	–	0.097	47.7
ING3	12.8	52.7	5.52	0.073	45.7
ING4	70.9	291.4	18.5	0.102	94.5
ING5	3.77	15.5	3.20	0.070	18.2
ING6	3.48	14.3	2.58	0.041	1.81
ING7	3.91	16.1	2.43	0.027	1.03

[a] Hydrolysis of **2** in a solution of 50 mM HEPES buffer (pH 7.3)/MeCN (1:1) at 10 °C with 2 equiv of cavities to 1 equiv of substrate. (HEPES = 2-[4-(2-hydroxyethyl)-1-piperazine]ethanesulfonic acid). $k_{impr.}$: pseudo-first-order rate constant in presence of the imprinted nanogel. [b] $k_{sol.}$: rate constant in HEPES buffer (pH 7.3)/MeCN (1:1). [c] $k_{contr.}$: rate constant in presence of the control nanogel. [d] Available cavities with amidinium groups determined by potentiometric titration in aqueous 0.1 N NaCl/MeCN (1:1) solution with 0.02 N aqueous HCl.

Control nanogels were prepared in analogy to the imprinted ones (**ING1**–**ING7**), but instead of the template diphenyl phosphate, formic acid was used (**CNG1**–**CNG7**; see the Supporting Information). The standard nanogel **ING1** shows clear catalytic activity, but it is lower than that of the corresponding insoluble macroporous polymers.[14] To obtain more rigid nanogels with better stabilization of the active site by more efficient cross-linking, we employed new methods of preparation (see the Supporting Information); some representative data is shown in Tables 1 and 2.

Higher monomer concentrations and higher degrees of cross-linking resulted in higher molecular weights and considerably higher polydispersities M_w/M_n, but at the same time the catalytic activity of the nanogels also increased. The potential for increasing the monomer concentration is limited because at concentrations above the critical concentration c_m (in the present case at around 1.5 wt%) macrogelation takes place. A further considerable improvement of the properties was achieved when the polymerization was performed in three stages with increasing temperatures (60, 70, and 80 °C). The most effective increase in the rigidity of the nanogel structure was obtained by a novel method we have called the "postdilution method". It is based on the observation that the

 © 2006 Wiley-VCH Verlag GmbH & Co. KGaA, Weinheim

in the homopolymerization at high EDMA concentration the cross-linking degree of the system reaches its maximum at a point just before macrogelation takes place.[15] To avoid macrogelation we stopped the polymerization at high concentration just prior to macrogelation and then diluted extensively with cyclopentanone to keep the concentration of the polymerization solution below c_m (0.1–1.5 wt.%). In this way further polymerization results in an increase of the ratio $M_{n,abs.}/M_n$, a measure of the density of the particles, from around 16 to values of 26–33 with EDMA as cross-linker (see Table 1). At the same time the polydispersity became lower, and most importantly, the catalytic activity was greatly improved.

Since the trifunctional cross-linker trimethylolpropanetrimethacrylate (TRIM) had a positive influence on the catalytic properties of the nanogels, it was used in the preparation of **ING4**. Here, all possibilities for improvement were combined, and a very efficient catalyst system was obtained with the highest $k_{impr.}/k_{sol}$ value of 291 and a $k_{impr.}/k_{contr.}$ value of 18.5. Like natural enzymes, **ING4** shows typical Michaelis–Menten kinetics for the catalysis of carbonate hydrolysis. A plot of initial reaction rates versus the substrate concentration shows saturation kinetics (see the Supporting Information). From this data the Michaelis constant $K_m = 1.82$ mM and the turnover number $k_{cat} = 7.27 \times 10^{-5}$ min^{-1} can be calculated. The $k_{cat.}/k_{uncat.}$ ratio reached the remarkable value of 2990. A control polymer (**CNG4**) showed considerably lower catalytic activity, and no saturation phenomena were observed (nearly a straight line in the plot in Figure SI-2).

These results clearly indicate that the catalysis is occurring inside the active site. Thus, it was possible for the first time to prepare a soluble imprinted nanogel with catalytic activity similar to that of insoluble imprinted polymers. A further improvement due to the solubility of the catalysts was not observed. In the preparation of the nanogels the yields and the number of obtained active sites were nearly quantitative. This procedure, therefore, should also be suitable for more sophisticated and efficient catalytic systems with rate enhancements of more than 100000 fold, as has been described previously.[7] In addition it should also be applicable to the frequently used noncovalent imprinting protocols based on weaker interactions[5b] since during the imprinting no water or other protic solvents are present.

After obtaining nanogels with high rigidity and good catalytic activity, we tried again to reduce the heterogeneity by controlling the molecular weight and the polydispersity of the catalysts. This could be achieved by using higher dilution during the preparation in the final step of the "postdilution method". **ING3**, **ING5**, and **ING6** were prepared under identical conditions, except the dilution was 1.0, 0.5, and 0.1%. As can be seen in Table 1 the $M_{n,abs.}$ dropped from 624 to 261 and to 44.3 kDalton. At the same time, the polydispersity M_w/M_n dropped from 6.0 to 3.6 and 1.54. The reason is a much lower aggregation of the primary particles. A polydispersity of 1.54 is an extremely good value for a radical polymerization. A calculation based on the experimental results for **ING6** show the existence of on average 1.8 active sites per particle. As expected, particles of higher molecular weight contain, on average, a higher number of active sites per particle. To obtain nanogels with an average of one active site per particle, we reduced the amount of template monomer **1** in the preparation of **ING7**. Thus we obtained for the first time soluble nanogels with molecular weights similar to those of natural enzymes, around 40 kDalton, very low polydispersity, and on average only one active site per particle.

We visualized and characterized these nanogels by scanning transmission electron microscopy (STEM).[16] **ING6** was prepared without drying the material in order to avoid any additional aggregation and was subsequently analyzed. RuO_4-stained particles of **ING6** in dilute chloroform solution were applied to a STEM copper grid covered by fenestrated carbon film. The STEM overview picture in Figure 1a shows a narrow size distribution, and at higher magnification (Figure 1b) spherical particles with diameters between 10 and 20 nm can be clearly seen. These particles represent single, intramolecularly cross-linked macromolecules that do not possess a marked fractal structure. The particles are rigid and do not collapse onto the support film. With the available data still no safe conclusions about the fine structure of the nanogels can be obtained from these images.

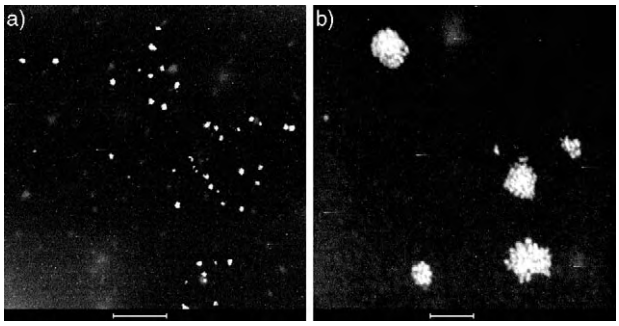

Figure 1. STEM pictures of **ING6**. a) Overview: RuO_4-stained nanoparticles (scale bar: 200 nm). The size distribution is small. b) At higher magnification the structure of the spherical particles can be seen (scale bar: 20 nm). The diameter of particles of 10–20 nm can be distinguished. The investigation was performed with a Philips Tecnai F30 analytical TEM instrument in STEM mode through a "high-angular annular dark field" detector (HAADF). The presence of Ru was confirmed through energy-dispersive X-ray spectroscopy with an Oxford Pentafet (Si/Li) EDX detector. Ru is homogeneously distributed on the nanogel and forms nanosized clusters on the surface of the polymer. Through a tilt series in the measurement of approximately $\pm 40°$ the shape and the size of the particles did not change.

Since these soluble particles of 40 kDalton can be prepared, on average, with one active catalytic site per particle and show Michaelis–Menten kinetics, a high analogy to natural enzymes was achieved. These catalysts can be analyzed and handled like enzymes but they are by far more stable. As with enzymes, it should also be possible to purify and enrich these nanogels by enzyme methodology, for example, by affinity chromatography. In addition to their importance as enzyme mimics, these novel soluble nanogels combining low molecular weight and low polydispersty with

 © 2006 Wiley-VCH Verlag GmbH & Co. KGaA, Weinheim

densely packed structures might find widespread use in different areas of science and technology.

Received: November 5, 2005
Revised: January 22, 2006
Published online: March 28, 2006

Keywords: enzyme models · homogeneous catalysis · molecular imprinting · nanogels · reaction kinetics

[1] For reviews see: a) A. J. Kirby, *Angew. Chem.* **1996**, *108*, 770 – 790; *Angew. Chem. Int. Ed. Engl.* **1996**, *35*, 707 – 724; b) W. B. Motherwell, M. J. Bingham, Y. Six, *Tetrahedron* **2001**, *57*, 4663 – 4686.
[2] a) D. J. Cram, *Nature* **1992**, *356*, 1009 – 1020; b) R. Breslow, S. D. Dong, *Chem. Rev.* **1998**, *98*, 1997 – 2011; c) C. Liang, J. M. J. Fréchet, *Prog. Polym. Sci.* **2005**, *30*, 385 – 402.
[3] W. Jencks, *Catalysis in Chemistry and Enzymology*, McGraw-Hill, New York, **1969**.
[4] a) R. A. Lerner, S. J. Benkovic, P. G. Schultz, *Science* **1991**, *252*, 659 – 667; b) D. Hilvert, *Annu. Rev. Biochem.* **2000**, *69*, 751 – 793.
[5] For reviews see: a) G. Wulff, *Angew. Chem.* **1995**, *107*, 1958 – 1979; *Angew. Chem. Int. Ed. Engl.* **1995**, *34*, 1812 – 1832; b) *Molecularly Imprinted Materials. Science and Technology* (Eds.: M. Yan, O. Ramstroem), Marcel Dekker, New York, **2005**.
[6] For reviews, see: a) G. Wulff, *Chem. Rev.* **2002**, *102*, 1 – 28; b) M. E. Davis, A. Katz, W. R. Ahmad, *Chem. Mater.* **1996**, *8*, 1820 – 1839.
[7] a) J.-Q. Liu, G. Wulff, *Angew. Chem.* **2004**, *116*, 1307 – 1311; *Angew. Chem. Int. Ed.* **2004**, *43*, 1287 – 1290; b) J.-Q. Liu, G. Wulff, *J. Am. Chem. Soc.* **2004**, *126*, 7452 – 7453.
[8] S. J. Zimmerman, M. S. Wendland, N. A. Rakow, I. Zharov, K. S. Suslick, *Nature* **2002**, *418*, 399 – 403.
[9] W. Funke, O. Okay, B. Joos-Müller, *Adv. Polym. Sci.* **1998**, *136*, 139 – 234.
[10] N. B. Graham, A. Cameron, *Pure Appl. Chem.* **1998**, *70*, 1271 – 1275.
[11] A. Biffis, N. B. Graham, G. Siedlaczek, S. Stalberg, G. Wulff, *Macromol. Chem. Phys.* **2001**, *2002*, 163 – 171.
[12] S. C. Maddock, P. Pasetto, M. Resmini, *Chem. Commun.* **2004**, 536 – 537.
[13] M. Antonietti, C. Rosenauer, *Macromolecules* **1991**, *24*, 3434 – 3442.
[14] A. G. Strikovsky, D. Kaspar, M. Grün, B. S. Green, J. Hradil, G. Wulff, *J. Am. Chem. Soc.* **2000**, *122*, 6295 – 6296.
[15] Y. Y. Chiu, L. J. Lee, *J. Polym. Sci. Part A* **1995**, *33*, 257 – 267.
[16] a) Z. L. Wang, *Adv. Mater.* **2003**, *15*, 1497 – 1514; b) R. Xie, U. Kolb, J. Li, T. Basché, A. Mews, *J. Am. Chem. Soc.* **2005**, *127*, 7480 – 7488; B. Rückert, U. Kolb, *MICRON* **2005**, *36*, 247 – 260.

 © 2006 Wiley-VCH Verlag GmbH & Co. KGaA, Weinheim

Metalation

DOI: 10.1002/anie.200504024

Mixed Mg/Li Amides of the Type $R_2NMgCl\cdot LiCl$ as Highly Efficient Bases for the Regioselective Generation of Functionalized Aryl and Heteroaryl Magnesium Compounds**

*Arkady Krasovskiy, Valeria Krasovskaya, and Paul Knochel**

The metalation of arenes is one of the most useful transformations in organic synthesis since it allows the regioselective functionalization of various aryl and heteroaryl derivatives.[1] Traditionally, strong bases such as alkyl lithium reagents (RLi) and lithium amides (R_2NLi) have been used for such deprotonations. However, these bases often lead to undesirable side reactions as a result of their high reactivity and their strong nucleophilicity (e.g. Chichibabin addition). Another serious limitation is the low stability of lithium amides in THF solutions at room temperature, which requires in situ generation of these reagents. Furthermore, the deprotonation of arenes by lithium bases requires very low temperatures (−78 to −90 °C), which complicates the scale-up of these reactions. Alternative methods have been developed using magnesium amides[2] such as **1**–**3**, amidozincates[3] of type **4**, and *n*BuLi/lithium aminoalkoxide aggregates which permit deprotonation of various heterocycles at the position α to the heteroatom (Scheme 1).[4] The problem of the low solubility of the magnesium amides R_2NMgCl (**1**) has been addressed by Eaton et al., who developed applications of magnesium amides of type R_2NMgR' (**2**) and $(R_2N)_2Mg$ (**3**). Nevertheless, for achieving high conversions it is usually necessary to use a large excess of the magnesium amides (2–12 equiv), which further complicates the reactions with electrophiles (up to 10 equiv of the electrophile may have to be used). Similarly, aminozincate requires the use of 3.5–4 equiv of an electrophile in subsequent quenching reactions.

Therefore, the development of an inexpensive, highly soluble magnesium base displaying high kinetic activity would be desirable. Recently, we found that the addition of lithium chloride to alkylmagnesium chlorides produces highly active reagents of the type $RMgCl_2^-Li^+$[5,6] and $R_2MgCl^-Li^+$,[7]

[*] Dr. A. Krasovskiy, V. Krasovskaya, Prof. Dr. P. Knochel
Department Chemie und Biochemie
Ludwig-Maximilians-Universität München
Butenandtstrasse 5–13, Haus F, 81377 München (Germany)
Fax: (+49) 89-2180-77680
E-mail: paul.knochel@cup.uni-muenchen.de

[**] We thank the Fonds der Chemischen Industrie, Merck Research Laboratories (MSD), and the DFG (SPP 1118 "Sekundäre Wechselwirkungen als Steuerungsprinzip zur gerichteten Funktionalisierung reaktionsträger Substrate") for financial support. We also thank Chemetall GmbH (Frankfurt) and BASF AG (Ludwigshafen) for generous gifts of chemicals.

Supporting information for this article is available on the WWW under http://www.angewandte.org or from the author.

WILEY InterScience DISCOVER SOMETHING GREAT
© 2006 Wiley-VCH Verlag GmbH & Co. KGaA, Weinheim

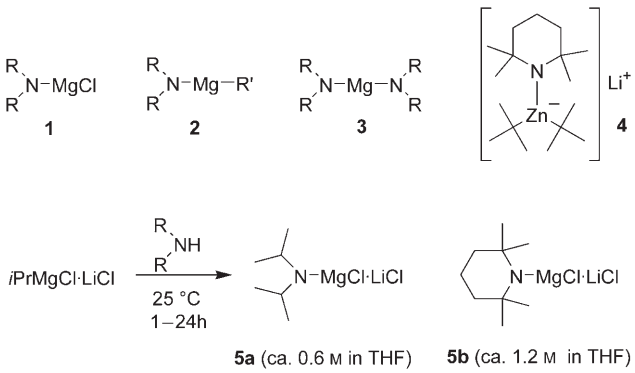

Scheme 1. Typical magnesium bases used for the magnesiation of arenes and heteroarenes and the preparation of the mixed Mg/Li amides.

which undergo Br/Mg exchange reactions with rates that are high compared to the those of the reactions with homoleptic reagents RMgX and R_2Mg without added LiCl.

We therefore prepared the corresponding mixed Mg/Li amides of type $R_2NMgCl{\cdot}LiCl$ **5** by reacting *i*PrMgCl·LiCl[5,6] with diisopropylamine or 2,2,6,6-tetramethylpiperidine (TMPH) in THF (25 °C, 1–24 h). The resulting Mg/Li reagents **5a** (R = *i*Pr) and **5b** (R_2N = 2,2,6,6-tetramethylpiperidyl) proved to have excellent solubility in THF (0.6 M and 1.2 M, respectively) as well as improved kinetic basicity and regioselectivity for the magnesiation of various aromatics and heteroaromatics.

In preliminary experiments, we examined the magnesiation of isoquinoline. Reaction with 2 equiv of **5a** provided only the magnesiated isoquinoline **6** after 12 h at 25 °C (Scheme 2). After iodolysis the iodoisoquinoline **7a** was

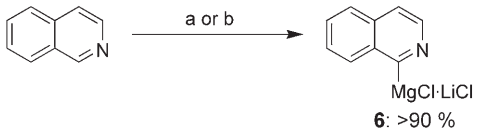

Scheme 2. Magnesiation of isoquinoline. a) **5a** (2 equiv), THF, 25 °C, 12 h; b) **5b** (1.1 equiv), THF, 25 °C, 2 h.

isolated in 81 % yield. In strong contrast, the sterically more hindered and less aggregated reagent **5b** led to complete magnesiation within 2 h at 25 °C. Remarkably, only 1.1 equiv of this base was required to achieve complete metalation. The resulting Grignard reagent **6** provided, after iodolysis, the isoquinoline **7a** in 92 % yield (entry 1, Table 1).

In the presence of substoichiometric amounts of CuCN·2 LiCl (20 mol %), the addition of benzoyl chloride (1.2 equiv) provided the ketone **7b** in 86 % yield (entry 2, Table 1). The presence of an excess of the magnesium amide often hampers palladium-catalyzed cross-couplings. We found that the Grignard reagents generated by deprotonation with **5b** (1.1 equiv) such as **6** were readily transmetalated to give the corresponding zinc derivative ($ZnCl_2$ (1.1 equiv), 0 °C, 5 min) and underwent a Negishi cross-coupling reaction using [$Pd(dba)_2$] (5 mol %), $P(2\text{-fur})_3$ (7 mol %) with ethyl 4-iodobenzoate (1.2 equiv; 50 °C, 12 h) leading to the arylated isoquinoline **7c** in 82 % yield.

This method of metalation is general, and 3-bromoquinoline was also metalated by **5b** (1.1 equiv, −25 °C, 0.5 h) leading to the 2-magnesiated quinoline **8** (entries 4 and 5). Thus, the quenching of **8** with I_2 and DMF provided the functionalized quinolines **9a** and **9b** in 87 and 91 % yield, respectively. Whereas the deprotonation of 2,6-dichloropyridine with $iPr_2NMgCl{\cdot}LiCl$ (**5a**) and lithium diisopropylamide (LDA)[9j] provided a 1:1 mixture of 3- and 4-magnesiated 2,6-dichloropyridine, the use of TMPMgCl·LiCl (**5b**) furnished only the 4-magnesiated pyridine **10**. Its reaction with typical electrophiles (I_2, DMF, and PhCHO) provided the expected products **11a–c** in 84–93 % yield (entries 6–8).

Interestingly, metalation of 3,5-dibromopyridine with LDA proceeded selectively at the 4-position,[7b] while in the case of TMPMgCl·LiCl (**5b**) (1.1 equiv, −25 °C, 0.5 h) regioselective metalation in the 2-position was observed, leading after the reaction with I_2 and DMF to the corresponding pyridines **13a** and **13b** in yields of 89 and 85 %, respectively (entries 9 and 10). The magnesiation of heterocycles bearing more acidic protons[8] such as thiazole, thiophene, furan, benzothiophene, and benzothiazole proceeded smoothly between 0 °C and 25 °C leading to the organomagnesium derivatives **14a–c** and **16a–b**. After trapping with standard electrophiles, the expected products **15a–c** and **17a–b** were obtained in 81–98 % yield (entries 11–15).

The metalation of pyrimidine derivatives is a challenging problem because of the propensity of these heterocycles to undergo addition reactions with organometallic reagents.[7b,9] We found that the inverse addition of the pyrimidine derivatives **18** and **19** to a THF solution of **5b** (1.2 equiv) at −55 °C provided completely regioselectively the corresponding magnesiated derivatives **20** and **21**, which react with a wide range of electrophiles leading to the functionalized pyrimidines **22–24** in good yields (Scheme 3).

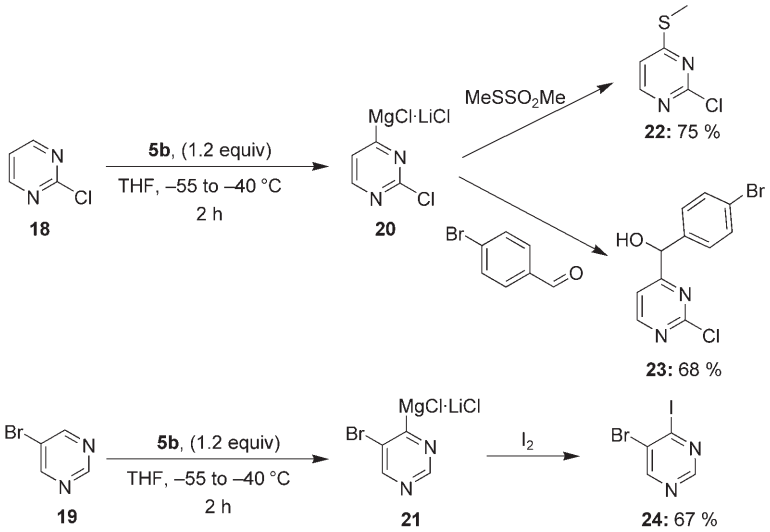

Scheme 3. Regioselective magnesiation of pyrimidines.

 © 2006 Wiley-VCH Verlag GmbH & Co. KGaA, Weinheim

Table 1: Products obtained by the magnesiation of heterocycles with **5b** and reaction with electrophiles.

Entry	Magnesium reagent[a]	*T* [°C], *t* [h][b]	Electophile	Product	Yield [%][c]
	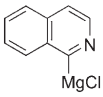			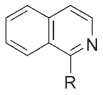	
1	**6**	25, 2	I_2	**7a**: R = I	92
2	**6**	25, 2	PhCOCl[d]	**7b**: R = COPh	86
3	**6**	25, 2	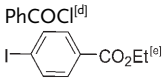	**7c**: R = 4-$EtO_2CC_6H_4$	82
	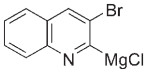			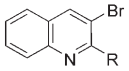	
4	**8**	−25, 0.3	I_2	**9a**: R = I	87
5	**8**	−25, 0.3	DMF	**9b**: R = CHO	91
	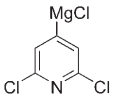			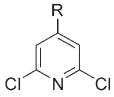	
6	**10**	25, 0.1	I_2	**11a**: R = I	93
7	**10**	25, 0.1	DMF	**11b**: R = CHO	90
8	**10**	25, 0.1	PhCHO	**11c**: R = CH(OH)Ph	84
	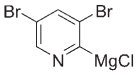			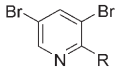	
9	**12**	−25, 0.5	I_2	**13a**: R = I	89
10	**12**	−25, 0.5	DMF	**13b**: R = CHO	85
	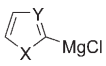				
11	**14a**: X = O, Y = CH	25, 24	DMF	**15a**: R = CHO	81
12	**14b**: X = S, Y = CH	25, 24	DMF	**15b**: R = CHO	90
13	**14c**: X = S, Y = N	0, 0.1	PhCHO	**15c**: R = CH(OH)Ph	94
	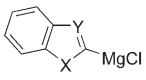			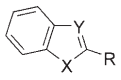	
14	**16a**: X = S, Y = CH	25, 24	DMF	**17a**: R = CHO	93
15	**16b**: X = S, Y = N	0, 0.1	I_2	**17b**: R = I	98

[a] Lithium chloride and TMPH are complexed to the Grignard reagent. [b] Reaction conditions for the deprotonation with **5b** (1.1 equiv). [c] Yield of isolated, analytically pure product. [d] A transmetalation with CuCN·2 LiCl (0.2 equiv) was performed. [e] Obtained by palladium-catalyzed cross-coupling after transmetalation with $ZnCl_2$.

The mixed Mg/Li amide **5b** is also well suited for the regioselective metalation of polyfunctional aromatic systems. Thus, the reaction of 2-phenylpyridine (**25**) in THF at 55 °C with **5b** (2.0 equiv) for 24 h provides the Grignard reagent **26**; this is a rare case where a phenyl ring is preferentially metalated over a pyridine ring.[10] After iodolysis, the *ortho*-iodinated product **27** was obtained in 80% yield. Interestingly, the metalation of polyfunctional arenes such as the bromodiester **28** and bromoester **29** also succeeded using only a stoichiomet-

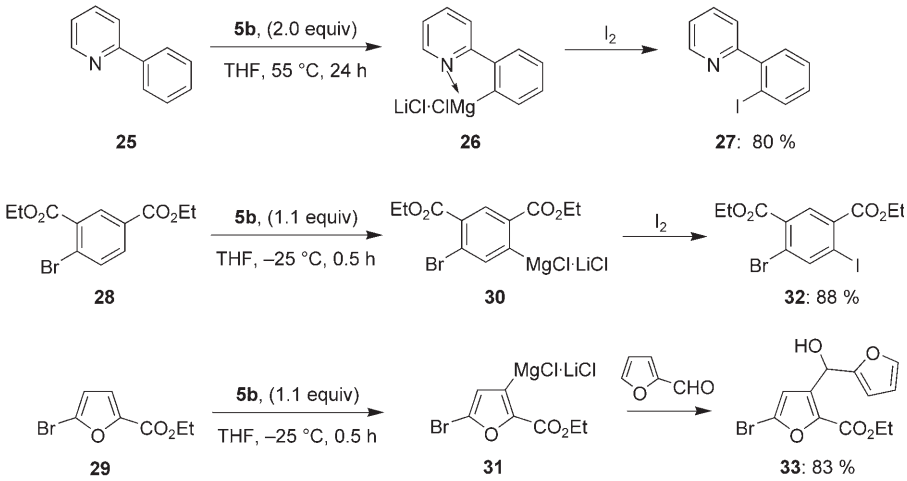

Scheme 4. Regioselective magnesiation of polyfunctional aromatic systems.

 © 2006 Wiley-VCH Verlag GmbH & Co. KGaA, Weinheim

ric amount of base **5b** (1.1 equiv) in THF (−25 °C, 0.5 h) leading regioselectively to the arylmagnesium species **30** and **31**, which after reaction with electrophiles furnished the polyfunctional aromatic derivatives **32** and **33** in 83–88% yields. (Scheme 4)

In summary, we have prepared new mixed Mg/Li-bases of the general type $R_2NMgCl{\cdot}LiCl$ which have a high kinetic activity because of the presence of LiCl which, we tentatively propose, breaks up oligomeric aggregates of magnesium amides. The use of TMPMgCl·LiCl, which has an excellent solubility and is stable for more than 6 months as THF solution at 25 °C, allows the regioselective functionalization of various aromatic and heteroaromatic compounds. It provides access to new magnesium species not readily available by Br/Mg-exchange reactions or previously reported metalation procedures. Extensions of this method are currently underway in our laboratories.

Experimental Section

1) Synthesis of **5b:** A dry and argon-flushed 250-mL Schlenk flask, equipped with a magnetic stirring bar and a septum, was charged with freshly titrated *i*PrMgCl·LiCl (100 mL, 1.2 M in THF, 120 mmol). TMPH (19.8 g, 126 mmol, 1.05 equiv) was added dropwise at room temperature. The reaction mixture was stirred at room temperature until gas evolution ceased (ca. 24 h).

2) Typical procedure: Synthesis of **7a**: A dry and argon-flushed 10-mL Schlenk flask, equipped with a magnetic stirring bar and a septum, was charged with **5b** (5 mL, 1.2 M in THF, 6.0 mmol). Isoquinoline (703 mg, 5.45 mmol) in THF (5 mL) was added dropwise at room temperature. During the addition the reaction mixture became red, and the metalation was complete after 2 h. (The reaction progress was checked by removal of reaction aliquots, which were quenched with a solution of I_2 in THF and analyzed by GC; the conversion was more than 98%.) A solution of I_2 in THF (6 mL, 1.0 M in THF, 6.0 mmol) was slowly added at −20 °C. The reaction mixture was quenched with sat. aqueous solution of NH_4Cl (10 mL). The aqueous layer was extracted with diethyl ether (4 × 10 mL), and the combined extracts were dried with Na_2SO_4 and concentrated in vacuo. The crude residue was purified by filter column chromatography (silica; CH_2Cl_2/pentane) affording **7a** (1.33 g, 92%) as slightly yellow crystals (m.p. 74–76 °C).

Received: November 11, 2005
Published online: March 28, 2006

Keywords: amides · Ggrignard reagents · heterocycles functionalization · lithium chloride · magnesium amides · mixed bases · regioselective metalation

[1] a) M. Schlosser, *Angew. Chem.* **2005**, *117*, 380; *Angew. Chem. Int. Ed.* **2005**, *44*, 376; b) A. Turck, N. Ple, F. Mongin, G. Quéguiner, *Tetrahedron* **2001**, *57*, 4489; c) F. Mongin, G. Quéguiner, *Tetrahedron* **2001**, *57*, 4059; d) M. Schlosser, *Eur. J. Org. Chem.* **2001**, *21*, 3975; e) D. M. Hodgson, C. D. Bray, N. D. Kindon, *Org. Lett.* **2005**, *7*, 2305; f) J.-C. Plaquevent, T. Perrard, D. Cahard, *Chem. Eur. J.* **2002**, *8*, 3300; g) C.-C. Chang, M. S. Ameerunisha, *Coord. Chem. Rev.* **1999**, *189*, 199; h) J. Clayden, *Organolithiums: Selectivity for Synthesis* (Eds.: J. E. Baldwin, R. M. Williams), Elsevier, **2002**; i) "The Preparation of Organolithium Reagents and Intermediates": F. Leroux, M. Schlosser, E. Zohar, I. Marek, *Chemistry of Organolithium Compounds* (Eds.: Z. Rappoport, I. Marek), Wiley, New York, **2004**, chap. 1, p. 435; j) K. W. Henderson, W. J. Kerr, *Chem. Eur. J.* **2001**, *7*, 3430; k) K. W. Henderson, W. J. Kerr, J. H. Moir, *Tetrahedron* **2002**, *58*, 4573; l) M. C. Whisler, S. MacNeil, V. Snieckus, P. Beak, *Angew. Chem.* **2004**, *116*, 2256; *Angew. Chem. Int. Ed.* **2004**, *43*, 2206; m) G. Queguiner, F. Marsais, V. Snieckus, J. Epsztajn, *Adv. Heterocycl. Chem.* **1991**, *52*, 187; n) M. Veith, S. Wieczorek, K. Fries, V. Huch, *Z. Anorg. Allg. Chem.* **2000**, *626*, 1237.

[2] a) M.-X. Zhang, P. E. Eaton, *Angew. Chem.* **2002**, *114*, 2273; *Angew. Chem. Int. Ed.* **2002**, *41*, 2169; b) Y. Kondo, Y. Akihiro, T. Sakamoto, *J. Chem. Soc. Perkin Trans. 1* **1996**, 2331; c) P. E. Eaton, C. H. Lee, Y. Xiong, *J. Am. Chem. Soc.* **1989**, *111*, 8016; d) P. E. Eaton, M.-X. Zhang, N. Komiya, C.-G. Yang, I. Steele, R. Gilardi, *Synlett* **2003**, *9*, 1275; e) P. E. Eaton, R. M. Martin, *J. Org. Chem.* **1988**, *53*, 2728; f) M. Shilai, Y. Kondo, T. Sakamoto, *J. Chem. Soc. Perkin Trans. 1* **2001**, 442.

[3] a) Y. Kondo, M. Shilai, M. Uchiyama, T. Sakamoto, *J. Am. Chem. Soc.* **1999**, *121*, 3539; b) T. Imahori, M. Uchiyama, T. Sakamoto, Y. Kondo, *Chem. Commun.* **2001**, *23*, 2450.

[4] P. Gros, Y. Fort, *Eur. J. Org. Chem.* **2002**, 3375.

[5] a) A. Krasovskiy, P. Knochel, *Angew. Chem.* **2004**, *116*, 3396; *Angew. Chem. Int. Ed.* **2004**, *43*, 3333; b) H. Ren, A. Krasovskiy, P. Knochel, *Chem. Commun.* **2005**, 543; c) H. Ren, A. Krasovskiy, P. Knochel, *Org. Lett.* **2004**, *6*, 4215.

[6] *i*PrMgCl·LiCl is commercially available from Chemetall GmbH (Frankfurt).

[7] a) A. J. Clarke, S. McNamara, O. Meth-Cohn, *Tetrahedron Lett.* **1974**, *15*, 2373–2376; b) Y. G. Gu, E. K. Bayburt, *Tetrahedron Lett.* **1996**, *37*, 2565.

[8] a) H. Froehlich, W. Kalt, *J. Org. Chem.* **1990**, *55*, 2993; b) C. Peyron, J.-M. Navarre, N. Van Craynest, R. Benhida, *Tetrahedron Lett.* **2005**, *46*, 3315; c) D. W. Slocum, P. L. Gierer, *J. Org. Chem.* **1976**, *41*, 3668.

[9] a) W. Schlecker, A. Huth, E. Ottow, J. Mulzer, *Liebigs Ann.* **1995**, *8*, 1441; b) W. Schlecker, A. Huth, E. Ottow, J. Mulzer, *J. Org. Chem.* **1995**, *60*, 8414; c) A. Bouillon, J.-C. Lancelot, V. Collot, P. R. Bovy, S. Rault, *Tetrahedron* **2002**, *58*, 3323; d) A. Bouillon, J.-C. Lancelot, J. S. de O. Santos, V. Collot, P. R. Bovy, S. Rault, *Tetrahedron* **2003**, *59*, 10043; e) A. Bouillon, J.-C. Lancelot, V. Collot, P. R. Bovy, S. Rault, *Tetrahedron* **2002**, *58*, 4369; f) A. Bouillon, J.-C. Lancelot, V. Collot, P. R. Bovy, S. Rault, *Tetrahedron* **2002**, *58*, 2885; g) H. Awad, F. Mongin, F. Trecourt, G. Queguiner, F. Marsais, *Tetrahedron Lett.* **2004**, *45*, 7873; h) D. L. Comins, M. O. Killpack, *J. Org. Chem.* **1990**, *55*, 69; i) R. Radinov, K. Chanev, M. Khaimova, *J. Org. Chem.* **1991**, *56*, 4793; j) S. Choppin, P. Gros, Y. Fort, *Org. Lett.* **2000**, *2*, 803.

[10] P. Gros, Y. Fort, *J. Org. Chem.* **2003**, *68*, 2028.

 © 2006 Wiley-VCH Verlag GmbH & Co. KGaA, Weinheim

Quantum Dynamics

DOI: 10.1002/anie.200504147

Periodic Electron Circulation Induced by Circularly Polarized Laser Pulses: Quantum Model Simulations for Mg Porphyrin**

*Ingo Barth and Jörn Manz**

Dedicated to our wives Tanja and Etsuko

During the last two decades, femtosecond laser pulses in the time domain from about five to several hundred fs (1 fs = 10^{-15} s) have been used for analysis and control of molecular reaction dynamics, supplemented by quantum simulations and predictions of the laser-driven nuclear wavepacket dynamics.[1–5] The recent advent of even shorter laser pulses from about one hundred attoseconds (1 as = 10^{-18} s) to a few fs has opened an analogous field of research, namely, the analysis and control of electron dynamics in the time domain in which the nuclei are essentially frozen.[6] The first purpose of the work described here was to design corresponding circularly polarized laser pulses to induce periodic unidirectional circulation of electronic wavepackets in ring-shaped molecules such as Mg porphyrin (see Figure 1).

Our work has been motivated by stimulating experimental and theoretical work in this field, including observations of ultrafast motions of electrons in atoms,[6] and quantum simulations of the measurement of periodic intramolecular electron transfer (PIET),[7] by means of high harmonic generation (HHG),[7–9] analogous to the tomographic imaging of molecular orbitals.[10] PIET may be expressed in terms of a coherent electronic wavepacket representing a "hybrid" superposition $(0,e)$ of the electronic ground (0) and excited (e) states, with energies E_0 and E_e, equal populations $P_j = |C_j|^2 = 0.5$ $(j = 0,e)$ and period $\tau_{e,0} = h/(E_e - E_0)$ [Eq. (1)].

$$|\Psi_{0,e}(t)\rangle = C_0|\Psi_0\rangle e^{-iE_0t/\hbar} + C_e|\Psi_e\rangle e^{-iE_et/\hbar} \quad (1)$$

Note that the preparation of periodic electron dynamics, for example, PIET, by means of few cycle laser pulses, has not been described in Ref. [7] or elsewhere.[30] The second purpose of our research was, therefore, to design laser pulses for the preparation of "hybrid"-type electronic states, analogous to Equation (1).

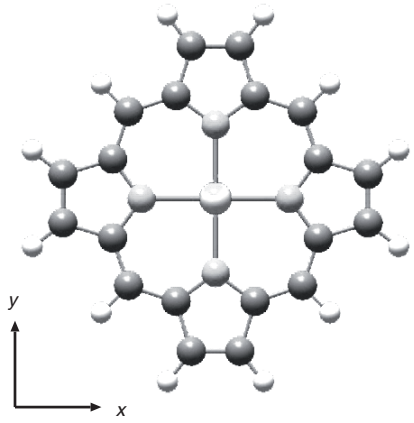

Figure 1. View of Mg porphyrin in the x/y plane. The laser pulse propagates out along the z axis.

Control of electronic motions by means of few cycle laser pulses has also been predicted[11,12] and demonstrated,[13] in particular for electronic population transfer from an initial electronic wave function to a final one by means of so-called "π pulses". The population dynamics for electronic wavepackets driven by π pulses is equivalent to that for nuclear ones (compare Refs. [12] and [14]). This analogy provides another motivation for our work. In Ref. [15] (compare with Ref. [16]) we designed circularly polarized π and π/2 pulses for specific complete or half population transfers, respectively, in oriented racemates such that ultimately the chirality of the laser pulse is transferred into that of nuclear wavepacket dynamics that yields pure enantiomers. In this paper, we shall show that the chirality of circularly polarized laser pulses can be transferred to unidirectional electron circulation, using analogous π/2 pulses as a reference.

As an example, we consider the Mg-porphyrin molecule oriented in the x/y plane (e.g. as achieved by means of laser pulses[7,10,17]), see Figure 1. The x and y components of the electric fields of four representative right circularly polarized laser pulses propagating along the z axis [Eqs. (2) and (3)]

$$\mathscr{E}_x(t) = \mathscr{E}_0 s(t)\cos(\omega t) \quad (2)$$

$$\mathscr{E}_y(t) = \mathscr{E}_0 s(t)\sin(\omega t) \quad (3)$$

with shape function [Eq. (4)] and intensities $I(t) = \varepsilon_0 c \mathscr{E}_0^2 s(t)^2$

$$s(t) = \sin^2\left(\frac{\pi t}{t_p}\right), \quad 0 \le t \le t_p \quad (4)$$

are plotted in Figure 2. The parameters are listed in the caption of Figure 2. The short pulse durations (full width at half maximum of the intensity) $\tau = 0.364\,t_p$ correspond to broad spectral widths $\Gamma = 3.295\,\hbar/\tau$. The resulting coherent

[*] I. Barth, Prof. Dr. J. Manz
Institut für Chemie und Biochemie
Freie Universität Berlin
Takustrasse 3, 14195 Berlin (Germany)
Fax: (+49) 30-838-54792
E-mail: jmanz@chemie.fu-berlin.de

[**] We thank Dr. M. Kitzler (Technische Universität Wien) and Dr. Y. Shigeta and Dr. K. Yagi (Tokyo University) for stimulating discussions of experimental applications and laser-driven electronic ring currents, as well as Prof. D. Diestler for polishing the first draft. Financial support by Deutsche Forschungsgemeinschaft (project Ma 515/23-1) and by the Fonds der Chemischen Industrie is also gratefully acknowledged.

 InterScience © 2006 Wiley-VCH Verlag GmbH & Co. KGaA, Weinheim

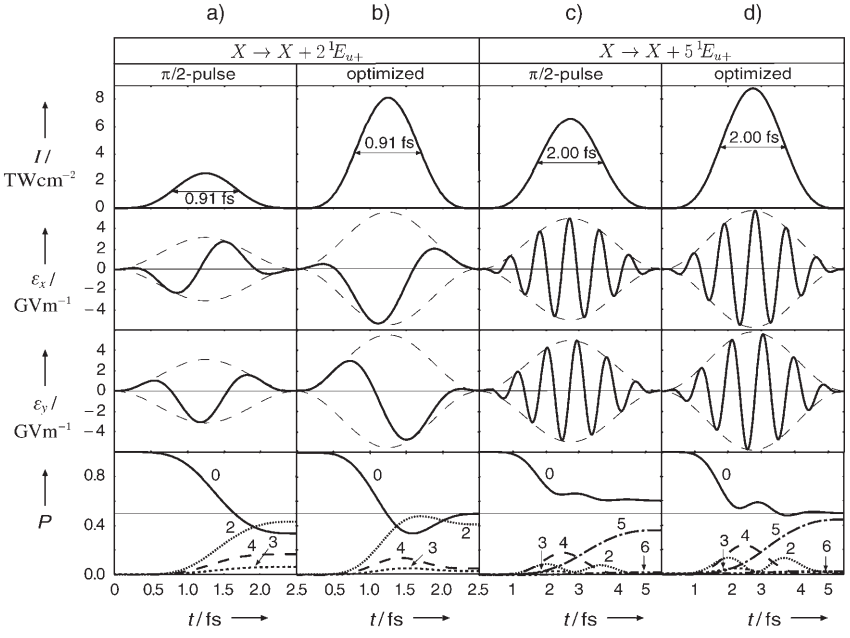

Figure 2. Circularly polarized π/2 and reoptimized π/2 laser pulses for half population transfer from the electronic ground state $X = 1\,^1A_{1g}$ to excited target states $2\,^1E_{u+}$ and $5\,^1E_{u+}$. The four rows show the time evolutions of the intensities, the *x* and *y* components of the electric fields, and the resulting populations of the ground (0) and excited states $j\,^1E_{u+}$ ($j = 2,\ldots,6$), respectively. The parameters of the laser pulses shown in columns (a), (b), (c), (d) are $\mathscr{E}_0 = 3.11$, 5.54, 4.98, and 5.77 GV m^{-1}, and $\hbar\omega = 2.66$, 1.94, 4.56, and 4.40 eV, respectively.

electronic wavepackets are calculated as solutions [Eq. (5)] of

$$|\Psi(t)\rangle = \sum_j C_j(t)|\Psi_j\rangle e^{-iE_jt/\hbar} \tag{5}$$

the time-dependent Schrödinger equation [Eq. (6)] starting

$$i\hbar|\dot{\Psi}(t)\rangle = (\mathscr{H}_{el} - \underline{\mathscr{E}}(t)\underline{M})|\Psi(t)\rangle \tag{6}$$

from the initial ($t = 0$) electronic ground state, $|\Psi_0\rangle = |\Psi_X\rangle$, $X = 1\,^1A_{1g}$, and using the semiclassical electronic dipole approximation. In Equations (5) and (6), $|\Psi_j\rangle$ denote the electronic eigenfunctions of the time-independent Schrödinger equation [Eq. (7)] with electronic Hamiltonian operator $\mathscr{H}_{el}$ (assuming fixed nuclei as shown in Figure 1) and with electronic eigenenergies E_j. Equivalently, we propagate Equation (8) for the time-dependent coefficients $C_j(t)$ and

$$i\hbar\dot{C}(t) = H(t)C(t) \tag{8}$$

corresponding populations $P_j(t) = |C_j(t)|^2$ of electronic states j, with matrix elements $H_{ij}(t) = -\underline{\mathscr{E}}(t)\langle\Psi_i|\underline{M}|\Psi_j\rangle e^{-i(E_j-E_i)t/\hbar}$, starting from $C_j(t{=}0) = \delta_{j0}$. For reasons of molecular symmetry, the right circularly polarized laser pulses with maximum intensities below 10^{13} W cm^{-2} yield exclusive population transfer from the electronic ground state $|\Psi_0\rangle$ to excited states $|\Psi_j\rangle = |\Psi_{j^1E_{u+}}\rangle = (|\Psi_{j^1E_{u,x}}\rangle + i|\Psi_{j^1E_{u,y}}\rangle)/\sqrt{2}$. The corresponding electronic energies E_j and matrix elements $\langle\Psi_0|\underline{M}|\Psi_j\rangle$ of the six j^1E_u states are adapted from quantum chemistry CASPT2 and TD-DFT results of Rubio et al. ($j = 1,\ldots,4$)[18] and Sundholm ($j = 5,6$),[19] respectively.

Our previous experience[15] suggests π/2 pulses for half population transfer from the initial ground state $|\Psi_0\rangle$ to a specific target state $|\Psi_j\rangle = |\Psi_{j^1E_{u+}}\rangle$. By analogy, the laser parameters should satisfy Equation (9), where $M = \max|\langle\Psi_0|\underline{M}|\Psi_{j^1E_{u+}}\rangle\mathscr{E}(t)|/\mathscr{E}_0$. Figure 2a,c

$$\frac{M\mathscr{E}_0 t_p}{\hbar} = \frac{\pi}{2} \tag{9}$$

show the π/2 pulses, designed exemplarily for selective half population transfers from $|\Psi_X\rangle$ to $|\Psi_{2^1E_{u+}}\rangle$ or $|\Psi_{5^1E_{u+}}\rangle$, within one or two cycles during $\tau = 0.91$ fs and 2.00 fs and with corresponding spectral widths $\Gamma = 2.38$ eV and 1.08 eV, respectively, together with the resulting population dynamics. As anticipated, the final populations of the initial and target states are indeed close to each other, but with significant deviations from the goal [$= 0.5$, see Eq. (1)], due to the rather broad spectral widths which cover several neighboring levels with the same symmetry, j^1E_{u+}, allowing their temporary populations. Fortunately, this deficiency may be compensated by reoptimizing the laser parameters ω and $\mathscr{E}_0$, starting from the π/2 pulses as a refererence. The "reoptimized π/2 pulses" and population dynamics are shown in Figure 2b,d, demonstrating preparations of almost perfect periodic "hybrid" electronic states [see Eq. (1)], $|\Psi_{X,2^1E_{u+}}\rangle$ and $|\Psi_{X,5^1E_{u+}}\rangle$, with corresponding periods $\tau_{2^1E_{u+},X} = 1.55$ fs and $\tau_{5^1E_{u+},X} = 0.91$ fs, respectively.

Thus, we have achieved the second goal of this paper. At the same time, we also reach the first one, that is, preparation of periodic unidirectional electron circulation. This is demonstrated by snapshots of the dynamics of the electronic wave packet after the laser pulse. Figure 3 shows the corresponding difference $\Delta\rho(t) = \rho(t) - \rho(0)$ of the resulting single electron density at time t after the laser pulse, minus the initial density, exemplarily for half population transfer from $|\Psi_X\rangle$ to $|\Psi_{5^1E_{u+}}\rangle$. Apparently, the optimized right circularly polarized π/2 pulse with period $2\pi/\omega = 0.94$ fs yields net right, periodic circulation of the shifted electron density $\Delta\rho(t)$, with a nearly identical period $\tau_{5^1E_{u+},X} = 0.91$ fs.

In conclusion, the present quantum simulations show that the chirality of the reoptimized π/2 right circularly polarized laser pulses may be transferred to state-selective right unidirectional net electron circulation. The unidirectionality is a consequence of selective preparation of hybrid states $|\Psi_{X,j^1E_{u+}}\rangle$ in the preoriented molecule. Likewise, the corresponding left circularly polarized laser pulses induce analo-

 © 2006 Wiley-VCH Verlag GmbH & Co. KGaA, Weinheim

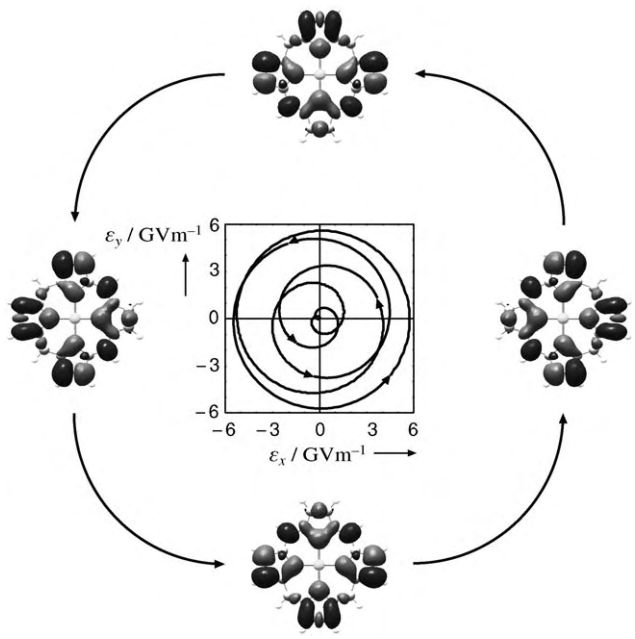

Figure 3. Reoptimized right circularly polarized $\pi/2$ laser pulse designed for half population transfer from the electronic ground state $X=1\,^1A_{1g}$ to the target state $5\,^1E_{u+}$, and the resulting periodic right electron circulation. The x and y components of the electric fields are shown as a polar plot (cf. Figure 2d). The electron circulation is illustrated by snapshots of the difference $\Delta\rho(t)$ of the single electron density $\rho(t)$ minus the initial density $\rho(0)$, at time $t=5.67$ fs and $t+k\tau_{5^1E_{u+},X}/4$, ($k=1,2,3,...$) with $\tau_{5^1E_{u+},X}=0.91$ fs. The target state $|\Psi_{5^1E_{u+}}\rangle$ corresponds to the $3e_{g+}$ to $2b_{1u}$ orbital transition (weight = 94%).[19] As a consequence, $\Delta\rho(t)$ may be approximated in terms of the (partial) transition of a single active electron, essentially from $3e_{g+}$ to $2b_{1u}$.

gous left unidirectional net electron circulation, represented by $|\Psi_{X,j^1E_{u-}}\rangle$. Similar ignitions of electron circulation are favored by molecular symmetries with degenerate representations of molecular states, for example, other ring-shaped molecules, or linear molecules which should support ignition of toroidal-type electron circulations, on a molecular scale, that is, much more compact and faster than circulation of Rydberg electrons along Kepler orbits around atoms.[20,21] The effect may be observed for example, by means of high harmonic generation, cf. Refs. [8,10,22,23], depending on special selection rules due to the symmetry of the molecule,[24] or by time-dependent asymmetric photoelectron spectra as suggested in Refs. [25,26].

Conservation of angular momentum implies that unidirectional electron circulations may be coupled to vibrational pseudorotations (Jahn–Teller effect, see also Ref. [27]) and to rotations of the molecular frame in the time domains beyond 100 fs and even picoseconds, respectively.[28] This is in accord with the present assumption of frozen nuclei in the sub-5 fs time domain. In contrast, extensions of the present scenario to longer pulse durations could call for simulations of nonfrozen nuclei, for example, they might move away from the Franck–Condon domain towards domains with different transition frequencies. This may be compensated by adequate chirping of the laser pulses.[11,29] In any case, it is advantageous to employ laser pulses with durations close to one or very few electronic cycles (e.g. $\tau \leq 2$ fs in the present case) because they support many electronic cycles before decay, for example, by coupled nuclear motions.

Moreover, by analogy with the results of Ref. [15], one may also design reoptimized π pulses for complete population transfer from the ground to excited electronic states $|\Psi_{j^1E_{u+}}\rangle$. These target states present stationary electronic ring currents instead of the present periodic electron circulation. Combinations of sequential reoptimized $\pi/2$ and π pulses could prepare excited hybrid states, for example, $|\Psi_{4^1E_{u+},5^1E_{u+}}\rangle$, with different periods, for example, $\tau_{4^1E_{u+},5^1E_{u+}}$.

Received: August 14, 2005
Revised: November 21, 2005
Published online: March 23, 2006

Keywords: electronic structure · laser chemistry · porphyrinoids · quantum dynamics

[1] A. H. Zewail, *Angew. Chem.* **2000**, *112*, 2688; *Angew. Chem. Int. Ed.* **2000**, *39*, 2586.
[2] M. Shapiro, P. Brumer, *Principles of the Quantum Control of Molecular Processes*, Wiley-VCH, Weinheim, **2003**.
[3] S. A. Rice, M. Zhao, *Optical Control of Molecular Dynamics*, Wiley, New York, **2000**.
[4] J. Manz in *Femtochemistry and Femtobiology: Ultrafast Reaction Dynamics at Atomic Scale Resolution, Nobel Symposium, Vol. 101* (Ed.: V. Sundström), Imperical College Press, London, **1997**, pp. 80–318.
[5] C. Daniel, J. Full, L. González, C. Lupulescu, J. Manz, A. Merli, Š. Vajda, L. Wöste, *Science* **2003**, *299*, 536.
[6] M. Hentschel, R. Kienberger, C. Spielmann, G. A. Reider, N. Milosevic, T. Brabec, P. Corkum, U. Heinzmann, M. Drescher, F. Krausz, *Nature* **2001**, *414*, 509.
[7] H. Niikura, D. M. Villeneuve, P. B. Corkum, *Phys. Rev. Lett.* **2005**, *94*, 083003.
[8] P. B. Corkum, *Phys. Rev. Lett.* **1993**, *71*, 1994.
[9] G. Lagmago-Kamta, A. D. Bandrauk, *Phys. Rev. A* **2005**, *71*, 053407.
[10] J. Itatani, J. Levesque, D. Zeidler, H. Niikura, H. Pépin, J. C. Kieffer, P. B. Corkum, D. M. Villeneuve, *Nature* **2004**, *432*, 867.
[11] J. Cao, C. J. Bardeen, K. R. Wilson, *Phys. Rev. Lett.* **1998**, *80*, 1406.
[12] P. Krause, T. Klamroth, P. Saalfrank, *J. Chem. Phys.* **2005**, *123*, 074105.
[13] J. Itatani, D. Zeidler, J. Levesque, M. Spanner, D. M. Villeneuve, P. B. Corkum, *Phys. Rev. Lett.* **2005**, *94*, 123902.
[14] M. Holthaus, B. Just, *Phys. Rev. A* **1994**, *49*, 1950.
[15] K. Hoki, D. Kröner, J. Manz, *Chem. Phys.* **2001**, *267*, 59.
[16] Y. Fujimura, L. González, K. Hoki, D. Kröner, J. Manz, Y. Ohtsuki, *Angew. Chem.* **2000**, *112*, 4785; *Angew. Chem. Int. Ed.* **2000**, *39*, 4586.
[17] H. Stapelfeldt, T. Seideman, *Rev. Mod. Phys.* **2003**, *75*, 543.
[18] M. Rubio, B. O. Roos, L. Serrano-Andrés, M. Merchán, *J. Chem. Phys.* **1999**, *110*, 7202.
[19] D. Sundholm, *Chem. Phys. Lett.* **2000**, *317*, 392.
[20] J. A. Yeazell, C. R. Stroud, *Phys. Rev. Lett.* **1988**, *60*, 1494.
[21] T. C. Weinacht, J. Ahn, P. H. Bucksbaum, *Phys. Rev. Lett.* **1998**, *80*, 5508.
[22] M. Kitzler, K. O'Keeffe, M. Lezius, *J. Mod. Opt.* **2005**, *53*, 57.
[23] M. Kitzler, M. Lezius, *Phys. Rev. Lett.* **2005**, *95*, 253001.
[24] O. E. Alon, V. Averbukh, N. Moiseyev, *Phys. Rev. Lett.* **1998**, *80*, 3743.
[25] A. D. Bandrauk, H. S. Nguyen, *Can. J. Chem.* **2004**, *82*, 831.

 © 2006 Wiley-VCH Verlag GmbH & Co. KGaA, Weinheim

[26] S. Chelkowski, A. D. Bandrauk, *Phys. Rev. A* **2005**, *71*, 053815.
[27] J. Manz, *J. Am. Chem. Soc.* **1980**, *102*, 1801.
[28] P. Král, T. Seideman, *J. Chem. Phys.* **2005**, *123*, 184702.
[29] K. Mishima, K. Yamashita, *J. Chem. Phys.* **1999**, *109*, 1801.
[30] Note added in proof: For the preparation and observation of a hybrid-type superposition state in the one-electron system H_2^+, see G. L. Yudin, S. Chelkowski, J. Itatani, A. D. Bandr'auk, P. B. Corkum, *Phys. Rev. A* **2005**, *72*, 051401(R); A. D. Bandrauk, S. Chelkowksi, H. S. Nguyen, *Int. J. Quantum Chem.* **2004**, *100*, 834.

 © 2006 Wiley-VCH Verlag GmbH & Co. KGaA, Weinheim

Heterogeneous Catalysis

DOI: 10.1002/anie.200503068

On the Role of Oxygen Defects in the Catalytic Performance of Zinc Oxide**

Sebastian Polarz, Jennifer Strunk, Vladislav Ischenko, Maurits W. E. van den Berg, Olaf Hinrichsen,* Martin Muhler, and Matthias Driess*

Metal oxides are highly important as components in heterogeneous catalysts.[1] It is also well established that as the building blocks of nanoscaled materials get smaller, surfaces become increasingly important in determining their properties.[2] Very early on, researchers found that catalytic activity is only indirectly related to the surface area;[3] in fact it depends on the density of active sites.[4] Although solid-state defects have been proposed to be the active sites in heterogeneous catalysis,[5] active centers have rarely been conclusively identified and the rational design of catalysts is still out of reach.

Processes in heterogeneous catalysis associated with the production of energy-storage molecules, for example, methanol as a storage molecule for hydrogen,[6,7] is presently of great interest. Low-pressure production of methanol is conducted industrially with catalysts containing Cu and ZnO as the active phases and alumina as the support.[7,8] Composites (Cu + ZnO), however, exhibit higher activities than that expected based on the performance of the single components. This was attributed to a strong metal–support interaction (SMSI) effect.[9] Nevertheless, the active sites in Cu/ZnO and even in the pure ZnO have not yet been identified experimentally.

Some important information concerning pure ZnO catalysts is already available: Generally, the catalytic activity of ZnO does not increase linearly with the increasing BET surface area.[10] It was concluded that the catalytic formation of methanol over ZnO is a structure-sensitive reaction requiring the presence of polar ZnO facets.[10] According to the most recent models of the methanol-synthesis reaction on the polar ZnO(000$\bar{1}$) surface,[11] oxygen vacancies formed on this surface of ZnO crystals serve as the active sites (Scheme 1).[12] However, there has been no definite experimental proof for this assumption.

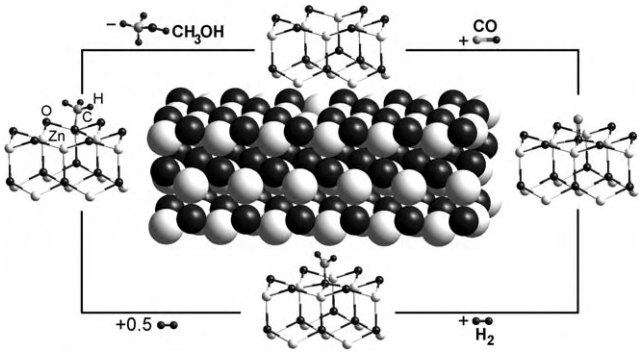

Scheme 1. Model for the activity of ZnO in the hydrogenation of CO. The space-filling model shows the (000$\bar{1}$) surface with one oxygen vacancy. The ball-and-stick models show the chemisorption of CO at the oxygen vacancy. More detailed information is given in Ref. [11].

We report here on the preparation of nanocrystalline ZnO materials containing different amounts of oxygen vacancies and on the catalytic performance of this model system. Our results indicate that oxygen vacancies are of fundamental importance for explaining the catalytic activity of pure ZnO in methanol synthesis.

The presence of oxygen vacancies in ZnO has been known for some time,[13] and a number of methods are suitable for the preparation of surface-rich and nanoscaled ZnO.[14] Still, to our knowledge no one has studied nanocrystalline ZnO with a varying degree of oxygen deficiencies and the effect on catalytic properties. One reason for this may be the thermodynamic instability of such vacancies at "normal" oxygen partial pressures.[15] One theoretical study implies that ZnO with oxygen defects is only metastable. Therefore, these materials may be accessible only by kinetically controlled bottom-up routes. We recently identified an organometallic precursor system from which ZnO can be prepared at temperatures as low as 150 °C.[16–19] These molecular precursors are characterized by a central Zn_4O_4 heterocubane cluster and thus represent zinc oxide preorganized on the

[*] Dr. S. Polarz, Dr. V. Ischenko, Prof. Dr. M. Driess
Technical University Berlin, Institute of Chemistry
Strasse des 17. Juni 135, 10623 Berlin (Germany)
Fax: (+49) 234-321-4378
E-mail: sebastian.polarz@tu-berlin.de
Dipl.-Chem. J. Strunk, Dr. M. W. E. van den Berg,
Prof. Dr. O. Hinrichsen, Prof. Dr. M. Muhler
Ruhr-Universität Bochum, Fakultät für Chemie
Universitätsstrasse 150, 44780 Bochum (Germany)
Fax: (+49) 30-314-297-32
E-mail: olaf@techem.ruhr-uni-bochum.de

[**] The authors gratefully acknowledge the Deutsche Forschungsgemeinschaft (DFG) for funding (Sonderforschungsbereich 558; Emmy Noether research group). We thank Dr. E. Bill and Prof. Dr. K. Wieghardt for the EPR measurements of our samples and for valuable discussions.

Supporting information for this article is available on the WWW under http://www.angewandte.org or from the author.

 © 2006 Wiley-VCH Verlag GmbH & Co. KGaA, Weinheim

molecular scale. In Figure 1a the methylisopropoxy derivative $[CH_3ZnOCH(CH_3)_2]_4$ is shown as an example.

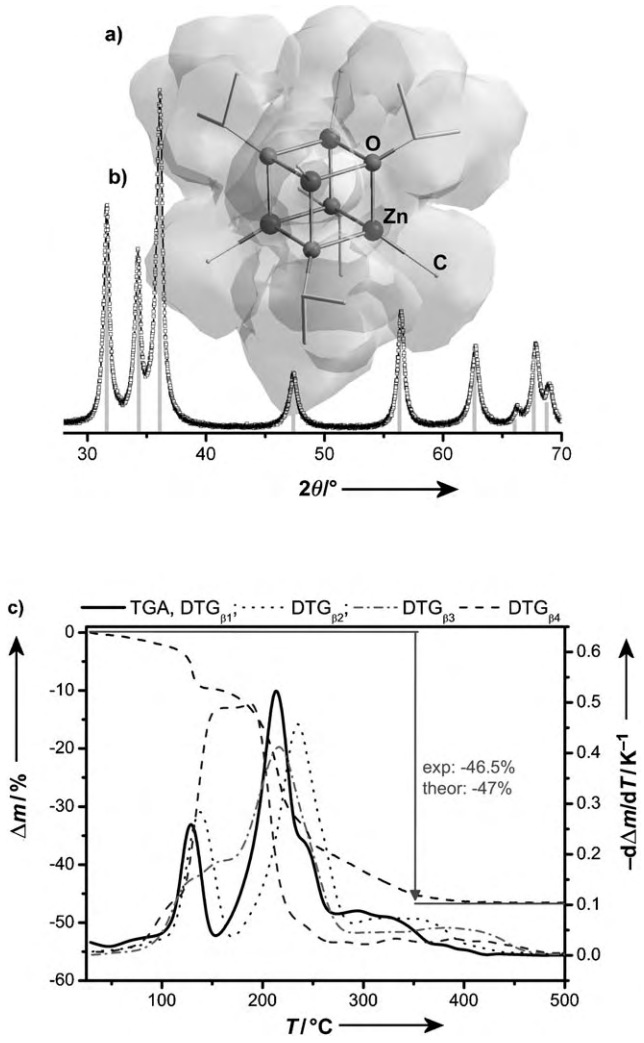

Figure 1. a) Molecular structure of the $[CH_3ZnOCH(CH_3)_2]_4$ highlighting the central Zn_4O_4 heterocubane motif; H atoms not shown. b) PXRD pattern of the material obtained from this precursor at $T_{end} = 350\,°C$ and a heating rate of $\beta_3 = 10\,K\,min^{-1}$, and the reference pattern of ZnO with hexagonal wurtzite structure (gray). c) TG curve for the thermolysis/oxidation of $[CH_3ZnOCH(CH_3)_2]_4$ in 80% N_2/20% O_2 and the first derivative of the TG trace (DTG) for the heating rates β_1–β_4.

The thermolysis of $[CH_3ZnOCH(CH_3)_2]_4$ in the presence of O_2 was studied by thermogravimetric analysis (TGA) at different heating rates β ranging from 1 $K\,min^{-1}$ to 30 $K\,min^{-1}$. It is evident that $[CH_3ZnOCH(CH_3)_2]_4$ is highly sensitive to kinetic factors in the decomposition process. At very low heating rates ($\beta_1 = 1\,K\,min^{-1}$) the thermolysis is characterized by two main mass-loss steps at $T = 128\,°C$ and 213 °C (Figure 1c). The remaining mass of 53.5% is in good agreement with the value expected for the quantitative transformation of the precursor to ZnO. At higher heating rates ($\beta_2 = 5\,K\,min^{-1}$ and $\beta_3 = 10\,K\,min^{-1}$, Figure 1b) the results can be explained by a broadening and superposition of the two DTG peaks (first derivative of the TGA data), but this is not possible for the highest heating rate ($\beta_4 = 30\,K\,min^{-1}$, Figure 1c). Only one broad step of mass loss is found centered at $T = 172\,°C$. The TGA results indicate that at higher heating rates formation of ZnO occurs under nonequilibrium conditions.

Interestingly, neither the chemical composition nor the particle size changes significantly with heating rate as proven by powder X-ray diffractometry (PXRD; not shown), elemental analysis, and IR spectroscopy. The IR spectra (see the Supporting Information) reveal that at 350 °C ZnO free of organic impurities could be obtained; only the features characteristic for the bulk ZnO reference sample are observed (ZnO stretching band at 440 cm^{-1}). Concerning this point, there is practically no difference between the samples heated at rates of 1 $K\,min^{-1}$ (β_2) and 30 $K\,min^{-1}$ (β_4). Therefore, we decided to heat our samples to $T_{end} = 350\,°C$ for their preparation. At this temperature one obtains pure, nanocrystalline ZnO with a mean particle diameter of roughly 13 nm as indicated by the PXRD pattern obtained for the sample with $\beta_3 = 10\,K\,min^{-1}$ (Figure 1b).[20] The purity of the obtained ZnO, in particular of its surface, was further confirmed by XPS measurements (see the Supporting Information).

Recently we were able to demonstrate by EPR spectroscopy that unpaired electrons are trapped at the sites of the oxygen vacancies.[18] The ZnO sample prepared from the *tert*-butoxy derivative $[CH_3ZnOCH(CH_3)_2]_4$ shows two EPR signals at *g*-values of around 1.96 and 2.0, the latter of which corresponds to the oxygen vacancies (Figure 2, top).

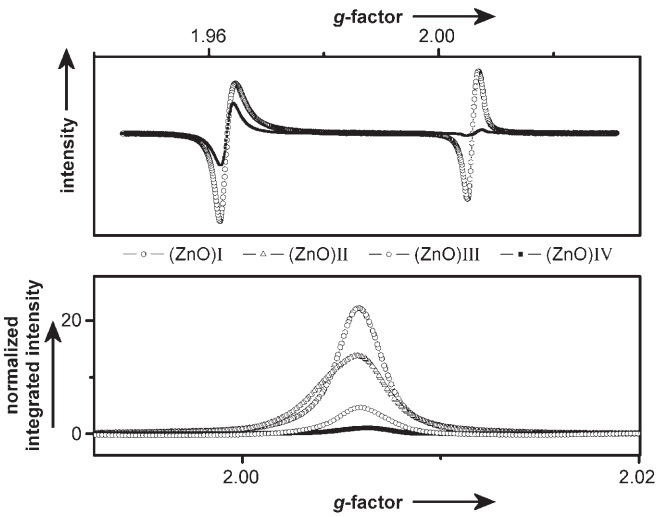

Figure 2. Top: EPR spectra of two ZnO samples prepared from $[CH_3ZnOC(CH_3)_3]_4$ at different heating rates of 5 $K\,min^{-1}$ (β_2, (ZnO)IV) and 30 $K\,min^{-1}$ (β_4, (ZnO)I). Bottom: The EPR data were normalized to the material with the lowest EPR signal ((ZnO)IV; see Table 1).

Details regarding the analysis of oxygen-deficient ZnO samples are beyond the scope of this paper, and the reader is referred to a separate publication.[18] An overview of the samples presented in the current study is given in Table 1. Initially, we believed that $[CH_3ZnOCH(CH_3)_2]_4$ is the ideal

 © 2006 Wiley-VCH Verlag GmbH & Co. KGaA, Weinheim

Table 1: Overview over the samples used for the catalytic investigations.

Sample	Precursor	Conditions
(ZnO)I	$[CH_3ZnOC(CH_3)_3]_4$	$\beta_4 = 30\ K\,min^{-1}$
(ZnO)II	$[CH_3ZnOC(CH_3)_3]_4$	$\beta_3 = 10\ K\,min^{-1}$
(ZnO)III	$[CH_3ZnOCH(CH_3)_2]_4$	$\beta_2 = 5\ K\,min^{-1}$
(ZnO)IV	$[CH_3ZnOC(CH_3)_3]_4$	$\beta_2 = 5\ K\,min^{-1}$

precursor for obtaining oxygen-deficient ZnO owing to the possible elimination of acetone and the corresponding formation of zinc hydride as the reactive transient species (Scheme 2, see the Supporting Information).[17,19]

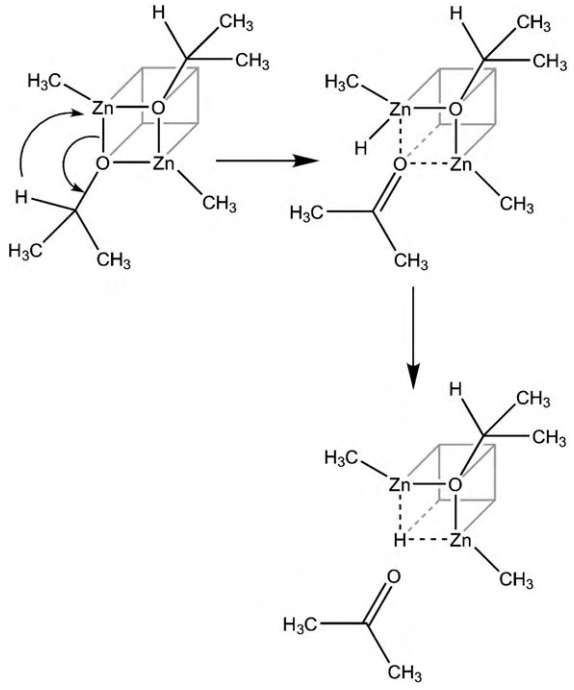

Scheme 2. Schematic representation of the loss of acetone from $[CH_3ZnOCH(CH_3)_2]_4$. For clarity only the front face of the "Zn_4O_4" cluster is shown. The products resulting from a β-hydride transfer must be regarded as intermediates in the formation of oxygen-deficient ZnO.

We tested our hypothesis whether the elimination of acetone is truly crucial for the formation of oxygen vacancies by comparison with a sample prepared from the *tert*-butoxy derivative $[CH_3ZnOC(CH_3)_3]_4$. Clearly, the elimination of an oxygen-containing leaving group from the *tert*-butoxy-substituted Zn_4O_4 core is rather unlikely because no β hydrogen atom is present. In fact, the intensity of the EPR signal corresponding to oxygen vacancies is smaller for a ZnO sample resulting from $[CH_3ZnOC(CH_3)_3]_4$ ((ZnO)IV) than that for a sample prepared from $[CH_3ZnOCH(CH_3)_2]_4$ ((ZnO)III; see Table 1 and Figure 2). The integrated intensity of the EPR signal corresponding to oxygen vacancies is five times higher for (ZnO)III than for (ZnO)IV, which indicates that the oxygen vacancy density is much lower for the latter sample. However, the effect was less pronounced than we had hoped.

Therefore, we raised the alternative hypothesis that more oxygen vacancies can be created if ZnO is prepared under enhanced nonequilibrium conditions. Figure 2a shows the results from EPR measurements of samples prepared from $[CH_3ZnOC(CH_3)_3]_4$ at $T_e = 350\,°C$ with different heating rates ((ZnO)IV: $\beta_2 = 5\ K\,min^{-1}$, (ZnO)I: $\beta_4 = 30\ K\,min^{-1}$). It can be seen that the EPR signal corresponding to oxygen vacancy sites at $g \approx 2.00$ is significantly higher for (ZnO)I.[18] The normalized, integrated intensity even 25 times greater (Figure 2b). Interestingly, $[CH_3ZnOCH(CH_3)_2]_4$ is less suitable for the formation of nanocrystalline ZnO with high oxygen-vacancy content, because at high heating rates we even observed the formation of elemental zinc (results not shown). Nevertheless, with $[CH_3ZnOC(CH_3)_3]_4$ as a precursor it is possible to obtain nanocrystalline ZnO samples with differing oxygen-vacancy content (Figure 2b).

Next, we tested the catalytic activity of the prepared samples for methanol synthesis (Figure 3) from using a

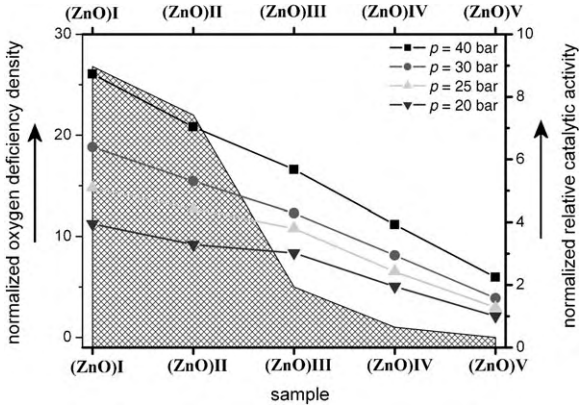

Figure 3. Correlation of the occurrence of oxygen vacancy sites (determined by EPR spectroscopy) to the normalized activity for CO hydrogenation at different pressures ($p = 20$–40 bar). The activities were normalized to the BET surface area of the respective ZnO powders and to the sample with lowest catalytic activity ((ZnO)V, a reference sample prepared by a conventional precipitation technique[10]).

feedgas mixture containing CO and H_2 (see the Experimental Section). Figure 3 indicates that a qualitative correlation exists between the catalytic activity and the amount of oxygen vacancies in the ZnO samples. While (ZnO)I has approximately over 25 times more oxygen vacancies than sample (ZnO)IV, its catalytic activity is only about four times higher. However, differences in scaling are expected since the catalytic activity is a surface property of the samples, while the EPR signal scales with the bulk volume of ZnO. Therefore, we conclude that the catalytic activity of ZnO does indeed depend on the amount of oxygen vacancies present.

Although there is a convincing correlation between the oxygen-deficiency content as determined by the EPR measurements, other factors like particle strain and the presence of more unstable crystal surfaces could also explain the higher catalytic performance of the kinetically produced ZnO samples.[18] If so, a similar trend in catalytic performance should also be observed for tests with CO_2 instead of CO. We reported earlier that CO_2 has a poisoning effect on pure ZnO

 © 2006 Wiley-VCH Verlag GmbH & Co. KGaA, Weinheim

catalysts probably arising from the quenching of oxygen defect sites.[11] This poisoning effect is caused by the reaction of CO_2 with the oxygen vacancy accompanied by the release of CO. It is important to note that CO_2 can quench only oxygen defect sites on the surface and no other structural defects such as dislocations etc.[18] Therefore, only two scenarios are possible: 1) The ZnO samples introduced here could display unusual activity also under CO_2-rich conditions, indicating that factors other than oxygen vacancies are responsible for the catalytic performance. 2) The unusual features in catalytic properties could be quenched by CO_2, and the zinc oxide samples would be comparable to the reference samples in CO_2. In this case oxygen vacancies play a crucial role.

Consequently, we determined the catalytic activity of the our samples in an atmosphere containing CO_2 and compared the data to those recorded previously on conventional ZnO samples (Figure 4; for further details about the reference samples see reference [10]). The samples (ZnO)I–(ZnO)IV and the reference samples display almost identical behavior. This strongly suggests that oxygen vacancies are indeed responsible for the increased catalytic activity under a CO atmosphere.

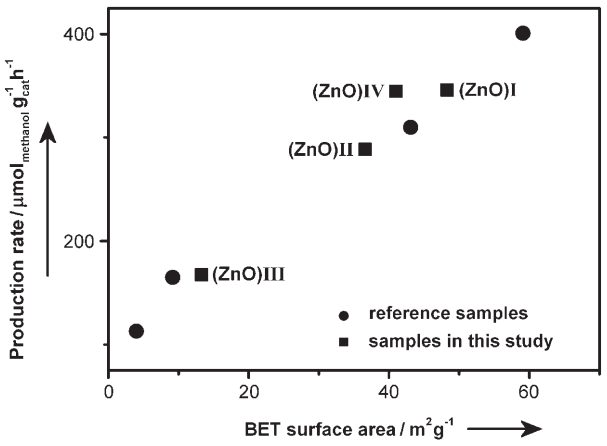

Figure 4. Catalytic performance of (ZnO)I–(ZnO)IV and of a reference sample[10] and in CO_2-containing synthesis gas (measurements at 30 bar).

In summary, samples with a set variation in oxygen-vacancy content can be prepared under kinetically controlled conditions by the low-temperature thermolysis of organometallic heterocubane Zn_4O_4 precursors. Catalytic investigations showed that oxygen vacancies in the ZnO lattice are very likely to represent the active sites in the hydrogenative conversion of CO to methanol.

Experimental Section

The heterocubane precursors and samples (ZnO)I–(ZnO)IV were prepared as reported in previous papers.[18,19] Sample (ZnO)V was prepared according to the literature.[10]

Catalytic measurements were performed in a previously described flow setup[21] with six gas lines: He (99.9999%), H_2 (99.9999%), 2% H_2/He (H_2: 99.9995%), 1% N_2O/He (N_2O: 99.9995%), 10% CO/He (CO: 99.9995%), and synthesis gas. Two different synthesis gas mixtures (purity ≥ 99.9995%) were used: 15% CO/H_2 and 6% CO/8% CO_2/64% H_2/He.[21] Fast online gas analysis was performed with a calibrated mass spectrometer (Balzers GAM422). In each test, 100 mg of the ZnO sample, previously pressed, crushed, and sieved to a particle size of 250–355 μm, was filled into a glass-lined stainless steel U-tube reactor. The catalyst bed was fixed by a glasswool plug on either side. The pretreatment of the samples comprised a heating procedure in 2% H_2/He (10 N mL min^{-1}, 5 K min^{-1}) from room temperature to 573 K and subsequently that temperature was maintained in dilute H_2 for 1 h. The reactor was flushed with He (10 N mL min^{-1}) for about 30 min without cooling, as a temperature of 573 K was also used for all catalytic activity tests. The temperature was measured and maintained throughout the test procedure by a thermocouple placed directly inside the catalyst bed. As the equilibrium yields in methanol synthesis are rather low at 573 K and atmospheric pressure, the reaction was carried out at 40, 30, 25, and 20 bar. At each pressure, conditions were maintained until steady state was reached.

Thermogravimetric analyses of the precursor were carried out with a thermogravimetric setup from Rubotherm. X-ray diffractograms were recorded with a Bruker AXS D8 Advance instrument using $Cu_{K\alpha}$ radiation ($\lambda = 1.5418$ Å) and a position-sensitive detector (PSD) diffractometer using $Cu_{K\alpha}$ radiation in the 2θ range from 25° to 85° with steps of 0.015°. Crystallite size and microstrain parameters were determined by full-profile LeBail fit of the experimental XRD pattern with subsequent decomposition of the reflection profile into Gaussian and Lorentzian parts, taking into account instrumental contribution to peak broadening. X-band EPR spectra were recorded with a Bruker Elexsys E500 EPR spectrometer with an ER077R magnet (75-mm pole cap distance), and an ER047 XG-T microwave bridge. The samples were irradiated with an Oriel high-pressure mercury lamp. The samples were loaded into quartz tubes and inserted into the microwave cavity. FT-IR spectra were recorded with a Bruker Vector 22 spectrometer (KBr pellets). The BET area was measured by static N_2 physisorption in the quartz U-tube of an Autosorb 1-C setup (Quantachrome). XPS spectra were recorded with a Scienta SES 2002 spectrometer using monochromated $Al_{K\alpha}$ radiation at 1486.6 eV. The X-ray source was operated at 14 kV and 55-mA emission current. Base pressure in the measurement chamber was less than 7×10^{-10} mbar. Survey spectra were recorded with a pass energy of 500 eV, whereas for the individual spectral lines 200 eV was used. The step size for the regions was 100 meV. Under these conditions, the Au $4f_{7/2}$ linewidth of a sputtered gold foil was 0.74 eV. All spectral lines were calibrated using the binding energy of the Zn $2p_{3/2}$ line at 1021.8 eV as a reference.

Received: August 29, 2005
Revised: February 13, 2006
Published online: March 28, 2006

Keywords: heterogeneous catalysis · methanol synthesis · oxygen vacancies · zinc oxide

[1] a) C. N. R. Rao, *Annu. Rev. Phys. Chem.* **1989**, *40*, 291; A. Fujimori, T. Mizokawa, *Curr. Opin. Solid State Mater. Sci.* **1997**, *2*, 18; b) Y. Tokura, *Curr. Opin. Solid State Mater. Sci.* **1998**, *3*, 175; c) R. J. Mortimer, *Chem. Soc. Rev.* **1997**, *26*, 147; d) P. Poizot, S. Laruelle, S. Grugeon, L. Dupont, J. M. Tarascon, *Nature* **2000**, *407*, 496.
[2] H. J. Freund, H. Kuhlenbeck, V. Staemmler, *Rep. Prog. Phys.* **1996**, *59*, 283.
[3] M. Boudart, *Cattech* **2001**, *5*, 81.
[4] H. S. Taylor, *Proc. R. Soc. London* **1925**, *108*, 105.

 © 2006 Wiley-VCH Verlag GmbH & Co. KGaA, Weinheim

[5] J. M. Thomas, E. L. Evans, J. O. Williams, *Proc. R. Soc. London Ser. A* **1972**, *331*, 417.
[6] a) G. A. Olah, *Angew. Chem.* **2005**, *117*, 2692; *Angew. Chem. Int. Ed.* **2005**, *44*, 2636; b) K. C. Waugh, *Catal. Today* **1992**, *15*, 51; c) J. Agrell, B. Lindström, L. J. Pettersson, S. G. Järas in *Catalysis—Specialist Periodical Reports 16* (Ed.: J. J. Spivey), Royal Society of Chemistry, Cambridge, **2002**, p. 67.
[7] L. Lloyd, D. E. Ridler, M. V. Twigg in *Catalyst Handbook* (Ed.: M. V. Twigg), Wolfe, London, **1989**.
[8] a) G. C. Chinchen, K. C. Waugh, D. A. Whan, *Appl. Catal.* **1986**, *25*, 101; b) M. Kurtz, H. Wilmer, T. Genger, O. Hinrichsen, M. Muhler, *Catal. Lett.* **2003**, *86*, 77.
[9] a) H. Wilmer, O. Hinrichsen, *Catal. Lett.* **2002**, *82*, 117; b) M. Kurtz, N. Bauer, C. Buscher, H. Wilmer, O. Hinrichsen, R. Becker, S. Rabe, K. Merz, M. Driess, R. A. Fischer, M. Muhler, *Catal. Lett.* **2004**, *92*, 49; c) M. Kurtz, N. Bauer, H. Wilmer, O. Hinrichsen, M. Muhler, *Chem. Eng. Technol.* **2004**, *27*, 1146.
[10] H. Wilmer, M. Kurtz, K. V. Klementiev, O. P. Tkachenko, W. Grünert, O. Hinrichsen, A. Birkner, S. Rabe, K. Merz, M. Driess, C. Wöll, M. Muhler, *Phys. Chem. Chem. Phys.* **2003**, *5*, 4736.
[11] M. Kurtz, J. Strunk, O. Hinrichsen, M. Muhler, K. Fink, B. Meyer, C. Wöll, *Angew. Chem.* **2005**, *117*, 2850; *Angew. Chem. Int. Ed.* **2005**, *44*, 2790.
[12] a) J. C. Lavalley, J. Saussey, T. Rais, *J. Mol. Catal.* **1982**, *17*, 289; b) H. H. Kung, *Catal. Rev. Sci. Eng.* **1980**, *22*, 235; c) S. A. French, A. A. Sokol, S. T. Bromley, C. R. A. Catlow, S. C. Rogers, F. King, P. Sherwood, *Angew. Chem.* **2001**, *113*, 4569; *Angew. Chem. Int. Ed.* **2001**, *40*, 4437; d) S. A. French, A. A. Sokol, S. T. Bromley, C. R. A. Catlow, P. Sherwood, *Top. Catal.* **2003**, *24*, 161; e) H. Lüth, G. W. Rubloff, W. D. Grobman, *Solid State Commun.* **1976**, *18*, 1427; f) W. Göpel, *Surf. Sci.* **1977**, *62*, 165.
[13] a) A. Poppl, G. Volkel, *Phys. Status Solidi A* **1989**, *115*, 247; b) B. S. Chiou, M. C. Chung, *J. Electron. Mater.* **1991**, *20*, 885; c) V. A. Gercher, D. F. Cox, J. M. Themlin, *Surf. Sci.* **1994**, *306*, 279.
[14] a) S. J. Pearton, D. P. Norton, K. Ip, Y. W. Heo, T. Steiner, *J. Vac. Sci. Technol.* **2004**, *22*, 932; b) Z. L. Wang, *J. Phys. Condens. Matter* **2004**, *16*, R829; c) R. Viswanatha, S. Sapra, B. Satpati, P. V. Satyam, B. N. Dev, D. D. Sarma, *J. Mater. Chem.* **2004**, *14*, 661; d) G. Rodriguez-Gattorno, P. Santiago-Jacinto, L. Rendon-Vazquez, J. Nemeth, I. Dekany, D. Diaz, *J. Phys. Chem.* **2003**, *107*, 12597; e) Z. S. Hu, G. Oskam, P. C. Searson, *J. Coll. Interf. Sci.* **2003**, *263*, 454; f) M. Shim, P. Guyot-Sionnest, *J. Am. Chem. Soc.* **2001**, *123*, 11651; g) E. A. Meulenkamp, *J. Phys. Chem.* **1998**, *102*, 5566.
[15] B. Meyer, *Phys. Rev. B* **2004**, *69*.
[16] a) S. Polarz, F. Neues, M. Van den Berg, W. Grünert, L. Khodeir, *J. Am. Chem. Soc.* **2005**, *127*, 12028; b) A. Roy, S. Polarz, S. Rabe, B. Rellinghaus, H. Zähres, F. E. Kruis, M. Driess, *Chem. Eur. J.* **2004**, *10*, 1565.
[17] D. Schröder, H. Schwarz, S. Polarz, M. Driess, *Phys. Chem. Chem. Phys.* **2005**, *7*, 1049.
[18] V. Ischenko, S. Polarz, D. Grote, V. Stavarache, K. Fink, M. Driess, *Adv. Funct. Mater.* **2005**, *15*, 1945.
[19] S. Polarz, A. Roy, M. Merz, S. Halm, D. Schröder, L. Scheider, G. Bacher, F. E. Kruis, M. Driess, *Small* **2005**, *1*, 540.
[20] E. Lifshin, *X-Ray Characterization of Materials*, Wiley-VCH, Weinheim, **1999**.
[21] T. Genger, O. Hinrichsen, M. Muhler, *Catal. Lett.* **1999**, *59*, 137.

 © 2006 Wiley-VCH Verlag GmbH & Co. KGaA, Weinheim

Block Copolymers

DOI: 10.1002/anie.200503514

Hockey-Puck Micelles from Oligo(*p*-benzamide)-*b*-PEG Rod–Coil Block Copolymers**

*Tobias W. Schleuss, Robert Abbel, Michael Gross, Dieter Schollmeyer, Holger Frey, Michael Maskos, Rüdiger Berger, and Andreas F. M. Kilbinger**

Rod–coil block copolymers (RCP) have recently received significant attention[1–3] as they provide a powerful means for the preparation of stable supramolecular architectures in solution and in the solid state. The conformational rigidity of one of the blocks has been achieved through the use of helical structures like polypeptides,[4] polyisocyanates,[5] polyisocyanides,[6] and polycarbodiimides[7] as well as π-conjugated polymers, for example, poly(*p*-phenylene)s,[8,9] poly(thiophene)s,[10] and poly(phenylquinoline)s.[11]

RCP with oligomeric rod block polymers (ORCP) are of particular interest as they may be used to form supramolecular aggregates on the nanometer-length scale that are much smaller than those achieved with RCPs consisting of polymeric rod blocks or coil–coil block copolymers.[12] Typical ORCP structures consist of a π-conjugated oligomer attached to a flexible solubilizing polymer chain. Stupp et al. have reported the supramolecular organization of a variety of structures in which the rod segment is based on oligomeric aromatic esters. Depending on the rod structure, ribbons[13] as well as mushroom-shaped aggregates[14] have been observed. Lee et al. have described supramolecular rod bundles[15] and supramolecular reactors[16] based on ORCP.

Chirally substituted electroactive π-conjugated oligomers have been incorporated into rod–coil architectures by Meijer et al. There, helical supramolecular organization in solution was investigated by circular dichroism spectroscopy and other

[*] Dipl.-Chem. T. W. Schleuss, Dipl.-Chem. R. Abbel, Dr. D. Schollmeyer, Prof. Dr. H. Frey, Dr. A. F. M. Kilbinger
Institut für Organische Chemie
Johannes Gutenberg-Universität Mainz
Duesbergweg 10–14, 55099 Mainz (Germany)
Fax: (+49) 6131-39-26138
E-mail: akilbing@uni-mainz.de

Dr. R. Berger
Max Planck Institut für Polymerforschung
Mainz (Germany)

Dipl.-Chem. M. Gross, Dr. M. Maskos
Institut für Physikalische Chemie
Johannes Gutenberg-Universität Mainz (Germany)

[**] The authors thank U. Rietzler for help with the SFM measurements, Prof. H.-J. Butt (Max Planck Institute for Polymer Research, Mainz) for kindly providing access to SFM equipment, and Prof. M. Schmidt (University of Mainz) for helpful discussions. A.F.M.K. and R.B. thank the German Research Foundation (DFG; SFB 625, "From Single Molecules to Nanoscopically Structured Materials") and the Fonds der Chemischen Industrie (FCI) for financial support.

Supporting information for this article is available on the WWW under http://www.angewandte.org or from the author.

 © 2006 Wiley-VCH Verlag GmbH & Co. KGaA, Weinheim

spectroscopic methods.[17] Many different and, sometimes unexpected, structures have been found for RCPs over the last few years. Layered structures,[18] arrowhead or zigzag structures,[18] and even double-hexagonal structures[12] have been observed in the bulk phase. Micelles,[19] vesicles,[20–23] and ribbonlike structures[24] have also been described. Most of the reported ORCP aggregate through relatively weak π–π interactions. To increase the association constant in solution or the phase stability in bulk, stronger noncovalent interactions are desirable.

We recently described the synthesis[25] and aggregation behavior[26] of a series of oligo(*p*-benzamide)-*b*-poly(ethylene glycol)monomethyl ethers (OPBA-MPEG) in which strong directional hydrogen bonds are responsible for the formation of supramolecular structures. Within the series of OPBA-MPEG rod–coil block copolymers, the block copolymer carrying the longest OPBA block (**1**, a hepta(*p*-benzamide), see Figure 1) showed the strongest aggregation; that is, the

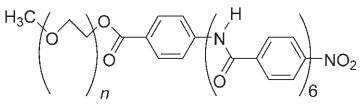

1: $n = 110$
2: $n = 45$

Figure 1. Hepta(*p*-benzamide)-*b*-poly(ethylene glycol)s **1** and **2** synthesized according to reported procedures.[25]

ratio of aggregated to nonaggregated species observed in GPC (chloroform) traces was the highest. Aggregation was also determined by a characteristic blue shift in the UV/Vis spectra (H aggregates)[27] and broadening of the aromatic resonances in the ^{1}H NMR spectra. In hydrogen-bond-disrupting solvents like *N*,*N*-dimethylformamide (DMF) and *N*,*N*-dimethylacetamide (DMAc) no aggregation could be observed by any of the above techniques, clearly indicating that hydrogen-bond formation is crucially important in the formation of supramolecular structures. While strong and defined aggregation was evident in these experiments, a clear picture of the aggregation process and the nature of the interaction forces, as well as the overall shape and geometry of the aggregate could not be obtained.

Here we present light-scattering data and scanning force microscope (SFM) images of high quality that show for the first time, to the best of our knowledge, the often proposed hockey-puck micelle for rod–coil architectures in great detail. Dynamic light-scattering (DLS) studies of a chloroform solution of **1** ($c = 0.6\ \mathrm{g\,L^{-1}}$) containing 6.25×10^{-4} M tetrabutylammonium bromide (TBABr) gave a hydrodynamic radius of $R_h = 21$ nm (see the Supporting Information) and a fairly narrow size distribution of the aggregates ($\mu_2^{90^\circ} = 0.04$).[28] Addition of TBABr was necessary to suppress residual electrostatic interaction between the micelles in solution. The residual electrostatic interaction is most likely due to traces of ionic impurities such as tri(*p*-benzamide), which bears a carboxylic acid group. Such trace impurities, while not detectable by standard analytical procedures, can coaggregate with the hepta(*p*-benzamide) rod–coil copolymers and cause significant electrostatic interactions in a nonpolar solvent like chloroform, thereby rendering the light-scattering measurement in the absence of salt additives meaningless. Static light-scattering experiments gave a radius of gyration of $R_g = 19.6$ nm. The characteristic ratio $\rho = R_g/R_h = 0.9$ is indicative of spherical aggregates with slightly ellipsoidal character.

A Zimm plot of **1** was recorded in chloroform and is shown in Figure 2. The refractive index increment of **1** in

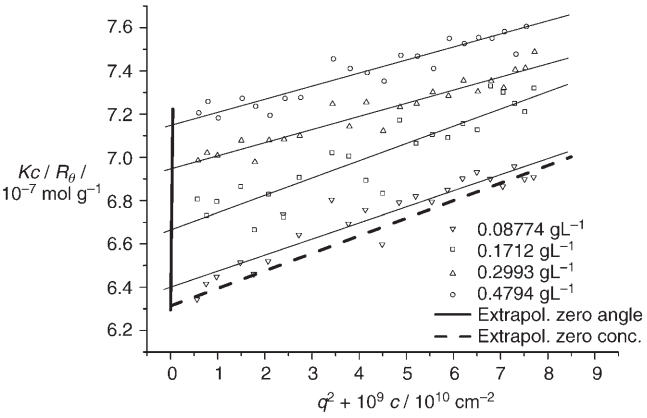

Figure 2. Zimm plot of **1** in chloroform. *K*: optical constant, *c*: concentration of dissolved sample, R_θ: Rayleigh ratio, *q*: scattering vector. Four different concentrations were obtained by diluting the sample inside the cuvette and subsequently each solution was measured at 20 different scattering angles. The laser wavelength was $\lambda_0 = 632.8$ nm. The data are plotted with an arbitrary refractive index increment of $dn/dc = 0.1000\ \mathrm{mL\,g^{-1}}$; $c_{TBABr} = 6.25 \times 10^{-4}$ M. Taking into account the experimental refractive index increment[29] of **1** in chloroform of $(dn/dc)_{exp} = 0.0736\ \mathrm{mL\,g^{-1}}$, one obtains the weight average of the molecular mass $M_w = 2.93 \times 10^6\ \mathrm{g\,mol^{-1}}$, the second virial coefficient of the osmotic pressure $A_2 = 5.2452 \times 10^{-5}\ \mathrm{mol\,mL\,g^{-2}}$, and the *z*-average of the squared radius of gyration $\langle R_g^2 \rangle_z = 3.8497 \times 10^{-12}\ \mathrm{cm^2}$ ($R_g = 19.6$ nm).

chloroform was determined to be $dn/dc = 0.0736\ \mathrm{mL\,g^{-1}}$. From the Zimm plot in Figure 2 a weight average molar mass for the aggregates of $M_w = 2.93 \cdot 10^6\ \mathrm{g\,mol^{-1}}$ could be calculated. This corresponds to an average aggregation number of $N_{agg} = 514$.

Aggregates of such dimensions are very well suited for visualization by scanning force microscopy (SFM). We chose tapping-mode SFM for characterization of the supramolecular structures, since it allows nondestructive imaging of the surface of soft polymer samples[30] and offers additional information about sample properties. To visualize single aggregates, highly dilute solutions of **1** ($c = 5\ \mathrm{mg\,L^{-1}}$) were prepared in chloroform and left to equilibrate at room temperature for at least twelve hours before film preparation. One drop of the solution was cast onto a freshly cleaved sheet of mica, the negatively charged surface of which offers good adhesion for hydrophilic polymers like polyethylene glycol (PEG). After evaporation of the solvent, the sample was examined by SFM in soft tapping mode using a silicon SFM tip.

As shown in Figure 3a, the particles are mainly spherical or slightly oval-shaped and have almost consistent dimensions, measuring 20–35 nm across and approximately 2 nm in

 © 2006 Wiley-VCH Verlag GmbH & Co. KGaA, Weinheim

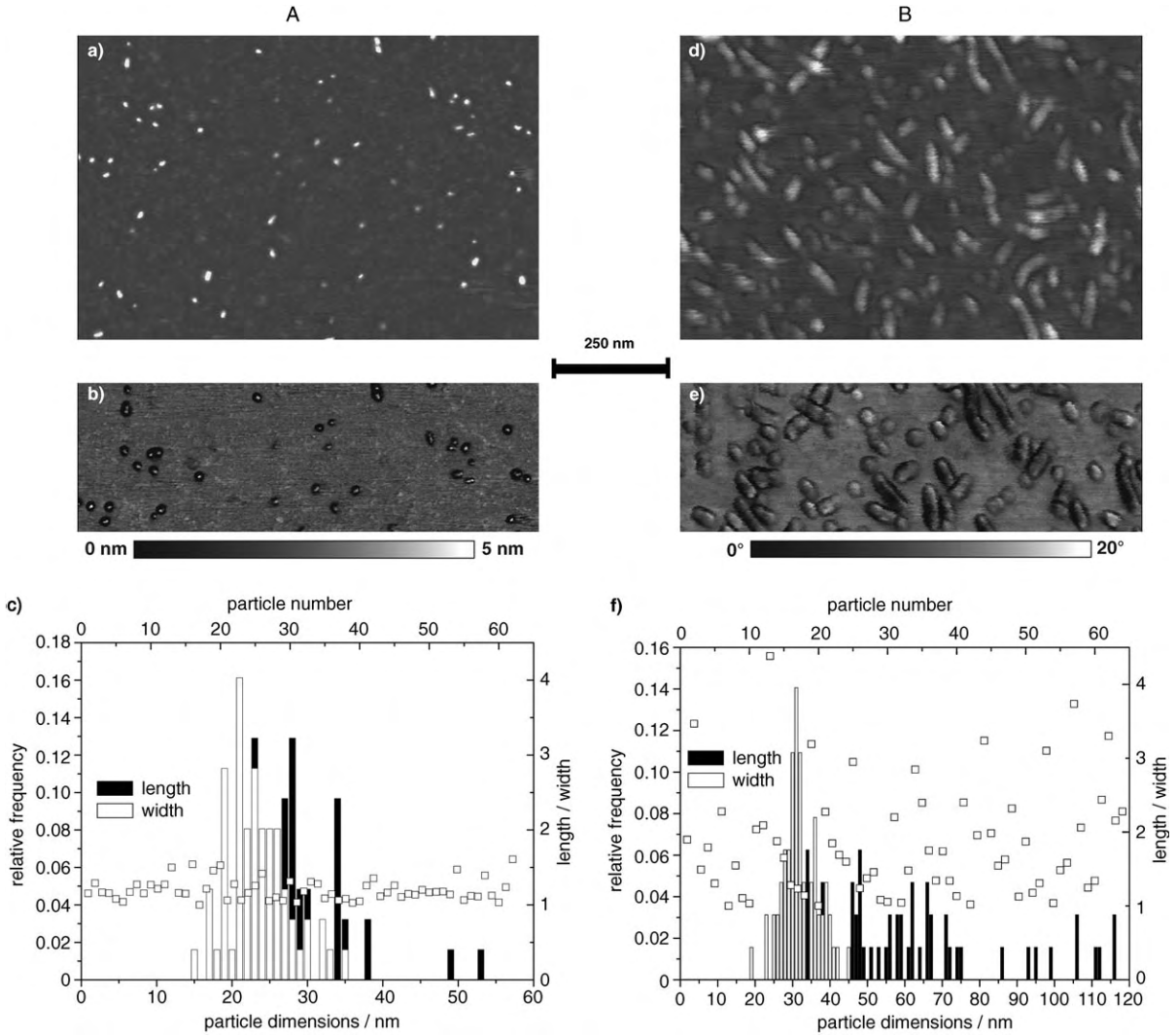

Figure 3. A. Tapping-mode SFM image showing spherical micelles of **1** on mica. The sample was prepared by drop-casting of a solution of **1** in chloroform ($c = 5\ mg\,L^{-1}$) onto freshly cleaved mica. a) Topography image, b) phase-contrast. c) Left and bottom axes (black and white bars): statistical analysis based on 62 micelles of **1**; for nonspherical shapes, the shorter axis was defined as the width and the longer axis as the length; top and right axes (□): a strong correlation between the length and width of the particles is observed. B. Tapping-mode SFM image showing rodlike micelles of **2** on mica. The sample was prepared by drop-casting of solution of **2** in chloroform ($c = 5\ mg\,L^{-1}$) onto freshly cleaved mica. d) Topography image, e) phase-contrast image. f) Left and bottom axes (black and white bars): statistical analysis based 64 micelles of **2**; top and right axes (□): length and width of the particles are not correlated.

height. The aggregates can be seen particularly well in the SFM phase-contrast image (Figure 3b). The phase-contrast image was also used to determine the in-plane particle dimensions. Besides the globular ones, few elongated aggregates were found. A statistical representation of the particle dimensions (Figure 3c) shows that the width and length distribution of the particles almost coincide. The narrow size distribution observed by SFM correlates well with the results obtained by DLS. The size of the aggregates was independent of solution concentration over a wide range of concentrations examined by SFM (2–50 $mg\,L^{-1}$).

Once the particles are deposited on mica, they are extremely stable; they can be clearly visualized by SFM even after being heated to 100 °C for several hours. In order to exclude false representation of the micelles by interactions between the mica surface and the aggregate, additional SFM experiments were carried out on amorphous carbon as well as SiO_2 (oxidized Si afer) and similar results were obtained (see the Supporting Information). Furthermore, the hydrodynamic radius of about 21 nm obtained by DLS measurements is in good agreement with the dimensions observed by SFM ($r = 10$–17.5 nm).

In addition, more concentrated solutions of **1** ($c = 0.05$–$1\ g\,L^{-1}$) were examined. For the highest concentrations investigated ($c = 1\ g\,L^{-1}$) we observed dendritic structures several hundred micrometers in length. Such structures are well-known to be caused by diffusion-limited aggregation (see the Supporting Information).[31]

Rod–coil block copolymers are believed to form hockey-puck micelles in coil-selective solvents;[32] however, there has

 © 2006 Wiley-VCH Verlag GmbH & Co. KGaA, Weinheim

been little experimental evidence in support of such unusual micelles.[33] To the best of our knowledge, this is the first time that such structures have been evidenced in great detail.

In analogy to micelles from low-molecular-weight amphiphiles the shape of the micelles is strongly influenced by the volume of the solvated head group, here, the hydrophilic PEG. To gain further insight into the formation of OPBA-PEG superstructures, rod–coil copolymer **2** was prepared in analogy to **1** but bearing a shorter PEG head group. Interestingly, the block copolymer bearing a tetra(*p*-benzamide) block, $MPEG_{2k}$-Ar_4-NH_2, an intermediate in the synthesis of **2**, showed strong aggregation in chloroform solution as determined by GPC, whereas for the analogous compound bearing a longer polymer chain, $MPEG_{5k}$-Ar_4-NH_2, no aggregation was observed.[26] This clearly shows that the length of the rod as well as the length of the coil segment strongly influence the overall ability of these rod–coil copolymers to form aggregates in nonpolar solvents.

Dynamic light-scattering (DLS) measurements of a solution of **2** in chloroform ($c = 0.3\ g\,L^{-1}$; 10^{-4} M TBABr) revealed a broader particle size distribution ($\mu_2^{90°} > 0.1$) than that of **1** ($\mu_2^{90°} = 0.04$, see above). The hydrodynamic radius of the aggregates of **2** (35 nm) was also larger than that observed for **1** (21 nm, see above). Static light-scattering (SLS) experiments with the same solution gave a radius of gyration of 57 nm and a ρ ratio R_g/R_h of 1.6, which indicates that the aggregates have an anisotropic shape.[34,35]

SFM measurements of thin films of **2** ($c = 5\ mg\,L^{-1}$) were carried out in the same way as described above for **1**. As can be seen in Figure 3 d,e, the aggregates observed are no longer spherical in shape but rodlike and elongated. The lengths of these rods differ over a range of ca. 80 nm, while the widths are very narrowly distributed (Figure 3 f). These results are in very good agreement with the data obtained from DLS.

The assumption that the rod–coil block copolymers form micelles in chloroform is supported by the fact that the shape of these aggregates changes from spherical to rodlike when the solvated head group is smaller; this is in analogy to the behavior of classical low-molecular-weight amphiphiles. The way these hockey-puck micelles are formed is most likely identical for compounds **1** and **2**. It is merely the size of the coil block that determines whether the micelle formed is more spherical or more elongated. The way these micelles are held together in the core, however, is fundamentally different from classical micelles. For a rod–coil hockey-puck micelle, the micellar core is believed to consist of a stack of rod segments arraged either as a monolayer or as a bilayer.[24,31,32,36]

As polymers **1** and **2** are amphiphilic, it should be possible to discriminate between the rigid hydrophobic micellar core and the softer hydrophilic corona by tapping-mode SFM. The SFM image in Figure 3 b reveals some fine structure at the core of the micelles. To investigate this further, the same sample was re-examined at higher resolution. To minimize possible interactions between the SFM tip and the polar PEG, SFM images of single micelles were recorded using hydrophobized SiO_2 cantilevers.[37] Samples of **1** were prepared in the same way as described above. The SFM phase-contrast image (Figure 4 b) clearly shows distinct micelles consisting of an anisotropic core approximately 10 nm in width and

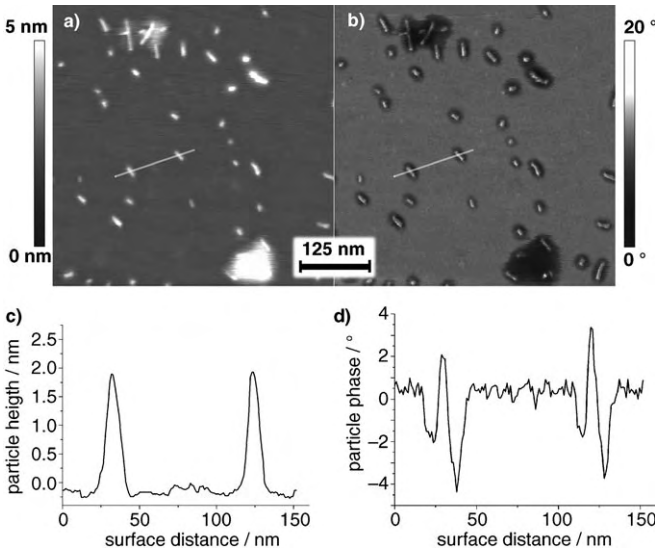

Figure 4. a) SFM tapping-mode image of **1** on mica. The sample was prepared by drop-casting of a solution of **1** in chloroform ($c = 5\ mg\,L^{-1}$) onto freshly cleaved mica and recorded with a plasma-cleaned and hydrophobized SFM tip; b) STM phase-contrast image; c) representative height profile through two of the micelles; d) corresponding phase profile (see bars across SFM images).

different lengths. The SFM image shows that the core is surrounded by a broad corona, presumably PEG. The hydrophobic tip leads to significantly fewer interactions with the PEG corona, resulting in a more distinct determination of the micelle core. The functionalized tip further offers the benefit of hydrophobic–hydrophobic interactions with the micelle core without being disturbed by nearby PEG. As a result, a more positive phase shift between the driving and oscillating frequency of the SFM cantilever at resonance frequency (Figure 4 d) can be achieved. To further minimize intermixing of hydrophobic/hydrophilic properties with the material's mechanic properties, the images were usually recorded in soft-tapping mode.[29,38] The size of the micelle core could be confirmed by applying hard tapping on the same sample. In the hard-tapping mode the phase-contrast image is dominated by the mechanical properties of the material. The heights of the micelles were constant within each sample. They varied, however, in the range of 2 to 4 nm depending on sample preparation and tapping parameters (Figure 4 a,c). Slight fluctuations of micelle height within one sample are most likely caused by differences of the PEG coils above and below the micelle core. To exclude artifacts in determining the width of the micelle core, a high-resolution SFM tip with a tip radius of curvature of < 1 nm was used. This measurement confirmed the previous width measurement of 10 nm.

Based on this data together with the data obtained from a single-crystal X-ray structure of tri(*p*-benzamide) **3**[25] (Figure 5) we propose a structural model for the hockey-puck micelles formed from OPBA-MPEG block copolymers. The dimensions of the micellar core (10 nm) determined by SFM cannot result from a monolayer of hepta(*p*-benzamide), the length of which is approximately 4.4 nm (extrapolated from the X-ray crystal structure of the trimer shown in Figure 5). It can, however, be explained by a bilayer model, in

 © 2006 Wiley-VCH Verlag GmbH & Co. KGaA, Weinheim

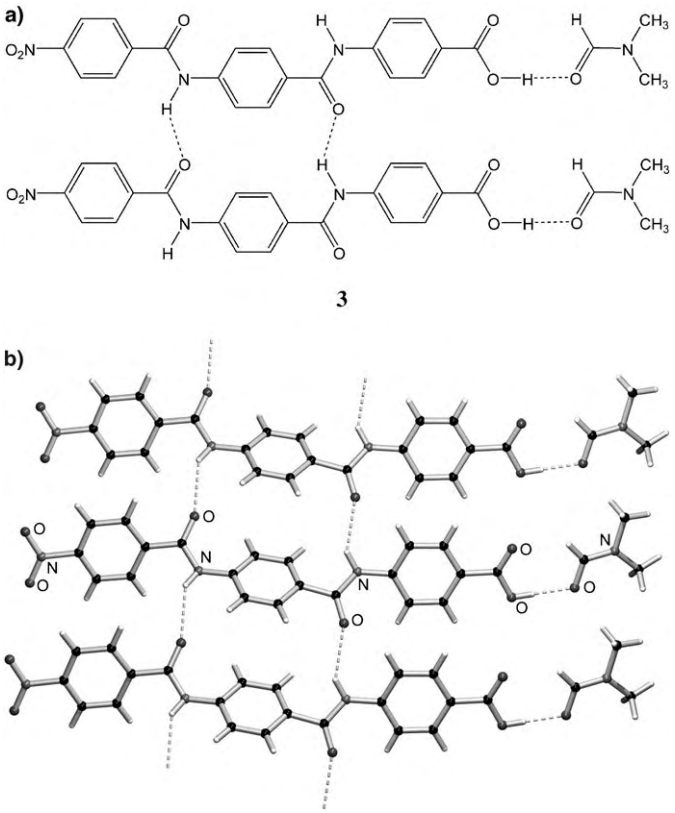

Figure 5. Intermolecular hydrogen bonding as the dominating force determining the aggregation of oligo(*p*-benzamide)s. a) Schematic representation of hydrogen bonds in trimer **3**.[25] b) Single-crystal X-ray structure of **3**.[39] Intermolecular hydrogen bonds are represented as dashed lines.

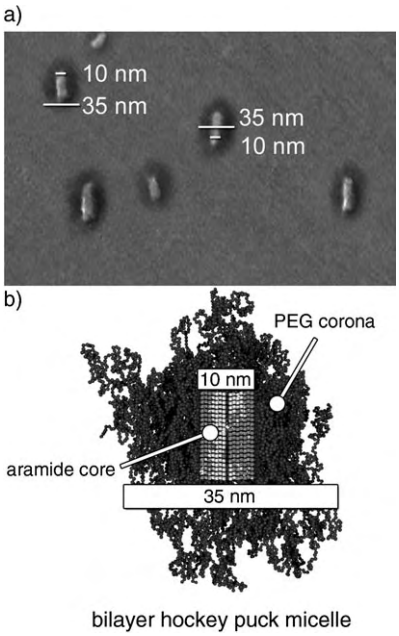

Figure 6. a) SFM tapping-mode images of **1**; b) a model of a bilayer hockey-puck micelle. The micellar core measures roughly 10 nm across, while the overall micelles have an average diameter of 35 nm. The height of the micelles is about 2 nm, corresponding to a stack of six bilayers formed by oligo(aramide)s.

which the C-termini of the oligoamide form the outside of the micellar core while the N-termini face each other. This type of aggregation is further supported by the X-ray crystal structure of the trimer **3** shown in Figure 5. A cross-section through the crystal structure shows that the C- and N-termini are on the side within an infinite hydrogen-bonded stack of rods. The uniform height of the micelles of roughly 2 nm suggests that about six hepta(*p*-benzamide) bilayers are stacked on top of each other by means of π–π interactions. The proposed model of the bilayer hockey-puck micelle is shown in Figure 6. In this model, two types of noncovalent interactions are present: one type (H bonds) is significantly stronger than the other (π–π interactions). Therefore, aggregation along the axis of stronger noncovalent interaction (length of the micelle) is more pronounced.

Analyzing the SFM image in Figure 4, we calculate an average number of ca. 90 hepta(*p*-benzamide)s in one π-stacked bilayer within the core of a micelle. Together with the data from the SFM height measurements, the overall aggregation number per micelle can be estimated to be $N_{agg,SFM} = 540$. This value is in very good agreement with that determined in static light-scattering experiments ($N_{agg,LS} = 514$).

As can be seen in Figures 4 and 6, the shape anisotropy of the micellar core is more pronounced than that of the overall micelle. This is most likely a result of the stretching of the PEG at the rod–coil boundary, resulting in stretched linear PEG in the vicinity of the core. The initial linear PEG becomes more coiled with increasing distance from the core, thereby canceling out the large axial ratio of the core itself to some degree.

We have shown that for large coil blocks, spherical micelles, and for smaller coil blocks, rodlike micelles, are predominantly formed. We are currently investigating the effect of further reducing the size and varying the chemical properties of the coil block on formation of supramolecular structures.

In conclusion, we have synthesized oligoaramide-PEG rod–coil block copolymers with different PEG lengths but identical rod lengths. These block copolymers aggregate strongly in nonpolar solvents. The aggregation was investigated by dynamic and static light scattering, and the aggregates were visualized by high-resolution SFM. Depending on the size of the PEG coil block, spherical or rodlike micelles were obtained and characterized. The core-shell structure of individual micelles was visualized by high-resolution SFM, and strong experimental evidence was found for the often proposed hockey-puck micelle. For the data obtained, a bilayer hockey-puck micelle model was proposed, in which the micellar core is stabilized by means of strong hydrogen bonds and π–π interactions. Such very stable noncovalent micelles with predictable geometry will play an important role in the preparation of well-defined functionalized nanoparticles. Owing to the high thermal and chemical stability of the deposited micelles, surface patterning, coating, and functionalization are also envisaged. Microphase-separated noncovalent block copolymers based on oligoaramides are currently being investigated.

 © 2006 Wiley-VCH Verlag GmbH & Co. KGaA, Weinheim

Experimental Section

All reactions were carried out in solvents of analytical quality (p.a.) purchased from Fischer Scientific. Poly(ethylene glycol) monomethyl ether ($M_w = 2000\ g\,mol^{-1}$, $5000\ g\,mol^{-1}$) was obtained from Fluka. All further chemicals were purchased from Acros Organics. All block copolymers were purified on a preparative GPC system eluting with DMF (Knauer HPLC Pump 64, MZ-GPC 250 × 30 mm GPC column, MZ-Gel SDplus, 10^3 Å 10μm (MZ-Analysentechnik); Knauer variable-wavelength monitor (UV detector at 254 nm); Shodex RI-71 refractive index detector) followed by freeze-drying from benzene solution.

SFM measurements were carried out on a Dimension 3100 instrument equipped with a Nanoscope IV Controller or a MultiMode connected to a NanoScope IIIa Controller using an E scanner. For SFM measurements, a standard solution ($1\ g\,L^{-1}$) was prepared and subsequently filtered through a 0.45-μm polytetrafluoroethylene (PTFE) syringe filter. This solution was diluted as required. Samples were prepared by drop-casting or spin-coating the dilute solution ($5\ mg\,L^{-1}$) onto freshly cleaved mica. Both film-casting techniques gave identical results. To achieve an equilibrium state, solutions were prepared at least 12 h before casting. Olympus tapping-mode silicon cantilevers (OMCL-AC160 TS-W2, $R_{Tip} < 10$ nm opening angle, spring constant $K_F = 42\ N\,m^{-1}$, $F_{res} = 300$ kHz) were used for measurements. For high-resolution imaging, Micro Mesh cantilevers with hydrophobic tip (DP15/HI′RES/AIBS/15, $R_{Tip} < 1$ nm opening angle, spring constant $K_F = 40\ N\,m^{-1}$, $F_{res} = 325$ kHz) were used.

All cantilevers were cleaned with Ar plasma immediately prior to use. Cantilever functionalization was carried out according to a general procedure: decalin, carbon tetrachloride, and chloroform were mixed in a 7:2:1 ratio and 1 vol% trimethylsilyl chloride was added. The solution was placed in a closed desiccator, and the plasma-cleaned SiO_2 cantilevers were placed in the gas phase above the solution for four days. Contact-angle measurements on the chip support were used to prove functionalization.

Dynamic and static light scattering experiments were performed with a Uniphase He/Ne laser ($\lambda = 632.8$ nm), an ALV-SP 86 goniometer, an ALV/High QE APD-Avalanche photodiode with fiber-optic detection, an ALV300 correlator, and a Lauda RC-6 thermostatization unit at angles between 30 and 150° in steps of 20° (DLS) or 5° (SLS). The temperature was kept constant at 293 K. The samples were filtered through Millex-LG filters (0.2 μm). The DLS data were analyzed by a cumulant fit and by a biexponential fit utilizing the simplex algorithmto yield the angular-dependent diffusion coefficient D_q. The extrapolation to zero-scattering angle gives the apparent diffusion coefficient D, which is translated into the sphere-equivalent apparent hydrodynamic radius (R_h) by application of the Stokes–Einstein relation.[42] The concentration and angular dependence of the Zimm plot of the static light-scattering data gives the weight average of the molecular mass M_w, the second virial coefficient of the osmotic pressure A_2, and the z-average of the squared radius of gyration $\langle R_g^2 \rangle_z$.

Received: October 4, 2005
Revised: January 7, 2006
Published online: March 28, 2006

Keywords: aggregation · block copolymers · micelles · nanostructures · scanning probe microscopy

[1] M. Lee, B.-K. Cho, W.-C. Zin, *Chem. Rev.* **2001**, *101*, 3869 – 3892.
[2] H.-A. Klok, S. Lecommandoux, *Adv. Mater.* **2001**, *13*, 1217 – 1229.
[3] M. Lee, Y.-S. Yoo, *J. Mater. Chem.* **2002**, *12*, 2161 – 2168.
[4] See, for example: D. Vernino, D. Tirrell, M. Tirrell, *Polym. Mater. Sci. Eng.* **1994**, *71*, 496 – 497.
[5] See for example: J. T. Chen, E. L. Thomas, C. K. Ober, G.-P. Mao, *Science* **1996**, *273*, 343 – 346.
[6] See, for example: J. J. L. M. Cornelissen, M. Fischer, R. J. M. Nolte, *Science* **1998**, *280*, 1427 – 1430.
[7] J. L. David, S. P. Gido, B. M. Novak, *Polym. Prepr. Am. Chem. Soc. Div. Polym. Chem.* **1998**, *39*, 433 – 434.
[8] X. F. Zhong, B. Francois, *Makromol. Chem.* **1991**, *192*, 2277 – 2291.
[9] B. Francois, X. F. Zhong, *Synth. Met.* **1991**, *41*, 955 – 958.
[10] T. Olinga, B. Francois, *Makromol. Chem. Rapid Commun.* **1991**, *12*, 575 – 582; T. Olinga, B. Francois, *J. Chim. Phys. Phys.-Chim. Biol.* **1992**, *89*, 1079 – 1084; B. Francois, T. Olinga, *Synth. Met.* **1993**, *57*, 3489 – 3494.
[11] S. A. Jenekhe, X. L. Chen, *Science* **1998**, *279*, 1903 – 1907.
[12] H.-A. Klok, J. F. Langenwalter, S. Lecommandoux, *Macromolecules* **2000**, *33*, 7819 – 7826.
[13] E. R. Zubarev, M. U. Pralle, E. D. Sone, S. I. Stupp, *J. Am. Chem. Soc.* **2001**, *123*, 4105 – 4106.
[14] S. I. Stupp, V. LeBonheur, K. Walker, L. S. Li, K. E. Huggins, M. Keser, A. Amstutz, *Science* **1997**, *276*, 384 – 389.
[15] Y. L. Jin, J.-H. Anh, M. Lee, *J. Am. Chem. Soc.* **2004**, *126*, 12208 – 12209.
[16] M. Lee, C.-J. Jang, J.-H. Ryu, *J. Am. Chem. Soc.* **2004**, *126*, 8082 – 8083.
[17] A. P. H. J. Schenning, A. F. M. Kilbinger, F. Biscarini, M. Cavallini, H. J. Cooper, P. J. Derrick, W. J. Feast, R. Lazzaroni, P. Leclere, L. A. McDonell, E. W. Meijer, S. C. J. Meskers, *J. Am. Chem. Soc.* **2002**, *124*, 1269 – 1275.
[18] J. T. Chen, E. L. Thomas, C. K. Ober, S. S. Hwang, *Macromolecules* **1995**, *28*, 1688; J. T. Chen, E. L. Thomas, C. K. Ober, G.-P. Mao, *Science* **1996**, *273*, 343 – 346.
[19] Y. Tu, X. Wan, D. Zhang, Q. Zhou, C. Wu, *J. Am. Chem. Soc.* **2000**, *122*, 10201 – 10205.
[20] D. M. Vriezema, J. Hoogboom, K. Velonia, K. Takazawa, P. C. M. Christianen, J. C. Maan, A. E. Rowan, R. J. M. Nolte, *Angew. Chem.* **2003**, *115*, 796 – 800; *Angew. Chem. Int. Ed.* **2003**, *42*, 772 – 776.
[21] F. Checot, A. Brulet, J. Oberdisse, Y. Gnanou, O. Mondain-Monval, S. Lecommandoux, *Langmuir* **2005**, *21*, 4308 – 4315.
[22] J. Rodriguez-Hernandez, S. Lecommandoux, *J. Am. Chem. Soc.* **2005**, *127*, 2026 – 2027.
[23] E. Bellomo, M. D. Wyrsta, L. Pakstis, D. J. Pochan, T. Deming, *J. Nat. Mater.* **2004**, *3*, 244 – 248.
[24] P. Leclere, A. Calderone, D. Marsitzky, V. Francke, Y. Geerts, K. Müllen, J. Bredas, R. Lazzaroni, *Adv. Mater.* **2000**, *12*, 1042 – 1046.
[25] R. Abbel, H. Frey, D. Schollmeyer, A. F. M. Kilbinger, *Chem. Eur. J.* **2005**, *11*, 2170 – 2176.
[26] R. Abbel, T. W. Schleuss, H. Frey, A. F. M. Kilbinger, *Macromol. Chem. Phys.* **2005**, *206*, 2067 – 2074.
[27] M. Pope, *Electronic Processes in Organic Chrystals and Polymers*, Oxford University Press, New York, **1999**.
[28] R. Pecora, *Dynamic Light Scattering*, Plenum, New York, **1985**.
[29] The refractive index increment was measured with a home-built Michelson interferometer as described in A. Becker, W. Köhler, B. Müller, *Ber. Bunsenges. Phys. Chem.* **1995**, *99*, 600.
[30] S. N. Magonov, *Encycl. Anal. Chem.* **2000**, 7432 – 7491.
[31] G. Reiter, J. U. Sommer, *Phys. Rev. Lett.* **1998**, *80*, 3771 – 3774; G. Reiter, J. U. Sommer, *J. Chem. Phys.* **2000**, *112*, 4376 – 4393; M. Wang, H.-G. Braun, E. Meyer, *Macromol. Rapid Commun.* **2002**, *23*, 853 – 858.
[32] D. R. M. Williams, G. H. Fredrickson, *Macromolecules* **1992**, *25*, 3561 – 3568.
[33] T. Mori, T. Watanabe, K. Minagawa, M. Tanaka, *J. Polym. Sci.* **2005**, *43*, 1569 – 1578.
[34] "Simultaneous Static and Dynamic Light Scattering: Application to Polymer Structure Analysis": M. Schmidt in *Dynamic*

 © 2006 Wiley-VCH Verlag GmbH & Co. KGaA, Weinheim

Light Scattering, The Method and Some Applications (Ed.: W. Brown), Clarendon Press, Oxford, **1993**, p. 372.
[35] A detailed analysis of the light-scattering data will be published elsewhere.
[36] H. Wang, W. You, P. Jiang, L. Yu, H. H. Wang, *Chem. Eur. J.* **2004**, *10*, 986 – 993.
[37] See, for example: R. Luginbühl, A. Szuchmacher, M. D. Garrison, J.-B. Lhoest, R. M. Overney, B. D. Ratner, *Ultramicroscopy* **2000**, *82*, 171 – 179.
[38] In particular, we have observed for lower setpoint ratios of around 0.6–0.7 that the micelles are deformed and that topography is altered. We observed that this deformation is reversible and that the micelle returned to its initial shape after the setpoint ratio was set again to 0.98.
[39] Crystal data for **3**: $C_{24}H_{22}N_4O_7$; $M_r = 478.45$; $0.02 \times 0.13 \times 0.19\ mm^3$; colorless; monoclinic; space group $P2_1/c$, $Z = 4$; $a = 24.540(5)$, $b = 5.363(2)$, $c = 17.078(3)$ Å, $\beta = 99.050(7)°$; $V = 2219.8(8)$ Å^3; $\rho_{calcd} = 1.432\ g\,cm^{-3}$; $Cu_{K\alpha}$ radiation ($\lambda = 1.54056$ Å); $2\theta_{max} = 148°$; $\omega/2\theta$-scans on a Turbo-CAD4; $T = 298$ K; 5140 reflections measured (all 4512 unique used); $-30 \le h \le 0$, $-6 \le k \le 0$, $-21 \le l \le 21$; Lorentz factor and absorption correction applied, no absorption correction ($\mu = 0.90\ mm^{-1}$) applied; structure solved with direct methods and refined with full-matrix least-squares on F^2 with SHELXL-97;[40] 4512 data and 316 parameters; R(1180 reflections $> 2\sigma(I)$, all data) = 0.1274, 0.3538; $wR2$(all data) = 0.4172; $S = 0.963$; hydrogen atoms riding; greatest final electron density difference excursions of +0.41, −0.46 e Å^{-3}.[41]
[40] G. M. Sheldrick, SHELXL-97, Program for Structure Refinement, University of Göttingen, Germany, **1997**.
[41] CCDC-283302 (**3**) contains the supplementary crystallographic data for this paper. These data can be obtained free of charge from The Cambridge Crystallographic Data Centre via www.ccdc.cam.ac.uk/data_request/cif.
[42] B. J. Berne, R. Pecora, *Dynamic Light Scattering*, J. Wiley, New York, **1976**.

 © 2006 Wiley-VCH Verlag GmbH & Co. KGaA, Weinheim

Intramolecular Sensitization

DOI: 10.1002/anie.200504091

Highly Efficient Photolabile Protecting Groups with Intramolecular Energy Transfer**

*Dominik Wöll, Julia Smirnova, Wolfgang Pfleiderer, and Ulrich E. Steiner**

DNA chips are widely used for genomic analysis.[1] Currently, high-density DNA chips can be synthesized with up to several hundred thousand different spots on an area of 1 cm^2.[2] In principle, the complete human genome can be probed with such a chip.[3] The required high spot densities can be achieved by photolithographic in situ DNA-chip synthesis. In this method, the oligonucleotides are synthesized step by step from protected nucleoside phosphitamides using photolithography with masks[4] or micromirror arrays[5] as suitable means for achieving parallel spatial addressability. This technique requires photolabile protecting groups[6] of high light sensitivity that release their substrate (in this case a nucleotide) in nearly quantitative yield. For the protecting groups currently in use for DNA-chip synthesis, the light sensitivity, suitably characterized by the product $\varepsilon\phi$ of the absorption coefficient and the photochemical quantum yield, reaches only moderate values. The widely used [(α-methyl-2-nitropiperonyl)oxy]carbonyl (MeNPOC) group[7] has a reasonable absorption coefficient at the wavelengths usually applied (in practice preferentially the mercury line at $\lambda = 366$ nm, $\varepsilon_{\mathrm{MeOH,366\,nm}} \approx 2500\ \mathrm{M^{-1}cm^{-1}}$), but the photochemical deprotection yield is quite small (3% in MeOH).[8] In contrast, the 2-(2-nitrophenyl)propoxycarbonyl (NPPOC) protecting group,[9] the reaction of which is represented in Scheme 1,[10] shows a much higher quantum yield (41% in MeOH), but has a significantly lower absorptivity ($\varepsilon_{\mathrm{MeOH,366\,nm}} \approx 230\ \mathrm{M^{-1}cm^{-1}}$). Thus, for both MeNPOC and NPPOC fairly long irradiation times are required during which undesired photoreactions may take place.

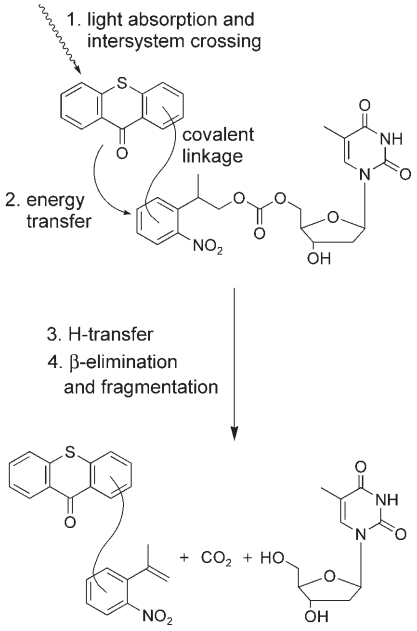

Scheme 1. Intramolecular sensitized photocleavage of a protecting group of the NPPOC type.

Sensitization is a suitable method to improve the light sensitivity of weakly absorbing photolabile protecting groups.[11,12] By using the triplet sensitizer thioxanthone to sensitize the photocleavage of NPPOC it has been possible to significantly improve the rate of photodeprotection in homogeneous solution as well as on a chip.[11] In this case, most of the light energy is absorbed by the sensitizer and can be

[*] D. Wöll, Dr. J. Smirnova, Prof. Dr. Dr. W. Pfleiderer, Prof. Dr. U. E. Steiner
Fachbereich Chemie, Universität Konstanz
Universitätstrasse 10, 78464 Konstanz (Germany)
Fax: (+49) 7531-88-3014
E-mail: ulrich.steiner@uni-konstanz.de

[**] We thank the Deutsche Forschungsgemeinschaft for financial support (project Ste 283/7-1) and NimbleGen GmbH, Waldkraiburg (Germany), for DNA chip experiments.

 © 2006 Wiley-VCH Verlag GmbH & Co. KGaA, Weinheim

transferred to the protecting group if an encounter with a triplet-excited sensitizer molecule takes place during the lifetime of the latter. Diffusion is the limiting factor for the effectiveness of energy transfer under such intermolecular sensitization conditions. Various examples of intramolecular triplet–triplet energy transfer have been described.[13]

In this communication, we report the development of novel photolabile protecting groups wherein a diffusion-independent enhancement of light sensitivity is achieved by covalently linking the protecting group to a sensitizer chromophore.[14] Recently the enhancement of photolysis of a photolabile protecting group by a covalently linked antenna molecule was also reported by the group of Corrie.[15]

The syntheses of the compounds shown in Scheme 2 have been described.[16] Except for compound **7**, the linkage of the

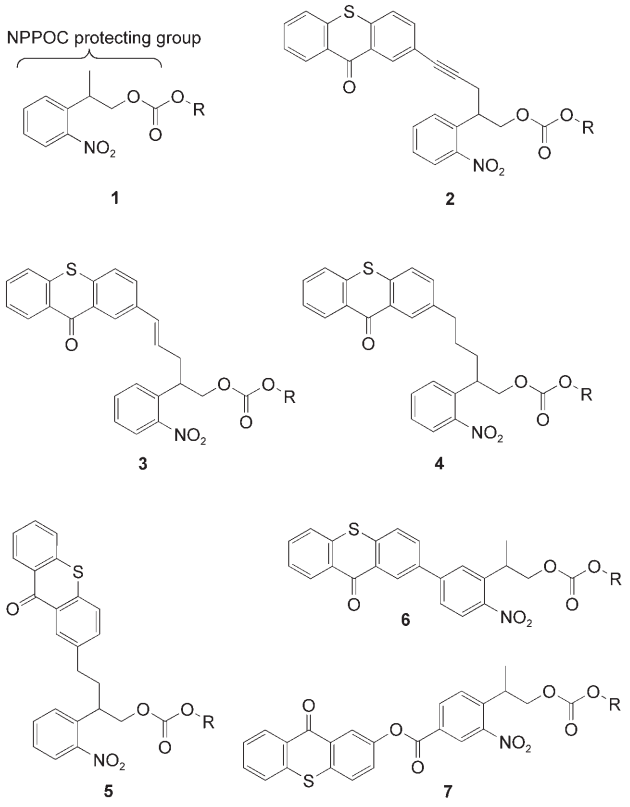

Scheme 2. Overview of the discussed compounds. R = 5′-*O*-thymidinyl.

o-nitrophenyl and thioxanthone chromophores at different positions and with different linkers was achieved by C–C coupling reactions (Sonogashira, Heck, Suzuki). For synthesizing the protected thymidines (R = 5′-*O*-thymidinyl) connected to the protecting group by means of a carbonate bridge, the free alcohols (R = H) were first treated with phosgene or phosgene substitutes and then with thymidine.

Figure 1 shows the absorption spectra of the protected thymidines. Except for compound **6**, the absorptions are essentially determined by the thioxanthone moiety. Significant spectral changes in the substituted thioxanthones appear in the second absorption band for the 2-vinyl- and the 2-ethynyl-substituted derivatives. The NPPOC chromophore

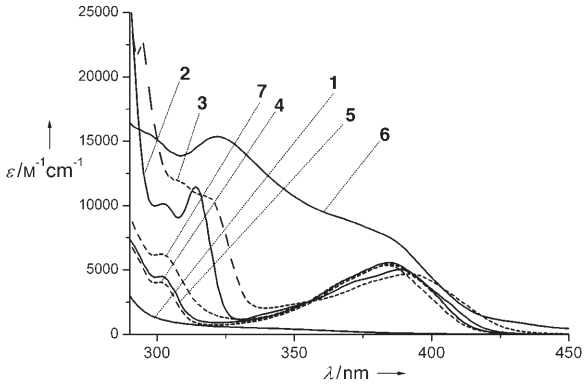

Figure 1. Absorption spectra of compounds **1**–**7** in methanol.

contributes only a fairly weak absorption; the thymidine moiety does not absorb at all in the spectral range shown. Compound **6** is the only one exhibiting a direct electronic coupling between the two chromophores through the π-electron system. As a result of the thioxanthone moiety the bichromophoric protecting groups **2**–**5** and **7** exhibit absorption coefficients at 366 nm 15 times higher, and compound **6** even about 35 times higher, than that of the NPPOC protecting group **1**. Thus, for unchanged photochemical quantum yield, an approximately 15 or 35 times higher light sensitivity would result. To test this expectation, the thymidines capped with the new protecting groups were subject to continuous irradiation for defined periods of time (conditions: 0.05 and 0.15 mM in methanol, photon irradiance about 2×10^{-8} Einstein $cm^{-2} s^{-1}$ as determined by azobenzene actinometry[17]). The products were separated by HPLC and analyzed by UV/Vis spectrometry. The decay kinetics of the starting compound is described by the rate law given in Equation (1). Here I_0 represents the photon irradiance, F the

$$\frac{dc}{dt} = -I_0 \frac{F\,d}{V} \frac{(1-10^{-A(t)})}{A(t)} \varepsilon\, c(t)\, \phi \qquad (1)$$

illuminated cross section, d the optical path length, V the volume of the solution, $A(t)$ the absorbance of the solution after irradiation time t, ε the molar absorption coefficient of the protected compound, c its concentration, and ϕ the quantum yield of the photodeprotection reaction. The quantum yield ϕ is determined by fitting the result $c(t)$ of the numerical integration of Equation (1) to the observed time dependence (Figure 2a).

The data in Table 1 indicate that the quantum yields of the bichromophoric protecting groups are somewhat lower than that of the NPPOC protecting group. However, this reduction of the quantum yield is overcompensated by the increased absorption coefficient such that the resulting overall enhancement of light sensitivity reaches a factor of up to 21 at 366 nm and 25 at 405 nm. For compounds **4**–**7** the yields of deprotected substrate range from 66 to 92% (Table 1). A further improvement of these values by systematic optimization of the reaction conditions should be possible. The poor thymidine yield of compounds **2** and **3** is a result of specific photochemical side reactions. Whereas the major reaction of

 © 2006 Wiley-VCH Verlag GmbH & Co. KGaA, Weinheim

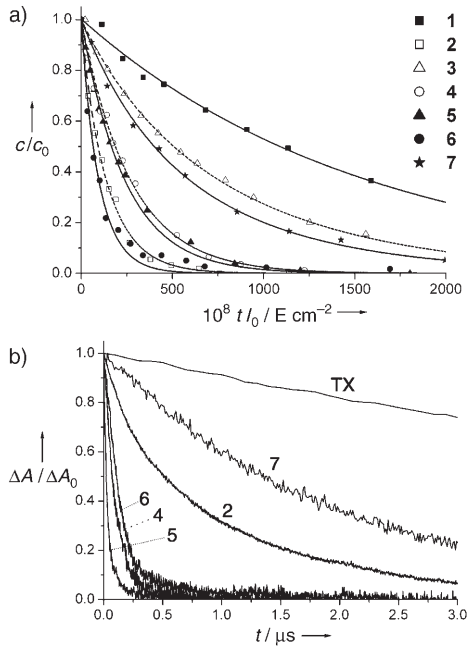

Figure 2. a) Decomposition kinetics of the protected thymidines **1**–**7** when continuously irradiated at $\lambda = 366$ nm. The photon irradiance I_0 was on the order of 2×10^{-8} Einstein cm^{-2} s^{-1}. Data points were calculated by integration of the HPLC peaks observed after the corresponding irradiation times. Curves were fitted to the data points according to Equation (1). b) Decay kinetics of the thioxanthone triplet observed by transient absorption at 600 nm after ns laser flash photolysis (excitation at 355 nm). No triplet signal could be observed for compound **3**.

compound **3** is a *trans–cis* isomerization, the main product from compound **2** is a rearrangement product of identical molar mass but with an as-yet unidentified structure.

Compounds **4** and **6** have already been tested for DNA-chip synthesis. Under optimized conditions, the cycle times could be reduced by a factor of 10 compared to the reaction time with NPPOC-T (compound **1**, R = 5′-*O*-thymidinyl). The yield per synthesis cycle was about 90%.

To prove that the increased light sensitivity is a result of an intramolecular triplet energy transfer, nanosecond laser flash spectroscopic experiments were performed. Transient absorption spectra as well as decay curves of the thioxanthone triplet were recorded. Following the change of the transient absorption spectra in time, the triplet–triplet absorption decay as well as the formation of the *aci*-nitro form of the NPPOC group, a known intermediate of the deprotection step of NPPOC,[10] could be detected.

In N_2-saturated solution, the thioxanthone triplet lifetimes for all bichromophoric compounds are much shorter than for unmodified thioxanthone (see Figure 2 and Table 1). The combination of this finding and the similarity of the quantum yields of sensitized and directly excited photoreaction of NPPOC proves that triplet quenching arises mainly from energy transfer. Not only the ground-state absorption spectrum of compound **6** (see Figure 1) but also its excited-state absorption spectrum differs significantly from the corresponding ones obtained for the other linked thioxanthones. In **6**, the two chromophores are strongly coupled and therefore cannot be regarded as independent. In this system, the lifetime of the observed transient is presumably determined by the intramolecular H-transfer step initiating the photoreaction. The photochemical quantum yield of **6** is comparable to that of the other linked thioxanthone–NPPOC conjugates connected by longer links with less direct coupling.

In aerated solution, molecular oxygen acts as triplet quencher in a close-to-diffusion-controlled reaction and reduces the triplet lifetime of all thioxanthone compounds to a value in the 100-ns range. Since this process competes with energy transfer it reduces the quantum yield of the photocleavage. If intramolecular energy transfer is fast or, as in compound **6**, if the lifetime of the triplet is short because of its fast reaction, the light sensitivity of the photoreaction depends much less on the oxygen content in solution than with a free triplet sensitizer. Therefore, the photokinetics of compounds **4**–**6** are not very sensitive to the presence of oxygen. This trend could also be demonstrated for the new protecting groups under conditions of continuous illumination in aerated solution. The reduced sensitivity towards oxygen is an important advantage for their application in the industrial production of DNA chips because an oxygen-free process would be technically more demanding.

Although the involvement of triplet–triplet energy transfer has been clearly demonstrated for the new compounds, it must be noted that sensitization of the photocleavage reaction cannot be explained exclusively on the basis of this mechanism. Such a conclusion follows from the observation of considerable fluorescence quenching, particularly in the cases with the shortest linkers, which is paralleled by a correspondingly reduced amount of triplet formation, but which does not

Table 1: Spectroscopic and photochemical data for compounds **1**–**7**.[a]

	ε [M^{-1} cm^{-1}]		ϕ		$\varepsilon\phi$ [M^{-1} cm^{-1}]		Thymidine yield		τ [µs]	
Cmpd.	366 nm	405 nm	366 nm	405 nm	366 nm	405 nm	366 nm	405 nm	N_2-sat.	Air-sat.
1	250	< 40	0.41	–	100	< 40	0.90	–	[b]	[b]
2	3500	2700	0.42	0.38	1500	1000	0.21	0.33	1.05	0.18
3	3100	3400	0.08	0.05	250	170	0.27	0.38	[c]	[c]
4	3800	2300	0.21	0.14	800	320	0.86	0.75	0.11	0.08
5	3900	2300	0.21	0.14	820	320	0.75	0.79	0.04	0.03
6	8200	2400	0.26	0.27	2100	650	0.66	0.89	0.13	0.12
7	4000	1800	0.09	0.09	360	160	0.92	0.82	3.6	0.22

[a] Molar decadic absorption coefficient ε, photochemical quantum yield ϕ, light sensitivity $\varepsilon\phi$, deprotected thymidine yield, and triplet lifetime τ. [b] For unsubstituted thioxanthone the triplet lifetime is 22.2 µs in N_2-saturated MeOH and 0.18 µs in air-saturated MeOH. [c] No transient with a lifetime in the nanosecond time range could be detected.

 © 2006 Wiley-VCH Verlag GmbH & Co. KGaA, Weinheim

go along with a decrease of the overall photochemical quantum yield. Detailed investigations to clarify the underlying mechanism are in progress.

In summary, a series of novel, highly light-sensitive photolabile protecting groups for light-controlled DNA synthesis has been developed. In these compounds the NPPOC protecting group is covalently linked to thioxanthone as an intramolecular antenna. The photochemical kinetics of these compounds under stationary irradiation conditions has been quantitatively investigated, and photochemical quantum yields as well as chemical yields of the photodeprotected substrate were determined for thymidine as a model substrate. The kinetics of triplet–triplet energy transfer between the antenna molecule and the photolabile protecting group has been investigated by laser flash spectroscopy. Besides triplet–triplet energy transfer, a sensitization mechanism involving the excited sensitizer singlet must be also involved, particularly in the systems with short linkers. As a result of the high light sensitivity of these new protecting groups, it should be possible to reduce the production time for the photolithographic synthesis of high-density DNA chips.

Received: November 17, 2005
Published online: March 23, 2006

Keywords: DNA chips · intramolecular energy transfer · photochemistry · protecting groups · sensitization

[1] An excellent overview is given in the special issue *Nat Genet.* **1999**, *21* (1), 1 – 60..
[2] K.-P. Stengele, U. E. Steiner, D. Wöll, W. Pfleiderer, S. Bühler, J. Bühler, R. Green, *Abstr. Pap. Solid Phase Synthesis & Combinatorial Libraries*, London, United Kingdom, **2003**; http://www.biocom.uk/sps2003.htm.
[3] NimbleGen Systems Inc., *NimbleGen Releases First Human Whole-Genome Array*, Pressemitteilung, Madison, WI, 28. Juli **2003**; http://www.nimblegen.com/news/press_rel/news_2003_07_28.html.
[4] S. P. A. Fodor, J. L. Read, M. C. Pirrung, L. Stryer, A. T. Lu, D. Solas, *Science* **1991**, *251*, 767 – 773.
[5] S. Singh-Gasson, R. D. Green, Y. Yue, C. Nelson, F. Blattner, M. R. Sussman, F. Cerrina, *Nat. Biotechnol.* **1999**, *17*, 974 – 978.
[6] "Photoremovable Protecting Groups in DNA Synthesis and Microarray Fabrication": M. C. Pirrung, V. S. Rana in *Dynamic Studies in Biology: Phototriggers, Photoswitches, and Caged Compounds* (Eds.: M. Goeldner, R. S. Givens), Wiley, New York, **2005**, p. 341.
[7] a) G. H. McGall, A. D. Barone, M. Diggelmann, S. P. A. Fodor, E. Gentalen, N. Ngo, *J. Am. Chem. Soc.* **1997**, *119*, 5081 – 5090; b) A. C. Pease, D. Solas, E. J. Sullivan, M. T. Cronin, C. P. Holmes, S. P. A. Fodor, *Proc. Natl. Acad. Sci. USA* **1994**, *91*, 5022 – 5026.
[8] The quantum yield for MeNPOC was determined under identical condition as for NPPOC (MeOH, irradiation at 366 nm).
[9] a) A. Hasan, K.-P. Stengele, H. Giegrich, P. Cornwell, K. R. Isham, R. A. Sachleben, W. Pfleiderer, R. S. Foote, *Tetrahedron* **1997**, *53*, 4247 – 4264; b) H. Giegrich, S. Eisele-Bühler, C. Hermann, E. Kvasyuk, R. Charubala, W. Pfleiderer, *Nucleosides Nucleotides* **1998**, *17*, 1987 – 1996; c) S. Bühler, I. Lagoya, H. Giegrich, K.-P. Stengele, W. Pfleiderer, *Helv. Chim. Acta* **2004**, *87*, 620 – 659.
[10] S. Walbert, W. Pfleiderer, U. E. Steiner, *Helv. Chim. Acta* **2001**, *84*, 1601 – 1611.
[11] D. Wöll, S. Walbert, K.-P. Stengele, T. J. Albert, T. Richmond, J. Norton, M. Singer, R. D. Green, W. Pfleiderer, U. E. Steiner, *Helv. Chim. Acta* **2004**, *87*, 28 – 45.
[12] a) C. Sundararajan, D. E. Falvey, *J. Am. Chem. Soc.* **2005**, *127*, 8000 – 8001; b) C. Sundararajan, D. E. Falvey, *Org. Lett.* **2005**, *7*, 2631 – 2634; c) A. Banerjee, K. Lee, D. E. Falvey, *Tetrahedron* **1999**, *55*, 12699 – 12710.
[13] S. Speiser, *Chem. Rev.* **1996**, *96*, 1953 – 1976 and references therein.
[14] U. E. Steiner, Universität Konstanz, D. Wöll, DE 10315772 (A1), WO 2004089529, **2004** [*Chem. Abstr.* **2004**, *141*, 366034].
[15] G. Papageorgiou, M. Lukeman, P. Wan, J. E. T. Corrie, *Photochem. Photobiol. Sci.* **2004**, *3*, 366 – 373; G. Papageorgiou, D. Ogden, J. E. T. Corrie, *J. Org. Chem.* **2004**, *69*, 7228 – 7233.
[16] J. Smirnova, D. Wöll, W. Pfleiderer, U. E. Steiner, *Helv. Chim. Acta* **2005**, *88*, 891 – 904.
[17] G. Gauglitz, *J. Photochem.* **1976**, *5*, 41 – 47; G. Gauglitz, S. Hubig, *J. Photochem.* **1981**, *15*, 255 – 257.

 © 2006 Wiley-VCH Verlag GmbH & Co. KGaA, Weinheim